Astrophysics and Space Science Library 458

Markus J. Aschwanden

New Millennium Solar Physics

ASSL

Springer

New Millennium Solar Physics

Astrophysics and Space Science Library

The Astrophysics and Space Science Library is a series of high-level monographs and edited volumes covering a broad range of subjects in Astrophysics, Astronomy, Cosmology, and Space Science. The authors are distinguished specialists with international reputations in their fields of expertise. Each title is carefully supervised and aims to provide an in-depth understanding by offering detailed background and the results of state-of-the-art research. The subjects are placed in the broader context of related disciplines such as Engineering, Computer Science, Environmental Science, and Nuclear and Particle Physics.

The ASSL series offers a reliable resource for scientific professional researchers and advanced graduate students.

More information about this series at http://www.springer.com/series/5664

Markus J. Aschwanden

New Millennium Solar Physics

Springer

Markus J. Aschwanden
Solar & Astrophysics Laboratory
Palo Alto, CA, USA

ISSN 0067-0057 ISSN 2214-7985 (electronic)
Astrophysics and Space Science Library
ISBN 978-3-030-13954-4 ISBN 978-3-030-13956-8 (eBook)
https://doi.org/10.1007/978-3-030-13956-8

Cover illustration: A prominence eruption on 2012 April 16 was captured by NASA's Solar Dynamics Observatory (SDO) mission with the Atmospheric Imager Assembly (AIA) instrument in the extreme ultraviolet wavelength of 304 Ångstrom, which radiates at chromospheric temperatures of about 50,000 K. Credit: NASA, SDO, AIA Team

This Springer imprint is published by the registered company Springer Nature Switzerland AG
The registered company address is: Gewerbestrasse 11, 6330 Cham, Switzerland

Dedicated to

Arnold O. Benz

who introduced me into the fantastic realms of solar physics

Preface

An introduction into the subject of solar physics has been previously presented in the textbook *Physics of the Solar Corona* by the same author, which covered most of the science of solar physics (except for the solar interior and surface), published in 2004, subject to a literature cutoff around 2000–2003. In order to provide an update of new results published during the new millennium (covering the years of 2000–2018), we present here a systematic overview of scientific progress and new results from the current space missions RHESSI, Hinode, STEREO, SDO, IRIS, and others, which all are still in operation during the time of writing.

This book is structured in order from inside to outside of the Sun, starting from the interior and proceeding through the convection zone, the photosphere, the chromosphere, the transition region, and the corona, to the interplanetary heliosphere, with an emphasis on solar flare and coronal mass ejection processes. The era of 2000–2018 has seen an exponential increase in scientific publications, which amounts to over 20,000 peer-reviewed articles in solar and heliophysics, currently growing with an average rate of $\approx$1000 solar publications per year. We divided the entire discipline of solar physics into 16 thematic chapters, and subdivided each chapter into 10 topics of current interest, each one containing separate literature references. We selected about 3600 publications that we describe and cite in this book, carefully weighted by the number of citations, citation rates, and representativeness in each of the 160 topics. In order to give the reader a measure of the impact of an individual publication cited here, we add to each reference the current number of citations $[c]$, as well as the citation rate per year $[c/y]$, which is the ratio of the number of article citations $[c]$ divided by the number of years $[y]$, calculated from information provided by NASA's *Astrophysics Data System (ADS)*. The annual citation rate should be a fair criterion to evaluate and compare the impact of old and new papers. We provide also the titles in the cited references, which often contain important information on the used solar data sources, instruments, and interpreted physical processes. For most part of the book, we entertain a high-level discussion of the cited work only, while technical details can be found in the cited original papers. A separate list of standard reviews on solar topics is given

at the end of the book (Appendix A), organized by the themes of the chapters. A comprehensive list of acronyms is given in Appendix C.

This book can be considered as a condensed update of the solar literature, while the previous literature before the new millennium (< 2000) is mostly provided in the textbook *Physics of the Solar Corona*. Consequently, original references to earlier publications (< 2000) are largely ignored here for space constraints. However, our selection of references should reflect a balanced subset of high-impact publications, typically with $c/y \gtrsim 5$ citations per year, or less if they contain unique information of recent interest. Therefore, the new millennium time interval that is covered here samples publications homogeneously during the time interval of 2000–2018, and each of the 160 topics represents an up-to-date "miniature review."

This book is intended to provide an overview of new trends and results published in high-impact papers, primarily designed for graduate students, PhD students, and professional researchers. Theoretical aspects and concepts are mostly treated in the textbook *Physics of the Solar Corona* and in other reviews listed at the end of this book. The contents of this book cover an overview on new solar instrumentation (Chap. 1), basic spectrosocpy (Chap. 2), the solar interior (Chap. 3), the photosphere (Chap. 4), the chromosphere (Chap. 5), the corona (Chaps. 6–11), solar flares (Chap. 12, 13), coronal mass ejections (Chap. 14, 15), and Sun–Earth connections (Chap. 16).

We acknowledge the NASA/ADS for most useful access to the solar and astrophysics literature, which we consulted in over 20,000 cases, as well as the support of this project from Lockheed Martin's *Solar and Astrophysics Laboratory (LMSAL)*, as well as partial support of this work from NASA's missions RHESSI, Hinode, STEREO, SDO, and IRIS. Permission to use material from the original publications has been obtained from the original authors and it is reproduced by permission of the copyright-holding publishers of the journals *ApJ*, *A&A*, *Solar Physics*, *Science*, *SSRv*, *Nature*, *LRSP*, *ApJSS*, *Nature Physics*, *EP&S*, and *PDU*. Images reproduced from NASA websites are made available by the *open data policy* of NASA.

This book is dedicated to my friend and teacher Prof. Arnold O. Benz, who introduced me into the fantastic realms of solar physics. Special thanks go also to Prof. Virginia Trimble, who encouraged me to write critical solar reviews over many years. The author is most indebted to a number of experts in solar physics who read and commented on individual chapters, which are listed in alphabetical order here: Tom Berger, Bart De Pontieu, Yuhong Fan, Lyndsay Fletcher, Nat Gopalswamy, Shadia Habbal, Gordon Holman, Judith Karpen, Bernhard Kliem, Sam Krucker, Alexander Kosovichev, Ryan Milligan, Valery Nakariakov, Hardi Peter, Ken Phillips, Don Reames, Pete Riley, Manuela Temmer, Jack Thomas, Alexander Warmuth, Sven Wedemeyer, Yi Ming Wang, Tongjiang Wang, Harry Warren, Thomas Wiegelmann, Amy Winebarger, Jean-Piere Wülser, and Peter Young.

Finally, I heartfully wish to thank my wife Carol J. Kersten, and my family, for enthusiastic support during the three-year writing period.

Palo Alto, CA, USA Markus J. Aschwanden
November 2018

Contents

Chapter 1
New Solar Instrumentation

1.1 Solar Missions Overview and Moore's Law

The exploration of our Sun has been pursued with ground-based instruments in optical and radio wavelengths before the start of the space age, which was initiated by the launch of *Sputnik* in October 1957. Besides some short-duration exploratory rocket flights, the first solar-dedicated space missions during the last century (see time line in Fig. 1.1a and Table 1.1) started with the satellite series of *Orbiting Solar Observatory OSO-1* to *OSO-8* (1962–1975), the *Apollo Telescope Mount (ATM)* onboard *Skylab* (1973–1974), the *Geostationary Operational Environmental Satellites (GOES)* series (1974–present), the *Solar Maximum Mission (SMM)* (1980–1989), the *Yohkoh* mission (1992–2000), the Russian *Complex ORbital Observatory Near-earth of Activity of the Sun (CORONAS)* series, starting with the *CORONAS-I* mission (1994–2001), the *Solar and Heliospheric Observatory (SOHO)* (1996–present), and the *Transition Region And Coronal Explorer (TRACE)* mission (1998–2010). The primary purpose of the *Compton Gamma-Ray Observatory (CGRO)* (1991–2000) was focused on astrophysical high-energy sources, but it was equally successful in detecting myriads of solar flares. These missions expanded our view of the Sun into extreme-ultraviolet, soft X-ray, hard X-ray, and gamma-ray wavelengths and were all very successfull in producing large solar datasets and new insights into the physics of the solar corona. The theory and observational results of the physics of the solar corona obtained during the last millennium has been described in detail in the textbook *"Physics of the Solar Corona. An Introduction"* (Aschwanden 2004). For recent reviews and textbooks (after 2000) see Appendix A.

In this book we are going to describe selected highlights of new theoretical and observational results that were obtained during the first two decades of this millennium (2000–2017), covering the era of the *Ramaty High Energy Solar Spectroscopic Imager (RHESSI)* mission (2002–2018), the *CORONAS-F* mission (2001–2005),

M. J. Aschwanden, *New Millennium Solar Physics*, Astrophysics and Space Science Library 458, https://doi.org/10.1007/978-3-030-13956-8_1

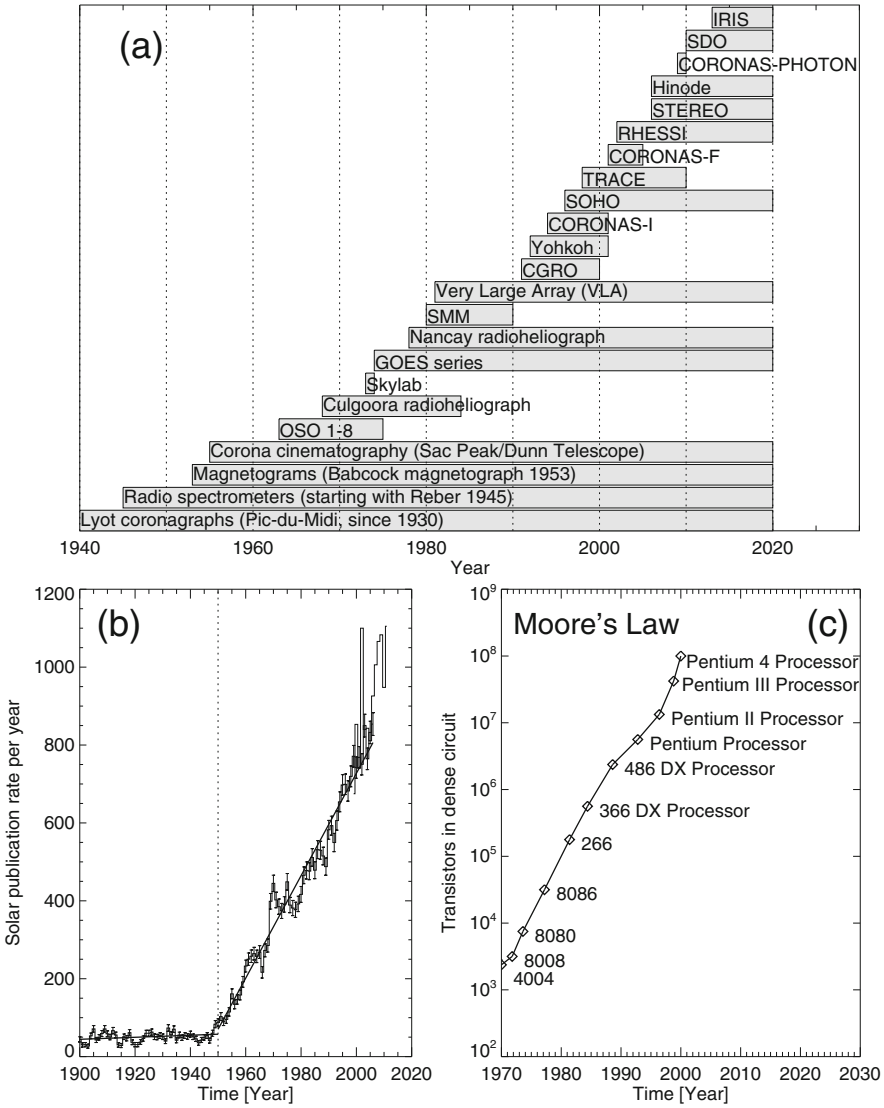

Fig. 1.1 (**a**) The operation periods of major ground-based instruments and solar-dedicated space missions during the era of 1940–2020. (**b**) The rate of publications in solar physics over the last century, based on NASA's Astronomical Database System (ADS). (**c**) Moore's law that states that the number of transistors (y-axis) in a dense integrated circuit doubles every 2 years (x-axis) (Credit: Wikipedia)

the *Solar Terrestrial Relations Observatory (STEREO)* mission (2006–present), the *Hinode* mission (2006–present), the *CORONAS-Photon* mission (2009), the *Solar Dynamics Observatory (SDO)* mission (2010–present), and the *Interface Region Imaging Spectrograph (IRIS)* mission (2013–present), see time line in Fig. 1.1a.

Table 1.1 Major solar space missions, acronyms, and period of performance

Formal instrument designation	Acronym, name	Performance
Orbiting Solar Observatory	OSO 1–8	1962–1975
Skylab	Skylab	1973–1974
Geostationary Operational Environmental Satellites	GOES	1974–present
Solar Maximum Mission	SMM	1980–1989
Compton Gamma Ray Observatory	CGRO	1991–2000
Solar-A	Yohkoh	1992–2000
CORONAS-I[a]	CORONAS-I	1994–2001
CORONAS-F[a]	CORONAS-F	2001–2005
CORONAS-Photon[a]	CORONAS-Photon	2009
Solar and Heliospheric Observatory	SOHO	1996–present
Transition Region and Coronal Explorer	TRACE	1998–2010
Ramaty High Energy Solar Spectroscopic Imager	RHESSI	2002–2018
Solar Terrestrial Relations Observatory	STEREO	2006–present
Solar-B	Hinode	2006–present
Solar Dynamics Observatory	SDO	2010–present
Interface Region Imaging Spectrograph	IRIS	2013–present

[a]CORONAS = Complex ORbital Observatory Near-earth of Activity of the Sun

The material described in this book is mostly based on the literature in solar physics that has been published during the new millennium, which comprises over $\approx 20,000$ refereed publications between 2000 and 2017. The annual growth of publications in solar physics is histogrammed in Fig. 1.1b. A solar *literature reference matrix* classified by solar phenomena versus physical processes is provided on one of the author's webpages.[1]

Progress in solar physics during the last decades is clearly driven by new space-based and ground-based instruments that produce massive floods of imaging data, with increasingly higher spatial resolution, time cadence, and spectral resolution. *Moore's law*, which states that the number of transistors on integrated circuits doubles approximately every 2 years (Fig. 1.1c), as it has been observed over the history of computing hardware ($\approx$ 1970–2010), obviously dominates also electronic computers and instrumental hardware in solar physics. The exponential increase in computer power enhances not only the cadence, resolution, and volume of solar imaging data, but allows us also to conduct more powerful data analysis of massive solar data sets using automated image processing and feature recognition techniques (Aschwanden 2010), as well as to perform high-powered computer simulations of solar and astrophysical plasma physics. For instance, the SDO feeds our solar data archives with a downlink data rate of 1.5 Terabytes a day, producing a staggering data flow of about one (4K $\times$ 4K) full-Sun image per second, taken in

[1] http://www.lmsal.com/~aschwand/publications/index.html.

10 different wavelength bands, compared with one image (2K × 2K) every 3 min from STEREO, or one (1K × 1K) image every 12 min from SOHO.

The space era enabled us to explore the Sun in all wavelengths that are absorbed by the Earth's atmosphere, especially in EUV, soft X-rays, hard X-rays, and gamma-rays. Access to these wavelengths is extremely important for solar and astrophysical observations, because they allow us to detect thermal or non-thermal bremsstrahlung emission, as well as nuclear gamma-ray line emission, which all are manifestations of high-temperature plasmas and high-energy particles. Without space-borne detectors in those wavelength regimes, we would have no way to explore magnetic reconnection or particle acceleration in astrophysical plasmas, two key processes that control the plasma dynamics in our universe.

A key factor that distinguishes solar from stellar physics is the adequacy of spatial resolution of imaging instruments. One of the highest spatial resolutions is achieved with the *Solar Optical Telescope (SOT)* onboard Hinode, which has an angular resolution of $\approx 0.2''$, corresponding to $\approx$ 150 km on the surface of the Sun. The *Atmospheric Imaging Assembly (AIA)* onboard SDO images the full Sun with a pixel size of $0.6''$ (with an angular resolution of $\approx 1.5''$ or $\approx$ 1000 km on the solar surface), which corresponds to about the distance that a coronal Alfvén wave travels in 1 s. This allows us to track and reconstruct coronal MHD waves with unprecedented clarity. Solar flares are produced by magnetic reconnection regions covering spatial scales of typically 1000–100,000 km, which can be probed with AIA in great detail.

The success of solar physics, of course, should not be measured by the new technical capabilities only, but more importantly, ought to be reflected in the quality and quantity of new published results. In order to give a glance on this aspect we plot the rate of peer-reviewed publications in solar physics over the last century in Fig. 1.1b. This histogram was obtained from annual searches of solar papers in NASA's *Astrophysical Database System (ADS)*.[2] The histogram shown in Fig. 1.1b contains an estimated $\approx 32,000$ (refereed) solar publications during the time interval of 1900–2012. Interestingly, the publication rate was extremely constant before 1950, with a leasurely average of $\approx$ 50 papers per year, while it suddenly started to grow afterward with an average increase of $\approx$ 13 papers per year, a trend that lasts already for six decades. Note also a remarkable spike after 1967, when the journal *Solar Physics* was founded. Technological and economical conditions after 1950 improved to such a degree that productivity in science rapidly accelerated. If we compare the progress in computer technology according to Moore's Law (2015) shown in Fig. 1.1c, we note that data storage and processing capacity grew exponentially after 1960, while science results measured in terms of publications grew linearly after 1950 (Fig. 1.1b), so we may conclude that science return scales approximately with the logarithm of the amount of available data, which clearly underscores the need for automated data processing methods.

[2] http://adsabs.harvard.edu/.

Table 1.2 Discoveries and key observations of RHESSI instrument

1.	Discovery of gamma-ray footpoint structures
2.	Energy content and spectrum of flare energetic electrons
3.	Ubiquitous nonthermal emission from the corona and bulk energization
4.	Double coronal X-ray sources
5.	Microflares
6.	Initial downward motion of X-ray sources
7.	Hard X-ray flare ribbons
8.	Location of superhot X-ray source
9.	Photospheric X-ray albedo
10.	511-keV positron annihilation line
11.	Measurement of the oblateness of the Sun
12.	Discovery of a huge flare from the soft-gamma-ray repeater SGR 1806-20
13.	Terrestrial gamma-ray flashes associated with lightenings or sprites

1.2 The RHESSI Mission

The *Reuven Ramaty High Energy Solar Spectroscopic Imager (RHESSI)*,[3] a rotation-modulated hard X-ray Fourier-type imager (Hurford et al. 2002), is a NASA Small Explorer Mission, operated and controlled from the ground systems at the University of Berkeley, a solar-dedicated space mission that was launched on 2002 February 5 and has been decommissioned on 2018 August 9.

RHESSI's primary mission is to explore the basic physics of particle acceleration and explosive energy release in solar flares. This is achieved through imaging spectroscopy in X-rays and gamma-rays with fine angular and energy resolution to reveal the locations and spectra of the accelerated electrons and ions and of the hottest flare plasma. RHESSI has greatly advanced our knowledge of solar flares, as the key discoveries from the first 10 years of the mission listed in Table 1.2 and the summaries of scientific results presented in Emslie et al. (2011) demonstrate.

Technical descriptions of the RHESSI instrument and first results are provided in Lin et al. (2002). A list of instrument characteristics is given in Table 1.3. The hardware of the RHESSI spacecraft includes the 9 bi-grid collimators and the spectrometer with 9 cryogenically cooled Ge detectors (Smith et al. 2002), a beryllium (Be) scattering element that enables hard X-ray polarimetry (McConnell et al. 2002), the *Solar Aspect System (SAS)*, and a *Roll Angle System (RAS)* to control the pointing and the roll angle of the rotating spacecraft (Fivian et al. 2002; Hurford and Curtis 2002).

The working principle of the RHESSI instrument is illustrated in Fig. 1.2: The spin-stabilized spacecraft carries an instrument that consists of nine subcollimators with grids of variable widths, which transmit soft and hard X-ray photons that are

[3] http://hesperia.gsfc.nasa.gov/rhessi2/.

Table 1.3 RHESSI instrument characteristics (adapted from Lin et al. 2002)

Parameter	Characteristics
Technique	Fourier-transform imaging with rotating modulation collimators
Angular resolution	2.3″ at 100 keV, increasing to 36″ at 15 MeV
Angular coverage	2″–180″
Field of view	Full Sun ($\approx 1°$)
Temporal resolution	$\approx$ 10 ms for coarse image, 2 s for fine image
Energy range	3 keV to 17 MeV
Energy resolution	$<$ 1 keV FWHM at 3 keV, increasing to $\approx$ 5 keV at 5 MeV
Detectors	9 two-segment *n*-type germanium (7.1 cm diameter times 8.5 cm), cooled to $<$ 75 K with Stirling-cycle mechanical cooler
Effective area	$\approx 10^{-3}$ cm^2 at 3 keV, $\approx$ 32 cm^2 at 10 keV (without attenuators), $\approx$ 60 cm^2 at 100 keV, $\approx$ 15 cm^2 at 5 MeV
Imager	9 pairs of tungsten grids, with pitches from 34 μm to 2.75 mm, 1.55 m front-to-rear grid separation
Aspect system	Sensor Aspect System (SAS) for Sun direction $<$ 1.5″
	Roll Aspect System (RAS) for roll angle resolution $<$ 3′
Spacecraft spin rate	15 rpm, pointing to 0.2° of Sun center
Spacecraft mass	291.1 kg
Spacecraft power	220.4 W
Spacecraft size	1.18 m diameter, 2.06 m height, 5.74 m solar panel span
Telemetry	4 Mbps, downlink
On-board storage	4 Gbyte solid state memory
Launch vehicle	Pegasus XL
Launch date	2002 February 5
Orbit	38° inclination, 587–600 km altitude

detected in form of nine modulated time profiles, which can be processed into two-dimensional images using Fourier transform methods. The grid spacings vary from 2.3″ to $\gtrsim$ 3′ in steps of $\sqrt{3}$, allowing sources to be imaged over a wide range of angular scales, from the sizes of flare loop footpoint diameters to sizes of entire active regions. The energy range spans from 3 keV to 17 MeV, where the energy resolution is $\lesssim$ 1 keV at 3 keV, and increases to $\approx$ 5 keV at 5 MeV, thanks to the technology of cryogenically cooled germanium detectors. This high energy resolution allows RHESSI to resolve essentially all solar gamma-ray lines for the first time. An automated shutter system allows a wide dynamic range ($> 10^7$) of flare intensities to be handled without instrument saturation. Time tagged data for every photon are stored temporarily in a solid-state memory, before telemetered to the ground control center at the University of Berkeley, which allows post-event selection of time intervals with higher data rates. The spin rate of the satellite is one rotation per 4 s, which allows a basic time resolution of 2 s, or higher if a light curve demodulation technique is employed. The rotational modulation of the hard X-ray collimators allows us to obtain many more Fourier components of the image than

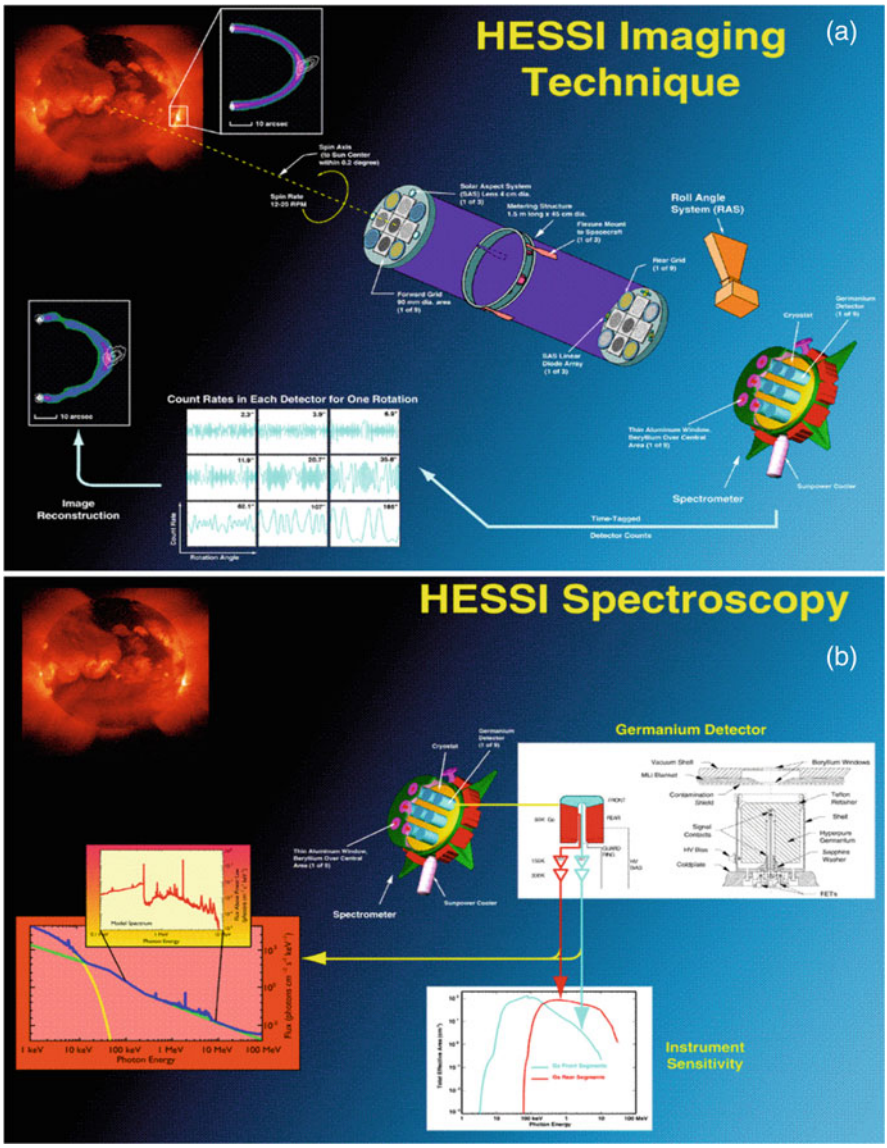

Fig. 1.2 (**a**) The RHESSI Imaging technique involves hard X-ray photons from the Sun, which pass through the slits of the front and rear grids of each of nine grid pairs to reach the germanium detector. The spacecraft rotates and the detector count rates are temporally modulated, which can be used to perform Fourier imaging. The germanium detectors are cryogenically cooled to provide high spectral resolution capable of resolving narrow gamma-ray lines and steep solar continuum spectra. (**b**) RHESSI spectroscopy covers hard X-ray wavelengths from energies of 1 keV up to gamma-ray wavelengths of 100 MeV. The Germanium detector design and the instrument sensitivity as a function of the photon energy is shown on the right side (Credit: NASA/GSFC, RHESSI Team)

the 9 basic components of the subcollimators, and thus yields finer details in the reconstructed images.

The major advances in solar hard X-ray observations provided by RHESSI are the capabilities of the first high-resolution hard X-ray imaging spectroscopy (Fig. 1.2, bottom), the first high-resolution gamma-ray line spectroscopy, and the first imaging above 100 keV, including the first imaging of gamma-ray lines (Hurford et al. 2003). Imaging with RHESSI reconstructs the Fourier components measured with the rotation-modulated collimators into spatial maps (Hurford et al. 2002), using specific algorithms such as *back-projection methods*, *Clean iterations*, *maximum entropy methods (MEM)*, *pixon reconstruction* (Metcalf et al. 1996), *forward-fitting methods* to modulated time profiles (Aschwanden et al. 2002), or to *uv-Fourier component visibilities*. Since RHESSI is a spinning spacecraft with a period of ≈ 4 s, time profiles with finer time bins require a demodulation of the RHESSI count rates (Arzner 2002). Nutation of the spinning spacecraft can also lead to instrumental oscillations in RHESSI count rates with periods of ≈ 75 s.

Spectroscopy is carried out by inversion of the electron energy injection spectrum from the observed bremsstrahlung photon spectrum, for instance with a *regularization inversion method* (Massone et al. 2003). The RHESSI data analysis software, *Solar SoftWare (SSW)* written in the *Interactive Data Language (IDL)*, is described in Schwartz et al. (2002).

1.3 The STEREO Mission

The most novel aspect of the STEREO mission capabilities is the stereoscopic vantage point from two different observing locations, which allows an unprecedented 3-D reconstruction of solar phenomena. The main scientific purpose of the STEREO mission is to understand the origin and propagation of *coronal mass ejections (CMEs)* and the related causes of the most severe nonrecurrent geomagnetic storms at Earth (Kaiser et al. 2008). STEREO measurements are used to study the mechanisms and sites of energetic particle acceleration, and to develop three-dimensional (3-D) time-dependent models of the magnetic topology, temperature, density, and velocity of the solar wind between the Sun and Earth. A conceptual cartoon of the STEREO observing strategy is shown in Fig. 1.3b, involving both remote-sensing and in-situ observations of a CME.

The specific tasks are:

1. Understand the causes of mechanisms of CME initiation.
2. Characterize the propagation of CMEs through the heliosphere.
3. Discover the mechanisms and sites of solar energetic particle acceleration in the low corona and in the interplanetary medium.
4. Develop a three-dimensional, time-dependent model of the magnetic topology, temperature, density, and velocity structure of the ambient solar wind.

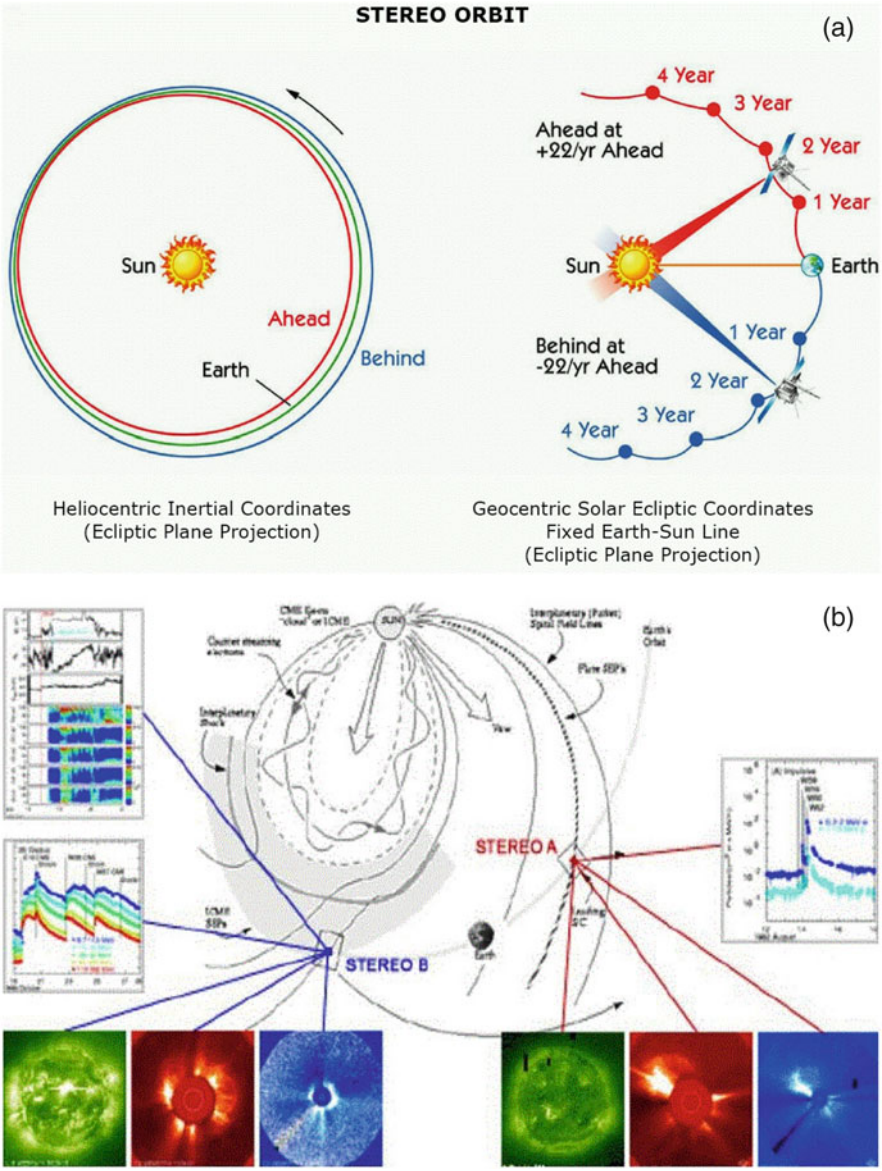

Fig. 1.3 (**a**) Orbital progression of the STEREO spacecraft Ahead and Behind over the mission life time (Credit: JHU/APL). (**b**) Possible STEREO/IMPACT observations of *solar energetic particles (SEPs)* at two magnetically disconnected locations in the heliosphere: STEREO-A is located on an open magnetic field line that is connected to the coronal flare region and will probe flare-accelerated particles, while STEREO-B probes SEPs in-situ in a CME-driven shock in interplanetary space at 1 AU (Credit: NASA, STEREO/IMPACT Team)

The twin *Solar TErrestrial RElations Observatory (STEREO)*[4] spacecraft were launched on 2006 October 26. At the end of January 2007 the two spacecraft separated and entered heliospheric orbits in opposite directions, STEREO-A(head) leading in East direction and STEREO-B(ehind) trailing in West direction around the Sun. They increase their separation by $\approx 45°$ per year, but maintain their average distance of $\approx 1.0 \pm 0.1$ AU from the Sun (Fig. 1.3a). Mission operations lost contact with the Behind observatory on 2014 October 1, just before its transit behind the Sun. There was a brief period of limited contact in the summer of 2016, but recovery efforts have been unsuccessfull since. The Ahead observatory continiues to operate nominally at the time of this writing. These particular orbits provide solar data that are suitable for small-angle stereoscopy of active regions in the solar corona at the beginning of the mission (or later whenever the separation angle is near zero or 180 degrees), while large-angle stereoscopy and tomography is feasible in most later years, designed to provide the 3-D reconstruction of coronal mass ejections that are launched in the solar corona and propagate through interplanetary space. Because of the varying distance of the two spacecraft from Earth, the data rate and telemetry is highest at the beginning of the mission, but drops continuously with increasing distance later in the mission. The STEREO mission concept was already anticipated in a number of pre-launch studies dating back to 1993.

Each of the two identical STEREO spacecraft contains a set of four instrument packages (Table 1.4): (i) the *Sun Earth Connection Coronal and Heliospheric Investigation (SECCHI)* suite; (ii) the *In-situ Measurements of PArticles and CME Transients (IMPACT)* experiment; (iii) the *PLAsma and SupraThermal Ion Composition (PLASTIC)* experiment; and (iv) the *STEREO/WAVES (SWAVES)* radio antenna system. The SECCHI suite of instruments includes two white light coronagraphs (COR1 and COR2), an extreme-ultraviolet imager (EUVI), and two heliospheric white light imagers (HI-1 and HI-2) which track CMEs out to 1 AU. The IMPACT suite of instruments measures in situ solar wind electrons, protons, heavier ions, magnetic field strengths, and magnetic field directions. The PLASTIC instrument measures the composition of heavy ions in the ambient plasma as well as protons and alpha particles. The SWAVES instrument uses radio waves to track the location of CME-driven shocks and the 3-D topology of open field lines along which particle flows, produced by solar flares. In addition, each of the 4 instrument packages produce a small real-time stream of selected data for space weather predictions used by the *National Oceanic and Atmospheric Administration (NOAA)*.

Technical descriptions of the STEREO instruments are documented in the special issue of *Space Science Reviews* volume **136** (2008), which includes a description of the STEREO spacecraft (Driesman et al. 2008), the SECCHI instrument suite (Howard et al. 2008), the IMPACT instrument suite (Luhmann et al. 2008; Acuna et al. 2008; Sauvaud et al. 2008; Lin et al. 2008; Mason et al. 2008; Mewaldt et al. 2008; Müller-Mellin et al. 2008; von Rosenvinge et al. 2008), the PLASTIC

[4] http://stereo.gsfc.nasa.gov/.

Table 1.4 STEREO instruments (adapted from Kaiser et al. 2008)

Instrument	Acronym	Purpose
SECCHI	COR1	Coronagraph 1.4–4.0 solar radii
	COR2	Coronagraph 2–15 solar radii
	EUVI	Extreme ultraviolet imager 1.6 solar radius
	HI-1	Heliospheric imager 8–45 solar radii
	HI-2	Heliospheric imager 35–215 solar radii
IMPACT	SWEA	Solar wind electrons up to 3 keV
	STE	Suprathermal electrons 2–100 keV
	SEPT	Electrons 20–400 keV; protons 60–7,000 keV
	SIT	Composition He-Fe 300–2,000 keV/nucleon
	LET	Protons, He, heavy ions to 40 MeV/nucleon
	HET	Protons, He to 100 MeV; electrons to 8 MeV
	MAG	Vector magnetic field up to 65,536 nT
PLASTIC	SWS	Protons, alpha dist. functions to 100 keV
		Heavy ions to 100 keV
	WAP	Wide angle heavy ions up to 100 keV
S/WAVES	HFR	Electric field 125 kHz–16 MHz
	LFR	Electric field 2.5–160 kHz
	FFR	Fixed frequency 32 or 34 MHz
	TDS	Time domain to 250 k sample/sec

instrument (Galvin et al. 2008), and the SWAVES radio instrument (Bougeret et al. 2008; Bale et al. 2008). Photometric calibration and background subtraction of the coronagraphs COR1 and COR2 are documented in Thompson and Reginald (2008) and Thompson et al. (2010), while performance, calibration, and stray light rejection of the heliospheric imagers HI-1 and HI-2 can be found in Eyles et al. (2009), Brown et al. (2009), Harrison et al. (2009), and Bewsher et al. (2010).

1.4 The Hinode Mission

As the successor of the *Yohkoh* (Solar-A) mission, Hinode aims to understand how magnetic energy gets transferred from the photosphere to the upper atmosphere and results in explosive energy releases. The principal scientific goals of the Hinode mission are the following (Kosugi et al. 2007):

1. To understand the processes of magnetic field generation and transport including the magnetic modulation of the Sun's luminosity.
2. To investigate the processes responsible for energy transfer from the photosphere to the corona and for the heating and structuring of the chromosphere and the corona.

3. To determine the mechanisms responsible for eruptive phenomena, such as flares and coronal mass ejections, and understand these phenomena in the context of the space weather of the Sun-Earth system.

The Japanese/US/UK *Hinode*[5] mission (named after the Japanese word for "sunrise"), formerly known as *Solar-B*, was launched on 2006 September 22, just a month before the STEREO mission. The satellite was maneuvred into a quasi-circular Sun-synchronous orbit that is stationary over the Earth day/night terminator, which allows near-continuous observation of the Sun. The first images from Hinode were captured on 2006 October 28. The Hinode satellite contains three telescopes; (i) the *Solar Optical Telescope (SOT)*; (ii) the *X-ray telescope (XRT)*; and (iii) the *Extreme-Ultraviolet Imaging Spectrometer (EIS)*, pictured in Fig. 1.4a. Technical data are listed in Table 1.5.

The SOT (Solar Optical Telescope) is of a Gregorian type with 0.5 meter aperture and with an angular resolution of $\approx 0.2''$ over a limited field-of-view of $328'' \times 164''$. The *Focal Plane Package (FPP)* consists of three optical instruments: the *Broadband Filter Imager (BFI)* produces images of the solar photosphere and chromosphere in 6 wide-band interference filters; the *Narrowband Filter Imager (NFI)* is a tunable Lyot-type birefringent filter capable of producing magnetogram and dopplergram images of the solar surface; and the *Spectro-Polarimeter (SP)* which produces the most sensitive vector magnetograph maps of the photosphere to date. The FPP also includes a *Correlation Tracker (CT)* which locks onto solar granulation to stabilize the SOT images to a fraction of an arcsecond.

The XRT (X-Ray Telescope) is a modified Wolter 1 type telescope design that uses grazing incidence optics to image the solar corona's hottest components (with temperatures of $T_e \approx 0.5$–10 MK) with an angular resolution that is about twice the CCD pixel size of $1''$, over an imaging field-of-view of 34 arcmin, which is slightly larger than the solar diameter and is capable to capture a full-Sun image when pointed at Sun center.

The EIS (Extreme-Ultraviolet Imaging Spectrometer) is a normal incidence spectrometer in the extreme ultraviolet (EUV) wavelength range, producing spatially resolved spectra in the two wavelength ranges of 17.0–21.2 nm (170–212 Å) and 24.6–29.2 nm (246–292 Å). The spatial resolution is $\approx 2''$ and the field-of-view is up to $560'' \times 512''$. The emission lines in the EIS wavelength bands are emitted at coronal temperatures ranging from 50,000 K to 20 MK.

Technical descriptions of the Hinode instruments are given in the special issues of *Solar Physics* volumes **243** (2007) and **249** (2008), containing descriptions of the mission (Kosugi et al. 2007), the XRT instrument (Golub et al. 2007; Kano et al. 2008), the EIS instrument (Culhane et al. 2007), and the SOT instrument (Tsuneta et al. 2008; Shimizu et al. 2008; Suematsu et al. 2008; Ichimoto et al. 2008). Post-launch instrumental studies of Hinode focused on the point spread function of SOT (Wedemeyer-Böhm 2008), magnetogram comparisons of SOT (Wang et al.

[5] http://hinode.msfc.nasa.gov/.

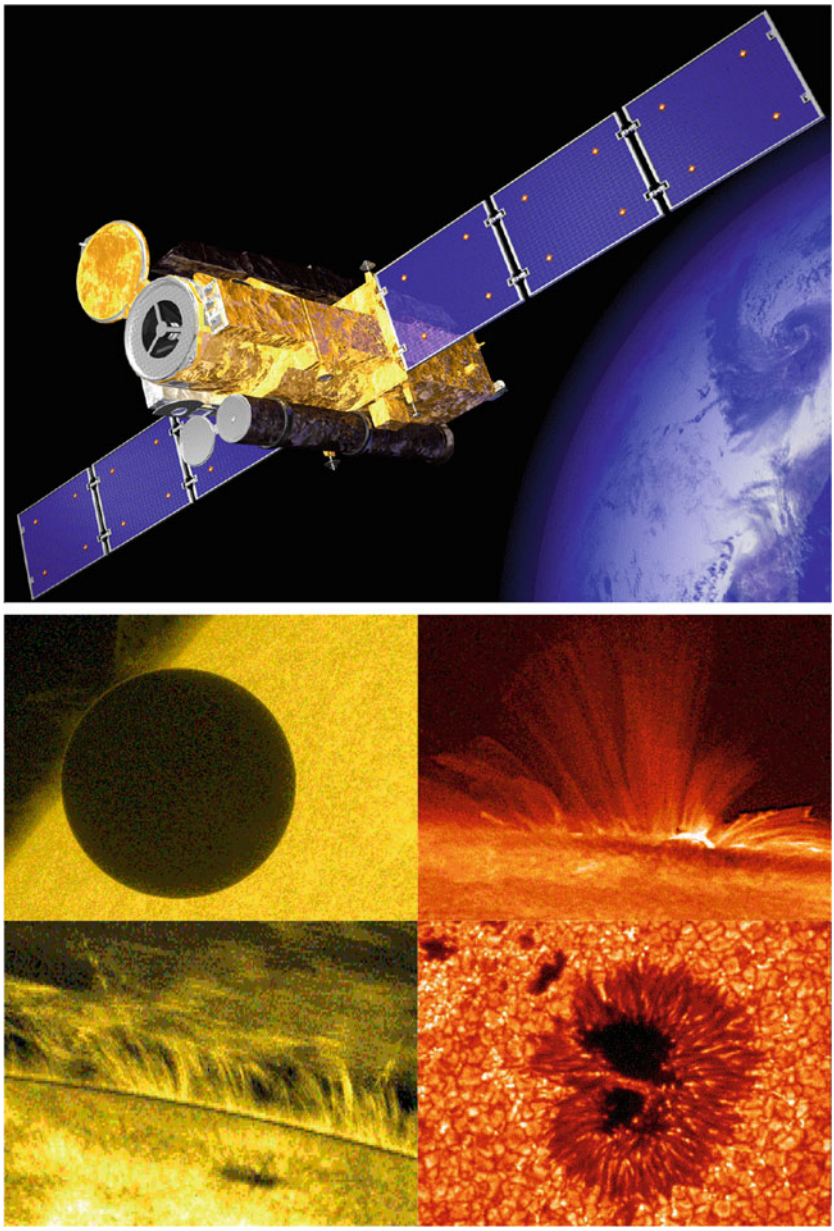

Fig. 1.4 *Top:* Artist's version of the *Hinode* spacecraft in a Sun-synchronous orbit. The large central cylinder with the open door is the SOT telescope, while the EIS/Hinode instrument is in the black box on top, and the XRT instrument is attached below the SOT. *Bottom:* Images obtained from Hinode that emphasize the high spatial resolution of SOT that is needed to resolve the finest observed features. *Middle left:* Venus transit on 2012 June 5; *Bottom left:* Prominence threads above the limb; *Middle right:* Postflare loops; *Bottom right:* Sunspot and solar granulation (Credit: Hinode Team)

Table 1.5 Hinode instrument characteristics (adapted from Kosugi et al. 2007)

Parameter	Characteristics
Spacecraft mass	900 kg (wet), 770 kg (dry)
Spacecraft power	1100 W
Spacecraft size	4.0 × 1.6 × 1.6 m
Data rate	Up to 2 Mbps
Telemetry rate	32 kbps (S-band), 4 Mbps (X-band)
On-board storage	8 Gbits
Orbit altitude	680 km (circular, Sun-synchronous, polar orbit)
Orbit inclination	98.1°
Orbit period	98 min
Attitude control	Three-axis stabilized
Absolute pointing	20″
Pointing determination	X/Y axes: 0.1″
Launch date	2006 September 22
Instruments	Solar Optical Telescope (SOT)
	X-ray telescope (XRT)
	Extreme-Ultraviolet Imaging Spectrometer (EIS)
Angular resolution	SOT: 0.2″, XRT: 2″, EIS: 2″
Field of view	SOT: 328″ × 164″, XRT: 34', EIS: ≤ 560″
Temporal resolution	SOT: 3.4 s, XRT: 2 s, EIS: scanning 1″ in 0.7 s
Spectral range	SOT: 3800–7000 Å, EIS: 170–212 Å, 246–292 Å, XRT: 6–60 Å

2009), polarimetric noise and scattering polarization of SOT (Tiwari et al. 2009), the intensity contrast and stray light correction of SOT (Danilovic et al. 2008; Mathew et al. 2009), the wavelength calibration of EIS (Brown et al. 2008; Del Zanna 2013), and the performance of the spectro-polarimeter (Lites et al. 2013).

Hinode is designed to address the fundamental question of how magnetic fields interact with the ionized atmosphere to produce solar variability, which should be accomplished by the unprecedented high spatial resolution of SOT/Hinode (see examples in Fig. 1.4), and to measure magnetic fields from space, which is only diffraction-limited, compared with ground-based optical telescopes that suffer degraded spatial resolution due to the seeing conditions in the Earth's atmosphere. The three instruments SOT, EIS, and XRT were selected to observe the response of the chromosphere and corona to changes in the photosphere by measuring the 3-D vector magnetic field. This should constrain the measurement of electric currents and free magnetic energies (defined as difference between the force-free non-potential and the potential field). The response of the solar atmosphere to magnetic field changes is measured by the EUV Imaging Spectrometer (EIS) and the X-Ray Telescope (XRT).

1.5 The SDO Mission

The *Solar Dynamics Observatory (SDO)*[6] is the first space-based mission of NASA's *Living With a Star (LWS)* program. The most useful capability of the SDO mission is the imaging of *"all the Sun all the time"*. SDO was launched on 2010 February 11, and was lifted into a circular geosynchronous orbit inclined by 28° about the longitude of the SDO-dedicated ground station in New Mexico (Fig. 1.5a). Science operations started on 2010 May 1. The SDO spacecraft contains three instruments, the *Atmospheric Imaging Assembly (AIA)*, the *Extreme Ultraviolet Variability Experiment (EVE)*, and the *Helioseismic and Magnetic Imager (HMI)*, built by NASA/GSFC, LMSAL, and LASP (University of Colorado). Technical data of the SDO observatory (Fig. 1.5a) are summarized in Table 1.6.

The AIA (Atmospheric Imaging Assembly) consists of four telescopes that employ normal-incidence, multilayer-coated optics to provide narrow-band imaging of seven extreme ultra-violet (EUV) band passes centered mostly on iron lines: Fe XVIII (94 Å), Fe VIII and XXI (131 Å), Fe IX (171 Å), Fe XII and XXIV (193 Å), Fe XIV (211 Å), He II (304 Å), and Fe XVI (335 Å). One telescope observes C IV (near 1600 Å) and the nearby continuum (1700 Å) and has a filter that observes in the visible light to enable coalignment with images from the other telescopes. The temperature diagnostics of the EUV emissions cover the range from $T_e = 6 \times 10^4$ K to $T_e = 20$ MK. The field-of-view of AIA images extends out to 1.5 solar radii, the CCD image contains 4096×4096 pixels with a pixel size of $0.6''$ and has a spatial resolution of ≈ 2 pixels. Images in all wavelengths are recorded with a cadence of 12 s, 24 hours a day, producing over a Terabyte of (uncompressed) data per day. Examples of coronal loops, filaments, and prominences imaged by AIA are shown in Fig. 1.5b–e.

The EVE (Extreme Ultraviolet Variability Experiment) measures the solar EUV irradiance from 0.1 to 105 nm (1–1050 Å) with unprecedented spectral resolution (0.1 nm), temporal cadence (10 s), and accuracy (20%). EVE includes several irradiance instruments: The *Multiple EUV Grating Spectrographs (MEGS)* instrument consists of a grazing-incidence spectrograph *MEGS-A)* that measures the solar EUV irradiance in the 5–37 nm range with 0.1 nm resolution, and a normal-incidence, dual-pass spectrograph *MEGS-B)* that measures the solar EUV irradiance in the 35–105 nm range with 0.1 nm resolution. In-flight calibration is provided by the *EUV Spectro-Photometer (ESP)*, which measures the solar EUV irradiance in broad bands between 0.1 and 39 nm. All these instruments are designed to accurately measure the solar irradiance in the entire EUV wavelength range and thus are very useful to study the solar impact on the Earth's ionosphere.

The Helioseismic and Magnetic Imager (HMI) onboard SDO is a vector magnetograph that is designed to measure the Doppler shift, intensity, and vector magnetic field at the solar photosphere using the 6173 Å Fe I absorption line. The instrument

[6] http://www.nasa.gov/mission_pages/sdo/main/index.html.

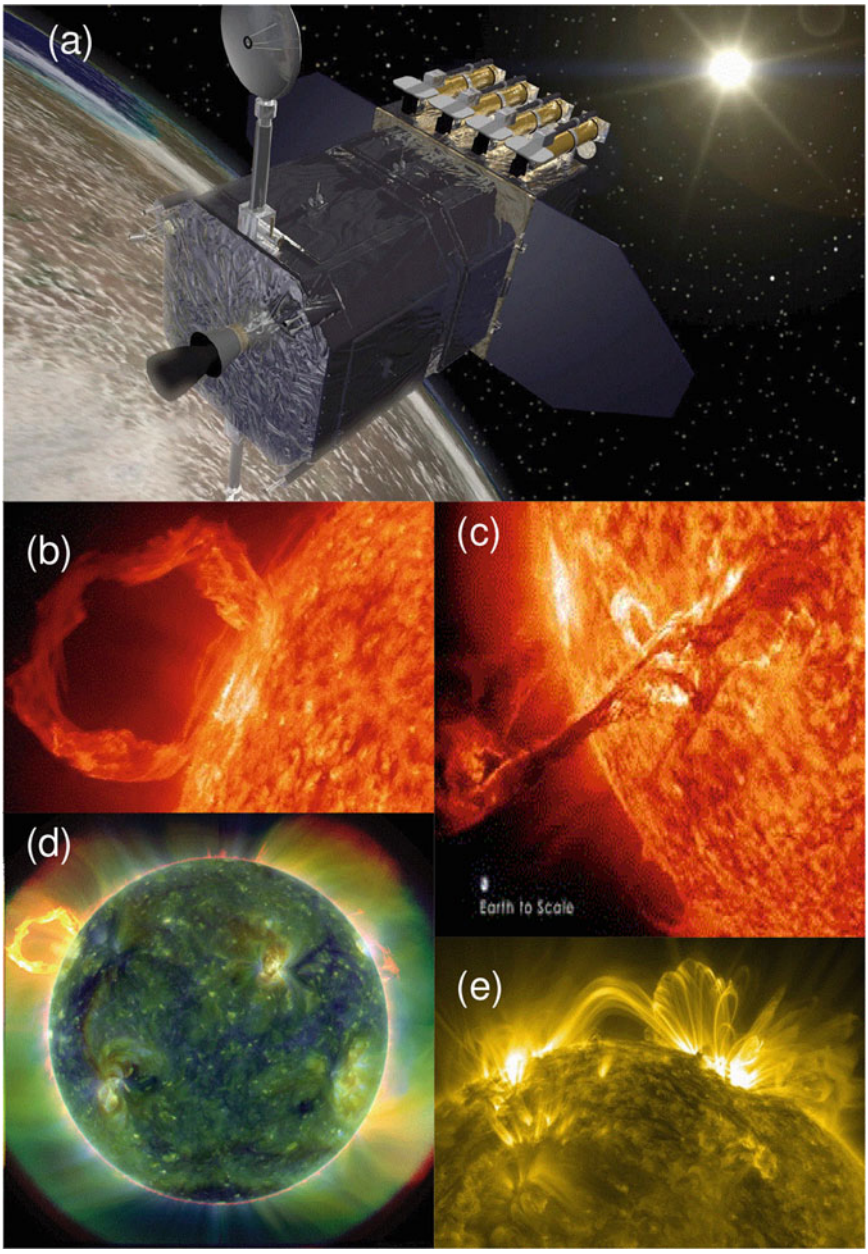

Fig. 1.5 (**a**) The *Solar Dynamics Observatory (SDO)* spacecraft is shown in an artist's impression. The four golden tubes represent the four *Atmospheric Imaging Assembly (AIA)* telescopes. Images taken by AIA/SDO: (**b**) Prominence observed with AIA in 304 Å on 2012 August 31; (**c**) An erupting filament that turns into a prominence; (**d**) Full disk EUV multi-wavelength image on 2012 August 31; (**e**) Two active regions near the limb bridged by transequatorial loops, observed by AIA on 2012 July 12 (Credit: NASA, SDO Team)

Table 1.6 SDO observatory characteristics

Parameter	Characteristics		
Spacecraft mass	3000 kg		
Spacecraft power	1500 W		
Spacecraft size	4.7 × 2.2 × 2.2 m		
Data rate	150 Mbps		
Orbit altitude	35,800 km		
Orbit inclination	28°		
Orbit period	Geosynchronous		
Attitude control	Three-axis stabilized		
Pointing accuracy	0.12″		
Launch date	2010 February 11		
Mission operation	NASA/GSFC		
SDO ground station	White Sands, New Mexico		
Instrument	AIA	HMI	EVE
CCD detector	4096 × 4096	4096 × 4096	1024 × 2048
Pixel size	0.6″	0.505″	
Angular resolution	1.5″	0.91″	
Field of view	41′ × 41′	34′ × 34′	
Temporal cadence	12 s	45 s	10 s
Spectral range	94–335 Å	6173 Å	1–1050 Å
	1600, 1700 Å		
	4500 Å		

consists of a front-window filter, a telescope, a set of waveplates for polarimetry, an image stabilization system, a blocking filter, a five-stage Lyot filter with one tunable element, two wide-field tunable Michelson interferometers, a pair of 4096^2 pixel CCD cameras with independent shutters, and associated electronics. Each camera takes a full-disk image in Doppler velocity, intensity, and line-of-sight field measurements with a cadence of 45 s, and at a slower cadence for the full vector magnetic field. The temporally uninterrupted observations of HMI play a key role for inversion techniques in helioseismology.

Technical descriptions of the SDO instruments are mostly given in the special issue of *Solar Physics* volume **275** (2012), such as descriptions of the SDO mission (Pesnell et al. 2012), the AIA instrument (Lemen et al. 2012; Boerner et al. 2012), the EVE instrument (Woods et al. 2012; Hock et al. 2012), and the HMI instrument (Scherrer et al. 2012; Schou et al. 2012a,b; Wachter et al. 2012; Zhao et al. 2012). Post-launch instrumental SDO studies concerned the fast inversion of Stokes vector profiles (Borrero et al. 2011), inter-comparisons of magnetograms (Liu et al. 2012), the photometric and thermal cross-calibration (Boerner et al. 2014), and the HMI vector magnetic field pipeline (Hoeksema et al. 2014; Centeno et al. 2014; Couvidat et al. 2016).

1.6 The IRIS Mission

The *Interface Region Imaging Spectrograph (IRIS)*[7] is a NASA small explorer mission mission that has been launched in 2013 and is still operating at the time of writing. This solar-dedicated observatory contains a multi-channel imaging spectrograph with a UV telescope, capable of obtaining spectra and slit-jaw images. The most novel aspect of the IRIS capabilities is the high-resolution and high-cadence spectroscopy and imaging of the transition from the photosphere to the corona.

The primary objective of the IRIS mission is the exploration of the interface between the solar chromosphere, transition region, and corona, in order to understand how the plasma flows generated by the internal magneto-convection drives coronal activity: (i) Which types of non-thermal energy dominate in the chromosphere and beyond? (ii) How does the chromosphere regulate mass and energy supply to corona and heliosphere? (iii) How do magnetic flux and matter rise through the lower atmosphere, and what role does flux emergence play in flares and coronal mass ejections?

For an overview of the IRIS instrument (Fig. 1.6) we extract a description from De Pontieu et al. (2014): The Interface Region Imaging Spectrograph (IRIS) small explorer spacecraft provides simultaneous spectra and images of the photosphere, chromosphere, transition region, and corona with 0.33–0.4 arcsec spatial resolution, 2-s temporal resolution, and $1\,\mathrm{km\,s^{-1}}$ velocity resolution over a field-of-view of up to 175×175 arcsec^2. IRIS was launched into a Sun-synchronous orbit on 27 June 2013 using a Pegasus-XL rocket and consists of a 19 cm UV telescope that feeds a slit-based dual-bandpass imaging spectrograph. IRIS obtains spectra in passbands from 1332–1358 Å, 1389–1407 Å, and 2783–2834Å, including bright spectral lines formed in the chromosphere (Mg II h 2803 Å and Mg II k 2796 Å) and transition region (C II 1334/1335 Å and Si IV 1394/1403 Å). Slit-jaw images in four different passbands (C II 1330, Si IV 1400, Mg II k 2796, and Mg II wing 2830 Å) can be taken simultaneously with spectral rasters that sample regions up to 130×175 arcsec^2 at a variety of spatial samplings (from 0.33 arcsec and up). IRIS is sensitive to emission from plasma at temperatures between 5000 K and 10 MK and will advance our understanding of the flow of mass and energy through an interface region, formed by the chromosphere and transition region, between the photosphere and corona. This highly structured and dynamic region not only acts as the conduit of all mass and energy feeding into the corona and solar wind, it also requires an order of magnitude more energy to heat than the corona and solar wind combined. The IRIS investigation includes a strong numerical modeling component based on advanced radiative-MHD codes to facilitate interpretation of observations of this complex region. Approximately eight Gbytes of data (after compression) are

[7] http://science.nasa.gov/missions/iris/.

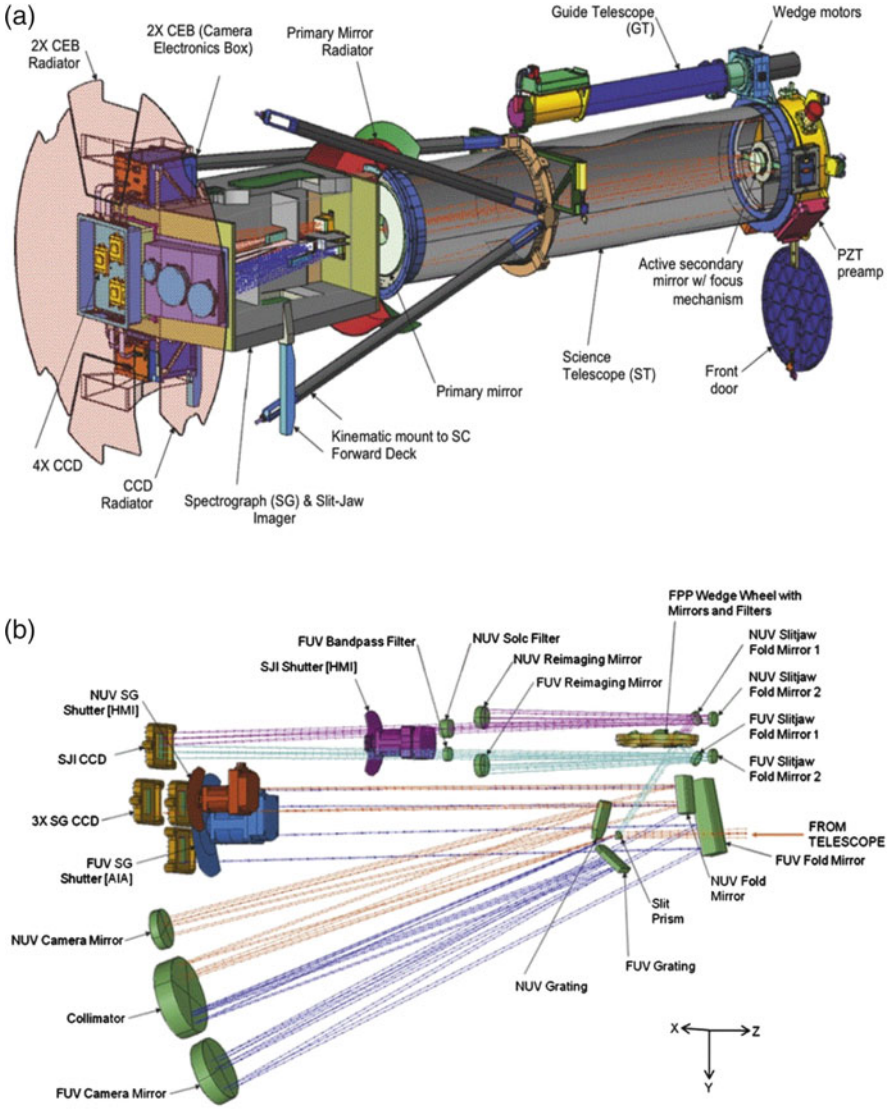

Fig. 1.6 (**a**) Conceptual design of the IRIS instrument. Sunlight enters from the right. The telescope measures 2.18 m from the CEB radiator to the front of the telescope. (**b**) Path taken by light in the FUV spectrograph (dark blue), NUV spectrograph (orange), FUV slit-jaw (light blue), and slit-jaw (purple), (De Pontieu et al. 2014)

Table 1.7 IRIS instrument characteristics (SJI=slit jaw imager; SG=spectrograph; FUV=far ultra-violet, NUV=near ultra-violet)

Characteristics	Parameter
Primary optics diameter	19 cm
Effective focal length	6.895 m
Field of view	175×175 arcsec^2 (SJI)
	0.33×175 arcsec^2 (SG—slit)
	130×175 arcsec^2 (SG—raster)
Spatial scale (pixel)	0.167 arcsec
Spatial resolution	0.33 arcsec (FUV)
	0.4 arcsec (NUV)
Spectral scale (pixel)	12.8 mÅ (FUV)
	26.5 mÅ (NUV)
Spectral resolution	26 mÅ (FUV SG)
	53 mÅ (NUV SG)
Bandwidth	55 Å (FUV SJI)
	4 Å (NUV SJI)
CCD detectors	Four e2v 2061×1056 pixels, thinned, back-illuminated
CCD cameras	Two 4-port readout cameras (SDO flight spares)
Detector full well	150,000 electrons
Typical exposure times	0.5 to 30 s
Flight computer	BAe RAD 6000
Mass	87 kg (Instrument), 96 kg (Spacecraft)
Power	55 W (Instrument), 247 W (Spacecraft)
Average downlink rate	0.7 Mbit s^{-1}
X-band downlink rate	13 Mbit s^{-1}
Total data volume	$\approx$20 Gbytes (uncompressed) per day

acquired by IRIS each day and made available for unrestricted use within a few days of the observation.

The IRIS instrument characteristics are given in Table 1.7. IRIS was designed to provide: (i) high spatial resolution (0.4 arcsec) spectroscopic and (context) imaging data over a field of view of at least 120 arcsec, providing diagnostics from the photosphere to the corona, with an emphasis on the chromosphere and transition region. (ii) A high signal-to-noise ratio for 2-s exposures for a few selected bright lines covering chromosphere and transition region, which allows a velocity determination with 1 km s^{-1} accuracy and 3 km s^{-1} spectral pixels. (iii) High-cadence spectral (20 s) and imaging (10 s) observations covering a small region of the Sun (5×120 arcsec) for periods of up to eight hours continuously. (iv) Eclipse-free observations for up to eight months per year with about 15 X-band passes per day and an average data rate of 0.7 Mbit s^{-1}. These capabilities are met by a design that includes the following: (i) A 19-cm Cassegrain telescope that feeds a dual-range UV spectrograph (SG) and slit-jaw imager, with 0.16 arcsec pixels and four 2061×1056 CCDs; (ii) A slit-jaw imager that includes four passbands with two

transition-region lines (C II 1335 Å and Si IV 1400 Å), one chromospheric line (Mg II k 2796 Å), and one photospheric passband (2830 Å), covering a field-of-view of 175 arcsec × 175 arcsec; (iii) A spectrograph with 0.33 arcsec wide and 175 arcsec long slit that covers FUV passbands from 1332 Å to 1358 Å and 1389 Å to 1407 Å, and an NUV passband from 2783 Å to 2835 Å. These passbands include lines formed over a wide range of temperatures from the photosphere (5000 K) to the corona (1 to 10 million K); (iv) CCD detectors with a full well of 150,000 electrons, with a camera-readout noise of <20 electrons, and data compression that is nearly lossless.

Understanding the observations of IRIS, which contains an imaging spectrograph (covering Mg II h and k lines) as well as a slit-jaw imager (centered at Mg II k) requires forward modeling of Mg II h and k line formation from 3-D radiation-MHD models, which is conducted in a series of papers; (i) using a quintessential model atom of Mg II and general formation properties of the Mg II h and k lines (Leenaarts et al. 2013a); (ii) describing the formation of Mg II h and k lines in the solar atmosphere (Leenaarts et al. 2013b); (iii) describing near-ultraviolet (NUV) spectra and images (Pereira et al. 2013); (iv) using the Mg II triplet lines as a new diagnostic for lower chromospheric heating (Pereira et al. 2015), and (v) exploiting the diagnostic potential of the C II lines at 133.5 nm (Rathore et al. 2015a,b; Rathore and Carlsson 2015) and the O I 135.56 nm line in the solar atmosphere (Lin and Carlsson 2015). IRIS observations also provide a critical quantitative measure of the energy radiated in the Balmer continuum (Heinzel and Kleint 2014).

1.7 The CORONAS Missions

The *Russian Federal Space Agency* (Roskosmos) launched a series of three solar-terrestrial science missions: *CORONAS-I* was launched on 1994 March 2 and decayed on 2001 March 4 (I stands for Izmiran, the site of the head institution, the *Institute of Terrestrial Magnetism, Ionosphere and Radio Wave Propagation*); *CORONAS-F* was launched on 2001 July 31 and re-entered the atmosphere on 2005 December 6 (F stands for FIAN, the Lebedev Institute of Physics); and *CORONAS-Photon* (or CORONAS-Foton; Fig. 1.7), which was launched on 2009 January 30, but lost power on 2009 December 1, and was declared as lost on 2010 April 18. The *CORONAS* project, an acronym for *Complex ORbital Observations Near-Earth of Activity of the Sun*, was envisioned to make observations during different phases of the 11-year solar cycle. The CORONAS satellite series was equipped with a variety of instruments including UV, EUV, and XUV imagers, X-ray and gamma-ray spectrometers, radio receivers, and particle counters.

CORONAS-I carried a total of 12 science instruments, including the *Terek* spectro-heliometer, the *RES-K* solar X-ray spectrograph, the *Helicon* solar gamma-ray detector, the *SUVR-SP-C* ultraviolet radiometer, the *DIFOS* optical photometer, and other instruments.

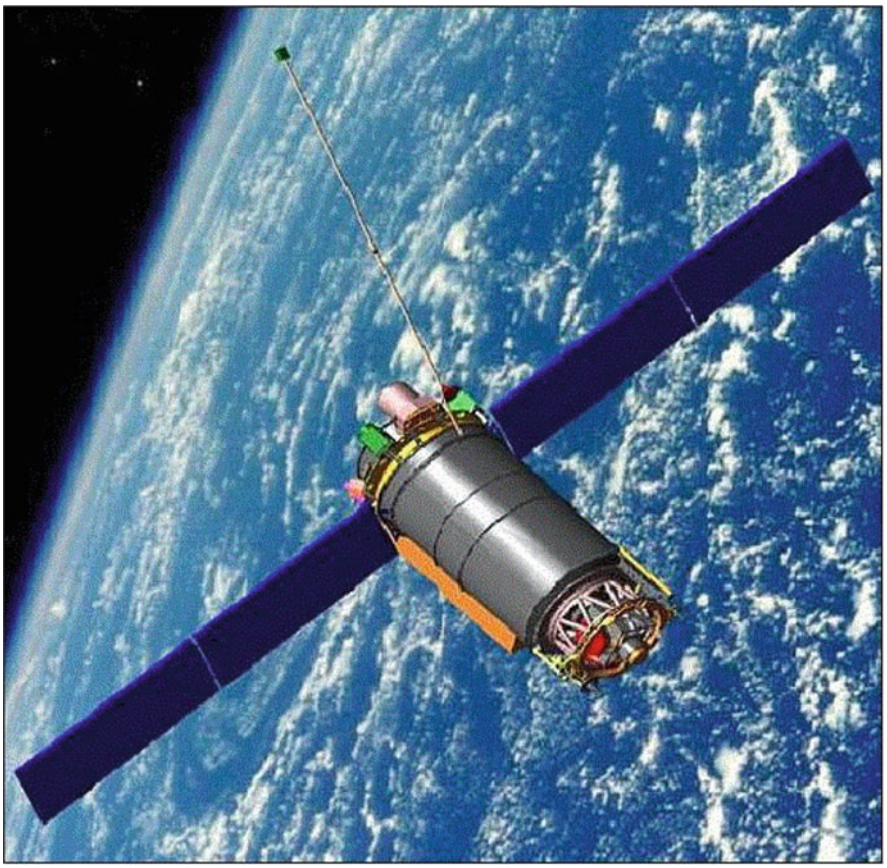

Fig. 1.7 Artist's view of the CORONAS-Photon spacecraft in orbit (Credit: Roskosmos)

CORONAS-F was equipped with 18 instruments: the Multichannel Solar Photometer *DIFOS*, the Full Sun XUV spectroscopy imaging *SPIRIT* (Reva et al. 2011), the Solar X-Ray Telescope *SRT*, the X-Ray Spectroheliograph *RES*, the X-Ray Spectrometer and Photometer *DIOGENESS*, the X-Ray Spectrometer *RESIK*, the Solar Spectropolarimeter *SPR*, the Flare Spectrometer *IRIS*, the Gamma Spectrometer *HELICON*, the X-Ray Spectrometer *RPS* (Pankov et al. 2006), the Time-Amplitude Spectrometer *AVS*, the Solar UV Radiometer *SUFR*, the Solar UV Spectrophotometer *VUSS*, the Solar Cosmic Rays Complex *SKL*, the Cosmic Ray Monitor *MKL*, the Spectrometer of Energy and Ion Chemical Composition *SKI*, the Solar Neutron and Gamma Ray Spectrometer *SONG*, and the X-ray polarimeter *PR-N*. Comprehensive studies of solar activity using the CORONAS-F satellite are summarized in Oraevsky and Sobelman (2002).

CORONAS-Photon is part of the international *Living with a Star (LWS)* program. The scientific payload complex contains: the high energy spectrometer

Natalya-2M (Kotov et al. 2011c), the Roentgen Telescope-2 *RT-2* (Kotoch et al. 2011; Sreekumar et al. 2011; Sarkar et al. 2011; Debnath et al. 2011; Nandi et al. 2011), the hard X-ray polarimeter-spectrometer *PENGUIN-M* (Kotov et al. 2011a), the X-ray and gamma-ray spectrometer *Konus-RF* (Kuznetsov et al. 2011a), the fast X-ray monitor *BRM* (Trofimov et al. 2011), the multi-channel ultraviolet monitor *PHOKA* (Kotov et al. 2011b), the solar telescope/imaging spectrometer *TESIS* (Kuzin et al. 2009, 2011a,b), which contains the *SphinX soft X-ray spectro-photometer* (Gburek et al. 2011a,b, 2013), the charged particle analyzer *Electron-M-PESCA* (Denisov et al. 2011), the satellite telescope of electrons and protons *STEP-F* (Dudnik et al. 2011, 2012), the magnetometer *SM-8M*, and the global solar oscillation experiment *SOKOL* (Levedev et al. 2011). Scientific goals and observational capabilities of the CORONAS-Photon mission are summarized in Kotov (2011).

The main goal of the CORONAS project is the investigation of energy accumulation and its transformation into energy of accelerated particles processes during solar flares; the study of the acceleration mechanisms, propagation and interaction of fast particles in the solar atmosphere; the study of the solar activity correlation with physical-chemical processes in the Earth upper atmosphere. The specific science tasks include: (i) Determine the distribution functions of accelerated electrons, protons and nuclei and their dynamics with high time resolution; (ii) Study the difference in the acceleration dynamics of electrons and protons (nuclei); (iii) Obtain the distribution function variations for high energy particles (up to a few GeV); (iv) Study the interacting particle angular anisotropy by statistical analysis of radiation spectra and linear polarization parameters of hard X-rays; (v) Study of directional effects in the region of high energy gamma radiation; (vi) Determination of mechanisms and requirements of electron and proton acceleration in different flare phases, and parameters of propagation region of accelerated particles; (vii) Determination of elemental abundance in the region of gamma-ray production by gamma spectroscopy and capture of low energy neutrons in the solar atmosphere; (viii) Determination of radiation generation altitudes by observation of deuteron line weakening from limb flares; (ix) Determination of energy spectra in view of accelerated protons and nuclei and dynamics of these spectra according to nuclear gamma-line ratio; (x) Study of light elements generation (D, ^{3}He, Li, Be) during flares; (xi) Research of chemical and isotopic compositions of nuclei accelerated in flare on the Earth orbit, and also energy and temporal parameters of flare electrons and protons; (xii) Monitoring of the Earth upper atmosphere by absorption of extreme ultraviolet of the quiet Sun; (xiii) Study of hard X-ray and gamma radiation from gamma-ray bursts; (xiv) Study of X-ray radiation from the bright local sources along the ecliptic plane. A summary of scientific results from the CORONAS-F mission is given in Kuznetsov et al. (2011b).

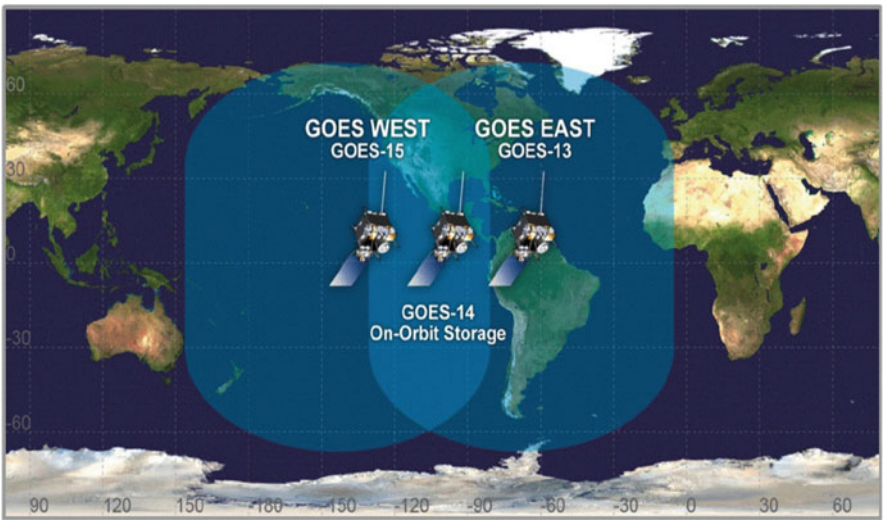

Fig. 1.8 The Geostationary Operational Environmental Satellites (GOES) operate from two primary locations, GOES East is located at 75°W and provides most of the U.S. weather information. GOES West is located at 135° over the Pacific Ocean. NOAA also maintains an on-orbit GOES satellite in the event of an anomaly or failure of GOES East or GOES West (Credit: NOAA, GOES Team)

1.8 Solar-Terrestrial Space Missions

In addition to the large space-based and solar-dedicated observatories[8] (e.g., SOHO, STEREO, Hinode, SDO) that were or became operational early in the new millennium, there is also an arsenal of other solar-terrestrial space missions, suborbital rocket flights, and balloon-borne detectors, that provided significant contributions to solar physics. In the following we will briefly mention a few of these missions that were operated in the new millennium, in order of launch dates.

The *Geostationary Operational Environmental Satellites (GOES)* (see Fig. 1.8) program, operated by the US *National Oceanic and Atmospheric Administration (NOAA)*, consists of a series of geostationary satellites (orbiting the Earth at a height of 35,790 km), which overlap in time so that there are always one to three spacecraft present and warrant an essentially uninterrupted time series of solar soft X-ray fluxes, besides continuous meteorological observations of the Earth (Table 1.8). The first (GOES-1) satellite was launched on 1974 October 16. In the meantime the series continued up to GOES-17, launched on 2018 March 17. GOES 12–15 had *soft X-ray imaging (SXI)* capability, and GOES 16 and 17 have EUV imaging *(SUVI)* capability. Operational and technical details of GOES solar instruments (after 2000)

[8] http://www.scholarpedia.org/article/Solar_Satellites.

Table 1.8 GOES history and status during the period of 1975–2017. GOES-M through GOES-P contain *Soft X-ray Imagers (SXI)*, and GOES-R and GOES-S contain *Solar X-ray Ultraviolet Imagers (SUVI)* [Credit: NOAA, www.goes-r.gov/mission/history.html]

Launch designation	Operational designation	Launch	Status
GOES-A	GOES 1	October 16, 1974	Decommissioned 1985
GOES-B	GOES 2	June 16, 1977	Decommissioned 1993
			Reactivated 1995–2001
GOES-C	GOES 3	June 16, 1978	Decommissioned 2016
GOES-D	GOES 4	September 9, 1980	Decommissioned 1988
GOES-E	GOES 5	May 22, 1981	Decommissioned 1990
GOES-F	GOES 6	April 28, 1983	Decommissioned 1992
GOES-G	N/A	May 3, 1986	Failed to orbit
GOES-H	GOES 7	February 26, 1987	Decommissioned 2012
GOES-I	GOES 8	April 13, 1994	Decommissioned 2004
GOES-J	GOES 9	May 23, 1995	Decommissioned 2007
GOES-K	GOES 10	April 25, 1997	Decommissioned 2009
GOES-L	GOES 11	May 3, 2000	Decommissioned 2011
GOES-M, SXI	GOES 12	July 23, 2001	Decommissioned 2013
GOES-N, SXI	GOES 13	May 24, 2006	Decommissioned
GOES-O, SXI	GOES 14	June 27, 2009	In on-orbit storage
GOES-P, SXI	GOES 15	March 4, 2010	In operation as GOES West
GOES-R, SUVI	GOES 16	November 19, 2016	In operation as GOES East
GOES-S, SUVI	GOES 17	March 1, 2018	Post-launch checkout

can be gleaned from Lemen et al. (2004), Hill et al. (2005), Pizzo et al. (2005), Väänänen et al. (2009), Evans et al. (2010), Neupert (2011), the NOAA website,[9] or the NASA/GOES website.[10] GOES is the longest-operated solar-observing program in space and provides a basically continuous data stream of soft X-ray fluxes in the two 0.5–4 Å and 1–8 Å wavelength bands, which are widely used for the classification of solar flare magnitudes. The logarithmic flux values are labeled with letters (A, B, C, M, X-class), which denote the order of magnitude of the peak flux on a logarithmic scale ($A = 10^{-8}$, $B = 10^{-7}$, $C = 10^{-6}$, $M = 10^{-5}$, $X = 10^{-4}$ W m^{-2}), subdivided with an additional digit (e.g., an X2 class flare has a flux of 2×10^{-4} W m^{-2}).

Interball[11] is an international solar-terrestrial program to study the Earth magnetosphere with two spacecraft, one flying through the magnetospheric geotail (i.e., the *Tail Probe*, launched on 1995 August 3), and one flying over the polar aurora (i.e., the *Auroral Probe*, launched on 1996 August 29). One of the instruments onboard,

[9] http://www.oso.noaa.gov/goes/.

[10] http://goespoes.gsfc.nasa.gov/project/index.html.

[11] http://www.iki.rssi.ru/interball/.

RF15, comprises a solar photometer and an imager, designed for multi-band high-resolution measurements of the integral solar flux in the energy range between 2 keV and 240 keV as well as for imaging of solar flares in the 2–8 keV energy range. The X-ray imager has rotation-modulated collimators, similar to RHESSI, and thus is capable of Fourier imaging of solar flares (Sylwester et al. 2000).

TIMED-SEE[12] is the *Solar EUV Experiment (SEE)* instrument onboard the NASA *Thermosphere Ionosphere Mesosphere Energetics and Dynamics (TIMED)* mission, developed at the *Laboratory for Atmospheric and Space Physics (LASP)* at the University of Colorado, launched on December 2001. It serves to study solar irradiance and variability, in the VUV wavelength range of 0–200 nm, including the soft X-ray (XUV) range of 0–30 nm, the extreme-ultraviolet (EUV) range of 0–120 nm, and the far ultraviolet (FUV) range of 120–200 nm. TIMED/SEE data also served for cross-calibration with SOHO/EIT irradiances (Woods et al. 2005, Hock and Eparvier 2008).

The *SMEI (Solar Mass Ejection Imager)*[13] is an instrument designed to detect the transient clouds of hot ionized gases that are launched by a *coronal mass ejection (CME)* from the solar surface and propagate through the entire interplanetary space and heliosphere. Of most interest are those CMEs that are directed towards Earth and have impacts on Earth-orbiting satellites, electrical power distribution networks, and long-distance radio communication. The SMEI spacecraft was launched on 2003 January 6, operated successfully for 8 years, and stopped data-taking on 2011 September 28. SMEI data were used for tomographic reconstruction of the density enhancements associated with the propagation of interplanetary CMEs, in conjunction with interplanetary scintillation data, and provided information for space weather forecasting (Eyles et al. 2003; Jackson et al. 2004).

The *SOlar Radiation and Climate Experiment (SORCE)*[14] is a NASA-sponsored satellite, operated by LASP at the University of Colorado, dedicated to both solar and terrestrial observations, making measurements in X-rays, ultraviolet, visible, and near-infrared wavelengths, and total solar radiation. The SORCE measurements specifically address long-term climate changes, natural variability and enhanced climate prediction, and atmospheric ozone and UV-B radiation. The SORCE spacecraft was launched on 2003 January 25 and placed into a 645 km orbit with 40° inclination. SORCE continues to make precise measurements of the *total solar irradiance (TSI)*, which started with the *ERB* instrument in 1979 and has been continued to the present with the *ACRIM* series of measurements. SORCE provides also the solar spectral irradiance from 1 nm to 2000 nm, accounting for 95% of the spectral contribution to TSI. SORCE carries four instruments: the *Spectral Irradiance Monitor (SIM)* (Rottman et al. 2005), the *Solar Stellar Irradiance Comparison Experiment (SOLSTICE)* (McClintock et al. 2005a; McClintock 2005b; Snow et al. 2005), the *Total Irradiance Monitor (TIM)* (Kopp et al. 2005), and the

[12] http://lasp.colorado.edu/see/index.html.

[13] http://www.sr.bham.ac.uk/~mpc/p2/smei/.

[14] http://lasp.colorado.edu/sorce/index.htm.

XUV Photometer System (XPS) (Woods and Rottman 2005, Woods et al. 2005, Woods et al. 2008). Technical documentations about SORCE are mostly given in the special issue of *Solar Physics* volume **230**.

SOXS/GSAT-2 is a *Solar X-ray Spectrometer (SOXS)* instrument on board the Indian *Geostationary Satellite (GSAT-2)*, launched on 2003 May 8 (Jain et al. 2005). SOXS records the full-Sun hard X-ray flux from 4 keV to 10 MeV with comparable (spectral) energy resolution as RHESSI. Scientific results from the SOXS mission include the detection of the Fe-line feature at 6.4 and 6.7 keV during solar flares (Jain et al. 2006).

1.9 Suborbital and Balloon Flights

Suborbital rocket flights provide short-interval trajectories into the upper atmosphere, typically lasting about 7 min, during which a short, well-planned, one-time measurement in space can be made. Solar rocket flights served mostly for testing new technologies, as a proof of concept for major space-borne missions to follow, and for cross-calibrating orbital instruments. Despite of the relatively short flight times, some rockets manage to produce new science results also, such as the Hi-C observations (see Chaps. 6, 8, and 9). Some of the notable solar rocket flights during the beginning of the twenty-first century include (Table 1.9): Two SWRI/LASP sounding rocket flights launched on 1997 May 15 and 1998 November 2 provided inter-calibration with the EUV imagers on SOHO and TRACE (Auchère

Table 1.9 Selected suborbital flights with solar observations

Instrument	Launch	Reference
SwRI/LASP (Southwest Research Institute)	1997 May 15	Auchère et al. (2001)
SwRI/LASP (Southwest Research Institute)	1998 Nov 2	
MOSES-I (Montana State University)	2006 Feb 8	Kankelborg and Martens (2001); Kankelborg and Thomas (2006)
MOSES-II (Montana State University)	2015 Aug 21	
XDT (XUV Doppler Telescope), ISAS	1998 Jan 31	Kano et al. (2000)
		Kobayashi et al. (2000)
EUNIS-06 (NASA/GSFC)	2006 Apr 12	Thomas and Davila (2001)
EUNIS-07 (NASA/GSFC)	2007 Nov 6	Wang et al. (2010)
EUNIS-13 (NASA/GSFC)	2013 Apr 23	Brosius et al. (2014)
Hi-C (NASA/MSFC)	2012 Jul 11	Kobayashi et al. (2014)
Hi-C (NASA/MSFC)	2018 May 29	
VAULT-II (NRL)	2014 Sept 30	Vourlidas et al. (2016)
CLASP	2015 Sept 3	Giono et al. (2017)
FOXSI-1 (Univ. Berkeley)	2012 Nov 2	Krucker et al. (2014)
FOXSI-2 (Univ. Berkeley)	2014 Dec 11	Ishikawa et al. (2017)
FOXSI-3 (Univ. Berkeley)	2018 Sept 7	

et al. 2001); the *MOSES (Multi-Order Solar EUV Spectrograph)* sounding rocket payload, built by Univ. Montana, flown on 2006 February 8, which demonstrated multi-order EUV tomography (Kankelborg and Martens 2001; Kankelborg and Thomas 2006); the *Solar XUV Doppler Telescope (XDT)* flown by ISAS on 1998 January 31, which demonstrated Doppler shift maps of the Fe XIV 211 Å line (Kano et al. 2000; Kobayashi et al. 2000); the *EUNIS-06* and 07 missions with a EUV normal-incidence spectrometer, first proposed by Thomas and Davila (2001), flown on 2006 April 12 and 2007 November 6, which provided absolute radiometric calibration in the wavelength band of 170–205 Å (Wang et al. 2010) and cross-calibration with CDS/SOHO and EIS/Hinode (Wang et al. 2011); the *Hi-C* sounding rocket flight on 2012 July 11, which carried a 0.2″ EUV imager and revealed spatially resolved magnetic braids in the solar corona with unprecedented spatial resolution (Cirtain et al. 2013; Kobayashi et al. 2014).

Balloon-borne telescopes have been flown to test detectors in wavelengths that are absorbed by the lower Earth's atmosphere (hard X-rays, soft X-rays, EUV) or to test telescopes in optical wavelengths with a superior atmospheric seeing compared with ground-based telescopes. Although some balloon flights have been conducted at low geographic latitudes (e.g., at NASA's Scientific Balloon Facility in Palestine, Texas), the preferred route for long-duration balloons is circling antarctica, where the air is very dry (yielding an optimum seeing at low moisture) and balloons return to the same launch site after a 2–3 week period (Fig. 1.9). Ultra-long-duration balloon flights up to 100 days over the Antarctica and the Arctic are anticipated to provide full annual coverage and at a lower cost than a space-borne payload. We briefly mention a few balloon flights with solar instrumentation: The *High Resolution Gamma-Ray and Hard X-Ray Spectrometer (HIREGS)* payload with hard X-ray and gamma-ray detectors, designed to detect solar and astrophysical high-energy radiation, was flown by the University of Berkeley Space Physics Research Group from November 1994 to January 1995 (Boggs et al. 1998). An 80-cm Ritchey-Chretien solar telescope *GENESIS* that acquired long time series of high spatial resolution (diffraction-limited 0.2″) and vector magnetograms was flown in January 2000 for 17 days in the stratosphere above Antarctica (Bernasconi et al. 2000), studying also the magnetic topology of so-called *Ellerman bombs*. A Japanese balloon-borne hard *X-ray Doppler Telescope (XDT)* to obtain high-resolution spectra (with 3 keV resolution) of solar flares over the energy range of 15–120 keV was flown on 2001 August 29 and 2002 May 24, detecting an M1.1 flare (Kobayashi et al. 2004).

The largest optical telescope flown on a balloon is the (German-built) 1 m aperture Gregory telescope *Sunrise*, which was launched on 2009 June 8 near Kiruna in northern Sweden and floated westward to land on Somerset island in northern Canada on 2009 June 13 (Solanki et al. 2010; Barthol et al. 2011). A reflight of Sunrise took place in 2013 also. The Sunrise telescope carried a UV filter imager and an imaging vector polarimeter (IMAX). The numerous scientific results obtained on the photospheric dynamics observed during this balloon flight are documented in over 20 publications in the special issue of *The Astrophysical Journal Letters* volume **723**.

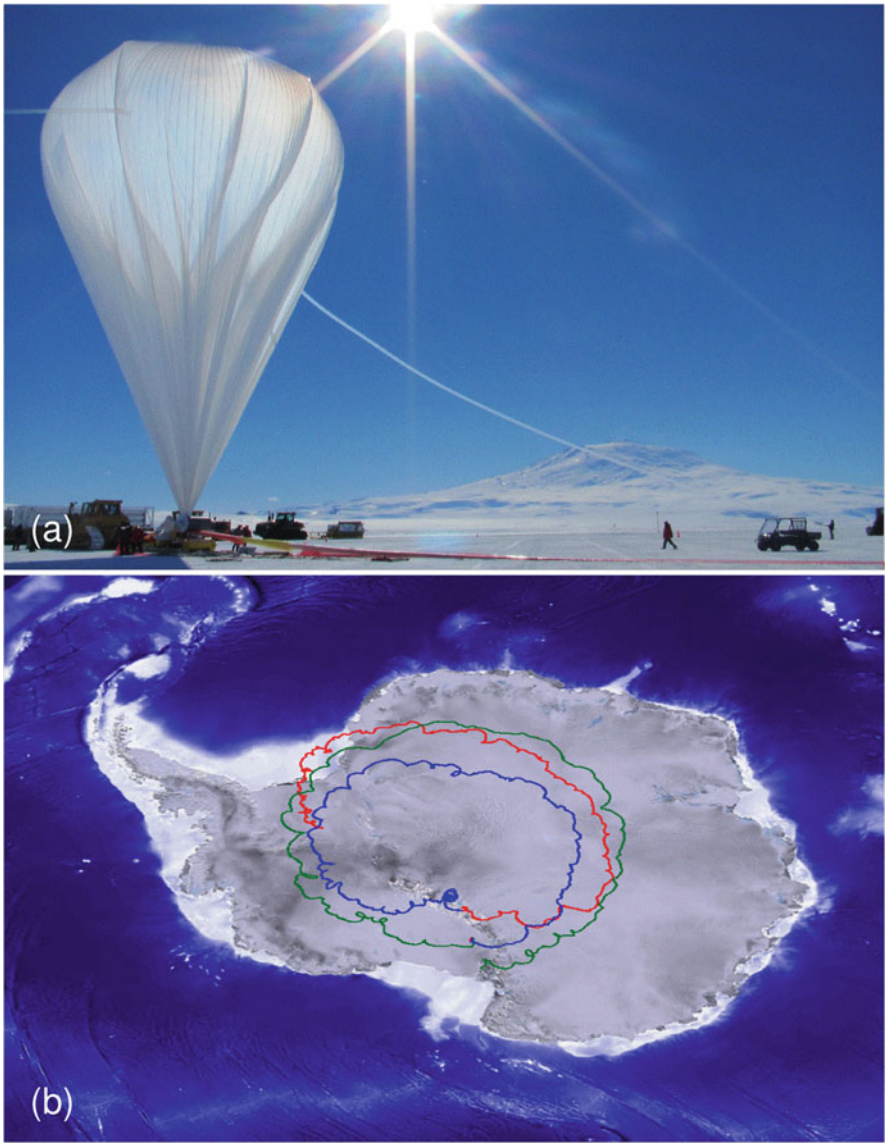

Fig. 1.9 (**a**) Large X-ray and gamma-ray detectors are flown on balloon-borne payloads around Antarctica, such as the Gamma-Ray Imager/Polarimeter for solar flares (GRIPS) and the stratospheric Terahertz Observatory (STO-II) payloads, to altitudes around 130,000 feet, which is above 99.5 percent of the Earth's atmosphere. Campaign preparations are made at McMurdo Station, Antarctica, in mid-October, with a launch pending on the formation of an anticyclone, expected by mid-December. (**b**) The anticyclone takes a balloon on a circular flight trajectory, keeping the balloon over the Antarctic land mass for extended periods of time. The groundtrack of the Super-Tiger mission (2012/2013) shows a record-breaking 55 day travel, after completing nearly three revolutions around the south pole (Credit: NASA, Univ. Berkeley, GRIPS Team)

1.10 Radio Instrumentation

Solar observations in radio wavelengths can be made with ground-based instruments, since the atmosphere is transparent in the radio band. First solar radio observations have been pioneered by Grote Reber as early as 1942, while the first solar radiospectrograph has been built at Penrith (Australia) in 1948. Since about 1970, a large number of radio spectrometers were built around the world and some are still in use for solar observations. A major breakthrough was the advent of radio interferometers, which came online since about 1980, such as the *Very Large Array (VLA)*, the *Owens Valley Radio Observatory (OVRO)*, the French *Nançay Radioheliograph (NRH)*, the Russian *RATAN-600*, or the Japanese *Nobeyama Radioheliograph* (Fig. 1.10), which are all still in use at the time of writing. In Table 1.10 we list the currently operating solar-observing radio interferometers. A more complete list of (radio and optical) ground-based observatories can be found on the *Max Millennium Program* website.[15]

The *Very Large Array (VLA)*[16] is the most powerful radio instrument regarding imaging quality, spatial resolution, and frequency range (metric, decimetric, microwaves), but since it is not solar-dedicated, solar flares are caught only rarely during the sparsely allocated observing time intervals of a few hours.

The *Owens Valley Solar Array (OVSA)*,[17] operated by the *New Jersey Institute of Technology (NJIT)*, is a solar-dedicated radio interferometer that is designed to image solar flares and active regions in microwaves. The ongoing OVSA expansion project complements the currently operating 7 antennas to a total of 15, in the frequency range of 1–18 GHz. Automated localization of solar flares is accomplished with the *Solar Radio Burst Locator (SRBL)* capability.

The *Nobeyama Radioheliograph (NoRH)*[18] (Fig. 1.10) has been the major workhorse of solar radio imaging during the last decades, and completed 25 years of service in 2017. The solar-dedicated NoRH consists of 84 dishes with a maximum baseline of 490 m in east/west direction, operating daily 8 hours since 1992. The NoRH produces full-Sun images, capturing active regions, flares, prominences, coronal mass ejections, and has even sufficient time resolution (0.1–1.0 s) to resolve rapid dynamic phenomena, such as flare loop oscillations.

The *Nançay Radioheliograph (NRH)*[19] is also a long-operating facility that images the Sun at 164, 236, 327, 410, and 432 MHz on a daily basis. The NRH also has the capability of flare multi-channel imaging with sub-second time resolution, which allows it to image the trajectories of type III bursts and coronal mass

[15] http://solar.physics.montana.edu/max_millennium/obs/GBO.html.

[16] http://www.vla.nrao.edu/.

[17] http://www.ovsa.njit.edu/.

[18] http://solar.nro.nao.ac.jp/.

[19] http://secchirh.obspm.fr/nrh.php.

Fig. 1.10 The Nobeyama Radioheliograph (NoRH) in Japan, consisting of 84 parabolic antennas with 80 cm diameter, arranged in two arms, one with a length of 490 m in east/west direction, the other with a length of 220 m in north-south direction. First observations were made in April 1992, and are continued already over 25 years (Credit: NRO/NAO, Japan)

Table 1.10 Solar-observing radio interferometers operational in the new millennium

Acronym	Instrument name and location	Frequency range	Imaging angular resolution
VLA	Very Large Array, New Mexico	80 MHz–4.3 GHz	0.05–700″
OVSA	Owens Valley Solar Array, California	1–18 GHz	7–128″
NoRH	Nobeyama Radioheliograph, Japan	17, 34 GHz	8–16″
NRH	Nançay Radioheliograph, France	164–432 MHz	120–300″
RATAN-600	Special Astrophysical Observatory, Russia	1–7 GHz	12–235″
SSRT	Siberian Solar Radio Telescope, Irkutsk	5.7 GHz	15″
GRH	Gauribidanur Radioheliograph, India	30–110 MHz	300″
BDA	Brazilian Decimetric Array, Brazil	1.2–1.7 GHz	90″
ALMA	Atacama Large Millimeter Array	84–950 GHz	0.5–4.8″

ejections. An overview on the last 65 years of solar radioastronomy is given in Pick and Vilmer (2008).

RATAN-600[20] is a circular array of reflectors that provides high spatial resolution in one scan dimension, in a large number (52) of frequency channels,

[20] http://www.sao.ru/ratan/.

which makes it ideal for frequency-tomography of active regions. 2-D image reconstruction with RATAN-600 data has been faciliated (Golubchina et al. 2002).

The *Siberian Solar Radio Telescope (SSRT)*[21] provides 2-D imaging of the Sun at 5.7 GHz and can switch to a very high time resolution of 56 ms during a flare mode. The current status and upgrades with a future SSRT-based radio heliograph are described in Grechnev (2003a,b).

First solar observations with the *Allen Telescope Array (ATA)*[22] interferometer, the first wide-field, panchromatic, snapshot radio camera for radio astronomy and SETI (Welch et al. 2009), located near Hat Creek (California), have demonstrated high-quality mapping of the Quiet Sun from 1.43 GHz to 6 GHz. Other radio interferometers came online in Gauribidanur (India)[23] in the low frequency range of 40–150 MHz, and the *Brazilian Decimetric Array (BDA)* in the 1.2–1.7 GHz range.

The *Low-Frequency Array (LOFAR)*,[24] built by the Netherlands astronomical foundation ASTRON, is the largest connected radio telescope using an array of about 20,000 small omni-directional antennas, distributed across the Netherlands, Germany, Great Britain, France, and Sweden. Initial LOFAR test stations became operational since 2003, and about 40 stations became operational by 2012. Although this array is mostly dedicated to astrophysical observations of extragalactic and cosmological sources, solar physics and space weather is also an item to be pursued (Bastian 2004; White et al. 2003).

The *Murchison Widefield Array (MWA)* is a low-frequency radio interferometer in Western Australia operating between 80 and 300 MHz. Phase I operations began in 2012 with 2048 dual-polarization dipole antennas arranged in 128 4x4 aperture arrays, and a Phase II upgrade was completed in 2017 that doubled the size of the array. Solar, heliospheric, and ionospheric science are among the instrument's primary science objectives (Bowman et al. 2013).[25]

The *Atacama Large Millimeter Array (ALMA)*[26] is located in the Atacama desert in Chile, where the very dry air conditions allow measurements in mm and sub-mmm wavelengths. The ALMA array consists of 66 radio dishes (with 7 and 12 m diameter) and began scientific observations in 2011 and became fully operational in 2013. The primary science objectives are star birth during the early universe and detailed imaging of local star and planet formation, but ALMA is also thought to be an ideal probe of the solar chromosphere (Loukitcheva et al. 2008). A review of the anticipated solar science to be accomplished with ALMA is compiled in Wedemeyer et al. (2016).

Besides solar radio interferometry that provides images of the Sun, there are a number of radio spectrometers in operation, which all switched from the analog

[21] http://ssrt.iszf.irk.ru/.

[22] http://ral.berkeley.edu/ata/.

[23] http://www.iiap.res.in/centers/radio.

[24] http://www.lofar.org.

[25] http://www.mwatelescope.org/.

[26] http://www.almaobservatory.org/.

recording technology of the last millennium to digital dynamic spectra, which display frequency spectra as a function of time with high time resolution. A world-wide net of solar radio spectrometers, called *e-CALLISTO (Compound Astronomical Low-cost Low-frequency Instrument for Spectroscopy in Transportable Observatory)*[27] has been created, which consists of identical programmable heterodyne receivers, connected through the internet, operating in the 45–870 MHz decimetric range (Benz et al. 2005, 2009). Host observatories of e-CALLISTO are distributed world-wide in over 30 countries.

Other new developments (after 2000) of solar radio spectrometers include: the *Ichon Solar Radio Spectrograph* in Korea, operating in the 30–2500 MHz frequency range and designed to track type II bursts during CMEs (Cho et al. 2003), the Chinese *Solar Broadband Radio Spectrometer (SBRS)* operating in frequency bands from 0.7 to 7.6 GHz with antennas in Bejing, Kunming, and Nanjing (Fu et al. 2004; Ji et al. 2003), the *ARTEMIS IV* solar radio spectrograph with a frequency range of 20–650 MHz, operating at Thermopylae, Greece (Alissandrakis et al. 2009), and the high-sensitivity *Assembly of Metric-band Aperture TElescope and Real-time Analysis System (AMATERAS)* of Tohoku University in Japan (Iwai et al. 2012).

1.11 Optical and Infrared Instrumentation

Last but not least, we will give also an overview of ground-based solar observatories and instrumental capabilities in optical and infrared wavelengths that substantially contributed to a better understanding of the physics of the solar corona during the last decades. A review on adaptive optics is given by Rimmele and Marino (2011).

A list of major optical solar telescopes[28] that are currently operating or in construction is given in Table 1.11. Some new instrumentation developed in the new millennium include: the SOLIS vector spectro-magnetograph (VSM) (Jones et al. 2002), the Fabry-Perot interferometer TESOS at VTT (Tritschler et al. 2002); the *Dutch Open Telescope (DOT)* (Hammerschlag et al. 2009); the *Multi Channel Subtractive Double Pass (MSDP)* of THEMIS (Gelly et al. 2008), solar polarimetry in near-UV with the Zürich Imaging Polarimeter ZIMPOL II (Gandorfer et al. 2004); the Goettingen Fabry-Perot spectrometer for GREGOR (Puschmann et al. 2006), the *Spectro-Polarimeter for Infrared and Optical Regions (SPINOR)* for the Dunn Solar Telescope at NSO (Socas-Navarro et al. 2006); the (new) Big Bear Solar Observatory's digital vector magnetograph with a 160 cm aperture (Goode et al. 2003); Stokes imaging polarimetry using image restoration at the *Swedish 1-m Solar Telescope (SST)* (Van Noort and Rouppe van der Voort 2008), the Tenerife Infrared Polarimeter II, the KIS/IAA *Visible Imaging Polarimeter (VIP)*, a post-focus instrument that upgrades the TESOS spectrometer at the VTT

[27] http://www.e-callisto.org/.

[28] http://en.wikipedia.org/wiki/List_of_solar_telescopes.

Table 1.11 A selection of currently operating large optical solar telescopes

Acronym	Telescope name	Aperture	Year	Location
DKIST	Daniel K.I. Solar Telescope	424 cm	...	Maui, US
GREGOR	GREGOR solar telescope	150 cm	2012-	Tenerife, Spain
BBSO	Big Bear Solar Observatory	160 cm	2008-	Big Bear, US
SST	Swedish 1-m Solar Telescope	100 cm	2002-	La Palma, Spain
DOT	Dutch Open Telescope	45 cm	1997-	La Palma, Spain
THEMIS	THEMIS Solar Telescope (France)	90 cm	1996-	Tenerife, Spain
VTT	Vacuum Tower Telescope (German)	70 cm	1989-	Tenerife, Spain
DST	Dunn Solar Telescope	76 cm	1969-	Sacramento Peak
KPNO	McMath-Pierce Solar Telescope	161 cm	1961-	Kitt Peak, US

(Beck et al. 2010); the *Rapid Oscillations in the Solar Atmosphere (ROSA)* high-cadence, synchronized multi-camera (Jess et al. 2010), and the *Interferometric Bidimensional Spectrometer (IBIS)* at the *Dunn Solar Telescope (DST)* with the *Spectro-Polarimeter (SP)* (Cavallini 2006). The next major optical solar facility is the *Daniel K. Inouye Solar Telescope (DKIST)* (Rimmele et al. 2012; Tritschler et al. 2016), which is currently under construction on the Hawaiian island Maui.

What is the significance of optical and infrared observations from ground-based telescopes to the understanding of the physics of the solar corona? In the following we outline a few topics of solar corona physics that have been pursued in the new millennium.

Solar Eclipse Observations: Solar eclipses observations (Fig. 1.11), the only natural method to see the faint corona without being blinded by the six orders of magnitude brighter photosphere in optical light, still produces high-quality science results, although we observed solar eclipses since millennia. A *Solar Eclipse Coronal Eclipse Imaging System (SECIS)* (Phillips et al. 2000) and new numerical methods of total solar eclipse photography processing (Druckmüller 2013) have been developed.

Coronagraphic Observations: Solar coronagraphs mimic natural solar eclipses by blocking out the bright visible light from the photospheric disk by an occulting disk, invented by Bernard Lyot in 1930. In order to eliminate the Rayleigh-scattered light in the Earth's atmosphere, ground-based coronagraphs are using the polarization to distinguish the (unpolarized) sky brightness from the polarized light of the corona, which is produced by near-perpendicular Thompson-scattering. Space-based coronagraphs are LASCO on SOHO, and COR-1 and COR-2 on STEREO. One of the most used ground-based instruments is the *Mark IV Coronagraph* operated by the *High Altitude Observatory (HAO)* on top of Mauna Loa, Hawaii.

Coronal Magnetometry: Measuring the magnetic field in the solar corona is a very important task, but current capabilities are very limited. A feasibility study of coronal magnetometry (Judge et al. 2001) recommends more dedicated instruments that measure the weak Zeeman-induced Stokes V signal in the Fe XIII line (10,746 Å) and the Hanle effect in the He I line (10,830 Å). Some first full-Stokes

Fig. 1.11 The solar eclipse of 2012 May 20 observed in Doyle, California. The time sequence illustrates the flashing-up of the solar corona during the totality, which is not visible at other times due to the immense brightness contrast (Credit: http://www.aaroads.com/blog/2012/05/22/)

spectro-polarimetric measurements of the forbidden Fe XIII coronal emission line yielded field strengths of $B \approx 4$ G at an altitude of $100''$ above the solar limb (Lin et al. 2004). The DKIST will have the capabilities to measure the magnetic field with high resolution in the photosphere (Fe I, 6303 Å and Mg I, 12,320 Å lines) and chromosphere (Ca II 8542 Å).

Coronal Loop Oscillations and Propagating Waves: There are a number of quasi-periodic coronal phenomena that have been detected in optical wavelengths, associated with standing oscillations or propagating MHD waves in coronal loops. Early detections were made during eclipses or with coronagraphs, and more recently with the SECIS equipment during the eclipse in Bulgaria (Williams et al. 2001, 2002), and in the 10,747 Å and 10,798 Å lines with the *Coronal Multi-channel Polarimeter (CoMP)*[29] at the NSO's Sacramento Peak Observatory (Tomczyk et al. 2007; Tomczyk and McIntosh 2009). The latter observations of oscillations or waves by Tomczyk et al. (2007) were found to be ubiquitous in the solar corona, although at such a small amplitude level that the waves can only be detected in Doppler shift, rather than from the spatial oscillation amplitude. Nevertheless, these observations in white light have spawned a broad discussion about the interpretation in terms of MHD fast-mode kink oscillations, Alfvénic waves, propagating waves, or quasi-periodic flows.

[29] http://www.cosmo.ucar.edu/CoMP.html.

Coupling of Photospheric and Coronal Phenomena: White-light observations reveal the sub-photospheric magneto-convection, magnetic flux emergence, the magnetic field evolution on the solar surface, but also the build-up of non-potential magnetic energy in form of sheared and twisted fields, which leads to eruptive filaments, flares, and coronal mass ejections. There are a number of solar phenomena that reveal a coupling between the photosphere, chromosphere, and corona, such as: acoustic shocks, spicular upflows, soft X-ray jets, explosive events, Ellerman bombs, chromospheric evaporation, nanoflares, bright points, etc. A key question is which of these mostly small-scale variability phenomena contribute to coronal heating. The observational verification of coupled phenomena between the chromosphere and corona requires high spatial and temporal resolution in many wavelengths. One suitable instrument for this task is the *Rapid Oscillations in the Solar Atmosphere (ROSA)* high-cadence, synchronized multi-camera solar imaging system, currently operated at the *Dunn Solar Telescope (DST)* at NSO (Jess et al. 2010). The space-based *Interface Region Imaging Spectrograph (IRIS)*, containing a multi-channel imaging EUV spectrograph has a complementary function to disentangle the interface between the solar chromosphere, transition region, and corona. Additional options that DKIST will provide in this endeavour are discussed in Rimmele et al. (2012) and Tritschler et al. (2016).

1.12 Future Solar Instrumentation

Here we give an outlook of new instrumentations that are currently under construction and expected to be commissioned by about 2018–2010, such as the *Parker Solar Probe*, the *Solar Orbiter*, and the *Daniel K.I. Solar Telescope (DKIST)*.

The *Solar Probe Plus (SPP)* NASA mission, renamed to the *Parker Solar Probe (PSP)* at the launch date (2018 August 12), will be the first spacecraft to fly into the low solar corona (Fox et al. 2016). The trajectory of the PSP is designed to approach the Sun closer and closer during a sequence of seven Venus flybys during nearly 7 years to gradually shrink its orbit around the Sun (Fig. 1.12), coming as close as 6.16×10^6 km (or 7.7 solar radii) in the perihelion, where it will have a speed of ≈ 200 km s^{-1} and an orbital period of 88 days, performing for 24 orbits (5.8 yrs) at least.[30]

The concept of sending a spacecraft as close as a few solar radii to the Sun has been discussed for over five decades, and finally became reality with the successful launch in 2018. The scientific objectives are: (i) Tracing the flow of energy that heats and accelerates the solar corona and solar wind; (ii) determining the structure and dynamics of the plasma and magnetic fields at the sources of the solar wind; and (iii) exploring mechanisms that accelerate and transport energetic particles.

[30] http://parkersolarprobe.jhuapl.edu/The-Mission/index.php.

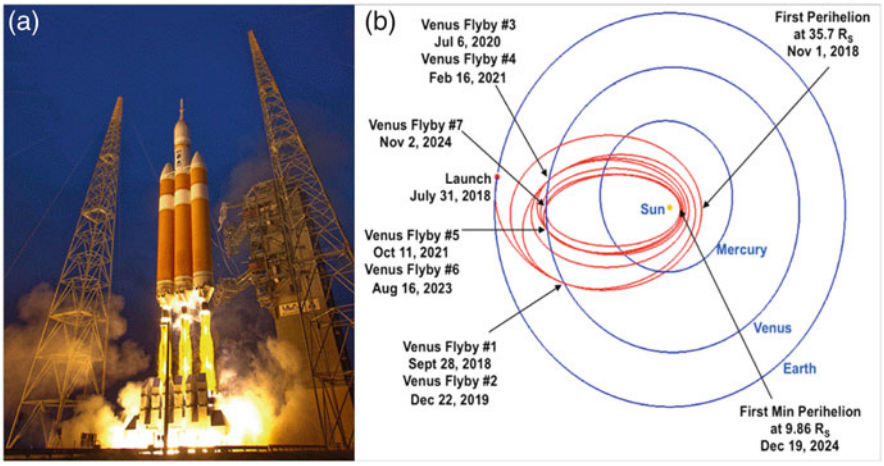

Fig. 1.12 (**a**) Launch of the Parker Solar Probe on 2018 August 12, 3:31 EDT (7:31 UTC), mounted on a Delta IV-Heavy with Upper Stage, and experiencing a maximum launch acceleration of 154 $km^2\ s^{-2}$ (Credit: ULA, NASA). (**b**) Trajectory of PSP, launched on 2018 August, Venus flyby on 2018 October 3, 4:44 am (08:44 UTC), and reaching first perihelion on 2018 Nov 5, 10:27 pm (03:27 UTC), (Credit: NASA)

To accomplish these scientific goals, the PSP is equipped with four major instruments: (i) The *FIELDS Experiment* that makes direct measurements of electric and magnetic fields and waves, Poynting flux, absolute plasma density and electron temperature, spacecraft floating potential and density fluctuactions, and radio emissions; (ii) the *Integrated Science Investigation of the Sun (IS⊙IS)* that makes observations of energetic electrons, protons, and heavy ions that are accelerated to high energies (10s of keV to 100 MeV) in the Sun's atmosphere and inner heliosphere and correlates them with solar wind and coronal structures; (iii) the *Wide-field Imager for Solar PRobe (WISPR)*, which will take images of the solar corona and inner heliosphere, providing images of the solar wind, shocks, and coronal structures; and (iv) the *Solar Wind Electrons Alphas and Protons (SWEAP)* Investigation, which will count the most abundant particles in the solar wind (electrons, protons, and helium ions) and measures their velocity, density, and temperature.

The most innovative technology that allows the spacecraft to function in such extreme environments close to the Sun uses an unprecedented heat protection capability, which consists of a 11.43 cm thick carbon-composite shield, which will need to withstand temperatures outside the spacecraft, reaching nearly 1377 degrees Celsius. The compact, solar-powered probe will house solar arrays that will retract and extend as the spacecraft swings toward or away from the Sun during several loops around the inner solar system, making sure that the panels stay at proper temperatures and power levels. At its closest passes the spacecraft must survive solar intensity of about 475 times what spacecraft experience while orbiting Earth.

The *Solar Orbiter*[31] is a planned Sun-observing space mission and is currently under development by the *European Space Agency (ESA)*. The mission is planned to be launched with an Atlas V from Cape Canaveral in Florida in 2020. The mission duration is planned for 7–10 years. Solar Orbiter will have a special trajectory that can observe the solar north and south pole regions, the sources of the fast solar wind in polar coronal holes. The satellite will be placed in an elliptic heliocentric orbit with a perihelion of 0.28 AU, an aphelion of 0.8–0.9 AU, and an inclination angle of 0–34 degrees with respect to the ecliptic plane. The orbit leads to a perihelion slightly inside of the planet Mercury, with a close approach (within $\approx$ 60 solar radii) to the Sun every five months, while the PSP approaches the Sun as close as 7.7 solar radii. Both the PSP and the Solar Orbiter are expected to coordinate observations.

The payload of the Solar Orbiter contains heliospheric in-situ instruments, such as the *Solar Wind Analyser (SWA)*, the *magnetometer (MAG)*, and *Radio and Plasma Wave Analyser (PRW); and solar-remote-sensing instruments, such as the Polarimetric and Helioseismic Imager (PHI), (Gandorfer et al. 2018; Alvarez-Herrero et al. 2017; Barandiaran et al. 2017), the EUV full-Sun and high-resolution imager (EUI)* (Schühle et al. 2018; Halain et al. 2016, 2017, 2018), the *Spectral Imager (SPICE)* (Caldwell et al. 2017; Peleikis et al. 2017); the *Spectrometer Telescope for Imaging X-rays (STIX)* (Limousin et al. 2016); the coronagraph *Multi Element Telescope for Imaging and Spectroscopy (METIS)* (Capobianco et al. 2018; Schühle et al. 2018; Casti et al. 2018; Antonucci et al. 2017; Da Deppo et al. 2017; Landini et al. 2017; Frassetto et al. 2017; Alvarez-Herrero et al. 2017; Verroi et al. 2017; Romoli et al. 2017; Uslenghi et al. 2017; Sandri et al. 2017; Pancrazzi et al. 2016; Dolei et al. 2016), and the *Heliospheric Imager (SoloHI)* (Thernisien et al. 2018). Initial studies are underway to predict the solar wind conditions during the PSP and the Solar Orbiter mission (Venzmer and Bothmer 2018).

There is some overlap in the science goals of the Solar Orbiter and of the PSP. The Solar Orbiter aims to understand: How and where do the solar wind plasma and magnetic field originate in the corona? How do solar transients drive heliospheric variability? How do solar eruptions produce energetic particle radiation that fills the heliosphere? How does the solar dynamo work and drive connections between the Sun and the heliosphere? However, the Solar Orbiter has comprehensive imaging and spectroscopy diagnostics to get a close look at the solar atmosphere and the interior, while the PSP does not.

The *Daniel K. Inouye Solar Telescope (DKIST)*[32] represents the most ambitious next-generation project of ground-based solar research, (formerly known as the *Advanced Technology Solar Telescope, ATST*), built on top of the mountain Haleakala on the Hawaiian island Maui (USA), and involves a collaboration of 22 institutions, coordinated under the auspices of NSO. The observatory site on Haleakala was chosen for its unsurpassed quality of the sky above the summit (at an altitude of 3084 m, Fig. 1.13a). DKIST is by far the largest existing solar telescope

[31] http://sci.esa.int/solar-orbiter.

[32] https://dkist.nso.edu.

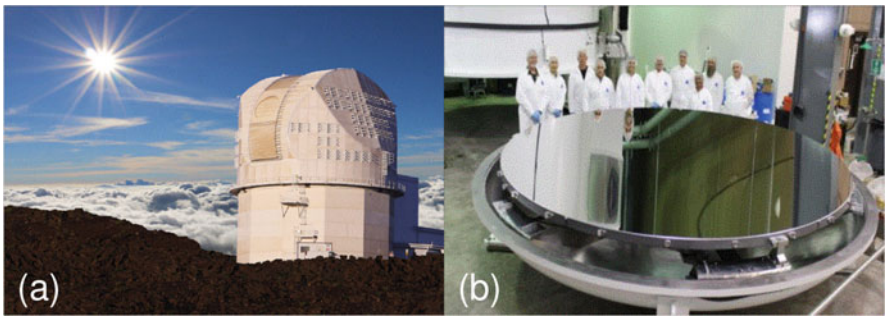

Fig. 1.13 (**a**) The Daniel K. Inouye Solar Telescope on the summit of Haleakala on the island Maui, at an altitude of 3084 m. (**b**) The DKIST primary mirror has been successfully aluminized in preparation for installation into the Telescope Mount Assembly, (Credit: NSO, NSF)

(see Table 1.11), which faciliates as key novel capability an unprecedented spatial resolution and very low stray light, enabling coronal observations of the magnetic field and MHD waves. The diameter of the primary mirror is 4.24 m (Fig. 1.13b), the diameter of the secondary mirror is 0.65 m, and the telescope is supported by an Altazimuth mount. NSO announced the start of ATST construction in November 2012. The ATST became renamed to DKIST for late Hawaiian senator Inouye in December 2013. The large enclosure components for DKIST reached Haleakala in July 2015. Northrop Grumman successfully delivered the deformable mirror for the world's largest solar telescope in July 2015. The primary mirror was delivered in August 2017, and completion of the DKIST observatory is expected in 2019/2020.

The DKIST first light instrument capabilities include: a *Visible Broadband Imager (VBI)*, a *Visible spectropolarimeter (ViSP)*, a *Visible Tunable Filter (VTF)*, a *Visible Broadband Imager (VBI)*, a *Diffraction Limited Near Infrared Spectropolarimeter (DL-NIRSP)*, a *Cryogenic Near Infrared Spectropolarimeter (Cryo-NIRSP)*, and a *Context Imager (Cryo-NIRSP)*. The DKIST is capable to observe the Sun in visible to near-infrared wavelengths in an off-axis Gregorian configuration that has an unobstructed aperture. Adaptive optics compensates for atmospheric turbulence, and should allow high-resolution observations down to scales of 20 km on the solar surface ($\approx$ 0.03 arcsec).

The planned science to be studied with DKIST encompasses a very broad range of targeted solar science topics (e.g., Rimmele et al. 2012; Tritschler et al. 2016), such as: (i) Flux tubes, the building blocks of solar and stellar magnetic fields; (ii) magnetic field generation, local dynamos and the solar cycle; (iii) magnetic and current helicity and its relevance to the dynamo problem; (iv) interaction of magnetic fields and mass flows; (v) flares and coronal mass ejections; (vi) inhomogeneous stellar atmospheres, (vii) magnetic fields and stellar coronae, and (viii) long-term studies of the Sun and solar cycles.

References

(1.1) Solar Missions Overview and Moore's Law

Aschwanden, M.J. 2004, 2005, *Physics of the solar corona - An introduction*, Praxis and Springer: New York, [660 c, 51 c/y].

Aschwanden, M.J. 2010, *Image processing techniques and feature recognition in solar physics*, (Invited review), SoPh 262, 235, [34 c, 5 c/y].

Moore, G. 2015, *Gordon Moore: The man whose name means progress, the visionary engineer reflects on 50 years of Moore's law*, IEEE Spectrum: Special report: 50 Years of Moore's law.

(1.2) The RHESSI Mission

Arzner, K. 2002, *Time-domain demodulation of RHESSI light curves*, SoPh 210, 213, [6 c, 0.4 c/y].

Aschwanden, M.J., Schmahl, E., RHESSI Team 2002, *Reconstruction of RHESSI solar flare images with a forward-fitting method*, SoPh 210, 193, [10 c, 0.6 c/y].

Emslie, A.G. et al. 2011, *High-energy aspects of solar flares: A RHESSI-inspired monograph* in the Special Issue of SSRv Volume 159, [5 c, 1 c/y].

Fivian, M., Hemmeck, R., McHedlishvili, A., et al. 2002, *RHESSI aspect reconstruction*, SoPh 210, 87, [17 c, 1 c/y].

Hurford, G.J., Schmahl, E.J., Schwartz, R.A., et al. 2002, *The RHESSI imaging concept*, SoPh 210, 61, [365 c, 24 c/y].

Hurford, G.J. and Curtis, D.W. 2002, *The PMTRAS roll aspect system of RHESSI*, SoPh 210, 101, [27 c, 2 c/y].

Hurford, G.J., Schwartz, R.A., Krucker, S., et al. 2003, *First gamma-ray images of a solar flare*, ApJ 595, 77, [94 c, 6 c/y].

Lin, R.P., Dennis, B.R., Hurford, G.J., et al. 2002, *The Reuven Ramaty High-Energy Solar Spectroscopic Imager (RHESSI)*, SoPh 210, 3, [1076 c, 69 c/y].

Massone, A.M., Piana, M., Conway, A. et al. 2003, *A regularization approach for the analysis of RHESSI X-ray spectra*, A&A 405, 325, [10 c, 0.7 c/y].

McConnell, M.L., Ryan, J.M., Smith, D.M., et al. 2002, *RHESSI as a hard X-ray polarimeter*, SoPh 210, 125, [31 c, 2 c/y].

Metcalf, T.R., Hudson, H.S., Kosugi, T., et al. 1996, *Pixon-based multiresolution image reconstruction for Yohkoh's hard X-ray telescope*, ApJ 466, 585, [102 c, 5 c/y].

Schwartz, R.A., Csillaghy, A., Tolbert, A.K., et al. 2002, *RHESSI data analysis software: Rationale and methods*, SoPh 210, 165, [79 c, 6 c/y].

Smith, D.M., Lin, R.P., Turin, P., et al. 2002, *The RHESSI spectrometer*, SoPh 210, 33, [268 c, 18 c/y].

(1.3) The STEREO Mission

Acuna, M.H., Curtis, D., Scheifele, J.L., et al. 2008; *The STEREO/IMPACT magnetic field experiment*, SSRv 136, 203, [126 c, 13 c/y].

Bale, S.D., Ullrich, R., Goetz, K., et al. 2008, *The electric antennas for the STEREO/ WAVES experiment*, SSRv 136, 529, [62 c, 6 c/y].

Bewsher, D., Brown, D.S., Eyles, C.J., et al. 2010, *Determination of the photometric calibration and large-scale flatfield of the STEREO heliospheric Imagers, I. HI-1*, SoPh 264, 433, [26 c, 3 c/y].

Bougeret, J.L., Goetz, K., Kaiser, M.L., et al. 2008, *S/WAVES: The radio and plasma wave investigation on the STEREO mission*, SSRv 136, 487, [194 c, 20 c/y].

Brown, D.S., Bewsher, D., and Eyles, C.J. 2009, *Calibrating the pointing and optical parameters of the STEREO heliospheric imagers*, SoPh 254, 185, [41 c, 5 c/y].

Driesman, A., Hynes, S., George, C. 2008, *The STEREO observatory*, SSRv 136, 17, [18 c, 2 c/y].

Eyles, C.J., Harrison, R.A., Davis, C.J., et al. 2009, *The heliospheric imagers onboard the STEREO mission*, SSRv 254, 387, [189 c, 22 c/y].

Galvin, A.B., Kistler, L.M., Popecki, M.A., et al. 2008, *The plasma and suprathermal ion composition (PLASTIC) investigation on the STEREO observations.*, SSRv 136, 437, [212 c, 22 c/y].

Harrison, R.A., Davies, J.A., Rouillard, A.P., et al. 2009, *Two years of the STEREO heliospheric imagers. Invited review*, SoPh 256, 219, [38 c, 4 c/y].

Howard, R.A., Moses, J.D., Vourlidas, A., et al. 2008, *Sun Earth Connection Coronal and Heliospheric Investigation (SECCHI)*, SSRv 136, 67, [830 c, 87 c/y].

Kaiser, M.L., Kucera, T.A., Davila, J.M. et al. 2008, *The STEREO mission: An introduction*, SSRv 136, 5, [629 c, 66 c/y].

Lin, R.P., Curtis, D.W., Larson, D.E., et al. 2008, *The STEREO IMPACT suprathermal electron (STE) instrument*, SSRv 136, 241, [29 c, 3 c/y].

Luhmann, J.G., Curtis, D.W., Schroeder, P., et al. 2008; *STEREO IMPACT investigation goals, measurements, and data products overview*, SSRv 136, 117, [151 c, 16 c/y].

Mason, G.M., Korth, A., Walpole, P.H., et al. 2008, *The suprathermal ion telescope (SIT) for the IMPACT/SEP investigation*, SSRv 136, 257, [38 c, 4 c/y].

Mewaldt, R.A., Cohen, C.M.S., Cook, W.R., et al. 2008, *The low-energy telescope (LET) and SEP central electronics for the STEREO mission*, SSRv 136, 285, [59 c, 6 c/y].

Müller-Mellin, R., Böttcher, S., Falenski, J., et al. 2008, *The solar electron and proton telescope for the STEREO mission*, SSRv 136, 363, [61 c, 6 c/y].

Sauvaud, J.A., Larson, D., Aoustin, C., et al. 2008; *The IMPACT solar wind electron analyzer (SWEA)*, SSRv 136, 227, [54 c, 6 c/y].

Thompson, W.T. and Reginald, N.L. 2008, *The radiometric and pointing calibration of SECCHI COR1 on STEREO*, SSRv 250, 443, [25 c, 3 c/y].

Thompson, W.T., Wei, K., Burkepile, J.T. et al. 2010, *Background subtraction for the SECCHI/COR telescope aboard STEREO*, SSRv 262, 213, [21 c, 3 c/y].

von Rosenvinge, T.T., Reames, D.V., Baker, R., et al. 2008, *The high energy telescope for STEREO*, SSRv 136, 391, [48 c, 5 c/y].

(1.4) The Hinode Mission

Brown, C.M., Feldman, U., Seely, J.F., et al. 2008, *Wavelengths and intensities of spectral lines in the 171–211 and 245–291 Å ranges from five solar regions recorded by the EIS on Hinode*, ApJS 176, 511, [104 c, 11 c/y].

Culhane, J.L., Harra, L.K., James, A.M., et al. 2007, *The EUV imaging spectrometer for Hinode*, SoPh 243, 19, [592 c, 56 c/y].

Danilovic, S., Gandorfer, A., Lagg, A., et al. 2008, *The intensity contrast of solar granulation: comparing Hinode SP results with MHD simulations*, A&A 484, L17, [80 c, 8 c/y].

Del Zanna, G. 2013, *A revised radiometric calibration for the Hinode/Eis instrument*, A&A 555, A47, [45 c, 10 c/y].

Golub, L., Deluca, E., Austin, G., et al. 2007, *The X-Ray telescope (XRT) for the Hinode mission*, SoPh 243, 63, [441 c, 42 c/y].

Ichimoto, K., Lites, B., Elmore, D., et al. 2008, *Polarization calibration of the Solar Optical Telescope (SOT) onboard Hinode*, SoPh 249, 233, [248 c, 26 c/y].

Kano, R., Sakao, T., Hara, H., et al. 2008, *The Hinode X-ray telescope (XRT): camera design, performance and operations*, SoPh 249, 263, [72 c, 8 c/y].

Kosugi, T., Matsuzaki, K., Sakao, T., et al. 2007, *The Hinode (Solar-B) mission: An overview*, SoPh 243, 3, [1063 c, 99 c/y].
Lites, B.W., Akin, D.L., Card, G., et al. 2013, *The Hinode Spectro-Polarimeter*, SoPh 283, 579, [73 c, 16 c/y].
Mathew, S.K., Zakharov, V., Solanki, S.K. 2009, *Stray light correction and contrast analysis of Hinode broad-band images*, A&A 501, L19, [38 c, 4 c/y].
Shimizu, T., Nagata, S., Tsuneta, S., et al. 2008, *Image stabilization system for Hinode (Solar-B) solar optical telescope*, SoPh 249, 221, [200 c, 21 c/y].
Suematsu, Y., Tsuneta, S., Ichimoto, K., et al. 2008, *The solar optical telescope of Solar-B (Hinode): The optical telescope assembly*, SoPh 249, 197, [286 c, 30 c/y].
Tiwari, S.K., Venkatakrishnan, P., Gosain, S., et al. 2009, *Effect of polarimetric noise of the estimation of twist and magnetic energy of force-free fields*, ApJ 700, 199, [22 c, 3 c/y].
Tsuneta, S., Ichimoto, K., Katsukawa, Y., et al. 2008, *The solar optical telescope for the Hinode mission: An overview*, SoPh 249, 167, [820 c, 86 c/y].
Wang, D., Zhang, M., Li. H., et al. 2009, *A cross-comparison of cotemporal magnetograms obtained with MDI/SOHO and SP/Hinode*, SoPh 260, 233, [15 c, 2 c/y].
Wedemeyer-Böhm, S. 2008, *Point spread functions for the solar optical telescope onboard Hinode*, A&A 487, 399, [50 c, 5 c/y].

(1.5) The SDO Mission

Boerner, P.F., Edwards, C., Lemen, J. et al. 2012, *Initial calibration of the Atmospheric Imaging Assembly (AIA) on the Solar Dynamics Observatory (SDO)*, SoPh 275, 41, [200 c, 36 c/y].
Boerner, P.F., Testa, P., Warren, H., et al. 2014, *Photometric and thermal cross-calibration of solar EUV instruments*, SoPh 289, 2377, [31 c, 9 c/y].
Borrero, J.M., Tomczyk, S., Kubo, M., et al. 2011, *VFISV: Very Fast Inversion of the Stokes Vector for the Helioseismic and Magnetic Imager*, SoPh 273, 267, [153 c, 24 c/y].
Centeno, R., Schou, J., Hayashi, K., et al. 2014, *The Helioseismic and Magnetic Imager (HMI) vector magnetic field pipeline: Optimization of the spectral line inversion code*, SoPh 289, 3531, [35 c, 10 c/y].
Couvidat, S., Schou, J., Hoeksema, J.T., et al. 2016, *Observables processing for the Helioseismic and Magnetic Imager instrument on the Solar Dynamics Observatory*, SoPh 291, 1887, [18 c, 12 c/y].
Hock, R.A., Chamberlin,P.C., Woods,T.N., et al. 2012, *Extreme ultraviolet Variability Experiment (EVE) multiple EUV grating spectrographs (MEGS): Radiometric calibrations and results*, SoPh 275, 145, [29 c, 5 c/y].
Hoeksema, J.T., Liu, Y., Hayashi, K., et al. 2014, *The Helioseismic and Magnetic Imager (HMI) vector magnetic field pipeline: Overview and performance*, SoPh 289, 3483, [133 c, 38 c/y].
Lemen, J.R., Title, A.M., Akin, D.J., et al. 2012, *The Atmospheric Imaging Assembly (AIA) on the Solar Dynamics Observatory (SDO)*, SoPh 275, 17, [1447 c, 263 c/y].
Liu, Y., Hoeksema, J.T., Scherrer, P.H., et al. 2012, *Comparison of line-of-sight magnetograms taken by the Solar Dynamics Observatory/Helioseismic and Magnetic Imager and Solar and Heliospheric Observatory/Michelson Doppler Imager*, SoPh 279, 295, [92 c, 17 c/y].
Pesnell, W.D., Thompson, B.J., and Chamberlin, P.C. 2012, *The Solar Dynamics Observatory (SDO)*, SoPh 275, 3, [767 c, 139 c/y].
Scherrer, P.H., Schou, J., Bush, R.I., et al. 2012, *The Helioseismic and Magnetic Imager (HMI) Investigation for the Solar Dynamics Observatory (SDO)*, SoPh 275, 207, [625 c, 114 c/y].
Schou, J., Borrero, J.M., Norton, A.A., et al. 2012a, *Polarization Calibration of the Helioseismic and Magnetic Imager (HMI) onboard the Solar Dynamics Observatory (SDO)*, SoPh 275, 327, [62 c, 11 c/y].

Schou, J., Scherrer, P.H., Bush, R.I., et al. 2012b, *Design and Ground Calibration of the Helioseismic and Magnetic Imager (HMI) Instrument on the Solar Dynamics Observatory (SDO)*, SoPh 275, 229, [667 c, 121 c/y].

Wachter, R., Schou, J., Rabello-Soares, M.C., et al. 2012, *Image quality of the Helioseismic and Magnetic Imager (HMI) onboard the Solar Dynamics Observatory (SDO)*, SoPh 275, 261, [35 c, 6 c/y].

Woods, T.N., Eparvier, F.G., Hock, R., et al. 2012, *Extreme ultraviolet Variability Experiment (EVE) on the Solar Dynamics Observatory (SDO): Overview of science objectives, instrument design, data products, and model developments*, SoPh 275, 115, [178 c, 32 c/y].

Zhao, J., Couvidat,S., Bogart,R.S., et al. 2012, *Time-distance helioseismology data analysis pipeline for helioseismic and magnetic imager onboard Solar Dynamics Observatory (SDO/HMI) and its initial results*, SoPh 275, 375, [30 c, 5 c/y].

(1.6) The IRIS Mission

De Pontieu, B., Title, A.M., Lemen, J.R., et al. 2014, *The Interface Region Imaging Spectrograph (IRIS)*, SoPh 289, 2733, [342 c, 98 c/y].

Heinzel, P., and Kleint, L. 2014, *Hydrogen Balmer continuum in solar flares detected by the Interface Region Imaging Spectrograph (IRIS)*, ApJ 794, L23, [30 c, 9 c/y].

Leenaarts, J., Pereira, T.M.D., Carlsson, M., et al. 2013a, *The formation of IRIS diagnostics. I. A quintessential model Atom of Mg II and general formation properties of the Mg II h and k Lines*, ApJ 772, 89, [55 c, 12 c/y].

Leenaarts, J., Pereira, T.M.D., Carlsson, M., et al. 2013b, *The formation of IRIS diagnostics. II. The formation of the Mg II h and k lines in the solar atmosphere*, ApJ 772, 90, [73 c, 16 c/y].

Lin, H.H., and Carlsson, M. 2015, *The formation of IRIS diagnostics. VII. The formation of the OI 135.56 nm line in the solar atmosphere*, ApJ 813, 34, [8 c, 3 c/y].

Pereira, T.M.D., Leenaarts, J., De Pontieu, B., et al. 2013, *The formation of IRIS diagnostics. III. Near-ultraviolet spectra and images*, ApJ 778, 143, [42 c, 9 c/y].

Pereira, T.M.D., Carlsson, M., De Pontieu, B., et al. 2015, *The formation of IRIS diagnostics. IV. The Mg II triplet lines as a new diagnostic for lower chromospheric heating*, ApJ 806, 14, [30 c, 12 c/y].

Rathore, B. and Carlsson, M. 2015, *The formation of IRIS diagnostics. V. A quintessential model atom of C II and general formation properties of the C II lines at 133.5 nm*, ApJ 811, 80, [10 c, 4 c/y].

Rathore, B., Carlsson, M., Leenaarts, J., and De Pontieu, B. 2015a, *The formation of IRIS diagnostics. VI. The diagnostic potential of the C II lines at 133.5 nm in the solar atmosphere*, ApJ 811, 81, [16 c, 6 c/y].

Rathore, B., Pereira, T.M.D., Carlsson, M., and De Pontieu, B. 2015b, *The formation of IRIS diagnostics. VIII. IRIS observations in the C II lines at 133.5 nm multiplet*, ApJ 814, 70, [3 c, 1 c/y].

(1.7) The CORONAS Missions

Debnath, D., Nandi, A., Rao, A.R., et al. 2011, *Instruments of RT-2 experiment onboard CORONAS-PHOTON and their test and evaluation I: Ground calibration of RT-2/S and RT-2/G*, Experimental Astronomy 29, 1.

Denisov, Y.I., Kalegaev, V.V., Myagkova, I.N., et al. 2011, *Experiment on the measurement of charged particle flows with ELECTRON-M-PESCA onboard the CORONAS-PHOTON solar research satellite*, SoSyR 45, 206, [3 c, 0.5 c/y].

Dudnik, A.V., Persikov, V.K., Zalyubovsky, I.I., et al. 2011, *High-sensitivity STEP-F spectrometer-telescope for high-energy particles of the CORONAS-PHOTON satellite experiment*, SoSyR 45, 212, [3 c, 0.5 c/y].

Dudnik, A.V., Podgorski, P., Sylwester, J., et al. 2012, *X-ray spectrophotometer SphinX and particle spectrometer STEP-F of the satellite experiment CORONAS- PHOTON. Preliminary results of the joint data analysis*, SoSyR 46/2, 160, [1 c, 0.2 c/y].

Gburek, S., Sylwester, J., Kowalinski, M., et al. 2011a, *SphinX soft X-ray spectrophotometer: Science objectives, design and performance*, SoSyR 45/3, 189, [17 c, 3 c/y].

Gburek, S., Siarkowski, M., Kepa, A., et al. 2011b, *Soft X-ray variability over the present minimum of solar activity as observed by SphinX*, SoSyR 45/3, 182, [8 c, 1 c/y].

Gburek, S., Sylwester, J., Kowalinski, M., et al. 2013, *SphinX: The Solar Photometer in X-Rays*, Solar Physics 283, 631. [2 c/y, 9 c].

Kotoch, T.B., Nandi, A., Debnath, D., et al. 2011, *Instruments of RT-2 experiment onboard CORONAS-PHOTON and their test and evaluation II: RT-2/CZT Payload*, Experimental Astronomy 29, 27, [3 c, 0.5 c/y].

Kotov, Y.D. 2011, *Scientific goals and observational capabilities of the CORONAS-PHOTON solar satellite project*, SoSyR 45, 93, [10 c, 2 c/y].

Kotov, Y.D., Glyankenko, A.S., Arkhangelsky, A., et al. 2011a, *Experimental study of parameters of X-ray radiation from solar flares using the PENGUIN-M instrument aboard the CORONAS-PHOTON spacecraft*, SoSyR 45, 135, [4 c, 0.6 c/y].

Kotov, Y.D., Kochemasov, A.V., Glyankenko, A.S., et al. 2011b, *PHOKA Experiment: Description of the equipment and first results*, SoSyR 45, 153, [3 c, 0.5 c/y].

Kotov, Y.D., Yurov, V.N., Lupar, E.E., et al. 2011c, *The NATALYA-2M spectrometer of high-energy radiations for the CORONAS-PHOTON space project*, SoSyR 45, 97, [1 c, 0.2 c/y].

Kuzin, S.V., Bogachev, S.A., Zhitnik, I.A., et al. 2009, *TESIS experiment on EUV imaging spectroscopy of the Sun*, AdSpR 43, 1001, [14 c, 2 c/y].

Kuzin, S.V., Zhitnik I.A., Shestov, S.V., et al. 2011a, *The TESIS Experiment on the CORONAS-PHOTON Spacecraft*, SoSyR 45, 162, [16 c, 2 c/y].

Kuzin, S.V., Shestov, S.V., Bogachev, S.A., et al. 2011b, *Processing method of images obtained during the TESIS/CORONAS-PHOTON experiment*, SoSyR 45, 174, [1 c, 0.2 c/y].

Kuznetsov, S.N., Kurt, V., Yushkov, B.Y., et al. 2011a, *Gamma-ray and high-energy-neutron measurements on CORONAS-F during the solar flare of 28 October 2003*, SoPh 268, 175, [23 c, 4 c/y].

Kuznetsov, S.N., Sobelman, I.I., Zhitnik, I.A. et al. 2011b, *Results of solar observations by the CORONAS-F payload*, AdSpR 47, 1538.

Levedev, N.I., Kuznetsov, V.D., Zhugzhda, Yu.D. et al. 2011, *Observations of global oscillations of the Sun in the SOKOL experiment onboard the CORONAS-PHOTON satellite*, SoSyR 45/3, 200, [1 c, 0.2 c/y].

Nandi, A., Palit, S., Debnath, D., et al. 2011, *Instruments of RT-2 experiment onboard CORONAS-PHOTON and their test and evaluation III: Coded aperture mask and Fresnel zone plates in RT-2/CZT Payload*, Experimental Astronomy 29, 55, [5 c, 0.8 c/y].

Oraevsky, V.N., and Sobelman, I.I. 2002, *Comprehensive studies of solar activity on the CORONAS-F satellite*, Astron. Lett. 28/6, 401.

Pankov, V.M., Prokhin, V.L., and Khavenson, N.G. 2006, *The RPS-1 X-ray CdTe spectrometer onboard the CORONAS-F satellite*, SoSyR 40, 314, [8 c, 0.7 c/y].

Reva, A., Shestov, S., Bogachev, S., et al. 2011, *Investigation of hot X-ray points (HXPs) using spectroheliograph Mg uc(xii) experiment data from CORONAS-F/SPIRIT*, SoPh 276, 97.

Sarkar, R., Mandal, S., Debneth, D., et al. 2011, *Instruments of RT-2 experiment onboard CORONAS-PHOTON and their test and evaluation IV: Background simulations using GEANT-4 toolkit*, Experimental Astronomy 29, 85, [5 c, 0.8 c/y].

Sreekumar, S.S., Vinod, P., Samuel, E., et al. 2011, *Instruments of RT-2 experiment onboard CORONAS-PHOTON and their test and evaluation V: Onboard software, data structure, telemetry and telecommand*, Experimental Astronomy 29, 109, [1 c, 0.2 c/y].

Trofimov, Y.A., Yurov, V.N., Kotov, Y.D., et al. 2011, *The Experiment with the fast X-Ray monotor (BRM) instrument onboard the CORONAS-PHOTON*, SoSyR 45, 146, [2 c, 0.3 c/y].

(1.8) Solar-Terrestrial Space Missions

Evans, J.S., Strickland, D.J., Woo, W.K., et al. 2010, *Early observations by the GOES-13 Solar Extreme Ultraviolet Sensor (EUVS)*, SoPh 262, 71, [10 c, 1 c/y].

Eyles, C.J., Simnett, G.M., Cooke, M.P., et al. 2003, *The Solar Mass Ejection Imager (SMEI)*, SoPh 217, 319, [144 c, 10 c/y].

Hill, S.M., Pizzo, V.J., Balch, C.C., et al. 2005, *The NOAA GOES-12 Solar X-Ray Imager (SXI). I. Instrument, operations, and data*, SoPh 226, 255, [69 c, 6 c/y].

Hock, R.A., and Eparvier, F.G. 2008, *Cross-calibration of TIMED SEE and SOHO EIT irradiances*, SoPh 250, 207, [3 c, 0.3 c/y].

Jackson, B.V., Buffington, A., Hick, P.P., et al. 2004, *The Solar Mass-Ejection Imager (SMEI) mission*, SoPh 225, 177, [99 c, 7 c/y].

Jain, R., Pradhan, A.K., Joshi, V., et al. 2006, *The Fe-line feature in the X-ray spectrum of solar flares: First results from the SOXS mission*, SoPh 239, 217, [9 c, 0.8 c/y].

Jain, R., Dave, H., Shah, A.B., et al. 2005, *Solar X-ray Spectrometer (SOXS) mission onboard GSAT2 Indian spacecraft: The low-energy payload*, SoPh 227, 89, [30 c, 2 c/y].

Kopp, G., Lawrence, G., and Rottman, G. 2005, *The Total Irradiance Monitor (TIM): Science results*, SoPh 230, 129, [112 c, 9 c/y].

Lemen, J.R., Duncan, D., Edwards, C., et al. 2004, *The solar X-ray imager for GOES*, SPIE 5171, 65, [14 c, 1 c/y].

McClintock, W.E., Snow, M., and Woods, T.N. 2005a, *Solar Stellar Irradiance Comparison Experiment II (SOLSTICE II): Pre-launch and on-orbit calibrations*, SoPh 230, 259, [50 c, 4 c/y].

McClintock, W.E., Rottman, G. J., and Woods, T.N. 2005b, *Solar Stellar Irradiance Comparison Experiment II (SOLSTICE II): Instrument concept and design*, SoPh 230, 225, [88 c, 7 c/y].

Neupert, W.M. 2011, *Intercalibration of solar soft X-Ray broadband measurements from SOLRAD 9 through GOES-12*, SoPh 272, 319, [6 c, 1 c/y].

Pizzo, V.J., Hill, S.M., Balch, C.C., et al. 2005, *The NOAA GOES-12 Solar X-Ray Imager (SXI). II. Performance*, SoPh 226, 283, [34 c, 3 c/y].

Rottman, G.J., Harder, J., Fontenla, J., et al. 2005, *The Spectral Irradiance Monitor (SIM): Early observations*, SoPh 230, 205, [27 c, 2 c/y].

Snow, M., McClintock, W.E., Rottman, G., et al. 2005, *Solar Stellar Irradiance Comparison Experiment II (SOLSTICE II): Examination of the solar stellar comparison technique*, SoPh 230, 295, [45 c, 4 c/y].

Sylwester, J., Farnik, F., Likin, O., et al. 2000, *Solar soft/hard X-ray photometer-imager aboard the Interball-Tail Probe*, SoPh 197, 337, [13 c, 1 c/y].

Väänänen, M., Alha, L., and Huovelin, J. 2009. *Cross-calibration of SMART-1 XSM with GOES and RHESSI*, SoPh 260, 479, [4 c, 0.5 c/y].

Woods, T.N., and Rottman, G. 2005, *XUV Photometer System (XPS): Solar variations during the SORCE mission*, SoPh 230, 375, [25 c, 2 c/y].

Woods, T.N., Rottman, G., and Vest, R. 2005, *XUV Photometer System (XPS): Overview and Calibrations*, SoPh 230, 345, [26 c, 2 c/y].

Woods, T.N., Chamberlin, P.C., Peterson, W.K., et al. 2008, *XUV Photometer system (XPS): Improved solar irradiance algorithm using CHIANTI Spectral Models*, SoPh 250, 235, [39 c, 4 c/y].

(1.9) Suborbital and Balloon Flights

Auchère, F., Hassler, D.M., Slater, D.C., et al. 2001, *SWRI/LASP sounding rocket inter-calibration with the EIT instrument on board SOHO*, SoPh 202, 269, [4 c, 0.4 c/y].

Barthol, P., Gandorfer, A., Solanki, S.K., et al. 2011, *The Sunrise mission*, SoPh 268, 1, [125 c, 19 c/y].

Bernasconi, P.N., Rust, D.M., Eaton, H.A., et al. 2000, *Balloon-borne telescope for high-resolution solar imaging and Polarimetry*, SPIEE 4014, 214, [9 c, 0.5 c/y].

Boggs, S.E., Lin, R.P., Feffer, P.T., et al. 1998, *A high resolution gamma-ray and hard x-ray spectrometer (HIREGS) for long duration balloon flights*, Adv. Spac. Res. 21/7, 1015, [4 c, 0.2 c/y].

Brosius, J.W., Daw, A.N., Rabin, D.M. 2014, *Pervasive faint Fe XIX emission from a solar active region with EUNIS-13: Evidence for nanoflare heating*, ApJ 790, 112, [28 c, 8 c/y].

Cirtain, J.W., Del Zanna, G., DeLuca, E.E. et al. 2013, *Energy release in the solar corona from spatially resolved magnetic braids*, Nature 493, Issue 7433, 501, [115 c, 26 c/y].

Giono, G., Ishikawa, R., Narukage, N., et al. 2017, *Polarization Calibration of the Chromospheric Lyman-Alpha SpectroPolarimeter for a 0.1VUV Range. Part II: In-Flight Calibration*, SoPh 292, 57, [3 c, 6 c/y].

Ishikawa, S.N., Glesener, L., Krucker, S., et al. 2017, *Detection of nanoflare-heated plasma in the solar corona by the FOXSI-2 sounding rocket*, Nature Astronomy 1, 771, [9 c, 9 c/y].

Kankelborg, C.C. and Martens, P.C.H. 2001, *Simultaneous EUV imaging and spectroscopy*, in "Solar Encounter", Proc. 1st Solar Orbiter Workshop, (eds. B. Battrick and H. Sawaya-Lacoste), ESA, ESTEC, Noordwijk, The Netherlands, ESA SP-493, 257.

Kankelborg, C.C. and Thomas, R.J. 2006, *Simultaneous imaging and spectroscopy of the solar atmosphere: Advantages and challenges of a 3-order slitless spectrograph*, SPIE 4498, 16.

Kano, R., Hara, H., Kobayashi,K., et al. 2000, *Initial results from the XUV Doppler Telescope (XDT)*, AdSpaR 25/9, 1739.

Kobayashi, K., Hara, H., Kano, R., et al. 2000, *On the Detection of solar coronal high-velocity fields ysing the XUV Doppler Telescope*, PASJ 52, 1165, [1 c, 0.06 c/y].

Kobayashi, K., Tsuneta, S., Tamura, T., et al. 2004, *Observation of solar flare hard X-Ray spectra using CdTe detectors*, AdSpaR 33/10, 1786.

Kobayashi, K., Cirtain, J., Winebarger, A.R., et al. 2014, *The high-resolution coronal imager (Hi-C)*, SoPh 289, 4393, [24 c, 7 c/y].

Krucker, S., Christe, S., Glesener, L., et al. 2014, *First Images from the Focusing Optics X-Ray Solar Imager*, ApJ 793, L32, [27 c, 8 c/y].

Solanki, S.K., Barthol, P., Danilovic, S., et al. 2010, *Sunrise: Instrument, mission, data, and first results*, ApJ 723, L127, [149 c, 20 c/y].

Thomas, R.J. and Davila, J.M. 2001, *EUNIS: A Solar EUV Normal-Incidence Spectrometer*, in "UV/EUV and visible space instrumentation for astronomy and solar physics", (eds. O.H. Siegmund, S. Fineschi, and M.A. Gummin), SPIE 4498, 161, [9 c, 0.5 c/y].

Vourlidas, A., Beltran, S.T., Chintzoglou, G., et al. 2016, *Investigation of the Chromosphere-Corona Interface with the Upgraded Very High Angular Resolution Ultraviolet Telescope (VAULT2.0)*, J. Astron. Instr. 5/1, 1640003, [2 c, 1 c/y].

Wang, T., Brosius, J.W., Thomas, R.J., et al. 2010, *Absolute radiometric calibration of the EUNIS-06 170–205 A channel and calibration update for coronal diagnostic spectrometer/normal-incidence spectrometer*, ApJS 186, 222, [6 c, 0.8 c/y].

Wang, T.J., Thomas, R.J., Brosius, J.W., et al. 2011, *Underflight calibration of SOHO/ CDS and Hinode/EIS with EUNIS-07*, ApJS 197, 32, [19 c, 3 c/y].

(1.10) Radio Instrumentation

Alissandrakis, C.E., Kontogeorgos, A., Tsitsipis, P., et al. 2009, *New developments in ARTEMIS IV solar radio spectrograph*, Earth Moon and Planets, 104, 93.

Bastian, T.S. 2004, *Low-frequency solar radiophysics with LOFAR and FASR*, Planetary and Space Science, 52, 1381, [22 c, 2 c/y].

Benz, A.O., Monstein,C., and Meyer,H. 2005, *CALLISTO - A new concept for solar radio spectrometers*, SoPh 226, 143, [25 c, 2 c/y].

Benz, A.O., Monstein,C., Meyer,H., et al. 2009, *A World-wide net of solar radio spectrometers: E-Callisto*, Earth, Moon, and Planets 104, 277, [39 c, 5 c/y].

Bowman, J.D., Cairns, I., Kaplan, D.L., et al. 2013; *Science with the Murchison Widefield Array*, Publ. Astron. Soc. Australia 30, e031, [196 c, 44 c/y].

Cho, K.S., Kim, K.S., Moon, Y.J., and Dryer, M. 2003, *Initial results of the Ichon solar radio spectrograph*, SoPh 212, 151, [8 c, 0.6 c/y].

Fu, Q.J., Ji, H., Qin, Z., et al. 2004, *A new solar broadband radio spectrometer (SBRS) in China*, SoPh 222, 167, [8 c, 0.6 c/y].

Golubchina, O.A., Zhekanis, G.V., Bogod,V.M., et al. 2002, *The construction of two-dimensional image of the Sun with radio telescope RATAN-600*, in "Solar Variability: From Core to outer Frontiers", European Space Agency Special Publication Vol. 506, (ed. Wilson,A.), ESA: ESTEC Noordwijk, The Netherlands, p. 939.

Grechnev, V.V. 2003a, *A method to analyze imaging radio data on solar flares*, SoPh 213, 103, [18 c, 1 c/y].

Grechnev, V.V. 2003b, *The Siberian Solar Radio Telescope (SSRT): The current state of the instrument, observations, and data*, SoPh 216, 239, [56 c, 4 c/y].

Iwai, K., Tsuchiya, F., Morioka, A., and Misawa, H. 2012, *IPRT/AMATERAS: A new metric spectrum observation system for solar radio bursts*, SoPh 277, 447, [9 c, 2 c/y].

Ji, H., Fu, Q., Liu, Y., et al. 2003, *A solar radio spectrometer at 5.2–7.6 GHz*, SoPh 213, 359, [9 c, 0.6 c/y].

Loukitcheva, M.A., Solanki, S.K., and White, S. 2008, *ALMA as the ideal probe of the solar chromosphere*, Astrophysics and Space Science 313, 197, [12 c, 1 c/y].

Pick, M., and Vilmer, N. 2008, *Sixty-five years of solar radioastronomy: Flares, coronal mass ejections and Sun-Earth connection*, Astronomy and Astrophysics Review 16, 1, [68 c, 7 c/y].

Wedemeyer, S., Bastian, T., Brajsa, R., et al. 2016, *Solar science with the Atacama large millimeter/submillimeter array: A new view of our Sun*. SSRv 200, 1, [24 c, 16 c/y].

Welch, J., Backer, D., Blitz, L., et al. 2009, *The Allen Telescope Array: The first widefield, panchromatic, snapshot radio camera for radio astronomy and SETI*, IEEE 97/8, 1438, [60 c, 7 c/y].

White, S.M., Kassim, N.E., and Erickson, W.C. 2003, *Solar radioastronomy with the LOFAR (LOw Frequency ARray) radio telescope*, in Proc. "Innovative Telescopes and Instrumentation for Solar Astrophysics", (eds. Keil, S.L. and Avakyan, S.V.), SPIE 4853, 111, [6 c, 0.4 c/y].

(1.11) Optical and Infrared Instrumentation

Beck, C., Bellot Rubio, L.R., Kentischer, T.J., et al. 2010, *Two-dimensional solar spectropolarimetry with the KIS/IAA visible imaging polarimeter*, A&A 520, A115, [14 c, 2 c/y].

Cavallini, F. 2006, *IBIS: A new post-focus instrument for solar imaging spectroscopy*, SoPh 236, 415, [172 c, 15 c/y].

Druckmüller, M. 2013, *A Noise adaptive fuzzy equalization method for processing solar extreme ultraviolet images*, ApJS 207, 25, [9 c, 2 c/y].

Gandorfer, A.M., Steiner, H.P., Aebersold, et al. 2004, *Solar polarimetry in the near UV with the Zurich Imaging Polarimeter ZIMPOL II*, A&A 422, 703, [65 c, 5 c/y].

Gelly, B., Le Men, C., Lopez Ariste, A., et al. 2008, *Design and implementation of an image stabilization device at the THEMIS solar telescope*, Experimental Astronomy, 22, 67, [2 c, 0.2 c/y].

Goode, P.R., Denker, C.J., Didkovsky, L.I., et al. 2003, *1.6-m Solar Telescope in Big Baer - the NST*, JKAS 36, 125, [9 c, 0.6 c/y].

Hammerschlag, R.H., Bettonvil, F.C.M., Jaegers, A.P.L., et al. 2009, *Open principle for large high-resolution solar telescopes*, Earth Moon and Planets, 104, 83, [3 c, 0.4 c/y].

Jess, D.B., Mathioudakis, M., Christian, D.J., et al. 2010, *ROSA: A high-cadence, synchronized multi-camera solar imaging system*, SoPh 261, 363, [63 c, 8 c/y].

Jones, H.P., Harvey, J.W., Henney, C.J., et al. 2002, *Data Analysis for the SOLIS vector spectromagnetograph*, ESA SP-505, p.15, [14 c, 1 c/y].

Judge, P.G., Casini, R., Tomczyk, S., et al. 2001, *Coronal magnetometry: a feasibility Study*, NCAR TN-466+STR (Technical memo).

Lin, H., Kuhn, J.R., and Coulter, R. 2004, *Coronal magnetic field measurements*, ApJ 613, L177, [163 c, 12 c/y].

Phillips, K.J.H., Read, P.D., Gallagher, P.T., et al. 2000, *SECIS: The Solar Eclipse Coronal eclipse Imaging System*, SoPh 193, 259, [29 c, 2 c/y].

Puschmann, K.G., Kneer, F., Seelemann, T., et al. 2006, *The new Goettingen Fabry-Perot spectrometer for two-dimensional observations of the Sun*, A&A 451, 1151, [59 c, 5 c/y].

Rimmele, T.R., and Marino, J. 2011, *Solar adaptive optics*, LRSP 8, 2, [32 c, 5 c/y].

Rimmele, T.R., Collados V.M., Berger, T., et al. (eds.) 2012, *The second ATST-EAST meeting: Magnetic fields form the photosphere to the corona*, PASP Vol. 463, 460.

Socas-Navarro, H., Dlmore, D., Pietarila, A., et al. 2006, *Spinor: Visible and infrared Spectro-polarimetry at the National Solar Observatory*, SoPh 235, 55, [58 c, 5 c/y].

Tomczyk, S., McIntosh, S.W., Keil, S.L., et al. 2007, *Alfvén waves in the solar corona*, Science 317, 1192, [394 c, 38 c/y].

Tomczyk, S., and McIntosh, S.W. 2009, *Time-distance seismology of the solar corona with CoMP*, ApJ 697, 1384, [144 c, 17 c/y].

Tritschler, A., Schmidt, W., Langhans, K., et al. 2002, *High-resolution solar spectroscopy with TESOS - Upgrade from a double to a triple system*, SoPh 211, 17, [46 c, 3 c/y].

Tritschler, A., Rimmele, T.T., Berukoff, S., et al. 2016, *Daniel K. Inouye Solar Telescope: High-resolution of the dynamic Sun*, Astron.Nachrichten 337/10, 1064, [7 c/y].

Van Noort, M.J., Rouppe van der Voort L.H.M. 2008, *Stokes imaging polarimetry using image restoration at the Swedish 1-m Solar Telescope*, A&A 489, 429, [42 c, 4 c/y].

Williams, D.R., Phillips, K.J.H., Rudawy, P., et al. 2001, *High frequency oscillations in a solar active region coronal loop*, MNRAS 326, 428, [82 c, 5 c/y].

Williams, D.R., Mathioudakis, M., Gallagher, P.T. et al. 2002, *An observational study of a magneto-acoustic waves in the solar corona*, MNRAS 326, 747, [78 c, 6 c/y].

(1.12) Future Solar Instrumentation

Alvarez-Herrero, A., Garcia, P.P., Laguna, H., et al. 2017; *The polarization modulators based on liquid crystal variable retarders for the PHI and METIS instruments for the solar orbiter mission*, Proc. SPIE 10563, id. 105632Z.

Antonucci, E., Andretta, V., Cesare, S., et al. 2017, *METIS, the Multi Element Telescope for Imaging and Spectroscopy: An instrument proposed for the Solar Orbiter mission*, Proc. SPIE 10566, id. 105660L, [1 c, 1 c/y].

Barandiaran, J., Zuluaga, P., Fernandez, A.B. et al. 2017, *Solar orbiter/PHI full disk telescope entrance window mechanical mount*, Proc. SPIE 10563, id. 1056319.

Caldwell, M.E., Morris, N., Griffin, D.K. et al. 2017, *The VUV instrument SPICE for Solar Orbiter: Performance ground testing*, Proc. SPIE 10397, id. 1039708.

Capobianco, G., Casti, M., Fineschi, S., et al. 2018, *Wide field of view liquid crystals-based modulator for the polarimeter of the Metis/Solar Orbiter*, Proc. SPIE 10698, id. 1069830.

Casti, M., Fineschi, S., Capobianco, G. et al. 2018, *Calibration of the liquid crystal visible-light polarimeter for the Metis/Solar Orbiter coronagraph*, Proc. SPIE 10698, id. 1069831.

Da Deppo, V., Poletto, L., Crescenzio, G. et al. 2017, *Preliminary error budget analysis of the coronagraphic instrument metis for the solar orbiter ESA mission*, Proc. SPIE 10564, id. 105643B.

Dolei, S., Spadaro, D., and Ventura, R. 2016, *Mapping the coronal hydrogen temperature in view of the forthcoming coronagraph observations by Solar Orbiter*, A&A 592, A173, [3 c, 2 c/y].

Fox, N.J., Velli, M.C., Bale, S.D., et al. 2016, *The Solar Probe Plus mission: Humanity's first visit to our star*, SSRv 204, 7, [79 c, 53 c/y].

Frassetto, F., Poletto, L., Fineschi, S. et al. 2017; *Internal checkup illumination sources for METIS coronagraph on solar orbiter*, Proc. SPIE 10563, id. 105635J.

Gandorfer, A., Grauf, B., Staub, J., et al. 2018, *The High Resolution Telescope (HRT) of the Polarimetric and Helioseismic Imager (PHI) onboard Solar Orbiter*, Proc. SPIE 10698, id. 106984N.

Halain, J.P., Rochus, P., Renotte, E. et al. 2016, *The qualification campaign of the EUI instrument of Solar Orbiter*, Proc. SPIE 9905, id. 99052X.

Halain, J.P., Mazzoli, A., Rochus, P., et al. 2017, *EUV high resolution imager on-board solar orbiter: optical design and detector performances*, Proc. SPIE 10564, id. 105643V.

Halain, J.P., Renotte, E., Auchere, F., et al. 2018, *The EUI flight instrument of Solar Orbiter: from optical alignment to end-to-end calibration*, Proc. SPIE 10699, id. 106990H.

Landini, F., Vives, S., Romoli, M., et al. 2017, *The optimization of the inverted occulter of the solar orbiter/METIS coronagraph/spectrometer*, Proc. SPIE 10564, id. 105640F.

Limousin, O., Meuris, A., Gevin, O., et al. 2016, *Flight production of Caliste-SO: the hard x-ray spectrometers for solar orbiter/STIX instrument*, Proc. SPIE 9905, id. 99050F.

Pancrazzi, M., Straus, T., Andretta, V., et al. 2016, *A virtual appliance as proxy pipeline for the Solar Orbiter/Metis coronagraph*, Proc. SPIE 9913, id. 99134L.

Peleikis, T., Kruse, M., Berger, L., et al. 2017, *Origin of the solar wind: A novel approach to link in situ and remote observations. A study for SPICE and SWA on the upcoming Solar Orbiter mission*, A&A 602, A24, [2 c, 2 c/y].

Rimmele, T.R., Collados V.M., Berger, T., et al. (eds.) 2012, *The second ATST-EAST meeting: Magnetic fields form the photosphere to the corona*, PASP Vol. 463, 460.

Romoli, M., Landini, F., Antonucci, E. et al. 2017, *METIS: the visible and UV coronagraph for solar orbiter*, Proc. SPIE 10563, id. 105631M.

Sandri, P., Sarra, P., Radaelli, P., et al. 2017, *Optical measurements of the mirrors and of the interferential filter of the Metis coronagraph on Solar Orbiter*, Proc. SPIE 10397, id. 1039716.

Schühle, U., Teriaca, L., Aznar Cuadrado, R., et al. 2018, *The solar orbiter Metis and EUI intensified CMOS-APS detectors: concept, main characteristics, and performance*, Proc. SPIE 10699, id. 1069934.

Thernisien, A.F.R., Howard, R., Korendyke, C., et al. 2018, *Stray light analysis and testing of the SoloHI (solar orbiter heliospheric imager) and WISPR (wide field imager for solar probe) heliospheric imagers*, Proc, SPIE 10698, id. 106980E.

Tritschler, A., Rimmele, T.T., Berukoff, S., et al. 2016, *Daniel K. Inouye Solar Telescope: High-resolution of the dynamic Sun*, Astron.Nachrichten 337/10, 1064, [7 c/y].

Uslenghi, M., Schühle, U., Teriaca, L., et al. 2017, *Characterization of the UV detector of Solar Orbiter/Metis*, Proc. SPIE 10397, id. 103971K.

Venzmer, M.S. and Bothmer, V. 2018, *Solar-wind predictions for the Parker Solar Probe orbit. Near-Sun extrapolations derived from an empirical solar-wind model based on Helios and OMNI observations*, A&A 611, A36.

Verroi, E., Da Deppo, V., Naletto, G., et al. 2017, *METIS-ESA solar orbiter mission internal straylight analysis*, Proc. SPIE 10563, id. 105631N.

Chapter 2
Atomic Physics and Spectroscopy

2.1 Photospheric Elemental Abundances

The chemical composition or the elemental abundances in the Sun and stars are of fundamental importance for modeling the nucleosynthesis in cosmology, stellar evolution models, or EUV and soft X-ray emission spectra from solar and stellar atmospheres. The *cosmic abundances* (or *solar system abundances*) are thought to settle universally to the same values in solar systems, after condensation from interstellar clouds, which naturally explains why the elemental abundances analyzed in meteorites ought to be identical to those measured with spectroscopy in the solar photosphere (called *photospheric abundances*), after normalization to the same (astronomical) log scale. Deviations from this rule occur for volatile elements, which can be quantified by the *condensation temperature* of an element or its compounds (see Lodders 2003 and references therein). Data from solar spectroscopy and meteorite analyses are combined to derive a recommended set of photospheric abundances, which are then used to derive *protosolar abundances* (which is identical to *solar system abundances*). The differences between protosolar and present-day solar abundances is explained by gravitational settling over the Sun's lifetime of some elements (e.g., He)—see Lodders (2003). An anomaly of coronal abundances is their enhancement or depletion with respect to photospheric abundances, characterized by a (single-digit) factor that expresses the *first ionization potential (FIP)* bias. Reviews on solar elemental abundances can be found in Feldman and Widing (2003, 2007), Asplund et al. (2005, 2009), Grevesse et al. (2007), Laming (2015), and Allende Prieto (2016).

In Table 2.1 we list the photospheric abundances for the 83 naturally occurring elements, along with the abundances in *C I-type carbonaceous meteorites*, as compiled in Lodders (2003). Lodders converted her compiled meteoritic abundances on a cosmochemical scale (Si = 10^6 atoms) to an astronomical (Russell) log scale using a photospheric Si abundance of 7.54, while recent (2015) photospheric abundances are slightly lower, i.e., 7.51 ± 0.03 (Grevesse et al. 2015; Scott et al.

M. J. Aschwanden, *New Millennium Solar Physics*, Astrophysics and Space Science Library 458, https://doi.org/10.1007/978-3-030-13956-8_2

Table 2.1 Elemental abundances derived from photospheric spectroscopy, abundances in C I chondrites, and first-ionization potential energies (adapted from Lodders 2003)

Element	Abundance[a] photosphere	Abundance[a] C I chondrites	FIP [eV]	Element	Abundance[a] photosphere	Abundance[a] C I chondrites
1 H	12.00[c]	8.28 ± 0.05	13.6	43 Tc	–	–
2 He	10.899 ± 0.01[c]	1.32	24.6	44 Ru	1.84 ± 0.07	1.80 ± 0.08[c]
3 Li	1.10 ± 0.10	3.28 ± 0.06[c]	5.4	45 Rh	1.12 ± 0.12	1.10 ± 0.02[c]
4 Be	1.15 ± 0.20	1.41 ± 0.08[c]	9.3	46 Pd	1.69 ± 0.04	1.70 ± 0.02[c]
5 B	2.7 ± 0.21	2.78 ± 0.04[c]	8.3	47 Ag	0.94	1.23 ± 0.06[c]
6 C	8.39 ± 0.04[c]	7.43 ± 0.06	11.3	48 Cd	1.77 ± 0.11	1.74 ± 0.03[c]
7 N	7.83 ± 0.11[c]	6.28 ± 0.07	14.5	49 In	1.56 ± 0.2	0.80 ± 0.03[c]
8 O	8.69 ± 0.05[c]	8.42 ± 0.02	13.6	50 Sn	2.0 ± 0.3	2.11 ± 0.04[c]
9 F	4.56 ± 0.30	4.46 ± 0.06[c]	17.4	51 Sb	1.0 ± 0.3	1.06 ± 0.07[c]
10 Ne	7.87 ± 0.10[c]	−1.09	21.6	52 Te	–	2.22 ± 0.04[c]
11 Na	6.30 ± 0.03[c]	6.30 ± 0.03	5.2[b]	53 I	–	1.54 ± 0.12[c]
12 Mg	7.54 ± 0.06	7.56 ± 0.02[c]	7.6[b]	54 Xe	2.27 ± 0.02[c]	−1.92
13 Al	6.47 ± 0.07	6.46 ± 0.02[c]	6.0[b]	55 Cs	–	1.10 ± 0.03[c]
14 Si	7.54 ± 0.05	7.54 ± 0.02[c]	8.1[b]	56 Ba	2.17 ± 0.07	2.19 ± 0.03[c]
15 P	5.49 ± 0.04	5.43 ± 0.04[c]	10.5	57 La	1.13 ± 0.03	1.18 ± 0.06[c]
16 S	7.20 ± 0.05	7.19 ± 0.04[c]	10.3	58 Ce	1.58 ± 0.09	1.61 ± 0.02[c]
17 Cl	5.50 ± 0.30	5.26 ± 0.06[c]	13.0	59 Pr	0.71 ± 0.08	0.78 ± 0.03[c]
18 Ar	6.55 ± 0.08[c]	−0.48	15.8[b]	60 Nd	1.50 ± 0.12	1.46 ± 0.03[c]
19 K	5.12 ± 0.13	5.09 ± 0.05[c]	4.3	62 Sm	0.99	0.95 ± 0.04[c]
20 Ca	6.36 ± 0.02[c]	6.32 ± 0.03	6.1[b]	63 Eu	0.52 ± 0.04	0.52 ± 0.04[c]
21 Sc	3.17 ± 0.10	3.07 ± 0.04[c]	6.6	64 Gd	1.12 ± 0.04	1.06 ± 0.02[c]
22 Ti	5.02 ± 0.06	4.92 ± 0.03[c]	6.8	65 Tb	0.28 ± 0.3	0.31 ± 0.03[c]
23 V	4.00 ± 0.02[c]	4.00 ± 0.03	6.8	66 Dy	1.14 ± 0.08	1.13 ± 0.04[c]
24 Cr	5.64 ± 0.13	5.66 ± 0.05[c]	6.8	67 Ho	0.53 ± 0.10	0.49 ± 0.02[c]
25 Mn	5.39 ± 0.03	5.50 ± 0.03[c]	7.4	68 Er	0.93 ± 0.06	0.95 ± 0.03[c]
26 Fe	7.45 ± 0.08	7.48 ± 0.03[c]	7.9[b]	69 Tm	(0.00 ± 0.15)	0.11 ± 0.06[c]
27 Co	4.92 ± 0.08	4.89 ± 0.03[c]	7.9	70 Yb	1.08 ± 0.15	0.94 ± 0.03[c]
28 Ni	6.22 ± 0.13	6.22 ± 0.03[c]	7.6[b]	71 Lu	0.06 ± 0.10	0.09 ± 0.06[c]
29 Cu	4.21 ± 0.04	4.26 ± 0.06[c]		72 Hf	0.88 ± 0.08	0.77 ± 0.04[c]
30 Zn	4.62 ± 0.15	4.64 ± 0.04[c]		73 Ta	–	-0.14 ± 0.03[c]
31 Ga	2.88 ± 0.10	3.10 ± 0.06[c]	6.0	74 W	(1.11 ± 0.15)	0.65 ± 0.03[c]
32 Ge	3.58 ± 0.05	3.62 ± 0.05[c]		75 Re	–	0.26 ± 0.04[c]
33 As	–	2.32 ± 0.05[c]		76 Os	1.45 ± 0.10	1.37 ± 0.03[c]
34 Se	–	3.36 ± 0.04[c]		77 Ir	1.38 ± 0.05	1.35 ± 0.03[c]
35 Br	–	2.59 ± 0.09[c]		78 Pt	1.74	1.67 ± 0.03[c]

(continued)

Table 2.1 (continued)

Element	Abundance[a] photosphere	Abundance[a] C I chondrites	FIP [eV]	Element	Abundance[a] photosphere	Abundance[a] C I chondrites
36 Kr	3.28 ± 0.08[c]	-2.24	14.0	79 Au	(1.01 ± 0.15)	0.83 ± 0.06[c]
37 Rb	2.60 ± 0.15	2.36 ± 0.06[c]	4.2	80 Hg	–	1.16 ± 0.18[c]
38 Sr	2.92 ± 0.05	2.91 ± 0.04[c]		81 Tl	(0.72–1.10)	0.81 ± 0.04[c]
39 Y	2.21 ± 0.02	2.20 ± 0.04[c]		82 Pb	2.00 ± 0.06	2.05 ± 0.04[c]
40 Zr	2.59 ± 0.04	2.60 ± 0.02[c]		83 Bi	–	0.68 ± 0.03[c]
41 Nb	1.42 ± 0.06	1.42 ± 0.03[c]		90 Th	–	0.09 ± 0.04[c]
42 Mo	1.92 ± 0.05	1.99 ± 0.04[c]		92 U	$< -0.47)$	-0.49 ± 0.04[c]

[a] Abundances are given on a logarithmic scale, $12.0 + log_{10}(A/A_H)$
[b] Abundances up to a factor of ≈ 4 times higher in corona and solar wind (low-FIP)
[c] Recommended values for protosolar or solar system abundances
(. . .) Values between parentheses are less accurate

2015a,b). Most of the abundances measured in the photosphere agree well with those in C I chondrites, as it can be seen for the 56 elements for which measurements from both sources exist. There are only a few elements that have exemptions, mostly the noble gases (He, Ne, Ar, Kr, Xe) with the atomic mass numbers (2, 10, 18, 36, 54), which hardly undergo any chemical reaction, since their outer shell of valence electrons is "full", and thus makes molecular bonding unlikely. Other exceptions are H, C, N, and O, with the atomic mass numbers (1, 6, 7, 8), which readily form gaseous compounds, and thus are depleted in meteorites. On the other side, lithium (Li) is processed in the Sun and thus is depleted in the photosphere by a factor of 150, compared with the Li abundance at the time of the birth of the Sun. There is also the problem that helium cannot be measured in the photosphere, because there is no spectroscopic helium line that is formed at a photospheric temperature around 5000 K. For the 56 elements for which a comparison between photospheric and meteoritic abundances can be done, the relative abundances agree within 10% for 31 elements, and within 15% for 41 elements (Lodders 2003). The so-called *recommended abundances* that form the standard abundances for *protosolar abundances* (also called *solar system abundances*), are essentially defined by the higher value of the photospheric or meteoritic abundance and are marked with the symbol * in Table 2.1.

The photospheric abundances listed in Table 2.1 give the mass fractions of hydrogen ($X = 0.7491$), helium ($Y = 0.2377$), and heavy elements ($Z = 0.0133$), leading to $Z/X = 0.0177$ (Lodders 2003). Substantial downward revisions of the solar abundance of oxygen measured from line formation (of O I and OH lines) in solar granulation resulted in a significant decrease in the solar metal mass fraction, to $Z = 0.0126$, or $Z/X = 0.0168$ (Asplund et al. 2004), compared with earlier values that had almost the double value. This has decreased the metal content in the solar convection zone by almost a factor of two. While this downward correction of the metallicity resolves a number of long-standing problems, the new 3-D solar model element abundances created a new challenge for helioseismology

(Asplund et al. 2005, 2009). While earlier oxygen abundances yielded agreement with helioseismology, the new (revised) oxygen abundances disagree. More accurate determinations of photospheric elemental abundances are investigated using upward revisions of the opacity tables (Basu and Antia 2004), 3-D time-dependent radiation-hydrodynamical simulations, instead of 1-D hydrostatic models (e.g., Caffau et al. 2008; Allende Prieto et al. 2002), improvements in atomic data to analyze the solar spectrum, including allowed and forbidden lines in O I and OH, and using helioseismology (Basu and Antia 2004).

The remaining differences are suspected to be due to some unknown fractionation, increased opacity, variations of the solar evolutionary history with episodes of mass loss by accretion, a metallicity that is higher in the radiative zone than in the convection zone, or the effects of turbulent kinetic flux within the solar convection zone (Laming 2015). The FIP and inverse FIP effects in solar and stellar coronae are modeled in terms of the ponderomotive force due to the propagation and/or reflection of MHD waves in the chromosphere, which act on chromospheric ions, but not neutrals, and this way can lead to ion-neutral fractionation (Laming 2015). The model explains the observed difference in solar FIP fractionation between the slow and fast solar wind, which is governed by closed and open magnetic fields. The observed helium depletion in the solar wind is explained by the sensitivity to the chromospheric altitude where ion-neutral separation occurs (Laming 2015).

Is the Sun a typical star? A study employing 11 solar twins and 10 solar analogs, selected by near-identical color-temperature relations and similar ages, revealed that the solar chemical abundances relative to iron depart from the mean abundance ratios in the solar twins (Fig. 2.1a), and that the Sun shows a $\approx$ 20% depletion of refractory elements (a class of metals that are extraordinarily resistant to heat and wear, such as Ti, V, Cr, Zr, etc.), relative to the volatile elements (H, N, C, O), in a comparison of solar twins (Melendez et al. 2009). The abundance differences

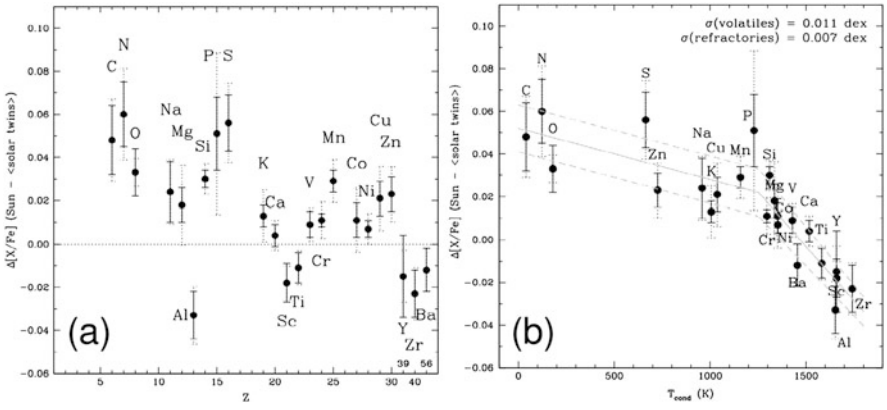

Fig. 2.1 Differences between [X/Fe] of the Sun (solid error bars) and the mean values in solar twins (dashed error bars) as a function of the atomic number Z (**a**) and as a function of the condensation temperature T_{cond} (**b**). The reference element is Fe (Melendez et al. 2009)

correlate strongly with the condensation temperatures of the elements (Fig. 2.1b). Thus, the Sun has an unusual chemical composition, but is not unique. These differences may already have arisen at the time when the Sun was formed, possibly when the molecular cloud that formed the Sun was cleansed from dust by radiation from hot luminous stars to a higher degree than in other stars. The amount of remaining dust may have also severe consequences for the formation of planets and the statistical probability of formation of life.

2.2 The First-Ionization-Potential (FIP) Effect

While the chemical composition of the photosphere is believed to by a universal standard, being essentially the same on the surface of the Sun and stars, and being the same at the solar equator or at the poles, in Quiet Sun regions or in active regions, the situation is different in the solar corona. Since the corona has a many orders of magnitude lower density than the photosphere, the elemental abundances are less accurately determined than in the photosphere. The 15 most abundant elements that could be measured in the corona consist of 7 non-volatile elements (Na, Mg, Al, Si, Ca, Fe, Ni), and 8 volatile elements (H, N, C, O), including the noble gases (He, Ne, Ar). The coronal abundances have been found to differ from the photospheric abundances for some elements, but also to vary at different parts of the corona and as a function of time. Early differences were found in the EUV and soft X-ray spectra recorded during rocket flights, in the slow solar wind, and in energetic particle data. It was found that elements with low *first-ionization potentials (FIP)* $\leq$ 10 eV were over-abundant (such as the non-volatile elements Na, Mg, Al, Si, Ca, Fe, and Ni, by about a factor of 4 relative to the high-FIP ($\geq$ 10 eV) elements (such as the volatile elements H, C, N, O) as compared with photospheric abundance ratios (Fig. 2.2). This FIP effect was interpreted in terms of a separation of ions from neutrals, a

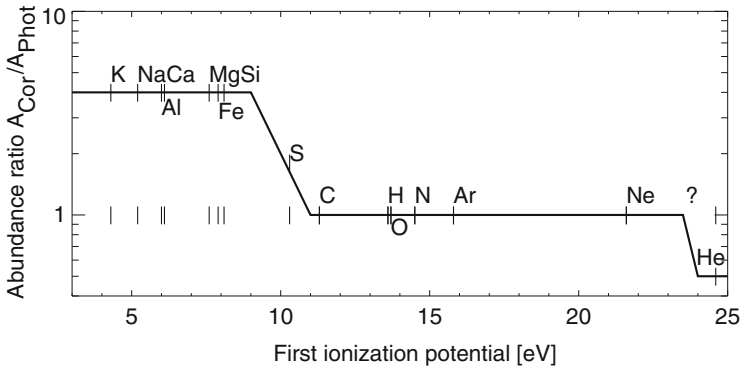

Fig. 2.2 Ratio of coronal to photospheric abundances versus their *first-ionization potential* (Feldman and Widing 2003)

process called *fractionation* that occurs at the base of the solar corona. Reviews on the FIP effect are given in Feldman and Laming (2000), Feldman and Widing (2003, 2007), Phillips et al. (2008), Laming (2015), and Allende Prieto (2016).

The coronal FIP bias has been scrutinized in more detail over the last decade, by studying the effects of non-equilibrium ionization on the FIP bias (Edgar and Esser 2000), by measuring the variation of the FIP bias off-limb as a function of altitude with SUMER/SOHO, or using EIS/Hinode spectra. In limb measurements above active regions or streamers, the absolute elemental abundances show a general FIP effect and decrease with height for all elements, which is consistent with the effect of gravitational settling, occurring more likely in closed loops where no significant outflow occurs (Ko et al. 2002). However, the FIP bias varies according to the choice of elements used in the ratios and on the location in the streamer where the FIP bias is measured. In some streamers it was concluded that both the low-FIP and high-FIP elements were depleted (Uzzo et al. 2003), or no abundance-depleted core was found (Uzzo et al. 2006). Measurements of elemental abundances with UVCS/SOHO in a post-CME current sheet in a very hot active region revealed first-ionization potential enhancement of 7–8 compared to the usual factor of 3–4 (Ciaravella et al. 2002).

A significant question concerns the absolute values of coronal and chromospheric abundances, in order to decide whether the FIP effect corresponds to an enrichment at low FIPs or a depletion of higher FIPs. A low-FIP enhancement suggests a fractionation in the lower chromosphere. Hybrid abundances were inferred also, which represent a compromise between low-FIP being enhanced and high-FIPs being depleted (Schmelz et al. 2012). The FIP effect was found to vary significantly from the solar minimum in a diffusive, quiet equatorial region (with a value of ≈ 4) compared with 2 years later, using SUMER/SOHO spectra of limb regions (Widing et al. 2005). In the following, we review some recent progress in abundance measurements of specific elements:

Iron (Fe): Determinations of the absolute abundance of iron, using a combination of EUV spectroscopy and density measurements from thermal bremsstrahlung at radio wavelengths have demonstrated that iron is enhanced by a factor of $\approx 4.0 \pm 0.8$ relative to the photosphere (White et al. 2000). Using the radiative cooling time from delays in different EUV temperature filters as a density diagnostics, a similar result with a FIP bias of 4.8 ± 1.7 was inferred for iron (Aschwanden et al. 2003). Iron abundances were also determined from the X-ray line complexes at 6.65 keV (Fe) and 8 keV (Fe/Ni) using RHESSI spectra during solar flares, yielding a FIP bias of 2.6 ± 0.6 compared with photospheric abundances (Phillips and Dennis 2012).

Helium (He): Absolute abundances of helium were measured at altitudes of $\approx 1.05 R_\odot$ above the solar limb with SUMER/SOHO, yielding a ratio of He/H$= 0.038 \pm 0.17$ (mass fraction $Y = 0.13$) using the revised oxygen abundance, or He/H$= 0.052 \pm 0.005$ (mass fraction $Y = 0.17$) from using H I Lyman series (Laming and Feldman 2001). The He/H ratio in open-field regions (in coronal holes) has been found never to be higher than 5% (Laming and Feldman 2003).

Potassium (K): The absolute abundance of potassium, the element with the lowest FIP potential of 4.3 eV, was for the first time measured from a solar flare with the RESIK crystal spectrometer on the *CORONAS-F* mission, yielding a FIP bias of a factor of 3 times the photospheric value (Phillips et al. 2003). Later, potassium lines were further analyzed with RESIK at 3.53–3.57 Å during a solar flare. A more detailed analysis of these lines with RESIK revealed a FIP enhancement of 5.5 (Sylwester et al. 2010a).

Sodium (Na): Highly ionized sodium lines were found to have coronal abundances with an enhancement of 3–4 over the photospheric values, based on flare data observed with FCS/SMM (Phillips et al. 2010).

Argon (Ar): Argon lines analyzed with RESIK/CORONAS-F at 3.9–3.7 Å were found to have very similar photospheric abundances (as determined by indirect methods) and coronal abundances (Sylwester et al. 2010b). There are no suitable photospheric argon or neon photospheric lines from which the FIP bias can be determined directly, and thus the argon abundance depends on the reference element, such as oxygen or calcium. Recent observations with EIS/Hinode near a sunspot during a flare revealed argon/calcium abundance ratios seven times greater than expected from photospheric abundances, which is an unprecedented anomaly, interpreted as due to an inverse FIP effect (Doschek and Warren 2016). The argon abundance apparently varies depending on the emitting photospheric feature (e.g., active region, or sunspot).

Chlorine (Cl): Chlorine abundances determined with RESIK show an enhancement of 1.8, compared with infrared measurements in sunspots (Sylwester et al. 2011). However, the abundance of chlorine was found to be constant for a large range of flare temperatures, using RESIK/CORONAS-F and GOES measurements, which argues for a fractionation process that is not modulated by the solar cycle activity level (Sylwester et al. 2011).

Silicon (Si) and Sulphur (S): Silicon is a low-FIP element (8.1 eV) and sulphur is an intermediate element (10.3 eV) between low and high-FIP elements, but a consistent enhancement of 3–4 was found in the outflows from active regions measured with EIS/Hinode (Brooks and Warren 2011).

Neon (Ne): The absolute neon abundance is controversial. Ne/O abundances of He/O=0.41 were reported from 21 *Chandra* stars (Drake and Testa 2005) and from revised neon abundances based on solar interior models. In contrast, solar observations yielded significantly lower values of Ne/O=0.15 during solar flares, observed with FCS/SMM (Schmelz et al. 2005), and Ne/O=0.18 $\pm$ 0.05 in solar supergranule cells, observed with CDS/SOHO (Young 2005), leading to a suggested photospheric abundance of Ne/O=0.17 $\pm$ 0.05, while updated work yielded Ne/O=0.24 $\pm$ 0.05 (Young 2018). Recent analysis of SUMER/SOHO data, using the intensity ratio between allowed Ne IX lines and the free-free continuum radiation observed close to the Ne IX line, restored the old abundances of $A_{Ne} = 8.11 \pm 0.12$ (Landi et al. 2007), which are a factor of 1.9 above the down-revised abundances of Asplund et al. (2004). Re-analysis of P-78 and SMM spectra revealed that the Ne/O ratio varies by a factor of two and increases with higher plasma temperatures in active regions (Drake 2011). Since

the neon abundance can not be measured in the photosphere, it is necessary to use a proxy, such as transition region, coronal, and stellar abundances.

2.3 The CHIANTI Atomic Database

The measurement of the most fundamental parameters in solar and astrophysics, such as temperatures and densities, is generally carried out with ultraviolet and soft X-ray line spectroscopy, which requires extensive atomic databases with wavelengths, widths, and intensities of atomic line transitions in the wavelength range of $\lambda \approx$ 1–2000 Å. The probably most widely used atomic database in solar physics is the so-called *CHIANTI* code (which is not an acronym), developed and maintained by collaborators at the George Mason University (USA), the University of Michigan (USA), and the University of Cambridge (UK). The first version of CHIANTI 1.01 was released in 1997, the code was then continually improved with more complete sets of atomic lines and higher accuracy of energy levels, and the latest version (at the time of writing), CHIANTI 8.0.7, was released in September 2015. The developments and upgrades of the CHIANTI code are described in a series of papers (Dere et al. 1997, 2001, 2009; Young et al. 1998, 2003; Landi et al. 1999, 2002, 2006, 2012, 2013; Landi and Phillips 2006; Landi and Young 2009; Young and Landi 2009; Del Zanna et al. 2015). Information on the CHIANTI code is accessible at the website *http://www.chiantidatabase.org/*.

What kind of data and calculations are involved in an atomic database? CHIANTI provides a database of atomic energy levels, wavelengths of line transitions, radiative rates, electron excitation rates, proton excitation rates, photo-excitation rates, for all ions that are abundant in cosmic plasmas, mostly in the 50–1100 Å wavelength range (Dere et al. 1997). CHIANTI also contains ionization and recombination rate coefficients that allow the equilibrium ionization fractions for all ions to be calculated (Arnaud and Rothenflug 1985; Arnaud and Raymond 1992; Dere 2007; Bryans et al. 2009). Together the CHIANTI atomic data sets yield diagnostics of emission line spectra, which are mostly produced by collisional excitation of a variety of ionization stages in astrophysical high-temperature plasmas. Some emission lines can only rarely be observed in laboratory experiments, and thus the line identification at their exact wavelength can be faciliated by the analysis of astrophysical observations. Theoretical calculations based on quantum mechanics often predict the wavelength of specific lines typically with an accuracy of $\approx$ 10%–20%, (though accuracies of 0.2% are claimed with the Cowan Hartree-Fock code,—see Merts and Torrey 1963), because the number of energy levels that need to be included, which can be several hundred per ion (Fig. 2.3), is always limited, and collision strengths of many transitions are often lacking. It is therefore no surprise that improvements of an atomic database is an endless effort that started since the discovery of quantum mechanics.

Iterative improvements of the CHIANTI atomic database are systematically carried out by comparing temperature-sensitive as well as density-sensitive line

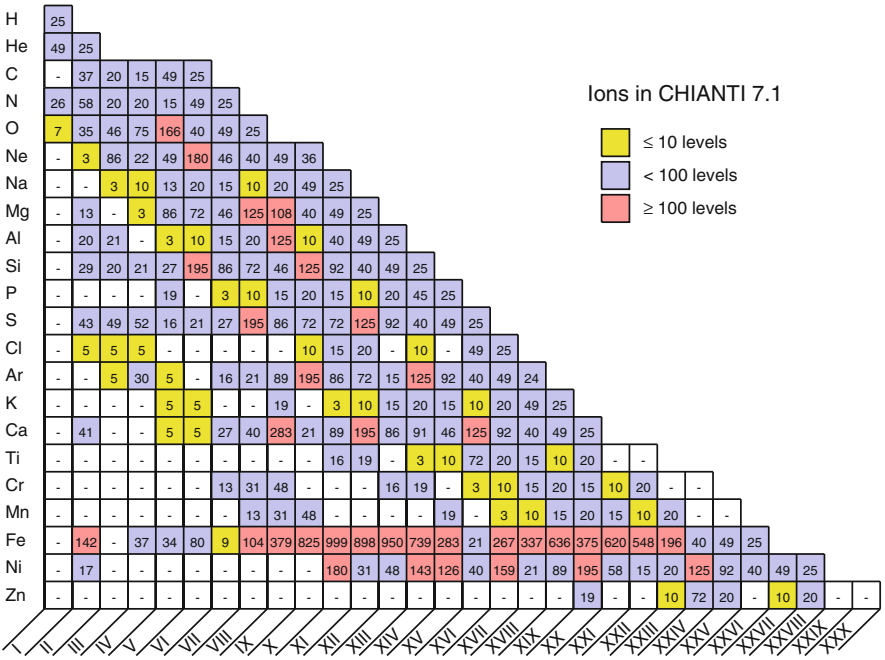

Fig. 2.3 Ions from hydrogen (H) to zinc (Zn) included in the CHIANTI database version 7.1. The y-axis indicates the atoms, the x-axis the ionization levels, and the number of atomic levels that are included in each model of an ion are listed in the boxes (Credit: Peter Young)

ratios from astrophysical spectra with theoretically predicted line ratios. These then allow an improved calibration of any spectrometer that observes the relevant lines. The procedure sometimes helps with the identification of lines with uncertain theoretical wavelengths. Where discrepancies between CHIANTI and measured line intensities exist, they point to potential mis-identifications, new identifications, line blending (unresolved spectral lines formed from different ions), possible calibration problems, data reduction errors, or inaccurate atomic data (Mason et al. 2002). Such cross-comparisons have been performed with solar data from: the SERTS rocket flight (235–450 Å); FCS/SMM (7–19 Å); CDS/SOHO (151–785 Å); SUMER/SOHO (500–1610 Å); EIS/Hinode (170–211 and 246–291 Å); the SDO (94 Å), RESIK/CORONAS-F and RHESSI spectra, and XPS/SORCE.

The iron ions are particularly difficult to represent with an accurate atomic model, but the temperature range of the solar corona ($T_e \approx$ 1–3 MK), active regions ($T_e \approx$ 2–8 MK), and solar flares ($T_e \approx$ 5–50 MK), produce highly ionized iron states from Fe VII to Fe XXIV, and thus iron lines were chosen for coronal temperature diagnostics in the design of most of the EUV temperature filters on SOHO/EIT, TRACE, and AIA/SDO. The CHIANTI database contains up to several hundred atomic levels per iron ion (Fig. 2.3). Benchmark studies were conducted for all iron ionization states between Fe VII and Fe XXIV. Other recent updates of the

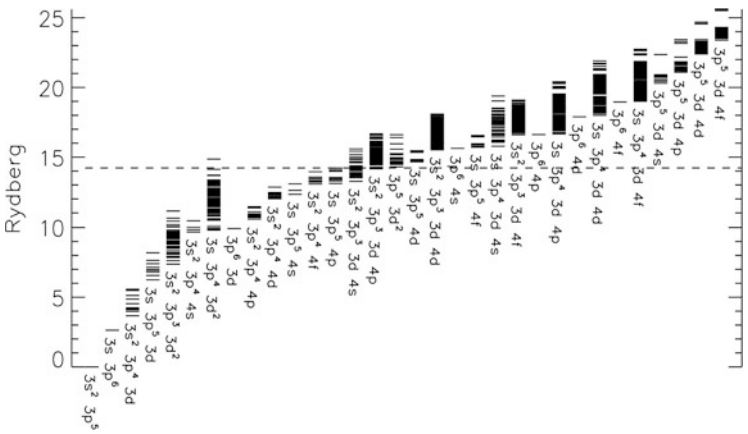

Fig. 2.4 The energies of individual atomic terms for Fe X $n = 4 \mapsto n = 3$ transitions are shown here as short horizontal lines in Rydberg (1 Ry = 13.6 eV); these include 218 terms in the CHIANTI database (Del Zanna et al. 2012)

CHIANTI atomic database include Ni XII, Be-like ions (such as C III, N IV, O V, Ne VII, Mg IX, Al X, Si XI, S XIII, Ar XV, Ca XVII, Ne XXIII, Ni XXV), O-like ions (such as P, Cl, K, Ti, Cr, Mn, Co), Mn VI, S X, Si XI, Si VII, Ca VIII, Ca XIII. A spectral atlas of the short wavelength range (7–19 Å) of the CHIANTI database is given in Landi and Phillips (2005).

The IRON project is another effort parallel to CHIANTI, dedicated to complete the atomic database of iron ions (e.g., Storey et al. 2000, 2005; Storey and Zeippen 2001). An example of term energies for Fe X for $n = 4 \mapsto n = 3$ transitions is shown in Fig. 2.4, taken from Del Zanna et al. (2012). New updates on the Fe X lines are particularly important to improve the AIA/SDO 94 Å filter response function (Del Zanna et al. 2012; Testa et al. 2012), where large discrepancies between predicted and observed count rates were reported (e.g., Aschwanden and Boerner 2011).

2.4 Solar Emission Line Spectroscopy

The solar EUV and soft X-ray spectrum, covering a wavelength range of $\lambda \approx$ 1–2000 Å, contains thousands of emission lines and continuum emission from free-free and free-bound transitions, produced in the high-temperature and low density plasma above the transition region and in the corona. Inversions and forward-fitting of temperature and density models to the observed EUV and soft X-ray line fluxes became an important diagnostic of the physical conditions in the solar corona and in flares. The line intensities can be used to calculate electron densities, electron temperatures, elemental abundances, and non-Maxwellian electron distributions. The line profiles and Doppler shifts give information on ion temperatures and

line broadening by nonthermal plasma flows and turbulence. The subject is most comprehensively treated in the textbook *Ultraviolet and X-ray Spectroscopy of the Solar Atmosphere* (Phillips et al. 2008), and further recent reviews can be found in Feldman and Widing (2007), Doschek and Feldman (2010), and in Kohl et al. (2006) for the extended corona.

The wavelength coverage of various high-resolution EUV and soft X-ray spectrometers operated onboard solar-dedicated spacecraft is compiled in Table 2.2, including the spacecraft Skylab, OSO-8, Hinotori, P-78, SMM, Coronas-I, Coronas-F, Yohkoh, SOHO, SORCE, Hinode, IRIS, and the rocket flights SERTS and EUNIS. Coverage of the solar UV and soft X-ray spectrum in the $\lambda \approx 1$–2000 Å range has been continuously improved over the last decade with the advent of new space-based spectrographs (Table 2.2), which provided higher spectral resolution and improved cross-calibrations, and this way enabled the identification of weaker

Table 2.2 Wavelength coverage of solar high-resolution EUV and soft X-ray spectrometers (adapted from Doschek and Feldman 2010)

Spacecraft	Instrument	Wavelength range (Å)	Reference
Skylab	EUV spectroheliograph S082A	150–350, 300–645	Tousey et al. (1977)
Skylab	EUV spectroheliograph S082B	970–3940	Bartoe et al. (1977)
Skylab	EUV spectroheliometer	280–1340	Reeves et al. (1977)
OSO-8	UV spectrometer (LPSP)	1025–3960 (6 bands)	Bonnet et al. (1978)
OSO-8	UV spectrometer, polarimeter	1170–3600	Bruner (1977)
Hinotori	Rotating Bragg X-ray spectrometer	1.72–1.95, 1.83–1.89	Tanaka (1982)
P78-1	Bragg X-ray spectrometers	1.82–8.53 (4 bands)	Doschek (1983)
P78-1	Bragg X-ray spectrometers	7.8–23.0	McKenzie et al. (1980)
SMM	BCS Bent Crystal Spectrometer	1.76–3.2 (8 bands)	Rapley et al. (2017)
SMM	FCS Flat Crystal Spectrometer	1.4–22.43 (7 bands)	Phillips et al. (1982)
Coronas-I	Spectroheliograph	180–210	Zhitnik et al. (1998)
Coronas-F	SPIRIT Spectroheliograph	280–330	Zhitnik et al. (2005)
Yohkoh	BCS Bent Crystal Spectrometer	1.76–5.11 (4 bands)	Culhane et al. (1991)
SOHO	SUMER EUV spectrometer	390–1610	Wilhelm et al. (1995)
SOHO	CDS EUV spectrometer	150–800	Harrison et al. (1995)
SOHO	UVCS coronagraph spectrometer	499–1242 (5 bands)	Kohl et al. (1995)
SORCE	SIM Spectral Irradiance Monitor	220–1630, 1600–2400	Harder et al. (2010)
Hinode	EIS EUV imaging spectrometer	170–210, 250–290	Culhane et al. (2007)
IRIS	FUV1 Far Ultraviolet	1331.56–1358.40	De Pontieu et al. (2014)
IRIS	FUV2 Far Ultraviolet	1390.00–1406.79	De Pontieu et al. (2014)
IRIS	NUV Near Ultraviolet	2782.56–2833.89	De Pontieu et al. (2014)
IRIS	SJI Slit-Jaw Imager	1330–5000 (6 bands)	De Pontieu et al. (2014)

atomic lines and blends. The EUV spectrum of the Quiet Sun comprises many emission lines from iron (Fe VIII to XV), oxygen (O IV to O VI), magnesium (Mg V to Mg VII), silicon (Si VII to X) and others, which enables unprecedented temperature and density diagnostics, in particular with the EIS/Hinode spectrometer (Young et al. 2007, 2009) and IRIS (De Pontieu et al. 2014) to be used. As a direct consequence of the coronal plasma dynamics, which perpetually disturbs local electron temperatures and densities, the EUV spectra vary distinctly among different locations on the Sun, as well as the EUV irradiance spectra from the entire Sun vary between different times, depending on the solar activity level. EUV irradiance spectra were produced from the full Sun with CDS/SOHO, SUMER/SOHO, SORCE, while local EUV spectra were obtained from Quiet-Sun regions with EIS/Hinode (Young et al. 2007, 2009), from coronal limb regions with SUMER/SOHO (Curdt et al. 2001, 2004), with EIS/Hinode (Brown et al. 2008; Del Zanna 2012), from coronal holes with SUMER/SOHO, or from prominences with SUMER/SOHO. Soft X-ray spectra were obtained from solar flares with FCS/SMM or with RESIK/CORONAS-F. An example of a small portion of the SUMER/SOHO spectral atlas (Curdt et al. 2004) is shown in Fig. 2.5, measured near the solar limb. EUV spectroscopy in active regions reveals flows and nonthermal velocities, which can be used to trace the magnetic field (Doschek et al. 2008). Two components of spectral emission profiles are ubiquitously found in the corona and transition

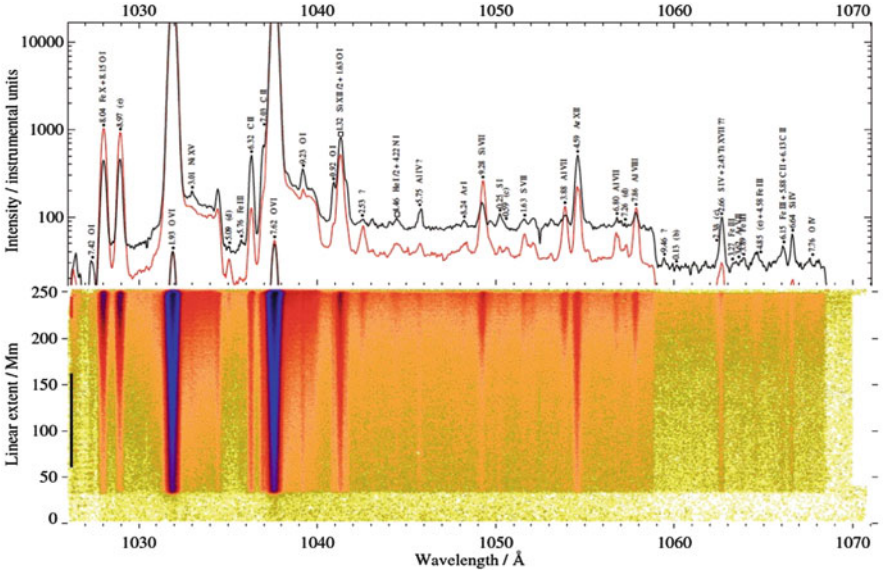

Fig. 2.5 A small portion of the solar EUV spectrum observed with SUMER/SOHO in the wavelength range of $\lambda = 1025$–1070 Å, featuring two O VI lines (1032.0 Å and 1037.6 Å), with the slit positioned in the South-East quadrant of the Sun and extending from near the limb (top of linear scale and red spectrum) to further away from the limb (bottom of linear scale and black spectrum) (Curdt et al. 2004)

region, one associated with a (single-Gaussian) stationary background, and one with an asymmetric, blueshifted (double-Gaussian) line profile due to upflows (with velocities of 50–150 km s^{-1} (Tian et al. 2011; Peter 2010). EUV spectra can also serve to infer density and temperature models of the chromosphere and transition region, for instance by modeling of the optically thick non-LTE radiative transfer for H, C I to C IV, and O I to O VI lines and continua, using SUMER/SOHO spectra (Avrett and Loeser 2008).

2.5 Instrumental Temperature Response Functions

The accuracy and success of solar spectroscopy depends on the instrumental wavelength coverage, sensitivity, and spectral resolution of the instruments. There are a number of (space-borne) solar-dedicated instruments with spectroscopic capabilities (see list of spectrometers in Table 2.2), which have either high spectral resolution with limited imaging capabilities (e.g., BCS/SMM, CDS/SOHO, SUMER/SOHO), or multi-wavelength imagers with high spatial resolution but limited spectral information (e.g. EIT/SOHO, TRACE, or EUVI/STEREO with four temperature filters each, or AIA/SDO with ten temperature filters). The combination of both capabilities leads to imaging spectrographs (e.g., EIS/Hinode or IRIS), but their limitation is governed by the trade-off between time cadence and field-of-view coverage. Each of these types of instruments can be used for temperature and density diagnostics of solar coronal features, but the optimum combination and relative importance of spectral, spatial, and temporal resolution depends on the observed phenomenon to be studied. For instance, flares require a rapid time cadence, with a small field-of-view, while full-Sun irradiance studies can be rastered slowly, but require full-Sun coverage, which can be accomplished by "mosaic tiling".

The prime instrument that currently provides both high spatial resolution and unprecedented multi-wavelength coverage is the *Atmospheric Imaging Assembly* (AIA) instrument onboard the *Solar Dynamics Observatory* (SDO), which started observations on 2010 March 29 and has produced since then essentially continuous data of the full Sun with four 4096 × 4096 detectors with a pixel size of 0.6″, corresponding to an effective spatial resolution of ≈ 1.6″. AIA/SDO contains ten different wavelength channels, three in white light and UV, and seven EUV channels, whereof six wavelengths (94, 131, 171, 193, 211, 335 Å) are centered on strong iron lines (Fe VIII, IX, XII, XIV, XVI, XVIII), covering the coronal range from $T \approx 0.6$ MK to $\gtrsim 16$ MK. AIA/SDO records a full set of near-simultaneous images in each temperature filter with a fixed cadence of 12 s. Instrumental descriptions can be found in Lemen et al. (2012) and Boerner et al. (2012, 2014). The nominal AIA/SDO response functions $R_\lambda(T)$ are shown in Fig. 2.6, based on the most recently available calibration (February 2012) that was updated with improved atomic emissivities according to the CHIANTI Version 7 code.

The AIA/SDO response to coronal holes, quiet Sun, active regions, and flare plasmas has been calculated in O'Dwyer et al. (2010). For this purpose, the contribution

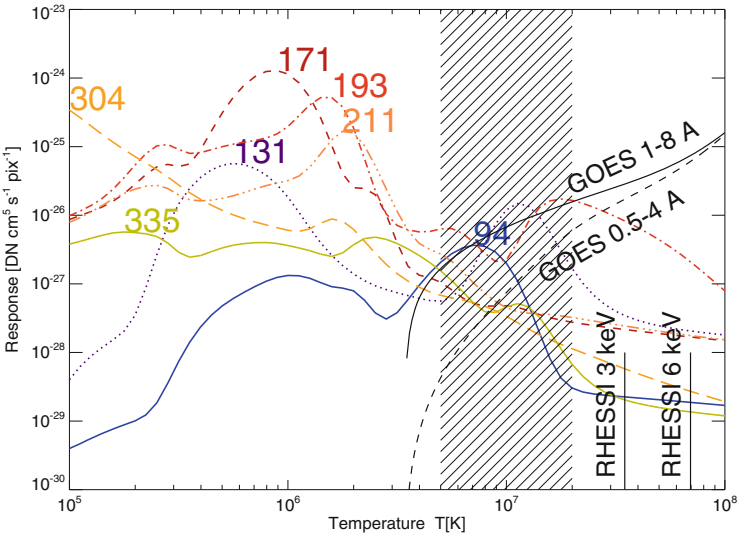

Fig. 2.6 Temperature-response functions for the seven coronal EUV channels of the AIA/SDO, according to the status as of 2012 December. The GOES 1–8 Å and 0.5–4 Å is also shown (in arbitrary flux units), along with the thermal energy of the lowest fittable RHESSI channels at 3 keV and 6 keV. The approximate peak temperature range of large flares ($T_p \approx$ 5–20 MK) is indicated with a hatched area (Aschwanden et al. 2015)

of spectral lines and continuum emission were determined in different regions of the solar corona, by calculating synthetic spectra with the CHIANTI database and sample differential emission measures for the different coronal regions. The synthetic spectra were convolved with the effective area of each channel. From this exercise it was found that the dominant contribution to the 131 Å channel under flare conditions does not come, as expected, from the Fe XX (132.84 Å) or the Fe XXIII (132.91 Å), but instead from the Fe XXI (128.75 Å) line. The dominant contribution to the 94 Å channel for Quiet-Sun conditions comes from the Fe X (94.01 Å) line. The authors recognize that other temperature ranges than those for which each channel was designed may be dominant, depending on the observed targets (active regions, Quiet-Sun, coronal holes, flare sites), which can affect the interpretation of the observed features (O'Dwyer et al. 2010).

A major inconsistency of the AIA/SDO temperature response function has been identified from fitting of differential emission measure (DEM) distributions (Aschwanden and Boerner 2011). The nominal response function of the AIA/SDO 94 Å filters was found to be inconsistent with the other five coronal temperature filters (131, 171, 193, 211, 335 Å) in the low-temperature part of $T \lesssim 2.0$ MK (or $log(T) \leq 6.3$). From self-consistent fits of 100 mostly isothermal (background-subtracted) coronal loop cross-sections, an empirical response function with an enhanced low-temperature response by an average correction factor of $q_{94} = 6.7 \pm 1.7$ was found to fit the data best. This empirical correction was suspected

to be due to a deficiency of missing Fe X lines in the CHIANTI code (Aschwanden and Boerner 2011), as well as missing Fe IX lines (Foster and Testa 2011). The same finding of a significant underestimate of plasma emission in the 94 and 131 Å channel, owing to a multitude of missing lines in CHIANTI in the 50–170 Å range, was corroborated by photometric and thermal cross-calibration, using AIA/SDO, EVE/SDO, and EIS/Hinode data (Boerner et al. 2014). A better agreement of the 94 and 131 Å fluxes was obtained also with a revised emissivity of Fe VIII in the CHIANTI code (Schmelz et al. 2013).

The AIA/SDO response functions shown in Fig. 2.6 reveal a good coverage over the temperature range of $T_e \approx$ 5–20 MK that is prevailing in active regions and flares, but the sensitivity at higher temperature ranges $T_e \gtrsim 20$ MK can be complemented by GOES, RHESSI, or EIS/Hinode data. A reliable reconstruction of the differential emission measure (DEM) distributions is model-dependent and often mathematically ill-defined due to the ambivalent double-peaked response functions of AIA/SDO and the incomplete knowledge of uncertainties in the instrumental response functions and elemental abundances. Combining different instruments with complementary wavelength and temperature coverage can help, but involves additional complications, caused by different spatial field-of-views, absolute calibration errors, and systematic errors in atomic excitation calculations (Judge 2010).

Some effort has been invested in in-flight calibration methods and inter-calibration of instruments with simultaneous and co-spatial observations, often with instruments on suborbital rocket flights. In-flight calibrations are necessary not only to test prelaunch calibrations, but also to monitor the time-dependent changes and degradation of detector sensitivities. In-flight calibrations were carried out by comparison of predicted and observed line ratios, e.g., for CDS/SOHO (Del Zanna et al. 2001, 2010; Lang et al. 2007; Kuin and Del Zanna 2007), or by irradiance comparisons between CELIAS-SEM/SOHO, EIT/SOHO, and CDS/SOHO (McMullin et al. 2002). Inter-calibrations have been undertaken between SUMER / SOHO and CDS / SOHO (Brooks et al. 2000; Pauluhn et al. 2001), between CDS/SOHO, EIT/SOHO, and the sounding rocket flight SERTS-97 (Thomas 2002), between CDS/SODO and the sounding rocket flight EUNIS-06 (Wang et al. 2010, 2011), between EIT/SOHO, CDS/SOHO, and TRACE (Brooks and Warren 2006), or between SWAP/PROBA2 and TRACE, SOHO, STEREO, SDO (Raftery et al. 2013). Other updates on instrumental response functions have been carried out for SXT/Yohkoh (Takeda 2011), for EIT/SOHO and TRACE (Tripathi et al. 2006), and for the dual GOES channels (White et al. 2005).

2.6 Differential Emission Measure Analysis Methods

The *differential emission measure (DEM)* distribution function is defined as an instrument-independent function that characterizes the electron and temperature of an optically-thin structure that emits EUV and soft X-rays. The observed EUV

or soft X-ray fluxes $f_\lambda(x, y)$ observed at an arbitrary location (x, y) in the solar corona at various wavelengths λ with imaging EUV detectors, can be calculated by convolving a DEM function $DEM(x, y, T)$ with the instrumental response functions $R_\lambda(T)$ (Fig. 2.6) of a particular temperature filter λ,

$$f_\lambda(x, y) = \int DEM(x, y, T)\, R_\lambda(T)\, dT \tag{2.6.1}$$

where the DEM function is defined as the squared electron density n_e^2 integrated along the line-of-sight z,

$$DEM(T) = n_e^2 \frac{dz}{dT} \quad [cm^{-5}K^{-1}]\,, \tag{2.6.2}$$

while the total emission measure DEM_{tot} of an area-integrated volume is

$$DEM_{tot}(T) = n_e^2 \frac{dV}{dT} \quad [cm^{-3}K^{-1}]\,, \tag{2.6.3}$$

Obviously, the determination of the DEM function requires an inversion of the temperature integral (Eq. 2.6.1), or a forward-fitting method of a parameterized model of the DEM function. For a compilation of various DEM methods applied to solar data see Table 2.3. We can classify the various DEM methods into four groups: (i) DEM inversion methods, (ii) DEM filter-ratio methods, (iii) DEM forward-fitting methods, and (iv) emission measure loci methods. However, some hybrid methods

Table 2.3 Differential emission measure (DEM) reconstruction methods

Methods	Methodical descriptions
DEM inversion methods	
Monte Carlo Markov Chain (MCMC)	Kashyap and Drake (1998)
Bayesian iterative method	Goryaev et al. (2010)
Bayesian inversion	Guennou et al. 2012a,b
Regularized inversion	Hannah and Kontar (2012)
Filter ratio methods	
Two-filter ratio	Weber et al. (2005)
Three-filter ratio	Aschwanden and Nightingale (2005)
Color-color	Noglik and Walsh (2007)
DEM forward-fitting methods	
Single or multi-Gaussian DEM	Aschwanden and Boerner (2011)
Spatial synthesis (Gaussian DEM)	Aschwanden et al. (2013)
Spatial synthesis (sparse solution)	Cheung et al. (2015)
Emission measure loci methods (EMI)	
Inverse response functions	Landi et al. (2002)

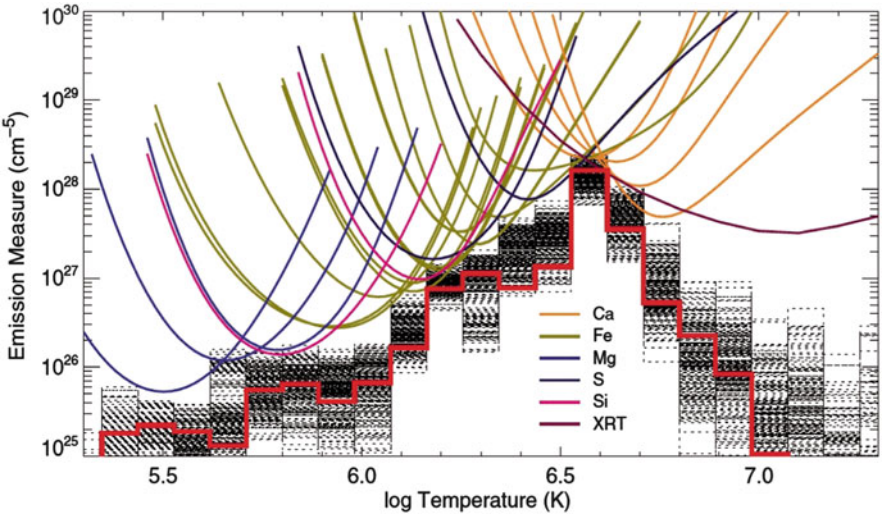

Fig. 2.7 Example of a reconstructed differential emission measure (DEM) distribution from the fluxes observed with EIS/Hinode and XRT in the core of an active region, using three different methods: forward-fitting (red histogram), MCMC method (dotted black histograms), and EMI method (color-coded response curves) (Warren et al. 2011)

could be classified into more than one group. Figure 2.7 shows an example of a DEM with three different visualizations.

On the theoretical side, the concept of DEM distributions and the ill-posed problem of their inversion from the observed optically-thin thermal radiation (produced by bremsstrahlung or free-free and free-bound emission), has been recognized early on. It was pointed out that systematic errors resulting from the incomplete calculations of atomic excitation levels and data noise represent a fundamental limitation in DEM inversions (Judge 2010). In principle, DEM inversion methods make no assumption on the functional form of the DEM distribution and attempt to invert it directly from the observed fluxes in different wavelengths. Examples of such DEM inversion methods are the *Monte Carlo Markov Chain (MCMC)* method (Kashyap and Drake 1998), the Bayesian iterative method (Goryaev et al. 2010), or the regularized inversion method (Hannah and Kontar 2012). Tests of isothermal DEMs with the MCMC method, including data noise and uncertainties in the atomic data, revealed that the MCMC method cannot resolve isothermal plasmas better than $\Delta log(T) \approx 0.05$, and that two isothermal components can not be resolved better than $\Delta log(T) \approx 0.2$ (Landi et al. 2012). Tests on synthetic single-Gaussian and multi-Gaussian DEMs with the *regularized inversion* technique yielded uncertainties of $\Delta log(T) \approx 0.1$–$0.5$ and a valid range of the retrieved DEM down by about two orders of magnitude from the peak of the DEM (Hannah and Kontar 2012).

A simplified approach to a DEM inversion is the line-ratio method, which should be used for isothermal (or near-isothermal) structures only, within a temperature range in which the line ratio has a unique solution,

$$\frac{f_{\lambda,1}}{f_{\lambda,2}} = \frac{\int DEM(T)\, R_{\lambda,1}(T)\, dT}{\int DEM(T)\, R_{\lambda,2}(T)\, dT} \approx \frac{R_{\lambda,1}(T)}{R_{\lambda,2}(T)} \,. \tag{2.6.4}$$

For instance, the TRACE 173 and 195 Å filters have a unique filter ratio within a temperature range of $T_e \approx 0.7$–1.8 MK. The ambiguity of two-filter ratios has been investigated for (isothermal) delta-like DEM and (multi-thermal) rectangular DEM functions (Weber et al. 2005). Triple-filter ratios (say $q_{1,2} = f_{\lambda,1}/f_{\lambda,2}$ and $q_{2,3} = f_{\lambda,2}/f_{\lambda,3}$) have less ambiguity over a larger temperature range, i.e., $\Delta T_e \approx [0.7, 2.8]$ MK for the TRACE 171, 195, and 284 Å filters, and thus allowing discrimination between narrow (isothermal) and broad (multi-thermal) DEM distributions (Aschwanden and Nightingale 2005). Triple-filter ratios can be visualized with a so-called *color-color method*, which plots the ratios $q_{1,2}$ and $q_{2.3}$ versus each other (Noglik and Walsh 2007).

The alternative approach to inversion methods is the forward-fitting technique, which requires a parameterization of the DEM function with a number of free parameters that should not exceed the number of constraints, which is the number of fluxes f_λ observed in different wavelengths. One of the most robust choices of a DEM function with a minimum of free parameters is a single-Gaussian (in the logarithm of the temperature), which has 3 free parameters only and is defined by the peak emission measure EM_p, the DEM peak temperature T_p, and the logarithmic Gaussian width σ_T (Eq. 2.6.5). The DEM parameter has the cgs-units [cm^{-5} K^{-1}],

$$DEM(T) = n_e^2 \frac{dz}{dT} = EM_p \exp\left(-\frac{[log(T) - log(T_p)]^2}{2\sigma_T^2}\right) , \tag{2.6.5}$$

where the total emission measure $EM = n_e^2 dz = \int DEM(T)\, dT$ is the temperature integral over the Gaussian DEM (in units of [cm^{-5}]). Besides single-Gaussian DEMs, double-Gaussians or multiple Gaussians are also frequently used,—see benchmark tests in Aschwanden et al. (2015).

A novel method consists of subdividing the observed space into small areas down to the pixel size of the image (which are more likely to encompass a narrower and simpler temperature distribution due to the smaller number of bright structures that are intersected) and then to perform a DEM reconstruction in every pixel, while the total DEM of the entire flare area or active region can then simply be added together. Such a *spatial-synthesis method* has been developed for AIA/SDO recently (Aschwanden et al. 2013). A similar spatial-synthesis method, generalized for sparse DEM solutions rather than Gaussian DEM solutions (for each pixel), has been developed and validated with AIA/SDO data also (Cheung et al. 2015).

An alternative formulation of a DEM distribution function is the so-called *emission measure loci method (EMI)* (Landi et al. 2002), which displays the inverse

response functions scaled by the observed line intensity (see example in Fig. 2.7). Such a diagram reveals whether a DEM is isothermal (in which case all inverse response functions intersect in one point) or multi-thermal (in which case the lower envelope of the inverse response functions outline a broadband DEM function).

2.7 Multi-Thermal Energy

The differential emission measure analysis of a solar phenomenon, such as a quiet coronal loop, an active region, or a flare, offers also a convenient formalism to calculate the exact amount of (multi-)thermal energy that is contained in the observed phenomena. If the structure of interest is isothermal (with a single temperature) and homogeneous (with a constant electron density), the thermal energy would be simply,

$$E_{th} = 3 n_e k_B T_e V \tag{2.7.1}$$

which is a product of the average electron density n_e, the electron temperature T_e, and the volume V. The DEM formalism discussed in the foregoing section allows us to replace the unknown electron density and volume with the total emission measure EM_{tot}, which results from the temperature integral (Eq. 2.6.3),

$$EM_{tot} = \int DEM_{tot}(T) dT = \int n_e^2 dV = n_e^2 V \ . \tag{2.7.2}$$

where n_e defines a mean electron density that is averaged over the volume V with a filling factor of unity. Inserting the total emission measure EM_{tot} (Eq. 2.7.2) into the expression for the thermal energy E_{th} yields then,

$$E_{th} = 3 k_B T_e \sqrt{EM_{tot}\ V} \ . \tag{2.7.3}$$

This allows us to calculate the thermal energy from the observables EM_{tot}, T_e, and V, but we have to be aware that this applies only to a strictly isothermal structure with a homogeneous density.

However, since the solar flare plasma is inhomogeneous and multi-thermal, we can calculate a more accurate expression for the total thermal energy when imaging observations are available. Ideally, such as in the case of an MHD simulation, the full 3D distributions of temperatures $T_e(x, y, z)$ and electron densities $n_e(x, y, z)$ are known, so that the most accurate expression for thermal energies can be computed by volume integration (e.g., Testa et al. 2012),

$$E_{th} = \int\int\int 3 n_e(x, y, z) k_B T_e(x, y, z)\ dx\ dy\ dz \ . \tag{2.7.4}$$

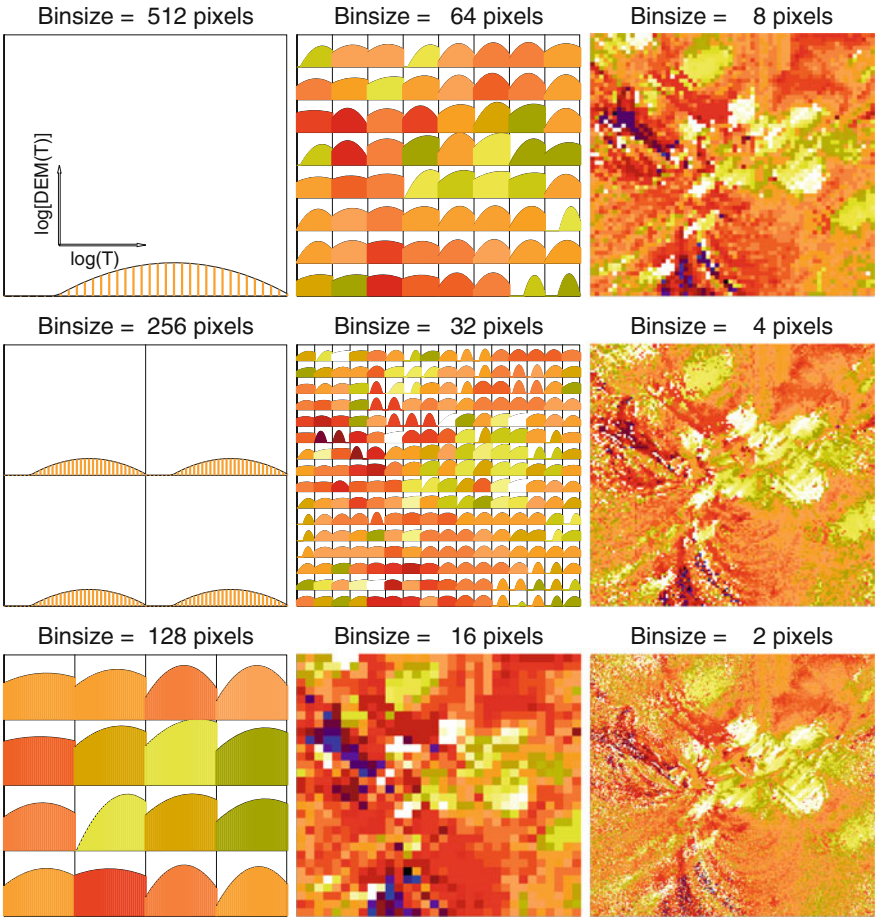

Fig. 2.8 The spatial synthesis DEM method is visualized by single-Gaussian DEM fits in macropixels of sizes decreasing by a factor 2, from $\Delta x = 512, 256, \ldots, 2$. A single-Gaussian DEM fit is executed in each macropixel to the fluxes of the 6 coronal AIA/SDO wavelengths and the peak temperature in each macropixel is visualized by color, covering the range $log(T) = [5.8, 7.45]$. The data are obtained from the GOES X2.2-class flare observed with AIA/SDO on 2011 February 15, 01:40 UT (Aschwanden et al. 2015)

For numerical computations, we use a discretized 3D volume (x_i, y_j, z_k) that is aligned in the z-direction with the line-of-sight, while images in different wavelengths have the 2-D coordinate system (x_i, y_i) with pixel size $\Delta x = \Delta y$. A DEM analysis yields an inversion of a DEM distribution $DEM_{ij}(T) = DEM(T; x_i, y_j)$ in every pixel (or macropixel) at location (x_i, y_j) (Fig. 2.8). The column depth emission measure is defined by

$$EM_{ij} = \int DEM_{ij}(T)\, dT = \int n_{ij}^2\, dz = n_{ij}^2\, L \tag{2.7.5}$$

which yields an average density n_{ij} along the line-of-sight column depth with length L at each pixel position (x_i, y_j). We can then define a thermal energy $E_{th,ij}$ for each column depth $L = V^{1/3}$ by summing all contributions EM_k from each temperature interval ΔT_k (Eq. 2.7.3),

$$E_{th,ij} = \sum_k 3k_B V^{1/2}\, T_{ijk}\, EM_{ij}^{1/2} = 3k_B V^{1/2} \sum_k \left[T_k^2\, DEM_{ij}(T_k)\, \Delta T_k \right]^{1/2} . \tag{2.7.6}$$

Note that the temperature bins ΔT_k are usually chosen equidistant in the logarithm of the temperature T_k, in a standard DEM analysis. The total thermal energy in the computation box can then be obtained by summing up the partial thermal energies EM_{ij} from all pixels (see examples of spatial summing in Fig. 2.9),

$$E_{th} = \sum_i \sum_j E_{th,ij} \Delta x^2 = 3k_B V^{1/2} \sum_i \sum_j \sum_k \left[T_k^2\, DEM_{ij}(T_k)\, \Delta T_k \right]^{1/2} \Delta x^2$$

$$= 3k_B V^{1/2} \sum_k \left[T_k^2 \sum_i \sum_j DEM_{ij}(T_k)\, \Delta T_k \right]^{1/2} \Delta x^2 \tag{2.7.7}$$

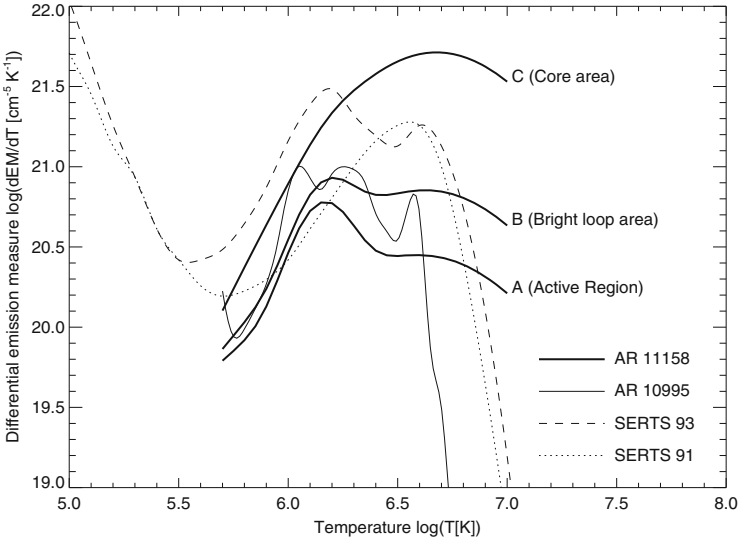

Fig. 2.9 Examples of differential emission-measure (DEM) distributions dEM/dT of the flaring active region NOAA 11158 observed on 2011 February 15 shortly before a GOES X2.2 flare was produced, summed in 3 different areas: entire active region (A), central bright loop area (B), and its core area (C), all computed with the spatial-synthesis method (Aschwanden et al. 2013). The DEMs are compared with other active regions, observed with STEREO and SERTS

where we can replace the partial DEM functions $DEM_{ij}(T_k)$ per column depths by the total DEM function $DEM(T_k)$,

$$DEM(T_k) = \sum_i \sum_j DEM_{ij}(T_k) \Delta x^2 \ , \tag{2.7.8}$$

which leads to the expression

$$E_{th} = 3k_B V^{1/2} \sum_k \left[T_k^2 \ DEM(T_k) \ \Delta T_k \right]^{1/2} \ . \tag{2.7.9}$$

We compare the thermal energy E_{th} (Eq. 2.7.9) computed in this way for a multi-thermal DEM distribution with the isothermal approximation (Eq. 2.7.3) by their ratio in Fig. 2.10, given for a set of thermal widths $\sigma_T = 0.1, 0.2, \ldots, 1.0$ in the single-Gaussian DEM function (Eq. 2.6.5) that is used for DEM modeling in each pixel. For small values, say $\sigma_T = 0.1$, the DEM distributions are almost isothermal, and thus the approximation (Eq. 2.7.3) is appropriate and we obtain a ratio near unity ($E_{iso}/E_{multi} \gtrsim 1$). For broader multi-thermal DEM functions, the ratio increases systematically, up to a factor of ≈ 30. At higher temperatures, the ratio decreases because the temperature range between the peak of the DEM and the upper limit (here at $T = 30$ MK) becomes increasingly smaller and thus has less weight in the asymmetric T^2-weighting of the thermal energy contributions. Observations have typically a thermal width of $\sigma_T \approx 0.5$, and thus the multi-thermal energy is about

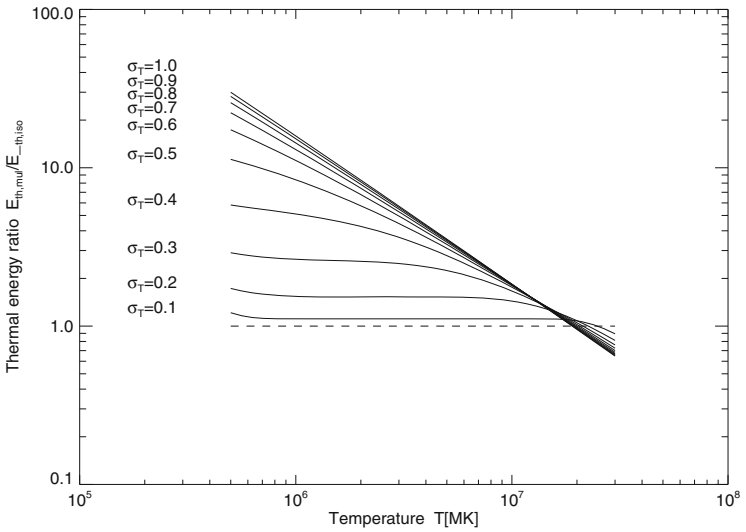

Fig. 2.10 Thermal energy ratio $E_{th,mul}/E_{th,ana}$ computed for narrow ($\sigma_T \approx 0.1$–0.5 and broad multi-temperature distributions ($\sigma_T \approx 0.5$–1.0), normalized by the isothermal approximation, in the range of $T = 0.5$–30 MK (Aschwanden et al. 2015)

a factor of $\approx$ 2–10 higher for flare peak temperatures of $T_p \approx$ 10–20 MK than the E_{th} in the isothermal approximation (Eq. 2.7.3).

2.8 Density-Sensitive Line Ratio Diagnostics

The DEM analysis provides an average electron density under the assumption of a filling factor of unity with respect to the volume over which the emission measure is integrated. Even when a coronal structure is spatially resolved (in transverse direction to the line-of-sight), the density inhomogeneities along the line-of-sight are still not resolved and cannot be measured with DEM modeling.

A more direct electron density measurement method exists that uses ratios of density-sensitive atomic lines. The ratio of two spectral lines emitted by the same ion is,

$$\frac{F_{i,j}}{F_{k,l}} = \frac{\int G_{i,j}(T, n_e) DEM(T) dT}{\int G_{k,l}(T, n_e) DEM(T) dT} , \tag{2.8.1}$$

where $DEM(T)$ is the differential emission measure distribution function (as a function of temperature), while $G_{i,j}(T, n_e)$ and $G_{k,l}(T, n_e)$ are the contribution functions of the two lines for the atomic transitions $(i \mapsto j)$ and $(k \mapsto l)$. Since the ion fractions and the elemental abundances are the same for the two lines, the ratio of the integrals (Eq. 2.8.1) depend on the populations of the upper levels i and k of the two lines, and on the Einstein coefficients for spontaneous radiation. The density sensitivity of the atomic population ratio can be due to the competing importance of collisional and relative de-excitation from upper levels, or the density sensitivity of the population of the lower level(s) from which the upper level is populated (Phillips et al. 2008). At least seven types of ratios are suitable for electron density diagnostics: (i) ratios of forbidden lines, (ii) ratios of allowed lines, (iii) ratios of both forbidden and allowed lines, (iv) ratios from high energy levels, (v) dielectronic satellite line spectra, (vi) ratios from different ions, and (vii) ratios of the collisional and resonantly scattered components of spectral lines (Phillips et al. 2008).

An example of a density-sensitive line ratio (Fe XIII lines) measured with EIS/Hinode is shown in Fig. 2.11. Density-sensitive line ratios were measured with CDS/SOHO, SUMER/SOHO, UVCS/SOHO, SERTS rocket flights, and most recently with EIS/Hinode, EVE/SDO, and IRIS. The target regions of electron density measurements cover Quiet Sun regions, active regions, flares, small flares, transient events, polar plumes, coronal holes, coronal streamers, loop footpoints, prominences, etc.

The EIS/Hinode (EUV Imaging Spectrometer) provides currently some of the best coronal density diagnostics (Watanabe et al. 2007; Feldman et al. 2008; Warren and Brooks 2009; Young 2009; Young et al. 2009; Ko et al. 2009), which allows electron densities to be determined with an unprecedented precision of up to $\pm 5\%$ in active regions (Young et al. 2009). In the recent study of Young et al. (2009), the

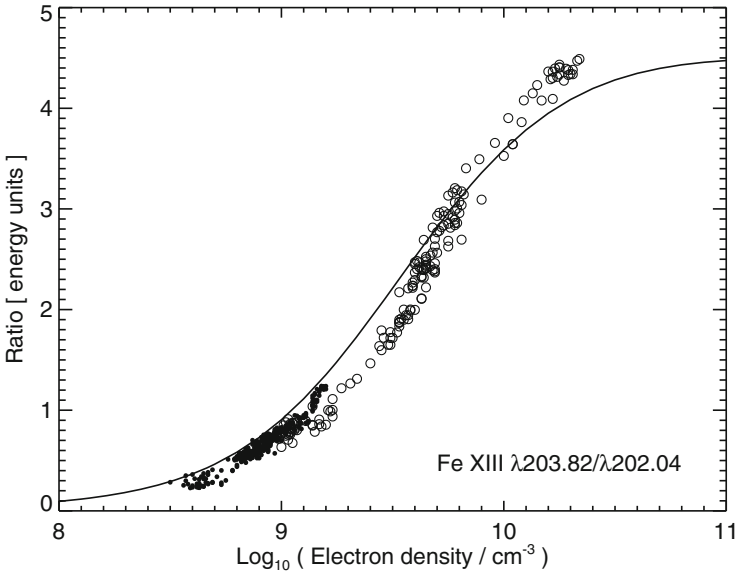

Fig. 2.11 A comparison of the measured variation of the Fe XIII λ203.82/λ202.04 intensity ratio with density compared to the predictions from the CHIANTI data base (continuous line). The measured densities are obtained from the Fe XIII λ196.54/λ202.04 ratio measured at two different days (filled and full circles) (Young et al. 2009)

most accurate density diagnostics was obtained from Fe XII (186.88Å/195.12Å) and (196.64Å/195.12Å), and from Fe XIII (196.54Å/202.04Å) and (203.82Å/202.04Å), with density values in the range of $n_e \approx 10^{8.5}$–$10^{11.0}$. However, the high precision measurements with EIS/Hinode demonstrated significant discrepancies, always giving higher densities with Fe XII ratios than those from Fe XIII ratios; this was identified as a problem with the CHIANTI atomic model (Young et al. 2009). Revised wavelengths of Fe XII 196.647 Å ±0.003 Å and Fe XIII 196.518 Å ±0.003 Å were suggested (Young et al. 2009), while in earlier studies the following line pairs were used: Fe XII 186.9 Å /195.1 Å and Fe XIII 203.8 Å /202.0 Å (Watanabe et al. 2007).

Progress has been made to resolve blends (i.e., lines that overlap in their wavelength width) using instruments with high spectral resolution (e.g., with EIS/Hinode), which leads to disentangled line ratios that are required for accurate electron density diagnostics (e.g., Ko et al. 2009). Measurements of near-isothermal temperature structures in the Quiet Sun observed with EIS/Hinode above the solar limb, indicate that the strong Fe and Si lines are generally consistent which each other, while a significant fraction of the weaker emission lines observed in the EIS/Hinode wavelength ranges cannot be understood with current atomic data of CHIANTI, see Table 2.4 (Warren and Brooks 2009). Iterating differential emission measure fits with more comprehensive atomic data (such as with newly identified

Table 2.4 Monte-Carlo Markov chain (MCMC) differential emission measure model applied to the Fe IX-Fe XVI lines (Warren and Brooks 2009)

Ion	Wavelength	I_{calc}	I_{obs}	I_{calc}/I_{obs}
Fe IX	188.497	43.13	31.28	1.09
Fe IX	189.941	18.02	15.36	1.17
Fe IX	197.862	24.50	21.02	1.17
Fe X	174.532	560.17	572.57	0.98
Fe X	177.239	304.81	308.28	0.99
Fe X	184.536	119.94	142.17	0.84
Fe XI	180.401	415.93	432.24	0.96
Fe XI	182.167	53.84	58.50	0.92
Fe XI	188.216	196.01	224.90	0.87
Fe XI	192.813	50.16	57.75	0.87
Fe XII	186.880	33.11	35.17	0.94
Fe XII	192.394	88.03	79.48	1.11
Fe XII	193.509	185.60	177.53	1.05
Fe XII	195.119	277.87	274.67	1.01
Fe XII	196.640	9.04	11.03	0.82
Fe XIII	196.525	1.71	2.71	0.63
Fe XIII	197.434	5.24	7.10	0.74
Fe XIII	200.021	6.37	9.43	0.68
Fe XIII	202.044	126.16	157.66	0.80
Fe XIII	203.826	27.46	25.02	1.10
Fe XIII	204.937	7.88	8.19	0.96
Fe XIV	211.316	30.71	39.47	0.78
Fe XIV	270.519	7.97	6.96	1.14
Fe XIV	274.203	17.19	18.31	0.94
Fe XV	284.160	28.72	21.20	1.35
Fe XVI	262.984	0.17	0.42	0.42

lines in the CHIANTI code) is an ongoing task to improve the accuracy and completeness of atomic data. For instance, among the Fe IX transitions in the wavelength range of 188–198 Å identified for the first time in EIS/Hinode spectra, the line at 197.86 Å was found to be unblended and close to the peak of the EIS/Hinode sensitivity curve, making it a valuable diagnostic of plasma near a temperature of $T_e \approx 0.8$ MK (Young 2009). The ratio of λ197.86 Å to the λ171.07 Å resonance line of Fe IX was found to be a good temperature diagnostic, independent of the density (Young 2009).

EIS/Hinode obtains high-resolution spectra in the wavelength ranges 170–210 Å and 250–290 Å. For hot plasma in non-flaring active regions, He II, Si VII, Ca XVII are found to be suitable for probing the chromosphere/transition region, while Fe XXIII, Fe XXIV lines are used for electron density diagnostics up to flare temperatures (Ko et al. 2009). In flaring conditions, EIS/Hinode yields electron density diagnostics in a range of $n_e \approx 10^{10}$–10^{13} cm^{-3}, by means of intensity ratios of lines emitted by Ti, Cr, and Mn ions (Phillips et al. 2008). EIS/Hinode observed the footpoints of flare loops during GOES C-class to X-class flare events (Milligan

2015). Milligan (2011) used five pairs of density-sensitive line ratios formed at different temperatures (Mg VII, Si X, Fe XII, Fe XIII, Fe XIV), obtaining densities approaching $n_e \lesssim 10^{11.5}$ cm^{-3}.

Similar electron densities ($n_e \approx 10^{11.2}$–$10^{12.1}$ cm^{-3}) are measured also with density-sensitive Fe XXI ratios during X-class flares with the EUV Variability Experiment (EVE) onboard SDO (Milligan et al. 2012). Since EVE/SDO spectra can be measured with a cadence of 10 s, the detailed evolution of these high-temperature electron densities can be monitored (Milligan et al. 2012). A review on EUV spectroscopy of the chromosphere/corona during flares is provided in Milligan (2015).

The most recent electron density diagnostics come from the *Interface Region Imaging Spectrograph (IRIS)*, which has passbands from 1332–1358 Å, 1389–1407 Å, to 2783–2834Å (De Pontieu et al. 2014). The O IV and S IV intercombination lines around 1400 Å provide a new density diagnostic (Polito et al. 2016). In observations of an active region loop, a near isothermal temperature $T_e \approx 10^5$ K and an iso-density of $n_e \approx 4 \times 10^{10}$ cm^{-3} was measured, while the densities increase up to $n_e \lesssim 10^{13}$ cm^{-3} during impulsive flares (using the S IV ratio). The S IV lines provide a higher range of density sensitivity than the O IV lines. Thus, IRIS corroborates density measurements from previous instruments (such as EIS/Hinode), although it operates in a non-overlapping spectral wavelength range.

2.9 Line Profile Diagnostics

The spectral line profile observed in EUV or soft X-rays contains a host of diagnostic information. Theoretically, radiative emission produced from a transition between two atomic levels E_i and E_j of an ion occurs at a fixed frequency $\nu_{i,j} = (E_j - E_i)/h$, with h being the Planck constant, which essentially defines a monochromatic line. This monochromatic line, however, has always a finite width, caused by a number of broadening mechanisms: (i) the *natural line profile* given by the intrinsic energy width of atomic energy levels, (ii) the *Doppler line profile* due to motion of the emitting ion along the line-of-sight, (iii) the *pressure line profile* due to interaction between the emitting ion and other particles in the plasma along a line-of-sight, and (iv) the *instrumental line profile* given by the finite spectral resolution of the optical components of the spectrograph (Phillips et al. 2008). These four effects mostly produce a symmetric line profile, which is often characterized by a Lorentzian or Gaussian function. On top of these omni-present effects there are additional physical mechanisms that modify a Gaussian line profile, such as thermal broadening due to local heating of the plasma, or plasma motion that produces asymmetric tails in form of redshifts (when the motion is away from the observer) or blueshifts (from motion towards the observer). The latter two effects are particularly interesting for diagnostics of plasma heating, plasma flows in the corona, chromospheric evaporation in flares, coronal condensation, turbulence, or the presence of waves.

All forms of motion of emitting ions produce a Doppler effect, which translates into a shifted wavelength of

$$\lambda = \lambda_0 \left(1 - \frac{v}{c}\right) , \tag{2.9.1}$$

where c is the speed of light, and plasma motion is generally non-relativistic ($v \ll c$), resulting into small line shifts. For a collisional or thermalized plasma, which has a Maxwell-Boltzmann distribution of velocities $f(v)$, the line profile $F(\lambda)$ can be approximated by a Gaussian function,

$$F(\lambda) = \frac{1}{\sqrt{\pi}\Delta\lambda} \exp - \left(\frac{(\lambda - \lambda_0)}{\Delta\lambda}\right)^2 , \qquad FWHM = \frac{\lambda_0}{c}\sqrt{4 \ln 2 \frac{2k_B T_i}{M_i}} , \tag{2.9.2}$$

where T_i is the ion temperature, M_i is the ion mass, FWHM is the full width at half maximum, and $\Delta\lambda = (\lambda_0/c)(2k_B T_i/M_i)^{1/2}$ is the Gaussian width. This is just the minimum line width for an ion with a given temperature T_i that can be measured in the coronal plasma. However, often there is additional line broadening observed due to non-thermal plasma motion or turbulence, which can be characterized by an additional non-thermal velocity v_{nth},

$$FWHM = \frac{\lambda_0}{c}\sqrt{4 \ln 2 \left(\frac{2k_B T_i}{M_i} + v_{nth}^2\right)} . \tag{2.9.3}$$

In observations of plasma flows in the transition region or corona, siphon flows in coronal loops, or upflows of heated plasma by chromospheric evaporation, a line profile can often be decomposed into two components, where the primary line profile is centered at the rest wavelength λ_0, and the secondary line profile is centered at a blueshifted or redshifted wavelength, depending on the direction of the plasma motion with respect to the observer. This effect allows spectroscopic detection of plasma flows that is most sensitive in parallel or anti-parallel direction to the line-of-sight of the observer, while imaging observations are most sensitive in the detection of plasma motion in perpendicular direction to the line-of-sight. This is another area where spectroscopic and imaging observations are nicely complementary. For instance, MHD kink-mode oscillations of coronal loops were first detected by the high-resolution imaging instrument TRACE, while ubiquitous small-amplitude Alfvénic waves in the solar corona were discovered by their Doppler shift with the *Coronal Multi-Channel Polarimeter (CoMP)* (Tomczyk et al. 2007). Evidence for the detection of Alfvén waves above the solar limb was obtained by the theoretically predicted correlation between the line broadening velocity Δv and the electron density $n_e(r)$ as a function of altitude above the limb,

$$\Delta v(r) = v_\varphi(r) \propto \rho^{-1/4}(r) \propto n_e^{-1/4}(r) , \tag{2.9.4}$$

where v_φ is the phase speed of Alfvén waves, $\rho = m_p n_i \approx m_i n_e$ is the mean mass density, n_e is the electron density, and $r \approx 1.0$–1.4 is the distance from Sun center.

Some recent work that used spectroscopic information of line profiles in order to investigate physical conditions in coronal phenomena includes:

Mass flows in transition region: The canonical variation of the Doppler velocity in a vertical direction across the transition region, $v_{nth}(h)$, starts with a minimum at $T \approx 10^4$ K, ramps up to ≈ 10 km s^{-1} at $T \approx 10^5$ K, and drops again from zero to slightly negative velocities at $T \approx 10^6$ K at the coronal base (Fig. 2.12) (Peter 2001; Dadashi et al. 2011). EIS/Hinode measurements reveal persistent redshifts in cooler lines and persistent blueshifts in hotter lines (Del Zanna 2008). Detailed modeling of the asymmetries of line profiles with EIS/Hinode show that the best fits are achieved with a combination of a narrow Gaussian line core and a broad minor wing component (Fig. 2.13). The broad minor component contributes 10%–20% to the emission, is about twice as wide as the core, shows strong blueshifts up to 50 km s^{-1}, especially in the footpoint regions of loops, and appears to be the main provider of heating and mass supply to the corona, perhaps related to type II spicules (Peter 2010).

Active regions: The largest nonthermal line widths in active regions, measured with EIS/Hinode, do not occur in the most intense regions. Measurements with EIS/Hinode reveal large areas of outflows (20–50 km s^{-1}) that can persist for at

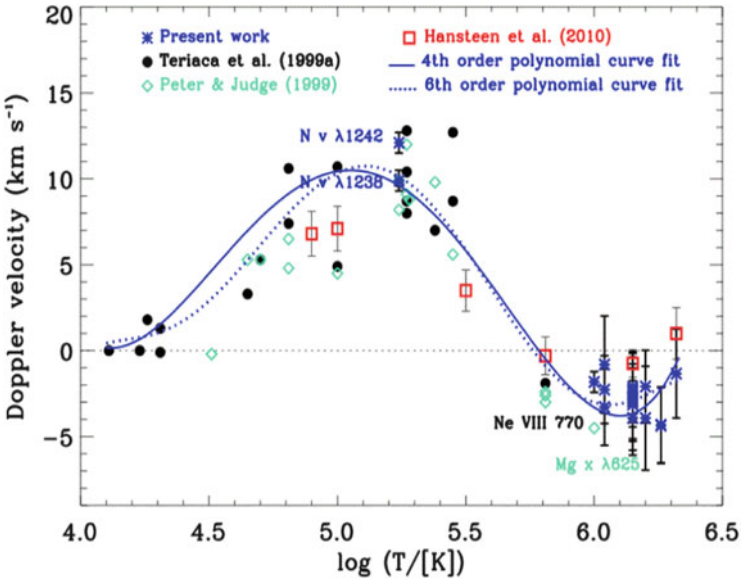

Fig. 2.12 Average Doppler shift (positive is red shift, negative is blue shift) in the quiet Sun at disk center of various ions measured from SUMER/SOHO and EIS/Hinode spectra (Dadashi et al. 2011)

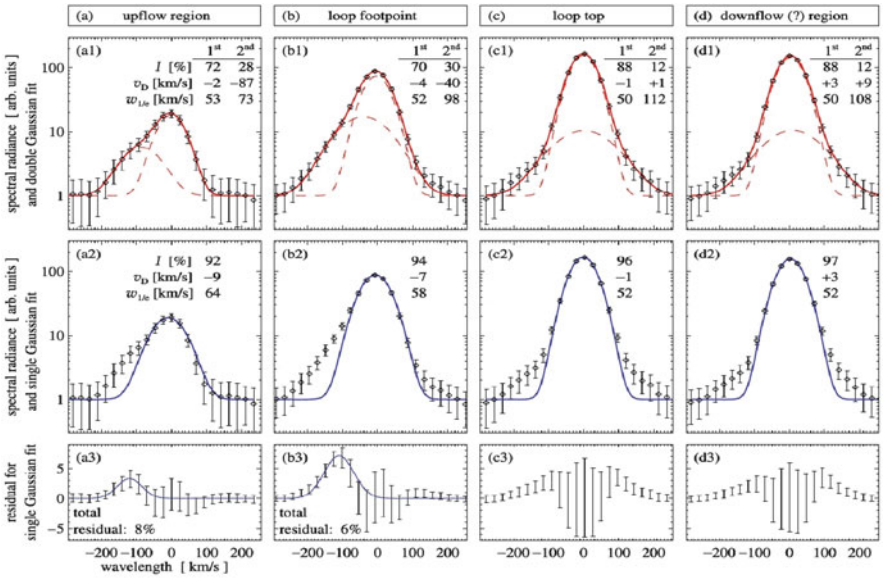

Fig. 2.13 Spectral line profiles of Fe XV (284 Å) measured with EIS/Hinode in 4 different regions (upflow region, loop footpoint, loop top, downflow region), fitted with double-Gaussians (top) and single Gaussians (middle), and the residuals of the single Gaussian fits (bottom row) (Peter 2010)

least a day, possibly feeding the slow solar wind along open field lines (Doschek et al. 2008).

Bright points: EIS/Hinode observations show X-ray bright points with nonthermal velocities of 220 km s^{-1}, but more often in the range of 10–20 km s^{-1}. Two distinctly different types of brightenings are distinguished depending on their non-thermal velocity behavior measured with EIS/Hinode, a fast type ($v_{nth} > 60$ km s^{-1}) associated with magnetic reconnection near the transition region, and a slow type ($v_{nth} < 60$ km s^{-1}) associated with magnetic emergence.

Alfvén waves above the limb: Line broadening measured with SUMER/SOHO was found to decrease with altitude above the limb as a function of the electron density according to the predictions of Alfvén waves (with the Alfvén speed being inversely proportional to the square root of the density). A line width reduction can also be interpreted in terms of resonant energy conversion from Alfvén to acoustic waves, or by ion-cyclotron absorption of high-frequency waves.

Fast solar wind: A correlation between the blueshift and brightness of UV lines measured with SUMER/SOHO suggests that the fast solar wind originates from the chromospheric magnetic network. Velocity distribution anisotropies can be studied from O VI line profiles. Polar coronal holes have larger line widths than the equatorial holes, suggesting a faster solar wind emanating from polar holes than from equatorial holes.

Solar flare chromospheric evaporation and cooling: Doppler shifts and excess line broadening indicate evidence for chromospheric evaporation during the impulsive flare phase (due to blueshifted upflows), as well as evidence for condensation or "coronal rain" during the postflare phase (due to redshifted downflows). EIS/Hinode observations revealed fast blueshifted soft X-ray jets, as well as an increase of nonthermal motions many hours before the flare begins, which was interpreted as the first spectroscopic evidence of a fast-mode shock wave in a flare.

From this sample of recent spectroscopic line profile diagnostics, especially using EIS/Hinode, we see that very quantitative measurements of mass flows and flow velocities can be obtained in the solar corona, which are crucial for modeling of inflows and outflows of magnetic reconnection processes, footpoint-driven upflows in the chromospheric evaporation scenario, hydrodynamic flow instabilities, coronal condensation and "rain", as well as for studying the source regions and heating of the slow and fast solar wind.

References

(2.1) Photospheric Elemental Abundances

Allende Prieto, C., Lambert, D.L., and Asplund, M. 2002, *A reappraisal of the solar photospheric C/O ratio* ApJ 573, L137, [338 c, 22 c/y].

Allende Prieto, C. 2016, *Solar and stellar photospheric abundances*, LRSP 13, 1, [2 c, 1 c/y].

Asplund, M., Grevesse, N., Sauval, A.J., et al. 2004, *Line formation in solar granulation. IV [O I], O I and OH lines and the photospheric O abundances*, A&A 417, 751, [656 c, 49 c/y].

Asplund, M., Grevesse, N., and Sauval, A.J. 2005, *The solar chemical composition*, (eds., T.G.Barnes III and Frank N.Bash), Astronomical Society of the Pacific Conference Series Vol. 336, 25, [1507 c, 121 c/y].

Asplund, M., Grevesse, N., Sauval, A.J. and Scott, P. 2009, *The chemical composition of the Sun*, ARAA 47, 481, [3260 c, 384 c/y].

Basu, S. and Antia, H.M. 2004, *Constraining solar abundances using helioseismology*, ApJ 606, L85, [185 c, 14 c/y].

Caffau, E., Ludwig, H.G., Steffen, M., et al. 2008, *The photospheric solar oxygen project. I. Abundances analysis of atomic lines and influence of atmospheric models.* A&A 488, 1031, [185 c, 19 c/y].

Feldman, U. and Widing, K.G. 2003, *Elemental abundances in the solar upper atmosphere derived by spectroscopic means*, SSRv 107/3, 665, [84 c, 6 c/y].

Grevesse, N., Asplund, M., and Sauval, A.J. 2007, *The solar chemical composition*, SSRv 130, 105, [389 c, 37 c/y].

Grevesse, N., Scott, P., Asplund, M., et al. 2015, *The elemental composition of the Sun, III. The heavy elements Cu to Th**, A&A 573, A27, [82 c, 33 c/y].

Laming, J.M. 2015, *The FIP and inverse FIP effects in solar and stellar coronae*, LRSP 12, 2, [55 c, 22 c/y].

Lodders, K. 2003, *Solar system abundances and condensation temperatures of the elements*, ApJ 591, 1220, [2138 c, 147 c/y].

Melendez, J., Asplund, M., Gustafsson, B., et al. 2009, *The peculiar solar composition and its possible relation to planet formation*, ApJ 704, L66, [193 c, 23 c/y].

Scott, P., Grevesse, N., Asplund, et al. 2015a, *The elemental composition of the Sun. I. The intermediate mass elements Na to Ca**, A&A 573, A25, [92 c, 37 c/y].
Scott, P., Asplund, M., Grevesse, N., et al. 2015b, *The elemental composition of the Sun. II. The iron group elements Sc to Ni**, A&A 573, A26, [116 c, 46 c/y].

(2.2) The First-Ionization-Potential (FIP) Effect

Allende Prieto, C. 2016, *Solar and stellar photospheric abundances*, LRSP 13, 1, [2 c, 1 c/y].
Aschwanden, M.J., Schrijver, C.J., Winebarger, A.R., et al. 2003, *A new method to constrain the iron abundance from cooling delays in coronal loops*, ApJ 588, L49, [10 c, 1 c/y].
Asplund, M., Grevesse, N., Sauval, A.J., et al. 2004, *Line formation in solar granulation. IV [O I], O I and OH lines and the photospheric O abundances*, A&A 417, 751, [656 c, 49 c/y].
Brooks, D.H. and Warren, H.P. 2011, *Establishing a connection between active region outflows and the solar wind: Abundance measurements with EIS/Hinode* ApJL 272, L13, [60 c, 9 c/y].
Ciaravella, A., Raymond, J.C., Li, J., et al. 2002, *Elemental abundances and post-coronal mass ejection current sheet in a very hot active region*, ApJ 575, 1116, [104 c, 7 c/y].
Doschek, G.A. and Warren, H.P. 2016, *The mysterious case of the solar argon abundance near sunspots in flares*, ApJ 825, 36, [11 c, 7 c/y].
Drake, J.J. 2011, *Neon insights from old solar X-rays: A plasma temperature dependence of the coronal neon content*, ApJ 743, 22, [6 c, 1 c/y].
Drake, J.J. and Testa, P. 2005, *The solar model problem solved by the abundance of neon in nearby stars*, Nature 436, Issue 7050, 525, [170 c, 14 c/y].
Edgar, R.J. and Esser, R. 2000, *Nonequilibrium ionization and first ionization potential effect diagnostics*, ApJ 538, 167, [6 c, 0.4 c/y].
Feldman, U. and Laming, J.M. 2000, *Element abundances in the upper atmospheres of the Sun and stars: Update of observational results*, Physica Scripta 61, 222, [164 c, 9 c/y].
Feldman, U. and Widing, K.G. 2003 , *Elemental abundances in the upper atmosphere derived by spectroscopic means*, SSRv 107/3, 665, [84 c, 6 c/y].
Feldman, U. and Widing, K.G. 2007, *Spectroscopic measurement of coronal compositions*, SSRv 130, 115, [18 c, 2 c/y].
Ko, Y.K., Raymond, J.C., Li,J., et al. 2002, *Solar and heliospheric observatory ultraviolet coronagraph spectrometer and Yohkoh Soft X-Ray Telescope observations of the high-temperature corona above an active region complex*, ApJ 578, 979, [34 c, 2 c/y].
Laming, J.M. and Feldman, U. 2001, *The solar helium abundance in the outer corona determined from observations with SUMER/SOHO*, ApJ 546, 552, [36 c, 2 c/y].
Laming, J.M. and Feldman, U. 2003, *The variability of the solar coronal helium abundance: Polar coronal holes compared to the Quiet Sun*, ApJ 591, 1257, [28 c, 2 c/y].
Laming, J.M. 2015, *The FIP and inverse FIP effects in solar and stellar coronae*, LRSP 12, 2, [33 c, 13 c/y].
Landi, E., Feldman, U., and Doschek, G.A. 2007, *Neon and oxygen absolute abundances in the solar corona*, ApJ 659, 743, [29 c, 3 c/y].
Phillips, K.J.H., Sylwester, J., Sylwester, B., and Landi, E. 2003, *Solar flare abundances of potassium, argon, and sulphur*, ApJ 589, L113, [35 c, 2 c/y].
Phillips, K.J.H., Feldman, U., and Landi, E. 2008, *Ultraviolet and X-ray Spectroscopy of the Solar Atmosphere*, Cambridge Astrophysics Series Vol., 44, Cambridge University Press, Cambridge, [74 c, 8 c/y].
Phillips, K.J.H., Sylwester, J., Sylwester, B., et al. 2010, *The solar X-ray continuum measured by RESIK*, ApJ 711, 179, [11 c, 2 c/y].
Phillips, K.J.H. and Dennis, B.R. 2012, *The solar flare iron abundance*, ApJ 748, 52, [9 c, 2 c/y].
Schmelz, J.T., Nasraoui, K., Roames, J.K., et al. 2005, *Neon lights up a controversy: The solar Ne/O abundance*, ApJ 634, L197, [68 c, 5 c/y].

Schmelz, J.T., Reames, D.V., von Steiger, R. et al. 2012, *Composition of the solar corona, solar wind, and solar energetic particles*, ApJ 755, 33, [84 c, 15 c/y.

Sylwester, J., Sylwester, B., Phillips, K.J.H., et al. 2010a, *Highly ionized potassium lines in solar X-ray spectra and the abundance of potassium*, ApJ 710, 804, [19 c, 3 c/y].

Sylwester, J., Sylwester, B., Phillips, K.J.H., et al. 2010b, *A solar spectroscopic absolute abundance of argon from RESIK*, ApJ 720, 1721, [12 c, 2 c/y].

Sylwester, B., Phillips, K.J.H., Sylwester, J., et al. 2011, *The solar flare chlorine abundance from RESIK X-ray spectra*, ApJ 738, 49, [11 c, 2 c/y].

Uzzo, M., Ko, Y.K., Raymond, J.C. et al. 2003, *Elemental abundances for the 1996 streamer belt*, ApJ 585, 1062, [22 c, 2 c/y].

Uzzo, M., Strachan, L., Vourlidas, A., et al. 2006, *Physical properties of a 2003 April quiescent streamer*, ApJ 645, 720, [14 c, 1 c/y].

White, S.M., Thomas, R.J., Brosius, J.W., et al. 2000, *The absolute abundance of iron in the solar corona*, ApJ 534, L203, [29 c, 2 c/y].

Widing, K.G., Landi, E., and Feldman, U. 2005, *Coronal element comparison observed by SOHO/SUMER in the quiet Southeast and Northwest limb regions at* 1.04 $R_{\odot}$, ApJ 622, 1211, [7 c, 0.6 c/y].

Young, P.R. 2005, *The element abundance FIP effect in the quiet Sun*, A&A 439, 361, [19 c, 2 c/y].

Young, P.R. 2018, *Element abundance ratios in the Quiet Sun transition region*, ApJ 855, 15, [5 c, 5 c/y].

(2.3) The CHIANTI Atomic Database

Arnaud, K. and Rothenflug, R. 1985, *An updated evaluation of recombination and ionization rates*, A&AS 60, 425, [1150 c, 35 c/y].

Arnaud, K. and Raymond, J. 1992, *Iron ionization and recombination rates and ionization equilibrium*, ApJ 398, 394, [648 c, 25 c/y].

Aschwanden, M.J. and Boerner, P. 2011, *Solar corona loop studies with AIA: I. Cross-sectional temperature structure*, ApJ 732, 81, [78 c, 12 c/y].

Bryans, P., Landi, E., and Savin, D.W. 2009, *A new approach to analyzing solar coronal spectra and updated collisional ionization equilibrium calculations. II. Updated ionization rate coefficients*, ApJ 691, 1540, [171 c, 20 c/y].

Del Zanna, G., Storey, P.J., Badnell, N.R., et al. 2012, *Atomic data for astrophysics: Fe X soft X-ray lines*, A&A 541, A90, [29 c, 5 c/y].

Del Zanna, G., Dere, K.P., Young, P.R., et al. 2015, *CHIANTI - An atomic database for emission lines. Version 8*, A&A 582, A56, [156 c, 62 c/y].

Dere, K.P, Landi, E., Mason,H.E., et al. 1997, *CHIANTI. An atomic database for emission lines*, A&A 125, 149, [1207 c, 59 c/y].

Dere, K.P., Landi, E., Young, P.R., et al. 2001, *CHIANTI - An atomic database for emission lines. IV. Extension to X-ray wavelengths*, ApJS 134, 331, [159 c, 10 c/y].

Dere, K.P. 2007, *Ionization rate coefficients for the elements hydrogen through zinc*, A&A 466, 771, [89 c, 8 c/y].

Dere, K.P., Landi, E., Young, P.R., et al. 2009, *CHIANTI - An atomic database for emission lines. IX. Ionization rates, recombination rates, ionization equilibria for the elements hydrogen through zinc and updated atomic data*, A&A 498, 915, [312 c, 37 c/y].

Landi, E., Landini, M., Dere,K.P., et al. 1999, *CHIANTI - An atomic database for emission lines. III. Continuum radiation and extension of the ion database*, A&AS 135, 339, [95 c, 5 c/y].

Landi, E., Feldman, U., and Dere, K.P. 2002, *CHIANTI - An atomic database for emission lines. V. Comparison with an isothermal spectrum observed with SUMER*, ApJS 139, 281, [91 c, 6 c/y].

Landi, E. and Phillips, K.J.H. 2005, *Spectral atlas of X-ray lines emitted during solar flares based on CHIANTI*, ApJS 160, 286, [29 c, 2.3 c/y].

Landi, E. and Phillips, K.J.H. 2006, *CHIANTI - An atomic database for emission lines. VIII. Comparison with solar flare spectra from the Solar Maximum Mission Flat Crystal spectrometer*, ApJS 166, 421, [26 c, 2 c/y].

Landi, E., Del Zanna,G., Young, P.R., et al. 2006, *CHIANTI - An atomic database for emission lines. VII. New Data for X-rays and other improvements*, ApJS 162, 261, [376 c, 33 c/y].

Landi,E. and Young, P.R. 2009, *CHIANTI - An atomic database for emission lines. X. Spectral atlas of a cold feature observed with Hinode/EIS*, ApJ 706, 1, [23 c, 3 c/y].

Landi, E., Del Zanna, G., Young, P.R. 2012, *CHIANTI - An atomic database for emission lines. XII. Version 7 of the database*, ApJ 744, 99, [187 c, 34 c/y].

Landi, E., Young, P.R., Dere, K.P., et al. 2013, *CHIANTI - An atomic database for emission lines. XIII. Soft X-ray improvements and other changes*, ApJ 763, 86, [248 c, 55 c/y].

Mason, H.E., Del Zanna, G., Dere, K.P., et al. 2002, *The CHIANTI atomic database and instrument calibration: A symbiosis*, in The Radiometric Calibration of SOHO, ESA SR-002, (eds. A. Pauluhn, M.C.E. Huber, and R. von Steiger, p.271.

Merts, A.L. and Torrey, M.D. 1963, *Some analytic solutions of the Hartree-Fock equations by an iterative least-squares method*, J. Chemical Physics 39/3, 694, [4 c, 0.1 c/y].

Storey, P.J., Mason, H.E., and Young, P.R. 2000, *Atomic data from the IRON Project. XL. Electron impact excitation of the Fe XIV EUV transitions*, A&AS 141, 285, [32 c, 2 c/y].

Storey, P.J. and Zeippen, C.J. 2001, *Coronal Fe IX line intensities and electron density diagnostics*, MNRAS 324, L7, [4 c, 0.2 c/y].

Storey, P.J., Del Zanna, G., Mason, H.E., et al. 2005, *Atomic data from the IRON Project*, A&A 433, 717, [36 c, 3 c/y].

Testa, P., Drake, J., and Landi, E. 2012, *Testing EUV/X-ray atomic data for the Solar Dynamics Observatory (SDO)*, ApJ 745, 111, [30 c, 5 c/y].

Young, P.R., Landi, E., and Thomas, R.J. 1998, *CHIANTI - An atomic database for emission lines. II. Comparison with the SERTS-89 active region spectrum, A&A 329, 291, [105 c, 5 c/y].*

Young, P.R., Del Zanna, G., Landi, E., et al. 2003, *CHIANTI - An atomic database for emission lines. VI. Proton rates and other improvements*, ApJS 144, 135, [252 c, 17 c/y].

Young, P.R. and Landi, E. 2009, *CHIANTI - An atomic database for emission lines. XI. Extreme-ultraviolet emission lines of Fe VII, Fe VIII, and Fe IX observed by Hinode/EIS*, ApJ 707, 173, [22 c, 3 c/y].

(2.4) Solar Emission Line Spectroscopy

Avrett, E.H., and Loeser, R. 2008, *Models of the solar chromosphere and transition region from SUMER and HRTS Observations: Formation of the Extreme-Ultraviolet Spectrum of Hydrogen, Carbon, and Oxygen*, ApJS 175, 229, [152 c, 16 c/y].

Bartoe, J.D.F., Brueckner, G.E., Purcell, J.D., et al. 1977, *Extreme ultraviolet spectrograph ATM experiment S082B*, Appl. Opt. 16, 879, [109 c, 3 c/y].

Bonnet, R.M., Lemaire, P., Vial, J.C. et al. 1978, *The LPSP instrument on OSO-8. II. - In-flight performance and preliminary results*, ApJ 221, 1032, [78 c, 2 c/y].

Brown, C.M., Feldman, U., Sheeley, J.F., et al. 2008, *Wavelengths and intensities of spectral lines in the 171–211 Å ranges from five solar regions recorded by the EUV Imaging Spectrometer (EIS) on Hinode*, ApJS 176, 511, [104 c, 11 c/y].

Bruner, E.C.Jr. 1977, *The University of Colorado OSO-8 spectrometer experiment. I. Introduction and optical design considerations* Space Sci. Instrum. 3, 369, [19 c, 0.5 c/y].

Culhane, J.L., Hiei, E., Doschek, G.A. et al. 1991, *The Bragg Crystal Spectrometer (BCS) for SOLAR-A*, SoPh 136, 89, [188 c, 7 c/y].

Culhane, J.L., Harra, L.K., James, A.M., et al. 2007, *The EUV Imaging Spectrometer (EIS) for Hinode*, SoPh 243, 19, [591 c, 56 c/y].

Curdt, W., Brekke, P., Feldman, U. et al. 2001, *The SUMER spectral atlas of solar-disk features*, A&A 375, 591, [201 c, 12 c/y].

Curdt, W., Landi, E., and Feldman, U. 2004, *The SUMER spectral atlas of solar coronal features*, A&A 427, 1045, [67 c/y].

Del Zanna, G. 2012, *Benchmarking atomic data for the CHIANTI atomic database: Coronal lines observed by Hinode EIS*, A&A 537, A38, [33 c, 6 c/y].

De Pontieu, B., Title, A.M., Lemen, J.R., et al. 2014, *The Interface Region Imaging Spectrograph (IRIS)*, SoPh 289, 2733, [336 c, 96 c/y].

Doschek, G.A. 1983, *Solar instruments on the P78-1 spacecraft*, SoPh 86, 9, [39 c, 1 c/y].

Doschek, G.A. and Feldman, U. 2010, *Topical Review: The solar UV-X-ray spectrum from 1.5 to 2000 A*, J. Phys. B: At. Mol. Opt, Phys. 43, 232001, [15 c, 2 c/y].

Doschek, G.A., Warren, H.P., Mariska, J.T., et al. 2008, *Flows and non-thermal velocities in solar active regions observed with the EIS on Hinode: A tracer of active region sources of heliospheric magnetic fields ?* ApJ 686, 1362, [114 c, 12 c/y].

Feldman, U. and Widing, K.G. 2007, *Spectroscopic measurement of coronal compositions*, SSRv 130, 115, [18 c, 2 c/y].

Harder, J.W., Thuillier, G., Richard, E.C. et al. 2010, *The SORCE SIM solar spectrum: Comparison with recent observations*, SoPh 263, 3, [35 c, 5 c/y].

Harrison, R.A., Sawyer, E.C., Carter, M.K. et al. 1995, *The CDS for the SOHO*, SoPh 162, 233, [567 c, 25 c/y].

Kohl, J.L., Esser, R., Gardner, L.D. et al. 1995, *The Ultraviolet Coronagraph Spectrometer (UVCS) for the Solar and Heliospheric Observatory*, SoPh 162, 313, [350 c, 16 c/y].

Kohl, J.L., Noci, G., Cranmer, S.R., et al. 2006, *Ultraviolet spectroscopy of the extended corona*, A&AR 13, 31, [118 c, 10 c/y].

McKenzie, D.L., Landecker, P.B., Broussard, R.M. et al. 1980, *Solar flare X-ray spectra between 7.8 and 23.0 Å* ApJ 241, 409, [105 c, 3 c/y].

Peter, H. 2010, *Asymmetries of solar coronal extreme ultraviolet emission lines*, A&A 521, A51, [58 c, 8 c/y].

Phillips, K.J.H., Leibacher, J.W., Wolfson, C.J., et al. 1982, *Solar flare X-ray spectra from the Solar Maximum Mission (SMM) Flat Crystal Spectrometer (FCS)*, ApJ 256, 774, [152 c, 4 c/y].

Phillips, K.J.H., Feldman, U., and Landi, E. 2008, *Ultraviolet and X-ray Spectroscopy of the Solar Atmosphere*, Cambridge Astrophysics Series Vol., 44, Cambridge University Press, Cambridge, [74 c, 8 c/y].

Rapley, C.G., Sylwester, J., and Phillips, K.J.H. 2017, *New results from the Solar Maximum Mission/Bent Crystal Spectrometer*, SoPh 292, 50, [1 c, 1 c/y].

Reeves, E.M., Huber, M.C.E., and Timothy, J.G. 1977, *Extreme UV spectroheliometer on the Apollo Telescope Mount (ATM)*, Appl. Opt. 16, 837, [102 c, 5 c/y].

Tanaka, K. 1982, *High-resolution solar flare X-ray spectra obtained with rotating spectrometers on the HINOTORI satellite*, ApJ 254, L59, [105 c, 3 y/c].

Tian, H., McIntosh, S.W., De Pontieu, B., et al. 2011, *Two components of the coronal emission revealed by EUV spectroscopic observations*, ApJ 738, 18, [63 c, 10 c/y].

Tousey, R., Bartoe, J.D.F., Brueckner, G.E., and Purcell, J.D. 1977, *Extreme ultraviolet spectroheliograph ATM experiment S082A*, Appl. Opt. 16, 870, [142 c, 4 c/y].

Wilhelm, K., Curdt, W., Marsch, E. et al. 1995, *SUMER - Solar Ultraviolet Measurements of Emitted Radiation*, SoPh 162, 189, [705 c, 31 c/y].

Young, P.R., Del Zanna, G., Mason, H.E., et al. 2007, *EUV emission lines and diagnostics observed with Hinode/EIS*, PASJ 59, S857, [139 c, 13 c/y].

Young, P.R., Watanabe, T., Hara, H., et al. 2009, *High-precision density measurements in the solar corona. I. Analysis methods and results for Fe XII and Fe XIII*, A&A 495, 587, [121 c, 14 c/y].

Zhitnik, I.A., Kuzin, S.V., Oraevskii, V.N. et al. 1998, *A spectral analysis of solar images in the range 180–210 Å with the RES-K spectroheliograph onboard the CORONAS-I satellite*, Astron. Lett. 24, 819, [7 c, 0.4 c/y].

Zhitnik, I.A., Kuzin, S.V., Urnov, A.M. et al. 2005, *Extreme vacuum ultraviolet solar spectra obtained during the SPIRIT experiment aboard CORONAS-F: A catalog of lines in the range 280–330 Å*, Astron. Lett. 31, 37, [10 c, 0.8 c/y].

(2.5) Instrumental Temperature Response Functions

Aschwanden, M.J. and Boerner, P. 2011, *Solar corona loop studies with AIA: I. Cross-sectional temperature structure*, ApJ 732, 81, [78 c, 12 c/y].

Boerner, P.F., Edwards, C., Lemen, J. et al. 2012, *Initial calibration of the Atmospheric Imaging Assembly (AIA) on the Solar Dynamics Observatory (SDO)*, SoPh 275, 41, [200 c, 36 c/y].

Boerner, P.F., Testa, P., Warren, H., et al. 2014, *Photometric and thermal cross-calibration of solar EUV instruments*, SoPh 289, 2377, [31 c, 9 c/y].

Brooks, D.H., Fischbacher, G.A., Fludra, A. et al. 2000, *A study of opacity in SOHO-SUMER and SOHO-CDS spectral observations. I. Opacity deduction at the limb*, A&A 357, 697, [12 c, 1 c/y].

Brooks, D.H. and Warren, H.P. 2006, *The intercalibration of SOHO EIT, CDS-NIS, and TRACE*, ApJS 164, 202, [26 c, 2 c/y].

Del Zanna, G., Bromage, B.J.I., Landi, E., et al. 2001, *Solar EUV spectroscopic observations with SOHO/CDS. I. An in-flight calibration study*, A&A 379, 708, [49 c, 3 c/y].

Del Zanna, G., Andretta, V., Chamberlin, P.C. et al. 2010, *The EUV spectrum of the Sun: long-term variations in the SOHO CDS NIS spectral responsivities*, A&A 518, A49, [18 c, 2 c/y].

Foster, A.R. and Testa, P. 2011, *Fe IX calculations for the Solar Dynamics Observatory (SDO)*, ApJL 740, L52, [22 c, 3 c/y].

Judge, P.G. 2010, *Coronal emission lines as thermometers*, ApJ 708, 1238, [19 c, 3 c/y].

Kuin, N.P.M. and Del Zanna, G. 2007, *The in-flight performance of the SOHO/CDS grazing incidence spectrometer*, SoPh 242, 187, [4 c, 0.4 c/y].

Lang, J., Brooks, D.H., Lanzafame, A.C. et al. 2007, *The in-flight monitoring and validation of the SOHO CDS normal incidence spectrometer radiometric calibration*, A&A 463, 339, [3 c, 0.3 c/y].

Lemen, J.R., Title, A.M., Akin, D.J., et al. 2012, *The Atmospheric Imaging Assembly (AIA) on the Solar Dynamics Observatory (SDO)*, SoPh 275, 17, [1445 c, 263 c/y].

McMullin, D.R., Judge, D.L., Hilchenbach, M. et al. 2002, *In-flight comparisons of solar EUV irradiance measurements provided by the CELIAS/SEM on SOHO*, in ESA SR-002, (eds., A. Pauluhn, M.C.E. Huber, and R. von Steiger), p.135, [12 c, 1 c/y].

O'Dwyer, O., Del Zanna G., Mason, H.E., et al. 2010, *SDO/AIA response to coronal hole, quiet Sun, active region, and flare plasma*, A&A 521, A21, [181 c, 24 c/y].

Pauluhn, A., Ruedi, I., Solanki, S.K. et al. 2001, *Intercalibration of SUMER and CDS on SOHO. II. SUMER detectors A and B and CDS NIS*, Appl. Optics 40/34, 6292, [18 c, 1 c/y].

Raftery, C.L., Bloomfield, D.S., Gallagher, P.T., et al. 2013, *Temperature response of the 171 Å passband of the SWAP imager on PROBA2, with a comparison to TRACE, SOHO, STEREO, and SDO*, SoPh 286, 111, [4 c, 1 c/y].

Takeda, A. 2011, *Characteristics of the re-calculated Yohkoh/SXT temperature response*, SoPh 273, 295, [4 c, 1 c/y].

Schmelz, J.T., Jenkins, B.S., and Kimble, J.A. 2013, *Atmospheric Imaging Assembly (AIA) response functions: solving the Fe VIII problems with Hinode/EIS bright point data*, SoPh 283, 325, [5 c, 1 c/y]

Thomas, R.J. 2002, *Underflight calibration of SOHO CDS by SERTS-97*, in "The radiometric calibration of SOHO", (eds. A. Pauluhn, M.C.E. Huber, and R. von Steiger), ESA SR-002, p.225, [5 c, 0.3 c/y].

Tripathi, D., Del Zanna, G., Mason, H.E. et al. 2006, *EIT and TRACE responses to flare plasma* A&A 460, L53, [10 c, 1 c/y].

Wang, T.J., Brosius, J.W., Thomas, R.J., et al. 2010, *Absolute radiometric calibration of the EUNIS-06 170–205 Å channel and calibration update for Coronal Diagnostic Spectrometer (CDS) incidence spectrometer*, ApJS 186, 222, [6 c, 1 c/y].

Wang, T.J., Thomas, R,J., Brosius, J.W., et al. 2011, *Underflight calibration of SOHO/ CDS and Hinode/EIS with EUNIS-07*, ApJS 197, 32, [19 c, 3 c/y].

White, S.M., Thomas, R.J., and Schwartz, R.A. 2005, *Updated expressions for determining temperatures and emission measures from GOES soft X-ray measurements*, SoPh 227, 231, [98 c, 8 c/y].

(2.6) Differential Emission Measure Analysis Methods

Aschwanden, M.J. and Nightingale, R.W. 2005, *Elementary loop structures in the solar corona analyzed from TRACE triple-filter images*, ApJ 633, 499, [106 c, 8 c/y].

Aschwanden, M.J. and Boerner, P. 2011, *Solar corona loop studies with AIA: I. Cross-sectional temperature structure*, ApJ 732, 81, [78 c, 12 c/y].

Aschwanden,M.J., Boerner, P., Schrijver, C.J., et al. 2013, *Automated temperature and emission measure analysis of coronal loops and active regions observed with the AIA on SDO*, SoPh 283, 5, [73 c, 16 c/y].

Aschwanden, M.J., Boerner, P., Caspi, A., et al. 2015, *Benchmark test of differential emission measure codes and multi-thermal energies in solar active regions*, SoPh 290, 2733, [8 c, 3 c/y].

Cheung, M.C.M., Boerner, P., Schrijver, C.J., et al. 2015, *Thermal diagnostics with the Atmospheric Imaging Assembly (AIA) on board the Solar Dynamics Observatory (SDO): A validated method for differential emission measure inversions*, ApJ 807, 143, [17 c, 7 c/y].

Goryaev, F.F., Parenti, S., Urnov, A.M., et al. 2010, *An iterative method in a probabilistic approach of the spectral inversion problem. Differential emission measure from line spectra and broadband data*, A&A 523, A44, [10 c, 1 c/y].

Guennou, C., Auchère, F., Soubrie, E., et al. 2012a, *On the accuracy of the differential emission measure diagnostics of solar plasmas. Application to SDO/AIA. I. Isothermal plasmas*, ApJS 203, 25, [17 c, 3 c/y].

Guennou, C., Auchère, F., Soubrie, E., et al. 2012b, *On the accuracy of the differential emission measure diagnostics of solar plasmas. Application to SDO/AIA. II. Multithermal plasmas*, ApJS 203, 26, [26 c, 5 c/y].

Hannah, I.G. and Kontar, E.P. 2012, *Differential emission measures from the regularized inversion of Hinode and SDO data*, A&A 539, A146, [105 c, 19 c/y].

Judge, P.G. 2010, *Coronal emission lines as thermometers*, ApJ 708, 1238, [19 c, 3 c/y].

Kashyap, V., and Drake, J.J. 1998, *Markov-Chain Monte Carlo reconstruction of emission measure distributions: Applications to solar extreme-ultraviolet spectra*, ApJ 503, 450, [125 c, 6 c/y].

Landi, E., Feldman, U., and Dere, K.P. 2002, *A comparison between coronal emission lines from an isothermal spectrum observed with the coronal diagnostic spectrometer and CHIANTI emissivities*, ApJ 574, 495, [23 c, 1 c/y].

Landi, E., Reale, F., and Testa, P. 2012, *Monte Carlo Markov chain DEM reconstruction of isothermal plasmas*, A&A 538, A111, [16 c, 3 c/y].

Noglik, J.B., and Walsh, R.W. 2007, *Investigation of a color-color method to determine temperatures along coronal structures using TRACE data*, ApJ 655, 1127, [10 c, 1 c/y].

Weber, M.A., Schmelz, J.T., DeLuca, E.E., and Roames, J.K. 2005, *Isothermal bias of the "filter ratio" method for observations of multithermal plasmas*, ApJ 635, L101, [35 c, 3 c/y].

Warren, H.P., Brooks, D.H., and Winebarger, A.R. 2011, *Constraints on the heating of high-temperature active region loops: Observations from Hinode and the Solar Dynamics Observatory (SDO)*, ApJ 734, 90, [78 c, 12 c/y].

(2.7) Multi-Thermal Energy

Aschwanden, M.J., Boerner, P., Schrijver, C.J., et al. 2013, *Automated temperature and emission measure analysis of coronal loops and active regions observed with the Atmospheric Imaging Assembly (AIA) on the Solar Dynamics Observatory (SDO)*, SoPh 283, 5, [73 c, 16 c/y].

Aschwanden, M.J., Boerner, P., Caspi, A., et al. 2015, *Benchmark test of differential emission measure codes and multi-thermal energies in solar active regions*, SoPh 290, 2733, [8 c, 3 c/y].
Testa, P., De Pontieu, B., Martinez-Syjkora, J., et al. 2012, *Investigating the reliability of coronal emission measure distribution diagnostics using 3-D MHD simulations*, ApJ 758, 54, [30 c, 5 c/y].

(2.8) Density-Sensitive Line Ratio Diagnostics

De Pontieu, B., Title, A.M., Lemen, J.R., et al. 2014, *The Interface Region Imaging Spectrograph (IRIS)*, SoPh 289, 2733, [336 c, 96 c/y].
Feldman, U., Landi, E., and Doschek, G.A. 2008, Line intensity ratios in the EIS range sensitive to electron densities in 10^7 K plasmas, ApJ 679, 843, [6 c, 1 c/y].
Ko, Y.K., Doschek, G.A., Warren, H.P., et al. 2009, Hot plasma in nonflaring active regions observed by the EIS on Hinode, ApJ 697, 1956, [30 c, 4 c/y].
Milligan, R.O. 2011, *Spatially resolved nonthermal line broadening during the impulsive phase of a solar flare*, ApJ 740, 70, [29 c, 5 c/y].
Milligan, R.O., Kennedy, M.B., Mathioudakis, M., et al. 2012, *Time-dependent density diagnostics of solar flare plasmas using SDO/EVE*, ApJ 755, 16, [24 c, 4 c/y].
Milligan, R.O. 2015, *Extreme ultra-violet spectroscopy of the lower solar atmosphere during solar flares (Invited review)*, SoPh 290, 3399, [15 c, 6 c/y].
Phillips, K.J.H., Feldman, U., and Landi, E. 2008, *Ultraviolet and X-ray Spectroscopy of the Solar Atmosphere*, Cambridge Astrophysics Series Vol., 44, Cambridge University Press, Cambridge, [74 c, 8 c/y].
Polito, V., Del Zanna, G., Dudik, J., et al. 2016, *Density diagnostics derived from the O IV and Si IV intercombination lines obsered by IRIS*, A&A 594, 64, [8 c, 5 c/y].
Warren, H.P. and Brooks, D.H. 2009, *The temperature and density structure of the solar corona. I. Observations of the Quiet Sun with the EUV Imaging Spectrometer (EIS) on Hinode*, ApJ 700, 762, [37 c, 4 c/y].
Watanabe, T., Hara, H., Culhane, L., et al. 2007, *Temperature and density structures of solar corona. A Test of iron line diagnostic capability of EIS instrument onboard Hinode*, PASJ 59, 5669, [13 c, 1 c/y].
Young, P.R., Watanabe, T., Hara, H., and Mariska, J.T. 2009, *High precision density measurements in the solar corona. I. Analysis methods and results fro Fe XII and Fe XIII*, A&A 495, 587, [121 c, 14 c/y].
Young, P.R. 2009, *New EUV Fe IX emission line identifications from Hinode/EIS*, ApJL 691, L77, [28 c, 3 c/y].

(2.9) Line Profile Diagnostics

Dadashi, N., Teriaca, L., and Solanki, S.K. 2011, The Quiet Sun average Doppler shift of coronal lines up to 2 MK, A&A 534, A90, [15 c, 2 c/y].
Del Zanna, G. 2008, *Flows in active region loops observed by Hinode EIS*, A&A 481, L49, [115 c, 12 c/y].
Doschek, G.A., Warren, H.P., Mariska, J.T., et al. 2008, *Flows and nonthermal velocities in solar active regions observed with the EIS on Hinode: A tracer of active region sources of heliospheric magnetic fields?*, ApJ 686, 1362, [114 c, 12 c/y].
Peter, H. 2001, *On the nature of the transition region from the chromosphere to the Corona of the Sun*, A&A 374, 1108, [115 c, 7 c/y].
Peter, H. 2010, *Asymmetries of solar coronal extreme ultraviolet emission lines*, A&A 521, A51, [56 c, 8 c/y].

Phillips, K.J.H., Feldman, U., and Landi, E. 2008, *Ultraviolet and X-ray Spectroscopy of the Solar Atmosphere*, Cambridge Astrophysics Series Vol., 44, Cambridge University Press, Cambridge, [74 c, 8 c/y].

Tomczyk, S., McIntosh, S.W., Keil, S.L., et al. 2007, *Alfvén waves in the solar corona*, Science 317, 1192, [391 c, 37 c/y].

Chapter 3
The Solar Interior

3.1 Solar Neutrino Problem Solved

Neutrinos allow us to look into the interior of the Sun, in particular by observing the neutrino fluxes that come from the Sun's core, which yield stringent tests whether we understand the nuclear physics and calculate the correct temperatures and densities in solar or stellar cores. The source of solar energy was solved in the 1920s, when Hans Bethe, George Gamov, and Carl von Weizsäcker identified the relevant nuclear chain reactions. The main nuclear reaction is the transformation of hydrogen into helium, where 0.7% of the mass is converted into radiation (according to Einstein's energy equivalence, $E = mc^2$), the so-called *p-p chain*, which starts with the fusion of two protons (^{1}H) into a nucleus of deuterium (^{2}He), and after chain reactions involving ^{3}He, ^{7}Be, and ^{7}Li produces helium (^{4}He),

$$\begin{aligned} p + p &\mapsto {}^2He + e^+ + \nu_e \\ {}^2He + p &\mapsto {}^3He + \gamma \\ {}^3He + {}^3He &\mapsto {}^4He + p + p \end{aligned} \tag{3.1.1}$$

or by the chain reaction starting with ^{3}He and ^{4}He,

$$\begin{aligned} {}^3He + {}^4He &\mapsto {}^7Be + \gamma \\ {}^7Be + e^- &\mapsto {}^7Li + \nu_e \\ {}^7Be + p &\mapsto {}^8B + \gamma \\ {}^7Li + p &\mapsto {}^8Be + \gamma \mapsto {}^4He + {}^4He \end{aligned} \quad . \tag{3.1.2}$$

M. J. Aschwanden, *New Millennium Solar Physics*, Astrophysics and Space Science Library 458, https://doi.org/10.1007/978-3-030-13956-8_3

The net effect of both chain reactions is

$$4p \mapsto {}^4He + 2e^+ + 2\nu_e + Q \,, \tag{3.1.3}$$

where Q=26.73 MeV also accounts for positron annihilation.

One can estimate the Sun's lifetime by dividing the available mass energy by the luminosity,

$$t_\odot \approx 0.1 \times 0.007\, m_\odot c^2 / L_\odot \approx 10^{10} \text{ years} \,, \tag{3.1.4}$$

where we assumed that only about a fraction of 0.1 of the total solar mass is transformed, because only the innermost core of the Sun is sufficiently hot to sustain nuclear reactions.

An alternative nuclear chain reaction occurring in the Sun and stars is the *Carbon-Nitrogen-Oxygen (CNO)* cycle,

$$\begin{aligned} {}^{12}C + p &\mapsto {}^{13}N + \gamma \\ {}^{13}N &\mapsto {}^{13}C + e^+ + \nu_e \\ {}^{13}C + p &\mapsto {}^{14}N + \gamma \\ {}^{14}N + p &\mapsto {}^{15}O + \gamma \\ {}^{15}O &\mapsto {}^{15}N + e^+ + \nu_e \\ {}^{15}N + p &\mapsto {}^{12}C + {}^4He \,. \end{aligned} \tag{3.1.5}$$

The p-p chain produces 98.5% of the solar energy, and the CNO cycle the remainder, but the CNO-cycle is faster in stars that are more massive than the Sun. New neutrino experiments set upper limits of 7.3% to the fraction of energy that the Sun produces via the CNO-cycle (Bahcall et al. 2003).

Neutrinos have extremely little interactions with matter, unlike photons, and thus most of the electronic neutrinos (ν_e), emitted by the fusion of hydrogen to helium in the central core, escape the Sun without interactions and a very small amount is detected at Earth. Solar neutrinos have been detected since 1967, with an average rate of 2.56 ± 0.23 SNU (solar neutrino units), pioneered by Raymond Davis Jr. using a chlorine tank in the Homestake Gold Mine in South Dakota, and by John Bahcall on the theoretical side, but the observed count rate was about a third of the theoretically expected value, 7.5 ± 1.0 SNU, causing the puzzling *neutrino problem* that persisted for the next 35 years (Bahcall et al. 2001). The theoretical prediction is based on solar (interior) models, which are also corroborated with the measurements of the helioseismological frequencies of the solar pressure-mode (p-mode) eigenfrequencies.

Six experiments have observed solar neutrinos. Three of them are radiochemical experiments: Homestake (chlorine detector), GALLEX (gallium detector), and SAGE (gallium detectors). These radiochemical detectors record all neutrinos above a fixed threshold energy, i.e., 0.87 MeV for chlorine, and 0.2 MeV for gallium. Radiochemical detectors record solar neutrinos by extracting neutrino-induced

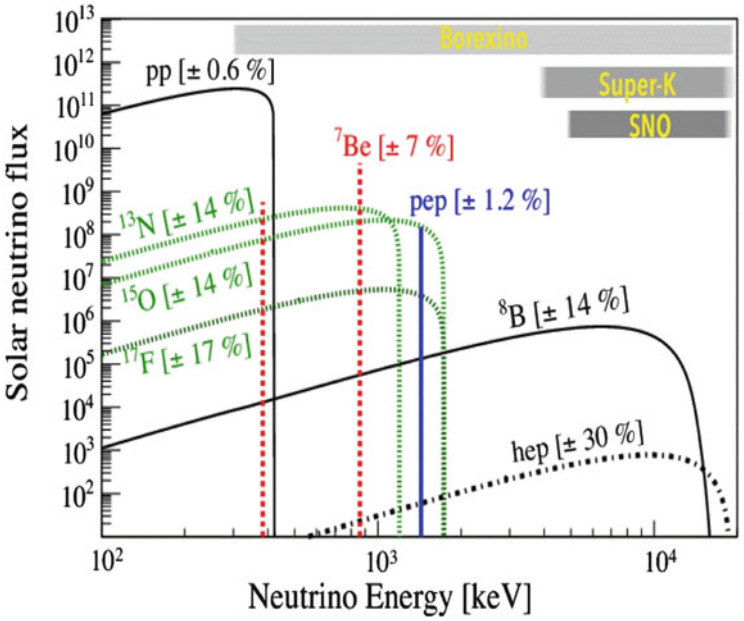

Fig. 3.1 The solar neutrino flux as a function of the neutrino energy is shown, predicted from the various nuclear reactions in the solar models. The grey bands in the top of the figure indicate in which energy ranges the SNO, the Super-Kamiokande, and Borexino are sensitive. Note that Super-Kamiokande and SNO can observe about 0.02% of the total flux, while Borexino may observe each type of predicted neutrinos (Credit: Borexino Consortium)

radioactive argon produced over an exposure time of the order of one month. The other three experiments, Kamiokande, Super-Kamiokande, and Sudbury Neutrino Observatory (SNO), measure the energies of electrons produced in neutrino interactions in water. Kamiokande and Super-Kamiokande use neutrino-electron scattering in ordinary (very pure) water, and SNO uses neutrino absorption and neutrino disassociation of deuterium in heavy water, measuring electrons produced by neutrino interactions at energies above 5 MeV (Fig. 3.1). However, a second solar neutrino problem arised from discrepancies between the pure-water and the chlorine experiments, which was a consequence of the different energy thresholds. And a third solar neutrino problem entered the scene with the GALLEX and SAGE results, which could not be reconciled with the expected rates of ^{7}Be neutrinos.

The last detector of this series of experiments is Borexino (in Gran Sasso, Italy), designed to study low-energy (sub-MeV) solar neutrinos of all three flavors (Fig. 3.1). Due to the improved background levels in Borexino, the total systematics uncertainty can be reduced down to the 3% level (Ianni 2014). Borexino is the first experiment to measure low-energy (< 1 MeV) solar neutrino events (from the pp chain) in real time (Haxton et al. 2013; Bellini et al. 2014).

From the theoretical side, Gribov and Pontecorvo (1969) predicted already 30 years ago that low-energy solar neutrinos undergo a "personality disorder" on their travel to Earth and oscillate into other flavors of muonic (ν_μ) and tauonic neutrinos (ν_τ), which turned out to be the solution of the *missing neutrino problem* for detectors that are only sensitive to the highest-energy (electronic) neutrinos, such as the Homestake chlorine tank, the gallium detectors *GALLEX* in Italy and *SAGE* in Russia. Only the *Kamiokande* and *Super-Kamiokande-I* pure-water experiments and the *Sudbury Neutrino Observatory* (*SNO*; Ontario, Canada) heavy-water experiments are somewhat sensitive to the muonic and tauonic neutrinos. It was the *SNO* that measured in 2001 for the first time all three lepton flavors and this way brilliantly confirmed the theory of *neutrino (flavor) oscillations* (Ahmad et al. 2002). The SNO detects ^{8}B solar neutrinos through the reactions:

$$\begin{aligned} \nu_e + d &\mapsto p + p + e^- \qquad (CC)\,, \\ \nu_x + d &\mapsto p + n + \nu_x \qquad (NC)\,, \\ \nu_x + e^- &\mapsto n_x + e^- \qquad (ES)\,, \end{aligned} \tag{3.1.6}$$

where (CC) is the charged current reaction that is sensitive exclusively to electron-type neutrinos, (NC) is the neutral current reaction that is equally sensitive to all active neutrino flavors ($x = e, \mu, \tau$), and (ES) is the elastic scattering reaction that is sensitive to all flavors. Sensitivity to these three reactions allows SNO to determine the electron and non-electron active neutrino components of the solar flux (Ahmad et al. 2002). A ^{8}B neutrino flux of $(5.44 \pm 0.99) \times 10^6$ cm^{-2} s^{-1} was theoretically predicted (Ahmad et al. 2001), while the actually observed ^{8}B neutrino flux measured with the NC reaction at SNO yielded a consistent value of $(6.42 \pm 1.59) \times 10^6$ cm^{-2} s^{-1} (Ahmad et al. 2002). With that result, the total number of electron neutrinos produced in the Sun are just as predicted by detailed solar models based on helioseismic p-mode observations with the BiSON, GOLF, GONG, LOWL, and MDI instruments (e.g., Turck-Chieze et al. 2001). This affirmative result represented a triumph for solar and astrophysicists, who correctly calculated solar and stellar evolution models and the associated generation of nuclear energies.

Today, after the successful solution of the neutrino problem, the measured neutrino fluxes are sufficiently accurate to constrain the helium abundance Y and heavy element abundances Z in the solar interior. A high-Z (metallicity) model with a convection zone depth of $R_{CZ} \approx 0.714$ and a He abundance ratio of $Y_{surf} \approx 0.245$ is found to fit the helioseismology data better than a Low-Z model with $R_{CZ} \approx 0.724$ and a surface He abundance ratio of $Y_{surf} \approx 0.232$ (Fig. 3.2).

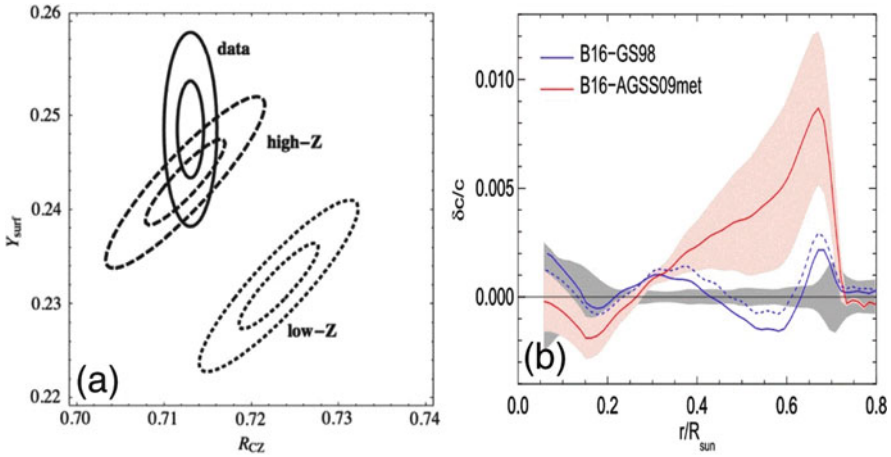

Fig. 3.2 (**a**) Comparison of observed quantities from helioseismology data (solid contours) with solar standard models, for the high-Z (dashed contours) and the low-Z (dotted contours) abundances, with the 1σ and 3σ contours indicated (Ianni 2014); (**b**) Fractional sound speed difference $(\delta c/c) = (c_{\odot} - c_{mod})/c_{mod}$. The grey shaded region shows the errors from the helioseismic inversion procedure, the red shaded region corresponds to errors from variations of the high-Z model, based on the chemical abundances of Grevesse et al. (2015). The blue curve corresponds to the low-Z model with abundances from Asplund et al. (2009), computed in Vinyoles et al. (2017)

3.2 New Solar Standard Models

Solar (or stellar) models essentially characterize the radial function of density $n(r)$ and temperature $T(r)$ inside the Sun (or star), taking the variation of hydrogen, helium, and heavy elements due to nuclear burning into account, from which the (pressure-driven) p-mode oscillation frequencies can be calculated and compared with the observed helioseismic oscillation frequencies. Newer developments of standard models are driven by improved laboratory measurements (e.g., nuclear reaction rates, opacity measurements) or more sophisticated remote-sensing observations (e.g., photospheric elemental abundances, acoustic modes, gravity modes, or neutrino fluxes). A most recent review on solar standard models and global helioseismology can be found in Basu (2016).

The basic assumptions of classical solar models are: (i) spherical symmetry (no rotation), (ii) the conservation of mass during its evolution (which is a valid assumption since the solar mass loss is only $\approx 10^{-14}$ of its mass per year), (iii) energy generation by hydrogen burning, (iv) energy transport by radiation and convection, and (v) homogeneous zero-age Sun with initial mass fractions of hydrogen X_0, helium Y_0, and metals for heavier elements Z_0 (normalized to $X_0 + Y_0 + Z_0 = 1$). Following Basu (2016), the continuity equation (in the absence

of flows) can then be written as a function of the radius r, the mass $m(r)$, and density $\rho(r)$,

$$\frac{dr}{dm} = \frac{1}{4\pi r^2 \rho} \,. \tag{3.2.1}$$

The momentum equation (in a quasi-stationary state and hydrostatic equilibrium) can then be expressed as a function of the pressure $p(r)$,

$$\frac{dp}{dm} = -\frac{Gm}{4\pi r^4} \,, \tag{3.2.2}$$

where G is the gravitational constant. The conservation of energy l in equilibrium, through a shell of radius r per unit time, as a function of the energy e release rate (per unit mass and time) by nuclear reactions, the energy loss rate e_ν due to neutrino fluxes, and the energy lost by expansion and contraction during their evolution, is

$$\frac{dl}{dm} = e - e_\nu - C_p \frac{dT}{dt} + \frac{\delta}{\rho}\frac{dp}{dt} \,, \tag{3.2.3}$$

where C_p is the specific heat at constant pressure, t is time, and δ is given by the equation of state and is defined as,

$$\delta = -\left(\frac{\partial \ln \rho}{\partial \ln T}\right)_{P,X_i} \,, \tag{3.2.4}$$

with X_i denoting the composition. The dependence of the temperature T on the mass m follows from Eq. (3.2.2) as,

$$\frac{dT}{dm} = -\frac{GmT}{4\pi r^4 p}\Delta \,, \tag{3.2.5}$$

where Δ is the dimensionless temperature gradient $d \ln T / d \ln P$ and depends on the assumption whether energy is being transported by radiation. If energy is transported by convection, the energy flux depends on the difference between the temperature gradient and the adiabatic gradient. An additional equation is needed that describes the change of the chemical composition, which includes nuclear reactions, the changes in the boundaries of the convection zone, diffusion, and gravitational settling (Basu 2016),

$$\frac{\partial X_i}{\partial t} = \frac{m_i}{\rho}\left[\sum_j r_{ji}(X_i, X_j) - \sum_k r_{ik}(X_i, X_k)\right] \,, \tag{3.2.6}$$

where m_i is the mass of the nucleus of each isotope i, r_{ji} is the rate at which isotope i is formed from isotope j, and r_{ik} is the rate at which isotope i is lost because it

turns into a different isotope k. While the solar model has been formulated solely as a function of the 1-D radial distance r, the motion of convection is a 3-D process, and thus needs to be approximated by spatial averages. The transition from the (inner) radiative zone to the (outer) convection zone requires additional empirical modeling, which is most commonly modeled in terms of the so-called mixing-length theory (Prandtl 1925). Also, diffusion acts against gravitational settling. The change of a chemical abundance X_i described by a spatially averaged diffusion process is,

$$\frac{\partial X_i}{\partial t} = D\nabla^2 X_i \ , \tag{3.2.7}$$

where D is the diffusion coefficient, and ∇^2 is the Laplacian operator. In the computation of solar standard models, the full set of equations that govern stellar structure and evolution are solved for a given chemical abundance X_i, where the mass m and time t are the two independent variables, for which solutions in the mass range of $0 \leq m \leq M$ (stellar structure) and time $t \geq t_0$ (stellar evolution) are sought. In fact, only the heavy element abundance is prescribed, while the helium abundance as well as the mixing-length parameter are determined by calibrating the solar models to the observed radius and luminosity.

The observables that constrain the solutions are the stellar radius, luminosity, surface temperature, and pressure. These observables are given for the Sun in Table 3.1.

A new generation of standard solar models includes recent updates on some important nuclear reaction rates, a more consistent treatment of the equation of state, and improved uncertainties of radiative opacities. The new solar standard models boiled down to two cases, one with a low, and one with a high metallicity (Z), called the low-Z and the high-Z model (see best-fit solutions for high-Z and low-Z models in Table 3.2 and Fig. 3.2a). While the observed radiation from the Sun traditionally has been fitted with 1-D semi-empirical photospheric models, 3-D radiative hydrodynamic simulations of the convection zone, photosphere, and chromosphere are used now. These new 3-D simulations predict metal abundances that are about a factor of two smaller than previous 1-D models. The 3-D models describe the granulation of the surface better, i.e., the widths, shifts, and asymmetries of spectral lines. Helioseismology, on the other hand, constrains the depth of the convection zone to $R_{CZ}/R_\odot = 0.713 \pm 0.001$ and the photospheric helium abundance to $Y_S = 0.2485 \pm 0.0035$ (Fig. 3.2a and Table 3.2). Helioseismic measurements exhibit

Table 3.1 Global parameters of the Sun (Basu 2016)

Quantity	Numerical value
Mass $M_\odot$	$1.98892(1 \pm 0.00013) \times 10^{33}$ g
Radius $R_\odot$	$6.9599(1 \pm 0.0001) \times 10^{10}$ cm
Luminosity $L_\odot$	$3.8418(1 \pm 0.004) \times 10^{33}$ erg s^1
Age $t_\odot$	$4.57(1 \pm 0.0044) \times 10^9$ years
Irradiance $S_\odot$	1361 W m^{-2}
Temperature $T_\odot$	5772 K

Table 3.2 Best-fit parameters for two solar standard models, the high-Z model B16-GS98 with abundances from Grevesse et al. (2015), and the low-Z model B16-AGSS09met with abundances from Asplund et al. (2009), computed by Vinyoles et al. (2017). The subscript S stands for the surface, C for the convection zone, 0 for the initial time, and α_{MLT} for mixing-length theory

Quantity	B16-GS98 (High-Z model)	B16-AGSS09met (Low-Z model)	Solar
Y_S	0.2426±0.0059	0.2317±0.0059	0.2485±0.0035
$R_{CZ}/R_\odot$	0.7116±0.0048	0.7223±0.0053	0.713±0.001
$< \delta c/c >$	0.0005±0.0004	0.0021±0.001	0
α_{MLT}	2.18±0.05	2.11±0.05	...
Y_0	0.2718±0.0056	0.2613±0.0055	...
Z_0	0.0187±0.0013	0.0149±0.0009	...
Z_S	0.0170±0.0012	0.0134±0.0008	...
Y_C	0.6328±0.0053	0.6217±0.0062	...
Z_C	0.0200±0.0014	0.0159±0.0010	...

a strong disagreement with recent low-Z solar standard models (with abundances from Asplund et al. 2009), while the agreement is almost perfect with high-Z models (with abundances from Grevesse et al. 2015). While spectroscopic measurements of photospheric abundances corroborate the low-Z model, the 3-D solar standard models support the high-Z model, which constitutes the so-called *"solar abundance problem"*.

The root cause of the solar abundance problem seems to be located in the overshoot region of the convection zone, where the semi-empirical mixing-length theory is generally applied. One finding suggests that the metal contribution to the radiative opacity is larger at the bottom of the convective envelope ($\approx$ 70%) than at the solar core ($\approx$ 30%). The new generation of solar standard models from the Barcelona group (B16), with updated atomic opacities, is compared in Fig. 3.2b for two elemental abundance cases, with the high-Z abundances (Grevesse et al. 2015) and the low-Z abundances (Asplund et al. 2009). Clearly, the high-Z model agrees much better with the helioseismic inversion than the low-Z abundances (Fig. 3.2a). When the sound speed differences in the narrow region of $0.65 < r/R_\odot < 0.70$ are excluded, the high-Z model improves from 2.7σ to 0.9σ, and the low-Z model from 4.7σ to 3.0σ (Vinyoles et al. 2017).

Another constraint on solar standard models are the observed neutrino fluxes. Comparisons of the predicted neutrino fluxes of $\Phi(^8B)$ and $\Phi(^7Be)$ computed with the low-Z or the high-Z abundances, however, shows that the neutrino fluxes are well described by both solar compositions (with low-Z or high-Z elemental abundances). Both, theoretical calculations of atomic radiative opacities, as well as revised nuclear reaction rates (that affect the energy and neutrino production in the Sun), are currently explored to solve the solar abundance problem (Ianni 2014).

3.3 Helioseismology: Meridional Flows

In the decade of 1960–1970, global oscillations were discovered on the solar surface in visible light, which became the field of *helioseismology*. Velocity oscillations were first measured by R. Leighton, and then interpreted in 1970 as standing sound waves in the solar convection zone by R. Ulrich, C. Wolfe, and J. Leibacher. These acoustic oscillations, also called *p-modes* (pressure-driven waves), excited by turbulent convection below the photosphere, are detectable from the fundamental up to (radial) harmonic order of $\approx$ 30, and are most conspicuous in dispersion diagrams, $\omega(k)$, where each harmonic shows up as a separate ridge, when the oscillation frequency (ω) is plotted as a function of the wavelength λ (i.e., essentially the solar circumference divided by the spherical harmonic degree). Frequencies of the p-mode correspond to periods of $\approx$5 min. An example of a p-mode standing wave is shown in Fig. 3.3a. Each mode is characterized by the number of radial, longitudinal, and latitudinal nodes, corresponding to the radial quantum number n, the degree l of spherical harmonic, and the azimuthal number m functions. For a spherically symmetric star, all modes with the same degree l and order n have the same frequency, while asphericities such as rotation and magnetic field cause frequency splitting in m. The frequency ν_{nlm} of a mode is defined as,

$$\nu_{nlm} = \nu_{nl} + \sum_{j=1}^{j_{max}} a_j(nl) P_j(m/L) \,, \tag{3.3.1}$$

where $L = \sqrt{l(l+1)}$, a_j are the splitting coefficients, and P_j are Legendre polynomials. Since the density and temperature increases monotonically with the depth inside the Sun, the sound speed varies as a function of radial distance from Sun center. P-mode waves excited at the solar surface propagate downward and are refracted towards the surface. The low harmonics penetrate very deep, while high harmonics are confined to the outermost layers of the solar interior. By measuring the frequencies at each harmonic, the sound speed can be inverted as a function of the depth, and this way the density and temperature profile of the solar interior can be inferred and unknown parameters of theoretical standard models can be inverted. Basic reviews on global seismology can be found in Kosovichev et al. (2000), Christensen-Dalsgaard (2002), Gough (2013), Kosovichev (2011), and Basu (2016).

Exploiting the Doppler effect, frequency shifts of the p-mode oscillations can be used to measure the internal velocity rates as a function of depth and latitude, as shown in Fig. 3.2b. A layer of rapid change in the internal rotation rate was discovered this way at the bottom of the convection zone, the so-called tachocline (at 0.712 ± 0.005 $R_\odot$, with a thickness of 0.04 ± 0.01 $R_\odot$). Using the so-called time-distance method, which measures and inverts the wave travel times between different points on the surface, local properties of convective and magnetic structures in the subsurface layers can be probed. Horizontal flows in supergranular cells in depths of $\approx$ 5 Mm were discovered, as well as meridional flows from the

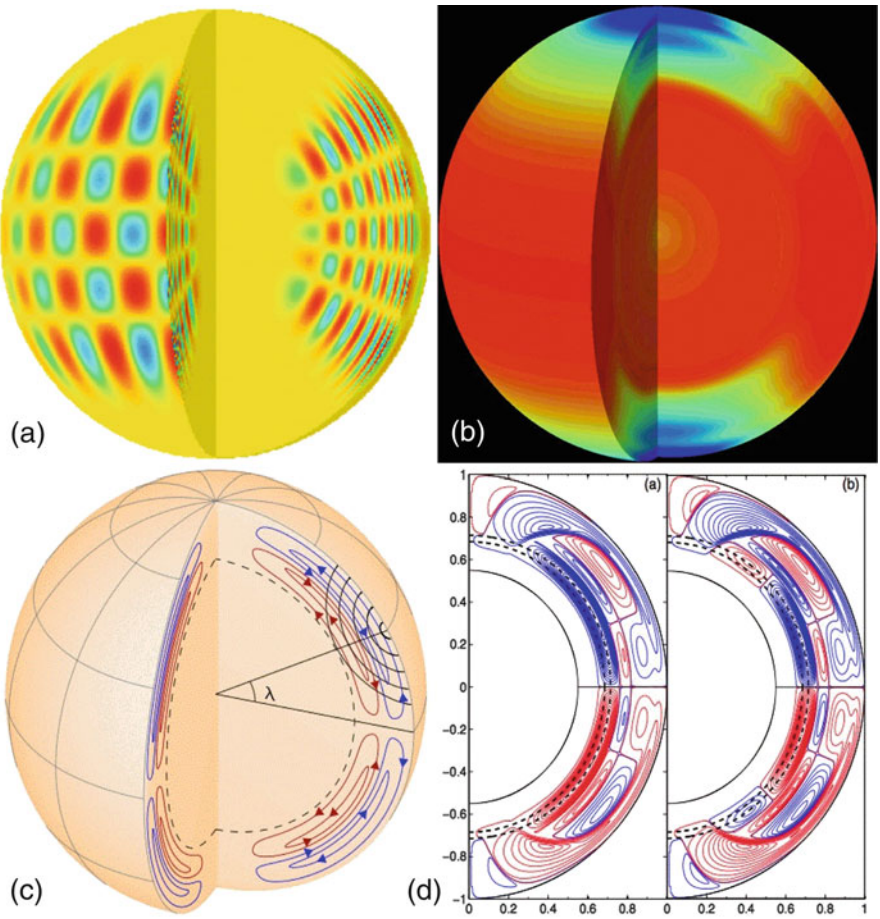

Fig. 3.3 (**a**) A global acoustic p-mode wave is visualized: The radial order is $n = 14$, the angular degree is $l = 20$, the angular order is $m = 16$, and the frequency was measured to $\nu = 2935.88 \pm 0.1$ μHz with MDI/SOHO. The red and blue zones show displacement amplitudes of opposite sign. (**b**) The internal rotation rate is shown with a color code, measured with MDI/SOHO during 1996 May–1997 April. The red zone show the fastest rotation rates ($P \approx 25$ days), dark blue the slowest ($P \approx 35$ days). Note that the rotation rate varies in latitude differently in the radiative and convective zones (Credit: MDI/SOHO Team). (**c**) Diagram of the deep-focusing time-distance measurement scheme, with black curves showing some acoustic wave paths. The dual meridional flow patterns are indicated in poleward (red) and equatorward (blue) circulation (Zhao et al. 2013). (**d**) Complicated meridional circulation patterns used in flux-transport dynamo models that can reproduce the butterfly patterns of the solar cycle. Red and blue contours indicate clockwise and counter-clockwise orientations (Hazra et al. 2014)

equator towards the North and South poles. Overturning convection motion was measured from granule-size ($\approx$ 1000 km) to supergranule-size ($\approx$ 30,000 km) structures (Hathaway et al. 2013). Furthermore, the time-distance method enabled 3-D tomography of sunspots and active regions (Kosovichev et al. 2000).

We turn now our attention to recent highlights in the measurement of meridional flows. Meridional flows in the solar interior provide information on the redistribution of angular momentum, transport of magnetic flux, the length of the solar cycle, and the time of the reversal of the Sun's polar field. It has long been recognized that the meridional flow is poleward at the surface and in the shallow interior down to a depth of at least 30 Mm, with a speed of $\approx$ 20 m s^{-1}. This average meridional flow speed is about two orders of magnitude smaller than the average solar rotation rate, and thus it is difficult to measure, especially at high latitudes. Conservation of mass demands that poleward flow must be compensated by equatorward flow at a different depth, the so-called *"conveyor belt"* scenario. The return flow was found beneath a depth of 0.77 $R_\odot$ (Rajaguru and Antia 2015). The meridional flow speed was also found to have a solar cycle dependence, with an anti-correlation between the flow speed and the magnetic flux strength (Zhao et al. 2014).

Using the first 2 years (2010–2012) of HMI/SDO data, measuring the acoustic travel times along north-south directions near the central meridian, and performing inversions using ray-path approximation sensitivity kernels, the interior meridional circulation was found to have a double cell profile (Zhao et al. 2013), with the equatorward flow extending from approximately 0.91 $R_\odot$ to 0.82 $R_\odot$ with a speed of $\approx$ 10 m s^{-1}, and a poleward flow in depths of 0.91 $R_\odot$ to 1.0 $R_\odot$ as well as 0.75–0.83 $R_\odot$ (Fig. 3.3c). A more comprehensive method to measure meridional circulation corrected for center-to-limb effects in the time-distance helioseismic method yields similar results, i.e., a three-layer flow structure with equatorward flows at 0.82–0.91 $R_\odot$ for low latitudes, and at 0.85–0.91 $R_\odot$ for higher latitudes (Chen and Zhao 2017).

Analyzing 18 Carrington rotations during a similar time span (2010–2011) with HMI/SDO data also, horizontal components of solar subsurface flows were measured with a ring-diagram analysis, up to high latitudes of 75° and in depths down to 16 Mm. The meridional flows were found to be poleward at most depths and latitudes, with a maximum of $\approx$ 20 m s^{-1} near 37.5° latitude (Komm et al. 2013). This confirms that both the travel-time technique (Zhao et al. 2013) and the ring-diagram technique (Komm et al. 2013) yield compatible results.

Schad et al. (2013, 2016) developed a novel global helioseismic analysis method that infers the meridional flow in the deep solar interior based on the perturbation of eigenfunctions of solar p-modes at low harmonics of $s = 1, \ldots, 8$. Obviously, the degree $s = 2$ is a special one, because it characterizes the dipole moment in terms of two hemispheric, oppositly directed meridional flows. Using MDI/SOHO data from the period 2004–2010 they find evidence for meridional flows down to the base of the convection zone (or tachocline). The notion that the meridional flow may consist of multiple cells has also been confirmed with GONG data (Kholikov et al. 2014). GONG data agree with HMI data for a shallow equatorward flow at a depth of 65 Mm, but unphysical solutions are found in deeper layers (Jackiewicz et al. 2015).

Complementary to the helioseismic inversions of the meridional flow patterns based on the observed Doppler shifts, numerical hydrodynamic simulations have been carried out, which have to pass the minimum test of reproducing the butterfly diagram of the solar cycle. Hazra et al. (2014) find that flux-transport dynamos can reproduce butterfly diagrams for far more complex multi-cell circulation patterns (Fig. 3.3d) than a simple one-cell (conveyor belt) scenario. Other simulations generate the meridional circulation from the differential rotation and turbulent Reynold stress (Dikpati 2014; Brun et al. 2011), or find Reynold stress forces in balance with the Coriolis force of a near surface shear layer in a depth range of (0.950–0.975) $R_\odot$ (Hotta et al. 2015).

3.4 Helioseismology: Solar Interior Rotation

The differential rotation of the Sun, with a fastest period of ≈27 days near the equator, and a slowest period of $\gtrsim 35$ days near the poles, was already known from sunspot observations in the seventeenth century. The rotational behavior inside the Sun, however, could only be measured by means of helioseismology within the last 40 years. Systematic helioseismic observations started with BiSON and ACRIM/SMM around 1980, and then mostly with GONG and MDI/SOHO in 1996. BiSON and GONG are ground-based, and ACRIM/SMM and MDI/SOHO are space-based instruments. For a historical review of measurements of the solar interior rotation and its variation see Howe (2009).

The rotation of the Sun introduces a "rotational splitting" of the helioseismic frequencies between modes of the same degree l and the azimuthal number m, because waves propagate with and against the direction (prograde and retrograde). The frequency splitting,

$$\delta\nu_{m,l} \approx (\nu_{-m,l} - \nu_{+m,l}) \,, \tag{3.4.1}$$

is proportional to the rotation rate multiplied by m to first order. Because modes of different m values sample different latitude ranges, we can invert the rotation rate as a function of latitude according to the azimuthal number m and degree l. Only the odd-order coefficients produce a rotational asymmetry, so the a_1 coefficients (Eq. 3.3.1) describe the rotation rate averaged over all latitudes, and the a_3 and higher coefficients (Eq. 3.3.1) describe the differential rotation.

From a series of low-degree helioseismology studies with data from LOWL, GOLF, MDI, VIRGO, and BiSON during 1999–2006, first reported from IPHIR measurements (Toutain and Kosovichev 1994), it was found that the interior solar rotation within a depth range of $\approx$ (0.2–0.7)$R_\odot$ is approximately constant with radius, and spherically symmetric, which means that no significant departure from rigid-body rotation has been found. These measurements could in principle be improved by using g-modes due to their higher sensitivity in the core in Sun center, rather than using p-modes, but the detection of g-modes is still unconfirmed. While

most of the radiative interior rotates as a solid-body, it was found that the base of the convection zone at 0.71 $R_\odot$ coincides with a region of strong radial shear, above which the convection zone exhibits a differential rotation pattern, mostly varying with latitude, which was dubbed the *tachocline*. The depth of the tachocline corresponds to a region where the global oscillation modes with $l \approx 20$ have their lower turning point, providing a spatial resolution of the inversion by 5–10% of the solar radius in radial direction. In other words, the velocity step function in the tachocline cannot be fully resolved with p-modes, and thus requires some modeling in comparisons with solar standard models (Fig. 3.2b). Modeling of the tachocline has been attempted with turbulent flows (mixing-length theory), "fossil" magnetic fields, and gravity waves, but even the most recent 3-D radiative hydrodynamic simulations are not able to reproduce a self-sustaining tachocline (Kitiashvili et al. 2016).

The solar rotation rate in the convection zone $(0.7–1.0)R_\odot$ can be probed with p-modes of degree $l \gtrsim 20$. Helioseismic inversions have been carried out with uninterrupted time series from ground-based GONG and space-based HMI/SOHO and HMI/SDO data. An example of GONG data inversion is shown in Fig. 3.4 (Howe et al. 2000, 2005). Once GONG and MDI were compared, it became clear that the two instruments produced significantly different solutions, especially at high latitudes, which were found to be caused by the different inversion algorithms, rather than by data-specific instrumental effects (Schou et al. 2002).

In order to understand the observed differential rotation patterns, a series of Babcock-Leighton solar dynamo model (or flux-transport dynamo model) simulations were conducted, driven by turbulent pumping (Guerrero and Gouveia Del Pion 2008). From these simulation results it was concluded that the Babcock-Leighton approach, the equatorward motion of the observed magnetic activity, is

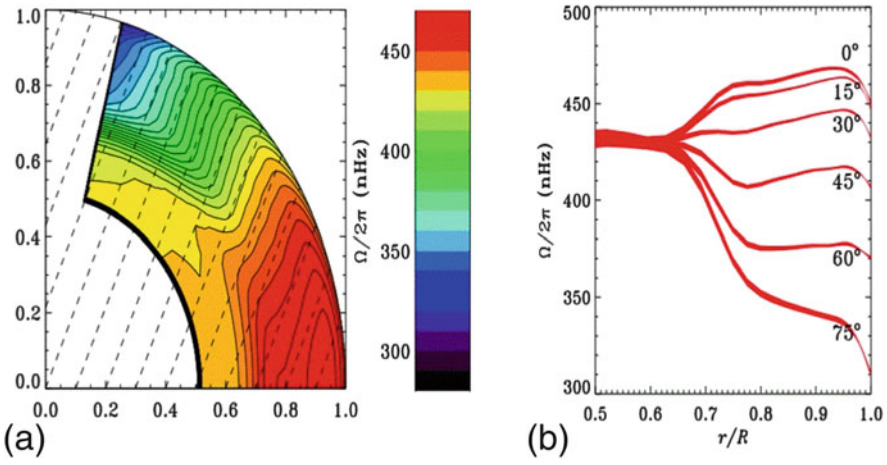

Fig. 3.4 Mean rotation profile from GONG data, shown in contours of constant rotation, (**a**) and cuts at constant latitude as a function of radius (**b**) (Howe et al. 2000, 2005)

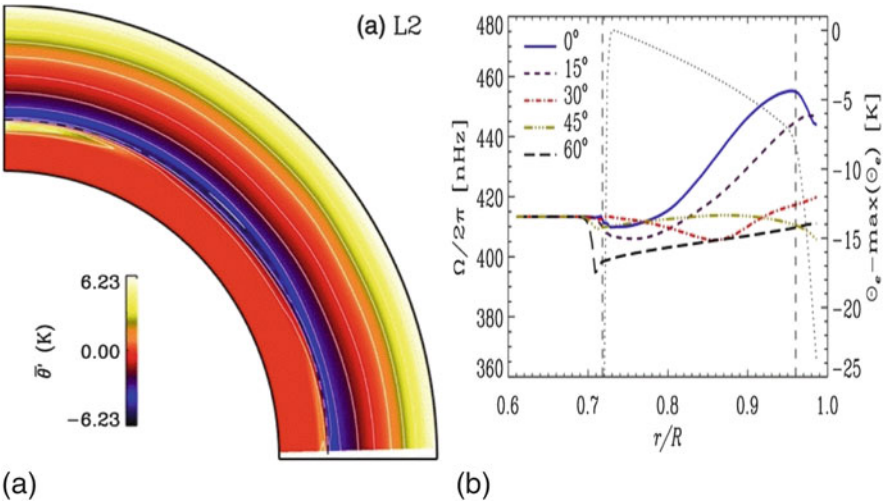

Fig. 3.5 Profile of the potential temperature obtained from the EULAG code (**a**), and radial profiles of the simulated angular velocity at different latitudes (**b**) (Guerrero et al. 2013)

governed by the latitudinal pumping of the toroidal magnetic field, rather than by a large-scale coherent meridional flow. Alternative numerical simulations are of the global modeling type, where all the HD and MHD equations are solved in spherical geometry with appropriate boundary conditions. One of them is the EULAG code (Fig. 3.5), which performs HD simulations (Guerrero et al. 2013). In this code, the establishment of mean flows depends on the balance between buoyancy and Coriolis forces, which can be controlled by the Rossby number. For smaller Rossby numbers (dominant rotation), the equator rotates faster than the poles, as observed on the Sun. The meridional flux transport exhibits a complicated multi-cellular pattern that mimics some features of helioseismic results, see results of helioseismic inversions (Fig. 3.3).

A given latitude zone does not exactly rotate with an invariant speed. In addition to the latitudinal dependence that defines the differential rotation rate, a so-called *torsional oscillation* pattern was discovered, which exhibits bands of faster and slower than average zonal (parallel to the equator) flows, which was found to be associated with the equatorward drift of the activity belt during a solar cycle (Howard and LaBonte 1980). Numerical simulations of this phenomenon, using a mean-field flux-transport dynamo model with a model-derived differential rotation profile and meridional flow, investigate the effects of various driving mechanisms on the torsional oscillations (Rempel 2007). Some of these simulations were successful in reproducing the poleward-propagating branch by a periodic forcing at mid-latitudes, but could not reproduce the equatorward-propagating branch (Howe et al. 2006), probably because they are controlled by Lorentz forces associated with a magnetic dynamo wave (Guerrero et al. 2016), or by torque forces induced by magnetic tension (Pipin and Kosovichev 2018).

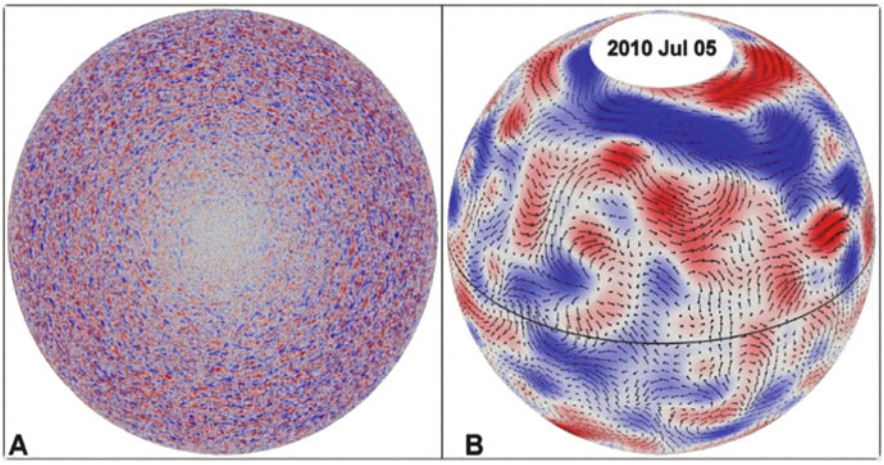

Fig. 3.6 (**a**) Supergranules are revealed by their Doppler velocity signal (red and blue). The flows in supergranules are largely horizontal. (**b**) Giant cells are revealed by tracking the motions of supergranules. Longitudinal velocities slower than the average rotation rate at that latitude are indicated with red, and vice versa with blue. The flow directions are indicated with vectors (Hathaway et al. 2013)

The differential rotation being fast near the equators and slow near the poles is opposite to what we expect from conservation of angular momentum. This fact implies that a rapidly rotating equator could only be maintained by forces or stresses that could act against the tendency to make the poles spin paster. The source of these forces or stresses can not be axisymmetric and are highly influenced by the Sun's rotation. Giant cells—very large (non-axisymmetric) convection cells with lifetimes longer than the Sun's rotation period—were proposed to be the solution (Hathaway et al. 2013). Early models of large convection cells in the Sun's convection zone indeed indicated that Reynold stresses (which show a correlation between flows in the direction of rotation with flows toward the equator) can maintain a rapidly rotating equator. Hathaway et al. (2013) demonstrated, after removal of axisymmetric velocity components, that giant cells become visible in the HMI data (Fig. 3.6), which adds another non-uniformity to the classical differential rotation pattern.

3.5 Local Helioseismology

Local helioseismology techniques were developed from the principles of wave propagation through inhomogeneous media, which include (i) the Fourier-Hankel decomposition technique, (ii) the ring-diagram analysis, (iii) time-distance helioseismology, (iv) helioseismic holography, and (v) direct modeling. Local helioseismology provides a 3-D view of the solar interior, modeling the entire wave field

observed on the solar surface, while global helioseismology probes the eigenmode frequencies only, and thus cannot detect longitudinal variations of flows in meridional planes. Local helioseismic methods can probe the evolution of phenomena in the interior of the Sun on global scales (rotational and torsional oscillations, meridional flows, vertical flows, variability at the tachocline), the evolution of active regions and sunspots (flows near complexes of magnetic activity, sunspot flows, far-side imaging, excitation of waves by flares), and convection patterns at the surface (supergranulation, giant cells). Reviews on theory and data analysis with local helioseismology methods are given in Gizon and Birch (2005), Gizon and Thompson (2007), Gizon et al. (2010), Thompson and Zharkov (2008), and Kosovichev (2011, 2012).

(i) The Fourier-Hankel spectral method was designed to study the relationship between inward and outward traveling waves around sunspots. The oscillation signal in an annular region around a sunspot is approximated with Hankel functions to the more exact combination of Legendre polynomials used in spherical geometry. Hankel analysis revealed that sunspots are strong absorbers of incoming p and f modes ($n = 0$), opposed to no absorption in Quiet-Sun regions.

(ii) The method of ring-diagram analysis is based on the computation and fitting of local $\mathbf{k}-\omega$ power spectra. A small patch (typically $15^\circ \times 15^\circ$) is tracked during its rotation across the disk, the partial images are remapped to compensate for the solar rotation, and the 3-D power spectra of the resulting data cube is used as basic input for the ring analysis. Flows introduce Doppler shifts in the oscillation spectrum and changes in the sound speeds alter the location of the rings, so that subsurface flows and sound-speed can be estimated from the shapes of the rings in the power spectrum.

(iii) The time-distance helioseismology method measures and models the travel times of solar waves between any two locations on the solar surface. A travel time anomaly (e.g., due to an inhomogeneity such as a sunspot or active region) contains the seismic signature of buried inhomogeneities within the proximity of the ray path that connects two surface locations, which can then be inverted to infer its spatial structure. The mean solar rotation is removed also, like in the ring-diagram method. The travel times of wave packets are measured from the (first-bounce) cross-covariance function. In the ray approximation, the travel time perturbation is approximated as an integral along the ray path. Other kernels that are used, are the Born approximation, the Rytov approximation, or the Fresnel zone approximation. Finally, a (velocity) perturbation to the solar model is then inverted from a particular set of observed travel times.

(iv) In the helioseismic holography method, the basic concept is that the wavefield, e.g., the line-of-sight Doppler velocity observed at the solar surface, can be used to make an estimate of the wavefield at any location in the solar interior at any instant of time. The estimate of the wavefield at some point in the solar interior is obtained by assuming that the observed wavefield (at the solar surface) is generated entirely either by waves diverging from

that point (for egression) or by waves converging towards that point (for ingression). The target point in the solar interior is called "the focus point", and the restricted area on the surface above the focus point is called "the pupil", in analogy to optics. The wavefield is generally characterized with the Green's functions. The main holographic methods include control-correlation techniques, acoustic power holography, phase-sensitive holography, and far-side imaging. An example of the geometry of far-side imaging is given in Fig. 3.7.

(v) A fifth local helioseismology technique is direct modeling, which estimates subsurface flows from direct inversion of the correlations seen in the wavefield in the Fourier domain. It is assumed that Fourier components of the physical wavefield are uncorrelated for horizontally homogeneous steady models with no flow. Also, departures from horizontal homogeneity or time-dependence generally introduce correlations into the wavefield.

We turn now to scientific results that were obtained with the various local helioseismology methods. Comparisons of solar rotation rates and torsional oscillations obtained with global helioseismology methods (by inversion of frequency-splitting) and local helioseismology (time-distance and ring diagram) methods were found to be in good agreement (Zhao and Kosovichev 2004). Theoretical explanations of torsional oscillations are multi-fold, including Reynolds stresses, suppression of

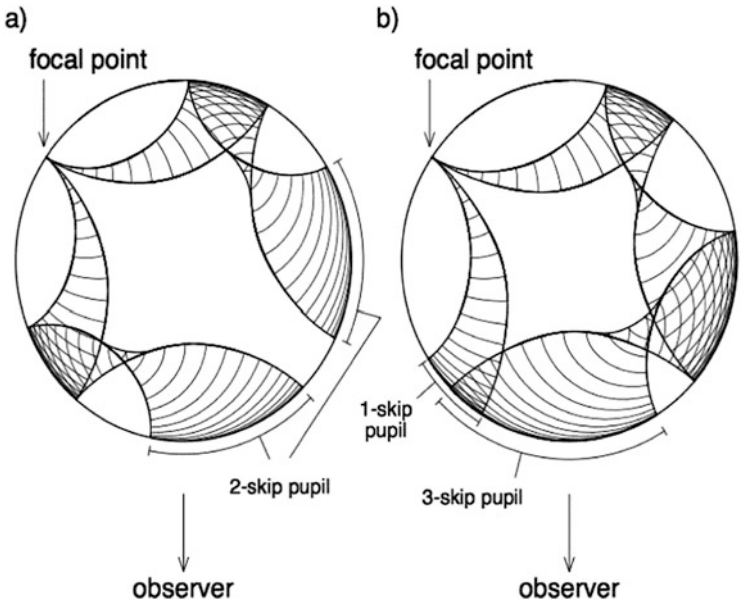

Fig. 3.7 Geometry for far-side imaging with holograpy: (**a**) Two-skip correlation scheme, (**b**) One-skip and three-skip correlation. In far-side imaging, the data (pupils) on the visible disk are used to estimate the wavefield at focal points on the far-side of the Sun (Braun and Lindsey 2001)

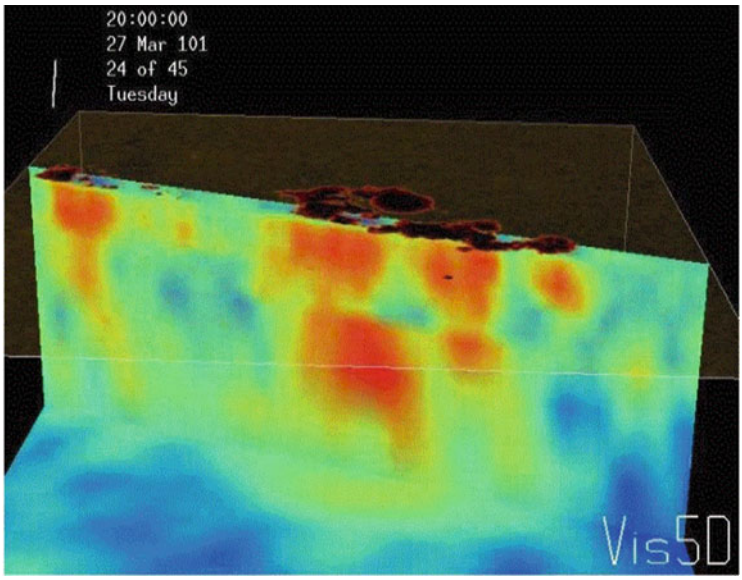

Fig. 3.8 A slice from a wave speed perturbation associated with active region AR9393 is shown, observed with MDI on 2001 March 25 until April 1, with positive/negative speed changes rendered with red/blue colors, (Kosovichev et al. 2000; Gizon and Birch 2005)

turbulent viscosity by active regions, or temperature perturbations due to the magnetic field (e.g., Rempel 2007). The measurement of variability at the tachocline has also been attempted, but was found to be very challenging with local helioseismology methods (Howe et al. 2000).

Travel time perturbations below active regions were studied using time-distance helioseismology (Fig. 3.8) by Kosovichev et al. (2000). Maximum wave-speed differences of $\approx$ 1 km s^{-1} between the Quiet Sun and a sunspot were detected in the subphotospheric zone, where Quiet Sun sound speeds are about 20 km s^{-1} at a depth of 4 Mm, and 35 km s^{-1} at 10 Mm (Zhao et al. 2001). This corresponds to a temperature change of 10%, possibly a direct effect of the magnetic field.

The first far-side imaging with helioseismic holography was accomplished by Lindsey and Braun (2000), where an active region was located on the far-side of the Sun (Fig. 3.9) based on a travel time deficit of $\approx$ 10 s, compared with the Quiet Sun. Far-side detections of active regions have been confirmed in 22 cases (without exception) by stereoscopic observations (with STEREO/EUVI), based on EUV 304 Å proxies of active regions (Liewer et al. 2017). The far-side imaging method is attractive for space weather predictions, as it allows about a week of warning before an active region appears at the East limb. Such a service is now provided on a routine basis. It helps also to create synoptic magnetic maps of the full Sun, which is most useful for heliospheric magnetic field models, for which the entire solar surface is needed to define a lower boundary.

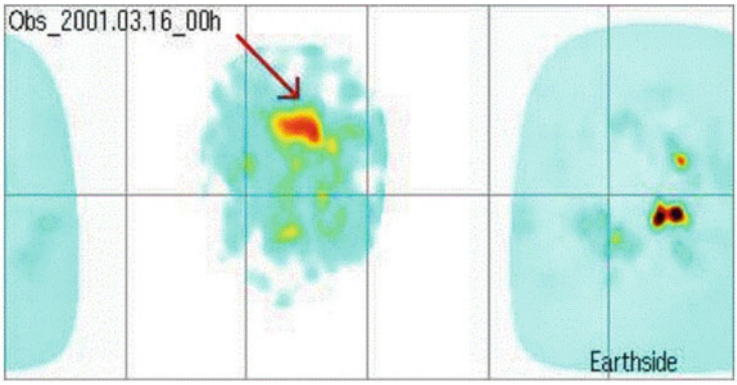

Fig. 3.9 Example of helioseismic far-side imaging of the Sun from March to June 2001. The large activity complex AR 9393 is seen for several rotation periods. The map is rendered as a synoptic map of the full Sun in the Carrington coordinate system. The solar Earthside is on the right side, and the solar far-side is in the middle of the map (Braun and Lindsey 2001; Gizon and Birch 2005)

Convection occurs on the Sun on various scales, most conspicuously on granulation scales of $\approx$ 1000 km, a bit less obvious on super-granular scales of $\approx 30,000$ km (which map to the chromospheric network), and possibly in giant cells. Local seismology methods, however, despite of their refined capabilities, were not yet able to measure the depth of supergranules.

3.6 Limit-Cycle Oscillations of the Solar Dynamo

A broad consensus exists now that the solar magnetic (2×11-year) cycle is caused by the inductive action of fluid motions pervading the solar interior (Charbonneau 2010). A selection of representative theoretical models includes: $\alpha\Omega$ mean-field models, interface dynamos, mean-field models including meridional circulation, shear instability models, buoyant instabilities of sheared magnetic layers, flux tube instability models, and Babcock-Leighton models (Charbonneau 2010, 2013).

The observational constraints for testing of theoretical solar dynamo models includes the granulation and supergranulation, the solar rotation, the (latitudinal and radial) differential rotation, torsional oscillations, meridional flows, the 11-year activity cycle, the 22-year magnetic cycle, Spörer's law, Hale's law, Joy's law, the Waldmeier effect, the north-south asymmetry, extended cycles, correlation between polar fields, the open flux and strength of the next cycle, magnetic fields at the surface advected by surface flow, coronal mass ejections, magnetic helicity fluxes, and grand minima and maxima (Cameron and Schüssler 2017a). *Spörer's law* describes the butterfly diagram of active regions that emerge at high latitudes at the beginning of the solar cycle and migrate progressively to lower latitudes during the solar cycle. *Joy's law* describes the east-west alignment of emerging bipolar active

regions (with the leading spots closer to the equator) in both hemispheres. *Hale's law* states that the magnetic polarity of active regions is oppositely oriented in both hemispheres, and alternates in successive sunspot cycles, so that a full magnetic solar cycle lasts $\approx$ 22 years. These statistical properties have been found to be consistent with the Babcock-Leighton dynamo model (for reviews see Charbonneau 2010). The global magnetic field of the Sun undergoes a cyclic transition from a global poloidal field to a highly-stressed toroidal field during an 11-year cycle. It explains the winding-up of the highly-stressed toroidal field as a consequence of the differential rotation, and the subsequent gradual decay due to meridional flows, ending up in a relaxed poloidal field in the minimum of the solar cycle. On top of the cyclical variations, secular changes related to the interplanetary magnetic field may play a role also (Solanki et al. 2000), which even affects the total solar irradiance, estimated to be ≈ 1 W m^{-2} (Wang et al. 2005).

There is a large number of studies on analytical and physical models of the solar dynamo, as well as numerical MHD simulations. The Babcock-Leighton-type model, one paradigm of a solar dynamo model, can reproduce the key features of the solar cycle (Cameron and Schüssler 2017a). The underlying flux-transport dynamo considers the axisymmetric part of the magnetic field and is based on the evolutionary equations of the azimuthal component of the vector potential (which determines the poloidal field) at the solar surface (Cameron and Schüssler 2017b),

$$a(\theta, t) = \frac{1}{\sin\theta} \int_0^\theta \sin\theta R_\odot^2 B_r|_{R=R_\odot} d\theta \tag{3.6.1}$$

while the radially integrated toroidal flux per radian is,

$$b(\theta, t) = \int_{R_b}^{R_\odot} B_\Phi r \, dr \, , \tag{3.6.2}$$

both as functions of colatitude θ, and time, where $R_\odot$ is the solar radius, and R_b is the radial location of the bottom of the solar convection zone. B_r and B_Φ are the radial and azimuthal components, respectively, of the magnetic field. The model has 4 free parameters. Introducing fluctuations in the source term for the poloidal field, the evolutionary equations given in Cameron and Schüssler (2017a) become stochastic differential equations. Random forcing in form of a 2-D Wiener process is applied in order to mimic the influence of noise. The numerical results for mildly supercritical, nonlinear dynamo action with this model, fully constrained by observed values of the solar cycle (e.g., cycle length of 11 yrs, and surface diffusivity $\eta_0 = 65$ km^2 s^{-1}), are shown in Fig. 3.10.

A recent highlight is the understanding of physical dynamo models (such as the Babcock-Leighton-type dynamo) in terms of self-organizing (nonlinear) limit-cycle processes (such as the Hopf bifurcation or the Lotka-Volterra equation, see Fig. 3.11). The variability of the solar cycle can then be understood in terms of a weakly nonlinear limit cycle affected by random noise (Cameron and Schüssler 2017b), quantified in normal form in terms of the Hopf bifurcation or Lotka-Volterra

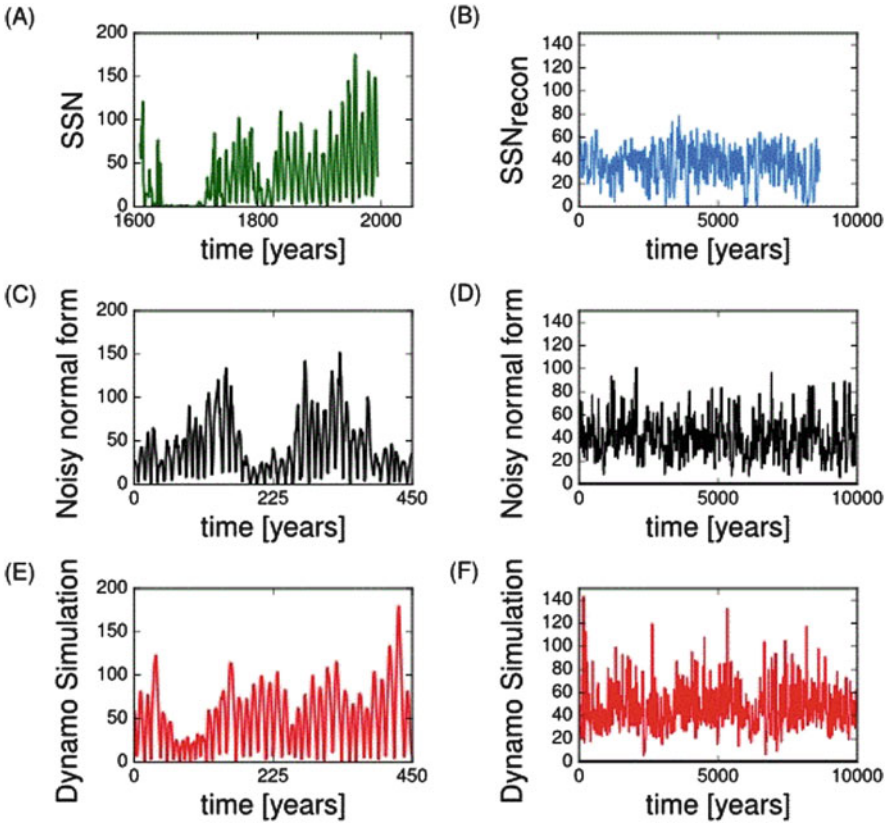

Fig. 3.10 (**a**) Time series of the observed sunspot numbers (SSN); (**b**) Sunspot number reconstructed from cosmogenic isotopes (SSN_{recon}); (**c**,**d**) Monte-Carlo simulations of a weakly nonlinear, noisy limit cycle (Hopf bifurcation normal-form model); (**e**,**f**) Results from Babcock-Leighton dynamo model with fluctuating sources (Cameron and Schüssler 2017b)

system. The presence of a limit cycle is a common property in coupled nonlinear dissipative systems, which is most easily understood in terms of the Lotka-Volterra equation system (Fig. 3.11), known as the predator-prey equation system in ecology,

$$\begin{aligned} \partial X/\partial t &= k_1 X - k_2 XY \\ \partial Y/\partial t &= -k_3 Y + k_2 XY \end{aligned} \quad . \tag{3.6.3}$$

This equation system has a periodic solution, which is called the limit cycle. Critical points occur when $dX/dt = 0$ and $dY/dt = 0$, which yields a stationary point in phase space at $X = k_3/k_2$ and $Y = k_1/k_2$. Applying the Lotka-Volterra equation system to the solar cycle, X represents the poloidal field and Y the toroidal field, k_1 the growth rate of the poloidal field, k_3 the growth rate of the toroidal field, and (k_2) a nonlinear interaction term between the two field components.

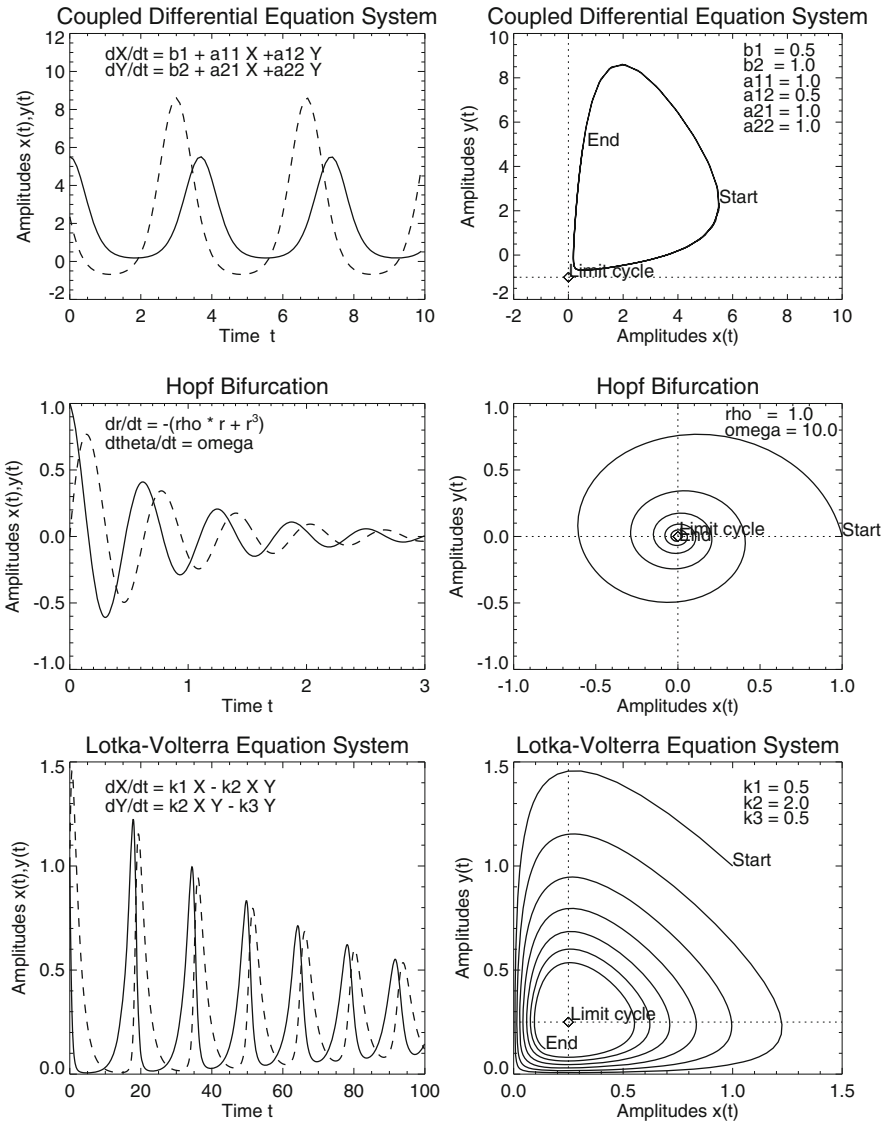

Fig. 3.11 The dynamic behavior near a limit cycle is shown for three different nonlinear systems: for coupled oscillators (top), the Hopf bifurcation (middle), and the Lotka-Volterra equation system (bottom). For each case the trajectories are shown in phase space $Y(X)$ (right panels), and as a function of time, $X(t)$ and $Y(t)$ (left panels), for the parameters indicated in the right panels. The system starts to oscillate far away from the limit cycle, but gradually approaches the attractor at the fixed point (X_0, Y_0) (Aschwanden et al. 2018)

The Lotka-Volterra equations describe the emergence and sustained oscillation in an open system far from equilibrium, as well as emergence of spontaneous self-organization. An application of the Lotka-Volterra system to the complex system of the solar cycle is discussed in Consolini et al. (2009), where a double dynamo mechanism is envisioned, one at the base of the convection zone (tachocline), and a shallow subsurface dynamo. The deeper dynamo dominates the poloidal field, while the shallower dynamo controls the toroidal field. In summary, the limit cycle represents a highly-ordered self-organizing 22-year pattern of the solar magnetic activity, which cannot be explained with a random process.

A chaotically modulated stellar dynamo was modeled also based on bifurcation theory, where modulation of the basic magnetic cycle and chaos occur as a natural consequence of a star that is in transition from a non-magnetic state to one with periodically reversing fields (Tobias et al. 1995).

3.7 Solar Cycle Prediction

Various observables of the solar magnetic cycle are: the sunspot number, the solar flare rate (above some threshold), the irradiance, the magnetic flux (i.e., the magnetic field strength integrated over the solar surface area), etc. For every physical model of the solar dynamo it is necessary to quantify how the observables are related to physical parameters, which can then be tested by predictions of the physical model. Reviews on the solar cycle can be found in Hathaway (2010, 2015), on the solar activity over millennia in Usoskin (2008, 2013, 2017), on the flux-transport mechanism in Sheeley (2005), and on solar cycle prediction in Petrovay (2010) and Pesnell (2012). In the review of Pesnell (2012), a summary and analysis of 75 different predictions of the amplitude of the latest Solar Cycle 24 is presented.

Here we describe one of the many prediction highlights, a method that establishes a tight correlation between the solar magnetic dipole moment and the sunspot number over the 25 last solar cycles (Svalgaard et al. 2005; Svalgaard and Cliver 2007, 2010; Svalgaard 2014), which represents a useful quantitative relationship between an observable (i.e., the sunspot number) and a physical parameter (i.e., the magnetic dipole moment). The method is based on Babcock's model of the solar cycle, which suggests that the polar magnetic fields near the cycle minimum can be used as a predictor of the size of the following sunspot cycle (Schatten et al. 1978). This method has been proven to be successful for the last four Cycles 21–25, including the critical lowest Cycle 24 (Svalgaard et al. 2005). The *Dipole Moment (DM)*, i.e., the difference between the polar fields measured from Wilcox Solar Observatory (WSO) data, with the convention that polar fields are confined to the average line-of-sight flux density (or field strength) above latitudes or 55° in the North and South, was found to be a convenient parameter for the purpose of prediction. It was found that the value of the dipole moment over the 3 years preceding the minimum is relatively constant, with only a slight decrease over time (due to the pole-ward migration of emerging new-cycle flux), and is sufficiently

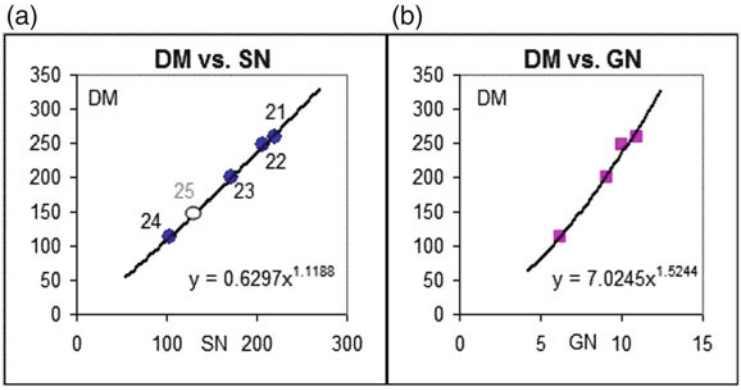

Fig. 3.12 (**a**) Correlation of dipole moment (DM) vs. the sunspot number (SN) for Cycles 21–25, and (**b**) correlation of DM versus the Group Number GN (Credit: NASA, HMI/SDO), HMI Science Nugget 78

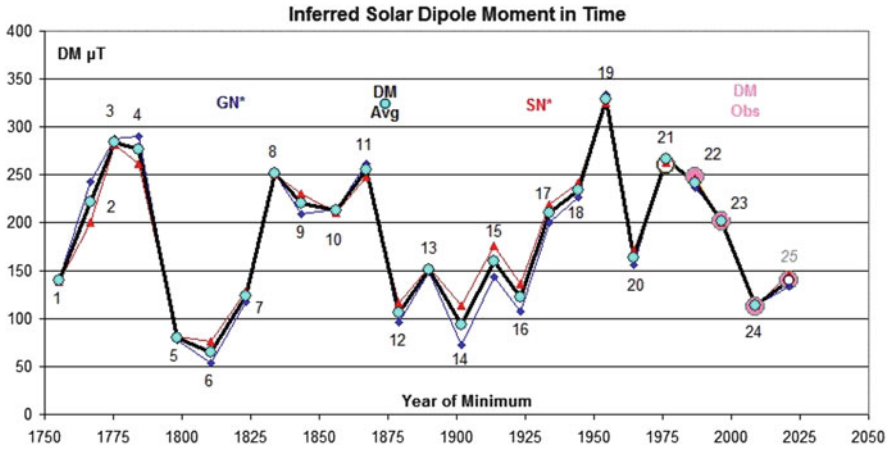

Fig. 3.13 The solar dipole moment (DM) inferred from the sunspot number (SN) (red symbols) and from the group number (GN) (blue symbols), for the cycles following the minima for which the DM is determined using the linear regression relationship shown in Fig. 3.12. The average DM for each cycle is shown in black (Credit: NASA, HMI/SDO), HMI Science Nugget 78)

stable so that its average single value was a good predictor, at least for the last four sunspot cycles (Fig. 3.12).

Relying on the success of the sunspot number (SN) and group number (GN) for predicting the last 4 cycles (for which magnetic data are available), one can then "post-dict" the solar dipole moment all the way back from Cycle 25 to Cycle 1, which is shown in Fig. 3.13. Since the cycles have two or more peaks, the average SN or GN of the two most active yearly values are used. Magnetic measurements were available since 1976, but the first measurements during

1976–1977 are diminished ($\approx$ 18%) due to excessive scattered light (Svalgaard and Schatten 2008) and suffered from being at (or after) the end of the 3-year pre-minimum interval ($\approx$ 12%), and thus were corrected by 30%.

The Dipole Moment (DM) for Cycles 1 to 24, reconstructed at the cycle minima from the sunspot number (SN) and group number (GN), as well as the average of their reconstructions is given in Table 3.3. A graphic representation of the DM and their reconstructions is given in Fig. 3.13. The inferred dipole moments (DM) can be used to predict the long-term evolution of solar and heliospheric (HMF) activity. For instance, the long-term variation of the HMF strength (at Earth) has been derived from geomagnetic data back to the 1840s (Svalgaard and Cliver 2010; Svalgaard 2014). The polar (solar) magnetic fields are believed to control the HMF when the low-latitude fields from active regions have died (or migrated) away at

Table 3.3 Time of minimum for the numbered solar cycles. Average group numbers (GN) and sunspot numbers (SN) for the two highest yearly values for each cycle. Dipole moment DM(μT) observed at WSO for the 3 years prior to the minimum, and the DM inferred from GN and SN, and their average, and the inferred heliospheric magnetic field (HMF) strength B(nT) at each minimum (Svalgaard and Cliver 2010)

Cycle	Year	Month	GN max	SN max	WSO(DM)	DM(GN)	DM(SN)	DM(avg)	B min
1	1755	5	7.17	124	...	142	138	140	...
2	1766	8	10.22	172	...	243	200	221	...
3	1775	6	11.41	234	...	287	281	284	...
4	1784	5	11.50	219	...	291	262	276	...
5	1798	6	4.85	77	...	78	81	80	...
6	1810	7	3.78	72	...	53	76	65	...
7	1823	4	6.37	116	...	118	129	123	...
8	1833	8	10.47	210	...	252	250	251	...
9	1843	7	9.25	195	...	209	230	219	5.00
10	1856	1	9.41	180	...	211	210	212	5.05
11	1867	4	10.74	209	...	262	248	255	5.83
12	1878	12	5.58	106	...	96	116	106	4.71
13	1890	2	7.42	136	...	149	154	151	5.04
14	1901	9	4.62	104	...	72	114	93	4.30
15	1913	6	7.23	154	...	143	177	160	4.32
16	1923	4	6.00	122	...	108	136	122	4.94
17	1933	9	9.01	187	...	200	219	210	5.09
18	1944	4	9.74	204	...	226	241	234	5.76
19	1954	4	12.59	266	...	334	324	329	5.38
20	1964	8	7.66	150	...	156	171	164	5.21
21	1976	3	10.93	220	260	269	262	266	5.78
22	1986	9	10.02	207	247	236	246	241	5.67
23	1996	5	9.08	172	201	203	200	201	5.01
24	2008	12	6.21	104	113	114	113	113	4.22
25	2021	1	6.90	130	149	133	146	140	4.75

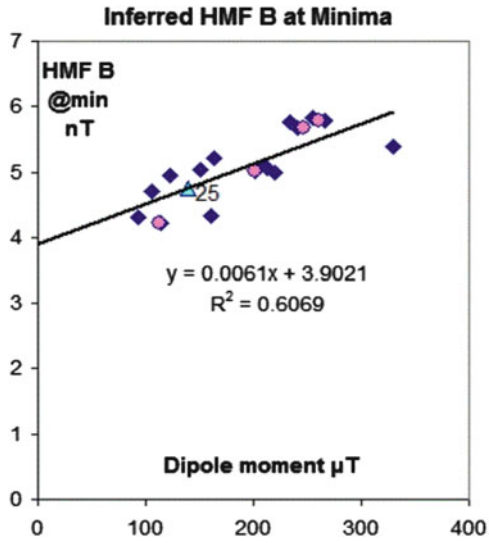

Fig. 3.14 The heliospheric magnetic field strength (at Earth) inferred from geomagnetic data at sunspot minimum vs. the solar dipole moment from the minima from SN and GN (blue diamonds), cycles 9–24, (Credit: NASA, HMI/SDO), HMI Science Nugget 78

solar minimum. This hypothesis is tested by plotting the magnetic field B at the cycle minimum against the dipole moment in Fig. 3.14. It appears that the excess of the magnetic field above a "floor" of $B = 3.9$ nT ($= 3.5 \times 10^{-5}$ Gauss) is proportional to the dipole moment, but the origin of the floor level is unknown (Svalgaard and Cliver 2007).

The use of polar fields at minimum as a predictor of the amplitude of the next solar cycle is based on dynamo theories such as the Babcock-Leighton model, which recently includes meridional flows also. For recent measurements of the polar magnetic field reversal and surface flux transport during Cycle 24 see Sun et al. (2015), for instance. The meridional flow speed sets the cycle period and influences both the strength of the polar fields and the amplitudes of the following cycles. A related prediction method is based on the *polar field precursor method* (Schatten 2005). Perhaps the strongest criticism of dynamo-based predictions is the inherent unpredictability of deterministically chaotic systems (Tobias et al. 2006; Bushby and Tobias 2007), such as a weakly nonlinear limit cycle affected by random noise (Sect. 3.6). Solar cycle predictions have also been made by using the $\alpha\Omega$-Parker model and an *Ensemble Kalman Filter*, a data assimilation method that takes into account uncertainties of a dynamo model and measurements (Kitiashvili and Kosovichev 2008; Kitiashvili 2016).

3.8 Magneto-Convection and Convective Dynamos

The solar convection zone, which approximately extends from 70% to 100% of a solar radius (where the solar interior is convectively unstable), has become increasingly important in recent years, because global-scale turbulent convective

motions under the influence of rotation and gravitational stratification redistributes momentum and energy, generating differential rotation, meridional circulation, and magnetic fields through hydromagnetic dynamo processes. Recent reviews that focus on the dynamics and magnetic fields in the solar convection zone can be found in Fan (2004), Fan (2009), Miesch (2005), Nordlund et al. (2009) and Stein (2012). The biggest progress in recent modeling of the convection zone is the transition from previous purely hydrodynamic modeling (without magnetic fields) to MHD modeling (with magnetic fields), as well as the transition from 1-D (radial) modeling of the convection zone to 3-D modeling encompassing the global convection zone.

Recently, global fully dynamic 3-D MHD convective dynamo simulations made headway in producing the solar-like cyclic behavior of the large-scale magnetic field and the self-consistent formation of buoyant, active region-like emerging tubes from dynamo-generated strong toroidal fields (Käpylä et al. 2012; Nelson et al. 2011; Augustson et al. 2015). Most of the previous simulations approximate the solar rotation with cylindrical iso-rotation contours throughout the convection zone.

As a representative highlight we exemplify the MHD simulations of a convective dynamo in the solar convective envelope (Fan and Fang 2014). The simulations of Fan and Fang (2014) present a convective dynamo simulation that is driven by the solar radiative diffusive heat flux and maintains a differential rotation profile that resembles closely to the observed solar differential rotation in the convective zone in terms of the pole-equator contrast and the more conical iso-contours of rotation in the mid-latitude. The code reproduces also a large-scale mean magnetic field with irregular cyclic behavior and polarity reversals.

The numerical code solves the anelastic MHD equations using a finite-difference spherical anelastic MHD scheme (Fan 2008; Fan and Fang 2014),

$$\nabla \cdot (\rho_0 \mathbf{v}) = 0 \,, \tag{3.8.1}$$

$$\rho_0 \left[\frac{\partial \mathbf{v}}{\partial t} + (\mathbf{v} \cdot \nabla)\mathbf{v} \right] = 2\rho_0 \mathbf{v} \times \Omega - \nabla p_1 + \rho_1 \mathbf{g} + \frac{1}{4\pi} (\nabla \times \mathbf{B}) \times \mathbf{B} + \nabla \cdot D_{ij} \,, \tag{3.8.2}$$

$$\rho_0 T_0 \left[\frac{\partial s_1}{\partial t} + (\mathbf{v} \cdot \nabla)(s_0 + s_1) \right] = \nabla \cdot (K \rho_0 T_0 \nabla s_1) - (D_{ij} \cdot \nabla) \cdot \mathbf{v} + \frac{1}{4\pi} \eta (\nabla \times \mathbf{B})^2 - \nabla \cdot \mathbf{F}_{rad} \,, \tag{3.8.3}$$

$$\nabla \cdot \mathbf{B} = 0 \,, \tag{3.8.4}$$

$$\frac{\partial \mathbf{B}}{\partial t} = \nabla \times (\mathbf{v} \times \mathbf{B}) - \nabla \times (\eta \nabla \times \mathbf{B}) \,, \tag{3.8.5}$$

$$\frac{\rho_1}{\rho_0} = \frac{p_1}{p_0} - \frac{T_1}{T_0} \,, \tag{3.8.6}$$

$$\frac{s_1}{c_p} = \frac{T_1}{T_0} - \frac{(\gamma - 1)}{\gamma} \frac{p_1}{p_0} \,, \tag{3.8.7}$$

where $s_0(\mathbf{r})$ is the entropy profile, $p_0(\mathbf{r})$ is the pressure profile, $\rho_0(\mathbf{r})$ is the density profile, $T_0(\mathbf{r})$ is the temperature profile, $\mathbf{g} = -g_0(\mathbf{r})\hat{\mathbf{r}}$ is the gravitational acceleration of a time-independent reference state of hydrostatic equilibrium and nearly adiabatic stratification, c_p is the specific heat capacity at constant pressure, γ is the ratio of specific heats, $\mathbf{v}$, $\mathbf{B}$, s_1, p_1, ρ_1, T_1 are the corresponding quantities that describe the changes from the reference state, Ω is the solid body rotation rate of the Sun, D_{ij} is the viscous stress tensor $D_{ij} = \rho_0 \nu[S_{ij} - (2/3)(\nabla \times \mathbf{v})\delta_{ij}]$, ν is the kinematic viscosity, δ_{ij} is the unit tensor, S_{ij} is the strain rate tensor, $\mathbf{F}_{rad} = -(16\sigma_s T_0^3/3\kappa\rho_0)(dT_0/dr)\hat{\mathbf{r}}$ is the radiative heat flux, K is the thermal diffusivity, η is the magnetic diffusivity, σ_s is the Stephan-Boltzman constant, and κ is the Rosseland mean opacity. The heating term $\mathbf{F}_{rad}$ due to the solar radiative diffusive heat flux drives a radial gradient of s_1 that drives the convection. The thermal diffusivity K, the viscosity ν, and the magnetic diffusivity η are set at the top of the domain and decrease all with depth following a $1/\sqrt{\rho_0}$ profile. The gravitational stratification of the domain includes approximately four scale heights. A computation grid with dimensions $[N_r \times N_\theta \times N_\Phi] = [96 \times 512 \times 768]$ is used. Some space-time slices of the simulations are shown in Fig. 3.15, rendered for the

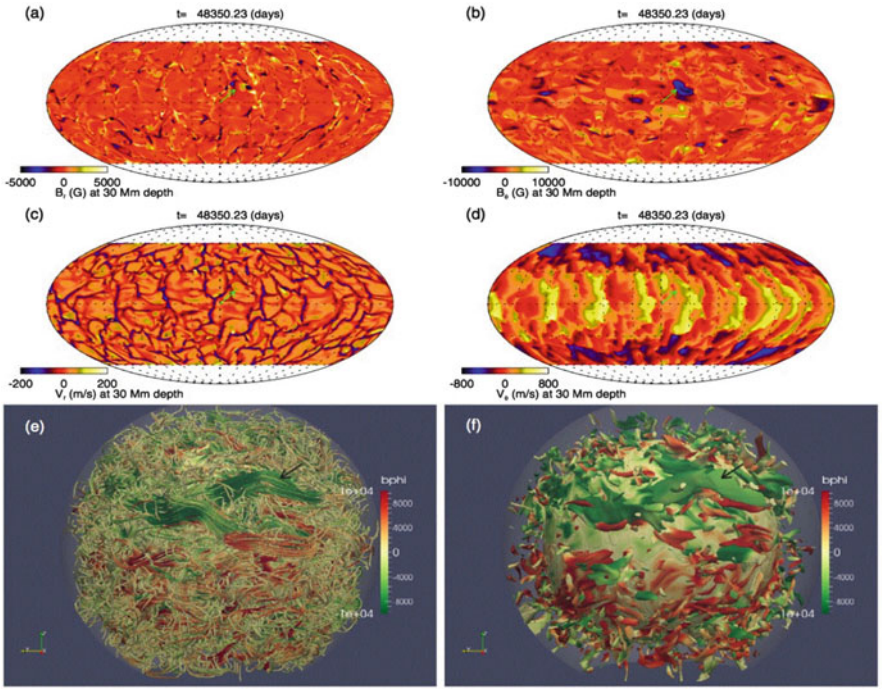

Fig. 3.15 Snapshots of (**a**) B_r, (**b**) B_Φ, (**c**) v_r, (**d**) v_Φ at a shell slice at the depth of 30 Mm below the photosphere, displayed on the full sphere in Mollweider projection. 3-D views of (**e**) the magnetic field lines and (**f**) the equipartition field iso-surfaces of $v_a/v_{rms} = 1$ with v_a being the Alfvén speed and v_{rms} being the rms convective velocity for the corresponding depth (Fan and Fang 2014)

radial magnetic field B_r (Fig. 3.15a), the azimuthal field B_Φ (Fig. 3.15b), the radial velocity v_r (Fig. 3.15c), and the azimuthal velocity v_Φ, in a shell slice at a depth of 30 Mm below the photosphere, and 3-D views are shown for the magnetic field lines (Fig. 3.15e) and the equipartition field iso-surfaces (Fig. 3.15f).

The anleastic approximation MHD code (Gough 1969; Gilman and Glatzmaier 1981; Glatzmaier 1984; Lantz and Fan 1999) is based on the assumptions of (i) near-adiabaticity $\delta \ll 1$, where $\delta = \nabla - \nabla_{ad}$ is the dimensionless super-adiabaticity with $\nabla = d \ln T / d \ln p$ and $\nabla_{ad} = (d \ln T / d \ln p)_{ad}$ denoting the actual and the adiabatic logarithmic temperature gradient of the fluid respectively, and the convective flow speed v_c is expected to be much smaller than the sound speed c_s, namely $v_c / c_s \approx \delta^{1/2} \ll 1$, and (ii) high plasma-$\beta$ parameter, $\beta = p/(B^2/8\pi) \gg 1$, i.e. a high thermal pressure compared with the magnetic pressure in the convection zone. The main feature of the anelastic approximation is that it filters out the sound waves so that the time step of numerical integration is not limited by the stringent acoustic time scale which is much smaller than the relevant dynamic time scales of interest as determined by the flow velocity and the Alfv́en speed (Fan 2009). It was shown that the anelastic formulation gives an accurate description of the magnetic buoyancy instabilities under the conditions of high plasma-β and nearly adiabatic stratification (Fan 2001). These conditions, however, break down near the top of the solar convection zone, where fully compressible MHD simulations are necessary for modeling flux emergence near the surface (Fig. 3.16).

The results of this study can be summarized as (quoted from Fan and Fang 2014): The convective dynamo produces a large-scale mean magnetic field that exhibits irregular cyclic behavior with oscillation time scales ranging from about 5 to 15 years and undergoes irregular polarity reversals. The mean axisymmetric toroidal magnetic field is of opposite sign in the two hemispheres and is concentrated at the bottom of the convection zone. The presence of the magnetic field is found to play an important role in the self-consistent maintenance of a solar-like differential rotation in the convective dynamo model. Without the magnetic fields, the convective flows drive a differential rotation with a faster rotating polar region. In the midst of magneto-convection, we found the emergence of strong super-equipartition flux bundles at the surface, exhibiting properties that are similar to emerging solar active regions.

Another global convective dynamo model has been simulated by Hotta et al. (2016), which represents hitherto the highest spatial resolution ever achieved in convective dynamo simulations with solar conditions (i.e., using the solar rotation rate). It further demonstrates the important role of the magnetic fields achieved by an efficient small-scale dynamo with high resolution, which acts as an effective viscosity to suppress the small-scale motions and thus allows a (cyclic) large-scale mean field to be maintained at high Reynolds number.

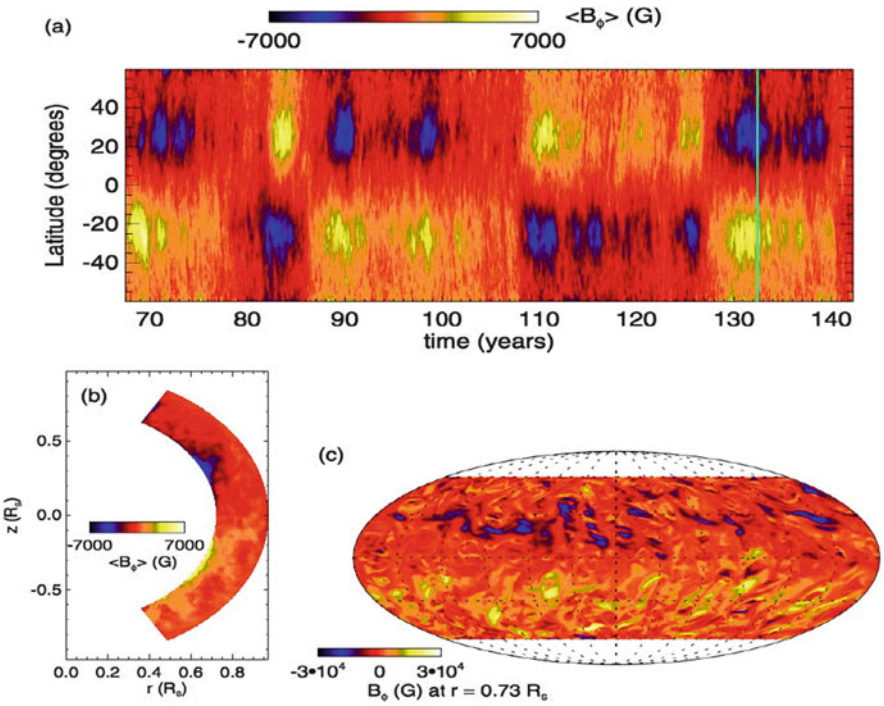

Fig. 3.16 (**a**) Latitude-time variation of mean (azimuthally averaged) toroidal magnetic field at a depth of $r = 0.73R_\odot$. (**b**) Azimuthally averaged toroidal magnetic field distribution in the meridional plane. (**c**) A shell slice of the toroidal magnetic field (Fan and Fang 2014)

3.9 Magnetic Flux Emergence

The origin of the coronal magnetic field, the birth of sunspots and associated active regions, are all rooted in the solar interior, where an invisible dynamo process generates magnetic fields that are transported by magnetic buoyancy to the solar surface, a process that is termed *"magnetic flux emergence"*.

The physics (or theory) of emerging flux is discussed in the review of Cheung and Isobe (2014), while the related magnetic fields in the solar convection zone are reviewed in Fan (2004, 2009). The buoyancy force, the main driver of flux emergence, depends on the pressure balance between a magnetic flux tube and the ambient unmagnetized fluid,

$$p + \frac{B^2}{8\pi} = p_e \,, \tag{3.9.1}$$

where p is the internal gas pressure in the flux tube, B is the magnetic field strength in the flux tube, and p_e is the pressure of the external fluid. The physical principles of

the 3-D MHD equations generally used to model emerging flux scenarios includes mass conservation, momentum conservation, energy conservation, and Faraday's law of electromagnetic induction (by eliminating the electric field),

$$\frac{\partial \mathbf{B}}{\partial t} = \nabla \times (\mathbf{u} \times \mathbf{B}) + \eta \nabla^2 \mathbf{B} \,, \tag{3.9.2}$$

where η is the Ohmic magnetic diffusivity and $\mathbf{u}$ is the velocity of the plasma motion. The first term on the right-hand side describes changes to the magnetic field as it is advected by plasma flows with speed $\mathbf{u}$, and the second term describes changes due to magnetic field diffusion. The relative importance of the terms is given by the Reynolds number,

$$R_m = \frac{vl}{\eta} \,, \tag{3.9.3}$$

where v is the velocity and l is the length scale. If $R_m \gg 1$, the advective term dominates, as it is generally the case for the solar corona, while the case with dominant diffusion ($R_m \ll 1$) is not relevant for typical solar conditions.

The diversity of MHD models used in numerical simulations of flux emergence is divided into three categories by Cheung and Isobe (2014), namely (i) *idealized models* that include energy sinks, energy sources, thermal conduction, neutral-ion effects, convective flows, and magnetic reconnection; (ii) *realistic models* that additionally include radiative transfer and *non-local thermodynamic equilibrium (NLTE)* effects, and (iii) *data-driven models* that are computed with time-dependent boundary conditions driven by observed real data on scales of entire active regions. Recently, the most developed numerical MHD models of flux emergence are provided by Martinez-Sykora et al. (2008, 2009, 2011), Cheung et al. (2007), Tortosa-Andreu and Moreno-Insertis (2009), Stein et al. (2011) and Rempel and Cheung (2014), which simulated the phenomenon of flux emergence from the convection zone through the photosphere, chromosphere, and corona, where the chromosphere is treated with radiative transfer that includes scattering (see example in Fig. 3.17).

Early simulations of emerging flux started with the insertion of a horizontal flux tube at some depth of the convection zone, which buoyantly rises towards the photosphere, while lateral pressure equilibrium causes a flattening into a horizontally extended sheet-like structure (Spruit 1987), which is reproduced in recent radiative MHD simulations (e.g., Cheung et al. 2010; Toriumi and Yokoyama 2011). During the upward motion of a flux emergence structure, various magnetic buoyancy instabilities kick in, such as the interchange mode (Kruskal-Schwarzschild instability $\mathbf{k} \perp \mathbf{B}$), or the undular mode (Parker instability, $\mathbf{k} \parallel \mathbf{B}$). The undular instability of a horizontal magnetic layer shapes the formation of arching flux tubes (Fan 2001a). The interaction of convective downflows with rising magnetic flux tubes undulates the magnetic field to form serpentine field lines that emerge into the photosphere (Cheung et al. 2008; Pariat et al. 2004). The horizontal expansion of a buoyantly

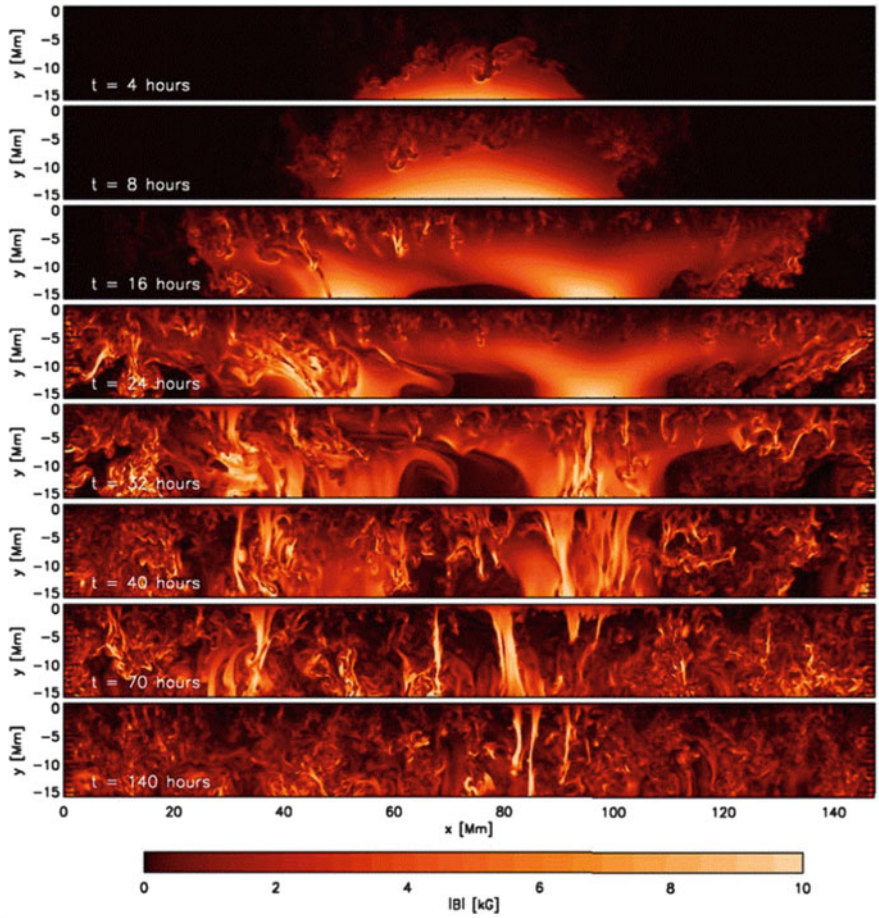

Fig. 3.17 Time evolution of the magnetic field strength $|B|$ during magnetic flux emergence on a vertical cut through the center of the domain along the x-axis. The first two snapshots show the subsurface field evolution prior to the appearance of flux in the photosphere, the remaining six snapshots correspond to the photospheric magnetograms (Rempel and Cheung 2014)

rising flux tube can be suppressed in the presence of an ambient magnetic field, for instance by the magnetic tension in the azimuthal component of a twisted flux tube (e.g., Matsumoto et al. 1993; Fan 2001b). The presence of Alfvén waves were found to play an important role in the simulation of buoyancy instabilities (Manchester 2001, 2004). Depending on the topology of the external flow field, an emerging flux tube can modify the local granulation pattern and lead to the transient appearance of dark lanes (Cheung et al. 2007).

While earlier MHD simulations of flux emergence started with the insertion of a flux tube to study the evolution during the buoyant rise, recent 3-D MHD simulations added the evolution of realistic magneto-convection dynamics to drive

the flux emergence process (Cheung and Isobe 2014). This immediately causes an asymmetry between upflows and downflows (Hurlburt et al. 1984), because upflowing material expands (in the center of granules) and downflows compress (in the intergranular lanes or network) due to mass conservation. Examples of convection-driven flux emergence can be seen in Abbett (2007) and Isobe et al. (2008), producing granular-scale Ω-loops as well as U-loops that are trapped by downflow lanes. Spontaneous formation of surface magnetic structures driven by a large-scale dynamo in strongly stratified convection has been demonstrated by Masada and Sano (2016). The emergence of a twisted flux tube into a pre-existing coronal arcade determines the helicity (Fan and Gibson 2003, 2004) and the orientation of S-shaped sigmoids and filaments (Gibson et al. 2004), but sigmoids are unreliable signatures of the sign and magnitude of magnetic twist (Abbett and Fisher 2003), and have a complex topology (Archontis et al. 2009). Some simulations are capable to create stable coronal flux ropes, tethered by overlying potential fields (Leake et al. 2013).

Another recent realistic radiation-MHD simulation of active region flux emergence and sunspot formation in the near surface layer has been conducted by Chen et al. (2017). It is driven at the lower boundary by the dynamo-generated emerging magnetic field and flow field, and it reproduces the observed asymmetric formation of sunspot groups and active regions with an earlier formation and more coherent leading sunspots.

3.10 Magnetic Helicity Injection and Condensation

Magnetic helicity is a measure of the helical twist, which can be observed most conspicuously in coronal loops. Inspecting soft X-ray images from the Sun, flaring active regions indeed show strong helical twist as it can be inferred from their sigmoidal geometry, while the magnetic field in old active regions, in the Quiet Sun, and in coronal holes generally exhibit negligible helical twist and fit a near-potential magnetic field. Consequently, we have the impression that magnetic helicity is generated in the interior of the Sun mostly during the emergence of strong-field active regions, which can be quantified with large-scale volumetric currents that produce only a global shear or twist, rather than field-line tangling (Schrijver 2007), as envisioned in the field line braiding concept of Parker (1972). Therefore, the apparent smoothness and laminarity of coronal loops and the absence of tangled field lines is a puzzling problem in the Parker (1988) nanoflare reconnection model. The problem with such reconnection-heating models is that any helicity injected into the corona as a result of random footpoint motions should conserve magnetic helicity in a high Lundquist-number system like the corona (Antiochos 2013). Even when helicity is injected on scales below currently resolved structures ($\lesssim 1''$), the helicity should build up and appear as twisting or tangling of the large-scale coronal field on larger scales, which is not observed.

Two alternative scenarios may be considered to explain the discrepancy between the theoretically envisioned complexity of tangled loops and the observationally inferred smoothness of coronal loops: (i) Photospheric motions produce equal and opposite helicity everywhere, so that no net helicity is injected into the corona, and (ii) the lack of helicity build-up is that the heating is not due to reconnection, but due to true diffusion, in which case helicity is not conserved, but both alternatives were discarded by Antiochos (2013), based on the difficulty to explain the observed Joy's law, Hale's law, the strongly preferred sign for the helicity injected into each hemisphere, and the required co-helicity of magnetic reconnection in numerical simulations. From this, Antiochos (2013) concludes that the net helicity is injected into each coronal hemisphere by the photosphere, and that reconnection preserves this helicity. The injected helicity then ends up as the magnetic shear in filament channels, the only locations in the solar corona where the magnetic field is strongly nonpotential, and hence, makes a large contribution to the total helicity.

We outline here a theoretical model for helicity injection and transport as described in Antiochos (2013). A rotated flux tube with size d, axial field B_r, and magnitude Θ, has an axial magnetic flux Φ_d of

$$\Phi_d = \pi d^2 B_p/4 \,, \tag{3.10.1}$$

which produces a twist-associated flux in the corona of,

$$\Phi_t = \Theta \Phi_d/\pi \,, \tag{3.10.2}$$

We consider now two twisted flux tubes produced by neighboring or overlapping photospheric rotation, so that the twist components of the flux tubes can reconnect, as shown in Fig. 3.18. The twist will cause the flux tubes to expand in the corona and their magnetic field lines to interact and possibly reconnect. There are two possibilities: Either two neighbored flux tubes have the same helicity (or sense of twist), and thus they will reconnect (Fig. 3.18 top or bottom), or they have opposite helicity, in which case they simply bounce and no topological change takes place (Fig. 3.18 middle).

The expected evolution of a reconnection-driven helicity cascade is shown in Fig. 3.19. As a result of reconnection, the helicity "condenses" onto the largest scale in the flux system, which is given by the scale L of the polarity inversion line that encompasses all the flux in the system. There are two conclusions from this scenario: (i) the global twist of the whole polarity inversion line is equivalent to a coherent localized shear there, which spans the length of a filament channel, and (ii) the helicity condensation mechanism is unaffected by the shape of the polarity inversion line. Furthermore, since the photospheric convection in either quiet or active regions is not observed to change with the solar cycle, the model predicts that the hemispheric helicity rule should hold independently of the solar cycle, as observed. Antiochos (2013) concludes that this simple physical model of helicity condensation can explain the smoothness of the closed-field corona, the accumulation of magnetic shear at photospheric polarity inversion lines (e.g.,

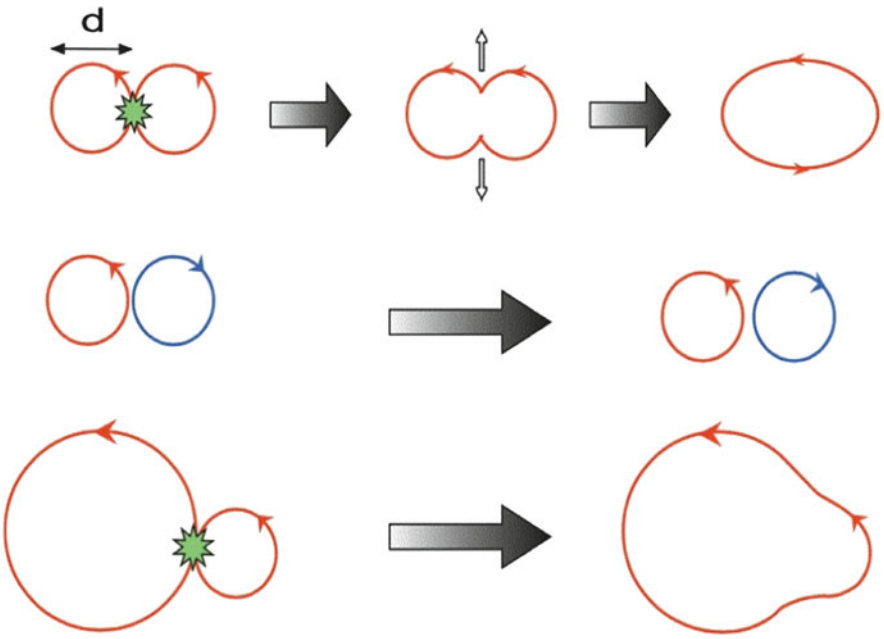

Fig. 3.18 Interaction of the twist component of interactive flux tubes. Red and blue circles correspond to oppositely oriented twist components of the magnetic field (Antiochos 2013)

filament channels), and the complex dynamics of the solar wind. The helicity condensation model predicts that the magnetic shear must accumulate at polarity inversion lines and coronal hole boundaries.

The first detailed quantitative MHD simulations of the reconnection evolution proposed by the helicity condensation model of Antiochos (2013) were conducted by Zhao et al. (2015), which demonstrated, contrary to common belief, that opposite helicity twists do not lead to significant reconnection in such a coronal system, whereas twists with the same sense of helicity do produce substantial reconnection. The shear was found always to propagate via reconnection to the boundary of the flow region while the total magnetic helicity is conserved, as predicted by the theoretical model of Antiochos (2013).

Numerical simulations of the helicity condensation model have been conducted for the case of a filament channel formation (Knizhnik et al. 2015). The 3-D simulations with the ARMS code drives photospheric twisting of a quasi-potential flux system that is bounded by a polarization inversion line and contains a coronal hole. The magnetic helicity injection is shown to inverse cascade-up to the largest allowable scales that define the closed flux system. It produces field lines that are both sheared and smooth, and are sheared in opposite senses at the polarization inversion line and the coronal hole, in agreement with the scenario pictured in Fig. 3.19.

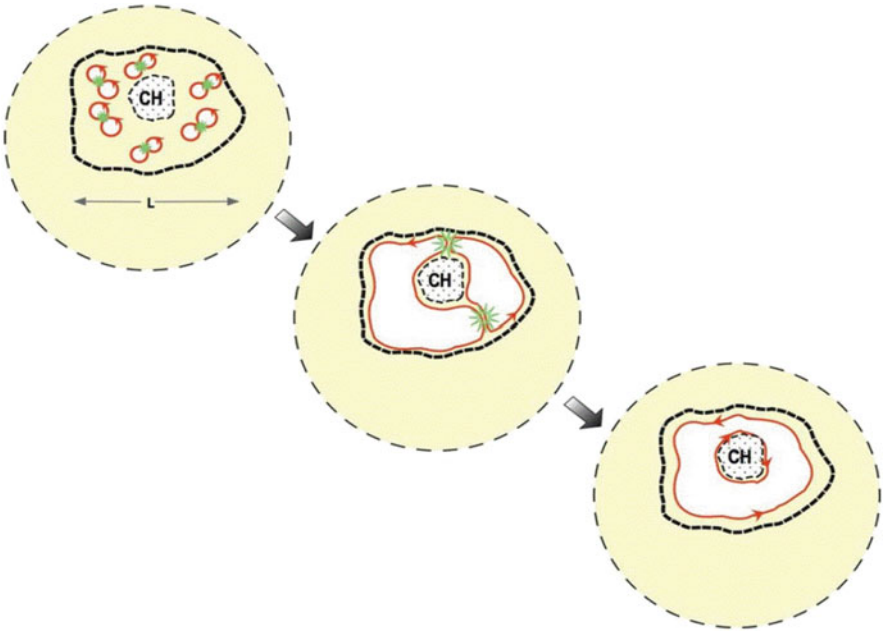

Fig. 3.19 Helicity condensation for interactive flux tubes around a coronal hole (CH), seen from the solar north pole. The expected evolution of the twist component of the magnetic field is marked with a red contour (Antiochos 2013)

More refined numerical 3-D simulations with bundles of parallel loops, where the footpoints of the field lines do not move in response to magnetic forces, but do respond to imposed boundary flows to mimic driving at the plasma-dominated photosphere, are shown in Knizhnik et al. (2017). From this study the following four main conclusions were obtained: (i) in agreement with the helicity condensation model of Antiochos (2013), the inverse cascade of helicity by magnetic reconnection in the corona results in the formation of filament channels localized about polarity inversion lines; (ii) this same process removes most complex fine structure from the rest of the corona, resulting in smooth and laminar coronal loops; (iii) the amount of remnant tangling in coronal loops is inversely dependent on the net helicity injected by the driving motions; and (4) the structure of the solar corona depends only on the helicity preference of the driving motions and not on their detailed time dependence.

Simulations of magnetic injection and condensation on the Sun on a global scale was conducted by Mackay et al. (2014), using a combination of magnetic flux transport and magneto-frictional relaxation model. The simulations show that; (i) on a north-south oriented polarization inversion line, both differential rotation and convective motions inject the same sign of helicity, which matches that required to reproduce the hemispheric pattern of filaments; (ii) on a high latitude east-west oriented polar crown or subpolar crown polarization inversion line, the vorticity of the cells has to be approximately 2–3 times greater than the local differential

rotation gradient in order to overcome the incorrect sign of helicity injection from differential rotation; (3) in the declining phase of the cycle, as a bipole interacts with the polar field, helicity condensation can reverse the effect of differential rotation along the east-west lead arm sometimes. The authors of this latter study consider the helicity-condensation model of Antiochos (2013) as an attractive third model of helicity injection, which acts over all latitudes, at all times, and can regenerate magnetic helicity in situ (even after eruptions), and is not sensitive to the orientation of the polarity inversion line irrespective or whether it contains a switchback.

Recent reviews related to this subject can be found on magnetic helicity, tilt, and twist (Pevtsov et al. 2014), on magnetic helicity and large scale magnetic fields (Blackman 2015), or on magnetic helicity estimations in models and observations of the solar magnetic field (Valori et al. 2016).

References

(3.1) Solar Neutrino Problem Solved

Ahmad, Q.R., Allen, R.C., Andersen, T.C., et al. 2001, *Measurement of the rate* $\nu_e + d \mapsto p + p + e^-$ *interactions produced by* ^8B *solar neutrinos at the Sudbury Neutrino Observatory (SNO)*, Phys.Rev.Lett. 87/7, 071301, [1520 c, 92 c/y].

Ahmad, Q.R., Allen, R.C., Andersen, T.C., et al. 2002, *Direct evidence for neutrino flavor transformation from neutral-current interactions in the Sudbury Neutrino Observatory*, Phys.Rev.Lett. 89/1, 011301-1, [1986 c, 128 c/y].

Bahcall, J.N., Pinsonneault, M.H., and Basu, S. 2001, *Solar models: Current epoch and time dependences, neutrinos, and helioseismological properties*, ApJ 555, 990, [648 c, 39 c/y],

Bahcall, J.N., Gonzalez-Garcia, M.C., and Pena-Garay, C. 2003, *Does the Sun shine by pp or CNO fusion reactions?* Phys.Rev.Lett. 90/13, 131301, [28 c, 2 c/y].

Bellini, G., Benziger, J., Bick, D., et al. 2014, *Final results of Borexino Phase-I on low-energy solar neutrino spectroscopy*, Phys.Rev. D 89/11, id. 112007, [98 c, 28 c/y].

Gribov, V. and Pontecorvo, B. 1969, *Neutrino astronomy and lepton charge*, Phys.Lett. B 28/7, 493, [558 c, 11 c/y].

Haxton, W.C., Hamish Robertson, R.G., and Serenelli, A.M. 2013, *Solar neutrinos: Status and prospects*, ARAA 51, 21, [82 c, 15 c/y].

Ianni, A. 2014, *Solar neutrinos and the solar model*, Physics of the Dark Universe 4, 44, [8 c, 2 c/y].

Turck-Chieze, S., Couvidat, S., Kosovichev, A.G. et al. 2001, *Solar neutrino emission deduced from a seismic model*, ApJ 555, 69, [130 c, 8 c/y].

(3.2) New Solar Standard Models

Asplund, M., Grevesse, N., Sauval, A.J., et al. 2009, *The chemical composition of the Sun*, ARAA 47, 481, [3297 c, 388 c/y].

Basu, S. 2016, *Global seismology of the Sun*, LRSP 13, 2, [8 c, 5 c/y].

Grevesse, N., Scott, P., Asplund, M., and Sauval, A.J. 2015, *The elemental composition of the Sun. III. The heavy elements Cu to Th*, A&A 573, A27, [64 c, 26 c/y].

Ianni, A. 2014, *Solar neutrinos and the solar model*, Physics of the Dark Universe 4, 44, [8 c, 2 c/y].

Prandtl, L. 1925, *Bericht über Untersuchungen zur ausgebildeten Turbulenz*, Zeitschr. Angew. Math. Mech. 5, 136.
Vinyoles, N., Serenelli, A.M.,Villante, F.L., et al. 2017, *A new generation of standard solar models*, ApJ 835, 202, [14 c, 14 c/y].

(3.3) Helioseismology: Meridional Flows

Basu, S. 2016, *Global seismology of the Sun*, LRSP 13, 2, [8 c, 5 c/y].
Brun, A.S., Miesch, M.S., and Toomre, J. 2011, *Modeling the dynamical coupling of solar convection with the radiative interior*, ApJ 742, 79, [84 c, 13 c/y].
Chen, R. and Zhao, J.W. 2017, *A comprehensive method to measure solar meridional circulation and the center-to-limb effect using time-distance helioseismology*, ApJ 849, 144.
Christensen-Dalsgaard, J. 2002, *Helioseismology*, Rev.Modern Phys. 74/4, 1073, [305 c, 20 c/y].
Dikpati, M. 2014, *Generating the Sun's global circulation from differential rotation and turbulent Reynolds stresses*, MNRAS 438, 2380, [13 c, 4 c/y].
Gough, D. 2013, *What have we learned from helioseismology, what have we really learned, and what do we aspire to learn?* SoPh 287, 9, [13 c, 3 c/y].
Hazra, G., Karak, B.B., and Choudhuri, A.R. 2014, *Is a deep one-cell meridional circulation essential for the flux transport solar dynamo*, ApJ 782, 93, [42 c, 12 c/y].
Hathaway, D.H., Upton, L., and Colegrove, O. 2013, *Giant convection cells found on the Sun*, Science 342, 1217, [37 c, 8 c/y].
Hotta, H., Rempel, M., and Yokoyama, T. 2015, *High-resolution calculation of the solar global convection with the reduced speed of sound technique: II. Near surface shear layer with the rotation*, ApJ 798, 51, [26 c, 10 c].
Jackiewicz, J., Serebryanskiy, A., and Kholikov, S. 2015, *Meridional flow in the solar convection zone. II. Helioseismic inversions of GONG data*, ApJ 805, 133, [22 c, 9 c/y].
Kholikov, S., Serebryanskiy, A., Jackiewicz, J. 2014, *Meridional flow in the solar convection zone. I. Measurements from GONG data*, ApJ 784, 145, [25 c, 7 c/y].
Komm, R., Gonzalez Hernandez I., Hill, F., et al. 2013, *Subsurface meridional flow from HMI using the ring-diagram pipeline*, SoPh 287, 85, [23 c, 5 c/y].
Kosovichev, A.G., Duvall, T.L.Jr., and Scherrer, P.H. 2000, *Time-distance inversion methods and results (Invited review)*, SoPh 192, 159, [240 c, 14 c/y].
Kosovichev, A.G. 2011, *Advances in global and local helioseismology: An introductory review*, Lecture Notes in Physics 832, 3, [12 c, 2 c/y].
Rajaguru, S.P. and Antia, H.M. 2015, *Meridional circulation in the convection zone: Time-distance helioseismic inferences from 4 years of HMI/SDO observations*, ApJ 813, 114, [28 c, 11 c/y].
Schad, A., Timmer, J., and Roth, M. 2013, *Global helioseismic evidence for a deeply penetrating solar meridional flow consistent with multiple flow cells*, ApJ 778, L38, [54 c, 12 c/y].
Schad, A., Jouve, L., Duvall, T.L.Jr., et al. 2016, *Recent developments in helioseismic analysis methods and solar data assimilation*, SSRv 196, 221, [1 c, 0.7 c/y].
Zhao, J.W., Bogart, R.S., Kosovichev, A.G., et al. 2013, *Detection of equatorward meridional flow and evidence of double-cell meridional circulation inside the Sun*, ApJ 774, L29, [131 c, 29 c/y].
Zhao, J.W., Kosovichev, A.G., Bogart, R.S. 2014, *Solar meridional flow in the shallow interior during the rising phase of Cycle 24* ApJ 789, L7, [13 c, 4 c/y].

(3.4) Helioseismology: Solar Interior Rotation

Guerrero, G. and de Gouveia Del Pion 2008, *Turbulent magnetic pumping in a Babcock-Leighton solar dynamo model*, A&A 485, 267 [80 c, 8 c/y].
Guerrero, G., Smolarkiewicz, P.K., Kosovichev, A.G. et al. 2013, *Differential rotation in solar-like stars from global simulations*, ApJ 779, 176, [44 c, 10 c/y].
Guerrero, G., Smolarkiewicz, P.K., Gouveia, D.P., et al. 2016, *Understanding solar torsional oscillations from global dynamo models*, ApJ 828, L3, [9 c, 6 c/y].
Hathaway, D.H., Upton, L., and Colegrove, O. 2013, *Giant convection cells found on the Sun*, Science 342, 1217, [37 c, 8 c/y].
Howard, R. and LaBonte B.J. 1980, *The Sun is observed to be a torsional oscillator with a period of 11 years*, ApJ 239, L33, [372 c, 10 c/y].
Howe, R. 2009, *Solar interior rotation and its variation*, LRSP 6, 1, [116 c, 14 c/y].
Howe, R., Christensen-Dalsgaard, J., Hill, J., et al. 2000, *Dynamic variations at the base of the solar convection zone*, Science 287, 2456, [318 c, 18 c/y].
Howe, R., Christensen-Dalsgaard, J., Hill, F., et al. 2005, *Solar convection-zone dynamics*, ApJ 634, 1405, [58 c, 5 c/y].
Howe, R., Rempel, M., Christensen-Dalsgaard, J., et al. 2006, *Solar convection zone dynamics: How sensitive are inversions to subtle dynamo features?* ApJ 649, 1155, [27 c, 2 c/y].
Kitiashvili, I.N., Kosovichev, A.G., Mansour, N.N., et al. 2016, *Dynamics of turbulent convection and convective overshoot in a moderate-mass star*, ApJ 821, L17, [6 c, 4 c/y].
Pipin, V.V. and Kosovichev, A.G. 2018, *Meridional circulation and torsional oscillations in a self-consistent solar dynamo model*, astro-ph arXiv1708.03073v1.
Rempel, M. 2007, *Origin of solar torsional oscillations*, ApJ 655, 651, [30 c, 3 c/y],
Schou, J., Howe, R., Basu, S., et al. 2002, *A comparison of solar p-mode parameters from the Michelson Doppler Imager (MDI) and the Global Oscillation Network Group (GONG): Splitting coefficients and rotation inversions*, ApJ 567, 1234, [87 c, 6 c/y].
Toutain, T. and Kosovichev, A.G. 1994, *A new estimate of the solar core rotation from IPHIR*, A&A 284, 265, [30 c, 1 c/y].

(3.5) Local Helioseismology

Braun, D.C. and Lindsey, C. 2001, *Seismic imaging of the far hemisphere of the Sun*, ApJL 560, L189, [39 c, 2 c/y].
Gizon, L. and Birch, A.C. 2005, *Local helioseismology*, LRSP 2, 6, [124 c, 10 c/y].
Gizon, L. and Thompson, M.J. 2007, *Outstanding problems in local helioseismology*, Astron.Nachrichten 328/3, 204, [7 c, 0.7 c/y].
Gizon, L., Birch, A.C., and Spruit, H. 2010, *Local helioseismology: 3-D imaging of the solar interior*, ARAA, 48, 289, [108 c, 14 c/y].
Howe, R., Christensen-Dalsgaard, J., Hill, J., et al. 2000, *Dynamic variations at the base of the solar convection zone*, Science 287, 2456, [318 c, 18 c/y].
Kosovichev, A.G., Duvall, T.L.Jr., and Scherrer, P.H. 2000, *Time-distance inversion methods and results (Invited review)*, SoPh 192, 159, [240 c, 14 c/y].
Kosovichev, A.G. 2011, *Advances in global and local helioseismology: An introductory review*, Lecture Notes in Physics 832, 3, [12 c, 2 c/y].
Kosovichev, A.G. 2012, *Local helioseismology of sunspots: Current status and perspectives*, SoPh 279, 323, [21 c, 4 c/y].
Liewer, P.C., Qiu, J., and Lindsey, C. 2017, *Comparison of helioseismic far-side active region detections with STEREO far-side EUV observations of solar activity*, SoPh 292, 146.
Lindsey, C. and Braun, D.C. 2000, *Seismic images of the far side of the Sun*, Science 287, 1799, [82 c, 5 c/y].
Rempel, M. 2007, *Origin of solar torsional oscillations*, ApJ 655, 651, [33 c, 3 c/y].

Thompson, M.J. and Zharkov, S. 2008, *Recent developments in local helioseismology*, SoPh 251, 225, [15 c, 2 c/y].
Zhao, J.W., Kosovichev, A.G., and Duvall, T.L.Jr. 2001, *Investigation of mass flows beneath a sunspot by time-distance helioseismology*, ApJ 557, 384, [192 c, 12 c/y].
Zhao, J.W. and Kosovichev, A.G. 2004, *Torsional oscillation, meridional flows, and vorticity inferred in the upper convection zone of the Sun by time-distance helioseismology*, ApJ 603, 776, [250 c, 19 c/y].

(3.6) Limit-Cycle Oscillations of the Solar Dynamo

Aschwanden, M.J., Scholkmann, F., Béthume, W. 2018, *Order out of randomness: Self-organization processes in astrophysics*, SSRv 214, 55.
Cameron, R. and Schüssler, M. 2017a, *An update of Leighton's solar dynamo model*, A&A 599, A52, [2 c, 2 c/y].
Cameron, R. and Schüssler, M. 2017b, *Understanding solar cycle variability*, ApJ 843, 111, [2 c, 2 c/y].
Charbonneau, P. 2005, 2010, *Dynamo models of the solar cycle*, LRSP 2, 2 (2005); 7, 3 (2010), [410 c, 47 c/y].
Charbonneau, P. 2013, *Solar and stellar dynamos*, in Saas-Fee Advanced Course 38, Swiss Society for Astrophysics and Astronomy, Steiner (ed.), 237p, e-book, [9 c, 1 c/y].
Consolini, G., Tozzi, R., and De Michelis, P. 2009, *Complexity in sunspot cycle*, A&A 506, 1381, [12 c, 1 c/y].
Solanki, S.K., Schüssler, M., and Fligge, M. 2000, *Evolution of the Sun's large-scale magnetic field since the Maunder minimum*, Nature 408/6811, 445, [173 c, 10 c/y].
Tobias, S.M., Weiss, N.O., and Kirk, V. 1995, *Chaotically modulated stellar dynamos*, MNRAS 273, 1150, [94 c, 4 c/y].

(3.7) Solar Cycle Prediction

Bushby, P.J. and Tobias, S.M. 2007, *On predicting the solar cycle using mean-field models*, ApJ 661, 1289, [45 c, 4 c/y].
Hathaway, D.H. 2010, 2015, *The solar cycle*, LRSP 7, 1 (2010), 12:4 (2015), [311 c, 61 c/y].
Kitiashvili, I., and Kosovichev, A.G. 2008, *Application of Data Assimilation Method for Predicting Solar Cycles*, ApJ 688, L49, [44 c, 5 c/y].
Kitiashvili, I. 2016, *Data assimilation approach for forecast of solar activity cycles*, ApJ 831, 15, [1 c, 1 c/y].
Pesnell, W.D. 2012, *Solar cycle predictions*, SoPh 281, 507, [52 c, 9 c/y].
Petrovay, K. 2010, *Solar cycle prediction*, LRSP 7, 6, [73 c, 10 c/y].
Schatten, K.H., Scherrer, P.H., Svalgaard, L., and Wilcox, J.M. 1978, *Using dynamo theory to predict the sunspot number during solar cycle 21*, GRL 5, 411, [172 c, 4 c/y].
Schatten, K.H. 2005, *Fair space weather for solar cycle 24*, GRL 32/21, L21106, [112 c, 9 c/y].
Sheeley, N.R. 2005, *Surface evolution of the Sun's magnetic field: A historical review of the flux-transport mechanism*, LRSP 2, 5, [50 c, 4 c/y].
Sun, X., Hoeksema, J.T., Liu, Y., et al. 2015, *On polar magnetic field reversal and surface flux transport during solar cycle 24*, ApJ 798, 114, [35 c, 14 c/y].
Svalgaard, L., Cliver, E.W., and Kamide, Y. 2005, *Sunspot cycle 24: Smallest cycle in 100 years ?* GRL 32, L01104, [195 c, 16 c/y].

Svalgaard, L. and Cliver, E.W. 2007, *A floor in the solar wind magnetic field*, ApJ 661, L203, [61 c, 6 c/y].
Svalgaard, L. and Schatten, K.H. 2008, *Predicting solar cycle 24*, AGU meeting 2008, abstract SH51A-1593.
Svalgaard, L. and Cliver, E.W. 2010, *Heliospheric magnetic field 1835–2009*, JGR 115, A09111, [56 c, 7 c/y].
Svalgaard, L. 2014, *Correction of errors in scale values for magnetic elements for Helsinki 2014*, Ann.Geophys. 32, 633. [12 c, 3 c/y].
Tobias, S., Hughes, D., and Weiss, N. 2006, *Unpredictable Sun leaves researchers in the dark*, Nature 442, 26, [28 c, 2 c/y].
Usoskin, I.G. 2008, 2013, 2017, *A history of solar activity over millennia*, LRSP 5, 3 (2008); 10, 1 (2013); 14, 3 (2017), [191 c, 52 c/y].
Wang, Y.M., Lean, J.L., and Sheeley, N.R.Jr. 2005, *Modeling the Sun's magnetic field and irradiance since 1713*, ApJ 625, 522, [335 c, 27 c/y].

(3.8) Magneto-Convection and Convective Dynamos

Augustson, K., Brun, A.S., Miesch, M., et al. 2015, *Grand minima and equatorward propagation in a cycling stellar convective dynamo*, ApJ 809, 149, [56 c, 22 c/y].
Fan, Y. 2001, *Nonlinear growth of the 3-D undular instability of a horizontal magnetic layer and the formation of arching flux tubes*, ApJ 546, 509, [51 c, 3 c/y].
Fan, Y. 2004, 2009, *Magnetic fields in the solar convection zone*, LRSP 1, 1 (2004), 6:4 (2009), [197 c, 23 c/y].
Fan, Y. 2008, *The 3-D evolution of buoyant magnetic flux tubes in a model solar convective envelope.* ApJ 676, 680, [67 c, 7 c/y].
Fan, Y. and Fang, F. 2014, *A simulation of convective dynamo in the solar convective envelope: Maintenance of the solar-like differential rotation and emerging flux*, ApJ 789, 35, [50 c, 14 c/y].
Gilman, P.A. and Glatzmaier, G.A. 1981, *Compressible convection in a rotating spherical shell. I. Anelastic equations*, ApJS 45, 335, [146 c, 4 c/y].
Glatzmaier, G.A. 1984, *Numerical simulations of stellar convective dynamos. I. The model and method*, J. Comput. Phys. 55, 46, [301 c, 9 c/y].
Gough, D.O. 1969, *The anelastic approximation for thermal convection*, J. Atmos.Sci. 26, 448, [128 c, 4 c/y].
Hotta, H., Rempel, M., and Yokoyama, T. 2016, *Large-scale magnetic fields at high Reynolds numbers in magnetohydrodynamic simulations*, Science 351, Issue 6280, 1427, [35 c, 23 c/y].
Käpylä, P.J., Mantere, M.J., and Brandenburg, A. 2012, *Cyclic magnetic activity due to trubulent convection in spherical wedge geometry*, ApJ 755, L22, [110 c, 20 c/y].
Lantz, S.R. and Fan, Y. 1999, *Anelastic MHD equations for modeling solar and stellar convection zones*, ApJ 121, 247, [85 c, 5 c/y].
Miesch, M.S. 2005, *Large-scale dynamics of the convection zone and tachocline*, LRSP 2, 1, [149 c, 12 c/y].
Nelson, N.H., Brown, B.P., Brun, A.S., et al. 2011, *Buoyant magnetic loops in a global dynamo simulation of a Young Sun*, ApJ 739, L38, [42 c, 6 c/y].
Nordlund, A, Stein, R.F., and Asplund, M. 2009, *Solar surface convection*, LRSP 6, 2, [169 c, 20 c/y].
Stein, R.F. 2012, *Solar surface magneto-convection*, LRSP 9, 4, [33 c, 6 c/y].

(3.9) Magnetic Flux Emergence

Abbett, W.P. and Fisher, G.H. 2003, *A coupled model for the emergence of active region magnetic flux into the solar corona*, ApJ 582, 475, [48 c, 3 c/y].

Abbett, W.P. 2007, *The magnetic connection between the convection zone in the Quiet Sun*, ApJ 665, 1469, [102 c, 10 c/y].

Archontis, V., Hood, A.W., Savcheva, A. et al. 2009, *On the structure and evolution of complexity in sigmoids: A flux emergence model*, ApJ 691, 1276, [45 c, 5 c/y].

Chen, F., Rempel, M., and Fan, Y. 2017, *Emergence of magnetic flux generated in a solar convective dynamo. I. The formation of sunspots and active regions, and the origin of their asymmetries*, ApJ 846, 149, [6 c, 6 c/y].

Cheung, M.C.M., Schüssler, M., and Moreno-Insertis, F. 2007, *Magnetic flux emergence in granular convection: radiative MHD simulations and observational signatures*, A&A 467, 703, [118 c, 11 c/y].

Cheung, M.C.M., Schüssler, M., Tarbell, T.D., et al. 2008, *Solar surface emerging flux regions" A comparative study of radiative MHD modeling and Hinode SOT observations*, ApJ 687, 1373, [127 c, 13 c/y].

Cheung, M.C.M., Rempel, M., Title, A.M. et al. 2010, *Simulation of the formation of a solar active region*, ApJ 720, 233, [159 c, 21 c/y].

Cheung, M.C.M. and Isobe, H. 2014, *Flux emergence (theory)*, LRSP 11, 3, [38 c, 11 c/y].

Fan, Y. 2001a, *Nonlinear growth of the 3-D undular instability of a horizontal magnetic layer and the formation of arching flux tubes*, ApJ 546, 509, [51 c, 3 c/y].

Fan, Y. 2001b, *The emergence of a twisted Ω-tube into the solar atmosphere*, ApJ 554, L111, [202 c, 12 c/y].

Fan, Y. and Gibson, S.E. 2003, *The emergence of a twisted magnetic flux tube into a preexisting coronal arcade*, ApJ 589, L105, [135 c, 9 c/y].

Fan, Y. and Gibson, S.E. 2004, *Numerical simulations of 3-D coronal magnetic fields resulting from the emergence of twisted magnetic flux tubes*, ApJ 609, 1123, [191 c, 14 c/y].

Fan, Y. 2004, 2009, *Magnetic fields in the solar convection zone*, LRSP 1, 1 (2004), 6, 4 (2009), [197 c, 23 c/y].

Gibson, S.E., Fan, Y., Mandrini, C., et al. 2004, *Observational consequences of a magnetic flux rope emerging into the corona*, ApJ 617, 600, [103 c, 8 c/y].

Hurlburt, N.E., Toomre, J., and Massaguer, J.M. 1984, *2-D compressible convection extending over multiple scale heights*, ApJ 282, 557. [143 c, 4 c/y].

Isobe, H., Proctor, M.R.E., and Weiss, N.O. 2008, *Convection-driven emergence of small-scale magnetic fields and their role in coronal heating and solar wind acceleration*, ApJ 679, L57, [63 c, 7 c/y].

Leake, J.E., Linton, M.G., and Török, T. 2013, *Simulations of emerging magnetic flux. I. The formation of stable coronal flux ropes*, ApJ 778, 99, [47 c, 10 c/y].

Manchester, W.IV. 2001, *The role of nonlinear Alfvén waves in shear formation during solar magnetic flux emergence*, ApJ 547, 503, [53 c, 3 c/y].

Manchester, W.IV. 2004, *Eruption of a buoyantly emerging magnetic flux rope*, ApJ 610, 588, [199 c, 15 c/y].

Martinez-Sykora, J., Hansteen, V., and Carlsson, M. 2008, *Twisted flux tube emergence from the convection zone to the corona*, ApJ 679, 871, [109 c, 11 c/y].

Martinez-Sykora, J., Hansteen, V., Carlsson, M. 2009, *Twisted flux tube emergence from the convection zone to the corona. II. Later states*, ApJ 702, 129, [53 c, 6 c/y].

Martinez-Sykora, J., De Pontieu, B., Testa, P., and Hansteen, V. 2011, *Forward modeling of emission in SDO/AIA passbands from dynamic 3-D simulations*. ApJ 743, 23, [25 c, 4 c/y].

Masada, Y., Sano, T. 2016, *Spontaneous formation of surface magnetic structure from large-scale dynamo in strongly stratified convection*, ApJ 822, L22, [6 c, 4 c/y].

Matsumoto, R., Taima, T., Shibata, K., et al. 1993, *3-D MHD of the emerging magnetic flux in the solar atmosphere*, ApJ 414, 357, [83 c, 3 c/y].

Pariat, E., Aulanier, G., Schmieder, B., et al. 2004, *Resistive emergence of undulatory flux tubes*, ApJ 614, 1099. [133 c, 10 c/y].
Rempel, M. and Cheung, M.C.M. 2014, *Numerical simulations of active region scale flux emergence: From spot formation to decay*, ApJ 785, 90, [45 c, 13 c/y].
Stein, R.F., Lagerfjärd, A., Nordlund, A., and Georgobiani, D. 2011, *Solar flux emergence simulations*, SoPh 268, 271, [55 c, 8 c/y].
Spruit, H. 1987, *Is there a weak mixed polarity background field? Theoretical arguments*, SoPh 110, 115, [99 c, 3 c/y].
Toriumi, S. and Yokoyama, T. 2011, *Numerical experiments on the two-step emergence of twisted magnetic flux tubes in the Sun*, ApJ 735, 126, [19 c, 3 c/y].
Tortosa-Andreu, A. and Moreno-Insertis, F. 2009, *Magnetic flux emergence into the solar photosphere and chromosphere*, A&A 507, 949, [43 c, 5 c/y].

(3.10) Magnetic Helicity Injection and Condensation

Antiochos, S.K. 2013, *Helicity condensation as the origin of coronal and solar wind structure*, ApJ 772, 72, [23 c, 5 c/y].
Blackman, E.G. 2015, *Magnetic helicity and large scale magnetic fields; A primer*, SSRv 188, 59, [17 c, 7 c/y].
Knizhnik, K.J., Antiochos, S.K., and DeVore, C.R. 2015, *Filament channel formation via magnetic helicity condensation*, ApJ 809, 137, [10 c, 4 c/y].
Knizhnik, K.J., Antiochos, S.K., and DeVore, C.R. 2017, *The role of magnetic helicity in structuring the solar corona*, ApJ 835, 85, [3 c, 3 c/y].
Mackay, D.H., DeVore, C.R., and Antiochos, S.K. 2014, *Global-scale consequences of magnetic helicity injection and condensation on the Sun*, ApJ 784, 164, [15 c, 4 c/y].
Parker, E. 1972, *Topological dissipation and the small-scale fields in turbulent gases*, ApJ 174, 499, [632 c, 14 c/y].
Parker, E. 1988, *Nanoflares and the solar x-ray corona*, ApJ 330, 474, [1063 c, 36 c/y].
Pevtsov, A.A., Berger, M.A., Nindos, A., et al. 2014, *Magnetic helicity, tilt, and twist*, SSRv 186, 285, [27 c, 8 c/y].
Schrijver, C.J. 2007, *Braiding-induced interchange reconnection of the magnetic field and the width of solar coronal loops*, ApJ 662, L119, [28 c, 3 c/y].
Valori, G., Pariat, E., Anfinogentov, S. et al. 2016, *Magnetic helicity estimations in models and observations of the solar magnetic field. Part I: Finite Volume Methods*, SSRv 201, 147, [7 c, 5 c/y].
Zhao, L., DeVore, C.R., Antiochos, S.K., et al. 2015, *Numerical simulations of helicity condensation in the solar corona*, ApJ 805, 61, [5 c, 2 c/y].

Chapter 4
The Photosphere and Sunspots

4.1 Solar Diameter and Oblateness

Recent debates about the accuracy of measuring the solar radius attribute an uncertainty (including systematic errors) of about $\sigma_R \pm 500$ km (e.g., Emilio et al. 2012), which amounts to a relative accuracy of $\sigma_R/R \approx 0.0007$. Space-based observations are considered to be more accurate than ground-based measurements, which are impacted by the seeing through the Earth atmosphere. Celestial mechanics is known to such a high degree of precision that the exact timing of a Venus or Mercury transit is well-known. The transits can be used to improve the errors of the plate scale of instruments like the *Helioseismic and Magnetic Imager (HMI)* onboard SDO, but also to accurately determine the solar radius at a specific instrument wavelength. The basic idea is to time the instant at which the planet enters (ingression) and exits (egression) the solar disk. A comparison between the measured transit duration and the duration predicted by the ephemeris as a function of the solar radius returns the exact value of this radius.

Recent space-based measurements have been conducted with the *Michelson Doppler Imager (MDI)* onboard the SOHO during the Mercury 2003 May 7 and 2006 November 8 transits (Emilio et al. 2012). From the MDI transit data, a solar radius of $960.12'' \pm 0.09''(696, 342 \pm 65$ km) was established. This value is consistent between the transits and consistent between different MDI focus settings after accounting for systematic effects. The total transit time was obtained with an accuracy of 4 s in 2003 and 1 s in 2006. The correction ΔR to a previous nominal value of the radius $R_\odot = 696, 000 \pm 40$ km) is calculated from,

$$\Delta R = \frac{\omega^2}{R_\odot} T \ \Delta T_{OC} \ , \tag{4.1.1}$$

where ω is the speed of Mercury relative to the Sun, T is the total length of the transit, and ΔT_{OC} is the difference between the observed and ephemeris duration of

M. J. Aschwanden, *New Millennium Solar Physics*, Astrophysics and Space Science Library 458, https://doi.org/10.1007/978-3-030-13956-8_4

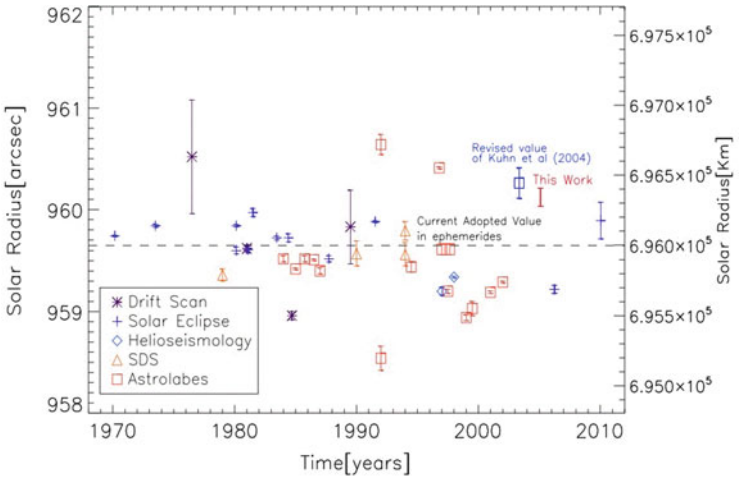

Fig. 4.1 Published measurements of the solar radius during 1970–2012, including methods such as drift scans, solar eclipses, helioseismology, *solar diameter sextant (SDS)* experiment, and astrolabe measurements. Astrolabe measurements are corrected for atmospheric and instrumental systematic effects. For references see Fig. 1 in Emilio et al. (2012)

the transit. No significant variation of the solar radius was observed over the 3 years between the two (2003, 2006) Mercury transits. A compilation of previous solar diameter measurements is shown in Fig. 4.1. Another Mercury transit was observed on 2016 May 9 with both the MDI/SOHO and HMI/SDO instruments, but the degradation of the MDI front window (which causes scattered light) and different orbits and transit paths prevented an accurate dual solar diameter measurement. The next Mercury transit will occur on 2019 November 11.

Another rare opportunity was the Venus transit on 2012 June 5 (Fig. 4.2). Venus crossings occur in two events separated by 8 years (such as on 2004 June 8 and 2012 June 5), but repeat only after 121.5 and 105.5 yrs. HMI/SDO observed the 2012 Venus transit, being the last one during this century (Emilio et al. 2015). The data have been corrected for the instrumental distortion, the point-spread function, and different background thresholds, using the information documented in Wachter et al. (2012). The obtained result is a solar radius of $959.57'' \pm 0.02$ (695, 946 ± 15 km), which is $0.55''$ smaller than the MDI result during the Mercury transit ($960.12''$), while the total uncertainty is estimated to be $0.27''$. At the same time, the Venus transit was observed with AIA, from which a solar radius of $963.04'' \pm 0.04''$ at 1600 Å, and $961.76'' \pm 0.03''$ at 1700 Å was obtained. The "visual" solar diameter depends on the wavelength (Rozelot et al. 2015). The "standard" solar radius (such as used for solar model calibrations), adopted by the IAU in 2015, was calculated using helioseismology measurements.[1] Recent measurements showed that it varies by 1–2 km during the solar cycle (Kosovichev and Rozelot 2018a).

[1] https://en.wikipedia.org/wiki/Solar_radius.

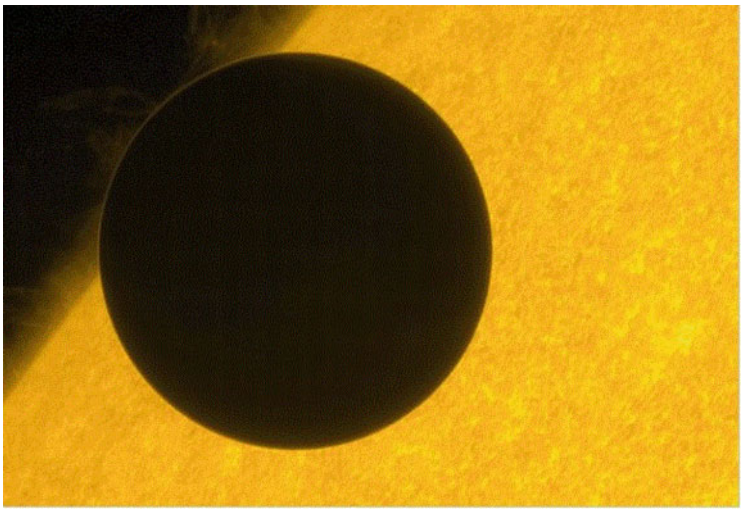

Fig. 4.2 Venus transit on 2012 June 5, observed with SOT/Hinode. Venus has a radius of 6051.8 km (Credit: Hinode Team)

Let us now turn from the solar diameter measurement to the solar oblateness measurement, which is the ratio between the equatorial and polar radius. Recent reviews about this topic can be found in Damiani et al. (2011) and Rozelot et al. (2015). Theoretically, the oblateness and centrifugal force would diminish the equatorial gravity compared to the polar gravity. The Earth has an oblateness of 1/298. The shape of the Sun is influenced by its internal rotation and the magnetic and fluid-flow stresses. The surface rotation rate, $v \approx 2$ km s^{-1} at the equator, predicts an oblateness (equator-pole radius difference) of 7.8 milli-arcsec, or $\approx 10^{-5}$. Observations with RHESSI revealed an unexpected larger flattening (Fig. 4.3) of 10.77 ± 0.44 milli arcsec (Fivian et al. 2008). The position of the limb correlates with the EUV 284 Å brightness of magnetic elements in the enhanced network, which can be used to correct for this systematic error, yielding a corrected oblateness of the non-magnetic Sun of 8.01 ± 0.14 milli arcsec, close to the theoretically expected value from rotation (Fivian et al. 2008).

According to Kuhn et al. (2012), the expected deviation of the solar-limb shape from a perfect circle is very small, but measurable with present instrumentation such as MDI/SOHO and HMI/SDO. Long-term measurements with MDI reveal that the Sun's oblate shape is distinctly constant and almost unaffected by the solar-cycle variability. Kuhn et al. (2012) find that the observed oblateness is significantly lower than theoretically expected, but by an amount that could be explained by a slower differential rotation in the outer few percent of the Sun. However, the most recent helioseismic measurements reveal rotation and asphericity variations in the near-surface shear layer during a solar cycle (Kosovichev and Rozelot 2018b).

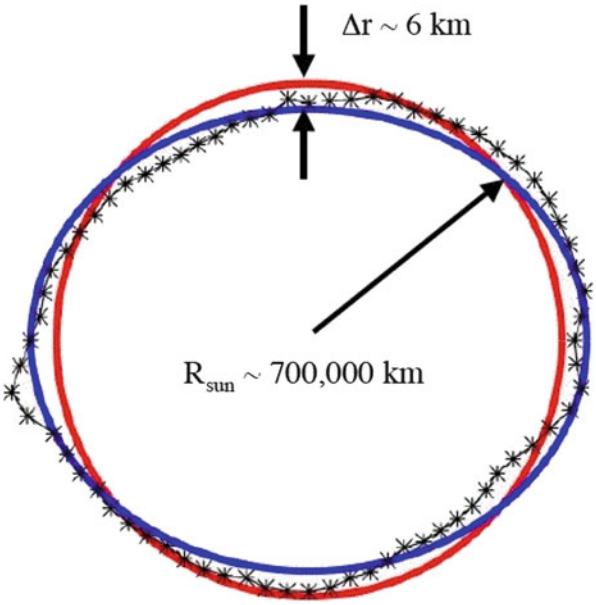

Fig. 4.3 The diagram depicts the Sun's oblateness, which is magnified by a factor of 10^4. The blue curve traces the Sun's shape averaged over a 3-month period. The black curve with asterisks traces a shorter 10-day average. The wiggles in the 10-day curve are correlated with strong magnetic ridges in the vicinity of sunspots. The red circle corresponds to a perfect sphere (Fivian et al. 2008)

How oblate is the Sun? Douglas Gough (2012) gives us the following answer: Le Verrier realized the unexplained perihelion precession of Mercury. Newcomb pointed out that this residual precession could be due to the oblateness of the Sun. Einstein demonstrated that the general theory of relativity explained almost all of the $43''$ per century perihelion precession of Mercury, assuming that the Sun is perfectly spherical without oblateness. Only 0.2% of the original discrepancy then remained to be explained otherwise, presumably by oblateness caused by the solar rotation. Gough (2012) suggests that turbulent stresses from convection could possibly contribute. Nevertheless, the analysis of HMI data (Kuhn et al. 2012) yields a too low oblateness and the conundrum remains: Why does the Sun appear to be so round?

4.2 Magnetic Flux Distribution

Although the global magnetic field of the Sun is roughly described by a poloidal dipole field during the minimum of the solar activity cycle, and with a toroidal field during the maximum, the distribution of the magnetic flux on the solar surface is much more complex. It is common practice to subdivide it into active regions

with sunspots (where the magnetic field is strongest and has mostly a closed-field configuration), Quiet Sun regions (where the field is weaker but still closed), and coronal hole regions (where the field is weak and has an open-field configuration by definition). The strongest fields are found in sunspots and amount to field strengths of $B \approx 1000$–6250 G (Okamoto and Sakurai 2018), while the weakest fields have field strengths of $B \approx 5$–10 G in the average. However, there appears to be a continuous distribution of magnetic field strengths and fluxes, ranging over five decades in flux, from $\Phi = BA \approx 2 \times 10^{17}$ to 10^{23} Mx (Parnell et al. 2009). If we associate the weakest field strengths of $B_{min} \approx 5$ G to the weakest fluxes, we obtain a length scale of $L_{min} \approx \sqrt{\Phi_{min}/B_{min}} \approx 2$ Mm, while the largest sunspots with a field strength of $B_{max} \approx 4000$ G are estimated to have a length scale of $L_{max} \approx \sqrt{\Phi_{max}/B_{max}} \approx 50$ Mm, or 7% of a solar radius (Fig. 4.4 left). The weakest magnetic field structures in the Quiet Sun are called "salt-and-pepper", while the smallest flux concentrations in active regions are referred to as "network" and "magnetic pores" (Fig. 4.4 right). Some studies claim that the Sun's magnetic field is structured over a range of seven orders of magnitude, where four of them are beyond the resolving power of current telescopes (Stenflo 2012). The recycling time of photospheric magnetic fluxes has been measured from 14 hrs (Hagenaar 2001) down to 1.4 hr (Close et al. 2004).

The most remarkable result of the measured magnetic flux structures is the finding of an approximate power law distribution that spans over 5 orders of magnitude (Fig. 4.5; Table 4.1; Parnell et al. 2009),

$$N(\Phi)d\Phi = \Phi^{-1.85\pm0.14}\, d\Phi \quad [\mathrm{Mx}^{-1}\mathrm{cm}^{-2}]\,, \tag{4.2.1}$$

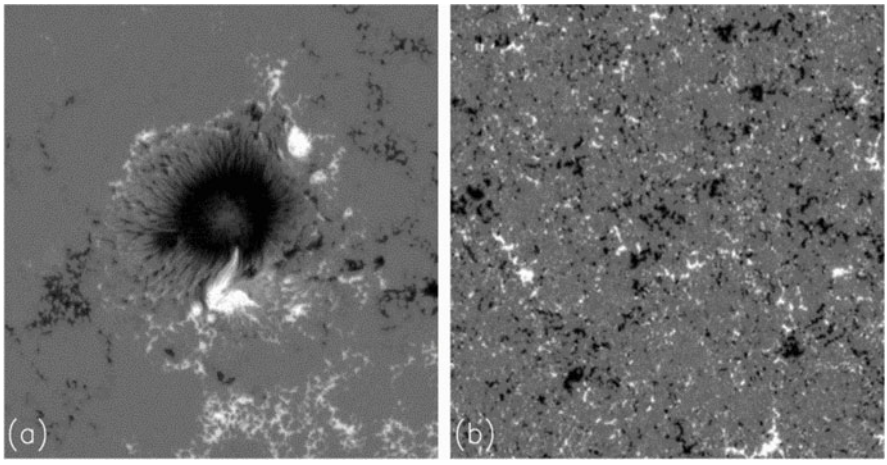

Fig. 4.4 Examples of a large sunspot structure (**a**) and the salt-and-pepper structure in the Quiet Sun (**b**), observed with the *Spectro-Polarimeter (SP)* onboard *SOT/Hinode*, which takes line profiles of the Stokes V parameter in the blue wing of the 6320 Å spectral absorption line, recorded over a slit of 0.15″ (Parnell et al. 2009)

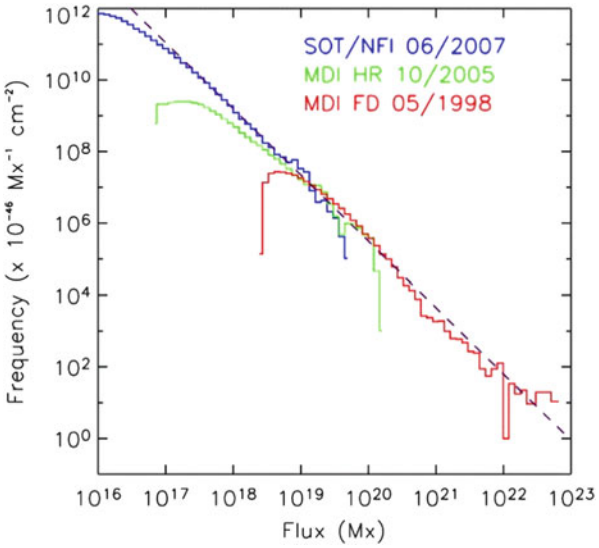

Fig. 4.5 Histogram of magnetic flux features observed with SOT/Hinode and MDI/SOHO. The dashed line represents a power law fit with a slope of $\alpha = -1.85$. Note the range of 5 decades in magnetic flux (Parnell et al. 2009)

This result, however, has been "stitched together" from three different data sets observed with two instruments, i.e., from NFI/SOT/Hinode, and full-disk and high-resolution data from MDI/SOHO. Moreover, the three data sets were observed at different times. A similar value was found also from cellular automaton simulations, i.e., $N(\Phi) \approx \Phi^{-1.5\pm0.05}$ (Fragos et al. 2004).

The question arises, whether this remarkable result can help us to understand the formation process of sunspots and pores in terms of the underlying solar dynamo. Magnetic features observed on the solar surface are believed to be created in the convection zone, either close to the photosphere by a "shallow dynamo", or in the tachocline at the bottom of the convection zone by a "deep dynamo". Schrijver et al. (1997) formulated a set of magneto-chemistry equations and predicted an exponential distribution function for the magnetic fluxes. Parnell (2002) used the same equations, but different assumptions, and predicted a Weibull distribution function. Moreover, simulations show that initially evenly distributed fields form self-organized magnetic structures, such as pores and sunspots (Kitiashvili et al. 2010), which may explain the break in the power law distribution at high magnetic flux values.

If magnetic flux is evenly distributed in the 3-D volume of the convection zone, such as generated by a deep dynamo process, fragmentation would lead to a scale-free size distribution of length scales, $N(L)dL \propto L^{-3}\, dL$, which translates into a size distribution of areas $A = L^2$ as,

$$N^{deep}(A)dA \propto N(L[A])\frac{dL}{dA}dA = A^{-2.0}dA\ . \tag{4.2.2}$$

On the other hand, if the magnetic flux is generated by a shallow dynamo near the surface only, fragmentation would lead to a scale-free size distribution of length scales, $N(L)dL \propto L^{-2}$, which translates into a size distribution of areas $A = L^2$ as,

$$N^{shallow}(A)dA \propto N(L[A])\frac{dL}{dA}dA = A^{-1.5}dA\,. \tag{4.2.3}$$

From cellular automaton simulations, a fractal dimension of $N(L) \propto L^{-1.73\pm0.05}$ was found (Fragos et al. 2004), which is closer to the power law slope value expected for the shallow case, with $N(L) \propto L^{-2}$.

From the the magnetic flux distribution $N(\Phi)$ and area distribution $N(A)$ we can infer a relationship for the scaling between the two parameters Φ and A, which we characterize with a power law exponent β,

$$\Phi \propto A^{\beta}\,. \tag{4.2.4}$$

From the characteristic values of magnetic features listed in Table 2 of Parnell et al. (2009) we find minimum values of $\Phi_{min} = 4.9 \times 10^{18}$ Mx and $A_{min} = 15$ Mm^2, and maximum values of $\Phi_{max} = 128 \times 10^{18}$ Mx and $A_{max} = 2140$ Mm^2 (from MDI data), from which we estimate an approximate power law exponent β of

$$\beta = \frac{\log\left(\Phi_{max}/\Phi_{min}\right)}{\log\left(A_{max}/A_{max}\right)} \approx 0.66\,. \tag{4.2.5}$$

Thus, we obtain the relationship $\Phi(A) \propto A^{0.66}$ from the Parnell et al. (2009) data. Furthermore, we can obtain a prediction of the scaling between the mean magnetic field strength B and the length scale L of each magnetic flux area, using the relationships $\Phi = AB$, $\Phi = A^{\beta}$, and $A = L^2$,

$$B \propto L^{2(\beta-1)} \propto L^{\delta} \propto L^{-0.68}\,, \tag{4.2.6}$$

which approximately agrees with the result of Mandrini et al. (2000), who found a universal scaling law between the mean magnetic field B and the loop length L, derived in the range of $50 \leq L \leq 300$ Mm,

$$B \propto L^{\delta} \approx L^{-0.88\pm0.30}\,, \tag{4.2.7}$$

Note that both data sets predict that the mean magnetic field strength decreases with the length scale of the magnetic area. The fact that the loop length statistics is different in coronal holes, Quiet Sun, and active regions, may complicate the scaling between loop lengths L_{loop} and the sizes L_{mag} of magnetic areas (Wiegelmann and Solanki 2004).

Nevertheless, this simple model based on the results of Parnell et al. (2009) can provide a diagnostic of whether the magnetic features are generated by a deep

Table 4.1 Magnetic flux and area distributions and related scaling laws

	Parnell et al. (2009)	Mandrini et al. (2000)
$N(\Phi) \propto \Phi^{a_\Phi}$	$a_\Phi = -1.85 \pm 0.14$	
$N^{deep}(A) \propto A^{a_A}$	$a_A = -2.0$	
$N^{shallow}(A) \propto A^{a_A}$	$a_A = -1.5$	
$\Phi \propto A^{\beta}$	$\beta = +0.66$	
$B \propto L^{\delta}$	$\delta = -0.68$	$\delta = -0.88 \pm 0.30$

dynamo (if the magnetic area distribution is $N(A) \propto A^{-2.0}$), or by shallow dynamos (if the magnetic area distribution is $N(A) \propto A^{-1.5}$) (see summary of power law slopes in Table 4.1). If both (shallow and deep) dynamos operate, a broken power-law is predicted.

4.3 Bimodal Magnetic Area Distributions

The mathematical form of statistical probability density functions (PDF) of various physical parameters can reveal physical scaling laws and the physical nature of the underlying generation process. For instance, power law (or log-normal) distributions indicate scale-free parameter ranges over which nonlinear energy dissipation processes operate, producing coherently amplified events. In contrast, exponential, Gaussian, or Poissonian distributions indicate random processes that produce incoherent events that are statistically independent. More generalized distribution functions include the Weibull distribution function, which exhibits shapes from a simple power law function to a Rayleigh distribution function (which is Gaussian-like), or the log-normal distribution function, which essentially is close to a Gaussian on a log-scale. The hope is that the mathematical form of a distribution function is generic to a specific physical process, so that it can be used as a diagnostic tool.

Motivated by such statistical arguments, fitting of occurrence frequency distribution functions were carried out for solar magnetic parameters, such as the magnetic flux (Parnell et al. 2009), or sunspot areas, sunspot group areas, and sunspot umbral areas (Meunier 2003; Baumann and Solanki 2005; Zharkov et al. 2005; Zhang et al. 2010; Schad and Penn 2010; Jiang et al. 2011; Nagovitsyn et al. 2012; Tlatov and Pevtsov 2014; Munoz-Jaramillo et al. 2015). Ultimately, the size distribution functions of these magnetic parameters observed in the photosphere are investigated in order to infer information on the size of the solar dynamo, which can have a global scale as large as the depth of the convection zone (the so-called "deep dynamo"), and additionally may consist of small-scale components (the so-called "shallow dynamo").

Tlatov and Pevtsov (2014) investigated the detailed relationship between the magnetic flux $\Phi = AB$, the field strength B, and the sunspot area A, using daily

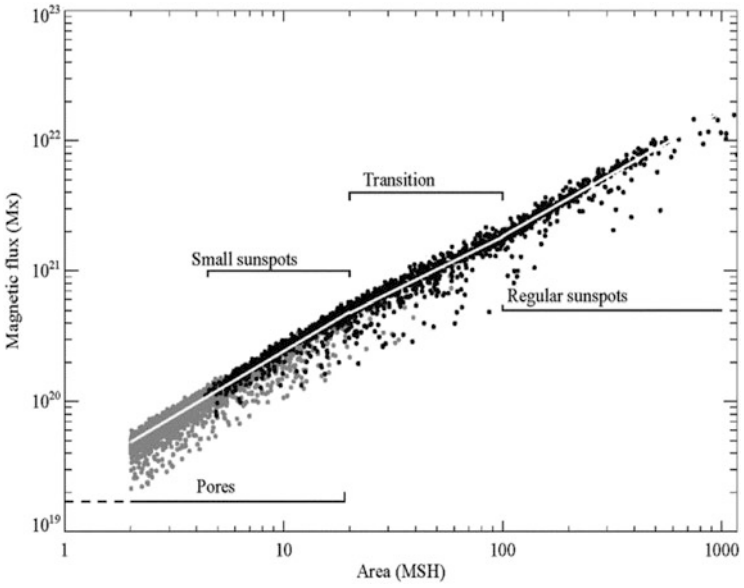

Fig. 4.6 The total magnetic flux $\Phi(A)$ as a function of the area of pores (gray) and sunspots (black). Piecewise linear fits are shown with a white line. The unit of the area is a *millionth solar hemisphere (MSH)* (Tlatov and Pevtsov 2014)

observations from HMI/SDO. The authors fit a function $B_{max} = c_0 + c_1 \log(A)$ to the data and find a bimodal distribution of magnetic fields, which can be expressed by different scaling factors c_0, yielding an average magnetic field strength of $B_{avg} \approx 800$ G for small sunspots and pores ($A \leq 20$ millionth of solar hemisphere, MSH), and of $B_{avg} \approx 600$ G for large sunspots ($A \geq 100$ MSH), with a continuous transition between the two area regimes (Fig. 4.6). The authors attribute this difference to the formation of a regular penumbra in small sunspots. When the sunspot penumbra starts forming, the magnetic field becomes more horizontal, and thus the relation between the vertical field strength and the area of sunspot changes.

Munoz-Jaramillo et al. (2015) study the best-fitting distribution functions for 11 different databases of sunspot areas, sunspot group areas, sunspot umbral areas, and magnetic flux, including the photo-heliographic results of the *Royal Greenwich Observatory (RGO)*, the *Solar Observing Optical Network (SOON)*, the *Pulkovo's catalog of solar activity (PCSA)*, the *Kislovodsk Mountain Astronomical Station (KMAS)*, the HMI/SDO, the *San Fernando Observatory (SFO)*, the *Kitt Peak Vacuum Telescope (KPVT)* bipolar magnetic region and *KPVT/SOLIS* datasets, and the *MDI/SOHO* dataset. An example of a HMI/SDO magnetogram is shown in Fig. 4.7, which illustrates the approximate self-similarity of bipolar magnetic structures over a scale range of about 2 orders of magnitude. A large active region may cover an area with a length scale of almost a half solar radius (Fig. 4.7a), which contains hierarchical subgroups of bipolar structures, as it can be seen when

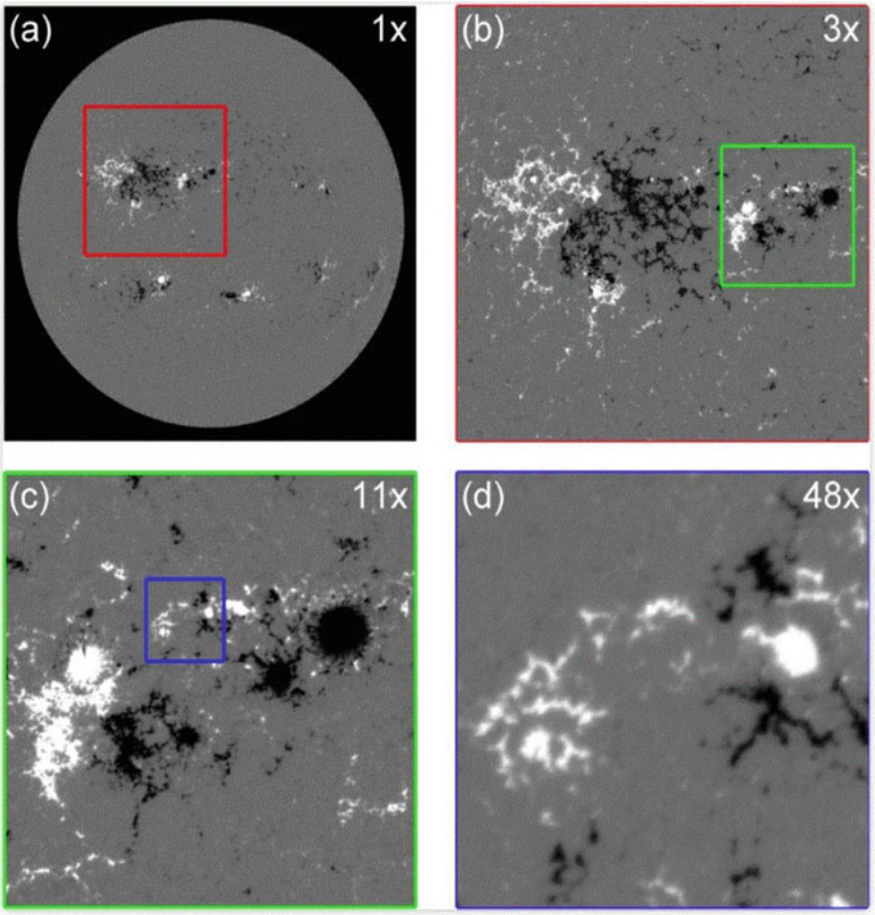

Fig. 4.7 A HMI/SDO magnetogram (2012 June 5) of a large-scale active region is shown (**a**), magnified 3× (**b**), 11× (**c**), and 48× (**d**), which approximately exhibits self-similarity for bipolar structures, spanning over 2 orders of magnitude in length, or 4 orders of magnitude in area (Munoz-Jaramillo et al. 2015)

magnified by a factor of 3 (Fig. 4.7b), a factor of 11 (Fig. 4.7c), or a factor of 48 (Fig. 4.7d). The authors fit log-normal, power law, exponential, and Weibull distribution functions and find that a linear combination of Weibull and log-normal distributions fit the data best, a bimodal function with a separation point around $\approx 10^{21}$–10^{22} Mx in magnetic flux, at $A \approx 10^2$ MSH (Fig. 4.8). The approximate power law shape of the Weibull distribution in the range of 10^{16}–10^{21} Mx found here is compatible with the power law fit of Parnell et al. (2009). The fact that a Weibull distribution was found to be a better fit than a power law function in Munoz-Jaramillo et al. (2015), appears to be a discrepancy to the power-law fits of Parnell et al. (2009), but could possibly be explained with the different detection

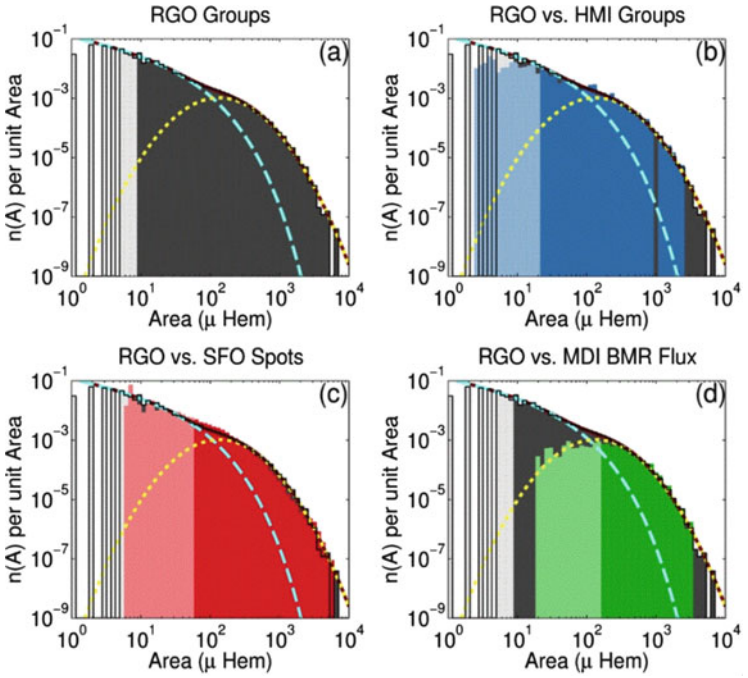

Fig. 4.8 Occurrence frequency size distributions of sunspot areas for 11 different data sets, consisting of a Weibull (dashed blue) and log-normal distributions (dotted yellow line) (Munoz-Jaramillo et al. 2015)

algorithms used in MDI/HR, MDI/FD, and SOT/NFI magnetograms, as well as with the different time durations and solar cycles of the selected data.

Based on the successful fit of bimodal distributions to 11 different datasets with different size ranges, Munoz-Jaramillo et al. (2015) interpret this result as evidence of two separate mechanisms giving rise to visible structures on the photosphere: one directly connected to the global component of the solar dyanmo (and the generation of bipolar active regions), and the other one with the small-scale component of the dynamo (and the fragmentation of magnetic structures due to their interaction with turbulent convection, with a transition between these two types of structures around 10^{21}–10^{22} Mx in flux, or $A \approx 10^2$ MSH). Future MHD simulations of turbulent convection, with flux-emergence and transport throughout the convection zone, may benefit from the additional constraint of these observed magnetic flux distributions and sunspot areas characterized by a bimodal Weibull-lognormal distribution function.

4.4 The Multi-Fractal Photosphere

While the umbra of a photospheric sunspot appears to be space-filling, its surface area A is expected to scale quadratically with its length scale L, i.e., $A \propto L^2$. Outside the umbra, however, a photospheric magnetogram reveals a lot of fragmented magnetic flux, especially in the plages of active regions, down to the ubiquitous salt-and-pepper structure on the entire solar surface. A representative measure of the degree of magnetic flux fragmentation is the fractal (or multi-fractal) dimension, e.g., the 2-D Hausdorff dimension D_2,

$$N(A) \propto A^{D_2} \ , \tag{4.4.1}$$

which defines a size distribution $N(A)$ of areas A with power law index D_2, where the range is limited by $0 < D_2 \leq 2$ for 2-D areas A (in a 2-D Euclidean space). If the fractal dimension is near $D_2 \approx 2$, the sampled structures consist of solid areas, which become curvi-linear near $D_2 \approx 1$, or even dotted near $D_2 \gtrsim 0$. Two widely used methods to infer the fractal dimension are the box-counting method (defined by $D_2 = \log A / \log(L)$), and the perimeter-area method (defined by $P \approx A^{D_2/2}$, with P being the perimeter length).

A compilation of fractal dimensions measured in photospheric magnetograms is given in Table 4.2. The solar granulation has a typical spatial scale of $L = 1000$ km, or a perimeter of $P = \pi L \approx 3000$ km. Roudier and Muller (1986) measured the areas A and perimeters P of 315 granules and found a power law relation $P \propto A^{D/2}$, with $D = 1.25$ for small granules (with perimeters of $P \approx 500$–4500 km) and $D = 2.15$ for large granules (with $P = 4500$–$15,000$ km). The smaller granules were interpreted in terms of turbulent origin, because the predicted fractal dimension of an isobaric atmosphere with isotropic and homogeneous turbulence is $D = 4/3 \approx 1.33$ (Mandelbrot 1977). Similar values were found by Hirzberger et al. (1997). Bovelet and Wiehr (2001) tested different pattern recognition algorithms (Fourier-based recognition technique FBR and multiple-level tracking MLT) and found that the value of the fractal dimension strongly depends on the measurement method. The MLT method yielded a fractal dimension of $D \approx 1.1$, independent of the spatial resolution, the heliocentric angle, and the definition in terms of temperature or velocity. Meunier (1999) evaluated the fractal dimension with the perimeter-area method and found $D = 1.48$ for supergranular structures to $D = 1.68$ for the largest structures, while the linear size-area method yielded $D = 1.78$ and $D = 1.94$, respectively. In addition, a solar cycle dependence was found by Meunier (2004), with the fractal dimension varying from $D = 1.09 \pm 0.11$ (minimum) to $D = 1.73 \pm 0.01$ for weak-field regions ($B_m < 900$ G), and $D = 1.53 \pm 0.06$ (minimum) to $D = 1.80 \pm 0.01$ for strong-field regions ($B_m > 900$ G), respectively. A fractal dimension of $D = 1.41 \pm 0.05$ was found by Janssen et al. (2003), but the value varies as a function of the center-to-limb angle and is different for a speckle-reconstructed image that eliminates seeing and noise.

Table 4.2 Area fractal dimension D_2 of scaling between length scale L and fractal area $A(L) \propto L^{D_2}$ of various solar phenomena observed in white light and in magnetograms

Wavelengths regime and phenomenon (reference in superscript)	Method	Area fractal dimension D
White-light of granules[a]	Perimeter area	1.25, 2.15
White-light of granules[b]	Perimeter area	1.3, 2.1
White-light of granular cells[b]	Perimeter area	1.16
White-light of granules[c]	Perimeter area	1.09
Magnetogram super-granulation[d]	Perimeter area	1.25
Magnetograms of small scales[e]	Perimeter area	1.41 ± 0.05
Magnetograms of active regions[f,g]	Linear size area	1.56 ± 0.08
Magnetograms of plages[h]	Linear size area	1.54 ± 0.05
Magnetograms of active regions[i]	Linear size area	1.78–1.94
	Perimeter area	1.48–1.68
Magnetograms of active regions[j]	Perimeter area	
– Total		1.71–1.89
– Cycle minimum		1.09–1.53
– Cycle rise		1.64–1.97
– Cycle maximum		1.73–1.80
Magnetograms Quiet Sun, active regions[k]	Box-counting	Multifractal
Magnetograms of active regions[l,m]	Box-counting	Multifractal
Magnetograms of active regions[n]	Box-counting	1.25–1.45

References: [a]Roudier and Muller (1986); [b]Hirzberger et al. (1997); [c]Bovelet and Wiehr (2001); [d]Paniveni et al. (2005); [e]Janssen et al. (2003); [f]Lawrence (1991); [g]Lawrence and Schrijver (1993); [h]Balke et al. (1993); [i]Meunier (1999); [j]Meunier (2004); [k]Lawrence et al. (1993); [l]Cadavid et al. (1994); [m]Lawrence et al. (1996); [n]McAteer et al. (2005)

A completely different approach to measure the fractal dimension D was pursued in terms of a 2-D diffusion process, finding fractal diffusion with dimensions in the range of $D \approx 1.3$–1.8 (Lawrence 1991) or $D = 1.56 \pm 0.08$ (Lawrence and Schrijver 1993) by measuring the dependence of the mean square displacement of magnetic elements as a function of time. Similar results were found by Balke et al. (1993). The results exclude Euclidean 2-D diffusion but are consistent with percolation theory for diffusion of clusters at a density below the percolation threshold (Lawrence and Schrijver 1993; Balke et al. 1993).

Fractal dimensions were also evaluated with a box-counting method, finding a range of $D \approx 1.30$–1.70 for chromospheric network structures in a temperature range of $T = 10^{4.5} - 10^6$ K (Gallagher et al. 1998), a value of $D \approx 1.4$ for so-called *Ellerman bombs* (Georgoulis et al. 2002), which are short-lived brightenings seen in the wings of the Hα line from the low chromosphere, or a range of $D \approx 1.25$–1.45 from a large survey of 9342 active region magnetograms (McAteer et al. 2005). In the most recent work it was found that the concept of mono-fractals has to be generalized to multi-fractals (Fig. 4.9) to quantify the spatial structure of solar magnetograms more accurately (Lawrence et al. 1993, 1996; Cadavid et al. 1994; McAteer et al. 2005; Conlon et al. 2008).

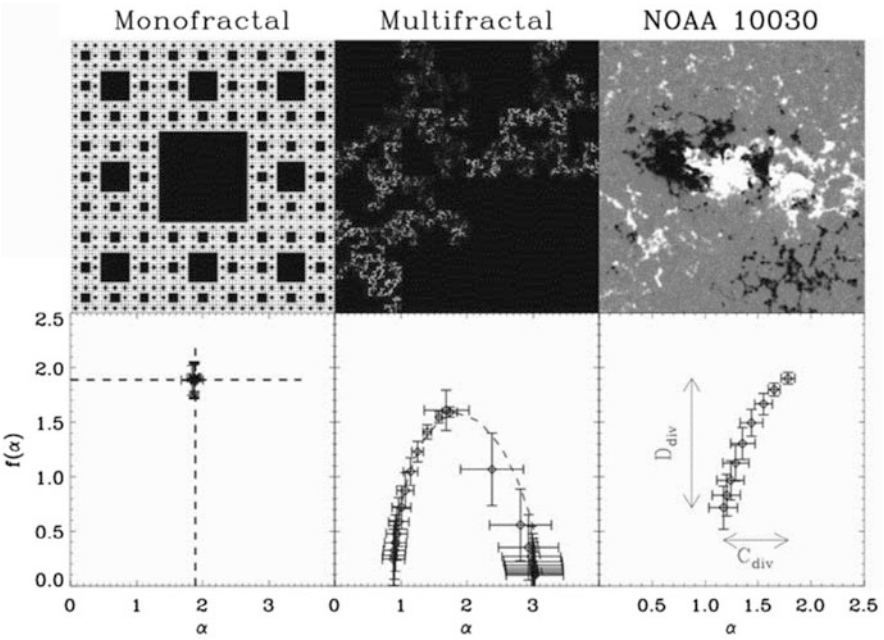

Fig. 4.9 *Top:* A monofractal image, a multi-fractal image, and a magnetogram of an active region. *Bottom:* Multi-fractal spectra with a spectrum of exponents $f(\alpha)$, each with relative strength or significance α (Conlon et al. 2008)

The physical understanding of solar (or stellar) granulation has been advanced by numerical magneto-convection models and N-body dynamic simulations, which predict the evolution of small-scale (granules) into large-scale features (meso or supergranulation), organized by surface flows that sweep up small-scale structures and form clusters of recurrent and stable granular features (Hathaway et al. 2000; Berrilli et al. 2005; Rieutord et al. 2008, 2010). The fractal structure of the solar granulation is obviously a self-organizing pattern that is created by a combination of subphotospheric magneto-convection and surface flows, which are turbulence-type phenomena.

The generation of magnetic structures that bubble up from the solar convection zone to the solar surface by buoyancy, observed as emerging flux phenomena in form of active regions, sunspots, and pores, can be statistically described as random, self-organization (SO), self-organized criticality (SOC), percolation, or diffusion process. Random processes produce incoherent structures, in contrast to the coherent magnetic flux concentrations observed in sunspots. A self-organization (SO) process needs a driving force and a counter-acting feedback mechanism that produces ordered structures (such as the convective granulation cells). A SOC process exhibits power law size distributions of avalanche sizes and durations. The finding of a fractal dimension in magnetic features alone is not a sufficient condition

to prove or rule out any of these processes. Nevertheless, it yields a scaling law between areas ($A \propto L^{D_2}$) or volumes ($V \propto L^{D_3}$) and length scales L that quantifies scale-free (fractal) processes in form of power laws and can straightforwardly be incorporated in SOC-like models.

4.5 Mini-Granulation

The solar photosphere exhibits a pattern of "bubbling" cells (like boiling water in a frying pan), which is called "photospheric granulation" and has been interpreted in terms of hydrodynamic convection cells (Fig. 4.10). The central part of a granulation cell is occupied with upflowing plasma, which then cools down and descends in the surrounding edges, which consequently appear to be darker than the center, because a cooler temperature corresponds to darker white-light emission. The photospheric temperature is $T_s = 5780$ K, the typical size of a granule is $w \approx 1500$ km, and the life time is about 8–20 min.

The underlying physical mechanism of convection has been studied in great detail in terms of the Rayleigh-Bénard instability, known as the Lorenz model (Lorenz 1963), described also in the monographs of Chandrasekhar (1961) and Schuster (1988). The basic ingredients of the (hydrodynamic) Lorenz model are the Navier-Stokes equation, the equation for heat conduction, and the continuity equation. The Lorenz model can describe the transition from heat conduction to convection rolls, where Lorenz discovered the transition from deterministic to chaotic system dynamics. Thus, the Lorenz model demonstrates that a temperature gradient (for instance below the photosphere) transforms (a possibly turbulent) random motion into a highly-organized rolling motion (due to the Rayleigh-Bénard instability) and this way organizes the plasma into nearly equi-sized convection rolls that have a specific size (such as $w \approx 1500$ km for solar granules). A self-organization process thus creates order (of granules with a specific size) out of randomness (of the initial turbulent spectrum). Since convection is the main energy transport process inside the Sun down to $0.7 R_\odot$, larger convection rolls than the granulation pattern can be expected. Krishan (1991) argues that the Kolmogorov turbulence spectrum $N(k) \propto k^{-5/3}$ extends to larger scales and possibly can explain the observed hierarchy of structures (granules, mesogranules, supergranules, and giant cells) by the same self-organization process (for a review of self-organization processes in astrophysics see Aschwanden et al. 2018).

At smaller scales, a subpopulation of mini-granular structures has been discovered recently, in the range of $w \approx 100$–600 km, predominantly confined to the wide dark lanes between regular granules, often forming chains and clusters, but being different from magnetic bright points (Abramenko et al. 2012). A set of TiO images of solar granulation acquired with the 1.6 meter *New Solar Telescope (NST)* at *Big Bear Solar Observatory (BBSO)* was utilized. The high-contrast speckle-reconstructed images of Quiet-sun granulation (Fig. 4.10), allowed to detect, besides the regular-size granules, the small granular-like features in dark inter-granular

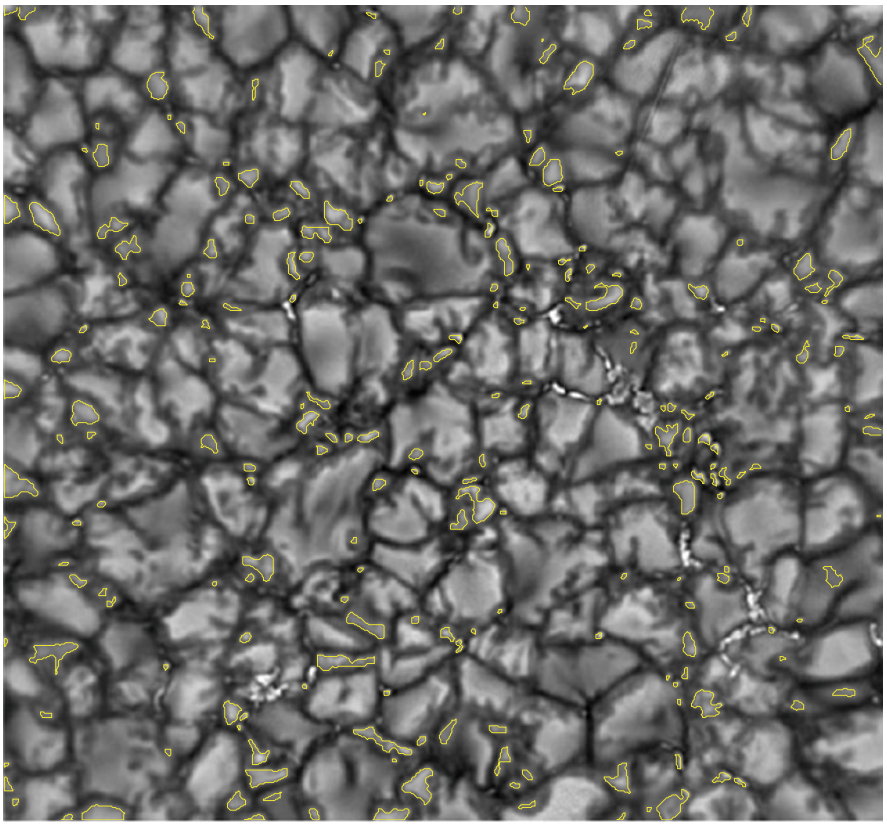

Fig. 4.10 A TiO image of the solar surface is shown, containing normal granules and mini-granules in a Quiet Sun region, observed with the *New Solar Telescope (NST)*. Mini-granules are outlined with yellow contours, which show granular-like features of sizes below 600 km located in dark intergranular lanes. Note that the mini-granules do not coincide with magnetic bright points (Abramenko et al. 2012)

lanes, named as *mini-granules*. Mini-granules are very mobile and short-lived. They are predominantly located in places of enhanced turbulence and close to strong magnetic fields in inter-granular lanes. The equivalent size of detected granules was estimated from the circular diameter of the granule area. The resulting *probability density functions (PDF)* for 36 independent snapshots are shown in gray in the left frame of Fig. 4.11). The average PDF (the red histogram) changes its slope in the scale range of $\approx$ 600–1300 km. This varying power law PDF is suggestive that the observed ensemble of granules may consist of two populations with distinct properties: regular granules and mini-granules. A decomposition of the observed PDF showed that the best fit is achieved with a combination of a power law function (for mini-granules) and a Gaussian function (for granules). Their sum fits the observational data (Fig. 4.11). Mini-granules do not display any characteristic

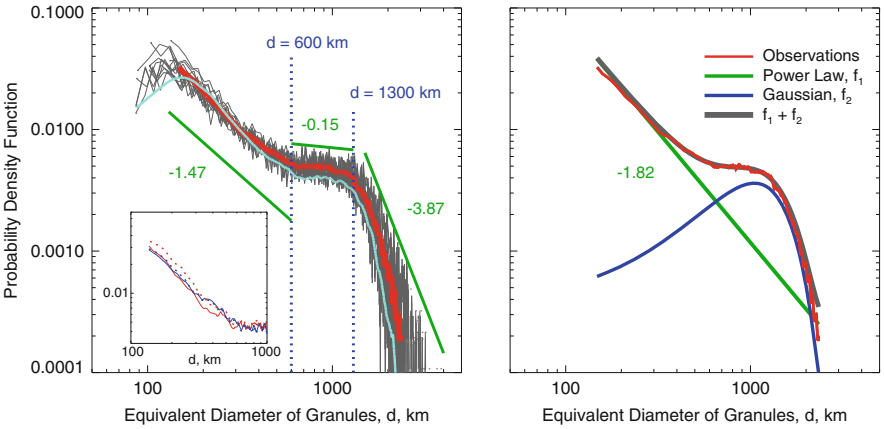

Fig. 4.11 The probability density function of the equivalent diameter of granules (in units of km) is shown, observed in Quiet Sun regions with the *New Solar Telescope (NST)*. The regular granules have a size of $w \approx 500$–2000 km, while the range of $w \approx 100$–500 km exhibits the new phenomenon of "mini-granules" (Abramenko et al. 2012)

("dominant") scale. This non-Gaussian distribution of sizes implies that a more sophisticated mechanism with more degrees of freedom may be at work, where any small fluctuation in density, pressure, velocity and magnetic field may have significant impact and affects the resulting dynamics. It is worth to note that a recent direct numerical simulation attempt (Van Kooten and Cranmer 2017) produced the PDF of granular size (Fig. 4.12) in agreement with the observed one in Fig. 4.11. The authors concluded that the population of mini-granules is intrinsically related to non-linear turbulent phenomena, whereas Gaussian-distributed regular granules originate from near-surface convection.

The size distribution of granulation cells in the solar photosphere does not form a power law distribution, but clearly shows a preferred spatial scale of $\approx$ 1500 km, which renders a regular spatial pattern, rather than a scale-free distribution. However, a power law distribution has been found for the newly discovered "mini-granules" in a size range of 100–600 km, which is not consistent with a self-organizing convective process that creates bubbles of equal sizes. The physical process of convection that is driven by a temperature gradient and the Rayleigh-Bénard instability is well-understood and known as the Lorenz model. A caveat is how much the magnetic field plays a role in the solar convection zone, requiring a model with magneto-convection and hydromagnetic (Parker and Kruskal-Schwarzschild) instabilities. In summary, two different physical mechanisms are required to explain the two different types of distribution functions for "regular granules" and "mini-granules": The Gaussian size distribution of regular granules is consistent with the self-organizing convection process, while the power law size distribution of "mini-granules" could be related to nonlinear turbulence (as simulated by Van Kooten and Cranmer 2017).

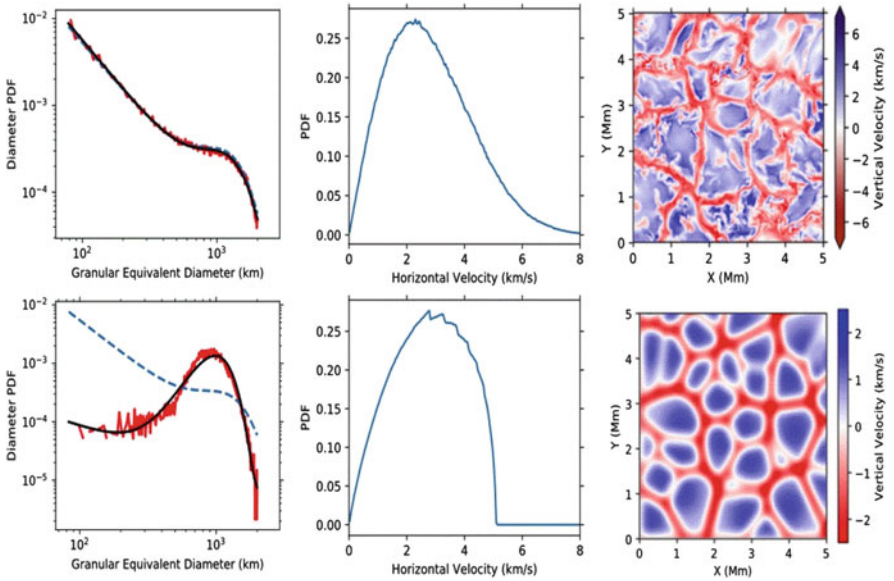

Fig. 4.12 Comparison of MURaM (top) and ROUGH (bottom) numerical MHD simulations of solar granulation, showing the probability distribution functions (PDF) of the granule sizes (left panels, red), and the fitted distributions of Abramenko et al. (2012), renomarlized to this plotting range and fitted to the simulated data (left panels, black), and the histogram of horizontal velocity magnitudes at all pixels in the simulation (middle panels), and velocity maps (right panels) (Van Kooten and Cranmer 2017)

4.6 Quiet-Sun and Polar Fields

Solar magnetism occurs on all scales, as mean field (poloidal and toroidal) components that cover the entire hemisphere, as well as on progressively smaller scales as active regions, sunspots, and magnetic pores, up to the diffraction limit of the largest telescopes (de Wijn et al. 2009; Lagg et al. 2017), or beyond (Stenflo 2012). Granular flows in the photosphere sweep flux into intergranular lanes, where it clumps into small concentrations of mostly vertical field with strengths in excess of 1000 G, coinciding with bright points and faculae in white light, best visible in plages of active regions.

In the Quiet Sun, supergranular flows are concentrated in the magnetic network that outline supergranular cells in intermittent patterns. The internetwork magnetic field in the Quiet Sun has been found to carry strong horizontal fields ubiquitously (Lites et al. 2008), which requires very sensitive magnetometers for their detection, such as SOT/SP onboard Hinode. These small-scale magnetic fields in the Quiet Sun have been called "granular fields" (Lin and Rimmele 1999), "horizontal Quiet-Sun fields" (Lites et al. 1996), or "seething fields" (Harvey et al. 2007). Internetwork fields have traditionally been measured with the Zeeman effect, while

the turbulent field has been probed mainly with the Hanle effect, which reveals small-scale "hidden" magnetic flux (Stenflo 2004). The weakest fluxes measured in internetwork features with present instrumentation has a magnetic flux of $\approx 10^{16}$ Mx (Fig. 4.5). The rate of magnetic flux in internetwork fields is found to be $\approx 10^2$ times larger than in ephemeral active regions, and about a factor of $\approx 10^4$ larger than in active regions, but the decay time scale is reciprocally shorter, so that it is not clear what component dominates the net flux emergence. Before the Hinode mission, typical average field strengths of $\approx$ 2–5 G were measured in Quiet Sun regions, while average field strengths of $\approx$ 20 G were measured in the internetwork with sub-arcsecond ($0.5''$) spatial resolution (Dominquez Cerdena et al. 2003), and $\approx$ 11 G with the Hinode Spectro-Polarimeter ($0.32''$) (Lites et al. 2008).

In the solar polar regions, where the global magnetic field is open and where the fast solar wind originates, magnetic field measurements are very challenging due to the variable seeing, combined with a strong intensity gradient and the foreshortening effect at the solar limb. A breakthrough took place with the Hinode/SOT instrument, which has a diffraction-limited spatial resolution of $0.2''$–$0.3''$. This instrument revealed many vertically oriented magnetic flux tubes with field strengths as strong as $\approx$ 1000 G within a latitude range of 70° and 90° (Tsuneta et al. 2008). Hinode observed the solar polar region on 2007 March 16 when the south pole was located 7° inside the visible solar disk. All 4 Stokes profiles were measured in two Fe I lines (6301.2 and 6301.5 Å) and the magnetic field strength B was inverted by fitting a Milne-Eddington atmosphere to the Stokes profiles. A view of the reconstructed magnetogram from the direction of the south pole is shown in Fig. 4.13, which exhibits isolated unipolar patches, some with field strengths reaching over 1000 G, while all have the same polarity, consistent with the global polarity of the south polar region. The polar coronal hole extends from 90° down to 60°–70° in latitude, and thus the entire polar region mapped in Fig. 4.13 represents the photospheric base of the polar coronal hole.

The magnetic landscape of the polar region is characterized by vertical kilogauss patches with super-equipartition field strength, a coherent polarity in each hemisphere, and ubiquitous weaker transient horizontal magnetic fields. Histograms of magnetic field strengths, intensities, and filling factors are shown in Fig. 4.14. The lifetime of the magnetic concentrations in the Quiet Sun has been estimated from MDI/SOHO data to be $\approx$ 1 hr for 2.5×10^{18} Mx fluxes, and $\approx$ 10 hrs for 10×10^{18} Mx fluxes. The total magnetic flux of this area is estimated to be $\Phi = 2 \times 10^{22}$ Mx, while the area covers $A = 2.1 \times 10^{18}$ cm^{-2} (Tsuneta et al. 2008). Combining the footpoint areas of all flux tubes with $B > 200$ G, an expansion factor of ≈ 345 is required to fill the entire space of the coronal hole, (for modeling of vertically expanding magnetic structures see examples in Fig. 4.15). If the polar field with the same total magnetic flux $\Phi \approx BfS$ were uniformly distributed (S being the total magnetic area and f being the filling factor), the estimated effective field strength would be about 10 G, as measured with SOT/SP in Quiet Sun regions. Thus the surface poloidal magnetic energy is approximately 90 times larger than in the case of a uniform magnetic field, if we take $B \approx 900$ G, corresponding to the peak of the energy probability density function shown in Fig. 4.14b. The equi-partition

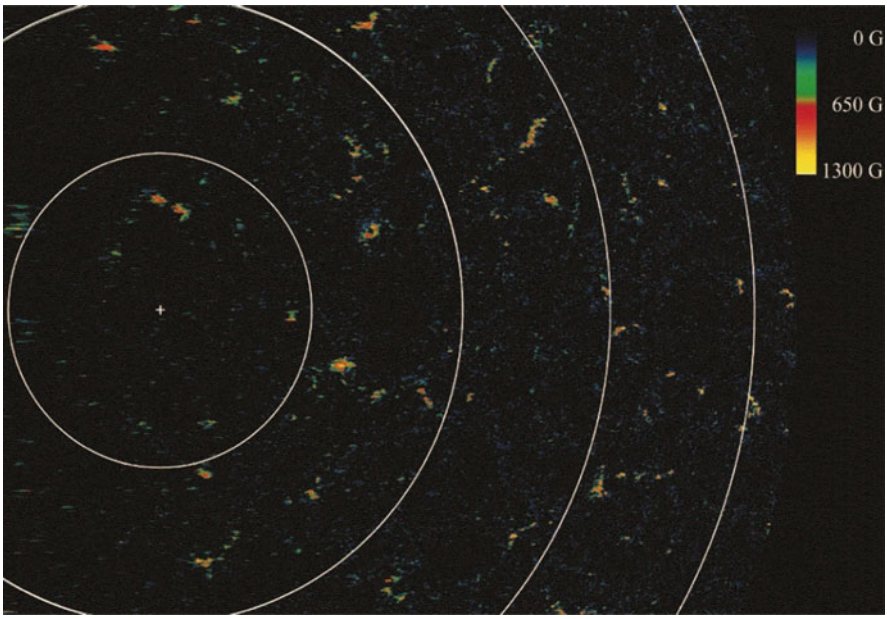

Fig. 4.13 South polar view of the magnetic field strength observed on 2007 March 16. The magnetic field strength (color-coded in the range of $B = 0$–1300 G) is rendered for pixels above a noise threshold (Tsuneta et al. 2008)

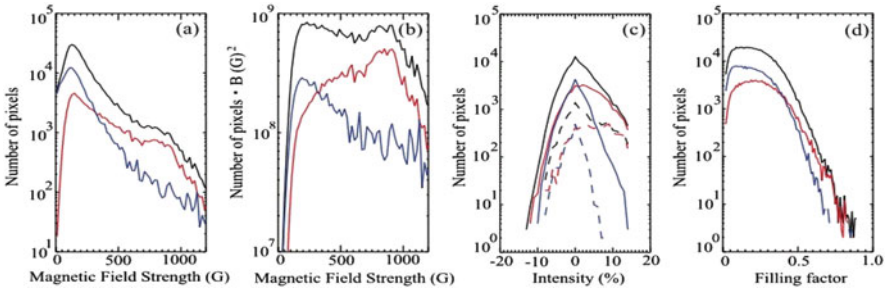

Fig. 4.14 Statistics of pixels as a function of the magnetic field strength (**a**,**b**), intensity (**c**), and filling factors (**d**). Red histograms indicate the vertical field, blue the horizontal field, and black the total field. The histogram is multiplied with the function B^2 in (**b**). Histograms of continuum intensity for magnetic field strengths of 300 B (solid lines) and 800 G (dashed lines) are shown in (**c**). All panels are for latitudes above 75° (Tsuneta et al. 2008)

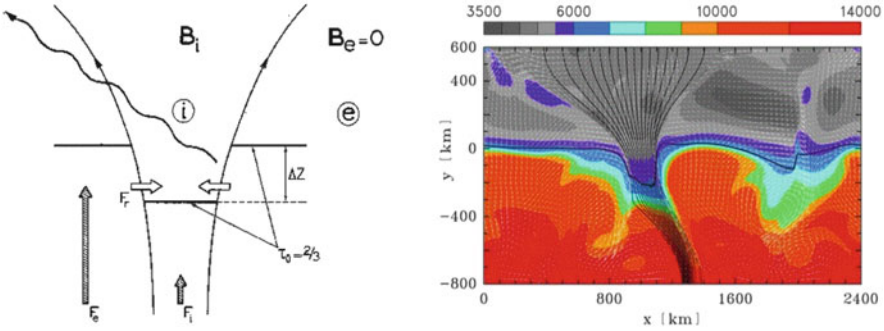

Fig. 4.15 Examples of modeling magnetic elements with vertically expanding fields: *Left:* Analytic magneto-static flux tube model. *Right:* a 2-D MHD model of a flux sheet (de Wijn et al. 2009)

field strength B_e, at which the magnetic energy is equal to the kinetic energy of the surface granular motion, is $B_e = (4\pi\rho v^2)^{1/2}$. The typical value of B_e is ≈ 400 G for granules, with a velocity of $v = 2 \times 10^5$ cm s^{-1}, indicating that the magnetic field strength for the majority of the patches is larger than the equi-partition field strength.

Tsuneta et al. (2008) interpret the findings as follows: The observed unipolar flux tubes scattered about the polar region are considered to represent poloidal seed for toroidal fields (Wang et al. 1989). Magnetic flux is transported to the polar regions by meridional flows and supergranular diffusion in the flux-transport dynamo model (Dikpati and Charbonneau 1999). Since the magnetic field takes the form of such isolated flux tubes with super-equipartition strength, instead of the diffuse weak mean field assumed in the flux-transport dynamo, flux transport on the Sun occurs by means of an aerodynamic (drag) force against the magnetic tension force and may be more complicated than in the mean field case assumed in the models (Tsuneta et al. 2008).

4.7 Penumbral Dynamics

The structure of a sunspot is determined by the local interaction of magnetic fields and by the magneto-convection near the solar surface (for recent reviews see: Solanki 2003; Thomas and Weiss 2004, 2008; Borrero and Ichimoto 2011; Rempel and Schlichenmaier 2011). The dark central umbra is surrounded by a filamentary penumbra, whose complicated fine structure has only recently been revealed by high-resolution observations. The magnetic field in the penumbra has an intricate interlocking-comb structure (Fig. 4.16), where some field lines with associated outflows of gas dive back down below the solar surface at the outer edge of the spot (Thomas et al. 2002). They stay submerged, although one would

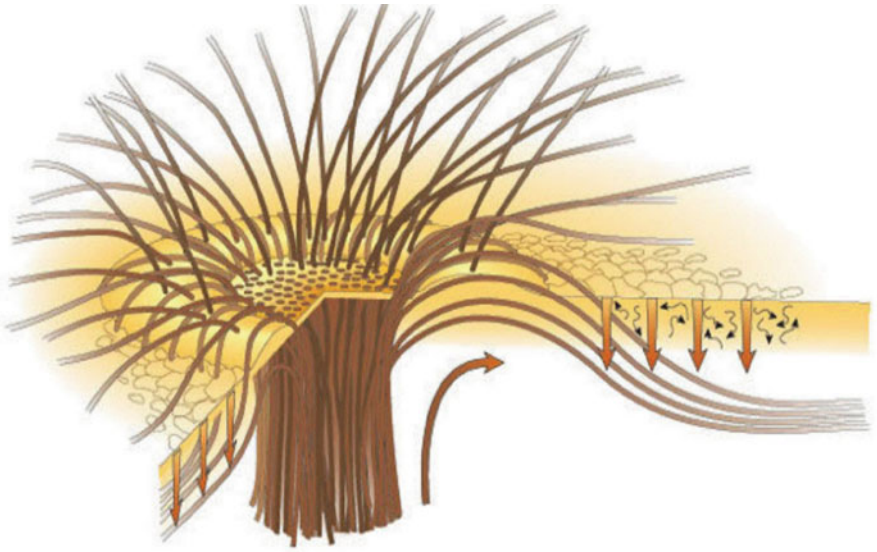

Fig. 4.16 Sketch showing the interlocking-comb structure of the magnetic field in the filamentary penumbra of a sunspot. The bright radial filaments, where the magnetic field is inclined (at about 40° to the horizontal in the outer penumbra), alternate with dark filaments in which the field is nearly horizontal. Within the dark filaments, some magnetic flux tubes (bundles of magnetic field) extend radially outward beyond the penumbra along an elevated magnetic canopy, while other returning flux tubes dive back below the surface. The sunspot is surrounded by a layer of small-scale granular convection (thin quiggly black arrow) embedded in the radial outflow (thick curved brown arrow) associated with a long-lived annular supergranule (the moat cell). The submerged parts of the returning flux tubes are held down by turbulent pumping (indicated by thick vertical brown arrow) due to granular convection in the moat. There is also a persistent horizontal outflow in the penumbra (the Evershed flow), which is mostly confined to thin, nearly horizontal, radial channels with the dark filaments (Thomas et al. 2002)

expect that magnetic buoyancy will bring them quickly back to the surface. Thomas et al. (2002) demonstrated that the field lines are kept submerged outside the spot by turbulent, compressible convection, which is dominated by strong coherent descending plumes. Moreover, this downward pumping of magnetic flux explains the origin of the interlocking-comb structure of the penumbral magnetic field, and the behaviour of other magnetic features near the sunspot.

While the penumbral model of Thomas et al. (2002) proposed a downward pumping mechanism with an interlocking comb structure (Fig. 4.16), alternative models were created with uncombed magnetic fields (Fig. 4.17), such as the *"embedded flux tube model"* (Solanki and Montavon 1993), or the *"field-free gap model"* (Spruit and Scharmer 2006; Scharmer et al. 2011). While each of these empirical models could explain a subset of observables, none of them could match all of them, such as the origin of the Evershed flow, the heat flux of the penumbral surface, the overturning convective motion, the inward migration of penumbral grains, or the asymmetric Stokes profiles observed in the penumbra.

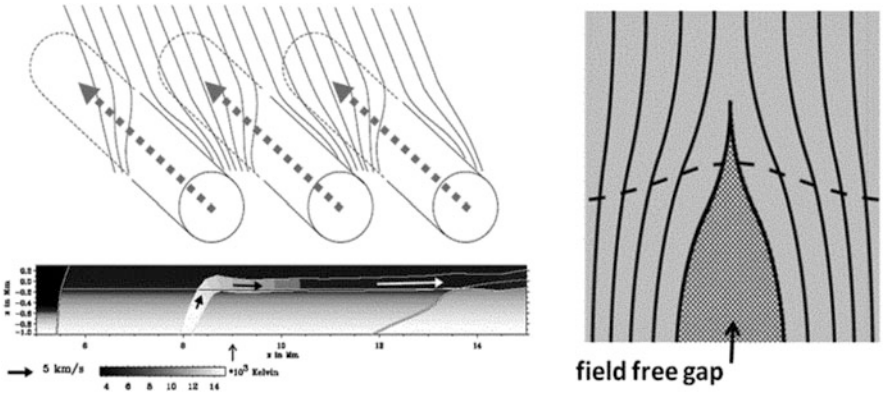

Fig. 4.17 Models for explaining the uncombed penumbral structure: the embedded flux tube model (top left; Solanki and Montavon 1993); the rising flux-tube model (bottom left: Schlichenmaier et al. 1998); the field-free gap model (right: Spruit and Scharmer 2006)

Recent Ca II 8542 Å data are found to be consistent with an inverse Evershed flow, where a critical (sonic) or supersonic siphon flow along super-penumbral flux tubes accelerates plasma that abruptly attains subcritical velocity through a standing shock in or near the penumbra (Choudhary and Beck 2018).

Ultimately, progress in sunspot modeling occurred once the transition from simplified empirical (analytical) models to radiative 3-D MHD simulations was achieved, which triggered a dramatic change in sunspot models (Rempel and Schlichenmaier 2011). Previous empirical models were formulated with magnetostatic MHD models, with parameterized energy transport, with predefined geometries (e.g., flux tubes, field-free gaps, convective rolls), which prevented a self-consistent explanation of all aspects of penumbral structure (energy transport, filamentation, Evershed flow). In recent 3-D radiative MHD simulations, overturning convection is the key element to understand energy transport, filamentation leading to fine structure, and the driving of strong outflows. In the big picture, these 3-D MHD simulations should also be able to explain the subsurface structure of sunspots as well as the sunspot formation.

Due to the formidable numerical challenges, recent 3-D radiative MHD simulations started first with the smallest structures of umbral dots, continued then to piece-wise sections of penumbrae, and finally reached full sunspots. Rempel et al. (2009) performed a simulation of an opposite polarity sunspot pair in a domain of $98 \times 49 \times 6$ Mm at a resolution of 32 km in the horizontal direction and 16 km in the vertical, requiring a total of 1.8×10^9 grid points (Fig. 4.18). This simulation presents for the first time an extended outer penumbra with a strong radial outflow that has a filling factor close to unity and average velocities of up of 5 km s^{-1} (and peak flow speed of 14 km s^{-1}). The location of regions with radial outflows is strongly related to the average inclination angle ($\gtrsim 45°$) of the magnetic field.

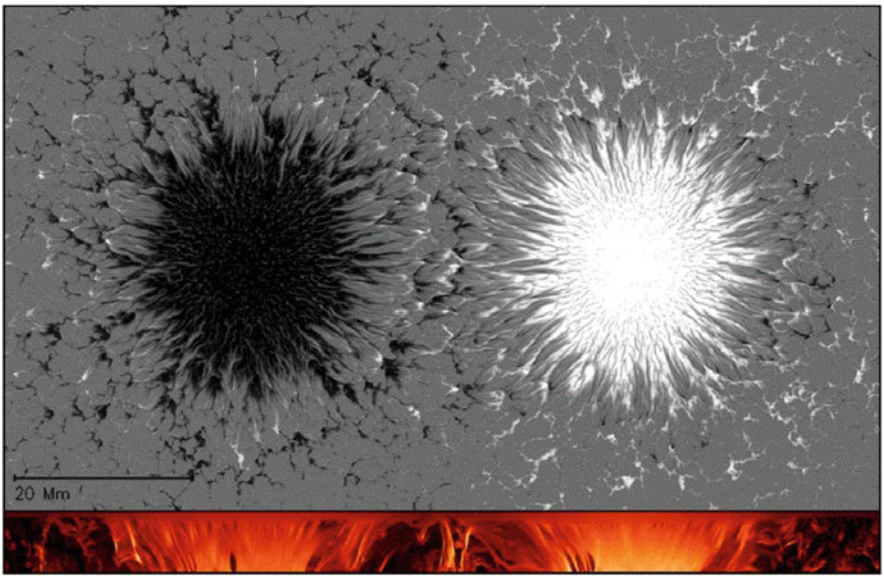

Fig. 4.18 Still image of a time-dependent 3-D radiative MHD simulation of an opposite polarity sunspot pair. The tope panel shows a magnetogram of the vertical field, with magnetic field values ranging from −3000 to +3000 G. The bottom panel depicts the magnetic field from a vertical cut through the center of both sunspots, with a range of 0 to 10,000 G (Rempel et al. 2009)

A unified picture of numerical simulations of the penumbra is discussed in Borrero and Ichimoto (2011). The *embedded flux-tube model*, or the *rising hot flux tube* with the dynamic evolution of the flux tube explains a number of observational aspects about the fine scale features of the penumbra, such as the origin of the Evershed flow, inward migration of penumbral grains, and asymmetric Stokes profiles observed in the penumbra, but faces difficulties when attempting to explain the heat transport to the penumbral surface. In the *field-free gap penumbral model*, the gap is formed by a convecting hot and field-free gas protruding upward into the background (oblique) magnetic fields of the penumbra, and is supposed to be the region that harbors the Evershed flow. It has an advantage in explaining the heat transport to the penumbral surface and twisting appearance of penumbral bright filaments, but does not address the origin of the Evershed flow. Thus, both the embedded flux-tube model and the field-free gap model have their own advantages but also considerable shortcomings. The recent 3-D radiative MHD simulations are able to reproduce the radial filamentary structure of the penumbra as seen in continuum images, the uncombed structure of the magnetic field, Evershed outflows along the filaments with a nearly horizontal magnetic field, and overturning convective motions in upwelling plumes. According to Rempel (2011), the Evershed flow is driven by vertical pressure forces in upflows that are deflected into the horizontal direction through the Lorentz-force generated by the horizontally stretched magnetic fields in flow channels, and the radial flow velocity reaches up to

8 km s^{-1} at the depth of $\tau_c = 1$ with a rapid decline toward the higher atmospheric layers. Thus, the recent 3-D radiative MHD simulations have begun to reproduce many details of fine scale dynamics and structure of the magnetic field observed in the penumbra.

4.8 Rotating Sunspots

The rotation of sunspots, first detected over a century ago (Evershed 1910), has at least two possible interpretations: either (1) a helically twisted vertical magnetic field structure is pushed upward through the photosphere, or (2) a vertically balanced structure is rotated by forces that act in the azimuthal direction of a rotationally symmetric sunspot. Either way, this dynamic phenomenon can reveal important information on the solar dynamo and its generation of magnetic fields inside the Sun. For examples of twisted sunspots, sigmoids, and quadrupoles see Fig. 4.19.

Observations of sunspot rotation in the new millennium were furnished in white-light from TRACE and in soft X-rays from *SXT/Yohkoh* data (Brown et al. 2003), exhibiting rotation angles about their umbral center up to 200° over a period of 3–5 days. From seven cases of identified rotating sunspots, two were found to be associated with sigmoid structures in soft X-rays, and six events associated with GOES C- to X-class flares. Using the *non-linear affine velocity estimator (NAVE)* method (Min and Chae 2009; Zhu et al. 2012; Wang et al. 2014), rotation angles up to 540° were measured (Min and Chae 2009). Among 82 sunspots with strong flux emergence, 63 showed rotational angular velocities larger than 0.4° hr^{-1} (Zhu et al. 2012). Using the travel-time delay method in local helioseismology, strong shear flows beneath a rapidly rotating sunspot was detected (Kosovichev 2002; Zhao and Kosovichev 2003). Sub-photospheric flows associated with sunspot rotations were also detected with the ring-diagram technique (Jain et al. 2012). From statistics of 103 years of sunspot data it was found that young groups rotate faster than old spot groups (Hiremath 2002; Ruzdjak et al. 2004), and that the observed rotation rates approximately match the rotation speed inferred from helioseismology (Hiremath 2002). Statistics of 182 rotating sunspots was gathered from MDI/SOHO, TRACE, an Hinode data, exhibiting a similar ratio of clockwise to counterclockwise rotations in both hemispheres (Yan et al. 2008).

The relationship between rotating sunspots and the triggering of a flare accompanied by a sigmoid eruption, most likely driven by a kink instability, is overwhelming. Evidence is given, e.g., for the case of the largest proton event (2001 November 4) in cycle 23 (Tian and Alexander 2006), the 2006 December 13 flare and CME event (Zhang et al. 2017), the 2003 August 5 flare (Yan and Qu 2007), flares in the super active region NOAA 10486 (Zhang et al. 2008), the X17 eruptive flare on 2003 October 28 (Kazachenko et al. 2010), the X2.2-class flare on 2011 February 15 in NOAA 11158 (Jiang et al. 2012; Vemareddy et al. 2012; Wang et al. 2014; Li and Liu 2015), the flare and CME events on 2000 February 9–10 in NOAA 08858

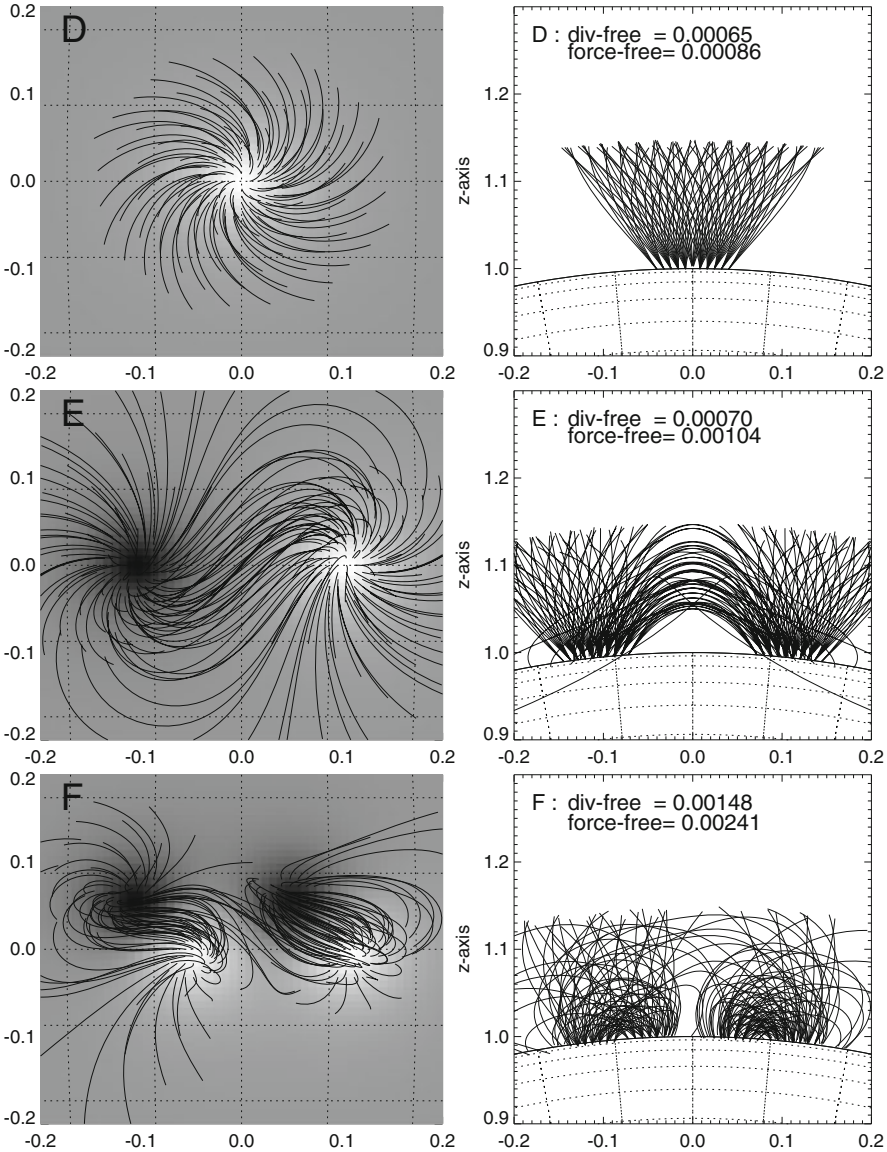

Fig. 4.19 The magnetic field of a rotated sunspot (top), a twisted dipole or sigmoid (middle), and a twisted quadrupole configuration (bottom) are shown, in form of a magnetogram (grey scale background images in left panels) and in form of extrapolated magnetic field lines, calculated with the *vertical current approximation nonlinear force-free field (VCA-NLFFF)* code (Aschwanden 2013)

(Yan et al. 2012), the M2.9 flare on 2010 October 16 in NOAA 11112 (Kumar et al. 2013), the X2.1 flare on 2011 September 3 in NOAA 11283 (Ruan et al. 2014), and the CME eruptions in AR 12158 (Vemareddy et al. 2016). A rotation-related flare occurs generally when the rotation rate of the sunspot reaches its maximum (Li and Liu 2015). However, rapid rotation is not always required, while shearing motion can be sufficient to account for the energetics and helicity content for some major flares also (Kazachenko et al. 2010). On one occasion, the sunspot rotation was observed to be reversed during an X1.6 flare, which may be caused by a change of the Lorentz torque in response to shrinkage of the coronal field during the flare (Bi et al. 2016). A high correlation between the sunspot rotation speed and the change in the total accumulated helicity is found, and the net current shows a synchronous change with the sunspot rotation rate (Wang et al. 2016)

On the theoretical side, the most common interpretation attributes the sunspot rotation to injection of helical twist into the corona, producing sigmoid-shaped dipolar configurations, which are more likely to lead to flaring and eruption of CMEs than untwisted active regions. Numerical MHD simulations of rotating sunspots with inflows from a magnetic pore were attempted to test whether flare triggering via kink instability occurs (Gerrard et al. 2003). 3-D MHD simulations of an emerging twisted magnetic flux tube from the convection zone (Fan 2009; Santos et al. 2011; Török et al. 2013; Sturrock et al. 2015; Sturrock and Hood 2016) show that significant rotational motion sets in within each magnetic polarity, producing a sigmoid-shaped, dipped core field in the corona. The rotational motion in the two polarities is a result of propagation of nonlinear torsional Alfvén waves along the flux tube, which transports significant twist from the tube's interior portion toward its expanded coronal portion, ultimately leading to eruption (Fan 2009). The flare/CME trigger in a rotating sunspot environment is conveyed by a horizontal Lorentz force, which can explain the connections between the rapid and irreversible photospheric vector magnetic field change and the observed short-term motions associated with a flare. In particular, the unbalanced torque provided by the horizontal Lorentz force change can explain the measured angular acceleration (Wang et al. 2014; Sturrock et al. 2015; Sturrock and Hood 2016). Magnetic modeling (with NLFFF codes) show that the evolution of an active region can be approximated by a time series of force-free equilibria, but when the sigmoid-shaped field exceeds a critical twist, this leads to a loss of equilibrium and can trigger the onset of multiple eruptions (Vemareddy et al. 2016). The free energy that is available for dissipation during a flare/CME event can directly be calculated with the *vertical current approximation nonlinear force free field (VCA-NLFFF)* code (Fig. 4.19), which takes the helical twist of rotating sunspots due to vertical currents into account (Aschwanden 2013).

4.9 Sunspot Light Bridges

A short description of light bridges is given in the review on the magnetic structure of sunspots (Borrero and Ichimoto 2011). Since the umbra of a sunspot is dominated by strong magnetic fields, convection is generally inhibited in the umbra, which is the reason why no granulation is visible in the umbra. However, when a sunspot decays, the magnetic field strength becomes weaker and magneto-convection takes over, which leads to the features of *umbral dots* and *light bridges*, both being manifestations of convection inside the umbra. Light bridges are usually seen along "fissures" where a sunspot forms or decays. Light bridges are elongated bright features that often split the umbra into two (or more) sections, connecting two different sides of the penumbra (Fig. 4.20). Light bridges and umbral dots share many similarities, for instance both feature a central dark lane and bright edges. Light bridges can be considered as an extreme form of elongated umbral dots. The larger size of light bridges allows the detection of both blue and redshifted velocities with arc-second resolution. Observations with sub-arcsecond resolution

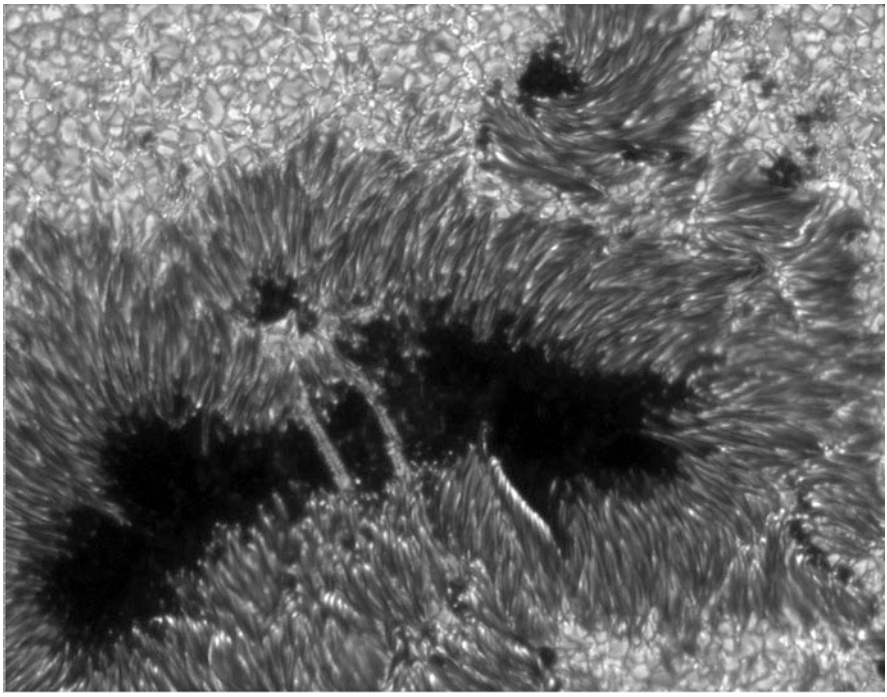

Fig. 4.20 This sunspot image, observed with the Swedish Vacuum Solar Telescope (SVST) on 2000 May 22 (using adaptive optics), shows two so-called *white-light bridges* during the decay phase of a large sunspot, extending over 5000 km and connecting the north and south umbral regions. As days progressed, the light bridge expanded to fill the void as the sunspots moved apart and decayed (Credit: G. Scharmer, L. Rouppe van der Voort, SVST)

clearly establish a connection between upflows and the central dark lane in light bridges, as well as between downflows and the bright edges of the light bridge, similar to the convective flow pattern in granulation cells outside the penumbra (Hirzberger et al. 2002; Berger and Berdyugina 2003; Rouppe van der Voort et al. 2010). Moreover, the magnetic field is weaker and slightly more inclined in light bridges than in the surrounding umbra, as it occurs in umbral dots also (Jurcak et al. 2006).

The formation process and evolution of light bridges in sunspots is not fully understood. Observations show evidence for plasma ejections along a light bridge of a stable and mature sunspot, in form of Hα surges as well as EUV jets at 171 Å, which could be a by-product of a magnetic reconnection process (Asai et al. 2001). Evidence for plasma ejection from a light bridge followed by Ellerman bombs, with opposite polarities in the light bridge with respect to the umbra, was interpreted also in terms of low-altitude magnetic reconnection, as a result of magnetic cancellation in the photosphere (Bharti et al. 2007). More jets ejected from a sunspot light bridge are reported in Liu (2012), Robustini et al. (2016), and Song et al. (2017). The formation process of a light bridge could be traced for several days with unprecedented resolution with SOT/Hinode (Katsukawa et al. 2007), finding that many umbral dots were observed to be emerging from the leading edges of penumbral filaments and rapidly intruding into the umbra. They found that the light bridges and the umbral dots had significantly weaker magnetic fields associated with upflows relative to the core of the umbra, which implies that there is hot gas with weak field strength penetrating from the subphotosphere to near the visible surface. They suggest that the emergence and the inward motion are triggered by a buoyant flux tube as well as subphotospheric flow crossing the sunspot (Katsukawa et al. 2007). Moreover, 3-D radiative MHD numerical simulations demonstrate that nearly field-free upflow plumes and umbral dots are a natural consequence of magneto-convection in an initially monolithic magnetic flux tube, and thus does not require the adoption of a cluster model to match the observed umbral dots (Schüssler and Vögler 2006).

Similarly, from SVST data it was concluded that the photospheric blue and redshifts observed in a granular light bridge are caused by the emergence of a small-scale, flat Ω-loop with highly inclined footpoints of opposite polarity that brings new magnetic field to the surface, which was the first time that magnetic flux was observed to emerge in the strongly magnetized environment of sunspots, pushed upwards by the convective flows of a granular light bridge (Louis et al. 2015). Lagg et al. (2014) find close similarities between Quiet-Sun granules and light bridge (Fig. 4.21), which points to the deep anchoring of granular light bridges in the underlying convection zone. The fast supersonic downflows in light bridge granules are most likely a result of invigorated convection due to radiative cooling into the neighboring umbra and the sampling of deeper layers adjacent to the slanted walls of the Wilson depression (Lagg et al. 2014).

Doppler shift analysis of SOT/Hinode observations reveal nonuniform flows with peak velocities of 250 and 180 m s^{-1} (Louis et al. 2008), supersonic downflows in light bridges with velocities of up to 10 km s^{-1}, which are the strongest photospheric

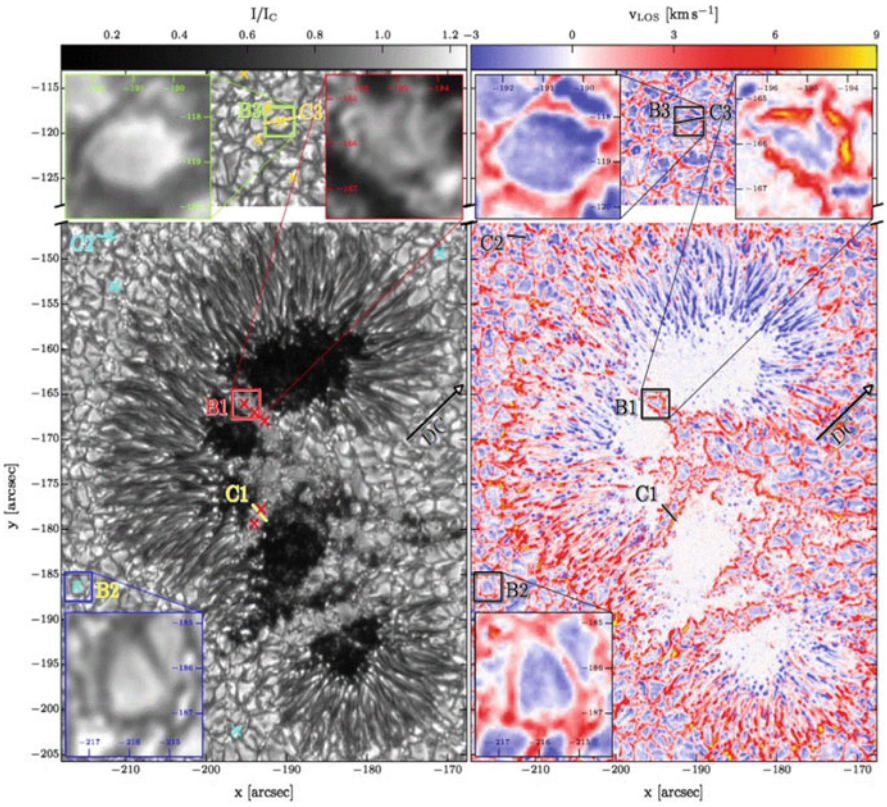

Fig. 4.21 Continuum map of AR 10926 of Stokes I (left) and line-of-sight velocity map (right; with red and blueshifts). The 3 boxes contain locations in light bridges (B1, C1) and in the Quiet Sun. Note the similar convection patterns in all 3 boxes (Lagg et al. 2014)

flows ever measured in light bridges (Louis et al. 2009; Shimizu 2011). IBIS data reveal downward velocities of 200 m s^{-1} in pores, and 150 m s^{-1} in the light bridge of a pore, which is consistent with the velocity structure of a convective roll (Giordano et al. 2008).

The global 5-min oscillations of the Sun exhibit interesting properties in sunspots with light bridges. The 5-min oscillations are suppressed in the umbra, while the 3-min oscillations occupy all cores of the sunspot umbra separated by light bridges (Fig. 4.21), and thus may either not be affected by umbral oscillations or share the same source (Yuan et al. 2014). Some sunspot light bridges exhibit oscillating light walls, probably excited by p-mode leakage from below the photosphere (Yang et al. 2015). Some light bridges were found to exhibit not only 5-min periods, but also persistent sub-minute oscillations (Yuan and Walsh 2016), or surge-like, intermittent pulses, probably excited by upward propagating slow-mode shocks (Zhang et al. 2017).

A first numerical simulation of flux emergence and accompanying light bridge formation was undertaken by Toriumi et al. (2015b), based on data of an active region that is likely to be produced by magnetic reconnection driven by magneto-convective evolution (Toriumi et al. 2015a). The convective upflow continuously transports horizontal fields to the surface layer and creates a light bridge structure.

4.10 Photospheric Waves and Oscillations

Helioseismology studies waves and oscillations in the solar interior but are detected on the solar surface (photosphere), a rich field that started after the discovery of the global 5-min oscillations in the 1970's. Coronal seismology, on the other hand, investigates standing and propagating waves and oscillations in the solar corona, which was initiated after the discovery of fast kink-mode oscillations in TRACE EUV movies in 1998. Expanding the discovery space of waves and oscillation phenomena in spatial and wavelength domains, we could envision "photo-seismology" and "chromo-seismology" for the two domains of the photosphere and chromosphere, but nobody has used these terms yet. Nevertheless, since the photosphere and the chromosphere are "sandwiched" between the solar interior and the corona, it is naturally expected that many of the helioseismic and coronal waves couple in upward and downward direction with structures seen in the photosphere and chromosphere. Consequently, we expect to see at least 4 different types of waves and oscillations in the photosphere: (i) coupled waves of the helioseismic global 5-min oscillations, also called p-mode leakage, (ii) coupled waves of fast and slow MHD modes from oscillating loops in the solar corona, and (iii) global spherically propagating waves in photospheric heights, also called running penumbral waves, and (iv) Moreton-Ramsey waves (observed in Hα wavelengths), chromospheric (or upper photospheric) signatures of large-scale global shock waves.

(i) The 5-min umbral oscillations are coherent amplifications with large spatial scales (typically a substantial fraction of the entire umbra), with periods of 4–7 min, and rms velocity amplitudes of 40–90 m s^{-1}, observed in lines that form in the low photosphere. There are also 3-min umbral oscillations of smaller spatial scales (3″–4″), observed in lines that form in the upper photosphere and chromosphere, with periods of order 2–3 min, and amplitudes of a few 100 m s^{-1}. The 5-min p-mode oscillations are believed to leak out of the photosphere and to propell spicules into chromospheric heights (De Pontieu et al. 2004). The photospheric velocity field and intensities are dominated by granular convection and p-modes. De Pontieu et al. (2004, 2005) demonstrated that the p-modes leak sufficient energy, on inclined magnetic flux tubes, from the global resonant cavity into the chromosphere, to power shocks that drive upward flows and form spicules. The nonverticality of the flux tube increases the acoustic cutoff period to values closer to the dominant periods of the photospheric oscillations, thus allowing tunneling or even direct propagation

into the corona (De Pontieu et al. 2005). Chromospheric velocity oscillations show a 3-min period with a clear sawtooth shape typical of propagating shock wave fronts, while photospheric velocity oscillations have basically a 5-min period, although the power spectrum shows a secondary peak in the 3-min band also (Centeno et al. 2006). The most recent observations with the *Fast Imaging Solar Spectrograph (FISS)* of the 1.6 m *Goode New Solar Telescope (NST)* clearly demonstrates the photospheric origin of 3-min oscillations (Fig. 4.22) in the photospheric Ni I (5436 Å), Fe I (5435 Å), and Na I D_2 5980 Å) lines (Chae et al. 2017). Photospheric oscillations were also detected in the infrared line 15,650 Å, which is sensitive to magnetic field oscillations (Bellot Rubio et al. 2000). MHD simulations of magneto-acoustic wave propagation from the photosphere to the low chromosphere show that the fast (magnetic) mode in the region $c_s < v_A$ does not reach the chromosphere and reflects back to the photosphere at a somewhat higher layer than the $c_s = v_A$ line (Khomenko and Collados 2006; Khomeno et al. 2008). This behavior is due to wave refraction, caused primarily by the vertical and horizontal gradients of the Alfvén speed. The slow (acoustic) mode continues up to the chromosphere along the magnetic field lines with increasing amplitude, which generates a wide range of periods at different distances from the sunspot axis (Khomenko and Collados 2006). Waves with

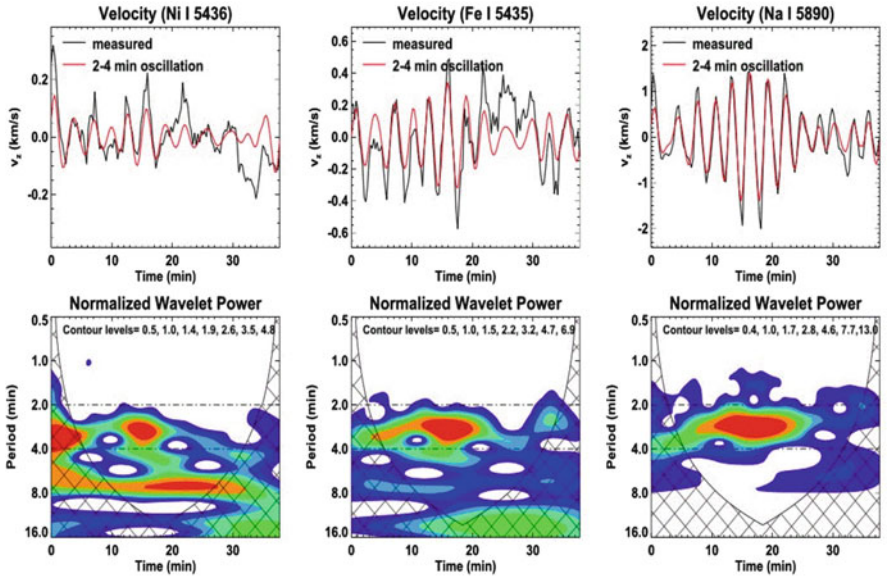

Fig. 4.22 Velocity oscillations (top panels) and wavelet periods (bottom panels) observed in a sunspot umbrae on 2015 June 16 with the *Fast Imaging Solar Spectrograph (FISS)* of the 1.6 m *Goode New Solar Telescope (NST)* in the photospheric Ni I (5436 Å), Fe I (5435 Å), and Na I D_2 5980 Å) lines (Chae et al. 2017)

frequencies above the acoustic cut-off propagate from the photosphere to the upper layers only in restricted areas of the Quiet Sun, a large fraction of the quiet chromosphere is occupied by "magnetic shadows", surrounding network regions, detected in the Ca II line (Vecchio et al. 2007). From IRIS observations (in the chromosphere and upper photosphere) a positive correlation was found between the maximum velocity and deceleration, a result that is consistent with numerical simulations of upward propagating magneto-acoustic shock waves (Tian et al. 2014). Some p-mode waves have been traced from the photosphere through the chromosphere all the way up into the corona via cross-correlation and time-distance helioseismic analysis (Zhao et al. 2016). Waves in different frequencies are found to travel along different paths (Zhao et al. 2016). In network regions, besides p-mode leakage as origin of photospheric oscillations, alternative mechanisms in terms of mode conversion, or reflection and refraction of waves on the magnetic canopy, have also been considered (Kontogiannis et al. 2010).

(ii) Fast kink-mode oscillations of coronal loops show periods in a typical range of $P \approx 2$–10 min, which depends on the loop length L and Alfvén velocity (v_A), or the tube speed c_k,

$$P_{kink} = \frac{2L}{c_k} = \frac{2L}{v_A}\left(1 + \frac{(\rho_e/\rho_0)}{2}\right)^{1/2}, \tag{4.10.1}$$

with ρ_e and ρ_0 the external and internal electron density, respectively. While the fast kink-mode displays the largest oscillating amplitude in the midpoint in transverse direction to the loop axis, the amplitude is substantially reduced near the photospheric footpoints of the loops, but might still be detectable in some wave phenomena coupled to photospheric features. It was proposed that some oscillating loops are so sensitive to the source position of wave excitation, so that rocking motions of the photospheric plasma associated with some flares cause a few loops to oscillate in (anti)phase in the fundamental mode, with a period and decay rate that are determined largely by the characteristics of the photosphere, rather than by the corona (Schrijver and Brown 2000). A coupling between oscillating microwave-emitting loops and p-mode oscillations leakage in a sunspot was found for a number of flare events, with periods around ≈ 3 min (Sych et al. 2009). Based on SOT/Hinode (Fujimura and Tsuneta 2009), ROSA (Morton et al. 2011; Grant et al. 2015; Freij et al. 2016), and with *Dutch Open Telescope (DOT)* (Freij et al. 2016) observations, both longitudinal (sausage-mode) and transverse (kink-mode) MHD waves were detected in photospheric fluxtubes.

(iii) Running penumbral waves are coherent outward-propagating wave fronts (with subtended angles of 90°–270°) readily observed in the penumbral chromosphere. The measured radial phase speeds vary in the range of 8–35 km s^{-1}, with a tendency of decreasing phase speed with distance. Recent studies have confirmed that running penumbral waves have the same nature as umbral flashes, both being slow-mode magneto-acoustic waves that propagate upward

and are guided by the inclined magnetic field of the penumbra (Bloomfield et al. 2007; Jess et al. 2013; Löhner-Böttcher and Bello Gonzalez 2015; Löhner-Böttcher et al. 2016). This magnetic field inclination increases from the inner to the outer penumbra, causing an increasing path length that appears as an outward propagation with decreasing velocity.

(iv) Moreton-Ramsey waves are also known as fast-mode MHD waves, which propagate globally along the spherical solar surface. STEREO observations determined altitude ranges of $\lesssim 0.15 R_\odot$ and speeds of $\approx$ 500–1500 km s^{-1} for these waves, generated in conjunction with large flares and CMEs. Other flare-related phenomenona with global propagation characteristics are the "sunquakes", first discovered by Kosovichev and Zharkova (1998), which are usually detected during the impulsive phase of the largest (M- and X-class) flares, but occasionally also in weak C-class flares (Sharykin et al. 2015), and is analyzed with helioseismic methods (e.g., Martinez-Oliveros et al. 2008). Helioseismic waves are believed to be initiated by the photospheric impact of electron (or proton) beams accelerated in the early impulsive phase of flares (e.g., Kosovichev 2007).

References

(4.1) Solar Diameter and Oblateness

Damiani, C., Rozelot, J.P., Lefebvre, S. et al. 2011, *A brief history of the solar oblateness. A review*, J.Atmos Solar-Terr. Phys. 73, 241, [24 c, 4 c/y].

Emilio, M., Kuhn, J.R., Bush, R.I., and Scholl, I.F. 2012, *Measuring the solar radius from space during the 2003 and 2006 Mercury transits*, ApJ 750, 135, [24 c, 4 c/y].

Emilio, M., Couvidat, S., Bush, R. I., et al. 2015, *Measuring the Solar Radius from Space during the 2012 Venus Transit*, ApJ 798, 48, [4 c, 2 c/y].

Fivian, M.D., Hudson, H.S., Lin, R.P. and Zahid, H.J. 2008, *A large excess in apparent solar oblateness due to surface magnetism*, Science 322, 560, [32 c, 3 c/y].

Gough, D. 2012, *How oblate is the Sun?*, Science 337, 1611, [9 c, 2 c/y].

Kosovichev, A. and Rozelot, J.P. 2018a, *Cyclic changes of the Sun's seismic radius*, ApJ 861, 90, [1 c, 1 c/y].

Kosovichev, A. and Rozelot, J.P. 2018a, *Solar cycle variations of rotation and asphericity in the near-surface shear layer*, JASTP 176, 21, [1 c, 1 c/y].

Kuhn, J.R., Bush, R., Emilio, M., and Scholl, I.F. 2012, *The precise solar shape and its variability*, Science 337, 1638, [26 c, 5 c/y].

Rozelot, J.P., Kosovichev, A., and Kilcik, A. 2015, *Solar radius variations: An inquisitive wavelength dependence*, ApJ 812, 91, [5 c, 2 c/y].

Wachter, R., Schou, J., Rabello-Soares, M.C. et al. 2012, *Image quality of the HMI onboard the SDO*, SoPh 275, 261, [35 c, 6 c/y].

(4.2) Magnetic Flux Distribution

Close, R.M., Parnell, C.E., Longcope, D.W. et al. 2004, *Recycling of the solar corona's magnetic field*, ApJ 612, L81, [52, 4 c/y].

Fragos, T., Rantsiou, E., and Vlahos, L. 2004, *On the distribution of magnetic energy storage in solar active regions* A&A 420, 719, [15 c, 1 c/y].

Hagenaar, H.J. 2001, *Ephemeral regions on a sequence of full-disk MDI magnetograms*, ApJ 555, 448, [152 c, 9 c/y].

Kitiashvili, I.N., Kosovichev, A.G., Wray, A.A., et al. 2010, *Mechanism of spontaneous formation of stable magnetic structures on the Sun*, ApJ 719, 307, [64 c, 9 c/y].

Mandrini, C.H., Démoulin, P., and Klimchuk, J.A. 2000, *Magnetic field and plasma scaling laws: Implications for coronal heating models*, ApJ 530, 999, [138 c, 8 c/y].

Okamoto, T. and Sakurai T. 2018, *Super-strong magnetic field in sunspots*, ApJ 852, L16.

Parnell, C.E. 2002, *Nature of the magnetic carpet. - I. Distribution of magnetic fluxes*, MNRAS 335, 389. [43 c, 3 c/y].

Parnell, C.E., DeForest, C.E., Hagenaar, H.J. et al. 2009, *A power-law distribution of solar magnetic fields over more than five decades in flux*, ApJ 698, 75, [10 c/y, 86 c].

Schrijver, C.J., Title, A.M., van Ballegooijen, A.A., et al. (1997), *Sustaining the quiet photospheric network: The balance of flux emergence, fragmentation, merging, and cancellation*, ApJ 487, 424, [289 c, 14 c/y].

Stenflo, J.O. 2012, *Scaling laws for magnetic fields on the Quiet Sun*, A&A 541, A17, [29 c, 5 c/y].

Wiegelmann, T. and Solanki, S.K. 2004, *Similarities and differences between coronal holes and the Quiet Sun: Are loop statistics the key?* SoPh 225, 227, [34 c, 3 c/y].

(4.3) Bimodal Magnetic Area Distributions

Baumann, I. and Solanki, S.K. 2005, *On the size distribution of sunspot groups in the Greenwich sunspot record 1874–1976*, A&A 443, 1061, [37 c, 3 c/y].

Jiang, J., Cameron, R.H., Schmitt, D. and Schüssler, M. 2011, *The solar magnetic field since 1700. I. Characteristics of sunspot group emergence and reconstruction of the butterfly diagram*, A&A 528, A82, [38 c, 6 c/y].

Nagovitsyn, Y.A., Pevtsov, A.A. and Livingston, W.C. 2012, *On a possible explanation of the long-term decrease in sunspot field strength*, ApJ 758, L20, [43 c, 8 c/y].

Meunier, N. 2003, *Statistical properties of magnetic structures: Their dependence on solar scale and solar activity*, A&A 405, 1107, [38 c, 3 c/y].

Munoz-Jaramillo, A., Senkpeil, R.R., Windmueller, J.C. et al. 2015, *Small-scale and global dynamos and the area and flux distributions of active regions, sunspot groups, and sunspots: A multi-database study*, ApJ 800, 48, [15 c, 6 c/y].

Parnell, C.E., DeForest, C.E., Hagenaar, H.J. et al. 2009, *A power-law distribution of solar magnetic fields over more than five decades in flux*, ApJ 698, 75, [86 c, 10 c/y].

Schad, T.A. and Penn, M.J. 2010, *Structural invariance of sunspot umbrae over the Solar Cycle: 1993–2004*, SoPh 262, 19, [19 c, 3 c/y].

Tlatov, A.G. and Pevtsov, A.A. 2014, *Bimodal distribution of magnetic fields and areas of sunspots*, SoPh 289, 1143, [18 c, 5 c/y].

Zhang, J., Wang, Y., and Liu, Y. 2010, *Statistical properties of solar active regions obtained from an automatic detection system and the computational bias*, ApJ 723, 1006, [26 c, 3 c/y].

Zharkov, S., Zharkova, V.V. and Ipson, S.S. 2005, *Statistical properties of sunspots in 1996–2004: I. Detection, north south asymmetry and area distribution*, SoPh 228, 377, [34 c, 3 c/y].

(4.4) The Multi-Fractal Photosphere

Balke, A.C., Schrijver, C.J., Zwaan,C., et al. 1993, *Percolation theory and the geometry of photospheric magnetic flux concentrations*, SoPh 143, 215 [43 c, 2 c/s].

Berrilli, F., Del Moro, D., Russo, S., et al. 2005, *Spatial clustering of photospheric structures*, ApJ 632, 677, [23 c, 2 c/s].
Bovelet, B. and Wiehr, E. 2001, *A new algorithm for pattern recognition and its application to granulation and limb faculae*, SoPh 201, 13, [41 c, 2 c/y].
Cadavid, A.C., Lawrence, J.K., Ruzmaikin, A., et al. 1994, *Multifractal models of small-scale magnetic fields*, ApJ 429, 391, [26 c, 1 c/y].
Conlon, P.A., Gallagher, P.T., McAteer, R.T.J., et al. 2008, *Multifractal properties of evolving active regions*, SoPh 248, 297, [41 c, 4 c/y].
Gallagher, P.T., Phillips, K.J.H., Harra-Murnion, L.K., et al. 1998, *Properties of the Quiet Sun EUV network*, A&A 335, 733, [65 c, 3 c/y].
Georgoulis, M.K., Rust, D.M., Bernasconi, P.N., et al. 2002, *Statistics, morphology, and energetics of Ellerman bombs*, ApJ 575, 506, [119 c, 8 c/y].
Hathaway, D.H., Beck, J.G., Bogart, R.S., et al. 2000, *The photospheric convection spectrum* SoPh 193, 299, [99 c, 6 c/y]. s
Hirzberger, J., Vazquez, M., Bonet, J.A., et al. 1997, *Time series of solar granulation images. I. Differences between small and large granules in quiet regions*, ApJ 480, 406, [72 c, 4 c/y].
Janssen, K., Voegler, A., and Kneer, F. 2003, *On the fractal dimension of small-scale magnetic structures in the Sun*, A&A 409, 1127, [42 c, 3 c/y].
Lawrence, J.K. 1991, *Diffusion of magnetic flux elements on a fractal geometry*, SoPh 135, 249, [32 c, 1 c/y].
Lawrence, J.K. and Schrijver, C.J. 1993, *Anomalous diffusion of magnetic elements across the solar surface*, ApJ 411, 402, [50 c, 2 c/y].
Lawrence, J.K., Ruzmaikin, A., and Cadavid, A.C. 1993, *Multifractal measure of the solar magnetic field*, ApJ 417, 805, [77 c, 3 c/y].
Lawrence, J.K., Cadavid, A.C., and Ruzmaikin, A.A. 1996, *On the multifractal distribution of solar magnetic fields*, ApJ 465, 425, [25 c, 1 c/y].
Mandelbrot, B.B. 1977, *Fractals: form, chance, and dimension*, Translation of *Les objects fractals*, W.H. Freeman, San Francisco, [569 c, 14 c/y].
McAteer, R.T.J., Gallagher, P.T., and Ireland, J. 2005, *Statistics of active region complexity. A Large-scale fractal dimension survey*, ApJ 662, 691, [63 c, 5 c/y].
Meunier, N. 1999, *Fractal analysis of Michelson Doppler Imager magnetograms: a contribution to the study of the formation of solar active regions.* ApJ 515, 801, [42 c, 2 c/y].
Meunier, N. 2004, *Complexity of magnetic structures: flares and cycle phase dependence*, A&A 420, 333, [17 c, 1 c/y].
Paniveni, U., Krishan, V., Sing, J., et al. 2005, *On the fractal structure of solar supergranulation*, SoPh 231, 1, [8 c, 0.6 c/y].
Rieutord, M., Meunier, N., Roudier, T., et al. 2008, *Solar supergranulation revealed by granule tracking*, A&A 479, L17, [32 c, 3 c/y].
Rieutord, M., Roudier, T., Rincon, F., 2010, *On the power spectrum of solar surface flows*, A&A 512, A4, [37 c, 5 c/y].
Roudier, T. and Muller, R. 1986, *Structure of solar granulation*, SoPh 107, 11, [93 c, 3 c/y].

(4.5) Mini-Granulation

Abramenko, V.I., Yurchyshyn, V.B., Goode, P.R., et al. 2012, *Detection of small-scale granular structures in the Quiet Sun with the New Solar Telescope*, ApJ 756, L27, [16 c, 3 c/y].
Aschwanden, M.J., Scholkmann, F., Béthume, W., et al. 2018, *Order out of randomness: Self-organization processes in astrophysics*, SSRv 214, 55.
Chandrasekhar, S. 1961, *Hydrodynamic and hydromagnetic Stability*, Clarendon Press, Oxford.
Krishan, V. 1991, *A model of solar granulation through inverse cascade*, MNRAS 250, 50, [20 c, 0.8 c/y].
Lorenz, E.N. 1963, *Deterministic nonperiodic flow*, J. Atmos. Sciences 20, 130, [4983 c, 91 c/y].

Schuster, H.G. 1988, *Deterministic Chaos*, VCH Verlag: Weinheim.
Van Kooten, S.J. and Cranmer, S.R. 2017, *Characterizing the motion of solar magnetic bright points at high resolution*, ApJ 850, 64, [1 c, 1 c/y].

(4.6) Quiet-Sun and Polar Fields

de Wijn, A.G., Stenflo, J.O., Solanki, S.K., et al. 2009, *Small-scale solar magnetic fields*, SSRv 144, 275, [116 c, 14 c/y].
Dikpati, M. and Charbonneau, P. 1999, *A Babcock-Leighton flux transport dynamo with solar-like differential rotation*, ApJ 518, 508, [478 c, 26 c/y].
Dominquez Cerdena, I., Sanchez, A., and Kneer, F. 2003, *Inter-network magnetic fields observed with sub-arcsec resolution*, A&A 407, 741, [96 c, 7 c/y].
Harvey, J.W., Branston, D., Henney, C.J., et al. 2007, *Seething horizontal magnetic fields in the quiet solar photosphere*, ApJ 659, L177, [98 c, 9 c/y].
Lagg, A., Lites, B., Harvey, J., et al. 2017, *Measurements of photospheric and chromospheric magnetic fields*, SSRv 210, 37, [6 c, 6 c/y].
Lin, H.S. and Rimmele, T. 1999, *The granular magnetic fields of the Quiet Sun*, ApJ 514, 448, [166 c, 9 c/y].
Lites, B.W., Leka, K.D., Skumanich, A., et al. 1996, *Small-scale horizontal magnetic fields in the solar photosphere*, ApJ 460, 1019, [131 c, 6 c/y].
Lites, B.W., Kubo, M., Socas-Navarro, H., et al. 2008, *The horizontal magnetic field flux of the Quiet-Sun internetwork as observed with the Hinode Spectro-Polarimeter*, ApJ 672, 1237, [309 c, 33 c/y].
Stenflo, J.O. 2004, *Solar physics: Hidden magnetism*, Nature 430, 304, [19 c, 1 c/y].
Stenflo, J.O. 2012, *Scaling laws for magnetic fields on the Quiet Sun*, A&A 541, A17, [29 c, 5 c/y].
Tsuneta, S., Ichimoto, K., Katsukawa, Y., et al. 2008, *The magnetic landscape of the Sun's polar region*, ApJ 688, 1374, [114 c, 12 c/y].
Wang, Y.M., Nash, A.G., and Sheeley, N.R.Jr. 1989, *Magnetic flux transport on the Sun*, Science 245, 712, [216 c, 8 c/y].

(4.7) Penumbral Dynamics

Borrero, J.M. and Ichimoto, K. 2011, *Magnetic structure of sunspots*, LRSP 8, 4, [67 c, 10 c/y].
Choudhary, D.P. and Beck, C. 2018, *Thermodynamic properties of the inverse Evershed flow at its downflow points*, ApJ 859, 139.
Rempel, M., Schüssler, M., Cameron, R.H., et al. 2009, *Penumbral Structure and Outflows in Simulated Sunspots*, Science, 325, 171, [135 c, 16 c/y].
Rempel, M. 2011, *Penumbral fine structure and driving mechanisms of large-scale flows in simulated sunspots*, ApJ 729, 5, [64 c, 10 c/y].
Rempel, M. and Schlichenmaier, R. 2011, *Sunspot modeling: From simplified models to radiative MHD simulations*, LRSP 8, 3, [35 c, 5 c/y].
Scharmer, G.B., Henriques, B.M.H., Kiselman, D. et al. 2011, *Detection of convective downflows in a sunspot penumbra*, Science, 333, 316, [50 c, 8 c/y].
Schlichenmaier, R., Jahn, K., and Schmidt, H.U. 1998, *Magnetic flux tubes evolving in sunspots. A model for the penumbral fine structure and the Evershed flow*, A&A 337, 897, [162 c, 8 c/y].
Solanki, S.K. and Montavon, C.A.P. 1993, *Uncombed fields as the source of the broad-band circular polarization of sunspots*, A&A 275, 283, [215 c, 9 c/y].
Solanki, S.K. 2003, *Sunspots: An overview*, A&ARv 11/2, 153, [387 c, 27 c/y].

Spruit, H.C. and Scharmer, G.B. 2006, *Fine structure, magnetic field and heating of sunspot penumbrae*, A&A 447, 343. [132 c, 11 c/y].
Thomas,J.H., Weiss, N.O., Tobias, S.M. et al. 2002, *Downward pumping of magnetic flux as the cause of filamentary structures in sunspot penumbrae*, Nature 420, 390, [86 c, 6 c/y].
Thomas, J.H. and Weiss, N.O. 2004, *Fine structure in sunspots*, ARvAA 42, 517, [85 c, 4 c/y].
Thomas, J.H. and Weiss, N.O. 2008, *Sunspots and starspots*, Cambridge, UK: Cambridge Unviersity Press, [61 c, 6 c/y].

(4.8) Rotating Sunspots

Aschwanden, M.J. 2013, *A nonlinear force-free magnetic field approximation suitable for fast forward-fitting to coronal loops*, SoPh 287, 323, [17 c, 4 c/y].
Bi, Y., Jiang, Y., Jang, J., et al. 2016, *Observation of a reversal of rotation in a sunspot during a solar flare*, Nature Communications 7, 13798, [6 c, 4 c/y].
Brown, D.S., Nightingale, R.W., Alexander, D., et al. 2003, *Observations of rotating sunspots from TRACE*, SoPh 216, 79, [144 c, 10 c/y].
Evershed, J. 1910, *Radial movement in sun-spots (Second paper)*, MNRAS 70, 217, [48 c, 0.4 c/y].
Fan, Y. 2009, *The emergence of a twisted flux tube into the solar atmosphere: Sunspot rotations and the formation of a coronal flux rope*, ApJ 697, 1529, [94 c, 11 c/y].
Gerrard, C.L., Brown, D.S., Mellor, C., et al. 2003, *MHD simulations of sunspot rotation and the coronal consequences*, SoPh 213, 39, [11 c, 0.8 c/y].
Hiremath, K.M. 2002, *Change of rotation rates of sunspot groups during their lifetimes: Clues ot the sites of origin of different flux tubes*, A&A 386, 674, [24 c, 2 c/y].
Jain, K., Komm, R.W., Gonzalez-Hernandez, I. et al. 2012, *Subsurface flows in and around active regions with rotating and non-rotating sunspots*, SoPh 279, 349, [9 c, 2 c/y].
Jiang, Y., Zheng, R., Yang, J., et al. 2012, *Rapid sunspot rotation associated with the X2.2 flare on 2011 February 15*, ApJ 744, 50, [43 c, 8 c/y].
Kazachenko, M.D., Canfield, R.C., Longcope, D.W., et al. 2010, *Sunspot rotation, flare energetics, and flux rope helicity: The Halloween flare on 2003 October 28*, ApJ 722, 1539, [18 c, 2 c/y].
Kosovichev, A.G. 2002, *Subsurface structure of sunspots*, Astron.Nachrichten 323, 186, [28 c, 2 c/y].
Kumar, P., Park, S.H., Cho, K.S., et al. 2013, *Multiwavelength study of a solar eruption from AR NOAA 1112. I. Flux emergence, sunspot rotation, and triggering of a solar flare*, SoPh 282, 503, [15 c, 3 c/y].
Li, A. and Liu, Y. 2015, *Sunspot rotation and the M-class flare in solar active region NOAA 11158*, SoPh 290, 2199, [5 c, 2 c/y].
Min, S.Y. and Chae, J.C. 2009, *The rotating sunspot in AR 10930*, SoPh 258, 203, [46 c, 5 c/y].
Ruan, G., Chen, Y., Wang, S. et al. 2014, *A solar eruption driven by rapid sunspot rotation*, ApJ 784, 165, [20 c, 6 c/y].
Ruzdjak, D., Ruzdjak, V., Brajsa, R., et al. 2004, *Deceleration of the rotational velocities of sunspot groups during their evolution*, SoPh 221, 225, [18 c, 1 c/y].
Santos, J.C., Büchner, J. and Otto, A. 2011, *3D MHD simulations of electric current development in a rotating sunspot: Active region NOAA 8210*, A&A 535, A111, [9 c, 1 c/y].
Sturrock, Z., Hood, A.W., Archontis, V., et al. 2015, *Sunspot rotation. I. A consequence of flux emergence*, A&A 582, A76, [7 c, 3 c/y].
Sturrock, Z. and Hood, A.W. 2016, *Sunspot rotation. II. Effects of varying the field strength and twist of an emerging flux tube*, A&A 593, A63, [3 c, 2 c/y].
Török, T., Temmer, M., Valori, G., et al. 2013, *Initiation of coronal mass ejections by sunspot rotation*, SoPh 286, 453, [33 c, 7 c/y].
Tian, L. and Alexander, D. 2006, *Role of sunspot and sunspot-group rotation in driving sigmoidal active region eruptions*, SoPh 233, 29, [38 c, 3 c/y].

Vemareddy, P., Ambastha, A., and Maurya, R.A. 2012, *On the role of rotating sunspots in the activity of solar active region NOAA 11158*, ApJ 761, 60, [42 c, 8 c/y].
Vemareddy, P., Cheng, X., and Ravindra, B. 2016, *Sunspot rotation as a driver of major solar eruptions in NOAA active region 12158.* ApJ 829, 24, [9 c, 6 c/y].
Wang, S., Liu, C., Deng, N., et al. 2014, *Sudden photospheric motion and sunspot rotation associated with the X2.2 flare on 2011 February 15*, ApJ 782, L31, [25 c, 6 c/y].
Wang, R., Liu, Y.D., Wiegelmann, T., et al. 2016, *Relationship between sunspot rotation and a major solar eruption on 12 July 2012*, SoPh 291, 1159, [3 c, 2 c/y].
Yan, X.L. and Qu, Z.Q. 2007, *Rapid rotation of a sunspot associated with flares*, A&A 468, 1083, [37 c, 4 c/y].
Yan, X.L., Qu, Z.Q., and Xu, C.L. 2008, *A statistical study on rotating sunspots: Polarities, rotation directions, and helicities*, ApJ 682, L65, [33 c, 3 c/y].
Yan, X.L., Qu, Z.Q., Kong, D.F., et al. 2012, *Sunspot rotation, sigmoidal filament, flare, and coronal mass ejection: The event on 2000 February 10*, ApJ 754, 16, [23 c, 4 c/y].
Zhang, J., Li, L., and Song, Q. 2017, *Interaction between a fast rotating sunspot and ephemeral regions as the origin of the major solar event on 2006 December 13*, ApJ 662, L35, [75 c, 7 c/y].
Zhang, Y., Liu, J., and Zhang, H. 2008, *Relationship between rotating sunspots and flares*, SoPh 247, 39, [50 c, 5 c/y].
Zhao, J.W. and Kosovichev, A.G. 2003, *Helioseismic observation of the structure and dynamics of a rotating sunspot beneath the solar surface*, ApJ 591, 446, [83 c, 6 c/y].
Zhu, C., Alexander, D., and Tian, L. 2012, *Velocity characteristics of rotation sunspots*, SoPh 278, 121, [7 c, 1 c/y].

(4.9) Sunspot Light Bridges

Asai, A., Ishii, T.T., and Kurokawa, H. 2001, *Plasma ejection from a light bridge in a sunspot umbra*, ApJ 555, L65, [62 c, 4 c/y].
Berger, T.E. and Berdyugina, S.V. 2003, *The observation of sunspot light-bridge structure and dynamics*, ApJ 589, L117, [33 c, 4 c/y].
Bharti, L., Rimmele, T., Jain, R., et al. 2007, *Detection of opposite polarities in a sunspot light bridge: Evidence of low-altitude magnetic reconnection*, MNRAS 376, 1291, [27 c, 3 c/y].
Borrero, J.M., and Ichimoto, K. 2011, *Magnetic structure of sunspots*, LRSP 8, 4, [67 c, 10 c/y].
Giordano, S., Berilli, F., Del Moro, D., et al. 2008, *The photospheric structure of a solar pore with a light bridge*, A&A 489, 747, [22 c, 2 c/y].
Hirzberger, J., Bonet, J.A., Sobotka, M. et al. 2002, *Fine structure and dynamics in a light bridge inside a solar pore*, A&A 383, 275, [33 c, 4 c/y].
Jurcak, J., Martinez Pillet, V., and Sobotka, M. 2006, *The magnetic canopy above light bridges*, A&A 453, 1079, [58 c, 5 c/y].
Katsukawa, Y., Yokoyama, T., Berger, T.E., et al. 2007, *Formation process of a light bridge revealed with the Hinode/SOT*, PASJ 59, S577, [38 c, 4 c/y].
Lagg, A., Solanki, S.K., van Noort, M., et al. 2014, *Vigorous convection in a sunspot granular light bridge*, A&A 568, A60, [26 c, 7 c/y].
Liu, S. 2012, *A coronal jet ejection from a sunspot light bridge*, PASA 29, 193, [6 c, 1 c/y].
Louis, R.E., Bayanna, A.R., Mathew, S.K., et al. 2008, *Dynamics of sunspot light bridges as revealed by high-resolution images from Hinode*, SoPh 252, 43, [32 c, 3 c/y].
Louis, R.E. Bellot Rubio, L.R., Mathew, S.K. and Venkatakrishnan, P. 2009, *Supersonic downflows in a sunspot light bridge*, ApJ 704, L29, [32 c, 4 c/y].
Louis, R.E., Bellot Rubio, L.R., de la Cruz Rodriquez J., et al. 2015, *Small-scale magnetic flux emergence in a sunspot light bridge*, A&A 584, A1, [9 c, 4 c/y].
Robustini, C., Leenaarts, J., de la Cruz Rodriquez, J., et al. 2016, *Fan-shaped jets above the light bridge of a sunspot driven by reconnection*, A&A 590, A57, [14 c, 9 c/y].

Rouppe van der Voort, L., Bellot Rubio, L.R., and Ortiz, A. 2010, *Upflows in the central dark lane of sunspot light bridges*, ApJ 718, L78, [24 c, 3 c/y].
Schüssler, M. and Vögler, A. 2006, *Magnetoconvection in a sunspot umbra*, ApJ 641, L73, [161 c, 14 c/y].
Shimizu, T. 2011, *long-term evolution of magnetic and dynamical properties in a sunspot light bridge*, ApJ 738, 83, [62 c, 7 c/y].
Song, D., Chae, J.C., Yurchyshyn, V. et al. 2017, *Chromospheric plasma ejections in a light bridge of a sunspot*, ApJ 835, 240, [5 c, 5 c/y].
Toriumi, S., Cheung, M.C.M., and Katsukawa, Y. 2015a, *Light bridge in a developing active region. I. Observation of light bridge and its dynamic activity phenomena*, ApJ 811, 137, [20 c, 8 c/y].
Toriumi, S., Cheung, M.C.M., and Katsukawa, Y. 2015b, *Light bridge in a developing active region. II. Numerical simulation of flux emergence and light bridge formation*, ApJ 811, 138, [15 c, 6 c/y].
Yang, S., Zhang, J., Jiang, F., et al. 2015, *Oscillating light wall above a sunspot light bridge*, ApJ 804, L27, [16 c, 6 c/y].
Yuan, D., Nakariakov, V.M., Huang, Z., et al. 2014, *Oscillations in a sunspot with light bridges*, ApJ 792, 41, [21 c, 6 c/y].
Yuan, D. and Walsh, R.W. 2016, *Abnormal oscillation modes in a waning light bridge*, A&A 594, A101, [7 c, 5 c/y].
Zhang, J., Tian, H., He, J., et al. 2017, *Surge-like oscillations above sunspots light bridges driven by magneoacoustic shocks*, ApJ 838, 2, [6 c, 6 c/y].

(4.10) Photospheric Waves and Oscillations

Bellot Rubio, L.R., Collados, M., Ruiz Cobo, B., et al. 2000, *Oscillations in the photosphere of a sunspot umbra from the inversion of infrared Stokes profiles*, ApJ 534, 989, [55 c, 3 c/y].
Bloomfield, D.S., Lagg, A., and Solanki, S.K. 2007, *The nature of running penumbral waves revisited*, ApJ 671, 1005, [58 c, 6 c/y].
Centeno, R., Collados, M., Trujillo Bueno, J. 2006, *Spectro-polarimetric investigation of the propagation of magneto-acoustic waves and shock formation in sunspot atmospheres*, ApJ 640, 1153, [91 c, 8 c/y].
Chae, J., Lee, J., Cho, K., et al. 2017, *Photospheric origin of three-minute oscillations in a sunspot*, ApJ 836, 18, [6 c, 6 c/y].
De Pontieu, B., Erdelyi, R., James, S.P. 2004, *Solar chromospheric spicules from the leakage of photospheric oscillations and flows*, Nature 430, 536, [286 c, 21 c/y].
De Pontieu, B., Erdelyi, R., and De Moortel, I. 2005, *How to channel photospheric oscillations into the corona*, ApJ 624, L61, [124 c, 10 c/y].
Freij, N., Dorotovic, I., Morton, R.J., et al. 2016, *On the properties of slow MHD sausage waves within small-scale photospheric magnetic structures*, ApJ 817, 44, [7 c, 5 c/y].
Fujimura, D. and Tsuneta, S. 2009, *Properties of MHD waves in the solar photosphere obtained with Hinode*, ApJ 702, 1443, [63 c, 7 c/y].
Grant, S.D.T., Jess, D.B., Moreels, M.G., et al. 2015, *Wave damping observed in upward propagating sausage-mode oscillations contained within a magnetic pore*, ApJ 806, 132, [14 c, 6 c/y].
Jess, D.B., Reznikova, V.E., Van Doorsselaere, T. et al. 2013, *The influence of the magnetic field on running penumbral waves in the solar chromosphere*, ApJ 779, 168, [40 c, 9 c/y].
Khomenko, E. and Collados, M. 2006, *Numerical modeling of magnetohydrodynamic wave propagation and refraction in sunspots*, ApJ 653, 739, [89 c, 8 c/y].
Khomeno, E., Centeno, R., Collados, M., et al. 2008, *Channeling 5-minute photospheric oscillations into the solar outer atmosphere through small-scale vertical magnetic flux tubes*, ApJ 676, L85, [55 c, 6 c/y].

Kontogiannis, I., Tsiropoula, G., Tziotziou, K., et al. 2010, *Oscillations in a network region observed in the Hα line and their relation to the magnetic field*, A&A 524, A12, [15 c, 2 c/y].

Kosovichev, A.G. and Zharkova, V.V. 1998, *X-ray flare sparks quake inside Sun*, Nature 393, Issue 6683, [170 c, 9 c/y].

Kosovichev, A.G. 2007, *The cause of photospheric and helioseismic responses to solar flares: High-energy electrons or protons?* ApJ 670, L65, [28 c, 3 c/y].

Löhner-Böttcher, J. and Bello Gonzalez, N. 2015, *Signatures of running penumbral waves in sunspot photosphere*, A&A 580, A53, [12 c, 5 c/y].

Löhner-Böttcher, J., Bello Gonzalez, N., and Schmidt, W. 2016, *Magnetic field reconstruction based on sunspot oscillations*, Astron.Nachr. 337, 1040, [2 c, 1 c/y].

Martinez-Oliveros, J.C., Moradi, H., and Donea, A.C. 2008, *Seismic emissions from a highly impulsive M6.7 solar flare*, SoPh 251, 613, [20 c, 2 c/y].

Morton, R.J., Erdelyi, R., Jess, D.B., et al. 2011, *Observations of sausage modes in magnetic pores*, ApJL 729, L18, [40 c, 6 c/y].

Schrijver, C.J. and Brown, D.S. 2000, *Oscillations in the magnetic field of the solar corona in response to flares near the photosphere*, ApJ 537, L69, [71 c, 4 c/y].

Sharykin, I.N., Kosovichev, A.G., and Zimovets, I.V. 2015, *Energy release and initiation of a sunquake in a C-class flare*, ApJ 807, 102, [11 c, 4 c/y].

Sych, R., Nakariakov, V.M., Karlicky, M., et al. 2009, *Relationship between wave processes in sunspots and quasi-periodic pulsations in active region flares*, A&A 505, 791, [87 c, 10 c/y].

Tian, H., DeLuca, K.K., McKillop, S. et al. 2014, *High-resolution observations of the shock wave behavior for sunspot oscillations IRIS*, ApJ 786, 137, [48 c, 14 c/y].

Vecchio, A., Cauzzi, G., Reardon, K.P. et al. 2007, *Solar atmospheric oscillations and the chromospheric magnetic topology*, A&A 461, L1, [85 c, 8 c/y].

Zhao, J.W., Felipe, T., Chen, R., et al. 2016, *Tracing p-mode waves from the photosphere to the corona in active regions*, ApJ 830, L17, [6 c, 4 c/y].

Chapter 5
The Chromosphere and Spicules

5.1 Chromospheric Models

Modeling of the solar chromosphere is challenging and the spectral diagnostic features formed in the chromosphere are few and difficult to interpret, and typically they are neither formed in the optically thin regime (unlike the corona), nor are they in the *local thermodynamic equilibrium (LTE)* (e.g., see reviews by Carlsson 2007, 2008).

Old models of the chromosphere, the so-called *semi-empirical models*, assumed a more or less homogeneous, gravitationally stratified sphere within a height range of 500–2000 km above the photosphere. Suitable observables that constrain semi-empirical models are UV lines and UV continuum emission, the Lyman-α line, the Ca II h and k lines, the hydrogen Balmer lines, and the helium 10,830 Å line, which originate from highly excited atomic levels and thus have a very temperature sensitive opacity. The most cited paper on semi-empirical models is the *Vernazza-Avrett-Loeser (VAL3)* paper (Vernazza et al. 1981). The solution of the non-LTE optically thick transfer equations for hydrogen, carbon, and other ions yields the intensity (flux) $I(\lambda)$ as a function of the wavelength λ, fitting the observed UV fluxes, while the temperature $T_e(h)$ as a function of height is a free function. These models have a temperature minimum at $\approx$ 500 km above the visible solar surface (optical depth unity at 5000 Å), a rapid temperature rise outwards to $\approx$ 6000 K at 1000 km height, and thereafter have a gradual temperature increase to 7000 K at 2000 km height, with a very rapid increase from there to coronal temperatures. The realism of the VAL3 model has been questioned because of the blatant ignorance of the observed dynamic and spatial inhomogeneities of chromospheric fine structure, as well as the large number of free parameters (e.g., temperature as a function of height, microturbulence as a function of height and angle, non-gravitational forces, shock waves), and because of the model-specific assumptions (e.g., ionization equilibrium, lateral homogeneity, static solution, and the unspecified energy source to maintain the chromospheric temperature) (see reviews by Carlsson 2007, 2008).

M. J. Aschwanden, *New Millennium Solar Physics*, Astrophysics and Space Science Library 458, https://doi.org/10.1007/978-3-030-13956-8_5

More recent semi-empirical models include more atomic (H, C, O) lines and energy balance between chromospheric radiative loss and coronal thermal conduction (Avrett and Loeser 2008), FUV and EUV irradiance computations (Fontenla et al. 2009), comparisons with IRIS Mg II k line profiles (Avrett et al. 2015), and they resolve the controversy about the temperature minimum value (Fontenla et al. 2007).

New models of the chromosphere include an energy equation, with energy balance between chromospheric heating and radiative loss, the turbulent motion driven by sub-photospheric convection, the effects of global p-modes, acoustic waves, and subsequent shock formation, initially with 1-D, and later with 3-D numerical hydrodynamic simulations. The magnetic field was initially ignored to reduce the computational load, but a non-magnetic solar chromosphere appears not to exist, not even in field-free internetwork regions (Carlsson and Stein 1995). The chromospheric observations and numerical simulations reveal a highly dynamic behavior of the chromosphere, which invalidate earlier *mean static models*. The inclusion of solar convection in 3-D hydrodynamic simulations, however, is difficult for three reasons: (i) The approximation of the LTE overestimates the local (collisional) coupling in chromospheric layers, (ii) the shock formation requires a very fine grid or a shock capturing scheme, and (iii) the non-equilibrium ionization for the proper evaluation of the energy balance in the chromosphere (Carlsson 2007).

3-D hydrodynamic simulations extending to the chromosphere with high spatial resolution were performed by Wedemeyer et al. (2004), using the CO^{5}BOLD code. The 3-D model includes the chromosphere, the photosphere, and the top of the convection zone, where acoustic waves are excited by convective motions. While the waves propagate upwards, they steepen into shocks, dissipate, and deposit their mechanical energy as heat in the chromosphere. The numerical simulations show for the first time a complex 3-D structure of the chromospheric layers, formed by the interaction of shock waves. A thermal bifurcation occurs, separating cold and hot regions, sufficiently hot (7000 K) to produce chromospheric UV emission, and at the same time sufficiently cold (2000 K) to form carbon monoxide molecules (Wedemeyer et al. 2004). These early simulations of the chromosphere, however, may not yield accurate temperatures, given a number of assumed simplifications (no scattering, no chromospheric losses, and no non-equilibrium ionization). These conditions were dealt with in more refined later models, which were made publicly available (Carlsson et al. 2016).

These later codes model the solar chromosphere in the interface between the solar surface and the solar corona, representing the transition from optically thick to thin radiation escape, from gas-pressure dominance to magnetic-pressure dominance, from a neutral to an ionized state, from MHD to plasma physics, and from near-equilibrium (LTE) to non-equilibrium conditions. The ionization of hydrogen in the solar chromosphere and transition region does not obey *local thermal equilibrium (LTE)*, because the ionization time scale is long compared with important hydrodynamical time scales, especially for magneto-acoustic shock processes, and thus needs non-equilibrium (NLTE) treatment (Leenaarts et al. 2007). Besides hydrogen, helium EUV resonance lines also require optically thick radiatative transfer and non-

equilibrium ionization treatment, in order to reproduce the oserved He II (304 Å and 256 Å) line intensities (Golding et al. 2016, 2017).

Simulations of the chromosphere with radiative-MHD codes and 3-D non-LTE radiative transfer have also been used to model the formation of the Hα line in the chromosphere (Leenaarts et al. 2012), with the finding that the Hα opacity is mainly sensitive to the mass density, and only weakly sensitive to the temperature. The Hα line core intensity is anti-correlated with the average formation height: the larger the average formation height, the lower the intensity. The line-core width measures the gas temperature in the line-forming region.

Using 2.5-D radiative MHD simulations with the Bifrost code (Fig. 5.1), Martinez-Sykora et al. (2012) investigated the importance of partial ionization in the chromosphere. The models cover the chromosphere from the upper convection zone up to the lower corona, solve the full MHD equations with non-gray and non-LTE radiative transfer, with thermal conduction along the magnetic field, using the generalized Ohm's law (with Ohmic diffusion, Hall diffusion, and ambipolar diffusion, which all strongly fluctuate in the chromosphere). It was found that Ohmic diffusion is $\approx 10^3$ times smaller than the Hall term in the chromosphere, and the Hall term is $\approx 10^3$ times smaller than the artificial (numerical) diffusion. In the chromosphere, it is found that the ambipolar diffusion is of the same order of magnitude or even larger than the numerical diffusion used to stabilize the code, which implies that the simulations may be more realistic than previously assumed (Martinez-Sykora et al. 2012).

Besides UV lines and continuum, chromospheric models can also be modeled and tested in radio, at millimeter, and sub-millimeter wavelengths. This can now most suitably be carried out with the new *Atacama Large Millimeter/Submillimeter Array (ALMA)* data. Especially the method of imaging with ALMA in small steps across the wavelength range could render a tomographic reconstruction of the chromospheric temperature structure, since the emission at a given radio frequency is convolved from a wide range of heights that depend on the electron density (Loukitcheva et al. 2015; Alissandrakis et al. 2017; Wedemeyer et al. 2016).

5.2 Chromospheric Fibrils

Fibrils are the chromospheric counterparts to coronal loops: Both appear as curvilinear structures, both follow more or less the local magnetic field, and both exhibit dynamic processes such as flows, oscillations, and waves. The major difference is their temperature regime and altitude range: chromospheric fibrils are filled with cool ($T_e \gtrsim 5000$ K) partially ionized gas, best visible in Hα, Ca II 8542 Å, Mg II 2796 Å h and k, Ca II h and k, and millimeter wavelengths, while coronal loops are filled with hot ($T_e \gtrsim 10^6$ K) fully ionized plasma. Fibrils are ubiquitous in the solar chromosphere, but appear darkest in Hα in active regions and in sunspot penumbral and super-penumbral surroundings. There is no tight definition about

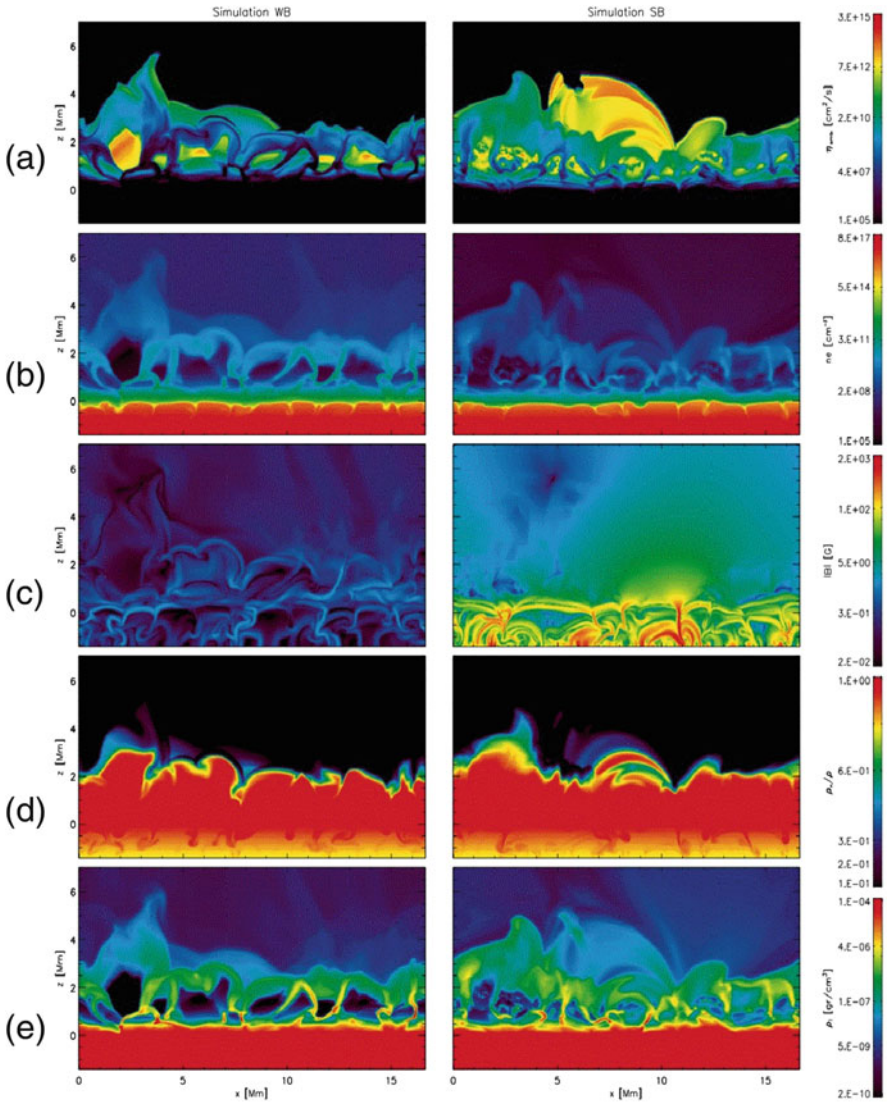

Fig. 5.1 2-D MHD simulation of chromosphere: (**a**) Ambipolar diffusion, (**b**) electron density, (**c**) absolute value of magnetic field, (**d**) ratio between neutral and total density, and (**e**) ion density are shown from top to bottom, for the weak field (left panels) and strong field models (right panels) (Martinez-Sykora et al. 2012)

the size, length, and width of chromospheric fibrils, but larger structures morph into filaments, prominences, and arch-filament systems.

A first question that is important to understand the origin and physical nature of chromospheric fibrils is how well they are aligned with the local magnetic

field. From measurements of the 3-D vector magnetic field using the Na I 5896 Å line with the *Stokes Polarimeter* at *Mees Solar Observatory (MSO)*, it was found that the magnetic field is not force-free in the photosphere, but becomes force-free at an altitude of $h \approx 400$ km in active regions (Metcalf et al. 1995), up to 1400–1800 km (Zhu et al. 2016). However, a lot of chromospheric structures in weak-field regions are magnetically closed inside the chromosphere (below a canopy height of $\lesssim 1500$ km), so that there is not always a link between the photospheric network and magnetic loops in the corona (Jendersie and Peter 2006). The non-potentiality of the magnetic field in the chromosphere has been measured with line-of-sight magnetograms at the *National Solar Observatory's Kitt Peak Observatory (NSO/KP)* using the Ca II 8542 Å line, which is primarily sensitive to the magnetic field at a height of $h \approx 800$ km (Choudhary et al. 2001; de la Cruz Rodriguez et al. 2012), but is sensitive over a wide range of heights in other wavelengths. 3-D numerical MHD simulations with the Bifrost code (Gudiksen et al. 2011) allow us to localize the contribution heights of the Ca II 8542 Å line in a range of $h \lesssim 1500$ km for the core of the line profile, confirmed also in 3-D Bifrost models (Leenaarts et al. 2009). A similar chromospheric height range has also been adopted in the hydrostatic models of Vernazza et al. (1981). The Ca II 8542 Å line is particularly suited to observe the fine structure of fibril-like features (Pietarila et al. 2009; Cauzzi et al. 2008), to measure their geometry and orientation, and to determine their magnetic field-alignment and non-potentiality (Jing et al. 2011). The field-alignment of chromospheric fibrils was tested by comparing *CRisp Imaging Spectro-Polarimeter* data (CRISP, Scharmer 2006) with *Spectro-Polarimeter for INfrared and Optical Regions data (SPINOR)*, (Socas-Navarro et al. 2006), and it was found that fibrils are often oriented along the magnetic field, but not always (de la Cruz Rodriguez and Socas-Navarro 2011). Also in MHD simulations it was found that some modeled fibrils are not field-aligned in the simulated volume of their particular magnetic field configuration (Leenaarts et al. 2015). In fact, Leenaarts et al. (2015) found that the horizontal component of the magnetic field aligns well with the plane-of-the sky direction of the observed fibrils, but the vertical component of the magnetic field is not necessarily aligned with the fibrils. IBIS observations from the *Dunn Solar Telescope (DST)* in New Mexico found that fibrils are aligned with the magnetic field with an uncertainty of $\mu \lesssim 10°$ (Schad et al. 2013). These IBIS observations were done with the He I 10,830 Å line, which typically forms somewhat higher in the chromosphere than the 8542 Å line. Tracing superpenumbral fibrils in Hα 6563 Å, Ca II 8542 Å, Mg II h and k 2796 Å and 2802 Å, He II 304 Å (with the *Rapid Oscillations in the Solar Atmosphere (ROSA)*, the *Interferometric Bidimensional Spectrometer (IBIS)*, IRIS, and AIA/SDO, using a code for automated tracing of curvi-linear structures (such as chromospheric fibrils or coronal loops) (Fig. 5.2), it was found that the median misalignment angle between chromospheric fibrils and the local magnetic field is only $\mu_2 \approx 4°$–$7°$, and that the plasma-β parameter is $\beta \approx 10^{-5}$–10^{-1} for all structures (Aschwanden et al. 2016). While these observationally constrained cases of chromospheric fibrils exhibit a good coalignment with the magnetic field,

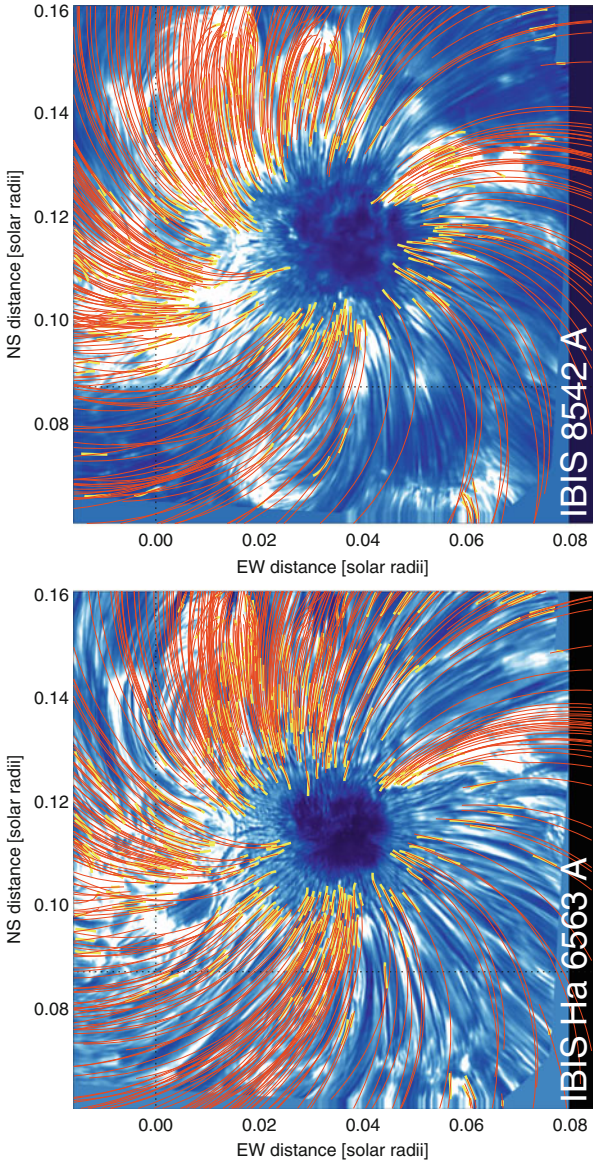

Fig. 5.2 An example of automated tracing of chromospheric superpenumbral fibrils: A subset of automatically traced loop segments (yellow curves) and best-fit magnetic field lines (red curves) are shown, overlaid on the Ca II 8542 Å image (top frame) and Hα 6563 Å image (bottom frame), observed by IBIS (Aschwanden et al. 2016)

theoretical 3-D radiative MHD simulations show that the magnetic field is often not well aligned with chromospheric features. This occurs in locations where the ambipolar diffusion is large, where ions and neutral populations decouple as the ion-neutral collision frequency drops, allowing the field to slip through the neutral population near the top of the chromosphere (Martinez-Sykora et al. 2016). It needs to be investigated whether the latter conclusions apply to super-penumbral fibrils (Aschwanden et al. 2016) also, which are located in strong magnetic field regions. Asensio Ramos et al. (2016) find that fibrils are often well aligned with the magnetic field azimuth in penumbral fibrils, with a standard deviation of $\approx 16^{\circ}$ in their dispersion. While chromospheric fibrils generally are thought to trace out low-lying, mainly horizontal magnetic fields that fan out from flux concentrations in the photosphere, high resolution ($0.1''$) images show evidence for two separate, but interlaced, components of the chromospheric magnetic field (Reardon et al. 2011).

The next important question to understand the formation and evolution of chromospheric fibril structures is their dynamic nature. Using the Bifrost 3-D radiative MHD code combined with high resolution data from the *Swedish 1 m Solar Telescope (SST)*, it was shown that jets in active regions are a natural consequence of upwardly propagating slow-mode magneto-acoustic shocks, generated by convective flows and p-mode oscillations in the lower photosphere, and leaking upward into the magnetized chromosphere (Hansteen et al. 2006). These jets in active regions appear to be generated by the same mechanism as some spicules and mottles in the Quiet Sun (Rouppe van der Voort et al. 2007). Analysis of high resolution Hα observations from SST shows for the first time spatially and temporally resolved dynamic fibrils in active regions (De Pontieu et al. 2007). The fibrils follow a parabolic path in their ascent and descent, where the observed deceleration is found to be only a fraction of solar gravity and incompatible with a ballistic path in solar gravity, but consistent with chromospheric shock waves that occur when convective flows and p-modes leak into the chromosphere (De Pontieu et al. 2007; Langangen et al. 2008).

5.3 Chromospheric Oscillations

With the term "chromospheric oscillations" we focus on any periodic or quasi-periodic dynamic phenomenon in the solar chromosphere, which includes both standing and propagating waves. Early observations found 3-min oscillations in the inter-network, or above the sunspot umbra, while no 3-min, but slower 5-min oscillations were detected in the network, at photospheric levels. Part of the 3–5 min power in plages and network regions exhibit the same oscillatory phenomenon as the shocks that drive dynamic spicules (De Pontieu and McIntosh 2010). Both network and internetwork regions produce intermittent oscillation episodes, occasionally as non-recurring long-lifetime events (McAteer et al. 2004). Some particular locations of the network are the so-called *network bright points (NBP)*, in which long-period waves with periods of 4–15 min were detected (McAteer et al. 2002). Besides the

two categories of 3-min and 5-min oscillations, a third category of oscillations is that of running waves, which move concentrically away from the umbra along penumbral structures. Photospheric and chromospheric oscillations were found to be strongly coupled for frequencies in the range of 2–8 mHz, or 2–8 min (Judge et al. 2001; Wikstol et al. 2000), characterized by cross-correlated oscillation power, phase delays (McIntosh et al. 2003; Muglach 2003; Kobanov et al. 2011), wavelet analysis (McAteer et al. 2004), and variations in wave speed, indicating a transition from dominant fast-magneto-acoustic waves to slow modes when moving from network into plages and umbrae (Bloomfield et al. 2006; Maurya et al. 2013). A systematic time lag of $\approx$ 50 s is found between chromospheric (He I, 10830 Å) and photospheric (Si I 10,827 Å) 5-min oscillations in solar faculae (Fig. 5.3) (Kobanov et al. 2011). Significant differences in oscillation power is also noted between inside a coronal hole relative to its boundary and Quiet-Sun regions (McIntosh and Smillie 2004). Reviews on chromospheric oscillations can be found focussing on high-frequency acoustic waves (Carlsson et al. 2007), or multi-wavelength studies of MHD waves (Jess et al. 2015).

High-frequency acoustic waves, which early on have been proposed to heat the Quiet chromosphere, have not been detected with TRACE (Krijger et al. 2001), and it was estimated that they are inadequate to balance the radiative losses in a static chromosphere by a factor of 5 (Carlsson et al. 2007).

How can the chromospheric oscillations be excited? There are at least three competing mechanisms to excite 3-min oscillations: the excitation of waves at the cutoff frequency, the wake of propagating shock waves, or a chromospheric resonator. In a gravitationally stratified atmosphere, acoustic waves from the solar interior can only propagate if they have a shorter period than the acoustic cut-off period, which is at $\approx$ 200 s (3.3 min). Numerical 3-D MHD simulations showed that small collapsing granules, where upflows are turned into downflows on a time scale smaller than 3 min, may be the photospheric excitation mechanism for the internetwork bright grains observed in the Ca II h and k lines (Skartlien et al. 2000). Oscillations in network bright points are believed to be produced by magneto-acoustic or magneto-gravity wave modes (McAteer et al. 2002). Later on, MHD simulations demonstrated that the (normally evanescent) 5-min p-mode waves can propagate by leakage from the photosphere through the chromosphere and up into the corona, if they are guided along inclined flux tubes. The non-verticality of the flux tube increases the acoustic cutoff period and this way allows tunneling or direct propagation in upward direction (De Pontieu et al. 2004, 2005). A consequence is that the exponential decrease of density with height leads to a nonlinear steepening of the tunneled photospheric oscillations in the chromosphere, so that magneto-acoustic shocks form, which lead to dynamic fibrils (De Pontieu et al. 2005). Waves with frequencies above the acoustic cut-off propagate from the photosphere to the chromosphere and corona in restricted areas of the Quiet Sun only. A large fraction of the Quiet chromosphere is occupied by *"magnetic shadows"* in form of surrounding network regions, as detected in the Ca II line (Vecchio et al. 2007). Chae et al. (2014) find patterns of outward propagation that apparently originate from inside the sunspot, propagate like running penumbral waves, and develop into the

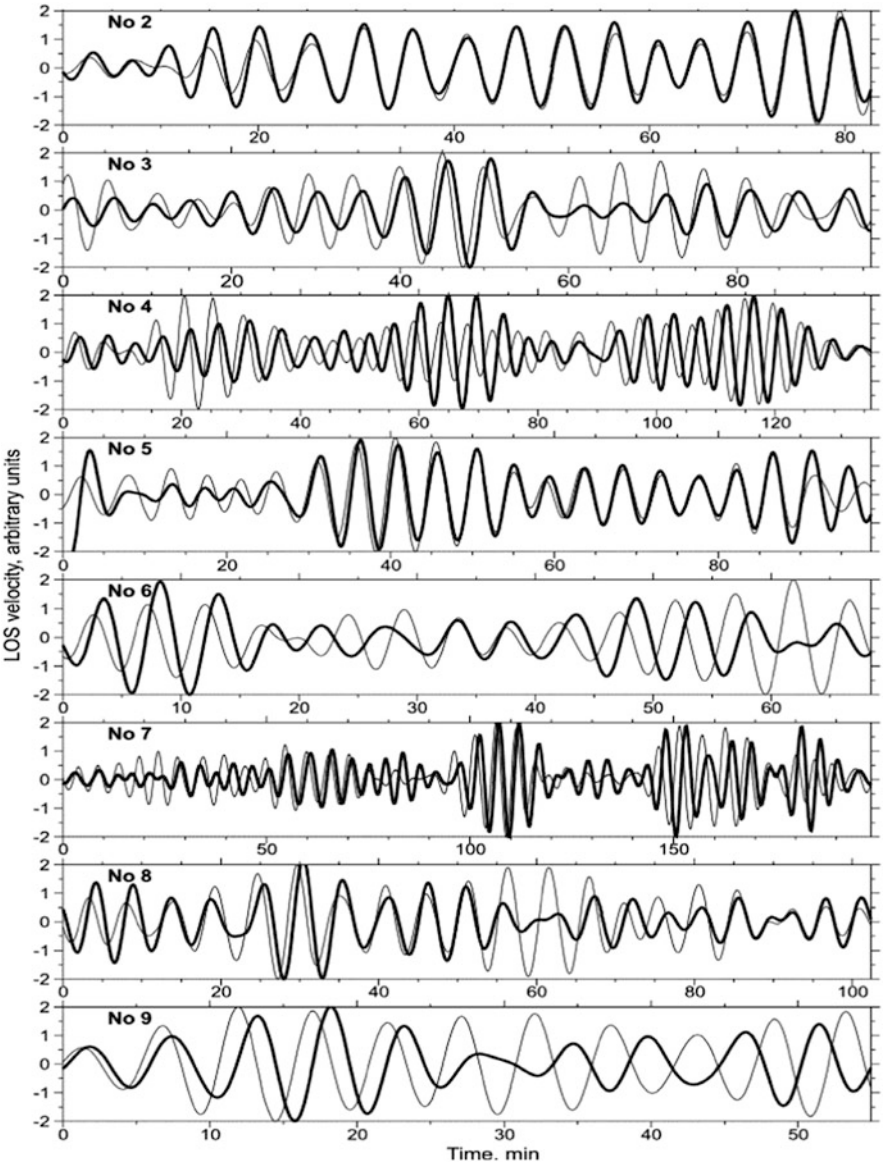

Fig. 5.3 Phase relationship between photospheric (thin curves) and chromospheric unshifted signals (thick curves) of line-of-sight velocity in 9 different faculae are shown. The signals have been filtered in a 1 mHz band around 3.5 mHz (Kobanov et al. 2011)

fibrils. The predominant period of these shock waves increases, often jumping with distance, from 3 min to 10 min. This short-to-long period transition seems to result from the selective suppression of a shock by the falling material of the preceding

shocks. Based on this scenario, it is proposed that the fibrils are driven by slow shock waves with long periods that are produced by the merging of shock waves with shorter periods propagating along the magnetic canopy (Chae et al. 2014).

MHD waves have fast-mode and slow-mode solutions, as well as kink-mode and sausage-mode branches in the dispersion relation. Sausage modes have faster periods than kink modes, because they scale with the Alfvénic travel time across (for sausage modes) or along (for kink modes) a resonant flux tube (or loop). Evidence for propagating MHD waves of the fast-sausage mode has been found for slender Ca II h fibrils observed with *Sunrise/SuFI*, with periods of 32 ± 17 s and 36 ± 25 s (Gafeira et al. 2017). MHD kink-mode waves, both standing and propagating modes, have been reported with periods of ≈ 120 s in chromospheric mottles, using the ROSA instrument (Kuridze et al. 2013), or with CRISP/SST in an chromospheric active region fibril (Pietarila et al. 2011; Stangalini et al. 2015). Kink waves have been detected during upward propagation, with a frequency above 2.6 mHz, with no sign of energy dissipation, which implies that most of the energy carried by kink waves (within < 17 mHz) flows upward to the corona (Stangalini et al. 2015).

Besides driven by p-modes, chromospheric oscillations can also be triggered by a (flare-driven) magnetic reconnection process, as observed in a dynamic fibril in an active region (Pietarila et al. 2011), or observed with the *New Vacuum Solar Telescope (NVST)* (at the Fuxian Solar Observatory of China) with a very short period of 25 s (Yang and Xiang 2016). Alternatively, a strong downflow event in a sunspot was found to trigger an oscillation with a period of 2.7 min, gradually increasing to 3.3 min, as observed with the 1.6 m *New Solar Telescope (NST)* (Kwak et al. 2016).

5.4 Chromospheric Alfvén Waves

The search for Alfvén waves in the solar chromosphere and corona has been considerably intensified over the last two decades, thanks to the availability of new high-resolution imagers sensitive to chromospheric temperatures (Hinode, IRIS), which triggered also more theoretical studies in "chromospheric seismology" (e.g., Erdelyi and Fedun 2007; Verth et al. 2010; Fedun et al. 2011). For theoretical concepts of Alfvén waves in the solar atmosphere see Fig. 5.4. Alfvén waves are non-compressional and do not modulate the plasma density, but perturb the plasma velocity (and magnetic field), which causes positive and negative Doppler shifts that can be detected as line broadening. Direct observations of Alfvén waves can be obtained with imaging instruments only if they have a sufficiently high spatial and temporal resolution.

Such a successful measurement has been accomplished with the *Solar Optical Telescope (SOT)* onboard Hinode, which has a spatial resolution of 150 km and a cadence of 5–8 s, enabling us to predict the amplitude and the energy flux of Alfvén waves (De Pontieu et al. 2007). Time series of chromospheric Ca II h-line (3968

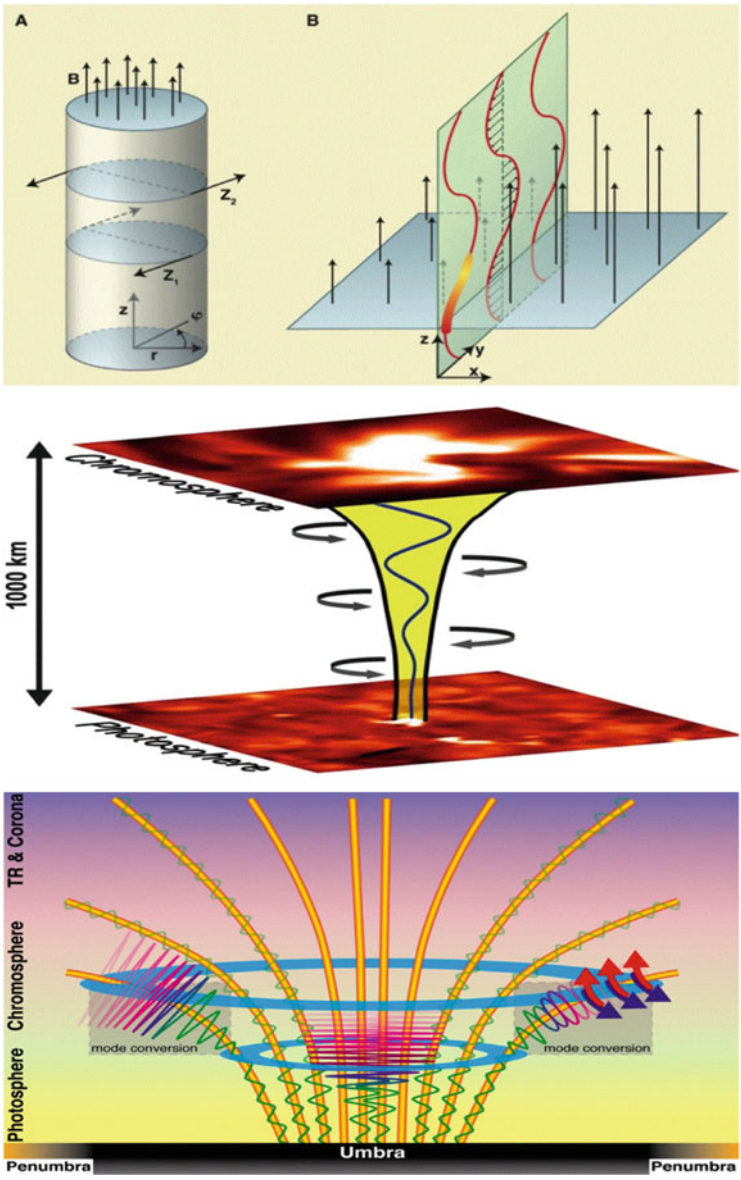

Fig. 5.4 *Top left:* Magnetic flux tube concept with Alfvénic displacements in z-directions. *Top right:* Alfvén waves propagating along a magnetic discontinuity in z-direction (Erdelyi and Fedun 2007). *Middle:* Torsional Alfvén waves propagating from the photosphere upward to the chromosphere (Jess et al. 2009). *Bottom:* Mode conversion of Alfvén waves resonantly amplifying magneto-acoustic waves and increasing the shock formation efficiency (left), and coupling of upwardly propagating magneto-acoustic oscillations into Alfvén waves (Grant et al. 2018)

Å) images taken with SOT reveal a multitude of thin ($\approx$ 200 km wide), dynamic, jet-like extrusions at the solar limb, called spicules. These spicules shoot upward at speeds of 20–150 km s^{-1}, reaching heights of 2000–10,000 km, and exhibit transverse displacements of 200–500 km and transverse velocities of 10–30 km s^{-1} during their short lifetimes of 10–300 s, with periods of $\approx$ 2.5–6 min (Okamoto and De Pontieu 2011). The oscillatory motions in transverse direction to the long axis of spicules are interpreted as Alfvénic wave motions (but could also be interpreted as MHD fast kink-mode waves, if a stable wave guide were to exist). The oscillatory motion of spicules seems to be ubiquitous in the chromosphere. The energy flux in the chromosphere is estimated to be $E = \rho v^2 v_A \approx (4\text{–}7) \times 10^6$ erg s^{-1} cm^{-2}, based on the Alfvén speed $v_A = B/\sqrt{\mu_0 \rho}$, the magnetic permeability μ_0, the observed velocity amplitude $v \approx 20$ km s^{-1}, the spicular mass density $\rho = (2.2\text{–}40) \times 10^{-14}$ g cm^{-6}, and the magnetic field of $B \approx 10$ G (De Pontieu et al. 2007). The energy flux that reaches the corona is thus on the order of $E \gtrsim 1.2 \times 10^5$ erg s^{-1} cm^{-2} for a transmission coefficient of 3 %. These numerical values have also been approximately reproduced with recent 3-D radiative MHD simulations. Therefore, the upward propagated energy flux is, in principle, sufficient to heat the Quiet-Sun corona and/or to power the solar wind (De Pontieu et al. 2007, 2011). However, evidence for Alfvénic heating waves requires both the detection of wave dissipation, as well as the heating of plasma, which has been seen in some isolated cases of prominences (Okamoto et al. 2015; Antolin et al. 2015) and spicules (Antolin et al. 2018).

After the promising detection of Alfvén waves with SOT/Hinode (De Pontieu et al. 2007), searches with other instruments followed. Ubiquitous upward propagating waves where reported from observations with the *Coronal Multi-Channel Polarimeter (CoMP)* at NSO, detected in intensity, line-of-sight velocity (Doppler shift), and linear polarization in the Fe XIII 10,747 Å line (Tomczyk et al. 2007). These wave-like coronal phenomena were interpreted as Alfvénic waves, but they exhibited much lower velocity amplitudes (in the order of 0.5 km s^{-1}) than measured for the chromospheric spicules (with a velocity amplitude of $v \approx 20$ km s^{-1}; De Pontieu et al. 2007). Also, CoMP has a lower spatial ($\approx$ 4.5 Mm) and temporal (30 s) resolution than SOT/Hinode. The apparent discrepancy between the chromospheric (De Pontieu et al. 2007) and the coronal measurements (Tomczyk et al. 2007) has raised concerns that these low-frequency Alfvénic motions do not contribute significantly to the energy balance of the corona, perhaps because the large chromospheric wave energy is dissipated or reflected before reaching the corona.

A new analysis using the (chromospheric) He II 304 Å and the (coronal) Fe IX 171 Å channels of AIA/SDO, which have a spatial resolution of 870 km and a temporal resolution of 8 s, confirmed the SOT/Hinode observations in the sense that it revealed spicular jets that shoot rapidly (20–150 km s^{-1}) upwards, often reaching heights of 20,000 km above the limb (McIntosh et al. 2011). Moreover, the AIA/SDO image sequences show a hot corona ($\approx$ 1–2 MK) that is replete with Alfvénic waves. Monte Carlo simulations show that the observations are compatible

with the presence of Alfvénic waves with amplitudes of 25 km s^{-1} in the coronal hole, or 20 km s^{-1} in the Quiet Sun, and periods of order 100–500 s (1.6–8 min) (McIntosh et al. 2011). It appears that the low-resolution observations with CoMP underestimate the oscillatory amplitudes and velocities of transverse wave motions, and hence predict an energy flux that is too low and insufficient to heat the Quiet corona or to accelerate the solar wind. This is likely because of the substantial superposition of waves when obserevd at low resolution with CoMP (McIntosh and De Pontieu 2012). Evidence has been found that links the large non-thermal broadening of coronal lines with the small-amplitude low-frequency waves observed with CoMP.

Alternative studies using SOUP/SST data detected an oscillatory signal in a *bright point group* that was interpreted as torsional Alfvén wave and provided an energy flux sufficient to heat the corona (Jess et al. 2009). Investigations with the new *Interface Region Imaging Spectrograph (IRIS)* instrument reported observations of prevalent twisting and torsional motions (10–20 km s^{-1}) on sub-arcsecond scales, driven by subphotospheric convection, permeating both the chromosphere and transition region, likely associated with rapid heating to transition region temperatures (De Pontieu et al. 2014).

A full physical understanding of the role of Alfvén waves in the chromosphere requires a comprehensive model of their generation in the convective zone and subsequent propagation through the photosphere, chromosphere, transition region, corona, solar wind, and into the heliosphere. A number of effects may play a role that need to be included in a comprehensive model, such as: damping of Alfvén mode oscillations by collisions between ions and neutrals in a partially ionized chromosphere (De Pontieu et al. 2001, 2011); the nonlinear generation of compressive waves and shocks (Suzuki and Inutsuka 2005); the bidirectional nature of outward propagating and reflected Alfvén waves (Cranmer and Ballegooijen 2005); wave reflection that leads to counter-propagating waves and turbulence in the photospheric and chromospheric parts of flux tubes (van Ballegooijen et al. 2011; Verdini and Velli 2007); the proton heating by the Kolmogorov dissipation of Alfvén waves in open-field regions (van der Holst et al. 2010), or the problem of exciting Alfvén waves at the photosphere due to a low-ionization fraction, which then causes near-total reflection at the transition region (Hansen and Cally 2012). Part of the later issue is resolved when taking into account the recent Biforst simulations that show that Alfvén waves can be generated in the middle to upper chromosphere where spicules are launched (Martinez-Sykora et al. 2017).

5.5 Type-II Spicules

Typical observational properties of chromospheric type-I spicules are (Fig. 5.5): heights of 7000–13,000 km, widths of 300–1500 km, lifetimes of 1–10 min, upward velocities of 25 km s^{-1}, temperatures of 5000–15,000 K, and densities of 3×10^{-13}

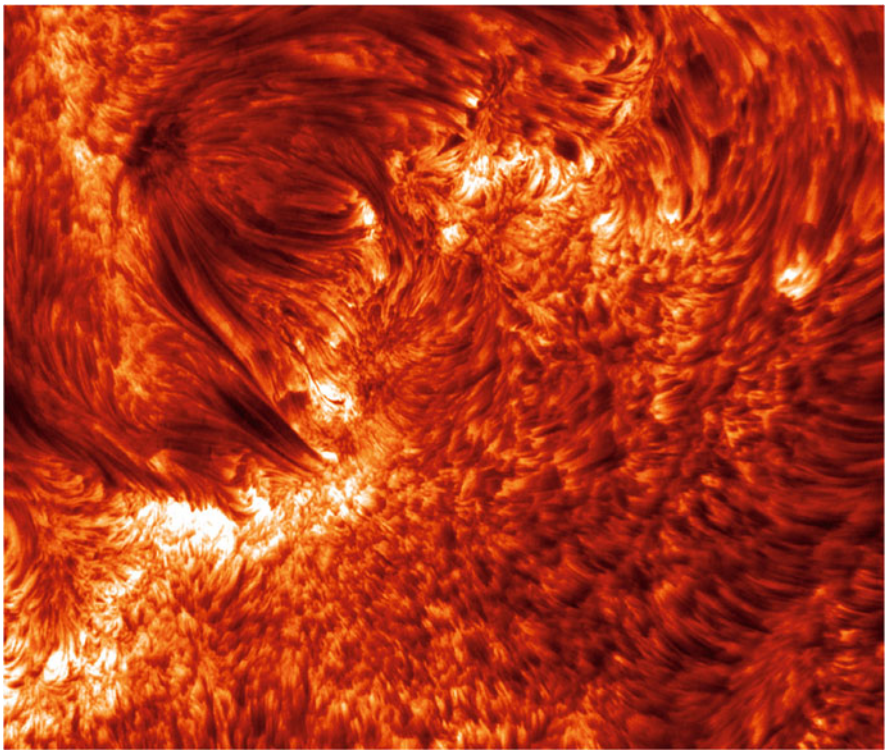

Fig. 5.5 High-resolution image of active region NOAA 10380 on 2003-Jun-16, located near the limb, showing chromospheric spicules (particularly in the right half of the image). The image was taken with the Swedish 1-meter Solar Telescope (SST) on La Palma, Spain, using a tunable filter, tuned to the blueshifted line wing of the Hα 6563 Å line. The spicules are jets of moving gas, flowing upward into the chromosphere with a speed of $\approx$ 15 km s^{-1}. The scale of the image is 65,000 $\times$ 45,000 km (Credit: Bart De Pontieu, SST)

g cm^{-3}. The distinction between type-I and type-II spicultes was first introduced by De Pontieu et al. (2007). Recent reviews can be found in Sterling (2000), Zaqarashvili and Erdelyi (2009), Tsiropoula et al. (2012), Moore et al. (2011), and Pereira et al. (2012). Other chromospheric phenomena that are more or less related to spicules are dark mottles (on disk), (dynamic) fibrils, UV and EUV spicules, macrospicules, surges, and mini-filament eruptions. A classification of suggested theoretical spicule models includes (for early references see Sterling 2000): (i) Strong pulse in the lower atmosphere; (ii) weak pulse in the lower atmosphere (rebound shock model); (iii) pressure-pulse in the higher atmosphere; (iv) Alfvén wave (low-frequency and high-frequency) models (Zaqarashvili and Erdelyi 2009); (v) magnetic reconnection for type-II spicules (e.g., De Pontieu et al. 2007; Sterling et al. 2010); (vi) Joule heating due to ion-neutral collisional damping (James et al. 2003); (vii) Leakage of global p-mode oscillations from photosphere, and formation

of shocks in chromosphere (De Pontieu et al. 2004; Zaqarashvili et al. 2007); (viii) MHD kink waves (Kukhianidze et al. 2006), and (ix) vortical flows which lead to torsional Alfvén waves that drive spicules (Iijima and Yokoyama 2017).

The advent of Hinode, TRACE, IRIS, and SST enabled spicule observations with unprecedented spatial and temporal resolution, which together with new 3-D radiative MHD simulations triggered a "renaissance" in spicule research. A first major clarification was a classification into two types of spicules (which we quote from the abstract of De Pontieu et al. 2007): *We use high-resolution observations of the Sun in Ca II h (3968 Å) from the Solar Optical Telescope on Hinode to show that there are at least two types of spicules that dominate the structure of the magnetic solar chromosphere. Both types are tied to the relentless magneto-convective driving in the photosphere, but have very different dynamic properties. "Type-I" spicules are driven by shock waves that form when global oscillations and convective flows leak into the upper atmosphere along magnetic field lines on 3–7 minute timescales. "Type-II" spicules are much more dynamic: they form rapidly (in* $\approx$*10 s), are very thin (*$\leq$ *200 km wide), have lifetimes of 10–150 s (at any one height) and seem to be rapidly heated to (at least) transition region temperatures, sending material through the chromosphere at speeds of order 50–150 km* s^{-1}*. The properties of type-II spicules suggest a formation process that is a consequence of magnetic reconnection, typically in the vicinity of magnetic flux concentrations in plages and network. Both types of spicules are observed to carry Alfvén waves with significant amplitudes of order 20 km/s.* Langangen et al. (2008) conducted a search for the on-disk counterparts of type-II spicules (observed at the limb) in IBIS data in the Ca II IR line and found *rapid blueshifted events (RBE)* with similar lifetimes, somewhat shorter lengths, and lower mass motion speeds, a discrepancy that was explained by line-of-sight projection and reduced-opacity effects. Other searches reported the discovery of the disk counterparts of type-II spicules using spectral imaging data in the Ca II 8542 Å and Hα lines with the *CRisp Imaging Spectro Polarimeter (CRISP)* at the *Swedish Solar Telescope (SST)* in La Palma, which successfully retrieved blue shifts of 20–50 km s^{-1} and other parameters (lifetimes, longitudinal and transverse velocities, occurrence rates) that have been observed in type-II spicules at the limb (Rouppe van der Voort et al. 2009; Sekse et al. 2012). In contrast, one study questioned the uniqueness of type-II spicules (Zhang et al. 2012), but an analysis of the same dataset by Pereira et al. (2012) confirmed the existence of rapidly evolving spicules. Besides the field-aligned flows (with 50–100 km s^{-1}) and the swaying transverse motion (with 15–20 km s^{-1}), additional torsional motions (of order 25–30 km s^{-1}) were measured in type-II spicules (De Pontieu et al. 2012), which add to the helicity transport. The first detections of type-II spicules with IRIS data reinforced earlier work (Pereira et al. 2014).

Spicules exhibit a number of oscillation and wave types, and thus became a promising diagnostic tool for chromospheric and coronal wave heating scenarios (see review by Zaqarashvili and Erdelyi 2009). Evidence for upward propagating high-frequency Alfvén waves has been identified from dynamic wave-like spicules observed by SOT/ Hinode, finding that spicules are modulated by high-frequency waves ($\leq$ 0.02 Hz) or periods of $\geq$ 50 s (He et al. 2009). In a statistical analysis,

a mixture of upward propagating, downward propagating, and standing waves was found for Alfvén waves moving along spicules. The downward propagating spicules may be caused by reflection of initially upward propagating waves, which may spoil seismology techniques in spicular regions (Okamoto and De Pontieu 2011). The origin of type-I spicule oscillations are believed to be produced by (photospheric) magneto-acoustic oscillations that are funneled upward along type-I spicules and undergo longitudinal-to-transverse mode conversion into waves at twice the initial driving frequency (Jess et al. 2012).

3-D radiative MHD simulations of spicule-like structures have been conducted with the *Oslo Staggered Code* and many observed features of type-I spicules could be reproduced (Martinez-Sykora et al. 2009). From these simulations it was concluded that type-I spicules can be driven by a variety of mechanisms, such as p-modes, collapsing granules, magnetic energy releases in the photosphere and chromosphere, or convective buffeting of flux concentrations. Subsequent simulations with the same code suggests a driver mechanism for type-II spicules in which material is rapidly ejected from the chromosphere to the corona, generating a strong Lorentz force that squeezes the chromospheric material and results in a vertical pressure gradient and propels the spicule along the magnetic field with accompanied Joule heating (Martinez-Sykora et al. 2011, 2017). Other MHD simulations of Alfvén wave propagation along an open flux tube revealed Alfvén wave resonance cavities, which is claimed to be one of the most effective mechanism to explain the dynamics of spicules and a sufficient energy flux to heat the corona (Matsumoto and Shibata 2010). In the most recent simulations, spicules are shown to occur when magnetic tension is amplified and transported upward through interactions between ions and neutrals or ambipolar diffusion, where the tension is impulsively released to drive flows, heat plasma (through ambipolar diffusion), and generate Alfvénic waves (Martinez-Sykora et al. 2017).

The most intriguing question about spicules was always whether they can account for the heating of the quiet corona. It was estimated already early on from numerical simulations that torsional Alfvén waves carry a sufficient energy flux to heat the Quiet corona (e.g., Saito et al. 2001), which possibly is also the case for MHD kink waves (Kukhianidze et al. 2006), while slow MHD waves have an insufficient energy flux (Saito et al. 2001). Type-II spicules and their co-generated Alfvén waves are estimated to carry an average energy flux of $\approx 7 \times 10^5$ erg cm^{-2} s^{-1}, sufficient to power the Quiet Sun corona and solar wind (De Pontieu et al. 2009, 2011; Moore et al. 2011). Mode conversion of magneto-acoustic oscillations is estimated to produce an energy flux of $\approx 3 \times 10^8$ erg cm^{-2} s^{-1} (Jess et al. 2012). Considering the rapid cooling due to adiabatic expansion, however, Klimchuk (2012) argued that type-II spicules are insufficient to heat the corona, which still remains a matter of debate. In contrast, 2.5-D radiative MHD simulations are found to converge towards coronal (fan) and spicular structures observed with AIA and IRIS (De Pontieu et al. 2017).

5.6 Chromospheric Jets: Observations

Jets originating from the solar chromosphere have been observed in cool temperatures in Hα (also called surges), as well as in hot temperatures in UV, EUV, and soft X-rays. These jets have often supersonic speeds (10–1000 km s^{-1}) and are collimated along straight open magnetic field lines, or appear to follow along untwisting helical field lines. Jets are commonly associated with flux emergence or moving magnetic features. Theoretical models involve magnetic reconnection processes where outflows are driven by the slingshot effect. In the following we describe a well-observed jet event where the kinematics could be clearly disentangled.

A chromospheric jet lasting for more than 1 hr has been observed on 2007 February 9 at 02:40 to 04:20 UT on the west limb, with the SOT/Hinode telescope (with a resolution of $\approx$ 0.16″ and a cadence of 8 s), as well as with TRACE, STEREO, and RHESSI) by Liu et al. (2009), see Figs. 5.6 and 5.7. A very small flare of GOES-class A4.9 occurred simultaneously. The SOT/Hinode observations were obtained in the Ca II h passband, sensitive to chromospheric temperatures of (1–2) $\times$ 10^4 K. The time series of images shown in Fig. 5.6 illustrates the time evolution of the jet ejection, starting with a precursor of the jet at 02:40 UT (Fig. 5.6a), while the jet is fully formed at 02:51:31 UT (Fig. 5.6c), then swings with a whip-like motion towards the jet axis (Fig. 5.6d), and moves upward in a rotating motion about the jet axis (Fig. 5.6e–g), while some downward fall back is observed later on (Fig. 5.6h). Interestingly, the streamlines of the falling material follow almost straight lines with no detectable transverse motion (Fig. 5.6h). The

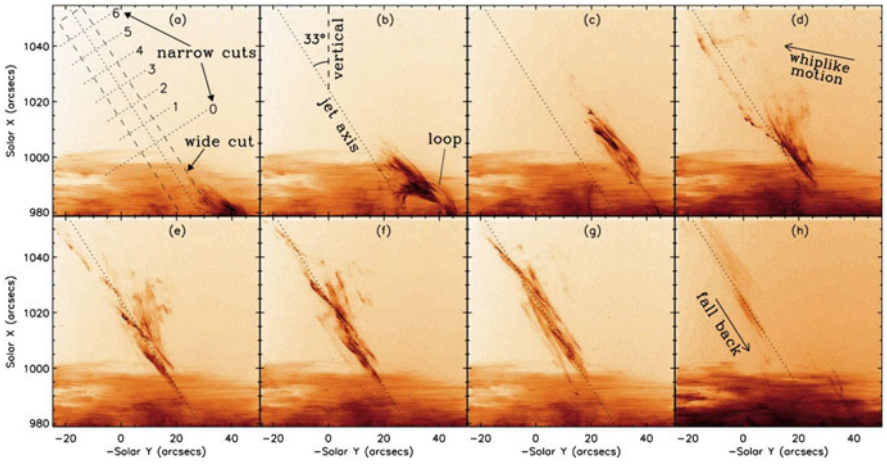

Fig. 5.6 Hinode Ca II h images of a chromospheric jet. The diagonal dotted line marks the jet axis, and the dashed lines mark a 10″ wide cut along the axis (Liu et al. 2009). (**a**) 02:47:30. (**b**) 02:50:02. (**c**) 02:51:31. (**d**) 02:53:23. (**e**) 02:54:11. (**f**) 02:54:43. (**g**) 02:55:15. (**h**) 03:10:35

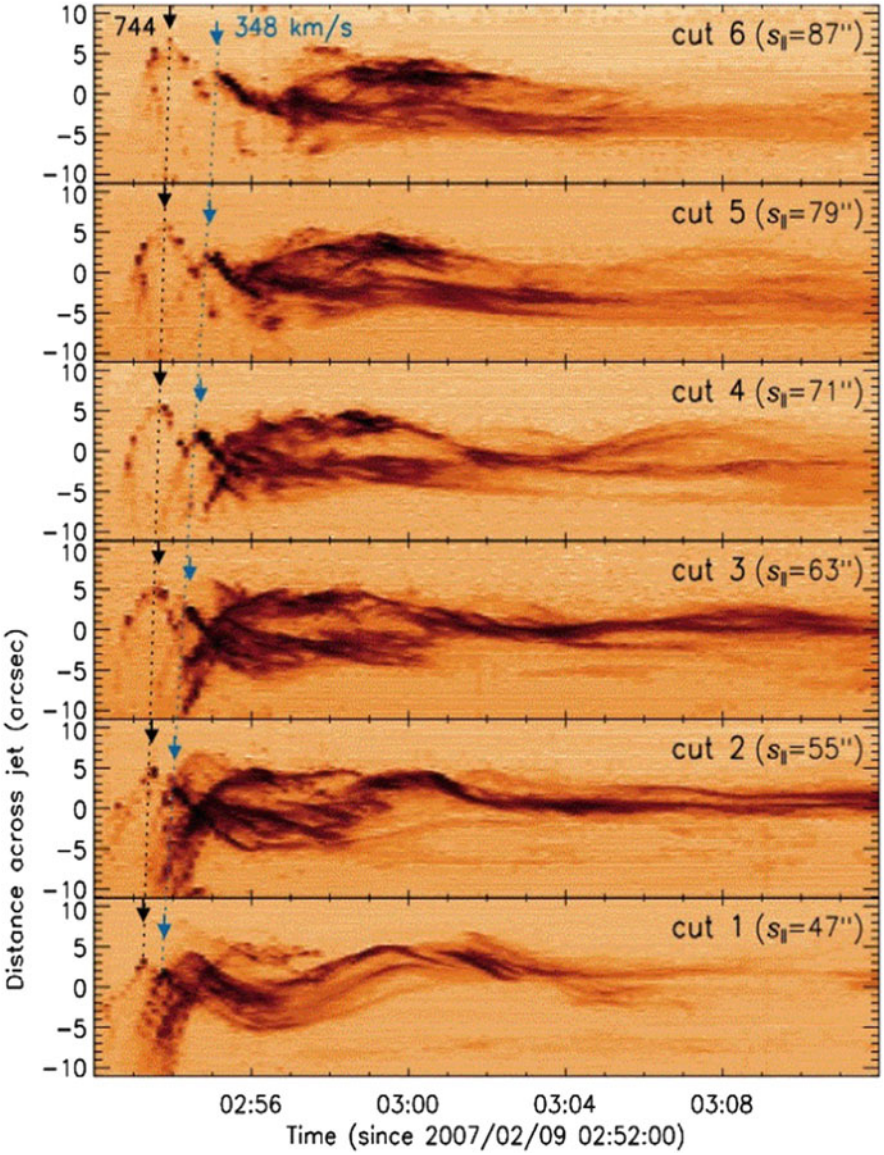

Fig. 5.7 Time-distance diagram from 1″ narrow cuts perpendicular to the jet, showing a damped oscillation. The two arrows in each panel point to the crests of the first two inverted-V-shaped tracks, indicating delays toward higher altitudes that correspond to an exciter speed of 744 and 348 km s^{-1} (Liu et al. 2009)

ejection occurred in three episodes separated by 12–14 min, with the downward velocities of the material decreasing with time. The upward velocities range from 438 to 33 km s^{-1}, while the downward velocities of the material falling back have

smaller values of $\approx 56 \pm 14$ km s^{-1}. The average acceleration amounts only to a fraction of the solar gravitational acceleration. The jet consists of fine threads (0.5″–2″ wide) which exhibit coherent, oscillatory transverse motions perpendicular to the jet axis (Fig. 5.7). The leading edge of the jet has a maximum speed of 744 ± 11 km s^{-1}, the transverse velocities vary from 151 to 26 km s^{-1}, the amplitudes are 6.0–1.9 Mm, and the periods are 250–536 s. These observations, which may be typical for many other jets also, are consistent with the scenario of untwisting helical threads (Fig. 5.7), which rotate about the axis of a single large cylinder and shed magnetic helicity into the upper atmosphere.

Chromospheric anemone jets (named after their morphological shape of a flower or sea anemone) were abundantly detected with SOT/Hinode so that they were considered as evidence for ubiquitous magnetic reconnection in the solar chromosphere/corona interface (Shibata et al. (2007). The typical characteristics measured with SOT/Hinode are lengths of 3″-7″ (2000–5000 km), widths of 0.2″–0.4″ (150–300 km), and speeds of 10–20 km s^{-1} (Shibata et al. 2007; Nishizuka et al. 2011). Based on previous observations with Yohkoh, the anemone shape is formed as a result of magnetic reconnection between an emerging magnetic dipole and a pre-existing uniform vertical (or slanted) field. The thermal energy of jets observed with SOT/Hinode is estimated to be of order $\approx 10^{26}$ erg (based on densities of $n_e \approx 10^{15}$ cm^{-3}, $T \approx 5000$ K), which is comparable with microflares, but larger than nanoflares ($\approx 10^{24}$ erg). The estimated average Poynting flux, however, is 10^3 erg cm^{-2} s^{-1} only (Shibata et al. 2007), mostly due to the relatively rare occurrence of jet events, which is several orders of magnitude below the coronal heating requirement.

Smaller *"micro-jet"* events were detected in umbral and penumbral chromospheres (Katsukawa et al. 2007; Rouppe van der Voort and de la Cruz Rodriguez 2013; Yurchyshyn et al. 2014), with estimated energies of 2×10^{23} erg (Katsukawa et al. 2007), which is even below the nanoflare limit.

Other small-scale jets are the so-called "IRIS network jets", which were observed in the magnetic network of the solar transition region and chromosphere, with observed speeds of 80–250 km s^{-1} (Tian et al. 2014), interpreted as the transition region counterparts of spicules (De Pontieu et al. 2017; Chintzoglou et al. 2018) and have been simulated with the Bifrost model.

Soft X-ray jets were detected in coronal holes also, one with a speed of ≈ 800 km s^{-1}, and several with a lower speed of ≈ 200 km s^{-1}, which is in the range of the fast and slow solar wind components (Cirtain et al. 2007). An erupting jet feature observed in a coronal hole was characterized as a *"blowout coronal jet"*, which is detected in soft X-rays and EUV, has velocities similar to type-II spicules, and exhibits spinning or unwinding during ejection (Sterling et al. 2010; Adams et al. 2014; Moore et al. 2015), sometimes associated with flares and/or radio type-III bursts (Hong et al. 2017).

A new phenomenon described as *"fast rotating swirls"* in the chromosphere was discovered by Wedemeyer-Böhm and Rouppe van der Voort (2009), which have rotating or vortex-like motions, similar to the helical jets (Liu et al. 2009) and

rotating sunspots on larger scales (Sect. 4.8). These events feature dark and bright rotating patches, which may consist of arcs, spiral arms, rings, or ring fragments. The fragments have a width or diameter of $\approx 0.2''$ and exhibit upflows with a Doppler shift of -2 to -7 km s^{-1}. A likely explanation is that the relative motion of associated bright points twists the magnetic field in the chromosphere, producing then propagating waves that spiral upwards, guided by the magnetic field structure, and produce the observed intensity signature of Doppler-shifted fragments (Wedemeyer-Böhm and Rouppe van der Voort 2009). Related phenomena are the ubiquitous torsional motions found in type II spicules (De Pontieu et al. 2012), possibly associated with Alfvénic waves, and driven by ion-neutral interactions or ambipolar diffusion (Martinez-Sykora et al. 2017).

A number of observed chromospheric jets lend evidence for the magnetic fan-spine topology, which can be characterized by an isolated coronal magnetic null point, surrounded by an anemone-like structure with opposite polarity, forming a fan surface (dome) below the null point and a spine above (e.g., Liu et al. 2011). Blobs in EUV jets were interpreted as plasmoids created by a magnetic reconnection process with tearing-mode instability and ejection along the jets (Zhang and Ji 2014). Other evidence for reconnection has been obtained from bidirectional flows in jets (Zhang and Zhang 2017).

5.7 Chromospheric Jets: Numerical Simulations

Recent numerical MHD simulations of jets have been performed mostly based on the theoretical scenario where jets are produced by a magnetic reconnection process that occurs between emerging flux and an overlying field structure in vertical or oblique direction.

Early resistive MHD simulations (Yokoyama and Shibata 1995, 1996) were criticized regarding their unrealistic temperatures ($T = 0.25$ MK) and densities (10^{12} cm^{-3}) for the solar corona, so that it was not possible to reproduce both the emerging flux and jets self-consistently, while a self-consistent treatment with more realistic coronal temperatures ($T \approx 1.0$ MK) was first performed in Nishizuka et al. (2008). Observations and matching MHD simulations are shown in Fig. 5.8 for a jet observed on the west limb in active region NOAA 10940 on 2007 February 9, 13:20 UT. The maximum height of the jet was $\approx 14,000$ km and the width of the jet was ≈ 6000 km. Figure 5.8a–c show Ca II h-line broadband filter snapshots taken with SOT/Hinode. The evolution of the modeled density and temperature in the MHD simulations are shown in Fig. 5.8d–i. In contrast to the values used in the Yokoyama and Shibata (1995) model, a higher coronal temperature ($T = 1.0$ MK) and a lower density ($n_e = 10^{10}$ cm^{-3}) was used. The resulting 2-D resistive MHD simulations with uniform gravitational field, but without thermal conduction, radiative cooling, or chromospheric evaporation, show that the jet is magnetically driven, rather than by the thermal pressure. The numerical simulations closely reproduce the observed co-existence of hot and cool jets adjacent to each other, as well as the generation and

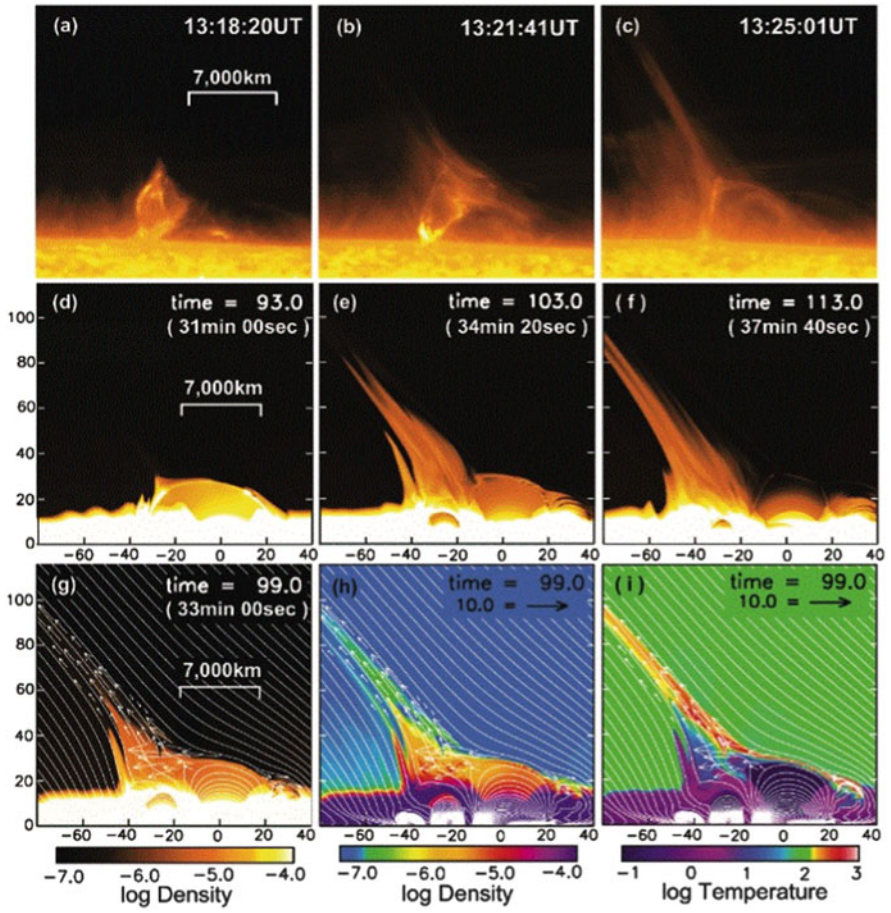

Fig. 5.8 Comparison between the Ca jet and simulated jets based on a reconnection model. (**a–c**) Ca II h broadband filter images of the Ca jet on 2007 February 9, taken with SOT/Hinode. (**d–f**) 2-D distributions of logarithmic electron density in the simulated jets. (**g–i**) 2-D distributions of density and temperatures of simulated jets (Nishizuka et al. 2008)

the propagation of Alfvén waves, and this way supports the magnetic reconnection model of Yokoyama and Shibata (1995).

Another approach is the scenario of shock wave-driven chromospheric jets, which has been simulated with a 1-D hydrodynamic code by Heggland et al. (2007). These simulations use a 1-D model of the upper atmosphere, with a monochromatic piston driven at the lower chromospheric boundary for creating magnet-acoustic waves. As these waves travel upward, the gain in amplitude steepens into shocks (because of the decreasing density with height), which then hit the transition region and thereby push the plasma upward. The code includes radiative loss due to collisional excitation of various ions (C, O, Ne, Fe), and due to thermal bremsstrahlung,

with thermal conduction, but ignores radiative transport. The simulations reproduce some features of dynamic fibrils (or jets), such as the "parabolic" height pattern of acceleration and deceleration, as wells as the correlation between velocity and deceleration, which largely confirms the scenario of jet formation by magneto-acoustic shock waves, which could explain type-I spicules.

In a similar scenario, but replacing the magneto-acoustic shock waves with a wave-induced magnetic reconnection model, where a monochromatic piston induces periodic reconnection, Heggland et al. (2009) simulated spicule-like jets with lengths and lifetimes that match observations. The 2-D code includes radiative loss and heat conduction and can render the time evolution of spectral signatures (such as Doppler shifts of Fe XII and Ca II IR), which are found to be similar to those of *"explosive events"*.

In a third study, Heggland et al. (2011) present results on the wave propagation and jet formation in the chromosphere obtained with the 2-D Bifrost code, which includes radiative loss, thermal conduction, artificial viscosity and resistivity, magnetic diffusivity, and radiative transfer, but omits time-dependent ionization. The boundary conditions are set by chromospheric waves with periods longer than the acoustic cutoff period. It is found that the velocity signal is dominated by waves with periods around 5 min in regions of strong inclined fields, whereas 3 min waves dominate in regions of weak or vertically oriented fields. Therefore, the field inclination is very important for long-period propagation, and consequently jets in inclined fields and those in vertical fields are different, in agreement with observations of dynamic fibrils.

Data-driven 3-D radiative MHD simulations are the present state-of-the-art, where the (observed) time-dependent boundary conditions (of the velocity and/or magnetic field) are used in each time step of the simulations. Such a code is used in Cheung et al. (2015), using IRIS, SOT/Hinode, and SDO data (Fig. 5.9). Simultaneous observations by SDO and Hinode show that the jets emanate from the source region comprising a pore embedded in the interior of a supergranule, leading to a spine-fan magnetic topology in the coronal field that is amenable to jet formation. It shows that the emergence of current-carrying magnetic field in the vicinity of the pore supplies the magnetic twist needed for recurrent helical jet formation (Cheung et al. 2015).

The motion of *moving magnetic features (MMF)* can lead to the production of a jet. A magnetic reconnection process with tearing-mode instability produces plasmoids that correspond to the observed moving blobs in anemone jets. An increase in the reconnection-driven thermal pressure at the base of the jet induces a train of slow-mode shocks that propagate upward (Yang et al. 2013; Takasao et al. 2013; Gonzalez-Aviles et al. 2017). Jet simulations with the global Alfvén wave solar model show that the outwardly propagating torsional Alfvén waves have a significant impact on the large-scale corona (Szente et al. 2017). The most recent simulations reproduce spicules that are driven by ion-neutral interactions or ambipolar diffusion (Martinez-Sykora et al. 2017).

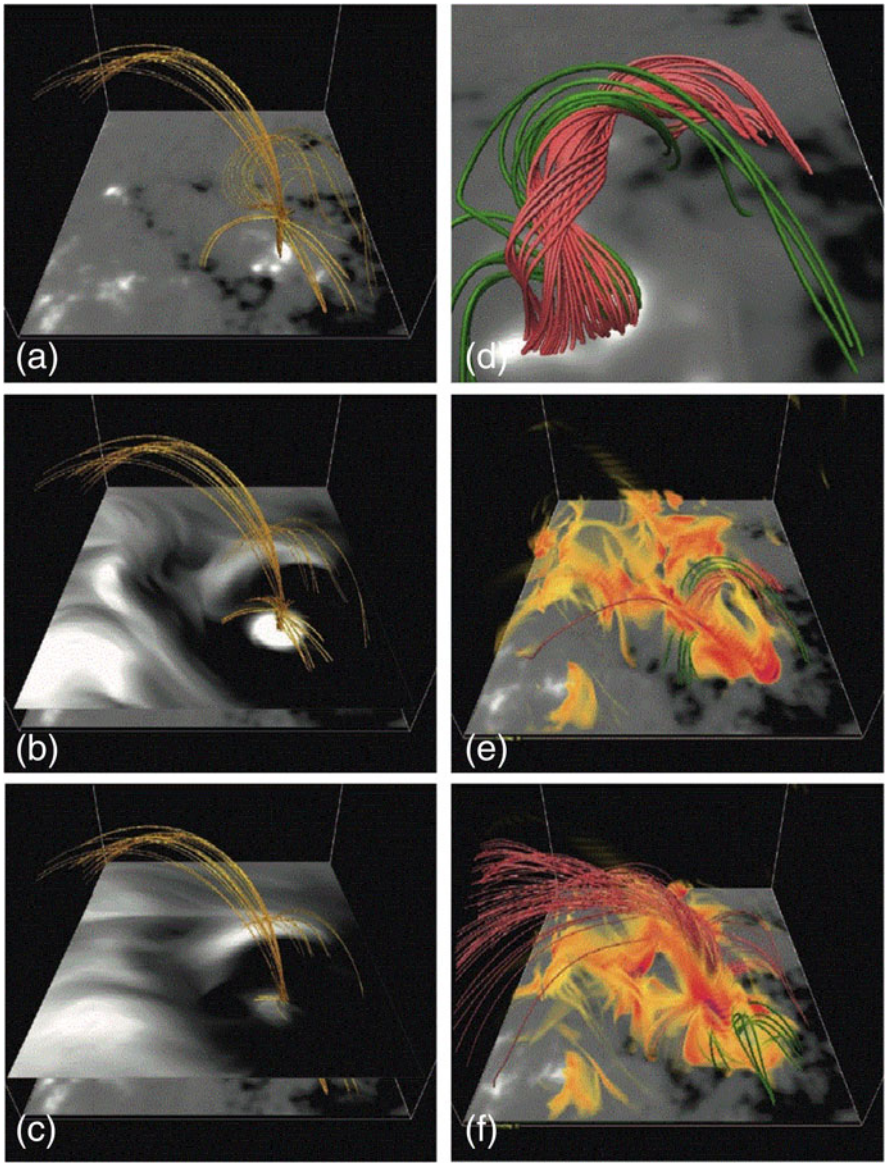

Fig. 5.9 Jet-like magnetic evolution in a data-driven model: (**a**) B_z at z=1.0 Mm, (**b**) B_z at z=4.0 Mm, (**c**) B_z at z=8.0 Mm. Magnetic configuration on 2013 July 21 at 11:02 UT in the vicinity of a coronal null point reveals a fan-spine topology, with the spine connecting the null point with the underlying parasitic polarity: (**d**) Close-up view of magnetic flux rope at 12:55 UT, (**e**) Magnetic field at 12:59 UT, (**f**) Magnetic field at 13:37 UT. Pink magnetic field lines are traced from a stationary grid of points. At 13:37 UT, field lines traced from the same set of points reveal a set of inclined twisted field lines aligned with the background inclined field. Green field lines are traced from $z = 0$ from the parasitic polarity. The semi-transparent orange/red surfaces in panels (**e**) and (**f**) indicate regions of strong current density (Cheung et al. 2015)

5.8 Ellerman Bombs

Historically, Ferdinand Ellerman from the *Mount Wilson Solar Observatory* reported in 1917 a phenomenon of bright emission in both wings of the Hα line, originating from several locations of the low chromosphere, which later has been referred to as *"Ellerman bomb"*, due to its short-lived ($\approx$ 10–20 min) and small-scale nature ($\lesssim 1.1''$–$1.8''$). Statistics, morphology, and energetics of 593 Ellerman bomb events observed with the balloon-borne *Flare Genesis Experiment* is described in Georgoulis et al. (2002): The preferential location of Ellerman bomb events was found to be in the low chromosphere, either above or in the absence of photospheric neutral magnetic lines. They are associated with photospheric downflows, and their location follows the transverse mass flows in the photosphere. Fractal dimensions for their area ($A \propto L^{1.4}$) and power-law functions were found for their duration, $N(D) \propto D^{-2.2}$, their area distribution, $N(A) \propto A^{-2.4}$, their maximum integrated contrast, $N(I_m) \propto I_m^{-3.5}$, and their total integrated contrast, $N(I_t) \propto I_t^{-2.1}$. The finding of a fractal dimension and power law distributions supports an interpretation in terms of a nonlinear energy dissipation process with self-organized criticality. Georgoulis et al. (2002) estimates also the total energy of Ellerman bomb events (including radiative loss and thermal conduction) and finds an energy range of $E \approx 10^{25}$–10^{26} erg, based on a temperature enhancement of $\Delta T \approx 2000$ K and time scales of order a few seconds. Because of this energy range, Fang et al. (2006) dubbed the Ellerman bomb events as "submicroflares". Using NICOLE inversions of spectropolarimetric data yield on average an energy of $(3.4 \pm 0.5) \times 10^{24}$ erg of stored magnetic energy to be dissipated during an Ellerman bomb event (Reid et al. 2016). The volumetric heating rate is $\varepsilon \approx (3/2) n k_B \Delta T \approx 0.9$ erg cm^{-3} s^{-1}. For the triggering mechanism of Ellerman bomb events, Georgoulis et al. (2002) suggest a stochastic magnetic reconnection process caused by the turbulent evolution of the low-lying magnetic fields and the continuous reshaping of separatrix layers.

In one study of Ellerman bomb events, Pariat et al. (2004) investigates the magnetic configuration, in particular the location of Ellerman bomb events with respect to the loci of *bald patches* (Fig. 5.10). Bald patches are defined by concave upward-curved (or horizontal) segments of magnetic field lines, in contrast to normal (bipolar or sigmoid) coronal loops that have an upward convex curvature. Pariat et al. (2004) find that Ellerman bomb events occur during flux emergence, and many of them are located near moving magnetic dipoles in which the vector magnetic field is nearly tangential (horizontal) to the photosphere. A linear force-free magnetic field extrapolation reveals that half (23 out of 47) of the Ellerman bomb events are cospatial with bald patches, while a third (15 out of 47) is located at the footpoints of very flat separatrix field lines passing through distant bald patches. This topology confirms that many Ellerman bomb events and bald patches are linked by a hierarchy of elongated flux tubes showing aperiodic spatial undulation (Fig. 5.11, left), whose wavelengths are typically above the threshold of the Parker instability. The rise of undulatory flux tubes is caused by the Parker instability,

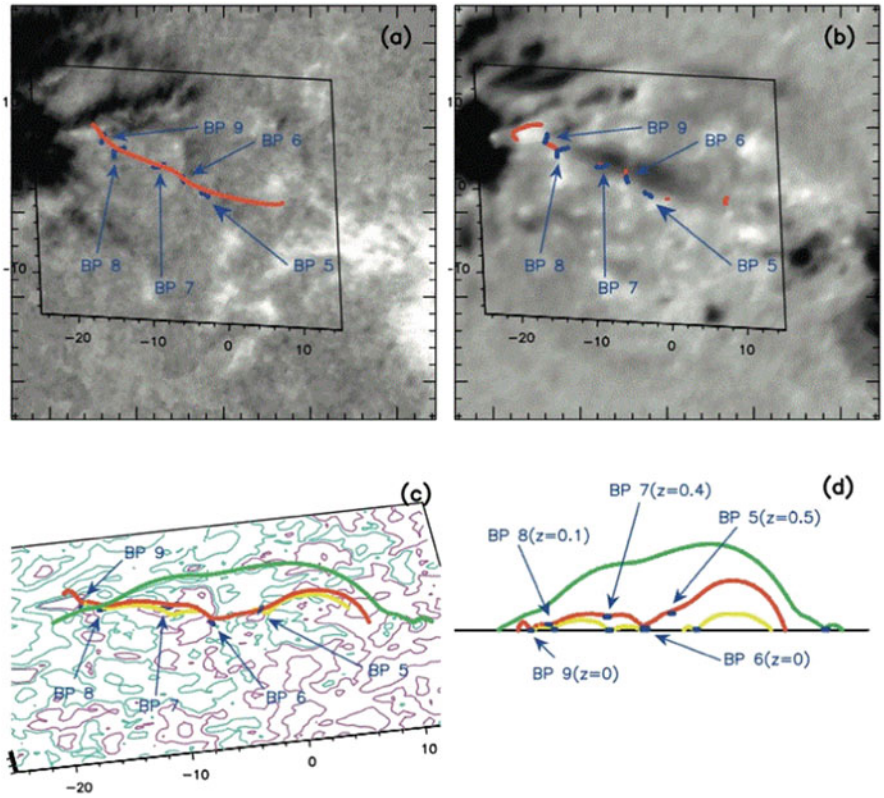

Fig. 5.10 Example of an undulatory flux tube: only one field line of the "serpentine flux tube" (red curve) is shown. The blue dots (denoted BP5-BP9) represent bald patches: (**a**) magnetogram, (**b**) Hα 0.8 Å filtergram, (**c**) projection view of undulatory flux with isocontours of $B_z = \pm 50$, 300, 900, and 1800 G, (pink for positive and blue for negative values), (**d**) side view of undulatory field lines (Pariat et al. 2004)

while the dipped lower parts emerge because of magnetic reconnection. Therefore, Ellerman bombs are the signature of the resistive emergence of undulatory flux tubes (Pariat et al. 2004).

Numerical 2-D MHD simulations were performed by Isobe et al. (2007) in order to study the effects of resistive processes in the dynamics of magnetic flux emergence and its relation to Ellerman bombs, using the scenario of flux emergence in the formation and expansion of Ω-shaped loops due to the Parker instability. Since the Parker instability has the largest growth rate at a finite wavelength $\lambda_p \approx (10\text{–}20) \times H$, where H is the scale height (≈ 200 km in the solar photosphere), a number of magnetic loops may rise from the initial flux sheet if it is sufficiently long. The MHD simulations indeed show multiple emerging loops expanding in the atmosphere like an undulating serpentine structure (Fig. 5.11, left), leading to magnetic reconnection and local heating that may account for Ellerman bombs, and

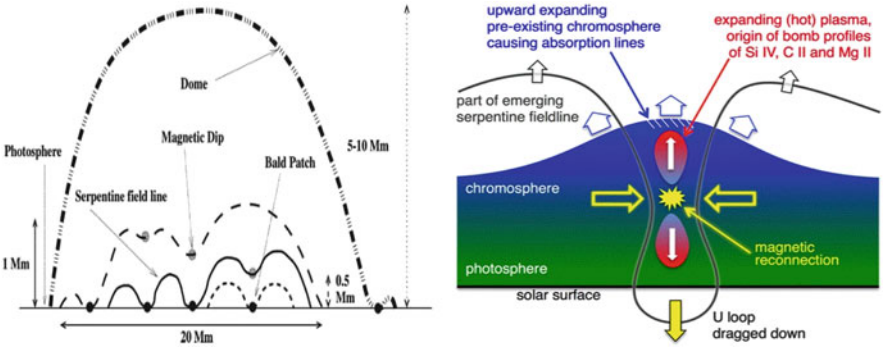

Fig. 5.11 *Left:* Sketch of the field lines overlying the emerging flux, indicating the locations of bald patches, serpentine field lines, and magnetic dips in a dipolar active region (Pariat et al. 2004). *Right:* Cartoon of a reconnection-driven Ellerman bomb scenario: An undulating magnetic field line emerges and the resulting U-loop gets dragged down. Being squeezed together, the magnetic field reconnects, and plasma is heated and accelerated deep into the atmosphere. The bidirectional outflow from the reconnection region causes the double-humped line profiles of Si IV, C II, and Mg II, while the cool material above causes the absorption lines (Peter et al. 2014)

produces high-temperature reconnection jets later on. Compression of the plasma in between the expanding loops forms cool and dense plasma structures, is similar to those observed in Hα surges (Isobe et al. 2007). Further simulation studies on flux emergence and *"sea-serpent"* shaped magnetic fields were accomplished with 3-D MHD codes (Archontis and Hood 2009; Pariat et al. 2009).

Further observational studies on Ellerman bombs focus on the correlation between the Hα and UV signatures of Ellerman bombs using BBSO and TRACE data (Qiu et al. 2000), Hα and Ca II 8542 Å line profile modeling using THEMIS data (Fang et al. 2006), spectrophotometric analysis of Ellerman bombs in the Ca II, Hα, and UV range (Pariat et al. 2007; Watanabe et al. 2008), the height of gas flows in an Ellerman bomb (Matsumoto et al. 2008), identification of Ellerman bombs in CRISP (SST) and SDO data (Watanabe et al. 2011; Vissers et al. 2013), simultaneous observations of Ellerman bombs with IRIS and SST (Vissers et al. 2015), and observations of Ellerman bombs in the He I D_3 and He I 10,830 Å line (Libbrecht et al. 2017). Vissers et al. (2013) conclude that Ellerman bombs are purely photospheric (magnetic reconnection) phenomena, rather than chromospheric, incapable of breaking through the overlying canopy. Ellerman bombs occur at sites of strong-field magnetic flux cancellation between small bipolar strong-field patches that rapidly move together over the solar surface (Vissers et al. 2013). Ellerman bombs in the photosphere appear to be shielded by overlying chromospheric fibrils in the cores of strong lines, which suggests that the reconnecting photospheric gas underneath is heated sufficiently to temporary stages of ionization normally assigned to the transition region and corona (Vissers et al. 2015).

Recent observations with IRIS have revealed pockets of hot gas ($T \approx (2\text{–}8) \times 10^4$ K) (Hansteen et al. 2017), potentially resulting from magnetic reconnection in the partially ionized lower solar atmosphere, which were dubbed *"IRIS bombs"* (Peter et al. 2014). A study identified 10 simultaneous IRIS bomb and Ellerman bomb events, but only 3 cases exhibited an unambiguous connection (Tian et al. 2016). A recent model that reconciles the emission and absorption in the various IRIS UV lines (Si IV, C II, and Mg II) (Peter et al. 2014), is depicted in Fig. 5.11 (right).

5.9 Chromosphere: Kelvin-Helmholtz Instability

The Kelvin-Helmholtz instability can occur in a single continuous fluid (if there is velocity shear) or at the interface between two fluids (if they have different velocities). In solar physics, studies on the *Kelvin-Helmholtz instability (KHI)* have increased dramatically since the new millennium, applied to a number of phenomena with velocity shear, such as surges, jets, plumes, and spicules in the photosphere and chromosphere, but also to the corona, coronal streamers, and the solar wind. A major motivation to study the KHI is the evolution from laminar to turbulent flows, which affects the efficiency of coronal heating. For reviews on this subject see Mishin and Tomozov (2016), Kuridze et al. (2016), and Zhelyazkov (2015).

An early numerical 2-D hydrodynamic simulation that demonstrates the evolution of the KHI in photospheric flows has been pioneered by Karpen et al. (1993). These numerical simulations show that typical photospheric flows are indeed susceptible to the KHI, with rapid nonlinear growth times approximately half of the granule lifetime. Approximately half of the initial kinetic energy is transferred to smaller spatial scales, the bulk being concentrated at the scale of the persistent KHI vortices ($\approx$ 100 km). Hence the KHI produces vortical structures in intergranular lanes comparable to a typical *fluxule* radius, which is precisely the right scale for maximum power transfer to the corona (Karpen et al. 1993). The numerical simulations were generalized to 2-D MHD (Keppens et al. 1999) and 3-D MHD codes (Keppens and Toth 1999), revealing the nonlinear dynamics of the KHI in magnetized jets (Fig. 5.12). Reconnection events speed up the buildup of a global plasma circulation, since the initial current sheet gets amplified by the vortex flow and can become unstable to tearing instabilities, forming magnetic islands (Keppens et al. 1999). The initially weak magnetic field becomes locally dominant in the nonlinear dynamics before and after saturation, and this way controls the jet deformation and eventual breakup (Keppens and Toth 1999). The response of a solar small-scale and weak magnetic flux tube to photospheric twisting motions was simulated with a 3-D MHD code (Murawski et al. 2016). The twists produce rotation of the magnetic field lines. A perturbation of magnetic field lines propagates upward, driving vertical and azimuthal flows as well as plasma compressions and rarefactions in the form of eddies. The eddies resulting from the sheared azimuthal

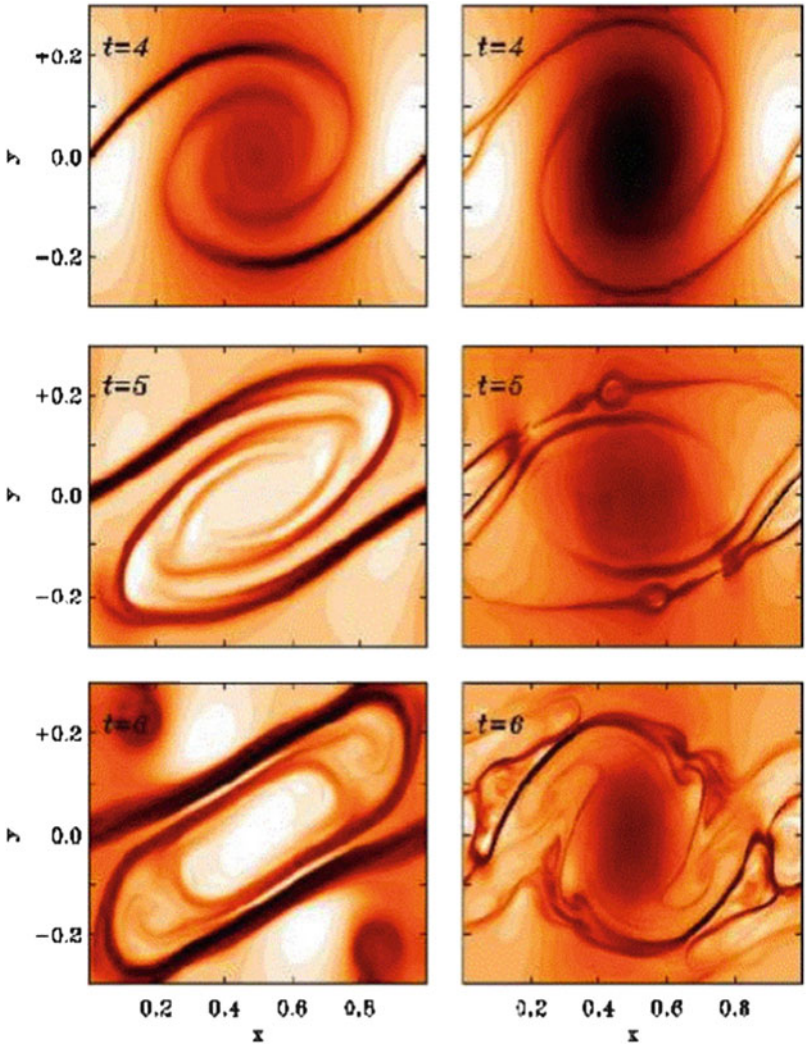

Fig. 5.12 Time evolution of the Kelvin-Helmholtz instability in the non-linear growth phase, computed with the 2-D MHD *Versatile Advection Code (VAC)*. The left panels show the plasma density, and the right frames show the magnetic field (or the reversed MHD case), (Keppens et al. 1999)

flow seed the KHI between the flux tube and the ambient medium (Murawski et al. 2016). Recent 2-D resistive MHD simulations show that the plasmoid instability and KHI along jets are both possible causes of the formation of blobs observed at EUV wavelengths (Ni et al. 2017).

Analytical studies focused on the KHI and shear instability with a helical flow around a magnetic flux tube, finding that a sharp jump of the azimuthal flow com-

ponent of a cylindric flux tube boundary always leads to KHI for sufficiently small wavelengths of the perturbation (Kolesnikov et al. 2004). A parametric study of the KHI growth rates finds that fluting-like modes can develop a KHI on timescales comparable to the period of kink oscillations of the flux tube. The azimuthal component of the magnetic field is believed to be responsible for suppressing the KHI in a stable coronal loop (Soler et al. 2010). The linear phase of the KHI at an interface between two partially ionized magnetized plamsas was investigated in the presence of a shear flow. For the particular case of turbulent plumes in prominences, it was concluded that sub-Alfvénic flow velocities can trigger the KHI thanks to the ion-neutral coupling (Soler et al. 2012). Turbulent flows in solar prominences with sub-Alfvénic velocities may be interpreted as consequences of the KHI in partially ionized plasmas (Martinez-Gomez et al. 2015). The conditions under which kink MHD waves propagating along photospheric uniformly twisted flux tubes with axial mass flow become unstable has been computed as a consequence of the KHI. It was found that this occurs above a threshold Alfvén-Mach number of 1.25, such as for flow speeds of 10 km s^{-1} inside the flux tube, and 12.5 km s^{-1} outside (Zhelyazkov and Zaqarashvili 2012). Twisted and rotating jets are unstable to KHI when the kinetic energy of rotation is more than the magnetic energy (Zaqarashvili et al. 2015). Azimuthal magnetic fields of 1–5 G can stabilize observed rotations in spicules (or macrospicules) and in soft X-ray and EUV jets, for instability growth times of several seconds for spicules (or macrospicules), and a few minutes for soft X-rays and EUV jets (Zaqarashvili et al. 2015). A study of the KHI in cool solar jets in the framework of Hall MHD finds that the stability of MHD modes depends upon 4 parameters: (i) the density contrast between the flux tube and its environment, (ii) the ratio of external and internal magnetic fields, (iii) the ratio of the Hall to the length scale l_{Hall}/a, and (iv) the value of the Alfvén Mach number defined as the ratio of the tube axial velocity to Alfvén speed inside the flux tube (Zhelyazkov and Dimitrov 2018). It is also established that the kink (m=1) mode is unstable to KHI for large density contrasts, depending on the threshold l_{Hall}/a, but not for small density contrast, nor in the case of the sausage (m=0) mode (Zhelyazkov and Dimitrov 2018).

The evolutionary conditions for the KHI in a Hα surge, observed in active region NOAA 8227 on 1998 May 30, were studied in Zhelyazkov et al. 2015). A jet with speeds in the range of 45–50 km s^{-1}, width of 7 Mm, and electron density of 3.83×10^{10} cm^{-3} is assumed to be confined in a twisted magnetic flux tube embedded in a magnetic field of 7 G. The temperature of the surge is $\approx 10^5$ K, surrounded by a coronal temperature of 2 MK. The resulting Alfvén speed is 78 km s^{-1}. Modeling of the magnetic field inside (helical) and outside (helical or uniform) the surge structure yields the result that the magnetic field configuration is unstable against the KHI instability only for negative mode numbers (m=−3, −4), and that the instability occurs at sub-Alfvénic critical flow velocities in the range of 25–50 km s^{-1} (Zhelyazkov et al. 2015).

Small-scale features, such as *rapid redshifted* and *blueshifted excursions*, appearing as *high-speed jets* in Hα line wings were analyzed in high-resolution *CRISP/SST* images (Kuridze et al. 2016). Modeling the jets as twisted magnetic

flux tubes moving along their axis and with an incompressible MHD code, these jets were found to be unstable to KHI with very short (few seconds) instability growth times and high upflow speeds. The generated vortices and unresolved turbulent flows associated with the KHI could be observed as a broadening of chromospheric spectral lines. Ion-neutral collisions may lead to fast heating of the KHI vortices over time scales comparable with the lifetime of the observed chromospheric jets (Kuridze et al. 2016). Transverse waves that are induced by KHI rolls are described in Antolin et al. (2018).

Although the dynamics of KHI has been studied theoretically, either with analytical or numerical methods, the observational detection and modeling of KHI conditions is very difficult in cool structures (photosphere, chromosphere, Hα surges, jets, spicules, prominences). Realistic modeling requires 3-D radiative MHD codes, while the same task is much more conducive for hot plasma structures (corona, flares, CMEs), where DEM modeling in optically thin (EUV and soft X-ray) emission is straightforward.

5.10 Chromospheric Heating Models

The heating problem of the solar chromosphere has been investigated in terms of two major physical mechanisms: (i) magneto-acoustic waves, and (ii) Alfvén waves or turbulence. Alternative heating mechanisms in the chromosphere include the dissipation of Pedersen currents, the Farley-Buneman instability, or Joule dissipation (e.g., as shown in Bifrost models by de la Cruz Rodriguez et al. 2012).

(i) Magneto-acoustic waves have been considered as a likely mechanism for heating of the chromosphere because acoustic waves are likely to be generated by sub-photospheric convection and global p-modes. Chromospheric heating models have traditionally been studied with time-dependent, one-dimensional, radiation-hydrodynamic numerical codes. However, it has been demonstrated that this model leads to unrealistic shock mergings, to the artificial formation of unusually strong shocks, and the artificial destruction of high-frequency acoustic power, so that comparisons with observations lead to a severe misjudgement of the nature of the chromospheric heating process (Ulmschneider et al. 2005). The detection of high-frequency (10–50 mHz or 20–100 s) acoustic waves were estimated to have an energy flux, based on TRACE 1600 Å data, that is about an order of magnitude too low to balance radiative losses, and thus cannot constitute the dominant heating mechanism of the solar chromosphere (Fossum and Carlsson 2005). Also SOT/Hinode Ca II h-line and blue continuum broadband observations show no dominant power at small spatial scales. The total energy flux in acoustic waves of frequency 5–40 mHz (or 25–200 s) entering the internetwork chromosphere of the Quiet Sun is estimated to be less than 0.8×10^6 erg cm^{-2} s^{-1}, which is inadequate to balance

the radiative losses in a static chromosphere by a factor of five (Carlsson et al. 2007).

Acoustic waves that drive shocks and lead to type-I spicules and dynamic fibrils were suggested by De Pontieu et al. (2004). The work of Fossum and Carlsson (2005) was criticized based on insufficient spatial resolution of the used TRACE data (Cuntz et al. 2007; Kalkofen 2007), but was addressed by Carlsson et al. (2007). It was shown that inclined magnetic fields at the boundaries of large-scale convective cells (supergranules) provide *"portals"* through which low-frequency < 5 mHz (or > 200 s) magneto-acoustic waves can propagate into the chromosphere, which opens up the feasibility of magneto-acoustic wave heating to balance the radiative losses of the chromosphere (Jefferies et al. 2006). Further support for heating of the magnetic network grains (observed in Ca II h and k) by magneto-acoustic waves was suggested based on 2-D MHD simulations of chromospheric shocks (Fig. 5.13) (Hasan and van Ballegooijen 2008). *Local thermodynamic equilibrium (LTE)* inversions of spectropolarimetric data in the Ca II h line core led to the conclusion that acoustic waves are steepening into shocks and this way can heat the chromosphere (De Pontieu et al. 2004; Beck et al. 2008). Recent work using Ca II line core data from IBIS suggests that the spatial correlation between Ca II maps of radiative losses and acoustic flux is 72%, and the deposited acoustic flux provides at least 23% of the energy radiated in the Quiet chromosphere, and 54% in plage regions, respectively (Sobotka et al. 2016).

An alternative chromospheric heating mechanism is the Farley-Buneman instability, which is triggered by the cross-field motion of the neutral component of the partially ionized gas at velocities in excess of the ion-acoustic velocity. This instability occurs in the solar chromosphere because electrons become strongly magnetized just above the photosphere, while heavy ions and protons remain unmagnetized, and only at the very top of the chromosphere do they become magnetized. Convective overshoot motions are the drivers of the Farley-Buneman instability and could in principle provide enough energy to account for the upper chromosphere radiative losses in the Quiet-Sun internetwork and network lanes (Fontenla et al. 2008). However, observational evidence for this process is still lacking.

(ii) Alfvén waves, kinetic Alfvén waves, or Alfvén turbulence are other contenders of heating mechanisms for the chromosphere. In a 3-D (reduced) MHD model for the propagation and dissipation of Alfvén waves in coronal loops (which include the chromospheric footpoints), waves on small spatial scales (less than 100 km) originate inside kilogauss flux elements located in the photosphere. The increase of the Alfvén speed with height in the chromosphere and transition region causes strong wave reflection, leading to counter-propagating waves and turbulence at the loop footpoints. Alfvén wave turbulence provides heating in both the coronal parts and in the chromospheric footpoints, if the random footpoint motions is 1–2 km s^{-1} and the time scales are 60–200 s, while the heating rate per unit volume in the chromosphere is two to three orders of magnitude higher in the chromosphere than in the corona

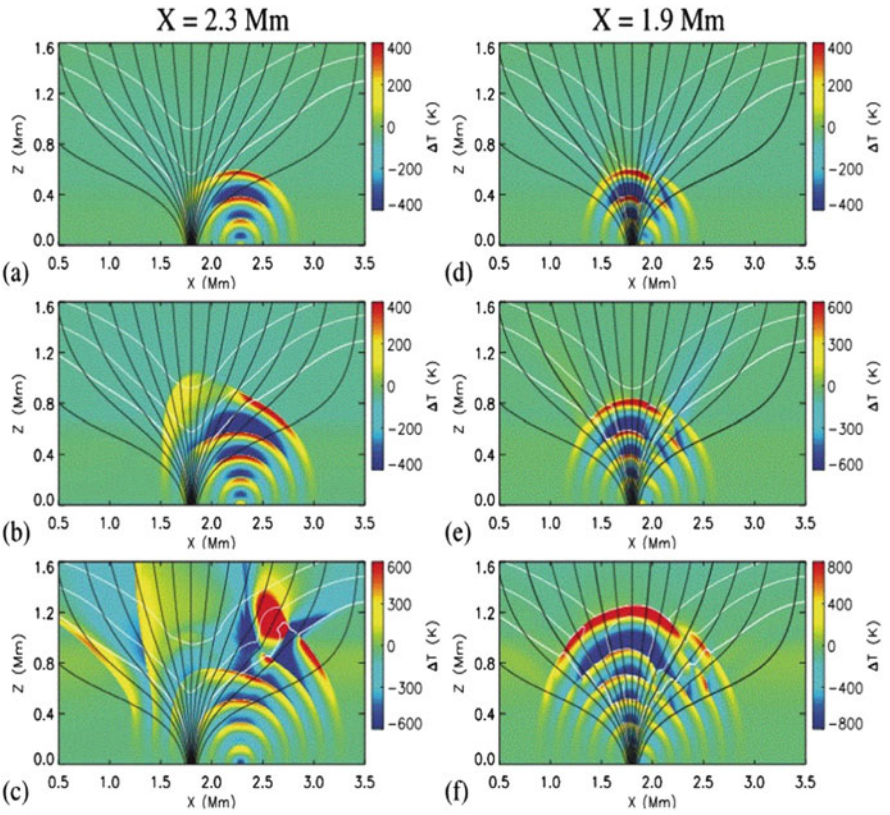

Fig. 5.13 Numerical 2-D MHD simulations of the propagation of magneto-acoustic waves and shock formation in the chromospheric network, depicted with temperature perturbation maps at (**a**) t=76 s, (**b**) 101 s, and (**c**) 140 s in a single tube due to a localized vertical periodic motion at $z = 0$, $x = 2300$ km (panels **a**–**c**) and $x = 1900$ km (panels **d**–**f**) with an amplitude of 750 m s^{-1} and a period of 24 s. The black curves indicate the magnetic field lines, and the white curves indicate contours of constant β, corresponding to $\beta = 0.1, 0.3$, and 1.0 (Hasan and van Ballegooijen 2008)

(van Ballegooijen et al. 2011). A 3-D (reduced) MHD model of Alfvén-wave-driven turbulence has been applied to open flux tubes in a coronal hole, near a streamer, and in a strong-field active region, and it was found that the heating rate variability of turbulent heating reproduces coronal *differential emission measure (DEM)* distributions, and this way opens the possibility that turbulent heating in the chromosphere by Alfvén waves can accelerate the solar wind in open flux tubes (Woosley and Cranmer 2015), although nonlinear coupling of Alfvén waves with slow-mode shock waves is expected also (Hollweg 1981; Arber et al. 2016). Direct observational evidence of Alfvén waves heating chromospheric plasma in a sunspot umbra through the formation of shock fronts is presented in Grant et al. (2018).

1.5-D non-ideal MHD simulations were used to test models of direct resistive dissipation of high-frequency Alfvén waves through Pedersen resistivity in chromospheric heating models (Arber et al. 2016). It was found that the Hall term does not affect the heating rates. If plasma compressibility is taken into account, shocks are produced through the ponderomotive coupling of Alfvén waves to slow modes, and shock heating dominates the resistive dissipation. The ponderomotive coupling of Alfvén waves to sound waves is found to be more important in chromospheric heating than Pedersen dissipation through ion-neutral collisions (Arber et al. 2016). Arguments for Pedersen dissipation are based on the fact that the combination of weak ionization and strong magnetization implies that the main MHD resistive heating mechanism is the dissipation of ion (mainly proton) Pedersen currents (Goodman 2011). Using the 2.5-D MHD code *Lare2d*, photosphere-driven Alfvén and kink waves propagating upwards into an expanding flux tube, embedded in a model chromosphere has been simulated (Brady and Arber 2016). It is shown that the ponderomotive coupling from Alfvén and kink waves into slow modes generates shocks, which both heat the upper chromosphere and drives spicules, consistent with the observed type-I spicules (Brady and Arber 2016). Using a 3-D MHD code that takes into account the ambipolar term from the generalized Ohm's law, it is shown that perturbations caused by magnetic waves can be effectively dissipated due to ambipolar diffusion (Shelyag et al. 2016). The dissipation of currents in the chromosphere is enhanced by orders of magnitude due to the action of ambipolar diffusion, as compared with the standard Ohmic diffusion (Khomenko and Collados 2012). Martinez-Sykora et al. (2012, 2017) use the most realistic model of the chromosphere (Bifrost) and show that ambipolar diffusion can efficiently heat the chromosphere. Also, Bifrost has shown that Joule heating of currents caused by braiding can heat the chromosphere (e.g., de la Cruz Rodriguez et al. 2012).

In sunspots, atmospheric models show a higher temperature than the surrounding Quiet Sun in the upper chromosphere, although they are dark in the photosphere. Comparisons between acoustic wave heating and kinetic Alfvén wave heating show that the heating by kinetic Alfvén waves can dominate sunspot chromospheric heating at heights above 850 km, probably due to increased ionization (Wu and Fang 2007). Resistive current dissipation contributes to heat the sunspot umbra in chromospheric heights, but more importantly in the penumbra (Socas-Navarro 2005).

In summary, although a number of physical models has been proposed to understand the highly inhomogeneous chromosphere and its most dynamic spicular structures, observational tests have been carried out with widely different levels of rigor, so that the ultimate answer of the dominant physical mechanism(s) is still outstanding.

References

(5.1) Chromospheric Models

Alissandrakis, C.E., Patsourakos, S., Nindos, A., et al. 2017, *Center-to-limb observations of the Sun with ALMA. Implications for solar atmospheric models*, A&A 605, A78, [2 c, 2 c/y].

Avrett, E.H. and Loeser, R. 2008, *Models of the solar chromosphere and transition region from SUMER and HRTS observations: Formation of the EUV spectrum of hydrogen, carbon, and oxygen*, ApJS 175, 229, [150 c, 16 c/y].

Avrett, E.H., Tian, H., Landi, E., et al. 2015, *Modeling the chromosphere of a sunspot and the Quiet Sun*, ApJ 811, 87, [4 c, 2 c/y].

Carlsson, M. and Stein, R.E. 1995, *Does a nonmagnetic solar chromosphere exist?* ApJ 440, L29, [268 c, 12 c/y].

Carlsson, M. 2007, *Modeling the solar chromosphere*, in ASP Conf. Ser. 368, The physics of chromospheric plasmas, (ed. P. Heinzel, R. Dorotovic, and R.J. Rutten), (San Francisco: ASP), 49, [15 c, 1 c/y].

Carlsson, M. 2008, *3D radiative transfer in stellar atmospheres*, Physica Scripta 133, 014012, [7 c, 1 c/y].

Carlsson, M., Hansteen, V.H., Gudiksen, B.V., et al. 2016, *A publicly available simulation of an enhanced network region of the Sun*, A&A 585, A4, [58 c, 39 c/y].

Fontenla, J.M., Balasubramaniam, K.S., and Harder, J. 2007, *Semiempirical models of the solar atmosphere. II. The Quiet-Sun chromosphere at moderate resolution*, ApJ 667, 1243, [63 c, 6 c/y].

Fontenla, J.M., Curdt, W., Haberreiter, M., et al. 2009, *Semiempirical models of the solar atmosphere. III. Set of non-LTE models for FUV and EUV irradiance computation*, ApJ 707, 482, [108 c, 13 c/y].

Golding, T.P., Leenaarts, J., and Carlsson, M. 2016, *Non-equilibrium helium ionization in an MHD simulation of the solar atmosphere*, ApJ 817, 125, [12 c, 8 c/y].

Golding, T.P., Leenaarts, J., and Carlsson, M. 2017, *Formation of the helium EUV resonance lines*, A&A 597, A102, [6 c, 6 c/y].

Leenaarts, J., Carlsson, M., Hansteen, V., et al. 2007, *Non-equilibrium hydrogen ionization in 2-D simulations of the solar atmosphere*, A&A 473, 625, [90 c, 9 c/y].

Leenaarts, J., Carlsson, M., Rouppe van der Voort, L. 2012, *The formation of the Hα line in the solar chromosphere*, ApJ 749, 136, [109 c, 20 c/y].

Loukitcheva, M., Solanki, S.K., Carlsson, M. et al. 2015, *Millimeter radiation from a 3-D model of the solar atmosphere*, A&A 575, A15, [22 c, 9 c/y].

Martinez-Sykora, J., De Pontieu, B., and Hansteen, V. 2012, *2-D radiative MHD simulations of the importance of partial ionization in the chromosphere*, ApJ 753, 161, [56 c, 10 c/y].

Vernazza, J.E., Avrett, E.H., and Loeser, R. 1981, *Structure of the solar chromosphere. III. Models of the EUV brightness components of the Quiet-Sun*, ApJS 45, 635, [1862 c, 51 c/y].

Wedemeyer, S., Freytag, B., Steffen, M., et al. 2004, *Numerical simulation of the 3-D structure and dynamics of the non-magnetic solar chromosphere*, A&A 414, 1121, [239 c, 18 c/y].

Wedemeyer, S., Bastian, T., Brajsa, R., et al. 2016, *Solar science with the Atacama Large Millimeter/ Submillimeter Array (ALMA) - A new view of our Sun*, SSRv 200, 1, [24 c, 16 c/y].

(5.2) Chromospheric Fibrils

Aschwanden, M.J., Reardon, K., and Jess, D.B. 2016, *Tracing the chromospheric and coronal magnetic field with AIA, IRIS, IBIS, and ROSA data*, ApJ 826, 61, [3 c, 2 c/y].

Asensio Ramos, A., de la Cruz Rodriguez, J., Martinez Gonzalez, M.J. et al. 2016, *Inference of the chromospheric magnetic field orientation in the Ca II 8542 Å line fibrils*, A&A 599, A133, [3 c, 3 c/y].

Cauzzi, G., Reardon, K.P., Uitenbroek, H., et al. 2008, *The solar chromosphere at high resolution with IBIS. I. New insights from the Ca II 854.2 nm line*, A&A 480, 515, [91 c, 10 c/y].

Choudhary, D.P., Sakurai, T., and Venkatakrishnan, P. 2001, *Chromospheric magnetic field of solar active regions*, ApJ 560, 439, [17 c, 1 c/y].

de la Cruz Rodriguez, J. and Socas-Navarro, H. 2011, *Are solar chromospheric fibrils tracing the magnetic field?* A&A 527, L8, [36 c, 5 c/y].

de la Cruz Rodriguez, J., Socas-Navarro, H., Carlsson, M., et al. 2012, *Non-local thermodynamic equilibrium inversions from a 3-D MHD chromospheric model*, A&A 543, A34, [44 c, 8 c/y].

De Pontieu, B., Hansteen, V.H., Rouppe van der Voort, L. et al. 2007, *High-resolution observations and modeling of dynamic fibrils*, ApJ 655, 624, [143 c, 14 c/y].

Gudiksen, B.V., Carlsson, M., Hansteen V.H. et al. 2011, *The stellar atmosphere simulation code Bifrost. Code description and validation*, A&A 531, A154, [137 c, 21 c/y].

Hansteen, V.H., De Pontieu, B., Rouppe van der Voort, L., et al. 2006. *Dynamic fibrils are driven by magneto-acoustic shocks*, ApJ 647, L73, [194 c, 17 c/y].

Jendersie, S. and Peter H. 2006, *Link between the chromospheric network and magnetic structures of the corona*, A&A 460, 901, [17 c, 1 c/y].

Jing, J., Yuan, Y, Reardon, K., et al. 2011, *Nonpotentiality of chromospheric fibrils in NOAA active region 11092 and 9661*, ApJ 739, 67, [14 c, 2 c/y].

Leenaarts, J., Carlsson, M., Hansteen, V., et al., 2009, *3-D non-LTE radiative transfer computation of the Ca 8542 infrared line from a radiation-MHD simulation*, ApJ 694, L128, [67 c, 8 c/y].

Leenaarts, J., Carlsson, M., Rouppe van der Voort, L. 2015, *On fibrils and field lines: the nature of Hα fibrils in solar chromosphere*, ApJ 802, 136, [22 c, 9 c/y].

Langangen, O., Carlsson, M., Rouppe van der Voort, L. 2008, *Spectroscopic measurements of dynamic fibrils in Ca II 8662 line*, ApJ 673, 1194, [22 c, 2 c/y].

Martinez-Sykora, J., De Pontieu, B., Carlsson, M., et al. 2016, *On the misalignment between chromospheric features and the magnetic field on the Sun*, ApJ 831, L1, [7 c, 5 c/y].

Metcalf, T.R., Jiao, L., Uitenbroek, H., et al. 1995, *Is the solar chromospheric magnetic field force-free?* ApJ 439, 474, [212 c, 9 c/y].

Pietarila, A., Hirzberger, J., Zakharov, V., et al. 2009, *Bright fibrils in Ca II K*, A&A 502, 647, [27 c, 3 c/y].

Reardon, K.P., Wang, Y.M., Muglach, K., et al. 2011, *Evidence for two separate but interlaced components of the chromospheric magnetic field*, ApJ 742, 119, [17 c, 3 c/y].

Rouppe van der Voort, L.H.M., De Pontieu, B., Hansteen, V.H. et al. 2007, *Magnetoacoustic shocks as a driver of Quiet-Sun mottles*, ApJ 660, L169, [69 c, 7 c/y].

Schad, T.A., Penn, M.J., and Lin, H. 2013, *He I vector magnetometry of field-aligned superpenumbral fibrils*, ApJ 768, 111, [30 c, 7 c/y].

Scharmer, G.B. 2006, *Comments on the optimization of high resolution Fabry-Perot filtergraphs*, A&A 447, 1111, [77 c, 7 c/y].

Socas-Navarro,H., Elmore, D., Pietarila, A., et al. 2006, *Spectro-polarimetric observations and non-LTE modeling of Ellerman bombs*, SoPh 235, 55, [34 c, 3 c/y].

Vernazza, J.E., Avrett, E.H., and Loeser, R. 1981, *Structure of the solar chromosphere. III. Models of the EUV brightness components of the Quiet-Sun*, ApJS 45, 635, [1862 c, 51 c/y].

Zhu, X., Wang, H., Du, Z., et al. 2016, *Forced field extrapolation of the magnetic structure of the fibrils in the solar chromosphere*, ApJ 826, 51, [1 c, 1 c/y].

(5.3) Chromospheric Oscillations

Bloomfield, D.S., McAteer, R.T., Mathioudakis, M., et al. 2006, *The influence of magnetic field on oscillations in the solar chromosphere*, ApJ 652, 812, [25 c, 2 c/y].

Carlsson, M., Hansteen, V.H., de Pontieu, B., et al. 2007, *Can high frequency acoustic waves heat the Quiet Sun chromosphere*, PASJ 59, S663, [62 c, 6 c/y].

Chae, J., Yang, H., Park, H., et al. 2014, *Superpenumbral fibrils powered by sunspot oscillations*, ApJ 789, 108, [15 c, 4 c/y].

De Pontieu, B., Erdelyi, R., and James, S.P. 2004, *Solar chromospheric spicules from the leakage of photospheric oscillations and flows*, Nature 430, 536, [292 c, 22 c/y].

De Pontieu, B., Erdelyi, R., and De Moortel, I. 2005, *How to channel photospheric oscillations into the corona*, ApJ 624, L61, [124 c, 10 c/y].

De Pontieu, B. and McIntosh, S.W. 2010, *Quasi-periodic signals in the solar corona: The signature of magnetoacoustic waves or high-velocity upflows?*, ApJ 722, 1013, [82 c, 11 c/y].

Gafeira, R., Jafarzadeh, S., Solanki, S.K., et al. 2017, *Oscillations on width and intensity of slender Ca II H fibrils from Sunrise/SuFI*, ApJSS 229, 7, [5 c, 5 c/y].

Jess, D.B., Morton, R.J., Verth, G., et al. 2015, *Multiwavelength studies of MHD waves in the solar chromosphere. An overview of recent results*, SSRv 190, 103, [35 c, 14 c/y].

Judge, P.G., Tarbell, T.D., and Wilhelm, K. 2001, *A study of chromospheric oscillations using the SOHO and TRACE spacecraft*, ApJ 554, 424, [79 c, 5 c/y].

Kobanov, N.I., Kustov, A.S., Chupin, S.A.k et al. 2011, *Oscillations in solar faculae. III. The phase relations between chromospheric and photospheric line-of-sight velocities*. SoPh 273, 39, [3 c, 0.5 c/y],

Krijger, J.M., Rutten, R.J., Lites, B.W., et al. 2001, *Dynamics of the solar chromosphere. III. Ultraviolet brightness oscillations from TRACE*, A&A 379, 1052, [113 c, 7 c/y].

Kwak, H., Chae, J., Song, D., et al. 2016, *Oscillatory response of the solar chromosphere to a strong downflow event above a sunspot*, ApJ 821, L30, [8 c, 5 c/y].

Kuridze, D., Verth, G., Mathioudakis, M., et al. 2013, *Characteristics of transverse waves in chromospheric mottles*, ApJ 779, 82, [38 c, 7 c/y].

Maurya, R.A., Chae, J., Park, H., et al. 2013, *Chromospheric sunspot oscillations in Hα and Ca II 8542 Å*, SoPh 288, 73, [1 c, 0.2 c/y].

McAteer, R.T.J., Gallagher, P.T., Williams, D.R., et al. 2002, *Long-period chromospheric oscillations in network bright points*, ApJ 567, L165, [30 c, 2 c/y].

McAteer, R.T.J., Gallagher, P.T., Bloomfield, D.S., et al. 2004, *Ultraviolet oscillations in the chromosphere of the Quiet Sun*, ApJ 602, 436, [30 c, 2 c/y].

McIntosh, S.W., Fleck, B., and Judge, P.G. 2003, *Investigating the role of plasma topography on chromospheric oscillations observed by TRACE*, A&A 405, 769, [34 c, 2 c/y].

McIntosh, S.W., and Smillie, D.G. 2004, *Characteristic scales of chromospheric oscillation wave packets*, ApJ 604, 924, [13 c, 1 c/y].

Muglach, K. 2003, *Dynamics of solar active regions. I. Photospheric and chromospheric oscillations observed with TRACE*, A&A 401, 685, [31 c, 2 c/y].

Pietarila, A., Cuadrado, R.A., Hirzberger J., et al. 2011, *Kink waves in an active region dynamic fibril*, ApJ 739, 92, [20 c, 3 c/y].

Skartlien, R., Stein, R.F., and Nordlund, A. 2000, *Excitation of chromospheric wave transients by collapsing granules*, ApJ 541, 468, [65 c, 4 c/y].

Stangalini, M., Giannattasio, F., and Jafarzadeh, S. 2015, *Non-linear propagation of kink waves to the solar chromosphere*. A&A 577, A17, [13 c, 5 c/y].

Vecchio, A., Cauzzi, G., Reardon, K.P. et al. 2007, *Solar atmospheric oscillations and the chromospheric magnetic topology*, A&A 461, L1, [85 c, 8 c/y].

Wikstol, O., Hansteen, V.H., Carlsson, M., et al. 2000, *Chromospheric and transition region internetwork oscillations: A signature of upward-propagating waves*, ApJ 531, 1150, [48 c, 3 c/y].

Yang, S. and Xiang, Y. 2016, *Oscillation of newly formed loops after magnetic reconnection in the solar chromosphere*, ApJ 819, L24, [3 c, 2 c/y].

(5.4) Chromospheric Alfvén Waves

Antolin, P., Okamoto, T.J., De Pontieu, B., et al. 2015, *Resonant absorption of transverse oscillations and associated heating in a solar prominence. II. Numerical aspects*, ApJ 809, 72, [48 c, 19 c/y].

Antolin, P., Schmit, D., Pereira, T.M.D., et al. 2018, *Transverse wave induced Kelvin-Helmholtz rolls in spicules*, ApJ 856, 44, [2 c, 2 c/y].

Cranmer, S.R. and Ballegooijen, A.A. 2005, *On the generation, and reflection of Alfvén waves from the photosphere to the distant heliosphere*, ApJSS 156, 265, [240 c, 19 c/y].

De Pontieu, B., Martens, P.C.H., and Hudson, H.S. 2001, *Chromospheric damping of Alfvén waves*, ApJ 558, 859, [118 c, 7 c/y].

De Pontieu, B., McIntosh, S.W., Carlsson, M., et al. 2007, *Chromospheric Alfvénic waves strong enough to power the solar wind*, Science 318, 1574, [460 c, 44 c/y].

De Pontieu, B., McIntosh, S.W., Hansteen, V.H., et al. 2009, *Observing the roots of solar coronal heating - in the chromosphere*, ApJ 701, L1, [195 c, 23 c/y].

De Pontieu, B., McIntosh, S.W., Carlsson, M., et al. 2011, *The origins of hot plasma in the solar corona*, Science 331, 6013, [212 c, 33 c/y].

De Pontieu, B., Rouppe van der Voort, L., McIntosh, S.W. 2014, *On the prevalence of small-scale twist in the solar chromosphere and transition region*, Science 346, 1255732, [42 c, 11 c/y].

De Pontieu, B., De Moortel, I., Martinez-Sykora, J., et al. 2017, *Observations and numerical models of solar coronal heating associated with spicules*, ApJ 845, L18, [8 c, 8 c/y].

Erdelyi, R. and Fedun, V. 2007, *Are there Alfvén waves in the solar atmosphere*, Science 318, 1572, [114 c, 11 c/y].

Fedun, V., Verth, G., Jess, D.B., and Erdelyi, R. 2011, *Frequency filtering of torsional waves by chromospheric magnetic field*, ApJ 740, L46, [33 c, 5 c/y].

Grant, S.D.T., Jess, D.B., Zaqarashvili, T.V. et al. 2018, *Alfvén wave dissipation in the solar chromosphere*, Nature Physics 14, 480.

Hansen, S.C. and Cally, P.S. 2012. *Benchmarking fast-to-Alfvén mode conversion in a cold MHD plasma. II. How to get Alfvén waves through the solar transition region*, ApJ 2012, ApJ 751, 31, [26 c, 5 c/y].

Jess, D.B., Mathioudakis, M., Erdelyi, R., et al. 2009, *Alfvén waves in the lower solar atmosphere*, Science 323, 1582. [220 c, 13 c/y].

Martinez-Sykora, J., De Pontieu, B., Hansteen, V.H. 2017, *On the generation of solar spicules and Alfvénic waves*, Science 356, 6344, 1269, [25 c, 25 c/y].

McIntosh, S.W., De Pontieu, B., Carlsson, M. et al. 2011, *Alfvénic waves with sufficient energy to power the Quiet solar corona and fast solar wind*, Nature 475, 477, [260 c, 40 c/y].

McIntosh, S.W. and De Pontieu, B. 2012, *Estimating the "dark" energy content of the solar corona*, ApJ 761, 138, [25 c, 5 c/y].

Okamoto, T.J. and De Pontieu, B. 2011, *Propagating waves along spicules*, ApJ 736, L24, [89 c, 14 c/y].

Okamoto, T.J., Antolin, P., De Pontieu, B., et al. 2015, *Resonant absorption of transverse oscillations and associated heating in a solar prominence. I. Observational aspects*, ApJ 809, 71, [42 c, 17 c/y].

Suzuki, T., and Inutsuka, S.I. 2005, *Making the corona and the fast solar wind: A self-consistent simulation for the low-frequency Alfvén waves from the photosphere to 0.3 AU*, ApJ 632, L49, [149 c, 12 c/y].

Tomczyk, S., McIntosh, S.W., Keil, S.L., et al. 2007, *Alfvén waves in the solar corona*, Science 317, 1192, [401 c, 38 c/y].

van Ballegooijen, A.A., Asgari-Targhi, M., Cranmer, S.R. et al. 2011, *Heating of the solar chromosphere and corona by Alfvén wave turbulence*, ApJ 736, 3, [166 c, 25 c/y].

van der Holst, B., Manchester, W.B.IV., Frazin, R.A., et al. 2010, *A data-driven, two-temperature solar wind model with Alfvén waves* ApJ 725, 1373, [63 c, 8 c/y].

Verdini, A. and Velli, M. 2007, *Alfvén waves and turbulence in the solar atmosphere and solar wind*, ApJ 662, 669, [124 c, 12 c/y].
Verth, G., Erdelyi, R., and Goossens, M. 2010, *Magnetoseismology: Eigenmodes of torsional Alfvén waves in stratified solar waveguides*, ApJ 714, 1637, [29 c, 4 c/y].

(5.5) Type-II Spicules

De Pontieu,B., Erdelyi,R., James,S.P. 2004, *Solar chromospheric spicules from leakage of photospheric oscillations and flows*, Nature 430, 536, [286 c, 21 c/y].
De Pontieu,B., McIntosh,S.W., Hansteen,V.H., et al. 2007, *A tale of two spicules: The impact of spicules on magnetic chromosphere*, PASJ 59, S655, [235 c, 22 c/y].
De Pontieu, B., Carlsson, M., Rouppe van der Voort, L.H.M. et al. 2012, *Ubiquitous torsional motions in type-II spicules*, ApJ 752, L12, [85 c, 15 c/y].
He, J.S., Tu, C.Y., Marsch, E., et al. 2009, *Upward propagating high-frequency Alfvén waves as identified from dynamic wave-like spicules observed by SOT on Hinode*, A&A 497, 525, [64 c, 8 c/y].
Iijima, H. and Yokoyama, T. 2017, *A 3-D MHD simulation of the formation of solar chromospheric jets with twisted magnetic field lines*, ApJ 848, 38, [9 c, 9 c/y].
James, S.P., Erdelyi, R., and De Pontieu, B. 2003, *Can ion-neutral damping help to form spicules*, A&A 406, 715, [29 c, 2 c/y].
Jess, D.B., Pascoe, D.J., Christian, D.J., et al. 2012, *The origin of type-I spicule oscillations*, ApJ 744, L5, [33 c, 6 c/y].
Klimchuk, J.A. 2012, *The role of type-II spicules in the upper solar atmosphere*, JGR 117, A12, [41 c, 7 c/y].
Kukhianidze, V., Zaqarashvili, T.V., and Khutsishvili, E., 2006, *Observation of kink waves in solar spicules*, A&A 449, L35, [62 c, 5 c/y].
Langangen, O., De Pontieu, B., Carlsson, M., et al. 2008, *Search for high velocities in the disk counterpart of type-II spicules*, ApJ 679, L167, [66 c, 7 c/y].
Martinez-Sykora, J., Hansteen, V., De Pontieu, B., et al. 2009, *Spicule-like structures observed in 3-D realistic MHD simulations*, ApJ 701, 1569, [64 c, 8 c/y].
Martinez-Sykora, J., Hansteen, V., Moreno-Inertis, F. 2011, *On the origin of the type-II spicules: Dynamic 3-D MHD simulations* ApJ 736, 9, [12 c, 2 c/y].
Martinez-Sykora, J., De Pontieu, B., Hansteen, V.H. 2017, *On the generation of solar spicules and Alfvénic waves*, Science 356, 6344, [25 c, 50 c/y].
Matsumoto, T. and Shibata, K. 2010, *Nonlinear propagation of Alfvén waves driven by observed photospheric motions: Application to the coronal heating and spicule formation*, ApJ 710, 1857, [60 c, 8 c/y].
Moore, R.L., Sterling, A.C., Cirtain, J.W., et al. 2011, *Solar X-ray jets, type-II spicules, granule-size emerging bipoles, and the genesis of the heliosphere*, ApJ 731, L18, [42 c, 6 c/y].
Okamoto, T. and De Pontieu, B. 2011, *Propagating waves along spicules*, ApJ 736, L24, [80 c, 12 c/y].
Pereira, T.M.D., De Pontieu, B., and Carlsson, M. 2012, *Quantifying spicules*, ApJ 759, 18, [65 c, 12 c/y].
Pereira, T.M.D., De Pontieu, B., Carlsson, M., et al. 2014, *An IRIS first view on solar spicules*, ApJ 792, L15, [50 c, 14 c/y].
Rouppe van der Voort,L., Leenaarts,J., De Pontieu,B., et al. 2009, *On-disk counterparts of type-II spicules in the Ca II 8542 and Hα lines*, ApJ 705, 272, [117 c, 14 c/y].
Saito, T., Kudoh, T., and Shibata, K. 2001, *What determines the height of spicules? I. Alfvén wave model and slow-wave model*, ApJ 554, 1151, [20 c, 1 c/y].
Sekse, D.H., Rouppe van der Voort, L., and De Pontieu, B. 2012, *Statistical properties of the disk counterparts of type-II spicules from simultaneous observations or rapid blueshifted excursions in Ca II 8542 and Hα*, ApJ 752, 108, [48 c, 9 c/y].

Sterling, A. 2000, *Solar spicules: A review of recent models and targets for future observations (Invited review)*, SoPh 196, 79, [173 c, 10 c/y].
Sterling, A.C., Moore, R.L., and DeForest, C. 2010, *Hinode/SOT observations of the source region and evolution of "Type-II" spicules at the solar polar limb*, ApJ 714, L1, [27 c, 4 c/y].
Tsiropoula, G., Tziotziou, K., Kontogiannis, I., et al. 2012, *Solar fine structures. I. Spicules and other small-scale, jet-like events at the chromospheric level: Observations and physical parameters*, SSRv 169, 181, [71 c, 13 c/y].
Zaqarashvili, T.V., Khutsishvili, E., Kukhianidze, V. et al. 2007, *Doppler-shift oscillations in solar spicules*, A&A 474, 627, [58 c, 6 c/y].
Zaqarashvili, T.V. and Erdelyi, R. 2009, *Oscillations and waves in solar spicules*, SSRv 149, [96 c, 11 c/s].
Zhang, Y.Z., Shibata, K., Wang, J.X., et al. 2012, *Revision of solar spicule classification*, ApJ 750, 16, [40 c, 7 c/y].

(5.6) Chromospheric Jets: Observations

Adams, M., Sterling, A.C., Moore, R.L. 2014, *A small-scale eruption leading to a blowout macrospicule jet in an on-disk coronal hole*, ApJ 783, 11, [27 c, 8 c/y].
Chintzoglou, G., De Pontieu, B., Martinez-Sykora, J. et al. 2018, *Bridging the gap: Capturing the Lyα counterpart of a type-II spicule and its heating evolution with VAULT2.0 and IRIS observations*, ApJ 857, 73.
Cirtain, J.W., Golub, L., Lundquist, L., et al. 2007, *Evidence for Alfvén waves in solar X-ray jets*, Science 318, 1580, [276 c, 26 c/y].
De Pontieu, B., Carlsson, M., Rouppe van der Voort, L.H.M., et al. 2012, *Ubiquitous torsional motions in type II spicules*, ApJ 752, L12, [96 c, 17 c/y].
De Pontieu, B., Martinez-Sykora, J., and Chintzoglou, G. 2017, *What causes the high apparent speeds in chromospheric and transition region spicules on the Sun ?*, ApJ 849, L7, [3 c, 3 c/y].
Hong, J., Jiang, Y., Yang, J., et al. 2017, *Minifilament eruption as the source of a blowout jet, C-class flare, and type-III radio burst*, ApJ 835, 35, [8 c, 16 c/y].
Katsukawa, Y., Berger, T.E., Ichimoto, K., et al. 2007, *Small-scale jetlike features in penumbral chromospheres*, Science 318, 1594, [104 c, 10 c/y].
Liu, W., Berger, T.E., Title, A.M., and Tarbell, T.D. 2009, *An intriguing chromospheric jet observed by Hinode: Fine structure kinematics and evidence of unwinding twists*, ApJ 707, L37, [58 c, 7 c/y].
Liu, W., Berger, T.E., Title, A.M., et al. 2011, *Chromospheric jet and growing loop observed by Hinode: New evidence of fan-spine magnetic topology resulting from flux emergence*, ApJ 728, 103, [50 c, 8 c/y].
Martinez-Sykora, J., De Pontieu, B., Hansteen, V.H., et al. 2017, *On the generation of solar spicules and Alfvénic waves*, Science 356, Issue 6344, 1269.
Moore, R.L., Sterling, A.C., Falconer, D.A. 2015, *Magnetic untwisting in solar jets that go into the outer corona in polar coronal holes*, ApJ 806, 11, [15 c, 6 c/y].
Nishizuka, N., Nakamura, T., Kawate, T., et al. 2011, *Statistical study of chromospheric anemone jets observed with Hinode/SOT*, ApJ 731, 43, [31 c, 5 c/y].
Shibata, S., Nakamura, T., Matsumoto, T. et al. 2007, *Chromospheric anemone jets as evidence of ubiquitous reconnection*, Science 318, 1591, [201 c, 19 c/y].
Sterling, A.C., Harra, L.K., and Moore, R.L. 2010, *Fibrillar chromospheric spicule-like counterpart to an EUV and soft X-ray blowout coronal jet*, ApJ 722, 1644, [39 c, 5 c/y].
Rouppe van der Voort, L. and de la Cruz Rodriguez, J. 2013, *Short dynamic fibrils in sunspot chromosphere*, ApJ 776, 56, [26 c, 6 c/y].
Tian, H., DeLuca, E.E., Cranmer, S.R., et al. 2014, *Prevalence of small-scale jets from the network of the solar transition region and chromosphere*, Science 246, 1255711, [71 c, 10 c/y].

Wedemeyer-Böhm, S. and Rouppe van der Voort, L. 2009, *Small-scale swirl events in the Quiet chromosphere*, A&A 507, L9, [79 c, 9 c/y].
Yurchyshyn, V., Abramenko, V., Kosovichev, A. et al. 2014, *High resolution observations of chromospheric jets in sunspot umbra*, ApJ 787, 58, [24 c, 7 c/y].
Zhang, Q.M. and Ji, H.S. 2014, *Blobs in recurring extreme-ultraviolet jets*, A&A 567, A11, [28 c, 8 c/y].
Zhang, Y. and Zhang, J. 2017, *Cusp-shaped structure of a jet observed by IRIS and SDO*, ApJ 834, 79, [5 c, 5 c/y].

(5.7) Chromospheric Jets: Numerical Simulations

Cheung, M.C.M., De Pontieu, B., Tarbell, T.D., et al. 2015, *Homologous helical jets: Observations by IRIS, SDO, and Hinode and magnetic modeling with data-driven simulations*, ApJ 801, 83, [25 c, 10 c/y].
Gonzalez-Aviles, J.J., Guzman, F.S., and Fedun, V. 2017, *Jet formation in solar atmosphere due to magnetic reconnection* ApJ 836, 24, [2 c, 2 c/y].
Heggland, L., De Pontieu, B., and Hansteen, V.H. 2007, *Numerical simulations of shock wave-driven chromospheric jets*, ApJ 666, 1277, [62 c, 6 c/y].
Heggland, L., De Pontieu, B., and Hansteen, V.H. 2009, *Observational signatures of simulated reconnection events in the solar chromosphere and transition region*, ApJ 702, 1, [44 c, 5 c/y].
Heggland, L., Hansteen, V.H., De Pontieu, B. et al. 2011, *Wave propagation and jet formation in the chromosphere*, ApJ 743, 142, [34 c, 5 c/y].
Martinez-Sykora, J., De Pontieu, B., Hansteen, V.H. 2017, *On the generation of solar spicules and Alfvénic waves*, Science 356, 6344, [25 c, 50 c/y].
Nishizuka, N., Shimizu, M., Nakamura, T., et al. 2008, *Giant chromospheric anemone jet observed with the Hinode and comparison with MHD simulations: Evidence of propagating Alfvén waves and magnetic reconnection*, ApJ 683, L83, [107 c, 11 c/y].
Szente, J., Toth, G., Manchester, W.B.IV., et al. 2017, *Coronal jets simulated with the global Alfvén wave solar model*, ApJ 834, 123, [3 c, 3 c/y].
Takasao, S., Isobe, H., and Shibata, K. 2013, *Numerical simulations of solar chromospheric jets associated with emerging flux*, PASJ 65, 62, [27 c, 6 c/y].
Yang, L., He, J., Peter, H., et al. 2013, *Numerical simulations of chromospheric anemone jets associated with moving magnetic features*, ApJ 777, 16, [31 c, 7 c/y].
Yokoyama,T. and Shibata,K. 1995, *Magnetic reconnection as the origin of X-ray jets and Hα surges on the Sun*, Nature 375, 42, [342 c, 15 c/y].
Yokoyama,T. and Shibata,K. 1996, *Numerical simulation of solar coronal X-ray jets based on the magnetic reconnection model*, PASJ 48, 353, [266 c, 12 c/y].

(5.8) Ellerman Bombs

Archontis, V. and Hood, A.W. 2009, *Formation of Ellerman bombs due to 3-D flux emergence*, A&A 508, 1469, [62 c, 7 c/y].
Fang, C., Tang, Y.H., Xu, Z., et al. 2006, *Spectral analysis of Ellerman bombs*, ApJ 643, 1325, [64 c, 6 c/y].
Georgoulis, M.K., Rust, D.M., Bernasconi, P.N., et al. 2002, *Statistics, morphology, and energetics of Ellerman bombs*, ApJ 575, 506, [120 c, 8 c/y].
Hansteen, V.H., Archontis, V., Pereira, T.M.D., et al. 2017, *Bombs and flares at the surface and lower atmosphere of the Sun*, ApJ 839, 22, [8 c, 8 c/y].
Isobe, H., Tripathi, D., and Archontis, V. 2007, *Ellerman bombs and jets associated with resistive flux emergence*, ApJ 657, L53, [84 c, 8 c/y].

Libbrecht, T., Joshi, J., de la Cruz Rodriquez, J., et al. 2017, *Observations of Ellerman bomb emission features in He I D_3 and He I 10,830 Å*, A&A 598, A33, [5 c, 5 c/y].
Matsumoto, T., Kitai, R., Shibata, K., et al. 2008, *Height dependence of gas flows in an Ellerman bomb*, PASJ 60, 95, [32 c, 3 c/y].
Pariat, E., Aulanier, G., Schmieder et al. 2004, *Resistive emergence of undulatory flux tubes*, ApJ 614, 1099, [134 c, 10 c/y].
Pariat, E., Schmieder, B., Berlicki, A., et al. 2007, *Spectrophotometric analysis of Ellerman bombs in the Ca II, Hα, and UV range*, A&A 473, 279, [50 c, 5 c/y].
Pariat, E., Masson, S., and Aulanier, G. 2009, *current buildup in emerging serpentine flux tubes*, ApJ 701, 1911, [39 c, 5 c/y].
Peter, H., Tian, H., Curdt, W., et al. 2014, *Hot explosions in the cool atmosphere of the Sun*, Science 346, 1255726, [60 c, 17 c/y].
Qiu, J., Ding, M.D., Wang, H., et al. 2000, *Ultraviolet and Hα emission in Ellerman bombs*, ApJ 544, L157, [53 c, 3 c/y].
Reid, A., Mathioudakis, M., Doyle, J.G., et al. 2016, *Magnetic flux cancellation in Ellerman bombs*, ApJ 823, 110, [15 c, 10 c/y].
Tian, H., Zhi, X., Jiansen, H., et al. 2016, *Are IRIS bombs connected to Ellerman Bombs"*, ApJ 824, 96, [27 c, 18 c/y].
Vissers, G.J.M., Rouppe van der Voort L.H.M., and Rutten, R.J. 2013, *Ellerman bombs at high resolution. II. Triggering, visibility, and effect on upper atmosphere*, ApJ 774, 32, [35 c, 14 c/y].
Vissers, G.J.M., Rouppe van der Voort, L.H.M., Rutten, R.J., et al. 2015, *Ellerman bombs at high resolution. III. Simultaneous observations with IRIS and SST*, ApJ 812, 11, [46 c, 18 c/y].
Watanabe, H., Kitai, R., Okamoto, K., et al. 2008, *Spectropolarimetric observation of an emerging flux region: Triggering mechanisms of Ellerman bombs*, ApJ 684, 736, [48 c, 5 c/y].
Watanabe, H., Vissers, G., Kitai, R., et al. 2011, *Ellerman bombs at high resolution. I. Morphological evidence for photospheric reconnection*, ApJ 736, 71, [54 c, c/y].

(5.9) Chromosphere: Kelvin-Helmholtz Instability

Antolin, P., Schmit, D., Pereira, T.M.D., et al. 2018, *Transverse wave induced Kelvin-Helmholtz rolls in spicules*, ApJ 856, 44, [2 c, 2 c/y].
Karpen, J.T., Antiochos, S.K., Dahlburg, R.B. et al. 1993, *The Kelvin-Helmholtz instability in photospheric flows: Effects on coronal heating and structure*, ApJ 403, 769, [30 c, 1 c/y].
Keppens, R. and Toth, G. 1999, *Nonlinear dynamics of Kelvin-Helmholtz unstable magnetized jets: 3-D effects*, Physics of Plasmas 6/5, 1461, [27 c, 1 c/y].
Keppens, R., Toth, G., Westermann, R.H.J. et al. 1999, *Growth and saturation of the Kelvin-Helmholtz instability with parallel and anti-parallel magnetic fields*, J. Plasma Physics 61, 1, [68 c, 4 c/y].
Kolesnikov, F., Bünte, M., Schmitt, D., et al. 2004, *Kelvin-Helmholtz and shear instability of a helical flow around a magnetic flux tube*, A&A 420, 737, [5 c, 0.4 c/y].
Kuridze, D., Zaqarashvili, T.V., Henriques, V., et al. 2016, *Kelvin-Helmholtz instability in solar chromospheric jets: Theory and observations*, ApJ 830, 133, [8 c, 4 c/y].
Martinez-Gomez, D., Soler, R., and Terradas, J. 2015, *Onset of the Kelvin-Helmholtz instability in partially ionized magnetic flux tubes*, A&A 578, A104, [10 c, 4 c/y].
Mishin, V.V. and Tomozov, V.M. 2016, *Kelvin-Helmholtz Instability in the Solar Atmosphere, Solar Wind and Geomagnetosphere*, SoPh 291, 3165, [1 c, 1 c/y].
Murawski, K., Chmielewski, P., Zaqarashvili, T.V., et al. 2016, *Numerical simulations of magnetic Kelvin-Helmholtz instability at a twisted solar flux tube*, MNRAS 459, 2566, [6 c, 4 c/y],
Ni, L., Zhang, Q.M., Murphy, N.A., et al. 2017, *Blob formation and ejection in coronal jets due to the plasmoid and Kelvin-Helmholtz instabilities*, ApJ 841, 27, [8 c, 16 c/y].

Soler, R., Terradas, J., Oliver, R., et al. 2010, *Kelvin-Helmholtz instability in coronal magnetic flux tubes due to azimuthal shear flows*, ApJ 712, 875, [27 c, 4 c/y].
Soler, R., Diaz, A.J., Ballester, J.L., et al. 2012, *Kelvin-Helmholtz instability in partially ionized compressible plasmas*, ApJ 749, 163, [25 c, 5 c/y],
Zaqarashvili, T.V., Zhelyazkov, I., and Ofman, L. 2015, *Stability of rotating magnetized jets in the solar atmosphere. I. Kelvin-Helmholtz instability*, ApJ 813, 123, [20 c, 8 c/y].
Zhelyazkov, I. and Zaqarashvili, T.V. 2012, *Kelvin-Helmholtz instability of kink waves in photospheric twisted flux tubes*, A&A 547, A14, [13 c, 2 c/y].
Zhelyazkov, I., Zaqarashvili, T.V., Chandra, R., et al. 2015, *Kelvin-Helmholtz instability in solar cool surges*, AdSpR 56/12, 2727, [10 c, 4 c/y].
Zhelyazkov, I. 2015, *On modeling the Kelvin-Helmholtz instability in solar atmosphere*, J. Astrophys. Astron. 36, 233, [5 c, 2 c/y].
Zhelyazkov, I. and Dimitrov, Z. 2018, *Kelvin-Helmholtz instability in a cool solar jet in the framework of Hall MHD: A case study*, SoPh 293, 11.

(5.10) Chromospheric Heating Models

Arber, T.D., Brady, C.S., and Shelyag, S. 2016, *Alfvén wave heating of the solar chromosphere: 1.5D Models*, ApJ 817, 94, [14 c, 9 c/y].
Beck, C., Schmidt, W., Rezaei, R., et al. 2008, *The signature of chromospheric heating in Ca II H spectra*, A&A 479, 213, [41 c, 4 c/y].
Brady, C.S. and Arber, T.D. 2016, *Simulations of Alfvén and kink wave driving of the solar chromosphere: Efficient heating and spicule launching*, ApJ 829, 80, [3 c, 2 c/y].
Carlsson, M., Hansteen, V.H., de Pontieu, B. 2007, *Can high frequency acoustic waves heat the Quiet Sun chromosphere?* PASJ 59, S663, [62 c, 6 c/y].
Cuntz, M., Rammacher, W., and Musielak, Z.E. 2007, *Acoustic heating of the solar chromosphere: Present indeed and locally dominant*, ApJ 657, L57, [25 c, 2 c/y].
de la Cruz Rodriguez, J., Socas-Navarro, H., Carlsson, M., et al. 2012, *Non-local thermodynamic equilibrium inversions from a 3-D MHD chromospheric model*, A&A 543, A34, [44 c, 8 c/y].
De Pontieu, B., Erdelyi, R., and James, S.P. 2004, *Solar chromospheric spicules from the leakage of photospheric oscillations and flows*, Nature 430, 536, [292 c, 22 c/y].
Fontenla, J.M., Peterson, W.K., and Harder J. 2008, *Chromospheric heating by the Farley-Buneman instability*, A&A 480, 839, [34 c, 4 c/y].
Fossum, A. and Carlsson, M. 2005, *High-frequency acoustic waves are not sufficient to heat the solar chromosphere*, Nature 435, 919, [93 c, 7 c/y].
Grant, S.D.T., Jess, D.B., Zaqarashvili, T.V. et al. 2018, *Alfvén wave dissipation in the solar chromosphere*, Nature Physics 14, 480.
Goodman, M.L. 2011, *Conditions for photospherically driven Alfvénic oscillations to heat the solar chromosphere by Pedersen current dissipation*, ApJ 735, 45, [17 c, 3 c/y].
Hasan, S.S. and van Ballegooijen, A.A. 2008, *Dynamics of the solar magnetic network. II. Heating the magnetized chromosphere*, ApJ 680, 1542, [68 c, 7 c/y].
Hollweg, J.V. 1981, *Alfvén waves in the solar atmosphere. II. Open and closed magnetic flux tubes*, SoPh 70, 25, [175 c, 5 c/y].
Jefferies, S.M., McIntosh, S.W., Armstrong, J.D., et al. 2006, *Magnetoacoustic portals and the basal heating of the solar chromosphere*, ApJ 648, L151, [128 c, 11 c/y].
Kalkofen, W. 2007, *Is the solar chromosphere heated by acoustic waves?* ApJ 671, 2154, [22 c, 2 c/y].
Khomenko, E., and Collados, M. 2012, *Heating of the magnetized solar chromosphere by partial ionization effects*, ApJ 747, 87, [60 c, 11 c/y].
Martinez-Sykora, J., De Pontieu, B., and Hansteen, V. 2012, *2-D radiative MHD simulations of the importance of partial ionization in the chromosphere*, ApJ 753, 161, [56 c, 10 c/y].

Martinez-Sykora, J., De Pontieu, B., Hansteen, V.H. 2017, *On the generation of solar spicules and Alfvénic waves*, Science 356, 6344, 1269, [25 c, 25 c/y].

Shelyag, S., Khomenko, E., De Vicente, A., et al. 2016, *Heating of the partially ionized solar chromosphere by waves in magnetic structures*, ApJ 819, L11, [8 c, 5 c/y].

Socas-Navarro H. 2005, *Are electric currents heating the magnetic chromosphere?* ApJ 633, L57, [38 c, 3 c/y].

Sobotka, M., Heinzel, P., Svanda, M., et al. 2016, *Chromospheric heating by acoustic waves compared to radiative cooling*, ApJ 826, 49.

Ulmschneider, P., Rammacher, W., Musielak, Z.E., et al. 2005, *On the validity of acoustically heated chromosphere models*, ApJ 631, L155, [25 c, 2 c/y]. s

van Ballegooijen, A.A., Asgari-Targhi, M., Cranmer, S.R., et al. 2011, *Heating of the solar chromosphere and corona by Alfvén wave turbulence*, ApJ 736, 3, [165 c, 25 c/y].

Woosley, L.N. and Cranmer, S.R. 2015, *Time-dependent turbulent heating of open flux tubes in the chromosphere, corona, and solar wind*, ApJ 811, 136, [10 c, 4 c/y].

Wu, D.J. and Fang, C. 2007, *Sunspot chromospheric heating by kinetic Alfvén waves*, ApJ 659, L181, [25 c, 2 c/y].

Chapter 6
The Quiet-Sun Corona

6.1 Solar Eclipses

Total solar eclipses provide a unique view of the faint solar corona, without the bright over-powering emission from the solar disk, enabling us to explore the electron density, temperature, thermodynamics, and related fundamental physics (Habbal et al. 2010a, 2011, 2013). In the past, solar eclipse observations were leading to fundamental tests of Einstein's theory of special relativity, by Sir Arthur Eddington in 1919, and to the discovery of coronal holes, by Max Waldmeier in 1957 (Bleeker et al. 2001).

The brightness of the white-light corona on 2008 August 1 and 2009 July 22, when solar activity was at its lowest in 100 years, was found to be $\approx 0.4 \times 10^{-6}$ of the total brightness of the Sun, which is the lowest ever observed (Hanaoka et al. 2012).

In a gravitationally stratified atmosphere, the electron density (or gas pressure) falls off exponentially with height, i.e., $n_e(h) \propto e^{-h/\lambda}$, where λ is the density scale height. EUV emission observed in ionized iron lines (such as Fe IX 171 Å or Fe XII 193 Å), has an intensity that is proportional to the squared density due to the collisional excitation mechanism. The emission in coronal forbidden lines, such as Fe X 6374 Å, Fe XI 7892 Å, Fe XIII 10,747 Å, and Fe XIV 5303 Å, is produced by collisional excitation (close to the Sun), and is dominated by resonant excitation when collisional excitation becomes too weak. Resonant absorption is proportional to the ion density, and the disk radiation at that wavelength. The different functional dependence of the emitted intensity in white-light and in EUV wavelengths has the consequence that EUV emission can only be observed in relatively low altitudes ($\lesssim 1.25 R_\odot$), while the white-light corona can be observed out to much larger distances from the Sun, which plays an important role during solar eclipses. In order to optimally enhance the fine structure of the corona in eclipse pictures, a *Fourier normalizing-radial-graded filter (FNRGF)* (Druckmüllerova et al. 2011), or an *Adaptive Circular Highpass Filter (ACHF)* is applied, see example in Fig. 6.1.

M. J. Aschwanden, *New Millennium Solar Physics*, Astrophysics and Space Science Library 458, https://doi.org/10.1007/978-3-030-13956-8_6

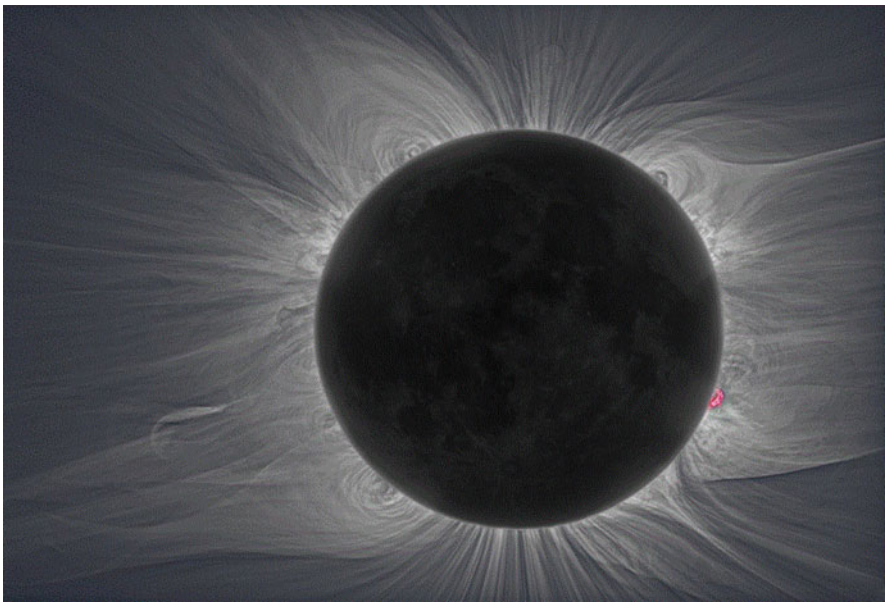

Fig. 6.1 White-light image of the corona taken by M. Druckmüller during the total solar eclipse of 2010 July 11. The image has been processed with the *Adaptive Circular Highpass Filter (ACHF)*, in order to enhance the fine structure (Habbal et al. 2011)

Electron density profiles $n_e(h)$ as a function of the radial distance from the Sun can be obtained from the white-light brightness by inversion of the line-of-sight integral, assuming Thomson scattering in the plane-of-sky. The density profile can be parameterized by a polynomial, e.g., $n_e(r) = \Sigma_k a_k r^{-k}, k = 1, \ldots n$ (Skomorovsky et al. 2012).

Temperature information in a solar eclipse picture can readily be obtained from the forbidden green and red line emission. The 4 eclipse pictures shown in Fig. 6.2 display the solar corona during the solar cycle minimum (2006) and near the solar cycle maximum (2010). There appears to be a bimodal distribution of temperature structures: Field lines extending outwards from the solar surface are dominated by cooler emission of Fe XI 7892 Å (peak $T = 1.1$ MK, red), while the bulges of streamers are dominated by the hottest emission of Fe XIV 5303 Å (peak $T = 1.8$ MK, green) (Habbal et al. 2013). Analysis of Fe XI 7892 Å images of the 2006 March 29 eclipse revealed localized increases in Fe XI density relative to the electron density, which is attributed to the dominance of radiative over collisional excitation in the formation of the Fe XI line (Habbal et al. 2007; Byhring et al. 2011). The 2006 and 2008 eclipses demonstrated that *prominence cavities* are intricate magnetic and density structures that are enshrouded with hot plasma (with a temperature of $\gtrsim 2.0$ MK) and twisted magnetic structures (Habbal et al. 2010b). Other diagnostic capabilities of forbidden lines are: (i) the inference of elemental abundances in the corona, which can be compared to their photospheric values,

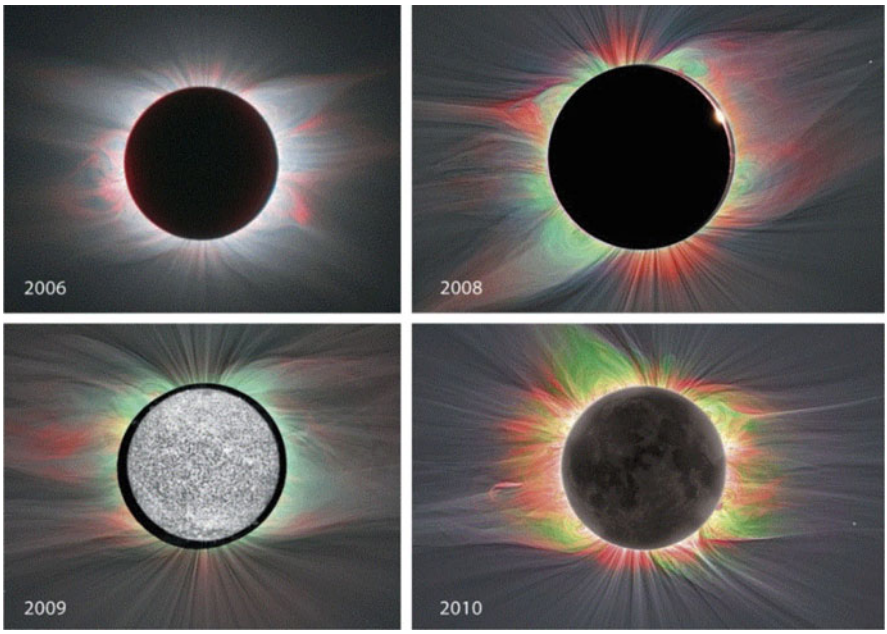

Fig. 6.2 Electron temperature distribution in the corona as inferred from narrow-band multi-wavelength observations form the eclipses of 2006, 2008, 2009, and 2010. Structures shown in grey are from the white-light images. Superimposed on this background is the emission from Fe XI 7892 Å ($T \approx 1.1$ MK; red), and Fe XIV 5303 Å ($T \approx 1.8$ MK; green), (Habbal et al. 2013)

(ii) the inference of the magnetic field direction and strength from polarization measurements, and (iii) the chemical composition of exogenic material from sun-grazing comets or near-solar asteroids (Habbal et al. 2013).

Coronal phenomena observed during eclipses include polar plumes, loop oscillations, quiescent or eruptive prominences (Alzate et al. 2017), tethered prominence-CME systems (Druckmüller et al. 2017), CMEs, erupting spicules and macrospicules, mass motion in the upper chromosphere, rays, streamers, the large-scale coronal magnetic field (Nandy et al. 2018), the center-to-limb variation of the solar brightness, the solar radius (Lamy et al. 2015), etc. Besides these widely-used phenomena, new morphologies of coronal structures in white-light eclipse images were discovered, such as *"smoke rings"*, *faint nested expanding loops, expanding bubbles*, and *twisted helical structures*, which are believed to be snapshots of the dynamical evolution of instabilities developing at prominence-corona interfaces, which propagate outward with the solar wind (Druckmüller et al. 2011). Unraveling of prominences and the outward expansion of the helical twisted field has been observed during eclipses also, which may point to the solar origin of interplanetary flux ropes (Habbal et al. 2014).

6.2 Quiet Sun: Flows and Jets

The more we improve the spatial and temporal resolution of solar observations, the more the term "Quiet Sun" becomes a misnomer. There are apparently ubiquitous Quiet-Sun phenomena that display transient flows and formation of jets, which involve "not-so-quiet", or even "violent" magneto-hydrodynamic processes. Nevertheless, the term is still useful to distinguish those parts of the corona that are not part of active regions (dominated by flare processes) or coronal holes (harboring the source regions of the fast solar wind). In the following we highlight recent observations of flow and jet phenomena in the Quiet Sun (Table 6.1).

Small-scale Hα upflow events were observed in the Quiet Sun with the BBSO, with typical sizes of $\approx$ 2.5″, blue-shifted velocities of $\approx$ 5 km s^{-1}, lifetimes of $\approx$ 1.4 min, and a birth rate of $\approx$ 78 events s^{-1} (Lee et al. 2000). They are different from dark mottles, which show both blue and red shifts (Lee et al. 2000).

Explosive events were observed with SUMER/SOHO in the Quiet Sun and exhibit bidirectional jets following a reconnection event, with high velocities of $\approx$ 100 km s^{-1}, spatial sizes of $\approx$ 2″ (1500 km), average lifetimes of $\approx$ 1 min, temperatures of 3×10^4–3×10^5 K, and a birth rate of $\approx$ 600 s^{-1} (Peter and Brkovic 2003). While the feature of bidirectional jets generally indicates magnetic reconnection, some explosive events were interpreted in terms of flux cancellation, or as a miniature CME with EUV dimming (Innes and Teriaca 2013).

Dynamic fibrils are thin jet-like extrusions that are formed in the vicinity of photospheric magnetic field concentrations, but extend out to the Quiet Sun and reach heights of 2000–10,000 km, and have durations of 3–10 min. Phenomena like dynamic fibrils, mottles, and spicules (Fig. 5.5) are all believed to be driven by magneto-acoustic shocks (Hansteen et al. 2006; De Pontieu et al. 2007a). Spicules

Table 6.1 A compilation of recent observations of Quiet-Sun transient phenomena, with interpretation of their drivers

Phenomenon	Interpretation	References
Hα upflow events	Magnetic reconnection	Lee et al. (2000)
Blinkers	Chromospheric heating	Peter and Brkovic (2003)
Dynamic fibrils	Magneto-acoustic shocks	Hansteen et al. (2006)
Spicules (limb) type-I	Magneto-acoustic shocks	De Pontieu et al. (2007a)
Spicules (limb) type-II	Magnetic reconnection	De Pontieu et al. (2007b)
Elongated dark mottles (disk)	Magneto-acoustic shocks	Rouppe van der Voort et al. (2007)
Reverse (soft X-ray) jet	Heat conduction or MHD wave	Shimojo et al. (2007)
Small-scale energy releases	Flux submergence	Potts et al. (2007)
High-speed upflows	Magnetic reconnection	McIntosh and De Pontieu (2009)
Miniature CMEs	Supergranular flows	Innes et al. (2009)
Explosive events	Magnetic reconnection	Innes and Teriaca (2013)
Jetlets in upper chromosphere	Fan-spine reconnection	Zeng et al. (2016)

are jet-like features at the limb, referred to as dynamic fibrils in active region plages, and as mottles in the Quiet Sun (Rouppe van der Voort et al. 2007).

Jetlets in the upper chromosphere can be triggered by magnetic fan-spine reconnection in emerging magnetic ephemeral regions (Filippov et al. 2007). The fan-spine geometry of the magnetic reconnection of a small-scale chromospheric jet event (Figs. 6.3 and 6.4) could be clearly resolved with the *New Solar Telescope (NST)* using 10,830 Å filtergrams (Zeng et al. 2016). Bi-directional flows were observed across the separatrix regions, suggesting that the jet was produced by magnetic reconnection in the upper chromosphere (Zeng et al. 2016). A jet propagating in a similar fan-spine geometry has been simulated by Wyper and DeVore (2016).

Reverse Soft X-ray Jets occur in the Quiet Sun at the secondary footpoint of a closed loop that produced a soft X-ray jet at the primary footpoint rooted in an active region. Such reverse jets have been observed with XRT/Hinode and are suspected to be produced by heat conduction, or by a MHD wave subsequent to the main jet (Shimojo et al. 2007).

Small-scale energy releases in the Quiet Sun can occur due to flux submergence, driven by the ubiquitous sub-photospheric convective downflows (Potts et al. 2007).

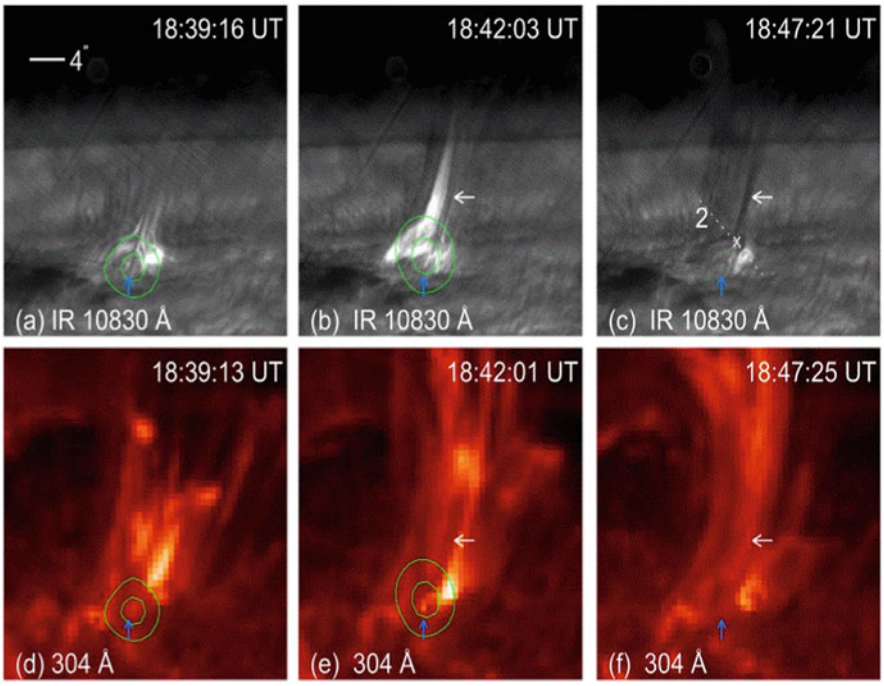

Fig. 6.3 Evolution of a jet event: 10,830 Å filtergrams (**a–c**), AIA 304 Å images (**d–f**). Green contours are RHESSI 6–12 keV emission, (Zeng et al. 2016)

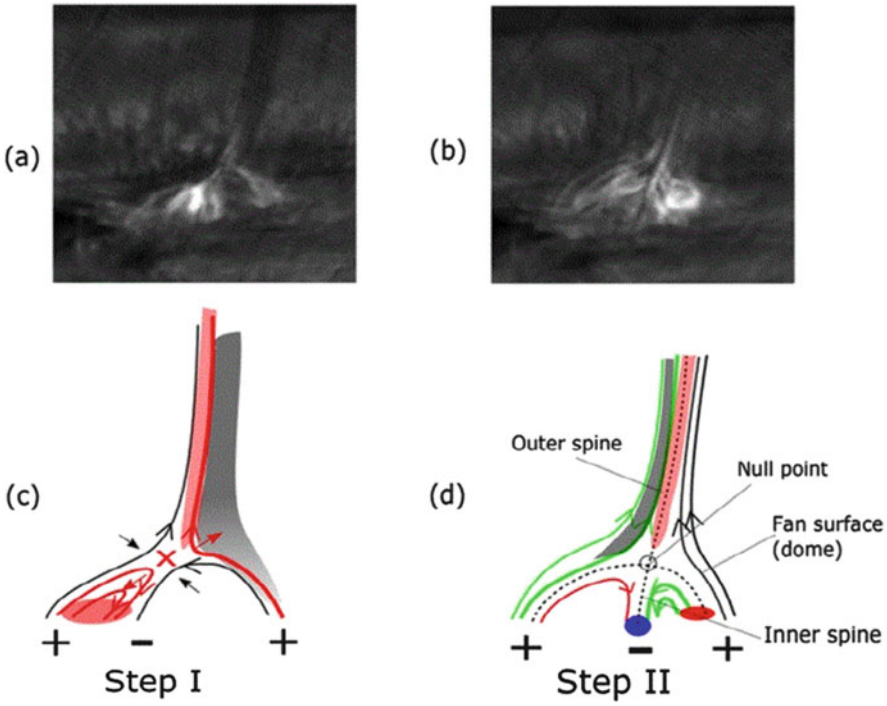

Fig. 6.4 Hα images (**a**,**b**) and diagram of fan-spine geometry of magnetic reconnection process (**c**,**d**), (Zeng et al. 2016)

Frequent high-speed (supersonic) mass downflows were inferred from SOT/Hinode measurements (Shimizu et al. 2008).

High-speed flows from the transition region into the corona in Quiet-Sun regions have been inferred from Si IV 1402 Å, C IV 1548 Å, N V 1238 Å, O VI 1031 Å, and Ne VIII 770 Å spectral lines observed with IRIS, which show a significant asymmetry in the blue wing of the emission line profiles. These high-speed upflows, preferentially occurring around the network regions, reveal upward velocities of order 40–100 km s^{-1} (McIntosh and De Pontieu 2009). This upflow component carries enough hot plasma to become significant for the energy and mass balance of the Quiet corona (McIntosh and De Pontieu 2009). These high-speed upflows are commensurable with speeds measured in type-II spicules (De Pontieu et al. 2007b). Plume-like structures, which generally carry high-speed outflows, are not only seen in coronal holes, but also in Quiet Sun regions (Tian et al. 2011). Ubiquitous Quiet-Sun jets have been detected also with IMAX/Sunrise and SOT/Hinode, based on the highly dynamic and strongly Doppler shifted Stokes V signals (Martinez Pillet et al. 2011), but no center-to-limb variation was detected (Rubio da Costa et al. 2015).

Miniature Coronal Mass Ejections (mini-CMEs) can be activated in the supergranular boundaries, where photospheric flows sweep up concentrations of

mixed polarity magnetic field. These mini-CMEs produce brightenings in EUV and faint waves with speeds of $\gtrsim 100$ km s^{-1}, with a rate of ≈ 1400 events per day on the whole Sun (Innes et al. 2009; Hong et al. 2011).

6.3 Quiet Sun: Cyclones and Tornadoes

Like the weather on Earth, cyclones, tornadoes, and hurricanes share the same property of rotational vortex motion. It is therefore no surprise that such vortical motions have been noticed in the solar corona recently (with SOHO and TRACE in late 1990s, and with SDO since 2010), mostly occurring in rotating prominences, but also in Quiet-Sun regions. Ancient reports of tornado-like prominences may go back as far as to Angelo Secchi in 1877.

While rotational motions on the Sun have been observed earlier, the discovery of *"cyclones"* rooted in *rotating network magnetic fields* was reported by Zhang and Liu (2011). The phenomenon of EUV cyclones is seen everywhere in the Quiet Sun, in all EUV channels of AIA/SDO (94, 131, 171, 193, 211, 304, 335 Å), and thus covers the full coronal temperature range of $T \approx 0.5$–2.5 MK. Observations and a *differential emission measure* analysis with EIS/Hinode suggest that there is more mass contribution in tornadoes at a temperature below $T = 1.0$ MK than in prominences (Levens et al. 2015). The rotational motion seen in EUV is also apparent in the line-of-sight magnetograms, and thus the rotating coronal plasma is tied to the rotation of the magnetic field, similar to the rotation of sunspots (Sect. 4.8). The rotation of cyclones has been tracked over several hours, but the lifetime of cyclones can last longer than 10 hours (Zhang and Liu 2011), up to 70–100 hrs in homologous cyclones (Xu et al. 2014). The rotation speed of cyclones was found in the range of $\approx 1°$–$5°$ per minute. After the cyclones rotate for several hours (Fig. 6.5), they can be followed by EUV brightenings (or microflares) and EUV waves. In a statistical survey of 388 *rotating network magnetic fields* near disk center, a mean unsigned magnetic flux of 4.0×10^{21} Mx (or 78% of the total network flux) was found, with the rotation showing a weak hemispheric preference (Zhang and Liu 2011). The rotation of the magnetic field about the vertical axis corresponds to an increase of the vertical current and helicity, as well as to an increase of the non-potential and free (magnetic) energy, and this way provides energy storage to be released in Quiet-Sun transients (see Sect. 6.2). Like magnetic tornadoes (Wedemeyer-Böhm et al. 2012), also other phenomena like cyclones may serve as energy channels into the solar corona, although this has still to be investigated. In a few cases, however, the causality may be reversed, i.e., flares may trigger a solar tornado (Panesar et al. 2013). The magnetic tornadoes appear to be driven by a combination of convective motion and conservation of angular momentum, while cyclones might be rather the result of a larger rotating magnetic field structure.

The likely explanation of the rotating motion of cyclones is the emergence of a helically twisted magnetic flux tube. In an observation by SOT/Hinode, such an emerging twisted flux tube, reminiscent of a cyclone, was found to produce

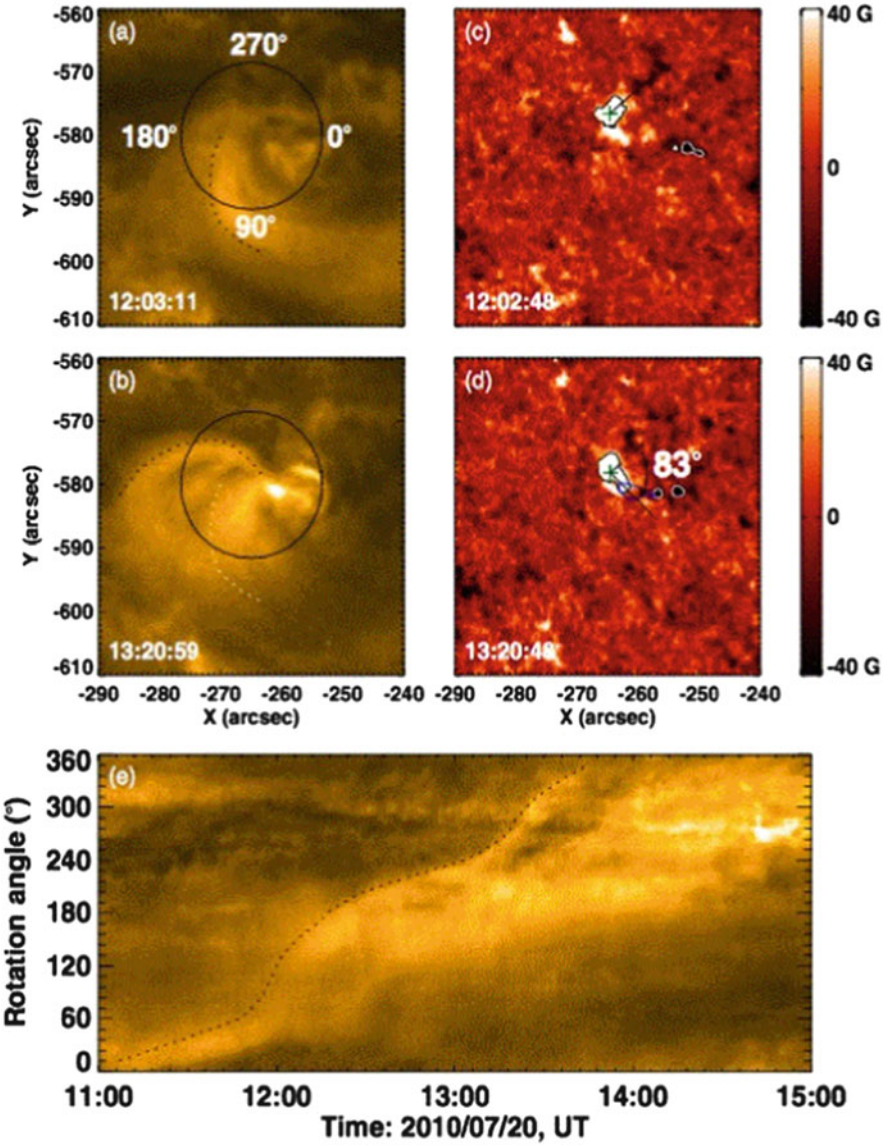

Fig. 6.5 AIA/SDO 171 Å images (**a**,**b**), HMI/SDO magnetograms (**c**,**d**), and a time-slice diagram of the rotation angle of a cyclone observed on 2010 July 20. (**e**) The rotation angle is 83° between the two times 12:03:11 UT and 13:20:59 UT (Zhang and Liu 2011)

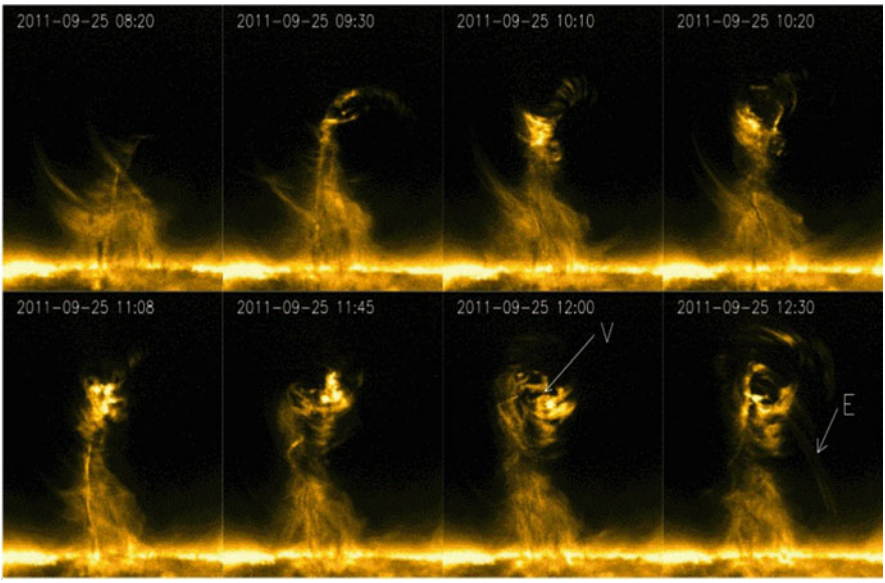

Fig. 6.6 Time evolution and rotation of a solar tornado seen in the AIA (171 Å) channel over ≈4 hrs, starting on 2011 September 25, 08:20 UT, at 8 different times (Li et al. 2012)

a chromospheric running wave, which could be reproduced with a 3-D MHD simulation (Magara et al. 2012).

Another type of solar tornadoes is the rotational flow and evolution of magnetic helicity in a *prominence cavity*. Such a configuration with a prominence seen at the limb and associated cavity, observed with AIA/SDO, has been reported by Li et al. (2012). The evolution during 3 hours shows material upflowing from the prominence core along a loop-like structure, accompanied by a rise ($\geq 50,000$ km) of the prominence core and the loop, producing small blobs and streaks of varying brightness rotating around the top part of the prominence and cavity (Fig. 6.6), mimicking a cyclone (Li et al. 2012). The cyclonic appearance is interpreted in terms of the expansion of helical structures into the cavity, and the movement of plasma along helical structures, which appears as a rotation when viewed along the helix axis (Li et al. 2012).

The relationship of so-called *solar magnetic tornadoes* with filaments or prominences became clearer when the rotational motion was disentangled above the limb, both in emission (He II 304 Å, Hα 6562.8 Å, Ca II K3 3934 Å, using AIA, NSO-GONG, and Meudon data), as well as in absorption (AIA, Fe IX 171 Å) (Su et al. 2012, 2014). A statistical study of 201 *giant tornadoes* yields an occurrence rate of 30 events to be present across the whole Sun, at a time near the solar maximum (Wedemeyer et al. 2013). The rotation of the tornadoes may progressively twist the magnetic field structure of a prominence until it becomes unstable and erupts (Wedemeyer et al. 2013). Recent studies focus on the helical kink instability of

prominences, which may be encountered in a tornado-like evolution (Wang et al. 2017).

As an alternative explanation, Panasenco et al. (2014) confronts us with the view that the tornado-like appearance of helically twisted prominences is mainly an illusion due to projection effects. Two different cases are discussed. One case of apparent vortical motion in prominence spines and barbs arises from the (mostly) 2-D counterstreaming plasma motion along the prominence spine and barbs, together with oscillations along individual threads. The other case of apparent rotational motion is observed in a prominence cavity and results from the 3-D plasma motion along the writhed magnetic fields inside and along the prominence cavity as seen projected on the limb. Thus, the "tornado" impression results either from counterstreaming and oscillations, or from the projection on the plane-of-the-sky of plasma along magnetic field lines, rather than from a true vortical motion around an (apparent) vertical or horizontal axis (Panasenco et al. 2014). Later spectroscopic work showed persistent blue and red Doppler shifts on the two opposite sides of the tornado (Su et al. 2014; Mghebrishvili et al. 2015; Schmieder et al. 2017; Yang et al. 2018), evidencing rotational motion of the tornado and weakening the *"vortical illusion"* argument of Panasenco et al. 2014). On the other side, tornado-like magnetic structures are only able to support prominences if sufficient twist or poloidal flows are present (Luna et al. 2015).

In contrast to cyclonic and tornado events in the Quiet-Sun corona, vortex motions have also been observed in the chromosphere. Observations with CRISP in the Ca II 8542 Å spectral line revealed *small-scale swirl events*, originally called *chromospheric swirls*, which typically consist of ring or ring fragments with widths of $\approx 0.2''$, diameters of $\approx 2''$, and Doppler shifts of -2 to -7 km s^{-1} (Wedemeyer-Böhm and Rouppe van der Voort 2009; Wedemeyer-Böhm et al. 2012). Numerical simulations show that the swirling motion, which occurs as photospheric vortex flows in the MHD simulations, indeed produces the spiral particle trajectories in the chromosphere (Wedemeyer and Steiner 2014).

6.4 Quiet Sun: Magnetic Field

The global magnetic field of the Sun can be modeled as a poloidal dipole during the solar minimum, turning into a toroidal field during the solar cycle maximum, according to the Babcock-Leighton dynamo model. In addition, strong local magnetic fields are produced by emerging flux in sunspots and active regions, which need to be superimposed onto the global field. The global magnetic field can then be further subdivided into zones of open magnetic fields (containing polar and trans-equatorial holes) and closed-field regions (the so-called Quiet Sun regions). In addition, there are ubiquitous and randomly distributed small-scale fields, called *salt-and-pepper* structure. Contrary to the general definition of coronal holes in terms of open field regions, closed loops were found to exist in coronal holes also, but their average length and height is lower than in the Quiet Sun (Wiegelmann and

Solanki 2004), essentially produced by the salt-and-pepper structure. We have to keep this compartmentalization in mind when we talk about the *Quiet-Sun magnetic field*.

The salt-and-pepper structure of positive and negative small-scale magnetic polarities appears to be randomly distributed on the photospheric solar surface, but a more careful examination of magnetograms reveals a hierarchy of network structures, mesogranular, supergranular, and giant cell structures, which all organize the inhomogeneous Quiet Sun magnetic field. The photospheric salt-and-pepper structure has also been called *"magnetic carpet"* and evolved into the *tectonic coronal heating model* (Priest et al. 2002), in analogy to geological tectonic plates that produce earthquakes (stressed energy releases) at their (network) boundaries (Fig. 6.7). The magnetic flux in the Quiet Sun is not static, but rather highly dynamic, as it emerges in ephemeral regions and quickly migrates to supergranule

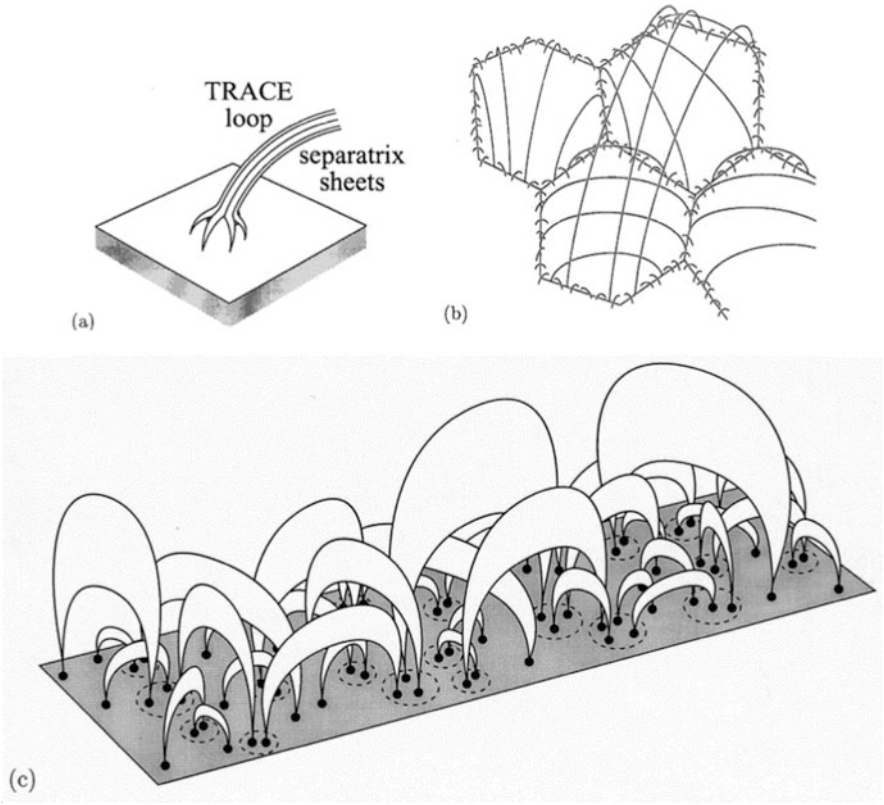

Fig. 6.7 (**a**) Coronal loop observed with TRACE, with a footpoint that ends as a spider of fingers separated by separatrix current sheets. (**b**) Over several supergranules a range of coronal loops (viewed from above) shows a mixture of short and long loops. (**c**) A 3-D view within the network indicates that the photospheric flux elements (dashed ovals) are in general connected to a range of neighbors (Priest et al. 2002)

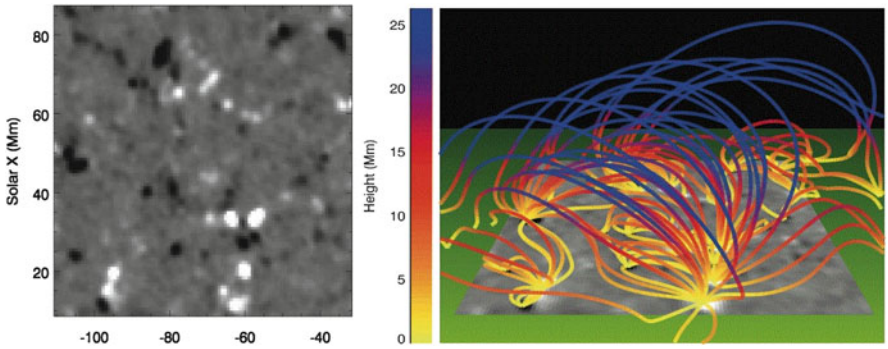

Fig. 6.8 *Left:* Magnetogram (80 × 80 pixels) showing the line-of-sight component of the photosphere, white is positive and black is negative magnetic polarity. *Right:* Magnetic field extrapolation based on the boundary condition of the observed magnetogram in left panel. The color indicates the height (from 0 to 25 Mm). Note that all field lines indicate a closed-field configuration, without open field lines (Close et al. 2004)

boundaries, merges, and cancels over time periods of 10–40 hrs. Most ($\approx$ 95%) of the photospheric flux closes low down in the chromosphere (Fig. 6.8), while only a small fraction ($\approx$ 5%) forms large-scale connections with the overlying corona. The time scale for magnetic flux connected to the Quiet-Sun corona is only $\approx$ 1.4 hr (Close et al. 2004), about 10% of the photospheric flux recycling time (Hagenaar 2001).

The measured magnetic field strength of the salt-and-pepper component depends very much on the spatial resolution of the instrument. Spectro-polarimetric measurements (Fe 6300 Å) of high-resolution data from Hinode (with 0.32″ resolution) indicate that the inter-network consists of very inclined $\approx$ 100 G fields, while the network exhibits a predominance of kG field concentrations (Orozco Suarez et al. 2007). The ubiquitous horizontal polarization on the edges of bright granules seen by Hinode are found to be invariant during a solar cycle, which lends support for a local dynamo (Buehler et al. 2013).

Modeling the Quiet Sun magnetic field by positioning flux concentrations on the edges of cells formed by Voronoi tesselation (to mimic the salt-and-pepper field) and applying observed loop scaling laws, it is found that the solar corona has a plasma-β close to unity, the corona exhibits dynamic fine structure, but no significant spatially averaged Doppler shift, which implies that the Quiet Sun corona is often neither quasi-steady nor force free, and thus MHD models are needed to model the coronal magnetic field (Schrijver and van Ballegooijen 2005).

The complexity of the solar magnetic field has been approached with topological methods (for a review see Longcope 2005), which characterizes the field by separators, separatrices, quasi-separatrix layers, null points, fans, spines, skeletons, and bald patches (related to "saddle points" in mathematical terminology). Topological models, such as the *magnetic charge topology model*, the *pointwise mapping model*, or the *submerged pole model* help to compartmentalize the magnetic

field into unipolar magnetic regions, to quantify magnetic connectivities between different polarities, and to understand the connectivity changes during a magnetic reconnection process. A relationship between the number of domains (D), number of magnetic unipolar sources (S), the number of separators (X), and the number of coronal nulls (N) is,

$$D = S + X - N - 1 \,. \tag{6.4.1}$$

The salt-and-pepper structure of the magnetic field in the Quiet Sun produces many *magnetic separators*, since many separators arise from each null point (Close et al. 2005). Based on a study with SOT/Hinode, null points are found mostly to be located above the bottom boundary layer in the photosphere (54%) and in the chromosphere (44%), with only a few null points in the corona (2%), which emphasizes the topological complexity in the chromosphere, while the corona exhibits a simpler field geometry, and coronal heating involving an X-point in a magnetic reconnection process is less likely than in the chromosphere (Régnier et al. 2008; Longcope and Parnell 2009). This is also consistent with modeling magnetic loops in the Quiet Sun using IMAX/Sunrise data, from which it is found that 91% of the magnetic energy in the mid-chromosphere (at a height of 1000 km) is in a field line whose stronger footpoint has a strength of more than 300 G, which is above the equipartition field strength with convection (Wiegelmann et al. 2010).

Dynamical models of the global solar magnetic field include differential rotation, supergranular diffusion, meridional flows, magnetic flux emergence (for a review see Mackay and Yeates 2012). The major requirement of global models is the interpolation of magnetograms to the back-side of the Sun, which became known as *synoptic magnetograms*. For the computation of such global coronal magnetic field models, a number of methods have been invented, such as the *Potential Field Source Surface (PFSS)* model, *Nonlinear Force-Free Field (NLFFF)* models, or *magneto-hydrostatic (MHS)* models (for a review see Wiegelmann et al. 2014, 2017). Comparisons between the extrapolation methods exemplify the dependence on the computational domain (Tadesse et al. 2015), and on the spatial resolution (DeRosa et al. 2015). Significant improvements of the computed NLFFF solutions can be obtained by fitting automatically detected loops and fibrils with the *Vertical Current Approximation (VCA-NLFFF)* code (Aschwanden et al. 2016). Another improvement of NLFFF codes involves "inductive" electric field solutions obtained from a surface flux-transport model (Weinzierl et al. 2016). A novel method involves the kinematics of *"EIT waves"* during their global propagation over the solar surface to calculate the magnetic field (Long et al. 2013).

6.5 Quiet Sun: Photosphere-Corona Connectivity

There is an intimate coupling between the photosphere and the corona, as exhibited by close correlations between the photospheric magnetic field strength B and the soft X-ray luminosity L_{SXR} of the corona. While some correlation $B \propto L_{SXR}$ is

expected in active regions (Benevolenskaya et al. 2002), where soft X-ray emission is produced by magnetic reconnection processes and subsequent plasma heating during flares, it is perhaps surprising to find a coupling in Quiet-Sun regions (Pevtsov and Acton 2011), even far away from flaring active regions.

A study on the soft X-ray luminosity and photospheric magnetic field was undertaken with SXT/Yohkoh and KPNO magnetograms during almost a full solar cycle (1991–1998), in 3 selected field-of-views at the central meridian (Pevtsov and Acton 2011). The soft X-ray luminosity decreased by a factor of 7 between 1991 (active Sun) and 1996 (quiescent Sun), while the unsigned magnetic flux decreased only by a factor of 2. The soft X-ray luminosity exhibited also variations on time scales of 9–12 months, which were not present in the magnetic flux, which implies that the Quiet-Sun magnetic elements (*chromospheric network, "magnetic carpet", or "salt-and-pepper fields"*) can at best account for a minimal contribution to the heating of the 1–2 MK corona, while the major contribution to coronal heating has to be associated with the stronger magnetic fields in active regions (Pevtsov and Acton 2011).

Another correlation study between the photospheric magnetic field and the EUV brightness of the coronal plasma was conducted by using MDI/SOHO magnetograms and EIT/SOHO Fe XII (195 Å) images for a total duration of 4 days (Handy and Schrijver 2001). The findings are that emerging bipoles in the Quiet Sun reach a typical length of $\approx$ 14 Mm before fading or reconnecting in a time period of $\approx$ 5–12 hrs, and the Quiet Sun decorrelates in $\approx$ 15 hrs. The majority of coronal loops in the Quiet Sun were found to be products of numerous small-scale magnetic flux concentrations coalescing in the photosphere, rather than being produced by a single large emerging bipole (Handy and Schrijver 2001).

A recent study explores the statistics and occurrence probability distributions of coronal EUV brightening events (observed with EUVI/STEREO) and the photospheric counterparts (detected in magnetograms from MDI/SOHO), sampled over a time duration of one month (Uritsky et al. 2013). Interestingly, the majority of coronal dissipation sites do not show an obvious correlation with the underlying photospheric field. However, both distributions are power law-like, suggesting that the multi-scale intermittent dissipation in the corona at spatial scales $>$ 3 Mm is controlled by turbulent photospheric convection. The complex topology of the photospheric network makes this coupling essentially nonlocal and non-deterministic. The lack of detailed correlations has been predicted by Schrijver and Title (2002), which is described as *stochastic coupling* of the solar photosphere with the corona (Uritsky et al. 2013). This is a fundamental property of nonlinear energy dissipation systems, in the sense that a random disturbance (in the photosphere) can be nonlinearly amplified to a small or large avalanche event (in the corona), a property that is also called *self-organized criticality*. Although both input (disturbances) and output (avalanche) events have similar (power law-like) occurrence (size) distribution, the size of an individual avalanche event cannot be predicted from the size of the triggering disturbance.

Magnetic field computations in the Quiet Sun are challenging because of the complex topology at the spatial resolution limit of current instrumentation. The topological domains of mixed-polarity magnetic potential fields have been analyzed

from TRACE and MDI/SOHO data, leading to the conclusions that (i) we should expect at best a weak correlation between coronal brightness and the magnetic flux in the underlying flux concentrations, (ii) that low-lying chromospheric field lines can be traced in Hα fibrils to obtain complementary information to traced EUV loops in coronal heights, and (iii) that Parker's prediction of footpoint braiding is more efficient low in the corona (rather than in the high corona) and in Quiet-Sun regions (rather than in active regions) (Schrijver and Title 2002). Magnetic field modeling of IMAX/Sunrise data exhibited a rapid connection recycling time of $\approx 3 \pm 1$ min in the upper atmosphere and $\approx 12 \pm 4$ min in the photosphere (Wiegelmann et al. 2013).

The magnetic connection between the solar photosphere and the corona has often been characterized with a wineglass-shaped magnetic canopy of network flux that fully encloses weakly magnetic regions below it (Fig. 6.9 left), which was

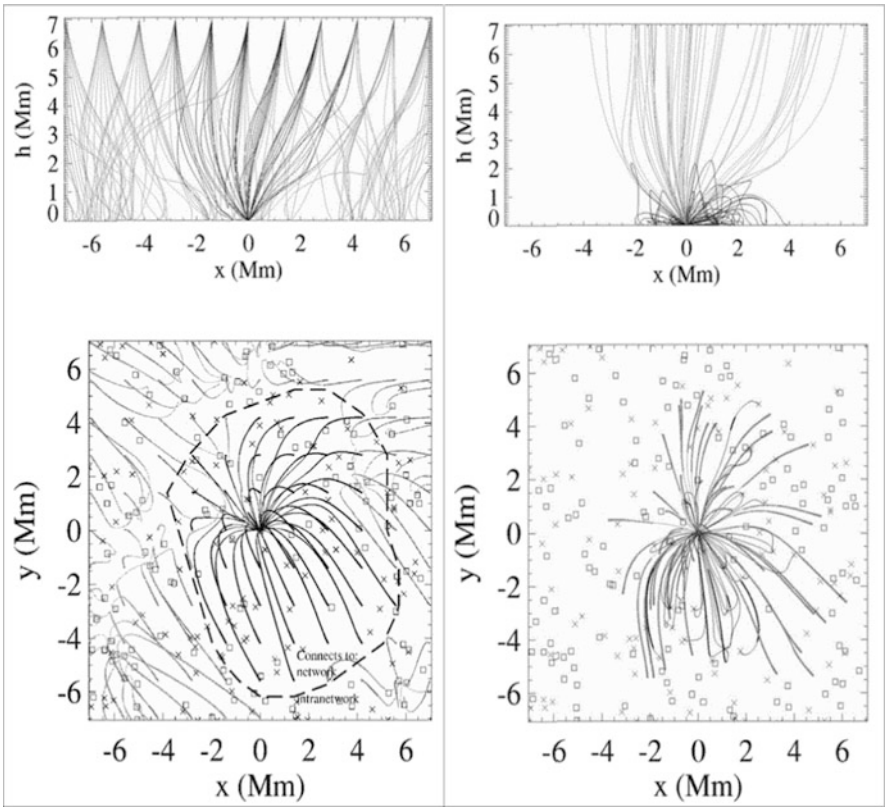

Fig. 6.9 *Left:* Magnetic field extrapolation from a regular grid at an altitude of $h = 7$ Mm, which illustrates the classical network canopy that covers the entire photosphere. *Right:* Magnetic field extrapolation from network concentrations with a flux of 3×10^{18} Mx in very Quiet-Sun regions, surrounded by a small-scale mixed polarity field (Schrijver and Title 2003)

later considered as fundamentally wrong (Schrijver and Title 2003). Instead, in the presence of a relatively strong internetwork field, as much as half of the coronal field over very Quiet Sun may be rooted in the mixed-polarity internetwork field throughout the supergranules (Fig. 6.9 right), rather than in the previously assumed network flux concentrations (Schrijver and Title 2003; Wedemeyer-Böhm et al. 2009). Even more pessimistic, magnetic field models with kG internetwork flux elements demonstrated that one cannot really determine with current instrumentation from observations, which regions on the Quiet-Sun surface, i.e., the network or internetwork, are connected to which parts of the corona through extrapolation techniques (Jendersie and Peter 2006).

Theoretical scenarios of the photosphere-corona coupling in the Quiet Sun involve post-reconnection shocks and sling-shot effects in the photosphere and chromosphere (Ryutova et al. 2001), the tectonic coronal heating model (Priest et al. 2002), magnetic reconnection in quasi-separatrix layers and hyperbolic flux tubes (Titov et al. 2002), generalized squashing factors for a covariant description of magnetic connectivity (Titov 2007), and 3-D MHD simulations of subphotospheric magneto-convection (e.g., Abbett 2007).

A summary diagram of the complex concepts of the photosphere-corona coupling is shown in Fig. 6.10, which includes phenomena such as granulation, supergranulation, photospheric network, p-modes, g-waves, small-scale canopies, weak fields, current sheets, shock waves, fibrils, dynamics fibrils, type-I and type-II spicules, Alfvén waves, etc. (Wedemeyer-Böhm et al. 2009; Lagg et al. 2017). The solar magnetism is a multi-scale system in which low-flux magnetism plays a crucial role, coupling different layers of the atmosphere (Martinez-Gonzalez et al. 2010).

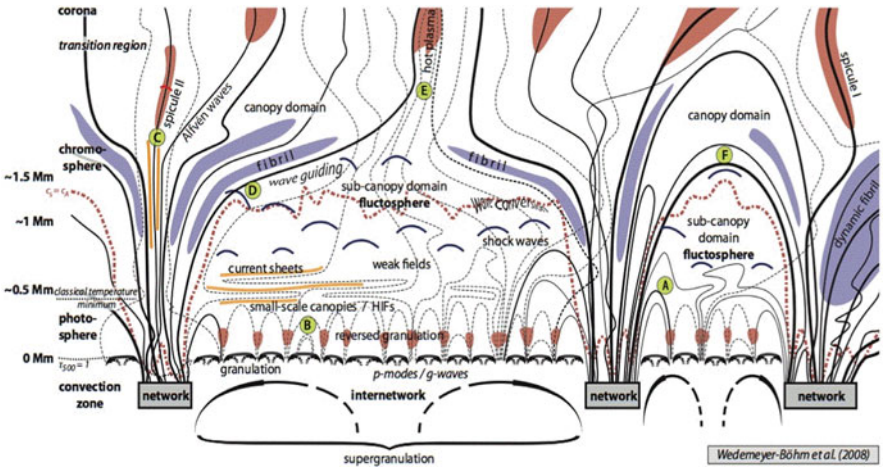

Fig. 6.10 Schematic diagram of the coupling between the convection zone, the photosphere, chromosphere, transition region, and corona (Wedemeyer-Böhm et al. 2009)

6.6 Quiet Sun: Alfvénic Waves

Theoretical studies concluded that dissipation of Alfvén waves is not an effective heating mechanism for the transition region and corona, although it may be for the chromosphere (e.g., Campos and Mendes 2000). In a partially ionized chromosphere, the dominant damping process of Alfvén waves is due to collisions between ions and neutrals (De Pontieu et al. 2001; Khodachenko et al. 2004; Leake et al. 2005; Song and Vasyliunas 2011; Tu and Song 2013). For a given wave frequency, the maximum damping always occurs at temperature minimum heights and in the coldest structures. Alfvén waves with frequencies above 0.6 Hz (or $\lesssim 1.7$ s) were found to be completely damped, and frequencies below 0.01 Hz (or $\gtrsim 100$ s) unaffected (Leake et al. 2005). The chromosphere behaves like a low-pass filter and the magnetic field strength determines the upper cutoff frequency. For coronal loops, the presence of a moderate amount of Alfvén wave damping in the chromosphere can enhance wave leakage at the loop footpoints (De Pontieu et al. 2001), which is a likely mechanism for damping of coronal loop oscillations, as first observed in TRACE data.

Early numerical simulations of small-scale flux tubes (with diameters of 100 km) in the granular network of the Quiet Sun have been studied in terms of strong currents conveyed by nonlinear torsional and compressional waves, and it was found that Alfvénic wave energies can be transferred upward in both untwisted and highly twisted flux tubes and eventually contribute to coronal heating (Sakai et al. 2001). Another simulation on dissipated Alfvén waves in an inhomogeneous 3-D force-free equilibrium model above a Quiet Sun region exhibited partial reflection of waves and demonstrated that a non-negligible fraction of the Alfvén wave energy is dissipated inside the corona (Malara et al. 2005), taking place mainly in magnetic separatrices (Malara et al. 2007).

The search for waves in the Quiet Sun corona started around the new millennium, with space-borne instruments (SOHO/EIT, Yohkoh), as well as with ground-based coronagraphs, e.g., in green-line (Fe XIV 5305 Å) spectra with the *Norikura Solar Observatory*, from which Alfvénic wave speeds of ≈ 500 km s^{-1} and sound waves with wave speeds of ≈ 100 km s^{-1} were reported (Sakurai et al. 2002). The line intensity and line width (of sound waves) did not show clear oscillations, but their phase relationship with the Doppler velocity $(\delta I/I) = 2(v/c_s)$ (with sound speed $c_s \propto \sqrt{T}$) indicated propagating waves rather than standing waves.

A breakthrough in the detection of Alfvén waves in the solar corona was accomplished with the *Coronal Multi-Channel Polarimeter (CoMP)* instrument at the *National Solar Observatory (NSO)* New Mexico, by using the Fe XIII 10,747 Å coronal emission line, which provided intensity, line-of-sight velocity, and linear polarization images (Tomczyk et al. 2007). Ubiquitous upward propagating waves were seen (Fig. 6.11), with phase speeds of 1000–4000 km s^{-1}, and trajectories consistent with the direction of the magnetic field inferred from the linear polarization measurements. The type of MHD waves that was most consistent with the observations was believed to be Alfvén waves, because the observed phase

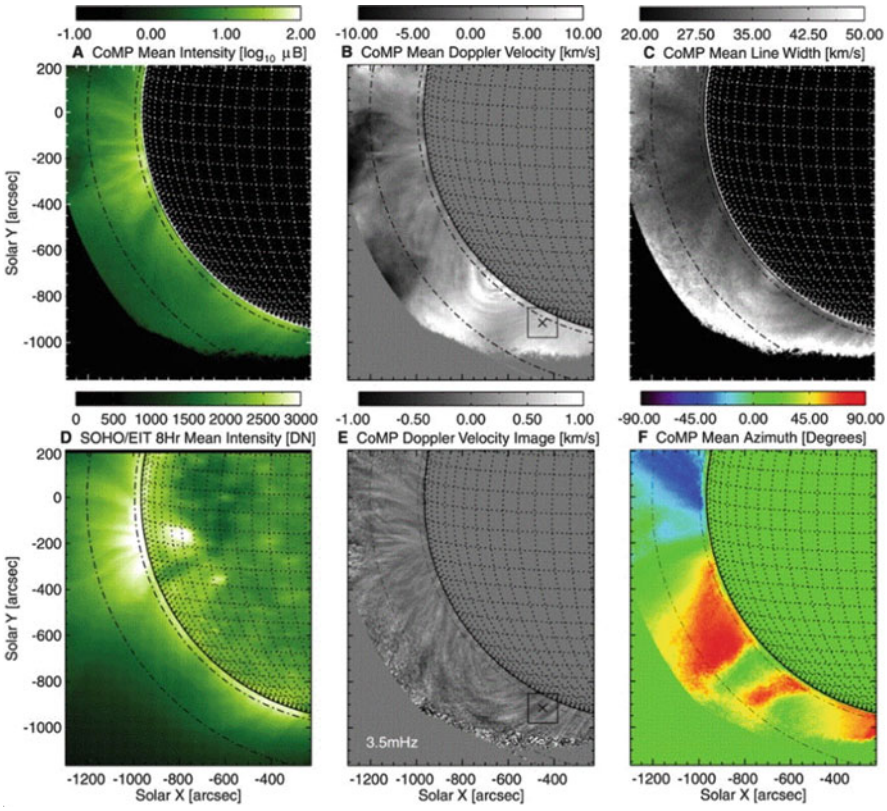

Fig. 6.11 (**a**) CoMP mean intensity [$\log_{10} \mu B$]; (**b**) CoMP mean Doppler velocity [km s^{-1}]; (**c**) CoMP mean line width [km s^{-1}]; (**d**) SOHO/EIT 8 hr mean intensity [DN]; (**e**) CoMP Doppler velocity image [km s^{-1}]; (**f**) CoMP mean azimuth [degrees] (Tomczyk et al. 2007)

speeds (1000–4000 km s^{-1}) are much larger than the sound speed ($\approx$ 200 km s^{-1}) and therefore the waves are not slow magneto-acoustic mode waves. The spatio-temporal properties of the velocity oscillations and the linear polarization measurements show that these waves propagate along the fields, which would not be the case for fast magneto-acoustic waves. The power of these detected Alfvén waves, however, was found to be insufficient to heat the corona.

While the previous detection of Alfvénic waves in the corona (Tomczyk et al. 2007) revealed oscillation amplitudes far too small (0.5 km s^{-1}) to supply the energy flux of (1–2) $\times$ 10^5 erg cm^{-2} s^{-1}, which is required to drive the fast solar wind or to balance the radiative losses of the Quiet Sun corona, new measurements were presented, using He II 304 Å and Fe IX 171 Å data from AIA/SDO, where transverse swaying motion of coronal loops (Fig. 6.12) were interpreted as the response to passing Alfvénic waves through plasma at $\approx$ 10^5 K (in the transition region) or at coronal temperatures (McIntosh et al. 2011). The ubiquitously observed

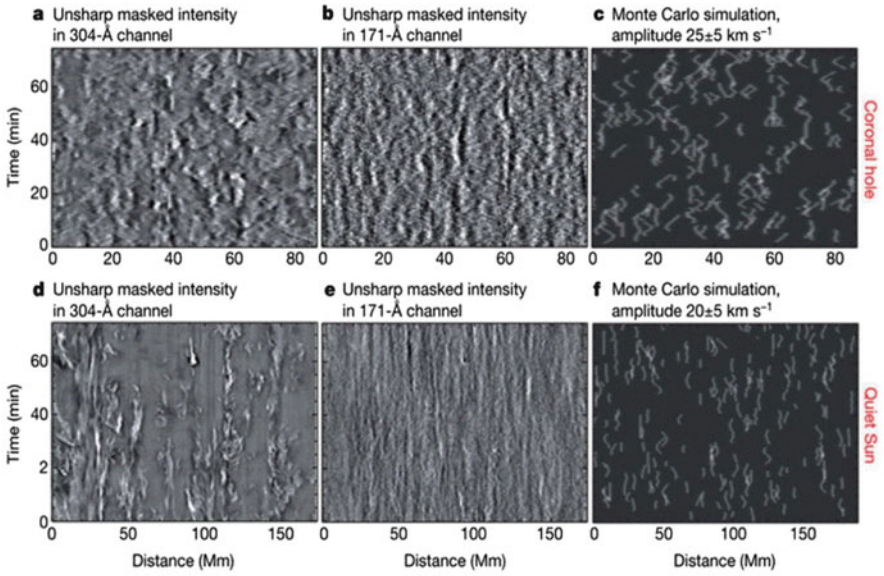

Fig. 6.12 Examining Alfvénic motion in coronal hole (top row) and Quiet Sun (bottom row) regions. (**a**–**e**) AIA/SDO space-time plots of unsharp masked intensity in the 304 Å (**a**,**d**) and 171 Å (**b**,**e**) channels 15 Mm above the solar limb. (**c**,**f**) Monte-Carlo simulations for Alfvénic waves with periods of 150–600 s and amplitudes of 25 ± 5 (**c**) and 20 ± 5 km s^{-1} (**f**). These simple simulations indicate that the spatio-temporal superposition of many independent bright features carrying Alfvénic waves with random phases leads to poor visibility of the extrema of the sinusoidal motion. The polarization of the Alfvénic wave is along the line-of-sight (McIntosh et al. 2011)

outward-propagating Alfvénic motions have periods of the order of 100–500 s throughout the quiescent atmosphere, and thus carry sufficient energy to heat the Quiet corona (McIntosh et al. 2011). Furthermore, compressible (sound waves) and incompressible wave modes (Alfvénic waves) have both been identified in on-disk observations also, which indicates a vast reservoir of wave energy in the chromosphere (Morton et al. 2012).

Analysis of CRISP/SST Hα 6562.8 Å observations revealed the ubiquitous presence of high-frequency ($\approx$ 12–42 mHz, or 20–80 s) torsional motions in thin spicular-type structures in the chromosphere of the Quiet Sun, which by means of numerical simulations were identified as *torsional Alfvén waves* (Srivastava et al. 2017). The associated high-frequency drivers in the chromosphere were estimated to contain a huge Poynting flux of $\approx 10^8$ erg cm^{-2} s^{-1}, while less than $\lesssim 1\%$ transmission to the corona would be sufficient to heat the corona and to energize the (supersonic) solar wind (Srivastava et al. 2017).

6.7 Quiet Sun: Heating Mechanisms

The *coronal heating problem* is one of the most prominent unsolved mysteries in solar physics. Bluntly stated: Why does the coronal temperature increase from $\approx$ 5800 K on the photospheric surface to several million degrees in the corona? A differentiation in the answer must be made for at least three different magnetic regimes in the solar corona: (i) active regions (with closed magnetic fields), (ii) the Quiet Sun region (with closed magnetic fields), and (iii) coronal holes (with open magnetic fields). The energy balance is somewhat different for open-field configurations, where the plasma can flow away, and for closed-field structures, where an equilibrium can be reached. The heating rates or Poynting fluxes required to balance conductive and radiative losses are therefore different in the three regimes, i.e., $E \approx 8 \times 10^5$ erg cm^{-2} s^{-1} ($T_e \approx 0.8$ MK) for coronal holes, $E \approx 3 \times 10^5$ erg cm^{-2} s^{-1} ($T_e \approx 1.5$ MK) for the Quiet Sun, and $E \approx 10^7$ erg cm^{-2} s^{-1} ($T_e \approx 2.5$ MK) for active regions, which is also reflected in the different (mean) temperatures. Most of the proposed physical heating mechanisms can be classified into two major categories, AC (alternating current) models such as faciliated by high-frequency waves, and DC (direct current) models such as generated by twisting and braiding of coronal loops. There has been significant progress and evidence for both types of models since the new millennium, so that the question has to be refined to the relative contributions of AC versus DC currents. Recent reviews on the coronal heating problem can be found in DeMoortel and Browning (2015) and Klimchuk (2015).

AC wave heating models experienced a strong boost after the detection of Alfvénic waves with SOT/Hinode, which detected Alfvén waves in chromospheric spicules with strong amplitudes of the order of 10–25 km s^{-1} and periods of 100–500 s. The energy flux in the chromosphere was estimated to be $E = \rho v^2 v_A \approx$ (4–7) $\times 10^6$ erg s^{-1} cm^{-2}, based on the Alfvén speed $v_A = B/\sqrt{\mu_0 \rho}$, the observed velocity amplitude $v \approx 20$ km s^{-1}, the spicular mass density $\rho = (2.2–40) \times 10^{-14}$ g cm^{-6}, and the magnetic field $B \approx 10$ G (De Pontieu et al. 2007). The energy flux that reaches the corona is thus on the order of $E \gtrsim 1.2 \times 10^5$ erg s^{-1} cm^{-2} for a transmission coefficient of 3%. These numerical values have also been approximately reproduced with recent 3-D radiative MHD simulations. Therefore, the upward propagating energy flux is sufficient to heat the Quiet-Sun corona and/or to power the solar wind (De Pontieu et al. 2007, 2011). Tomczyk et al. (2007) detected Alfvénic waves in the corona also, but the oscillation amplitudes turned out to be far too small (0.5 km s^{-1}) to supply the energy flux of $E \approx$ (1–2) $\times 10^5$ erg cm^{-2} s^{-1} required to heat the Quiet Sun corona. On the other hand, by using He II 304 Å and Fe IX 171 Å data from AIA/SDO, outward-propagating Alfvénic motions with periods of $\approx$ 100–500 s were detected throughout the quiescent atmosphere, which were interpreted in terms of passing Alfvénic waves that also carried sufficient energy to heat the Quiet Sun corona (McIntosh et al. 2011). In addition, CRISP/SST Hα 6562.8 Å observations revealed the ubiquitous presence of high-frequency ($\approx$ 12–42 mHz, or 20–80 s) torsional motions in thin spicular-

type structures in the chromosphere of the Quiet Sun, which by means of numerical simulations were identified as *torsional Alfvén waves*, requiring only $\lesssim$ 1% transmission to the corona to match the coronal heating requirement (Srivastava et al. 2017). Using EIS/Hinode spectral data and a magnetic field model, an energy in the range of $E \approx (1.3\text{–}5.5) \times 10^5$ erg cm^{-2} s^{-1} was found at the footpoint of Quiet-Sun loops, which amounts to more than 80% of the coronal heating requirement and was interpreted as further evidence for wave heating of the Quiet-Sun corona (Hahn and Savin 2014). Of course, besides the energy input into the corona, the dissipation mechanisms in the corona are equally important to identify in the solution of the solar heating problem.

DC heating models include stress-induced reconnection, stress-induced current cascades, or stress-induced turbulence models. The most prominent DC heating model is due to Parker, who envisioned random braiding of coronal field lines that leads through cumulative build-up of non-potential magnetic energy to magnetic reconnection events. The basic reconnection physics is similar in large-scale flares and small-scale coronal heating events (also called nanoflares), but the major issue is whether the small-scale heating events involve spatially resolved loops that can be observed and modeled individually as "monolithic elements", or whether the small-scale heating events cannot be resolved and consequently can only be modeled as a statistical phenomenon. A pioneering new result was made with the *High-resolution Coronal Imager (Hi-C)* during a rocket flight on 2012 July 11, taking images in the Fe XII 193 Å line (sensitive to a temperature of $T_e \approx 1.5$ MK), with a spatial resolution of $0.2''$ ($\approx$ 150 km). The Hi-C data show evidence of magnetic field braiding and axial twist in loops along their length (Fig. 6.13), magnetic reconnection, and subsequent heating in the low corona, while AIA/SDO with a resolution of $1.2''$ (900 km) did not resolve the braiding, but detected a flare with a temperature of $\approx$ 7 MK (Cirtain et al. 2013). In another subsequent braiding and untwisting event, a total (magnetic) free energy of $E_{tot} \approx 10^{29}$ erg was estimated. Cirtain et al. (2013) emphasize that the observed magnetic configurations imply true braiding, not just helical twisting by rotation. The braiding is driven by the ubiquitous small-scale, convection-driven motion of the photospheric feet of the magnetic field, and thus provides a true DC-like energy source for the corona (Cirtain et al. 2013). Although this particular observation reveals the unmistakable topology of braiding in the corona, it needs to be demonstrated how frequently energy releases due to braiding-induced reconnection occur, and whether their dissipated energy matches the coronal heating requirement.

Besides the method of direct imaging, a frequent approach of the coronal heating problem is the 1-D hydrodynamic modeling of the spatial heating function in coronal loops, which should tell us at least whether the data are consistent with uniform, footpoint, or apex heating (Serio et al. 1981; Priest et al. 2000). Most of the fitted data were found to be consistent with footpoint heating (e.g., Aschwanden et al. 2000; Winebarger et al. 2003). Also in the flux-tube tectonic model, the strongest heating is expected in the "carpet" near the footpoints of coronal loops, due to the preponderance of supergranular downflows in the chromosphere (Priest et al. 2002). Synthesizing recent observations, ten arguments were brought forward that yield

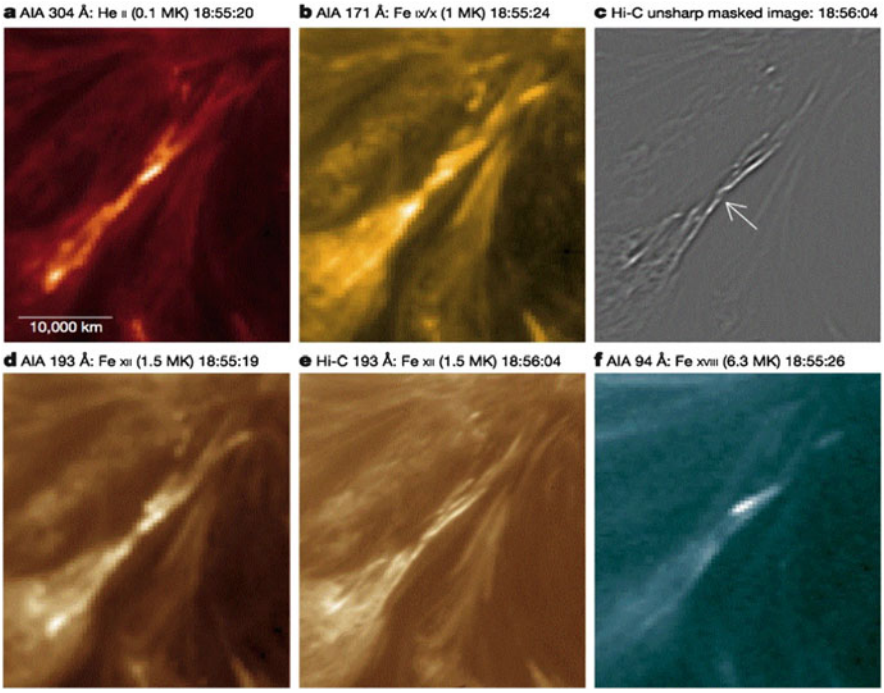

Fig. 6.13 A twisted coronal loop structure seen at different coronal temperatures by AIA and Hi-C: (**a**) AIA 304 Å, He II (0.1 MK); (**b**) AIA 171 Å, Fe IX/X (1.0 MK); (**c**) Hi-C unsharp masked; (**d**) AIA 193 Å, Fe XII (1.5 MK); (**e**) Hi-C 193 Å, Fe XII (1.5 MK); (**f**) AIA 94 Å, Fe XVIII (6.3 MK), (Cirtain et al. 2013)

strong evidence for (footpoint) heating of the corona with input from chromospheric sources (Aschwanden et al. 2007), based on: (i) the temperature evolution of coronal loops, (ii) the over-density of hot coronal loops, (iii) upflows into coronal loops, (iv) the Doppler blue-shift in coronal loops, (v) upward propagating MHD waves, (vi) the energy balance in coronal loops, (vii) the magnetic complexity in the transition region, (viii) the altitude of observed microflares and EUV nanoflares, (ix) the cross-section of elementary loops, and (x) 3-D simulations of coronal heating. More accurate atomic calculations (of Fe lines) would help also to improve the coronal temperature and heating diagnostics. Improved density measurements with EIS/Hinode in the Quiet Sun above the limb established a temperature distribution that is strongly peaked at $\approx$ 1.0 MK, but has a significant tail at higher temperatures that cannot be understood with current atomic data (Warren and Brooks 2009). A hot-temperature component in the Quiet Sun could be detectable with RHESSI, but new upper limits in the 3–200 keV range, which are substantially lower than previous ones, constrain several physical processes that could contribute to the Quiet Sun hard X-ray flux, such as coronal thin-target emission, microflares, cosmic rays, or generation of axions inside the Sun (Hannah et al. (2010)).

One theoretical concept of coronal heating processes, introduced by Eugene Parker in the 1980s, is the so-called *nanoflare model*. In the review of Klimchuk (2015), 10 key aspects of this model have been highlighted, which should be understood before we can consider the problem to be solved: (i) All coronal heating is impulsive; (ii) the details of coronal heating matter; (iii) the corona is filled with elemental magnetic strands; (iv) the corona is densely populated with current sheets; (v) the strands must reconnect to prevent an infinite build-up of stress; (vi) nanoflares repeat with different frequencies; (vii) what is the characteristic magnitude of energy release? (viii) what causes the collective behaviour responsible for loops? (ix) what are the onset conditions for energy release? (x) chromospheric nanoflares are not a primary source of coronal plasma. The biggest problem of this concept is the ambiguity and (or undetectability) of individual (unresolved) nanoflare structures.

6.8 Quiet Sun: EUV Nanoflare Energetics

The plausibility and viability of any proposed coronal heating mechanism usually has been buttressed by a back-of-the-envelope estimate of the coronal heating rate requirement, which entails an energy balance between the heating rate and the conductive and radiative loss rate. Such energy estimates are often made by assuming typical values for the involved physical parameters. Typical parameter values, however, are only valid for incoherent random processes (leading to Gaussian-like distributions), but are ill-defined for nonlinear processes with coherent growth of avalanching events (leading to scale-free, power law-like distributions). The scale-free range $[x_1, x_2]$ of power law distributions $N(x) \propto x^{-\alpha}$ is usually bound by a lower threshold x_1 (above which complete sampling is assumed), and by an upper bound x_2 (which is given by the largest observed event). The total energy contained in a distribution can then conveniently be obtained by integrating the power law distributions over the scale-free range (also called *inertial range*). The peak of the power law distribution is usually found to be close to the threshold of complete sampling, rather than being a typical (mean) value of a Gaussian random distribution. Size distributions (also called *frequency distributions* or *occurrence rate distributions*) of different data sets, should only be compared for equal threshold values x_1 and equal time ranges $[t_1, t_2]$ of the data sets, unless they are properly normalized to the same total number of events and the same threshold. Substantial progress has been accomplished over the last three decades by quantifying the (power law-like) size distributions of Quiet Sun small-scale events (or EUV nanoflares), rather than estimating (ill-defined) typical values.

Before we review the statistics and energetics of small-scale events in the Quiet Sun, we have to clarify the nomenclature of the so-called *nanoflare* events. There is an observational and a theoretical meaning of this term. The observations refer to *large flares* in the energy range of $E \approx 10^{30}$–10^{33} erg, to *microflares* in the energy range of $E \approx 10^{27}$–10^{30} erg, and to *nanoflares* in the energy range of $E \approx 10^{24}$–10^{27} erg (Fig. 6.14). While large flares are detected in hard X-rays,

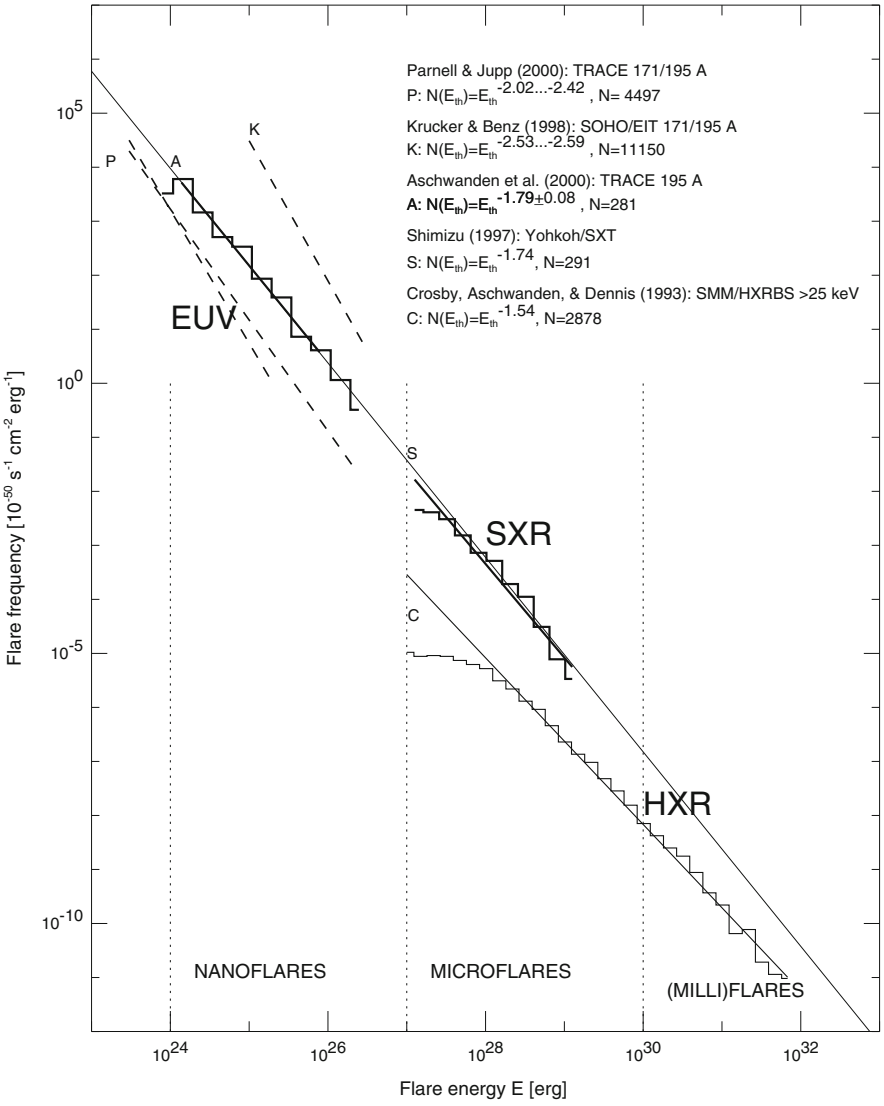

Fig. 6.14 Composite flares frequency distribution in a normalized scale in units of 10^{50} flares per time unit (s^{-1}), and energy unit (erg^{-1}). The diagram includes EUV flares analyzed in Krucker and Benz (1998), Parnell and Jupp (2000), Aschwanden et al. (2000), and compared with soft X-ray brightenings (Shimizu 1997), and hard X-ray flares (Crosby et al. 1993). All flare energies are specified in terms of the thermal energy $E_{th} = 3n_e k_B T_e V$, except for the hard X-ray flares. An overall power law slope of $\alpha = 1.8$ is indicated, extending over the entire energy domain of 10^{24}–10^{32} erg (Aschwanden et al. 2000)

microflares are seen in soft X-rays, and nanoflares in EUV wavelengths. These nanoflares observed in EUV show all characteristics of large flares (cooling delay, small post-flare loops, etc), and appear to consist of resolved flare loops with widths of $w \approx 1.0$–1.5 Mm (Krucker and Benz 1998; Parnell and Jupp 2000; Aschwanden et al. 2000). On the other side, the term *"nanoflares"* has also been used in the theoretical concept of Eugene Parker (1988), who estimates an energy of $E \approx 10^{24}$ erg for a "typical" small-scale magnetic reconnection event that smoothes out the apparent braiding of coronal loops. The major discrepancy between these two definitions of *nanoflare events* is that the observational definition is based on resolved (post-flare) loop structures, while the theoretical definition hypothesizes unresolved loop strands, so it is an issue of resolved versus unresolved structures. In order to disambiguate this dual definition of the term *nanoflares* we will use the two terms *"EUV nanoflares"* and *"Parker nanoflares"*, with the understanding that the former is based on resolved elementary loops (being observational structures), while the latter assumes unresolved elementary loops (being a theoretical hypothesis).

Three statistical studies on the energy size distribution of *EUV nanoflares* in the Quiet Sun were conducted by Krucker and Benz (1998), Parnell and Jupp (2000), and Aschwanden et al. (2000). All three studies selected EUV data (EIT/SOHO, TRACE), a field-of-view in the Quiet Sun (away from active regions), used similar (but independently developed) automated event detection algorithms, and obtained similar energy ranges, but somewhat different power law slopes α of the energy size distribution (Fig. 6.14): $\alpha \approx 2.3$–2.6 (Krucker and Benz 1998); $\alpha \approx 2.4$–2.6 (Parnell and Jupp 2000); $\alpha \approx 1.8$ (Aschwanden et al. 2000). The differences in these power slopes can easily be explained by a number of systematic effects, such as: the selection of events, the model of the line-of-sight depth, and/or different detection thresholds, etc. (Aschwanden et al. 2000; Benz and Krucker 2002). Taking the fractal geometry of the EUV nanoflare volume and a broader temperature coverage of EUV and soft X-ray wavelengths into account, the slope of the power law distribution of EUV nanoflare energies flattens to $\alpha \approx 1.54 \pm 0.03$ (Aschwanden and Parnell 2002). There is a critical power law slope value of $\alpha_{crit} = 2$ that implies divergence of the integral at the lower (or upper) end of the size distribution, depending on whether the slope is larger (or smaller) than this critical value. If this criterion is applied, there is more energy in EUV nanoflares than in large flares for measurements of $\alpha > 2$ (Krucker and Benz 1998; Parnell and Jupp 2000), and vice versa for $\alpha < 2$ (Aschwanden et al. 2000). However, the extrapolation of the power law size distribution to unobserved energies that are many orders of magnitude smaller remains questionable (Benz and Krucker 2002), and may invalidate the importance of nanoflare heating of the Quiet Sun corona by unresolved Parker nanoflares. Parnell and Jupp (2000) find that EUV nanoflares occur in 16% of the solar surface only, in regions with the brightest EUV emission, which are presumably the regions connected to the strongest magnetic fields (i.e., active regions), which does not explain *Parker nanoflare* heating in the EUV-faint parts of the Quiet Sun. Harrison et al. (2003) proposed a unification of Quiet-Sun transient-event phenomena, for instance blinkers, network flares, cell brightenings, and EUV brightenings appear to have the same physical characteristics, which could be added

Table 6.2 Frequency distributions of small-scale phenomena observed in Quiet Sun regions (Aschwanden et al. 2000)

Phenomenon	Number of events N	Powerlaw slope α_E	Energy range E_1, E_2 10^{24} [erg]	Total flux F [erg cm^{-2} s^{-1}]
EUV transients, EIT, 171+195[a]	233	2.45 ± 0.15	10–300	0.7×10^5
EUV transients, EIT 195[b]	228	1.35 ± 0.20	1–100	...
EUV transients, EIT 195[c]	277	1.45 ± 0.20	10–100	...
Nanoflares, TRACE, 171+195[d]	5131	2.48 ± 0.11	0.3–60	0.2×10^5
Nanoflares, TRACE+SXT[e]	281	1.53 ± 0.02	10–10^6	0.5×10^5
Blinkers, CDS, O V[f]	790	1.34 ± 0.08	0.01–0.3	...
Explosive ev., SUMER C III[g]	3403	2.8 ± 0.1	0.05–2	0.45×10^5
Explosive ev., SUMER Ne IV[g]	2505	2.8 ± 0.1	0.6–10	0.16×10^5
Explosive ev., SUMER O VI[g]	5531	3.3 ± 0.4	0.1–2	0.79×10^5
Explosive ev., SUMER Ne VIII[g]	2907	2.8 ± 0.5	0.06–1	0.03×10^5
Quiet Sun heating requirement				3.0×10^5

[a]Krucker and Benz (1998); [b]Berghmans et al. (1998); [c]Berghmans and Clette (1999); [d]Parnell and Jupp (2000) [corrected for a factor of 100 in original paper]; [e]Aschwanden et al. (2000); [f]Brkovic et al. (2001); [g]Winebarger et al. (2002)

to the EUV nanoflare events and this way boost the overall energy input into the Quiet Sun corona.

In Table 6.2 we compile frequency distributions of small-scale phenomena that have been reported from the Quiet Sun and calculate their total energy flux F based on the observed energy ranges $[E_1, E_2]$ and the power law slopes α_E. EUV transients, nanoflares and microflares generally are found in the energy range of $E \approx 10^{24}$–10^{26} erg and the integrated flux over the entire observed frequency distribution lies in the range of $F \approx (0.5 \pm 0.2) \times 10^5$ erg^{-1} cm^{-2} s^{-1}, which makes up about one sixth of the total heating requirement of the Quiet corona, roughly covering the radiative losses in the Quiet Sun corona. A similar flux was also measured for explosive events in C III, Ne IV, and O VI (Winebarger et al. 2002), which fits into the picture that explosive events and nanoflares are probably controlled by the same physical process as a magnetic reconnection process in the transition region. This conclusion is also supported by the comparable amounts of thermal plasma inside the transition region (as detected in the cooler EUV lines in C III, Ne IV, and O VI) as well as in the lower corona (in the hotter EUV lines of Fe IX/X and Fe XII). Other phenomena such as blinkers carry several orders of magnitude less energy ($E \approx 10^{22}$–3×10^{23}; Brkovic et al. 2001), and thus seem to be energetically less important for coronal heating.

6.9 Quiet Sun: Fluxtube Braiding

The theoretical concept of fluxtube braiding as a coronal heating mechanism of the Quiet Sun, introduced by Parker (1972) as *topological dissipation and the small-scale fields in turbulent gases*, became testable once the first 3-D MHD numerical simulations (Gudiksen and Nordlund 2002, 2005a,b) of a realistic-looking corona, displaying a number of loop-like structures, became available (Peter et al. 2004).

Of course, the efficiency of fluxtube braiding completely depends on how the system is driven, and how the time-dependent boundaries of the computation box are defined. In the first simulations (Gudiksen and Nordlund 2002, 2005a,b; Peter et al. 2004), the initial magnetic field was obtained from a potential field extrapolation of a MDI/SOHO magnetogram of active region NOAA 9114. The lower boundary is stressed by a time-dependent velocity field, constructed from a Voronoi tesselation that reproduces the granulation pattern (Schrijver et al. 1997), while the velocity field reproduces the geometric pattern as well as the amplitude power spectrum of the velocity and vorticity (Peter et al. 2004). In this MHD simulation, the braiding of the magnetic field by the photospheric motions rapidly produces an intermittent corona in both time and space with a typical temperature of $\approx$ 1 MK, during the whole simulated time span of $\approx$ 50 min. The time- and space-averaged heating function decreases exponentially with height, producing a heat input of $E \approx (2\text{–}8) \times 10^6$ erg cm^{-2} s^{-1} that is sufficient to heat the corona (in the chosen active region, and supposedly in Quiet Sun regions also). Using the electron density, temperature, and velocity from the MHD model, the emissivity for a number of UV and EUV emission lines could be synthesized, which matched the typical observed values, so that Peter et al. (2004) concluded that the fluxtube braiding mechanism is a prime candidate for being the dominant heating process of the magnetically closed corona of the Sun and solar-like stars. More advanced simulations of coronal heating through footpoint braiding have been conducted by Hansteen et al. (2015), including a convection zone, where granulation and associated flows are driven by self-consistent convection. On smaller scales, heating is concentrated in current sheets with widths set by the numerical resolution.

Following Parker's braiding concept, the plasma volumes of coronal loops should repeatedly be spliced, leading to an increase of loop width with time, with a diffusion coefficient of 93 ± 9 km^2 s^{-1} (Schrijver 2007), which matches the dispersion coefficient of the granular random walk up to several hours. Consequently, loop width observations indicate that granular braiding is statistically countered by frequent coronal (interchange) reconnection events, which in turn explains the general absence of entangled coronal field structures in the quiescent corona (Schrijver 2007).

Other measures of the degree of braiding involves the *squashing factor* Q (a property of magnetic field line mapping) and *quasi-separatrix layers (QSL)*, for which it is found that the maximum values of Q increase exponentially, as the degree of braiding of the magnetic field is increased, while myriads of thin QLSs form, and thus QSLs are not good predictors or current features in this class of braided fields

(Wilmot-Smith et al. 2009a). An analytical braiding model with parallel electric fields shows that loss of equilibrium is an inevitable consequence of the braiding process, probably via magnetic reconnection events (Wilmot-Smith et al. 2009b).

The dynamics of a braiding loop pair has been explored with a resistive 3-D MHD code, starting with an initial near force-free field, and leading to a long-wavelength instability and formation of two thin current sheets, including an elliptic magnetic field structure about the reconnection site, and resulting in an untwisting of the global field (Wilmot-Smith et al. 2010). A myriad of thin current layers form via a cascade process, triggering multiple reconnection events, and finally ending in a non-linear force-free field of two flux tubes of oppositely-signed twist embedded in a uniform background field (Pontin et al. 2011). Similar simulations leading to heating of the braided loops are described in Wilmot-Smith et al. (2011), Wilmot-Smith (2015), Pontin and Hornig (2015).

The braiding of coronal loop strands can be modeled in terms of a self-organized criticality model, similar to a forest fire model, in which the frequency distributions of coherent braid sequences as well as flare energies follow power law distributions (Berger and Asgari-Targhi 2009, 2015). A similar cut-and-splice model of loop strands has been modeled by Morales and Charbonneau (2008), which mimics the braiding of loop strands and reproduces the power law distributions typical for self-organized criticality models. It is suggested that the braiding-associated reconnection in the corona can be understood in terms of a self-organized criticality model driven by convective rotational motions, similar to those observed at the photosphere (Knizhnik et al. 2018).

What observational tests can be designed for braiding loops? A more specific question is: if energy release occurs in a coronal loop containing braided magnetic flux, should we expect a clearly observable signature in emissions? Pontin et al. (2017) attempt to answer this question by using MHD simulations and forward modeling of synthesized EUV images (Fig. 6.15). They demonstrate that the presence of braided magnetic field lines does not guarantee a braided appearance to the observed intensities. However, in all cases they considered, the evolution of the braided loop is accompanied by localized heating regions as the loop relaxes. An inspection of the Hi-C movies that contain braided structures (Cirtain et al. 2013) reveals emission patterns indicative of braiding on multiple spatial scales (Pontin et al. 2017). There is also a superposition effect that doubles the (optically thin) EUV brightness at the intersections of two equally bright crossing loop segments, which needs to be taken into account in forward-modeling and data analysis of braided loops. Another important distinction that needs to be folded into 3-D modeling of loops is twisting versus braiding geometries (Prior and Yeates 2016a). The electric current structures of the final states of simulated flux ropes differ significantly between the braided field (which has a diffuse nature), and the twisted field (which displays a clear sigmoid), and could be observable (Prior and Yeates 2016a,b). In addition, quasi-periodic flows within a velocity range of 13–185 km s^{-1} have been detected in braided structures, possibly outflows from reconnection sites (Pant et al. 2015), which can be compared with MHD simulations.

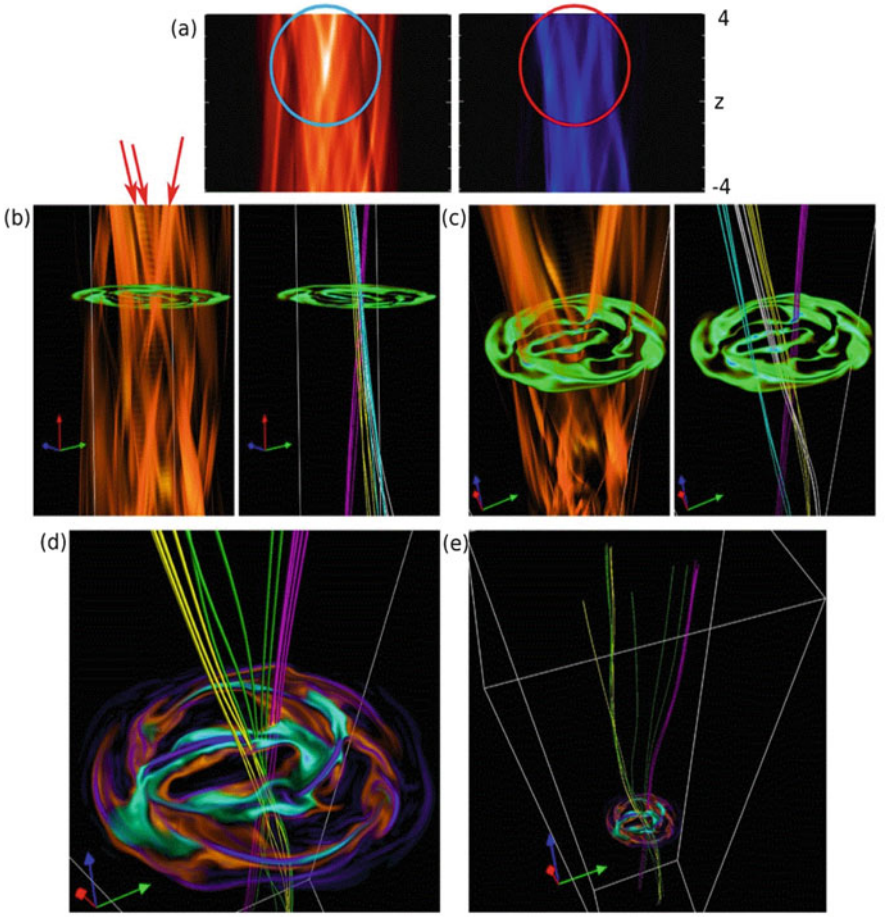

Fig. 6.15 Braiding simulation: (**a**) Close-up of a braiding structure from a synthesized EUV image in Fe XII 193 Å (red-orange) and Fe XV 284 Å (blue); (**b–e**) Different aspect angles and field-of-views. The shading in the cross-sections show regions of Fe XII emission (orange), Fe XV (cyan), and current density (purple), (Pontin et al. 2017)

Estimates of the energy input from magnetic braiding have been inferred within a range of 10^6–3.5×10^8 erg cm^{-2} s^{-1}, based on SP/Hinode data (Yeates et al. 2014). Applying a nonlinear force-free magnetic field reconstruction to the braided structure observed by Cirtain et al. (2013) yields a free energy that is about 100 times larger than estimated previously, which strengthens the possibility of the active region corona being heated by field line braiding (Thalmann et al. 2014).

6.10 Quiet Sun: Radio Emission

A recent review on radio emission of the Quiet Sun and active regions is provided in Shibasaki et al. (2011). Solar radio emission is traditionally divided into a background component (Quiet Sun), a slowly-varying component (associated mostly with active regions), and a sporadic (flare-related) burst component, but new measurements reveal considerable variability even for the Quiet Sun component. With the high-resolution observations of ALMA, even the background component became more dynamic, of course. Most of the Quiet Sun emission is produced by thermal bremsstrahlung in *local thermodynamic equilibrium (LTE)*, originating in chromospheric heights. An overview of contribution functions in the wavelengths from $\lambda = 3$ cm down to $\lambda = 70$ nm is shown in Fig. 6.16. The height-dependent temperatures $T_e(h)$, densities $n_e(h)$, and free-free opacities $\tau(h)$ have been calculated from an atmospheric model (Sect. 5.1), such as the semi-empirical Avrett and Loeser (2008) model (Fig. 6.16, red curves), or the Fontenla et al. (2007, 2009) models, which describe the average Quiet Sun chromosphere and transition region up to $T = 1.6$ MK and the Quiet Sun spectrum in the wavelength range of $\lambda = 0.04$–40 mm. Most of the radio emission at $\lambda = 3$ cm and shorter wavelengths originates below the transition region, with a small contribution from the transition region itself and no contribution from the corona. The brightness temperature as a function of wavelength has been calculated by Loukitcheva et al. (2004), based on static atmospheric models (Avrett and Loeser 2008), as well as based on the dynamic simulations of Carlsson and Stein (2002) (Fig. 6.16, bottom right panel). Their conclusion was that the dynamic picture of the solar internetwork chromosphere is consistent with the currently available mm and sub-mm brightness observations. Extending the chromospheric spectrum to the corona (say up to a wavelength of $\lambda = 20$ cm) requires a two-component model with an optically thick chromosphere and an isothermal corona. In order to match the radio polar brightening observed by the Nobeyama radioheliograph at 17 GHz, a spicular component with holes and faculae is needed (Selhorst et al. 2005, 2010). Modeling of the microwave polar brightening and its solar cycle variation has remained to be a persistent problem because of the sensitivity of the gyroresonance component to the magnetic field (Gopalswamy et al. 2012; Kim et al. 2017; Shimojo et al. 2017a).

A powerful new instrument that faciliates chromospheric modeling with unprecedented high spatial resolution is the *Atacama Millimeter/Submillimeter Array (ALMA)* in Chile (Wooten and Thompson 2009). ALMA consists of up to 66 antennas, configurable on baselines from 150 m to 15 km, and operates in the frequency range of 84–950 GHz. ALMA became operational during 2016 and produced already a number of studies. First high-resolution synthesized images were obtained during the solar-commissioning campaign in December 2015 (Shimojo et al. 2017b). White et al. (2017) used a fast-scanning method to make single-dish maps of the full Sun (Fig. 6.17). A first comparison of millimeter continuum maps from ALMA with UV maps in Mg II from IRIS demonstrated a detailed correspondence down to the fine structure of penumbral fibrils, but revealed a temperature difference

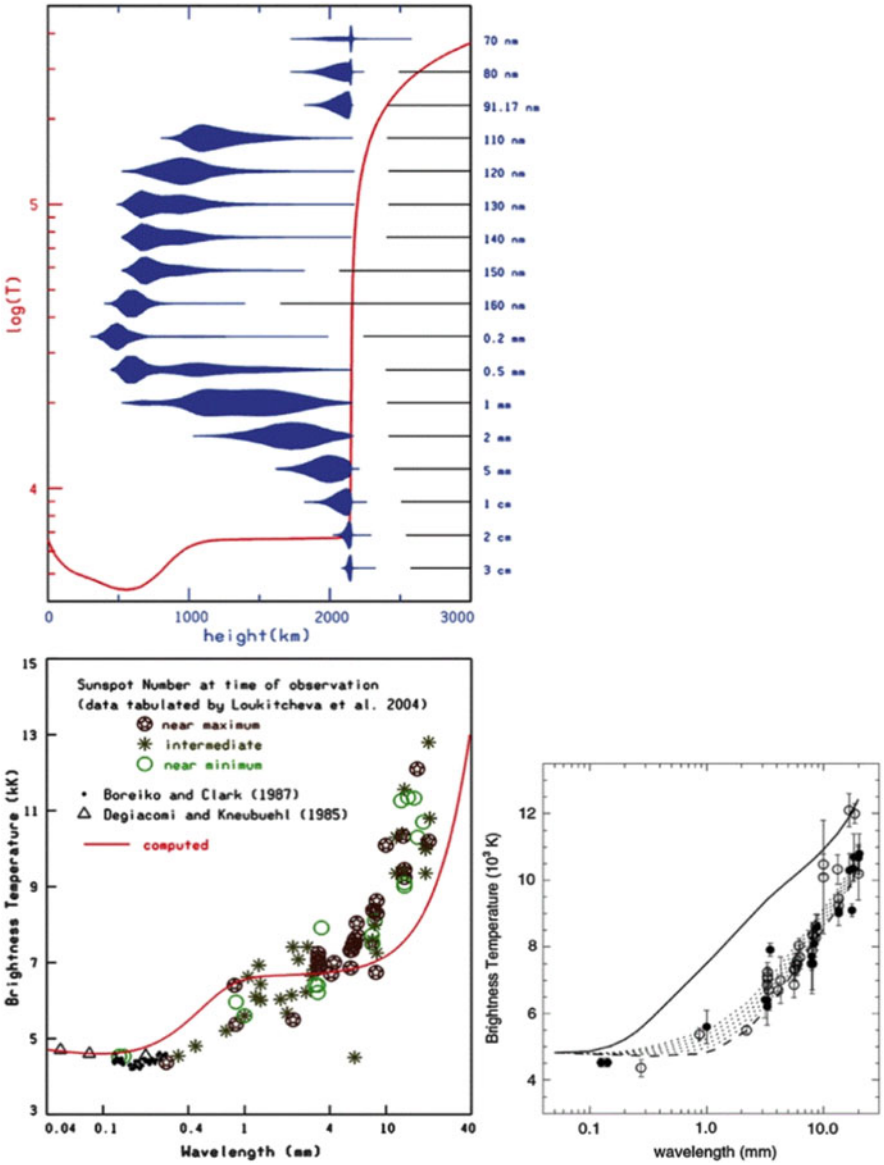

Fig. 6.16 Contribution functions at microwave and millimeter wavelengths according to the model of Avrett and Loeser (2008) (top panel), the corresponding spectrum (bottom left panel), and spectra computed by Loukitcheva et al. (2004) (bottom right), based on the FAL model F in networks (solid line), and based on the dynamic simulations by Carlsson and Stein (2002) (dotted lines). Data points near solar maximum (minimum) are represented with open (filled) circles, (Shibasaki et al. 2011)

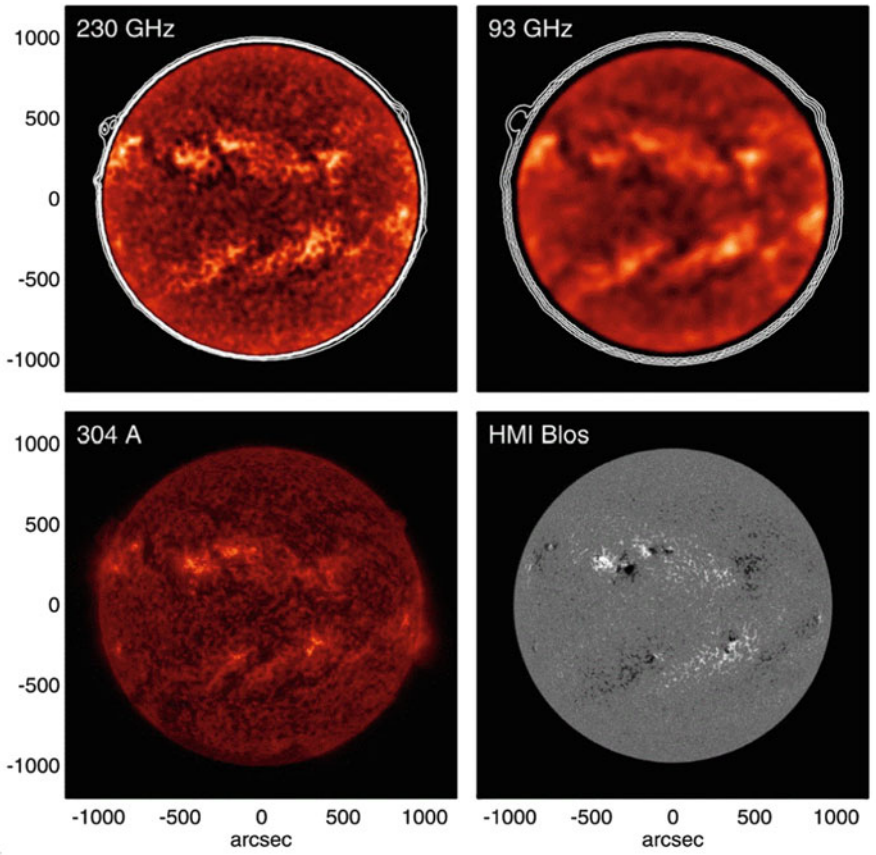

Fig. 6.17 ALMA fast-scanning observations of the Sun on 17 December 2015 at 230 GHz (5300–7400 K) and 93 GHz (6700–8800 K) (top panels), compared with a He II 304 Å AIA/SDO images (bottom left panel) and a HMI/SDO magnetogram (lower right panel), (White et al. 2017)

of 35% between the radio brightness temperature and the Mg II temperature (Bastian et al. 2017), which is currently re-analyzed. For the first time, millimeter observations of sunspots have resolved the umbral/penumbral brightness structure at chromospheric heights, revealing a temperature difference of $\approx$ 600 K between the inner part of the umbra and the surrounding Quiet Sun (Loukitcheva et al. 2017b). One strategy is to use the circular polarization of free-free emission to infer the chromospheric magnetic field. 3-D non-LTE radiative MHD simulations of the Quiet Sun have been carried out to test the chromospheric field diagnostics from free-free radiation at mm and sub-mm wavelengths (Loukitcheva et al. 2017a). The most recent review on solar science carried out with ALMA is given in Wedemeyer et al. (2016).

Another new radio interferometer that came online is the *Allen Telescope Array (ATA)*, a radio interferometer near Hat Creek, California, consisting of 42 antennas configured with baselines up to 300 m. First full-Sun maps were obtained in microwave frequencies (1.43–6.0 GHz) during 2009–2010, produced for the first time without mosaic assembling (Saint-Hilaire et al. 2012).

References

(6.1) Solar Eclipses

Alzate, N., Habbal, S.R., Druckmüller, M., et al. 2017, *Dynamics of large-scale coronal structures as imaged during the 2012 and 2013 total solar eclipses*, ApJ 848, 84, [1 c, 1 c/y].

Bleeker, J.A.M., Geiss, J., and Huber, M.C.E. (eds.) 2001. *The Century of Space Science*, p.220, Kluwer Academic Publishers, Dordrecht.

Byhring, H.S., Cranmer, S.R., Lie-Svendsen, O., et al. 2011, *Modeling iron abundance enhancements in the slow solar wind*, ApJ 732, 119, [5 c, 1 c/y].

Druckmüller, M., Habbal, S.R., and Morgan H., 2011, *Discovery of new class of coronal structures in white light eclipse images*, ApJ 785, 14, [14 c, 4 c/y].

Druckmüller, M., Habbal, S.R., Alzate, N., et al. 2017, *Tethered prominence-CME systems captured during the 2012 November 13 and 2013 November 3 total solar eclipses*, ApJ 851, L41, [1 c, 1 c/y].

Druckmüllerova, H., Morgan, H., and Habbal, S.R. 2011, *Enhancing coronal structures with the Fourier normalizing-radial-graded filter*, ApJ 737, 88, [9 c, 1 c/y].

Habbal, S.R., Morgan, H., Johnson, J., et al. 2007, *Localized enhancements of Fe^{+10} density in the coronal as observed in Fe XI 789.2 nm during the 2006 March 29 total solar eclipse*, ApJ 663, 598, [22 c, 2 c/y].

Habbal, S.R., Druckmüller, M., Morgan, H. et al. 2010a, *Mapping the distribution of electron temperature and Fe charge states in the corona with total solar eclipse observations*, ApJ 708, 1650, [34 c, 5 c/y].

Habbal, S.R., Druckmüller, M., Morgan, H., et al. 2010b, *Total solar eclipse observations of hot prominence shrouds*, ApJ 719, 1362, [44 c, 6 c/y].

Habbal, S.R., Druckmüller, M., Morgan, H. et al. 2011, *Thermodynamics of the solar corona and evolution of the solar magnetic field as inferred from the total eclipse observations of 2010 July 11*, ApJ 734, 120, [35 c, 5 c/y].

Habbal, S.R., Morgan, H., Druckmüller, M. et al. 2013, *Probing the fundamental physics of the solar corona with lunar solar occultation observations*, SoPh 285, 9, [12 c, 3 c/y].

Habbal, S.R., Morgan, Y., and Druckmüller, M. 2014, *Exploring the prominence-corona connection and its expansion into the outer corona using total solar eclipse observations*, ApJ 793, 119, [5 c, 1 c/y].

Hanaoka, Y., Kikuta, Y., Nakazawa, J., et al. 2012, *Accurate measurements of the brightness of the white-light corona at the total solar eclipses on 1 August 2008 and 22 July 2009*, SoPh 279, 75, [8 c, 1 c/y].

Lamy, P., Prado, J.Y., Floyd, O., et al. 2015, *A novel technique for measuring the solar radius from eclipse light curves - Results for 2010, 2012, 2013, and 2015*, SoPh 290, 2617, [4 c, 2 c/y].

Nandy, D., Bhowmik, P., Yeates, A.R., et al. 2018, *The large-scale coronal structure of the 2017 August 21 great American eclipse: An assessment of solar surface flux transport model enabled predictions and observations*, ApJ 853, 72.

Skomorovsky, V.I., Trifonov, V.D., Mashnich, G.P., et al. 2012, *White-light observations and polarimetric analysis of the solar corona during the eclipse of 1 August 2008*, SoPh 277, 267, [9 c, 2 c/y].

(6.2) Quiet Sun: Flows and Jets

De Pontieu, B., Hansteen, V.H., Rouppe van der Voort, L. 2007a, *High-resolution observations and modeling of dynamic fibrils*, ApJ 655, 624, [143 c, 14 c/y].
De Pontieu, B., McIntosh, S.W., Hansteen, V.H., et al. 2007b, *A tale of two spicules: The impact of spicules on the magnetic chromosphere*, PASJ 59, S655, [235 c, 22 c/y].
Filippov, B., Koutchmy, S., and Vilinga, J. 2007, *On the dynamic nature of the prolate solar chromosphere: Jet formation*, A&A 464, 1119, [12 c, 1 c/y].
Hansteen, V.H., De Pontieu, B., Rouppe van der Voort, L. 2006, *Dynamic fibrils are driven by magneto-acoustic shocks*, ApJ 647, L73, [194 c, 17 c/y].
Hong, J., Jiang, Y., Zheng, R., et al. 2011, *A micro CME associated blowout EUV jet*, ApJ 738, L20, [43 c, 7 c/y].
Innes, D.E., Genetelli, A., Attie, R., et al. 2009, *Quiet Sun mini-CMEs activated by supergranular flows*, A&A 495, 319, [47 c, 6 c/y].
Innes, D.E. and Teriaca, L. 2013, *Quiet Sun explosive events: Jets, Splashes, and Eruptions*, SoPh 282, 453, [14 c, 3 c/y].
Lee, C.Y., Chae, J.C., and Wang, H. 2000, *Dynamical characteristics of small-scale Hα upflow events on the Quiet Sun*, ApJ 545, 1124, [20 c, 1 c/y].
Martinez Pillet, V., del Toro Iniesta, J.C., and Quintera Noda C. 2011, *Ubiquitous Quiet-Sun jets*, A&A 530, A111, [17 c, 3 c/y].
McIntosh, S.W. and De Pontieu, B. 2009, *High-speed transition region and coronal upflows in the Quiet Sun*, ApJ 707, 524, [63 c, 7 c/y].
Peter, H., Brkovic, A. 2003, *Explosive events and transition region blinkers: Time variability of non-Gaussian Quiet-Sun EUV spectra*, A&A 403, 287, [14 c, 1 c/y].
Potts, H.E., Khan, J.I., and Diver, D.A. 2007, *Small-scale energy release driven by supergranular flows on the Quiet Sun*, SoPh 245, 55, [7 c, 0.7 c/y].
Rouppe van der Voort, L.H., De Pontieu, B., Hansteen, V.H., et al. 2007, *Magnetoacoustic shocks as a driver of Quiet-Sun mottles*, ApJ 660, L169, [69 c, 6 c/y].
Rubio da Costa, E., Solanki, S.K., Danilovic, S., et al. 2015, *Center-to-limb properties of small, photospheric Quiet-Sun jets*, A&A 574, A95, [3 c, 1 c/y].
Shimizu, T., Lites, B.W., Katsukawa, Y., et al. 2008, *Frequent occurrence of high-speed local mass downflows on the solar surface*, ApJ 680, 1467, [41 c, 4 c/y].
Shimojo, M., Narukage, N., Kano, R., et al. 2007, *Fine structures of solar X-ray jets observed with the X-Ray Telescope (XRT) aboard Hinode*, PASJ 59, S745, [42 c, 4 c/y].
Tian, H., McIntosh, S.W., Habbal, S.R., et al. 2011, *Observation of high-speed outflow on plume-like structures of the Quiet Sun and coronal holes with SDO/AIA*, ApJ 736, 130, [52 c, 8 c/y].
Wyper, P.F. and DeVore, C.R. 2016, *Simulations of solar jets confined by coronal loops*, ApJ 820, 77, [9 c, 6 c/y].
Zeng, Z., Chen, B., Haisheng J., et al. 2016, *Resolving the fan-spine reconnection geometry of a small-scale chromospheric jet event with the New Solar Telescope (NST)*, ApJ 819, L3, [5 c, 3 c/y].

(6.3) Quiet Sun: Cyclones and Tornadoes

Levens, P.J., Labrosse, N., Fletcher, L., et al. 2015, *A solar tornado observed by EIS. Plasma diagnostics*, A&A 582, A27, [13 c, 5 c/y].
Li, X., Morgan, H., Leonard, D., et al., 2012, *A solar tornado observed by AIA/SDO: Rotational flow and evolution of magnetic helicity in a prominence cavity*, ApJ 752, L22, [67 c, 12 c/y].
Luna, M., Moreno-Insertis, F., and Priest, E. 2015, *Are tornado-like magnetic structures able to support solar prominence plasma ?* ApJ 808, L23, [10 c, 4 c/y].
Magara, T., An, J.M., Lee, H., et al. 2012, *Chromospheric running wave from a solar cyclone produced through the emergence of a twisted magnetic flux tube*, PASJ 64, L4.

Mghebrishvili, I., Zaqarashvili, T.V., Kukhianidze, V., et al. 2015, *Dynamics of a solar prominence tornado observed by SDO/SIS on 2012 November 7–8*, ApJ 810, 89, [4 c, 2 c/y].
Panasenco, O., Martin, S.F., and Velli, M. 2014, *Apparent solar tornado-like prominences*, SoPh 289, 603, [32 c, 9 c/y].
Panesar, N.K., Innes, D.E., Tiwari, S.K., et al. 2013, *A solar tornado triggered by flares ?* A&A 549, A105, [30 c, 7 c/y].
Schmieder, B., Mein, P., Mein, N., et al. 2017, *Hα shifts in a tornado in the solar corona*, A&A 597, A109, [5 c, 10 c/y].
Su, Y., Wang, T., Veronig, A., et al., 2012, *Solar magnetized "tornadoes": Relation to filaments*, ApJ 756, L41, [50 c, 9 c/y].
Su, Y., Gömöry, P., Veronig, A., et al. 2014, *Solar magnetized tornadoes: Rotational motion in a tornado-like prominence*, ApJ 785, L2, [24 c, 7 c/y].
Wang, W., Liu, R., and Wang, Y. 2017, *Tornado-like evolution of a kink-unstable solar prominence*, ApJ 834, 38, [3 c, 3 c/y].
Wedemeyer-Böhm, S. and Rouppe van der Voort, L. 2009, *Small-scale swirl events in the Quiet-Sun chromosphere*, A&A 507, L9, [79 c, 9 c/y].
Wedemeyer-Böhm, S., Scullion, E., Steiner, O., 2012, *Magnetic tornadoes as energy channels into the solar corona*, Nature 486, 505, [157 c, 29 c/y].
Wedemeyer, S., Scullion, E., Rouppe van der Voort, L. et al., 2013, *Are giant tornadoes the legs of solar prominences ?* ApJ 774, 123, [39 c, 9 c/y].
Wedemeyer, S. and Steiner, O. 2014, *On the plasma flow inside magnetic tornadoes on the Sun*, PASJ 66, S108, [15 c, 4 c/y].
Xu, X., Zhang, J., Li, T., et al. 2014, *Homologous cyclones in the Quiet Sun*, ApJ 782, L15, [4 c, 1 c/y].
Yang, Z., Tian, H., Peter, H., et al. 2018, *Two solar tornadoes observed with the IRIS*, ApJ 852, 79, [1 c, 1 c/y].
Zhang, J. and Liu, Y. 2011, *Ubiquitous rotating network magnetic fields and EUV cyclones in the Quiet Sun*, ApJ 741, L7, [42 c, 6 c/y].

(6.4) Quiet Sun: Magnetic Field

Aschwanden,M.J., Reardon,K., and Jess,D.B. 2016, *Tracing the chromospheric and coronal magnetic field with AIA, IRIS, IBIS, ROSA*, ApJ 826, 61, [5 c, 3 c/y].
Buehler, D., Lagg, A., Solanki, S.K. 2013, *Quiet Sun magnetic fields observed by Hinode: Support for a local dynamo*, A&A 555, A33, [35 c, 8 c/y].
Close, R.M., Parnell, C.E., Longcope, D.W. et al. 2004, *Recycling of the solar corona's magnetic field*, ApJ 612, L81, [52 c, 4 c/y].
Close, R.M., Parnell, C.E., and Priest, E.R. 2005, *Separators in 3-D Quiet-Sun magnetic fields*, SoPh 225, 21, [32 c, 2 c/y].
DeRosa, M.L., Wheatland, M.S., Leka, K.D., et al. 2015, *The influence of spatial resolution on nonlinear force-free modeling*, ApJ 811, 107, [24 c, 10 c/y].
Hagenaar, H.J. 2001, *Ephemeral regions on a sequence of full-disk MDI magnetograms*, ApJ 555, 448, [153 c, 9 c/y].
Long,D.M., Williams,D.R., Régnier,S., et al. 2013, *Measuring the magnetic field strength of the Quiet solar corona using EIT waves*, SoPh 288, 567, [15 c, 3 c/y].
Longcope, D.W. 2005, *Topological methods for the analysis of solar magnetic fields*, LRSP 2, 7, [107 c, 9 c/y].
Longcope, D.W. and Parnell, C.E. 2009, *The number of magnetic null points in the Quiet Sun corona*, SoPh 254, 51, [47 c, 6 c/y].
Mackay, D.H. and Yeates, A.R. 2012, *The Sun's global photospheric and coronal magnetic fields: Observations and Models*, LRSP 9, 6, [69 c, 12 c/y].

Orozco Suarez, D., Bellot Rubio, L.R., Del Toro Iniesta, J.C., et al. 2007, *Quiet-Sun internetwork magnetic fields from the inversion of Hinode measurements*, ApJ 670, L61, [162 c, 15 c/y].
Priest, E.R., Heyvaerts, J.F., Title, A.M. 2002, *A flux-tube tectonics model for solar coronal heating driven by the magnetic carpet*, ApJ 576, 533, [152 c, 10 c/y].
Régnier, S., Parnell, C.E., and Haynes, A.L. 2008, *A new view of Quiet-Sun topology from Hinode/SOT*, A&A 484, L47, [44 c, 5 c/y].
Schrijver, C.J. and van Ballegooijen, A.A. 2005, *Is the Quiet Sun corona a quasi-steady, force-free environment?* ApJ 630, 552, [36 c, 3 c/y].
Tadesse, T., Wiegelmann, T., and MacNeice, P.J. 2015, *Effect of the size of the computational domain on spherical nonlinear force-free modeling of a coronal magnetic field using SDO/HMI data*, SoPh 290, 1159, [1 c, 0.4 c/y].
Weinzierl, M., Yeates, A.R., Mackay, D.H., et al. 2016, *A new technique for the photospheric driving of non-potential solar coronal magnetic field simulations*, ApJ 823, 55, [7 c, 3 c/y].
Wiegelmann, T. and Solanki, S.K. 2004, *Similarities and differences between coronal holes and Quiet Sun: Are loop statistics the key?* SoPh 225, 227, [34 c, 3 c/y].
Wiegelmann, T., Solanki, S.K., Borrero, J.M., et al. 2010, *Magnetic loops in the Quiet Sun*, ApJ 723, L185, [25 c, 3 c/y].
Wiegelmann, T., Thalmann, J.K., and Solanki, S.K. 2014, *The magnetic field in the solar atmosphere*, Astron.Astrophys.Rev. 22, 78, [39 c, 11 c/y].
Wiegelmann, T., Petrie, G.J.D., and Riley, P. 2017, *Coronal magnetic field models*, SSRv 210, 249, [8 c, 16 cy].

(6.5) Quiet Sun: Photosphere-Corona Connectivity

Abbett, W.P. 2007, *The magnetic connection between the convective zone and corona in the Quiet Sun*, ApJ 665, 1469, [102 c, 10 c/y].
Benevolenskaya, E.E., Kosovichev, A.G., Lemen, J.R., et al. 2002, *Large-scale solar coronal structures in soft X-rays and their relationship to the magnetic flux*, ApJ 571, 181, [34 c, 2 c/y].
Handy, B.H. and Schrijver, C.J. 2001, *On the evolution of the solar photospheric and coronal magnetic field*, ApJ 547, 1100, [21 c, 1 c/y].
Jendersie, S. and Peter, H. 2006, *Link between the chromospheric network and magnetic structures of the corona*, A&A 460, 901, [17 c, 1 c/y].
Lagg, A., Bruce, L., Harvey, J., et al. 2017, *Measurements of photospheric and chromospheric magnetic fields*, SSRv 210, 37, [6 c, 6 c/y].
Martinez-Gonzalez, M.H., Manso Sainz, R., Sensio Ramos, A., et al. 2010, *Small magnetic loops connecting the Quiet surface and the outer atmosphere of the Sun*, ApJ 714, L94, [41 c, 5 c/y].
Pevtsov, A.A. and Acton, L.W. 2011, *Soft X-ray luminosity and photospheric magnetic field in Quiet Sun*, ApJ 554, 416, [34 c, 2 c/y].
Priest, E.R., Heyvaerts, J.F., and Title, A.M. 2002, *A flux-tube tectonics model for solar coronal heating driven by the magnetic carpet*, ApJ 576, 533, [152 c, 10 c/y].
Ryutova, M., Habbal, S., Woo, R., et al. 2001, *Photospheric network as the energy source for the Quiet-Sun corona*, SoPh 200, 213, [23 c, 1 c/y].
Schrijver, C.J. and Title, A.M. 2002, *The topology of a mixed-polarity potential field, and interferences for the heating of the Quiet solar corona*, SoPh 207, 223, [57 c, 4 c/y].
Schrijver, C.J. and Title, A.M. 2003, *The magnetic connection between the solar photosphere and the corona*, ApJ 597, L165, [104 c, 7 c/y].
Titov, V.S., Hornig, G., and Démoulin, P. 2002, *Theory of magnetic connectivity in the solar corona*, JGR 107, A8, CiteID 1164, [163 c, 11 c/y].
Titov, V.S. 2007, *Generalized squashing factors for covariant description of magnetic connectivity in the solar corona*, ApJ 660, 863, [76 c, 7 c/y].

Uritsky, V.M., Davila, J.M., Ofman, L. et al. 2013, *Stochastic coupling of solar photosphere and corona*, ApJ 769, 62, [19 c, 4 c/y].
Wedemeyer-Böhm, S., Lagg, A., and Nordlund, A. 2009, *Coupling from the photosphere to the chromosphere and the corona*, SSRv 144, 317, [48 c, 6 c/y].
Wiegelmann, T., Solanki, S.K., Borrero, J.M., et al. 2013, *Evolution of the fine structure of magnetic fields in the Quiet Sun: Observations from Sunrise/IMAX and Extrapolations*, SoPh 283, 253, [10 c, 2 c/y].

(6.6) Quiet Sun: Alfvénic Waves

Campos, L.M.B.C. and Mendes, P.M.V.M. 2000, *On the dissipation rates for Alfvén waves in the solar transition region*, SoPh 191, 257, [5 c, 0.3 c/y].
De Pontieu, B., Martens, P.C.H., and Hudson, H.S. 2001, *Chromospheric damping of Alfvén waves*, ApJ 558, 859, [116 c, 7 c/y].
Khodachenko, M.L., Arber, T.D., Rucker, H.O. 2004, *Collisional and viscous damping of MHD waves in partially ionized plasmas of the solar atmosphere*, 422, 1073, [82 c, 6 c/y].
Leake, J.E., Arber, T.D., and Khodachenko, M.L. 2005, *Collisional dissipation of Alfvén waves in a partially ionized solar chromosphere*, A&A 442, 1091, [63 c, 5 c/y].
Malara, F., De Franceschis, M.F., and Veltri, P. 2005, *Dissipation of Alfvén waves in complex 3-D coronal force-free structures*, A&A 443, 1033, [8 c, 0.7 c/y].
Malara, F., Veltri, P., and De Franceschis, M.F., 2007, *Alfvén wave dissipation and topological properties of 3-D coronal force-free magnetic fields*, A&A 467, 1275, [8 c, 0.8 c/y].
McIntosh, S.W., De Pontieu, B., Carlsson, M., et al. 2011, *Alfvénic waves with sufficient energy to power the Quiet solar corona and fast solar wind*, Nature 475, 477, [261 c, 40 c/y].
Morton, R.J., Verth, G., Jess, D.B., et al. 2012, *Observations of ubiquitous compressive waves in the Sun's chromosphere*, Nature Comm. 3, 1315, [60 c, 11 c/y].
Sakai, J.I., Minamizuka, R., Kawata, T., et al. 2001, *Nonlinear torsional and compressional waves in a magnetic flux tube with electric current near the Quiet solar photospheric network*, ApJ 550, 1075, [13 c, 1 c/y].
Sakurai T., Ichimoto, K, Raju, K.P., et al. 2002, *Spectroscopic observation of coronal waves*, SoPh 209, 265, [53 c, 3 c/y].
Song, P. and Vasyliunas, V.M. 2011, *Heating of the solar atmosphere by strong damping of Alfvén waves*, JGR 116, A9, CiteID A09104, [21 c, 3 c/y].
Srivastava, A.K., Shetye, J., Murawski, K., et al. 2017, *High-frequency torsional Alfvén waves as an energy source for coronal heating*, Nature Scientific Reports 7, 43147, [9 c, 9 c/y].
Tomczyk, S., McIntosh, S.W., Keil, S.L., et al. 2007, *Alfvén waves in the solar corona*, Science 317, 1192, [402 c, 38 c/y].
Tu, J. and Song, P. 2013, *A study of Alfvén wave propagation and heating the chromosphere*, ApJ 777, 53, [16 c, 9 c/y].

(6.7) Quiet Sun: Heating Mechanisms

Aschwanden, M.J., Nightingale, R.W., and Alexander, D. 2000, *Evidence for nonuniform heating of coronal loops inferred from multi-thread modeling of TRACE data*, ApJ 541, 1059, [234 c, 13 c/y].
Aschwanden, M.J., Winebarger, A., Tsiklauri, D., et al. 2007, *The coronal heating paradox*, ApJ 659, 1673, [75 c, 7 c/y].
Cirtain,J.W., Golub,L., Winebarger,A.R., et al. 2013, *Energy release in solar corona from spatially resolved magnetic braids*, Nature 493, 501, [118 c, 26 c/y].

DeMoortel, I. and Browning, P. 2015, *Recent advances in coronal heating*, Philosophical Transactions Royal Society A 373, 2042, p.20140269, [27 c, 11 c/y].
De Pontieu,B., McIntosh,S.W., Carlsson,M., et al. 2007, *Chromospheric Alfvénic waves strong enough to power the solar wind*, Science 318, 1574, [460 c, 44 c/y].
De Pontieu, B., McIntosh, S.W., Carlsson, M., et al. 2011, *The origins of hot plasma in the solar corona*, Science 331, 6013, [212 c, 33 c/y].
Hahn, M., and Savin, D.W. 2014, *Evidence for wave heating of the Quiet-Sun corona*, ApJ 795, 111, [15 c, 4 c/y].
Hannah, I.G., Hudson, H.S., Hurford, G.J., et al. 2010, *Constraining the hard X-ray properties of the Quiet Sun with new RHESSI observations*, ApJ 724, 487, [24 c, 3 c/y].
Klimchuk, J.A. 2015, *Key aspects of coronal heating*, Royal Society of London Philosophical Transactions Series A, 373, p.20140256, [44 c, 18 c/y].
McIntosh, S.W., De Pontieu, B., Carlsson, M., et al. 2011, *Alfvénic waves with sufficient energy to power the Quiet solar corona and fast solar wind*, Nature 475, 477, [261 c, 40 c/y].
Priest, E.R., Foley, C.R., Heyvaerts, J., et al. 2000, *A method to determine the heating mechanisms of the solar corona*, ApJ 539, 1002, [96 c, 5 c/y].
Priest, E.R., Heyvaerts, J.F., and Title, A.M. 2002, *A flux-tube tectonic model for solar coronal heating driven by the magnetic carpet*, ApJ 576, 533, [152 c, 10 c/y].
Serio, S., Peres, G., Vaiana, G.S., et al. 1981, *Closed coronal structures. II. - Generalized hydrostatic model*, ApJ 243, 288, [272 c, 7 c/y].
Srivastava, A.K., Shetye, J., Murawski, K., et al. 2017, *High-frequency torsional Alfvén waves as an energy source for coronal heating*, Nature Scientific Reports 7, 43147, [9 c, 9 c/y].
Tomczyk, S., McIntosh, S.W., Keil, S.L., et al. 2007, *Alfvén waves in the solar corona*, Science 317, 1192, [402 c, 38 c/y].
Warren, H.P. and Brooks, D.H. 2009, *The temperature and density structure of the solar corona. I. Observations of the Quiet Sun with the EIS/Hinode*, ApJ 700, 762, [37 c, 4 c/y].
Winebarger, A.R., Warren, H.P., and Mariska, J.T. 2003, *TRACE and SXT active region loop observations: Comparisons with static solutions of the hydrodynamic equations*, ApJ 587, 439, [111 c, 8 c/y].

(6.8) Quiet Sun: EUV Nanoflare Energetics

Aschwanden, M.J., Tarbell, T.D., Nightingale, R.W., et al. 2000, *Time variability of the "Quiet" Sun observed with TRACE. II. Physical parameters, temperature evolution and energetics of EUV Nanoflares*, ApJ 535, 1047, [214 c, 12 c/y].
Aschwanden, M.J., and Parnell, C. 2002, *Nanoflare statistics from first principles: Fractal geometry and temperature synthesis*, ApJ 572, 1048, [112 c, 7 c/y].
Benz, A.O. and Krucker, S. 2002, *Energy distribution of microevents in the Quiet solar corona*, ApJ 568, 413, [76 c, 5 c/y].
Berghmans, D., Clette, F., and Moses, D. et al. 1998, *Quiet Sun EUV transient brightenings and turbulence. A panoramic view by EIT on board SOHO*, A&A 336, 1039, [106 c, 5 c/y].
Berghmans, D. and and Clette, F. 1999, *Active region EUV transient brightenings - First results by EIT of SOHO JOP80*, SoPh 186, 207, [186 c, 10 c/y].
Brkovic, A., Solanki, S.K., and Rüedi, I. 2001, *Analysis of blinkers and EUV brightenings in the Quiet Sun observed with CDS*, A&A 373, 1056, [35 c, 2 c/y].
Crosby, N.B., Aschwanden, M.J., Dennis, B.R. 1993, *Frequency distributions and correlations of solar X-ray flare parameters*, SoPh 143, 275, [345 c, 14 c/y].
Harrison, R.A., Harra, L.K., Brkovic, A., et al. 2003, *A study of the unification of Quiet-Sun transient-event phenomena*, A&A 409, 755, [22 c, 2 c/y].
Krucker, S. and Benz, A.O. 1998, *Energy distribution of heating processes in the Quiet solar corona*, ApJ 501, L213, [192 c, 10 c/y].
Parker, E.N. 1988, *Nanoflares and the solar X-ray corona*, ApJ 330, 474, [1025 c, 35 c/y].

Parnell, C.E. and Jupp, P.E. 2000, *Statistical analysis of the energy distribution of nanoflares in the Quiet Sun*, ApJ 529, 554, [188 c, 11 c/y].
Shimizu, T. 1997, *Studies of transient brightenings (microflares) discovered in solar active regions*, PhD Thesis, Natl. Astron. Obs., Mitaka, Tokyo, Japan.
Winebarger, A.R., Emslie, A.G., Mariska, J.T. et al. 2002, *Energetics of explosive events observed with SUMER*, ApJ 565, 1298, [30 c, 2 c/y].

(6.9) Quiet Sun: Fluxtube Braiding

Berger, M.A. and Asgari-Targhi, M. 2009, *Self-organized braiding and the structure of coronal loops*, ApJ 705, 347, [34 c, 5 c/y].
Berger, M.A., Asgari-Targhi, M., and Deluca, E.E. 2015, *Self-organized braiding in solar coronal loops*, J. Plasma Phys. 81/4, 395810404, [34 c, 5 c/y].
Cirtain, J.W., Golub, L., Winebarger, A.R., et al. 2013, *Energy release in the solar corona from spatially resolved magnetic braids*, Nature 493, 501, [118 c, 26 c/y].
Gudiksen, B.V. and Nordlund, A. 2002, *Bulk heating and slender magnetic loops in the solar corona*, ApJ 572, L113, [106 c, 7 c/y].
Gudiksen, B.V. and Nordlund, A. 2005a, *An ab initio approach to the solar coronal heating problem*, ApJ 618, 1020, [173 c, 14 c/y].
Gudiksen, B.V. and Nordlund, A. 2005b, *An ab initio approach to the solar coronal loops*, ApJ 618, 1031, [90 c, 7 c/y].
Hansteen, V., Guerreiro, N., De Pontieu, B., et al. 2015, *Numerical simulations of coronal heating through footpoint braiding*, ApJ 811, 106, [28 c, 11 c/y].
Knizhnik, K.J., Uritsky, V.M., Klimchuk, J.A., et al. 2018, *Power-law statistics of driven reconnection in the magnetically closed corona*, ApJ 853, 82.
Morales, L., and Charbonneau, P. 2008, *Self-organized critical model of energy release in an idealized coronal loops*, ApJ 682, 654, [23 c, 2 c/y].
Pant, V., Datta, A., and Banerjee, D. 2015, *Flows and waves in braided solar coronal magnetic structures*, ApJ 801, L2, [1 c, 0.4 c/y].
Parker, E.N. 1972, *Topological dissipation and the small-scale fields in turbulent gases*, ApJ 174, 499, [635 c, 14 c/y].
Peter, H., Gudiksen, B.V., and Nordlund, A. 2004, *Coronal heating through braiding of magnetic field lines*, ApJ 617, L85, [78 c, 6 c/y].
Pontin, D.I., Wilmot-Smith, A.L., Hornig, G., et al. 2011, *Dynamics of braided coronal loops. II. Cascade to multiple small-scale reconnection events*, A&A 525, A57, [50 c, 8 c/y].
Pontin, D.I. and Hornig, G. 2015, *The structure of current layers and degree of field-line braiding in coronal loops*, ApJ 805, 47, [11 c, 4 c/y].
Pontin, D.I., Janvier, M., Tiwari, S.K., et al. 2017, *Observable signatures of energy release in braided coronal loops*, ApJ 837, 108, [3 c, 3 c/y].
Prior, C. and Yeates, A.R. 2016a, *Twisted versus braided magnetic flux ropes in coronal geometry. I. Construction and relaxation*, A&A 587, A125, [1 c, 0.7 c/y].
Prior, C. and Yeates, A.R. 2016b, *Twisted versus braided magnetic flux ropes in coronal geometry. II. Comparative behaviour*, A&A 591, A16, [3 c, 2 c/y].
Schrijver, C.J., Hagenaar, H.J., and Title, A.M. 1997, *On the patterns of the solar granulation and supergranulation*, ApJ 475, 328, [61 c, 3 c/y].
Schrijver, C.J. 2007, *Braiding-induced interchange reconnection of the magnetic field and the width of solar coronal loops*, ApJ 662, L119, [29 c, 3 c/y].
Thalmann, J.K., Tiwari, S.K., and Wiegelmann, T. 2014, *Force-free field modeling of twist and braiding-induced magnetic energy in an active region corona*, ApJ 780, 102, [15 c, 4 c/y].
Wilmot-Smith, A.L., Hornig, G., and Pontin, D.I. 2009a, *Magnetic braiding and quasi-separatrix layers*, ApJ 704, 1288, [33 c, 4 c/y].

Wilmot-Smith, A.L., Hornig, G., and Pontin, D.I. 2009b, *Magnetic braiding and parallel electric fields*, ApJ 696, 1339, [42 c, 5 c/y].
Wilmot-Smith, A.L., Pontin, D.I., and Hornig, G. 2010, *Dynamics of braided coronal loops. I. Onset of magnetic reconnection*, A&A 516, A5, [46 c, 6 c/y].
Wilmot-Smith, A.L., Pontin, D.I., Yeates, A.R., et al. 2011, *Heating of braided coronal loops*, A&A 536, A67, [22 c, 3 c/y].
Wilmot-Smith, A.L. 2015, *An overview of flux braiding experiments*, Phil.Trans. Royal Soc. A 373, 20140265, [10 c, 3 c/y].
Yeates, A.R., Bianchi, F., Welsch, B.T. et al. 2014, *The coronal energy input from magnetic braiding*, A&A 564, A131, [7 c, 2 c/y].

(6.10) Quiet Sun: Radio Emission

Avrett, E.H. and Loeser, R. 2008, *Models of the solar chromosphere and transition region from SUMER and HERTS observations: Formation of the EUV spectrum of hydrogen, carbon, and oxygen*, ApJS 175, 229, [152 c, 16 c/y].
Bastian, T.S., Chintzoglou, G., De Pontieu, B., et al. 2017, *A first comparison of millimeter continuum and Mg II ultraviolet line emission from the solar chromosphere*, ApJ 845, L19, [1 c, 2 c/y].
Carlsson, M. and Stein, R.F. 2002, *Dynamic hydrogen ionization*, ApJ 572, 626, [139 c, 9 c/y].
Fontenla, J.M., Balasubramaniam, K.S., and Harder J. 2007, *Semiempirical models of the solar atmosphere. II. The Quiet-Sun low chromosphere at moderate resolution*, ApJ 667, 1243, [64 c, 6 c/y].
Fontenla, J.M., Curdt, W., Haberreiter, M., et al. 2009, *Semiempirical models of the solar atmosphere. III. Set of non-LTE models for Far-Ultraviolet/EUV irradiance computation*, ApJ 707, 482, [111 c, 13 c/y].
Gopalswamy, N., Yashiro, S., Mäkelä, P., et al. 2012, *Behavior of solar cycles 23 and 24 revealed by microwave observations*, ApJ 750, L42, [47 c, 9 c/y].
Kim, S., Park, J.Y., and Kim, Y.H. 2017, *Solar cycle variation of microwave polar brightening and EUV coronal hole observed by Nobeyama Radioheliograph and SDO/AIA*, J. Korean Astron. Soc. 50/4, 125.
Loukitcheva, M., Solanki, S.K., Carlsson, M., et al. 2004, *Millimeter observations and chromospheric dynamics*, A&A 419, 747, [56 c, 4 c/y].
Loukitcheva, M., White, S.M., Solanki, S.K., et al. 2017a, *Millimeter radiation from a 3-D model of the solar atmosphere. II. Chromospheric magnetic field*, A&A 601, A43.]
Loukitcheva, M.A., Iwai, K., Solanki, S.K., et al. 2017b, *Solar ALMA observations: Constraining the chromosphere above sunspots*, ApJ 850, 35, [5 c, 5 c/y].
Saint-Hilaire, P., Hurford, G.J., Keating, G., et al. 2012, *Allen Telescope Array multi-frequency observations of the Sun*, SoPh 277, 431, [2 c, 0.4 c/y].
Selhorst, C.L., Silva, A.V.R., Costa, J.E.R. 2005, *What determines the radio polar brightening ?* A&A 440, 367, [5 c, 0.4 c/y].
Selhorst,C.L., Gimenez de Castro,C.G., Varela Saraiva,A.C., 2010, *How are the EUV and radio polar limb-brightenings correlated?*, A&A 509, A51, [7 c, 1 c/y].
Shibasaki, K., Alissandrakis, C.E., and Pohjolainen, S. 2011, *Radio emission of the Quiet Sun and active regions (Invited Review)*, SoPh 273, 309, [47 c, 7 c/y].
Shimojo, M., Iwai, K., Asai, A., et al. 2017a, *Variation of the solar microwave spectrum in the last half century*, ApJ 848, 62.
Shimojo, M., Bastian, T.S., Hales, A.S., et al. 2017b, *Observing the Sun with the Atacama Large Millimeter/ submillimeter Array (ALMA): High-resolution interferometric imaging*, SoPh 292, 87, [4 c, 4 c/y].
Wedemeyer, S., Bastian, T., Brajsa, R., et al. 2016, *Solar science with the Atacama Large Millimeter / Submillimeter array - A new view of our Sun*, SSRv 200, 1, [32 c, 22 c/y].

White, S.M., Iwai, K., Phillips, N.M., et al. 2017, *Observing the Sun with the Atacama large millimeter/ submillimeter array (ALMA)*: Fast-scan single-dish mapping, SoPh 292, 88, [7 c, 7 c/y].

Wooten, A. and Thompson, A.R. 2009, *The Atacama Large Millimeter/submillimeter Array*, IEEE Proc. 97, 1463, [125 c, 15 c/y].

Chapter 7
Coronal Holes and Jets

7.1 Coronal Holes: Magnetic Field

The term *coronal hole* has at least three definitions: (i) the darkest patches on the solar surface as measured in UV and soft x-rays; (ii) the lowest intensity regions measured above the limb, seen either during a total solar eclipse or with an occulting coronagraph; and (iii) open-field (or open-flux) regions, which are equivalent to the footpoints of the time-steady solar wind flows (for reviews see Cranmer 2009; Wang 2009). The term "coronal holes" (or *"koronale Löcher"* in German) was coined by Max Waldmeier around 1956, based on the reduced brightness of the white-light corona in polar regions as seen during (total) solar eclipses. The area on the disk covered by the open magnetic field is largest during the minimum of the solar cycle, when the global field becomes mostly poloidal and covers the (northern and southern) polar caps. However, coronal holes occur not only in the polar regions, but occasionally extend to lower latitudes and may even bridge the equator (trans-equatorial holes). Besides the large-scale coronal holes, there is also some evidence of open magnetic flux in the vicinity of active regions (Fisk and Zurbuchen 2006; Wang 2017).

Modeling of the magnetic field in coronal holes has been performed by calculating a *potential field source surface (PFSS)* model with an axisymmetric geometry, including the effects of flux emergence and surface transport processes, evolving over one or several solar cycles (Wang and Sheeley 2003), as well as flux transport simulations of open flux or coronal hole evolution over the solar cycle using non-axisymmetric photospheric field configurations (Wang et al. 2002). More complex magnetic topologies with separatrix footprints of parasitic polarities in coronal hole linkages are modeled in Titov et al. (2011). A benchmark test of the nonpotential magnetic field observed during the 2015 March eclipse and compared with seven different models, has been conducted in Yeates et al. (2018).

M. J. Aschwanden, *New Millennium Solar Physics*, Astrophysics and Space Science Library 458, https://doi.org/10.1007/978-3-030-13956-8_7

EIT/SOHO data reveal that the rate of emergence of new magnetic flux is systematically lower (by a factor of ≈ 2) in coronal holes, relative to the surrounding Quiet Sun (Abramenko et al. 2006). A follow-on study of Hagenaar et al. (2008) found that the lower emergence rate of small bipoles applies equally to unipolar regions inside and outside coronal holes (i.e., the lower emergence rate is not related to the presence of open flux). The lower emergence rate in strongly unipolar regions appears to occur due to two main factors: (i) the minority-polarity flux is rapidly cancelled by the dominant polarity; or (ii) because of instrumental or other effects (such as "bleeding" between pixels), where small pockets of minority-polarity flux may be present but undetectable. Indeed, Wang et al. (2016) found several examples of bright plumes where the HMI magnetograms showed no minority-polarity flux at the plume base, but the corresponding EUV images showed small loop-like structures. Subsequently, an examination of unipolar plage areas in active regions revealed multitudes of small loop-like features in AIA 171 Å and 193 Å images where no minority-polarity flux was visible in the corresponding HMI magnetograms (Wang 2016).

SOT/Hinode observations reveal vertically oriented magnetic flux tubes in polar coronal holes, with field strengths as strong as 1 kG, scattered in latitude between 70° and 90° (Fig. 4.13; Tsuneta et al. 2008). These kG "islands" have all the same polarity, consistent with the global (dominant) polarity of the polar region (Tsuneta et al. 2008; Shimojo and Tsuneta 2009). In addition, polar regions are also found to have ubiquitous horizontal fields (Tsuneta et al. 2008).

Some interesting dynamics occurs at the coronal hole boundaries, especially in trans-equatorial coronal holes. The boundary separates open-field from closed-field regions. It was noted that the trans-equatorial coronal holes rotate rigidly, while the underlaying photospheric fields rotate differentially, which makes magnetic reconnection necessary to maintain the rigid rotation of a coronal hole. Recent AIA/SDO observations reveal many EUV jets, which appear to be the signatures of magnetic reconnection, as observed in 193 Å images, and some jets occur repetitively at the same sites (Fig. 7.1). The evolution of the jets is associated with the emergence and cancellation of magnetic fields (Yang et al. 2011). Both the east and west coronal hole boundaries shift westward, and the shift velocities are close to the velocities of rigid rotation, indicating that magnetic reconnection at coronal hole boundaries maintains the rigid rotation of coronal holes (Yang et al. 2011). While there have been several studies that claim or imply that the small jets observed near coronal hole boundaries affect their rotational behavior (e.g., Yang et al. 2011; Madjarska et al. 2004), the evidence for this has been purely circumstantial and not physically convincing. As Wang and Sheeley (2004) emphasize, the quasi-rigid behavior of the boundaries is determined by the global coronal field, with the required reconnection processes occuring at the streamer cusps far above the solar surface. The small jets triggered by emerging ephemeral regions may cause short-term fluctuations in the hole boundaries, but they are not responsible for their systematic quasi-rigid rotation (which is mainly determined by the large-scale distribution of active regions).

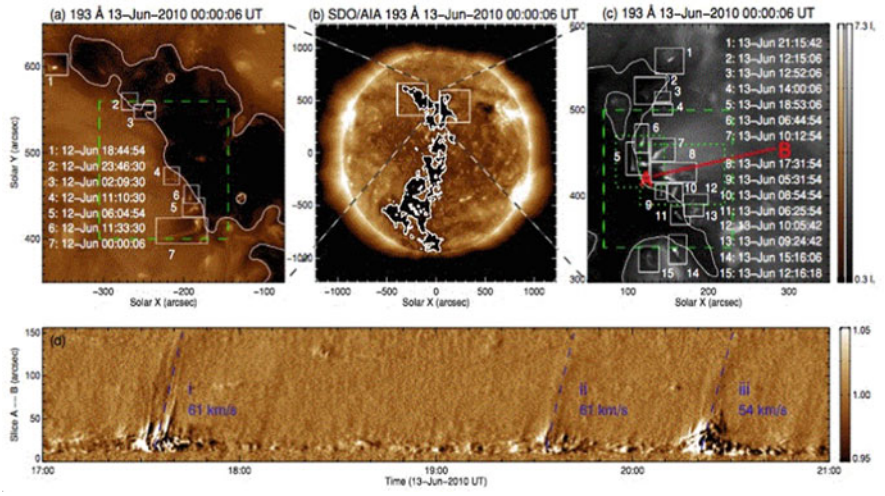

Fig. 7.1 AIA/SDO 193 Å full-disk image (middle top) obtained on 2010 June 13, showing an *equatorial extension of polar coronal holes*, and sub-images (left and right top). Bottom panel: running ratio space-time plot along slit A-B (red line in top right panel). The contours represent coronal hole boundaries. The white rectangles in the left and right top panels show jets occurring at the coronal hole boundaries at different times (Yang et al. 2011)

Since the global solar magnetic field oscillates between poloidal and toroidal field configurations, the parameters of coronal holes vary in synchrony. The total open flux and radial interplanetary field component varies roughly as the Sun's total dipole strength (Wang et al. 2009), rather than as the photospheric flux or the sunspot number (Wang et al. 2000). The dipole strength tends to peak a few years after sunspot maximum. The quasi-rigid rotation of coronal holes is maintained by continuous footpoint exchange (i.e., *interchange reconnection*) between open and closed field lines (Wang 2009). However, the polar magnetic field does not restore to the same magnetic field strength after every solar cycle. The Sun's polar fields are currently $\approx$ 40% weaker than they were during the previous three sunspot minima. The weakening has been accompanied by a corresponding decrease in the *interplanetary magnetic field (IMF)* strength, by a $\approx$ 20% shrinkage in the polar coronal hole areas, and by a reduction in the solar-wind mass flux over the poles (Wang et al. 2009).

The long-term evolution of coronal hole areas and open magnetic flux is now measured with automated coronal hole boundary detection algorithms (Scholl and Habbal 2008; Krista and Gallagher 2009; Lowder et al. 2014, 2017), using He I 10,830 Å KP/NSO, EIT/SOHO, MDI/SOHO, XRT/Hinode, EUVI/STEREO A+B, and AIA/SDO data. Some of the statistical results are: The total area of coronal holes measured with EIT/SOHO images and PFSS varies between 5% and 17% of the total solar surface area (during 1996–2010), and 5% and 10% for AIA and EUVI measurements (during 2010–2013) (Lowder et al. 2014). The total unsigned open

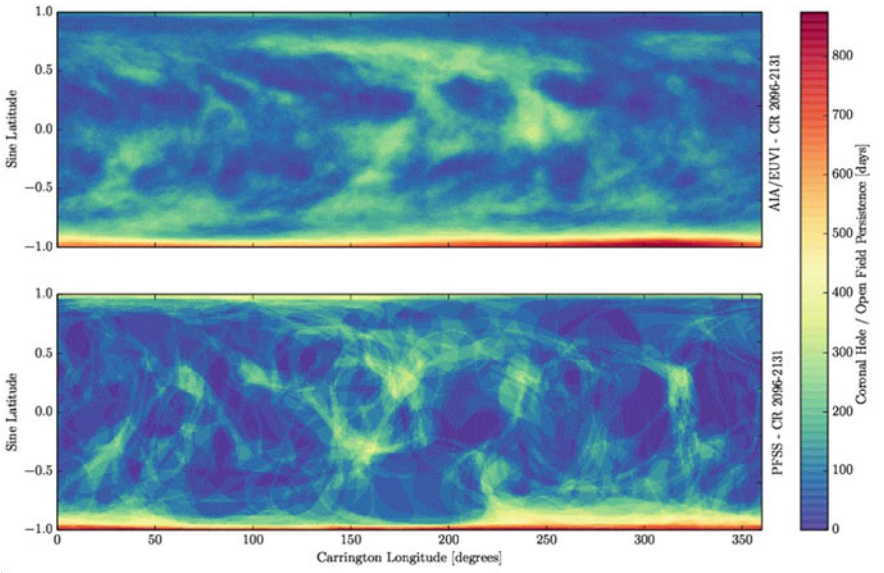

Fig. 7.2 Coronal hole persistence map for a combination of AIA 193 Å and EUVI 195 Å data sets (top), along with a corresponding map generated using spherical harmonic coefficients obtained from the Wilcox Solar observatory and a PFSS open field reconstruction (bottom). Persistence is scaled in days of consecutive appearance of coronal hole (or open field) for each pixel (Lowder et al. 2014)

flux varies within (2–5) $\times$ 10^{22} Mx for EIT, and (2–4) $\times$ 10^{22} Mx for AIA (Lowder et al. 2014). A coronal hole persistence map is shown in Fig. 7.2 (for a definition of a persistence map see Lowder et al. 2014). The low-latitude coronal holes are not well measured in He I 10,830 Å, with EIT, or the static PFSS, but are well retrieved with AIA and EUVI (Lowder et al. 2014). The northern and sourthern polar regions show a clear asymmetry, with a time lag between hemispheres, in the appearance and disappearance of polar coronal holes (Lowder et al. 2017). Flux tubes rooted in coronal holes expand super-radially up to a distance of $\approx$ 10–15 solar radii, while they become radial beyond, according to MHD modeling of streamer observations, and larger (smaller) coronal holes result in longer (shorter) duration high-speed solar wind streams (Krista and Gallagher 2009).

7.2 Coronal Holes: Plumes

Polar plumes are thin, long ray-like structures that project beyond the limb of the Sun's polar regions, maintaining their identity over distances of several solar radii. Observations of plumes have been conducted in white-light during solar eclipses, with coronagraphs (LASCO/SOHO, COR1, and COR2/STEREO),

with full-disk images in extreme-ultraviolet (EIT/SOHO, TRACE, EUVI/STEREO A+B, EIS/Hinode, AIA/ SDO), and even in interplanetary space with *in situ* measurements. Thus plumes are observed in coronal holes in polar regions, as well as in coronal holes on the disk. New studies focus on their 3-D reconstruction, hydrodynamic modeling, their role as waveguides for MHD waves, and the sources of the solar wind. Some motivating questions are: Does the solar wind emanante from plumes or from the ambient coronal hole wherein they are embedded? Do plumes have a role in the solar wind acceleration and mass loading? (see reviews by Wilhelm et al. 2011 and Poletto 2015).

An uncertainty in modeling the magnetic field of plumes is the assumption of radial expansion versus super-radial expansion. Almost all of the coronal field is super-radial, while the radial assumption is usually made to simplify theoretical modeling. From EUV/SOHO and LASCO/SOHO data it was inferred that the expansion is consistent with super-radial expansion and inconsistent with radial expansion (DeForest et al. 2001). A new method to determine the 3-D magnetic field geometry is stereoscopy with the EUVI/STEREO A+B spacecraft. Two methods were employed for 3-D reconstruction of polar plumes: tomography using filtered back-projection and including differential rotation of the Sun, and stereoscopic triangulation (de Patoul et al. 2013). Super-radial expansion was established with stereoscopic methods for 10 plumes, and it was found that the magnetic field along plumes is more horizontal than expected for a dipole field (Feng et al. 2009).

Hydrodynamic modeling of flows in plumes appears to be full of surprises. UV spectroscopy with CDS/SMM, yielded a near-isothermal temperature of $T_e = 0.8$ MK and an electron density of $n_e = 1.2 \times 10^9$ cm^{-3} for one plume, whose density is about twice that of the surrounding inter-plume density (Del Zanna et al. 2003). Both the electron temperature and the effective ion temperature of plumes are found to be lower than those in the environment (Wilhelm 2000). Outflow velocities in plumes (0–65 km s^{-1}) are found to be much slower than the ambient coronal expansion speed (105–150 km s^{-1}), as inferred from the O VI 1032 and 1037 Å lines (Giordano et al. 2000). High-speed jets with a mean velocity of $\approx$ 135 km s^{-1} in the temperature range of $T_e \approx$ 0.5–1.5 K are found in the footpoints of almost all analyzed polar plumes, observed at the limb with STEREO (McIntosh et al. 2010). AIA observations suggest that high-speed outflows originate mainly from the magnetic network in Quiet Sun regions and coronal holes, and that the plume flows observed with AIA are highlighted by the denser plasma contained therein (Tian et al. 2011). Bright points and polar plumes seen in Ne VIII 7700 Å do not show signatures of outflows (Wilhelm et al. 2000). The higher densities, lower temperatures, and lower outflow speeds can all be explained by the presence of an additional heating source, located very close to the plume base (Wang 1994). The extra heating is conducted downward through the transition region, evaporating more material from below; the higher densities lead to increased radiative cooling and thus to lower temperatures. The additional energy input is most likely due to reconnection between the unipolar network flux and minority-polarity flux, which would also account for the mini-jets seen by McIntosh et al. (2010) and by Raouafi and Stenborg (2014).

Dark upflows observed in vertically structured prominences have been indentified as plumes that develop turbulence, including occasional Kelvin-Helmholtz vortex motion (Berger et al. 2008, 2010). Hydrodynamic models with two fluids (ions and electrons), with coupling via Coulomb collisions, and with heat transport mainly by electrons, leads to energy deposition very close to the coronal base, raising the density, and decreasing the flow speed along the plume (Grappin et al. 2011). The observed densities and temperatures can be matched if the magnetic field is assumed to fall off with radius as $B(r) \propto r^{-4}$ (Grappin et al. 2011).

The basic magnetic topology of a plume is analogous to that of a jet or of a "pseudostreamer" (a streamer surrounded by open flux of the same polarity, with an X-point instead of a Y-point at its cusp). Below the cusp point, the field diverges rapidly; above the cusp, it reconverges (while remaining super-radial). The net expansion factor is thus smaller than for the ambient coronal hole. Plumes represent flux tubes that are suitable wave guides for the propagation of slow (magneto-acoustic) and fast (Alfvénic) MHD waves (see review by Banerjee et al. 2007). Slow magneto-acoustic waves, however, experience a nonlinear steepening as they propagate away from the Sun, leading to enhanced dissipation due to the compressive viscosity at the wave front within the first solar radii above the surface (Ofman et al. 2000b; Gupta 2014). Observations with UVCS/SOHO revealed quasi-periodic variation of the polarized brightness at a heliocentric distance of 1.9 solar radii, which is interpreted as compressional wave packets propagating along the plumes (Ofman et al. 2000a). Propagating slow magneto-acoustic waves undergo strong damping (i.e., small dissipation lengths) within the first 10 Mm altitude range, while the waves are weakly damped in larger heights (Gupta 2014). A statistical study on the damping of slow magneto-acoustic waves in polar plumes and interplumes yields an inverse power law dependence of the damping length on the periodicity (i.e., short-period oscillations have longer damping lengths) (Fig. 7.3). Short-period (2–6 min) are found to be more abundant than the long-period (7–30 min) counterparts (Mandal et al. 2018).

Alfvénic waves are detected also, besides the slow (magneto-acoustic) waves. Measuring the line broadening of plumes with EIS/Hinode and its height dependence, it was found that it matched the theoretical expectation of the relationship $\langle \delta v \rangle^2 \propto \rho^{-1/4}$ between the mean square nonthermal velocity $\langle \delta v \rangle$ and the plamsa mass density ρ for Alfvén waves, confirming the existence of undamped radially propagating linear Alfvén waves (Banerjee et al. 2009). Simultaneous measurements with AIA/SDO and the *Coronal Multi-channel Polarimeter (CoMP)* enabled the detection of both slow magneto-acoustic waves (with intensity modulation of $\approx$ 1%, speed of 120 km s^{-1}, periods of 15 min) and fast Alfvénic waves (with a velocity amplitude of 0.5 km s^{-1}, a phase speed of 830 kms^{-1}, and periods of 5 min) on the same plume structure (Liu et al. 2015).

Analyzing a plume in a polar coronal hole over its entire lifetime of $\approx$ 40 hrs with AIA/SDO led to the following findings: A plume started $\approx$ 2 hrs after a bright point appeared, and became undetectable $\approx$ 1 hr after the bright point disappeared. Outflow speeds of (30–300) km s^{-1} were observed that are consistent with wave motions. If these outflows persist when propagating out to the heliosphere, and if

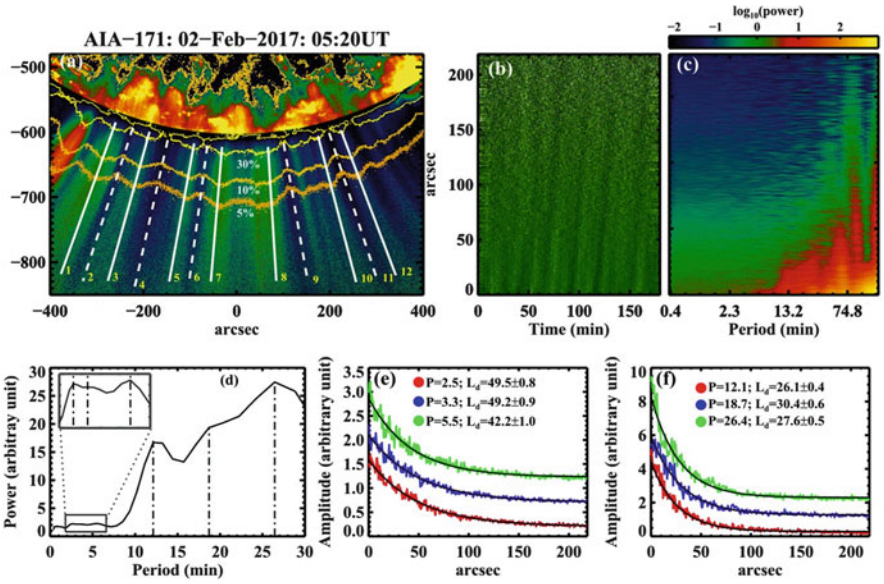

Fig. 7.3 Analysis of frequency-dependent damping in slow (magneto-acoustic) waves propagating along plumes (in near-vertical) direction to the solar surface. Panel (**a**) shows an AIA 171 Å image, processed with a radial filter to enhance the polar features. Overplotted yellow contours denote different intensity levels (in percent of the on-disk intensity), obtained from the original image. Solid and dashed white lines represent the locations of artificial slits used for the generation of time-distance maps. An enhanced time-distance map, generated from slit 3, is shown in panel (**b**), whereas the corresponding period-distance map is shown in panel (**c**). Panel (**d**) displays a template power spectrum constructed from the period-distance map showing different periods present in the data. Panels (**e**), (**f**) present the amplitude variation with distance for each of the detected periods. In these plots, the black solid lines show the fitted exponential decay function to the data. The obtained damping lengths L_d corresponding to individual periods P are indicated in each panel (Mandal et al. 2018)

plumes cover $\approx$ 10% of a typical coronal hole area, these flows could account for $\approx$ 50% of the solar wind mass (Pucci et al. 2014). Whether polar plumes or interplume regions contribute more to the source of the fast solar wind is still debated. UV line broadening at the O VI lines 1032 and 1037 Å indicate that the interplume regions produce a higher outflow speed at 1.7 solar radii than plumes (Teriaca et al. 2003).

In a recent study using HMI and AIA data, it was shown that coronal plumes form when unipolar network elements converge to form dense clumps, and fade as the clumps disperse again in the supergranular flow field (Wang et al. 2016). The plume lifetime is thus closely related to the evolutionary timescale of the supergranular network. The converging supergranular flows also carry trapped minority-polarity flux, driving reconnection with the unipolar network elements.

7.3 Coronal Holes: Jets

Soft X-ray jets are considered to be "miniature versions" of solar flares, produced by some magnetic reconnection process. In contrast to flares they have the appearance of collimated plasma beams, following a straight or slightly twisted geometry. Flows along these channels exhibit two distinct velocities, either magneto-acoustic speeds ($v \approx 200$ km s^{-1}), or Alfvénic speeds ($v \approx 800$ km s^{-1}) (Cirtain et al. 2007). They have widths in the range of $w = 2$–20 Mm, lengths that are much longer than their widths, and their duration or lifetime amounts to 100–2500 s. The high occurrence frequency and relatively high velocity of apparent outflows indicate that the jets may contribute to the high-speed solar wind (Cirtain et al. 2007; Tian et al. 2014), as well as to radio type III bursts (Innes et al. 2016), and to ^{3}He-rich particle events (Wang et al. 2006). An occurrence frequency of ≈ 60 X-ray jets per day has been sampled with XRT/Hinode data (Savcheva et al. 2007). The X-ray jets were found to have a prevalence to originate from the networks of the solar transition region and chromosphere (Kamio et al. 2009; Tian et al. 2014), in coronal holes, as well as in Quiet Sun regions, but they are more prominent in coronal holes due to the better contrast. A study of 79 polar jets based on EUVI/STEREO and white-light observations provides statistics on their morphology: 37 *Eiffel-tower types*, 12 *lambda types*, 5 *micro-CME types*, and 25 unclassified; while 31 cases exhibit helical magnetic fields (Nistico et al. 2009). Some *micro-sigmoid structures* were found also, which have been considered as progenitors of coronal jets (Raouafi et al. 2010). For a review on coronal jets see Raouafi et al. (2016).

The first stereoscopic 3-D reconstruction of a polar coronal jet was accomplished with the EUVI/STEREO instrument, using triangulation with a separation angle of $\approx 11^\circ$ between the two spacecraft STEREO/A and B, proving that the observed helical structure is real and does not result from possible projection effects as it would appear from a singe viewpoint (Patsourakos et al. 2008). This observation suggests also that the magnetic untwisting is the driving mechanism of the upward acceleration of the jet (from speeds of 10–20 km s^{-1} to ≈ 300 km s^{-1}). The kinematics of the untwisting motion in a polar jet is fully resolved in AIA observations (Chen et al. 2011).

A distinction of X-ray jets has been made between the standard reconnection picture (with null-point and fan-separatrix topology), which occurs in two thirds of polar X-ray jets, and a non-standard mechanism with a blowout eruption (where the X-ray jet is the counterpart of erupting-loop Hα macrospicules), occurring in one third of polar X-ray jets (Moore et al. 2010, 2013). There is a growing notion that the majority of jets in coronal holes are actually blowout jets, based on numerical simulations (Archontis and Hood 2013; Pariat et al. 2015; Wyper et al. 2018) and on observational grounds (Sterling et al. 2015; Adams et al. 2014; Panesar et al. 2018). Furthermore, even small-scale filament eruptions may act as drivers of X-ray jets in coronal holes (Sterling et al. 2015, 2016). Further cases with growing complexity are reported, such as one case that involves two mini-prominences, a blowout jet, bidirectional flows, and a cusp-shaped jet with a spire and an arch base (Zhang and Zhang 2017).

The leading model proposed for solar polar jets is magnetic reconnection with null-point and fan-separatrix topology (Pariat et al. 2009, 2010). The major challenge in explaining the observations is that reconnection must occur in short bursts to produce jets, in contrast to quasi-continuous structures such as plumes. The viability of this model has been demonstrated by 3-D MHD simulations of Pariat et al. (2009, 2010). Observations exhibit a higher occurrence frequency than previously believed, which led to the concept of recurring jets with a homologous behavior, where jets recur at the same location with similar morphological features. This feature could be reproduced in the 3-D MHD simulations by continuous driving of magnetic stressing at the photospheric boundary (Pariat et al. 2010). In a parametric study it was explored how the magnetic field inclination and photospheric field distribution affects the two morphologically different types of solar jets (straight and helical), see Fig. 7.4, which can account for the observed two types of standard jets and blowout jets (Pariat et al. 2015). 3-D MHD simulations that include spherical geometry, gravity, and solar wind, provide evidence that jet propagation is sustained through the outer corona, in form of a traveling nonlinear

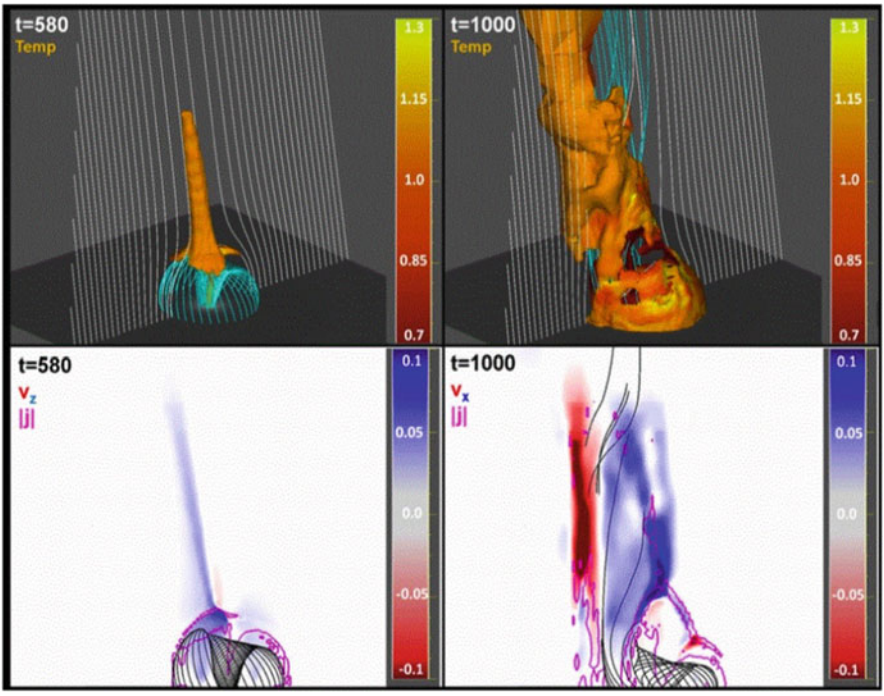

Fig. 7.4 Morphology of the straight jet (left panels) and the helical jet (right panel). Isosurfaces of plasma density are shown (top panels), the 2-D distribution of the velocity component v_z (bottom left panel), and the 2-D distribution of the velocity component v_x (bottom right panel). Blue and red indicate flows towards and away from the observer. The black field lines are all initially closed and correspond to the cyan field lines in the upper panel. The magenta lines are isocontours of the electric current density magnitude in the plane (Pariat et al. 2015)

Alfvén wave front, trailed by slower-moving plasma density enhancements that are compressed and accelerated by the wave, which explain microstreams and torsional Alfvén waves detected in situ in the solar wind (Karpen et al. 2017).

In other 3-D MHD models (see also Sect. 5.7), magnetic reconnection is driven by emerging flux from beneath the photosphere (rather than by twisting), where a thin current sheet is formed at the boundary of the emerging plasma, which then launches an X-ray jet in upward direction in a *vault-and-jet structure*, *inverted-Y structure*, or *"Eiffel-tower shape"* (Moreno-Insertis et al. 2008; Schmieder et al. 2013). New evidence of the fan-spine magnetic reconnection topology resulting from flux emergence has been provided by Liu et al. (2011). The simplified magnetic scenario is depicted in Fig. 7.5, while the different evolutionary steps in

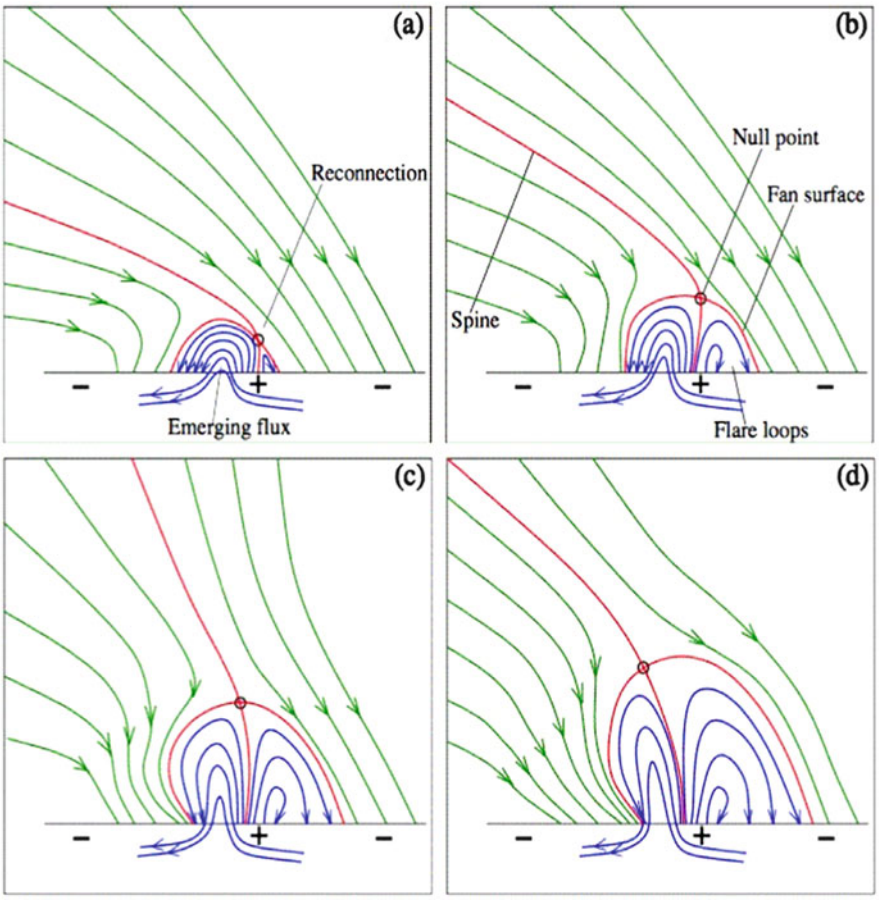

Fig. 7.5 2-D cut of jet model with fan-spine geometry driven by magnetic flux emergence, showing the unipolar surrounding magnetic field (green curves), the closed field lines inside the dome (blue curves), the separatrix or fan surface (closed field line in red), and the spine field line (open field line in red), (Liu et al. 2011)

the formation of the coronal jet includes initial rotation, rupture of a loop, swinging lateral motion, upward ejecta, mass downflows, collimation of jet along the spine, transverse oscillations, bifurcation at a null point, and formation of an *inverted-Y* geometry (Liu et al. 2011). Another 3-D MHD experiment produced a (hot and fast) coronal jet followed by several eruptions, tether-cutting reconnection, a twisted Ω-loop-like rope, the kink instability or torus instability, and mini-CMEs (Moreno-Insertis and Galsgaard 2013), reminiscent of the blowout eruptions reported by Moore et al. (2010). The recurrence behavior generally observed in the formation of X-ray jets has been related to repetitive accumulation and dissipation of vertical electric currents (Guo et al. 2013).

7.4 Coronal Holes: Blowout Jets

A magnetic dichotomy subdivides solar coronal jets into *standard jets* (in two thirds of the cases) and into *blowout jets* (in one third), based on examination of X-ray jets observed with XRT/Hinode (Moore et al. 2010, 2013), but there is a growing consensus that the majority of coronal hole jets are actually blowout jets (Archontis and Hood 2013; Pariat et al. 2015; Wyper et al. 2018; Sterling et al. 2015; Adams et al. 2014; Panesar et al. 2018). The standard jets fit the standard (interchange) reconnection scenario (e.g., Shibata et al. 2007), while the *blowout X-ray jets* display the following distinguishing features: (i) X-ray brightening inside the base arch in addition to the outside bright point that standard jets have; (ii) blowout eruption of the base arch's core field, often carrying a filament of cool ($T \approx 10^4$–10^5 K) plasma, and (iii) an extra jet-spire strand rooted close to the bright point (Moore et al. 2010). Thus the main difference is the base arch, which has not enough shear and twist to erupt in the case of standard jets. Standard jets include so-called solar X-ray jets, EUV jets, Hα surges, as well as EUV macrospicules (Fig. 7.6), while blowout jets appear to have a different magnetic topology, degree of magnetic twist, and eruptive type of (breakout) magnetic reconnection (Fig. 7.7). Type II spicules have also been considered to be a subpopulation of blowout jets, but occurring on much smaller horizontal size scales (Sterling et al. 2010). The new type of blowout jets could provide a link between standard collimated jets and coronal mass ejections (CMEs). A *"stealth CME"* event, which leaves no coronal trace in EUV (dimming) behind, is generally observed to exhibit a slow time evolution that is typical for the steamer-blowout CME class (Robbrecht et al. 2009).

A typical observation of a blowout jet observed with AIA/SDO and Hinode at the boundary of a polar coronal hole yields the following parameters: temperature $T_e = 1.6$ MK, density $n_e = (0.9\text{–}1.7) \times 10^8$ cm^{-3}, line-of-sight velocity $v \lesssim 250$ km s^{-1}, and angular rotation speed $v_{rot} = (9\text{–}12) \times 10^{-3}$ rad s^{-1} (Young and Muglach 2014). Physical parameters measured by Pucci et al. (2013) from both a standard jet and a blowout jet are juxtaposed in Table 7.1. The resulting blowout enthalpy flux ($\approx F_E \approx 1.7 \times 10^7$ erg cm^{-3}) is 1.6 times larger than the enthalpy flux of the standard jet. Further data analysis of standard jets and blowout jets can

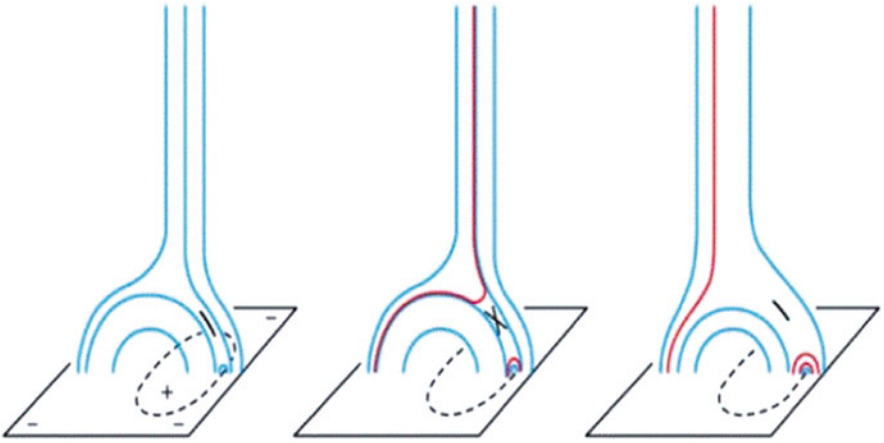

Fig. 7.6 Cartoon of the magnetic topology (blue lines) and reconnection of the *standard jet model*, shown in 3 steps from left to right. The dashed ovals are the polarity inversion lines around the positive flux of an emerging arch. The reconnection site is marked with a cross in the middle frame. The red field lines mark structures with reconnection-heated plasma (Moore et al. 2010)

be found in Liu et al. (2011), Adams et al. (2014), Li et al. (2015, 2017), or Shen et al. (2017).

Numerical 3-D MHD simulations of plasma jets have been conducted that mimic the launching of a hot and fast coronal jet followed by several violent eruptions (Moreno-Insertis and Galsgaard 2013), which ressembles a mini-CME, and together with the physical properties suggests that this experiment may provide a model for the blowout jets proposed by Moore et al. (2010). Similar 3-D MHD simulations (with the ARMS code) were carried out for two different scenarios, i.e., for straight jets and for helical jets, which appear to correspond to the morphological (observational) distinction of standard jets and blowout jets (Pariat et al. 2015). Numerical simulations demonstrated also direct evidence that the untwisting motion of blowout jets is associated with the propagation of torsional Alfvén waves in the corona (Lee et al. 2015; Pariat et al. 2016).

Interestingly, both types of coronal jets can occur sequentially in time, i.e., a straight jet precedes the onset of a helical jet, and the reconnection occurring during the straight-jet phase influences the triggering of the helical jet (Pariat et al. 2015). A similar scenario was observed where two cospatial jets were successively observed (with AIA/SDO), with a first jet exhibiting a typical fan-spine geometry, while the second jet displays a blowout morphology when a mini-filament erupts upward, leaving behind a hard X-ray emission source at the base, accompanied by a C-class flare and an interplanetary type-III radio burst (observed with WAVES/WIND) (Hong et al. 2017). Another event was described as simultaneous appearance of bubble-like and jet-like CMEs, dynamically related to the blowout jet with cool and hot components next to each other (Shen et al. 2012). The interpretation was that external reconnection causes the jet-like CME and the rising of a filament,

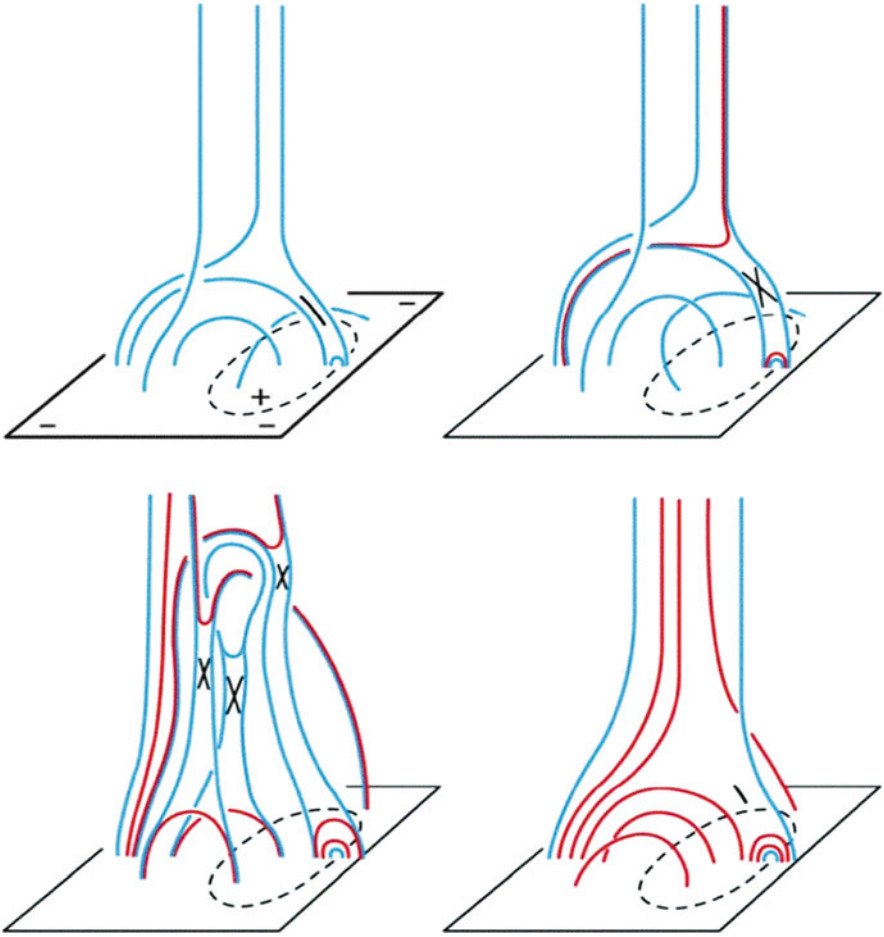

Fig. 7.7 Cartoon of the magnetic topology (blue lines), eruption, and reconnection of the *blowout jet model*, shown in 4 time steps. The dashed ovals are the polarity inversion lines around the positive flux of an emerging arch. The reconnection site is marked with a cross. The red field lines mark structures filled with reconnection-heated plasma. The time evolution shows initially a highly sheared configuration (top left), the onset of the breakout reconnection as the sheared core field begins to erupt (top right), reconnection and heated field lines during the blowout eruption of the sheared-core base arch, and the X-ray jet at the onset of its decay phase (Moore et al. 2010)

while internal reconnection starts underneath the rising filament and causes the bubble-like CME subsequently (Shen et al. 2012). A very similar evolution has been simulated with a 3-D MHD code, where external reconnection leads to the formation of a standard (straight) jet with inverse-Y geometry, while internal reconnection of sheared field lines in the emerging flux region produces an erupting magnetic flux rope, the erupting plasma blows out the ambient field, and it unwinds as it is ejected

Table 7.1 Physical parameters of two types of jets, including the temperature, column emission measure, density, magnetic field, and velocity, averaged over the event duration and along the jets (Pucci et al. 2013)

Parameter	Standard jet	Blowout jet
T_e	1.6×10^6 K	$(1.8–2.0) \times 10^6$ K
CEM	8×10^{25} cm^{-5}	1×10^{26} cm^{-5}
n_e	6×10^8 cm^{-3}	6×10^8 cm^{-3}
B	2.8 G	4.5 G
v	250 km s^{-1}	400 km s^{-1}

into the upper corona, and thus occurs as a transition from a standard jet to a blowout jet (Archontis and Hood 2013).

Magnetic modeling of coronal jet sites involves anemone-like fan-spine topologies for standard jets, while a bald patch topology has been found to be present at least two days before a blowout jet event (Chandra et al. 2017).

7.5 Coronal Holes: Boundaries

A review on coronal holes and its open magnetic flux and boundaries is given in Wang (2009), which summarizes the essential facts that define the time evolution of coronal hole boundaries: Coronal holes are low-density regions of the corona which appear dark in X-rays and which contain "open" magnetic flux, along which plasma escapes into the heliosphere. Like the rest of the Sun's large-scale field, the open flux originates in active regions but is subsequently redistributed over the solar surface by transport processes, eventually forming the polar coronal holes. The total open flux and radial interplanetary field component vary roughly as the Sun's total dipole strength, which tends to peak a few years after sunspot maximum. An inverse correlation exists between the rate of flux-tube expansion in coronal holes and the solar wind speed at 1 AU. In the rapidly diverging fields present at the polar hole boundaries and near active regions, the bulk of the heating occurs at low heights, leading to an increase in the mass flux density at the Sun and a decrease in the asymtotic wind speed. The quasi-rigid rotation of coronal holes is maintained by continual footpoint exchanges between open and closed field lines, with the reconnection taking place at the streamer cusps. At much lower heights within the hole interiors, "interchange reconnection" between small bipoles and the overlying open flux also gives rise to coronal jets and polar plumes (Wang 2009).

The total area of coronal holes (or areas with open magnetic flux) covers $\approx 20\%$ of the solar surface during the minimum of the solar 11-year cycle, and decreases to $\approx$ 5% during the maximum. At the same time, the average footpoint field in coronal holes increases from $\approx$ 5 G during the sunspot minimum to $\approx$ 20 G during the sunspot maximum. The total open flux, which is the product of these two quantities, i.e., $\Phi = AB$, thus remains constant within a factor of 2 (Wang 2009).

This anti-correlation $A(t) \propto B(t)^{-1}$ between the coronal hole area A and field strength B is mainly a consequence of photospheric flux transport: the open flux is initially concentrated near the edges of active regions, but occupies a progressively larger area and decreases in strength as it diffuses over the solar surface (Wang 2009). In EUV wavelengths, the areas of polar coronal holes cover a maximum fraction of $\approx$ 6% based on EIT/SOHO images during 1996–2010 (Hess Webber et al. 2014), or $\approx$ 5%–17% (Lowder et al. 2014), and $\approx$ 5%–10% based on AIA/SDO and EUVI/STEREO during 2010–2013 (Lowder et al. 2014). A detailed comparison between EIT, AIA+EUVI, and PFSS measurements indicates that coronal holes in low latitudes contribute significantly to the total open magnetic flux (Lowder et al. 2014).

The adjustment of the quasi-rigid rotation of coronal holes to the differential rotation (in latitude) of the photospheric surface requires continual magnetic disconnection and reconnection at the coronal hole boundary. SXT/Yohkoh observations (e.g., Kahler and Hudson 2002) suggest that *"interchange reconnection"* switches the footpoint connections between open and closed magnetic field lines, whenever new active regions emerge (Wang and Sheeley 2004). Evidence for magnetic reconnection at coronal hole boundaries has been furnished by (i) SUMER observations of bidirectional jets with near-cospatial blueshifts and redshifts (Madjarska et al. 2004, 2012; Aiouaz 2008), (ii) SOHO/EIT and SOHO/MDI observations of an active region that emerges close to a coronal hole and forms closed loops that leads to a retreat of the hole (Baker et al. 2007), (iii) AIA/SDO observations of many EUV jets associated with the emergence and cancellation of magnetic fields (Yang et al. 2011), and (iv) SOT/Hinode observations that show that all brightening events are associated with bipolar regions and are caused by magnetic flux emergence followed by flux cancellation (Huang et al. 2012). A correlation between the intensities in coronal holes and Quiet Sun has been found in the transition region, but not in the corona, which suggests that continuous reconnection occurs in coronal altitudes (Raju et al. 2005). The lack of changes in the diffuse coronal hole boundaries implies that gradual magnetic reconnection occurs high in the lower corona with large loops and weak magnetic fields. Magnetic reconnection at a coronal hole boundary can occur in a quasi-oscillatory manner, as observed with SUMER/SOHO for a chain of explosive events with 3–5 min periods (Doyle et al. 2006; Madjarska et al. 2012). The emergence and disappearance continuously expand or contract coronal holes, so that coronal hole boundaries change on time scales of days down to hours (Madjarska and Wiegelmann 2009).

The life time of trans-equatorial coronal holes is generally limited to a few solar rotations, but can be persistent in one form or another up to 2 years (Wang et al. 2010). The evolution of jets in coronal hole boundaries is much faster ($\approx$ 10 min) in comparison (e.g., Yang et al. 2011).

The interchange reconnection often results into the production of a jet that escapes along open field lines, and thus can contribute to the solar wind. Investigating a large statistical sample of brightenings observed with XRT/Hinode at the boundaries of equatorial, polar, and transient coronal holes (Fig. 7.8) shows that

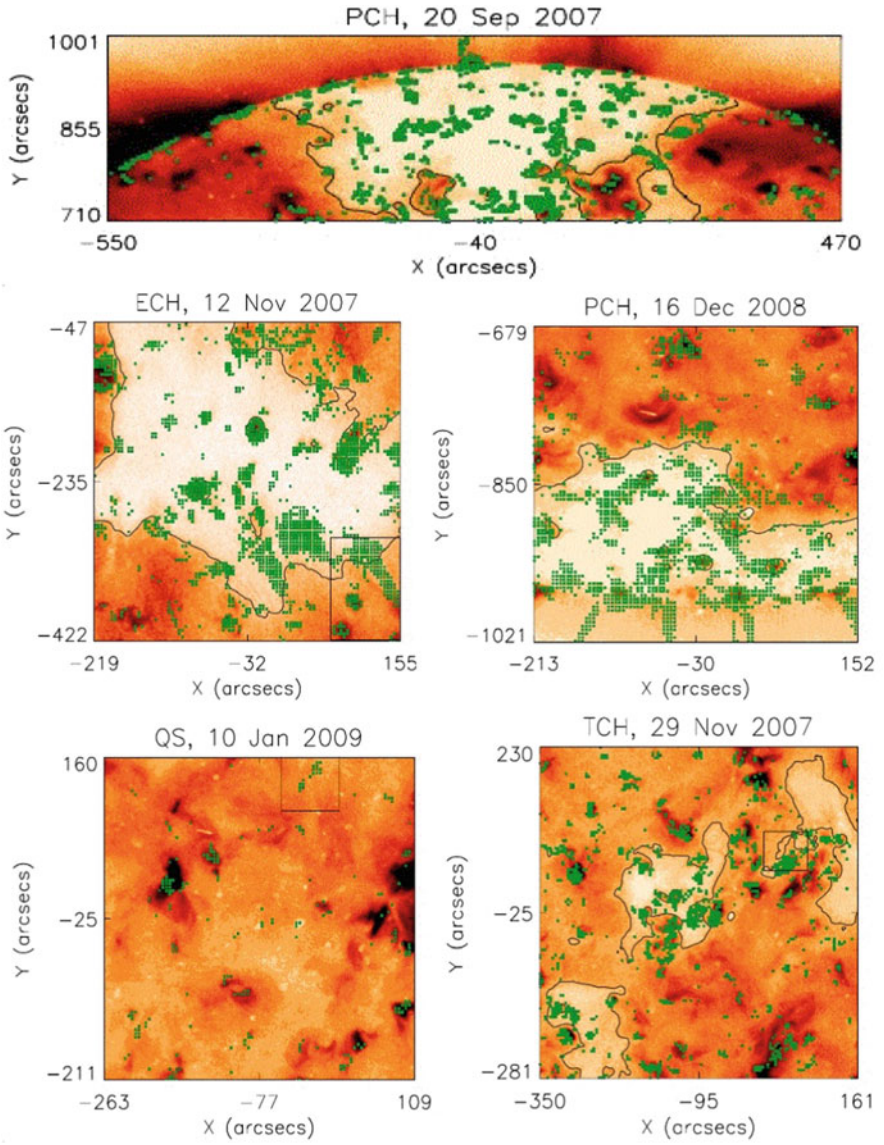

Fig. 7.8 Polar coronal hole (top), equatorial coronal hole (middle left), polar coronal hole (middle right), Quiet Sun (bottom left), and Quiet Sun with transient coronal holes (bottom right) with the positions of the corresponding identified pixels over-plotted. The coronal hole boundaries are outlined with a black contour. The orange background images display the soft X-ray flux observed with XRT/Hinode, with the Al Poly filter that has a temperature peak at $\log T_{max} \approx 6.9$ (Subramanian et al. 2010)

$\approx$ 70% of the events produce expanding loop structures or collimated outflows, which may represent sources of the slow solar wind (Subramanian et al. 2010).

Numerical simulations with 3-D MHD codes (ARMS) explore the reconnection-driven dynamics of coronal hole boundaries by embedding a small (active region) bipole into a global (solar) dipole field and driving a rotational motion. Due to the applied stress, the bipole expands outward and reconnects with the surrounding closed flux, eventually tunneling through the streamer boundary and encountering the open flux of the coronal hole, which results into interchange reconnection between closed and open fields (Edmondson et al. 2009, 2010). Further detailed calculations (with the ARMS code) of the dynamical response of a prototypical coronal hole boundary (between a coronal hole and a streamer), with driving by supergranule-like motions, are carried out in Higginson et al. (2017), producing flux interchanging episodes over 50 times in one day.

The magnetic topology of coronal hole linkages has been investigated with an analytical magnetic field (source surface) model (Titov et al. 2011), and the following results were found: (i) A coronal hole boundary can join stably to the separatrix boundary of a parasitic polarity region; (ii) A single parasitic polarity region can produce multiple null points and the corona and separator lines connecting these null points; (iii) The coronal holes are not connected by an open-field corridor of finite width, but instead are linked by a singular line that coincides with the separatrix footprint of the parasitic polarity. The correct topological model is important in order to understand possible connectivities between the coronal hole boundaries and the solar wind in the heliosphere.

7.6 Coronal Holes: MHD Waves

Reviews can be found on MHD waves in coronal holes (Ofman et al. 2005; Banerjee et al. 2011; Banerjee and Krishna Prasad 2016), or on coronal holes in general (Cranmer 2009), or on MHD waves near coronal null points in particular (McLaughlin et al. 2011). MHD waves in coronal holes are thought to be important to heat the slow solar wind and to accelerate the fast solar wind. The slow solar wind ($v \approx 400$ km s^{-1}) can be produced by thermal expansion, as predicted by Parker, for which MHD waves may contribute as a heating process (rather than by direct acceleration). The fast solar wind ($v \approx 800$ km s^{-1}), however, needs an additional source of momentum and energy transfer, which could be supplied by low-frequency MHD waves in coronal holes.

MHD wave activity in the fast solar wind has been detected in situ by *Helios*, *Ulysses*, *Wind*, and the *Advanced Composition Explorer (ACE)*, as well as by remote sensing with EUV imagers such as *UVCS/SOHO*, *SUMER/SOHO*, and *EIT/SOHO*.

Observational evidence of MHD waves in coronal holes comes from : (i) in situ measurements of power spectra in interplanetary space that show f^{-1} spectra at low frequencies ($f < 10^{-4}$ Hz), and $f^{-5/3}$ (Kolmogorov turbulence) spectra at high frequencies, beyond 1 AU; (ii) detection or large-amplitude low-frequency Alfvén waves beyond 0.3 AU; (iii) interplanetary scintillation measurements; (iv) remote-sensing observations of periodic density fluctuations with periods of ≈ 10 min that are consistent with propagating slow MHD mode waves (Ofman et al. 2000); and (v) non-thermal line broadening in Si VIII emission observed with SUMER/SOHO, which obeys the scaling law $\langle \delta v \rangle^2 \propto \rho^{-1/4}$ between the mean square nonthermal velocity $\langle \delta v \rangle$ and the plasma mass density ρ, as expected for Alfvén waves (Banerjee et al. 2009). Some observations confine the acceleration region of the fast solar wind to $< 10 R_\odot$, or $< 3 R_\odot$.

A self-consistent simulation for the low-frequency Alfvén waves from the photosphere to 0.3 AU was achieved by Suzuki and Inutsuka (2005), using a 1-D MHD model with radiative cooling and thermal conduction, which shows that the coronal heating and the fast solar wind acceleration in coronal holes are natural consequences of the footpoint fluctuations of the magnetic field at the photosphere (with $\langle \delta v_\perp \rangle = 0.7$ km s^{-1} and periods of 20 s to 30 min). The heating and acceleration of the plasma is mainly accomplished by the nonlinear generation of compressive waves and shocks, matching the observed temperatures of $T_e \approx 1$ MK and fast wind velocity $v \approx 800$ km s^{-1} (Suzuki and Inutsuka 2005).

Theoretical 2.5-D models of MHD wave propagation in coronal holes employ the visco-resistive MHD equations to define the background plasma in an open magnetic field, that diverges radially, or super-radially, and the Parker's 1-D solar wind solution to define the initial density and velocity radial structure (Ofman 2005). Launching a disturbance in this background field allows then to study the dissipation of MHD waves by phase mixing or resonant absorption. Such 2.5-D simulations have been performed for plume and inter-plume regions in coronal holes, some with generalizations to nonlinear MHD waves, and to three fluids (electrons, protons, and He^{++} ions).

These MHD simulations, however, cannot reproduce the ion temperature anisotropies in the fast solar wind (as observed with UVCS/SOHO), which appear to require ion-cyclotron wave resonances (Markovskii 2001; Hollweg and Markovskii 2002; Zhang 2003; Zhang et al. 2005). The generation of ion-cyclotron waves in a coronal hole may be initiated by a plasma instability that is driven by current fluctuations of a global resonance MHD mode (Markovskii 2001). The dispersion relation shows that ions can resonate with a purely right-hand circularly polarized wave if the propagation is oblique (Hollweg and Markovskii 2002; Ofman 2005). Reflection of Alfvén waves is a further ingredient that was introduced in coronal hole and solar wind models, which reduces the dissipation length of Alfvénic waves and this way makes coronal heating and solar wind acceleration more efficient

(Hollweg and Isenberg 2007). As an alternative to ion-cyclotron resonances, it was proposed that low-frequency Alfvén wave turbulence could provide additional energy to be absorbed in the corona (or coronal holes) (via stochastic heating) and this way may increase the perpendicular ion temperature $T_{\perp,i}$, in agreement with the observed O^{+5} temperature anisotropies (Chandran 2010). A unification of semi-empirical atmospheric models and MHD Alfvén wave turbulence models has been attempted with the motivation to provide a tool for space weather prediction (Sokolov et al. 2013).

Besides MHD waves, propagating along a guide magnetic field upward through the corona, there are also global MHD waves that propagate spherically over the solar surface, triggered by a local disturbance such as by a flare or CME. These global MHD waves have also been called *"EIT waves"*, based on the instrument of their discovery, or *"EUV waves"*, based on their wavelength (Wang 2000). An interesting property of these spherically propagating waves is that they are deflected away from active regions and coronal holes (e.g., Gopalswamy et al. 2009), where the wave speed v_f is large,

$$v_f^2 = \frac{1}{2}\left[v_A^2 + c_s^2 + \sqrt{(v_A^2 + c_s^2)^2 - 4v_A^2 c_s^2 \cos^2\delta}\right] \tag{7.6.1}$$

where v_A is the Alfvén speed, c_s the sound speed, and δ is the angle between the wave vector and the magnetic field. These global waves are also refracted upward as they propagate away from their origin, since v_f falls off rapidly with height. The average surface-projected expansion speeds are $v \approx 200$ km s^{-1}. Wave refraction occurs most strongly near null-points, where the Alfvén speed goes to zero, which defines the most efficient location of heating by fast MHD waves (McLaughlin et al. 2011; Pucci et al. 2014). Interactions of EUV waves with active regions and coronal holes can also lead to disappearance of primary waves and emergence of secondary waves nearby (Li et al. 2012). Stereoscopic observations in quadrature enabled the triangulation of three EUV waves reflected from coronal holes (Fig. 7.9), exhibiting starting velocities of $\approx$ 310–500 km s^{-1} and final velocities that match the initial velocities of the primary waves (Kienreich et al. 2013). In all three events, the primary and reflected waves obey the Huygens-Fresnel principle, as the incident angle with $\approx 10°$ to the normal is of the same magnitude as the angle of reflection (Kienreich et al. 2013). The phenomenon of wave deflection (reflection or refraction) confirms the nature of wave optics (i.e., a change of the refractive index corresponds to a change in phase speed).

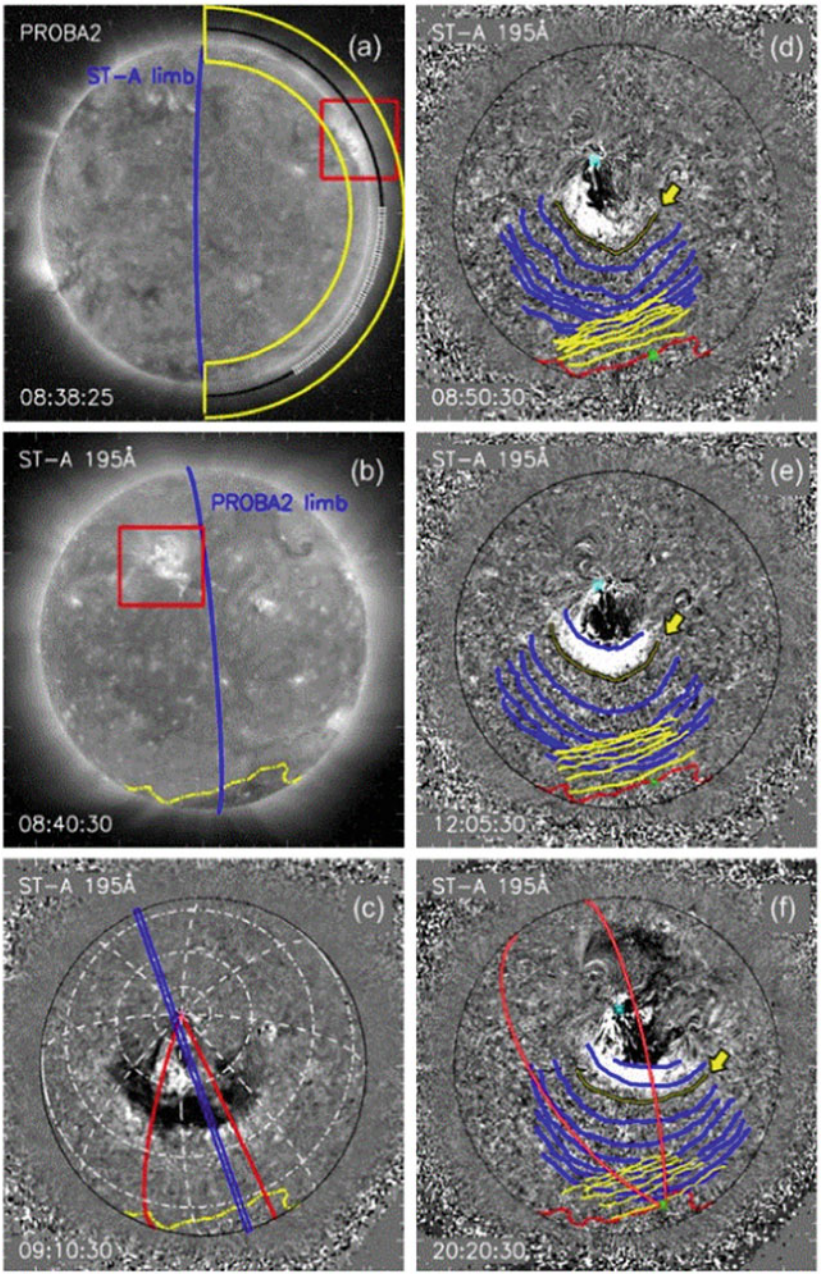

Fig. 7.9 (**a**) PROBA2, (**b**) STEREO-A images of a global EUV wave observed on 2011 January 27. The EUV wave source region (NOAA 11149) is marked with red boxes. (**c**)–(**f**) Median-filtered 10-min STEREO-A 195 Å images. (**d**)–(**f**) Running difference images with outgoing wave fronts (blue curves) and reflected wave fronts (yellow curves). Note that the first reflected wave front is coincident with the last outgoing wave front (Kienreich et al. 2013)

7.7 Coronal Holes: Heating Mechanisms

The coronal heating requirements for mechanisms operating in coronal holes are similar to those in the Quiet Sun, except that the mean coronal temperature and electron density is somewhat lower in coronal holes, which translates into somewhat lower conductive and radiative losses, but the energy loss due to the solar wind is higher in coronal holes (due to the open magnetic field), so that the total coronal losses are somewhat larger in coronal holes ($F \approx 8 \times 10^5$ erg cm^{-2} s^{-1}) than in the Quiet Sun ($F \approx 3 \times 10^5$ erg cm^{-2} s^{-1}), (Withbroe and Noyes 1977). It is therefore not surprising that the same coronal heating mechanisms in terms of DC and AC heating models have been proposed for coronal holes as it is the case for Quiet Sun heating (Sect. 6.7). One of the major challenges for modeling comes from the UVCS/SOHO measurements that indicate preferential (perpendicular) heating and acceleration of positive ions (O^{+5}, Cranmer et al. 2008) within the first few solar radii of the high-speed solar wind. The idea to energize ions by the dissipation of ion cyclotron resonant waves requires high-frequency MHD waves which have not been observed yet. A turbulent cascade is one possible way of generating small-scale fluctuations from a pre-existing population of low-frequency MHD waves. Reviews on heating processes in coronal holes can be found in Hollweg and Isenberg (2002), Marsch (2006), and Cranmer (2009).

One of the most cited papers on coronal heating models for open magnetic fields (applicable to coronal holes, as well as to streamers and open-field channels in active regions) is due to Cranmer et al. (2007), which presents a self-consistent approach for coronal heating and solar wind acceleration from anisotropic MHD turbulence, improving on earlier work (e.g., Hu et al. 2000; Isenberg 2001, 2004; Isenberg et al. 2001; Tu and Marsch 2001; Hollweg and Isenberg 2002). These models yield self-consistent solutions that combine (i) chromospheric heating driven by an empirically guided acoustic wave spectrum; (ii) coronal heating from Alfvén waves that have been partially reflected, then damped by anisotropic turbulent cascade; and (iii) solar wind acceleration from gradients of gas pressure, acoustic wave pressure, and Alfvén wave pressure (Cranmer et al. 2007). The radial gradient of the Alfvén speed affects wave reflection and damping, and different magnetic expansion factors reproduce the dichotomy of slow and fast solar wind. In essence, these models explain both coronal heating and solar wind acceleration in terms of (Alfvénic) wave dissipation and turbulent cascade. One model of MHD turbulence cascade uses a combination of advection and diffusion in wavenumber space, which leads to a highly anisotropic fluctuation spectrum, resulting into (i) Landau damping with parallel electron heating, and/or (ii) ion cyclotron resonance with perpendicular proton heating (Fig. 7.10), as observed in the proton and ion anisotropies (Cranmer and van Ballegooijen 2003). Analytical models deal with Alfvén wave reflection and turbulent heating in the solar wind from the solar surface all the way to 1 AU, employing the Heinemann-Olbert equations, which describe non-compressive MHD fluctuations in an inhomogeneous medium with a background flow parallel to the background magnetic field (Chandran and Hollweg 2009).

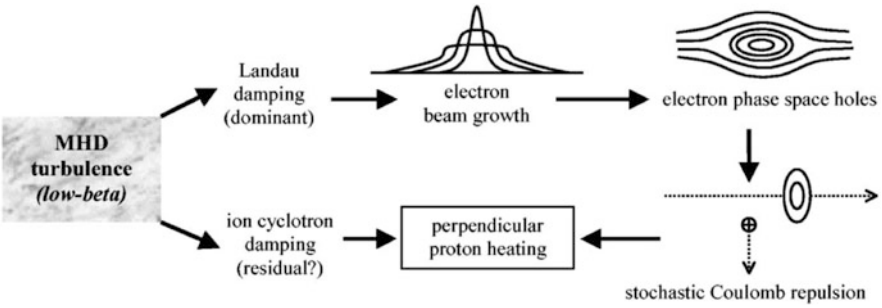

Fig. 7.10 Diagram of the major physical processes of a coronal hole heating model with Alfvénic turbulence. The relative amount of turbulent dissipation that directly heats the protons (bottom) and electrons (top) depends on the ratio of advection and diffusion in wavenumber space. The nonlinear development of parallel electron beams into phase-space holes that can interact with protons is also illustrated (Cranmer and van Ballegooijen 2003)

Another variant of a turbulence-driven coronal heating model that explains the generation of fast solar wind in coronal holes has been presented by Verdini et al. (2010). It relies on heating that is dominated by turbulent dissipation of MHD fluctuations transported upward into the solar atmosphere. Scale-separated transport equations include large-scale fields, transverse Alfvénic fluctuations, and a small compressive dissipation due to parallel shears near the transition region. The model has almost no free parameters and accounts for proton temperature, density, wind speed, and fluctuation amplitude as observed. In contrast to the model of Cranmer et al. (2007), it employs strong turbulence closure (instead of weak turbulence perturbations) and the internal energy of protons (instead of electron heat conduction). Also it needs a small component of compressive heating near the coronal base to account for fast solar wind streams, perhaps conveyed by type II spicules, or by fast switch-on MHD shock trains, produced by linearly polarized Alfvén fast MHD waves and acoustic slow MHD waves (Suzuki 2004).

Solar wind turbulence models contain multiple species, such as three-fluid models (with electrons, protons, alpha particles) (Ofman 2004), or four-fluid models (three-fluid plus a minor ion, e.g., O^{5+}) (Hu et al. 2000). The larger the number of species included in the dispersion relation is, the stronger preferential acceleration and heating produced by the waves for the heavy ions close to the Sun will be. Minor ions may be treated approximately as test particles in the solar wind. It was suggested that preferential perpendicular heating of coronal hole minor ions can be conveyed by the second-order Fermi mechanism (Isenberg and Vasquez 2007, 2009). The preferential effects naturally arise from the ability of minor ions to simultaneously resonate with several modes in a spectrum of inward- and outward-propagating waves, while protons can encounter only a single resonance for a given particle parallel speed. The multiply resonant interaction available to minor ions is equivalent to a second-order Fermi acceleration of these thermal particles. This effect can explain that the observed heavy ions in the fast solar wind are hotter and

flow faster than the proton population (Isenberg and Vasquez 2007, 2009). The same conclusion holds for more sophisticated models that include the effects of gravity, charge-separation electric field, and mirroring in the decreasing magnetic field of a super-radially expanding flux tube (Isenberg and Vasquez 2009). However, there is still the problem of proton heating: Field-aligned Alfvén waves are considered to be sources of proton heating, but the dissipated energy is insufficient to account for the observed distribution of accelerated protons (Markovskii et al. 2009).

While we discussed mostly AC heating models in terms of dissipation of Alfvénic waves so far, there are also DC heating models in terms of (Parker's) footpoint braiding, undergoing interchange reconnection in a turbulent corona (Rappazzo et al. 2012). Coronal heating models that simulate the field line footpoint shuffling by convective motion show that reconnection can occur continuously in unipolar field regions with no neutral points. Photospheric motions induce an MHD turbulent cascade in the coronal field that creates the necessary small scales, where a sheared magnetic field component orthogonal to the strong axial field is created locally and can reconnect. Reduced MHD simulations of such a model show that the slow wind may originate everywhere along loop coronal hole boundary regions, and can explain slow solar wind outflows (Rappazzo et al. 2012).

Hahn and Savin (2013) developed a novel method to measure energy dissipation by Alfvén waves in a polar coronal hole. Previous work has shown that line widths decrease with height in coronal holes, which is interpreted as a signature of wave damping, but failed to derive the energy lost by the waves, because the line width depends on both the non-thermal velocity v_{nt} and the ion temperature T_i. With the new method, these two parameters were measured separately, which yielded an initial flux density of $E_H = (6.7 \pm 0.7) \times 10^5$ erg cm^{-2} s^{-1} (Fig. 7.11), which is sufficient to heat the coronal hole and to accelerate the solar wind during the 2007–2009 solar minimum.

7.8 Coronal Holes: Fast Solar Wind Acceleration

What physical mechanism does accelerate the solar wind? A list of four different categories of physical processes for preferential heating and acceleration of minor ions in coronal holes is given in Table 7.2 (from Cranmer 2009). The first group envisions reconnection events that are triggered by convective motion, such as they are hypothesized in type-II spicules (McIntosh et al. 2011). The second group based on MHD turbulence cascade is the currently most studied mechanism for solar wind acceleration. For the third group on low-frequency Alfvénic waves it is not known whether the effective polarization is sufficiently large to provide a significant fraction of the ion thermal speeds. Also the forth group on velocity filtration is doubtful since hydrogen and iron ions have never been observed to settle into different gravitational scale heights as theoretically predicted.

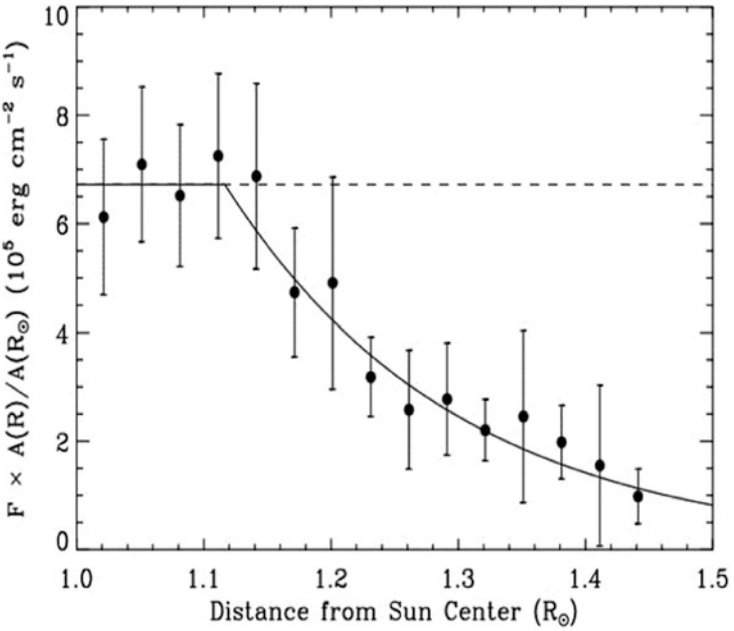

Fig. 7.11 The wave energy density flux F, multiplied by the expansion factor $A(R)/A(R_{\odot})$, measured with EIS/Hinode from O VI, Mg VII, Si VII, Si X, Fe VIII, Fe IX, Fe X, Fe X1 lines in a polar coronal hole, observed on 2009 Apr 23, 12:42–15:17 UT (Hahn and Savin 2013)

Clues on the origin and acceleration of the fast solar wind was inferred from the observed preferential heating and acceleration of O VI ions (Kohl et al. 1998; Antonucci et al. 2000; Tu and Marsch 2001) and the blueshift in He I and Ne VIII lines (Wilhelm et al. 2000). These in-situ measurements of the solar wind as well as remote-sensing observations of coronal holes have strongly implicated the resonant interaction with ion-cyclotron waves as the responsible mechanism for heating and acceleration of coronal hole ions to generate the fast solar wind (e.g., Hollweg 2000; Hu et al. 2000; Isenberg 2001; Hollweg and Isenberg 2002). A majority of studies on the acceleration of the fast solar wind in coronal holes finds supporting evidence for the idea that coronal heating and solar wind acceleration (in open magnetic flux tubes) occurs as a result of wave dissipation and turbulent cascade (Cranmer et al. 2007; Verdini et al. 2010). Self-consistent models managed to combine: (i) chromospheric heating driven by an acoustic wave spectrum, (ii) coronal heating from Alfvén waves (partially reflected and damped by anisotropic turbulence cascade), and (iii) solar wind acceleration from gradients of gas pressure, acoustic wave pressure, and Alfvén wave pressure (Cranmer et al. 2007). The radial gradient of the Alfvén speed affects where the waves are reflected and damped, and thus whether energy is deposited below or above the Parker critical point (Cranmer et al. 2007; Tu and Marsch 2001; Suzuki and Inutsuka 2005). What determines the solar wind speed? Larger coronal "expansion factors" of the magnetic field give rise

Table 7.2 Overview of physical processes suggested for preferential heating and acceleration of minor ions in coronal holes (Cranmer 2009)

Physical process	References
Reconnection events in the low corona generate	
Ion cyclotron resonant Alfvén waves	Tu and Marsch (1997), Cranmer (2000, 2001)
Electron beams $\mapsto$ ion cyclotron waves	Markovskii and Hollweg (2002, 2004)
Fast collisionless shocks	Lee and Wu (2000)
MHD turbulence in the extended corona generates	
Ion cyclotron waves ("parallel cascade?"), with	
$\gg$ Alfvén and fast-mode nonlinear coupling	Chandran (2005)
$\gg$ Three-wave (ion-sound/parametric) coupling	Yoon (2008)
$\gg$ Fermi-like diffusion between inward/outward wave resonances	Isenberg et al. (2001)
Kinetic Alfvén waves ("perpendicular cascade"), with	
$\gg$ Shear instabilities $\mapsto$ ion cyclotron waves	Markovskii et al. (2006)
$\gg$ Nonlinear wave-particle resonances	Voitenko and Goossens (2003, 2004)
$\gg$ Debye-scale electron holes	Matthaeus et al. (2003), Cranmer and van Ballegooijen (2003)
Oblique MHD waves (high $k_\parallel$, high $k_\perp$)	Li and Habbal (2001)
Current sheets $\mapsto$ coherent Fermi acceleration	Dmitruk et al. (2004)
Transverse density gradients $\mapsto$ drift currents	Markovskii (2001); Zhang (2003)
Low-frequency Alfvén waves in the corona directly undergo	
Polarization drift $\mapsto$ lower-hybrid waves	Singh and Khazanov (2004); Khazanov and Singh (2007)
Nonresonant stochastic heating	Lu and Li (2007); Wu and Yoon (2007)
Stochastic heating at fractional cyclotron resonance	Chen et al. (2001); Guo et al. (2008)
Heavy ion velocity filtration	Pierrard and Lamy (2003); Pierrard et al. (2004)

to a slower and denser wind, a higher temperature at the coronal base, less intense Alfvén waves at 1 AU, and correlative trends for commonly measured ratios of ion charge states and FIP-sensitive abundances that are in general agreement with observations (Cranmer et al. 2007).

In what distance from the solar surface is the fast solar wind accelerated? Comparison with theoretical models indicates acceleration of H I and O VI ions in interplume locations at distances of 1.75 and 2.0 solar radii (Teriaca et al. 2003; Giordano et al. 2000).

Observations of the transition region reveal how ubiquitous outward-propagating Alfvénic motions permeate the outer solar atmosphere with periods of the order 100–500 s (1.6–8.3 min) and are energetic enough to accelerate the fast solar wind (McIntosh et al. 2011).

7.9 Coronal Holes: Radio Emission

Radio emission originating from coronal holes is generally produced by free-free bremsstrahlung emission and maps out coronal features (in the microwave wavelength range), to chromospheric features (in the millimeter and sub-millimeter wavelength range), because the free-free opacity decreases with higher frequencies (or increases with longer wavelengths). The free-free absorption coefficient α_{ff}, which indicates the sensitivity of the radio brightness temperature on the electron density n_e, ion density n_i, electron temperature T_e, frequency ν, and column depth z is given by,

$$\alpha_{ff} \approx 10^{-2} \frac{n_e(z) \sum_i Z_i^2 n_i(z) \ln \Lambda}{\nu^2 T^{3/2}(z)} \; . \tag{7.9.1}$$

The observed radio brightness, which is a function of the line-of-sight integral or the free-free opacity α_{ff}, thus samples the chromosphere or corona at a temperature level T_{radio} where the opacity becomes unity, and thus can be compared with UV, EUV, or soft X-ray images only if their temperatures are compatible (e.g., $T_{radio} \approx T_{EUV}$). Quantitative comparisons thus require self-consistent models of the density $n_e(h)$ and temperature $T_e(h)$ as a function of the altitude $h(x, y)$ in each location (x, y). Such multi-wavelength studies of EUV, FUV, and UV emission in coronal holes have been conducted for radio emission at 150–450 MHz (Mercier and Chambe 2009, 2012), at 151 MHz, 327 MHz, 5.7 GHz, 17 GHz (Prosovetsky and Myagkova 2011), at 5.7 MHz (Krissinel et al. 2000), at 5.7 and 17 GHz (Maksimov et al. 2006), at 17 GHz (Moran et al. 2001; Selhorst et al. 2010, 2017; Kim et al. 2017), at 37 GHz (Brajsa et al. 2007), or at 87 GHz (Pohjolainen 2000). The instruments used for these studies include the *Siberian Solar Radio Telescope (SSRT)*, the *Nobeyama Radio Heliograph (NoRH)*, the *Nançay Radio Heliograph (NRH)*, and the *Metsähovi Observatory*.

An example of radio brightness temperature maps and corresponding magnetic features is shown in Fig. 7.12. Coronal holes generally appear as low brightness temperature regions in centimeter and millimeter wavelengths. However, high brightness temperature regions can occur at the boundaries of coronal holes (Brajsa et al. 2007). A radial displacement of brightness temperatures was interpreted as a consequence of heating by dissipation of Alfvén waves (Maksimov et al. 2006). The increase in the solar wind velocity up to ≈ 600 km s^{-1} was found to correlate with a decrease in the UV flux of the solar disk (Prosovetsky and Myagkova 2011). Also, a solar cycle variation of the polar limb-brightening effect was noted (Selhorst et al. 2010; Kim et al. 2017). The *Siberian Solar Radio Telescope (SSRT)* provides imaging at 5.7 and 17 GHz. A criterion has been established at SSRT that dark features in radio images, if this feature is dark in both 5.7 and 17 GHz, corresponds to a filament or filament channel, rather than to a coronal hole (Grechnev et al. 2003).

A more sophisticated method of modeling coronal electron density and electron temperature profiles is a (rotational) tomographic method, which was applied to *Mauna Loa Solar Observatory (Mark-IV)* K-coronameter data, which showed good agreement between EIT/SOHO and Mark-IV white-light data (Butala et al. 2005).

Coronal holes generally do not produce flare-related phenomena, but new observations indicate that they can play an important role for flare-like signatures in close proximity to their boundaries, such as ^{3}He-rich solar energetic particle events (Bucik et al. 2014, 2018), or micro-type III radio bursts (Morioka et al. 2007). Especially for trans-equatorial holes, continuous reconnection at their boundaries is required to compensate for the difference between the differential rotation speed in the corona and the rigid rotation speed in the photosphere (Sect. 7.5).

Radio emission in coronal holes and outward into interplanetary space can detect density fluctuations by Faraday rotation, using *interplanetary scintillation (IPS)* techniques. If ion cyclotron waves are obliquely propagating, as expected in the MHD turbulent cascade scenario of the fast solar wind (Sect. 7.8), they will be compressive, and the corresponding density fluctuations will induce phase, intensity, and Faraday rotation fluctuations on radio signals (from pulsars) passing through the corona (Hollweg 2000). Faraday rotation has indeed been detected in 13 polarized radio sources occulted by the solar corona (mostly by streamers), observed with the *Very Large Array (VLA)* at frequencies of 1465 and 1665 MHz, and sampled in an elongation range of (5–14)$R_\odot$ (Mancuso and Spangler 2000). The rotation measure RM is given by

$$RM = \frac{e^3}{2\pi m_e^2 c^4} \int_L n_e \, \mathbf{B} \cdot \mathbf{ds} \,, \tag{7.9.2}$$

from which electron density fluctuations $n_e(r)$ and magnetic field fluctuations $\mathbf{B}(r)$ can be constrained. Rotation measures of order $RM \approx$ (1–2) rad m^{-2} were detected, but occurring on time scales of several hours, which is many orders of magnitude longer than the kHz range required in some MHD turbulence cascade models (Hollweg 2000). However, radio fluctuation spectra during the solar

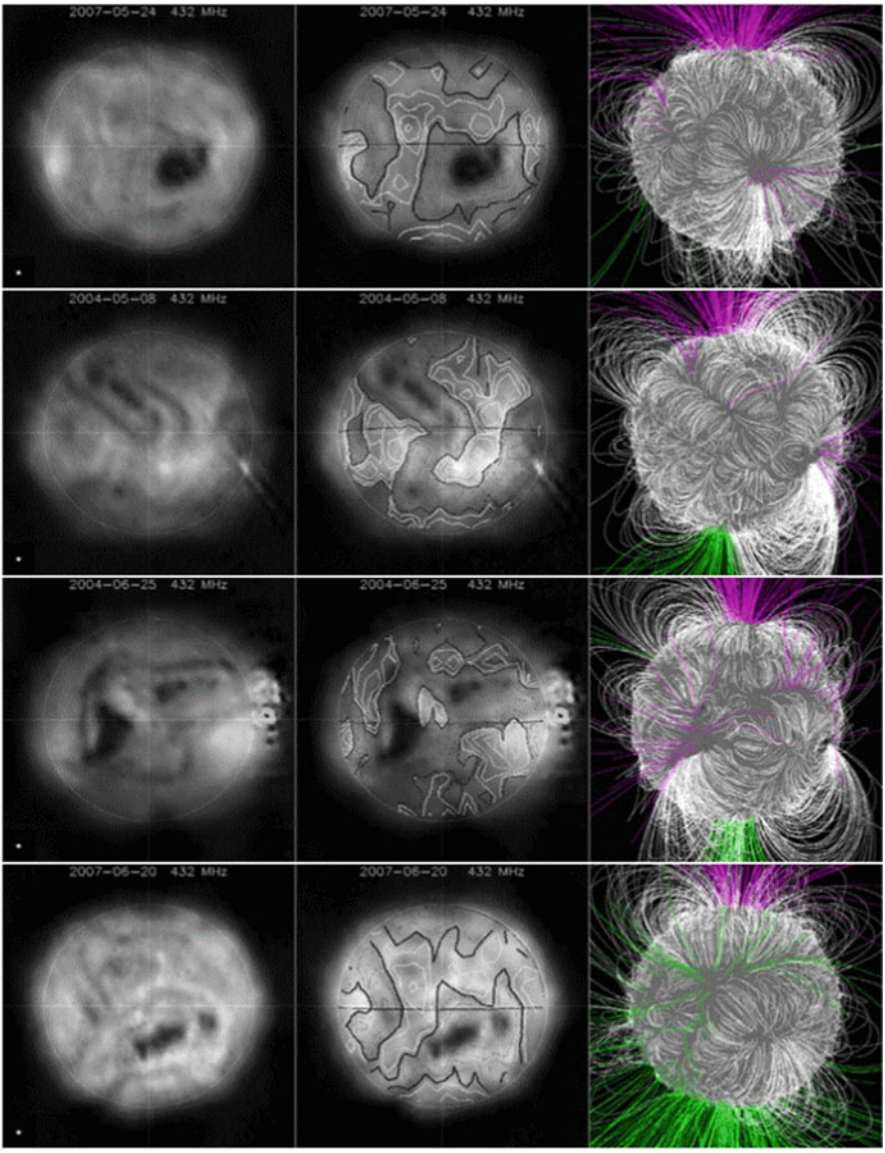

Fig. 7.12 Comparison between radio images at 432 MHz and magnetic features for four days (from top to bottom). From left to right: the radio image from the *Nançay Radioheliograph*, then superimposed with the *Wilcox Solar Observatory (WSO)* magnetogram contours (middle) and the *Potential Field Solar Surface (PFSS)*. Closed field lines are indicated with white color, open field lines with magenta and green color, where the positive magnetic polarity is magenta and the negative polarity is green. Note the radio darkening in the polar caps and in some filaments. Observing dates are indicated in the radio images (Mercier and Chambe 2012)

conjunctions of the *Ulysses* and *Galileo* spacecraft show a low-frequency turnover at frequencies $\approx$ 0.1 mHz that has been interpreted as an outer scale of density turbulence in the coronal plasma (Wohlmuth et al. 2001).

7.10 Coronal Holes: Solar Cycle Modulation

Measurements of the variation of coronal hole areas during solar cycles require long-term monitoring of the magnetic field with the same instrument. One method is the use of *Mount Wilson Observatory (MWO)* or *Wilcox Solar Observatory (WSO)* magnetograms, which are consistently available over at least three solar cycles now, and by applying a *potential field source surface (PFSS)* extrapolation method to map out coronal holes based on the open field regions (Luhmann et al. 2002). This method is particularly justified in the case of rigidly corotating solar wind streams (Luhmann et al. 2009). However, the generally assumed value of 2.5 $R_\odot$ for the source surface value typically used in PFSS applications should sometimes be lowered to $\approx$ 1.5–1.9 $R_\odot$, such as during cycles 22 and 23 minimum periods, in order to obtain best results in matching coronal hole areas (Lee et al. 2011). Newer methods include automated detection of EUV polar coronal holes (Kirk et al. 2009; Barra et al. 2009). A review on solar wind sources and their variations over the solar cycle is given in Schwenn (2006).

The area $A(t)$ of polar coronal holes waxes and wanes with the solar cycle, which couples with the mean open magnetic field strength $B(t)$, since the magnetic flux $\Phi(t) = A(t)B(t)$ is constant to first order. Since the properties of the high-speed solar wind streams depend on the geometry of the open field lines (such as the radial or super-radial expansion between the coronal base and the source surface level at $\approx$ 1.5–2.5 $R_\odot$), the fast solar wind speed is modulated with the solar cycle too. Moreover, there are substantial areas of low-latitude coronal holes which experience additional modulation from flare activity in nearby active regions with plages and open fields. A butterfly diagram of the magnetic flux during Cycles 23 and 24 is shown in Fig. 7.13 (Golubeva and Mordvinov 2017), where the appearance frequency of coronal holes is marked with yellow contours.

Although the periodicity of the 11-year solar cycle is fairly stable, other characteristics of the solar cycle can vary enormously, for instance the almost complete absence of the solar magnetic field during the Maunder minimum. Such nonlinear and intermittent behavior is typical for self-organizing processes, even when their periodicity converges towards a stable limit cycle (Sects. 3.6–3.7).

A recent anomaly of the solar cycle is the "weakness" of Cycle 24 (2008–2020) at the sunspot minimum in 2008. The solar polar fields are currently $\approx$ 40% weaker than they were during the previous minima, accompanied by a decrease in the interplanetary magnetic field (IMF) strength, by a $\approx$ 20% shrinkage in the polar coronal hole areas, and by a reduction in the solar wind mass flux over the poles (Wang et al. 2009). Also the low-latitude coronal holes were larger in the 2007 solar minimum relative to the previous cycle (Abramenko et al. 2010). The evolution

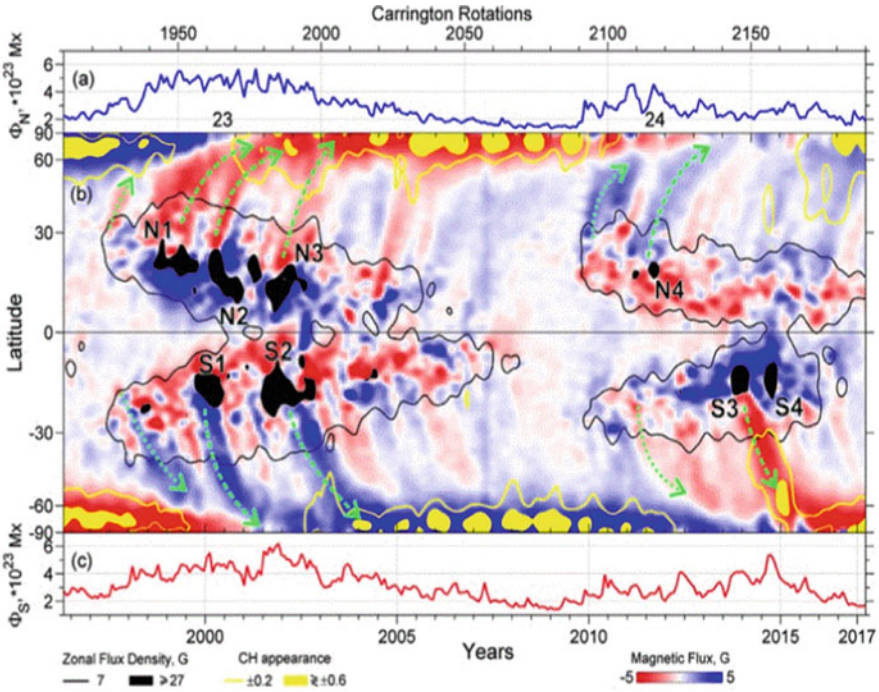

Fig. 7.13 Time-latitude analysis of magnetic flux and coroal holes in Cycles 23 and 24 (numbered in top panel). Variations in absolute magnetic flux in the northern and southern hemispheres are shown in the top (**a**) and bottom (**c**) panels, respectively. The time-latitude diagram is shown in panel (**b**). The longitude-averaged magnetic fields are plotted in red-to-blue colors. Black contours of 7 G in modulus depict the boundaries of sunspot activity zones. Domains of high zonal flux density above 27 G in modulus are shown in black. Green arrows point out the remnant flux surges. Domains of coronal holes at a level above 0.6 in modulus are shown in yellow. Yellow contours correspond to a coronal hole appearance of ±2 (Golubeva and Mordvinov 2017)

of coronal holes during the solar minimum had also implications for the high-speed solar wind: The large low-latitude coronal holes present until 2008 remained important sources of recurrent high-speed solar wind streams (de Toma 2011). Vice versa, high-latitude coronal holes were found to affect the properties of the solar wind in the ecliptic plane during solar cycles 21 to 23 (Tlatov et al. 2014). There was also an asymmetry in the phase delay between northern and southern polar holes (Fig. 7.14). The northern hemisphere went through polar-field reversal and reached solar maximum conditions in mid-2012, while the southern hemisphere reached it by end of 2013 (Karna et al. 2014; Lowder et al. 2014; Hess Webber et al. 2014).

To address the question of why the polar fields are so weak, the evolution of the photospheric field and radial IMF strength was simulated by employing a surface transport model that includes the effects of active region emergence, differential rotation, supergranular convection, and a poleward bulk flow (Wang et al. 2009), finding that the observed evolution can be reproduced if the amplitude of the surface

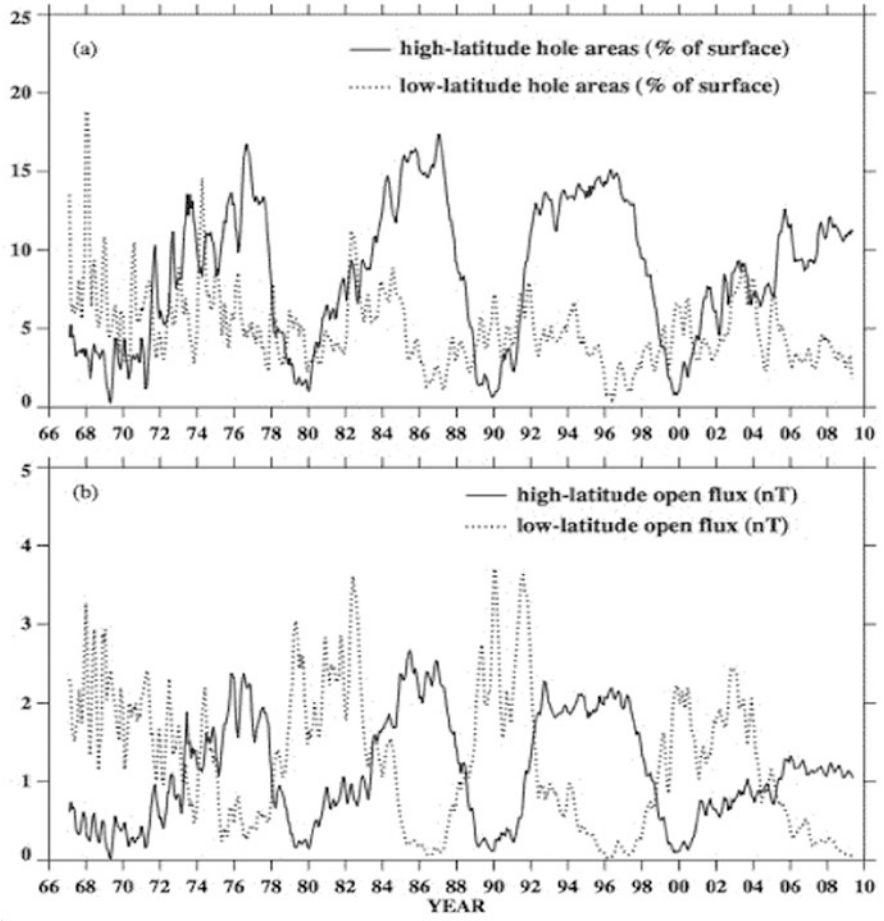

Fig. 7.14 (**a**) Percentage of the solar surface occupied by high-latitude ($|L| > 45°$) and low-latitude ($|L| < 45°$) open flux during 1997–2009. (**b**) Open flux originating from high latitudes and low-latitudes, expressed as field strengths (nT) at 1 AU. The PFSS extrapolation was applied to an average of the MWO and WSO photospheric field, and 3-month running means are plotted (Wang et al. 2009)

meridional flow is varied by as little as 15% (between 14.5 and 17 m s^{-1}), with the higher average speeds being required during the long cycles 20 and 23. The weakness of Cycle 24 was already predicted in 2005 (Schatten 2005). No such anomaly was noted in polar coronal hole characteristics during cycles 22 (1986–1995) and 23 (1996–2007) (Harvey and Recely 2002).

References

(7.1) Coronal Holes: Magnetic Field

Abramenko, V.L., Fisk, L.A., and Yurchyshyn, V.B. 2006, *The rate of emergence of magnetic dipoles in coronal holes and adjacent Quiet-Sun regions*, ApJ 641, L65, [21 c, 2 c/y].

Cranmer, S.R. 2009, *Coronal holes*, LRSP 6, 3, [126 c, 15 c/y].

Fisk, L.A. and Zurbuchen, T.H. 2006, *Distribution and properties of open magnetic flux outside of coronal holes*, JGR 111/A9, CiteID A09115, [34 c, 3 c/y].

Hagenaar, H.J., DeRosa, M.L., and Schrijver, C.J. 2008, *The dependence of ephemeral region emergence on local flux imbalance*, ApJ 678, 541, [39 c, 4 c/y].

Krista, L.D. and Gallagher, P.T. 2009, *Automated coronal hole detection using local intensity thresholding techniques*, SoPh 256, 87, [48 c, 6 c/y].

Lowder, C., Qiu, J., and Leamon, R., et al. 2014, *Measurements of EUV coronal holes and open magnetic flux*, ApJ 783, 142, [11 c, 3 c/y].

Lowder, C., Qiu, J., and Leamon, R. 2017, *Coronal holes and open magnetic flux over cycles 23 and 24*, SoPh 292, 18, [6 c, 12 c/y].

Madjarska, M.S., Doyle, J.G., and van Driel-Gesztelyi, L. 2004, *Evidence of magnetic reconnection along coronal hole boundaries*, ApJ 603, L57, [48 c, 4 c/y].

Scholl, I.F. and Habbal, S.R. 2008, *Automatic detection and classification of coronal holes and filaments based on EUV and magnetogram observations of the solar disk*, SoPh 248, 425, [35 c, 4 c/y].

Shimojo, M. and Tsuneta, S. 2009, *The relation between magnetic fields and coronal activities in the polar coronal hole*, ApJ 706, L145, [15 c, 2 c/y].

Titov, V.S., Mikic, Z., Linker, J.A., et al. 2011, *Magnetic topology of coronal hole linkages*, ApJ 731, 111, [51 c, 8 c/y].

Tsuneta, S., Ichimoto, K., Katsukawa, Y., et al. 2008, *The magnetic landscape of the Sun's polar region*, ApJ 688, 1374, [112 c, 12 c/y].

Wang, Y.M., Lean, J., and Sheeley, N.R.Jr. 2000, *The long-term variation of the Sun's open magnetic flux*, GRL 27/4. 505, [133 c, 8 c/y].

Wang, Y.M., Sheeley, N.R.Jr., and Lean, J. 2002, *Meridional flow and the solar cycle variation of the Sun's open magnetic flux*, ApJ 580, 1188, [66 c, 4 c/y].

Wang, Y.M. and Sheeley, N.R.Jr. 2003, *On the topological evolution of the coronal magnetic field during the solarc cycle*, ApJ 599, 1404, [54 c, 4 c/y].

Wang, Y.M. and Sheeley, N.R.Jr. 2004, *Footpoint switching and the evolution of coronal holes*, ApJ 612, 1196, [57 c, 4 c/y].

Wang, Y.M. 2009, *Coronal holes and open magnetic flux*, SSRv 144, 383, [46 c, 5 c/y].

Wang, Y.M., Robbrecht, E., and Sheeley, N.R.Jr., 2009, *On the weakening of the polar magnetic field during solar cycle 23*, ApJ 707, 1372, [130 c, 15 c/y].

Wang, Y.M., Warren, H.P., and Muglach, K. 2016, *Converging supergranular flows and the formation of coronal plumes*, ApJ 818, 203, [2 c, 2 c/y].

Wang, Y.M. 2016, *The ubiquitous presence of looplike fine structure inside solar active regions*, ApJ 820, L13, [2 c, 2 c/y].

Wang, Y.M. 2017, *Small coronal holes near active regions as sources of solar wind*, ApJ 841, 94, [4 c, 4 c/y].

Yang, S., Zhang, J., Li, T., et al. 2011, *SDO observations of magnetic reconnection at coronal hole boundaries*, ApJ 732, L7, [26 c, 4 c/y].

Yeates, A.R., Amari, T., Contopoulos, I., et al. 2018, *Global non-potential magnetic models of the solar corona during the March 2015 eclipse*, SSRv 241, 99.

(7.2) Coronal Holes: Plumes

Banerjee, D., Erdelyi, R., Oliver, R., et al. 2007, *Present and future observing trends in atmospheric magnetoseismology*, SoPh 246, 3, [162 c, 15 c/y].

Banerjee, D., Pérez-Suárez, D., and Doyle, J.G. 2009, *Signatures of Alfvén waves in the polar coronal holes as seen by EIS/Hinode*, A&A 501, L15, [56 c, 7 c/y].

Berger, T.E., Shine, R.A., Slater, G.L., et al. 2008, *Hinode/SOT observations of solar quiescent prominence dynamics*, ApJ 676, L89, [175 c, 18 c/y].

Berger, T.E., Slater, G., Hurlburt, N., et al. 2010, *Quiescent prominence dynamics observed with the Hinode SOT. Turbulent upflow plumes*, ApJ 716, 1288, [115 c, 15 c/y].

DeForest, C.E., Lamy, P.L., and Llebaria, A. 2001, *Solar polar plume lifetime and coronal hole expansion: Determination from long-term observations*, ApJ 560, 490, [41 c, 2 c/y].

Del Zanna, G., Bromage, B.J.I., and Mason, H.E. 2003, *Spectroscopic characteristics of polar plumes*, A&A 398, 743, [45 c, 3 c/y].

de Patoul, J., Inhester, B., Feng, L., et al. 2013, *2-D and 3-D polar plume analysis from the three vantage positions of STEREO/EUVI A, B, and SOHO/EIT*, SoPh 283, 207, [6 c, 1 c/y].

Feng, L., Inhester, B., Solanki, S.K., et al. 2009, *Stereoscopic polar plume reconstructions from STEREO/SECCHI images*, ApJ 700, 292, [19 c, 2 c/y].

Giordano, S., Antonucci, E., Noci, G., et al. 2000, *Identification of the coronal sources of the fast solar wind*, ApJ 531, L79, [71 c, 4 c/y].

Grappin, R., Wang, Y.M., and Pantellini, F. 2011, *Two-temperature models for polar plumes: Cooling by means of strong base heating*, ApJ 727, 30, [7 c, 1 c/y].

Gupta, G.R. 2014, *Observations of dissipation of slow magneto-acoustic waves in a polar coronal hole*, A&A 568, A96, [17 c, 5 c/y],

Liu, J., McIntosh, S.W., De Moortel, I., et al. 2015, *On the parallel and perpendicular propagating motions visible in polar plumes: An incubator for (fast) solar wind acceleration ?* ApJ 806, 273, [7 c, 3 c/y].

Mandal, S., Prasad, K., and Banerjee, D. 2018, *A statistical study on the frequency-dependent damping of the slow-mode waves in polar plumes and interplumes*, ApJ 853, 134.

McIntosh, S.W., Innes, D.E., De Pontieu, B. et al. 2010, *STEREO observations of quasi-periodically driven high-velocity outflows in polar plumes*, A&A 510, L2, [56 c, 7 c/y].

Ofman, L., Romoli, M., Poletto, G. et al. 2000a, *UVCS WLC observations of compressional waves in the south polar coronal hole*, ApJ 529, 592, [84 c, 5 c/y].

Ofman, L., Nakariakov, V.M., and Sehgal, N. 2000b, *Dissipation of slow magnetosonic waves in coronal plumes*, ApJ 533, 1071, [88 c, 5 c/y].

Poletto,G. 2015, *Solar Coronal Plumes*, LRSP 12, 7, [6 c, 2 c/y].

Pucci, S., Poletto, G., Sterling, A.C., et al. 2014, *Birth, life, and death of a solar coronal plume*, ApJ 793, 86, [6 c, 3 c/y].

Raouafi, N.E. and Stenborg, G. 2014, *Role of transients in the sustainability of solar coronal plumes*, ApJ 787, 118, [15 c, 4 c/y].

Teriaca, L., Poletto, G., Romoli, M., et al. 2003, *The nascent solar wind: Origin and acceleration*, ApJ 588, 566, [74 c, 5 c/y].

Tian, H., McIntosh, S.W., Habbal, S.R., et al. 2011, *Observation of high-speed outflow on plume-like structures of the Quiet Sun and coronal holes with SDO/AIA*, ApJ 736, 130, [51 c, 10 c/y].

Wang, Y.M. 1994, *Polar plumes and the solar wind*, ApJ 435, L153, [83 c, 4 c/y].

Wang, Y.M., Warren, H.P., and Muglach, K. 2016, *Converging supergranular flows and the formation of coronal plumes*, ApJ 818, 203, [2 c, 1 c/y].

Wilhelm, K. 2000, *Solar spicules and macrospicules observed by SUMER*, A&A 360, 351, [66 c, 4 c/y].

Wilhelm, K., Dammasch, I.E., Marsch, E., et al. 2000, *On the source regions of the fast solar wind in polar coronal holes*, A&A 353, 749, [90 c, 5 c/y].

Wilhelm, K., Abbo, L., Auchère, F., et al. 2011, *Morphology, dynamics and plasma parameters of plumes and inter-plume regions in solar coronal holes*, A&ARv 19, 35, [42 c, 6 c/y].

(7.3) Coronal Holes: Jets

Adams, M., Sterling, A.C., Moore, R.L., et al. 2014, *A small-scale eruption leading to a blowout macrospicule jet in an on-disk coronal hole*, ApJ 783, 11, [32 c, 9 c/y].

Archontis, V. and Hood, A.W. 2013, *A numerical model of standard to blowout jets*, ApJ 769, L21, [50 c, 11 c/y].

Chen,H., Zhang,J., Ma,S. 2011, *Kinematics of an untwisting solar jet in polar coronal hole observed by SDO/AIA*, Res.Astron.Astrophys. 12, 573, [30 c, 5 c/y].

Cirtain, J.W., Golub, L., Lundquist, L., et al. 2007, *Evidence for Alfvén waves in solar X-ray jets*, Science 318, 1580, [278 c, 26 c/y].

Guo, Y., Démoulin, P., Schmieder, B., et al. 2013, *Recurrent coronal jets induced by repetitively accumulated electric currents* A&A 555. A19, [43 c, 10 c/y].

Innes, D.E., Bucik, R., Guo, L.J., et al. 2016, *Observations of solar X-ray and EUV jets and their related phenomena*, Astron.Nachrichten 337, 1024, [12 c, 8 c/y].

Kamio, S., Hara, H., Watanabe, T., et al. 2009, *Distribution of jets and magnetic fields in a coronal hole*, A&A 502, 345, [16 c, 2 c/y].

Karpen, J.T., DeVore, C.R., Antiochos, S.K., et al. 2017, *Reconnection-driven coronal hole jets with gravity and solar wind*, ApJ 834, 62, [7 c, 7 c/y].

Liu, W., Berger, T.E., Title, A.M., et al. 2011, *Chromospheric jet and growing loop observed by Hinode: New evidence of fan-spine magnetic topology resulting from flux emergence*, ApJ 728, 103, [49 c, 8 c/y].

Moore, R.L., Cirtain, J.W., Sterling, S.C., et al. 2010, *Dichotomy of solar coronal jets: Standard jets and blowout jets*, ApJ 720, 757, [122 c, 16 c/y].

Moore, R.L., Sterling, S.C., Falconer, D.A., et al. 2013, *The cool component and the dichotomy, lateral expansion, and axial rotation of solar X-ray jets*, ApJ 769, 134, [50 c, 11 c/y].

Moreno-Insertis, F., Galsgaard, K., Ugarte-Urra, I. 2008, *Jets in coronal holes: Hinode observations and 3-D computer modeling*, ApJ 673, L211, [147 c, 15 c/y].

Moreno-Insertis, F. and Galsgaard, K. 2013, *Plasma jets and eruptions in solar coronal holes: A 3-D flux emergence experiment*, ApJ 771, 20, [63 c, 14 c/y].

Nistico, G., Bothmer, V., Patsourakos, S., et al. 2009, *Characteristics of EUV coronal jets observed with STEREO/SECCHI*, SoPh 259, 87, [79 c, 9 c/y].

Panesar, N.K., Sterling, A.C., Moore, R.L., et al. 2018, *Magnetic flux cancelation as the trigger of solar coronal jets in coronal holes*, ApJ 853, 189, [8 c, 8 c/y].

Pariat, E., Antiochos, S.K., and DeVore, C.R. 2009, *A model for solar polar jets*, ApJ 691, 61, [191 c, 22 c/y].

Pariat, E., Antiochos, S.K., and DeVore, C.R. 2010, *3-D modeling of quasi-homologous solar jets*, ApJ 714, 1762, [102 c, 14 c/y].

Pariat, E., Dalmasse, K., DeVore, C.R., et al. 2015, *Model for straight and helical solar jets. I. Parametric studies of the magnetic field geometry*, A&A 573, A130, [43 c, 17 c/y],

Patsourakos,S., Pariat,E., and Vourlidas,A. 2008, *STEREO SECCHI stereoscopic observations constraining initiation of polar coronal jets*, ApJ 680, L73, [98 c, 10 c/y].

Raouafi, N.E., Georgoulis, M.K., Rust, D.M., et al. 2010, *Micro-sigmoids as progenitors of coronal jets: Is eruptive activity self-similarly multi-scaled ?* ApJ 718, 981, [31 c, 4 c/y].

Raouafi, N.E., Patsourakos, S., Pariat, E., et al. 2016, *Solar coronal jets: Observations, theory, and modeling*, SSRv 201, 1, [26 c, 17 c/y].

Savcheva, A., Cirtain, J., DeLuca, E.E., et al. 2007, *A study of polar jet parameters based on Hinode XRT observations*, PASJ 59, S771, [101 c, 10 c/y].

Sterling, A.C., Moore, R.L., Falconer, D.A., et al. 2015, *Small-scale filament eruptions as the driver of X-ray jets in solar coronal holes*, Nature 523, 437, [55 c, 22 c/y].

Sterling, A.C., Moore, R.L., Falconer, D.A., et al. 2016, *Minifilament eruptions that drive coronal jets in a solar active region*, ApJ 821, 100, [17 c, 11 c/y].

Schmieder, B., Guo, Y., Moreno-Insertis, F., et al. 2013, *Twisting solar coronal jet launched at the boundary of an active region*, A&A 559, A1, [46 c, 10 c/y].

Tian, H., DeLuca, E.E., Cranmer, S.R., et al. 2014, *Prevalence of small-scale jets from the networks of the solar transition region and chromosphere*, Science 346, id. 1255711, [72 c, 21 c/y].
Wang, Y.M., Pick, M., and Mason, G.M. 2006, *Coronal holes, jets, and the origin of ^{3}He-rich particle events*, ApJ 639, 495, [95 c, 8 c/y].
Wyper, P.F., DeVore, C.R., and Antiochos, S.K. 2018, *A breakout model for solar coronal jets with filaments*, ApJ 852, 98, [6 c, 6 c/y].
Zhang, Y. and Zhang, J. 2017, *Cusp-shaped structure of a jet observed by IRIS and SDO*, ApJ 834, 79.

(7.4) Coronal Holes: Blowout Jets

Adams, M., Sterling, A.C., Moore, R.L., et al. 2014, *A small-scale eruption leading to a blowout macrospicule jet in an on-disk coronal hole*, ApJ 783, 11, [28 c, 8 c/y].
Archontis, V. and Hood, A.W. 2013, *A numerical model of standard to blowout jets*, ApJL 769, L21, [50 c, 11 c/y].
Chandra, R., Mandrini, C.H., Schmieder, B., et al. 2017, *Blowout jets and impulsive eruptive flares in a bald-patch topology* A&A 598, A41, [6 c, 6 c/y].
Hong, J., Jiang, Y., Yang, J., et al. 2017, *Minifilament eruption as the source of a blowout jet, C-Class flare, and type-III radio burst*, ApJ 835, 35, [8 c, 8 c/y].
Lee, E.J., Archontis, V., and Wood, A.W. 2015, *Helical blowout jets in the Sun: Untwisting and propagation of waves*, ApJ 798, L10, [15 c, 6 c/y].
Li, X., Yang, S., Chen, H., et al. 2015, *Trigger of a blowout jet in a solar corona mass ejection associated with a flare*, ApJL 814, L13, [17 c, 7 c/y].
Li, H., Jiang, Y., Yang, J., et al. 2017, *Blowout surge due to interaction between a solar filament and coronal loops*, ApJ 842, L20, [4 c, 4 c/y].
Liu, C., Deng, N., Liu, R., et al. 2011, *A standard-to-blowout jet*, ApJ 735, L18, [49 c, 8 c/y].
Moore, R.L., Cirtain, J.W., Sterling, A., et al. 2010, *Dichotomy of solar coronal jets: Standard jets and blowout jets*, ApJ 720, 757, [122 c, 16 c/y].
Moore, R.L., Sterling, A.C., Falconer, D.A., et al. 2013, *The cool component and the dichotomy, lateral expansion, and axial rotation of solar X-ray jets*, ApJ 769, 134, [50 c, 11 c/y].
Moreno-Insertis, F. and Galsgaard, K. 2013, *Plasma jets and eruptions in solar coronal holes: A 3-D flux emergence experiment*, ApJ 771, 20, [70 c, 16 c/y].
Panesar, N.K., Sterling, A.C., Moore, R.L., et al. 2018, *Magnetic flux cancelation as the trigger of solar coronal jets in coronal holes*, ApJ 853, 189, [8 c, 8 c/y].
Pariat, E., Dalmasse, K., DeVore, C.R., et al. 2015, *Model for straight and helical solar jets. I. Parametric studies of the magnetic field geometry*, A&A 573, A130, [44 c, 18 c/y],
Pariat, E., Dalmasse, K., DeVore, C.R., et al. 2016, *A model for straight and helical solar jets. II. Parametric study of the plasma beta*, A&A 596, A36, [13 c, 9 c/y].
Pucci, S., Poletto, G., Sterling, A.C., et al. 2013, *Physical parameters of standard and blowout jets*, ApJ 776, 16, [24 c, 5 c/y].
Robbrecht, E., Patsourakos, S., and Vourlidas, A. 2009, *No trace left behind: STEREO observations of a coronal mass ejection without low coronal signatures*, ApJ 701, 283, [93 c, 11 c/y].
Shen, Y., Liu, Y., Su, J., et al. 2012, *On a coronal blowout jet: The first observation of a simultaneously produced bubble-like CME and a jet-like CME in a solar event*, ApJ 745, 164, [61 c, 11 c/y].
Shen, Y., Liu, Y.D., Su, J. 2017, *On a solar blowout jet: Driving mechanism and the formation of cool and hot components*, ApJ 851, 67, [3 c, 3 c/y].
Shibata, S., Nakamura, T., Matsumoto, T. et al. 2007, *Chromospheric anemone jets as evidence of ubiquitous reconnection*, Science 318, 1591, [201 c, 19 c/y].
Sterling, A.C., Harra, L.K., and Moore, R.L. 2010, *Fibrillar chromospheric spicule-like counterparts to an EUV and soft X-ray blowout coronal jet*, ApJ 722, 1644, [40 c, 5 c/y].

Sterling, A.C., Moore, R.L., Falconer, D.A., et al. 2015, *Small-scale filament eruptions as the driver of X-ray jets in solar coronal holes*, Nature 523, 437, [55 c, 22 c/y].
Wyper, P.F., DeVore, C.R., and Antiochos, S.K. 2018, *A breakout model for solar coronal jets with filaments*, ApJ 852, 98, [6 c, 6 c/y].
Young, P.R. and Muglach, K. 2014, *Solar Dynamics Observatory and Hinode observations of a blowout jet in a coronal hole*, SoPh 289, 3313, [30 c, 9 c/y].

(7.5) Coronal Holes: Boundaries

Aiouaz, T. 2008, *Evidence of relentless reconnection at boundaries of supergranular network lanes in Quiet Sun and coronal hole*, ApJ 674, 1144, [13 c, 1 c/y].
Baker, D., van Driel-Gesztelyi, L., and Attrill, G.D.R. 2007, *Evidence for interchange reconnection between a coronal hole and an adjacent emerging flux region*, Astron.Nachrichten 328, 773, [16 c, 2 c/y].
Doyle, J.G., Popescu, M.D., and Taroyan, Y. 2006, *Repetitive occurrence of explosive events at a coronal hole boundary*, A&A 446, 327, [37 c, 3 c/y].
Edmondson, J.K., Lynch, B.J., Antiochos, S.K., et al. 2009, *Reconnection-driven dynamics of coronal-hole boundaries*, ApJ 707, 1427, [29 c, 3 c/y].
Edmondson, J.K., Antiochos, S.K., Lynch, B.J., et al. 2010, *Interchange reconnection and coronal hole dynamics*, ApJ 714, 517, [33 c, 4 c/y].
Hess Webber, S.A., Karna, N., Pesnell, W.D., et al. 2014, *Areas of polar coronal holes from 1996 through 2000*, SoPh 289, 4047, [9 c, 3 c/y].
Higginson, A.K., Antiochos, S.K., DeVore, C.R., et al. 2017, *Dynamics of coronal hole boundaries*, ApJ 837, 113, [6 c, 6 c/y].
Huang, Z., Madjarska, M.S., Doyle, J.G., et al. 2012, *Coronal hole boundaries at small scales. IV. SOT view. Magnetic field properties of small-scale transient brightenings in coronal holes*, A&A 548, A62, [24 c, 4 c/y].
Kahler, S.W. and Hudson, H.S. 2002, *Boundary structures and changes in log-lived coronal holes*, ApJ 574, 467, [34 c, 4 c/y].
Lowder, C., Qiu, J., Leamon, R., et al. 2014, *Measurements of EUV coronal holes and open magnetic flux*, ApJ 783, 142, [11 c, 3 c/y].
Madjarska, M.S., Doyle, J.G., and van Driel-Gesztelyi, L. 2004, *Evidence of magnetic reconnection along coronal hole boundaries*, ApJ 603, L57, [45 c, 3 c/y].
Madjarska,M.S., Wiegelmann,T. 2009, *Coronal hole boundaries evolution at small scales. I. EIT 195 and TRACE 171 Å view*, A&A 503, 991, [20 c, 2 c/y].
Madjarska,M.S., Huang,Z., Doyle,J.G., et al. 2012, *Coronal hole boundaries evolution at small scales: III. EIS and SUMER views*, A&A 545, A67, [25 c, 5 c/y].
Raju, K.P., Bromage, B.J.I., Chapman, S.A., et al. 2005, *Correlation between coronal hole and Quiet Sun intensities: Evidence for continuous reconnection*, A&A 432, 341, [15 c, 1 c/y].
Subramanian,S., Madjarska,M.S., Doyle,J.G. 2010, *Coronal hole boundaries evolution at small scales. II. XRT view. Can small-scale outflows at coronal hole boundaries be a source of the slow solar wind?* A&A 516, A50, [41 c, 5 c/y].
Titov, V.S., Mikic, Z., Linker, J.A., et al. 2011, *Magnetic topology of coronal hole linkages*, ApJ 731, 111, [51 c, 8 c/y].
Wang, Y.M. and Sheeley, N.R.Jr. 2004, *Footpoint switching and the evolution of coronal holes*, ApJ 612, 1196, [55 c, 4 c/y].
Wang, Y.M. 2009, *Coronal holes and open magnetic flux*, SSRv 144, 383, [46 c, 5 c/y].
Wang,Y.M., Robbrecht,E., Rouillard,A.P. et al. 2010, *Formation and evolution of coronal holes following the emergence of active regions*, ApJ 715, 39, [23 c, 3 c/y].
Yang, S., Zhang, J., Li, T., et al. 2011, *SDO observations of magnetic reconnection at coronal hole boundaries*, ApJ 732, L7, [26 c, 4 c/y].

(7.6) Coronal Holes: MHD Waves

Banerjee, D., Pérez-Suárez, D., and Doyle, J.G. 2009, *Signatures of Alfvén waves in the polar coronal holes as seen by EIS/Hinode*, A&A 501, L15, [56 c, 7 c/y].

Banerjee, D., Gupta, G.R., and Teriaca, L. 2011, *Propagating MHD waves in coronal holes*, SSRv 158, 267, [42 c, 6 c/y].

Banerjee, D. and Krishna Prasad, S. 2016, *MHD waves in coronal holes*, in "Low-Frequency Waves in Space Plasmas" (eds. A. Keiling, D.H. Lee, and Nakariakov, V.), Geophys.Monograph Ser. 216, 419, [6 c, 4 c/y].

Chandran, B.D.G. 2010, *Alfvén wave turbulence and perpendicular ion temperatures in coronal holes*, ApJ 720, 548, [51 c, 7 c/y].

Cranmer, S.R. 2009, *Coronal holes*, LRSP 6, 3, [131 c, 15 c/y].

Gopalswamy, N., Yashiro, S., Temmer, M., et al. 2009, *EUV wave reflection from a coronal hole*, ApJ 691, L123, [102 c, 12 c/y].

Hollweg, J.V. and Markovskii, S.A. 2002, *Cyclotron resonances of ions with obliquely propagating waves in coronal holes and the fast solar wind*. JGR 107/A6, CiteID 1080, [12 c, 1 c/y].

Hollweg, J.V. and Isenberg, P.A. 2007, *Reflection of Alfvén waves in the corona and solar wind: An impulse function approach* JGR 112(A8), CitedID A08102, [26 c, 2 c/y].

Kienreich, I.W., Muhr, N., Veronig, A.M., et al. 2013, *STEREO-A and PROBA-2 quadrature observations of reflections of three EUV waves from a coronal hole*, SoPh 286, 201, [17 c, 4 c/y].

Li, T., Zhang, J., Yang, S. et al. 2012, *SDO/AIA observations of secondary waves generated by interactions of the 2011 June 7 global EUV wave with solar coronal structures*, ApJ 746, 13, [50 c, 9 c/y].

Markovskii S.A. 2001, *Generation of ion cyclotron waves in coronal holes by a global resonant MHD mode*, ApJ 557, 337, [44 c, 3 c/y].

McLaughlin, J.A., Hood, A.W., and de Moortel, I. 2011, *Review article: MHD wave propagation near coronal null points of magnetic fields*, SSRv 158, 205, [42 c, 6 c/y].

Ofman, L. 2005, *MHD waves and heating in coronal holes*, SSRv 120, 67, [61 c, 5 c/y].

Ofman, L., Romoli, M., Poletto, G. et al. 2000, *UVCS WLC observations of compressional waves in the south polar coronal hole*, ApJ 529, 592, [84 c, 5 c/y].

Ofman, L., Davila, J.M., Nakariakov, V.M., et al. 2005, *High-frequency Alfvén waves in multi-ion coronal plasma: Observational implications*, JGR 110(A9), CiteID A09102, [18 c, 1 c/y].

Pucci, F., Onofri, M., and Malara, F. 2014, *Evolution of MHD waves in low layers of a coronal hole*, ApJ 796, 43, [6 c, 2 c/y].

Sokolov, I.V., van der Holst, B., Oran, R., et al. 2013, *MHD waves and coronal heating: Unifying empirical and MHD turbulence models*, ApJ 764, 23, [53 c, 12 c/y].

Suzuki, T.K. and Inutsuka, S.I. 2005, *Making the corona and the fast solar wind: A self-consistent simulation for the low-frequency Alfvén waves from the photosphere to 0.3 AU*, ApJ 632, L49, [150 c, 12 c/y].

Wang, Y.M. 2000, *EIT waves and fast-mode propagation in the solar corona*, ApJ 543, L89, [153 c, 9 c/y].

Zhang, T.X. 2003, *Preferential heating of particles by H-cyclotron waves generated by a global MHD mode in solar coronal holes*, ApJ 597, L69, [16 c, 1 c/y].

Zhang, T.X., Wang, J.X., and Xiao, C.J. 2005, *Resonant heating of ions by parallel propagating Alfvén waves in solar coronal holes*, Chin.J.Astron.Astrophys. 5(3), 285, [5 c, 0.4 c/y].

(7.7) Coronal Holes: Heating Mechanisms

Chandran, B.D.G. and Hollweg, J.V. 2009, *Alfvén wave reflection and turbulent heating in the solar wind from 1 solar radius to 1 AU: An analytical treatment*, ApJ 707, 1659, [54 c, 6 c/y].
Cranmer, S.R. 2009, *Coronal holes*, LRSP 6, 3, [126 c, 15 c/y].
Cranmer, S.R. and van Ballegooijen, A.A. 2003, *Alfvénic turbulence in the extended solar corona: Kinetic effects and proton heating*, ApJ 594, 573, [141 c, 10 c/y].
Cranmer, S.R., van Ballegooijen, A.A., and Edgar, R.L. 2007, *Self-consistent coronal heating and solar wind acceleration from anisotropic MHD turbulence*, ApJSS 171, 520, [291 c, 28 c/y].
Cranmer, S.R., Panasyuk, A.V., and Kohl, J.L. 2008, *Improved constraints on the preferential heating and acceleration of oxygen ions in the extended solar corona*, ApJ 678, 1480, [53 c, 6 c/y].
Hahn, M. and Savin, D.W. 2013, *Observational quantification of the energy dissipated by Alfvén waves in a polar coronal hole: Evidence that waves drive the fast solar wind*, ApJ 776, 78, [18 c, 4 c/y].
Hollweg, J.V. and Isenberg, P.A. 2002, *Generation of the fast solar wind: A review with emphasis on the resonant cyclotron interaction*, JGR 107(A7), CitedID 1147, [198 c, 13 c/y].
Hu, Y.Q., Esser, R., and Habbal, S.R. 2000, *A four-fluid turbulence-driven solar wind model for preferential acceleration and heating of heavy ions*, JGR 105(A3), 5093, [52 c, 3 c/y].
Isenberg, P.A. 2001, *The kinetic shell model coronal heating and acceleration by ion cyclotron waves: II. Inward and outward propagating waves*, JGR 160(A12), 29249, [44 c, 3 c/y].
Isenberg, P.A., Lee, M.A., and Hollweg, J.V. 2001, *The kinetic shell model of coronal heating and acceleration by ion cyclotron waves: I. Outward propagating waves*, JGR 106(A4), 5649, [68 c, 4 c/y].
Isenberg, P.A. 2004, *The kinetic shell model of coronal heating and acceleration by ion cyclotron waves. III. The proton halo and dispersive waves*, JGR 109(A3), CiteID A03101, [36 c, 3 c/y].
Isenberg, P.A. and Vasquez, B.J. 2007, *Preferential perpendicular heating of coronal hole minor ions by the Fermi mechanism*, ApJ 668, 546, [35 c, 3 c/y].
Isenberg, P.A. and Vasquez, B.J. 2009, *Preferential acceleration and perpendicular heating of minor ions in a collisionless coronal hole*, ApJ 696, 591, [26 c, 3 c/y].
Markovskii, S.A., Vasquez, B.J., and Hollweg, J.V. 2009, *Proton heating by nonlinear field-aligned Alfvén waves in solar coronal holes*, ApJ 695, 1413, [25 c, 3 c/y].
Marsch, E. 2006, *Kinetic physics of the solar corona and solar wind*, LRSP 3, 1, [293 c, 25 c/y].
Ofman, O. 2004, *Three-fluid model of the heating and acceleration of the fast solar wind*, JGR 109(A7), A07102, [37 c, 3 c/y].
Rappazzo, A.F., Matthaeus, W.H., Ruffolo, D., et al. 2012, *Interchange reconnection in a turbulent corona*, ApJ 758, L14, [22 c, 4 c/y].
Suzuki, T.K. 2004, *Coronal heating and acceleration of the high/low-speed solar wind by fast/slow MHD shock trains*, MNRAS 349, 1227, [45 c, 3 c/y].
Tu, C.Y. and Marsch, E. 2001, *On cyclotron wave heating and acceleration of solar wind ions in the outer corona*, JGR 106(A5), 8233, [89 c, 5 c/y].
Verdini, A., Belli, M., Matthaeus, W.H., et al. 2010, *A turbulence-driven model for heating and acceleration of the fast wind in coronal holes*, ApJ 708, L116, [83 c, 11 c/y].
Withbroe, G.L. and Noyes, R.W. 1977, *Mass and energy flow in the solar chromosphere and corona*, ARAA 15, 363, [564 c, 14 c/y].

(7.8) Coronal Holes: Fast Solar Wind Acceleration

Antonucci, E., Dodero, M.A., and Giordano, S. 2000, *Fast solar wind velocity in a polar coronal hole during solar minimum*, SoPh 197, 115, [88 c, 5 c/y].
Chandran, B.D.G. 2005, *Weak compressible MHD turbulence in the solar corona*, Phys.Rev.Lett. 95, 265,004, [94 c, 8 c/y].

Chen, L., Lin, Z., and White, R. 2001, *On resonant heating below the cyclotron frequency*, Phys.Plasmas 8, 4713, [103 c, 6 c/y]

Cranmer, S.R. 2000, *Ion cyclotron wave dissipation in the solar corona: The summed effect of more than 2000 ion species*, ApJ 532, 1197, [126 c, 7 c/y].

Cranmer, S.R. 2001, *Ion cyclotron diffusion of velocity distributions in the extended solar corona*, JGR 106, 24,937, [54 c, 3 c/y].

Cranmer, S.R. and van Ballegooijen, A.A. 2003, *Alfvénic turbulence in the extended solar corona: kinetic effects and proton heating*, ApJ 594, 573, [141 c, 10 c/y].

Cranmer, S.R., van Ballegooijen, A.A., and Edgar, R.L. 2007, *Self-consistent coronal heating and solar wind acceleration from anisotropic MHD turbulence*, ApJSS 171, 520, [291 c, 28 c/y].

Cranmer, S.R. 2009, *Coronal holes*, LRSP 6, 3, [132 c, 16 c/y].

Dmitruk, P., Matthaeus, W.H., and Seenu, N. 2004, *Test particle energization by current sheets and nonuniform fields in MHD turbulence*, ApJ 617, 667, [124 c, 9 c/y].

Giordano, S., Antonucci, E., Noci, G., et al. 2000, *Identification of the coronal sources of the fast solar wind*, ApJ 531, L79, [71 c, 4 c/y].

Guo, Z., Crabtree, C., and Chen, L. 2008, *Theory of charged particle heating by low-frequency Alfvén waves*, Phys. Plasmas 15, 032,311, [15 c, 2 c/y].

Hollweg, J.V. 2000, *Cyclotron resonance in coronal holes: A five-beam turbulence model*, JGR 105(A7), 15699, [49 c, 3 c/y].

Hollweg, J.V. and Isenberg, P.A. 2002, *Generation of the fast solar wind: A review with emphasis on the resonant cyclotron interaction*, JGR 107(A7), CiteiD 1147, [198 c, 13 c/y].

Hu, Y.Q., Esser, R., and Habbal, S.R. 2000, *A four-fluid turbulence-driven wind model for preferential acceleration and heating of heavy ions*, JGR 105(A3), 5093, [52 c, 3 c/y].

Isenberg, P.A. 2001, *Heating of coronal holes and generation of the solar wind by ion-cyclotron resonance*, SSRv 95, 119, [37 c, 2 c/y].

Isenberg, P.A., Lee, M.A., and Hollweg, J.V. 2001, *The kinetic shell model of coronal heating and acceleration by ion cyclotron waves: I. Outward propagating waves*, JGR 106(A4), 5649, [68 c, 4 c/y].

Khazanov, I. and Singh, N. 2007, *Ion and electron acceleration by large-scale shear Alfvén waves via cross-field instabilities*, GRL 34, L20111, [4 c, 0.4 c/y].

Kohl, J.L., Noci, G., Antonucci, E., et al. 1998, *UVCS/SOHO empirical determinations of anisotropic velocity distributions in the solar corona*, ApJ 501, L127, [364 c, 19 c/y].

Lee, L.C. and Wu, B.H. 2000, *Heating and acceleration of protons and minor ions by fast shocks in the solar corona*, ApJ 535, 1014, [62 c, 4 c/y].

Li,X. and Habbal, S.R. 2001, *Damping of fast and ion cyclotron oblique waves in the multi-ion fast solar wind*, JGR 106, 10,669, [34 c, 2 c/y].

Lu, Q. and Li, X. 2007, *Heating of ions by low-frequency Alfvén waves*, Phys. Plasmas 14, 042,303, [32 c, 3 c/y].

Markovskii, S.A. 2001, *Generation of ion-cyclotron waves in coronal holes by a global resonant MHD mode*, ApJ 557, 337, [44 c, 3 c/y].

Markovskii, S.A. and Hollweg, J.V. 2002, *Electron heat flux instabilities in coronal holes; Implications for ion heating*, GRL 29, 1843, [9 c, 0.6 c/y].

Markovskii, S.A. and Hollweg, J.V. 2004, *Intermittent heating of the solar corona by heat flux generated ion cyclotron waves*, ApJ 609, 1112, [29 c, 2 c/y].

Markovskii, S.A., Vasquez, B.J., Smith, C.W. et al. 2006, *Dissipation of the perpendicular turbulent cascade in the solar wind*, ApJ 639, 1177, [53 c, 5 c/y].

Matthaeus, W.H., Dmitruk, P., Oughton, S., et al. 2003, *Turbulent dissipation in the solar wind and corona*, in Proc *Solar Wind Ten*, Proc. (eds. Velli, M., Bruno, R., Malara, R., AIP Conf. Proc, AIP 679, 427, [18 c, 1 c/y].

McIntosh, S.W., de Pontieu, B., Carlsson, M., et al. 2011, *Alfvénic waves with sufficient energy to power the quiet solar corona and fast solar wind*, Nature 475, 477, [262 c, 40 c/y].

Pierrard, V. and Lamy, H. 2003, *The effects of the velocity filtration mechanism on the minor ions of the corona*, SoPh 216, 47, [13 c, 0.9 c/y].

Pierrard, V., Lamy, H., and Lemaire, J. 2004, *Exospheric distribution of minor ions in the solar wind*, GJR 109(A2), A02118, [37 c, 3 c/y].
Singh, N. and Khazanov, I. 2004, *Numerical simulation of waves driven by plasma currents generated by low-frequency Alfvén waves in a multi-ion plasma*, JGR 109/A5, A05210.
Suzuki, T. and Inutsuka, S.I. 2005, *Making the corona and the fast solar wind: a self-consistent simulation for the low-frequency Alfvén waves from the photosphere to 0.3 AU*, ApJ 632, L49, [151 c, 12 c/y].
Teriaca, L., Poletto, G., Romoli, M., et al. 2003, *The nascent solar wind: Origin and acceleration*, SpJ 588, 566, [74 c, 5 c/y].
Tu, C.Y. and Marsch, E. 1997, *Two-fluid model for heating of the solar corona and acceleration of the solar wind by high-frequency waves*, SoPh 171, 363, [182 c, 9 c/y].
Tu, C.Y. and Marsch, E. 2001, *On cyclotron wave heating and acceleration of solar wind ions in the outer corona*, JGR 106(A5), 8233, [90 c, 5 c/y].
Verdini, A., Velli, M., Matthaeus, W.H., et al. 2010, *A turbulence-driven model for heating and acceleration of the fast wind in coronal holes*, ApJ 708, L116, [83 c, 11 c/y].
Voitenko, Y.M. and Goossens, M. 2003, *Kinetic excitation mechanisms for ion-cyclotron kinetic Alfvén waves in Sun-Earth connection*, SSRv 107, 387, [22 c, 2 c/y].
Voitenko, Y.M. and Goossens, M. 2004, *Cross-field heating of coronal ions by low-frequency kinetic Alfvén waves*, ApJ 605, L149, [78 c, 6 c/y].
Wilhelm, K., Dammasch, I.E., Marsch, E., et al. 2000, *On the source regions of the fast solar wind in polar coronal holes*, A&A 353, 749, [90 c, 5 c/y].
Wu, C.S. and Yoon, P.H. 2007, *Proton heating via nonresonant scattering off intrinsic Alfvénic turbulence*, Phys.Rev.Lett. 99, 075,001, [55 c, 5 c/y].
Yoon, P.H. and Fang, T.M. 2008, *Parallel cascade of Alfvén waves*, Plasma Phys. Control. Fusion 50, 085,007, [20 c, 2 c/y].
Zhang, T.X. 2003, *Preferential heating of particles by H-cyclotron waves generated by a global MHD mode in solar coronal holes*, ApJ 597, L69, [16 c, 1 c/y].

(7.9) Coronal Holes: Radio Emission

Brajsa, R., Benz, A.O., Temmer, M., et al. 2007, *An interpretation of the coronal holes' visibility in the millimeter wavelength range*, SoPh 245, 167, [10 c, 1 c/y].
Bucik, R., Innes, D.E., Mall, U., 2014, *Multi-spacecraft observations of recurrent ^{3}He-rich solar energetic particles*, ApJ 786, 71, [16 c, 5 c/y].
Bucik, R., Innes, D.W., Mason, G.M., et al. 2018, *^{3}He-rich solar energetic particles in helical jets on the Sun*, ApJ 852, 76.
Butala, M.D., Frazin, R.A., and Kamalabadi, F. 2005, *3-D estimates of the coronal electron density at times of extreme solar activity*, JGR 110(A9), A09S09, [9 c, 1 c/y].
Grechnev, V.V., Lesovoi, S.V., Smolkov, G.Y., et al. 2003, *The Siberian solar radio telescope: The current state of the instrument, observations, and data*, SoPh 216, 239, [58 c, 4 c/y].
Hollweg, J.V. 2000, *Compressibility of ion cyclotron and whistler waves: Can radio measurements detect high frequency waves of solar origin in the corona?* JGR 105(A4), 7573, [30 c, 2 c/y].
Kim, S., Park, J.Y., and Kim, Y.H. 2017, *Solar cycle variation of microwave polar brightening and EUV coronal hole observed by Nobeyama Radioheliograph and SDO/AIA*, J.Korean Astron.Soc. 50, 125.
Krissinel, B.B., Kuznetsova, S.M., Maksimov, V.P. 2000, *Some features of manifestations of coronal holes in microwave emission*, PASJ 52, 909, [9 c, 0.5 c/y].
Maksimov, V.P., Prosovetsky, V., Grechnev, V., et al. 2006, *On the relation of brightness temperatures in coronal holes at 5.7 and 17 GHz*, PASJ 58, 1, [9 c, 1 c/y].

Mancuso, S. and Spangler, S.R. 2000, *Faraday rotation and models for the plasma structure of the solar corona*, ApJ 539, 480, [43 c, 2 c/y].
Mercier, C. and Chambe, G. 2009, *High dynamic range images of the solar corona between 150 and 450 MHz*, ApJ 700, L137, [9 c, 1 c/y].
Mercier, C. and Chambe, G. 2012, *Morphology of the quiet Sun between 150 and 450 MHz as observed with the Nançay Radioheliograph*, A&A 540, A18, [5 c, 1 c/y].
Moran, T., Gopalswamy, N., Dammasch, I.E., et al. 2001, *A multi-wavelength study of solar coronal-hole regions showing radio enhancements*, A&A 378, 1037, [12 c, 1 c/y].
Morioka, A., Miyoshi, Y., Masuda, S., et al. 2007, *Micro-type III radio bursts*, ApJ 657, 567, [12 c, 1 c/y].
Pohjolainen, S. 2000, *On the origin of polar radio brightenings at short millimeter wavelengths*, A&A 361, 349, [12 c, 1 c/y].
Prosovetsky, D.V. and Myagkova, I.N. 2011, *The connection of solar wind parameters with radio and UV emission from coronal holes*, SoPh 273, 525, [3 c, 0.5 c/y].
Selhorst, C.L., Gimenez de Castro, C.G., Varela Saraiva, A.C., et al. 2010, *How are the EUV and radio polar limb-brightenings correlated?* A&A 509, A51, [7 c, 1 c/y].
Selhorst, S.C., Simoes, P.J.A., Oliveria e Silva, A.J., et al. 2017, *Association of radio polar cap brightening with bright patches and coronal holes*, ApJ 851, 146.
Wohlmuth, R., Plettemeier, D., Edenhover, P., et al. 2001, *Radio fluctuation spectra during the solar conjunctions of the Ulysses and Galileo spacecraft*, SSRv 97, 9, [14 c, 1 c/y].

(7.10) Coronal Holes: Solar Cycle Modulation

Abramenko, V., Yurchyshyn, V., Linker, J., et al. 2010, *Low-latitude coronal holes at the minimum of the 23 solar cycle*, ApJ 712, 813, [47 c, 6 c/y].
Barra, V., Delouille, V., Kretzschmar, M., et al. 2009, *Fast and robust segmentation of solar EUV images: algorithm and results for solar cycle 23*, A&A 505, 361, [27 c, 3 c/y].
de Toma, G. 2011, *Evolution of coronal holes and implications for high-speed solar wind during the minimum between Cycles 23 and 24*, SoPh 274, 195, [62 c, 10 c/y].
Golubeva, E.M. and Mordvinov, A.V. 2017, *Rearrangements of open magnetic flux and formation of polar coronal holes in Cycle 24*, SoPh 292, 175.
Harvey, K. and Recely, F. 2002, *Polar coronal holes during cycles 22 and 23*, SoPh 211, 31, [108 c, 7 c/y].
Hess Webber, S.A., Karna, N., Pesnell, W.D., et al. 2014, *Areas of polar coronal holes from 1996 through 2010*, SoPh 289, 4047, [9 c, 3 c/y].
Karna, N., Hess Webber, S.A., and Pesnell, W.D. 2014, *Using polar coronal hole area measurements to determine the solar polar magnetic field reversal in solar cycle 24*, SoPh 289, 3381, [14 c, 4 c/y].
Kirk, M.S., Pesnell, W.D., Young, C.A., et al. 2009, *Automated detection of EUV polar coronal holes during solar cycle 23*, SoPh 257, 99, [47 c, 6 c/y].
Lee, C.O., Luhmann, J.G., Hoeksema, J.T., et al. 2011, *Coronal field opens at lower height during the solar cycles 22 and 23 minimum periods: IMF comparison suggests the source surface should be lowered*, SoPh 269, 367, [37 c, 6 c/y].
Lowder, C., Qiu, J., Leamon, R., et al. 2014, *Measurements of EUV coronal holes and open magnetic flux*, ApJ 783, 142, [11 c, 3 c/y].
Luhmann, J.G., Li, Y., Arge, C.N., et al. 2002, *Solar cycle changes in coronal holes and space weather cycles*, JGR 107(A8), CiteID 1154, [56 c, 4 c/y].
Luhmann, J.G., Lee, C.O., Li, Y., et al. 2009, *Solar wind sources in the late declining phase of Cycle 23: Effects of the wak solar polar field on high speed streams*, SoPh 256, 285, [45 c, 5 c/y].

Schatten, K. 2005, *Fair space weather for solar cycle 24*, GRL 32(21), CiteID L21106, [105 c, 8 c/y].

Schwenn, R. 2006, *Solar wind sources and their variations over the solar cycle*, SSRv 124, 51, [59 c, 5 c/y].

Tlatov, A., Tavastsherna, K., and Vail'eva, V. 2014, *Coronal holes in solar cycles 21 to 23*, SoPh 289, 1349, [8 c, 2 c/y].

Wang, Y.M., Robbrecht, E., and Sheeley, N.R.Jr. 2009, *On the weakening of the polar magnetic fields during solar cycle 23*, ApJ 707, 1372, [131 c, 15 c/y].

Chapter 8
Active Regions

8.1 Active Regions: Magnetic Field Modeling

Magnetically, the Sun can be compartmentalized into boxes around active regions that can be modeled separately, since the mean magnetic field strength in the surrounding Quiet Sun regions and in coronal holes is about three orders of magnitude lower. An example of a (dipolar) active region is shown in Fig. 8.1, as observed with HMI/SDO and AIA/SDO in various wavelengths. The magnetic field in solar active regions has traditionally been modeled with three basic magnetic field extrapolation methods, with (i) a potential field, (ii) a linear force-free field (LFFF), and (iii) a non-linear force-free field (NLFFF) model. The first two options are considered to be over-simplified nowadays, while most of the recent developments have been dedicated to the third option, a non-potential field that is force-free and divergence-free, fulfilling the coupled equation system,

$$(\nabla \times \mathbf{B}) = \alpha \mathbf{B} \,, \tag{8.1.1}$$

$$\mathbf{B} \cdot \nabla \alpha = 0 \,, \tag{8.1.2}$$

where the α-parameter is invariant along a field line of $\mathbf{B}$, but has a different value for each field line, or remains a constant for the special case of a linear force-free field, and becomes zero for a potential field. The curl of the magnetic field is the current density, i.e., $\mathbf{J} = (c/4\pi)(\nabla \times \mathbf{B})$. Most of the NLFFF codes use the vector magnetic field vectors $\mathbf{B}(x, y, z) = [B_x(x, y, z), B_y(x, y, z), B_z(x, y, z)]$ at the photospheric level $z = z_{phot}(x, y)$ as a lower boundary condition of the computation box. About a dozen of NLFFF codes have been developed and implemented in recent years, including (i) the optimization method, in which the solution field is evolved to minimize a volume integral until it becomes divergence free and force free (Wheatland et al. 2000; Wiegelmann 2004); (ii) the evolutionary magneto-frictional method, which solves the magnetic induction equation using a velocity field that

M. J. Aschwanden, *New Millennium Solar Physics*, Astrophysics and Space Science Library 458, https://doi.org/10.1007/978-3-030-13956-8_8

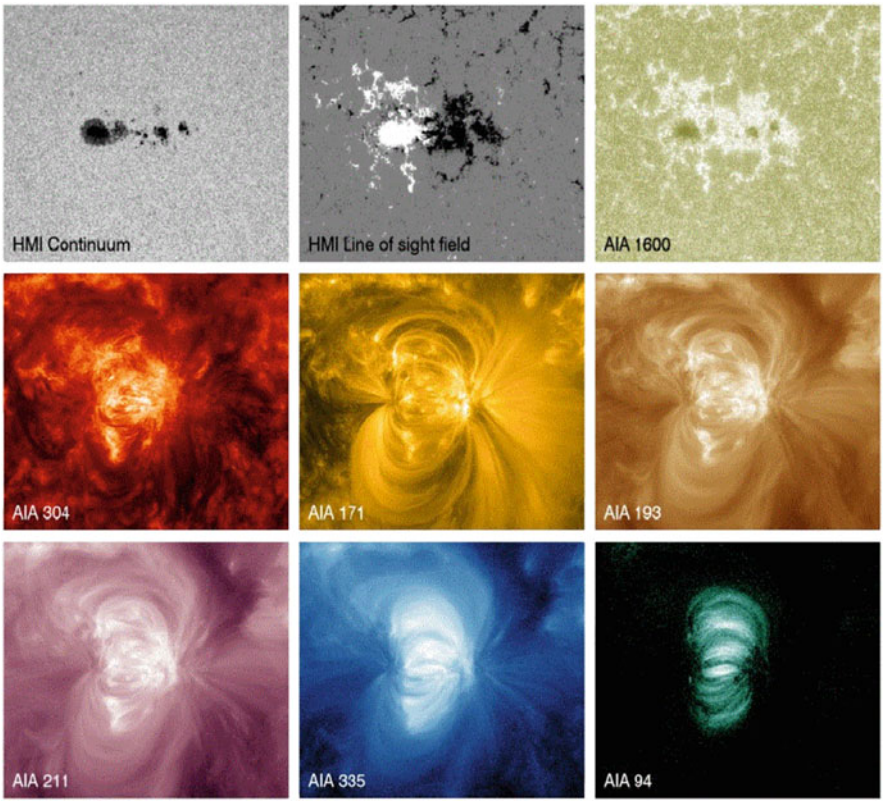

Fig. 8.1 *Top left:* HMI/SDO continuum; *Top middle:* HMI/SDO line-of-sight magnetogram; *Top right:* AIA/SDO 1600 Å ; *Second and third row:* AIA/SDO coronal wavelengths. The various UV and EUV wavelengths display the photospheric magnetic field (AIA 1600), coronal dipolar loops (AIA 171 and 193 Å), fans at the leading sunspot in the west and in the following sunspot in the east (171 Å), moss structure (193 Å), and hot loops in the core of the active region (94, 211, 335 Å), (Credit: NASA, SDO Team, Harry Warren)

advances the solution to a more force-free state (Yang et al. 1986; Valori et al. 2007); and (iii) Grad-Rubin-style current-field iteration procedures, in which currents are added to the domain, and the magnetic field is recomputed in an iterative fashion (Grad and Rubin 1958; Amari et al. 2006; Wheatland 2006). Further details and a performance comparison of these codes are given in Schrijver et al. (2006) and Metcalf et al. (2008). For reviews on coronal magnetic field modeling see Wiegelmann and Sakurai (2012), or Wiegelmann et al. (2014), Wiegelmann et al. (2017a).

Given the dozen of various NLFFF codes available for calculating a nonlinear force-free field for any active region that is observed near the solar center, the obvious question did arise how well the results of these codes agree with each other, which was assessed in a benchmark test, using identical boundary conditions, for the

case of active region NOAA 10953 (De Rosa et al. 2009). The following 3 issues were assessed: (i) vector magnetic field data covering larger areas are needed (then available from SOT/Hinode in this case) so that more electric currents associated with the full active regions of interest are measured, (ii) the modeling algorithms need a way to accomodate the various uncertainties in the boundary data, and (iii) a more realistic physical model is needed to approximate the photosphere-to-corona interface in order to better transform the forced photospheric magnetograms into adequate approximations of nearly force-free fields at the base of the corona (De Rosa et al. 2009). The influence of the spatial resolution on NLFFF modeling was found to increase the free energy with higher resolution (De Rosa et al. 2015).

The biggest impediment for NLFFF modeling is the non-force-freeness of the photospheric vector magnetograph data. One attempt to cure this problem is the modification of the transverse field components (B_x, B_y) in the photosphere with a method that minimizes the noise, the force, and the torque of the photospheric field, a procedure that was called "preprocessing of vector magnetograph data" (Wiegelmann et al. 2006, 2012). Another attempt uses the Bayesian probability to modify the boundary values on current density, using field-line connectivity information from two different force-free solutions (Wheatland and Régnier 2009). A third approach to take the non-forcefree nature of the photosphere and lower chromosphere into account is the application of a magneto-hydrostatic (MHS) model (Zhu et al. 2013; Gilchrist et al. 2016; Wiegelmann et al. 2017b; Zhu and Wiegelmann 2018).

An alternative approach to circumvent the non-force-freeness of the photosphere is the *vertical current approximation nonlinear force-free field (VCA-NLFFF)* method, which uses information of the topology of the magnetic field from automatically traced coronal loops seen in EUV or soft X-ray images (Aschwanden 2013a,b; Aschwanden and Malanushenko 2013). The usage of coronal loop data for magnetic field reconstruction is based on the fundamental assumption that the loops are supposedly field-aligned, which is justified in every coronal region where the plasma β-parameter (i.e., the ratio of the thermal to the magnetic pressure) is smaller than unity, which is generally true for most active regions (Gary 2001). The VCA-NLFFF code transforms a line-of-sight magnetogram map $B_z(x, y)$ into a number of buried unipolar magnetic charges, where the magnetic field falls of with the square of the distance, and it fits a vertical current to each unipolar magnetic charge (expressed with a nonlinear force-free α coefficient). In other words, the photospheric transverse field components $[B_x(x, y, z), B_y(x, y, z)]$ are constrained by the observed topology of coronal loops, rather than by a preprocessing procedure used in other NLFFF codes. The analytical solution of the force-free magnetic field $\mathbf{B}(\mathbf{r})$, which is divergence-free and force-free to second order (in the α parameter), is based on an approximation of vertical currents, which produce helically twisted loop geometries,

$$B_r(r, \theta) = B_0 \left(\frac{d^2}{r^2} \right) \frac{1}{(1 + b^2 r^2 \sin^2 \theta)} , \tag{8.1.3}$$

$$B_\varphi(r,\theta) = B_0 \left(\frac{d^2}{r^2}\right) \frac{br\sin\theta}{(1+b^2r^2\sin^2\theta)} \,, \tag{8.1.4}$$

$$B_\theta(r,\theta) \approx 0 \,, \tag{8.1.5}$$

$$\alpha(r,\theta) \approx \frac{2b\cos\theta}{(1+b^2r^2\sin^2\theta)} \,, \tag{8.1.6}$$

where $(B_r, B_\varphi, B_\theta)$ are the magnetic field components in spherical coordinates, and d is the depth of the buried magnetic charge. The potential field solution is obtained in the limit of $b = 0$ or $\alpha = 0$ (no currents). The 3-D solutions of the VCA-NLFFF code have also been cross-compared with stereoscopically triangulated 3-D coordinates of coronal loops, besides the automated 2-D tracing method (Aschwanden 2013a). The automated loop tracing is obtained with the *Oriented Coronal CUrved Loop Tracing (OCCULT)* code (Aschwanden et al. 2013). Differences between a photospheric extrapolation (NLFFF) method and the coronal forward-fitting (VCA-NLFFF) code were found to be small for the nonpotential magnetic field strength **B**, but revealed a factor of 4 discrepancy for the free energy (Aschwanden et al. 2014). Further quantitative comparisons of preprocessed NLFFF and the VCA-NLFFF method are in progress (Warren et al. 2018).

A variant of the loop forward-fitting magnetic reconstruction method was also developed by Malanushenko et al. (2014). The main differences to the VCA-NLFFF code are: (i) visual tracing of individual loops, and (ii) a modified Grad-Rubin method instead of fitting the vertical-current approximation. Taking information from EUV images into account for NLFFF modeling (in addition to vector magnetograms) has also been accomplished with a *magnetic stereoscopy method* (Chifu et al. 2015, 2017).

8.2 Active Regions: Magnetic Nonpotentiality

If we model a magnetic field of an active region with a potential field, which is uniquely defined by a line-of-sight magnetogram $B_z(x, y)$, we obtain a stable (stationary) magnetic field solution $\mathbf{B}_p(\mathbf{r})$ that corresponds to the lowest level of energy, E_p,

$$E_p = \int\int\int \frac{B_p^2(x,y,z)}{8\pi} dx\, dy\, dz \,. \tag{8.2.1}$$

If we calculate a non-potential field solution $\mathbf{B}_{np}(\mathbf{r})$ (that fulfills the divergence-freeness and force-freeness), for instance for a helically twisted loop (see Sect. 8.1),

the non-potential energy E_{np} is always larger than the potential energy,

$$E_{np} = \int\int\int \frac{B_{np}^2(x, y, z)}{8\pi} dx\, dy\, dz \geq E_p\,. \tag{8.2.2}$$

Consequently, the free energy E_{free}, defined as the difference between the nonpotential energy E_{np} and the potential energy E_p, is by definition always positive (or zero in the case of a potential field),

$$E_{free} = E_{np} - E_p \geq 0\,. \tag{8.2.3}$$

The significance of the free energy E_{free} is that it represents a firm upper limit how much magnetic energy can be dissipated during a magnetic reconnection process (such as occurring in solar flares and in coronal mass ejections). It is therefore also an absolute predictor of the maximum energy that can be released during a flare. A lot of magnetic modeling of active regions is thus focused on the questions whether the magnetic field is nearly potential and thus predicts quiescent conditions for an active region, or how strongly nonpotential the field is during flaring conditions.

Alternatively, if we define the free magnetic energy as the quantity of maximum magnetic energy that can be dissipated, an analytical definition may be difficult. On the one hand, the excess energy of a NLFFF solution above the potential energy may not be completely released due to helicity constraints. On the other hand, NLFFF models may underestimate the free einergy in regions with non-vanishing plasma beta (photosphere, chromosphere), where MHS models can obtain more energy than NLFFF models.

An example is the free energy computed for active region NOAA 8151 (Régnier et al. 2002), for which the total nonpotential energy is $E_{np} = 6.4 \times 10^{31}$ erg, the total potential energy is $E_p = 3.8 \times 10^{31}$ erg, leaving $E_{free} = E_{np} - E_p = 2.6 \times 10^{31}$ or 40% that can be released, in form of untwisting the highly twisted flux tubes or flux rope. The evolution of the free energy $E_{free}(t)$ in a major active region (NOAA 11158) has been traced with a *nonlinear force-free field (NLFFF)* code during 5 days and the degree of nonpotentiality has been quantified with the ratio $q_{np}(t) = E_{np}(t)/E_p(t) \approx 1.05$–$1.50$. The evolutionary time profiles of the currents, nonpotential energy, and potential energy are shown in Fig. 12.7, and some corresponding maps of the magnetic vector field, the vertical current density, EUV emission, and NLFFF field lines are depicted in Fig. 8.2. The time profile exhibits a steady build-up of free energy in the active region before the X2.2 flare occurs, but only a small fraction of the free energy ($\approx 4\%$) is dissipated during this major flare, so there is still a lot of free energy left that could produce more large flares. This demonstrates how important it is to monitor the nonpotential field for flare forecasting. While the NLFFF calculations are computationally expensive, a simpler method based on the magnetic connectivity at the lower boundary was found to be useful to estimate a lower limit on the free energy (Georgoulis et al. 2012).

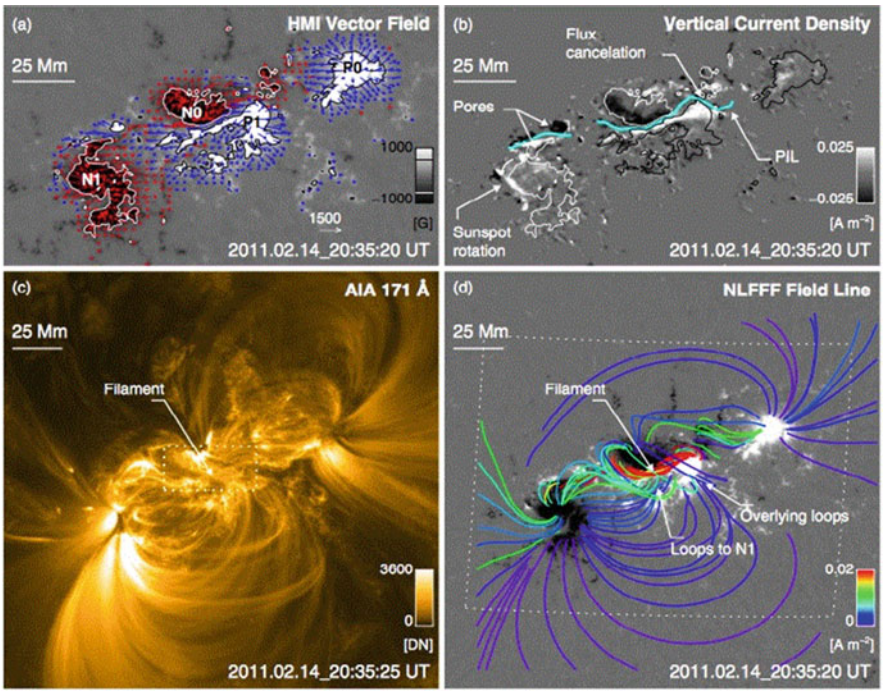

Fig. 8.2 Observations and modeling results for 2011 February 14 20:35 UT, about 5 hrs before the X-class flare, showing the remapped HMI vector magnetogram (**a**), the vertical current density (**b**), the AIA 171 Å image (**c**), and selected field lines (**d**) (Sun et al. 2012)

The nonpotentiality of active regions has been investigated in a statistical study of 95 active regions by comparison of TRACE EUV images with *potential field source surface (PFSS)* extrapolations (Schrijver et al. 2005). Significant nonpotentiality of the overall active region coronal field was found to occur (i) when new flux has emerged within or very near a region within the last $\approx$ 30 hrs, resulting in complex polarity separation lines, or (ii) when rapidly evolving, opposite-polarity concentrations are in contact (at $4''$ resolution). If these two criteria are met by more than 15% of the region's flux, the nonpotentiality of active region coronae is correctly identified in 88% of the cases (Schrijver et al. 2005). Flares are found to occur 2.4 times more frequently in active regions with nonpotential coronae than in near-potential regions (see also Sect. 16.8 for solar flare predictions). It is concluded that currents associated with coronal nonpotentiality have a characteristic growth and decay time scale of $\approx$ 10–30 hrs (Schrijver et al. 2005). Alternatively, the nonpotentiality of active regions was quantified in terms of the length of the strong-shear main neutral line L_{SSM} in the case of bipolar active regions, or the length of the strong-gradient main neutral line L_{SGM} in the case of multi-polar active regions, which can serve as a criterion for the prediction of coronal mass ejections (Falconer et al. 2008). A similar criterion with strong-field, high-gradient polarity inversion

lines was found to correlate well with the occurrence rate of X-class flares (Schrijver 2016). Force-free modeling of braiding loop strands as observed with the high-resolution imager *Hi-C* (0.1″ pixels) reveals that the free energy is underestimated by a factor of up to ≈ 100, which demonstrates how sensitively the calculation of the nonpotentiality depends on the spatial resolution of the instrument (Thalmann et al. 2014).

There are a number of physical processes that contribute to a nonpotential field. One of the simplest methods is a vertical current above a unipolar magnetic field concentration, which causes twisting along the vertical axis of a coronal flux tube and is used for the parameterization of the VCA-NLFFF code (see Sect. 8.1). Another method is the vertical Lorentz force and cross-field currents in the photospheric layer of active regions (Georgoulis and LaBonte 2004). A third method is the *flux rope insertion* method, which mimics the emergence of a twisted flux rope and ramps up the electric currents in the coronal part of an active region during this process (Bobra et al. 2008; Titov et al. 2014). A fourth method is the reconstruction of the 3-D geometry with stereoscopic triangulation (Sandman et al. 2009; Aschwanden and Sandman 2010).

8.3 Active Regions: Magnetic Helicity

The magnetic helicity of an active region, $H = \int_V \mathbf{A} \cdot \mathbf{B}\, dV$ (with $\mathbf{A}$ the vector potential field and $\mathbf{B}$ the magnetic field), measures the sum of linkages between all possible pairs of field lines, and thus measures the twist of helical fields. Berger and Field (1984) derived the Poynting theorem for the helicity in an open volume,

$$\frac{dH}{dt} = \oint 2(\mathbf{B} \cdot \mathbf{A_p}) v_z dS + \oint -2(\mathbf{v} \cdot \mathbf{A}_p) B_z dS, \tag{8.3.1}$$

where $\mathbf{A}_p$ is the vector potential of the potential field, which fulfills force-freeness and divergence-freeness,

$$\nabla \times \mathbf{A}_p \cdot \hat{\mathbf{z}} = B_z, \quad \nabla \cdot \mathbf{A}_p = 0, \quad \mathbf{A}_p \cdot \hat{\mathbf{z}} = 0\,. \tag{8.3.2}$$

According to Eq. (8.3.1), the helicity of magnetic fields in an open volume may change either by the passage of helical field lines through the surface (the first term) or by the shuffling horizontal motion of field lines on the surface (the second term). The twist observed in an emerging flux tube may originate either from the dynamo process operating at the base of the convection zone or from interaction of the rising fluxe tube with convection zone flow such as turbulent motion and differential rotation (Chae 2001). While previous studies focused on the effect of differential rotation (DeVore 2000), the study of Chae (2001) puts more emphasis on the possible existence of surface motions other than differential rotation and their possible role in accumulating the magnetic helicity of coronal magnetic fields.

Chae (2001) indeed finds that the change of magnetic helicity of coronal fields, dH/dt, based on a time series analysis of active region NOAA 8011 observed with MDI/SOHO during 40 hrs, is dominated by the helicity transport through the solar surface via the shuffling motion of photospheric footpoints, modulated with periods of one to several hours, rather than by the previously assumed shear motions resulting from differential rotation (DeVore 2000). Analyzing the latitude distribution of helicity exhibits a larger scatter than expected from measurement errors, which also implies that the generation of helicity is of random, turbulent nature, such as convective motion in the photosphere (Hagino and Sakurai 2004). Also later studies based on HMI data conclude that photospheric (random) shear motion contributes most of the helicity accumulated in the corona (Liu et al. 2014b).

In an extension of the approach of Chae (2001), Kusano et al. (2002) developed a method to compute the total helicity flux together with the (free) energy flux, which enabled also a separate determination of the helicity fluxes due to the shear motion (such as differential rotation) and the vertical motion (such as an emerging sigmoid), finding that both processes contributed equally to the helicity injection, and that the two processes supplied magnetic helicity of opposite signs into this active region. Generally, helicity is better conserved than the free energy.

Observing active region NOAA 7978 during seven solar rotations, Démoulin et al. (2002a) analyzed the long-term budget of the relative magnetic helicity and finds that the helicity injection caused by the differential rotation can neither explain the helicity of coronal fields (at least a factor of 2.5–4 larger), nor that of the helicity of CMEs ejected into the interplanetary space (a factor of 4–20 larger), and thus conclude that the main source of helicity is the inherent twist of the magnetic flux tube (sigmoids) forming in active regions, transferred to the corona either by continuous emergence of the flux tube or by torsional Alfvén waves. Démoulin et al. (2002b) also conclude that shearing motions are a relatively inefficient way to bring magnetic helicity to the corona, compared with helicity carried by a significantly twisted flux tube. Similar conclusions were drawn from the analysis of 35 CMEs ejected during five solar rotations (Green et al. 2002). Nindos et al. (2003) confirm that the helicities carried away by CMEs is a factor of $\lesssim 4$ larger than injected by differential rotation, but the authors note large uncertainties in the length scale of magnetic clouds that are used in helicity calculations. A survey of magnetic helicity injection in active regions that produce 48 X-flaring (and 345 non-X-flaring active regions) reveals that a necessary condition for the occurrence of an X-flare is that: (i) the peak helicity flux has a magnitude of $H > 6 \times 10^{36}$ Mx^2 s^{-1}, (ii) the weak hemispherical preference of helicity injection (positive in the south and negative in the north) caused by the solar differential rotation applies, (iii) the injected helicity is proportional to the squared magnetic flux, and (iv) most of the X-flare regions generated the helicity needed for a CME within a few days, down to a few hours (LaBonte et al. 2007).

Methods to estimate magnetic helicity in the solar context are reviewed by Valori et al. (2016), including the *Coulomb-Thalmann method* (Thalmann et al. 2011), the *Coulomb-Yang method* (Yang et al. 2013), the *Coulomb-Rudenko method* (Rudenko and Myshyakov 2011), or the *deVore gauge method* (DeVore 2000).

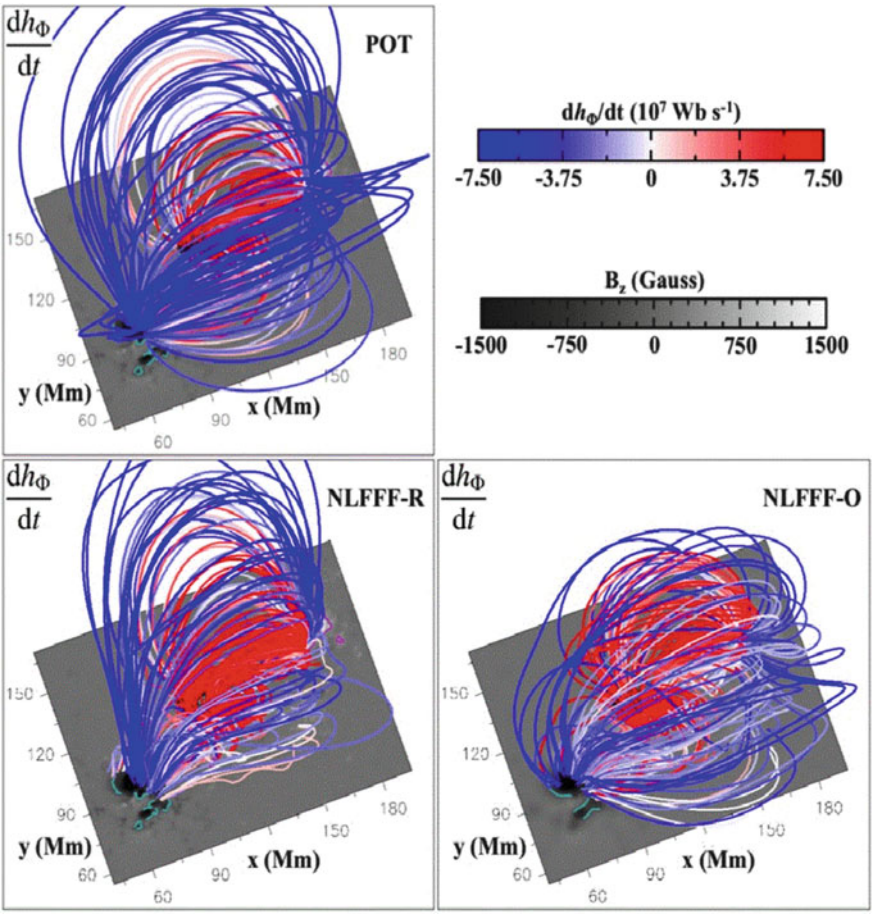

Fig. 8.3 3-D representation of the connectivity-based helicity flux density for three different force-free field extrapolations. The magnetic field lines were integrated from the same randomly selected photospheric footpoints for all three extrapolations. They are colored according to dH/dt (Eq. 8.3.1). Purple and cyan solid lines show $B_z = \pm 500$ G isocontours from the force-free field extrapolation. Note the quadrupolar magnetic field configuration with oppositely directed magnetic field lines and opposite signs (blue and red color) of the helicity flux (Dalmasse et al. 2018)

A recent example of helicity studies in solar active regions with the helicity flux density method (Dalmasse et al. 2018) is shown in Fig. 8.3. This connectivity-based helicity flux density method takes the 3-D nature of magnetic helicity into account by explicit knowledge of the magnetic field connectivity, which is subject to the same force-freeness restrictions as magnetic field extrapolation codes are (Sect. 3.1). The results of the magnetic helicity flux dH/dt for three different magnetic field modeling codes (one a potential field code and the two other being NLFFF codes) are shown in Fig. 8.3, demonstrating that the major features of the

connectivity-based helicity flux density method are robust (with regard to different field extrapolation methods), and allow for studying the transfer of magnetic helicity in active regions, and to relate it to their flaring activity.

Comparing the mutual-helicity injection in Quiet Sun regions and in active regions observed over a whole solar cycle ($\approx$ 11 years), it was concluded that the helicity injection by (random) surface motions in Quiet-Sun regions is negligible to the active region helicity flux rate (Welsch and Longcope 2003). The hemispheric sign rule of helicity is found to be satisfied in the solar maximum phase, but may not be so in the solar minimum phase (Hagino and Sakurai 2005; Pevtsov et al. 2008). The hemispheric rule preference varies greatly in different studies, from $\approx$58% to 82%. In a study using HMI/SDO data, a preference of 75%$\pm$7% was found for 151 active regions (Liu et al. 2014a). This may suggest that, prior to emergence of magnetic tubes, either the sign of twist does not have a hemispheric preference, or the twist is relatively weak (Liu et al. 2014a).

For other aspects of helicity see also Sect. 3.10 (on magnetic helicity injection and condensation) and Sect. 14.3 (on CME helicity).

8.4 Active Regions: Tomography Methods

A major boost in 3-D modeling came with the advent of the STEREO mission, which was launched in 2006 and allows us for the first time to carry out instantaneous stereoscopic triangulation and tomography of coronal structures. We can subdivide the 3-D reconstruction methods into *stereoscopic methods* (using triangulation with two different aspect angles), and *tomographic methods* (synthesized from many aspect angles, either using the solar rotation to vary the aspect angles or to use multi-spacecraft data). The methods depend also very much on the wavelength: white-light inversions involve Thomson scattering, EUV and soft X-ray tomography deals with optically thin thermal (free-free) emission, and radio tomography uses the wavelength-dependent opacity of optically thick free-free and gyroresonance emission (Table 8.1). In addition, helioseismic tomography in the interior of the Sun is also practiced (e.g., Jensen et al. 2001), which is close to seismic tomography in earthquakes and geology. For reviews see Aschwanden (2011a,b).

Table 8.1 Tomographic 3-D reconstruction methods of solar structures

Aspect angle variation	Method	Wavelength range	Parameter
Solar rotation	Tomography	White light	Electron density
Solar rotation	Tomography	EUV, Soft X-ray	Emission measure
Multi-spacecraft	Tomography	EUV, Soft X-ray	Emission measure
Solar rotation	Frequency tomography	Radio	Free-free opacity
Solar interior depth	Helioseismic tomography	White light	Sound speed

Computed Tomography (CT) scans in medical science make use of computer-processed combinations of many X-ray measurements taken from different angles to produce cross-sectional (tomographic) images (virtual "slices") of specific areas of a scanned object, allowing the user to see inside the object without cutting. An analogous method can be applied to the solar corona using soft X-ray emission, EUV emission, or free-free bremsstrahlung emission in radio wavelengths. A major difference to CT scans is that the variation of aspect angles cannot be completed by a rapid rotation of the detectors around the Sun, but rather has to rely on the solar rotation itself, which takes ≈27 days to complete a full scan, or ≈14 days for a half scan. Consequently, this tomographic method is limited to coronal or heliospheric structures that do not vary significantly during this time interval. Solar rotation-based tomography methods to determine the 3-D electron density distribution $n_e(x, y, z)$ were developed using C2/LASCO/SOHO polarized brightness white-light images in the range of 2.4–6.0 $R_\odot$ (Frazin and Janzen 2002; Morgan and Habbal 2010), *Mauna Loa Solar Observatory Mark-IV* data in a height range of 1.14–2.7 $R_\odot$ (Butala et al. 2005), COR1/STEREO data (Wang et al. 2017), *Solar Mass Ejection Imager (SMEI)* data (Jackson et al. 1998; Jackson and Hick 2002), or interplanetary scintillation data (Dunn et al. 2005).

Alternative methods to reconstruct the 3-D coronal magnetic field have been explored with vector tomography that exploit measurements of the longitudinal Zeeman effect (Kramar et al. 2006) and the Hanle effect (Kramar et al. 2013, 2016).

Solar rotation-based tomography has also been applied to soft X-ray and EUV data to reconstruct the 3-D electron density distribution $n_e(x, y, z)$ and 3-D temperature distribution $T_e(x, y, z)$ of of the solar corona and active regions. The observed flux F_λ,

$$F_\lambda(x, y) = \int \int n_e^2(x, y, z, T) R_\lambda(T) dT \, dz \, , \tag{8.4.1}$$

where $R_\lambda(T)$ is the instrumental temperature response function, has a square dependence on the electron density $n_e(x, y, z, T)$, and thus yields actually a better contrast than Thomson scattering in white light, which is proportional to the electron density. The simplest tomographic reconstruction method is the backprojection method, which yields a probability distribution based on the linear addition of projections from different directions. One of the first attempts to reconstruct the 3-D density distribution of the solar corona by means of solar-rotation tomography was done using a two-week's dataset of soft X-ray images from *Yohkoh* (Hurlburt et al. 1994). Another inversion method that has been used for solar tomography is the robust, regularized, positive estimation scheme (Frazin 2000; Frazin and Janzen 2002). The combination of differential emission measure analysis and solar rotation tomography allows us in principle to reconstruct the average density $n_e(x, y, z)$ and temperature $T_e(x, y, z)$ in each voxel (Frazin et al. 2005b; Frazin and Kamalabadi 2005). A tomographic 3-D reconstruction of the minimum corona electron density in a height range of 1.00–1.25 solar radii, based on a local emission measure analysis, has been performed by Vasquez et al. (2010), using EUVI/STEREO/A and B images

sampled during 27 days, or with EUV data from EIT/SOHO and EUVI/STEREO (Lloveras et al. 2016). Besides the problem of under-constrained inversion, the time variability is an additional challenge, which can be overcome with Kalman filtering (Frazin et al. 2005a; Butala et al. 2010).

Solar rotation-based tomography in radio wavelengths requires images at many wavelengths, from which in principle the electron density and temperature can be inverted. Let us consider the case of free-free (bremsstrahlung) emission, which has a *free-free absorption coefficient* $\alpha_\nu(z)$ for thermal electrons that depends on the ambient ion density $n_i(z)$, electron density $n_e(z)$, and temperature $T_e(z)$, at position z along a given observer's line-of-sight, and radio frequency ν as,

$$\alpha_{ff}(z,\nu) \approx 9.786 \times 10^{-3} \frac{n_e(z) \sum_i Z_i^2 n_i(z)}{\nu^2 T^{3/2}(z)} \ln \Lambda \,, \tag{8.4.2}$$

where $\ln \Lambda(z) \approx 20$ is the *Coulomb integral*, which yields the *free-free opacity* $\tau_{ff}(z,\nu)$ as a function of position z by integrating over the column depth range $z' = [-\infty, z]$,

$$\tau_{ff}(z,\nu) = \int_{-\infty}^{z} \alpha_{ff}[T_e(z'), n_e(z'), \nu]\, dz' \,. \tag{8.4.3}$$

From the free-free opacity we obtain the *radio brightness temperature* $T_B(\nu)$ at the observer's frequency ν with a further integration of the opacity along the line-of-sight,

$$T_B(\nu) = \int_{-\infty}^{0} T_e(z) \exp^{-\tau_{ff}(z,\nu)} \alpha_{ff}(z,\nu)\, dz \,. \tag{8.4.4}$$

The observed quantity is the *flux density* $I(\nu)$, which can be calculated from the *brightness temperature* $T_B(\nu)$ with the *Rayleigh-Jeans approximation* at radio wavelengths, integrated over the solid angle Ω_S of the radio source,

$$I(\nu) = \frac{2\nu^2 k_B}{c^2} \int T_B d\Omega_S \,. \tag{8.4.5}$$

These expressions describe how the radio brightness observed at a particular frequency ν depends on the 3-D density $n_e(x,y,z)$ and temperature distribution $T_e(x,y,z)$ of an observed source (e.g., an active region), and this way defines the inversion problem that has to be solved to obtain the 3-D density distribution $n_e(x,y,z)$.

Tomographic reconstructions in the solar corona can be achieved by synthesizing radio images at many frequencies ν, a method that is called *frequency tomography* (Aschwanden et al. 1995). High-resolution solar images in radio wavelengths became readily available around 1980, with radio interferometers such as the *Very Large Array (VLA)* or the *Owens Valley Radio Observatory (OVRO)*, at frequencies

of $\gtrsim 1$ GHz. Reasonably stable radio-emitting structures in the solar corona are the optically thick layers of free-free emission in active regions (Aschwanden and Bastian 1994a,b), or the gyroresonance layers above sunspots (Aschwanden et al. 1995; Lee et al. 1999; Nita et al. 2011), which can be imaged on a daily basis and the altitude of their source centroids can be triangulated from the parallax effect.

Regarding geometric 3-D reconstructions, we have to be aware that the frequency tomography method allows only to invert the electron density $n_e(\nu)$ and temperature $T_e(\nu)$ as a function of the radio frequency ν, while an additional opacity model $\nu(z)$ is required to map the radio frequency into a geometric coordinate z for each line-of-sight. In a statistical way, such additional information on the absolute height $h(\nu) = z(\nu)\cos\theta$ (at an angle θ from Sun center) can be obtained from solar-rotation stereoscopy. Further tomographic information on the magnetic field can be obtained from the circular polarization of free-free emission, quasi-transverse layers, and coronal abundances, leading to 3-D coronal magnetography (Lee et al. 1999; Ryabov et al. 2005; Nita et al. 2011).

8.5 Active Regions: High-Temperature Emission

While the EUV emission of active regions is concentrated in a "low-temperature regime" of $T_e \approx$ 1–2 MK, complementary observations in soft X-rays exhibit a "hot-temperature component" with temperatures in the range of $T_e \approx$ 2–6 MK, even during non-flaring times, which both have to be accomodated in coronal heating models of active regions. The capability of measuring high temperatures in the range of $T_e \approx$ 5–10 MK is now available by combining instruments such as SXT/Yohkoh, UVCS/SOHO, EIS/Hinode, XRT/Hinode, and AIA/SDO.

We review some recent papers pertinent to high-temperature emission in non-flaring active regions, in chronological order (Table 8.2). Using *Ultraviolet Coronagraph Spectrometer (UVCS/SOHO)* and *Soft X-ray Telescope (SXT/Yohkoh)* data of an active region that appears to be the base of a small streamer, observed at an altitude of 1.22–1.6 $R_\odot$ above the limb, two temperature structures were measured, a low-temperature component with $T_e \approx 1.5$ MK, and a hot-temperature component with $T_e \approx 3.0$ MK, based on the high-temperature lines Fe XVIII (974 Å), Ne IX (1248 Å), and Fe XV (284 Å). Analyzing high-temperature Ca lines (Ca XIV, XV, XVI, XVII) and the Fe XVII (254.87 Å) line from *Extreme-Ultraviolet Imaging Spectrometer (EIS/Hinode)* data, high-temperature components in the range of $T_e \approx$ 2.5–4.0 MK were measured, although some inconsistencies in the CHIANTI atomic physics database were noted (Warren et al. 2008). Using the *X-Ray Telescope (XRT/Hinode)* (with Al, C, Ti, Be filter combinations), a weak but significant high-temperature component of $T_e > 10$ MK in active regions was reported, in addition to a temperature component of $T_e \approx$ 2.0–3.2 MK (Schmelz et al. 2009), but this claim remained controversial because of the almost three orders of magnitude lower emission measure (than the differential emission measure peak

Table 8.2 High-temperature measurements in active regions (or associated streamers above the active regions)

Low-temperature	High-temperature	Instrument	Reference
1.5 MK	3.0 MK	UVCS/SOHO, SXT/Yohkoh	Ko et al. (2002)
	2.5–4.0 MK	EIS/Hinode	Warren et al. (2008)
	2.9–3.2 MK, >10 MK (?)	XRT/Hinode	Schmelz et al. (2009)
1.0 MK	6 MK	EIS/Hinode	Ko et al. (2009)
	2–3 MK, 4–15 MK	EIS/Hinode	Reale et al. (2009)
0.3–2.0 MK	4 MK	AIA/SDO, XRT+EIS/Hinode	Warren et al. (2011)
0.3–2.0 MK	4 MK	AIA/SDO, XRT+EIS/Hinode	Warren et al. (2012)
<1 MK	1.5–2.5 MK	AIA/SDO, EIS/Hinode	Del Zanna (2013)
	2.0–2.5 MK, >8 MK (?)	FOXSI, XRT+EIS/Hinode	Ishikawa et al. (2014)
	3.5–6.3 MK	AIA/SDO, EIS/Hinode	Mackovjak et al. (2014)
	3.0–5.0 MK	EIS/Hinode, FCS/SMM	Del Zanna and Mason (2014)
	2.5–4.0 MK	AIA/SDO	Del Zanna et al. (2015)
	3.1–4.4 MK	NuSTAR	Hannah et al. (2016)
0.3–2.0 MK	2.0–6.3 MK	All instruments	

of the low-temperature component). Ko et al. (2009) analyzed the high-temperature line Ca XVII (192.858 Å) from EIS/Hinode data, which has a formation temperature of $T_e \approx 6$ MK, but is blended with two Fe XI and six O V lines. Nevertheless, Ko et al. (2009) manage to measure the hot $T_e \approx 6$ MK component in the core of an active region, which is surrounded by cooler 1.0 MK plasma. Combining EUV images observed with AIA/SDO, XRT/Hinode, and EIS/Hinode, which yields one of the best-constrained *differential emission measure (DEM)* distributions of an active region over a temperature range of $T_e \approx 10^{5.5}$–$10^{7.3} = 0.3$–20 MK (Fig. 8.4), Warren et al. (2011) find a DEM peak of at $T_e \approx 10^{6.6} = 4.0$ MK, which falls off by about 3 orders of magnitude at a maximum temperature of $T_{max} \lesssim 10^7 = 10$ MK (Fig. 8.5), with no evidence for higher temperatures. A systematic survey of high-temperature emission in 15 different active regions fully confirmed this result that the DEM distributions are strongly peaked at $T_e \approx 4.0$ MK, with no evidence for significant emission at $T_e \gtrsim 10$ MK (Warren et al. 2012). A high-temperature component of 10 MK plasma appears to be absent at a level of at least two orders of magnitude down from the DEM peak, according to a DEM study of 12 active region loops (Schmelz et al. 2013), in contrast to earlier claims (Schmelz et al. 2009). A DEM study was performed by combining XRT/Hinode and EIS/Hinode data with the *Focusing Optics X-ray Solar Imager(FOXSI)* sounding

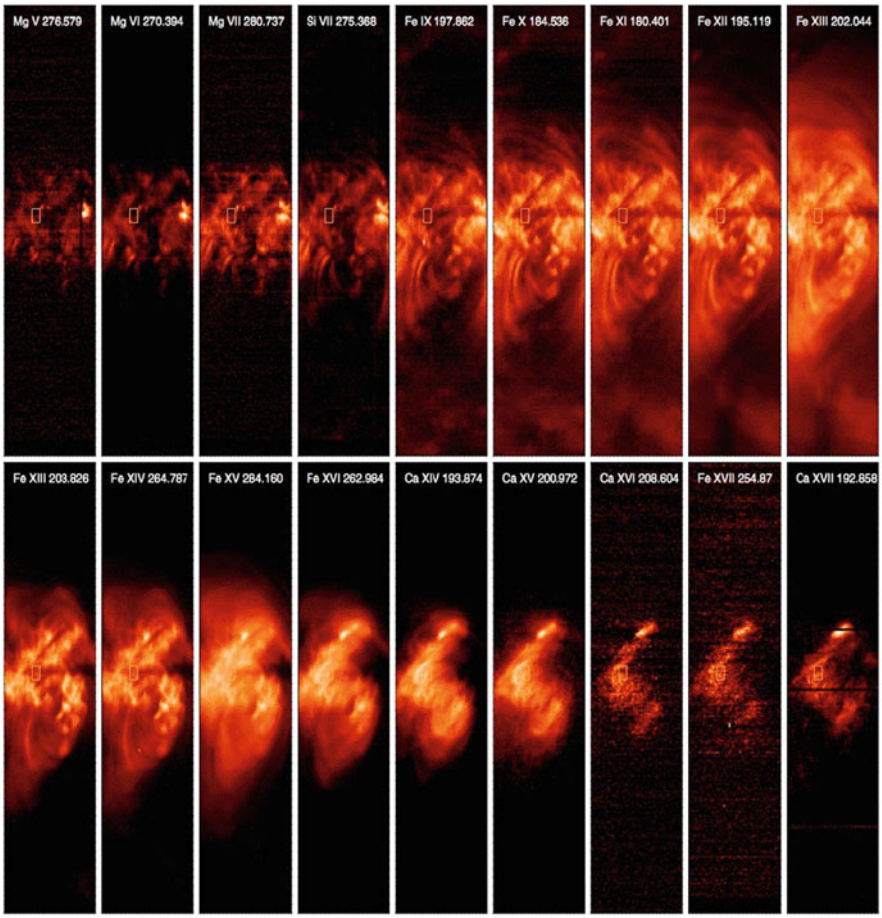

Fig. 8.4 EIS observations of AR 11089 in various emission lines, sorted by increasing formation temperature. The field of view is $120'' \times 384''$ (Warren et al. 2011)

rocked payload data (Ishikawa et al. 2014). The Hinode-derived DEM predicts a DEM peak at $T_e = 2.0$–2.5 MK, with significant emission above $T_e \geq 8$ MK, which is contradicted by the FOXSI observations that significantly constrain emission above $T_e \geq 8.0$ MK, suggesting that the Hinode-derived DEM analysis has larger uncertainties at higher temperatures and that $T_e \geq 8$ MK above an emission measure of $EM = 3 \times 10^{44}$ cm^{-3} can be excluded for this active region (Ishikawa et al. 2014). DEM reconstructions of active regions using non-Maxwellian κ-distributions yielded DEM peak temperatures of $T_e \approx 10^{6.55}$–$10^{6.8} \approx 3.5$–6.3 MK (Mackovjak et al. 2014).

Finally, first observations of quiescent active regions using the *Nuclear Spectroscopic Telescope Array (NuSTAR)*, a focusing hard X-ray telescope, yielded an (isothermal) emission measure peak of $T_e = 3.1$–4.4 MK and emission measures of

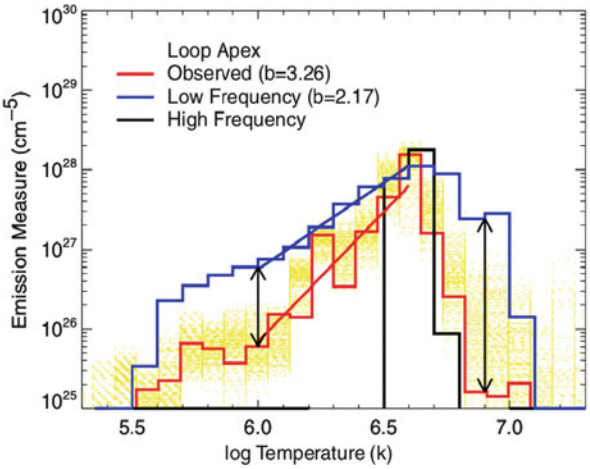

Fig. 8.5 Emission measure distributions derived from high-frequency (black) and low-frequency (blue) heating simulations sampled at the loop apex. The arrows indicate the differences between the observation and the low-frequency model at log(T)=6.0 and 6.9. The power law indices $EM \propto T^b$ are indicated for several of the emission measure distributions (Warren et al. 2011)

$EM = (1–8) \times 10^{46}$ cm^{-3} for an active region (Hannah et al. 2016). No emission above $T_{max} = 5$ MK is observed, and an upper limit of $EM \approx 10^{46}$ cm^{-3} for $T_e = 5$ MK is obtained, or an upper limit of $EM \approx 10^{43}$ cm^{-3} for $T_e = 12$ MK, respectively, which are at least an order of magnitude stricter than previous limits (Hannah et al. 2016).

We compiled the ranges of low and high temperatures reported from DEM modeling for active regions in Table 8.2. The resulting ranges are $T_e \approx 0.3–2.0$ MK for the low-temperature component, and $T_e \approx 2.0–6.3$ MK for the high-temperature component, which is not much different from initial SXT/Yohkoh results, which reported that high-temperature plasmas reach temperatures of $T_e \approx 5–6$ MK (Hara et al. 1992). Thus we can conclude that the cores of (non-flaring) active regions have a characteristic high-temperature range of $T_e \approx 2–6$ MK, while the periphery of active regions consists of *fan loops* with a low-temperature component of $T_e \approx 0.5–2.0$.

8.6 Active Regions: Plasma Outflows

The slow solar wind ($v \approx 400$ km s^{-1}) mostly originates from the edges of active regions and streamers, wherever magnetic open field channels exist that serve as conduits for hot plasma to escape from the lower corona towards the interplanetary space. Progress in the identification of the source regions of the slow solar wind has been made mostly with the EIS/Hinode instrument (after the launch of Hinode

Table 8.3 Measurements of plasma outflows from active regions

Velocity range	Duration	Instrument	Reference
40 km s^{-1}	$\approx$ 10 hrs	EIS/Hinode	Harra et al. (2007)
20–100 km s^{-1}	$>$ 13 min	EIS/Hinode	Harra et al. (2008)
20–50 km s^{-1}	$>$1 day	EIS/Hinode	Doschek et al. (2008)
5–30 km s^{-1}	Few days	EIS/Hinode, TRACE	DelZanna (2008)
$<$ 100 km s^{-1}	Few days	EIS/Hinode	Brooks and Warren (2012)

in 2006), which has excellent diagnostics of line widths in the hot (soft X-ray) temperature range. At the edge of active regions, located adjacent to coronal holes, patterns of continuous outflows of soft X-ray emitting plasmas were identified along open magnetic field lines and into the upper corona. Estimates of temperature and density of the outflowing plasmas suggest a mass loss rate of $\approx$ 1/4 of the total mass loss rate of the solar wind (Sakao et al. 2007).

Steady, quasi-stationary plasma outflows in non-flaring open-field regions (compiled in Table 8.3), are most likely to be associated with sources of the (slow) solar wind. Persistent outflows (at least for 13 min) from the edges of active regions have been measured with EIS/Hinode, with velocities of $v \approx$ 20–100 km s^{-1} (Harra et al. 2008). Persistent outflows over much longer time intervals (of a day at least) have been measured with EIS/Hinode (Doschek et al. 2008; Doschek 2012), with outflow speeds of $v \approx$ 20–50 km s^{-1}, and correlated with nonthermal velocities (Fe XII at 195.12 Å, $T_e \approx$ 1.2–1.4 MK). Persistent redshifts (downflows) and blueshifts (upflows) in the order of $v \approx$ 5–30 km s^{-1} were measured with EIS/Hinode and TRACE at hot/cool temperature interfaces (3 MK/1 MK) of an active region (DelZanna 2008). Following an active region over several solar rotations, outflows were detected with UVCS/SOHO in the intermediate corona throughout the whole active region lifetime, which strongly suggests that outflows are persistent over several solar rotations and contribute to the slow solar wind (Zangrilli and Poletto 2016).

Intermittent plasma outflows could be associated with flares and *coronal mass ejections (CMEs)*, rather than representing (steady) sources of the (slow) solar wind. However, there may be many borderline cases. Harra et al. (2007) observed coronal dimming related to a CME in an extended region away from the flare core, with outflow speeds of $\lesssim$ 40 km s^{-1}, and prolonged steady outflows of material from the corona, which was interpreted as a possible source of the slow solar wind.

The magnetic topology in active region outflow regions has been found to contain field lines that display strong gradients of magnetic connectivity, namely *quasi-separatrix layers (QSLs)*, or in the limit of infinitely thin QSLs, separatrices (Baker et al. 2009). The strongest active region outflows coincide also with QSL areas of strong magnetic field. It has been suggested that magnetic reconnections in QSLs are viable drivers of active region outflows and sources of the slow solar wind (Baker et al. 2009). Numerical 3-D MHD simulations of the evolution of an active region suggest that a horizontal expansion can generate outflows with speeds up to 45 km

s^{-1} (Murray et al. 2010), and mimic an emerging flux region (Harra et al. 2012). Following the solar rotation across the disk, the plasma outflows are found to be consistent with (i) fan-like structures rooted in QSLs, (ii) temperature stratification in altitude, and (iii) broad range of velocities in the outflows (Démoulin et al. 2013). Connections between the chromospheric nascent solar wind, the observed excessive outflow speed of over 200 km s^{-1} in the lower corona, and the corresponding intermediate-speed solar wind stream in interplanetary space have been observed together (He et al. 2010). It was observed with EIS/Hinode that some outflows occur also in closed-field regions and may not connect to the heliospheric solar wind (van Driel-Gesztelyi et al. 2012). Culhane et al. (2014) followed one active region across the disk (Fig. 8.6), measured the outflows with EIS/Hinode, and modeled the global magnetic field with the PFSS code (Fig. 8.7), finding that the active region was completely covered by the closed field of a helmet streamer, so that it was not clear how any of the outflowing active region-associated plasma could reach the source surface at 2.5 $R_{\odot}$ and contribute to the solar wind. An additional two-step magnetic reconnection process appears to be required to connect with the heliosphere.

The time evolution of plasma outflows in active regions can exhibit quasi-periodic modulation, but the interpretation is not unique in terms of waves or outflows from the intensity variation alone (Tian et al. 2011).

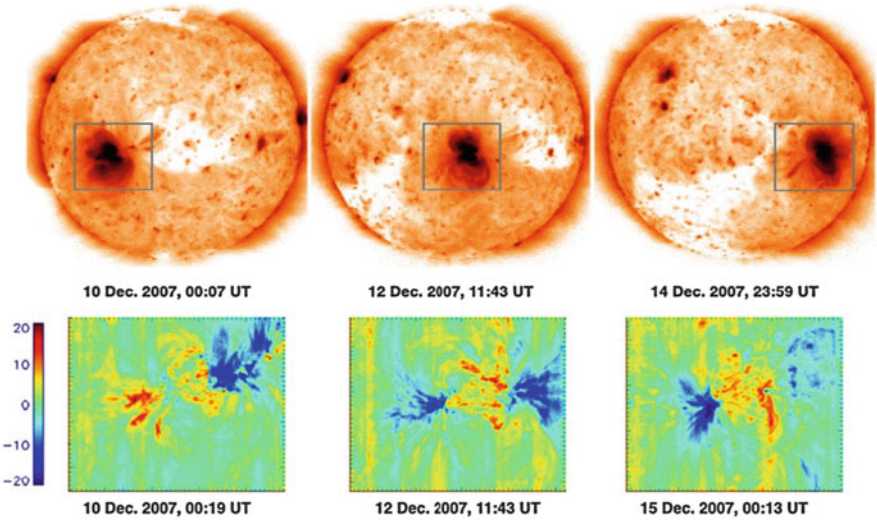

Fig. 8.6 Active region NOAA 10978 images and velocity maps for the interval 10–15 December 2007. *Top row:* XRT/Hinode Ti/Poly X-ray images for 10, 12, and 14 December 2007, with inverse contrast. *Bottom row:* Corresponding EIS/Hinode velocity maps obtained from Fe XII (195.21 Å) emission line profiles. Velocity scale is in km s^{-1} (bottom left). EIS raster size is 460″ by 384 ″ in the horizontal (x) and vertical (y) directions. Note the locations of plasma upflows (blue) (Culhane et al. 2014)

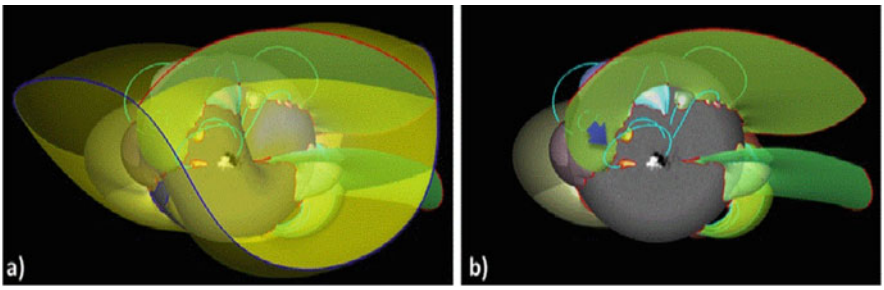

Fig. 8.7 Potential Field Source Surface (PFSS) model showing large-scale topological structures on 12 December 2007 around active region NOAA 10978 (Fig. 8.6). Panel (**a**) includes the semi-transparent yellow helmet-streamer separatrix surface, while (**b**) does not, so as to better show the magnetic configuration around active region NOAA 10978. The blue line in (**a**) shows the *Heliospheric Current Sheet (HCS)*. The active region is entirely covered by the streamer with no topological link between plasma upflows and open field. The spine field line (cyan; indicated by the blue arrow in panel (**b**) of a low-altitude null-point (red dot) to the East of the active region which is linked to the western upflow region, indicates that the upflowing plasma is channeled towards Quiet-Sun regions along long loops (Culhane et al. 2014)

Some other evidence for a direct connection between coronal plasma outflows and the solar wind comes from the consistency of elemental abundances (Brooks and Warren 2011), as well as from the *first ionization potential (FIP)* effect and asymmetries in the line profiles of active region outflows (Brooks and Warren 2012).

There appears to be a coupling between plasma outflows in different regions of the Sun. Active regions can lead to enhanced plasma outflows in neighboring coronal holes (Habbal et al. 2008). Also, coronal rays can represent signatures of outflows from active regions propagating in the inner corona along open field lines into the heliosphere (Slemzin et al. 2013). A correlation has been found between Doppler measurements and force-free magnetic field extrapolations, yielding altitudes of ≈20 Mm for radiation of Ne^{7+} ions, and ≈5 Mm for radiation of C^{3+} (Tu et al. 2005), which constrains the acceleration height of the solar wind.

8.7 Active Regions: Heating

After we discussed heating models in the chromosphere (Sect. 5.10), in the Quiet Sun (Sect. 6.7), in coronal holes (Sect. 7.7), and in coronal loops (Sect. 9.7), we turn now to active regions, which harbor the strongest magnetic fields on the solar surface and require the highest Poynting flux ($E \approx 10^7$ erg cm^{-2} s^{-1}) to maintain their high-temperature regime of $T_e \approx$ 2–6 MK (Sect. 8.5). Here we focus on heating processes in active regions as a whole, while hydrodynamic modeling of single active region loops or flare loops are treated elsewhere (Sects. 9, 13). Recent reviews

on coronal heating are given in DeMoortel and Browning (2015) and Klimchuk (2006, 2015).

There are essentially four different "schools of thought" on coronal heating processes in (non-flaring) active regions: (i) The Parker-nanoflare concept that envisions "microscopic" unresolved magnetic reconnection events, uniformly distributed throughout the corona; (ii) "macroscopic" or "monolithic" (observationally resolved) magnetic reconnection events that occur in the chromosphere and transition region, which includes EUV-emitting nanoflares and soft X-ray-emitting *active region transient brightenings (ARTB)*, both thought to be miniature versions of standard flares; (iii) MHD turbulence; and (iv) wave heating (e.g., by torsional Alfvén waves). Another classification reduces these four options into two groups: stressing models (DC) and wave models (AC) (Mandrini et al. 2000).

Coronal heating models can also be subdivided according to their time variability: steady or impulsive time evolution. Most of the recent studies find that impulsive and intermittent heating behavior is more consistent with observations of EUV loops (e.g., Ugarte-Urra et al. 2006; Hara et al. 2008), while steady heating is found in soft X-ray-emitting cores of active regions only (Warren et al. 2010; Winebarger et al. 2011; Tripathi et al. 2011). Low-frequency nanoflaring was found to be consistent with the observed DEM distributions $EM(T) \propto T^{\alpha}$ in 36%–77% (Bradshaw et al. 2012; Cargill 2014), and quasi-steady *"nanoflare trains"* were found to be consistent with 86%–100% of observed active region cores (Reep et al. 2013; Cargill et al. 2015). Pervasive faint Fe XIX emission was considered as evidence for continuous nanoflare heating (Brosius et al. 2014), although the intensity of Fe XIX lines relative to lines formed at 4 MK where not considered.

(i) The *Parker nano-flare concept* builds on the hypothesis that random braiding of coronal field lines leads through cumulative build-up of non-potential magnetic energy to magnetic reconnection events that reduce the magnetic stress. Parker (1988) estimated a typical energy of an individual nanoflare event to be in the order of $E \approx 10^{24}$ erg. Since footpoint braiding of loops is driven by convective motion, a natural spatial scale for the cross-section of a nanoflare heating event is the scale of a granule (≈ 1 Mm). This argument would predict that imaging instruments with arcsecond or poorer spatial resolution would not resolve an individual nanoflare event, so that we have to model them as a *multi-thread bundle* consisting of unresolved "microscopic" strands. However, cross-field transport in a multi-thread or multi-strand bundle is inhibited in the low-β corona, which predicts statistically independent electron temperatures and densities in individual strands (Fig. 8.8 left), and thus contradicts the EUV observations of smooth and near-isothermal loops. Recent models resolve this dilemma by appealing to a *"nanoflare storm"* scenario (Viall and Klimchuk 2011, 2012), where multiple nanoflaring strands coordinate their time patterns, temperatures, densities, and cooling delays (by some unknown cross-field coordination mechanism). However, large cooling delays cannot be explained by impulsive heating (Lionello et al. 2016).

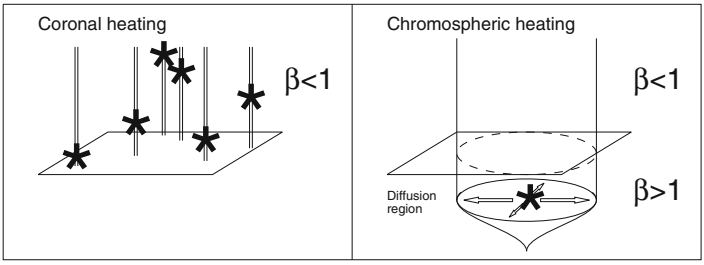

Fig. 8.8 *Left:* Parker's original scenario predicts nanoflares distributed through out the corona in $\beta < 1$ regions, in which individual nanoflares are stochastically distributed in space and time. *Right:* In a modified scenario where the nanoflare-associated magnetic reconnection events occur in the chromosphere or transition region, with $\beta > 1$, the heated plasma can expand across the field and fill out the diffusion region of the magnetic reconnection region, producing loops with widths corresponding to a photospheric granule size

(ii) A more plausible scenario is to assume that Parker's hypothesized nanoflares occur in a high-β regime in the chromosphere and transition region (rather than throughout the corona), where cross-field transport is enabled over a typical spatial scale of magneto-convection (which is the size of a photospheric granule, $w \approx 1$ Mm, or the size of the network, a few Mm) (Fig. 8.8 right), which naturally explains the observed near-isothermal cross-section of EUV-emitting coronal loops, the overdensity in EUV-emitting coronal loops, and the nonuniform, footpoint-concentrated heating function (Aschwanden et al. 2000, 2007; Aschwanden 2001; Schrijver et al. 2004; Schmieder et al. 2004). Footpoint-concentrated heating undergoes catastrophic cooling and produces *"coronal rain"*, which can be used as a marker of the heating mechanism also (Antolin et al. 2010). Nanoflares were supposedly detected in the transition region with *"moss"* structure with Hi-C, having 0.3″ spatial resolution and 15 s time resolution (Testa et al. 2013). Energetically, there is observational evidence for *EUV-emitting nanoflares* with energies of $E \approx 10^{24}$–10^{26} erg in the Quiet Sun (Fig. 6.14), which produce temperatures of $T_e \approx 1$–2 MK, and are likely to occur in active regions too. In addition, we observe also soft X-ray-emitting transient brightenings in active regions with energies of $E \approx 10^{27}$–10^{29} erg (Fig. 6.14) that explain the high-temperature emission of $T_e \approx 2$–6 MK (Sect. 8.5).

(iii) Numerical simulations of Parker's field line braiding model in the framework of reduced MHD exhibits anisotropic turbulence that transports energy from larger scales, where energy is injected by photospheric motions, to the small scales, where it is dissipated (Rappazzo et al. 2007). Weak turbulence regimes and steeper (Kolmogorov) spectra occur in stronger loop fields and lead to larger heating rates than in weak field regions (Rappazzo et al. 2008),

(iv) Torsional Alfvén waves are incompressible and thus need a mechanism such as mode conversion (leading to shock heating), phase mixing, resonant absorption, or turbulent cascade in order to heat the plasma. Conducting a

parametric study with a 1.5 MHD code, it was demonstrated that the regimes under which Alfvén wave heating produces hot and stable coronae are rather narrow (Antolin and Shibata 2010). However, from modeling of propagating Alfvén waves that nonlinearly interact with counter-propagating Alfvén waves, using HMI and AIA/SDO data, it was found that the hot loops are located in the active region core, while the loops at the periphery have large expansion factors and are predicted to be thermally unstable (Asgari-Targhi and van Ballegooijen 2012; Asgari-Targhi et al. 2013). Magnetic braiding appears to be a highly dynamic process (AC heating), rather than the classical picture of a quasi-static DC heating (van Ballegooijen et al. 2014).

8.8 Active Regions: 3-D MHD Simulations

In order to obtain more realistic models of the solar corona and the loops that make up an active region, we enter a new era where 1-D hydrodynamic models based on the flux tube concept become replaced by 3-D numerical MHD codes that are initiated and advanced in time with *"data-driven"* boundary conditions. It has been recognized that the chromosphere, which represents a lower boundary of a coronal computation box encompassing an active region, is highly dynamic and requires a realistic treatment of radiative transfer. The ionization of hydrogen in the chromosphere is dominated by collisional excitation in the Ly α transition, followed by photo-ionization by Balmer continuum photons (Carlsson and Stein 2002).

The first numerical MHD code of this kind uses sixth-order differential operators and fifth-order translational operators on a staggered mesh to solve the fully compressible MHD equations, with radiative cooling and Spitzer conductivity along the magnetic field included in the energy equation (Gudiksen and Nordlund 2002). The physical equations of this compressible MHD code are defined in Gudiksen and Nordlund (2005a,b), later called the *Bifrost* code (Gudiksen et al. 2011):

$$\frac{\partial \rho}{\partial t} = -\nabla \cdot \rho \mathbf{u} \,, \tag{8.8.1}$$

$$\frac{\partial \rho \mathbf{u}}{\partial t} = -\nabla \cdot (\rho \mathbf{u}\mathbf{u} - \tau) - \nabla P + \mathbf{J} \times \mathbf{B} + \rho \mathbf{g} \,, \tag{8.8.2}$$

$$\mu \mathbf{J} = \nabla \times \mathbf{B} \,, \tag{8.8.3}$$

$$\mathbf{E} = \eta \mathbf{J} - \mathbf{u} \times \mathbf{B} \,, \tag{8.8.4}$$

$$\frac{\partial \mathbf{B}}{\partial t} = -\nabla \times \mathbf{E} \,, \tag{8.8.5}$$

$$\frac{\partial e}{\partial t} = -\nabla \cdot e\mathbf{u} - P\nabla \cdot \mathbf{u} - \nabla \cdot \mathbf{F}_{Spitzer} + Q_{visc} + Q_{Joule} - n_{ion} n_e \Lambda \,, \tag{8.8.6}$$

where ρ is the mass density, $\mathbf{u}$ is the velocity vector, τ is the viscous stress tensor, P is the gas pressure, $\mathbf{J}$ is the electric current density, $\mathbf{B}$ is the magnetic flux density, $\mathbf{g}$ is the gravitational acceleration, μ is the vacuum permeability, $\mathbf{E}$ is the electric field strength, η is the magnetic diffusivity, e is the internal energy per unit volume, $\mathbf{F}_{Spitzer}$ is the energy flux due to the Spitzer conductivity along the magnetic field, Q_{visc} is the viscous heating, Q_{Joule} is the Joule heating, and $\Lambda(T)$ is the radiative cooling function for the optically thin coronal plasma, with n_{ion} and n_e being the number density of ions and electrons. The data-driven part of the original *Bifrost* code consists of a velocity field at the lower boundary that has randomly phased 2-D Fourier components and mimics an observed power spectrum, consistent with observed granulation turnover times. The basic 3-D MHD code has been developed further by including radiative transfer in an isothermal scattering atmosphere, hydrogen ionization, thermal conduction, magnetic field advection, and chromospheric radiation, so that the detailed shapes of observed spectral lines can be explained. A detailed description and validation of the *Bifrost* code is given in Gudiksen et al. (2011). The non-equilibrium ionization of hydrogen was improved by including non-equilibrium ionization of helium in addition, which was found to be important for the dynamics and thermal structure of the upper chromosphere and transition region (Golding et al. 2016). The massive parallel computation in solving the 3-D non-local thermal equilibrium (NLTE) radiative transfer problem has been substantially speeded up by using non-linear multigrid methods (Bjorgen and Leenaarts 2017). The most recent developments in 3-D MHD codes includes the *Bifrost* code with partial ionization (Martinez-Sykora et al. 2012).

Besides the *Bifrost* code, other codes with similar capabilities have been used to simulate flux emergence in active regions, such as the *ANMHD* and *ZEUS-3D* code (Abbett and Fisher 2003). Using similar 3-D MHD codes, the (intermittent) heating of an active region is found to be in the transition region from the chromosphere to the corona (Bingert and Peter 2011; MacTaggart 2011). Sigmoidal structures in active regions are simulated by Savcheva et al. (2012). Field-line braiding in active regions is found to be the dominant heating process on the observed spatial scales (Bourdin et al. 2013). A minimum flux density of $\approx$ 200 G is needed in the photosphere to heat a field line to coronal temperatures of $\approx$ 1 MK by Ohmic dissipation (Bourdin et al. 2015). Statistics of Ohmic heating events reveals power law distributions as expected in self-organized criticality (SOC) events, as well as energies of $\approx 10^{24}$ erg that are compatible with so-called nanoflares (Bingert and Peter 2013). The formation of an active region can be driven by the emergence of a sunspot pair (Chen et al. 2014). Substantial net currents are found to be present in active regions long before a flare occurs or a CME erupts (Török et al. 2014). Neutralized currents are in general produced only in the absence of magnetic shear at the photospheric polarity inversion line (Dalmasse et al. 2015). The δ-sunspot formation can be simulated with the emergence of two pairs of bipolar sunspots (Fang and Fan 2015). The Rosner-Tucker-Vaiana scaling law appears to fit hot (soft X-ray emitting) loops, but not cool (EUV-emitting) loops (Bourdin et al. 2016).

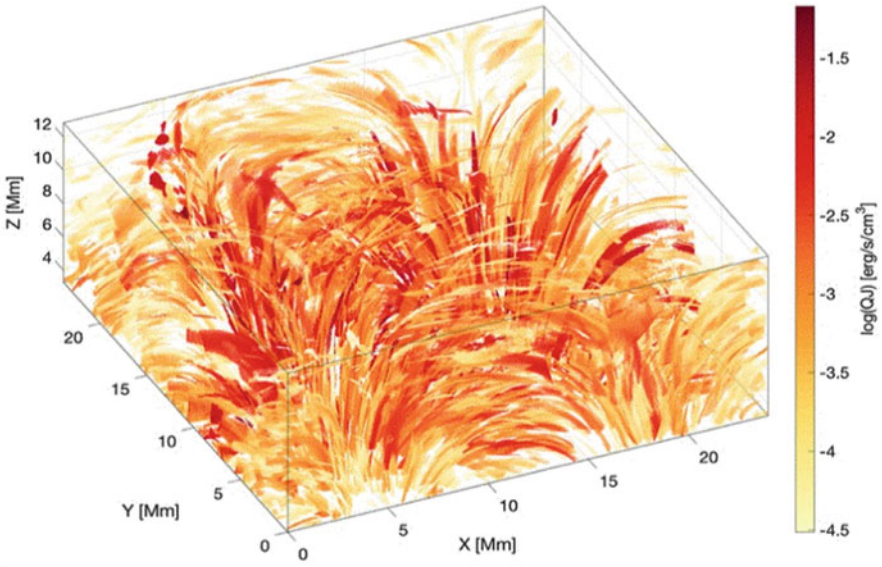

Fig. 8.9 3-D rendering of 4136 identified features of the Joule heating term, in which each color represents a different feature of Joule heating, on a logarithmic scale. The energy output from the resolved features is 12% of the Joule heating output, while the remaining 88% consist of background heating, numerical noise, and unresolved features (Kanella and Gudiksen 2017)

Kanella and Gudiksen (2017) identified over 4000 individual coronal heating events (Fig. 8.9) during a simulation run, mostly in the low corona, while heating decreases with height.

A related method is the magneto-frictional method, which uses the squared current density $\mathbf{J}^2$ as a proxy for the emissivity, rather than solving the full MHD equations (including electron density and temperature), and thus can be inferred from magnetograph data alone. This method has been applied to SOT/Hinode data to simulate the emerging flux in an active region (Cheung et al. 2008), the formation of an active region (Cheung et al. 2010), the evolution of an active region observed with AIA (Cheung and DeRosa 2012), or the evolution of an active region from spot formation (by flux emergence) to decay (Rempel and Cheung 2014).

An alternative method of modeling active regions is forward-fitting of a parameterized multi-loop model, where the geometry of individual loops is prescribed by a potential or force-free magnetic field model. Loops in a quasi-force-free coronal magnetic field are filled with plasma according to a steady-state energy balance model, and fitted to SXT/Yohkoh images, which required filling factors of $\approx (1\text{–}5) \times 10^{-2}$ to match the observed temperatures (Lundquist et al. 2008). The geometry of 70 coronal loops in an active regions was stereoscopically triangulated and used as a skeleton for a 3-D magnetic field. Each loop was filled with hot plasma according to a hydrostatic equilibrium, and then fitted to observed EUV images,

which yields the results that EUV loops with temperatures of $T_m \lesssim 3$ MK tend to be super-hydrostatic, while hotter loops with $T_m \approx 4$–7 MK are near-hydrostatic (Aschwanden et al. 2009).

8.9 Active Regions: Correlations

There is a broad concensus that the high-temperature plasma in active regions is produced by some magnetic reconnection process, which implies a correlation between the coronal soft X-ray flux and the photospheric magnetic field. Moreover, a comparison of soft X-ray images with full disk magnetograms shows a clear spatial correlation between the locations of the brightest soft X-ray emission and the photospheric location of bipolar magnetic active regions, which also confirms that magnetic fields play an essential role in the heating of the active region corona (Table 8.4).

A statistical study of 333 vector magnetograms of active regions, observed during 1991–1995 with the *Soft X-Ray Telescope (SXT)* onboard Yohkoh, with magnetograms observed with the Haleakala Stokes Polarimeter at the Mees Solar Observatory (Maui, Hawaii) was conducted by Fisher et al. (1998). In this study it was found that the X-ray intensity I_X is best correlated with the total unsigned magnetic flux Φ_{tot}, i.e., $I_X \approx 1.2 \times 10^{26}$ erg s^{-1} $(\Phi_{tot}/10^{22}$ Mx $)^{1.19}$. This observational finding constrains scaling laws of various coronal heating models. However, a puzzling result of the study by Fisher et al. (1998) is that the heating appears to be unrelated to the current, so that the soft X-ray emission is almost solely determined by the total unsigned magnetic flux.

Using similar data (1996–1997), SXT/Yohkoh images and MDI/SOHO magnetograms, by binning the data per day and spatially into nine latitude bins (each spanning 15°), a strong correlation between the soft X-ray flux F_X and the unsigned magnetic field $|B_z|$ was found in all low-latitude ($-30°$ to $+30°$) bands (Wolfson et al. 2000). Soft X-ray temperatures were restricted to $T_e \approx 1$–3 MK in both studies (Fisher et al. 1998; Wolfson et al. 2000), but both the Quiet Sun and active regions are included in Wolfson et al. (2000).

Table 8.4 Correlations found in active regions for the parameters of the soft X-ray intensity I_X, the soft X-ray flux F_X, the total unsigned magnetic flux Φ_{tot}, the unsigned magnetic field strength $|B|$, and the area A

Correlation	References
$I_X \propto \Phi_{tot}^{1.19}$	Fisher et al. (1998)
$F_X \propto \lvert B\rvert^{1.43...1.80}$	Wolfson et al. (2000)
$I \propto \Phi^{1.0}$	Handy and Schrijver (2001)
$I_{AlMg} \propto \lvert B\rvert^{1.4...2,2}$	Benevolenskaja et al. (2002)
$I_X \propto \lvert B\rvert^{1.87,...,1.94}$	van Driel-Gesztelyi et al. (2003)
$\lvert\Phi\rvert \propto A^{1.18,...,1.21}$	Meunier (2003)
$\lvert B\rvert \propto A^{0.38,...,0.43}$	Meunier (2003)
$F_H \propto B^{1.0\pm0.3} L^{-1.0\pm0.5}$	Schrijver et al. (2004)
$F_H \propto B^1 L^{-1}$	Warren and Winebarger (2006)

Similarly, using EIT/SOHO and MDI/SOHO data over a short period of 5 days (1997 August 10–14), Handy and Schrijver (2001) measured the lifetimes, dimensions, and orientations of small-scale coronal brightenings in active regions and found a linear relationship between the integrated unsigned photospheric magnetic flux $|B|$ and the total Fe XII loop intensity, where the region of integration was chosen by selecting a region surrounding the brightening visible in EIT and also including the footpoints as observed by MDI.

Benevolenskaja et al. (2002) used soft X-ray data from SXT/Yohkoh, magnetogram data from the *Kitt Peak Solar Observatory (KPSO)*, for the period of an entire solar cycle (1991–2001), and EUV data from EIT/SOHO during 1996–2001, and found a tight correlation between the soft X-ray intensity I_{AlMg} (aluminium magnesium filter) and the unsigned magnetic field strength $|B|$, i.e. $I_{AlMg} \propto |B|^n$, but the power index varied between $n \approx 1.4$–1.8 during the solar maximum to $n \lesssim 2.2$ during the minimum of the solar cycle. These power indices n are significantly higher than the value of $n \approx 1.2$ found by Fisher et al. (1998).

Analyzing the long-term evolution of active region NOAA 7978 from birth to decay, during a time duration of five solar rotations, using MDI/SOHO, SXT/Yohkoh, and BCS/Yohkoh data, van Driel-Gesztelyi et al. (2003) found a scaling between the soft X-ray intensity I_X and the magnetic field strength $|B|$, i.e., i.e. $I_X \propto |B|^n$, with $n = 1.87, \ldots, 1.94$ for SXT/Yohkoh data. In the same work, correlations between other parameters were found (area, temperature, emission measure, density, pressure), which constrain physical scaling laws.

A long dataset (7184 images between 1996–2002) of MDI/SOHO full-disk magnetograms was sampled in order to characterize the magnetic flux Φ and areas A (Meunier 2003). The correlations found in this study, i.e., $|\Phi| \propto A^{1.18,\ldots,1.21}$ and $|B_{mean}| \propto A^{0.38,\ldots,0.43}$, however, depend on the solar cycle.

Schrijver et al. (2004) parameterize a scaling law of the heating flux F_H as a function of the magnetic field strength B (at the chromospheric base), and the loop half length L, with the relationship $F_H \propto B^\alpha L^\beta$, with α and β being free parameters. Starting from full-sphere magnetic field maps, the corona is populated with $\approx 50,000$ coronal field lines with quasi-static atmospheres (Rosner et al. 1978; Serio et al. 1981), where the heating rate is balanced by conductive and radiative loss ($F_{heat} = F_{cond} + F_{rad}$). The theoretical model, which has only two free parameters (α, β), is then forward-fitted to observed EUV images (from EIT/SOHO) and soft X-ray images (from SXT/Yohkoh), by varying the two variables α and β. The best match to X-ray and EUV observations of the corona over active regions and their environments is found for $F_H \approx 4 \times 10^{14} B^{1.0\pm0.3} L^{-1.0\pm0.5}$, (in units of erg cm^{-2} s^{-1}, for B in Mx cm^{-2}, and L in cm). The best-fit coronal filling factor equals unity. The empirical scaling law found this way, is also consistent with the theoretical scaling law of Parker (1983), where heating is driven by field line braiding, where the reconnection field moves across neutral sheets with Alfvén velocity v_A, amounting to the work P done on the coronal field with strength B,

$$P \propto w \left(\frac{B^2}{4\pi}\right) \frac{w}{v} \frac{h}{L}\,, \tag{8.9.1}$$

(for loops of width h that is likely set by the granulation scale and for characteristic driver velocity w), yielding

$$P \propto \frac{B}{L}\rho^{1/2} . \tag{8.9.2}$$

Warren and Winebarger (2006) model followed up on the work of Schrijver et al. (2004) by using the same scaling law $F_H \propto B/L$ and fitting intensity images of 26 active regions observed with EIT/SOHO and SXT/Yohkoh (Fig. 8.10). The comparisons show close agreement with the observed emission at high temperatures (in soft X-rays), but significant discrepancies are found at the lower temperatures (in EUV).

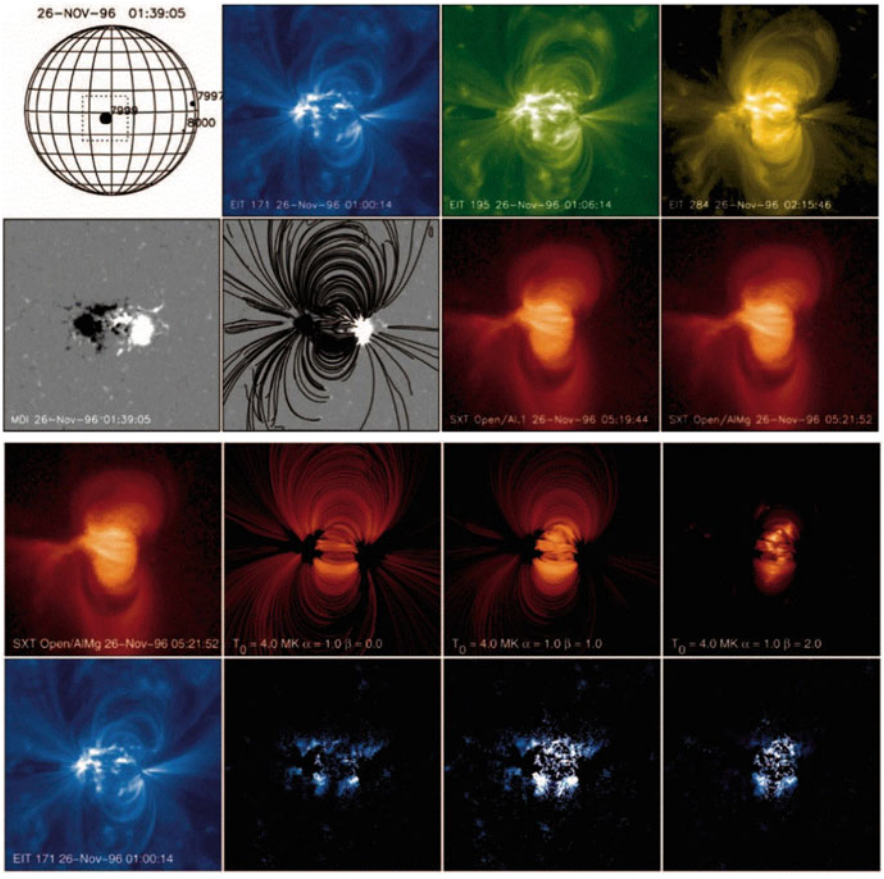

Fig. 8.10 *Top two rows and first column:* Images from active region NOAA 7999 on 1996 November 26, from EIT, MDI, and SXT, and magnetic field extrapolation. *Bottom two rows from second to fourth column:* Synthetic SXT AlMg and EIT 171 Å images, for different power law indices α and β in the heating scaling law $F_H \propto B^{\alpha} L^{\beta}$, (Warren and Winebarger 2006)

8.10 Active Regions: Coronal Streamers

Coronal streamers, also called *helmet streamers* (due to their morphological shape), are bright loop-like structures which develop over active regions. In lower coronal heights, streamers show a bipolar structure of closed magnetic loops that connect regions of opposite magnetic polarity. Since streamers have been observed with coronagraphs or during eclipses mostly, they can be seen over the solar limb only, which requires a substantial tilt or latitude offset between the northern and southern magnetic polarity, a condition that is met for a subset of all active regions only. At larger coronal heights, streamers shape into a pointed cusp, which naturally occurs when the solar wind drags and elongates the high-reaching active region loops outward along open magnetic field lines of the heliospheric current sheet, sometimes accompanied by out-streaming plasmoid blobs. The transition from a closed-field configuration in low coronal altitudes to an open-field configuration in the heliosphere can naturally be explained by the transition from a low plasma-β parameter ($\beta < 1$) to a high plasma-β parameter ($\beta > 1$), which can occur already at heights of $r \gtrsim 1.2 R_\odot$ (Gary 2001). There is also a dichotomy of magnetic configurations: *helmet streamers* separate open field lines of opposite magnetic polarity, located near boundaries of coronal holes, and possibly contributing to the acceleration of the slow solar wind, while *pseudostreamers* separate open filed lines of the same polarity, located inside coronal holes, and possibly contributing to the acceleration of the fast solar wind (Wang et al. 2007). A recent comparison of global non-potential magnetic models of the solar corona and streamers observed during the 2015 March eclipse has been presented in Yeates et al. (2018).

The dynamics of coronal streamers includes plasma blobs ejected continually from the cusplike bases of the streamers, fine raylike structures pervading the outer streamer belt, and inflows that occur mainly during times of high solar activity, phenomena that are believed to involve magnetic reconnection processes, in which plasma and magnetic flux are exchanged between closed and open field regions of the corona (Wang et al. 2000a). Narrow CMEs, called *"streamer puffs"*, were found to move along streamers, probably produced by means of opening an outer loop of a flare arcade (Bemporad et al. 2005). Various forms of *streamer detachments* or *streamer blowouts* are interpreted as magnetic reconnections of rising loops, where an outgoing helical flux rope and an ingoing arcade of collapsing loops collide (Sheeley and Wang 2007). CMEs can excite *streamer waves* with periods of $\approx$ 1 hr, wavelengths of $\approx$ 2–4$R_\odot$, amplitudes of a few tens of solar radii, and a propagating phase speed of $\approx$ 300–500 km s^{-1} (Chen et al. 2010). A *coronal mass ejection (CME)* was found to be deflected toward the current sheet of a larger helmet streamer due to an imbalance in the magnetic pressure and tension forces, but finally merges with the streamer (Zuccarello et al. 2012). CME-streamer interactions in conjunction with type II radio burst detections can localize electron acceleration sites caused by CME-driven shocks (Feng et al. 2012).

Analysis of CDS/SOHO and UVCS/SOHO data in an altitude range of $r = 1.02$–$1.6 R_\odot$ shows that abundances in the low corona (covered by CDS) do not show deviations from photospheric abundances, but abundances in the upper corona

(covered by UVCS) show a depletion of all element abundances, but no clear evidence of a *first ionization potential (FIP)* effect in streamers is found (Parenti 2000).

In many UVCS/SOHO observations (in an altitude range of 2.6–5.1$R_\odot$) there is evidence that outflows in streamers display acceleration by the slow solar wind. Frazin et al. (2003) measures outflow velocities of $v \approx$ 80–180 km s^{-1} and finds anisotropic velocity distributions of O^{5+} in the streamer legs and stalks. From a 2.5-D MHD simulation it is found that enhanced abundances of O^{5+} ions in the legs of a streamer, caused by the Coulomb friction with the outflowing protons, explains the observed enhancement of the oxygen line emission and traces the source regions of the slow solar wind in coronal streamers (Ofman 2000).

The characteristics of coronal streamer structures vary with the solar cycle. During the rising phase of the solar cycle 23 for instance, the latitudinal spreading of the streamer belt is a consequence of the increased rate of magnetic flux emergence in sunspot latitude, which led to a weakening of the Sun's axisymmetric dipole moment, to a rapid growth in the nonaxisymmetric components of the coronal field, and hence to a strong tilting and warping of the plasma current sheet (Wang et al. 2000b).

The STEREO mission provided a boost for 3-D reconstruction and tomography of coronal streamers. Using a higher cadence of 4 polarized brightness (pB) images per day from LASCO C2, instead of 1 pB image per day, the quality of tomographic reconstruction could be dramatically improved (Frazin et al. 2007), especially at a height of 2.5 $R_\odot$ that serves as a reference level of magnetic *potential-field source surface (PFSS)* models. 3D reconstructions of coronal streamers from LASCO images at 2.5 $R_\odot$ were compared with PFSS magnetic field lines and were found to coincide closely with the heliospheric current sheet, often associated with strong magnetic field active regions (Liewer et al. 2001). Based on this it was concluded that many of the bright streamers are the result of scattering from regions of enhanced density associated with active region outflows, and not a result of line-of-sight viewing through folds in a warped current sheet with uniform density (Liewer et al. 2001). However, more detailed tomography with LASCO data revealed double plasma sheets and triple current sheets that are not reproduced by standard PFSS extrapolations (Saez et al. 2005, 2007) (Fig. 8.11, top left), visible also in pseudo-tomography maps that subtract a *Fourier normalized-radial gradient filter (FNRGF)*, but do not preserve the electron density (Morgan et al. 2009; Morgan and Habbal 2010; Morgan 2011) (Fig. 8.11, right). True tomography of the 3D density distribution with two simultaneous spacecraft observations (STEREO/A and B, COR-1) was first performed by Kramar et al. (2009) (Fig. 8.11, bottom left), which demonstrated that the equatorial streamer belt is largely consistent with the variation of the current sheet derived from magnetic potential field models (Kramar et al. 2009, 2014).

While streamers were mostly considered as static objects in tomographic reconstruction, dynamic phenomena were also tracked with stereoscopic triangulation, such as streamer blobs that gradually expand outward (Sheeley et al. 2009), and become swept up and compressed by the fast solar wind from low-latitude coronal

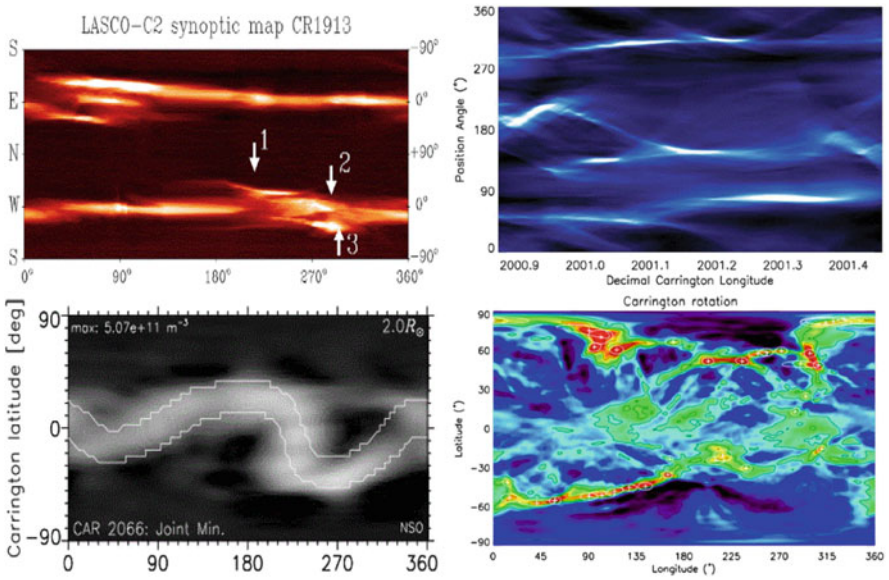

Fig. 8.11 Examples of tomographic streamer belt reconstructions. *Top left:* Streamer belt density reconstruction with LASCO C-2 at $r = 2.5\,R_\odot$ (Saez et al. 2005); *Bottom left:* Electron density at height $r = 2.0\,R_\odot$ reconstructed from STEREO COR-1, overlaid with magnetic field contours from NSO/GONG (Kramar et al. 2009); *Right:* Qualitative density maps at $r = 4.0\,R_\odot$ reconstructed from LASCO C-2 data (Morgan et al. 2009) (top), (Morgan and Habbal 2010) (bottom)

holes (Sheeley and Rouillard 2010), or slow streamer-blowout CMEs that are considered as a natural consequence of the corona's adjustment to the long term evolutionary driving of the photospheric magnetic field (Lynch et al. 2010). The thermodynamics and kinematics of coronal streamers was also simulated with resistive MHD models and PFSS magnetic models, which allowed the authors to test steady-state flows versus polytropic solutions (Airapetian et al. 2011).

References

(8.1) Active Regions: Magnetic Field Modeling

Amari, T., Boulmezaoud, T.Z., and Aly, J.J. 2006, *Well posed reconstruction of the solar coronal magnetic field*, A&A 446, 691, [94 c, 8 c/y].

Aschwanden, M.J. 2013a, *A nonlinear force-free magnetic field approximation suitable for fast forward-fitting to coronal loops. I. Theory*, SoPh 287, 323, [17 c, 4 c/y].

Aschwanden, M.J. and Malanushenko, A. 2013, *A nonlinear force-free magnetic field approximation suitable for fast forward-fitting to coronal loops. II. Numeric Code and Tests*, SoPh 287, 345, [20 c, 4 c/y].

Aschwanden, M.J. 2013b, *A nonlinear force-free magnetic field approximation suitable for fast forward-fitting to coronal loops. III. The Free Energy*, SoPh 287, 369, [14 c, 3 c/y].
Aschwanden, M.J. 2013a, *Nonlinear force-free magnetic field fitting to coronal loops with and without stereoscopy*, ApJ 763, 115, [17 c, 4 c/y].
Aschwanden, M.J., De Pontieu, B., and Katrukha, E. 2013, *Optimization of Curvi-Linear Tracing Applied to Solar Physics and Biophysics*, Entropy, 15(8), 3007, [11 c, 2 c/y].
Aschwanden, M.J., Sun, X.D., and Liu, Y. 2014, *The magnetic field of active region 11158 during the 2011 February 12–17 flares: Differences between photospheric extrapolation and coronal forward-fitting methods*, ApJ 785, 34, [23 c, 7 c/y].
Chifu, I., Inhester, B., and Wiegelmann, T. 2015, *Coronal magnetic field modeling using stereoscopy constraints*, A&A 577, A123, [4 c, 2 c/y].
Chifu, I., Wiegelmann, T., and Inhester, B. 2017, *Nonlinear force-free coronal magnetic stereoscopy*, ApJ 837, 10, [1 c, 1 c/y].
De Rosa, M.L., Schrijver, C.J., Barnes, G., et al. 2009, *A critical assessment of nonlinear force-free field modeling of the solar corona for active region 10953*, ApJ 696, 1780, [230 c, 27 c/y].
De Rosa, M.L., Wheatland, M.S., Leka, K.D., et al. 2015, *The influence of spatial resolution on nonlinear force-free modeling*, ApJ 811, 107, [22 c, 9 c/y].
Gary, G.A. 2001, *Plasma beta above a solar active region: Rethinking the paradigm*, SoPh 203, 71, [259 c, 16 c/y].
Gilchrist,S.A., Braun, D.C., and Barnes, G. 2016, *A fixed-point scheme for the numerical construction of magnetohydrostatic atmospheres in three dimensions*, SoPh 291, 3583, [3 c, 3 c/y].
Grad, H. and Rubin, H. 1958, in Peaceful Uses of Atomic Energy: Proc. Second UN International Atomic Energy Conference, 31 (Geneva: UN), 190.
Malanushenko, A., Schrijver, C.J., De Rosa, M.L., et al. 2014, *Using coronal loops to reconstruct the magnetic field of an active region before and after a major flare*, ApJ 783, 102, [31 c, 9 c/y].
Metcalf, T.R., De Rosa, M.L., Schrijver, C.J. et al. 2008, *Nonlinear force-free modeling of coronal magnetic fields. II. Modeling a filament arcade and simulated chromospheric and photospheric vector fields*, SoPh 247, 269, [152 c, 16 c/y].
Schrijver et al. 2006 *Nonlinear force-free modeling of coronal magnetic fields Part I: A quantitative comparison of methods*, SoPh 235, 161, [215 c, 19 c/y].
Valori, G., Kliem, B., and Fuhrmann, M. 2007, *Magnetofrictional extrapolations of Low and Lou's force-free equilibria* SoPh 245, 263, [42 c, 4 c/y].
Warren, H.P., Crump, N.A., Ugarte-Urra, I. et al. 2018, *Towards a quantitative comparison of magnetic field extrapolations and observed coronal loops*, ApJ 860, 46.
Wheatland, M.S., Sturrock, P.A., and Roumeliotis, G. 2000, *An optimization approach to reconstructing force-free fields*, ApJ 540, 1150, [249 c, 14 c/y].
Wheatland, M.S. 2006, *A fast current-field iteration method for calculating nonlinear force-free fields*, SoPh 238, 29, [33 c, 3 c/y].
Wheatland, M.S. and Régnier, S. 2009, *A self-consistent nonlinear force-free solution for a solar active region magnetic field*, ApJ 700, L88, [42 c, 5 c/y].
Wiegelmann, T. 2004, *Optimization code with weighting function for the reconstruction of coronal magnetic fields*, SoPh 19, 87, [270 c, 20 c/y].
Wiegelmann, T., Inhester, B., and Sakurai, T. 2006, *Preprocessing of vector magnetograph data for a nonlinear force-free magnetic field reconstruction* SoPh 233, 215, [212 c, 18 c/y].
Wiegelmann, T., Thalmann, J.K., Inhester, B., et al. 2012, *How should one optimize nonlinear force-free coronal magnetic field extrapolations from SDO/HMI vector magnetograms?* SoPh 281, 37, [62 c, 11 c/y].
Wiegelmann,T., and Sakurai, T. 2012, *Solar force-free magnetic fields*, LRSP 9, 5, [97 c, 18 c/y].
Wiegelmann,T., Thalmann, J. K., and Solanki, S.K. 2014, *The magnetic field in the solar atmosphere*, A&AR 22, 78, [38 c, 11 c/y].
Wiegelmann,T., Petrie, G.J.D., and Riley,P. 2017a, *Coronal magnetic field models*, SSRv 210, 249, [10 c, 10 c/y].

Wiegelmann,T., Neukirch, T., Nickeler, D.H., et al. 2017b, *Magneto-static modeling from Sunrise/IMaX: Application to an active region observed with Sunrise II*, ApJSS 229, 18, [7 c, 7 c/y].
Yang, W.H., Sturrock, P.A., and Antiochos, S.K. 1986, *Force-free magnetic fields - The magneto-frictional method*, ApJ 309, 383, [189 c, 6 c/y].
Zhu, X.S., Wang, H.N., Du, Z.L., et al. 2013, *Forced field extrapolation: Testing a magnetohydrodynamic (MHD) relaxation method with a flux-rope emergence model*, ApJ 768, 119, [15 c, 3 c/y].
Zhu, X.S. and Wiegelmann, T. 2018, *On the extrapolation of magneto-hydrodstatic equilibria on the Sun*, ApJ 866, 130.

(8.2) Active Regions: Magnetic Nonpotentiality

Aschwanden, M.J. and Sandman, A.W. 2010, *Bootstrapping the coronal magnetic field with STEREO: unipolar potential field modeling*, AJ 140, 723, [23 c, 3 c/y].
Bobra, M.G., van Ballegooijen, A.A., and DeLuca, E.E. 2008, *Modeling magnetic fields in solar active regions*, ApJ 672, 1209, [75 c, 8 c/y].
Falconer, D.A., Moore, R.L., and Gary, G.A. 2008, *Magnetogram measures of total nonpotentiality for prediction of solar coronal mass ejections from active regions of any degree of magnetic complexity*, ApJ 689, 1443, [33 c, 3 c/y].
Georgoulis, M.K. and LaBonte, B.J. 2004, *Vertical Lorentz force and cross-field currents in the photospheric magnetic fields of solar active regions*, ApJ 615, 1029, [27 c, 2 c/y].
Georgoulis, M.K., Tziotziou, K., and Raouafi, N.E., 2012, *Magnetic energy and helicity budgets in the active region solar corona. II. Nonlinear force-free approximation*, ApJ 759, 1, [29 c, 5 c/y].
Régnier, S., Amari, T., and Kersale, E. 2002, *3-D coronal magnetic field from vector magnetograms: non-constant α force-free configuration of the active region NOAA 8151*, A&A 392, 1119, [88 c, 6 c/y].
Sandman, A.W., Aschwanden, M.J., DeRosa, M.L., et al. 2009, *Comparison of STEREO/ EUVI loops with potential magnetic field models*, SoPh 259, 1, [31 c, 4 c/y].
Schrijver, C.J., De Rosa, M.L., Title, A.M., et al. 2005, *The nonpotentiality of active region coronae and the dynamics of the photospheric magnetic field*, ApJ 628, 501, [88 c, 7 c/y].
Schrijver, C.J. 2016, *The nonpotentiality of coronae of solar active regions, the dynamics of the surface magnetic field, and the potential for large flares*, ApJ 820, 103, [7 c, 5 c/y].
Sun, X., Hoeksema, J.T., Liu, Y., et al. 2012, *Evolution of magnetic field and energy in a major eruptive active region based on SDO/HMI observation*, ApJ 748, 77, [184 c, 33 c/y].
Thalmann, J.K., Tiwari, S.K., and Wiegelmann, T. 2014, *Force-free field modeling of twist and braiding-induced magnetic energy in an active region corona*, ApJ 780, 102, [16 c, 5 c/y].
Titov, V.S., Török, T., Mikic, Z., et al. 2014, *A method for embedding circular force-free flux ropes in potential magnetic fields*. ApJ 790, 163, [16 c, 5 c/y].

(8.3) Active Regions: Magnetic Helicity

Berger, M.A. and Field, G.B. 1984, *The topological properties of magnetic helicity*, J. Fluid Mech. 147, 133, [714 c, 21 c/y].
Chae, J. 2001, *Observational determination of the rate of magnetic helicity transport through the solar surface via the horizontal motion of field line footpoints*, ApJ 560, L95, [186 c, 11 c/y].
Dalmasse, K., Pariat, E., Valori, G., et al. 2018, *Studying the transfer of magnetic helicity in solar active regions with the connectivity-based flux density method*, ApJ 852, 141.

Démoulin, P., Mandrini, C.H., van Driel-Gesztelyi, L., et al. 2002a, *What is the source of the magnetic helicity shed by CMEs? The long-term helicity budget of AR 7978*, A&A 382, 650, [163 c, 11 c/y].

Démoulin, P., Mandrini, C.H., van Driel-Gesztelyi, L., et al. 2002b, *The magnetic helicity injected by shearing motions*, SoPh 207, 87, [73 c, 5 c/y].

DeVore, C.R. 2000, *Magnetic helicity generation by solar differential rotation*, ApJ 539, 944, [167 c, 10 c/y].

Green, L.M., Lopez Fuentes, M.C., Mandrini, C.H., et al. 2002, *The magnetic helicity budget of a CME-prolific active region*, SoPh 208, 43, [124 c, 8 c/y].

Hagino, M. and Sakurai, T. 2004, *Latitude variation of helicity in solar active regions*, PASJ 56, 831, [89 c, 6 c/y].

Hagino, M. and Sakurai, T. 2005, *Solar-cycle variation of magnetic helicity in active regions*, PASJ 57(3), 481, [57 c, 5 c/y].

Kusano, K., Maeshiro, T., Yokoyama, T. et al. 2002, *Measurement of magnetic helicity injection and free energy loading into the solar corona*, ApJ 577, 501, [173 c, 11 c/y].

LaBonte, B.J., Georgoulis, M.K., and Rust, D.M. 2007, *Survey of magnetic helicity injection in regions producing X-class flares*, ApJ 671, 955, [79 c, 8 c/y].

Liu, Y., Hoeksema, J.T., and Sun X. 2014a, *Test of the hemispheric rule of magnetic helicity in the Sun using the HMI data*, ApJ 783, L1, [14 c, 5 c/y].

Liu, Y., Hoeksema, J.T., Bobra, M. et al. 2014b, *Magnetic helicity in emerging solar active regions*, ApJ 785, 13, [19 c, 5 c/y].

Nindos, A., Zhang, J., and Zhang, H. 2003, *The magnetic helicity budget of solar active regions and coronal mass ejections*, ApJ 594, 1033, [112 c, 8 c/y].

Pevtsov, A.A., Canfield, R.C., Sakurai, T., et al. 2008, *On the solar cycle variation of the hemispheric helicity rule*, ApJ 677, 719, [39 c, 4 c/y].

Rudenko, G.V. and Myshyakov, I.I. 2011, *Gauge-invariant helicity of force-free magnetic fields in a rectangular box*, SoPh 270, 165, [16 c, 2 c/y].

Thalmann, J.K., Inhester, B., and Wiegelmann, T. 2011, *Estimating the relative helicity of coronal magnetic fields*, SoPhy 272, 243, [19 c, 3 c/y].

Valori, G., Pariat, E., Anfinogentov, S., et al. 2016, *Magnetic helicity estimations in models and observations of the solar magnetic field. Part I: Finite volume methods*. SSRv 201, 147, [8 c, 5 c/y].

Welsch, B.T. and Longcope, D.W. 2003, *Magnetic helicity injection by horizontal flows in the Quiet Sun. I. Mutual-helicity flux*, ApJ 588, 620, [73 c, 5 c/y].

Yang, S., Buechner, J., Santos, J.C., et al. 2013), *Evolution of relative magnetic helicity: Method of computation and its application to a simulated solar corona above an active region*, SoPh 283, 369, [14 c, 3 c/y].

(8.4) Active Regions: Tomography Methods

Aschwanden, M.J. and Bastian, T.S. 1994a, *VLA stereoscopy of solar active regions. I. Method and tests*, ApJ 426, 425, [35 c, 2 c/y].

Aschwanden, M.J. and Bastian, T.S. 1994b, *VLA stereoscopy of solar active regions. II. Altitude, relative motion, and center-to-limb darkening at 20 cm emission*, ApJ 426, 434, [38 c, 2 c/y].

Aschwanden, M.J., Lim, J., Gary, D.E., et al. 1995, *Solar rotation steoroscopy in microwaves*, ApJ 454, 512, [39 c, 2 c/y].

Aschwanden, M.J. 2011a, *Solar stereoscopy and tomography*, LRSP 8, 1, [19 c, 3 c/y].

Aschwanden, M.J. 2011b, *3-D reconstruction of active regions with STEREO*, J.Atmos. Solar-Terr.Phys 73(10), 1082, [7 c, 1 c/y].

Butala, M.D., Frazin, R.A., and Kamalabadi, F. 2005, *3-D estimates of the coronal electron density at times of extreme solar activity*, JGR 110(A9), CiteID A09S09, [9 c, 0.7 c/y].

Butala, M.D., Hewett, R.J., Frazin, R.A., et al. 2010, *Dynamic 3-D tomography of the Sun* SoPh 262, 495, [21 c, 3 c/y].

Dunn, T., Jackson, B.V., Hick, P.P., et al. 2005, *Comparative analyses of the CSSS calculation in the UCSD tomographic solar observations*, SoPh 227, 339, [19 c, 2 c/y].

Frazin, R.A. 2000, *Tomography of the solar corona. I. A robust, regularized, positive estimation method*, ApJ 530, 1026, [44 c, 3 c/y].

Frazin, R.A. and Janzen, P. 2002, *Tomography of the solar corona. II. Robust, regularized, positive estimation of the 3-D electron density distribution from LASCO-C2 polarized white-light images*, ApJ 570, 408, [56 c, 4 c/y].

Frazin, R.A., Butala, M.D., Kemball, M.D., and Kamalabadi, F. 2005a, *Time-dependent reconstruction of nonstationary objects with tomographic or interferometric measurements*, ApJL 635, L197, [19 c, 2 c/y.

Frazin, R.A., Kamalabadi, F., and Weber, M.A. 2005b, *On the combination of differential emission measure analysis and rotational tomography for 3-D solar EUV imaging*, ApJ 628, 1070, [27 c, 2 c/y].

Frazin, R.A. and Kamalabadi, F. 2005, *Rotational tomography for 3-D reconstruction of the white-light and EUV corona in the post-SOHO era*, SoPh 228, 219, [23 c, 2 c/y].

Hurlburt, N.E., Martens, P.C.H., Slater,G.L., et al. 1994, *Volume reconstruction of magnetic fields using solar imagery*, in *Solar Active Region Evolution: Comparing Models with Observations*, (eds, Balasubramaniam, K.S. and G.W.Simon), Astronomical Society of the Pacific (ASP), Conf.Ser.Vol. 68, 30.

Jackson, B.V., Hick, P.L., Kojima, M., et al. 1998, *Heliospheric tomography using interplanetary scintillation observations. I. Combined Nagoya and Cambridge data*, JGR 103, 12049, [100 c, 5 c/y].

Jackson, B.V. and Hick, P.L., 2002, *Corotational tomography of heliospheric features using global Thomson scattering data*, SoPh 211, 345, [17 c, 1 c/y].

Jensen, J.M., Duvall, T.L.Jr., and Jacobsen, B.H. (2001), *Imaging an emerging active region with helioseismic tomography*, ApJ 553, L193, [60 c, 4 c/y].

Kramar, M., Inhester, B., and Solanki, S.K. 2006, *Vector tomography for the coronal magnetic field. I. Longitudinal Zeeman effect measurements*, A&A 456, 665, [26 c, 2 c/y].

Kramar, M., Inhester, B., Lin, H. 2013, *Vector tomography for the coronal magnetic field. II. Hanle effect measurements*, ApJ 775, 25, [14 c, 3 c/y].

Kramar, M., Lin, H., and Tomczyk, S. 2016, *Direct observation of solar coronal magnetic fields by vector tomography of the coronal emission line polarization*, ApJL 819, L36, [4 c, 4 c/y].

Lee, J.W., White, S.M., Kundu, M.R., et al. 1999, *A test for coronal magnetic field extrapolations*, ApJ 510, 413, [40 c, 2 c/y].

Lloveras, D.G., Nuevo, F.A., Vasquez, A.M., et al. 2016, *Comparative analysis of solar minima with EUV tomography*, BAAA 58, 272, [1 c, 0.7 c/y].

Morgan, H. and Habbal, S.R. 2010, *Observational aspects of the 3-D coronal structure over a solar activity cycle*, ApJ 710, 1, [21 c, 3 c/y].

Nita, G.M., Fleishman, G.D., Jing, J., et al. 2011, *3-D structure of microwave sources from solar rotation stereoscopy versus magnetic extrapolations*, ApJ 737, 82, [9 c, 1 c/y].

Ryabov, B.I., Maksimov, V.P., Lesovoi, S.V., et al. 2005, *Coronal magnetography of solar active region 8356 with the SSRT and NoRH radio heliographs*, SoPh 226, 223, [9 c, 0.7 c/y].

Vasquez, A.M., Frazin, R.A., and Manchester, Ward B.IV. 2010, *The solar minimum corona from differential emission measure tomography*, ApJ 715, 1352, [28 c, 4 c/y].

Wang, T.J., Reginald, N.L., Davila, J.M., et al. 2017, *Variation in coronal activity from solar cycle 24 minimum to maximum using 3-D reconstructions of the coronal electron density from STEREO/COR1*, SoPh 292, 97, [2 c, 2 c/y].

(8.5) Active Regions: High-Temperature Emission

Del Zanna, G. 2013, *The multi-thermal emission in solar active regions*, A&A 558, A73, [66 c, 15 c/y].

Del Zanna, G. and Mason, H.E. 2014, *Elemental abundances and temperatures of quiescent solar active region cores from X-ray observations*, A&A 565, A14, [25 c, 7 c/y].

Del Zanna, G. Tripathi, D., Mason, H., et al. 2015, *The evolution of the emission measure distribution in the core of an active region*, A&A 573, A104, [11 c, 4 c/y].

Ishikawa, S.N., Glesener, L., Christe, S., et al. 2014, *Constraining hot plasma in a non-flaring solar active region with FOXSI hard X-ray observations*, PASJ 66, S15, [12 c, 3 c/y].

Hannah, I.G., Grefenstette, B.W., Smith, D.M., 2016, *The first X-ray imaging spectroscopy of quiescent solar active regions with NuSTAR*, ApJ 820, L14, [14 c, 9 c/y].

Hara, H., Tsuneta, S., Lemen, J.R., et al. 1992, *High-temperature plasmas in active regions observed with the SXT aboard Yohkoh*, PASJ 44, L135, [135 c, 5 c/y].

Ko, Y.K., Raymond, J.C., Ciaravella, A., et al. 2002, *SOHO UV coronagraph spectrometer and Yohkoh SXT observations of the high-temperature corona above an active region complex*, ApJ 578, 979, [35 c, 2 c/y].

Ko, Y.K., Doschek, G.A., Warren, H.P., et al. 2009, *Hot plasma in nonflaring active regions observed by the EIS on Hinode*, ApJ 697, 1956, [86 c, 10 c/y].

Mackovjak, S., Dzifacova, E., and Dudik, J. 2014, *Differential emission measure analysis of active region cores and quiet Sun for the non-Maxwellian κ-distributions*, A&A 564, A130, [8 c, c 2/y].

Reale, F., Testa, P., Klimchuk, J.A., et al. 2009, *Evidence of widespread hot plasma in a nonflaring coronal active region from Hinode/X-Ray Telescope*, ApJ 698, 756, [63 c, 7 c/y].

Schmelz, J.T., Saar, S.H., DeLuca, E.E., et al. 2009, *Hinode XRT detection of hot emission from quiescent active regions: A nanoflare signature?* ApJ 693, L131, [69 c, 8 c/y].

Schmelz, J.T., Pathak, S., Jenkins, B.S., et al. 2013, *Deeper by the dozen: Understanding the cross-field temperature distributions of coronal loops*, ApJ 764, 53, [13 c, 3 c/y].

Warren, H.P., Feldman, U., and Brown, C.M. 2008, *Solar observations of high-temperature emission with the EIS on Hinode*, ApJ 685, 1277, [23 c, 2 c/y].

Warren, H.P., Brooks, D.H., and Winebarger, A.R. 2011, *Constraints on the heating of high-temperature active region loops: Observations from Hinode and the SDO*, ApJ 734, 90, [78 c, 12 c/y].

Warren, H.P., Winebarger, A.R., and Brooks, D.H. 2012, *A systematic survey of high-temperature emission in solar active regions*, ApJ 759, 141, [85 c, 15 c/y].

(8.6) Active Regions: Plasma Outflows

Baker, D., van Driel-Gesztelyi, L., Mandrini, C.H. et al. 2009, *Magnetic reconnection along quasi-separatrix layers as a driver of ubiquitous active region outflows*, ApJ 705, 926, [82 c, 10 c/y].

Brooks, D.H. and Warren, H.P. 2011, *Establishing a connection between active region outflows and the solar wind: Abundance measurements with EIS/Hinode*, ApJ 727, L13, [60 c, 9 c/y].

Brooks, D.H. and Warren, H.P. 2012, *The coronal source of EUV profile asymmetries in solar active region outflows*, ApJ 760, L5, [24 c, 4 c/y].

Culhane, J.L., Brooks, D.H., van Driel-Gesztelyi, L., et al. 2014, *Tracking solar active region outflow plasma from its source to the near-Earth environment*, SoPh 289, 3799, [3 c, 1 c/y].

DelZanna, G. 2008, *Flows in active region loops observed by Hinode EIS*, A&A 481, L49, [115 c, 12 c/y].

Démoulin, P., Baker, D., Mandrini, C.H., et al. 2013, *The 3-D geometry of active region upflows deduced from their limb-to-limb evolution*, SoPh 283, 341, [14 c, 3 c/y].

Doschek, G.A., Warren, H.P., Mariska, J.T., et al. 2008, *Flows and nonthermal velocities in solar active regions observed with the EIS on Hinode: A tracer of active region sources of heliospheric magnetic fields?* ApJ 686, 1362, [114 c, 12 c/y].
Doschek, G.A. 2012, *The dynamics and heating of active region loops*, ApJ 754, 153, [22 c, 4 c/y].
Habbal, S.R., Scholl, I.F., and McIntosh, S.W. 2008, *Impact of active regions on coronal hole outflows*, ApJ 683, L75, [6 c, 0.6 c/y].
Harra, L.K., Hara, H., Imada, S., et al. 2007, *Coronal dimming observed with Hinode: Outflows related to a coronal mass ejection*, PASJ 59, S801, [59 c, 6 c/y].
Harra, L.K., Archontis, V., Pedram, E., et al. 2012, *The creation of outflowing plasma in the corona at emerging flux regions: Comparing observations and simulations*, SoPh 278, 47, [18 c, 3 c/y].
Harra, L.K., Sakao, T., Mandrini, C.H., et al. 2008, *Outflows at the edges of active regions: contribution to solar wind formation ?* ApJ 676, L147, [117 c, 12 c/y].
He, J.S., Marsch, E., Tu, C.Y., et al. 2010, *Intermittent outflows at the edge of an active region - A possible source of the solar wind?* A&A 516, A14, [33 c, 4 c/y].
Murray, M.J., Baker, D., van Driel-Gesztelyi, et al. 2010, *Outflows at the edges of an active region in a coronal hole: A signature of active region expansion?* SoPh 261, 253, [36 c, 5 c/y].
Sakao, T., Kano, R., Narukage, N., et al. 2007, *Continuous plasma outflows from the edge of a solar active region as a possible source of solar wind*, Science 318, 1585, [131 c, 12 c/y].
Slemzin, V., Harra, L., Urnov, A., et al. 2013, *Signatures of slow solar wind streams from active regions in the inner corona*, SoPh 286, 157, [15 c, 3 c/y].
Tian, H., McIntosh, S.W., and De Pontieu, B. 2011, *The spectroscopic signature of quasi-periodic upflows in active region timeseries*, ApJ 727, L37, [70 c, 11 c/y].
Tu, C.Y., Zhou, C., Marsch, E., et al. 2005, *Solar wind origin in coronal funnels*, Science 308, Issue 5721, 519, [178 c, 14 c/y].
van Driel-Gesztelyi, L., Culhane, J.L., Baker, D., et al. 2012, *Magnetic topology of active regions and coronal holes: Implications for coronal outflows and the solar wind*, SoPh 281, 237, [34 c, 6 c/y].
Zangrilli, L. and Poletto, G. 2016, *Evolution of active region outflows throughout an active region lifetime*, A&A 594, A40, [4 c, 2 c/y].

(8.7) Active Regions: Heating

Antolin, P. and Shibata, K. 2010, *The role of torsional Alfvén waves in coronal heating*, ApJ 712, 494, [43 c, 6 c/y].
Antolin, P., Shibata, K., and Vissers, G. 2010, *Coronal rain as a marker for coronal heating mechanisms*, ApJ 716, 154, [56 c, 7 c/y].
Aschwanden, M.J., Nightingale, R.W., and Alexander, D. 2000, *Evidence for nonuniform heating of coronal loops inferred from multithread modeling of TRACE data*, ApJ 541, 1059, [234 c, 13 c/y].
Aschwanden, M.J. 2001, *An evaluation of coronal heating models for active regions based on Yohkoh, SOHO, and TRACE observations*, ApJ 560, 1035, [91 c, 6 c/y].
Aschwanden, M.J., Winebarger, A., Tsiklauri, D. et a. 2007, *The coronal heating paradox*, ApJ 659, 1673, [75 c, 7 c/y].
Asgari-Targhi, M. and van Ballegooijen, A.A. 2012, *Model for Alfvén wave turbulence in solar coronal loops: Heating rate profiles and temperature fluctuations*, ApJ 746, 81, [40 c, 7 c/y].
Asgari-Targhi, M., van Ballegooijen, A.A., Cranmer, S.R., et al. 2013, *The spatial and temporal dependence of coronal heating by Alfvén wave turbulence*, ApJ 773, 111, [37 c, 8 c/y].
Bradshaw, S.J., Klimchuk, J.A., and Reep, J.W. 2012, *Diagnosing the time-dependence of active region core heating from the emission measure. I. Low-frequency nanoflares*, ApJ 758, 53, [38 c, 7 c/y].

Brosius, J.W., Daw, A.N., and Rabin, D.M. 2014, *Pervasive faint Fe XIX emission from a solar active region observed with EUNIS-13: Evidence for nanoflare heating*, ApJ 790, 112, [28 cm 8 c/y].

Cargill, P.J. 2014, *Active region emission measure distributions and implications for nanoflare heating*, ApJ 784, 49. [27 c, 8 c/y].

Cargill, P.J., Warren, H.P., and Bradshaw, S.J. 2015, *Modelling nanoflares in active regions and implications for coronal heating mechanisms*, Phil.Trans.Royal Soc. A, 373, 20140260, [13 c, 5 c/y].

DeMoortel, I. and Browning, P. 2015, *Recent advances in coronal heating*, Philosophical Transactions Royal Society A 373, 2042, p.20140269, [27 c, 11 c/y].

Hara, H., Watanabe, T., Harra, L.K., et al. 2008, *Coronal plasma motions near footpoints of active region loops revealed from spectroscopic observations with Hinode EIS*, ApJ 678, L67, 125 c, 13 c/y].

Klimchuk, J.A. 2006, *On solving the coronal heating problem*, SoPh 234, 41, [468 c, 41 c/y].

Klimchuk, J.A. 2015, *Key aspects of coronal heating*, Royal Society of London Philosophical Transactions Series A, 373, p.20140256, [44 c, 18 c/y].

Lionello, R., Alexander, C.E., Winebarger, A.R., et al. 2016, *Can large time delays observed in light curves of coronal loops be explained in impulsive heating ?* ApJ 818, 129, [9 c, 6 c/y].

Mandrini, C.H., Démoulin, P., and Klimchuk, J.A. 2000, *Magnetic field and plasma scaling laws: Their implications for coronal heating models*, ApJ 530, 999, [141 c, 8 c/y].

Parker, E.N. 1988, *Nanoflares and the solar X-ray corona*, ApJ 330, 474, [1025 c, 35 c/y].

Rappazzo, A.F., Velli, M., Einaudi, G., et al. 2007, *Coronal heating, weak turbulence, and scaling laws*, ApJ 657, L47, [91 c, 9 c/y].

Rappazzo, A.F., Velli, M., Einaudi, G., et al. 2008, *Nonlinear dynamics of the Parker scenario for coronal heating*, ApJ 677, 1348, [120 c, 13 c/y].

Reep, J.W., Bradshaw, S.J., and Klimchuk, J.A. 2013, *Diagnosing the time dependence of active region core heating from the emission measure. II. Nanoflare trains*, ApJ 764, 193, [25 c, 6 c/y].

Schmieder, B., Rust, D.M., Georgoulis, M.K., et al. 2004, *Emerging flux and the heating of coronal loops*, ApJ 601, 530, [62 c, 5 c/y].

Schrijver, C.J., Sandman, A.W., Aschwanden, M.J., et al. 2004, *The coronal heating mechanism as identified by full-sun visualizations*, ApJ 615, 512, [97 c, 7 c/y].

Testa, P., De Pontieu, B., Martinez-Sykora, J., et al. 2013, *Observing coronal nanoflares in active region moss*, ApJ 770, L1, [49 c, 11 c/y].

Tripathi, D., Klimchuk, J.A., and Mason, H.E. 2011, *Emission measure distribution and heating of two active region cores*, ApJ 740, 111, [50 c, 8 c/y].

Ugarte-Urra, I., Winebarger, A.R., and Warren, H.P. 2006, *An investigation into the variability of heating in a solar active region*, ApJ 643, 1245, [44 c, 4 c/y].

van Ballegooijen, A.A., Asgari-Targhi, M., and Berger, M.A. 2014, *On the relationship between photospheric footpoint motions and coronal heating in solar active regions*, ApJ 787, 87, [34 c, 10 c/y].

Viall, N.M. and Klimchuk, J.A. 2011, *Patterns of nanoflare storm heating exhibited by an active region observed with SDO/AIA*, ApJ 738, 24, [63 c, 10 c/y].

Viall, N.M. and Klimchuk, J.A. 2012, *Evidence for widespread cooling in an active region observed with the SDO/AIA*, ApJ 753, 35, [56 c, 10 c/y].

Warren, H.P., Winebarger, A.R., and Brooks, D.H. 2010, *Evidence for steady heating: Observations of an active region core with Hinode and TRACE*, ApJ 711, 228, [51 c, 7 c/y].

Winebarger, A.R., Schmelz, J.T., Warren, H.P., et al. 2011, *Using a differential emission measure and density measurements in an active region core to test a steady heating model*, ApJ 740, 2, [74 c, 11 c/y].

(8.8) Active Regions: 3-D MHD Simulations

Abbett, W.P. and Fisher, G.H. 2003, *A coupled model for the emergence of active region magnetic flux tube into the solar corona*, ApJ 582, 475, [48 c, 3 c/y].

Aschwanden, M.J., Wuelser, J.P., Nitta, N., et al. 2009, *First 3-D reconstruction of coronal loops with STEREO A+B spacecraft. III. Instant stereoscopic tomography of active regions*, ApJ 695, 12, [27 c, 3 c/y].

Bingert, S. and Peter, H. 2011, *Intermittent heating in the solar corona employing a 3D MHD model*, A&A 530, A112, [70 c, 11 c/y].

Bingert, S. and Peter, H. 2013, *Nanoflare statistics in an active region 3D MHD coronal model*, A&A 550, A30, [23 c, 5 c/y].

Bjorgen, J.P. and Leenaarts, J. 2017, *Numerical non-LTE 3D radiative transfer using a multigrid method*, A&A 599, A118.

Bourdin, P.A., Bingert, S., and Peter, H. 2013, *Observationally driven 3D MHD model of the solar corona above an active region*, A&A 555, A123, [28 c, 6 c/y].

Bourdin, P.A., Bingert, S., and Peter, H. 2015, *Coronal energy input and dissipation in a solar active region 3D MHD model*, A&A 580, A72, [7 c, 3 c/y].

Bourdin, P.A., Bingert, S., and Peter, H. 2016, *Scaling laws of coronal loops compared to a 3D MHD model of an active region*, A&A 589, A86, [5 c, 3 c/y].

Carlsson, M. and Stein, R.F. 2002, *Dynamic hydrogen ionization*, ApJ 572, 626, [139 c, 9 c/y].

Chen, F., Peter, H., Bingert, S., et al. 2014, *A model for the formation of the active region corona driven by magnetic flux emergence*, A&A 564, A12, [17 c, 5 c/y].

Cheung, M.C.M., Schüssler, M., Tarbell, T.D., et al. 2008, *Solar surface emerging flux regions: A comparative study of radiative MHD modeling and Hinode SOT observations*, ApJ 687, 1373, [127 c, 13 c/y].

Cheung, M.C.M., Rempel, M., Title, A.M., et al. 2010, *Simulation of the formation of a solar active region*, ApJ 720, 233, [167 c, 22 c/y].

Cheung, M.C.M. and DeRosa, M.L. 2012, *A method for data-driven simulations of evolving solar active regions*, ApJ 757, 147, [42 c, 8 c/y].

Dalmasse, K., Aulanier, G., Démoulin, P., et al. 2015, *The origin of net electric currents in solar active regions*, ApJ 810, 17, [8 c, 3 c/y].

Fang, F., and Fan, Y. 2015, *δ-sunspot formation in simulation of active region scale flux emergence*, ApJ 806, 79, [9 c, 4 c/y].

Golding, T.P., Leenaarts, J., and Carlsson, M. 2016, *Nonequilibrium helium ionization in an MHD simulation of the solar atmosphere*, ApJ 817, 125, [9 c, 6 c/y].

Gudiksen, B.V. and Nordlund, A. 2002, *Bulk heating and slender magnetic loops in the solar corona*, ApJ 572, L113, [106 c, 7 c/y].

Gudiksen, B.V. and Nordlund, A. 2005a, *An Ab initio approach to solar coronal loops*, ApJ 618, 1031, [90 c, 6 c/y]

Gudiksen, B.V. and Nordlund, A. 2005b, *An Ab initio approach to the solar coronal heating problem*, ApJ 618, 1020, [173 c, 11 c/y].

Gudiksen, B.V., Carlsson, M., Hansteen, V.H. et al. 2011, *The stellar atmospher simulation code Bifrost. Code description and validation*, ApJ 531, 154, [140 c, 22 c/y].

Kanella, C. and Gudiksen, B.V. 2017, *Identification of coronal heating events in 3D simulations*, A&A 603, A83, [1 c, 1 c/y].

Lundquist, L.L, Fisher, G.H., and McTiernan, J.M. 2008, *Forward modeling of active region coronal emissions. I. Methods and testing.* ApJSS 179, 533, [26 c, 3 c/y].

MacTaggart, D. 2011, *Flux emergence within mature solar active regions*, A&A 531, A108, [12 c, 2 c/y].

Martinez-Sykora, J., De Pontieu, B., and Hansteen, V. 2012, *2-D radiative MHD simulations of the importance of partial ionization in the chromosphere*, ApJ 753, 161, [58 c, 11 c/y].

Rempel, M. and Cheung, M.C.M. 2014, *Numerical simulations of active region scale flux emergence: From spot formation to decay*, ApJ 785, 90, [51 c, 15 c/y].

Savcheva, A., Pariat, E., van Ballegooijen, A., et al. 2012, *Sigmoidal active region on the Sun: Comparison of a MHD simulation and a nonlinear force-free field model*, ApJ 750, 15, [71 c, 13 c/y].
Török, T., Leake, J.E., Titov, V.S., et al. 2014, *Distribution of electric currents in solar active regions*, ApJ 782, L10, [25 c, 7 c/y].

(8.9) Active Regions: Correlations

Benevolenskaja, E.E., Kosovichev, A.G., Lemen, J.R., et al. 2002, *Large-scale solar coronal structures in soft X-rays and their relationship to the magnetic flux*, ApJ 571, L181, [34 c, 2 c/y].
Fisher, G.H., Longcope, D.W., Metcalf, T.R., et al. 1998, *Coronal heating in active regions as a function of global magnetic variables*, ApJ 508, 885, [115 c, 6 c/y].
Handy, B.N. and Schrijver, C.J. 2001, *On the evolution of the solar photospheric and coronal magnetic field*, ApJ 547, 1100, [21 c, 1 c/y].
Meunier, N. 2003, *Statistical properties of magnetic structures: Their dependence on scale and solar activity*, A&A 405, 1107, [83 c, 3 c/y].
Parker, E.N. 1983, *Magnetic neutral sheets in evolving fields - Part Two - Formation of the solar corona*, ApJ 264, 642, [436, 13 c/y].
Rosner, R., Tucker, W.H., and Vaiana, G.S. 1978, *Dynamics of the quiescent solar corona*, ApJ 220, 643, [1301 c, 33 c/y].
Schrijver, C.J., Sandman, A.W., Aschwanden, M.J., et al. 2004, *The coronal heating mechanism as identified by full-Sun visualizations*, ApJ 615, 512, [97 c, 7 c/y].
Serio, S., Peres, G., Vaiana, G.S., et al. 1981, *Closed coronal structures. II. Generalized hydrostatic model*, ApJ 243, 288, [272 c, 7 c/y].
van Driel-Gesztelyi, L., Démoulin, P., Mandrini, C.H., et al. 2003, *The long-term evolution of AR 7978: The scalings of the coronal plasma parameters with the mean photospheric magnetic field*, ApJ 586, 579, [36 c, 2 c/y].
Warren, H.P. and Winebarger, A.R. 2006, *Hydrostatic modeling of the integrated soft X-ray and extreme ultraviolet emission in solar active regions*, ApJ 645, 711, [55 c, 5 c/y].
Wolfson, R., Roald, C.B., Sturrock, P.A., et al. 2000, *Coronal X-ray brightness and photospheric magnetic field: A study in correlations*, ApJ 539, 995, [18 c, 1 c/y].

(8.10) Active Regions: Coronal Streamers

Airapetian, V., Ofman, L., Sittler, E.C. et al. 2011, *Probing the thermodynamics and kinematics of solar coronal streamers*, ApJ 728, 67, [10 c, 2 c/y].
Bemporad, A., Sterling, A.C., Moore, R.L., et al. 2005, *A new variety of coronal mass ejection: Streamer puffs from compact ejective flares*, ApJ 635, L189, [41 c, 3 c/y].
Chen, Y., Song, H.Q., Li, B., et al. 2010, *Streamer waves driven by coronal mass ejections*, ApJ 714, 644, [32 c, 4 c/y].
Feng, S.W., Chen, Y., Kong, X.L., et al. 2012, *Radio signatures of coronal mass ejection streamer interaction and source diagnostics of type II radio burst*, ApJ 753, 21, [29 c, 5 c/y].
Frazin, R.A., Cranmer, S.R., and Kohl, J.L. 2003, *Empirically determined anisotropic velocity distributions and outflows of O^{5+} ions in a coronal streamer at solar minimum*, ApJ 597, 1145, [59 c, 4 c/y].
Frazin, R.A., Vasquez, A.M., Kamalabadi, F., et al. 2007, *3-D tomographic analysis of a high-cadence LASCO-C2 polarized brightness sequence*, ApJ 671, L201, [23 c, 2 c/y].
Gary, G.A. 2001, *Plasma beta above a solar active region: Rethinking the paradigm*, SoPh 203, 71,[262 c, 16 c/y].

Kramar, M., Jones, S., Davila, J., et al. 2009, *On the tomographic reconstruction of the 3D electron density for the solar corona from STEREO COR1 data*, SoPh 259, 109, [27 c, 3 c/y].

Kramar, M., Airapetian, V., Mikic, Z., et al. 2014, *3D coronal density reconstruction and retrieving the magnetic field structure during solar minimum*, SoPh 289, 2927, [14 c, 4 c/y].

Liewer, P.C., Hall, J.R., De Jong, M. et al. 2001, *Determination of 3-D structure of coronal streamers and relationship to the solar magnetic field*, JGR 106/A8, 15903, [26 c, 2 c/y].

Lynch, B.J., Li, Y., Thernisien, A.F.R. et al. 2010, *Sun to 1 AU propagation and evolution of a slow streamer-blowout coronal mass ejection*, JGR 115/A7, A07106, [31 c, 4 c/y].

Morgan, H., Habbal, S.R., and Lugaz, N. 2009, *Mapping the structure of the corona using Fourier backprojection tomography*, ApJ 690, 1119, [17 c, 2 c/y].

Morgan, H. and Habbal, S.R. 2010, *Observational aspects of the 3-D coronal structure over a solar activity cycle*, ApJ 710, 1, [21 c, 3 c/y].

Morgan, H. 2011, *The rotation of the white light solar corona at height 4 R_{sun} from 1996 to 2010: Tomographical study of Large Angle and Spectrometric Coronagraph C2 Observations*, ApJ 738, 189, [10 s, 2 c/y].

Ofman, L. 2000, *Source regions of the slow solar wind in coronal streamers*, GRL 27/18, 2885, [36 c, 2 c/y].

Parenti, S., Bromage, B.J.I. 2000, *Characteristics of solar coronal streamers. Element abundance, temperature and density from coordinated CDS and UVCS SOHO observations*, A&A 363, 800, [61 c, 3 c/y]

Saez, F., Zhukov, A.N., Lamy, P., et al. 2005, *On the 3-D structure of the streamer belt of the solar corona*, A&A 442, 351, [18 c, 1 c/y].

Saez, F., Llebaria, A., Lamy, P., et al. 2007, *3-D reconstruction of the streamer belt and other large-scale structures of the solar corona. I. Method*, A&A 473, 265, [22 c, 2 c/y].

Sheeley, N.R.Jr. and Wang, Y.M. 2007, *In/out pairs and the detachment of coronal streamers*, ApJ 655, 1142, [43 c, 4 c/y].

Sheeley, N.R., Lee, D.D.H., Casto, K.P. et al. 2009, *The structure of streamer blobs*, ApJ 694, 1471, [51 c, 6 c/y].

Sheeley, N.R.Jr. and Rouillard, A.P. 2010, *Tracking streamer blobs into the heliosphere*, ApJ 715, 300, [21 c, 3 c/y].

Wang, Y.M., Sheeley, N.R., Socker, D.G., et al. 2000a, *The dynamical nature of coronal streamers*, JGR 105, A11, 25133, [120 c, 7 c/y].

Wang, Y.M., Sheeley, N.R.Jr., and Rich, N.B. 2000b, *Evolution of coronal streamer structure during the rising phase of solar cycle 23*, GRL 27/2, 149, [44 c, 3 c/y].

Wang, Y.M., Sheeley, N.R., and Rich, N.B. 2007, *Coronal pseudostreamers*, ApJ 658, 1340, [109 c, 10 c/y].

Yeates, A.R., Amari, T., Contopoulos, I., et al. 2018, *Global non-potential magnetic models of the solar corona during the March 2015 eclipse*, SSRv 214, 99.

Zuccarello, F.P., Bemporad, A., Jacobs, C., et al. 2012, *The role of streamers in the deflection of coronal mass ejections: Comparison between STEREO 3-D reconstructions and numerical simulations*, ApJ 744, 66, [53 c, 10 c/y].

Chapter 9
Coronal Loops

9.1 Coronal Loops: Stereoscopy and 3-D Geometry

The most ubiquitous structures in the solar corona are *loops*, often appearing with approximately semi-circular geometry, obviously representing visible manifestations of closed magnetic field lines. The magnetic field is not directly visible in any wavelength, but our knowledge of its topology and geometry is based on our understanding that some field-aligned coronal structures become filled with hot plasma that radiates in EUV and soft X-rays, and this way illuminates selected bundles of magnetic field lines. The super-position of myriads of illuminated loops in multi-polar active regions can lead to EUV and soft X-ray images with fairly complex topology, but in principle can be rendered with a suitable 3-D magnetic field model and hydrostatic 1-D loop models for each field line, as demonstrated for active regions observed with SXT/Yohkoh (Gary 1997; Lundquist et al. 2008), or with full-Sun visualizations (Schrijver et al. 2004).

A number of exercises have been conducted to adjust a theoretical magnetic field model to the observed 2-D projections of coronal loops, such as radial stretching of a potential field (Gary and Alexander 1999), varying the α-parameters in linear force-free field models (Wiegelmann and Neukirch 2002), forward-fitting of a series of submerged dipoles (Sandman and Aschwanden 2011), or varying the α-parameters in vertical current approximations of nonlinear force-free fields (Aschwanden 2013). What became clear even in the pre-STEREO era is that the 3-D geometry of observed coronal loops is not consistent with potential fields, as demonstrated for a sample of $\approx$ 60 loops in an active region observed with SOHO/EIT and reconstructed with the solar-rotation stereoscopy method (Aschwanden et al. 1999, 2000).

The launch of STEREO in 2006 augmented previous solar rotation-based methods with a new opportunity to conduct true stereoscopy, performed with two identical spacecraft with a suitable separation angle. The very first results from EUVI/STEREO/A and B reported the triangulation of $\approx$ 50 loops viewed at a

M. J. Aschwanden, *New Millennium Solar Physics*, Astrophysics and Space Science Library 458, https://doi.org/10.1007/978-3-030-13956-8_9

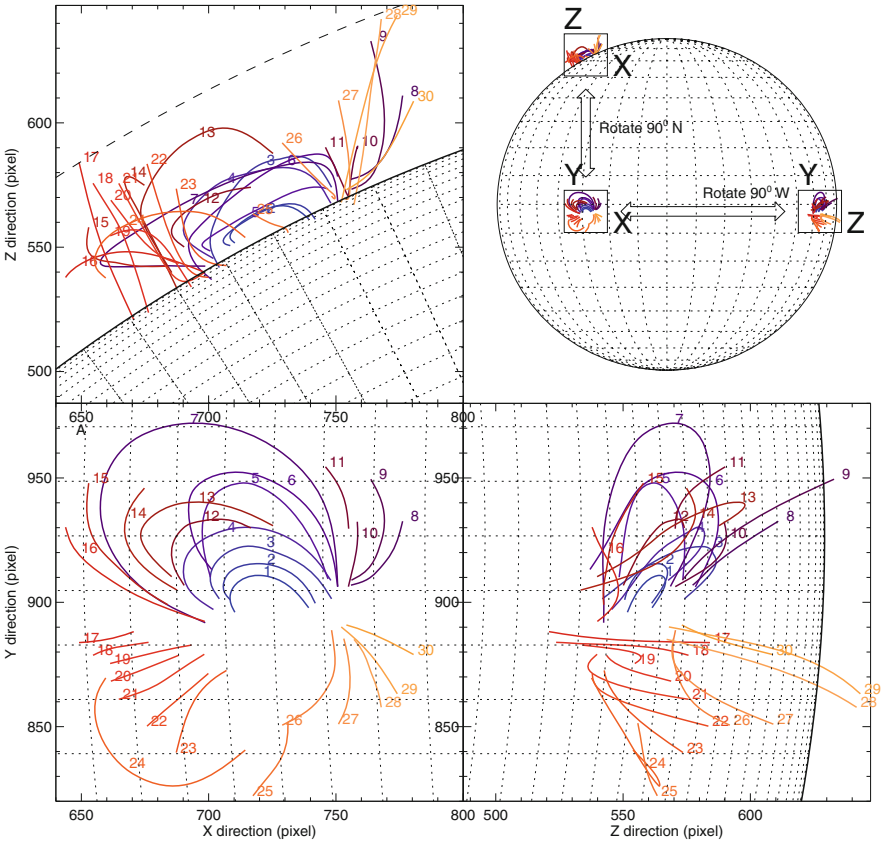

Fig. 9.1 3-D representation of 30 stereoscopically triangulated loops observed with EUVI/STEREO/A and B on 2007 May 9: in the XY plane (bottom left); in the ZX plane or rotated by 90° to the west (bottom right); and in the XZ plane, rotated by 90° to the north (top left). A synopsis of the rotations of the three perspectives is shown in the top right frame (Aschwanden et al. 2008)

spacecraft separation angle of $\approx$ 12° (Feng et al. 2007). The stereoscopic 3-D geometry of only $\approx$ 10 (out of 50) loops could locally be modeled with a linear force-free model, while no model could fit all triangulated loops, leading to the conclusion that linear force-free models are not adequate to explain the observed 3-D geometry of active region loops. Somewhat earlier on, when the STEREO/A and B had a spacecraft separation angle of 7°, a number of 30 loop structures (7 complete and 23 partial segments) were stereoscopically triangulated (Fig. 9.1), yielding the height range, stereoscopic height measurement errors, the loop plane inclination angles, and measurements of the coplanarity and circularity of the loops (Aschwanden et al. 2008). The loops were found to have large inclination angles from the vertical ($\theta \approx 36°–73°$), curvature radius variations of 3%–30%, and deviations from planarity by 3%–13% of the loop baselines (Fig. 9.2). The

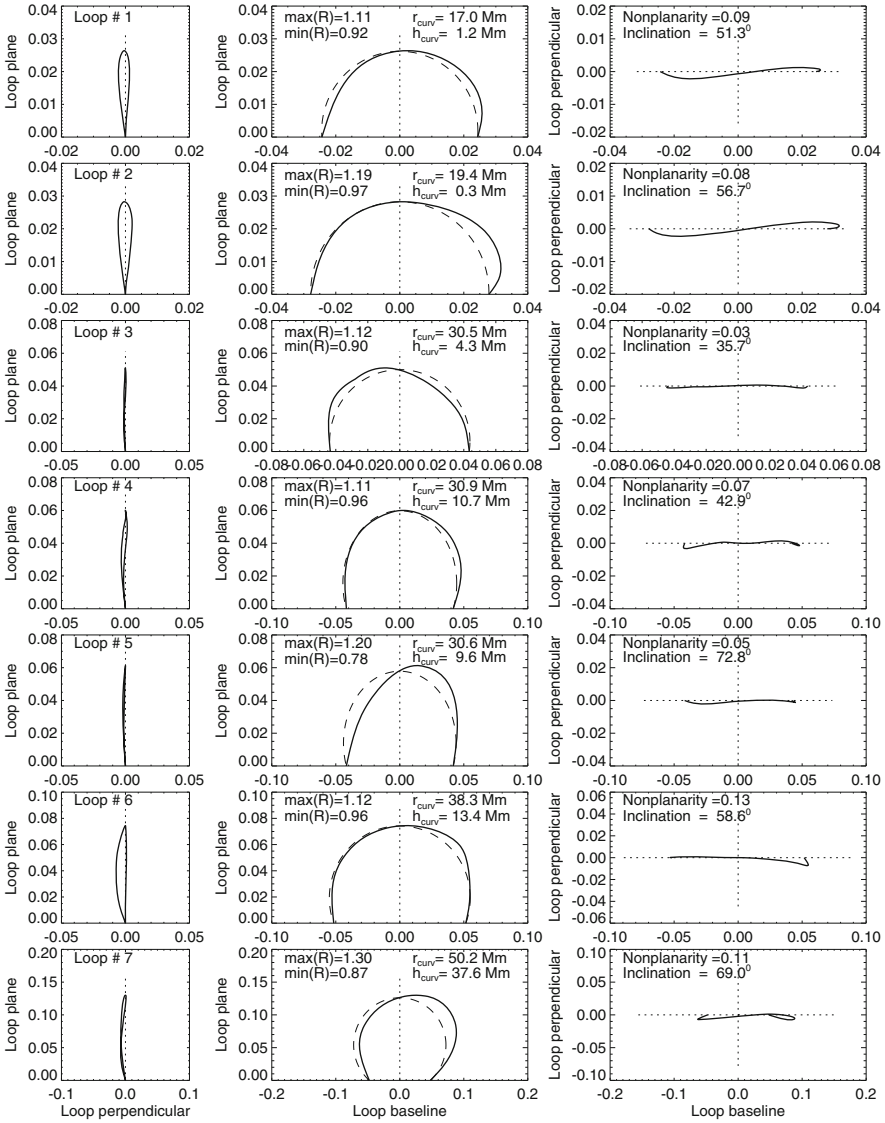

Fig. 9.2 Projections of 7 complete loops (of the same set as shown in Fig. 9.1) are shown in the loop plane (middle panels) and in orthogonal directions, from the side (left panels), and from top (right panels). The loop plane is defined by the two footpoints and the loop top above the midpoint between the footpoints. A circle is also interpolated through these 3 points in order to visualize the circularity (dashed linestyle). Note the deviations from coplanarity in the side view (left panel) and top view (right panel) (Aschwanden et al. 2008)

knowledge of the exact 3-D geometry of a loop with respect to the observers line-of-sight has important consequences for determining the correct vertical density scale height (used in hydrostatic models), the aspect angle of loop cross-sections (used in inferring electron densities from optically thin emission measures), the absolute flow speeds (used in siphon flow models), the correct loop length (used in loop scaling laws), as well as the 3-D vectors of the coronal magnetic field (used in testing theoretical magnetic field extrapolation models). Extreme deviations from a semi-circular geometry were found in oscillating loops, which appear to have strong helical twist (Aschwanden 2009). Stereoscopic triangulation of coronal loops is feasible from small ($\gtrsim 6°$) to large angles ($\lesssim 170°$) of the spacecraft separation, but the ambiguity in the identification of corresponding loop pairs becomes more severe for large angles $\gtrsim 30°$ (Aschwanden et al. 2012).

Statistics of geometric parameters is useful for testing physical scaling laws. For coronal loops, which often ressemble slender long structures, we can measure their length L and their width w. The loop lengths range from the smallest detectable size of $L_{min} \approx 1$ Mm to the size of the largest active region, $L_{max} \lesssim 250$ Mm, so they cover at least two orders of magnitude in scale, generally outlining incomplete segments of magnetic field lines.

9.2 Coronal Loops: Cross-Sectional Widths

The reduction from 3-D to 1-D hydrodynamics in coronal loops requires the definition of a cross-sectional dependence of a flux tube area $A(s)$ as a function of the loop length coordinate s, which is assumed to be constant in the simplest case. Another fundamental assumption is the monolithic structure of coronal loops, which is likely to break down for large loop widths. It is therefore imperative to measure the width of coronal loops with high-resolution instruments and to test their homogeneity (in the case of monolithic loops) or inhomogeneity (in the case of multi-stranded loops).

Cross-sectional widths of coronal loops have been measured with many different instruments (Dunn/SacPeak, Pic du Midi, Skylab, NRAO, VLA, ASE rocket, CSIRO, LMSAL rocket, SXT/Yohkoh, EIT/SOHO, TRACE, EIS/Hinode, CRISP, AIA/SDO, Hi-C, SOT/Hinode, IRIS) and wavelengths (optical, Hα, Lyα, EUV, soft X-rays, and radio). A compilation of 53 studies on loop width measurements is depicted in Fig. 9.3, showing the loop widths (on the x-axis) sorted by increasing widths (on the y-axis). The numbered references are listed in the original paper (Aschwanden and Peter 2017), from which we cite the most recent ones with the highest spatial resolution only (after 2010): Aschwanden and Wülser (2011 [37]); Aschwanden and Boerner (2011 [38]); Aschwanden and Schrijver (2011 [39]); Aschwanden et al. (2013 [43]); Mulu-Moore et al. (2011 [40]); Brooks et al. (2012 [41], 2013 [45], 2016 [51]); Antolin and Rouppe van der Voort (2012 [42]); Peter et al. (2013 [44]); Winebarger et al. (2013 [46], 2014 [49]);

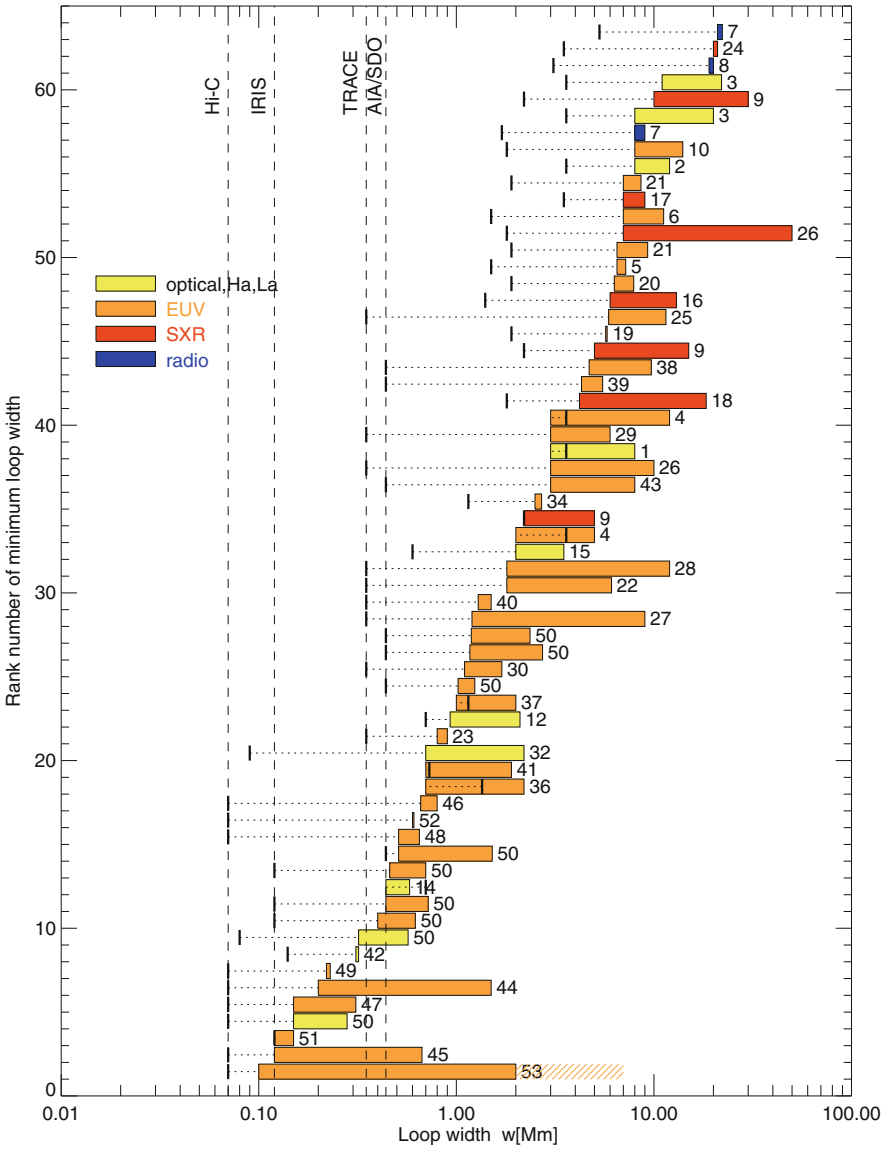

Fig. 9.3 Compilation of loop width measurements from literature during 1963–2017: The measured ranges are represented by blocks, colored by wavelength regimes (yellow=optical, Hα, Lα; orange=EUV, red=SXR, and blue=radio), labeled with the reference number cited in the text, and sorted by the increasing minimum width on the y-axis. The instrumental pixel size (or resolution if pixel size is not known) is indicated with a black thick bar for each measurement (adapted from Aschwanden and Peter 2017)

Morton and McLaughlin (2013 [47]); Alexander et al. (2013 [48]); Antolin et al. (2015 [50]); Tiwari et al. (2016 [52]); Aschwanden and Peter (2017 [53]).

The graphical representation in Fig. 9.3 divides the loop width measurements into 4 wavelength regimes by color (optical + Hα + Lyα, EUV, soft X-rays, and radio), and ranks the width ranges by the smallest detected width in ascending order. There are several trends visible in Fig. 9.3. Minimum loop widths have been measured from $w \approx 20$ Mm down to $w_{min} \approx 0.1$ Mm. The finest loop widths have been detected preferentially in EUV, while the loop widths measured in soft X-rays and optical wavelengths tend to be significantly larger, and are found to be largest in radio wavelengths. Since coronal loops in EUV and soft X-rays are produced by optically thin line emission, the density contrast of individual loops is much "crisper" than in structures detected in the optically thick regime of free-free and gyroresonance emission in radio wavelengths.

In Fig. 9.3 we can see also that the smallest loop widths are typically measured approximately at 2–4 pixels above the instrumental pixel sizes, which is partially explained by the point spread function that typically amounts to $w_{psf} \approx 2.5$ pixels in most EUV imagers (TRACE, AIA/SDO, STEREO, IRIS, Hi-C). Some additional scatter in the order of $w_{noise} \approx 1$ pixel is due to the noise in the background subtraction, so that the observed loop width w is broadened by,

$$w \approx \sqrt{w_{true}^2 + w_{psf}^2 + w_{noise}^2} \,, \tag{9.2.1}$$

if we add the uncertainties in quadrature. We may ask whether the distribution of loop sizes continues at the low end, if future instruments faciliate higher spatial resolutions. However, several studies with the highest available spatial resolution, with a pixel size of $w_{pixel} \approx 0.1'' \approx 70$ km for the Hi-C instrument, have demonstrated that AIA resolves many of the loops, as shown in Fig. 9.4. The smallest loops measured from recent Hi-C studies cover ranges of $w = 200$–1500 km (Peter et al. 2013), $w = 117$–667 km (Brooks et al. 2013), $w = 150$–310 km (Morton and McLaughlin 2013), $w = 120$–150 km (Brooks et al. 2016), with a most frequent width of $w \approx 500$ km (Aschwanden and Peter 2017).

There is no widely accepted theoretical model for the cross-sectional widths of coronal loops. The intrinsic loop widths supposedly reveal the cross-sectional area over which energy is deposited in a magnetic flux tube during an elementary heating event. However, since the basic coronal heating mechanism is still elusive, one can not predict the range of loop widths. Parker's nanoflare scenario envisions unresolved loop strands, while heating mechanisms with cross-field diffusion in a high-β regime predict monolithic resolved loops (Fig. 8.8). If the latest Hi-C measurements with finite loop widths with a most frequent value of $w \approx 500$ km hold up, we have to conclude that nanoflare strands with widths $w \lesssim 500$ km are negligible in the energy budget of the heating process. The particular value of $w \approx 500$ km apparently demarcates two types of granulation in the solar photosphere: the mini-granulation with a width range of $w \approx 100$–600 km (Abramenko et al. 2012), and the regular granules which have a Gaussian distribution with a mean of $w \approx 1000$ km.

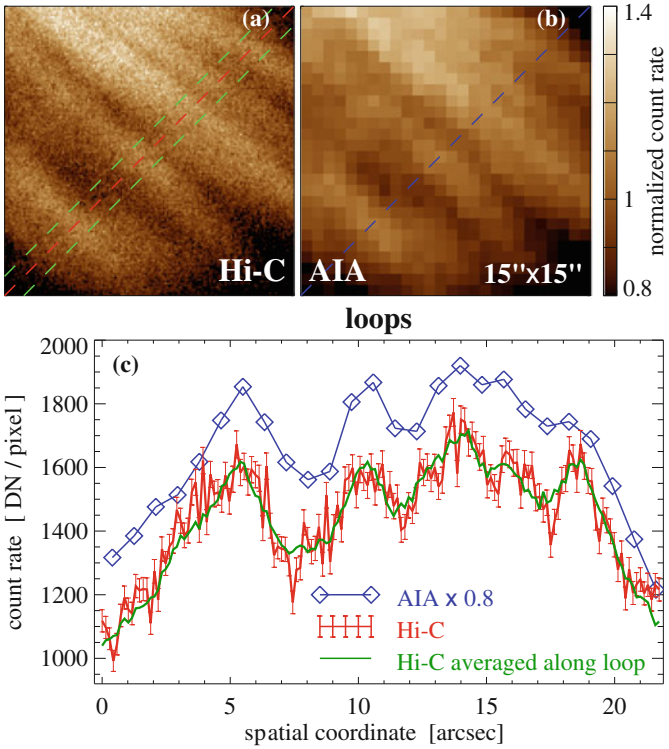

Fig. 9.4 Hi-C 193 Å observations with a pixel size of 0.1″ (**a**), compared with AIA 195 Å observations with a pixel size of 0.6″ (**b**), and cross-sectional profiles (**c**), across a bundle of loops (hashed diagonal lines in top panels). Note that 4–5 loop structures are fully resolved with AIA, while Hi-C shows data noise without additional significant fine structure (from Peter et al. 2013)

9.3 Coronal Loops: Multi-Strand Structure

Hydrodynamic modeling of coronal loops during the last two decades has been generalized from a single flux-tube concept to a multi-stranded macroscopic loop system, which has a number of consequences: (1) the observed macroscopic loops may indeed consist of finer unresolved strands, in particular for instruments with poor spatial resolution, which makes the measured physical parameters instrument-dependent (Fig. 9.5); (2) modeling a multi-stranded loop system introduces additional degrees of freedom (such as filling factors) that makes the interpretation of observables more ambiguous; and (3) the discrimination between homogeneous (monolithic) single loops and the inhomogeneous (multi-stranded) loop systems is tied to macroscopic versus microscopic coronal heating mechanisms, similar to the dichotomy between large-scale flares (for which we resolve the magnetic reconnection geometry) and nanoflares (which we do not resolve). Observationally, the majority of loops measured with arcsecond resolution instruments (TRACE, AIA)

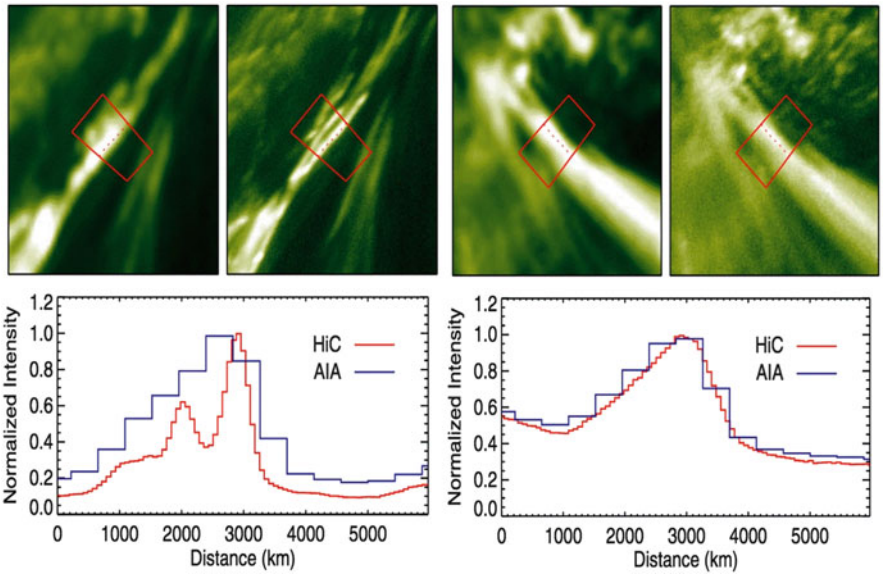

Fig. 9.5 Examples of a multi-strand loop that is resolved with Hi-C but not with AIA (left panels) and a monolithic loop that is fully resolved with both Hi-C and AIA (right panels). For each case, the AIA and Hi-C images at 193 Å are shown, along with intensity profiles (Brooks et al. 2013)

were found to be isothermal (Aschwanden and Nightingale 2005), which is consistent with resolved single loop strands, rather than with multi-stranded loop structures (unless all strands have the same temperature).

Let us review a few lessons we learned from multi-strand loop modeling and observations. The flat temperature profile along coronal loops can be reproduced by both a footpoint-heated monolithic loop or by an ensemble of uniformly heated loops (Reale and Peres 2000), as well as by an ensemble of footpoint-heated loops (Mendoza-Briceno et al. 2002). The discrepancy between the observed decay times of warm loops and the theoretical lifetime inferred from time-dependent hydrostatic simulations can be reconciled with a multi-strand system (Fig. 9.6), while it fails for most monolithic loops (Warren et al. 2002, 2003). Electron density and temperature diagnostics does not discriminate between the spatial form of the heating function in multi-strand (nanoflare) hydrodynamic simulations (Patsourakos and Klimchuk 2005; Sarkar and Walsh 2008, 2009). The temperature of the cold corona ($T_e \approx 1.0$–1.5 MK) as well as the fuzziness of the warm corona ($T_e \approx 2$–3 MK) can be reproduced with nanoflare simulations in a multi-strand corona (Reale et al. 2005, 2011; Guarrasi et al. 2010). Multi-strand hydrodynamic simulations produce modest line broadening (e.g., Ne VII and Mg X) that is consistent with observations (Patsourakos and Klimchuk 2006; Taroyan et al. 2006). Nonthermal widths of hot loops (1–4 MK) measured in non-flaring regions did reveal only small nonthermal velocities ($v = 17.6 \pm 5.3$ km s^{-1}) (Brooks et al. 2016).

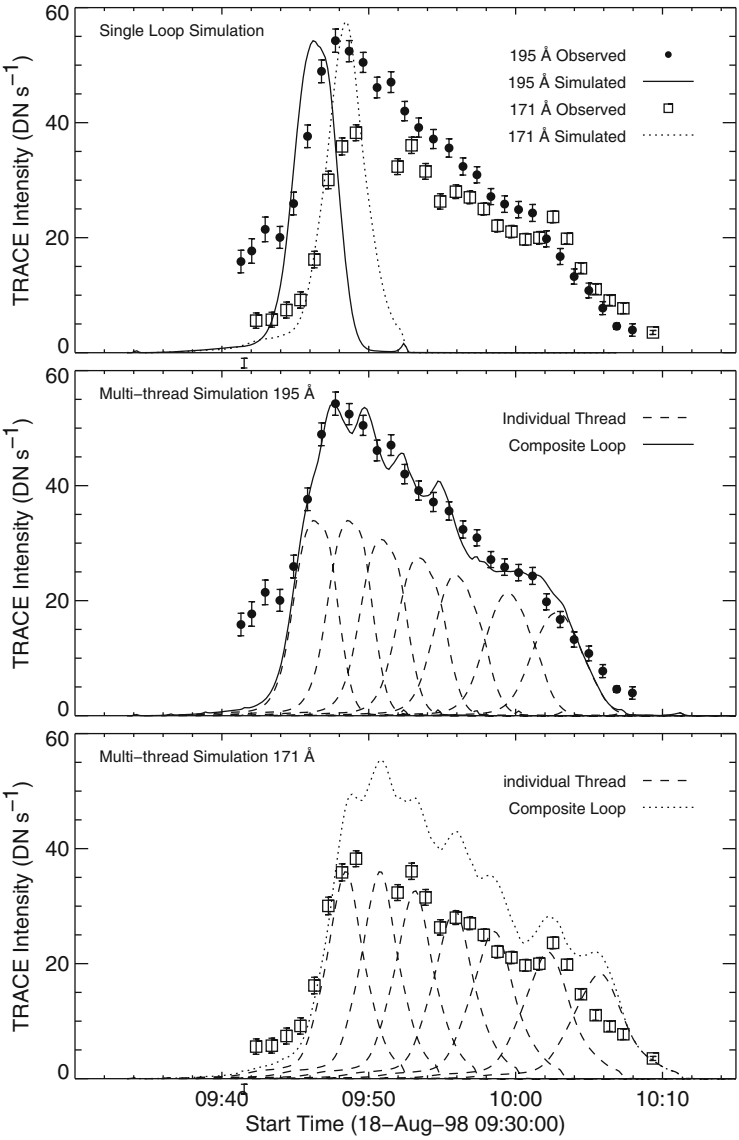

Fig. 9.6 Simulated and observed light curves for the TRACE active region loop observed on 1998 August 18. *Top:* Simulated light curve for a single loop. The delay between the 195 and 171 Å intensities in the simulated light curve matches the observations, but the loop cools too quickly. *Middle and Bottom:* Simulated light curve for a series of threads that are heated sequentially. The initial thread matches the observed delay. Subsequent threads have the same heating duration but smaller peak heating rates (Warren et al. 2003)

Multi-stranded loop models cannot reproduce both the transition region DEM distribution and the coronal DEM distribution with a unique set of parameters (Susino et al. 2010, 2013; Reale and Ciaravella 2006; Winebarger et al. 2011; Mulu-Moore et al. 2011). Hi-C observations (Fig. 9.4) over-resolve some single loops, which have cross-sectional widths of $w \approx 100$–500 km (Peter et al. 2013), implying that most loops with a width of $w \gtrsim 500$ km are likely to be composite or multi-stranded loops (Aschwanden and Peter 2017). Other nanoflare simulations determine filling factors (Jain and Yashiro 2002), spontaneous current sheets in filamentary loop systems (Petrie 2006), statistical models of the inhomogeneous corona (Aschwanden et al. 2007), the effects of filter-ratio analysis on the flat temperature profile in multi-stranded loop models (Bourouaine and Marsch 2010), the multi-thermal and multi-stranded nature of coronal rain (Antolin et al. 2015), or the effects of low-frequency versus high-frequency nanoflare heating (Bradshaw and Klimchuk 2015).

9.4 Coronal Loops: Cross-Sectional Temperature

The 1-D flux tube concept of a coronal loop in principle implies a homogeneous electron pressure, density, and temperature across the loop cross-section. In order to verify the cross-sectional temperature structure of coronal loops, multi-wavelength images observed with EIT/SOHO, TRACE, and AIA/SDO have been analyzed in great detail. The main question focused on the discrimination between monolithic (isothermal) and unresolved multi-stranded (multi-thermal) loop cross-sections. Monolithic (macroscopic) loops are by definition homogeneous in temperature and density across their cross-section, and thus require cross-field transport of plasma from a heating source that is spatially resolved with current instrumentation. In contrast, multi-stranded loop cross-sections are inhomogeneous in temperature and density. They display a broad multi-temperature (differential emission measure) distribution, because the unresolved strands are independently heated by microscopic heating sources, as envisioned in the original nanoflare heating scenarios.

How is the temperature structure measured across a coronal loop or multi-stranded loop system ? In the simplest method, a loop segment has to be identified in an image data set with (n_λ) multiple wavelengths, which yields a set of fluxes $F_i, i = 1, \ldots, n_\lambda$ to which a differential emission measure (DEM) analysis is applied (see Sect. 2.6 and Table 2.3 for an overview of different DEM methods). The outcome of the DEM analysis yields then either a narrow ($\Delta T/T$) $\ll 1$ or a broad DEM distribution ($\Delta T/T \approx 1$). Narrow temperature peaks indicate a near-isothermal structure, while broad DEMs imply a multi-thermal distribution. There are a number of systematic effects that can make the results ambiguous. For instance, if an instrument has a poor spatial resolution, a bundle of closely-spaced loop strands appear as a single loop, which constitutes a strong bias for a broad multi-thermal structure. Moreover, if a loop is observed near or beyond the limb, the observed loop flux is likely to be contaminated by large foreground and

background fluxes, which creates a bias for broad multi-thermal structures, since the target loop and the background are likely to have different temperatures. Therefore, clean results depend very much on the availability of high-resolution instruments, an accurate DEM inversion method, and careful background modeling. A selection of results on the thermality of loop cross-sections is provided in Table 9.1.

Table 9.1 Measurements of isothermal ($\sigma_T = \Delta T/T \lesssim 0.1$) and multi-thermal coronal loop cross-sections. The number of widths specifies how many loop (or thread) widths have been measured in each reference

Instrument	Wavelengths Å	Number of widths	Temperature range	Ref.
CDS, SXT	310–380, 517–633	13	Isothermal, multi-thermal	[1]
TRACE	171, 195	200	Isothermal, multi-thermal	[2]
SUMER, SXT	660–1600	45	Near-isothermal	[3]
CDS, TRACE	173	5	Isothermal	[4]
CDS, TRACE	173, 195	5	Near-isothermal	[5]
XDT, SXT, EIT, CDS	210–213,171,195,284	9	Multi-thermal	[6]
EIT, SUMER	668–1463	5	Isothermal	[7]
EIT	171, 195, 284	50	...	[8]
CDS	310–380, 517–633	3	Multi-thermal	[9]
TRACE	171, 195, 284	3500	Isothermal (84%)	[10]
CDS, EIT	150–785	3	Multi-thermal	[11]
CDS, TRACE	150–785	10	Isothermal	[12]
CDS	150–785	2	Isothermal, multi-thermal	[13]
EIS	171–212, 245–291	20	Near-isothermal	[14]
EIS	171–212, 250–290	1	Multi-thermal	[15]
SUMER	500–1600	3	Near-isothermal	[16]
EIS	170–210, 250–290	2	Near-isothermal	[17]
CDS, TRACE	171, 195, 284	2	Isothermal, multi-thermal	[18]
XRT, EIS	170–210, 250–290	5	Multi-thermal	[19]
AIA	94,131,171,193,211,335	1	Multi-thermal	[20]
AIA	94,131,171,193,211,335	12	Multi-thermal	[21]
EIS, XRT	186–274	1	Multi-thermal	[22]
AIA	94,131,171,193,211,335	12	Isothermal, multi-thermal	[23]
AIA	94,131,171,193,211,335	100	Isothermal (66%)	[24]
AIA	94,131,171,193,211,335	6	Near-isothermal	[25]
AIA	94,131,171,193,211,335	2892	$\sigma_T = 0.24 \pm 0.20$	[26]
AIA	94,131,171,193,211,335	12	Isothermal, multi-thermal	[27]

References: Schmelz (2002) [1]; Schmelz et al. (2001 [1], 2003 [8], 2005 [9], 2007 [13], 2008 [15], 2009 [18], 2010a [19], 2010b [20], 2011a [21], 2011b [22], 2011c [23], 2013 [27]); Testa et al. (2002) [2]; Warren and Warshall (2002) [3]; Del Zanna (2003) [4]; Del Zanna and Mason (2003) [5]; Nagata et al. (2003) [6]; Warren and Winebarger (2003) [7]; Aschwanden and Nightingale (2005) [10]; Schmelz and Martens (2006) [11]; Cirtain et al. (2007) [12]; Warren et al. (2008) [14]; Landi and Feldman (2008) [16]; Tripathi et al. (2009) [17]; Aschwanden and Boerner (2011) [24]; Brooks et al. (2011) [25]; Aschwanden et al. (2013) [26]

A number of criticisms have been raised concerning the various used DEM analysis methods, such as: (1) over-restricted temperature range, i.e., EIT with $T \approx$ 1–2 MK (Schmelz et al. 2003); (2) atomic lines missing in the CHIANTI code, e.g., in the 94 Å band (Aschwanden and Boerner 2011; Del Zanna 2013; Landi and Klimchuk 2010); (3) insufficient spatial resolution, i.e. CDS/SOHO data with a point-spread function of $6'' \times 8''$ (Schmelz 2002; Schmelz et al. 2001, 2003, 2005, 2007, 2009; Del Zanna 2003; Del Zanna and Mason 2003; Cirtain et al. 2007); (4) the ambiguity of the 2-filter-ratio technique (Weber et al. 2005; Martens et al. 2002); (5) the lack of background subtraction (Schmelz et al. 2001; Schmelz 2002); (6) over-smoothing of the fitted DEM function (Schmelz et al. 2001; Aschwanden 2002; Landi and Feldman 2008); (7) isothermal bias for over-estimates of the photometric uncertainty (Patsourakos and Klimchuk 2007); or (8) the choice of the radiative loss function (Reale and Landi 2012; Sasso et al. 2012). What matters additionally is the dynamical condition of a loop: quiescent active region loops often exhibit a narrow (near-isothermal) DEM (if they are spatially resolved), while flaring loops tend to exhibit broadband (multi-thermal) DEMs (e.g., Warren et al. 2013). A statistical rule-of-thumb was found that elementary loop strands: (i) are near-isothermal ($\Delta T \lesssim 0.2$ MK), (ii) have a small width ($w \leq 2$ Mm), and (iii) have a faint contrast ($\lesssim 30\%$) (Aschwanden 2005). Comparing the 27 studies listed in Table 9.1 it appears that isothermal (or near-isothermal) loops are more likely to be detected at "warm coronal temperatures" ($T \approx$ 1–2 MK), using instruments with the highest spatial resolution (TRACE with $0.5''$ and AIA with $0.6''$ pixels), and after proper background subtraction. Loops or multi-strand loop systems are also detected at hotter (flare-like) temperatures ($T \approx$ 3–30 MK), with instruments that have soft X-ray coverage (SXT, CDS, EIS, XRT). However, since these instruments have a relatively poor spatial resolution and often were analyzed without background subtraction, we can not decide whether hot loops are isothermal or multi-thermal.

9.5 Coronal Loops: Flows

Plasma flows in coronal loops require a generalization of static models (with velocity $v = 0$) in the 1-D hydrodynamic equations, enabling the calculation of simple steady-flow solutions ($v = const$), as well as siphon-flow solutions, which are driven by a pressure imbalance between the loop footpoints. An essential feature of steady flow solutions is their acceleration with increasing height (because the electron density decreases due to gravitational stratification and momentum conservation), which can exceed the sound speed and become supersonic and form stationary shocks. There is a wealth of flow patterns that can occur in the solar corona, such as blueshifted upflows, redshifted downflows, siphon flows, turbulent flows, shocks generated by critical or supersonic flows, reconnection inflows, reconnection outflows, etc. In the following we will review new measurements (Table 9.2) and hydrodynamic modeling after 2000, which were mostly obtained with EIS/Hinode and AIA/SDO.

Table 9.2 Flow measurements in the solar corona ($T \approx 0.5$–3.0 MK) after 2000

Observer	Instrument	Wavelength Å	Temperature T_e [MK]	Flow speed v (km s^{-1})
Winebarger et al. (2002)	SUMER, TRACE	780–1610	0.6–2.0	15–40
Feldman et al. (2003)	SUMER	780–1610	2.6–6.6	20–35
Singh et al. (2005)	NOGIS	5303, 6374	0.7	48
Brosius (2005)	CDS, EIT	171–629	0.2–2.0	15–25
Brosius and Landi (2005)	CDS, EIT	171–629	0.2–2.0	52
Doyle et al. (2006)	TRACE, SUMER	171, 1550	0.2–1.0	120
Hara et al. (2008)	EIS	166–211, 246–291	2.0	10–30
Doschek et al. (2008)	EIS	166–211, 246–291	1.2–1.4	20–50
Del Zanna (2008)	EIS	166–211, 246–291	1.0–3.0	5–30
Tripathi et al. (2009)	EIS	166–211, 246–291	1.0–2.0	<60
Warren et al. (2011)	EIS	166–211, 246–291	0.4–2.2	<40
Raju et al. (2011)	Fabry-Perot	5303	1.8–3.1	20–40
Ugarte-Urra and Warren (2011)	EIS	166–211, 246–291	0.6–1.0	40–130
McIntosh et al. (2012)	EIS, AIA	166–211, 246–291	< 1	10, 50–150
Tripathi et al. (2012a)	EIS, AIA	166–211, 246–291	0.6–1.6	4–20
Tripathi et al. (2012b)	EIS, AIA	166–211, 246–291	0.6–1.6	0±5
Su et al. (2012)	AIA,SOT,EIS	171, 304, 3968	1.0–3.0	80–200
Orange et al. (2013)	EIS	171–212, 250–290	0.6–1.0	5–60
Baker et al. (2017)	EIS	171–212, 250–290	0.6–1.0	11–32

The interpretation of the Dopplershift of flows depends very much on the heliographic position. Near disk center we expect a maximum blueshift for upflows, which should vanish when seen near the limb. Such a center-to-limb pattern in the directivity was indeed observed in upflows ($v \approx 20$ km s^{-1}) near the footpoints of active region loops with EIS/Hinode (Hara et al. 2008; Doschek et al. 2008), persistent for at least a day (Doschek et al. 2008), and extending into the heliosphere and solar wind (Doschek et al. 2008). The center-to-limb variation introduces systematic changes in the line shift, from which the inclination and angular spread can be measured (Démoulin et al. 2013; Baker et al. 2017). Besides persistent blueshifted upflows (Patsourakos et al. 2014), persistent redshifts were observed near loop footpoints in active regions too (Del Zanna 2008). This apparent co-spatial co-existence of blueshifted outflows and redshifted downflows was disentangled as two different temperature regimes: redshifted emission at transition region temperatures and blueshifted emission at coronal temperatures (Tripathi et al. 2009; Warren et al. 2011; Kamio et al. 2011). This dichotomy of flows was called *"coronal contra-flow"* or *"chromosphere-corona mass cycle"* (McIntosh et al. 2012). The emission in the blue wing was found to propagate upward fast ($v = 50$–150 km s^{-1}) and to contribute a few percents to the total emission only, while the *"draining"* of cooler material descends slowly ($v \approx 10$ km s^{-1}) while radiatively cooling (McIntosh et al. 2012), forming a complex near-cospatial mass cycle. Upflows with

velocities of $v = 48$ km s^{-1} forming loops with life times of 4 hrs were also observed in optical wavelengths (Singh et al. 2005). Strong blueshifts of $v \approx 20$–40 km s^{-1} were measured in the solar corona during a total eclipse (Raju et al. 2011). Other velocity measurements in upflows and downflows were reported also by Brosius (2005), Brosius and Landi (2005), Tripathi et al. (2012a), Orange et al. (2013), Kano et al. (2014), see compilation in Table 9.2. Most of the observed upflow events have been interpreted as a result of a local magnetic reconnection process that triggers chromospheric evaporation. Using magnetic extrapolations in the upflow regions, it was found that flows occur in thin, fan-like structures rooted in quasi-separatrix layers, between over-pressure active region loops and neighboring under-pressure loops (Démoulin et al. 2013).

On the theoretical side, 1-D hydrodynamic simulations have been carried out to calculate steady-flow solutions, but observational evidence is scarce. It was found that a sufficiently large heating asymmetry can produce the observed loop over-density (Winebarger et al. 2002), but very short pressure scale heights are needed, so that most of the warm ($T = 1$–2 MK) EUV loops cannot be explained by flows (Patsourakos et al. 2014). A transient motion along a cool loop observed with TRACE and SUMER has been modeled in terms of a siphon flow model, but the transient lasted only a few minutes, which is much shorter than expected for quasi-steady siphon flows (Doyle et al. 2006). The observed flows in a loop structure located in the penumbra of a sunspot were found to match theoretical predictions of chromospheric and coronal siphon flows, with accelerating upflowing plasma at one footpoint with low field strength and decelerating downflowing plasma at the other end (Fig. 9.7), possibly forming a tube shock (Bethge et al. 2012). High-velocity

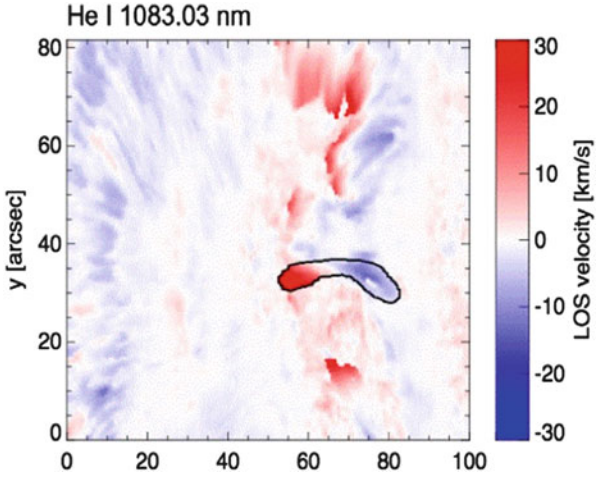

Fig. 9.7 Line-of-sight velocities (upflows in blueshift and downflows in redshift) observed in the He I line (10,830 Å) of a cool loop rooted in the penumbra of a sunspot, observed with TIP/VTT, Tenerife (Bethge et al. 2012)

flows can be generated by the generalized magneto-Bernoulli mechanism (Mahajan et al. 2002). Multi-species hydrodynamic simulations show the Coulomb coupling of the electrons and ions induces drag that counteracts the tendency of ions to settle into gravitational stratification (Lenz 2004). Ions and protons couple well in the line-forming region (Byhring et al. 2008). The coronal helium is found not to *"drain"*, leading to extreme increases of the helium abundance from the upper chromosphere to the corona (Killie et al. 2005).

9.6 Coronal Loops: Catastrophic Cooling

Hot coronal loops ($T_e \gtrsim 3$ MK) mostly cool by conductive energy loss, while radiative energy loss dominates later on (in warm loops with $T_e \approx 1$–3 MK). At even lower loop temperatures ($T_e < 1$ MK), radiative losses are no longer balanced by gains through heat conduction or in-situ heating, and therefore the radiatively-driven thermal instability sets in. This phase of the loop evolution is called *"catastrophic cooling"* or *"condensation"*. During this condensation phase, cold plasma blobs collapse and fall from the corona back to the chromosphere, a phenomenon that is also called *"coronal rain"*, which is observed in active regions, post-flare loops, eruptive filaments, and prominences (see examples in Fig. 9.8).

Recent observations of coronal rain with the CRISP instrument at SST in the H-α and Ca II H wavelengths quantify the dynamics (average falling speeds of $v \approx 70$ km s^{-1} and mass drain rate of $dm/dt \approx (1.5\text{–}5) \times 10^9$ g s^{-1}), geometric shapes (average lengths of $L \approx 710$ km and widths of $w \approx 310$ km), trajectories (along the magnetic field, with fall times of $\tau \approx 1$–10 min), and thermodynamic

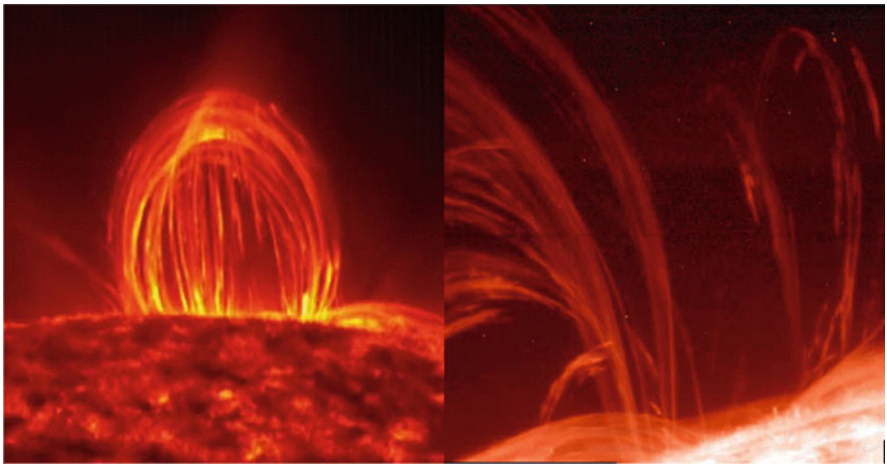

Fig. 9.8 Observations of coronal rain: *Left:* AIA/SDO observations on 2012-07-19 at 304 Å; *Right:* IRIS observations on 2015-03-06, 19:03:29 UT at 2796 Å (Credit: NASA, IRIS Team)

properties (average temperatures $T_e < 7000$ K) and densities ($n_e \approx (0.2\text{–}2.5) \times 10^{11}$ cm^{-3}) of the condensations (Antolin and Rouppe van der Voort 2012; Antolin et al. 2015). The formation of flare-driven coronal rain was observed in 5 phases: heating, evaporation, conductive cooling for ≈ 2 min, radiative enthalpy cooling for 1.3 hrs, and catastrophic cooling during 0.6–2.0 min, leading to rain strands with periods of 55–70 s (Scullion et al. 2016). These measurements confirm that the acceleration is largely below the effective gravity along loops, and that the trajectories follow the coronal magnetic field. The maximum descending speed was found to be correlated with the ratio of electron densities inside and outside the falling blobs (Oliver et al. 2016). While the falling of coronal condensations is easiest observed above the limb, the phenomenon is also found "on-the-disk", with similar physical parameters (Antolin et al. 2012; Ahn et al. 2014), which could explain also part of the ubiquitous redshifts observed on the disk. Combining the CRISP/SST measurements with AIA and IRIS, coronal rain is found to be highly multi-thermal and multi-stranded, with a high degree of co-spatiality in the multi-wavelength (optical and EUV) emissions (Antolin et al. 2015). The funneling effect of the upward diverging magnetic field streamlines the coronal rain into a more continuous and persistent stream at low altitudes, just before it impacts the chromosphere (Antolin et al. 2015).

Recent numerical 1-D hydrodynamic simulations of the condensation of plasma in cool ($T_e < 1$ MK) short loops ($L = 10$ Mm) exhibit a cyclic pattern of chromospheric evaporation, condensation, motion of the condensation region to either side of the loop, and finally loop reheating with a period of 1–2 hrs (Müller et al. 2003). It is found that the radiatively-driven thermal instability occurs about an order of magnitude faster than the Rayleigh-Taylor instability, which can occur in a loop with a density inversion at its apex also (Müller et al. 2003). Simulations with different heating functions reveal that the process of catastrophic cooling is not initiated by a drastic decrease of the total loop heating rate, but rather results from a loss of equilibrium at the loop apex as a natural consequence of (even steady) footpoint heating (Müller et al. 2004; Peter et al. 2012). In the case of repetitive impulsive heating, the cycle period to maintain a short loop at coronal temperatures is very sensitive to the loop length, for instance $T_{cycle} \approx 3$ min for $L = 5\text{–}10$ Mm (Mendoza-Briceno et al. 2002).

Much longer cycles, with periods of $T = 3.8\text{–}9.0$ hrs (lasting over several days), where found in some active region loops, which were interpreted in terms of thermal non-equilibrium evaporation and condensation cycles also (Froment et al. 2015, 2017). The time evolution of plasma temperatures $T(t)$ and emission measure EM, as well as phase diagrams of $T - EM$, are shown in Fig. 9.9 for three cases (with mean periods of 3.8, 5.0, and 9.0 hours).

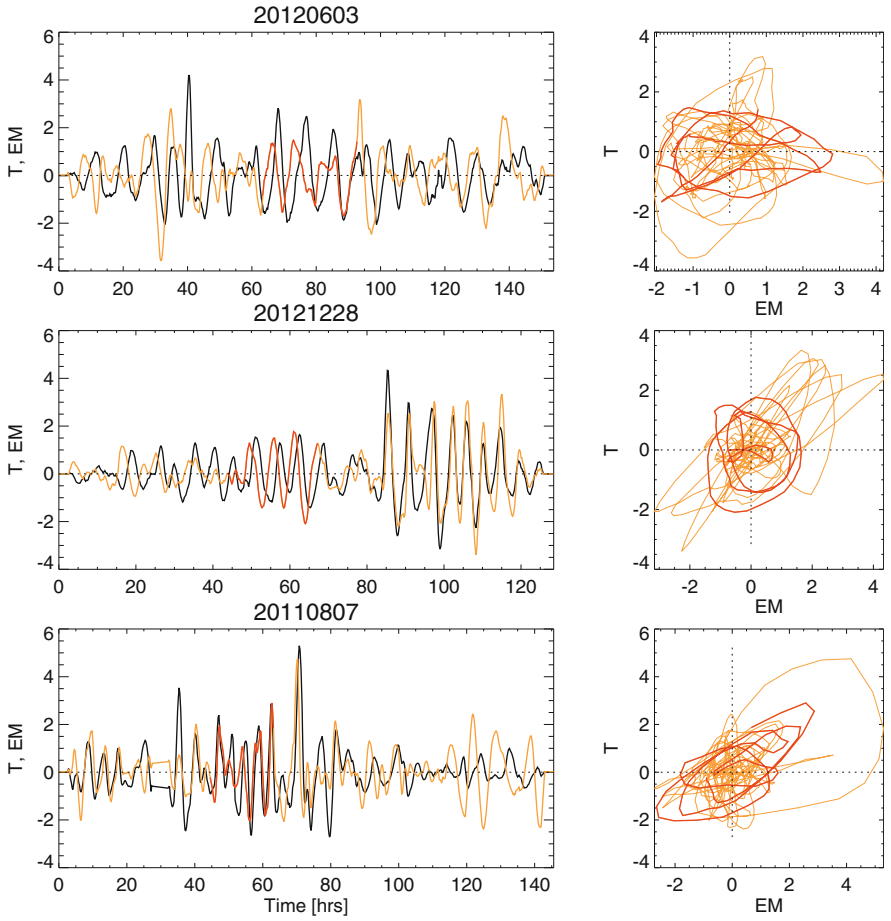

Fig. 9.9 Smoothed time profiles of the emission measure $EM(t)$ (black in left panels) and the electron temperature $T_e(t)$ (red in left panels, and phase diagram $T_e(EM)$ (right panels) of three loop episodes observed in an active region with AIA/SDO. A moving average background has been subtracted in all time profiles, and the amplitudes are normalized by their standard deviation from the means. A quasi-stationary time interval with near-elliptical phase trajectories is colored with red. The quasi-periodicity and the phase delay indicate a limit-cycle behavior of the evaporation-condensation cycle in solar flares (Froment et al. 2015)

Periodically repeating heating-condensation cycles were found to be coupled with transverse kink-mode oscillations in some active region loops (Kohutova and Verwichte 2016, 2017a,b; Verwichte and Kohutova 2017; Verwichte et al. 2017), see Fig. 9.10.

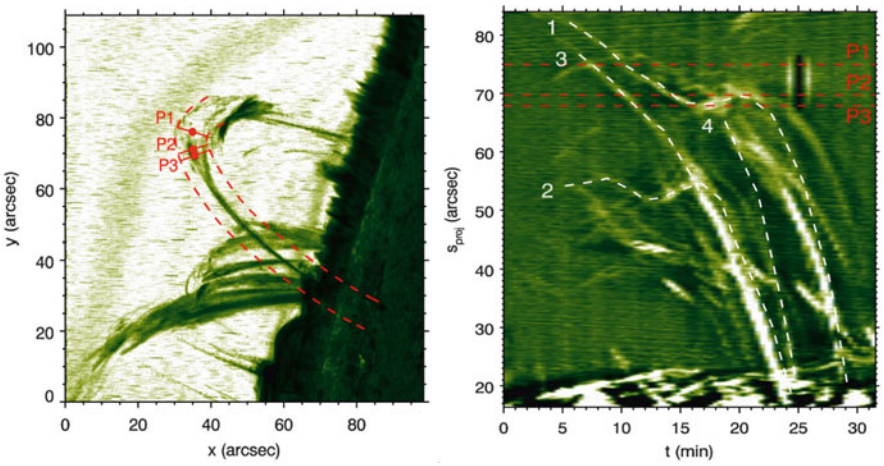

Fig. 9.10 Observations of coronal rain in an oscillating loop: *Left:* Hinode/SOT Ca II H band observations on 2012-04-16, 15:04 UT; *Right:* Time-slice plot with time on x-axis and altitude on y-axis (Verwichte et al. 2017)

9.7 Coronal Loops: Heating Function

The heating function term $E_h(s,t)$ in the hydrodynamic energy equation has (a generally unknown) time and spatial dependence. In 1-D hydrodynamic flux tube models (with loop length coordinate s), which is often approximated assuming an adiabatic state, the energy balance is given by (e.g., Rosner et al. 1978),

$$E_h(s,t) - E_c(s,t) - E_r(s,t) = 0\,. \tag{9.7.1}$$

Here E_h is the volumetric heating rate, E_c is the conductive energy loss rate, and E_r is the radiative energy loss rate. The three most common spatial heating functions of loops are the uniform, footpoint, and apex heating functions. The spatial shape of the nonuniform heating function is generally parameterized with an exponential function (e.g., Serio et al. 1981), and the time dependence has been approximated with a Gaussian function,

$$E_H(s,t) = H_0 \, \exp\left(-\frac{(t-t_m)^2}{2\tau_{heat}^2}\right) \exp\left(-\frac{s}{s_H}\right) \begin{cases} s_H > 0 & \text{for footpoint heating} \\ s_H = \infty & \text{for uniform heating} \\ s_H < 0 & \text{for apex heating} \end{cases} \tag{9.7.2}$$

were t_m is the time of maximum heating, τ_{heat} the gaussian width of the heating time interval, s_H is the heating scale height, and H_0 is the volumetric heating rate at the footpoint.

One obvious case we can rule out at this stage is the uniform heating function (constant in space and time), because it would not be able to explain the observed over-density of cool loops in EUV (Lenz et al. 1999; Aschwanden et al. 1999, 2000). None of the heating function approximations fits the observed density profiles derived from DEM forward-fitting or inversions, which created a new conundrum that violated previous steady-state models. Besides the over-density with respect to the RTV steady-state solution, EUV loops were found to reveal super-hydrostatic scale heights and exceptionally flat temperature profiles. These critical loop properties led to the diagnostic decision tree as shown in Fig. 9.11. The ratio of the radiative to the conductive cooling time,

$$\left(\frac{\tau_{rad}}{\tau_{cond}}\right) \approx \frac{T^4}{n_e^2 L^2} \tag{9.7.3}$$

was found to vary over orders of magnitude for cool and hot coronal loops (Fig. 9.12), but can be reproduced with simulations of impulsively heated loop strands (Klimchuk 2006, 2009).

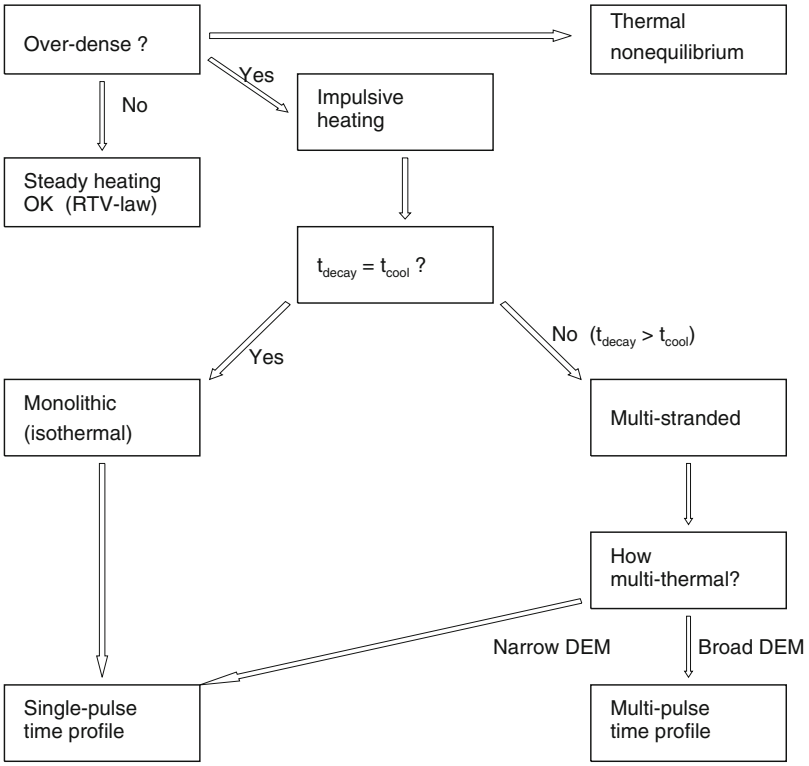

Fig. 9.11 Flow chart of the diagnostics of coronal loop heating scenarios, starting from the observed electron density, the observed decay time (compared with the theoretical cooling time), and the temperature widths of the DEMs (adapted from Klimchuk 2009)

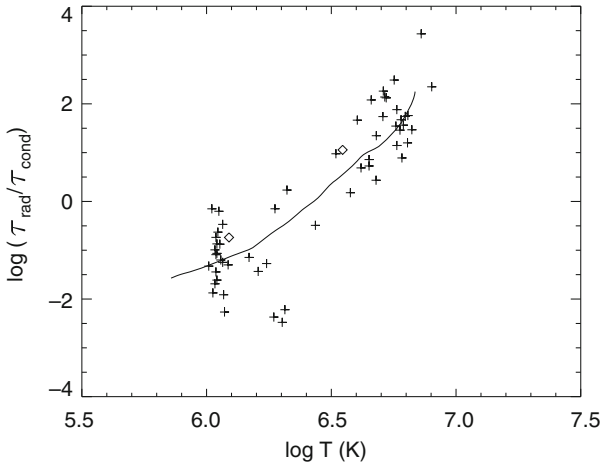

Fig. 9.12 Ratio of radiative to conductive cooling times versus temperature of loops observed with TRACE and SXT/Yohkoh (crosses). The solid curve is the cooling track of an impulsively heated loop strand simulation (Klimchuk 2006, 2009)

Another case that is unlikely is the loop apex heating scenario. Although a statistical temperature increase is generally observed in the corona above the limb, which has been interpreted in terms of a temperature profile of a single loop that is heated from the top (Reale 2002), this temperature gradient is more naturally explained in terms of the hydrostatic weighting bias in an inhomogeneous solar corona (Aschwanden and Nitta 2000). Consequently, only the case of footpoint heating survives as a realistic spatial heating function of coronal loops.

For the temporal dependence, delta-functions, rectangular, triangular, or Gaussian functions have been employed. Fortunately we have additional constraints that restrict the time-dependence of the heating function in loops, namely the observed life time (or decay time) of a loop, which has to match the cooling time as obtained in hydrodynamic simulations. However, hydrodynamic simulations of the time evolution of coronal loops exhibited that the simulated life times of loops were found to be always shorter than the observed life times (Warren et al. 2002, 2003), which led to the conclusion that a sequence of subsequentially (overlapping and superimposed) heating episodes only can explain the observed time evolution of active region loops (Fig. 9.6), so that an active region loop consists of a collection of small-scale strands (or filaments) that are impulsively heated and are cooling through the EUV passbands (Warren et al. 2002, 2003; Winebarger et al. 2003; Mulu-Moore et al. 2011). While the decay time discrepancy is based on multi-stranded loops observed with TRACE, it has not been tested yet whether monolithic loops with finer widths exhibit the same decay time discrepancy, such as the finest loops discovered in Hi-C data down to $w \approx 100$–500 km (Peter et al. 2013; Brooks et al. 2013; Aschwanden and Peter 2017; see Figs. 9.4 and 9.5). Multi-stranded hydrodynamic models have also difficulty to reproduce the diffuse hot plasma in an

active region (Warren et al. 2010a). On the other side, steady-state heating was found to be consistent with hot loops observed with XRT in the core of active regions, as well as with *"moss"* structures at the footpoint of high-temperature loops (Warren et al. 2010b).

Special cases of the heating function have been simulated: the *explosive heating* scenario with very fast heating to high temperatures, which leads to near-saturated thermal conduction (Bradshaw and Cargill 2006, 2013); simulations with nonuniform loop cross-section areas, nonuniform heating, asymmetric loop shapes, and asymmetric heating (Mikic et al. 2013); periodic and overlapping heating pulses that mimic quasi-steady heating (Testa et al. 2005); heating pulses in a multi-stranded system randomly distributed in time (Patsourakos and Klimchuk 2006; Guarrasi et al. 2010); or turbulent heating rates (Chae et al. 2002).

9.8 Coronal Loops: The 0-D EBTEL Code

The hydrodynamics of the solar corona is generally simplified in terms of one-dimensional (1-D) flux tubes that represent rigid conduits for plasma flows, since the plasma-β parameter is less than unity in most coronal regions, which implies that the magnetic pressure exceeds the thermal pressure and thus forms impenetrable flux tubes without cross-field transport. The reduction of the coronal hydrodynamics to a 1-D problem can further be simplified to a 0-D problem, since thermal conduction and flows tend to smooth out plasma gradients along the magnetic field. An efficient 0-D hydrodynamic code, called the *"enthalpy-based thermal evolution of loops" (EBTEL)* code has been developed that approximately describes the evolution of the average temperature, pressure, density, and differential emission measure (DEM) distribution inside a coronal loop strand, where the enthalpy plays a major role in the energy budget (Klimchuk et al. 2008; Cargill et al. 2012a,b). The motivation for creating such an efficient hydrodynamic code came from the desire to model coronal loops as a superposition of thousands of (observationally unresolved) miniature loops, also called *"elemental loop strands"*, as they are invoked in nanoflare heating models.

We outline the derivation of the 0-D hydrodynamic EBTEL model according to Klimchuk et al. (2008). The 1-D time-dependent hydrodynamic equation for energy conservation is,

$$\frac{\partial E}{\partial t} = -\frac{\partial}{\partial s}(Ev) - \frac{\partial}{\partial s}(Pv) - \frac{\partial F_c}{\partial s} + Q - n^2\Lambda(T) + \rho g_{\parallel} v \,, \tag{9.8.1}$$

where E is the combined thermal and kinetic energy density (defined as $E = P/(\gamma - 1)$ in terms of the adiabatic index γ in Cargill et al. 2012a),

$$E = \frac{3}{2}P + \frac{1}{2}\rho v^2 \,, \tag{9.8.2}$$

s is the spatial coordinate along the magnetic field, n is the electron number density, T is the electron temperature, P is the total pressure, v is the bulk velocity, F_c is the conductive heat flux, Q is the volumetric heating rate (equivalent to $E_H(s,t)$ in Sect. 9.7), $g_\parallel$ is the gravity component along the magnetic field, and $\Lambda(T)$ is the optically thin radiative loss function. The usual assumptions of 1-D hydrodynamic codes are applied, such as symmetric loops and constant loop cross-sections, which are still a matter of debate. Furthermore, neglecting the kinetic energy (assuming subsonic flows) and gravity terms (for loops shorter than the gravitational scale height), we obtain,

$$\frac{3}{2}\frac{\partial P}{\partial t} \approx -\frac{5}{2}\frac{\partial}{\partial s}(Pv) - \frac{\partial F_c}{\partial s} + Q - n^2\Lambda(T) \; . \tag{9.8.3}$$

Integrating Eq. (9.8.3) over the loop length L and applying a vanishing velocity and heat flux at the apex due to the loop symmetry, we obtain,

$$\frac{3}{2}L\frac{\partial\langle P\rangle}{\partial t} \approx \frac{5}{2}(P_0 v_0) + F_0 + L\langle Q\rangle - R_c \; , \tag{9.8.4}$$

where L is the coronal loop half length, the quantities $\langle P\rangle$ and $\langle Q\rangle$ indicate spatial averages along the coronal loop section, P_0 is the pressure and v_0 is the velocity at the footpoint of the loop (at the base of the corona), $(5/2)P_0v_0$ is the enthalpy flux, F_0 is the heat flux, and $R_c \approx \langle n^2\rangle\Lambda(\langle T\rangle)L$ is the radiative cooling rate per unit cross-sectional area in the corona. A similar averaging can be applied to the transition region,

$$\frac{3}{2}l\frac{\partial\langle P_{tr}\rangle}{\partial t} \approx \frac{5}{2}(P_0 v_0) + F_0 + l\langle Q_{tr}\rangle - R_{tr} \; , \tag{9.8.5}$$

where l is the length from the coronal base to the apex, and R_{tr} is the radiative cooling rate in the transition region. Assuming that the enthalpy flux is proportional to the temperature, therefore being much smaller at the top of the chromosphere than in the corona, i.e., $l \ll L$, it can be ignored in Eq. (9.8.5), leading to,

$$\frac{5}{2}(P_0 v_0) \approx -F_0 - R_{tr} \; . \tag{9.8.6}$$

In static equilibrium, the heat flux and radiative power is balanced, i.e., $|F_0| = R_{tr}$, which yields with Eqs. (9.8.4) and (9.8.6),

$$\frac{\partial\langle P\rangle}{\partial t} \approx \frac{2}{3}\left[\langle Q\rangle - \frac{1}{L}(R_c + T_{tr})\right] \; . \tag{9.8.7}$$

This equation reflects the energetics of the combined corona and transition region system, with a source term $\langle Q\rangle$ and loss term $(R_c + R_{tr})/L$.

After we quantified the pressure evolution $\partial\langle P\rangle/\partial t$ we want to derive the density evolution $\partial\langle n\rangle/\partial t$, which is obtained by setting the time derivative of the electron

column density $\langle n \rangle L$ equal to the flux of electrons through the coronal base, i.e., $\partial(\langle n \rangle L)/\partial t = J_0 \approx nv$, and using the ideal gas law $P = 2k_B nT$,

$$\frac{\partial \langle n \rangle}{\partial t} = \frac{c_2}{5c_3 k_B L \langle T \rangle}(F_0 + R_{tr}) \ , \tag{9.8.8}$$

where the constants refer to the temperature ratios $c_2 = \langle T \rangle / T_a$ and $c_3 = T_0/T_a$, T_a being the apex temperature, and T_0 the coronal base temperature. The classical expression for the heat flux is

$$F_0 = -\kappa_0 T^{5/2} \frac{\partial T}{\partial s} \approx -\frac{2}{7}\kappa_0 \frac{T_a^{7/2}}{L} \ . \tag{9.8.9}$$

Combining then Eqs. (9.8.7) and (9.8.8) with the ideal gas law leads then to the temperature evolution $\partial \langle T \rangle / \partial t$,

$$\frac{\partial \langle T \rangle}{\partial t} \approx \langle T \rangle \left(\frac{1}{\langle P \rangle} \frac{\partial \langle P \rangle}{\partial t} - \frac{1}{\langle n \rangle} \frac{\partial \langle n \rangle}{\partial t} \right) \ , \tag{9.8.10}$$

Similarly, the plasma velocity at the base of the corona can be obtained from the electron flux J_0,

$$v_0 = \frac{c_3}{c_2} \frac{2k_B \langle T \rangle J_0}{\langle P \rangle} \ . \tag{9.8.11}$$

The numerical EBTEL code uses the three evolutionary equations for the pressure (Eq. 9.8.7), the density (Eq. 9.8.8), and the temperature (Eq. 9.8.10) to calculate the time evolutions $P(t)$, $n(t)$, $T(t)$ in incremental time steps, starting from some initial conditions at time $t = 0$. An example of such a time-dependent 0-D solution is shown in Fig. 9.13, which is compared with a classical 1-D hydrodynamic solution using the *Adaptive Refined Godunov Solver (ARGOS)* code (Antiochos et al. 1999), demonstrating an agreement within $\approx 20\%$ in most time steps. The EBTEL code contains some variable parameters that can be adjusted based on 1-D hydrodynamic simulations, such as $c_1 = R_{tr}/R_c = 4.0$, $c_2 = \langle T \rangle / T_a = 0.87$, and $c_3 = T_0/T_a = 0.5$. Modifications of the EBTEL code include the energy flux and particle flux of nonthermal electron beams (Klimchuk et al. 2008). Generally, the differential emission measure (DEM) distributions computed with the EBTEL code, using the scenario of strong evaporation (by thermal conduction only) and strong condensation (when the heat flux is much less than the radiative losses), are not valid when nonthermal particles are important, such as in the case of beam-driven evaporation during solar flares. A key advantage of the 0-D EBTEL code is that it requires about four orders of magnitude less computation time than traditional 1-D hydrodynamic codes (such as ARGOS).

Improvements of the EBTEL model include gravitational stratification, a physically motivated treatment of radiative cooling (Cargill et al. 2012a), and nonequilibrium ionization (Bradshaw and Klimchuk 2011). Comparisons of the EBTEL code

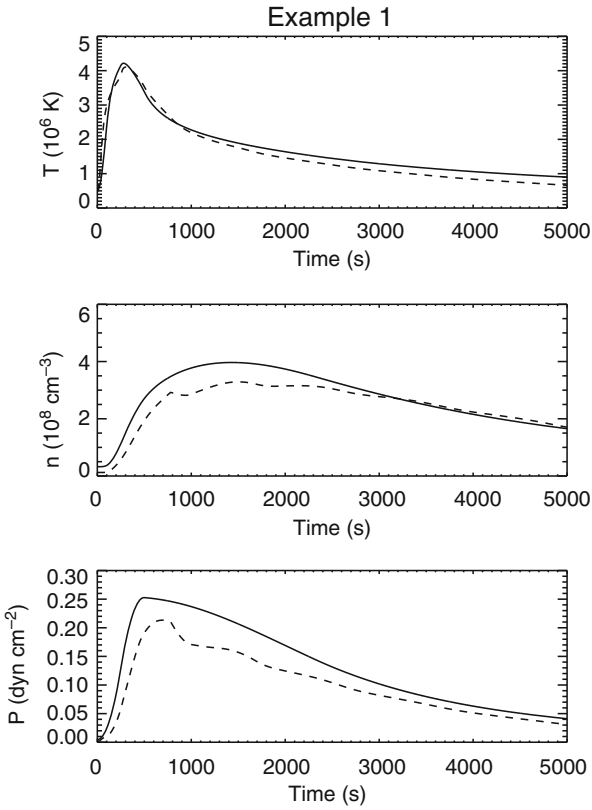

Fig. 9.13 Evolution of the coronal-averaged temperature (top), electron density (middle), and pressure (bottom), for a loop strand heated impulsively over a duration of 500 s. The solid curves are computed with the 0-D EBTEL code, while the dashed curves are computed with the 1-D ARGOS code. Classical heat flux is assumed (Klimchuk et al. 2008)

with other 0-D hydrodynamic models (Kuin and Martens 1982; Kopp and Poletto 1993; Cargill 1994; Fisher and Hawley 1990; Aschwanden and Tsiklauri 2009) have been conducted in Cargill et al. (2012b). Applications of the EBTEL code to solar flare data involves EIS/Hinode and AIA/SDO observations (e.g., Raftery et al. 2009; Ugarte-Urra and Warren 2014; Viall and Klimchuk 2012).

9.9 Coronal Loops: 1-D Hydrodynamics

1-D hydrodynamic codes have been the work horse for modeling of coronal loops or prominences for several decades. The one-dimensionality is a natural consequence of the fact that coronal plasma can only follow the magnetic field lines in the low plasma-β corona. All parameters in 1-D flux tubes have a dependence on the 1-

D spatial coordinate s, as well as on the time t, such as the electron temperature $T(s,t)$, the electron density $n(s,t)$ or mass density $\rho(s,t) = m_p n(s,t)$, the velocity $v(s,t)$, the heating rate $Q(s,t)$, the conductive flux $F_c(s,t)$, the pressure $P(s,t)$, the internal energy $E(s,t) = (3/2)P(s,t) + (1/2)\rho(s,t)v^2(s,t)$, and the radiative loss rate $E_r(s,t) = n^2(s,t)\Lambda(T(s,t))$. A hydrodynamic code, such as the ARGOS code (Antiochos et al. 1999), solves the time evolution of these parameters from the transport equations for mass, momentum, and energy in a 1-D plasma,

$$\frac{\partial}{\partial t}\rho + \frac{\partial}{\partial s}(\rho v) = 0 \,, \tag{9.9.1}$$

$$\frac{\partial}{\partial t}(\rho v) + \frac{\partial}{\partial s}(P + \rho v^2) = -\rho g_{\parallel} \,, \tag{9.9.2}$$

$$\frac{\partial E}{\partial t} = -\frac{\partial}{\partial s}(Ev) - \frac{\partial}{\partial s}(Pv) - \frac{\partial F_c}{\partial s} + Q - n^2\Lambda(T) + \rho g_{\parallel} v \,, \tag{9.9.3}$$

where the conductive flux F_c is,

$$F_C(s) = \left[-\kappa T^{5/2}(s)\frac{dT(s)}{ds}\right] = -\frac{2}{7}\kappa\frac{d}{ds}\left[T^{7/2}(s)\right] \,, \tag{9.9.4}$$

with $\kappa = 9.2 \times 10^{-7}$ (erg s^{-1} cm^{-1} K$^{-7/2}$) the classical Spitzer conductivity. The least known parameter is the spatio-temporal heating function $Q(s,t)$, for which various parameterizations have been used to mimic uniform, footpoint, or apex heating (Sect. 9.7). There exist also various parameterizations of the radiative loss function $\Lambda(T)$, usually approximated by piece-wise power law functions. While numerical codes have been designed to solve the coupled equation system of Eqs. (9.9.1–9.9.4), attempts have been made to simplify the analytical function that approximates the radiative loss function (e.g., Landini and Landi 2002; Dudik et al. 2009; Martens 2010; Bradshaw 2008), to specify various shapes of the spatial heating function (Serio et al. 1981), to quantify analytical approximations of the numerical solutions (Aschwanden and Tsiklauri 2009), or to include nonequilibrium ionization (e.g., Bradshaw and Mason 2003, Bradshaw 2008).

The radiative loss function $\Lambda(T)$ is generally approximated with piece-wise power law functions, following the initial characterization by Rosner et al. (1978). An alternative form is used by Landini and Landi (2002),

$$E_r = -n^2\Lambda(T) = -C\frac{p_0^2}{T^{2.5}} \,, \tag{9.9.5}$$

with $C \approx 2 \times 10^{12}$ K$^{5/2}$ cm^3 s^{-1} erg^{-1}, based on radiative loss calculations in an optically thin plasma using the Arcetri Spectral Code in the 10^4–10^8 K temperature range (Landi and Landini 1999). Similarly, Martens (2010) characterizes the radiative loss function with a power law function

$$E_r = -n^2\Lambda(T) = -\chi_0\, p_0^2\, T^{-(2+\gamma)} \,, \tag{9.9.6}$$

where $\chi_0 = 10^{12.41}$ is in cgs-units, while the heating function is rendered with a similar power law relation,

$$Q = Q_0 \, p_0^{\beta} \, T^{\alpha} \, . \tag{9.9.7}$$

This parameterization makes the energy equation (Eq. 9.9.3) integrable and an analytical solution is obtained for the hydrostatic temperature profile $T(s)$ and the RTV-type scaling law $P_0 L \propto T_{max}^3$, for a selection of heating functions $Q(s)$, as well as for a loop cross-section that is expanding with height (Martens 2010). A similar power law approach is used in analytical models of static coronal loops by Dudik et al. (2009), namely

$$E_r = -n^2 \Lambda(T) = -\chi_0 \, n_e^2 \, T^{-\sigma} \, , \tag{9.9.8}$$

with a coefficient of $\sigma = -1/2$ (Kuin and Martens 1982). In numerical models one can also interpolate the values calculated with an atomic data base, e.g., CHIANTI (see Sect. 2.3).

An analytical approximation of the temperature profile $T(s)$ can be obtained by neglecting the radiative loss during the initial heating phase (Aschwanden and Tsiklauri 2009), so that the heating rate $Q(s)$ essentially balances the conductive loss rate $\nabla F_c(s)$, which yields a differential equation of second order in the spatial coordinate s,

$$E_H(s) = \frac{d}{ds}\left[-\kappa T^{5/2}(s) \frac{dT(s)}{ds} \right] = -\frac{2}{7}\kappa \frac{d^2 T(s)^{7/2}}{ds^2} \, . \tag{9.9.9}$$

This second-order differential equation can be turned into an double-integral equation by expressing it as an explicit function of $T(s)$,

$$T(s) = \left[\int ds \int -\frac{7}{2\kappa} E_H(s) \, ds \right]^{2/7} \, . \tag{9.9.10}$$

which yields the following solution for the case of uniform heating,

$$T^{uni}(s) = T_2 \left[\left(\frac{s}{L} \right) \left(2 - \frac{s}{L} \right) \right]^{2/7} \, . \tag{9.9.11}$$

The evolution of the electron density $n(t)$ in the loop can be understood in terms of the *Neupert effect*, which in essence states that the accumulated density in a heated loop is an integral function of the heating rate, because the chromospheric evaporation rate into the coronal loop is a function of the chromospheric heating rate or energy input. If we neglect cooling during the heating phase, free energy is continuously added to the loop in form of evaporating material, which increases the density in the loop monotonously, peaking at the end of the heating phase. Parameterizing the heating function $Q(t)$ with a Gaussian function yields a Gaussian

temperature profile $T(t) \propto Q(t)$, while the density function follows the integral of the Gaussian function, $n(t) \propto \int Q(t)ds$, which predicts a maximum of the density function $n(t)$ at approximately the half decay time of the heating function, as sketched in Fig. 9.14. The analytical approximations of the temperature $T(t)$ and density profiles $n(t)$ have been found to agree well with numerical hydrodynamic simulations (Aschwanden and Tsiklauri 2009), as shown in Fig. 9.14. A typical characteristic of the temperature-density phase diagram (Fig. 9.14, right panel) is the hysteresis curve of the density peak lagging behind the temperature peak, following the *Jakimiec power law relationship*,

$$\frac{T(t)}{T_p} \approx \left(\frac{n(t)}{n_p}\right)^2 , \tag{9.9.12}$$

which was found to scale approximately with a power law slope of ≈ 2, as found in many earlier hydrodynamic simulations (e.g., Jakimiec et al. 1992; Serio et al. 1981; Sylwester et al. 1993).

While most hydrodynamic simulations of coronal loops assume ionization equilibrium, this assumption has been scrutinized by solving the detailed ionization

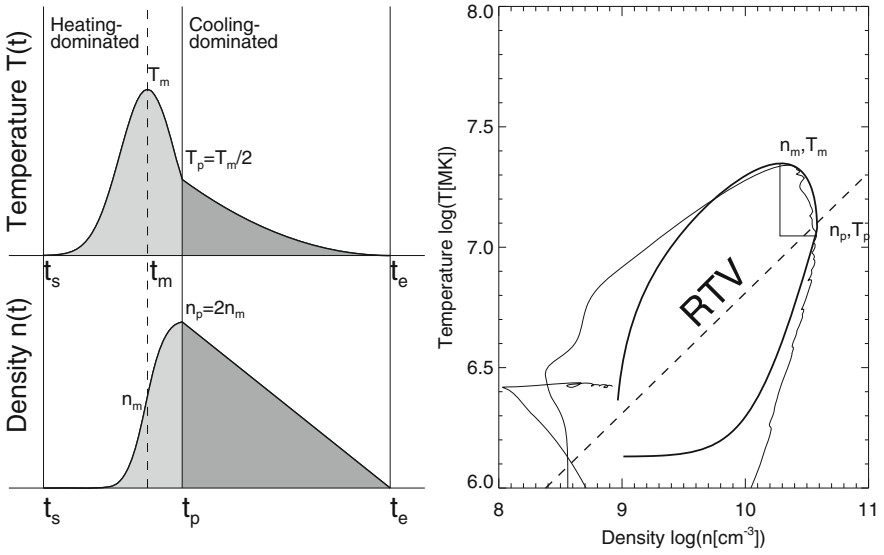

Fig. 9.14 Hydrodynamic time evolution of the electron temperature $T(t)$ and density $n_e(t)$ of a simulation of an impulsively-heated flare loop (see Aschwanden and Tsiklauri 2009), shown as time profiles (left panel) and as an evolutionary phase diagram $T_e(n_e)$ (right panel). The evolution of the hydrodynamic simulation is shown as exact numerical solution (curve with thin linestyle in right panel), and as an analytical approximation (curves with thick linestyle in both panels), along with the prediction $T_e \propto n_e^{1/2}$ of the RTV scaling law for uniform steady heating (dashed line in right panel) (Aschwanden and Shimizu 2013)

balance equation for each ion of the fifteen most abundant elements of the solar atmosphere for the case of a cooling loop (Bradshaw and Mason 2003). The ionization balance equation for each ion is,

$$\frac{\partial Y_i}{\partial t} + \frac{\partial}{\partial s}(Y_i v) = n(I_{i-1}Y_{i-1} + R_i Y_{i+1} - I_i Y_i - R_{i-1}Y_i) \,, \tag{9.9.13}$$

where Y_i denotes the fractional population of ion level i of element Y, the coefficients I_i and R_i are the ionization and recombination rates from/to ion level i, n is the electron number density, t is the time, and s is the spatial location along the loop. Significant deviations from equilibrium are found in the coronal and footpoint regions of the loop, especially in low-density coronal regions that cause the recombination rate to be rarer. For another case of a loop subjected to transient heating near the apex, an up to 5 times lower plasma emissivity is found in equilibrium compared with nonequilibrium emissivity, almost entirely due to the response of the coronal Fe ions (Bradshaw and Mason 2003).

9.10 Coronal Loops: Magnetic Modeling

Some new developments of magnetic field modeling in active regions are described in Sect. 8.1. It was realized that none of the magnetic field extrapolation methods warrants that the theoretically calculated field lines match the the observed geometry of coronal loops, as observed in EUV or in soft X-rays. Since the plasma β-parameter in the solar corona is generally less than unity, coronal loops visible in EUV or soft X-rays are supposed to trace the coronal magnetic field. There are two new strategies that take the observed loop geometry into account: (i) stereoscopic triangulation (which became feasible with the STEREO mission), and (ii) automated loop tracing in EUV and soft X-ray images, which both provide stringent constraints for 3-D modeling of the coronal magnetic field.

Since it was recognized that the photosphere and lower chromosphere are generally not force-free (Metcalf et al. 1995), the force-free extrapolation of coronal magnetic field lines from a non-force-free lower boundary, which is the *modus vivendi* for *non-linear force-free field (NLFFF)* codes using photospheric magnetograms (or vector data), the accuracy of NLFFF codes became questionable. A refinement of the NLFFF optimization method was proposed by introducing a weighting function that minimizes the force balance between the non-force-free photosphere and the force-free lower boundary of the computation box, which is a magneto-hydrostatic approach (Wiegelmann 2004). Well-posed boundaries are studied in Amari et al. (2006). A method of preprocessing was developed which drives the observed non-force-free data towards suitable boundary conditions for force-free extrapolation codes, minimizing the force balance and the torque-free condition (Wiegelmann et al. 2006; Metcalf et al. 2008; Wiegelmann et al. 2012). A benchmark test of 9 different NLFFF codes (including optimization,

magneto-frictional, Grad-Rubin based, and Green's function-based methods) has been arranged in Schrijver et al. (2006), which demonstrated that the agreement is always best in the lower central region of the volume, where the field and electrical currents are strongest and the effects of boundary conditions weakest, while the solutions in the outer domains show a high sensitivity on the specific boundary conditions. The fastest-converging and best-performing model for these analytical test cases turned out to be the Wheatland et al. (2000) optimization algorithm, as implemented by Wiegelmann (2004). A similar benchmark test with 6 different NLFFF codes was carried out by Metcalf et al. (2008), revealing differences in the free energy by about a factor of 2 for the different codes. The non-force-free boundary problem, however, can be circumvented with force-free codes that fit coronal loop features, rather than photospheric data, for instance with stereoscopic loop detection codes (Aschwanden 2013a), or with automated loop tracing codes (Aschwanden et al. 2014). The most comprehensive benchmark test of 12 NLFFF codes was carried out by De Rosa et al. (2009), using Hinode/SOT-SP, Hinode/XRT, EUV/STEREO, and MDI/SOHO observations. The following critical requirements for successful NLFFF modeling were assessed: (i) sufficiently large areas of vector magnetic field data are needed, (ii) the uncertainties in the boundary data need to be incorporated in the NLFFF algorithms, and (iii) a more realistic physical model is needed to approximate the photosphere-to-corona interface (De Rosa et al. 2009). It was shown that the incorporation of measurement errors implemented into the various NLFFF codes significantly improves the quality of NLFFF solutions from imperfect boundary conditions (Wiegelmann and Inhester 2010; Wiegelmann et al. 2012).

Using various methods of potential field methods (potential field source surface (PFSS), unipolar charges, dipolar models) and non-potential force-free field methods (NLFFF), it was shown that all these theoretical magnetic field models exhibit a misalignment of order $\approx 20°$–$40°$ with respect to the observed loop directions measured in EUVI/STEREO images, compared either with their 2-D projections, or with the 3-D coordinates as triangulated from stereoscopic observations (Sandman et al. 2009; Aschwanden and Sandman 2010; Sandman and Aschwanden 2011). A residual misalignment of $\approx 11°$–$17°$ has been attributed to the non-potentiality of active regions (Aschwanden and Sandman 2010).

Newly developed NLFFF codes include: a magneto-hydrostatic approach (Flyer et al. 2004); a Grad-Rubin method based on partial derivatives instead of finite differences (Song et al. 2006); NLFFF codes in spherical geometry instead of Cartesian geometry (Wiegelmann 2007); the so-called flux insertion method based on the geometry of observed Hα filaments (Van Ballegooijen 2004; Van Ballegooijen et al. 2007; Bobra et al. 2008; Titov et al. 2014); the vertical current approximation VCA-NLFFF code (Aschwanden 2013b,c, 2016; Aschwanden and Malanushenko 2013); and a stereoscopic triangulation code using automatically traced coronal loops (Aschwanden et al. 2014). An example of a VCA-NLFFF solution with automatically traced loops is shown in Fig. 9.15.

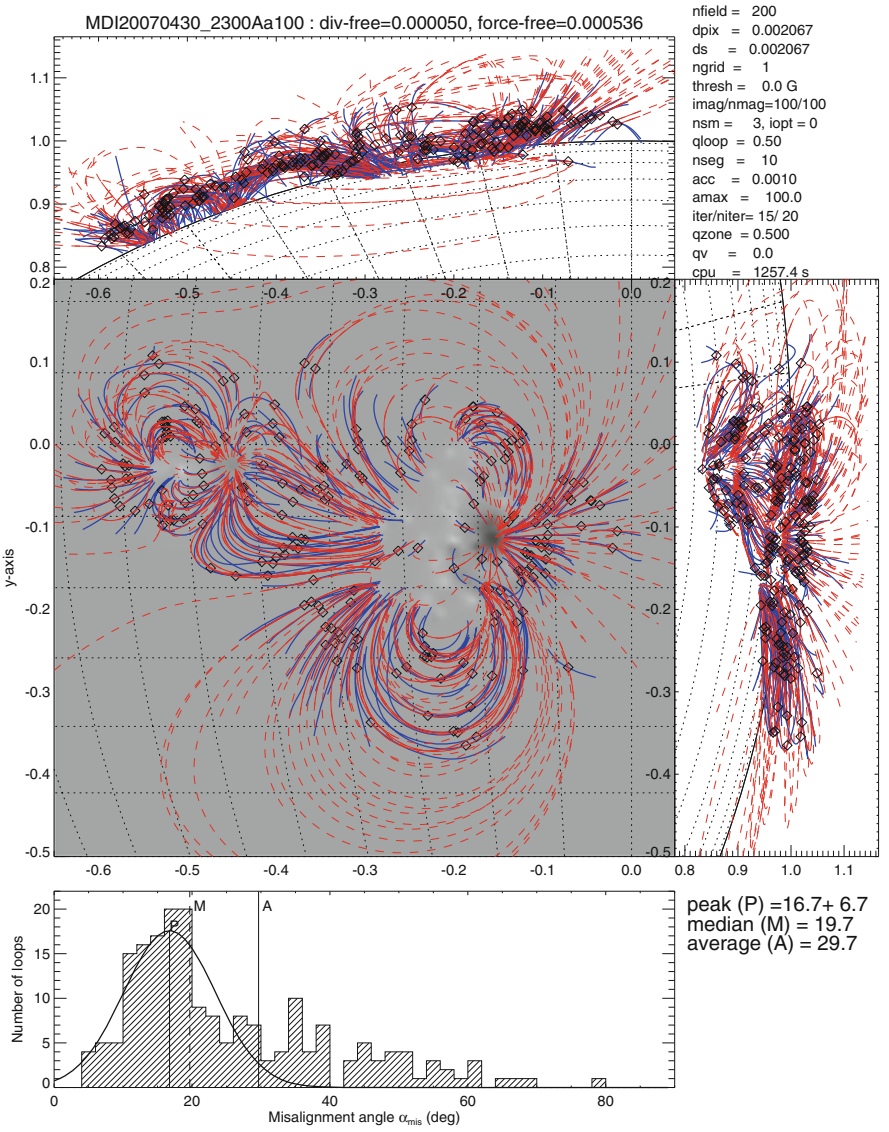

Fig. 9.15 Active region NOAA 10953, observed on 2007 April 30, 23:00 UT: Stereoscopically triangulated loops observed with EUVI/STEREO (blue curves) are compared with a solution of the VCA-NLFFF code (red curves), overlaid on a MDI/SOHO magnetogram. The upper 3 panels represent orthogonal views, and the histogram (bottom) shows the distribution of 3-D misalignment angles, with an average of $\mu_3 = 16.7^\circ \pm 6.7^\circ$ (Aschwanden et al. 2012)

References

(9.1) Coronal Loops: Stereoscopy and 3-D Geometry

Aschwanden, M.J., Newmark, J.S., Delaboudiniere, J.P., et al. 1999, *3-D stereoscopic analysis of solar active region loops. I. SOHO/EIT observations at temperatures of (1.0–1.5)* $\times 10^6$ *K*, ApJ 515, 842, [218 c, 12 c/y].

Aschwanden, M.J., Alexander, D., Hurlburt, N., et al. 2000, *3-D stereoscopic analysis of solar active region loops. II. SOHO/EIT observations at temperatures of 1.5–2.5 MK*, ApJ 531, 1129, [88 c, 5 c/y].

Aschwanden, M.J., Wülser,J.P., Nitta,N., et al. 2008, *First 3-D reconstruction of coronal loops with the STEREO A and B spacecraft. I. Geometry*, ApJ 679, 827, [78 c, 8 c/y].

Aschwanden, M.J. 2009, *The 3-D geometry, motion, and hydrodynamic aspects of oscillating coronal loops*, SSRv 149, 31, [40 c, 5 c/y].

Aschwanden, M.J., Wülser, J.P., Nitta, N., et al. 2012, *Solar stereoscopy with STEREO /EUVI A and B spacecraft from small (6°) to large (170°) spacecraft separation angles*, SoPh 281, 101, [6 c, 2 c/y].

Aschwanden, M.J. 2013, *A nonlinear force-free magnetic field approximation suitable for fast forward-fitting to coronal loops. I. Theory*, SoPh 287, 323, [17 c, 4 c/y].

Feng, L., Inhester, B., Solanki, S.K., et al. 2007, *First stereoscopic coronal loop reconstruction from STEREO SECCHI images*, ApJ 671, L205, [53 c, 5 c/y].

Gary, G.A. 1997, *Rendering 3-D solar coronal structures*, SoPh 174, 241, [15 c, 0.7 c/y].

Gary, G.A. and Alexander, D. 1999, *Constructing the coronal magnetic field by correlating parameterized magnetic field lines with observed coronal plasma structures*, SoPh 186, 123, [35 c, 2 c/y].

Lundquist, L.L, Fisher, G.H., and McTiernan, J.M. 2008, *Forward modeling of active region coronal emissions. I. Methods and testing*. ApJSS 179, 533, [26 c, 3 c/y].

Sandman, A.W. and Aschwanden, M.J. 2011, *A new method for modeling the coronal magnetic field with STEREO and submerged dipoles*, SoPh 270, 503, [17 c, 3 c/y].

Schrijver, C.J., Sandman, A.W., Aschwanden, M.J., et al. 2004, *The coronal heating mechanism as identified by full-Sun visualizations*, ApJ 615, 512, [97 c, 7 c/y].

Wiegelmann, T., and Neukirch, T. 2002, *Including stereoscopic information in the reconstruction of coronal magnetic fields*, SoPh 208, 233, [46 c, 3 c/y].

(9.2) Coronal Loops: Cross-Sectional Widths

Abramenko, V.I., Yurchyshyn, V.B., Goode, P.R., et al. 2012, *Detection of small-scale structures in the Quiet Sun with the New Solar Telescope (NST)*, ApJ 756, L27, [18 c, 3 c/y].

Alexander, C.E., Walsh, R.W., Régnier, S., et al. 2013, *Anti-parallel EUV flows observed along active region filament threads with Hi-C*, ApJ 775, L32, [24 c, 5 c/y].

Antolin, P., Vissers, G., Pereira, T.M.D., et al. 2015, *The multithermal and multi-stranded nature of coronal rain*, ApJ 806, 81, [34 c, 14 c/y].

Antolin, P. and Rouppe van der Voort, L. 2012, *Observing the fine structure of loops through high-resolution spectroscopic observations of coronal rain with the CRISP instrument at the Swedish Solar Telescope*. ApJ 745, 152, [80 c, 15 c/y].

Aschwanden, M.J. and Wülser, J.P. 2011, *3-D reconstruction of active regions with STEREO*, JASTP 73, 1082, [7 c, 1 c/y].

Aschwanden, M.J. and Boerner, P. 2011, *Solar corona loop studies with the AIA. I. Cross-temperature structure* ApJ 732, 81, [79 c, 12 c/y].

Aschwanden, M.J. and Schrijver, C.J. 2011, *Coronal loop oscillations observed with AIA. Kink mode with cross-sectional and density oscillations*, ApJ 736, 102, [88 c, 14 c/y].

Aschwanden, M.J., Boerner, P., Schrijver, C.J., et al. 2013, *Automated temperature and emission measure analysis of coronal loops and active regions observed with the AIA on the SDO*, SoPh 283, 5, [78 c, 17 c/y].

Aschwanden, M.J. and Peter, H. 2017, *The width distribution of loops and strands in the solar corona. - Are we hitting rock bottom*, ApJ 840, 4, [7 c, 7 c/y].

Brooks, D.H., Warren, H.P., and Ugarte-Urra, I. 2012, *Solar coronal loops resolved by Hinode and the SDO*. ApJ 755, L33, [50 c, 9 c/y].

Brooks, D.H., Warren, H.P., Ugarte-Urra, I., et al. 2013, *High spatial resolution observations of loops in the solar corona*, ApJ 772, L19, [47 c, 10 c/y].

Brooks, D.H., Reep, J.W., and Warren, H.P. 2016, *Properties and modeling of unresolved fine structure loops observed in the solar transition region by IRIS*, ApJ 826, L18, [4 c, 3 c/y].

Morton, R.J. and McLaughlin, J.A. 2013, *Hi-C and AIA observations of transverse MHD waves in active regions*, A&A 556, C1.

Mulu-Moore, F.M., Winebarger, A.R., Warren, H.P., et al. 2011, *Determining the structure of solar coronal loops using their evolution*, ApJ 733, 59, [23 c, 4 c/y].

Peter, H., Bingert, S., Klimchuk, J.A., et al. 2013, *Structure of solar coronal loops: From miniature to large-scale*, A&A 556, A104, [52 c, 12 c/y].

Winebarger, A.R., Walsh, R.W., Moore, R., et al. 2013, *Detecting nanoflare heating events in subarcsecond inter-moss loops using Hi-C*, ApJ 771, 21, [32 c, 7 c/y].

Winebarger, A.R., Cirtain, J., Golub, L., et al. 2014, *Discovery of finely structured dynamics solar corona observed in the Hi-C Telescope*, ApJ 787, L10, [11 c, 3 c/y].

Tiwari, S.K., Moore, R.L., Winebarger, A.R., et al. 2016, *Transition-region/coronal signatures of magnetic setting of sunspot penumbral jets: Hinode (SOT/FG), Hi-C, and SDO/AIA observations*, ApJ 816, 92, [9 c, 6 c/y].

(9.3) Coronal Loops: Multi-Strand Structure

Antolin, P., Vissers, G., Pereira, T.M.D., et al. 2015, *The multithermal and multi-stranded nature of coronal rain*, ApJ 806, 81, [34 c, 14 c/y].

Aschwanden, M.J. and Nightingale, R.W. 2005, *Elementary loop structures in the solar corona analyzed from TRACE triple-filter images*, ApJ 633, 499, [108 c, 9 c/y].

Aschwanden, M.J., Nightingale, R.W., and Boerner, P. 2007, *A statistical model of the inhomogeneous corona constrained by triple-filter measurements of elementary loop strands with TRACE*, ApJ 656, 577, [26 c, 2 c/y].

Aschwanden, M.J. and Peter, H. 2017, *The width distribution of loops and strands in the solar corona. - Are we hitting rock bottom ?* ApJ 840, 4, [7 c, 7 c/y].

Bourouaine, S. and Marsch, E. 2010, *Multi-strand coronal loop model and filter-ratio analysis*, ApJ 708, 1281, [2 c, 0.3 c/y].

Bradshaw, S.J. and Klimchuk, J.A. 2015, *Chromospheric nanoflares as a source of coronal plasma. II. Repeating nanoflares*, ApJ 811, 129, [7 c, 3 c/y].

Brooks, D.H., Warren, H.P., Ugarte-Urra, I., et al. 2013, *High spatial resolution observations of loops in the solar corona*, ApJ 772, L19, [47 c, 10 c/y].

Brooks, D.H., Reep, J.W., and Warren, H.P. 2016, *Properties and modeling of unresolved fine structure loops observed in the solar transition region by IRIS*, ApJ 826, L18, [4 c, 3 c/y].

Guarrasi, M., Reale, F., and Peres, G. 2010, *Coronal fuzziness modeled with pulse-heated multi-stranded loop systems*, ApJ 719, 576, [25 c, 3 c/y].

Jain, R. and Yashiro, S. 2002, *Filling factors and magnetic field strengths of nanoflare-heated coronal active regions: Yohkoh and MDI observations*, A&A 394, 1111, [6 c, 0.4 c/y].

Mendoza-Briceno, C.A., Erdelyi, R., and Di G. Sigaloti, L. 2002, *Coronal loop heating by random energy releases*, ApJ 579, L49, [27 c, 2 c/y].

Mulu-Moore, F.M., Winebarger, A.R., and Warren, H.P. 2011, *Can a long nanoflare storm explain the observed emission measure distributions in active region cores ?* ApJ 742, L6, [20 c, 3 c/y].

Patsourakos, S. and Klimchuk, J.A. 2005, *Coronal loop heating by nanoflares: The impact of the field-aligned distribution of the heating on loop observations*, ApJ 628, 1023, [42 c, 3 c/y].
Patsourakos, S. and Klimchuk, J.A. 2006, *Nonthermal spectral line broadening and the nanoflare model*, ApJ 647, 1452, [93 c, 8 c/y].
Peter, H., Bingert, S., Klimchuk, J.A., et al. 2013, *Structure of solar coronal loops: From miniature to large-scale*, A&A 556, A104, [52 c, 12 c/y].
Petrie, G.J.D. 2006, *Filamentary loop systems and spontaneous current sheets in the solar corona*, ApJSS 166, 378, [7 c, 0.6 c/y].
Reale, F. and Peres, G. 2000, *TRACE-derived temperature and emission measure profiles along long-lived coronal loops:* ApJ 528, L45, [80 c, 5 c/y].
Reale, F., Nigro, G., Malara, F., et al. 2005, *Modeling a coronal loop heated by MHD turbulence nanoflares*, ApJ 633, 489, [17 c, 1 c/y].
Reale, F. and Ciaravella, A. 2006, *Analysis of a multi-wavelength time-resolved observation of a coronal loop*, A&A 449, 1177, [15 c, 1 c/y].
Reale, F., Guarrasi, M., Testa, P., et al. 2011, *SDO discovers thin high temperature strands in coronal active regions*, ApJ 736, L16, [34 c, 5 c/y].
Sarkar, A. and Walsh, R.W. 2008, *Hydrodynamic simulation of a nanoflare-heated multistrand solar atmospheric loop*, ApJ 683, 516, [10 c, 1 c/y].
Sarkar, A. and Walsh, R.W. 2009, *EUV observational consequences of the spatial localization of nanoflare heating within a multistranded atmospheric loop*, ApJ 699, 1480, [5 c, 0.6 c/y].
Susino, R., Lanzafame, A.C., Lanza, A.F., et al. 2010, *Signatures of impulsive localized heating in the temperature distribution of multi-stranded coronal loops*, ApJ 709, 499, [19 c, 3 c/y].
Susino, R., Spadaro, D., Lanzafame, A.C., et al. 2013, *Properties of multistranded, impulsively heated hydrodynamic loop models*, A&A 552, A17, [0 c, 0 c/y].
Taroyan, Y., Bradshaw, S.J., and Doyle, J.G. 2006, *Nanoflare heating of coronal loops: hydrodynamic response and observational consequences*, A&A 446, 315, [23 c, 2 c/y].
Warren, H.P., Winebarger, A.R., and Hamilton, P.S. 2002, *Hydrodynamic modeling of active region loops*, ApJ 579, L41, [95 c, 6 c/y].
Warren, H.P., Winebarger, A.R., and Mariska, J.T. 2003, *Evolving active region loops observed with the TRACE. II. Time-dependent hydrodynamic simulations*, ApJ 593, 1174, [108 c, 7 c/y].
Winebarger, A.R., Schmelz, J.T., Warren, H.P., et al. 2011, *Using a differential emission measure and density measurements in an active region core to test a steady heating model*, ApJ 740, 2, [75 c, 12 c/y].

(9.4) Coronal Loops: Cross-Sectional Temperature

Aschwanden, M.J. 2002, *The differential emission measure distribution in the multiloop corona*, ApJ 580, L79, [25 c, 2 c/y].
Aschwanden, M.J. 2005, *Three criteria to discriminate between elementary and composite coronal loops*, ApJ 634, L193, [19 c, 2 c/y.
Aschwanden, M.J. and Nightingale, R.W. 2005, *Elementary loop structures in the solar corona analyzed from TRACE triple-filter images*, ApJ 633, 499, [108 c, 9 c/y].
Aschwanden, M.J. and Boerner, P. 2011, *Solar corona loop studies with the AIA. I. Cross-sectional temperature structure*, ApJ 732, 81, [79 c, 12 c/y].
Aschwanden, M.J., Boerner, P., Schrijver, C.J., et al. 2013, *Automated temperature and emission measure analysis of coronal loops and active regions observed with the AIA on SDO*, SoPh 283, 5, [78 c, 17 c/y].
Brooks, D.H., Warren, H.P., and Young, P.R. 2011, *EUV spectral line formation and the temperature structure of active region fan loops: Observations with Hinode/EIS and SDO/AIA*, ApJ 730, 85, 28 c, 4 c/y.

Cirtain, J.W., Del Zanna, G., DeLuca, E.E. et al. 2007, *Active region loops: Temperature measurements as a function of time from joint TRACE and SOHO CDS observations*, ApJ 655, 598, [31 c, 3 c/y.

Del Zanna, G. 2003, *Solar active regions: The footpoints of 1 MK loops*, A&A 406, L5, [30 c, 2 c/y].

Del Zanna, G. and Mason, H.E. 2003, *Solar active regions: SOHO/CDS and TRACE observations of quiescent coronal loops*, A&A 406, 1089, [130 c, 9 c/y].

Del Zanna, G. 2013, *The multi-thermal emission in solar active regions*, A&A 558, 73, [56 c, 12 c/y.

Landi, E. and Feldman, U. 2008, *The thermal structure of an active region observed outside the solar disk*, ApJ 672, 674, [26 c, 3 c/y].

Landi, E. and Klimchuk, J.A. 2010, *On the isothermality of solar plasmas*, ApJ 723, 320, [18 c, 2 c/y].

Martens, P.C.H., Cirtain, J.W., and Schmelz, J.T. 2002, *The inadequacy of temperature measurements in the solar corona through narrowband filter and line ratios*, ApJ 577, L115, [73 c, 5 c/y].

Nagata, S.I., Hara, H., Kano, R. et al. 2003, *Spatial and temporal properties of hot and cool coronal loops*, ApJ 590, 1095, [29 c, 2 c/y].

Patsourakos, S. and Klimchuk, J.A. 2007, *The cross-field thermal structure of coronal loops from triple-filter TRACE observations*, ApJ 667, 591, [19 c, 2 c/y].

Reale, F. and Landi, E. 2012, *The role of radiative losses in the late evolution of pulse-headed loops/strands*, A&A 543, A90, [15 c, 3 c/y].

Sasso, C., Andretta, V., Spandaro, D., et al. 2012, *Solar low-lying cool loops and their contribution to the transition region EUV output*, A&A 537, A150, [7 c, 1 c/y].

Schmelz, J.T., Scopes, R.T., Cirtain, J.W. et al. 2001, *Observational constraints on coronal heating models using CDS and SXT data*, ApJ 556, 896, [98 c, 6 c/y].

Schmelz, J.T. 2002, *Are coronal loops isothermal ?* ApJ 578, 161, [44 c, 3 c/y].

Schmelz, J.T., Beene, J.E., Nasraoui, K. et al. 2003, *The effect of background subtraction on the temperature of EIT coronal loops*, ApJ 599, 604, [37 c, 3 c/y].

Schmelz, J.T., Nasraoui, K., Richardson, V.L. et al. 2005, *All coronal loops are the same: Evidence to the contrary*, ApJ 627, L81, [21 c, 2 c/y].

Schmelz, J.T. and Martens, P.C.H. 2006, *Multithermal analysis of a SOHO/CDS coronal loop*, ApJ 636, L49, [34 c, 3 c/y].

Schmelz, J.T., Nasraoui, K., Del Zanna, G. et al. 2007, *CDS observations of isothermal and multithermal coronal loops*, ApJ 658, L119, [22 c, 2 c/y].

Schmelz, J.T., Scott, J., Rightmire, L.A. 2008, *May Day! Coronal loop temperatures from the Hinode EIS*, ApJ 684, 115, [12 c, 1 c/y].

Schmelz, J.T., Nasraoui, K., Rightmire, L.A. 2009, *Are coronal loops isothermal or multithermal ?* ApJ 691, 503, [24 c, 3 c/y].

Schmelz, J.T., Kimble, J.A., Jenkins, B.S. et al. 2010a, *AIA multithermal loop analysis: First results*, ApJ 725, L34, [16 c, 2 c/y].

Schmelz, J.T., Saar, S.H., Nasraoui, K. et al. 2010b, *Multi-stranded and multi-thermal solar coronal loops: Evidence from Hinode XRT and EIS data*, ApJ 723, 1180, [32 c, 4 c/y].

Schmelz, J.T., Worley, B.T., Anderson, D.J. et al. 2011a, *Isothermal and multithermal analysis of coronal loops observed with AIA. II. 211 A selected loops*, ApJ 739, 33, [18 c, 3 c/y].

Schmelz, J.T., Rightmire, L.A., Saar, S.H. et al. 2011b, *Warm and fuzzy: Temperature and density analysis of an Fe XV EIS Loop*, ApJ 738, 146, [17 c, 3 c/y].

Schmelz, J.T., Jenkins, B.S., Worley, B.T. et al. 2011c, *Isothermal and multithermal analysis of coronal loops observed with AIA*, ApJ 731, 49, [37 c, 6 c/y].

Schmelz, J.T., Pathak, S., Jenkins, B.S. et al. 2013, *Deeper by the Dozen: Understanding the cross-field temperature distributions of coronal loops*, ApJ 764, 53, [13 c, 3 c/y].

Testa, P., Peres, G., Reale, F., and Orlando, S. 2002, *Temperature and density structure of hot and cool loops derived from the analysis of TRACE data*, ApJ 580, 1159, [52 c, 4 c/y].

Tripathi, D., Mason, H.E., Dwivedi, B.N. et al. 2009, *Active region loops: Hinode/EIS observations*, ApJ 694, 1256, [87 c, 10 c/y].
Warren, H.P. and Warshall, A.D. 2002, *Temperature and density measurements in a quiet coronal streamer*, ApJ 571, 1999, [20 c, 1 c/y].
Warren, H.P. and Winebarger, A.R. 2003, *Density and temperature measurements in a solar active region*, ApJ 596, L113, [19 c, 1 c/y].
Warren, H.P., Ugarte-Urra, I., Doschek, G.A., et al. 2008, *Observations of active region loops with the EIS on Hinode*, ApJ 686, L131, [75 c, 8 c/y].
Warren, H.P., Mariska, J.T., and Doschek, G.A. 2013, *Observations of thermal flare plasma with the EUVE*, ApJ 770, 116, [22 c, 5 c/y].
Weber, M.A., Schmelz, J.T., DeLuca, E.E., et al. 2005, *Isothermal bias of the "filter ratio" method for observations of multithermal plasma*, ApJ 635, L101, [35 c, 3 c/y].

(9.5) Coronal Loops: Flows

Baker, D., Janvier, M., Démoulin, P., et al. 2017, *Apparent and intrinsic evolution of active region upflows*, SoPh 292, id.46.
Bethge, C., Beck, C., Peter, H. et al. 2012, *Siphon flow in a cool magnetic loop*, A&A 537, A130, [12 c, 2 c/y].
Brosius, J.W. 2005, *Mass flows in a disappearing sunspot plume*, ApJ 622, 1216, [19 c, 2 c/y].
Brosius, J.W. and Landi, E. 2005, *Properties of a sunspot plume observed with the CDS aboard the SOHO*, ApJ 632, 1196, [13 c, 1 c/y].
Byhring, H.S., Esser, R., and Lie-Svendsen, O. 2008, *The funnel geometry of open flux tubes in the low solar corona constrained by O VI and Ne VIII outflow*, ApJ 673, L91, [5 c, 0.5 c/y].
Del Zanna, G. 2008, *Flows in active region loops observed by Hinode EIS*, A&A 481, L49, [115 c, 12 c/y].
Démoulin, P., Baker, D., Mandrini, C.H. et al. 2013, *The 3-D geometry of active region upflows deduced from their limb-to-limb evolution*, SoPh 283, 341, [14 c, 3 c/y].
Doschek, G.A., Warren, H.P., Mariska, J.T., et al. 2008, *Flows and nonthermal velocities in solar active regions observed with the EIS on Hinode: A tracer of active region sources of heliospheric magnetic fields ?* ApJ 686, 1362, [115 c, 12 c/y].
Doyle, J.G., Taroyan, Y., Ishak, B. et al. 2006, *Study of a transient siphon flow in a cold loop*, A&A 452, 1075, [20 c, 2 c/y].
Feldman, U., Landi, E., and Curdt, W. 2003, *Nonthermal mass motions within the high-temperature plasma above a complex solar active region*, ApJ 585, 1087, [6 c, 0.4 c/y].
Hara, H., Watanabe, T., Harra, L.K. et al. 2008, *Coronal plasma motions near footpoints of active region loops revealed from spectroscopic observations with Hinode EIS*, ApJ 678, L67, [125 c, 13 c/y].
Kamio, S., Peter, H., Curdt, W., et al. 2011, *Continuous upflows and sporadic downflows observed in active regions*, A&A 532, A96, [26 c, 4 c/y].
Kano, R., Ueda, K., and Tsuneta, S. 2014, *Photospheric properties of warm EUV loops and hot X-ray loops*, ApJ 782, L32, [3 c, 1 c/y].
Killie, M.A., Lie-Svendsen, O., and Leer, E. 2005, *The helium abundance of quiescent coronal loops*, ApJ 632, L155, [7 c, 0.6 c/y].
Lenz, D.D. 2004, *Effects of flow on structure and abundances in multispecies solar coronal loops*, ApJ 604, 433, [7 c, 0.5 c/y].
Mahajan, S.M., Nikol'skaya, K.I., Shatashvili, N.L. et al. 2002, *Generation of flows in the solar atmosphere due to magnetofluid coupling*, ApJ 576, L161, [14 c, 1 c/y].
McIntosh, S.W., Tian, H., Sechler, M. et al. 2012, *On the Doppler velocity of emission line profiles formed in the "coronal Contraflow" that is the chromosphere-corona mass cycle*, ApJ 749, 60, [31 c, 6 c/y].

Orange, N.B., Chesny, D.L., Oluseyi, H.M. et al. 2013, *Direct observations of plasma upflows and condensation in a catastrophically cooling solar transition region loop*, ApJ 778, 90, [3 c, 0.7 c/y].
Patsourakos, S., Klimchuk, J.A., and Young, P.R. 2014, *Core and wing densities of asymmetric coronal spectral profiles: Implications for the mass supply of the solar corona*, ApJ 781, id. 58, [12 c, 3 c/y].
Raju, K.P., Chandrasekhar, T., and Ashok, N.M. 2011, *Analysis of coronal green line profiles: Evidence of excess blueshifts*, ApJ 736, 164, [5 c, 0.8 c/y].
Singh, J., Sakurai, T., Kiyoshi, I. et al. 2005, *Spectroscopic studies of solar corona VII. Formation of a coronal loop by evaporation*, SoPh 226, 201, [6 c, 0.5 c/y].
Su, J.T., Liu, Y., Shen, Y.D. et al. 2012, *Observation of high-speed outflows in coronal loops associated with photospheric magnetic field evolution*, ApJ 760, 82, [7 c, 1 c/y].
Tripathi, D., Mason, H.E., Dwivedi, B.N. et al. 2009, *Active region loops: Hinode EIS observations*, ApJ 694, 1256, [88 c, 10 c/y].
Tripathi, D., Mason, H.E., Del Zanna, G. et al. 2012a, *Observations of plasma upflow in a warm loop with Hinode/EIS*, ApJ 754, L4, [13 c, 2 c/y].
Tripathi, D., Mason, H.E., and Klimchuk, J.A. 2012b, *Active region moss: Doppler shifts from the Hinode/EIS observations*, ApJ 753, 37, [14 c, 2.5 c/y].
Ugarte-Urra, I. and Warren, H.P. 2011, *Temporal variability of active region outflows*, ApJ 730, 37, [32 c, 5 c/y].
Warren, H.P., Ugarte-Urra, I., Young, P., et al. 2011, *The temperature dependence of solar active region outflows*, ApJ 727, 58, [49 c, 8 c/y].
Winebarger, A.R., Warren, H., Van Ballegooijen, A. et al. 2002, *Steady flows detected in EUV loops*, ApJ 567, L89, [113 c, 7 c/y].

(9.6) Coronal Loops: Catastrophic Cooling

Ahn, K., Chae, J.C., Cho, K.S. et al. 2014, *Active region coronal rain event observed by the Fast Imaging Solar Spectrograph on the NST*, SoPh 289, 4117, [8 c, 1 c/y].
Antolin, P. and Rouppe van der Voort, L. 2012, *Observing the fine structure of loops through high-resolution spectroscopic observations of coronal rain with the CRISP instrument at the Swedish Solar Telescope (SST)*, ApJ 745, 152, [80 c, 15 c/y.
Antolin, P., Vissers, G., and Rouppe van der Voort, L. 2012, *On-Disk rain*, SoPh 280, 457, [27 c, 5 c/y].
Antolin, P., Vissers, G., Pereira, M.D., et al. 2015, *The multithermal and multi-stranded nature of coronal rain*, ApJ 806, 81, [34 c, 14 c/y].
Froment, C., Auchère, F., Bocchialini, K. et al. 2015, *Evidence for evaporation-incomplete condensation cycles in warm solar coronal loops*, ApJ 807, 158, [17 c, 7 c/y].
Froment, C., Auchére, F., Aulanier, G. et al. 2017, *Long-period intensity pulsations in coronal loops explained by thermal non-equilibrium cycles*, ApJ 835, 272, [5 c, 5 c/y].
Kohutova, P. and Verwichte, E. 2016, *Analysis of coronal rain observed by IRIS, Hinode/SOT, and SDO/AIA: Transverse oscillations, kinematics, and thermal evolution*, ApJ 827, 39, [7 c, 5 c/y].
Kohutova, P. and Verwichte, E. 2017a, *Dynamics of plasma condensations in a gravitationally stratified coronal loop*, A&A 602, A23, [2 c, 2 c/y].
Kohutova, P. and Verwichte, E. 2017b, *Excitation of vertical coronal loop oscillations by plasma condensations*, A&A 606, 120.
Mendoza-Briceno, C.A., Erdelyi, R., and Di G. Sigaloti, L. 2002, *Coronal loop heating by random energy releases*, ApJ 579, L49, [27 c, 2 c/y].
Müller, D.A.N., Hansteen, V.H., and Peter, H. 2003, *Dynamics of solar coronal loops. I. Condensation in cool loops and its effect on transition region lines*, A&A 411, 605, [100 c, 7 c/y.

Müller, D.A.N., Peter, H., and Hansteen, V.H. 2004, *Dynamics of solar coronal loops. II. Catastrophic cooling and high-speed downflows*, A&A 424, 289, [85 c, 6 c/y].

Oliver, R., Solar, R., Terradas, J. et al. 2016, *Dynamics of coronal rain and descending plasma blobs in solar prominences. II. Partially ionized case*, ApJ 818, 128, [7 c, 5 c/y].

Peter, H., Bingert, S., Kamio, S. et al. 2012, *Catastrophic cooling and cessation of heating in the solar corona*, A&A 537, A152, [13 c, 2 c/y].

Scullion, E., Rouppe van der Voort, L., Antolin, P. et al. 2016, *Observing the formation of flare-driven coronal rain*, ApJ 833, 184, [5 c, 3 c/y]

Verwichte, E. and Kohutova, P. 2017, *Excitation and evolution of vertically polarized transverse loop oscillations by coronal rain*, A&A 601, L2, [1 c, 1 c/y].

Verwichte, E., Antolin, P., Rowlands, G. et al. 2017, *Kinematics of coronal rain in a transversely oscillating loop: Ponderomotive force and rain-excited oscillations*, A&A 598, A57, [5 c, 5 c/y].

(9.7) Coronal Loops: Heating Function

Aschwanden, M.J., Newmark, J.S., Delaboudiniere, J.P., et al. 1999, *3-D stereoscopic analysis of solar active region loops. I. SOHO/EIT observations at temperatures of* $(1.0–1.5) \times 10^6$ *K*, ApJ 515, 842, [219 c, 12 c/y].

Aschwanden, M.J., Nightingale R.W., and Alexander, D. 2000, *Evidence for nonuniform heating of coronal loops inferred from multithread modeling of TRACE data*, ApJ 541, 1059, [234 c, 14 c/y].

Aschwanden, M.J. and Nitta, N. 2000, *The effect of hydrostatic weighting on the vertical temperature structure of the solar corona*, ApJ 535, L59, [35 c, 2 c/y].

Aschwanden, M.J. and Peter, H. 2017, *The width distribution of loops and strands in the solar corona. - Are we hitting rock bottom*, ApJ 840, 4, [7 c, 7 c/y].

Bradshaw, S.J. and Cargill, P.J. 2006, *Explosive heating of low-density coronal plasma*, A&A 458, 987, [58 c, 5 c/y].

Bradshaw, S.J. and Cargill, P.J. 2013, *The influence of numerical resolution on coronal density in hydrodynamic models of impulsive heating*, ApJ 770, 12, [36 c, 8 c/y].

Brooks, D.H., Warren, H.P., Ugarte-Urra, I. et al. 2013, *High spatial resolution observations of loops in the solar corona*, ApJ 772, L19, [47 c, 10 c/y].

Chae, J.C., Poland, A.I., and Aschwanden, M.J. 2002, *Coronal loops heated by MHD turbulence. I. A model of isobaric Quiet-Sun loops with constant cross sections*, ApJ 581, 726, [14 c, 1 c/y].

Guarrasi, M., Reale, F., and Peres, G. 2010, *Coronal fuzziness modeled with pulse-heated multi-heated multi-stranded loop systems*, ApJ 719, 576.

Klimchuk, J.A. 2006, *On solving the coronal heating problem*, SoPh 234, 41, [471 c, 41 c/y].

Klimchuk, J.A. 2009, *Coronal loop models and those annoying observations ?* (Keynote), in "The Second Hinode Science Meeting", ASP Conf. Ser. Vol. 415, (eds. B.Lites et al.), p.221.

Lenz, D.D., DeLuca, E.E., Golub, L., et al. 1999, *Temperature and emission-measure profiles along long-lived coronal loops observed with the TRACE*, ApJ 517, L155, [145 c, 8 c/y].

Mikic, Z., Lionello, R., Mok, Y., et al. 2013, *The importance of geometric effects in coronal loop models*, ApJ 773, 94, [34 c, 10 c/y].

Mulu-Moore, F.M., Winebarger, A.R., Warren, H.P., et al. 2011, *Determining the structure of solar coronal loops using their evolution*, ApJ 733, 59, [23 c, 4 c/y].

Patsourakos, S. and Klimchuk, J.A. 2006, *Nonthermal spectral line broadening and the nanoflare model*, ApJ 647, 1452, [93 c, 8 c/y].

Peter, H., Bingert, S., Klimchuk, J.A., et al. 2013, *Nanoflare statistics in an active region 3D MHD coronal model*, AA 556, A104, [23 c, 5 c/y].

Reale, F. 2002, *More on the determination of the coronal heating function from Yohkoh data*, ApJ 580, 566, [38 c, 2 c/y].

Rosner, R., Tucker, W.H., and Vaiana, G.S. 1978, *Dynamics of the quiescent solar corona*, ApJ 220, 643, [1301 c, 33 c/y].
Serio, S., Peres, G., Vaiana, G.S., et al. 1981, *Closed coronal structures. II. Generalized hydrostatic model*, ApJ 243, 288, [272 c, 7 c/y].
Testa, P., Peres, G., and Reale, F. 2005, *Emission measure distribution in loops impulsively heated at the footpoints*, ApJ 622, 695, [31 c, 2 c/y].
Warren, H.P., Winebarger, A.R., and Hamilton, P.S. 2002, *Hydrodynamic modeling of active regions*, ApJ 579, L41, [95 c, 6 c/y].
Warren, H.P., Winebarger, A.R., and Mariska, J.T. 2003, *Evolving active region loops observed with the TRACE. II. Time-dependent hydrodynamic simulations*, ApJ 593, 1174, [108 c, 7 c/y].
Warren, H.P., Kim, D.M., DeGiorgi, M., et al. 2010a, *Modeling evolving coronal loops with observations from STEREO, Hinode, and TRACE*, ApJ 713, 1095, [17 c, 2 c/y].
Warren, H.P., Winebarger, A.R., and Brooks, D.H. 2010b, *Evidence for steady heating: Observations of an active region core with Hinode and TRACE*, ApJ 711, 228, [51 c, 7 c/y].
Winebarger, A.R., Warren, H.P., and Seaton, D.B. 2003, *Evolving active region loops observed with the TRACE. I. Observations*, ApJ 593, 1164, [88 c, 6 c/y].

(9.8) Coronal Loops: The 0-D EBTEL Code

Antiochos, S.K., MacNeice, P.J., Spicer, D.S., et al. 1999, *The dynamic formation of prominence condensations*, ApJ 512, 985, [145 c, 8 c/y].
Aschwanden, M.J. and Tsiklauri, D. 2009, *The hydrodynamic evolution of impulsively heated coronal loops: Explicit analytical approximations*, ApJSS 185, 171, [15 c, 2 c/y].
Bradshaw, S.J. and Klimchuk, J.A. 2011, *What dominates the coronal emission spectrum during the cycle of impulsive heating and cooling ?* ApJSS 194, 26., [53 c, 8 c/y]
Cargill, P.J. 1994, *Some implications of the nanoflare concept*, ApJ 422, 381, [188 c, 8 c/y].
Cargill, P.J., Bradshaw, S.J., and Klimchuk, J.A. 2012a, *Enthalpy-based thermal evolution of loops. II. Improvements to the model*, ApJ 752, 161, [43 c, 8 c/y].
Cargill, P.J., Bradshaw, S.J., and Klimchuk, J.A. 2012b, *Enthalpy-based thermal evolution of loops. III. Comparison of 0-D models*, ApJ 758, 5, [24 c, 4 c/y].
Fisher, G.H. and Hawley, S.L. 1990, *An equation for the evolution of solar and stellar flare loops*, ApJ 357, 243, [67 c, 2 c/y].
Klimchuk, J.A., Patsourakos, S., and Cargill, P.J. 2008, *Highly efficient modeling of dynamic coronal loops*, ApJ 682, 1351, [153 c, 16 c/y].
Kopp, R.A. and Poletto, G. 1993, *Coronal heating by nanoflares: Individual events and global energetics*, ApJ 418, 496, [39 c, 2 c/y].
Kuin, N.P.M. and Martens, P.C.H. 1982, *On the thermal stability of hot coronal loops. The coupling between chromosphere and corona*, A&A 108, L1, [68 c, 2 c/y].
Raftery, C.L., Gallagher, P.T., Milligan, R.O., et al. 2009, *Multi-wavelength observations and modelling of a canonical solar flare*, ApJ 494, 1127, [44 c, 5 c/y].
Ugarte-Urra, I. and Warren, H.P. 2014, *Determining heating timescales in solar active region cores from AIA/SDO Fe XVIII images*, ApJ 783, 12, [14 c, 4 c/y].
Viall, N.M. and Klimchuk, J.A. 2012, *Evidence for widespread cooling in an active region observed with the SDO/AIA*, ApJ 753, 35, [60 c, 11 c/y].

(9.9) Coronal Loops: 1-D Hydrodynamics

Antiochos, S.K., MacNeice, P.J., Spicer, D.S., et al. 1999, *The dynamic formation of prominence condensations*, ApJ 512, 985, [145 c, 8 c/y].
Aschwanden, M.J. and Tsiklauri, D. 2009, *The hydrodynamic evolution of impulsively heated coronal loops: Explicit analytical approximations*, ApJS 185, 171, [15 c, 2 c/y].
Aschwanden, M.J. and Shimizu, T. 2013, *Multi-wavelength observations of the spatio-temporal evolution of solar flares with AIA/SDO. II. Hydrodynamic scaling laws and thermal energies*, ApJ 776, 132, [14 c, 3 c/y].
Bradshaw, S.J. 2008, *A re-interpretation of the energy balance in active region loops following new results from Hinode EIS*, A&A 486, L5.
Bradshaw, S.J. and Mason, H.E. 2003, *A self-consistent treatment of radiation in coronal loop modelling*, A&A 401, 699, [60 c, 4 c/y].
Dudik, J., Dzifcakova, E., Karlicky, M., et al. 2009, *Analytical model of static coronal loops*, A&A 502, 957, [2 c, 0.2 c/y].
Jakimiec,J., Sylwester,B., Sylwester,J., et al. 1992, *Dynamics of flaring loops. II. Flare evolution in the density-temperature diagram*, A&A 253, 269, [93 c, 4 c/y].
Kuin, N.P.M. and Martens, P.C.H. 1982, *On the thermal stability of hot coronal loops. The coupling between chromosphere and corona*, A&A 108, L1, [68 c, 2 c/y].
Landi, E. and Landini, M. 1999, *Radiative losses of optically thin coronal plasmas*, A&A 347, 401, [46 c, 2 c/y].
Landini, M. and Landi, E. 2002, *Models for solar magnetic loops. I. A simple theoretical model and diagnostic procedure*, A&A 383, 653, [9 c, 0.6 c/y].
Martens, P.C.H. 2010, *Scaling laws and temperature profiles for solar and stellar coronal loops with nonuniform heating*, ApJ 714, 1290, [23 c, 3 c/y].
Rosner, R., Tucker, W.H., and Vaiana, G.S. 1978, *Dynamics of the quiescent solar corona*, ApJ 220, 643, [1301 c, 33 c/y].
Serio, S., Peres, G., Vaiana, G.S., et al. 1981, *Closed coronal structures. II. Generalized hydrostatic model*, ApJ 243, 288, [272 c, 7 c/y].
Sylwester, B., Sylwester, J., Serio, S. et al. 1993, *Dynamics of flaring loops. III. Interpretation of flare evolution in the emission measure-temperature diagram*, A&A 582, 486, [57 c, 2 c/y].

(9.10) Coronal Loops: Magnetic Modeling

Amari, T., Boulmezaoud, T.Z., and Aly, J.J. 2006, *Well posed reconstruction of the solar coronal magnetic field*, A&A 446, 691, [94 c, 8 c/y].
Aschwanden, M.J. and Sandman, A.W. 2010, *Bootstrapping the coronal magnetic field with STEREO: Unipolar potential field modeling*, Astron. J. 140, 723, [23 c, 3 c/y].
Aschwanden, M.J., Wuelser, J.P., Nitta, N.V. et al. 2012, *First 3-D reconstruction of coronal loops with the STEREO A+B spacecraft. IV. Magnetic modeling with twisted force-free fields*, ApJ 756, 124, [21 c, 4 c/y].
Aschwanden, M.J. 2013a, *Nonlinear force-free magnetic field fitting to coronal loops with and without stereoscopy*, ApJ 763, 115, [17 c, 4 c/y].
Aschwanden, M.J. 2013b, *A nonlinear force-free magnetic field approximation suitable for fast forward-fitting to coronal loops. I. Theory*, SoPh 287, 323, [17 c, 4 c/y].
Aschwanden, M.J. and Malanushenko, A. 2013, *A nonlinear force-free magnetic field approximation suitable for fast forward-fitting to coronal loops. II. Numeric Code and Tests*, SoPh 287, 345, [20 c, 4 c/y].
Aschwanden, M.J. 2013c, *A nonlinear force-free magnetic field approximation suitable for fast forward-fitting to coronal loops. III. Free energy*, SoPh 287, 369, [15 c, 3 c/y].
Aschwanden, M.J., Xu, Y., and Jing, J. 2014, *Global energetics of solar flares. I. Magnetic energies*, ApJ 797, 50, [26 c, 7 c/y].

Aschwanden, M.J. 2016, *The vertical-current approximation nonlinear force-free field code - Description, performance, tests, and measurements of magnetic energies dissipated in solar flares*, ApJSS 224, 25, [8 c, 5 c/y].

Aschwanden, M.J., Reardon, K., and Jess, D.B. 2016, *Tracing the chromosphere and coronal magnetic field with AIA, IRIS, IBIS, and ROSA data*, ApJ 826, 61, [5 c, 3 c/y].

Bobra, M.G., van Ballegooijen, A.A. and DeLuca, E.E. 2008, *Modeling nonpotential fields in solar active regions*, ApJ 672, 1029, [79 c, 8 c/y].

De Rosa, M.L., Schrijver, C.J., Barnes, G., et al. 2009, *A critical assessment of nonlinear force-free field modeling of the solar corona for active region 10953*, ApJ 696, 1780, [230 c, 27 c/y].

Flyer, N., Fornberg, B., Thomas, S. et al. 2004, *Magnetic field confinement in the solar corona. I. Force-free magnetic fields*, ApJ 606, 1210, [46 c, 3 c/y].

Metcalf, T.R., Jiao, L., Uitenbroek, H., et al. 1995, *Is the solar chromospheric magnetic field force-free ?* ApJ 439, 474, [212 c, 9 c/y].

Metcalf, T.R., DeRosa, M.L., Schrijver, C.J. et al. 2008, *Nonlinear force-free modeling of coronal magnetic fields. II. Modeling a filament arcade and simulated chromospheric and photospheric vector fields*, SoPh 247, 269, [151 c, 16 c/y].

Sandman,A W., Aschwanden, M.J., Derosa, M.L., et al. 2009, *Comparison of STEREO/ EUVI loops with potential magnetic field models*, SoPh 259, 1, [31 c, 4 c/y].

Sandman, A.W. and Aschwanden, M.J. 2011, *A new method for modeling the coronal magnetic field with STEREO and submerged dipoles*, SoPh 270, 503, [17 c, 3 c/y].

Schrijver, C.J., DeRosa, M.L., Metcalf, T.R. et al. 2006, *Nonlinear force-free modeling of coronal magnetic fields Part I: A quantitative comparison of methods*, SoPh 235, 161, [215 c, 19 c/y].

Song, M.T., Fang, C., Tang, Y.H. et al. 2006, *A new and fast way to reconstruct a nonlinear force-free field in the solar corona*, ApJ 649, 1084, [39 c, 3 c/y].

Titov, V.S., Török, T., Mikic, Z., et al. 2014, *A method of embedding circular force-free flux ropes in potential magnetic fields*, ApJ 790, 163, [15 c, 4 c/y].

Van Ballegooijen, A.A. 2004, *Observations and modeling of a filament on the Sun*, ApJ 612, 519, [151 c, 12 c/y].

Van Ballegooijen, A.A., DeLuca, E.E., Squires, K. et al. 2007, *Modeling magnetic flux ropes in the solar atmosphere*, Atmos. Terr. Phys. 69, 24, [12 c, 1 c/y].

Wheatland, M.S., Sturrock, P.A., and Roumeliotis, G. 2000, *An optimization approach to reconstructing force-free fields*, ApJ 540, 1150, [250 c, 14 c/y].

Wiegelmann, T. 2004, *Optimization code with weighting function for the reconstruction of coronal magnetic fields*, SoPh 219, 87, [276 c, 20 c/y].

Wiegelmann, T., Inhester, B., and Sakurai, B. 2006, *Preprocessing of vector magnetograph data for a nonlinear force-free magnetic field reconstruction*, SP 223, 215, [217 c, 19 c/y].

Wiegelmann, T. 2007, *Computing nonlinear force-free coronal magnetic fields in spherical geometry*, SoPh 240, 227, [46 c, 4 c/y].

Wiegelmann, T. and Inhester, B. 2010, *How to deal with measurement errors and lacking data in nonlinear force-free magnetic field modeling ?* A&A 516, A107, [64 c, 9 c/y].

Wiegelmann, T., Thalmann, J.K., Inhester, B. et al. 2012, *How should one optimize nonlinear force-free coronal magnetic field extrapolations from SDO/HMI vector magnetograms*, SoPh 281, 37, [66 c, 12 c/y].

Chapter 10
Coronal Loop Oscillations and Waves

10.1 Coronal Loop Oscillations: Transverse Waves

The new field of "*coronal seismology*" started with the discovery of transverse loop oscillations detected with the TRACE instrument, which were interpreted as standing fast kink-mode waves (Aschwanden et al. 1999; Nakariakov et al. 1999), although the theoretical framework of MHD waves (including fast kink modes, fast sausage modes, and slow magneto-acoustic waves) has been developed and applied to solar (non-imaging) data at least two decades earlier (see reviews in Roberts 2000; Nakariakov and Verwichte 2005; Banerjee et al. 2007; Ruderman and Erdelyi 2009; Wang 2011, 2016; Nakariakov et al. 2016). After the demise of TRACE, unprecedented details of oscillating loops were investigated with AIA/SDO (e.g., Aschwanden and Schrijver 2011; White and Verwichte 2012; White et al. 2012), catalogued in Goddard et al. (2016).

Coronal standing fast kink mode waves were initially modeled in terms of linearized waves in (straight) homogeneous cylindrical flux tubes, but more realistic models include the effects of gravitational stratification, geometric expansion with height, curvature of the guiding magnetic field, non-circular cross-section, geometric loop shape, (helical) magnetic twist, and wave damping (e.g., see review by Ruderman and Erdelyi 2009).

An initial inspection of 255 flares (from GOES class C3 to X2) revealed loop oscillations in 6%, triggered by flares, CMEs, or filament destabilizations (Schrijver et al. 2002). Almost all of the loop oscillations start at some distance away from the center of the triggering disturbance, suggesting a spherically expanding wave (Schrijver et al. 2002). The coronal loop oscillations further exhibit deviations from strictly periodic pulses, spatially asymmetric oscillations, nonlinear transverse motions, which also point towards flare-induced impulsively generated MHD waves that propagate forth and back in the loops and decay quickly by wave leakage or damping (Aschwanden et al. 2002). Some transverse loop oscillations were found to occur dominantly in hot coronal lines during the formation of hot post-flare loops

M. J. Aschwanden, *New Millennium Solar Physics*, Astrophysics and Space Science Library 458, https://doi.org/10.1007/978-3-030-13956-8_10

(Li and Gan 2006; White et al. 2012). A statistical study of 120 oscillating loops in 58 events observed with AIA/SDO revealed that 44 events (76%) are associated with CMEs, 57 events (98%) are associated with low coronal eruptions, and 53 events (91%) with flares (Zimovets and Nakariakov 2015), similarly to the results of Schrijver et al. (2002).

It was immediately recognized that the measurement of the fast kink mode period P, the length of the oscillating loop L, and the electron density n_e, provides a measurement of the mean magnetic field B in an oscillating loop, which became the most prominent tool of the *coronal seismology* method (Nakariakov and Ofman 2001).

The observability of various MHD oscillation modes depends on the electron density contrast between inside and outside of the loop cross-section, and is optimal for compressible waves, e.g., for slow magneto-acoustic waves or fast sausage modes (Cooper et al. 2003).

Coupled fast kink oscillations have been observed in a post-flare loop arcade, exhibiting multiple oscillation modes, likely to correspond to the fundamental and second harmonic mode (Verwichte et al. 2004; De Moortel and Brady 2007; Guo et al. 2015).

Kink mode oscillations generally show loop displacements in transverse direction to the loop plane, which imposes the least deformation or compression of plasma inside the oscillating loop, but displacements in the (vertical) loop plane, called *vertical polarization mode*, have been observed too (Wang and Solanki 2004; Verwichte et al. 2006; Aschwanden and Schrijver 2011; White et al. 2012). In the vertical mode, some kink-mode oscillations are also found to be coupled to the cross-sectional radius and to the electron density variation (Aschwanden and Schrijver 2011), similar to a fast sausage mode (Fig. 10.1).

Coronal loops in hydrodynamic equilibrium have typical gravitational scale heights of $H \approx 50$ Mm (for $T_e \approx 1$ MK temperature loops). The density variation along the loop changes the Alfvén velocity $v_A \propto B/\sqrt{n_e}$ along the loop, but the effects on the amplitude profile of a kink-mode oscillation is found to be below the present measurement accuracy (Erdelyi and Verth 2007; Verth et al. 2007). Besides the gravitational density variation along loops, the magnetic flux tube divergence should also be taken into account in transverse loop oscillation models (Verth and Erdelyi 2008). Furthermore, an elliptical cross-section instead of a cylindrical shape may also affect the fundamental to harmonic period ratio in emerging coronal loops (Morton and Erdelyi 2009).

The loop curvature, which is mostly neglected in simple flux tube models of oscillating loops, is found to introduce wave leakage into the system, because of changes in the equilibrium, as demonstrated with a curved slab geometric model (Van Doorsselaere et al. 2009). On top of the circular loop curvature, a helical twist may occur in addition, which transforms a simple kink eigen-mode into a torsional Alfvén wave scenario (Antolin and Verwichte 2011).

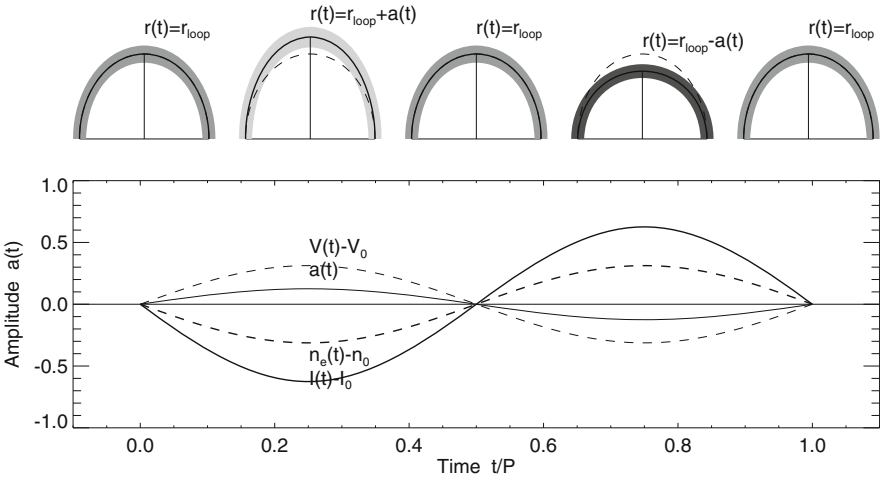

Fig. 10.1 Schematic of sinusoidal modulation of the loop vertical radius $r(t) = r_{loop} + a(t)$, volume $V(t) - V_0$, density $n_e(t) - n_0$, and flux intensity $I(t) - I_0$ during one full oscillation period, as observed on 2010 October 16, 19:05 UT, with AIA/SDO. Note that the density and intensity vary in anti-correlation to the loop amplitude, indicated with the grey-scale shading of the loops (Aschwanden and Schrijver 2011)

10.2 Coronal Loop Oscillations: Wave Damping

Coronal loop oscillations generally display damping of their transverse amplitude over the duration of a few oscillation periods, as it is expected for an impulsively generated exciter mechanism, but *"decay-less"* maintenance of quasi-steady oscillations is observed in a some cases also, which challenges traditional damping mechanisms. A number of physical mechanisms have been invoked for the damping of coronal loop oscillations, such as non-ideal MHD effects (resistivity, viscosity, Ohmic dissipation, plasma heating, plasma cooling), lateral wave leakage, footpoint wave leakage, phase mixing, and resonant absorption (Roberts 2000).

The damping due to resonant absorption (acting in the inhomogeneous regions of a flux tube where energy is transferred from the kink mode to Alfvén azimuthal oscillations) is analytically treated in Ruderman and Roberts (2002), who suggest that those loops with density inhomogeneities on a small scale (compared with the loop cross-sectional width) are able to support (observable) coherent oscillations for any length of time, while loops with a smooth cross-sectional density variation do not exhibit pronounced oscillations. Resonant damping of loops with elliptic cross-sections were found to have a similar decrement as circular loops (Ruderman 2003). Resonant absorption is selective because the damping length is inversely proportional to the frequency, so that the radial inhomogeneity causes coronal wave guides to be a natural low-pass filter of the high frequency components dissipated in the lower corona (Terradas et al. 2010). A compilation of many kink mode periods

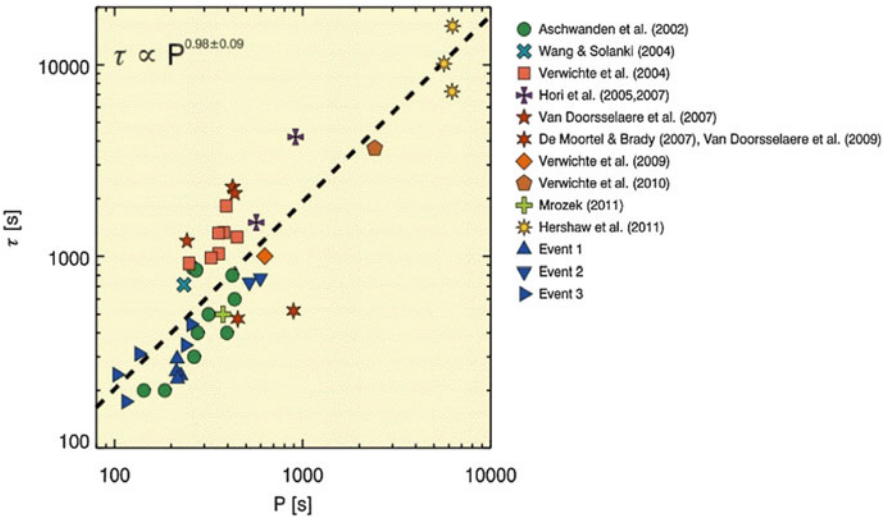

Fig. 10.2 The linear relationship of the periods P and damping times τ_d as inferred from previous studies of transverse coronal loop oscillations and one prominence oscillation (White and Verwichte 2012)

P and damping times τ_d from different observers and instruments reveals a good correlation between the two time scales, i.e., $\tau_d \propto P^{0.98\pm0.09}$ (Fig. 10.2), which is a strong endorsement for the interpretation of a resonant absorption damping mechanism (White and Verwichte 2012). In a more comprehensive statistical study, a linear fit of $\tau_d = (1.53 \pm 0.03)\,P$ was obtained (Goddard et al. 2016).

Early observational tests of damping times measured with TRACE revealed the best agreement for the phase mixing mechanism (leading to rapid dissipation of Alfvén waves due to the variation of the Alfvén speed across the wave front, and to formation of small scales), but an anomalously high viscosity is needed (Ofman and Aschwanden 2002). Other mechanisms (such as wave leakage, ideal decay of kink modes, radiative cooling, resonant absorption) showed less agreement (Ofman and Aschwanden 2002). However, if the ratio of the inhomogeneity length scale to the radius of the loop is allowed to vary from loop to loop, resonant absorption without invoking anomalously low Reynolds numbers can explain the observed loop oscillations also (Goossens et al. 2002; Aschwanden et al. 2003). Multiple (fundamental and second harmonic) oscillation modes observed with TRACE in a flare loop arcade were found to be consistent with both phase mixing and resonant absorption, although the damping times were found to be longer compared with previous studies (Verwichte et al. 2004).

Damping times by wave leakage was found to be too long to explain the observed decays, except for very short or thick loops (Cally 2003). Lateral leakage in wave damping includes also the mechanism of wave tunneling, where waves either leak straight out into the external medium, or have to overcome an evanescent barrier

(Verwichte et al. 2006). The damping of kink mode oscillations with vertical polarization has been studied by using the full MHD equations in a curved flux tube, and it was found that the decay rate increases with longer wavelength, increasing β-parameter, and decreasing contrast, and it was suggested that wave leakage through tunneling is the dominant damping mechanism of the observed kink-mode oscillations (Brady and Arber 2005; Brady et al. 2006; Verwichte et al. 2006). Using a toroidal model with a power law density profile, it was found that the kink mode couples to an Alfvén mode and enables wave leakage by tunneling, so that resonant damping and wave leakage occur together (Terradas et al. 2006a,b).

The simultaneous observation of fundamental and first overtone (second harmonic) kink mode oscillation yields a period ratio P_2/P_1, which can be used to infer the density scale height (Andries et al. 2005), but the result depends strongly on the assumed loop geometry (Dymova and Ruderman 2006a,b). Fundamental and second harmonic standing kink modes have been spatially resolved with AIA/SDO (Pascoe et al. 2016a).

Most of the coronal oscillating loops are observed in EUV wavelengths, at temperatures of $T_e \approx$ 1–2 MK, where radiative cooling is efficient. Consequently, the observed life time of a detected loop in 171 or 193 Å amounts to 10–20 min only, which is commensurable with the typical kink-mode periods (of $P \approx$ 3–5 min), and thus the assumption of an equilibrium state (of electron density and temperature) is violated, and the density dependence of the kink mode period, i.e., $P_{kink} = (2L/v_{A0})\sqrt{[1 + (\rho_e/\rho_0)]/2}$, needs to be taken into account (Aschwanden and Terradas 2008). The loop cooling time has also an important influence on the measured damping times, as well as on the fundamental/harmonic period ratio P_2/P_1 (Morton and Erdelyi 2009).

There are observations of coronal loop oscillations that do not show any (exponential) damping during the detected life time, at least over the duration of $\approx$ 4 oscillation periods (e.g., Aschwanden and Schrijver 2011). For a special set of loop oscillations, which have relatively small displacement amplitudes ($A \lesssim 1$ Mm) and periods in the range of $P \approx$ 2.5–11 min, a "*decay-less*" time evolution (or near-constant amplitude) was found, a behavior that was explained in terms of a damped harmonic resonator affected by a non-resonant continuously operating external force (Anfinogentov et al. 2013; Nistico et al. 2013), or by a self-oscillation mechanism that results from the interaction of the loops with quasi-steady flows, analogous to a bow moving across a violin string (Nakariakov et al. 2016). Such low-amplitude kink oscillations appear to be common according to a recent statistical study of 21 active regions (Anfinogentov et al. 2015). In another statistical study of 58 kink oscillation events observed with AIA the following results were found: a kink speed range of $c_k = (800–3300)$ km s^{-1}, a linear relationship of the period with loop length $P \propto L$, a linear relationship between period and damping time $P \propto \tau_p$, and both exponential and non-exponential damping (Goddard et al. 2016). There are also some indications of a nonlinear damping mechanism, but the the relationship between damping time and oscillation amplitude is not clear-cut (Goddard and Nakariakov 2016). Using the highest quality data available from AIA, the damping time profile was found to fit a Gaussian function better than an exponential profile in

some cases, which was interpreted in terms of mode coupling (Pascoe et al. 2016b,c, 2017).

10.3 Coronal Loop Oscillations: Vertical Polarization

The orientation of the plane in which a loop oscillation takes place is also called polarization: *horizontal polarization* corresponds to an oscillation amplitude that is oriented in transverse (or perpendicular) direction to the loop plane, while *vertical polarization* corresponds to an oscillation amplitude in the loop plane. Most of the reported coronal loop oscillations (observed with TRACE and AIA/SDO) exhibit horizontal polarization (e.g., Aschwanden et al. 2002), while evidence for vertical oscillations was found by Wang and Solanki (2004). Horizontal and vertical oscillations are two different solutions of the kink modes in a curved, line-tied loop. Horizontal oscillations produce little change in the loop length, and therefore, show nearly incompressible Alfvénic properties. Vertical oscillations are associated with expanding and shrinking motion, so that this mode should lead to compression and rarefaction of the plasma, i.e., density perturbations, if the plasma content and the cross-section of the loop remain unchanged over a wave period. Note that this compressibility is introduced by the nonlinearity connected with the effects of a finite amplitude, but is not a property of the MHD mode itself (Wang and Solanki 2004).

The two polarizations can be observationally distinguished either directly from displacement measurements in EUV images, or from difference images, which reveal a density increase at the front of moving loop segments, and a rarefaction in the wake of the moving loop segment (Fig. 10.3). Wang and Solanki (2004) analyzed an oscillating loop detected in the 195 Å passband of TRACE on 2002 April 17, 10:35 UT, which has a loop length of $L \approx 300$–400 Mm, an inclination angle of $\theta \approx 20°$–$40°$, an oscillation velocity of $v_{osc} \approx 130$ km s^{-1}, a period of $P = 3.9$ min, and a decay time of $\tau_d = 11.9$ min. The measured displacement amplitude is consistent with an intensity variation of $\approx 13\%$ due to density changes produced by the change of the loop length, while the observations reveal a considerably larger contrast, but still suggest that these oscillations correspond to a compressible fast MHD mode.

Another well-observed case was reported from an AIA/SDO observation on 2010 October 16, 19:05 UT, triggered by an M2.9 GOES class flare, located far away from the flare site in a narrow-angle CME cone (Aschwanden and Schrijver 2011). This unique event featured a kink-mode oscillation with vertical polarization, coupled cross-sectional and density oscillations with identical periods (Fig. 10.1), no significant damping, a kink mode period of $P = 6.3$ min, multiple interacting oscillating loops, a cool temperature $T_e \approx 0.5$ MK of the loop plasma, a density ratio of $n_e/n_i = (v_A/v_{Ae})^2 = 0.08$, and a magnetic field strength of $B_{kink} = 4.0 \pm 0.7$ G. The coupling of the kink mode and the cross-sectional oscillation (Fig. 10.1) can be explained as a consequence of the loop length variation in a vertically polarized

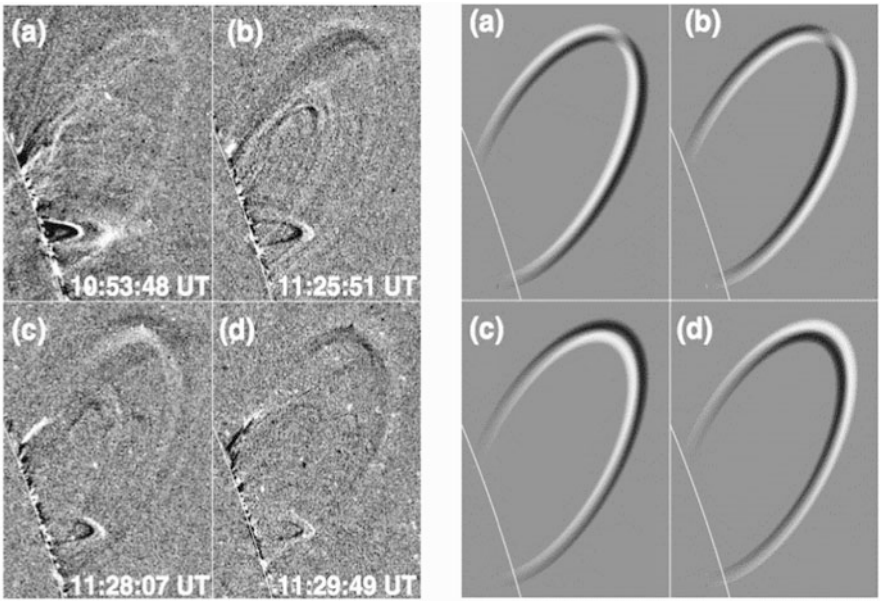

Fig. 10.3 *Left:* TRACE observations of an oscillating loop on 2002 April 17; (**a**) A difference image before the event, which is produced by subtracting the image at 10:35:06 from the image at 10:53:48 UT; (**b**)–(**d**) Running difference images with an interval of $\approx$ 2 min. Black indicates where the loop was in the earlier image, and white where it has moved to. *Right:* Difference images of simulated loop oscillations, with a geometry derived from the observation based on a circular loop model: (**a**)–(**b**) Horizontal oscillations, and (**c**)–(**d**) vertical oscillations (Wang and Solanki 2004)

mode. The seismological period P_{kink},

$$P_{kink} = \frac{2L_{osc}}{c_k} = \frac{2L_{osc}}{v_A}\sqrt{\frac{1+\rho_e/\rho_i}{2}} \tag{10.3.1}$$

was found to agree with the period P derived from the potential field model (quantified by the magnetic field $B(s)$ and Alfvén speed $v_A(s)$),

$$P = \int_0^P dt = \int_0^{2L} \frac{1}{v_A(s)} ds \; . \tag{10.3.2}$$

In addition, an average field strength $< B >$ can be defined by

$$< B >= L \left[\int B(s)^{-1} ds \right]^{-1} \; . \tag{10.3.3}$$

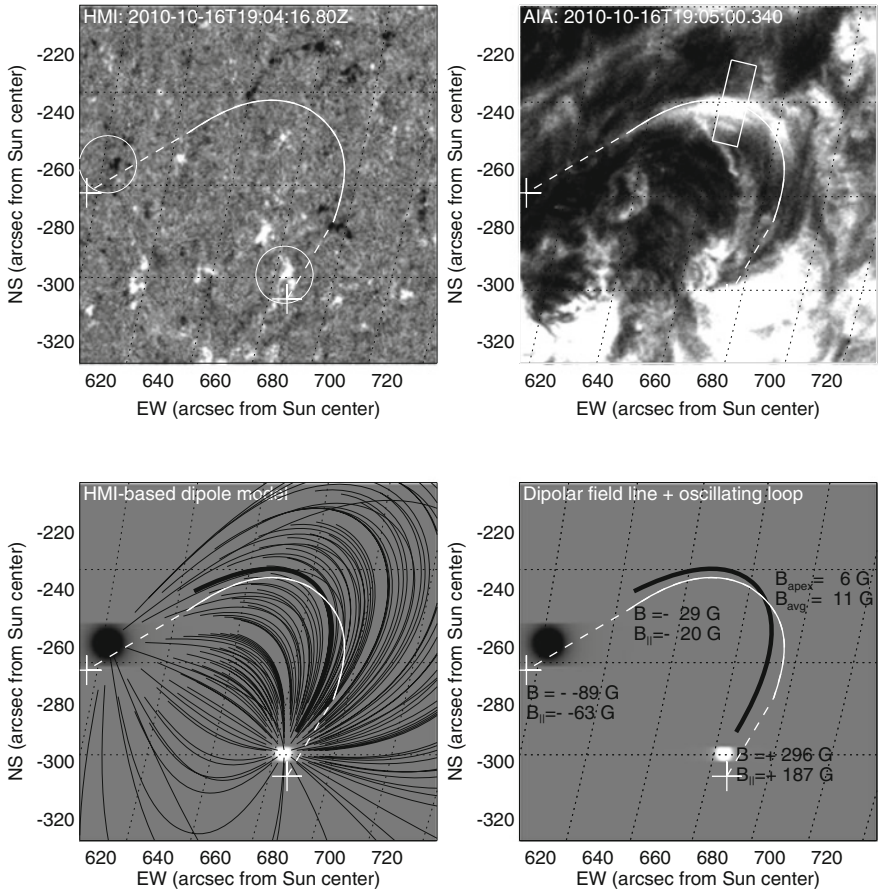

Fig. 10.4 HMI magnetogram (top left), AIA 171 Å image (top right), and HMI-based dipolar potential field model (bottom panels) of the oscillating loop (white curve). A field line that closely coincides with the oscillating loop is shown separately (bottom right; black curve), constrained by the longitudinal magnetic field observed in the HMI magnetogram with $B_{\|1} = 187$ G and $B_{\|2} = -63$ G (Aschwanden and Schrijver 2011)

The dipolar magnetic field model in the environment of the vertically oscillating loop is shown in Fig. 10.4, where the inclination angle between the loop plane and the vertical plane amounts to $\theta \approx 20°$.

Vertical oscillations were also observed during the formation of hot post-flare loops, which represent the first reports of kink mode oscillations found exclusively in hot coronal lines (Li and Gan 2006; White et al. 2012). The 94 and 131 Å filters of AIA/SDO are sensitive to flare temperatures of $T_e \approx 9$–11 MK. Interestingly, the hot oscillating loop is not observed to cool down to the cooler AIA channels, but disappears from all bandpasses at the end of the oscillation. It is suggested that these (5 min) oscillations in hot plasma are a direct byproduct of a magnetic reconnection

process (White et al. 2012), rather than due to a blast wave excitation mechanism that is often proposed for cooler transverse loop oscillations.

Vertical oscillations can be modeled with a 2-D geometry, because the time-dependent motion is all confined in the loop plane, while transverse oscillations require a 3-D geometry. Numerical 2-D MHD simulations have been been carried out for curved flux tubes in equilibrium by Brady and Arber (2005), which show that the decay rate increases with longer wavelengths, with increasing plasma β-parameter, and with decreasing density contrast ratio. These simulations show leaky waves where wave energy is transported away from the flux tube due to the finite radius of curvature, a wave tunneling effect that could explain the high decay (damping) rate observed in the event of Wang and Solanki (2004). Analytical and numerical models predict lateral wave leakage and tunneling effects with a damping rate that is shorter than observed (Verwichte et al. 2006a,b; Selwa et al. 2007), but consistent with numerical simulations (Verwichte et al. 2006c). Further 2-D MHD simulations were performed by implementing an impulsive excitation mechanism (for vertical kink standing waves), embedded in an arcade with a magnetic potential field, including the field line curvature and nonlinearity of the excitation mechanism, and the damping of standing fast magnetosonic waves (Selwa et al. 2005a). These simulations reproduce the rapid damping time and the anti-correlation between displacement and density observed in the case of Wang and Solanki (2004). Generalizing the 2-D MHD model to multiple (up to five) loop strands, it is found that only those loops exhibit collective (synchronized) oscillations that are in closest proximity (with a distance comparable to the strand width), while more distant strands show a weak coupling (Gruszecki et al. 2006).

10.4 Coronal Loop Oscillations: 3-D Kinematics

The time-dependent 3-D reconstruction of oscillating coronal loops should reveal us the 3-D kinematics of the physical excitation mechanism. One expects that the Lorentz force, i.e., $\mathbf{F} = \mathbf{v} \times \mathbf{B}$, can be inferred from the the plasma motion velocity $\mathbf{v}$ in a given coronal magnetic field $\mathbf{B}$, a force that is produced during the launch of coronal mass ejections, for instance, and can lead to large-amplitude kink-mode oscillations. We discussed already the excitation of loop oscillations in horizontal and vertical polarization (Sect. 10.3), which is related to distinctly different solutions of MHD wave modes. There is also ubiquitous convective motion occurring below the solar photosphere, which may cause displacements of loop footpoints and consequently may produce small-amplitude oscillations of coronal loops. However, before quantitative models of the 3-D kinematics of coronal loops can be built, the 3-D geometry and 3-D motion needs to be inferred from observations, which has recently been enabled with stereoscopic data from EUVI/STEREO.

Two examples of stereoscopic 3-D reconstructions of the geometry of oscillating loops are shown in Aschwanden (2009), one for a location near the solar disk center

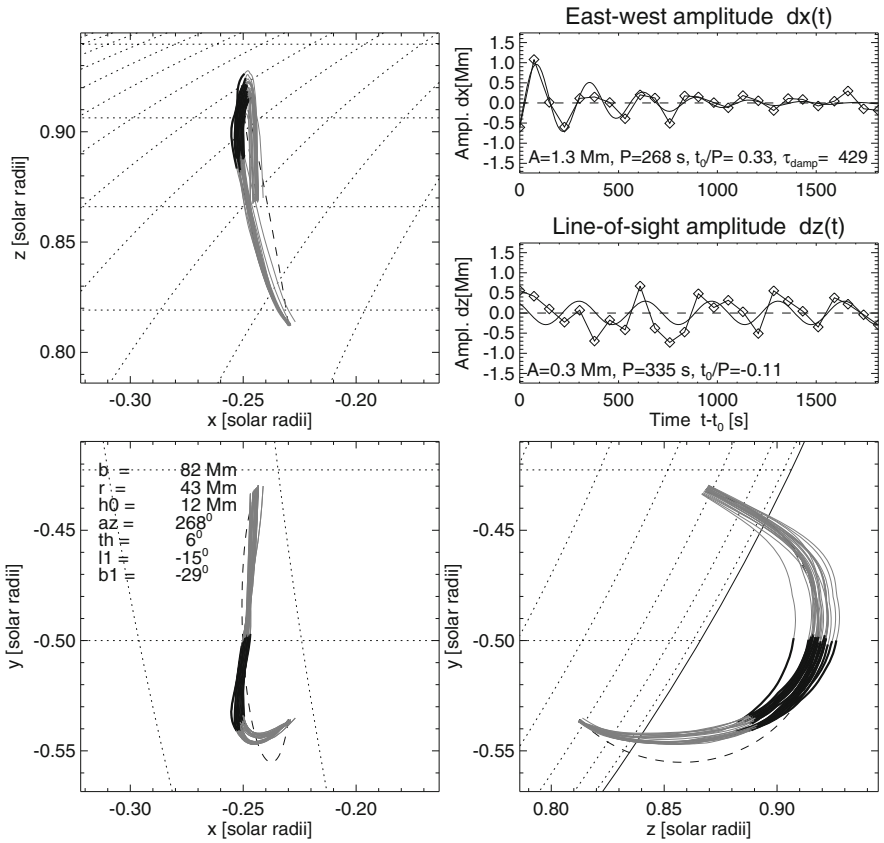

Fig. 10.5 3D reconstruction of loop oscillations for a sequence of TRACE 171 Å images in the time interval of 1998 July 14, 12:59–13:35 UT. The method of the 3D loop geometry with the curvature radius maximization method is visualized, with the loops traced at different times and rendered as grey curves. In addition we show the average loop amplitude $dx(t)$ in the horizontal x-direction and $dz(t)$ in the vertical z-direction (top right panels), for the middle loop segment (in the segment $0.5 < (s/L) < 0.7$ starting from north, marked with black curves), as well as a fit of an exponentially damped sine function to the observed time profiles (Aschwanden 2009)

(Fig. 10.5), and one for a loop seen side-on near the solar limb (Fig. 10.6). Three views in orthogonal directions are shown in Figs. 10.5 and 10.6. The first loop mostly oscillates in vertical direction, since the oscillation amplitudes show a larger spread in the vertical direction (Fig. 10.5, bottom right) than in horizontal direction (Fig. 10.5, bottom left). The second loop, on the other side, exhibits a sigmoid-shaped geometry, while the oscillations can be characterized by torsional motion (Fig. 10.6). There is obviously an infinite number of oscillatory solutions of curved flux tubes, with curved, kinked, and helically twisted shapes, depending on what initial displacement the loop oscillation is triggered by an external force. Another oscillating loop (2010 October 16, 19:05 UT) was found to be located far away

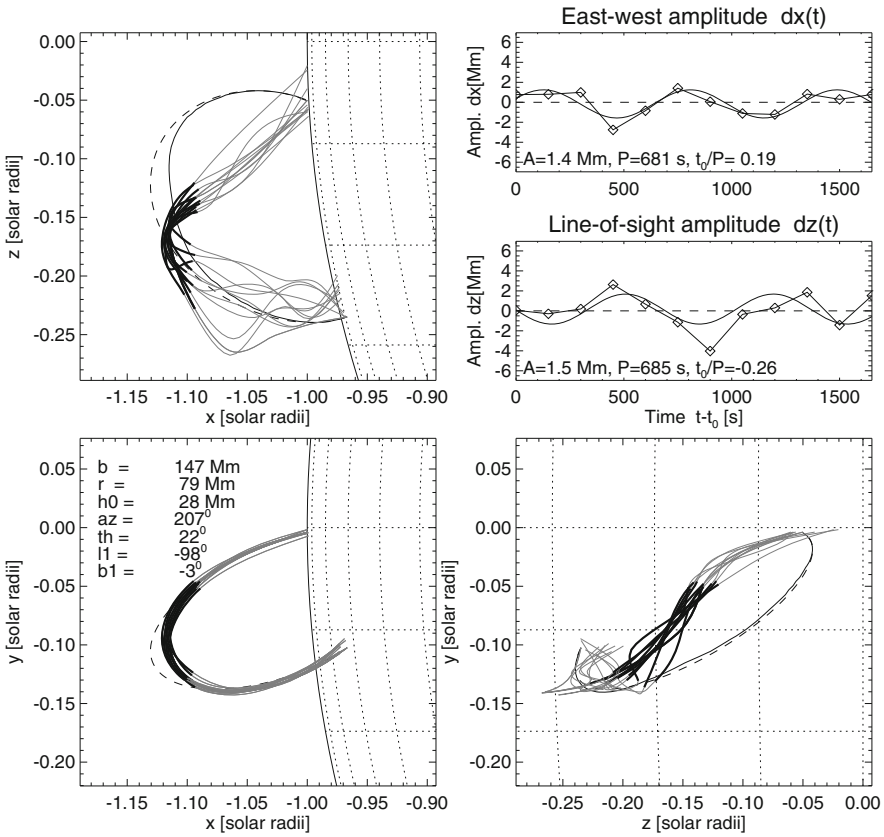

Fig. 10.6 3-D reconstruction of loop oscillations for a sequence of 16 EUVI/A+B 171 Å images in the time interval of 2007 June 27, 17:58–18:26 UT, using the stereoscopic triangulation method. The loop tracings in EUVI/A are rendered in the $x - y$ plane (left bottom panel), while the orthogonal reconstruction are shown in the $x-z$ plane (top left panel) and in the $z-y$ plane (bottom right panel). The loop tracings are rendered with grey curves, the semi-circular fit with a dashed curve, and the curvature radius maximization method with a thin black curve. The oscillation amplitudes averaged in the loop segments $0.3 < s/L < 0.6$ (marked with thick black curves) are shown in x-direction (east-west amplitude $dx(t)$ in top right panel) and in the z direction (line-of-sight amplitude $dz(t)$ in middle right panel) (Aschwanden 2009)

from the flare site (256 Mm) and was hit by a CME-associated global wave that propagated with a speed of $v_{CME} \approx 2000$ km s^{-1}, reached the loop after 132 s, and excited a delayed near-vertical oscillation (Aschwanden and Schrijver 2011). This is one of the few cases where the interaction between the exciter and the oscillating loop is unambiguously disentangled.

While stereoscopic triangulation of oscillating loops is often difficult due to the confusion of multiple loops overlapping each other on top of a time-variable background (that consists of other oscillating loops), alternative methods use a

simple geometrical 3-D model that is forward-fitted to data, such as the de-projection of 2-D loop tracings using the strategy of curvature radius maximization in 3-D space (Aschwanden 2009), or forward-fitting of a semi-circular loop model to the 2-D projections in corresponding EUVI/STEREO image pairs (Verwichte et al. 2009). From reconstructing transverse loop oscillations during the 2007 June 27 event it was found that the oscillation is a fundamental horizontally polarized fast magneto-acoustic kink mode, the loop length is $L = 340 \pm 15$ Mm, the oscillation period is $P = 10.5 \pm 0.5$ min, the damping time is $\tau_d = 17 \pm 5$ min, density variations occur during the transverse oscillation mode (caused by line-of-sight integration), and the magnetic field is $B = 11 \pm 2$ G. Since the intensity variations observed in oscillating loops are ambiguous, they can be produced either by compression and rarefaction (in adiabatically expanding loops) or by line-of-sight integration effects (White and Verwichte 2012; Cooper et al. 2003). 3-D reconstructions of the geometry of oscillating loops are necessary. Unfortunately the oscillating loop was located near the limb, which prevents comparisons with magnetic field models extrapolated from magnetograms.

The excitation mechanisms of loop oscillations are not well understood. Traditional models assume a flare- or CME-generated blast wave that hits the surrounding loops at the launch site of a CME, but this simple model does not explain a lot of characteristics of oscillating loops, such as the selectivity, the polarization, and directivity. An alternative model that captures the excitation of horizontally-polarized transverse oscillations by their interaction with CME-induced vertical flows due to the effect of vortex shedding was proposed by Nakariakov et al. (2009). This mechanism can essentially be understood by three orthogonal force components, where a loop is aligned along the magnetic field **B**, the CME-generated flows stream with velocity **v** in upward direction around the loop, which creates an alternate aerodynamic force **F** perpendicular to the loop. The oscillations are excited most effectively when the force is in resonance with the natural kink mode frequency (Nakariakov et al. 2009). Another observation that could not be reconciled with a CME-generated blast wave model was found in a hot soft X-ray emitting oscillating loop that did not cool through the EUV wavelengths, and thus may be directly connected with a hot plasma diffusion region of a magnetic reconnection process (White and Verwichte 2012).

10.5 Coronal Loop Oscillations: Multi-Stranded Loop Systems

A multi-stranded loop system may have a different dynamics than a monolithic loop, unless all strands become synchronized to the same periodic rhythm (in wave phase and period) by some collective resonant behavior. This may depend on how close the multiple strands are located, because individual loop strands at large distances obviously experience a weak coupling. If neighbored loops are out of

phase, the mutual coupling may lead to strong damping. Alternatively, complex system dynamics may occur such as in a system of coupled pendulums, subject to a self-organization process. These questions have been studied from observations with high-resolution imagers such as TRACE, AIA/SDO, and SOT/Hinode, as well as by analytical models and numerical MHD simulations.

From the observational point of view, oscillating loop strands are unique in the sense that they move over a slowly-varying background, and this way produce a much cleaner separation of the EUV emission of a target loop from the background forest of loops, thanks to the "scanning ability" of the oscillation amplitude. Statistics of loop widths revealed distributions with most frequent values of $w = 1430 \pm 340$ km, based on TRACE data (Aschwanden and Nightingale 2005), down to a most frequent value of $w \approx 500$ km based on Hi-C data (Aschwanden and Peter 2017), see Sect. 9.2 for a complete compilation, and Sect. 9.3 for a discussion of multi-strand structures.

Ofman (2005) investigated the oscillation of multi-threaded loops by solving the resistive 3-D MHD equations to model straight cylindrical multi-stranded loops and found that the coupling between closely spaced strands affects the damping rate of the oscillations, which becomes stronger for higher Lundquist numbers, compared to the monolithic loop. Gruszecki et al. (2006) performed 2-D numerical simulations of multi-strand scenarios containing two up to five strands and found that only strands that are very close to each other (at a distance comparable to the strand width) change the collective behavior of kink oscillations. More distant strands exhibit weak coupling, but their dynamics is essentially that of separate oscillating loops.

Observations with SOT/Hinode in the Ca II H line (3968 Å), which has a spatial resolution of $\approx 0.2''$ (145 km on the solar surface) exhibited oscillations in thin threads with a width of $\approx 0.5''$ (360 km) of cool plasma flowing with speeds of $v \approx 74$–123 km s^{-1}, while the fundamental kink mode oscillations have a phase speed of 1250 km s^{-1} (Ofman and Wang 2008). This observation documented for the first time plasma flows in an oscillating multi-thread structure (Ofman and Wang 2008). As an alternative to the multiple kink wave scenario, a torsional Alfvén wave scenario was considered also to explain the oscillatory motion of the coronal rain in the condensation phase, as observed with SOT/Hinode (Antolin and Verwichte 2011). Coupling between the kink mode and the torsional Alfvén mode during the decay of transverse kink oscillations has also been simulated with a 3-D MHD code (Pascoe et al. 2012).

A commonly accepted damping mechanism of fast kink oscillations is resonant absorption, which acts in inhomogeneous regions of a flux tube, where energy is transferred from the kink mode to Alfvén azimuthal oscillations. Such an inhomogeneous model has been simulated in terms of a number of ten closely spaced strands (Terradas et al. 2008). The global motion of this bundle of strands, excited by an external disturbance, demonstrates conversion into unresolved Alfvénic motions due to resonant absorption, which attenuate the collective kink oscillations (Fig. 10.7; Terradas et al. 2008). A simpler system with only two loop strands is simulated with an ideal MHD code to study the collective oscillatory properties (Luna et al. 2008).

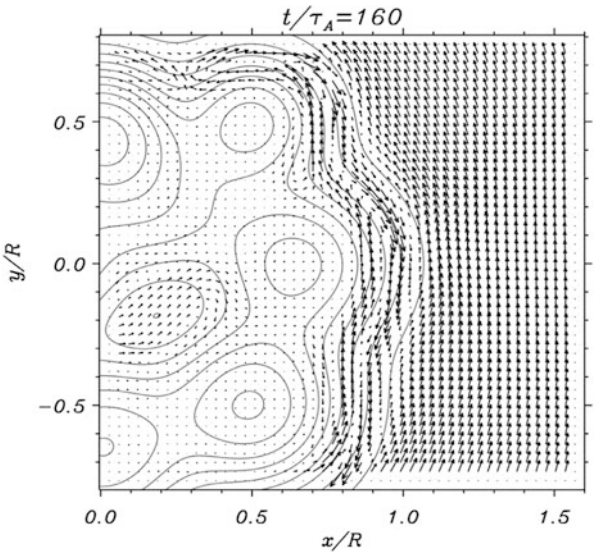

Fig. 10.7 Time evolution of the velocity field during a simulation of a multi-strand coronal loop system. The initial stage of the evolution of the bundle of loops is dominated by a complicated set of internal reflections of the wave front between the different strands. During a transitory phase, several wave fronts propagating from the bundle into the external medium are found, corresponding to the emission of leaky modes (Terradas et al. 2008)

It was found that the system supports four trapped normal modes, two in phase and two in anti-phase, and the excitation of multiple eigen-modes can lead to a beat frequency between the two resonant loop strands (Luna et al. 2008). Extending this multi-strand model to 7 strands, loops that have similar kink frequencies are found to oscillate collectively with a frequency that is slightly different from that of the individual kink mode (Luna et al. 2009). The individual kink frequencies were found to depend on the loop density, but not on their radius, and thus a coupling between kink oscillations of neighboring loops takes place when they have similar densities (Luna et al. 2009). A similar multi-thread system containing 10 loop threads was simulated with a 3-D MHD code by De Moortel and Pascoe (2012), finding that only a small fraction of the kinetic energy provided by the footpoint motions is observed in a line-of-sight integrated multi-thread system, which makes it nearly impossible to identify the wave mode of an individual thread.

Based on the SOT/Hinode observations (Ofman and Wang 2008), an oscillating multi-thread system (with four threads) exhibits twisted and tangled threads, non-force-free magnetic fields, and flows, which has been simulated with a 3-D MHD code by Ofman (2009), applying a rotating velocity field at the thread footpoints. It is found that twisted loop oscillations result in a filamented current and velocity structure that cannot be described by the fundamental kink mode. When parallel flow is present, the oscillation induces nonlinear compressive modulation of the

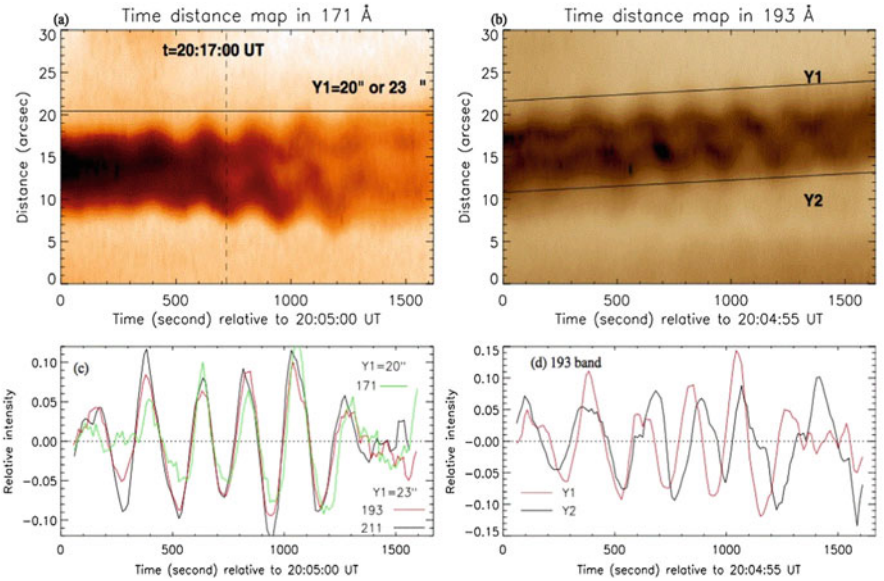

Fig. 10.8 Time-slice diagrams of (**a**) 171 Å and (**b**) 193 Å flux of the oscillating loop, time profiles of the 171, 193, and 211 Å relative intensities at two positions (Y1, Y2) (**c**,**d**). Note that the two amplitudes, which are collective and coherent initially, drift apart due to slightly different oscillation periods in the second time interval (**b**,**d**) (Wang et al. 2012)

flow and density in the threads, where a twisted loop oscillates and damps faster than the parallel-threaded loop (Ofman 2009).

Growing transverse oscillations were observed in a multi-stranded loop observed with AIA/SDO (Fig. 10.8), where two closely space oscillating loop strands slowly drift apart after they start out with a well-synchronized oscillation amplitude and phase in a collective way, while the decoherence probably occurs due to a slight difference in the initial periods of the two threads (Wang et al. 2012). The unusual growth of the transverse oscillation amplitude is interpreted in terms of a continuous non-periodic driving force, driven by the magnetic deformation of a CME, which deposits energy into the loop system at a rate that is faster than its loss (Wang et al. 2012).

A multi-stranded system, previously simulated in terms of a small (finite) number of individual strands, can arise also from the Kelvin-Helmholtz instability, similar to the development of turbulence, which deforms the cross-sectional area of loops, even for low-amplitude waves in long and thin loops (Fig. 10.15). Vortices generated by the instability are velocity sheared regions with enhanced emissivity that host current sheets. Strands result as a complex combination of the vortices and the line-of-sight angle, they last for time scales of a period, and they can be observed for a spatial resolution of a tenth of a loop radius (Antolin et al. 2014).

10.6 Coronal Loop Oscillations: Magnetic Field

The major trust of *"coronal seismology"* is the capability of measuring the magnetic field B in a coronal location, an important piece of information that is not directly available from photospheric magnetograms, and can be calculated only approximately from magnetic field extrapolations based on Stokes polarimetry. For reviews see Roberts (2000), Nakariakov and Verwichte (2005), Banerjee et al. (2007), Ruderman and Erdelyi (2009), and Nakariakov et al. (2016).

The method of coronal seismology is mostly applied to fast kink mode oscillations. The measurement of the kink mode period P_{kink} (which is twice the Alfvénic crossing time) and length L of the oscillating loop yields the Alfvén velocity v_A, or more accurately the kink speed c_k, i.e., $P_{kink} \approx 2L/c_k \approx 2L/v_A$. The Alfvén speed $v_A = B/\sqrt{4\pi\rho_0}$ essentially is defined by the magnetic field strength B and the mass density $\rho_0 = \mu m_H n_0$ or electron density n_0 inside the oscillating flux tube, while the kink speed depends additionally on the electron density n_e outdisde of the flux tube. From this we can express the magnetic field B as a function of $[P_{kink}, L, n_0, n_e]$

$$B_{kink} = \frac{L}{P_{kink}} \sqrt{8\pi\rho_0(1 + \rho_e/\rho_0)} \; . \tag{10.6.1}$$

This expression, however, assumes a constant magnetic field B_{kink} along an oscillating loop, which generally is not realistic (although it is consistent with the model of a constant cross-section of EUV loops). It is therefore more accurate to compare this magnetic field value derived from the kink mode period with the mean field strength $< B >$ integrated along the oscillating loop,

$$< B >= L \left[\int B(s)^{-1} ds \right]^{-1} \; , \tag{10.6.2}$$

where the variation of the magnetic field $B(s)$ along the loop coordinate s can be modeled from a potential or non-potential field model. Such a self-consistency test of the equality $< B > \approx B_{kink}$ has been rarely pursued, although it would constrain the 3-D magnetic field in the corona to a much stronger degree than the canonical single-value measurement based on Eq. (10.6.1). A dipolar potential field was forward-fitted to the projected geometry of an oscillating loop (Aschwanden and Schrijver 2011), which yielded an average field of $B = 11$ G, and $B = 6$ G at the apex, while the footpoints exhibit field strengths of $B = -89$ G and $B = 296$ G (Fig. 10.4), which clearly demonstrates the inadequacy of the assumption of a constant magnetic field along an oscillating loop.

Nakariakov and Ofman (2001) estimate the errors of the method to determine the (mean) coronal magnetic field by coronal loop oscillations and conclude that the largest uncertainties come from projection effects and departures from a circular

loop geometry. The estimated error is

$$\delta B_0 = \sqrt{(\delta L)^2 + (\delta P)^2 + (\delta \rho_0/2)^2}\,, \tag{10.6.3}$$

with typical uncertainties in the loop length $\delta L \approx 10\%$, oscillation period $\delta P \approx 3\%$, and density $\delta \rho_0 \approx 50\%$, which yields a combined error of $\delta B_0 \lesssim 30\%$. The saving grace is that uncertainties in density or density ratios enter the equation for the magnetic field with a square root dependence only (Eq. 10.6.1).

The first attempt to put coronal seismology estimates of the magnetic field strength to the test was conducted by De Moortel and Pascoe (2009), using an ideal MHD code (LARE3D). The magnetic field configuration was incorporated by an infinite 2-D arcade magnetic field ($B \propto 1/r$), and a pressure pulse was implemented to initialize a kink mode oscillation. The magnetic field inferred from the simulated oscillation (using Eq. 10.6.1) was found to be substantially different from the actual (input) magnetic field value, differing by $\approx 50\%$. In a more realistic coronal model, agreement within $\approx 15\%$ was found between the magnetic field values inferred from coronal seismology and the simulated 3-D magnetic field (Chen and Peter 2015).

It is not clear from what effect this discrepancy occurs. It is conceivable that the infinite loop arcade with a field dependence that scales with the curvature radius as $B \approx 1/r$ is rather unphysical, given the fact that a bipolar field generated by two oppositely magnetic charges produces a finite structure that scales as $B \approx 1/r^2$ (Eqs. 8.1.3–8.1.6). Thus, more realistic magnetic field configurations are needed in order to put coronal seismology to the test. Unfortunately, magnetic field modeling cannot be carried out near the limb, where most of the loop oscillations have been observed.

Another study that compared two different methods to determine the Alfvén speed and magnetic field inside an oscillating flux tube was conducted by Verwichte et al. (2013): (i) with the seismological method, and (ii) with a potential field (PFSS) extrapolation. Both methods applied to two different loops (Fig. 10.9) were found to be consistent with each other, but the average Alfvén speed based on loop travel time is not necessarily a good measure to compare with seismological results, which explains earlier reported discrepancies. Instead, the effect of density and magnetic stratification on the wave mode has to be taken into account

Coronal seismology can also be applied to slow mode (magneto-acoustic) waves, because the magnetic field strength is a function of the Alfvén speed and tube speed c_t of the slow mode,

$$P = \frac{2L}{c_t}\,, \qquad c_t = \left(\frac{1}{c_s^2} + \frac{1}{v_A^2}\right)^{-1/2}\,. \tag{10.6.4}$$

The magnetic field strength B can then be expressed in terms of the observables (electron density $n_9 = n_e/10^9$ cm^{-3}, period P, loop length L, and plasma

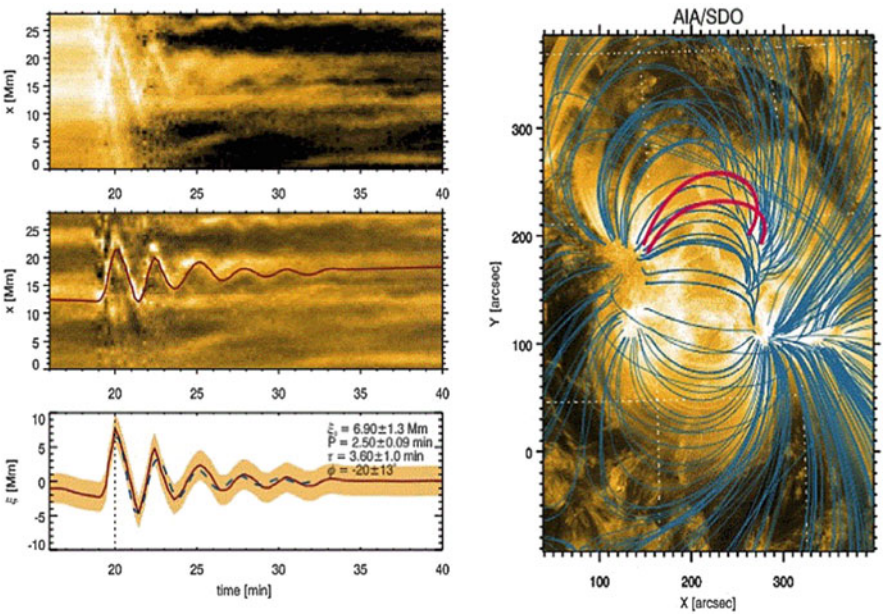

Fig. 10.9 *Left:* Time-distance diagram of the intensity for the path at $s = 0.5L$, for the 2011 September 6, 22:00 UT, event. *Right:* Potential field source surface (PFSS) magnetic field extrapolation of active region NOAA 11283 on 2011 September 7, 00:00 UT. The oscillating loops are marked with red color (Verwichte et al. 2013)

temperature $T_6 = T_e/10^6$ K) (Fig. 10.10; Wang et al. 2007),

$$B = \left(\frac{n_9}{C_1}\right)^{-1/2} \left(\frac{P^2}{4L^2} - \frac{1}{C_2 T_6}\right)^{-1/2} , \tag{10.6.5}$$

with the constants $C_1 = 4.8 \times 10^3$ and $C_2 = 2.3 \times 10^4$. Using this method for a set of seven events observed with SUMER in Fe XIX, magnetic field strengths of $B = 34 \pm 14$ G were measured (Wang et al. 2007). Similar values were determined from SOT/Hinode observations, such as $B = 20 \pm 7$ G (Ofman and Wang 2008), or $B = 32 \pm 5$ G (Jess et al. 2016).

10.7 Coronal Loop Oscillations: Longitudinal Waves

In the same year when the fast kink mode oscillations of coronal loops have been discovered, periodic perturbations that propagate in outward direction have been reported also, which were interpreted as slow magneto-acoustic waves (DeForest and Gurman 1998; Berghmans and Clette 1999; De Moortel et al. 2000). For reviews

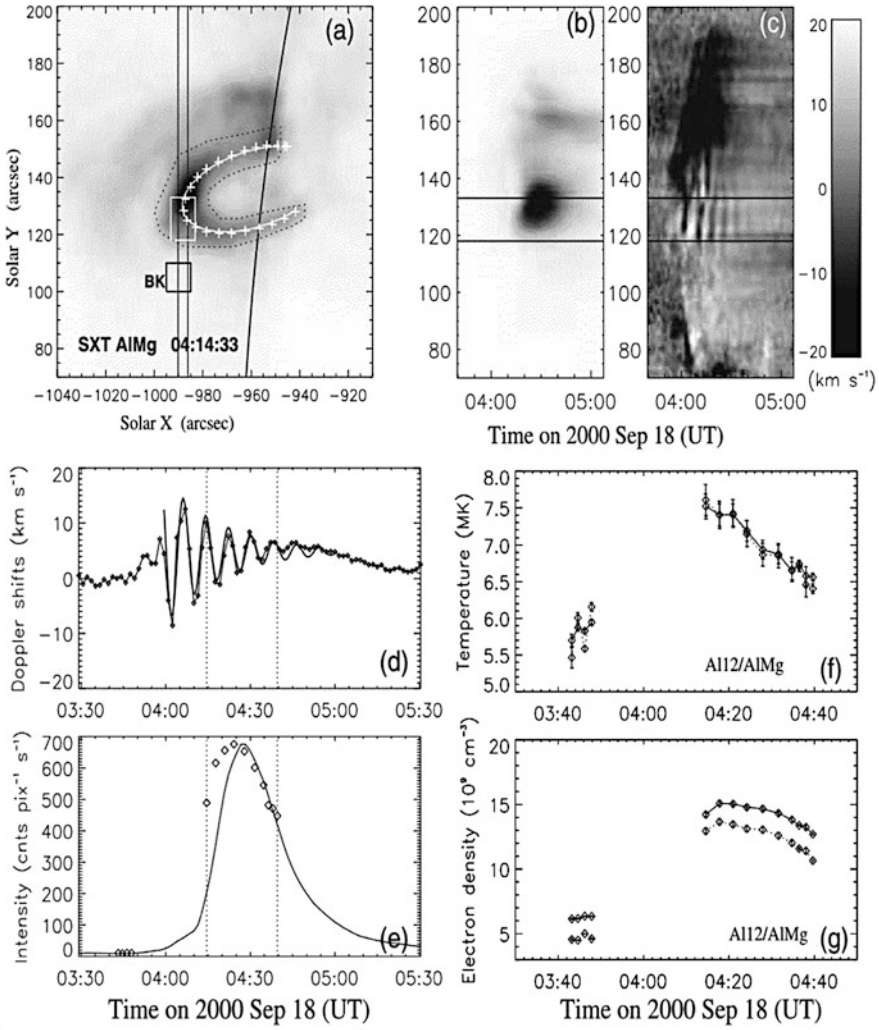

Fig. 10.10 Loop oscillation event observed with SUMER on 2000 September 18, 04:00 UT: oscillations of soft X-ray loop (**a**), line-of-sight integrated intensity (**b**) and Doppler shift (**c**), and time evolution of Doppler shift (**d**), intensity (**e**), temperature (**f**), and electron density (**g**), (Wang et al. 2007)

see De Moortel (2009) and Wang (2011). These longitudinal waves were detected with TRACE in the 171 Å (Fe IX) bandpass, using a wavelet analysis, featuring periods of $P \approx 3$–7 min, velocities of $v \approx 79$–165 km s^{-1}, and carrying an energy (Poynting) flux of $F \approx 4 \times 10^2$ erg cm^{-2} s^{-1} (De Moortel et al. 2000). The interpretation in terms of slow longitudinal magneto-acoustic waves is supported by the fact that the observed propagation speed is close to the sound speed (≈ 150

km s^{-1} for a plasma with a typical coronal temperature $T \approx 1.0$ MK), as well as the fact that the detected EUV brightness modulations are caused by density variations as expected for the compressive magneto-acoustic waves. It was also noted that the proximity of the observed periods to the global photospheric 5-min period could indicate some coupling between the photosphere and the corona (De Moortel et al. 2000). Simultaneous multi-wavelength observations of slow waves with different instruments (EIT and TRACE) and relatively high cadence (15–25 s) corroborated the expected dependence of the propagation speed on the temperature, i.e., mean projected speeds of 95 km s^{-1} in the 171 Å line were found, and 110 km s^{-1} in the hotter 195 Å line, respectively (Robbrecht et al. 2001). A statistical study of 38 events with longitudinal oscillations identified the source at the footpoints of large diffuse coronal (fan) loops in active regions, with a mean velocity of $v \approx 122 \pm 43$ km s^{-1}, an amplitude flux to background ratio of 4.1% ± 1.5%, with periods of $P = 282 \pm 93$ s, and an energy flux of $E = 342 \pm 126$ erg cm^{-2} s^{-1} (De Moortel et al. 2002a). It was concluded that the observed density oscillations are unlikely to be flare-driven, but that (slightly enhanced) thermal conduction alone can account for the observed damping lengths, and additionally can explain the correlation between propagation and damping length (De Moortel et al. 2002b). Oscillating (fan) loops that are situated above sunspots reveal periods of $P = 172 \pm 32$ s, while loops rooted in the penumbra outside sunspots have periods of $P = 321 \pm 74$ s, which reflects the global oscillation periods in sunspot umbras and penumbrae (De Moortel et al. 2002c).

In contrast, loop oscillations detected with SUMER/SOHO in the Fe XIX line at hot temperatures ($T > 6$ MK) showed Doppler oscillations with periods of $P =$ 14–18 min and exponential decay times of $\tau_d =$ 12–19 min, which were interpreted to be flare-driven oscillations and incompressible waves, due to the absence of brightness modulations (Wang et al. 2002). A statistical study of 54 events with Doppler shift oscillations observed with SUMER/SOHO and TRACE reveal periods in the range of $P =$ 7–31 min and decay times of $\tau_d =$ 6–37 min (Wang et al. 2003a). It was concluded from this extended data set that the oscillations are slow magneto-acoustic standing waves in hot loops, based on the phase speed equaling the sound speed, the intensity fluctuations lagging the Doppler shift by 1/4 period, and the scaling of dissipation times (Wang et al. 2003a,b). Small flares or micro-flares are proposed as a trigger (e.g., Wang 2011). Analyzing the spectral features of loop oscillations observed with the SUMER/SOHO spectrograph (Fe XIX and Fe XXI lines) suggests that initial hot flows support the model of single footpoint (asymmetric) excitation, but contradicts chromospheric evaporation as the trigger (Wang et al. 2005). Two harmonics with periods of 12 and 25 min were observed also with EIS/Hinode (Fig. 10.11), which documents that a suitably broadband exciter can produce overtones also (Wang et al. 2009a), possibly caused by the leakage of the photospheric p-modes through the chromosphere, transition region, and into the corona (Wang et al. 2009b). Another survey of persistent Dopplershift oscillations observed with EIS/Hinode leads to two types of events: (i) type-II spicules (with persistent blueshifts), and (ii) kink/Alfvén wave oscillations in the upper parts of loops (rather than flows) (Tian et al. 2012).

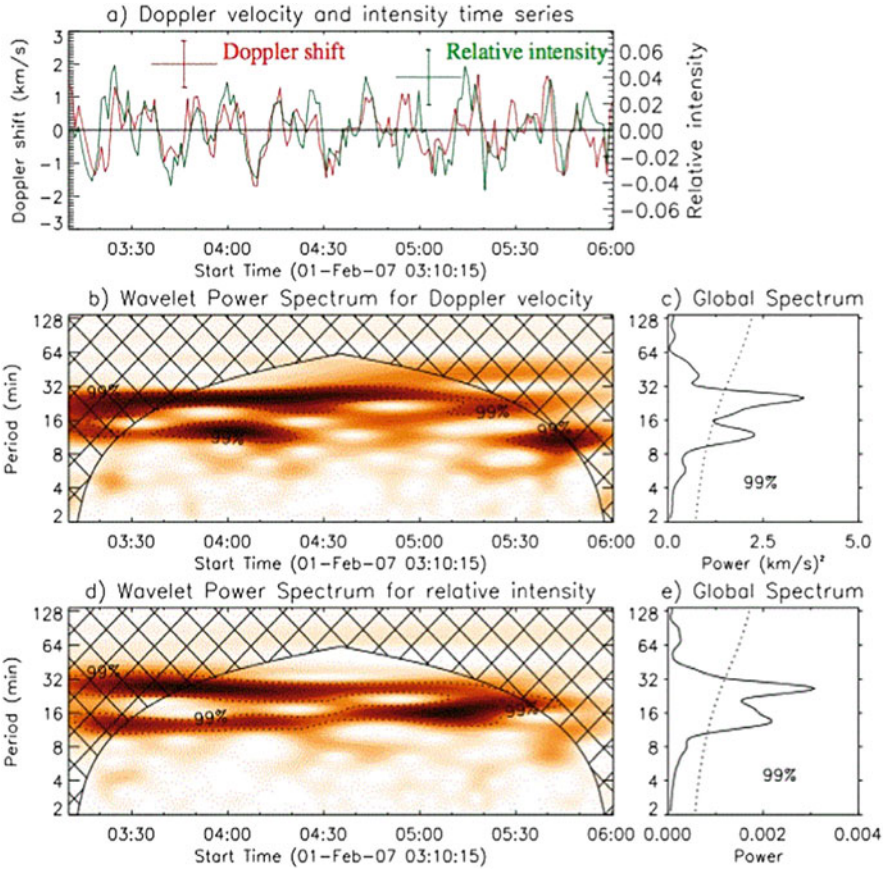

Fig. 10.11 Wavelet analysis for oscillation observed with EIS/Hinode on 2007 February 1, 00:12 UT, in active region NOAA 10940, showing the time profiles (**a**), and wavelet power spectra of the Doppler shift (**b**), and the relative intensity (**d**). The positive Doppler shift represents the blueshifted emission. Note the harmonic ratio of two periods (12 and 25 min) that persist through the entire event (Wang et al. 2009a)

A theoretical 1-D MHD model of propagating slow magneto-acoustic waves in coronal loops has been presented by Nakariakov et al. (2000), which incorporates the effects of nonlinearity, dissipation due to finite viscosity, thermal conduction, and gravitational stratification. The wave evolution was found to be controlled mostly by dissipation and stratification. Downward propagating waves are detected much rarer than upward propagating waves, which is expected due to their strong decay near the apex as predicted by the theoretical model (Nakariakov et al. 2000). Including a broad-band spectrum in the generation of slow magneto-acoustic waves was found to boost the Poynting flux to levels commensurable with the coronal heating requirement (Tsiklauri and Nakariakov 2001). 1-D MHD simulations with hot loop temperatures (as observed with SUMER/SOHO, $T > 6$ MK), confirmed

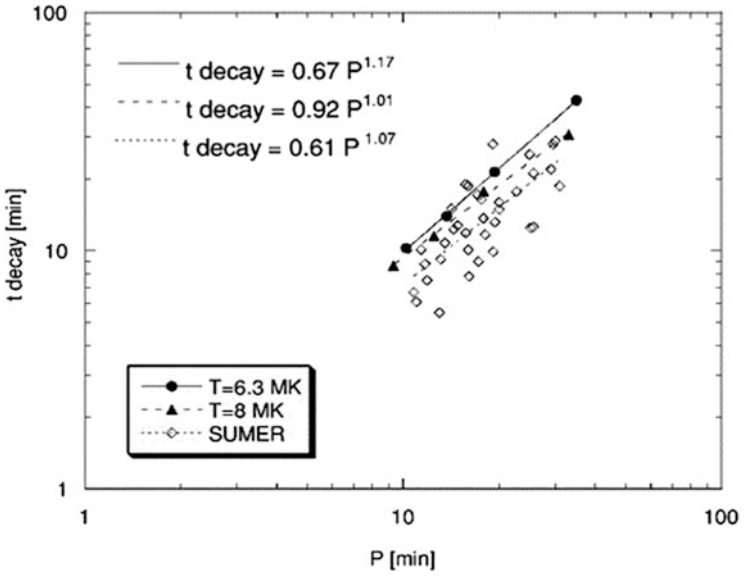

Fig. 10.12 Scaling between the exponential damping time scale τ_d with the slow magneto-acoustic oscillation period P for different samples of events, which all are consistent with a linear scaling law, i.e., $\tau_d \propto P$ (Ofman and Wang 2002)

that the large thermal conduction (which depends on temperature as $T^{2/5}$) leads to rapid damping of the slow magneto-acoustic waves (Ofman and Wang 2002), as inferred by De Moortel et al. (2002b) and De Moortel and Hood (2003). Observations suggest a linear relationship between the oscillation decay time and period, i.e., $\tau_d \propto P$ (Fig. 10.12). In the case of high thermal conduction, the slow magneto-acoustic waves become isothermal and the relative amplitude of the temperature variations in this wave tends to become zero, while the waves are damped mostly by compressive viscosity (Mendoza-Briceno et al. 2004). A 1-D MHD analytical model shows that a standing acoustic wave can be excited by an impulsive heat deposition at the chromospheric footpoint of a loop if the duration of the pulse matches the fundamental mode period (Taroyan et al. 2005).

Recent studies based on AIA/SDO data revealed great progress in the diagnostic of propagating and standing slow-mode waves, both in numerical simulations and observations. 3-D MHD simulations reproduce the observed slow magnetosonic waves and persistent upflows by a common impulsive trigger at the base of active regions (Ofman et al. 2012). Any upflow pulse inevitably excites slow magnetosonic wave disturbances that propagate along a loop (Wang et al. 2013). The confusion between propagating magnetosonic waves and spectroscopically inferred upflows has been clarified by simulations that confirm that reflected slow mode waves are propagating waves (Fang et al. 2015). A number of new AIA/SDO studies show

evidence for flare-excited slow-mode waves (Kumar et al. 2013, 2015; Wang et al. 2015, 2018; Mandal et al. 2016; Nistico et al. 2017).

10.8 Coronal Loop Oscillations: Optical and Radio

In the previous sections we mostly described coronal loop oscillations and waves as observed from space-based missions in EUV and soft X-ray wavelengths (such as with TRACE, AIA, Hinode), but there is also complementary physical information from ground-based observations in optical and radio wavelengths. Optical emission from the solar corona is very faint (compared with the six orders of magnitude brighter photospheric emission) and thus requires occultation of the solar disk, as it is naturally arranged during solar eclipses, or artificially obtained with coronagraphs. Radio emission mechanisms, on the other hand, include free-free bremsstrahlung and gyroresonance emission from active regions (and thus possibly from oscillating coronal loops), as well as gyrosynchrotron and coherent emission produced by relativistic (nonthermal) electrons and plasma instabilities, which can be modulated in a periodic way by loop oscillations and MHD waves .

Searches for loop oscillations and propagating waves in the white-light corona have been organized during most recent solar eclipses. CCD movies were digitized with a rate of 10 Hz (100 ms) through a filter in the coronal green line at 5303 Å (Fe XIV), observed during the 1994 November 3 (Putre, Chile) and 1998 February 26 (Aruba, Carribean island), but no evidence for oscillations was found (Pasachoff et al. 2000). A similar analysis of the 1999 August 11 eclipse (Romania, Bulgaria) indicated some marginal signal in the frequency band of 0.75–1.0 Hz (Pasachoff et al. 2002), while high cadence observations with the *Solar Eclipse Corona Imaging System (SECIS)* discovered a 6-s intensity oscillation (with a wavelet analysis) in an active region coronal loop (Williams et al. 2001), with a frequency range of 0.15–0.25 Hz (4–7s) (Katsiyannis et al. 2003), which however were disputed by Rudawy et al. (2004). This oscillation has been associated with a fast-mode magneto-acoustic wave that travels through the loop apex with a velocity of $v = 2100$ km s^{-1} (Williams et al. 2002). Further SECIS observations of the 2001 June 21 eclipse (Lusaka, Zambia) and wavelet analysis with a search in the frequency range of 0.06–10 Hz (0.1–17s) revealed a number of possible, but statistically insignificant periodicities (Rudawy et al. 2010). It appears that the low-amplitude oscillations seen with CoMP in the Quiet Sun (Sect. 6.6) do not produce significant oscillatory intensity fluctuations that could be detected with SECIS during eclipses (Rudawy et al. 2010). High-resolution spectroscopy of the solar corona was performed during the total solar eclipse of 2009 July 22 (China, India, Japan) using the 5303 Å (Fe IX) green line, and periodicities in the range of 25–50 s (20–40 Hz) were detected in intensity, velocity, and line width (Figs. 10.13 and 10.14; Singh et al. 2011).

From spectroscopic analysis of the green line profiles observed with the coronagraph at the Norikura Solar Observatory, Doppler velocities, line intensities,

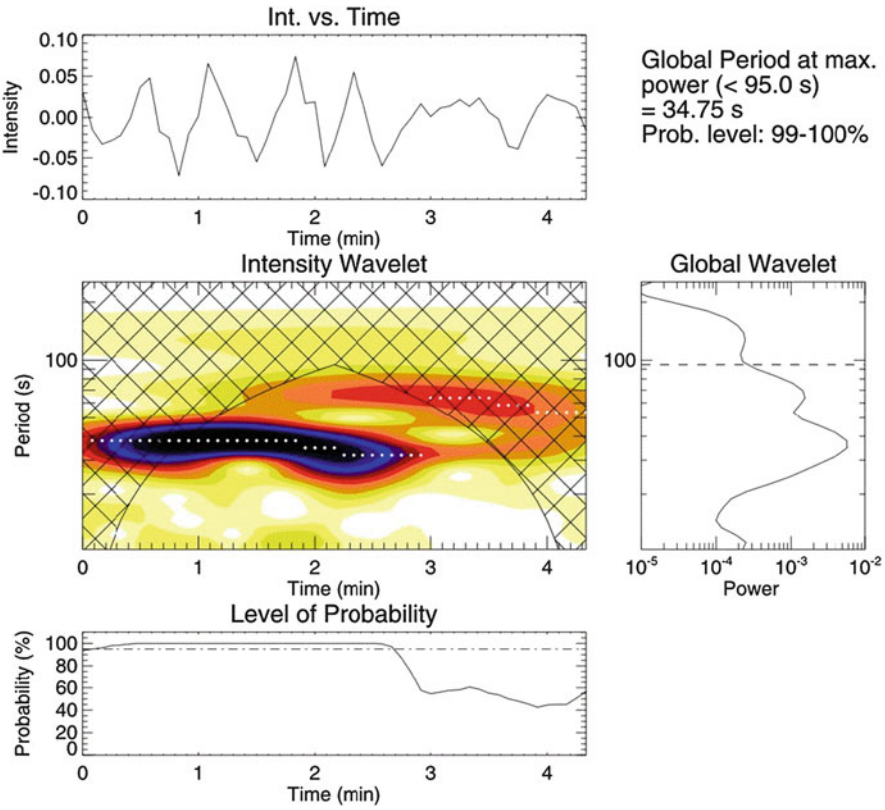

Fig. 10.13 Intensity oscillation time profile (top left), wavelet power spectrum (middle left), level of probability (bottom left), and power spectrum (middle right), observed with a broad passband interference filter with transmission from 5000 to 6600 Å during the 2009 July 22 eclipse in China (Singh et al. 2011)

and line widths were derived, from which a Fourier analysis revealed power in the frequency ranges of 1–3 mHz (6–17 min) and 5–7 mHz (2–3 min), possibly indicating propagating Alfvénic waves (Sakurai et al. 2002), although the density and the associated line intensities are not expected to vary for the incompressible Alfvén waves.

In the microwave domain, *quasi-periodic oscillations (QPOs)* of active region sources have been detected frequently, most prominently at 3 min (which is the global p-mode period in sunspots), but also more long-term periodicities in the range of ≈10–100 min (Gelfreikh et al. 2006; Nagovitsyn et al. 2013). Wide ranges of solar oscillation periods were detected in Quiet Sun areas, i.e., 3–15, 35–70, and 90 min, based on Fast Fourier transforms, global wavelet spectra, Morlet wavelets, and Fisher randomization tests (Kallunki and Riehokainen 2012). A delay of about 50 s was found between the optical (Sayan Solar Observatory) and radio (Nobeyama

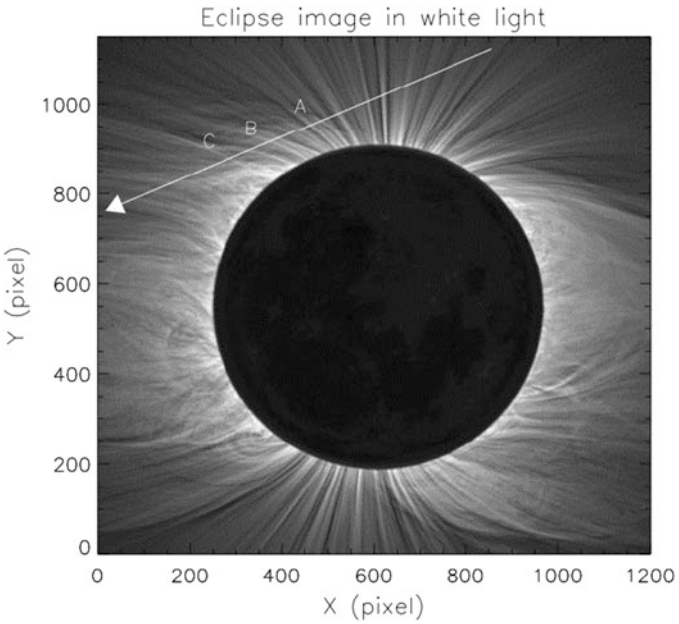

Fig. 10.14 White-light image of the 2009 July 22 solar eclipse recorded by Miroslav Druckmüller at the Enewetak Atoll, Marshall Islands, which is a context image for the measurements shown in Fig. 10.13) (Singh et al. 2011)

radioheliograph) observations of 3-min and 5-min oscillations, which implies that an MHD wave travels upward inside the umbral magnetic tube of the sunspot (Abramov-Maximov et al. 2011). Oscillations with periods of 10–15 min were found to dominate in coronal loops above faculae regions (Kobanov and Chelpanov 2014).

Fast sausage MHD standing oscillations modulate the electron density in a coronal loop due to periodic adiabatic expansions and contractions, which modulates also the gyrosynchrotron emission because of its dependence on the electron density and magnetic field, and thus can be used as a diagnostic of MHD oscillations and the effect of Razin suppression (Reznikova et al. 2014; Kuznetsov et al. 2015).

Detection and remote sensing of coronal kinetic Alfvén waves by means of radio observations has been proposed by means of nonlinear interaction of kinetic Alfvén waves with the extraordinary (x-) and ordinary (o-) mode radio waves (Sirenko et al. 2002). A model of the Alfvén speed in the global solar corona can be achieved by representing active regions with magnetic dipoles, which is a useful ingredient to study the propagation of type II radio bursts (Warmuth and Mann 2005).

10.9 Coronal Loop Oscillations: MHD Simulations

Magnetohydrodynamic (MHD) simulations of oscillations and waves can reveal the fundamental plasma physics of resonant systems in the solar corona, which can be cross-compared with analytical flux tube models of standing eigen-modes and propagating waves. MHD simulations may even uncover computational errors and incorrect analytical solutions. The availability of 1-D, 1.5-D, 2-D, 2.5-D, and 3-D MHD codes has triggered a new industry of simulations in the new millennium (see also Sect. 8.8 on 3-D MHD simulations in active regions). For a review on 3-D MHD numerical modeling of coronal oscillations see Ofman (2009b) and Pascoe (2014).

Damping of coronal loop oscillations has been simulated for the processes of chromospheric leakage (1.5-D code, Ofman 2002; 2-D code, Selwa et al. 2007a), and resonant absorption (1-D LEDA code; Van Doorsselaere et al. 2004). Footpoint leakage is found to be important in analytical models (De Pontieu et al. 2001) to explain the rapid damping of loop oscillations, while numerical 1.5-D simulations disagree (Ofman 2002). Differences in the width of the nonuniform layer in the case of resonant absorption were found to differ by 25% between the analytical and numerical models (Ofman 2002). Nevertheless, chromospheric wave leakage was found to be more efficient in 2-D MHD simulations than observed (Selwa et al. 2007a).

The propagation and evolution of impulsively generated Alfvénic pulses in solar loop arcades has been simulated with a 2.5-D compressible (ideal) MHD code, taking into account the gravitational stratification (Del Zanna et al. 2005). 3-D numerical simulations (with the LARE3D code) of footpoint-driven transverse waves propagating in a low-β plasma demonstrate that an inhomogeneous density structure causes resonant absorption and leads to coupling of the kink mode with the Alfvén mode (Pascoe et al. 2010).

The excitation and damping of slow magneto-acoustic standing waves has been simulated with 1-D MHD equations, including nonlinearity, thermal conduction, heating, and cooling of the loop plasma, which produced strong damping on typical time scales of $\approx$ 13 min (Selwa et al. 2005a). Slow magneto-acoustic waves are found to be excited faster in curved loops than in 1-D slabs due to the combined effect of the pulse inside and outside the loop, according to 2-D MHD simulations (Selwa et al. 2007b). Flows cause a phase shift in the perturbed velocity amplitude and an increase in wave period (Kumar et al. 2016).

Vertical oscillations were simulated with a 2-D MHD code (in the loop plane), which could reproduce the excitation and damping of fast magneto-acoustic waves (Selwa et al. 2005b), which was generalized to a multi-stranded scenario (Gruszecki et al. 2006), solving the 3-D resistive MHD equations (Ofman 2009a). It was found that twisted loop oscillations result in filamented current and velocity structures that cannot be described by the fundamental kink mode, and a twisted loop oscillates and damps faster than parallel-threaded loops (Ofman 2009a). Excitation of vertical kink waves in a coronal loop arcade by a periodic driver was simulated with a 2-D

ideal MHD code and demonstrated that the observed attenuation (damping) times can be reproduced by adopting a periodic driver rather than an impulsive excitation, possibly also explaining the high selectivity of responding loops (Selwa et al. 2010). Other 2-D MHD simulations of magneto-acoustic oscillations in a gravitationally stratified corona show the dependence of the excitation on the shape of the initial velocity pulse, which can be modeled with a 1-D rebound shock model (Konkol et al. 2012).

The fast standing sausage mode in a potential field geometry has been simulated with a 2-D MHD code by Pascoe and Nakariakov (2016). The upward expansion of the loop diameter affects the geometric oscillation pattern so that longitudinal harmonics of order ($n > 1$) have anti-nodes that are shifted towards the loop apex and the amplitude of anti-nodes near the loop apex is smaller than those near the footpoints. The MHD simulations are consistent with standing sausage modes observed in a flaring loop, with the global mode ($n = 1$) and the third harmonic ($n = 3$) excited simultaneously (Pascoe and Nakariakov 2016).

The selectivity of oscillating loops in an active region was simulated with a dipolar 3-D magnetic field and with a 3-D resistive MHD code, and it was found that the magnetic field inferred from the observed kink oscillation period overestimates the input magnetic field, and that vertical kink waves in a 3-D stratified geometry are damped mainly due to wave leakage in the horizontal direction (Selwa and Ofman 2010; Selwa et al. 2011). 3-D MHD modeling of vertical kink oscillations in an active region with the shape of a plasma curtain reproduces the nonlinear fast magnetosonic pulse, propagation, and damping of an event observed with AIA/SDO, and retrieves a more accurate magnetic field than a 1-D slab model, which emphasizes the importance of using more realistic 3-D magnetic field models for improving coronal seismology (Ofman et al. 2015).

The phenomenon of decay-less loop oscillations has been modeled with a 3-D MHD code in terms of the Kelvin-Helmholtz instability (KHI) that often accompanies transverse MHD waves (Fig. 10.15), resulting from the combination of periodic brightenings produced by the KHI and the coherent motion of the KHI vortices amplified by resonant absorption (Antolin et al. 2016). It reflects the low damping characteristics of the local azimuthal Alfvén waves resonantly coupled to the kink mode (Antolin et al. 2016). A 3-D MHD simulation of the inhomogeneous density structure is shown in Fig. 10.16 for comparison.

10.10 Coronal Loop Oscillations: Harmonics

Like a violinist can play overtones on the strings, the excitation of overtones can also be produced in oscillating coronal loops, if a suitable shape of the initial spatial displacement profile along the loop is produced (via the Lorentz force exerted by a CME, a flare, or a shear flow). Harmonic (integer-number) frequencies generally indicate resonant systems and have been observed in many systems in solar physics, such as in the periodicity of solar activity (154-day period and subharmonics),

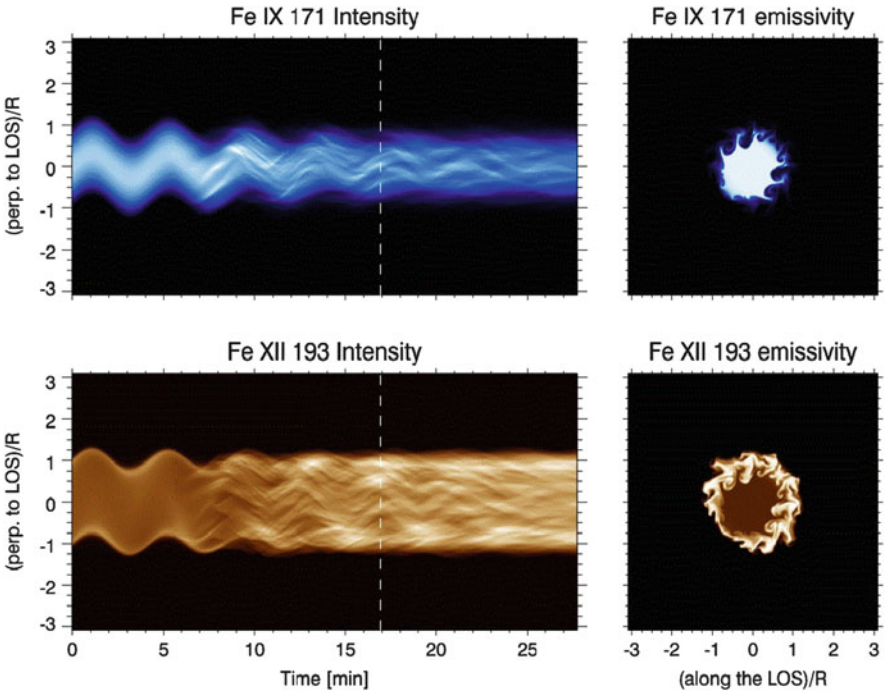

Fig. 10.15 Numerical 3-D MHD simulation of the Kelvin-Helmholtz instability. *Left panels:* Time-distance diagrams for the forward modeling of the numerical model in the Fe IX 171 Å (in blue, top panel) and Fe XII 193 Å (in brown, bottom panel) intensity for a slit placed perpendicular at the apex of the loop, at a 45° line-of-sight angle and at numerical (highest) spatial resolution. *Right panels:* Snapshot of the cross-section of the emissivity for each line for the time indicated by the dashed line in the time-distance diagrams. The cross-section is rotated by the same line-of-sight angle (Antolin et al. 2016)

harmonic radio burst frequencies (type I, type II, type III, zebra bursts), harmonic bands of decimetric millisecond spike bursts, gyroresonance emission at multiple harmonics, electron cyclotron maser radio emission at harmonics, wave harmonics in magnetic network (Srivastava 2010), multiple harmonics of fast MHD waves in prominences (Srivastava et al. 2013), harmonic periods in transverse loop oscillations (Verwichte et al. 2004; De Moortel and Brady 2007; Van Doorsselaere et al. 2007; Pascoe et al. 2016).

Fast kink mode MHD oscillations were detected with TRACE for the 2001 April 15, 20:24 UT, event near the limb, where an arcade of (nine traced) postflare loops were observed. A wavelet analysis revealed two groups of periodic signatures at $P_1 = 240$ s (4 min) and $P_2 = 400$ s (6.7 min), which were interpreted as multiple (fundamental and second harmonic) oscillation modes with a period ratio of $P_2/P_1 = 1.67$ (Verwichte et al. 2004). The multiple oscillation modes were found to have different amplitude profiles along the loop length, which indicates the presence of a second harmonic (Verwichte et al. 2004). In a sequence of TRACE

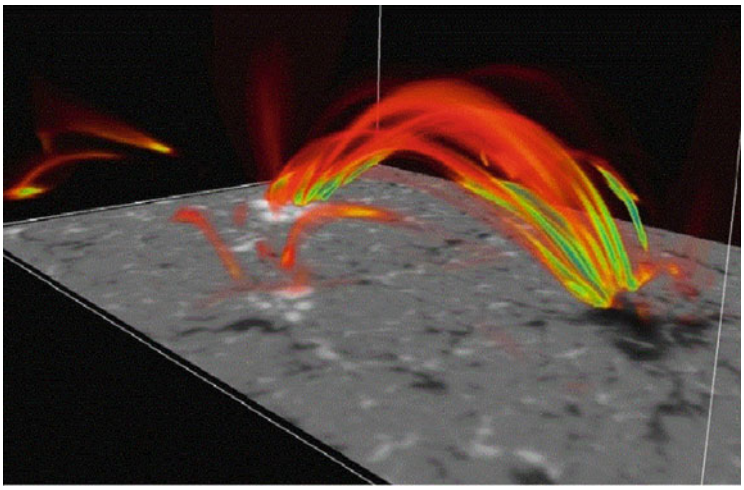

Fig. 10.16 A visualization of a 3-D MHD model of a multi-thread structure in an active region is shown, computed with the 3-D Pencil code (Credit: Internat. Max Planck Research School for Solar System Science)

171 Å observations taken on 2001 May 13, 02:52 UT, (S-shaped) second-harmonic (n=2) fast MHD kink waves ($P = 577$–672 s) (Fig. 10.17), with higher harmonics (n=4) of $P = 250$–346 s also present, but lacking the fundamental mode, which must be due to some particularity of the flare-induced excitation and/or damping mechanism (De Moortel and Brady 2007). Wang et al. (2009a) detected low-frequency slow magneto-acoustic waves in fan-like coronal loops with EIS/Hinode and found harmonic periods of 12 and 25 min (Fig. 10.11). This indicates that a suitably broadband exciter can produce overtones (Wang et al. 2009a), possibly caused by the leakage of the photospheric p-modes through the chromosphere, transition region, and into the corona (Wang et al. 2009b). Observations of two harmonics in horizontally polarized kink waves were reported based on AIA/SDO data by Guo et al. (2015), with periods of $P_1 = 530 \pm 13$ s, and $P_2 = 300 \pm 28$ (334 ± 22 s) in southern (northern) half loop segment. Thus there is an asymmetry in the southern/northern loop halfs, from which it was inferred that the density stratification and the temperature difference effects are larger than the magnetic field variation effect on the period ratio (Guo et al. 2015). Fitting the time-dependent displacements of a standing kink mode oscillation with two damped sine functions with different periods P_1 and P_2 and a damping time τ_d, the two components of the fundamental and second longitudinal harmonics were determined as $P_1 = 5.0 \pm 0.6$ min, $P_2 = 2.2 \pm 0.2$ min, and $P_1/2P_2 = 1.15 \pm 0.22$ (Pascoe et al. 2016). This method of fitting the loop shapes directly should be more accurate than previous time profiles taken from some arbitrary spatial position of an oscillating loop.

Evidence for harmonics of standing waves has also been found for cool loops, observed with CDS/SOHO in the transition region O V (629.73 Å) line (O'Shea

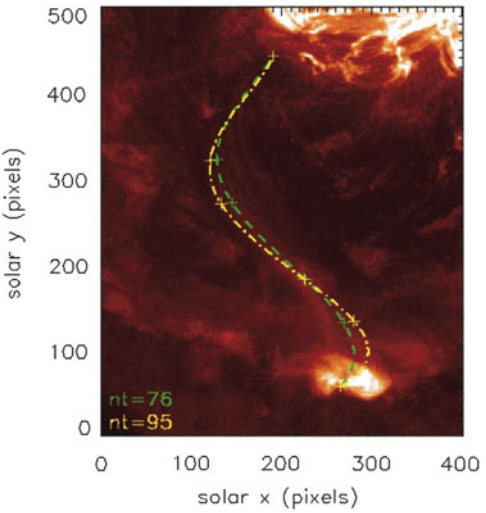

Fig. 10.17 Polynomial fit to the loop displacements at two different times: $nt = 76$ (dashed line) and $nt = 95$ (dot-dashed line), for an oscillating loop event observed with TRACE 171 Å during 2001 May 13, 02:52 UT. Note the S-shape of the loop, which corresponds to the second harmonic (transverse) kink mode. The displacements between the two times approximately represents the amplitude of the kink mode. The fundamental kink mode is absent (De Moortel and Brady 2007)

et al. 2007). The propagating disturbances have sub-sonic velocities of $v \approx 12$–24 km s^{-1}, suggesting that they are moved either by slow mode (acoustic or magneto-acoustic) wave propagation or by flare-triggered bulk flows. The detected periods have a range of 164–476 s (2.1–6.1 MHz), but harmonic frequencies do not match the expected ratio of 1:2 (O'Shea et al. 2007). Analyzing power spectra of He 256.32 Å intensity oscillations with EIS/Hinode near the south pole of the Sun reveal harmonic emission at $P_1 = 14.33$ min and $P_2 = 8.51$ min, with a period ratio of $P_2/P_1 = 1.68$, which corresponds to a (probably non-hydrostatic) density scale height of $H = 0.57$ Mm in the cavity-canopy loop interface (Srivastava 2010). Harmonic intensity oscillations were also observed in a prominence-like loop system observed with AIA/SDO in the 304 Å wavelength, exhibiting periods of 667 s and 305 s (with a period ratio of $P_1/P_2 = 2.18$ (Srivastava et al. 2013).

Deviations of the harmonic ratio of kink mode periods from the "ideal value" of $P_1/P_2 = 2$ was calculated from the frequency shift due to the presence of density stratification (Andries et al. 2005). This effect can be understood in terms of the density dependence of the Alfvénic phase speed that enters the harmonic period ratio. Conversely, the difference between this ratio and the ideal value of 2 can be used as a seismological tool to obtain information about the density scale height in oscillating loops (Andries et al. 2005). Van Doorsselaere et al. (2007) re-analyzed the event observed by Verwichte et al. (2004) and found a period ratio of $P_1/P_2 = 1.795 \pm 0.051$, which yields a density scale height of $H \approx 109$ Mm that corresponds either to a hydrostatic loop temperature of $T \approx 2.0$ MK, or to a super-hydrostatic scale height if a lower temperature of $T = 1.0$ MK is assumed. While a semi-circular loop shape was assumed in previous derivations of the harmonic ratio P_1/P_2 (Andries et al. 2005), further calculations show that the harmonic period ratio strongly depends on the assumed loop geometry (Dymova and Ruderman 2006a,b). Elliptical instead of circular cross-sections affect the fundamental to harmonic

period ratio P_2/P_1 also, as well as the loop cooling time and the associated damping time (Morton and Erdelyi 2009). Density stratification causes the anti-nodes of the first harmonic to shift towards the loop footpoints, which amounts to about 5.6 Mm for a loop with half length of $L = 100$ Mm and a density scale height of $H = 50$ Mm, which represents another magneto-seismology tool (Verth et al. 2007). Further numerical 2-D simulations of vertical loop oscillations showed that an initial velocity pulse located off-center excites both the fundamental (n=1) and the harmonic modes (n=2), which results into a movement of the node around the loop apex. Since the fundamental mode (n=1) acquires more energy than its first harmonic (n=2), this explains why the latter is so rarely detected within a coronal loop (Wasiljew and Murawski 2009).

The fast standing sausage mode has been simulated with a 2-D MHD code in a potential field geometry by Pascoe and Nakariakov (2016). The upward expansion of the loop diameter in a divergence-free field shifts the nodes of a standing wave, so that longitudinal harmonics of order ($n > 1$) have anti-nodes that are shifted towards the loop apex, and the amplitude of anti-nodes near the loop apex is smaller than those near the footpoints. The MHD simulations are consistent with standing sausage modes observed in a flaring loop, with the global mode ($n = 1$) and the third harmonic ($n = 3$) excited simultaneously (Pascoe and Nakariakov 2016).

References

(10.1) Coronal Loop Oscillations: Transverse Waves

Antolin, P. and Verwichte, E. 2011, *Transverse oscillations of loops with coronal rain observed by Hinode/SOT*, ApJ 736, 121, [40 c, 6 c/y].

Aschwanden, M.J., Fletcher, L., Schrijver, C.J., et al. 1999, *Coronal loop oscillations observed with the TRACE*, ApJ 520, 880, [598 c, 32 c/y].

Aschwanden, M.J., De Pontieu, B., Schrijver, C.J., et al. 2002, *Transverse oscillations in coronal loops observed with TRACE. II. Measurements and physical parameters*, SoPh 206, 99, [265 c, 17 c/y].

Aschwanden, M.J. and Schrijver, C.J. 2011, *Coronal loop oscillations observed with AIA - Kink mode with cross-sectional and density oscillations*, ApJ 736, 102, [89 c, 14 c/y].

Banerjee, D., Erdelyi, R., Oliver, R., et al. 2007, *Present and future observing trends in atmospheric magnetoseismology* (Review), SoPh 246, 3, [167 c, 16 c/y].

Cooper, F.C., Nakariakov, V.M., and Williams, D.R. 2003, *Short period fast waves in solar coronal loops*, A&A 409, 325, [59 c, 4 c/y].

De Moortel, I. and Brady, C.S. 2007, *Observation of higher harmonic coronal loop oscillations*, ApJ 664, 1210, [66 c, 6 c/y].

Erdelyi, R. and Verth, G. 2007, *The effect of density stratification on the amplitude profile of transversal coronal loop oscillations*, A&A 462, 743, [70 c, 7 c/y].

Goddard, C.R., Nistico, G., Nakariakov, V.M., et al. 2016, *A statistical study of decaying kink oscillations detected using SDO/AIA*, A&A 585, 137, [23 c, 15 c/y].

Guo, Y., Erdelyi, R., Srivastava, A.K., et al. 2015, *MHD seismology of a coronal loop system by the first two modes of standing kink waves*, ApJ 799, 151, [16 c, 6 c/y].

Li, Y.P. and Gan, W.Q. 2006, *The oscillatory shrinkage in TRACE 195 Å at 20 MK*, ApJ 644, L97, [35 c, 3 c/y].

Morton, R.J. and Erdelyi, R. 2009, *The effect of elliptic shape on the period ratio P_1/P_2 of emerging coronal loops*, A&A 502, 315, [23 c, 3 c/y].
Nakariakov,V.M., Ofman,L., DeLuca,E., et al. 1999, *TRACE observations of damped coronal loop oscillations: Implications for coronal heating*, Science 285, 862, [582 c, 31 c/y].
Nakariakov, V.M. and Ofman, L. 2001, *Determination of the coronal magnetic field by coronal loop oscillations*, A&A 372, 53, [313 c, 19 c/y].
Nakariakov, V.M. and Verwichte, E. 2005, *Coronal waves and oscillations*, LRSP 2, 3, [261 c, 21 c/y].
Nakariakov, V.M., Pilipenko, V., Heilig, B., et al. 2016, *MHD oscillations in the solar corona and Earth's magnetosphere: Towards consolidated understanding*, SSRv 200, 75, [43 c, 29 c/y].
Roberts, B. 2000, *Waves and oscillations in the corona (Invited review)*, SoPh 193, 139, [206 c, 12 c/y].
Ruderman, M.S. and Erdelyi, R. 2009, *Transverse oscillations of coronal loops*, SSRv 149, 199, [102 c, 12 c/y].
Ruderman, M.S., and Roberts, B. 2002, *The damping of coronal loop oscillations*, ApJ 577, 475, [290 c, 18 c/y].
Schrijver, C.J., Aschwanden, M.J., and Title, A.M. 2002, *Transverse oscillations in coronal loops observed with TRACE. I. An overview of events, movies, and a discussion of common properties and required conditions*, SoPh 206, 69, [171 c, 11 c/y].
Van Doorsselaere, T., Verwichte, E., and Terradas, J. 2009, *The effect of loop curvature on coronal loop kink oscillations*, SSRv 149, 299, [39 c, 5 c/y].
Verth, G., Van Doorsselaere, T., Erdelyi, R. 2007, *Spatial magneto-seismology: Effect of density stratification on the first harmonic amplitude profile of transversal coronal loop oscillations*, A&A 475, 341, [53 c, 5 c/y].
Verth, G. and Erdelyi, R. 2008, *Effect of longitudinal magnetic and density inhomogeneity on transversal coronal loop oscillations*, A&A 486, 1015, [95 c, 10 c/y].
Verwichte, E., Nakariakov, V.M., Ofman, L., et al. 2004, *Characteristics of transverse oscillations in a coronal loop arcade*, SoPh 223, 77, [197 c, 15 c/y].
Verwichte, E., Foullon, C., and Nakariakov, V.M. 2006, *Seismology of curved coronal loops with vertically polarised transverse oscillations*, A&A 452, 615, [48 c, 4 c/y].
Wang, T.J. and Solanki, S.K. 2004, *Vertical oscillations of a coronal loop observed by TRACE*, A&A 421, L33, [135 c, 10 c/y].
Wang, T.J. 2011, *Standing slow-mode waves in hot coronal loops: Observations, modeling, and coronal seismology*, SSRv 158, 397, [71 c, 11 c/y].
Wang, T.J., 2016, *Waves in Solar Coronal Loops in Low-Frequency Waves in Space Plasmas*, (eds. by A. Keiling, D.H. Lee, V. Nakariakov), Geophysical Monograph Series, Vol. 216, Wiley, p.395, [9 c, 6 c/y].
White, R.S., Verwichte, E., and Foullon, C. 2012, *First observation of a transverse vertical oscillation during the formation of a hot post-flare loop*, A&A 545, A129, [31 c, 6 c/y].
White, R.S. and Verwichte, E. 2012, *Transverse coronal loop oscillations seen in unprecedented detail by AIA/SDO*, A&A 537, A49, [65 c, 12 c/y].
Zimovets, I.V. and Nakariakov, V.M. 2015, *Excitation of kink oscillations of coronal loops: Statistical study*, A&A 577, A4, [28 c, 11 c/y].

(10.2) Coronal Loop Oscillations: Transverse Damping

Andries, J., Arregui, I., and Goossens, M. 2005, *Determination of the coronal density stratification from the observation of harmonic coronal loop oscillations*, ApJ 624, L57, [168 c, 13 c/y].
Anfinogentov, S., Nistico, G., and Nakariakov, V.M. 2013, *Decay-less kink oscillations in coronal loops*, A&A 560, 107, [43 c, 10 c/y].
Anfinogentov, S., Nakariakov, V.M., and Mathioudakis, M. 2015, *Decayless low-amplitude kink oscillations: A common phenomenon in the solar corona ?* A&A 583, 136, [32 c, 13 c/y].

Aschwanden, M.J., Nightingale, R.W., Jesse, A., et al. 2003, *Observational tests of damping by resonant absorption in coronal loop oscillations*, ApJ 598, 1375, [103 c, 7 c/y].

Aschwanden, M.J. and Terradas, J. 2008, *The effect of radiative cooling on coronal loop oscillations*, ApJ 686, 127, [37 c, 4 c/y].

Aschwanden, M.J. and Schrijver, C.J. 2011, *Coronal loop oscillations observed with AIA - Kink mode with cross-sectional and density oscillations*, ApJ 736, 102, [89 c, 14 c/y].

Brady, C.S., and Arber, T.D. 2005, *Damping of vertical coronal loop kink oscillations trough wave tunneling*, A&A 438, 733, [49 c, 4 c/y].

Brady, C.S., Verwichte, E., and Arber, T.D. 2006, *Leakage of waves from coronal loops by wave tunneling*, A&A 449, 389, [30 p, 3 c/y].

Cally, P.S. 2003, *Coronal leaky tube waves and oscillations observed with TRACE*, SoPh 217, 95, [35 c, 2 c/y].

Dymova, M.V. and Ruderman, M.S. 2006a, *Resonantly damped oscillations of longitudinally stratified coronal loops*, A&A 457, 1059, [55 c, 5 c/y].

Dymova, M.V. and Ruderman, M.S. 2006b, *The geometry effect on transverse oscillations of coronal loops*, A&A 459, 241, [41 c, 4 c/y].

Goddard, C.R., Nistico, G., Nakariakov, V.M., et al. 2016, *A statistical study of decaying kink oscillations detected using SDO/AIA*, A&A 585, 137, [23 c, 15 c/y].

Goddard, C.R. and Nakariakov, V.M. 2016, *Dependence of kink oscillation damping on the amplitude*, A&A 590, L5, [10 c, 7 c/y].

Goossens, M., Andries, J., and Aschwanden, M.J. 2002, *Coronal loop oscillations. An interpretation in terms of resonant absorption of quasi-mode kink oscillations*, A&A 394, L39, [217 c, 14 c/y].

Morton, R.J. and Erdelyi, R. 2009, *The effect of elliptic shape on the period ratio P_1/P_2 of emerging coronal loops*, A&A 502, 315, [23 c, 3 c/y].

Nakariakov, V.M., Anfinogentov, S.A., Nistico, G., et al. 2016, *Undamped transverse oscillations of coronal loops as a self-oscillatory process*, A&A 591, L5, [9 c, 2 c/y].

Nistico, G., Nakariakov, V.M., and Verwichte, E. 2013, *Decaying and decayless transverse oscillations of a coronal loop*, A&A 552, A57, [68 c, 15 c/y].

Ofman, L. and Aschwanden, M.J. 2002, *Damping time scaling of coronal loop oscillations deduced from TRACE observations*, ApJ 576, L153, [147 c, 9 c/y].

Pascoe, D.J., Goddard, C.R., Nakariakov, V.M. 2016a, *Spatially resolved observation of the fundamental and second harmonic standing kink modes using SDO/AIA*, A&A 593, 53, [7 c, 5 c/y].

Pascoe, D.J., Goddard, C.R., Nistico, G., et al. 2016b, *Damping profile of standing kink oscillations observed by SDO/AIA*, A&A 585, 6, [20 c, 13 c/y].

Pascoe, D.J., Goddard, C.R., Nistico, G., et al. 2016c, *Coronal loop seismology using damping of standing kink oscillations by mode coupling*, A&A 589, A136, [12 c, 8 c/y].

Pascoe, D.J., Anfinogentov, S., Nistico, G., et al. 2017, *Coronal loop seismology using damping of standing kink oscillations by mode coupling. II. Additional physical effects and Bayesian analysis*, A&A 600, 78, [7 c, 7 c/y].

Roberts, B. 2000, *Waves and oscillations in the corona (Invited review)*, SoPh 193, 139, [206 c, 12 c/y].

Ruderman, M.S., and Roberts, B. 2002, *The damping of coronal loop oscillations*, ApJ 577, 475, [290 c, 18 c/y].

Ruderman, M.S. 2003, *The resonant damping of oscillations of coronal loops with elliptic cross-sections*, A&A 409, 287, [55 c, 4 c/y].

Terradas, J., Oliver, R., and Ballester, J.L. 2006a, *Damping of kink oscillations in curved coronal loops*, ApJ 650, L91, [47 c, 4 c/y].

Terradas, J., Oliver, R., and Ballester, J.L. 2006b, *Damped coronal loop oscillations: Time-dependent results*, ApJ 642, 533, [57 c, 5 c/y].

Terradas, J., Goossens, M., and Verth, G. 2010, *Selective spatial damping of propagating kink waves due to resonant absoprtion*, A&A 524, 23, [71 c, 9 c/y].

Verwichte, E., Nakariakov, V.M., Ofman, L., et al. 2004, *Characteristics of transverse oscillations in a coronal loop arcade*, SoPh 223, 77, [197 c, 15 c/y].
Verwichte, E., Foullon, C., and Nakariakov, V.M. 2006, *Fast magneto-acoustic waves in curved coronal loops. II. Tunneling modes*, A&A 449, 769, [41 c, 4 c/y].
White, R.S. and Verwichte, E. 2012, *Transverse coronal loop oscillations seen in unprecedented detail by AIA/SDO*, A&A 537, A49, [65 c, 12 c/y].

(10.3) Coronal Loop Oscillations: Vertical Polarization

Aschwanden, M.J., De Pontieu, B., Schrijver, C.J., et al. 2002, *Transverse oscillations in coronal loops observed with TRACE. II. Measurements and physical parameters*, SoPh 206, 99, [265 c, 17 c/y].
Aschwanden, M.J. and Schrijver, C.J. 2011, *Coronal loop oscillations observed with AIA - Kink mode with cross-sectional and density oscillations*, ApJ 736, 102, [89 c, 14 c/y].
Brady, C.S., and Arber, T.D. 2005, *Damping of vertical coronal loop kink oscillations trough wave tunneling*, A&A 438, 733, [49 c, 4 c/y].
Gruszecki, M., Murawski, K., Selwa, M., et al. 2006, *Numerical simulations of vertical oscillations of a multi-stranded coronal loop*, A&A 460, 887, [22 c, 2 c/y].
Selwa, M., Murawski, K., Solanki, S.K., et al. 2005a, *Numerical simulations of vertical oscillations of a solar coronal loop*, A&A 440, 385, [38 c, 3 c/y].
Selwa, M., Murawski, K., Solanki, S.K., et al. 2007, *Energy leakage as an attenuation mechanism for vertical kink oscillations in solar coronal wave guides*, A&A 462, 1127, [32 c, 3 c/y].
Verwichte, E., Foullon, C., and Nakariakov, V.M. 2006a, *Seismology of curved coronal loops with vertically polarised transverse oscillations*, A&A 452, 615, [48 c, 4 c/y].
Verwichte, E., Foullon, C., and Nakariakov, V.M. 2006b, *Fast magneto-acoustic waves in curved coronal loops*, A&A 446, 1139, [49 c, 4 c/y].
Verwichte, E., Foullon, C., and Nakariakov, V.M. 2006c, *Fast magneto-acoustic waves in curved coronal loops. II. Tunneling modes*, A&A 449, 769, [41 c, 4 c/y].
Wang, T.J. and Solanki, S.K. 2004, *Vertical oscillations of a coronal loop observed by TRACE*, A&A 421, L33, [135 c, 10 c/y].
White, R.S., Verwichte, E., and Foullon, C. 2012, *First observation of a transverse vertical oscillation during the formation of a hot post-flare loop*, A&A 545, A129, [31 c, 6 c/y].

(10.4) Coronal Loop Oscillations: 3-D Kinematics

Aschwanden, M.J. 2009, *The 3-D geometry, motion, and hydrodynamic aspects of oscillating coronal loops*, SSRv 149, 31, [40 c, 5 c/y].
Aschwanden, M.J. and Schrijver, C.J. 2011, *Coronal loop oscillations observed with AIA - Kink mode with cross-sectional and density oscillations*, ApJ 736, 102, [89 c, 14 c/y].
Cooper, F.C., Nakariakov, V.M., and Williams, D.R. 2003, *Short period fast waves in solar coronal loops*, A&A 409, 325, [59 c, 4 c/y].
Nakariakov, V.M., Aschwanden, M.J., and VanDoorsselaere,T. 2009, *The possible role of vortex shedding in the excitation of kink-mode oscillations in the solar corona*, A&A 502, 661, [30 c, 4 c/y].
Verwichte, E., Aschwanden, M.J., Van Doorsselaere, T., et al. 2009, *Seismology of a large coronal loop from EUVI/STEREO observations of its transverse oscillation*, ApJ 698, 397, [62 c, 7 c/y].
White, R.S., Verwichte, E., and Foullon, C. 2012, *First observation of a transverse vertical oscillation during the formation of a hot post-flare loop*, A&A 545, A129, [31 c, 6 c/y].
White, R.S. and Verwichte, E. 2012, *Transverse coronal loop oscillations seen in unprecedented detail by AIA/SDO*, A&A 537, A49, [65 c, 12 c/y].

(10.5) Coronal Loop Oscillations: Multi-Stranded Loop Systems

Antolin, P. and Verwichte, E. 2011, *Transverse oscillations of loops with coronal rain observed by Hinode/SOT*, ApJ 736, 121, [40 c, 6 c/y].
Antolin, P., Yokoyama, T., and Van Doorsselaere, T. 2014, *Fine strand-like structure in the solar corona from MHD transverse oscillations*, ApJ 787, L22, [43 c, 12 c/y].
Aschwanden, M. and Nightingale, R.W. 2005, *Elementary loop structures in the solar corona analyzed from TRACE triple-filter images*, ApJ 633, 499, [108 c, 9 c/y].
Aschwanden, M.J. and Peter, H. 2017, *The width distribution of loops and strands in the solar corona. - Are we hitting rock bottom*, ApJ 840, 4, [7 c, 7 c/y].
De Moortel, I. and Pascoe, D.J. 2012, *The effects of line-of-sight integration on multi-strand coronal loop oscillations*, ApJ 746, 31, [39 c, 7 c/y].
Gruszecki, M., Murawski, K., Selwa, M., et al. 2006, *Numerical simulations of vertical oscillations of a multi-stranded coronal loop*, A&A 460, 887, [22 c, 2 c/y].
Luna, M., Terradas, J., Oliver, R., et al. 2008, *Transverse oscillations of two coronal loops*, ApJ 676, 717, [32 c, 3 c/y].
Luna, M., Terradas, J., Oliver, R., et al. 2009, *Transverse oscillations of systems of coronal loops*, ApJ 692, 1582, [23 c, 3 c/y].
Ofman, L. 2005, *3-D MHD models of active region loops*, Adv.Spac.Res. 36, 1572, [23 c, 2 c/y].
Ofman, L. and Wang, T.J. 2008, *Hinode observations of transverse waves with flows in coronal loops*, A&A 482, L9, [101 c, 11 c/y].
Ofman, L. 2009, *3-D MHD models of twisted multi-threaded coronal loop oscillations*, ApJ 694, 502, [32 c, 4 c/y].
Pascoe, D.J., Hood, A.W., de Moortel, I., et al. 2012, *Spatial damping of propagating kink waves due to mode coupling*, A&A 539, A37, [54 c, 10 c/y].
Terradas, J., Arregui, I., Oliver, R., et al. 2008, *Resonant absorption in complicated plasma configurations: Applications to multi-stranded coronal loop oscillations*, ApJ 679, 1611, [54 c, 6 c/y].
Wang, T.J., Ofman, L., Davila, J.M., et al. 2012, *Growing transverse oscillations of a multi-stranded loop observed by SDO/AIA*, ApJ 751, L27, [48 c, 9 c/y].

(10.6) Coronal Loop Oscillations: Magnetic Field

Aschwanden, M.J. and Schrijver, C.J. 2011, *Coronal loop oscillations observed with AIA - Kink mode with cross-sectional and density oscillations*, ApJ 736, 102, [89 c, 14 c/y].
Banerjee, D., Erdelyi, R., Oliver, R., et al. 2007, *Present and future observing trends in atmospheric magnetoseismology* (Review), SoPh 246, 3, [167 c, 16 c/y].
Chen, F. and Peter, H. 2015, *Using coronal seismology to estimate the magnetic field strength in a realistic coronal model*, A&A 581, A137, [7 c, 3 c/y].
De Moortel, I. and Pascoe, D.J. 2009. *Putting coronal seismology estimates of the magnetic field strength to the test*, ApJ 699, L72, [24 c, 3 c/y].
Nakariakov, V.M. and Ofman, L. 2001, *Determination of the coronal magnetic field by coronal loop oscillations*, A&A 372, 53, [313 c, 19 c/y].
Nakariakov, V.M. and Verwichte, E. 2005, *Coronal waves and oscillations*, LRSP 2, 3, [262 c, 21 c/y].
Nakariakov, V.M., Pilipenko, V., Heilig, B., et al. 2016, *MHD oscillations in the solar corona and Earth's magnetosphere: Towards consolidated understanding*, SSRv 200, 75, [43 c, 29 c/y].
Ofman, L. and Wang, T.J. 2008, *Hinode observations of transverse waves with flows in coronal loops*, A&A 482, L9, [101 c, 11 c/y].
Roberts, B. 2000, *Waves and oscillations in the corona (Invited Review)*, SoPh 193, 139, [206 c, 12 c/y].

Ruderman, M.S. and Erdelyi, R. 2009, *Transverse oscillations of coronal loops*, SSRv 149, 199, [102 c, 12 c/y].
Verwichte, E., Van Doorsselaere, T., Foullon, C., et al. 2013, *Coronal Alfvén speed determination: Consistency between seismology using AIA/SDO transverse loop oscillations and magnetic extrapolation*, ApJ 767, 16, [29 c, 6 c/y].
Wang, T.J., Innes, D.E., and Qiu, J. 2007, *Determination of the coronal magnetic field from hot-loop oscillations observed by SUMER and SXT*, ApJ 656, 598, [45 c, 4 c/y].

(10.7) Coronal Loop Oscillations: Longitudinal Waves

Berghmans, D. and Clette, F. 1999, *Active region EUV transient brightenings - First results by EIT of SOHO JOP80*, SoPh 186, 207, [190 c, 10 c/y].
DeForest, C.E. and Gurman, J.B. 1998, *Observation of quasi-periodic compressive waves in solar polar plumes*, ApJ 501, L217, [295 c, 15 c/y].
De Moortel, I., Ireland, J., and Walsh, R.W. 2000, *Observation of oscillations in coronal loops*, A&A 355, L23, [210 c, 12 c/y].
De Moortel, I., Ireland, J., Walsh, R.W., et al. 2002a, *Longitudinal intensity oscillations in coronal loops observed with TRACE I. Overview of measured parameters*, SoPh 209, 61, [134 c, 9 c/y].
De Moortel, I., Hood, A.W., Ireland, J., 2002b, *Longitudinal intensity oscillations in coronal loops observed with TRACE II. Discussion of measured parameters*, SoPh 209, 89, [83 c, 5 c/y].
De Moortel, I., Ireland, J., Hood, A.W., et al. 2002c, *The detection of 3 and 5 minute period oscillations in coronal loops*, A&A 387, L13, [144 c, 9 c/y].
De Moortel, I., and Hood, A.W. 2003, *The damping of slow MHD waves in solar coronal magnetic fields*, A&A 408, 755, [100 c, 7 c/y].
De Moortel, I. 2009, *Longitudinal waves in coronal loops*, SSRv 149, 65, [100 c, 12 c/y].
Fang, X., Yuan, D., van Doorsselaere, T., et al. 2015, *Modeling of reflective propagating slow-mode wave in a flaring loop*, ApJ 813, 33, [13 c, 5 c/y].
Jess, D.B., Rezmolpva. V.E., Ryans, R.S.I., et al. 2016, *Solar coronal magnetic fields derived using seismology techniques applied to omnipresent sunspot waves*, Nature Phys. 12, 179, [16 c, 11 c/y].
Kumar, P., Innes, D.E., and Inhester, B. 2013, *SDO/AIA observations of a reflecting longitudinal wave in a coronal loop*, ApJ 779, L7, [19 c, 4 c/y].
Kumar, P., Nakariakov, V.M., and Cho, K.S. 2015, *X-ray and EUV observations of simultaneous short and long period oscillations in hot coronal arcade loops*, ApJ 779, L7, [19 c, 4 c/y].
Mandal, S., Yuan, D., Fang, X., et al. 2016, *Reflection of propagating slow magneto-acoustic waves in hot coronal loops: Multi-instrument observations and numerical modeling*, ApJ 828, 72, [7 c, 5 c/y].
Mendoza-Briceno, C.A., Erdelyi, R., and Sigalotti, L. Di. G. 2004, *The effects of stratification on oscillating coronal loops*, ApJ 605, 493, [77 c, 6 c/y].
Nakariakov, V.M., Verwichte, E., Berghmans, D., et al. 2000, *Slow magneto-acoustic waves in coronal loops*, A&A 362, 1151, [121 c, 7 c/y].
Nistico, G., Polito, V., Nakariakov, V.M., et al. 2017, *Multi-instrument observations of a failed flare eruption associated with MHD waves in a loop bundle*, A&A 600, A37, [4 c, 4 c/y].
Ofman, L. and Wang, T.J. 2002, *Hot coronal loop oscillations observed by SUMER: Slow magnetosonic wave damping*, ApJ 580, L85, [167 c, 11 c/y].
Ofman, L., Wang, T.J., and Davila, J.M. 2012, *Slow magnetosonic waves and fast flows in active region loops*, ApJ 754, 111, [44 c, 8 c/y].
Robbrecht, E., Verwichte, D., Berghmans, D., et al. 2001, *Slow magneto-acoustic waves in coronal loops: EIT and TRACE*, A&A 370, 591, [127 c, 8 c/y].
Taroyan, Y., Erdelyi, R., Doyle, J.G. et al. 2005, *Footpoint excitation of standing acoustic waves in coronal loops*, A&A 438, 713, [51 c, 4 c/y].

Tian, H., McIntosh, S.W., Wang, T.J., et al. 2012, *Persistent Doppler shift oscillations observed with Hinode/EIS in the solar corona: Spectroscopic signatures of Alfvénic waves and recurring upflows*, ApJ 759, 144, [45 c, 8 c/y].
Tsiklauri, D. and Nakariakov, V.M. 2001, *Wide-spectrum slow magneto-acoustic waves in coronal loops*, A&A 379, 1106, [58 c, 4 c/y].
Wang, T.J., Solanki, S.K., Curdt, W., et al. 2002, *Doppler shift oscillations of hot solar coronal plasma seen by SUMER: A signature of loop oscillations ?* ApJ 574, L101, [171 c, 11 c/y].
Wang, T.J., Solanki, S.K., Curdt, W., et al. 2003a, *Hot coronal loop oscillations observed with SUMER: Examples and statistics*, A&A 406, 1105, [127 c, 9 c/y].
Wang, T.J., Solanki, S.K., Innes, D.E., et al. 2003b, *Slow-mode standing waves observed by SUMER in hot coronal loops*, A&A 402, L17, [117 c, 8 c/y].
Wang, T.J., Solanki, S.K., Innes, D.E., et al. 2005, *Initiation of hot coronal loop oscillations: Spectral features*, A&A 435, 753, [60 c, 5 c/y].
Wang, T.J., Ofman, L., Davila, J.M., et al. 2009a, *Hinode/EIS observations of propagating low-frequency slow magneto-acoustic waves in fan-like coronal loops*, A&A 503, L25, [70 c, 8 c/y].
Wang, T.J., Ofman, L., and Davila, J.M. 2009b, *Propagating slow magneto-acoustic waves in coronal loops observed by Hinode/EIS*, ApJ 696, 1448, [61 c, 7 c/y].
Wang, T.J. 2011, *Standing slow-mode waves in hot coronal loops: Observations, modeling, and coronal seismology*, SSRv 158, 397, [71 c, 11 c/y].
Wang, T.J., Ofman, L., and Davila, J.M. 2013, *3-D MHD modeling of propagating disturbances in fan-like coronal loops*, ApJ 775, L23, [32 c, 7 c/y].
Wang, T.J., Ofman, L., Sun, X., et al. 2015, *Evidence of thermal conduction suppression in a solar flaring loop by coronal seismoloy of slow-mode waves*, ApJ 811, L13, [13 c, 5 c/y].
Wang, T.J., Ofman, L., Sun, X., et al. 2018, *Effect of transport coefficients on excitation of flare-induced standing slow-mode waves in coronal loops*, ApJ 860, 107.

(10.8) Coronal Loop Oscillations: Optical and Radio

Abramov-Maximov, V.E., Gelfreikh, G.B., Kobanov, N.I., et al. 2011, *Multilevel Analysis of Oscillation Motions in Active Regions of the Sun*, SoPh 270, 175, [16 c, 2 c/y].
Gelfreikh, G.B., Nagovitsyn, Y.A., and Nagovitsyna, E.Y. 2006, *Quasi-periodic oscillations of microwave emission in solar active regions*, PASJ 58, 29, [40 c, 3 c/y].
Kallunki, J., and Riehokainen, A. 2012, *The statistical study of quasi-periodic oscillations of the radio emission in solar quiet regions*, Astron.Nachrichten 333, 20.
Katsiyannis, A.C., Williams, D.R., McAteer, R.T.J., et al. 2003, *Eclipse observations of high-frequency oscillations in active region coronal loops*, A&A 406, 709, [53 c, 4 c/y].
Kobanov,N.I., and Chelpanov, A. A. 2014, *The relationship between coronal fan structures and oscillations above faculae regions*, Astronomy Reports, 58, 272, [6 c, 2 c/y].
Kuznetsov, A.A., Van Doorsselaere, T., and Reznikova, V.E. 2015, *Simulations of gyrosynchrotron microwave emission from an oscillating 3D magnetic loop*, SoPh 290, 1173, [5 c, 2 c/y].
Nagovitsyn, Y.A., Nagovitsyna, E.Y., and Abramov-Maximov, V.E. 2013, *Long-term oscillations in solar active regions based on magnetic fields and radio emission*, Astron.Rep. 57, 636, [3 c, 0.7 c/y].
Pasachoff, J.M., Babcock, B.A., Russell, K.D., et al. 2000, *A search at two eclipses for short-period waves that heat the corona*, SoPh 195, 281, [4 c, 0.3 c/y].
Pasachoff, J.M., Babcock, B.A., Russell, K.D., et al. 2002, *Short period waves that heat the corona detected at the 1999 eclipse*, SoPh 207, 241, [22 c, 1 c/y].
Reznikova, V.E., Antolin, P., and Van Doorsselaere, T. 2014, *Forward modeling of gyrosynchrotron intensity perturbations by sausage modes*, ApJ 785, 86, [10 c, 3 c/y].
Rudawy, P., Phillips, K.J.H., Gallagher, P.T., et al. 2004, *Search for 1–10 Hz modulations in coronal emission with SECIS during the August 11, 1999 eclipse*, A&A 416, 1179, [11 c, 1 c/y].

Rudawy, P., Phillips, K.J.H, Buczylko, A., et al. 2010, *Search for rapid changes in the visible light corona during the 21-June 2001 total solar eclipse*, SoPh 267, 305, [5 c, 0.7 c/y].
Sakurai, T., Ichimoto, K., Raju, K.P., et al. 2002, *Spectroscopic Observation of Coronal Waves*, SoPh 209, 265, [53 c, 3 c/y].
Singh,J., Hasan, S.S., Gupta, G.R., et al. 2011, *Spectroscopic observation of oscillations in the corona during the total solar eclipse of 22 July 2009*, SoPh 270, 213, [16 c, 2 c/y].
Sirenko, O., Voitenko, Y., and Goossens, M. 2002, *Nonlinear interaction of kinetic Alfvén waves and radio waves in the solar corona*, A&A 390, 725, [8 c, 0.5 c/y].
Warmuth,A., and Mann, G. 2005, *A model of the Alfvén speed in the solar corona*, A&A 435, 1123, [66 c, 5 c/y].
Williams, D.R., Phillips, K.J.H., Rudawy, P., et al. 2001, *High-frequency oscillations in a solar active region coronal loop*, MNRAS 326, 428, [84 c, 5 c/y].
Williams, D.R., Mathioudakis, M., Gallagher, P.T., et al. 2002, *An observational study of a magneto-acoustic wave in the solar corona*, MNRAS 336, 747, [81 c, 5 c/y].

(10.9) Coronal Loop Oscillations: MHD Simulations

Antolin, P., De Moortel, I., Van Doorsselaere, T., et al. 2016, *Modeling observed decay-less oscillations as resonantly enhanced Kelvin-Helmholtz vortices from transverse MHD waves and their seismological application*, ApJ 830, L22, [7 c, 5 c/y].
Del Zanna, L., Schaekens, E., and Velli, M. 2005, *Transverse oscillations in solar coronal loops induced by propagating Alfvénic pulses*, A&A 431, 1095, [34 c, 3 c/y].
De Pontieu, B., Martens, P.C.H., and Hudson, H.S. 2001, *Chromospheric damping of Alfvén waves*, ApJ 558, 859, [117 c, 7 c/y].
Gruszecki, M., Murawski, K., Selwa, M., et al. 2006, *Numerical simulations of vertical oscillations of a multi-stranded coronal loop*, A&A 460, 887, [22 c, 2 c/y].
Konkol, P., Murawski, K., and Zaqarashvili, T.V. 2012, *Numerical simulations of magneto-acoustic oscillations in a gravitationally stratified solar corona*, A&A 537, A96, [6 c, 1 c/y].
Kumar, N., Kumar, A., and Murawski, K. 2016, *Propagation and damping of slow MHD waves in a flowing viscous coronal plasma*, Astrophys.Spac.Science 361, 143.
Ofman, L. 2002, *Chromospheric leakage of Alfvén waves in coronal loops*, ApJ 568, L135, [53 c, 3 c/y].
Ofman, L. 2009a, *3-D MHD models of twisted multi-threaded coronal loop oscillations*, ApJ 694, 502, [32 c, 4 c/y].
Ofman, L. 2009b, *Progress, challenges, and perspectives of the 3-D MHD numerical modeling of oscillations in the solar corona*, SSRv 149, 153, [31 c, i4 c/y].
Ofman, L., Parisi, M., and Srivastava, A.K. 2015, *3-D MHD modeling of vertical kink oscillations in an active region plasma curtain*, A&A 582, A75, [2 c, 1 c/y].
Pascoe, D.J., Wright, A.N., and De Moortel, I. 2010, *Coupled Alfvén and kink oscillations in coronal loops*, ApJ 711, 990, [66 c, 9 c/y].
Pascoe, D.J. 2014, *Numerical simulations for MHD coronal seismology*, Res.Astron. Astrophys. 14, 805, [15 c, 4 c/y].
Pascoe, D.J., Wright, A.N., and De Moortel, I. 2010, *Coupled Alfvén and kink oscillations in coronal loops*, ApJ 711, 990, [66 c, 9 c/y].
Pascoe, D.J. and Nakariakov, V.M. 2016, *Standing sausage modes in curved coronal slabs*, A&A 593, 52 c, [4 c, 3 c/y].
Selwa, M., Murawski, K., and Solanki, S.K. 2005a, *Excitation and damping of slow magnetosonic waves in a solar coronal loop*, A&A 436, 701, [47 c, 4 c/y].
Selwa, M., Murawski, K., Solanki, S.K., et al. 2005b, *Numerical simulations of vertical oscillations of a solar coronal loop*, A&A 440, 385, [38 c, 3 c/y].
Selwa, M., Murawski, K., Solanki, S.K., et al. 2007a, *Energy leakage as an attenuation mechanism for vertical kink oscillations in solar coronal wave guides*, A&A 462, 1127, [32 c, 3 c/y].

Selwa, M., Ofman, L., and Murawski, K. 2007b, *Numerical simulations of slow standing waves in a curved solar coronal loop*, ApJ 668, L83, [31 c, 3 c/y].
Selwa, M. and Ofman, L. 2010, *The role of active region topology on excitation, trapping and damping of coronal loop oscillations*, ApJ 714, 170, [12 c, 2 c/y].
Selwa, M., Murawski, K., Solanki, S.K., et al. 2010, *Excitation of vertical kink waves in a solar coronal arcade loop by a periodic driver*, A&A 512, A76, [8 c, 1 c/y].
Selwa, M., Ofman, L., and Solanki, S.K. 2011, *The role of active region loop geometry. I. How can it affect coronal seismology ?* ApJ 726, 42, [12 c, 2 c/y].
Van Doorsselaere, T., Andries, J., Poedts,S., et al. 2004, *Damping of coronal loop oscillations. Calculations of resonantly damped kink oscillations on "thick" boundaries*, ApJ 606, 1223, [109 c, 8 c/y].

(10.10) Coronal Loop Oscillations: Harmonics

Andries, J., Arregui, I., and Goossens, M. 2005, *Determination of the coronal density stratification from the observation of harmonic coronal loop oscillations*, ApJ 624, L57, [168 c, 13 c/y].
De Moortel, I. and Brady, C.S. 2007, *Observation of higher harmonic coronal loop oscillations*, ApJ 664, 1210, [66 c, 6 c/y].
Dymova, M.V. and Ruderman, M.S. 2006a, *Resonantly damped oscillations of longitudinally stratified coronal loops*, A&A 457, 1059, [55 c, 5 c/y].
Dymova, M.V. and Ruderman, M.S. 2006b, *The geometry effect on transverse oscillations of coronal loops*, A&A 459, 241, [41 c, 4 c/y].
Guo, Y., Erdelyi, R., Srivastava, A.K., et al. 2015, *MHD seismology of a coronal loop system by the first two modes of standing kink waves*, ApJ 799, 151, [16 c, 6 c/y].
Morton, R.J. and Erdelyi, R. 2009, *The effect of elliptic shape on the period ratio P_1/P_2 of emerging coronal loops*, A&A 502, 315, [23 c, 3 c/y].
O'Shea, E., Srivastava, A.K., Doyle, J.G., et al. 2007, *Evidence for wave harmonics in cool loops*, A&A 473, L13, [42 c, 4 c/y].
Pascoe, D.J., Goddard, C.R., Nakariakov, V.M. 2016, *Spatially resolved observation of the fundamental and second harmonic standing kink modes using SDO/AIA*, A&A 593, 53, [7 c, 5 c/y].
Pascoe, D.J. and Nakariakov, V.M. 2016, *Standing sausage modes in curved coronal slabs*, A&A 593, 52 c, [4 c, 3 c/y].
Srivastava, A.K. 2010, *Evidence of wave harmonics in a brightened magnetic network observed from Hinode/EIS*, New Astronomy 15/7, 621, [4 c, 0.5 c/y].
Srivastava, A.K., Dwivedi, B.N., and Kumar, M. 2013, *Observations of intensity oscillations in a prominence-like loop system as observed by SDO/AIA: Evidence of multiple harmonics of fast magneto-acoustic waves*, Astrophys. and Space Science 345, 25, [10 c, 2 c/y].
Van Doorsselaere, T., Nakariakov, V.M., and Verwichte, E. 2007, *Coronal loop seismology using multiple transverse loop oscillation harmonics*, A&A 473, 959, [102 c, 10 c/y].
Verth, G., Van Doorsselaere, T., Erdelyi, R. 2007, *Spatial magneto-seismology: Effect of density stratification on the first harmonic amplitude profile of transversal coronal loop oscillations*, A&A 475, 341, [53 c, 5 c/y].
Verwichte, E., Nakariakov, V.M., Ofman, L., et al. 2004, *Characteristics of transverse oscillations in a coronal loop arcade*, SoPh 223, 77, [197 c, 15 c/y].
Wang, T.J., Ofman, L., Davila, J.M., et al. 2009a, *Hinode/EIS observations of propagating low-frequency slow magneto-acoustic waves in fan-like coronal loops*, A&A 503, L25, [71 c, 8 c/y].
Wang, T.J., Ofman, L., and Davila, J.M. 2009b, *Propagating slow magneto-acoustic waves in coronal loops observed by Hinode/EIS*, ApJ 696, 1448, [61 c, 7 c/y].
Wasiljew, A. and Murawski,K. 2009, *Numerical simulations of the first harmonic kink mode of vertical oscillations of a solar coronal loop*, A&A 498, 863, [3 c, 0.4 c/y].

Chapter 11
Filaments and Prominences

11.1 Filaments/Prominences: Stereoscopy

Filaments (when seen in absorption on the solar disk) or prominences (when seen in emission above the limb) reveal the location of the magnetic neutral line in active regions and often represent progenitors of CMEs. What mainly distinguishes filaments from ordinary coronal loops or flux tubes is that their temperature is much cooler, and their density is much higher than the surrounding corona, and thus they are likely to be fed by upflows of heated dense chromospheric plasma that cools off by condensation. They may exist in a quiescent state for a long time, but eventually they may become magnetically unstable and may initiate the eruptive state of a *coronal mass ejection (CME)*, at which point they are called *eruptive filament* or eruptive prominence.

The STEREO mission provided for the first time a stereoscopic view on these spatially complex quiescent or eruptive filaments (or prominences). Some attempts of 3-D reconstructions of quiescent EUV filaments were made in the pre-STEREO era, using the solar rotation to vary the aspect angle of EIT/SOHO images. The best observed erupting filament during the STEREO era occurred on 2007 May 19 (Li et al. 2008; Gissot et al. 2008; Liewer et al. 2009; Bone et al. 2009; Xu et al. 2010), early in the STEREO mission when the two spacecraft were separated by 8.5°, at an angle that is most suitable for stereoscopy. The complex evolution of a quiescent and active filament, from the formation, interaction, to the merging, with repeated heating via magnetic reconnection preceding the eruption, has been observed with STEREO in the 2007 May 19 event. The filament could be followed with STEREO/EUVI 304 Å from $\approx$ 12 hours before to about 2 hours after the eruption, yielding the 3-D trajectory of the erupting filament (Liewer et al. 2009). The filament was stereoscopically triangulated and the height of the EUV emission was determined to be $\approx$ 48 $\pm$ 10 Mm prior to eruption (Gissot et al. 2008; Liewer et al. 2009; Xu et al. 2010), which was higher than the location of Hα emission (Xu et al. 2010). The trajectory of the erupting filament was

M. J. Aschwanden, *New Millennium Solar Physics*, Astrophysics and Space Science Library 458, https://doi.org/10.1007/978-3-030-13956-8_11

determined with the optical-flow algorithm *Velociraptor* (Gissot et al. 2008). The magnetic field topology was found to be highly nonpotential, with a multipolar configuration, hosting frequent flares, multiple filament eruptions, and CMEs (Li et al. 2008). The 3-D reconstruction of the filament and the chromospheric ribbons in the early stage of the eruption suggest that simultaneous heating occurred in the rising filament plasma and in the chromosphere below, as expected from a flare-like magnetic reconnection process (Liewer et al. 2009). Simultaneous analysis of SOT/Hinode, TRACE, and EUVI data led to the conclusion that a pre-eruption sheared-core magnetic field is gradually destabilized by evolutionary tether-cutting flux cancellation, which is driven by converging photospheric flows, where the main filament ejection is triggered by flux cancellation between the positive flux elements and the surrounding negative field (Sterling et al. 2010). Comparisons of He II and Hα images show that emission in He II occurs together with the disappearance in Hα, and thus the disappearance results from heating and motion, rather than from draining and loss of filamentary material (Liewer et al. 2009).

Stereoscopic observations of eruptive filaments can provide quite different 3-D perceptions than envisioned from a single direction. For instance, a filament appearance was reported on 2008 May 22, where Hα observations showed up- and down-flows in adjacent locations along a filament, suggesting plasma motions along a twisted flux rope, while STEREO A+B (with a separation angle of 52°) revealed an untwisting flux rope in He II 304 Å images (Gosain et al. 2009). Multi-spacecraft observations of the 2007 May 9 prominence eruption at the west limb with STEREO indicate that the prominence has a "hook-shaped" mainly 2-D planar structure, suggesting the absence of a 3-D flux rope (Bemporad 2009; Bemporad et al. 2009), and this kind of structure is envisaged in many flare-CME models (e.g., Raouafi 2009). Stereoscopic movies of the eruptive filament of 2008 March 25 clearly reveal that the 3-D geometry of the erupting twisted filament is consistent with the kink-unstable flux rope model (Aschwanden et al. 2009; Fig. 11.14 therein). Stereoscopic triangulation yields the true 3-D velocity and acceleration of rising filaments, which were found in the gradual filament eruption to be as slow as $v = 102$ km s^{-1} and $a = dv/dt = 3$ m s^{-2}, over a time span of 17 hours, followed by a gradual CME (Li et al. 2010). Other stereoscopic observations feature an initial mass off-loading phase that may trigger the rise and catastrophic loss of equilibrium of a flux rope (Seaton et al. 2011), a rotating erupting prominence (Thompson et al. 2012), a 4-D reconstruction of an eruptive prominence, (Fig. 11.1; Chifu et al. 2012), and a filament eruption observed from three viewpoints (Filippov 2013).

The 3-D geometry of filaments has often been approximated by horizontal and vertical slabs, or by planar sheet-like structures. A method to estimate the width and inclination of such filament sheets has been applied to STEREO He II 304 Å data (Gosain and Schmieder 2010). The automated detection of filaments in He 304 Å images is often difficult due to the varying brightness level of the background, but useful methods have been developed to remove this background (Artzner et al. 2010). Automated detection of limb prominences in He II 304 Å data has been developed, which can discriminate limb prominences from active regions or the

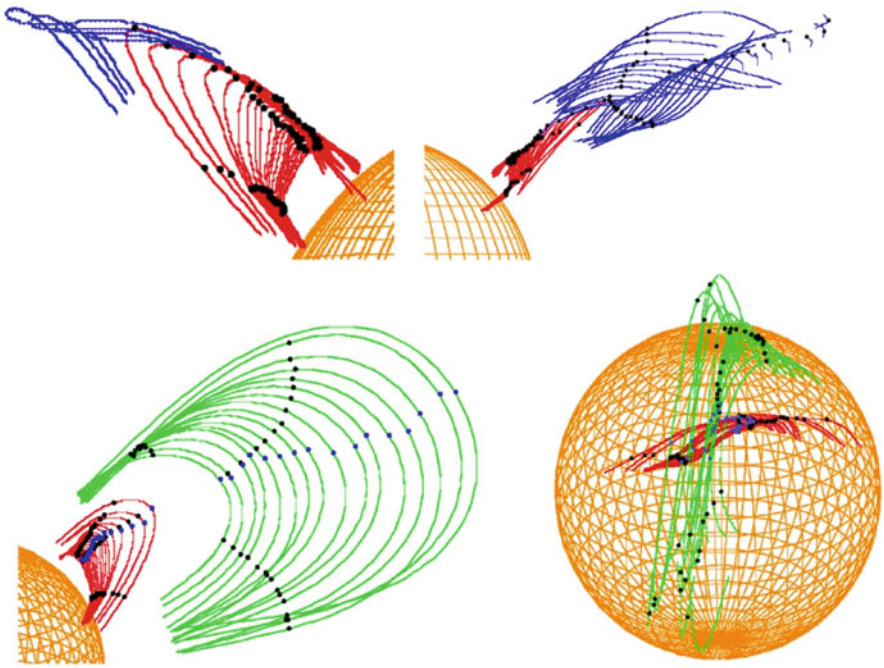

Fig. 11.1 The 3-D reconstruction of an erupting prominence, observed on 2010 August 1, from EUV images (red), the reconstruction of the CME core (blue) and the CME leading edge (green) using COR1/STEREO images. The reconstructed curves of the prominence and the CME core (top right panel) and of the prominence and leading edge of the CME from two different view directions (bottom panels) (Chifu et al. 2012)

quiet corona in 93% of the cases (Labrosse et al. 2010). Another algorithm, the *Solar Limb Prominence Catcher and Tracker (SLIPCAT)*, produced a catalog of 9477 well-tracked prominences during the 2007 April - 2009 October period of STEREO 304 Å observations (Wang et al. 2010). The statistical results showed that most prominences occur below a latitude of 60°, have a length of $\approx$ 50 Mm, a height of $\approx$ 26 Mm, and 80% show no obvious motion (Wang et al. 2010). Another statistical study of 68 quiescent filament channels with STEREO/EUVI and Hinode/XRT revealed an asymmetry in the morphology due to the variation in axial flux of the flux rope along the channel (Su et al. 2010).

11.2 Filaments/Prominences: Magnetic Field

Filaments (or prominences) have been used as probes of the magnetic field (for a review see Mackay et al. 2010), since the magnetic field lines are frozen into the fluid and have to move along with it, in a fluid with infinite electric conductivity.

They lie above photospheric *polarity inversion lines* and occur within *filament channels*, in which the chromospheric fibrils rooted in neighbored network elements are aligned with the polarity inversion lines. Mackay et al. (2010) subdivides filaments into three groups: (i) *active region filaments* (in multiple bipolar pairs of sunspots), *intermediate filaments* (at the border of active regions), and (iii) *quiescent filaments* (in the Quiet Sun), including the *polar crown filaments*. Filaments typically consist of three structural components: a spine, barbs, and two extreme ends.

The magnetic field in a filament channel has a strong axial component that carries electric currents, while twisted filament strands are helically wrapped around the axial field. This magnetic configuration cannot accurately be modeled with a potential field or a linear force-free field, but rather needs a *nonlinear force-free field (NLFFF)* model. One 3-D model of a filament channel has been constructed by inserting a twisted flux rope into a potential field representing the overlying coronal arcade (van Ballegooijen 2004). The flux rope has an axial flux of 3.4×10^{19} Mx and a poloidal flux of 3.7×10^{9} Mx cm^{-1}. In this model, the observed sinistral filament is supported by a right-helical flux rope, which is held down by an overlying arcade that is anchored in the neighboring network elements (van Ballegooijen 2004; van Ballegooijen et al. 2007).

The same filament that was observed with MDI/SOHO on 2005 October 10 was modeled with the flux rope insertion method by van Ballegooijen (2004), and has been used as a benchmark test for magnetic modeling of a filament with different NLFFF codes, including optimization, magneto-frictional, and Grad-Rubin-like codes (Metcalf et al. 2008). The codes were applied to both forced "photospheric" and more force-free "chromospheric" vector magnetic field boundary data derived from the model. Preprocessing of the forced photospheric boundary does improve the extrapolations, but the solutions depend strongly on the spatial resolution and degree of smoothing of the magnetograms (Fig. 11.2), and the uncertainty of the free energy amounts to a factor of two.

A similar NLFFF model using the flux-rope insertion method was developed by Bobra et al. (2008), constrained by Hα observations and TRACE data, where the flux rope geometry is forward-fitted to the observations, with the finding of a relatively weak twist of the flux rope. They find that the axial fluxes of the flux ropes are close to the upper limit for stability of the force-free equilibrium, but no major eruptions occurred in the two modeled active regions, either several days before or after the observations, which suggests that magnetic energy can be released very gradually and that the build-up of free energy does not necessarily lead to large flares or CMEs. In contrast, Su et al. (2009) modeled a different active region and found that the flux rope present in that region has an axial flux well below the threshold for eruption. Consequently, neither the evolution of the instability criterion, nor the evolution of free energy provide reliable forecasting for flares or CMEs. Nevertheless, a twisted flux rope is considered to be the basic magnetic structure of a filament (Canou and Amari 2010).

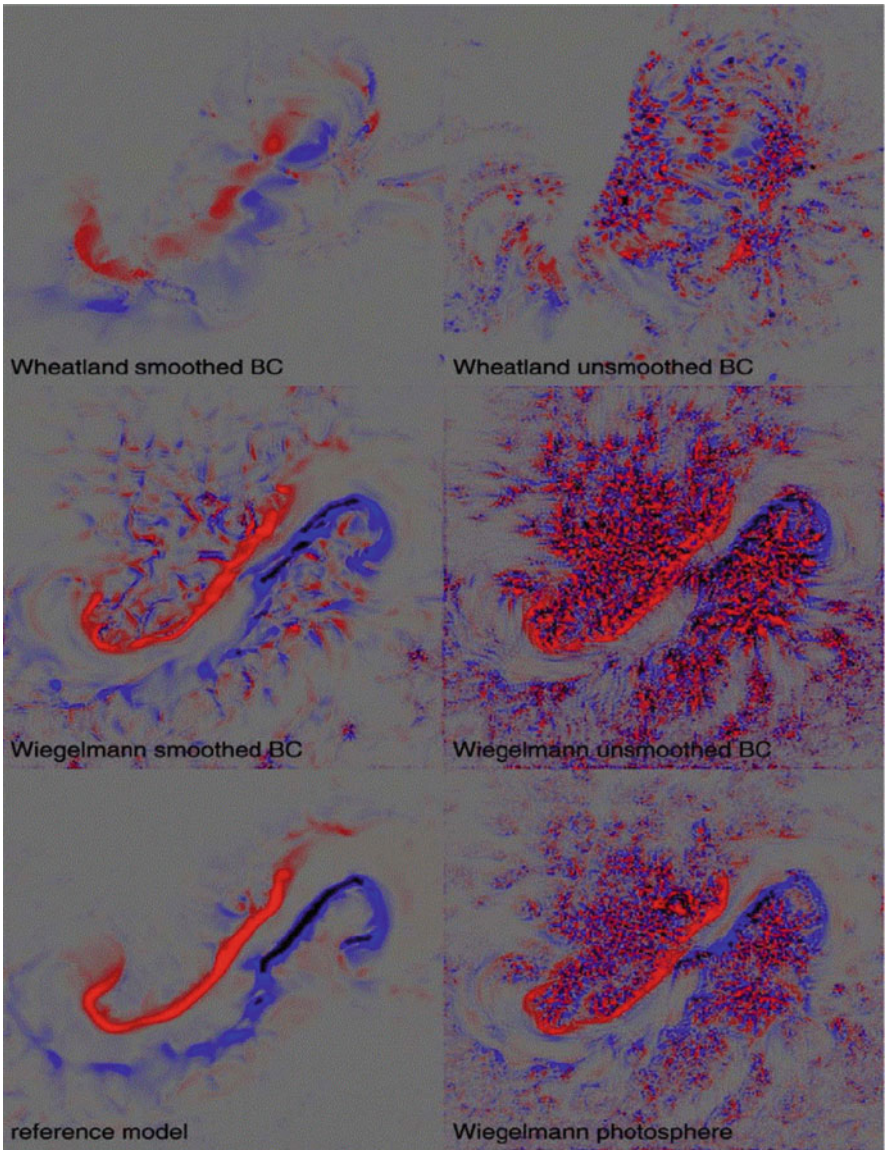

Fig. 11.2 Plots of the vertical current density J_z at a height of $h = 0.0004\ R_\odot$, for four photospheric test cases using preprocessed magnetograms (top two rows), as well as for the reference model and for Wiegelmann's solution without preprocessing (bottom row). Smoothing the input vector magnetogram during the preprocessing removes high-frequency currents, which otherwise propagate upward into the corona (Metcalf et al. 2008)

A typical feature of quiescent prominences is the magnetic dip, which supports the dense prominence plasma against gravity. Recent attempts use a 3-D NLFFF code to model magnetic dips filled with realistic prominence plasma in hydrostatic equilibrium, from which synthetic hydrogen Lyman-α spectra are produced and compared with observations (Gunar et al. 2013). Magnetic fields of order $B \approx 7$–25 G are found with this model, yielding a plasma-β of 0.07–0.1, which indicates no significant distortions of the magnetic field by the mass. Successful magnetic prominence models should match three well-defined morphological structures: (i) the vertical region seen in absorption in EUV, (ii) the extended region of numerous quasi-vertical fine-structure threads that are bright in Lyman-α, and sometimes (iii) the bubble lying underneath an area of tangled fine structures (Gunar et al. 2014). Three perspectives of a magnetic field model are depicted in Fig. 11.3, showing a juxtaposition of a theoretical model and AIA/SDO observations.

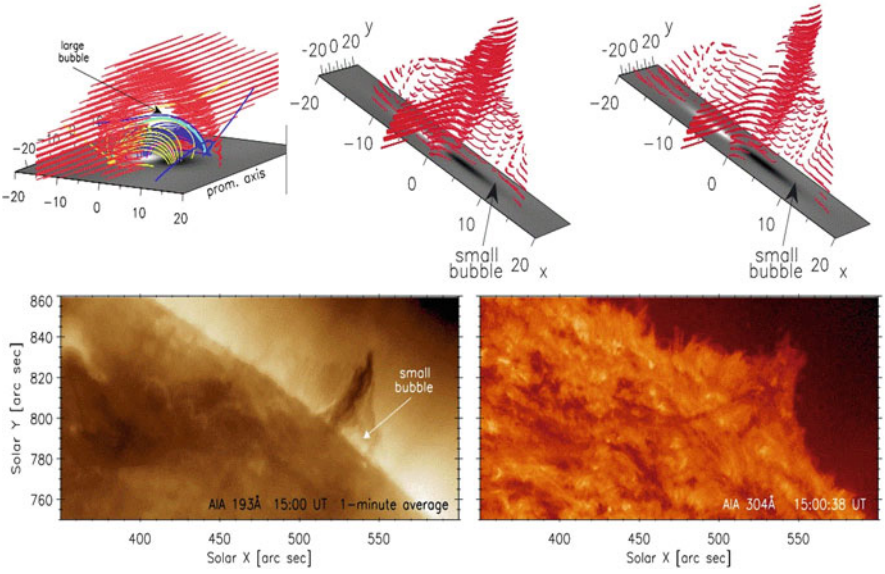

Fig. 11.3 A magnetic field model of the prominence compared to AIA/SDO observations. *Top left:* Original magnetic field model of the prominence with a symmetric unsheared bipole (Dudik et al. 2012, Fig. 6 therein). Magnetic dips up to a height of 300 km are shown in red. Spine and fan field lines of the positive and negative magnetic null-points are shown in yellow and blue. An arrow points to a small bubble within the prominence created by the bipole. *Top middle:* The same model, projected off-limb at 30° of solar latitude. The small bubble within the right foot is denoted by an arrow. *Top right:* Asymmetric model in the same off-limb projection. Dimensions are given in units of 1000 km. *Bottom row:* AIA/SDO 304 Å observations of the prominence together with the on-disk filament (right), while a weak filament channel is visible in AIA/SDO 193 Å (left) (Gunar et al. 2014)

The formation of small-scale magnetic fields in active region filaments were observed during four days by NVST, SDO, and Hinode (Yan et al. 2015) and were described as follows: Shearing motion of the opposite magnetic polarities and sunspot rotation plays an important role in the formation of (two) active-region filaments. Analyzing the nonlinear force-free field extrapolation in the photosphere, twisted structures were found in the two active region filaments prior to their eruptions, implying that the magnetic fields were dragged by shearing motion between opposite magnetic polarities and became more horizontal. The sunspot rotation twisted the horizontal magnetic field and finally formed the twisted active region filaments (Yan et al. 2015).

Magnetic field measurements in prominences have also been accomplished using the Hanle and Zeeman effect in spectropolarimetric measurements of the He I 10,830 Å triplet, but such measurements are scarce (Orozco Suarez et al. 2014), while future measurements with DKIST should be feasible.

11.3 Filaments/Prominences: Formation

What is the formation process of filaments? Theoretical mean field models applied to random footpoint motions that cause small-scale twisting and braiding of field lines have been developed, focussing on the formation of filament channels. It is found that magnetic flux cancellation plays an important role in the formation of filament channels, but the observed hemisphere pattern of dextral and sinistral channels remain a mystery (van Ballegooijen et al. 2000). A "head-to-tail linkage model" (i.e.,. a quadrupolar magnetic configuration where the tail of the first dipole links to the head of the second dipole) was presented by Martens and Zwaan (2001). A sequence of magnetic flux convergence and cancellation episodes produce loop-like filament segments with a half-turn in this model. The combined working of Hale's polarity law, Joy's tilt angle law, and the differential rotation introduce a strong hemispheric preference in the chirality of filaments formed poleward of the sunspot belt, in agreement with observations (Martens and Zwaan 2001).

Observationally, it is found that the formation of filaments is accompanied by an associated large canceling magnetic feature and by a persistent pattern of shear motion in the neighborhood of the filament, both together producing a much larger rate of helicity change than the differential rotation alone (Chae et al. 2001). This indicates that the filament formation represents only a small part of a much bigger magnetic structure, such as a flux rope and an overlying sheared arcade (Chae et al. 2001). A pair consisting of a quiescent filament and an active region filament was observed (on 2007 May 19, 12:50 UT) in an attempt to merge, but became repeatedly heated by magnetic reconnection, before it finally erupted (Bone et al. 2009). Another dual structure was identified as a flux rope in one section of the filament, and as a sheared arcade with dipping in another section of the filament (Guo et al. 2010). Dual active region filaments

were observed to form twisted active region filaments, caused by rotating sunspots (Yan et al. 2015). The flux rope structure seems to be prevailing in both quiescent and activated filaments, being present in both cool and hot plasma prominence material (Cheng et al. 2014). Kuckein et al. (2012) divides a filament into two parts, a low-lying part that stays trapped in the photosphere and is manifested in form of pores and orphan penumbrae, and an upper part in the chromosphere that can be detected by He lines. On a smaller scale, every filament consists of complex fine structure, some controlled by laminar flows along threads, while other parts of filaments/prominences reveal turbulence, manifested by condensation of plasma flows in different directions (Schmieder et al. 2014). Laminar parts of filaments are made of very thin threads, with widths of $\lesssim 0.3''$ or $\lesssim 250$ km (Lin et al. 2005a). Filaments develop barbs very rapidly, on time scales of 10 min, as inferred from flows in the spine and barbs (Joshi et al. 2013), where 65% of the observed end points of barbs fall within the network boundaries (Lin et al. 2005b).

Some numerical MHD models of filaments start with a sheared double arcade model, but the origin of the magnetic shear is not clear. It could be the result of the partial emergence of twisted flux tubes from below, or direct subsurface motions near the polarity inversion line (Luna et al. 2012). The 2.5-D MHD model of Xia et al. (2012) captures all phases of the filament/prominence formation. The formation results from concentrating heating in the chromosphere, followed by plasma evaporation and later rapid condensation in the corona due to thermal instability (Xia et al. 2012; Kaneko and Yokoyama 2015). Concentrating heating in the lower atmosphere supplies mass to the filament/prominence constantly (Xia et al. 2012). Heated dense chromospheric plasma material gets mixed with prominence matter up to very large heights, which offers an explanation for the evaporation-condensation cycle (Keppens et al. 2015). Recent simulations show the filament/prominence formation and evolution in an elongated magnetic flux rope as a result of in-situ plasma condensations fueled by continuous plasma evaporation from the chromosphere (Xia and Keppens 2016). The prominence is born and maintained in a fragmented, highly dynamic state (Fig. 11.4) with continuous reappearance of multiple blobs and thread structures that move mainly downward, dragging along mass-loaded field lines (Xia and Keppens 2016).

A useful resource of kinematic parameters of erupting filaments and prominences is the online catalog compiled by McCauley et al. (2015), based on AIA/SDO observations of 904 events. Examples of the four different types of filaments/prominences are shown in Fig. 11.5. Events with evident twist have significantly faster CME speeds and fast-rise onset heights, which suggests relationships between these values and flux rope helicity.

In general there are two main mechanisms put forward for prominence mass accumulation in magnetic dip (flux rope) structures: (i) one posits that hot plasma is lifted along the field lines via "footpoint non-equilibrium" and then radiatively cools in the dips to form the observed prominence (e.g., Karpen et al. 2001; Luna et al. 2012); and (ii) the other posits that relatively cool plasma is created aloft by

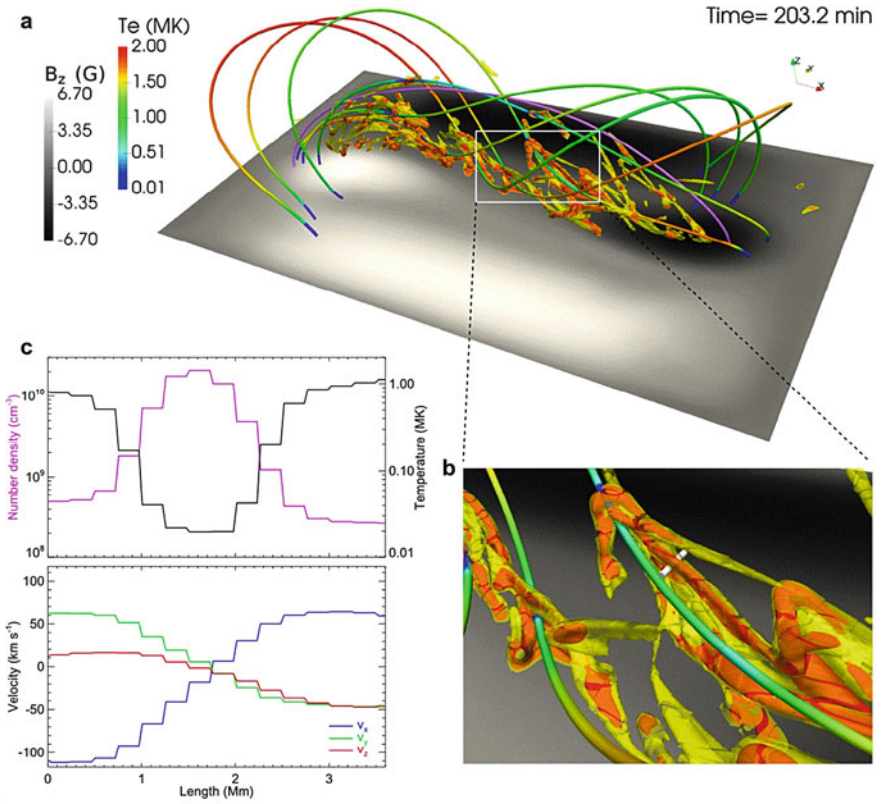

Fig. 11.4 (**a**) A global view of the prominence with yellow translucent density contours, (**b**) Close-up view of region in white box, and (**c**) density, temperature, and velocity profile as a function of the length across the cross-section of a filament thread, (Xia and Keppens 2016)

condensation from hotter coronal plasma in an overlying coronal cavity flux rope (Berger et al. 2012; Liu et al. 2012). These two paradigms are discussed in more detail in the context of non-equilibria (Sect. 11.5) and cavities (Sect. 11.9).

11.4 Filaments/Prominences: MHD

The formation of a filament-prominence system is envisioned to occur by a sequence of flux convergence and cancellation (magnetic reconnection) episodes in a filament channel, which strings the filament threads into a single twisted structure, and by the combined workings of Hale's polarity law, Joy's law, differential rotation, and helicity condensation produces a strong hemispheric preference in the chirality (Martens and Zwaan 2001).

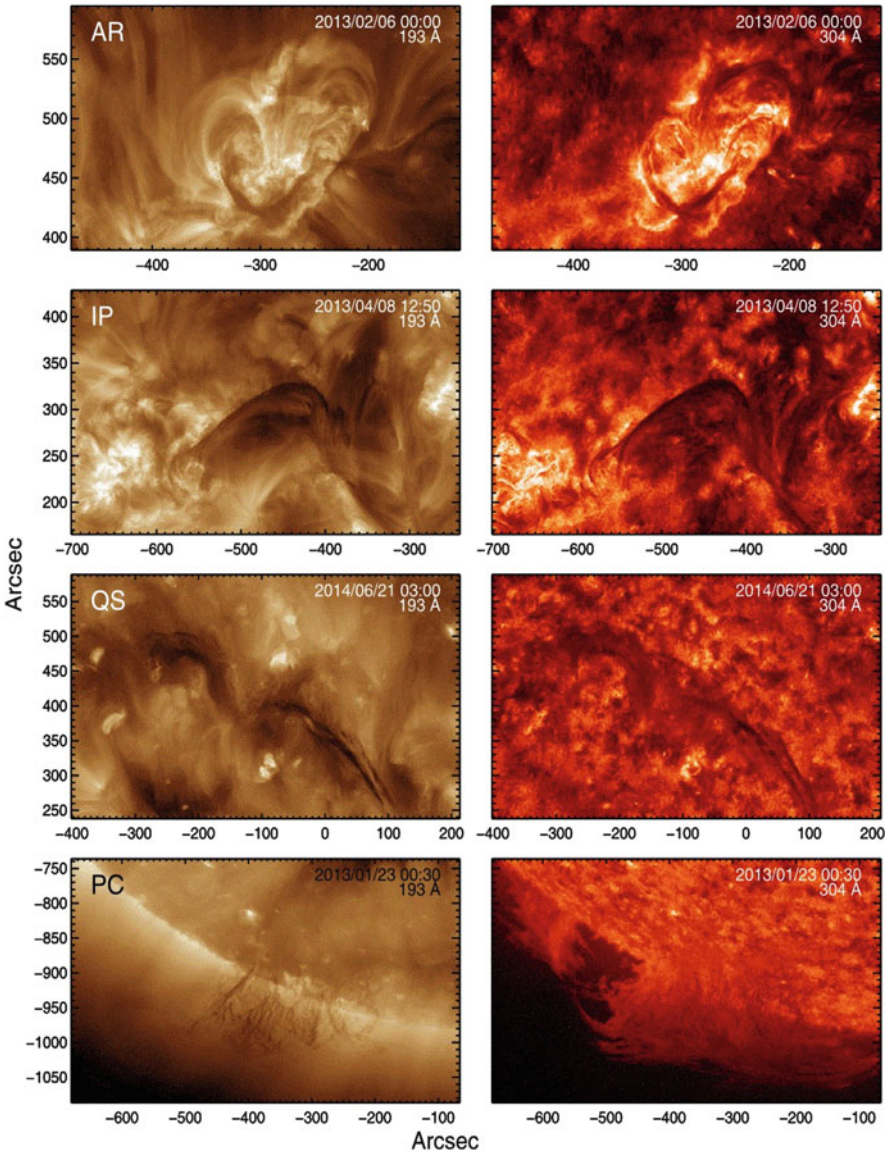

Fig. 11.5 Examples of three main types of filaments/prominences: active region (AR), intermediate (IP), and quiescent (QS) including polar crown (CP). The images are taken from AIA/SDO in the 193 and 304 Å wavelengths (McCauley et al. 2015)

An unsettled question is the support mechanism and long-term stability of quiescent filaments or prominences, since they last from a few hours to several months. The original model of Kippenhahn and Schlüter (1957) is based on an equilibrium between the gradient of the gas pressure ∇p, gravity $\rho \mathbf{g}$, and the Lorentz force ($\mathbf{j} \times \mathbf{B}$). A generalized Kippenhahn-Schlüter equilibrium and steady-flow solutions of the MHD equations was developed for isothermal prominence sheets (Low and Petrie 2005), predicting counter-streaming layers of prominence plasma (Petrie and Low 2005), as observed in large polar crown filaments (Lin et al. 2003; Schmieder et al. 2010) and in quiescent prominences (Shen et al. 2015). A DEM analysis reveals a higher emission measure and temperature inside a coronal cavity, compared with the overlying cooler prominence material (Fig. 11.6, Shen et al. 2015).

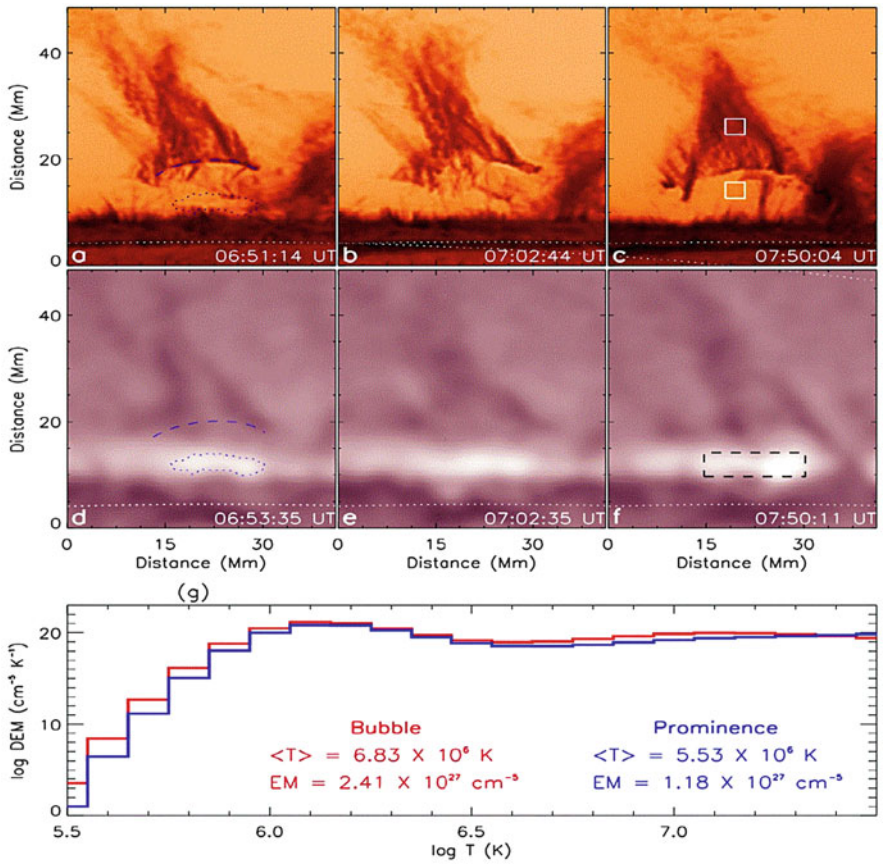

Fig. 11.6 Spatial and temporal evolution of a bubble and the vertical prominence foot. (**a**)–(**c**): NVST Hα negative images. (**d**)–(**f**): AIA 211 Å images. (**g**): Differential emission measure (DEM) curves from two boxes in the bubble and in the prominence, (Shen et al. 2015)

Numerical 1-D MHD simulations of a low-lying prominence demonstrated that helical field threading and enveloping the body of the prominence settles into a stable equilibrium, despite the substantial amount of reconnection and twist in the magnetic field (DeVore and Antiochos 2000). Numerical 1-D hydrodynamic simulations demonstrated that a filament thread with a dipped geometry, that is constantly heated at the footpoints, does not settle into an equilibrium, but undergoes a repetitive cycle of evaporation and condensation (Krall and Antiochos 1980; Antiochos et al. 2000; DeVore and Antiochos 2000). Chae et al. (2008) find that vertical threads in quiescent prominences are stacks of plasma supported against gravity by the sagging of initially horizontal magnetic field lines. Laboratory experiments (in agreement with MHD simulations) demonstrate that a large-scale arched magnetic field that straddles the prominence and effectively straps it down, can stabilize a prominence and inhibit eruption (Hansen and Bellan 2001).

The magnetic field configuration of filaments and prominences is another unsolved problem. We often assume that the observed curvilinear filament morphology follows the magnetic field, but we preferentially observe vertical fine structure at the limb, while we are biased towards horizontal structures on the disk. Moreover, the plasma-β parameter is larger than unity in chromospheric heights, where the filament material originates, and thus does not necessarily follow the magnetic field lines. If the vertical threads would follow the magnetic field, a magnetic levitation mechanism by incompressible MHD waves would be needed to keep the filament stable (Pecseli and Engvold 2000). A 3-D linear magneto-hydrostatic field model, constrained with an observed magnetogram, was able to predict the chirality, helicity, and morphology of an observed filament (Aulanier et al. 2000). The dips were found mostly to exhibit inverse polarity, but narrow regions with normal polarity were found also (Aulanier et al. 2002). A 2.5-D axisymmetric MHD model reproduced the formation of a prominence at the base of a helmet streamer (Linker et al. 2001). A 2-D magneto-hydrostatic (MHS) equilibrium model of vertical prominence threads includes 2-D multi-level non-LTE radiative transfer (Heinzel and Anzer 2001). Using MHD and hydrodynamic models of a long-lived filament demonstrated that the observed magnetic flux changes can produce a flux rope and the co-spatiality of the dipped (upward concave) portion of the field lines with the observed filament (Fig. 11.8; Lionello et al. 2002). A 2-D magneto-hydrostatic model of prominences in near-potential fields can reproduce the three-part structure, a cool dense prominence within a cavity/flux rope embedded in a hot corona (Petrie 2007; Petrie et al. 2007). The magnetic helicity of helical flux rope geometries can be characterized by the the twist and writhe, which plays a role for the onset of the kink instability in erupting filaments (Török et al. 2010). Solar prominences consisting of vertical threads are also called *hedgerow prominences*, which may be supported by tangled magnetic fields with field strengths of $\approx$ 10 G (VanBallegooijen and Cranmer 2010). However, 3-D MHD simulations rather suggest that the observed vertical threads are the result of the Rayleigh-Taylor instability (Fig. 11.7).

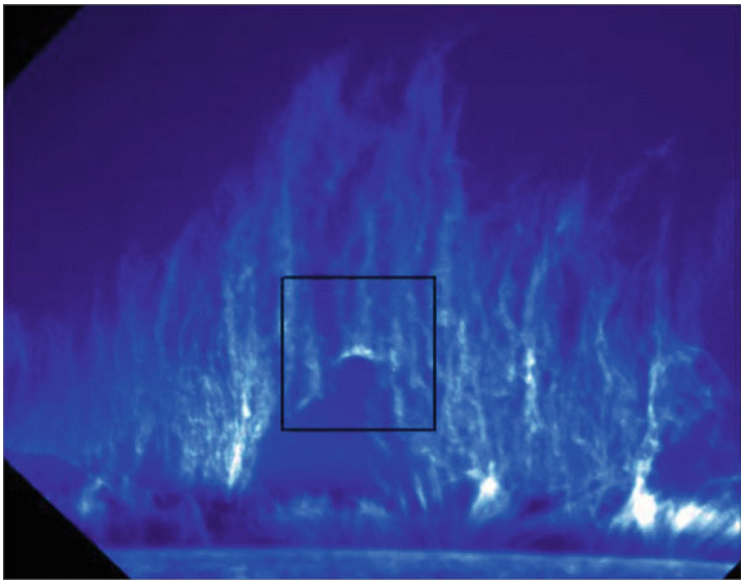

Fig. 11.7 A quiescent prominence observed on 2007 October 3, 03:30 UT, in the Ca II H line (3968.5 Å), with the Hinode/SOT instrument. The plumes (fingers of low-density material rising through the dense prominence material), are likely to be created by the Rayleigh-Taylor instability (see Sect. 11.8), Hillier et al. (2012)

11.5 Filaments/Prominences: Non-Equilibrium

Are long-lived quiescent filaments or prominences in a stationary equilibrium ? The long life of a quiescent prominence as a macroscopic structure from days to weeks or more suggest that static equilibrium is a reasonable first approximation to describe the prominence. Of course, high-resolution movies reveal that only the location of prominences appears to be quasi-static (for instance Fig. 11.9), while the fine structure exhibits rapid variations down to time scales of minutes.

Equilibrium models generally assume that the prominence material is supported against gravity through the magnetic tension force of dipped coronal magnetic fields. Therefore it appears that magnetic dips are a necessary prerequisite for prominence formation. However, there are two major reasons why this is not the case. First, numerous observations of constant motion, flows, and counterflows in prominences imply that stable gravitational support is not necessary, and second, footpoint heating produces a cycle of chromospheric upflows, thermal instability, and subsequent condensation (Antiochos et al. 2000; Karpen et al. 2003), regardless whether a dip in the magnetic field of a prominence exists or not (Karpen et al. 2001). 3-D MHD models of prominences have been configured either as sheared 3-D arcades, or as helically twisted flux ropes. Simulations of their relaxation to a static equilibrium revealed narrow regions of stable dips of inverse, as well as

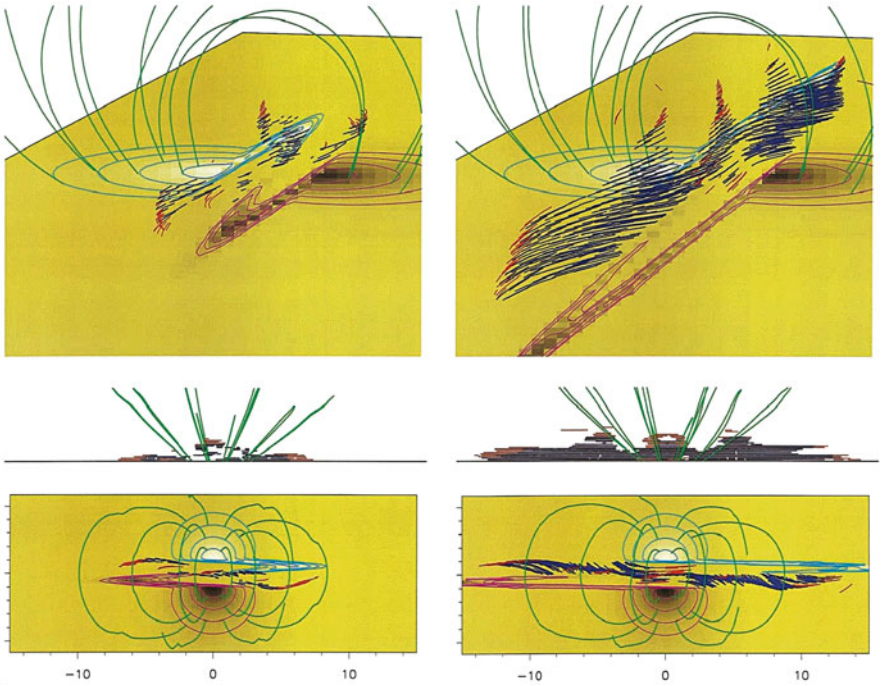

Fig. 11.8 Distribution of normal parity (red) and inverse polarity (dark blue) magnetic dips in sheared arcades surrounded by potential loops (green). The case in the left panel corresponds to small footpoint shearing, and the right panel to large footpoint shearing (Antiochos et al. 2000)

normal polarity (Fig. 11.8; Aulanier et al. 2002). MHD simulations that include hydrodynamic effects showed that observed magnetic flux changes can produce a flux rope and that the dipped (upward concave) portions of the field lines form in the approximate location of the observed prominence, and that condensations form in the dipped portions of the field lines (Fig. 11.9; Lionello et al. 2002). Condensations form readily in long, low-lying magnetic field lines when heating is localized near the chromosphere (Karpen et al. 2005; Karpen and Antiochos 2008).

Low and Petrie (2005) present a generalized *Kippenhahn-Schlüter* equilibrium and steady-flow solutions of the MHD equations. These solutions are constructed of arrays of laminated isothermal Kippenhahn-Schlüter prominence sheets, whose temperature, sag angles, and dip position may vary from sheet to sheet. The sheets can move at arbitrary constant uniform velocities relative to each other within their planes, and their dimensions differ from the characteristic hydrostatic scale lengths. This model also explains the observed vertical and horizontal velocities as naturally arising from steady rigid motions of plasma in local force equilibrium, but global non-equilibrium (Low and Petrie (2005). Another *magneto-hydrostatic (MHS)* model shows that no externallongitudinal field is needed for a prominence equilibrium, while a magnetic arcade with a magnetic field strength of a few Gauss

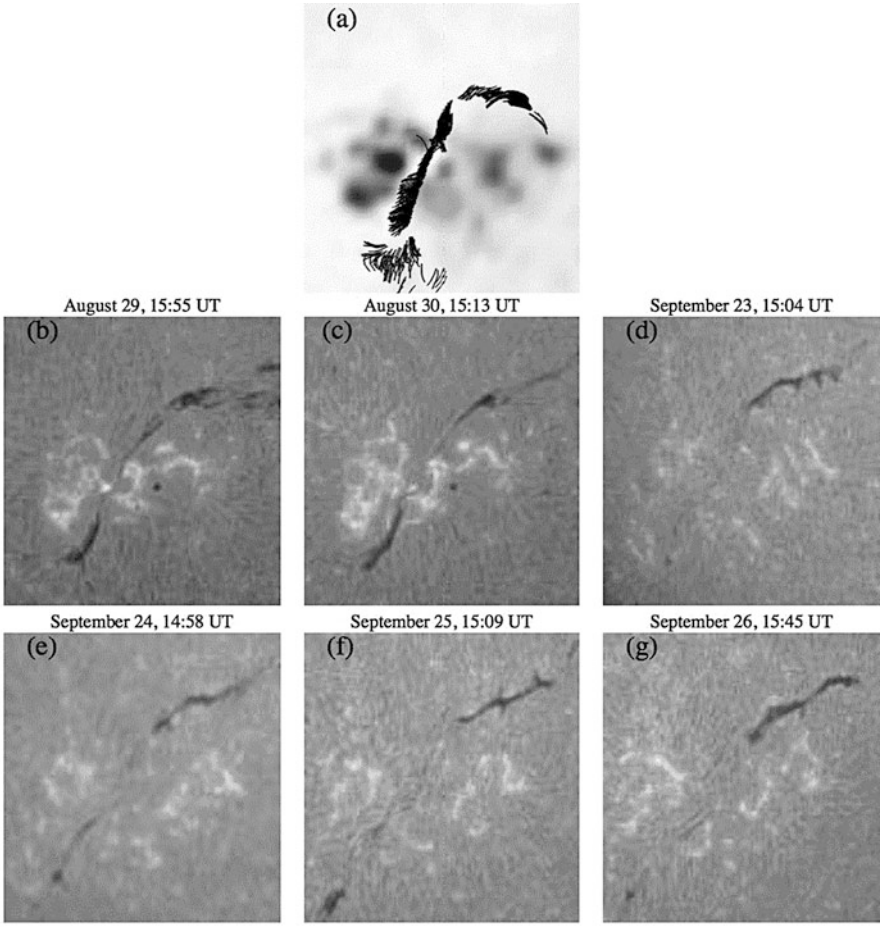

Fig. 11.9 Observations of Hα images obtained from Sacramento Peak Observatory (panels **b**–**g**), observed over a period of a month, and magnetic field reconstruction with a 3-D MHD code, overlayed on a magnetogram (panel **a**), Lionello et al. 2002

only, can maintain the equilibrium of cool dense filaments at heights of $\approx$ 50 Mm (Solov'ev 2010).

The static equilibrium of the Kippenhahn-Schlüter diffusive plasma slab, suspended vertically in a bowed magnetic field, under frozen-in condition, subject to thermal balance among optically thin radiation, heating, and field-aligned thermal conduction, was revisited by Low et al. (2012a), who found that the everywhere-analytical solutions to this nonlinear problem select an extremely restricted subset of physically admissable states of the system. A second study investigates the transverse response of a magnetic field to the independent relaxation of its flux tubes of fluid (Low et al. 2012b). The magnetic response is found to form

spontaneous discrete currents in an intermittent fashion, which can explain the dynamic structures seen in quiescent prominences by SOT/Hinode and AIA/SDO (Low et al. 2012b).

While the prominence material is supported against gravity through the magnetic tension of dipped coronal magnetic fields in equilibria models, hydrodynamic forces are likely to play an important role, as evident from the many observed gravity-driven flows. Some 2.5-D models have o-points or x-points below the prominence dip, but convergence to a prominence-like equilibrium is not warranted with such configurations (Hillier and van Ballegooijen 2013).

Besides the dynamic non-equilibrium of (macroscopic) prominence structures, there is also a thermodynamic non-equilibrium on the (microscopic) atomic level. Analysis of spectra and images of prominence plasma is not trivial, since non-LTE (departure from local thermodynamic equilibrium) radiative transfer models are required (see recent review by Labrosse et al. 2010). A simple inversion of spectroscopic data usually fails when the lines become optically thick at certain wavelengths, which requires complex non-LTE radiative transfer theory, and the associated multi-level radiative transfer problems. The solution of the radiative transfer problem involves the coupled equations of radiative transfer, statistical equilibrium, and other constraint equations. The forward-modeling approach starts with an initial prominence model (defined by the spatial distribution of temperature, pressure, and gas density), from which the excitation and ionization balance for each given species is evaluated, the opacities and emissivities are determined, and finally the emergent synthetic spectrum is calculated and compared with the observations. This procedure is iterative and the final models are called *semi-empirical models*, provided that they are at least partially data-driven (Labrosse et al. 2010).

Theoretical models, on the other hand, incorporate the non-LTE physics into the global *radiation magneto-hydrodynamical (RMHD)* models, which are not data-driven and are called *ab initio models*.

11.6 Filaments/Prominences: Oscillations and Waves (Observations)

We could call this section *filament seismology* or *prominence seismology* as well, besides the well-established fields of *coronal seismology* and *helioseismology*. It appears that coronal filaments (or prominences) display an equally rich palette of MHD resonance phenomena as it was found for coronal loops (Chap. 10). There are a number of review papers that specifically focus on MHD waves and oscillations in filaments and prominences (Oliver and Ballester 2002; Ballester 2005, 2006; Tripathy et al. 2009; Oliver 2009; Mackay et al. 2010; Lin 2011; Arregui and Ballester 2011a; Arregui et al. 2018; Arregui 2012).

MHD waves in coronal seismology are usually divided into fast (propagating with Alfvénic phase speed) and slow mode or magneto-acoustic waves (propagating

with sound speed). The fast MHD waves are further subdivided into sausage modes ($m = 0$), kink modes ($m = 1$), and fluting modes ($m = 2, 3, \ldots$). Kink modes are essentially incompressible and display transverse displacements, while sausage modes exhibit cross-sectional and density oscillations. Slow mode waves are compressible also and thus exhibit density oscillations. All these MHD modes have been observed in filaments and prominence threads, but the specific MHD mode is often not properly determined, because of a lack of density and magnetic field measurements (which leaves the Alfvén speed undefined).

Both, fast kink-mode oscillations and slow-mode (magneto-acoustic) waves have been detected in filaments and prominences, both in form of standing eigen-modes and propagating waves, as a large number of observations attests. Grouping the observations by instruments, oscillations and periodic waves were detected with: the *Vacuum Tower Telescope (VTT)* of the *Sacramento Peak Observatory* (Terradas et al. 2002), the *Big Bear Solar Observatory (BBSO)* (Jing et al. 2003), the *Coronal Diagnostic Spectrometer (CDS)* onboard SOHO (Pouget et al. 2006; Bocchialini et al. 2011), the *Extreme-ultraviolet Imaging Telescope (EIT)* onboard SOHO (Foullon et al. 2004, 2009; Pinter et al. 2008; Hershaw et al. 2011; Asai et al. 2012), the *Michelson Doppler Imager (MDI)* onboard SOHO, and the *Nobeyama Radio Heliograph (NoRH)* (Isobe et al. 2007), the *Solar Ultraviolet Measurements of Emitted Radiation (SUMER)* onboard SOHO (Chen et al. 2008), the *Solar Optical Telescope (SOT)* onboard Hinode (Okamoto et al. 2007; Berger et al. 2008; Terradas et al. 2008; Ning et al. 2009; Zhang et al. 2012; Hillier et al. 2013), the *Extreme-Ultraviolet Imager (EUVI)* onboard STEREO (Gosain and Foullon 2012), the *Atmospheric Imager Assembly (AIA)* onboard SDO (Li and Zhang 2012; Srivastava et al. 2013), the AIA/SDO, SOT/Hinode, and the *Télescope Héliographique pour l'Etude due Magnétisme et des Instabilités Solaires (THEMIS)* with the *MulTi-Raies (MTR)* (Schmieder et al. 2013), the AIA/SDO and the *Solar Magnetic Activity Research Telescope (SMART)* of the *Hida Observatory* (Shen et al. 2014a), the AIA/SDO, SMART, and STEREO (Shen et al. 2014b), the AIA/SDO and *Helioseismic and Magnetic Imager (HMI)* onboard SDO (Luna et al. 2014), the AIA/SDO and STEREO (Bi et al. 2014), the AIA/SDO (Joshi et al. 2016; Shen et al. 2017; Qu et al. 2017), the *Multi-channel Subtractive Double Pass (MSDP)* in Bialkov and Ondrejov (Zapior et al. 2015), and the *Global Oscillation Network Group (GONG)* of the *National Solar Observatory (NSO)* (Pant et al. 2015; Efremov et al. 2016; Luna et al. 2017).

The most interesting new findings of these filament and prominence oscillations include: (i) the discovery of coronal transverse MHD waves travelling with Alfvénic speed in a solar prominence detected above the limb by SOT/Hinode (Fig. 11.10; Okamoto et al. 2007); (ii) the discovery of upflowing magneto-acoustic waves in quiescent prominences as detected with SOT/Hinode (Berger et al. 2008); (iii) the first simultaneous observation of a Hα Moreton wave, EUV wave, and filament/prominence oscillations, as observed with EIT/SOHO (Asai et al. 2012).

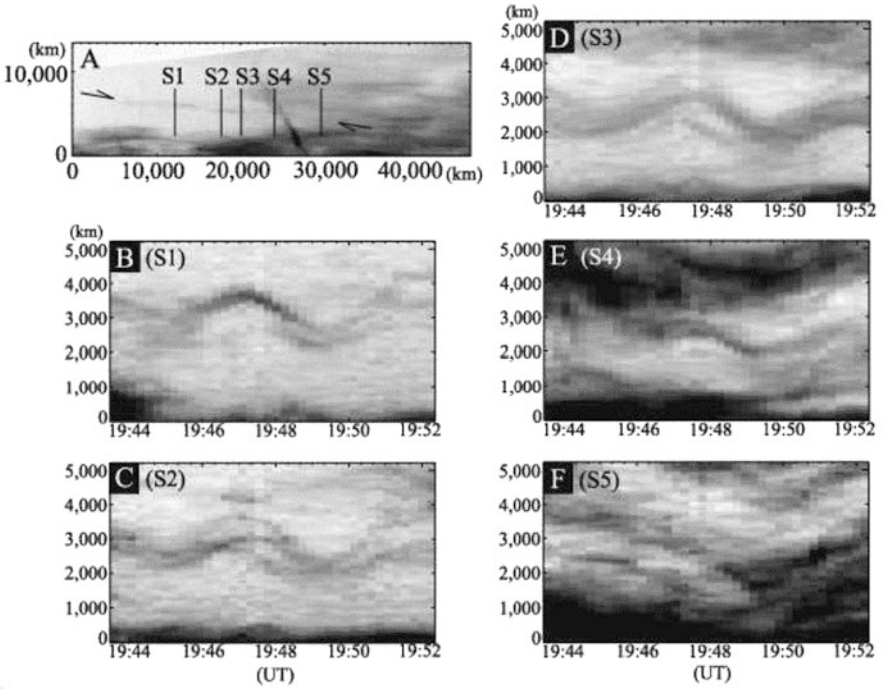

Fig. 11.10 Coronal transverse MHD waves travelling with Alfvénic speed are shown, as observed with SOT/Hinode. Prominence threads undergo synchroneous oscillation along their entire length (extending over 16,000 km here) (**a**), Lines S1 to S5 indicate the locations of height versus time plots shown in (**b**) to (**f**). Height-time plots (shown in negative contrast) for the locations indicated in (**a**). Maximum and minimum amplitudes occur at nearly the same locations (Okamoto et al. 2007)

11.7 Filaments/Prominences: Oscillations and Waves (Theory)

Theoretical understanding of oscillations and waves in filaments and prominences has been deepened in a similar way as for coronal loops (Chap. 10), by investigating physical excitation and damping mechanisms, modeling second-order effects (density stratification, temperature gradients, magnetic field dips) that modify the oscillation period or wavelengths, and by numerical simulations of analytical solutions or numerical MHD simulations, especially using the concept of multi-thread fine structure. Theoretical reviews are listed in the previous section 11.6.

Most of the observed oscillations in quiescent filaments or prominences are found to have a finite life time, and a variety of damping mechanisms has been considered, such as: radiative loss during the cooling phase in slow magneto-acoustic modes (Terradas et al. 2001, 2005), radiative loss, thermal conduction, and heating (Carbonell et al. 2004, 2006; Soler et al. 2007a, 2008), ion-neutral collisions

(Forteza et al. 2007, 2008; Soler et al. 2009c, 2015a), turbulent viscosity (Singh et al. 2007), resonant absorption (Arregui et al. 2008, 2011b; Soler et al. 2009b; Okamoto et al. 2015; Antolin et al. 2015), phase mixing (Soler and Terradas 2015), partial ionization (Carbonell et al. 2010; Soler et al. 2011; Barcelo et al. 2011), damping by mass accretion (Ruderman and Luna 2016), and the effect of time-dependent background temperature (Ballester et al. 2016).

Among the many damping effects, the mechanism of resonant absorption has been considered most frequently. High spatial, temporal, and spectral resolution observations with SOT/Hinode show a compelling signature of resonant absorption, which dissipates transverse wave energy into heat, based on the observed coherence in the transverse direction, the 180° phase difference between transverse motion and line-of-sight velocity, and significant heating from the chromosphere to higher temperatures (Okamoto et al. 2015). Comparison with advanced numerical simulations support a scenario in which transverse oscillations trigger a *Kelvin-Helmholtz instability (KHI)* at the boundaries of oscillating threads via resonant absorption, leading to numerous thin current sheets in which wave energy is dissipated and plasma is heated (Okamoto et al. 2015; Antolin et al. 2015). Various heating models with dissipation by resonant absorption are shown in Fig. 11.11.

Modeling of fast MHD waves focus on the cutoff frequency (Diaz et al. 2002, 2003), the coupling of multi-fibril oscillations (Diaz et al. 2005; Diaz and Roberts 2006; Soler et al. 2009a; Luna et al. 2012b; Luna and Karpen 2012; Soler and Luna 2015), the dispersion relation (Diaz et al. 2002; Soler et al. 2007b), partial ionization (Soler et al. 2009c, 2010), flows in filament threads (Soler and Goossens 2011; Soler et al. 2012), MHD equilibria (Blokland and Keppens 2011a,b), the magnetic field geometry (Luna et al. 2012a,b, 2016a), longitudinal filament oscillations (Zhang et al. 2013), period ratio of transverse thread oscillations (Soler et al. 2015b), the pendulum model (Luna et al. 2016b; Soler et al. 2016), the mirror current effect (Kolotkov et al. 2016), Alfvén wave heating of prominences (Soler et al. 2016), longitudinal oscillations with two magnetic dips (Zhou et al. 2017), and finite amplitude transverse oscillations (Kolotkov et al. 2018).

11.8 Rayleigh-Taylor and Kelvin-Helmholtz Instability

The *Rayleigh-Taylor instability (RTI)*, of which the *interchange instability* is a subset, occurs at the interface between two fluids of different densities, where the heavier fluid is balanced by a lighter fluid underneath. The classical hydrodynamic RTI is governed by the gravity force at an interface with a negative density gradient. The instability condition is fulfilled when the density gradient of the unperturbed plasma has an opposite direction to gravity, i.e., $(\mathbf{g}\cdot\partial n_0/\partial z) < 0$. A famous example in astrophysics is the Crab nebula (Hester et al. 1996), where the RTI is manifested by numerous filigree structures in the supernova remnant. The generalization of the RTI from hydrostatic to hydromagnetic conditions in astrophysical plasmas involves the magnetic field, also called the *Kruskal-Schwarzschild instability* (for $\mathbf{k}\cdot\mathbf{B} = 0$)

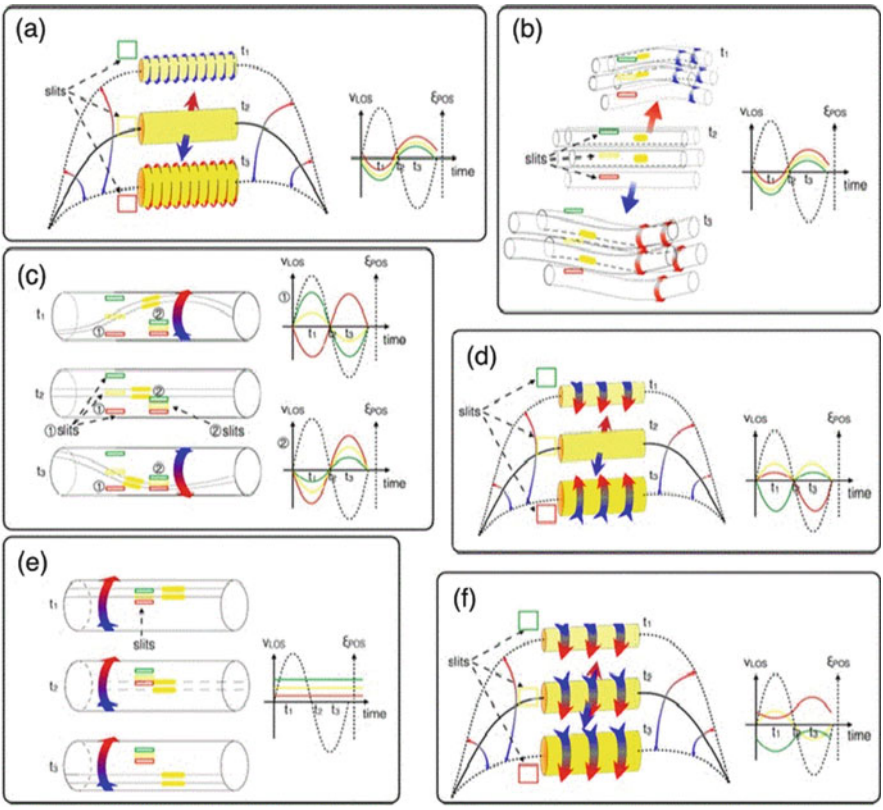

Fig. 11.11 Schematic representation of various heating models that dissipate wave energy by resonant absorption: kink wave (m=1) (**a**), mulitple kink waves (m=1) (**b**), torsional Alfvén wave (m=0) (**c**), torsional Alfvén wave coupled with kink wave (**d**), rotation (**e**), and rotation coupled with kink waves (**e**), (Okamoto et al. 2015)

or *Parker instability* (for $\mathbf{k} \cdot \mathbf{B} \neq 0$). Evidence for RTI operating in the plasma of the solar corona has recently been emphasized for hot plasma in active regions, quiescent prominences, and coronal cavities.

The origin of filamentary structures in active regions was previously interpreted as isolated bundles of magnetic field that rise from the photosphere carrying the dense gas, while new numerical 3-D MHD simulations of emerging flux demonstrated that the filamentary structure and the intermittent nature of the heating arises spontaneously from the magnetic Rayleigh-Taylor instability and explains the patchy brightenings seen in soft X-rays associated with jets (Isobe et al. 2005). SOT/Hinode observations revealed two new modes in quiescent solar prominences: large-scale (20–50 Mm) "arches" or "bubbles" that "inflate" from below into prominences, and smaller-scale (2–6 Mm) dark turbulent upflows, which were explained by the RTI taking place at the boundary between the buoyant bubbles and

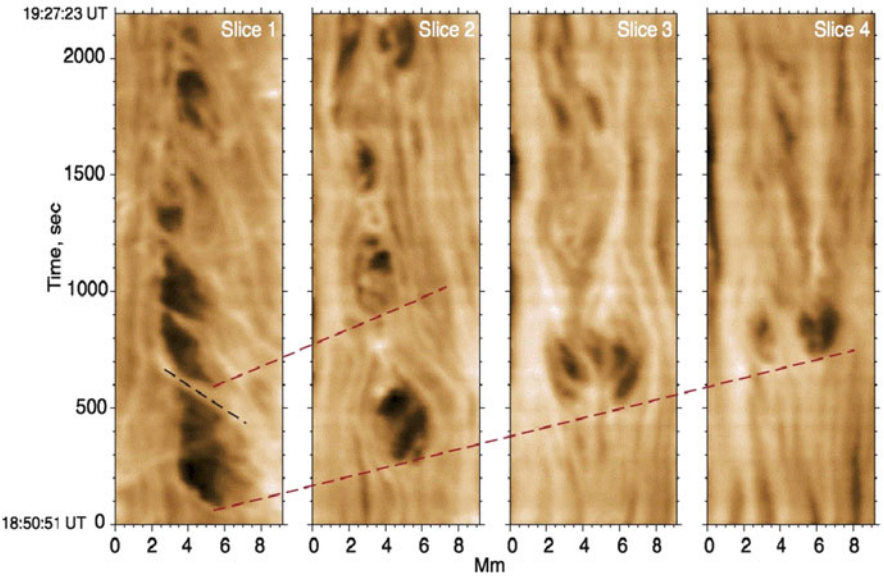

Fig. 11.12 Time slices of a plume in a prominence observed with AIA/SDO. The linear features indicate moving features with velocities of 14.7 km s^{-1} (lower red), 12.0 km s^{-1} (upper red), and 17.6 km s^{-1} (black), (Berger et al. 2010)

the overlying prominence (Berger et al. 2010). Examples of time-slice diagrams of moving features in the turbulent upflows are shown in Fig. 11.12. Turbulent flows in plumes of quiescent prominences were already noted earlier (Berger et al. 2008). Temperatures of $T = 0.25$–1.2 MK have been measured in "bubble" features of "polar-crown" prominences, which is 25–120 times hotter than the overlying prominence, and this way explains the buoyancy in cavity-prominence systems that drive the RTI (Berger et al. 2011). There are essentially two observed phenomena that result from the RTI: (i) the plumes that rise through quiescent prominences from low density bubbles forming below them, and (ii) the material that is falling back to the solar surface (Hillier 2018).

Numerical 3-D MHD simulations investigated the nonlinear instability of the Kippenhahn-Schlüter prominence model and the magnetic RTI (Hillier et al. 2011), the formation of upflows in plumes (Hillier et al. 2012a), reconnection-triggered downflows (Hillier et al. 2012b), the plasma-β parameter (Hillier et al. 2012c), and turbulence using SOT/Hinode dopplergrams (Hillier et al. 2017). The plasma-β value was found to be in the range of $\beta \approx 0.5$–1.1, which almost equates the magnetic to the thermal pressure, in a rising plume of a prominence (Hillier et al. 2012c). MHD simulations up to a height of 30 Mm show rapidly evolving convection motions where hot bubbles interplay with falling pillars, upwelling pillars that form bubbles, impacting Rayleigh-Taylor fingers that reflect on transition region plasma (perhaps being a property of the model's boundary condition),

ensuring mixing of heated dense chromospheric material with prominence matter up to large heights, and explain the evaporation-condensation cycle (Keppens et al. 2015). The RTI plays an important role in the dissipation of waves by resonant absorption, where the RTI extracts the energy from resonant layers and dissipates it through vortices and current sheets, which rapidly degenerates into turbulence (Antolin et al. 2015).

Analytical work that investigates the eigenmodes of a Cartesian slab model for filament threads under the presence of gravity finds that the Rayleigh-Taylor mode becomes stable when the magnetic field is increasing, and in the limit of strong magnetic fields it transforms essentially to the sausage magnetic mode (Terradas et al. 2012). In active region prominences, the stabilizing effect of the magnetic tension might be enough to suppress the RTI for a wide range of wavelengths (Terradas et al. 2012).

Another type of *mixing instability* (of disparate fluids) is the *Kelvin-Helmholtz instability (KHI)*, which occurs when there is a velocity shear in a single continuous fluid, or where there is a velocity gradient at an interface between two fluids that move with different velocities, i.e., $v_1 \neq v_2$. Examples of KHI include wind blowing over the water surface, clouds, the ocean, Saturn's bands, Jupiter's Red Spot, and hot plasmas in the solar corona. More specifically, solar applications include fast *coronal mass ejecta (CMEs)* (Fig. 11.13; Ofman and Thompson 2011; Foullon et al. 2011). A somewhat related model is the gravity-driven *droplet model* that has been applied to quiescent prominence downflows (Haerendel and Berger 2011).

An example of a fast CME with KHI has been presented by Foullon et al. (2011). The CME is detected in the 131 Å high-temperature channel ($T \approx 11$ MK) of AIA/SDO, which expands with a speed of $v_{ejecta} \approx 833$ km s^{-1}, while substructures have a phase speed of $v_{phase} = 417$ km s^{-1}, forming a bubble at the leading edge and multiple *rolled-up vortices* behind. Obviously, the KHI criterion of $v_{ejecta} \neq v_{phase}$ is fulfilled, which explains the vortices at the interface between the lateral CME flank and the background plasma. Another observation of a vortex-shaped feature in an active region, detected with AIA/SDO in all wavebands, was reported by Ofman and Thompson (2011), which was interpreted in terms of the KHI (Fig. 11.13). A similar morphological shape with quasi-periodic spacings has been reported by Gary and Moore (2004), which has been interpreted as a multiple-turn helical magnetic flux rope, but this quasi-regular spacing pattern could equally well be interpreted as a chain of multiple rolled-up vortices of the KHI.

Numerical 2-D simulations of coronal jets driven by flux emergence along the lower boundary show that the KHI develops with moderately high plasma-β and leads to the formation of bright vortex-like blobs above the high magnetosonic Mach number regions that appear along the jet. Both the plasmoid instability and the KHI along the jet cause formation of blobs that can be observed in EUV (Ni et al. 2017).

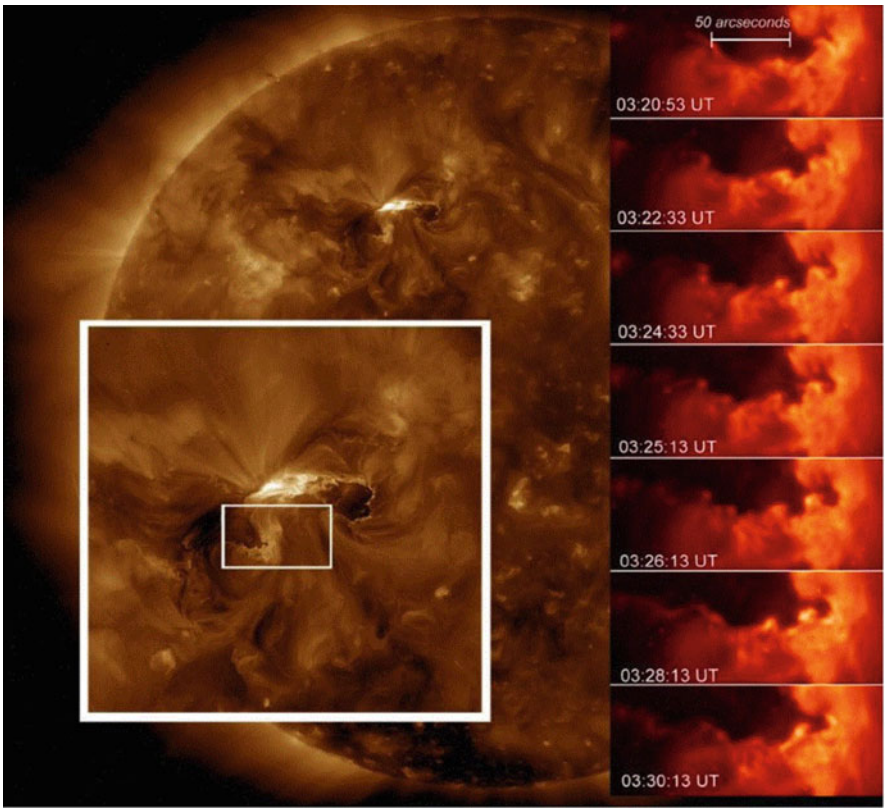

Fig. 11.13 Site of the CME eruption on 2010 April 8, 02:34 UT, observed with AIA/SDO in 193 Å. The small box captures the evolution of the Kelvin-Helmholtz instability as observed in 211 Å (right panels), (Ofman and Thompson 2011)

11.9 Coronal Cavities

A particular magnetic topology is the "coronal cavity", which is the limb manifestation of a longitudinally extended polar-crown filament channel (or tunnel), and has a lower density than the surrounding corona. The morphology of coronal cavities has been compared to the three-part morphology structure of CMEs, seen in white-light observations as (i) a bright expanding loop, (ii) followed by a relatively dark cavity, and (iii) a bright core associated with an erupting prominence/filament (Gibson et al. 2006). Coronal cavities are ubiquitous (at heights of $\lesssim 1.6 R_{\odot}$), as they are the coronal limb counterparts to filament channels, and their life time can extend from hours to several solar rotations, often ending as part of an eruption. One dominant polar crown cavity existed for more than a year (Karna et al. 2017).

Quiescent filament cavities can also be detected as brightness temperature depressions in metric radio wavelengths (Marque 2004).

The formation process of a coronal cavity has been attributed to the emergence of a helical magnetic flux rope that undergoes magnetic reconnection with lower coronal fields, possibly carrying material into the coronal cavity (Okamoto et al. 2010), or to turbulent upflow plumes (Berger et al. 2010). The dynamics of cavities is driven by spinning motions with velocities of $v \approx 5$–10 km s^{-1} (Wang and Stenborg 2010), and may be involved in cyclones and tornadoes (Sect. 6.3, Li et al. 2012). The hitherto not understood buoyancy of prominence bubbles has been identified to be caused by the 25–120 times hotter temperature ($T \approx 0.25$–1.2 MK) than in the overlying prominence, suggesting a novel explanation for the coronal cavity-prominence systems in terms of magneto-thermal convection (Berger et al. 2011). EUV observations with AIA/SDO in 304 and 171 Å suggest that a polar crown cavity represents a density depletion sitting above denser polar crown filament plasma drained down by gravity (Régnier et al. 2011). AIA/SDO 304 Å observations suggest prominence formation via in situ condensation of hot plasma from the coronal cavity (Berger et al. 2012). Strong shear flow across a bubble boundary leads to an apparent coupled Kelvin-Helmholtz Rayleigh-Taylor instability (Berger et al. 2017). The eruption of a coronal cavity is generally caused by a flare and/or CME, which produces hot and cool filamentary material that disappear suddenly when the cavity appears (Fig. 11.14; Long et al. 2018).

Modeling of the electron density of a cavity requires a model that includes both the coronal cavity as well as non-cavity features in front and behind, such as an axisymmetric torus that encircles the Sun at a constant latitude (Fuller et al. 2008), a tunnel-like cavity with elliptical cross-section and a Gaussian variation of height along the tunnel length (Gibson et al. 2010), dark bubbles with surrounding threads (Berlicki et al. 2011), several short cylindrical cavity cores (Reeves et al. 2012), or a long tube with an elliptical cross-section (Karna et al. 2015). The 3-D geometry and morphology of coronal cavities has been reconstructed also with tomographic methods (Vasquez et al. 2009) and from stereoscopic analysis using STEREO data (Gibson et al. 2010). Depressions in form of dark bubbles seen in Lyman-α, C III, and S VI lines have been modeled with 2-D *radiative magneto-hydrostatic (RMHS)* codes (Berger et al. 2011). By forward-fitting *Coronal Multi-Channel Polarimeter (CoMP)* observables from analytic MHD models of spheromak-type magnetic flux ropes, it was shown that such flux ropes oriented along the line-of-sight predict a bright ring of linear polarization surrounding a region where the linear polarization strength is relatively depleted (Dove et al. 2011). Forward-modeling (rather than line-ratio techniques) are more reliable for temperature and density diagnostics of cavities (Schmit and Gibson 2011; Reeves et al. 2012; Kucera et al. 2012). Overestimates of the EUV line intensity by factors of 4–10 suggest filling factors, uncertainties in the density diagnostics, and elemental abundance effects (Kucera et al. 2012). The 3-D geometry of one polar crown cavity was reconstructed with the limb synoptic map method, yielding a long tube with an elliptical cross-section with a length-to-width ratio of 11:1 and 7:1, a length of 1360 Mm, a longitude range of 170°, a tilt in latitude, and a temperature slightly hotter than its surroundings (Karna et al. 2015). The majority of cavities possess multiple rings with different line-of-sight velocities (Bak-Steslicka et al. 2016).

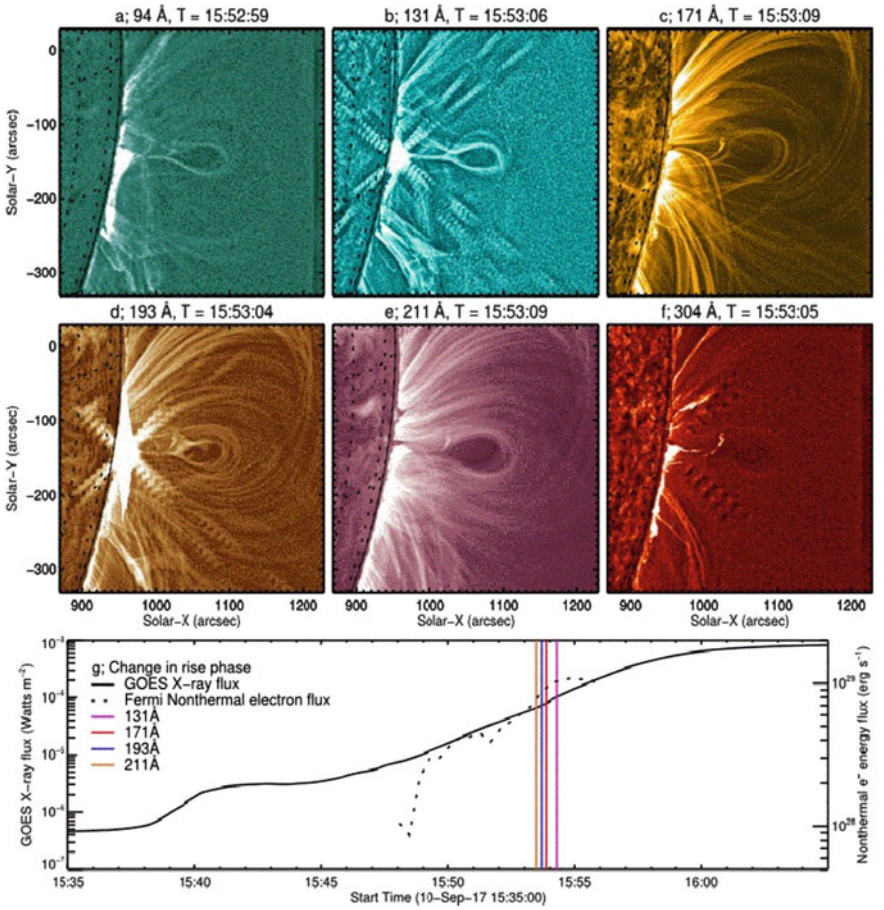

Fig. 11.14 Eruption from 2017 September 10 at 15:53:06 UT, as observed by AIA/SDO in the 91 (**a**), 131 (**b**), 171 (**c**), 193 (**d**), 211 (**e**), and 304 Å (**f**) passbands. Each image has been highpass-filtered. The GOES soft X-ray flux is shown in panel g. The diagonal ripples are caused by the telescope diffraction pattern. The pre-flare phase shows the restructuring of the active region prior to the eruption and formation of the cavity (Long et al. 2018)

The magnetic topology of bubbles in quiescent prominences has been studied with a linear force-free field model and was found to be complex, involving magnetic reconnection at a separator (Dudik et al. 2012; Shen et al. 2015). Using the flux rope insertion method, a solar polar crown prominence was modeled, but was found not to reproduce the observed vertical threads, nor the formation of the dense-column structure (Su and van Ballegooijen 2012). CoMP observations indicate that cavities possess a "lagomorphic" signature in linear polarization, indicating twist or shear extending up into the cavity above the neutral line, which can be explained by a magnetic flux rope model (Bak-Steslicka et al. 2013). Using coronal

(linear) polarization measurements, it is possible to distinguish between the models of cylindrical flux ropes, spheromak flux ropes, and sheared arcades (Rachmeler et al. 2013).

11.10 Filaments/Prominences: Eruptions

What is the relationship between eruptive prominences (or filaments) and the more powerful *coronal mass ejection (CMEs)* events, since both are eruptive phenomena? An overwhelming fraction of 72% of eruptive prominences were found to be associated with CMEs (Gopalswamy et al. 2003), or at least 56% (Jing et al. 2004). Early studies using white-light data from the Mk III K-Coronameter at the *Mauna Loa Solar Observatory (MLSO)* and the C2/LASCO/SOHO coronagraph on SOHO show that eruptive prominences are more strongly associated with CMEs than active region prominences, and that the associated CMEs generally have cores, while active region prominences do not (Gilbert et al. 2000). A useful resource of kinematic parameters of erupting filaments and prominences is the online catalog compiled by McCauley et al. (2015), based on AIA/SDO observations of 904 events. Events with evident twist have significantly faster CME speeds and fast-rise onset heights, which suggests relationships between these values and flux rope helicity (McCauley et al. 2015). Erupting quiescent filaments are closely related to flares also (with an association rate of 95% according to Jing et al. 2004). They are most conspicuously triggered by the flare-controlled converging motion of the chromospheric (bipolar) ribbons (with typical velocities of $v \lesssim 15$ km s^{-1}) (Wang et al. 2003).

The driver of erupting filaments (and sigmoids) has been attributed to the kink instability (Rust and LaBonte 2005; Williams et al. 2005; Liu et al. 2016), although twisted non-uniform fields may produce partial eruptions only (Bi et al. 2015). There are probably two driving processes staged in succession: (i) tether weakening by breakout-like quadrupolar reconnection as a release mechanism for the previously confined flux rope, and (ii) the MHD helical kink instability for the subsequent expansion of the flux rope (Williams et al. 2005; Sterling and Moore 2005). The progress of the events is broadly consistent with flux cancellation leading to formation of a helical flux rope that subsequently erupts due to onset of a magnetic instability and runaway tether cutting (Sterling et al. 2011). The majority of erupting prominences exhibit a separation of escaping and falling-back material at heights of $h = 1.20$–$1.35\ R_\odot$, probably with the assistance of an X-type neutral line during a magnetic reconnection process as postulated in flux rope models (Gilbert et al. 2000; Chae 2003). While prominences are considered as quasi-stable pre-eruptive states of CMEs, the stability of this equilibrium may depend on the vertical magnetic field gradient and a critical height range (Filippov and Den 2001).

Precursor brightenings in soft X-rays often signal reconnection events localized beneath the erupting footpoint at one side of a quiescent prominence, before destabilization and eruption of the entire prominence occurs (Chifor et al. 2006).

Reeves et al. (2015) observe a slow initial rise phase with a velocity of $v \approx 0.4$ km s^{-1} followed by a rapid acceleration with a final velocity of $v \approx 250$ km s^{-1}. From brightenings in IRIS data during the transition between these two phases they conclude that the eruption trigger for the fast part of the eruption is likely to be a tether-cutting mechanism, rather than a break-out mechanism (Reeves et al. 2015). During the precursor phase, propagation of the magnetic reconnection process along the polarity inversion line as well as separation away from the polarity inversion line are dynamically coupled (Tripathi et al. 2006). Moreover, a magnetic reconnection process may also trigger prominence oscillations and intermittent emerging flux before the the loss of equilibrium (Chen et al. 2008; Bi et al. 2014; Zhang et al. 2015). The breakout mechanism may even trigger both a sympathetic partial eruption, as well as a full filament eruption (Shen et al. 2012).

Multi-wavelength observations of a large-scale flux rope eruption above a kinked small filament reveals the formation of a hard X-ray source (12–25 keV) there, indicating particle acceleration that reached heights up to $h = 80$–100 Mm, following the slow rise of the flux rope ($v \approx 100$ km s^{-1}), surrounded by a cool compression front (or CME frontal loop) (Kumar and Cho 2014).

Filament eruptions can be confined, partially erupting, or fully erupting, but their fragmentation and evolution is hard to predict. A very fast acceleration (≈ 3–5 km s^{-2}) was observed for the filament eruption during the flare of 2014 March 29, although the final speed was similar to CMEs. There was also a low-lying twisted second filament near the erupting filament, which did not participate in the eruption, but vanished later (Kleint et al. 2015). During the 2011 September 8 flare, a partial filament eruption occurred, a magnetic null point and the corresponding spine and separatrix surface was found above a fragmented polarity inversion line, while the ejection of a runaway filament part caused a very small CME only (Zhang et al. 2015).

The eruption of a filament/prominence may cause the birth of a new prominence in the aftermath. AIA/SDO observed for the first time such an evolution, where initially a transequatorial loop system is visible that confines an earlier eruption, while nine hours later a new prominence with a mass of $\approx 10^{14}$ g is formed that drains most of its mass in one day (Liu et al. 2012).

Other consequences of a filament eruption is the fall-back of material that did not reach the escape velocity, sometimes causing impacting of dark cool prominence material over a large area (Fig. 11.15). Following the 2011 June 7 eruption, a kinetic energy of $E \approx (0.8\text{–}6) \times 10^{27}$ erg was estimated for the impacting material, which exceeded the radiated energy substantially ($E \approx (0.2\text{–}3) \times 10^{26}$ erg) (Gilbert et al. 2013).

Filament eruptions generally carry less kinetic energy than CMEs, but not always. Four *solar energetic particle (SEP)* events were found to be associated with filament eruptions outside of active regions (Gopalswamy et al. 2015). Fast CMEs and shock formation at larger distances from the Sun ($\gtrsim (2\text{–}3) R_\odot$) seem to be the primary characteristics of filament eruption events.

Stereoscopic observations help to disentangle the 3-D structure of erupting prominences. A long prominence composed of a series of vertical threads was iden-

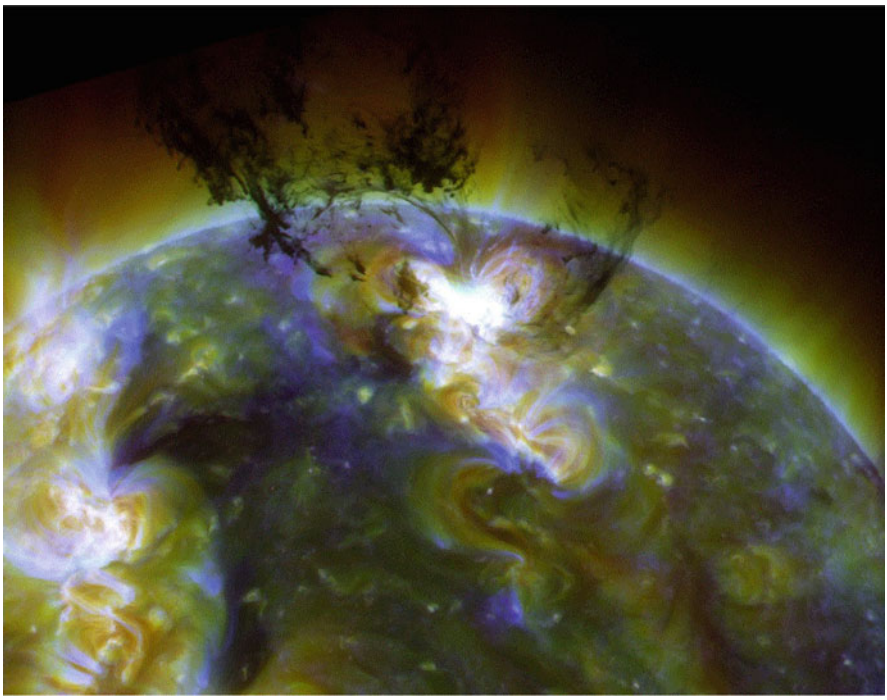

Fig. 11.15 AIA/SDO observed this spectacular eruption on 2011 June 7, where a massive amount of cool dark material is lifted into the corona, while most of this material falls back to the Sun, impacting a substantial fraction of the solar surface (Credit: NASA, SDO/AIA, LMSAL)

tified for the erupting polar crown prominence on 2012 March 12 with STEREO, which was modeled with various magnetic models (sheared arcade model, twisted flux rope model, and unstable models with hyperbolic flux tubes), (Su et al. 2015).

References

(11.1) Filaments/Prominences: Stereoscopy

Artzner, G., Gosain, S., and Schmieder, B., 2010, *A technique for removing background features in SECCHI-EUVI He II 304 filtergrams: Application to the filament eruption of 22 May 2008*, SoPh 262, 437, [8 c, 1 c/y].

Aschwanden, M.J., Wuelser, J.P., Nitta, N.V., et al. 2009, *Solar flare and CME observations with STEREO/EUVI*, SoPh 256, 3, [30 c, 4 c/y].

Bemporad, A. 2009, *Stereoscopic reconstruction from STEREO/EUVI imagers data of the 3-D shape and expansion of an eruptive prominence*, ApJ 701, 298, [22 c, 3 c/y].

Bemporad, A., Del Zanna ,G., Andretta, V., et al. 2009, *Multispacecraft observations of a prominence eruption*, Ann. Geophys. 27, 3841, [4 c, 0.5 c/y].

Bone, L.A., van Driel-Gesztelyi, L., Culhane, J.L., et al. 2009, *Formation, interaction and merger of an active region and a quiescent filament prior to their eruption on 19 May 2007*, SoPh 259, 31, [25 c, 3 c/y].

Chifu, I., Inhester, B., Mierla, M. et al. 2012, *First 4-D reconstruction of an eruptive prominence using three simultaneous view directions*, SoPh 281, 121, [2 c, 0.4 c/y.

Filippov, B. 2013, *A filament eruption on 2010 October 21 from three viewpoints*, ApJ 773, 10, [19 c, 4 c/y].

Gissot, S.F., Hochedez, J.F., Chainais, P. et al. 2008, *3-D reconstruction from SECCHI-EUVI images using an optical-flow algorithm: Method description and observations of and erupting filament*, SoPh 252, 397, [27 c, 3 c/y].

Gosain, S., Schmieder, B., Venkatakrishnan, P. et al. 2009, *3-D evolution of a filament disappearance event observed by STEREO*, SoPh 259, 13, [23 c, 3 c/y.

Gosain, S. and Schmieder, B. 2010, *Estimation of width and inclination of a filament using He II 304 Å observations by STEREO/EUVI*, Annal. Geophys. 28, 149, [5 c, 0.7 c/y.

Labrosse, N., Dalla, S., and Marshall, S. 2010, *Automatic detection of limb prominences in 304 Å EUV images*, SP 262, 449, [16 c, 2 c/y].

Li, Y., Lynch, B.J., Stenborg, G. et al. 2008, *The solar magnetic field and coronal dynamics of the eruption on 2007 May 19*, ApJ 681, L37, [28 c, 3 c/y].

Li, T., Zhang, J., Zhao, H., et al. 2010, *3-D shape and evolution of two eruptive filaments*, ApJ 720, 144, [17 c, 2 c/y.

Liewer, P.C., De Jong, E.M., Hall, J.R., et al. 2009, *Stereoscopic analysis of the 19 may 2007 erupting filament*, SoPh 256, 57, [63 c, 7 c/y].

Raouafi, N.E. 2009, *Observational evidence for coronal twisted flux rope*, ApJ 691, L128, [8 c, 1 c/y].

Seaton, D.B., Mierla, M., Berghmans, D., et al. 2011, *SWAP-SECCHI observations of a mass-loading type solar eruption*, ApJ 727, L10, [17 c, 2 c/y].

Sterling, A.C., Chifor, C., Mason, H.E., et al. 2010, *Evidence for magnetic flux cancellation leading to an ejective solar eruption observed by Hinode, TRACE, STEREO, and SoHO/MDI*, A&A 521, A49, [28 c, 4 c/y].

Su, Y., van Ballegooijen, A., and Golub, L. 2010, *Structure and dynamics of quiescent filament channels observed by Hinode/XRT and STEREO/EUVI*, ApJ 721, 901, [11 c, 1 c/y].

Thompson, W.T., Kliem,.B., and Török, T. 2012, *3-D Reconstruction of a rotating erupting prominence*, SP 276, 241, [32 c, 6 c/y.

Wang, Y., Cao, H., Chen, J. et al. 2010, *Solar limb prominence Catcher and Tracker (SLIPCAT): An automated system and its preliminary statistical results*, ApJ 717, 973, [21 c, 3 c/y.

Xu, Y., Jing, J. and Wang, H. 2010, *Measurements of filament height in Hα and EUV 304 Å*, SoPh 264, 81, [11 c, 1 c/y].

(11.2) Filaments/Prominences: Magnetic Field

Bobra, M.G., van Ballegooijen, A.A., and DeLuca, E.E. 2008, *Modeling nonpotential magnetic fields in solar active regions*, ApJ 672. 1209, [79 c, 8 c/y].

Canou, A. and Amari, T. 2010, *A twisted flux rope as the magnetic structure of a filament in active region 10953 observed by Hinode*, ApJ 715, 1566, [65 c, 9 c/y].

Dudik, J., Aulanier, G., Schmieder, B., et al. 2012, *Magnetic topology of bubbles in quiescent prominences*, ApJ 761, 9, [33 c, 6 c/y].

Gunar, S., Mackay, D.H., Anzer, U., et al. 2013, *Non-linear force-free magnetic dip models of quiescent prominence fine structure*, A&A 551, A3, [16 c, 4 c/y].

Gunar, S., Schwartz, P., Dudik, J., et al. 2014, *Magnetic field and radiative transfer modelling of a quiescent prominence*, A&A 567, A123, [14 c, 4 c/y].

Mackay, D.H., Karpen, J.T., Ballester, J.L., et al. 2010, *Physics of solar prominences: II - Magnetic structure and dynamics*, SSRv 151/4, 333, [281 c, 37 c/y].

Metcalf, T.R., De Rosa, M.L., Schrijver, C.J. et al. 2008, *Nonlinear force-free modeling of coronal magnetic fields. II. Modeling a filament arcade and simulated chromospheric and photospheric vector fields*, SoPh 247, 269, [151 c, 16 c/y].
Orozco Suarez, D., Asensio Ramos, A., and Trujillo Bueono J. et al. 2014, *The magnetic field configuration of a solar prominence inferred from spectropolarimetric observations in the He I 10,830 Å triplet*, A&A 566, A46, [27 c, 8 c/y].
Su, Y., van Ballegooijen, A.A., Lites, B.W., et al. 2009, *Observations and nonlinear force-free field modeling of active region 10953*, ApJ 691, 105, [45 c, 5 c/y].
van Ballegooijen, A.A. 2004, *Observations and modeling of a filament on the Sun*, ApJ 612, 519, [146 c, 11 c/y].
van Ballegooijen, A.A., DeLuca E.E., Squires, K., et al. 2007, *Modeling magnetic flux ropes in the solar atmosphere*, J.Atmos.Solar-Terr.Phys. 69, 24, [12 c, 1 c/y].
Yan, X.L., Xue, Z.K., Pan G.M., et al. 2015, *The formation and magnetic structures of active region filaments observed by NVST, SDO and Hinode* ApJSS 219, 17, [24 c, 10 c/y].

(11.3) Filaments/Prominences: Formation

Berger, T.E., Liu, W., and Low, B.C. 2012, *SDO/AIA detection of solar prominence formation within a coronal cavity*, ApJ 758, L37, [57 c, 10 c/y].
Bone, L.A., van Driel-Gesztelyi, L., Culhane, J.L., et al. 2009, *Formation, interaction and merger of an active region and a quiescent filament prior to their eruption on 19 May 2007*, SoPh 259, 31, [25 c, 3 c/y].
Chae, J., Wang, H., Qiu, J., et al. 2001, *The formation of a prominence in active region NOAA 8668. I. SOHO/MDI observations of magnetic field evolution*, ApJ 560, 476, [141 c, 9 c/y].
Cheng, X., Ding, M.D., Zhang, J., et al. 2014, *On the relationship between a hot-channel-like solar magnetic flux rope and its embedded prominence*, ApJ 789, L35, [31 c, 9 c/y].
Guo, Y., Schmieder, B., Démoulin, P., et al. 2010, *Coexisting flux rope and dipped arcade sections along one solar filament*, ApJ 714, 343, [90 c, 12 c/y].
Kaneko, T. and Yokoyama, T. 2015, *Numerical study on in situ prominence formation by radiative condensation in the solar corona*, ApJ 806, 115, [8 c, 3 c/y].
Karpen, J.T., Antiochos, S.K., Hohensee, M. et al. 2001, *Are magnetic dips necessary for prominence formation ?*, ApJ 553, L85, [114 c, 7 c/y].
Keppens, R., Xia, C., and Porth, O. 2015, *Solar prominences: Double, double . . . boil and bubble*, ApJ 806, L13, [13 c, 5 c/y].
Kuckein, C., Martinez Pillet, V., and Centeno, R. 2012, *An active region filament studied simultaneously in the chromosphere and photosphere. I. Magnetic structure*, A&A 539, A131, [51 c, 9 c/y].
Joshi, A.D., Srivastava, N., Mathew, S., et al. 2013, *Rapid formation and disappearance of a filament barb*, SoPh 288, 191, [8 c, 2 c/y].
Lin, Y., Engvold, O., Rouppe van der Voort, L. et al. 2005a, *Thin threads of solar filaments*, SoPh 226, 239, [162 c, 13 c/y].
Lin, Y., Wiik, J.E., Engvold, O., et al. 2005b, *Solar filaments and photospheric network*, SoPh 227, 283, [37 c, 3 c/y].
Liu, W., Berger, T.E., and Low, B.C. 2012, *First SDO/AIA observations of solar prominence formation following an eruption: Magnetic dips and sustained condensation and drainage*, ApJ 745, L21, [51 c, 9 c/y].
Luna, M., Karpen, J.T., and DeVore, C.R. 2012, *Formation and evolution of a multi-threaded solar prominence*, ApJ 746, 30, [54 c, 10 c/y].
Martens, P.C. and Zwaan, C. 2001, *Origin and evolution of filament-prominence systems*, ApJ 558, 872, [105 c, 6 c/y].

McCauley, P.I., Su, Y.N., Schanche, N., et al. 2015, *Prominence and filament eruptions observed by the SDO: Statistical properties, kinematics, and online catalog*, SoPh 290, 1703, [32 c, 13 c/y].

Schmieder, B., Tian, H., Kucera, T., et al. 2014, *Open questions on prominences from coordinated observations by IRIS, Hinode, SDO/AIA, THEMIS, and the Meudon/MSDP*, A&A 569, A85, [28 c, 8 c/y].

van Ballegooijen, A.A., Priest, E.R., and Mackay, D.H. 2000, *Mean field model for the formation of filament channels on the Sun*, ApJ 539, 983, [130 c, 7 c/y].

Xia, C., Chen, P.F., and Keppens 2012, *Simulations of prominence formation in the magnetized solar corona by chromospheric heating*, ApJ 748, L26, [50 c, 9 c/y].

Xia, C. and Keppens, R. 2016, *Formation and plasma circulation of solar prominences*, ApJ 823, 22, [19 c, 13 c/y].

Yan, X.L., Xue, Z.K., Pan, G.M., et al. 2015, *The formation and magnetic structures of active-region filaments observed by NVST, SDO, and Hinode*, ApJSS 219, 17, [34 c, 14 c/y].

(11.4) Filaments/Prominences: MHD

Antiochos, S.K., MacNeice, P.J. and Spicer,D.S. 2000, *The Thermal Nonequilibrium of Prominences*, ApJ 536, 494, [54 c, 3 c/y].

Aulanier, G., Srivastava, N., and Martin, S.F. 2000, *Model prediction for an observed filament*, ApJ 543, 447, [51 c, 3 c/y].

Aulanier, G., DeVore, C.R., and Antiochos, S.K. 2002, *Prominence magnetic dips in 3-D sheared arcades*, ApJ 567, L97, [64 c, 4 c/y].

Chae, J.C., Ahn, K.S., Lim, E.K., et al. 2008, *Persistent horizontal flows and magnetic support of vertical threads in a quiescent prominence*, ApJ 689, L73, [52 c, 5 c/y].

DeVore, C.R. and Antiochos, S.K. 2000, *Dynamical formation and stability of helical prominence magnetic fields*, ApJ 539, 954, [125 c, 7 c/y].

Hansen, J.F. and Bellan, P.M. 2001, *Experimental demonstration of how strapping fields can inhibit solar prominence eruptions*, ApJ 563, L183, [32 c, 2 c/y].

Heinzel, P. and Anzer, U. 2001, *Prominence fine structures in a magnetic equilibrium: 2-D models with multilevel radiative transfer*, A&A 375, 1082, [80 c, 5 c/y].

Hillier, A., Richard, H., and Tripathi D. 2012, *Determination of prominence plasma β from the dynamics of rising plumes*, ApJ 761, 106, [13 c, 2 c/y].

Lin, Y., Engvold, O., and Wiik J.E. 2003, *Counterstreaming in a large polar crown filament*, SoPh 216, 109, [109 c, 8 c/y].

Linker, J.A., Lionello, R., Mikic, Z., et al. 2001, *MHD modeling of prominence formation within a helmet streamer*, JGR 106, A11, 25165, [88 c, 5 c/y].

Lionello, R., Mikic, Z., Liker, J.A., et al. 2002, *Magnetic field topology in prominences*, ApJ 581, 718, [58 c, 4 c/y].

Low, B.C. and Petrie, G.J.D. 2005, *The internal structures and dynamics of solar quiescent prominences*, ApJ 626, 551, [39 c, 3 c/y].

Kippenhahn, R. and Schlüter, A. 1957, *Eine Theorie der solaren Filamente*, Zeitschrift für Astrophysics 43, 36, [483 c/y].

Krall, K.R. and Antiochos, S.K. 1980, *The evolution of active region loop plasma*, ApJ 242, 374, [25 c, 0.7 c/y].

Martens, P.C. and Zwaan, C. 2001, *Origin and evolution of filament-prominence systems*, ApJ 558, 872, [105 c, 6 c/y].

Pecseli, H. and Engvold, O. 2000, *Modeling of prominence threads in magnetic fields: Levitation by incompressible MHD waves*, SoPh 194, 73, [33 c, 2 c/y].

Petrie, G.J.D. and Low, B.C. 2005, *The dynamical consequences of spontaneous current sheets in quiescent prominences*, ApJSS 159, 288, [24 c, 2 c/y].

Petrie, G.J.D., Blokland, J.W.S., and Keppens, R. 2007, *Magnetohydrostatic solar prominences in near-potential coronal magnetic fields*, ApJ 665, 830, [11 c, 2 c/y].
Petrie, G.J.D. 2007, *Potential magnetic field around a helical flux rope current structure in the solar corona*, ApJ 661, 551, [2 c, 0.2 c/y].
Schmieder, B., Chandra, R., Berlicki, A., et al. 2010, *Velocity vectors of a quiescent prominence observed by Hinode/SOT and the MSDP (Meudon)*, A&A 514, A68, [51 c, 7 c/y].
Shen, Y., Liu, Y., Liu, Y.D., et al. 2015, *Fine magnetic structure and origin of counter-streaming mass flows in a quiescent solar prominence*, ApJ 814, L17, [18 c, 7 c/y].
Török, T., Berger, M.A., and Kliem, B. 2010, *The writhe of helical structures in the solar corona*, A&A 516, A49, [65 c, 9 c/y].
VanBallegooijen, A.A. and Cranmer, S.R. 2010, *Tangled magnetic fields in solar prominences*, ApJ 711, 164, [50 c, 7 c/y].

(11.5) Filaments/Prominences: Non-Equilibrium

Antiochos, S.K., MacNeice, P.J., and Spicer, D.S. 2000, *The thermal nonequilibrium of prominences*, ApJ 536, 494, [54 c, 3 c/y].
Aulanier, G., DeVore, C.R., and Antiochos, S.K. 2002, *Prominene magnetic dips in 3-D sheared arcades*, ApJ 567, L97, [64 c, 4 c/y].
Hillier, A. and van Ballegooijen, A.A. 2013, *On the support of solar prominence material by the dips of a coronal flux tube*, ApJ 766, 126, [24 c, 5 c/y].
Karpen, J.T., Antiochos, S.K., Hohensee, M. et al. 2001, *Are magnetic dips necessary for prominence formation ?*, ApJ 553, L85, [114 c, 7 c/y].
Karpen, J.T., Antiochos, S.K., Klimchuk, J.A. 2003, *Constraints on the magnetic field geometry in prominences*, ApJ 593, 1187, [50 c, 3 c/y].
Karpen, J.T., Tanner, S.E.M., Antiochos, S.K., et al. 2005, *Prominence formation by thermal nonequilibrium in the sheared-arcade model*, ApJ 635, 1319, [43 c, 3 c/y].
Karpen, J.T. and Antiochos, S.K. 2008, *Condensation formation by impulsive heating in prominences*, ApJ 676, 658, [49 c, 5 c/y].
Labrosse, N., Heinzel, P., Vial, J.-C., et al. 2010, *Physics of solar prominences: I. - Spectral diagnostics and Non-LTE modelling*, SSRv 151, 243, [215 c, 29 c/y].
Lionello, R., Mikic, Z., and Linker, J.A. 2002, *Magnetic field topology in prominences*, ApJ 581, 718, [58 c, 4 c/y].
Low, B.C. and Petrie, G.J.D. 2005, *The internal structures and dynamics of solar quiescent prominences*, ApJ 626, 551, [39 c, 3 c/y].
Low, B.C., Berger, T., Casini, R., et al. 2012a, *The hydromagnetic interior of a solar quiescent prominence. I. Coupling between force balance and steady energy transport*, ApJ 755, 34, [24 c, 4 c/y].
Low, B.C., Liu, W., Berger, T., et al. 2012b, *The hydromagnetic interior of a solar quiescent prominence. II. Magnetic discontinuities and cross-field mass transport*, ApJ 757, 21, [23 c, 4 c/y].
Solov'ev, A.A. 2010, *The structure of solar filaments. Prominences in the corona free from external magnetic field*, Astron.Rep. 54, 86, [18 c, 2 c/y].

(11.6) Filaments/Prominences: Oscillations and Waves (Observations)

Arregui, I. and Ballester, J.L. 2011a, *Damping mechanisms for oscillations in solar prominences*, SSRv 158, 169, [25 c, 4 c/y].
Arregui, I. 2012, *Prominence oscillations*, LRSP 9/1, [70 c, 13 c/y].
Arregui, I., Oliver, R., and Ballester J.L. 2018, *Prominence oscillations*, LRSP 15, 3.

Asai, A., Ishii, T.T., Isobe, H., et al. 2012, *First simultaneous observation of an Hα Moreton wave, EUV wave, and filament/prominence oscillations*, ApJ 745, L18, [62 c, 11 c/y].
Ballester, J.L. 2005, *Theoretical advances in prominence seismology*, SSRv 121, 105, [9 c, 1 c/y].
Ballester, J.L. 2006, *Seismology of prominence-fine structures: Observations and theory*, SSRv 122, 129, [10 c, 1 c/y].
Berger, T.E., Shine, R.A., Slater, G.L., et al. 2008, *Hinode SOT observations of solar quiescent prominence dynamics*, ApJ 676, L89, [179 c, 19 c/y].
Bi, Y., Jiang, Y., Yang, J. et al. 2014, *Solar filament material oscillations and drainage before eruption*, ApJ 790, 100, [17 c, 5 c/y].
Bocchialini, K., Baudin, F., Koutchmy, S., et al. 2011, *Oscillatory motions observed in eruptive filaments*, A&A 533, A96, [20 c, 3 c/y].
Chen, P.F., Innes, D.E. and Solanki, S.K. 2008, *SOHO/SUMER observations of prominence oscillation before eruption*, A&A 484, 487, [43 c, 5 c/y].
Efremov, V.I., Parfinenko, L.D., and Lolovev, A.A. 2016, *Ultra low-frequency oscillations of a solar filament observed by the GONG network*, SoPh 291, 3357, [3 c, 2 c/y].
Foullon, C., Verwichte, E., and Nakariakov, V.M. 2009, *Ultra-long-period oscillations in EUV filaments near to eruption: Two-wavelength correlation and seismology*, ApJ 700, 1658, [28 c, 3 c/y].
Foullon, C., Verwichte, E., and Nakariakov, V.M. 2004, *Detection of ultra-long-period oscillations in an EUV filament*, A&A 427, L5, [38 c, 3 c/y].
Gosain, S and Foullon, C. 2012, *Dual trigger of transverse oscillations in a prominence by EUV fast and slow coronal waves: SDO/AIA and STEREO/EUVI observations*, ApJ 761, 103, [13 c, 2 c/y].
Hershaw, J., Foullon, C., Nakariakov, V.M. et al. 2011, *Damped large amplitude transverse oscillations in an EUV solar prominence, triggered by large-scale transient coronal wave*, A&A 531, A53, [42 c, 6 c/y].
Hillier, A, Morton, R.J., and Erdelyi, R. 2013, *A statistical study of transverse oscillations in a quiescent prominence*, ApJ 779, L16, [22 c, 5 c/y].
Isobe, H., Tripathi, D., Asai, A., et al. 2007, *Large-amplitude oscillation of an erupting filament as seen in EUV, Hα, and microwave observations*, SoPh 246, 89, [33 c, 3 c/y].
Jing, J., Lee, J.W., Spirock, J., et al. 2003, *Periodic motion along a solar filament initiated by a subflare*, ApJ 584, L103, [67 c, 5 c/y].
Joshi, N.C., Filippov, B., Schmieder, B., et al. 2016, *Interaction of two filament channels of different chiralities*, ApJ 825, 123, [4 c, 3 c/y].
Li, T., and Zhang, J. 2012, *SDO/AIA observations of large-amplitude oscillations in a solar filament*, ApJ 760, L10, [34 c, 6 c/y].
Lin, Y. 2011, *Filament thread-like structures and their small-amplitude oscillations*, SSRv 158, 237, [50 c, 8 c/y].
Luna, M., Knizhnik, K., Muglach, K., et al. 2014, *observations and implications of large-amplitude longitudinal oscillations in a solar filament*, ApJ 785, 79, [26 c, 7 c/y].
Luna, M. Su, Y., Schmieder, B., et al. 2017, *Large-amplitude longitudinal oscillations triggered by the merging of two solar filaments: Observations and magnetic field analysis*, ApJ 850, 143, [3 c, 3 c/y].
Ning, Z., Cao, W., Okamoto, T.J. et al. 2009, *Small-scale oscillations in a quiescent prominence observed by Hinode/SOT*, A&A 499, 595, [44 c, 5 c/y].
Okamoto, T.J., Tsuneta, S., Berger, T.E., et al. 2007, *Coronal transverse MHD waves in a solar prominence*, Science 318, 1577, [237 c, 23 c/y].
Oliver, R. and Ballester, J.L. 2002, *Oscillations in quiescent solar prominences observations and theory (Invited review)*, SoPh 206, 45, [125 c, 8 c/y].
Oliver, R. 2009, *Prominence seismology using small amplitude oscillations*, SSRv 149, 175, [41 c, 5 c/y].
Pant, V., Srivastava, A.K., Banerjee, D., et al. 2015, *MHD seismology of a loop-like filament tube by observed kink waves*, Res.Astron.Astrophys 15, 1713, [4 c, 2 c/y].

Pinter, B., Jain, R., Tripathi, D., et al. 2008, *Prominence seismology: Wavelet analysis of filament oscillations*, ApJ 680, 1560, [21 c, 2 c/y].

Pouget, G., Boccialini, K., and Solomon, J. 2006, *Oscillations in a solar filament: First observation of long periods in the He I 584.44 Å line, modelling and diagnostic*, A&A 450, 1189, [27 c, 2 c/y].

Qu, Z.N., Jiang, L.Q., and Chen, S.L. 2017, *Observations of a fast-mode magnetosonic wave propagating along a curving coronal loop on 2011 November 11*, ApJ 851, 41, [3 c, 3 c/y].

Schmieder, B., Kucera, T.A., and Knizhnik, K.2013, *Propagating waves transverse to the magnetic field in a solar prominence*, ApJ 777, 108, [33 c, 7 c/y].

Shen, Y., Ichimoto, K., Takako, I., et al. 2014a, *A chain of winking (oscillating) filaments by an invisible extreme-ultraviolet wave*, ApJ 786, 151, [29 c, 8 c/y].

Shen, Y. and Liu, Y.D., Chen, P.F., et al. 2014b, *Simultaneous transverse oscillations of a prominence and a filament and longitudinal oscillation of another filament induced by a single shock wave*, ApJ 795, 130, [26 c, 7 c/y].

Shen, Y., Liu, Y., Tian, Z., et al. 2017, *On a small-scale EUV wave: Driving mechanism and the associated oscillating filament*, ApJ 851, 191, [3 c, 3 c/y].

Srivastava, A.K., Dwivedi, B.N., and Mukul, K. 2013, *Observations of intensity oscillations in a prominence-like cool loop system as observed by SDO/AIA: Evidence of multiple harmonics of fast magneto-acoustic waves*, Astrophys.Space Science 345, 25, [10 c, 2 c/y].

Terradas, J., Molowny-Horas, R., Wiehr, E., et al. 2002, *2-D distribution of oscillations in a quiescent solar prominence*, A&A 393, 637, [70 c, 5 c/y].

Terradas, J., Arregui, I., Oliver, R., et al. 2008, *Transverse oscillations of flowing prominence threads observed with Hinode*, ApJ 678, L153, [48 c, 5 c/y].

Tripathy, D., Isobe, H., and Jain, R. 2009, *Large amplitude oscillations in prominences*, SSRv 149, 283, [60 c, 7 c/y].

Zapior, M., Pavel, K., Rudawy, P., et al. 2015, *Simultaneous observations of solar prominence oscillations using two remote telescopes*, SoPh 290, 1647, [3 c, 1 c/y].

Zhang, Q.M., Chen, P.F., Xia, C., et al. 2012, *Observations and simulations of longitudinal oscillations of an active region prominence*, A&A 542, A52, [40 c, 7 c/y].

(11.7) Filaments/Prominences: Oscillations and Waves (Theory)

Antolin, P., Okamoto, T.J., De Pontieu, B. 2015, *Resonant absorption of transverse oscillations and associated heating in a solar prominence. II. Numerical aspects*, ApJ 809, 72, [40 c, 16 c/y].

Arregui, I., Terradas, J., Oliver, R. et al. 2008, *Damping of fast MHD oscillations in quiescent filament threads*, ApJ 682, L141, [48 c, 5 c/y].

Arregui, I., Soler, R., Ballester, J.L., et al. 2011b, *MHD kink waves in 2-D non-uniform prominence threads*, A&A 533, A60, [27 c, 4 c/y].

Ballester, J.L., Carbonell, M., Soler, R., et al. 2016, *Prominence oscillations: Effects of a time-dependent background temperature*, A&A 591, A109, [3 c, 2 c/y].

Barcelo, S., Carbonell, M., and Ballester, J.L. 2011, *Time damping of non-adiabatic MHD waves in a partially ionised prominence medium: Effect of a background flow*, A&A 525, A60, [11 c, 2 c/y].

Blokland, J.W.S. and Keppens, R. 2011a, *Toward detailed prominence seismology. I. Computing accurate 2.5D MHD equilibria*, A&A 532, A93, [13 c, 2 c/y].

Blokland, J.W.S. and Keppens, R. 2011b, *Toward detailed prominence seismology. II. Charting the continuous MHD spectrum*, A&A 532, A94, [11 c, 2 c/y].

Carbonell, M., Oliver, R., and Ballester, J.L. 2004, *Time damping of linear non-adiabatic MHD waves in an unbounded plasma with solar coronal properties*, A&A 415, 739, [53 c, 4 c/y].

Carbonell, M., Terradas, J., Oliver, R., et al. 2006, *Spatial damping of linear non-adiabatic magneto-acoustic waves in a prominence medium*, A&A 460, 573, [20 c, 2 c/y].

Carbonell, M., Forteza, P., Oliver, R., et al. 2010, *The spatial damping of MHD waves in a flowing partially ionised prominence plasma*, A&A 515, A80, [15 c, 2 c/y].
Diaz, A.J., Oliver, R., and Ballester, J.L. 2002, *Fast MHD oscillations in cylindrical prominence fibrils*, ApJ 580, 550, [71 c, 5 c/y].
Diaz, A.J., Oliver, R., and Ballester, J.L. 2003, *Fast MHD oscillations of a 3-D prominence fibril*, A&A 402, 781, [24 c, 2 c/y].
Diaz, A.J., Oliver, R., and Ballester, J.L. 2005, *Fast MHD oscillations in a multifibril Cartesian prominence model*, A&A 440, 1167, [36 c, 3 c/y].
Diaz, A.J. and Roberts, B. 2006, *Fast MHD oscillations in a fibril prominence model*, SoPh 236, 111, [15 c, 1 c/y].
Forteza, P., Oliver, R., Ballester, J.L., et al. 2007, *Damping of oscillations by ion-neutral collisions in a prominence plasma*, A&A 461, 731, [66 c, 6 c/y].
Forteza, P., Oliver, R., and Ballester, J.L. 2008, *Time damping of non-adiabatic MHD waves in and unbounded partially ionised prominence plasma*, A&A 492, 223, [26 c, 3 c/y].
Kolotkov, D.Y., Nistico, G., and Nakariakov, V.M. 2016, *Transverse oscillations and stability of prominences in a magnetic field dip*, A&A 590, A120, [4 c, 3 c/y].
Kolotkov, D.Y., Nistico, G., Rowlands, G., et al. 2018, *Finite amplitude transverse oscillations of a magnetic rope*, JASTR 172, 40.
Luna, M. and Karpen, J. 2012, *Large-amplitude longitudinal oscillations in a solar filament*, ApJ 750, L1, [38 c, 7 c/y].
Luna, M., Diaz, A.J., and Karpen, J. 2012a, *The effects of magnetic-field geometry on longitudinal oscillations of solar prominences* ApJ 757, 98, [24 c, 4 c/y].
Luna, M., Karpen, J.T., and DeVore, C.R. 2012b, *Formation and evolution of a multi-threaded solar prominence*, ApJ 746, 30, [54 c, 10 c/y].
Luna, M., Diaz, A.J., Oliver, R., et al. 2016a, *The effects of magnetic-field geometry on longitudinal oscillations of solar prominences: Cross-sectional area variation for thin tubes*, A&A 593, A64, [3 c, 2 c/y].
Luna, M., Terradas, J., Khomenko, E. 2016b, *On the robustness of the pendulum model for large-amplitude longitudinal oscillations in prominences*, ApJ 817, 157, [15 c, 10 c/y].
Okamoto, T.J., Antolin, P., De Pontieu, B. 2015, *Resonant absorption of transverse oscillations and associated heating in a solar prominence. I. Observational aspects*, ApJ 809, 71, [37 c, 15 c/y].
Ruderman, M.S. and Luna, M. 2016, *Damping of prominence longitudinal oscillations due to mass accretion*, A&A 591, A131, [5 c, 3 c/y].
Singh, K.A.P., Dwivedi, B.N., and Hasan, S.S. 2007, *Spatial damping of compressional MHD waves in prominences*, A&A 473, 931, [5 c, 0.5 c/y].
Soler, R., Oliver, R., and Ballester, J.L. 2007a, *The effect of the solar corona and the attenuation of small-amplitude prominence oscillations. I. Longitudinal magnetic field*, A&A 471, 1023, [25 c, 2 c/y].
Soler, R., Oliver, R., and Ballester, J.L. 2007b, *Oscillatory modes of a prominence-PCTR-corona slab model*, SoPh 246, 73, [6 c, 0.6 c/y].
Soler, R., Oliver, R., and Ballester, J.L. 2008, *Nonadiabatic MHD waves in a cylindrical prominence thread with mass flow*, ApJ 684, 725, [38 c, 4 c/y].
Soler, R., Oliver, R., and Ballester, J.L. 2009a, *Propagation of nonadiabatic magneto-acoustic waves in a threaded prominence with mass flows*, ApJ 693, 1601, [19 c, 2 c/y].
Soler, R., Oliver, R., Ballester, J.L., et al. 2009b, *Damping of filament thread oscillations: effect of the slow continuum*, ApJ 695, L166, [32 c, 4 c/y].
Soler, R., Oliver, R., and Ballester, J.L. 2009c, sl MHD waves in a partially ionized filament thread, ApJ 699, 1553, [55 c, 7 c/y].
Soler, R., Oliver, R., and Ballester, J.L. 2010, *Time damping of non-adiabatic MHD waves in partially ionized prominence plasma: effect of helium*, A&A 512, A28, [25 c, 3 c/y].
Soler, R., Oliver, R., and Ballester, J.L. 2011, *Spatial damping of propagating kink waves in prominence threads*, ApJ 726, 102, [15 c, 2 c/y].
Soler, R. and Goossens, M. 2011, *Kink oscillations of flowing threads in solar prominences*, A&A 531, A167, [8 c, 1 c/y],

Soler, R., Ruderman, M.S., and Goossens, M. 2012, *Damped kink oscillations of flowing prominence threads* A&A 546, A82, [8 c, 1 c/y].
Soler, R. and Luna, M. 2015, *Damped transverse oscillations of interacting coronal loops*, A&A 582, 120, [1 c, 0.4 c/y].
Soler, R. and Terradas, J. 2015, *MHD kink waves in nonuniform solar flux tubes: Phase mixing and energy cascade*, ApJ 803, 43, [14 c, 6 c/y].
Soler, R., Ballester, J.L., and Zaqaraschvili, T.V. 2015a, *Overdamped Alfvén waves due to ion-neutral collisions in the chromosphere*, A&A 573, 79, [19 c, 8 c/y].
Soler, R., Goossens, M., and Ballester, J.L. 2015b, *Prominence seismology using the period ratio of transverse thread oscillations*, A&A 575, 123, [4 c, 2 c/y].
Soler, R., Terradas, J., Oliver, R., et al. 2016, *The role of Alfvén wave heating in solar prominences*, A&A 592, A28, [7 c, 5 c/y].
Terradas, J., Oliver, R., and Ballester, J.L. 2001, *Radiative damping of quiescent prominence oscillations*, A&A 378, 635, [39 c, 2 c/y].
Terradas, J., Carbonell, M., Oliver, R., et al. 2005, *Time damping of linear non-adiabatic magneto-acoustic waves in a slab-like quiescent prominence*, A&A 434, 741, [37 c, 3 c/y].
Zhang, Q.M., Chen, P.F., Xia, C. et al. 2013, *Parametric survey of longitudinal prominence oscillation simulations*, A&A 554, A124, [24 c, 5 c/y].
Zhou, Y.H., Zhang, L.Y., Ouyang, Y., et al. 2017, *Solar filament longitudinal oscillations along a magnetic field tube with two dips*, ApJ 839, 9, [6 c, 6 c/y].

(11.8) Rayleigh-Taylor and Kelvin-Helmholtz Instability

Antolin, P., Okamoto, T.J., De Pontieu, B., et al. 2015, *Resonant absorption of transverse oscillations and associated heating in a solar prominence. II. Numerical aspects*, ApJ 809, 72, [41 c, 16 c/y].
Berger, T.E., Shine, R.A., Slater, G., et al. 2008, *Hinode SOT observations of solar quiescent prominence dynamics*, ApJ 676, L89, [180 c, 19 c/y].
Berger, T.E., Slater, G., Hurlburt, N., et al. 2010, *Quiescent prominence dynamics observed with the Hinode Solar Optical Telescope. I. Turbulent upflow plumes.* ApJ 716, 1288, [114 c, 15 c/y].
Berger, T.E., Testa, P., Hillier, A., et al. 2011, *Magneto-thermal convection in solar prominences*, Nature 472, 7342, [127 c, 20 c/y].
Foullon, C., Verwichte, E., Nakariakov, V.M. et al. 2011, *Magnetic Kelvin-Helmholtz instability at the Sun*, ApJ 729, L8, [88 c, 14 c/y].
Gary, G.A. and Moore, R.L. 2004, *Eruption of a multiple-turn helical magnetic flux tube in a large flare: Evidence for external and internal reconnection that fits the breakout model of solar magnetic eruptions*, ApJ 611, 545, [103 c, 8 c/y].
Haerendel, G. and Berger, T.E. 2011, *A droplet model of quiescent prominence downflows*, ApJ 731, 82, [16 c, 2 c/y].
Hester, J.J., Stone, J.M., Scowen, A., et al. 1996, *WFPC2 studies of the Crab nebula. III. Magnetic Rayleigh-Taylor instabilities and the origin of the filaments*, ApJ 456, 225, [116 c, 5 c/y].
Hillier, A., Isobe, H., Shibata, K., et al. 2011, *Numerical simulations of the magnetic Rayleigh-Taylor instability in the Kippenhahn-Schlüter prominence model*, ApJ 736, L1, [49 c, 8 c/y].
Hillier, A., Berger, T.E., Isobe, H., et al. 2012a, *Numerical simulations of the magnetic Rayleigh-Taylor instability in the Kippenhahn-Schlüter model. I. Formation and upflows*, ApJ 746, 120, [51 c, 9 c/y].
Hillier, A., Isobe, H., Shibata, K., et al. 2012b, *Numerical simulations of the magnetic Rayleigh-Taylor instability in the Kippenhahn-Schlüter model. II. Reconnection-triggered downflows*, ApJ 756, 110, [30 c, 5 c/y].
Hillier, A., Richard, H., and Tripathi D. 2012c, *Determination of prominence plasma β from the dynamics of rising plumes*, ApJ 761, 106, [13 c, 2 c/y].

Hillier, A., Matsumoto, T., and Ichimoto, K. 2017, *Investigating prominence turbulence with Hinode SOT Dopplergrams*, A&A 597, A111, [3 c, 3 c/y].
Hillier, A. 2018, *The magnetic Rayleigh-Taylor instability in solar prominences*, Rev. Modern Plasma Phys. 2, 1.
Isobe, H., Miyagoshi, T., Shibata, K., et al. 2005, *Filamentary structure on the Sun from the magnetic Rayleigh-Taylor instability*, Nature 434, 478, [109 c, 9 c/y].
Keppens, R., Xia, C., and Porth, O. 2015, *Solar prominences: "Double, Double . . . Boil and Bubble"*, ApJ 806, L13, [13 c, 5 c/y].
Ni, L., Zhang, Q.M., Murphy, N.A., et al. 2017, *Blob formation and ejection in coronal jets due to the plasmoid and Kelvin-Helmholtz instabilities*, ApJ 841, 27, [9 c, 9 c/y].
Ofman, L. and Thompson, B.J. 2011, *SDO/AIA observation of Kelvin-Helmholtz instability in the sola corona*, ApJ 734, L11, [59 c, 9 c/y].
Terradas, J., Oliver, R., and Ballester, J.L. 2012, *The role of Rayleigh-Taylor instabilities in filament threads*, A&A 541, A102, [11 c, 2 c/y].

(11.9) Filaments/Prominences: Cavities

Bak-Steslicka, U., Gibson, S.E., Fan, Y., et al. 2013, *The magnetic structure of solar prominence cavities: New observational signature revealed by coronal magnetometry*, ApJ 770, L28, [57 c, 13 c/y].
Bak-Steslicka, U., Gibson, S.E., and Chmielewska, E. 2016, *Line-of-sight velocity as a tracer of coronal cavity magnetic structure*, Front.Astron.Space Sci. 3, 7, [5 c, 3 c/y].
Berger, T.E., Slater, G., Hurlburt, N., et al. 2010, *Quiescent prominence dynamics observed with the Hinode Solar Optical Telescope. I. Turbulent upflow plumes.* ApJ 716, 1288, [114 c, 15 c/y].
Berger, T.E., Testa, P., Hillier, A., et al. 2011, *Magneto-thermal convection in solar prominences*, Nature 472, 7342, [127 c, 20 c/y].
Berger, T.E., Liu, W., and Low, B.C. 2012, *SDO/AIA detection of solar prominence formation within a coronal cavity*, ApJ 758, L37, [57 c, 10 c/y].
Berger, T.E., Hillier, A., and Liu, W. 2017, *Quiescent prominence dynamics observed with the Hinode/SOT. II. Prominence bubble boundary layer characteristics and the onset of a coupled Kelvin-Helmholtz Rayleigh-Taylor instability*, ApJ 850, 60, [1 c, 1 c/y].
Berlicki, A., Gunar, S., Heinzel, P., et al. 2011, *2-D radiative-magnetohydrostatic model of a prominence observed by Hinode, SOHO/SUMER and Meudon/ MSDP*, A&A 530, A143, [19 c, 3 c/y].
Dove, J.B., Gibson, S.E., Rachmeler, L.A., et al. 2011, *A ring of polarized light: Evidence for twisted coronal magnetism in cavities*, ApJ 731, L1, [60 c, 9 c/y].
Dudik, J., Aulanier, G., Schmieder, B., et al. 2012, *Magnetic topology of bubbles in quiscent prominences*, ApJ 761, 9, [49 c, 9 c/y].
Fuller, J., Gibson, S.E., de Toma, G. et al. 2008, *Observing the unobservable ? Modeling coronal cavity densities*, ApJ 678, 515, [42 c, 4 c/y].
Gibson, S.E., Foster, D., Burkepile, J., et al. 2006, *The calm before the storm: The link between quiescent cavities and coronal mass ejections*, ApJ 641, 590, [158 c, 14 c/y].
Gibson, S.E., Kucera, T.A., Tastawicki, D., et al. 2010, *3-D morphology of a coronal prominence cavity*, ApJ 724, 1133, [100 c, 13 c/y].
Karna, N., Zhang, J., Pesnell, W.D., et al. 2015, *Study of the 3-D geometric structure and temperature of a coronal cavity using the limb synoptic map method*, ApJ 810, 124, [8 c, 3 c/y].
Karna, N., Zhang, J., and Pesnell, W.D. 2017, *The formation and maintenance of the dominant southern polar crown cavity of cycle 24*, ApJ 835, 135.
Kucera, T.A., Gibson, S.E., Schmit, D.J., et al. 2012, *Temperature and EUV intensity in a coronal prominence cavity and streamer*, ApJ 757, 73, [29 c, 5 c/y].

Li, X., Morgan, H., Leonard, D., et al., 2012, *A solar tornado observed by AIA/SDO: Rotational flow and evolution of magnetic helicity in a prominence cavity*, ApJ 752, L22, [112 c, 20 c/y].
Long, D.M., Harra, L.K., Matthews, S.A., et al. 2018, *Plasma evolution within an erupting coronal cavity*, ApJ 855, 74, [1 c, 1 c/y].
Marque, C. 2004, *Radio metric observations of quiescent filament cavities*, ApJ 602, 1037, [35 c, 3 c/y].
Okamoto, T.J., Tsuneta, S., and Berger, T.E. 2010, *A rising cool column as a signature of helical flux emergence and formation of prominence and coronal cavity*, ApJ 719, 583, [27 c, 4 c/y].
Rachmeler, L.A., Gibson, S.E., Dove, J.B., et al. 2013, *Polarimetric properties of flux ropes and sheared arcades in coronal prominence cavities*, SoPh 288, 617, [32 c, 7 c/y].
Reeves, K.K., Gibson, S.E., Kucera, T.A., et al. 2012, *Thermal properties of a solar coronal cavity observed with the X-ray telescope on Hinode*, ApJ 746, 146, [43 c, 8 c/y].
Régnier, S., Walsh, R.W., and Alexander, C.E. 2011, *A new look at a polar crown cavity as observed by SDO/AIA. Structure and dynamics*, A&A 533, L1, [70 c, 11 c/y].
Schmit, D.J. and Gibson, S.E. 2011, *Forward modeling cavity density: A multi-instrument diagnostic*, ApJ 733, 1, [31 c, 5 c/y].
Shen, Y., Liu, Y., Liu, Y.D., et al. 2015, *Fine magnetic structure and origin of counter-streaming mass flows in a quiescent solar prominence*, ApJ 814, L17, [24 c, 10 c/y].
Su Y. and van Ballegooijen, A. 2012, *Observations and magnetic field modeling of a solar polar crown prominence*, ApJ 757, 168, [62 c, 11 c/y].
Vasquez, A.M., Frazin, R.A., and Kamalabadi, F. 2009, *3-D temperatures and densities of the solar corona via multi-wavelength EUV tomography: Analysis of prominence cavities*, SoPh 256, 73, [44 c, 5 c/y].
Wang, Y.M. and Stenborg, G. 2010, *Spinning motions in coronal cavities*, ApJ 719, L181, [55 c, 7 c/y].

(11.10) Filaments/Prominences: Eruptions

Bi, Y., Jiang, Y., Yang, J., et al. 2014, *Solar filament material oscillations and drainage before eruption*, ApJ 790, 100, [18 c, 5 c/y].
Bi, Y., Jiang, Y., Yang, Y., et al. 2015, *Partial eruption of a filament with twisting non-uniform fields*, ApJ 805, 48, [13 c, 5 c/y].
Chae, J. 2003, *The formation of a prominence in NOAA active region 8668. II. TRACE observations of jets and eruption associated with canceling magnetic features*, ApJ 584, 1084, [48 c, 3 c/y].
Chen, P.F., Innes, D.E., and Solanki, S.K. 2008, *SOHO/SUMER observations of prominence oscillation before eruption*, A&A 484, 487, [43 c, 5 c/y].
Chifor, C., Mason, H.E., Tripathi, D., et al. 2006, *The early phases of a solar prominence eruption and associated flare: a multi-wavelength analysis*, A&A 458, 965, [57 c, 5 c/y].
Filippov, B.P. and Den, O.G. 2001, *A critical height of quiescent prominences before eruption*, JGR 106, 25177, [49 c, 3 c/y].
Gilbert, H.R., Holzer, T.E., Burkepile, J., et al. 2000, *Active and eruptive prominences and their relationship to coronal mass ejections*, ApJ 537, 503, [125 c, 7 c/y].
Gilbert, H.R., Inglis, A.R., Mays, M.L., et al. 2013, *Energy release from impacting prominence material following the 2011 June 7 eruption*, ApJ 776, L12, [30 c, 7 c/y].
Gopalswamy, N., Shimojo, M., Lu, W., et al. 2003, *Prominence eruptions and coronal mass ejection: A statistical study using microwave observations*, ApJ 586, 562, [189 c, 13 c/y].
Gopalswamy, N., Mäkelä, P., Akiyama, S., et al. 2015, *Large solar energetic particle events associated with filament eruptions outside of active regions*, ApJ 806, 8, [24 c, 10 c/y].
Jing, J., Yurchyshyn, V.B., Yang, G., et al. 2004, *On the relation between filament eruptions, flares, and coronal mass ejections*, ApJ 614, 1054, [72 c, 5 c/y].

Kleint, L., Battaglia, M., Reardon, K., et al. 2015, *The fast filament eruption leading to the X-flare on 2014 March 29*, ApJ 806, 9, [28 c, 11 c/y].

Kumar, P. and Cho, K.S. 2014, *Multiwavelength observation of a large-scale flux rope eruption above a kinked small filament*, A&A 572, 83, [18 c, 5 c/y].

Liu, W., Berger, T.E., and Low, B.C. 2012, *First SDO/AIA observations of solar prominence formation following an eruption: Magnetic dips and sustained condensation and drainage*, ApJ 745, L21, [51 c, 9 c/y].

Liu, R., Kliem, B., Titov, V.S., et al. 2016, *Structure, stability, and evolution of magnetic flux ropes from the perspective of magnetic twist*, ApJ 818, 182, [51 c, 34 c/y].

McCauley, P.I., Su, Y.N., Schanche, N., et al. 2015, *Prominence and filament eruptions observed by the SDO: Statistical properties, kinematics, and online catalog*, SoPh 290, 1703, [33 c, 13 c/y].

Reeves, K.K., McCauley, P.I., and Tian, Hui 2015, *Direct observations of magnetic reconnection outflow and CME triggering in a small erupting solar prominence*, ApJ 807, 7, [13 c, 5 c/y].

Rust, D.M. and LaBonte, B.J. 2005, *Observational evidence of the kink instability in solar filament eruptions and sigmoids*, ApJ 622, L69, [95 c, 8 c/y].

Shen, Y., Liu, Y., Su, J., et al. 2012, *Sympathetic partial and full filament eruptions observed in one solar breakout event*, ApJ 750, 12, [60 c, 11 c/y].

Sterling, A.C. and Moore, R.L. 2005, *Slow-rise and fast-rise phases of an erupting solar filament, and flare emission onset*, ApJ 630, 1148, [86 c, 7 c/y].

Sterling, A.C., Moore, R.L., and Freeland, S.L., 2011, *Insights into filament eruption onset form SDO Observations*, ApJ 731, 3, [30 c, 5 c/y].

Su, Y., van Ballegooijen, A., McCauley, P., et al. 2015, *Magnetic structure and dynamics of the erupting solar polar crown prominence on 2012 March 12*, ApJ 807, 144, [20 c, 8 c/y].

Tripathi, D., Isobe, H., and Mason, H.E. 2006, *On the propagation of brightening after filament/prominence eruptions, as seen by SOHO/EIT*. A&A 453, 1111, [57 c, 5 c/y].

Wang,H., Qiu, J., Jing, J., et al. 2003, *Study of ribbon separation of a flare associated with a quiescent filament eruption*, ApJ 593, 564, [88 c, 6 c/y].

Williams, D.R., Török, T., Démoulin, P., et al. 2005, *Eruption of a kink-unstable filament in NOAA active region 10696*, ApJ 628, L163, [143 c, 11 c/y].

Zhang, Q.M., Ning, Z.J., Guo, Y., et al. 2015, *Multiwavelength observations of a partially eruptive filament on 2011 September 8*, ApJ 805, 4, [28 c, 11 c/y].

Chapter 12
Flares: Nonthermal Particles

12.1 Flare Gamma-Rays

Information on the highest energies of particles produced during solar flares, measured in gamma-ray wavelengths with photon energies of $E \gtrsim 300$ keV, has been obtained by very few instruments on a routine basis in the new millennium, such as from the *Ramaty High-Energy Spectroscopic Imager (RHESSI)* and from the *Fermi* spacecraft, and occasionally from the CORONAS-F mission and the *INTErnational Gamma-Ray Astrophysics Laboratory (INTEGRAL)* ESA mission. Recent reviews can be found on energetic ions in solar flares from gamma-ray and neutron observations (Vilmer et al. (2011)), on electron acceleration and propagation in solar flares (Holman et al. 2011), and on future hard X-ray and gamma-ray spectroscopy (Holman 2016).

A key result of the RHESSI mission is the discovery of gamma-ray footpoint structures, obtained from the first gamma-ray images of a solar flare at all, observed during the X4.8-class flare on 2002 July 23. This event turned out to be also the largest solar flare observed by RHESSI. Double ion footpoints have been imaged at 2.223 MeV (where the spectrum is dominated by a gamma-ray line). The narrow deuterium line at 2.223 MeV is formed by the thermalization and capture of neutrons produced in collisions. The ion footpoints were found to be slightly but significantly displaced ($20'' \pm 6''$) from the electron precipitation sites usually seen in $\gtrsim 25$ keV hard X-rays (Fig. 12.1), which poses an interesting new problem for particle acceleration models in terms of the standard thick-target flare model (Hurford et al. 2003, 2006; Smith et al. 2003; Lin et al. 2003; Schrijver et al. 2006). The spectral line profiles of Ne, Mg, Si, Fe, C, and O were for the first time resolved, exhibiting Doppler redshifts of 0.1%–0.8% and FWHM broadening of 0.1%–2.1%. Interpretations of the large redshifts in terms of inclined magnetic fields or extreme beaming of the ions were considered, while a bulk downward motion of the plasma

M. J. Aschwanden, *New Millennium Solar Physics*, Astrophysics and Space Science Library 458, https://doi.org/10.1007/978-3-030-13956-8_12

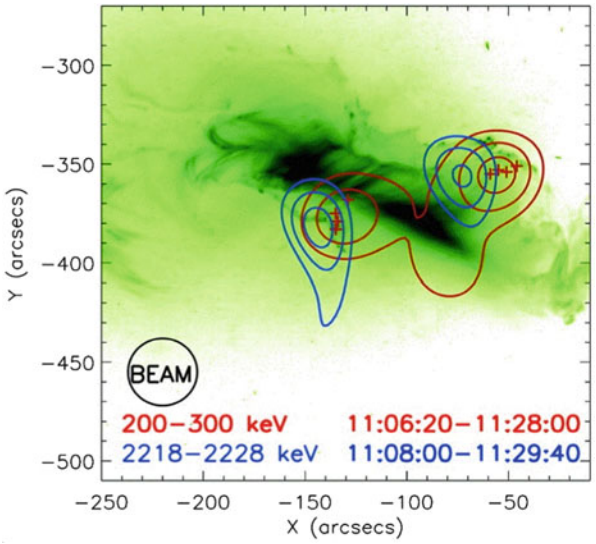

Fig. 12.1 Locations of the gamma-ray footpoint sources of the 2.2 MeV neutron capture line (blue contours) and the electron bremsstrahlung footpoint sources in the energy range of 200–300 keV, observed with RHESSI during the X4.8-class flare on 2002 July 23 (red contours). The green background image outlines the flare arcade as seen in EUV (from TRACE). The spatial resolution of RHESSI is indicated with a circular "beam size" pattern (Hurford et al. 2003)

in which the accelerated ions interact was ruled out (Smith et al. 2003). Other RHESSI-observed events with imaging of the neutron capture line include the flares of 2003 October 28, 2003 October 29, 2003 November 2 (Hurford et al. 2006), and 2005 January 20 (Masson et al. 2009; Kurt et al. 2010). The fact that the gamma-ray producing ions appear to be accelerated in highly localized regions (with a size of $\lesssim 20''$), indicates that they are accelerated by the coronal flare reconnection process, rather than by a widespread shock driven by a *coronal mass ejection (CME)* (Hurford et al. 2006; Lin 2006). Close correlations suggest that electrons with ≥ 0.3 MeV and protons with > 30 MeV are accelerated by a common mechanism (Shih et al. 2009).

Positron production by fast ions in solar flares may occur via the decay of radioactive daughter nuclei, beta decay of excited states of target nuclei, or via pion (plus) production, e.g., in $p(p, n\pi^+ X)p'$. RHESSI resolved the spectral width of the 511 keV positron annihilation line, with a line width of typically $\gtrsim 5$ keV, which indicates a temperature of the accelerated-ion interaction region around $T \approx 10^5$ K, which is much higher than the expected value of $T \approx 10^4$ K in the chromosphere (Share et al. 2004). Although the energy contained in high-energy particles may have been enough to heat the plasma, the rate of deposition is not correlated with the temperature determined by the 511 keV line width, and this raises questions about the energy source (Share et al. 2004). Interactions of flare-accelerated ions in the solar atmosphere can synthesize radioactive nuclei, whose

decay can produce observable, delayed gamma-ray lines in the aftermath of large flares, which amounts to ≈ 2 days for the β^+ radioisotopes in the 511 keV positron-electron line (Tatischeff et al. 2006).

Only about 20 solar flare events have ever been observed with significant pion production, and 18 flares were detected with Fermi/LAT above $>$ 100 MeV (Ackermann et al. 2014), and three of them behind the limb (Ackermann et al. 2017; Pesce-Rollins et al. 2015). Some of the most recent events have been observed in a wide energy range by both RHESSI and CORONAS-F (Kuznetsov et al. 2011; Trottet et al. 2008; Masson et al. 2009). Often there are two acceleration episodes, a first during the impulsive flare phase, and a second during a prolonged decay phase, lasting up to 20 hrs (Ajello et al. 2014). In the 2005 January 20 event, the first relativistic protons detected at Earth are accelerated together with relativistic electrons and with protons that produce pion-decay gamma-rays during the second episode (Masson et al. 2009). High-energy gamma radiation was detected with the *SOlar Neutrons and Gamma rays (SONG)* instrument onboard CORONAS-F up to energies of $>$ 100 MeV, suggesting decay of neutral pions by $>$ 300 MeV protons, as observed during the 2001 August 25, X5.3 flare (Kurt et al. 2010), and during the 2003 October 28, X17.2 flare (Kuznetsov et al. 2011).

Modeling of gamma-ray emission profiles, resulting from the bombardment of energetic ions impacting the chromosphere, using the observed nuclear de-excitation line profiles, requires an atmospheric model of the magnetic field, density, and temperature. A recent model addresses particle transport and interaction (in both hydrostatic and dynamically extended atmospheres) and includes energy losses due to Coulomb collisions, removal by nuclear reactions, magnetic mirroring in the converging magnetic flux, and MHD pitch-angle scattering in the corona, treated via the quasi-linear formalism (Murphy et al. 2007).

Quasi-periodic pulsations in gamma-ray emission have rarely been reported, probably because of insufficient signal-to-noise ratios, but a period of $P_1 \approx 40$ s has been detected during the solar flare of 2005 January 1, at photon energies up to 2–6 MeV with the SONG/CORONAS-F, as well as with RHESSI and the Nobeyama radio heliograph (Nakariakov et al. 2010). A second periodicity of $P_2 = 13$ s was noted also in the same flare, which was interpreted as second harmonic of the sausage MHD mode (Nakariakov et al. 2010).

12.2 Flare Hard X-Ray Ribbons

A common morphological structure of flares in the chromospheric regions is a pair of near-parallel *ribbons*, straddling along both sides of a magnetic polarity inversion line, and thus has conjugate (or opposite) magnetic polarity. The corresponding coronal structure is called a *flare arcade*, a sequence of nested loops that outline the post-reconnection magnetic field, with the footpoints anchored in the ribbons. The chromospheric double ribbons that are often visible in EUV, UV, or white-light, are generally not seen as a contiguous structure in hard X-rays, probably due to the

limited dynamic range of Fourier imaging, but RHESSI imaged larger segments of them in some flares (Fletcher and Hudson 2002; Liu et al. 2007; Dennis and Pernak 2009; Krucker et al. 2011). For a review see Fletcher et al. (2011).

Hard X-ray observations with the *Hard X-Ray Telescope (HXT)* onboard *Yohkoh* showed evidence for flare footpoint brightenings that precede the onset of the hard X-ray emission, but the spatio-temporal correlation indicates that the energy release occurs in different loops during the preflare and during the impulsive flare phase (Warren and Warshall 2001). The 2000 July 14 flare revealed for the first time $>$ 30 keV hard X-ray emission along the entire two-ribbon structure, suggesting that magnetic reconnection and particle acceleration occurs in the entire flaring region (Masuda et al. 2001). Moreover, the transverse separation of the ribbons indicates that magnetic reconnection progresses from low-lying highly sheared loops in the beginning of the flare to higher-lying and less sheared loops near the top of the flare arcade (Masuda et al. 2001; Aschwanden and Alexander 2001; Fletcher and Hudson 2001). Also a correlation between the footpoint motion and the hard X-ray flux was found for this flare (Fletcher and Hudson 2002). The limb X1.5 flare of 2002 April 21 indeed showed a centroid motion of the thermal 12–25 keV source in upward direction, with an initial velocity of $v \approx 10$ km s^{-1}, confirming the interpretation that magnetic reconnection moves to higher altitudes, as predicted in classical flare models (Gallagher et al. 2002).

RHESSI observations provide higher spatial resolution than HXT/Yohkoh to trace the hard X-ray sources along flare ribbons, which is especially important for measuring the motion of the centroids of the relatively crude hard X-ray blobs (compared with the much thinner ribbons seen in EUV and Hα). During the 2002 July 23 gamma-ray flare, a systematic motion of the $>$ 30 keV hard X-ray source along a ribbon was measured during a time interval of more than 10 min (Krucker et al. 2003), and similarly during the 2001 April 10 X2.3 flare (Asai et al. 2003). One of the longest hard X-ray ribbons was spotted in the 2005 May 13 flare (Fig. 12.2; Liu et al. 2007). Comparing Hα with UV/EUV flare ribbons, the flare ribbons have the tendency to spread systematically outwards of the magnetic polarity inversion line, while their appearance becomes more ordered as the flare progresses. On the other hand, the hard X-ray footpoint sources frequently move along the Hα or UV/EUV ribbons, while the ribbons move away from the polarity inversion line, and are found at locations distinguished by their high magnetic field strengths (Temmer et al. 2007), or their high magnetic flux transfer rates (Liu et al. 2008). The evolution of reconnection along two (conjugate) flare ribbons has been traced in detail in the 2002 November 9 flare and it was found that the reconnection process is not modulated simultaneously in the entire flare region, but occurs in a sequence of intermittent bursts that progresses along the flare arcade (Fig. 12.3; Grigis and Benz 2005).

The flare ribbon expansion can be used to test magnetic reconnection models (e.g. Qiu and Cheng 2017). The energy release rate can be written as a product of the Poynting flux into the reconnection region, $S = B_c^2 v_i/(4\pi)$, and the area of the

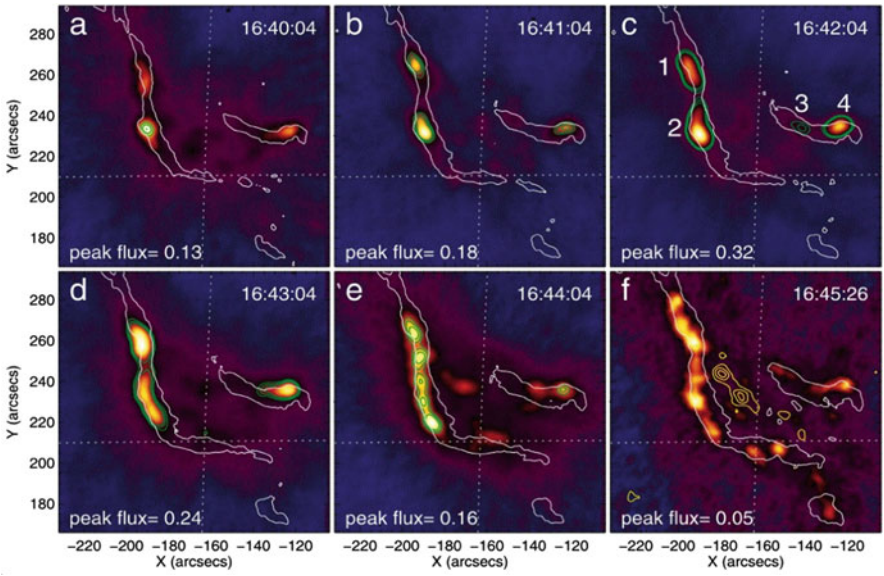

Fig. 12.2 The colored images represent a time sequence of RHESSI 25–50 keV hard X-ray images, integrated in 1 min time intervals. RHESSI images are reconstructed with the CLEAN algorithm. The white contours outline the TRACE 1600 Å ribbons taken near the center of each RHESSI time interval. Note the very long ribbon seen in hard X-rays (at the end of the flare, panel **f**), which almost matches the ribbon seen in ultraviolet at 1600 Å (Liu et al. 2007)

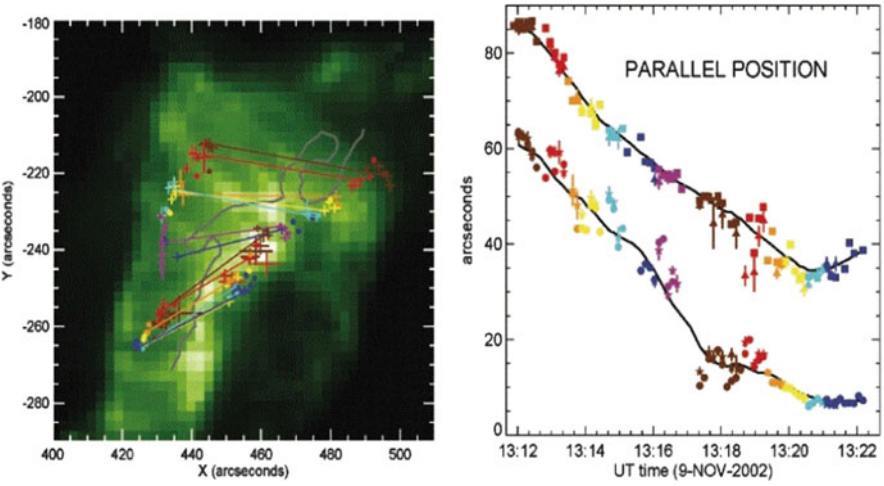

Fig. 12.3 *Left:* EIT/SOHO 195 Å image of the flare arcade observed during the 2002 November 12 flare. The colored lines indicate the magnetic connectivity at different times of the flare. *Right:* Time evolution of the source positions of the centroids of hard X-ray emission parallel to the ribbon curves. The color code marks different time intervals (Grigis and Benz 2005)

reconnection region, A, (Asai et al. 2004),

$$\frac{dE}{dt} = SA = 2\frac{B_c^2}{4\pi} v_i A \ , \tag{12.2.1}$$

where B_c is the magnetic field strength in the corona, and v_i is the inflow velocity into the reconnection region. With this method, Asai et al. (2004) found that the magnetic field strength of the Hα kernels associated with hard X-ray sources are about 3 times larger than those at the Hα kernels without hard X-ray sources. However, many flares display a more complex magnetic topology than envisioned from standard 2-D reconnection models, sometimes 3-D reconnection models are required that evolve as sigmoid-to-arcade transformations (Jing et al. 2007; Liu et al. 2007). The reconnection rates are never uniform along the flare ribbons, but are much larger at the locations where hard X-ray footpoints are observed (Temmer et al. 2007).

While most flare ribbons show some curvature, a few exhibit a completely circular geometry, which suggests a fan-spine magnetic topology involving reconnection at a 3-D coronal null point (Wang and Liu 2012). In the 2012 October 23 flare, three ribbons are visible, with two highly elongated ones inside and outside of a quasi-circular one, respectively (Yang et al. 2015). Many flares occur in a sigmoid geometry, where two J-shaped ribbons are matched, which are modeled with the inserted flux rope model and contain locations with prominent quasi-separatrix layers (Savcheva et al. 2015, 2016).

Modeling the energetics of flare ribbons with a temperature and emission measure analysis using GOES, EVE/SDO, AIA/SDO, and RHESSI data, substantial amounts of hot flare plasma (up to temperatures of $T_e \approx 10$ MK) was detected in the flare ribbons, during the pre-impulsive and early-impulsive flare phase (Fletcher et al. 2013).

The flare hard X-ray sources, which illuminate only short segments of the chromospheric flare ribbons at any time, generally appear as unresolved point sources (Dennis and Pernak 2009; Krucker et al. 2011), and may additionally be broadened by the theoretically predicted photospheric X-ray albedo. According to Kontar et al. (2006), back-reflected hard X-ray photons from the photosphere have been detected, where the solar surface acts like a *Compton mirror*.

12.3 Coronal Hard X-Rays

RHESSI provides imaging of hard X-rays within a dynamic range of about an order of magnitude, limited mostly by the fringes and sidelobes produced by Fourier imaging methods. During solar flares, the brightness of hard X-ray emission is generally strongest at the flaring footpoints (which are part of the flare ribbons), so that the fainter emission from coronal hard X-ray sources is outshone. If the bright footpoints are occulted by the solar limb, it is possible to detect much fainter

hard X-ray emission from coronal sources. Thus non-thermal hard X-ray emission is generally detected at the footpoints of flare loops (Krucker and Lin 2008), but RHESSI detects it also at coronal heights above flare loops (Battaglia and Benz 2007; Krucker et al. 2008; Ishikawa et al. 2011; Krucker et al. 2010), in occulted flares (Krucker et al. 2007b, 2010; Krucker and Lin 2008), in the preflare phase (Lin et al. 2003), in the absence of footpoint emission (Veronig and Brown 2004), associated with jets (Bain and Fletcher 2009), and cospatial with coronal mass ejections (Krucker et al. 2007a).

One of the most occulted flares occurred during 2002 October 27, which is associated with a SEP event and a very fast CME. Observed from Earth, the flare site is $40.4° \pm 3.5°$ behind the solar limb and the occultation height is $h = 1.5 \times 10^5$ km $\approx 0.35 \ R_\odot$ (Krucker et al. 2007b). Acceleration of electrons appears to take place in the high corona, where about 10% of all electrons are nonthermal at ≥ 10 keV (Krucker et al. 2007a).

While the location of the primary magnetic reconnection process and the associated particle acceleration site has been identified earlier (with HXT/Yohkoh) at a coronal height h that corresponds roughly to a factor of $h/d \approx 1.5$ times the footpoint separation d, either from direct imaging of a limb flare (Masuda et al. 1994), or from electron time-of-flight measurements (Aschwanden et al. 1996). The new RHESSI observations went a step further and established double coronal X-ray Sources. RHESSI detected such double hard X-ray sources in some suitably oriented limb flares, which reveal a vertically symmetric energy gradient below and above a supposed X-point reconnection site (Figs. 12.4 and 12.5; Sui and Holman 2003; Liu et al. 2008). The higher energies in the inner region (relative to the X-point) show mainly nonthermal emission, while the outer regions show thermal emission (Liu et al. 2008). Below the X-point, *reconnection outflows* are predicted by the standard reconnection scenario, which indeed have been observed with TRACE during the 2002 July 23 flare (Asai et al. 2004).

Another novel discovery of RHESSI is the initial downward motion of the centroid of the nonthermal hard X-ray sources. This unexpected initial downward motion of coronal hard X-ray sources has been observed in a number of flares, apparently associated with the propagation of reconnection along flare ribbons (Sui et al. 2004; Veronig et al. 2006; Ji et al. 2008). Models with a collapsing trap embedded in a standard 2-D magnetic reconnection model fit the data, if the the loop top source is assumed to be thermal bremsstrahlung from "superhot" ($T \approx 35$–45 MK) plasma (Veronig et al. 2006).

The standard scenario of magnetic reconnection above a neutral inversion line predicts a progressive separation of the flare ribbons and related altitude increase of the magnetic reconnection X-point. A further consequence is that the footpoint reconnection rate (or reconnection speed) is proportional to the (non-thermal) hard X-ray flux (Eq. 12.2.1). In the X1.5-class flare of 2002 July 23 this is indeed the case in one footpoint ribbon, while it is not the case in the other (conjugate) footpoint ribbon (Lin et al. 2003).

Veronig and Brown (2004) identified a new class of solar hard X-ray-emitting flares that display no footpoints, which were interpreted as coronal flare loops

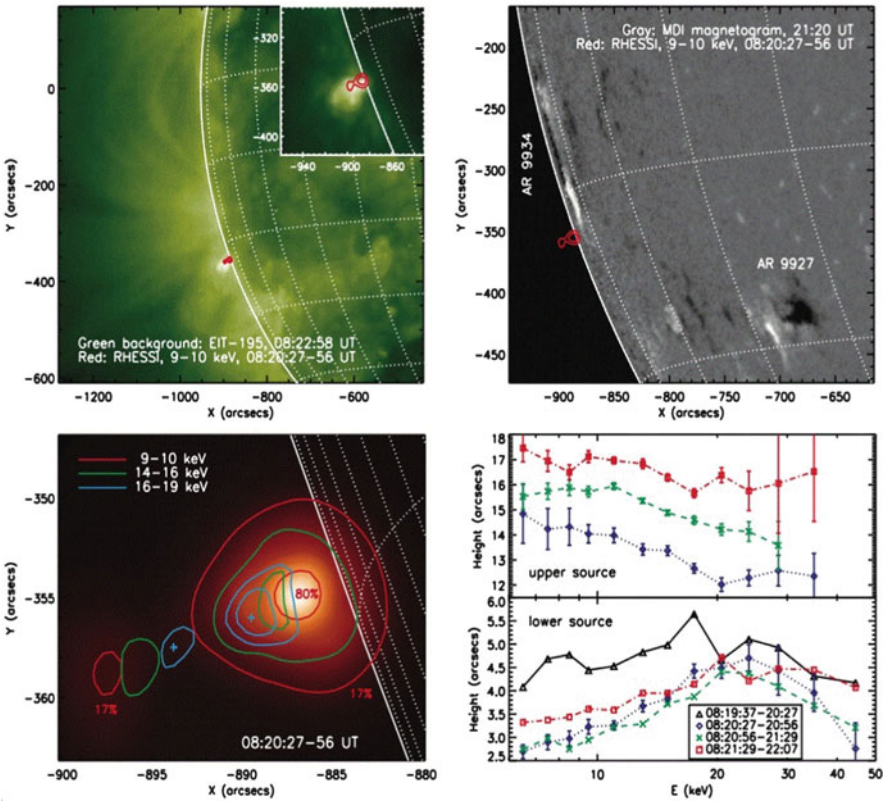

Fig. 12.4 Double coronal hard and soft X-ray sources observed by RHESSI, showing evidence for magnetic reconnection and particle acceleration. *Upper left:* EIT/SOHO 195 Å image observed at 2002 April 30, at 08:22 UT, superimposed with (red) RHESSI contours ot 9–10 keV. *Upper right:* MDI/SOHO magnetogram taken at 21:20 UT (some 13 hrs after the flare), overplotted with (red) RHESSI 9–10 keV contours. *Lower left:* RHESSI contours in three energy bands (9–10, 14–16, and 16–19 keV). *Lower right:* Height above the limb of the centroids for the upper and lower coronal sources, plotted as a function or energy, (Liu et al. 2008)

with such high densities that they are collisionally thick at electron energies up to $\gtrsim 50$ keV. It was shown that (i) the loop column densities are consistent with the nonthermal coronal thick-target model, (ii) chromospheric evaporation occurs by thermal conduction from the loop rather than by electron beam heating, and (iii) the hot loop temperature being in balance of thick-target collisional heating and (mainly) conductive heating (Veronig and Brown 2004).

Spectral analysis of coronal hard X-ray sources show soft-hard-soft evolution for both coronal and footpoint sources. However, the coronal source is nearly always softer than the footpoints (Battaglia and Benz 2006), which indicates that the location where electrons are accelerated to the highest energies (where they produce the hardest spectrum) lies between the coronal hard X-ray source and the

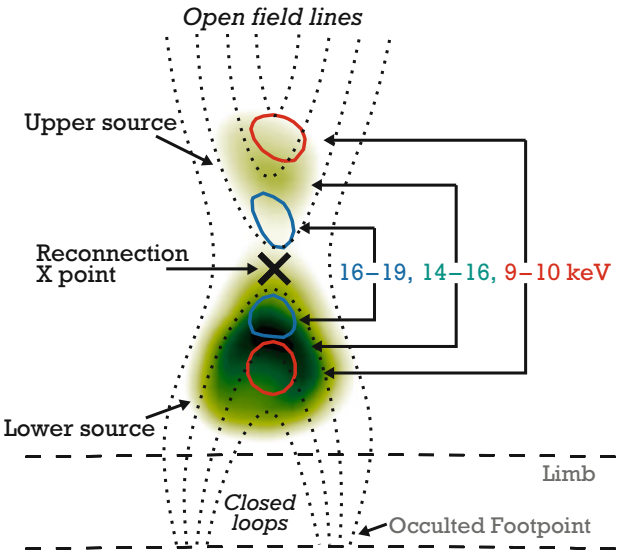

Fig. 12.5 Schematic diagram of the physical scenario superimposed on the RHESSI observations (contours at 9–10 and 16–19 keV) as a manifestation of the stochastic acceleration model. The dotted curves represent the magnetic field (Liu et al. 2008)

chromospheric footpoints. However, a thin-thick target model cannot account for the observed relations between the non-thermal spectra of coronal and footpoint sources (Battaglia and Benz 2007), while it is found to be consistent in partially occulted flares (Krucker et al. 2007b; Krucker and Lin 2008).

Superhot X-Ray sources ($T > 30$ MK) were detected in large coronal altitudes (even during the pre-impulsive flare phase), and thus are of coronal origin, rather than caused by chromospheric evaporation, which generally produces a high-temperature component of ≈ 20 MK also (Caspi and Lin 2010).

12.4 Modeling of Hard X-ray Spectra

Hard X-ray spectra from RHESSI have a high spectral resolution of $\approx$ 1 keV and allow us unambiguously to separate the thermal (exponential-like function) from the non-thermal (power law-like) spectral component, so that the thermal and non-thermal flare photons can be accurately separated (in photon space). However, there is one big problem that the low-energy cutoff of the nonthermal component (in particle energy space) cannot be easily determined. This low-energy cutoff is defined by the lowest energy where an electron can be accelerated out of the thermal distribution. The knowledge of this low-energy cutoff is necessary to avoid a singularity (and a huge over-estimate) of the extrapolated nonthermal spectrum

and related flux at the lowest energies. A correction term for the assumed *"cold-target"* energy loss in the thermal energy range eliminates the low-energy cutoff singularity (Emslie 2003). Spectral fitting with a broken power law function in terms of the thick-target model yields a low-energy cutoff varying between 20 and 40 keV during a large flare (Holman et al. 2003). A low-energy cutoff can be constrained by both hard X-ray and simultaneous microwave spectra (Holman 2003). Equipartition between thermal and nonthermal energy is found to be compatible with the data (Saint-Hilaire and Benz 2005). Sui et al. (2005) use a new method that combines spatial, spectral, and temporal analysis, based on the assumption that spiky time structures indicate non-thermal emission, while smooth time structures are expected for dominant thermal emission. A similar method was used based on analyzing the energy-dependent timing of thermal emission, where nonthermal hard X-ray emission shows extremely small electron time-of-flight delays in the order of $\lesssim$ 10–100 ms for nonthermal electrons, while thermal emission is controlled by conductive cooling and exhibits much larger delays in the order of a few seconds to a few tens of seconds. This method yields cross-over energies of $\epsilon_{th} = 18.0 \pm 3.4$ keV (where the hard X-ray spectrum transits from thermal to nonthermal emission), (Aschwanden 2007). These values can be considered as upper limits of the low-energy cutoff. A radically different approach to determine the low-energy cutoff was proposed by Kontar et al. (2015), based on a modification of the (warm) temperature regime due to chromospheric heating, evaporation, and turbulence, opposed to the standard cold-target model. The warm-target model of Kontar et al. (2015) has been applied to a large data set of solar flares, including 191 M- and X-class flares observed with AIA/SDO, which yields mean temperature of $T_e = 8.6$ MK in the thick-target region of flares, and a low-energy cutoff of $\epsilon_{wt} = 6.2 \pm 1.6$ keV (Aschwanden et al. 2016). The nonthermal energy exceeds the thermal energy in 85% of the events, which largely confirms the warm thick-target model of Kontar et al. (2015). As an alternative to the combination of thermal and nonthermal two-component spectra, a kappa distribution may be used instead, which has a Maxwellian-like core in addition to the power law tail, and has the nice feature that no assumption on the low-energy cutoff is required (Oka et al. 2013), but one should be aware that the kappa distribution is a mathematical convenience that is not derived from a physical model. Bain and Fletcher (2009) derived a physical model, but a specific velocity dependence is required for the energy diffusion in the acceleration region in order to obtain a kappa distribution.

Another effect of the thick-target model that needs to be included in fitting RHESSI hard X-ray spectra is the *non-uniform target ionization*. The decrease of ionization with depth in the atmosphere reduces long-range collisional energy losses and so enhances the hard X-ray bremsstrahlung efficiently there, elevating the high energy end of the hard X-ray spectrum by factors of up to 2.8 above that of an ionized target (Kontar et al. 2002). Evidence for such a spectrum was obtained by Su et al. (2011).

The spectral evolution of hard X-ray fluxes during impulsive solar flares was found to exhibit a correlation between the spectral index γ and the non-thermal flux

at 35 keV, which may be related to the generally observed soft-hard-soft evolution during the impulsive flare phase (Grigis and Benz 2004).

The effects of Compton backscattering were theoretically studied, where incoming photons become scattered in the dense chromosphere or photosphere, and this way contribute to a source broadening and to modified hard X-ray spectra (Massone et al. 2004; Saint-Hilaire and Benz 2005; Kontar et al. 2006, 2011; Kasparova et al. 2007). A major assumption in some backscattering models is the isotropy of the downward directed radiation (Kontar et al. 2006). Also, low-energy cutoffs inferred from mean electron spectra can sometimes be an artefact of the albedo (Kasparova et al. 2007).

The finite size of coronal hard X-ray sources has been investigated by forward-fitting of source visibilities in different energy bands, from which it was found that the average source sizes σ increase slowly with photon energy ϵ as $\sigma \propto \epsilon^{1/2}$ (Xu et al. 2008). This behavior is neither consistent with the predictions of a single-loop thermal model, nor with a model in which nonthermal electrons are injected into a constant-density structure from a compact acceleration region. On the other hand, it was concluded that the data are consistent with a nonthermal collisional model that incorporates an extended acceleration region (Xu et al. 2008), while other studies of the same flare events imply that hard X-rays come predominantly from the corona rather than from the more usual chromospheric footpoints (Dennis et al. 2018).

Fitting of hard X-ray spectra in a survey of partially occulted flares revealed that the coronal sources show faster time variations in the order of tens of seconds (than the thermal hard X-ray emission at $E \lesssim 15$ keV), which is likely to be thin-target emission in the corona from flare-accelerated electrons (Krucker and Lin 2008).

One generic model for hard X-ray emission is stochastic acceleration of particles by turbulence, where electrons accelerated at or very near the loop top produce thin-target bremsstrahlung emission there, and then escape downward producing thick-target emission at the loop footpoints. The model starts with the Fokker-Planck equation for the density spectrum of accelerated electrons, averaged over the turbulent acceleration region, includes the direct acceleration rate by turbulence, a particle diffusion rate, and a particle loss rate (by Coulomb collisions). Petrosian and Chen (2010) and Chen and Petrosian (2013) fitted this model to the 2003 November 3 flare and found an energy-dependence of the particle escape time T_{esc} scaling as,

$$T_{esc}(E) = 0.3\ \mathrm{s} \left(\frac{E}{100\ \mathrm{keV}} \right)^{\kappa}, \quad \kappa = 0.83 \pm 0.10\,, \tag{12.4.1}$$

and a scattering time τ_{scat}^{turb} due to turbulence,

$$\tau_{scat}^{turb}(E) = 0.016\ \mathrm{s} \left(\frac{E}{100\ \mathrm{keV}} \right)^{\lambda}, \quad \lambda = 1.90 \pm 0.14\,. \tag{12.4.2}$$

The energy-dependence of the escape time and the scattering time are shown in Fig. 12.6. Note that the escape time by turbulent scattering indicates a significantly

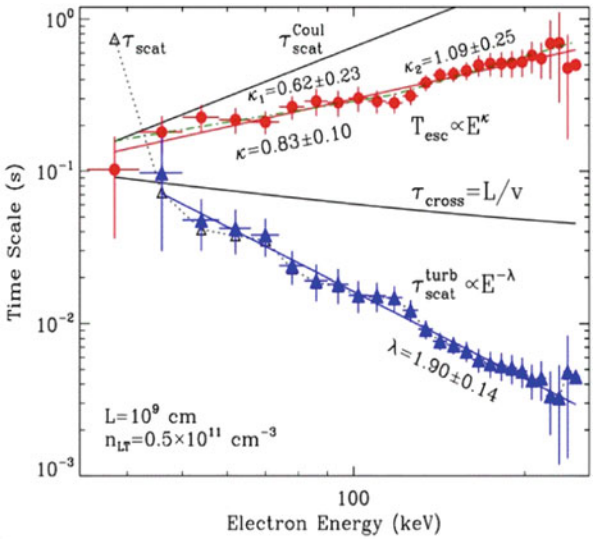

Fig. 12.6 Spectral modeling of the 2003 November 3 flare observed with RHESSI. The escape time (filled circles) and turbulence scattering time (filled triangles) in the loop top acceleration region are shown, both fitted with a power law dependence. The Coulomb collisional scattering rate $\tau_{scat}^{coul}(E) \propto E^{1.5}$ is shown in the top of the diagram (Petrosian and Chen 2010)

different scaling than what is expected for models with pure collisional Coulomb scattering (τ_{scat}^{Coul}), such as collisional trap models that have an escape time corresponding to the collisional deflection time (of scattering into the loss-cone),

$$\tau^{defl}(E) \approx 0.95 \text{ s} \left(\frac{E}{100 \text{ keV}}\right)^{3/2} \left(\frac{n_e}{10^{11}\, cm^{-3}}\right)^{-1} \left(\frac{20}{\ln \Lambda}\right) , \qquad (12.4.3)$$

with $\ln \Lambda$ being the Coulomb logarithm. Other statistical studies found that the energy-dependent time delays of $\approx$ 20–200 keV hard X-ray emission is consistent with the weak-diffusion limit (e.g., Aschwanden et al. 1997), opposed to the result of significant turbulent scattering in the 2003 November 3 flare modeled by Petrosian and Chen (2010), but the authors point out that this result may not be representative of typical flares, which have generally softer spectra for the loop top sources.

12.5 Rapid Magnetic Changes During Flares

Since magnetic reconnection dissipates part of the local magnetic energy during flares, the non-potential magnetic energy, or the free energy (i.e., the difference between the non-potential and potential magnetic energy) is expected to be reduced during a flare. Potential fields are stable because they represent the lowest state

of energy and cannot be dissipated by a magnetic reconnection process. Earlier studies describe rapid changes of magnetic fluxes associated with flares, without distinguishing between potential and non-potential magnetic field components (Wang et al. 2002; Yurchyshyn et al. 2004), while more recent studies quantify the fraction of dissipated free energy (e.g., Schrijver et al. 2008; Sun et al. 2012; Aschwanden et al. 2014).

Analyzing the line-of-sight component B_z of 6 X-class flares it was found that they all had an increase in the magnetic flux of the leading polarity of order of a few times 10^{20} Mx, while each event exhibited a permanent decrease in the magnetic flux of the following polarity (Wang et al. 2002; Yurchyshyn et al. 2004). The fact that the magnetic changes are permanent proves that they are due to an irreversible change in the reconnection topology, and not due to a reversible disturbance during a flare. The penumbral fields change from a highly inclined to a more vertical configuration, which leads to penumbral decay (Liu et al. 2005). Rapid changes in the magnetic gradient occurred in each of the analyzed events, corresponding to a magnetic gradient increase for converging motions, and to a gradient decrease for diverging motions (Wang 2006).

Using *Global Oscillation Network Group (GONG)* magnetograms in a statistical study of 15 X-class flares it was found that 75% of the locations exhibited flare-associated magnetic field changes within less than 10 min of the flare start, in a range of $B \approx 30$–300 G, while the changes corresponded to a decrease in two-thirds of the cases (Sudol and Harvey 2005).

Possible explanations for the rapid magnetic flux changes were proposed in terms of (i) the emergence of very inclined flux loops, (ii) a re-orientation of the magnetic field direction, (iii) expansion of the sunspot with less Zeeman saturation, or (iv) relaxation of penumbral fields by upward reconnecting magnetic fields above the photosphere (Wang et al. 2002; Yurchyshyn et al. 2004, Sudon and Harvey 2005). Combining the findings it became clear that magnetic reconnection plays a role in all cases. When an active region is away from the solar disk center, the reconnected transverse fields cause an apparent increase of the flux in the polarity towards the limb, and a decrease for the polarity closer to the disk center (Wang 2006).

The Lorentz force per unit area in the vertical direction,

$$\delta F_z = \frac{1}{4\pi}\left(B_z \delta B_z - B_x \delta B_x - B_y \delta B_y\right) \tag{12.5.1}$$

has been calculated from *Big Bear Solar Observatory (BBSO)* magnetograph data, which confirmed that the photospheric magnetic field responds to coronal field restructuring, and that the photospheric magnetic field near the polarity inversion line becomes more horizontal, as expected for the newly formed low-lying fields resulting from tether-cutting reconnection (Wang and Liu 2010; Wang et al. 2012; Petrie 2013). A detailed model of the Lorentz forces acting during the abrupt magnetic changes of the X2.2 flare is presented in Petrie (2013), while the Lorentz-force method applied to other flares is discussed in Petrie (2014).

Nonlinear force-free magnetic field (NLFFF) modeling of solar flares was conducted with Hinode/SOT vector magnetic field data and 14 NLFFF codes, revealing strong electrical currents that emerge together with the magnetic flux before a flare in a large-scale twisted flux rope topology, liberating a free magnetic energy of $\approx 10^{32}$ erg during a X3.4 GOES-class flare (Schrijver et al. 2008). It was concluded that (i) strong electrical currents emerge together with magnetic flux preceding the flare, (ii) that these currents are carried in an ensemble of thin strands, (iii) that the global pattern of these currents and field lines are compatible with a large-scale twisted flux rope topology, and (iv) that the magnetic energy change of $\Delta E \approx 10^{32}$ erg is sufficient to power the X3.4 flare and its associated CME (Schrijver et al. 2008).

The evolution of the magnetic field during major eruptive flares exhibits fast magnetic flux emergence (over 5 days) and strong shearing motion, leading to a quadrupolar sunspot complex that produced several major eruptions, including the first X-class flare (2011 February 14) of Solar Cycle 24 (Fig. 12.7). Magnetic (NLFFF) modeling yields free energies of $\approx 2.6 \times 10^{32}$ erg (Sun et al. 2012). During the flare, the photospheric field changes rapidly: the horizontal field was enhanced by 28% in the core region, and it becomes more inclined and more parallel to the polarity inversion. The flare-associated changes in the magnetic field were found to be consistent with the coronal "implosion" or tether-cutting reconnection model (Sun et al. 2012; Liu et al. 2012).

NLFFF modeling in a major statistical study of $\approx$ 400 M- and X-class flares using AIA/SDO and HMI/SDO data was performed with the goal to determine the potential energies E_P, the non-potential energies E_{NP}, the free energies $E_{free} = E_{NP} - E_P$, and the fraction of dissipated magnetic energies E_{diss} during flares, based on the difference of the free energy before and after the flares (Aschwanden et al. 2014). The underlying NLFFF model was based on the *vertical current approximation (VCA-NLFFF)*, which produces energy decreases by untwisting of helical (sigmoidal) coronal field lines. The free energies varied in the range of $E_{free}/E_p \approx$ 1%–25%, and the flare-dissipated energies amount to a substantial fraction of the free energy with a scaling of $E_{diss} \propto E_{free}^{0.9}$. A study of flare-rich but CME-poor active regions revealed that confined flares may leave weaker photospheric and coronal imprints of rapid magnetic changes than their eruptive counterparts (Sun et al. 2015).

Variations of the magnetic field may be caused even in the preflare phase, detectable as preflare brightenings, or as opposite-polarity magnetic flux elements, where the magnetic orientation of small bipoles is opposite to that of the ambient main polarities (Wang et al. 2017; Xu et al. 2017).

First detections of chromospheric magnetic field changes during an X1-class flare were made with IBIS Ca II 8542 Å by Kleint (2017). Photospheric magnetic changes are predominantly located near a polarity inversion line, and chromospheric changes occur near the footpoints of loops (Kleint 2017).

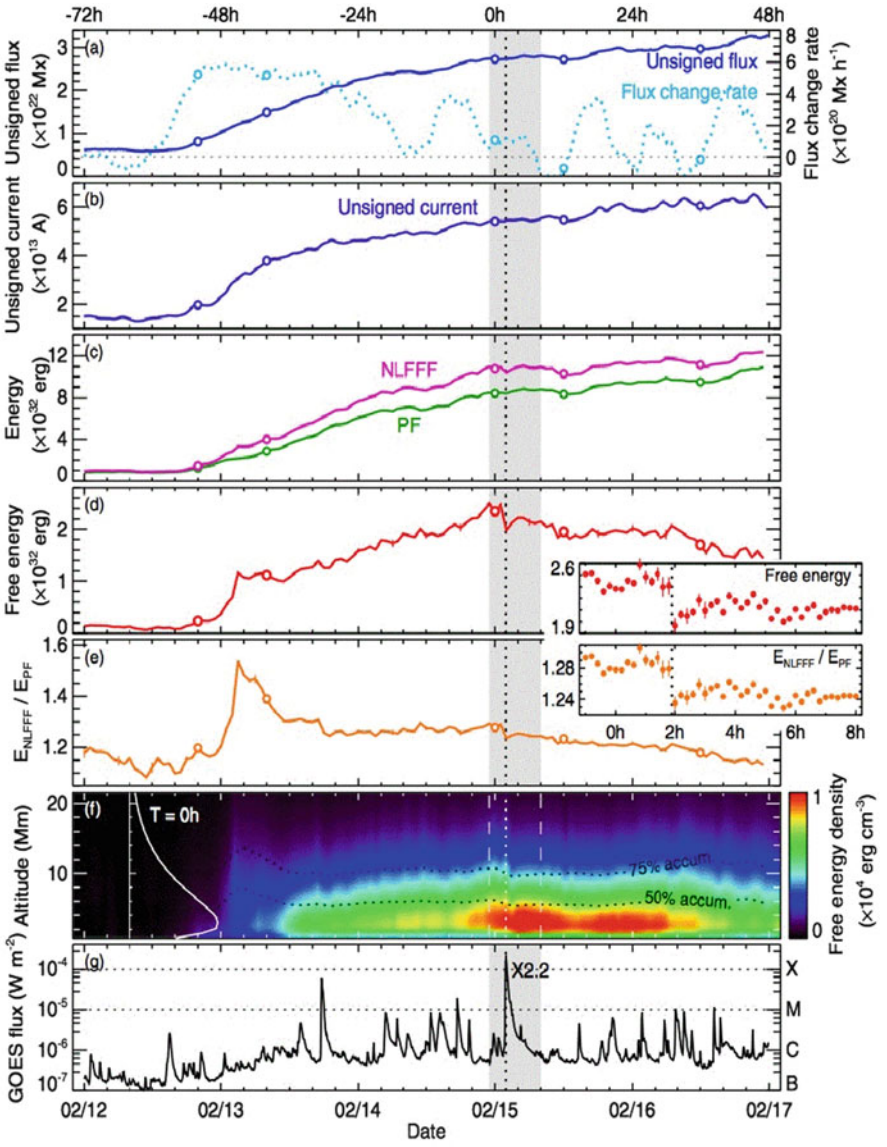

Fig. 12.7 Evolution of magnetic energy and related quantities of active region NOAA 11158 over 5 days (2011 February 12–17): (**a**) Total unsigned magnetic flux and flux change rate, (**b**) total unsigned current, (**c**) non-potential and potential field energy, (**d**) free energy, (**e**) ratio of nonpotential to potential energy (with insert for the X2.2 flare), (**f**) time-altitude diagram of average magnetic free energy density, and (**g**) GOES soft X-ray flux (1–8 Å), (Sun et al. 2012)

12.6 Magnetic Reconnection and Particle Acceleration

From magnetospheric in-situ measurements, laboratory experiments, analytical and numerical models, it is well known that particles are accelerated near the X-points in DC electric fields associated with magnetic reconnection (Drake et al. 2006; Chen et al. 2008; Che et al. 2011). If a reconnection process has multiple X-points, which is a characteristic of the secondary tearing-mode and coalescence instability, also known as *bursty reconnection mode*, the multitude of X-points strongly enhances the number of accelerated particles and their maximum energy, in comparison to single X-point reconnection (Kliem et al. 2000). The *impulsive bursty reconnection regime* produces plasmoids intermittently, by tearing and coalescence of magnetic islands near X-points, and this way modulates the local electric field at X-points, filamentary electric currents, the rate of accelerated (nonthermal) particles, and the associated fluxes observed in bursty hard X-ray emission and in quasi-periodic decimetric radio emission (Kliem et al. 2000). The energy spectra of accelerated particles during multi-island magnetic reconnection have been derived to have a power-law distribution function $\propto E^{-1.5}$ (Drake et al. 2013).

Magnetic reconnection at an X-point appears to be driven by lateral inflows and longitudinal outflows of plasma, where the particles become re-organized in the local diffusion region of vanishing anti-parallel magnetic fields. The first evidence of reconnection inflow in a solar flare was inferred from EUV observations of an X-point (visible in form of a cusp) with plasmoid ejection, formation of magnetic islands, and lateral inflow motions with a speed of $v \approx 5$ km s^{-1}, which corresponds to a reconnection rate or Alfvén Mach number of $M_A = 0.001$–0.03 (Yokoyama et al. 2001). Simultaneous observations of reconnection inflows and outflows were identified in the 2010 August 18 flare, with inflow speeds of $v_{in} = 12$–90 km s^{-1} and outflow speeds of $v_{out} = 220$–280 km s^{-1} (Takasao et al. 2012).

The spatial structure of the bursty reconnection mode is thought to be fractal, but continuously driven by ejection of (fractal) plasmoids, also called *plasmoid-induced reconnection in a fractal current sheet* (Shibata and Tanuma 2001). The initial plasmoid ejection was already part of the standard CSHKP flare model. The fractal structure of the current sheet is thought to occur with the following chain reaction: primary tearing, sheet thinning, Sweet-Parker current sheet, secondary tearing, further sheet thinning, etc. (Fig. 12.8). These processes occur repeatedly at smaller scales until a microscopic scale (either the ion Larmor radius or the ion inertial length) is reached where anomalous resistivity or collisionless reconnection occurs. The current sheet eventually has a fractal structure with many plasmoids, magnetic islands, and X-points of various sizes (Shibata and Tanuma 2001). The first relaxation episode after the initial thinning and (primary) tearing instability can explain the initial downward motion of the flare hard X-ray source before the hard X-ray source gradually moves upward (Sui et al. 2004; Ji et al. 2008), which is also called the *collapsing trap* (Veronig et al. 2006). The initial downward motion may also create large-scale Alfvén wave pulses and turbulent cascades, which can accelerate particles in the denser low-altitude regions and ameliorate the

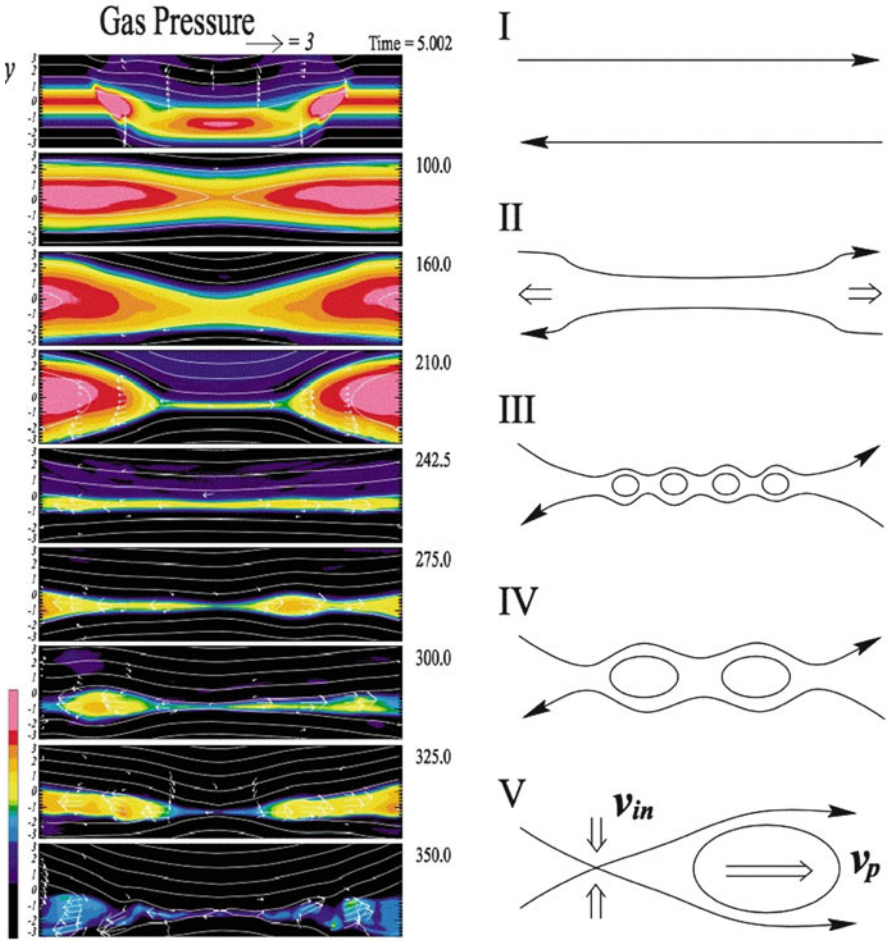

Fig. 12.8 *Right:* The scenario of plasmoid-induced reconnection in a fractal current sheet, which involves: The initial current sheet (I), current sheet thinning and evolution into Sweet-Parker sheet (II), secondary tearing of Sweet-Parker sheet (III), coalescence of magnetic islands (IV), and ejections of plasmoids (V). *Left:* Numerical simulation of the same scenario with time evolution (from top to bottom panel), where the color scale corresponds to the gas pressure, (Shibata and Tanuma 2001)

number problem (Fletcher and Hudson 2008). However, particle acceleration near the footpoints of flare loops disagrees with electron time-of-flight measurements (Aschwanden et al. 1996).

The magnetic field configuration during the reconnection process was found to have a sigmoid structure (Ji et al. 2008; Zhao et al. 2016; Li and Zhang 2015), an X-shaped ribbon structure (Li et al. 2016), a sheared arcade that evolved into a less sheared postflare arcade (Aulanier et al. 2012), a fan-spine magnetic

topology (Sun et al. 2013), J-shaped ribbons (Janvier et al. 2014), hooked flare ribbons (Zhao et al. 2016), or quasi-separatrix layers (Aulanier et al. 2006; Janvier et al. 2013, 2016; Dudik et al. 2014; Zhao et al. 2016). A further class of magnetic configurations are δ-sunspots, which have been broken down into the 4 categories of spot-spot, spot-satellite, quadrupole, and inter-active region cases (Toriumi and Takasao 2017; Toriumi et al. 2017).

The electric field E_c in reconnecting current sheets has been inferred during flares in terms of the Lorentz force, i.e., $E_c = v_{\parallel} B_n$, exerted by the horizontal flare footpoint motion $v_{\parallel}$ and the normal component of the magnetic field B_n, yielding a footpoint motion of $v_{\parallel} \approx 20$–100 km s^{-1} and an electric field of $E_c \approx 90$ V cm^{-1} (Qiu et al. 2002). Correlations between the hard X-ray flux and the upward motion were found, which confirmed the theoretically expected relationship between the reconnection rate and the flux of accelerated electrons (Sui et al. 2004).

Evidence for the X-point structure of magnetic reconnection in flares has been provided by the observation of double hard X-ray sources symmetrically located above and below a coronal X-point (Sui and Holman 2003; Liu et al. 2008, Sect. 12.3)

The time evolution of *bursty reconnection* is highly intermittent and dynamic, which has also been modeled with a *slipping magnetic reconnection* scenario in *quasi-separatrix layers (QSL)*, where successive reconnection occurs that is seen as an apparent "flipping" or "slipping" motion (Aulanier et al. 2006; Janvier et al. 2013, 2016; Dudik et al. 2014; Li and Zhang 2015).

12.7 Microflares and Nanoflares

The size distribution of flares extends from maximum values of $E \lesssim 10^{33}$ erg down to $E \gtrsim 10^{24}$ erg, which covers about 9 orders of magnitude (Fig. 6.14; Aschwanden et al. 2000b). Small-sized flares with an energy range of 10^{27}–10^{29} erg, the smallest events that are detected in hard X-ray wavelengths, are also called *microflares*, while even smaller events are named *nanoflares*. RHESSI registered hard and soft X-rays from over 25,000 microflares (Christe et al. 2008; Hannah et al. 2007, 2008, 2010, 2011; Stoiser et al. 2007), which were found to be distributed evenly in the northern and southern mid-latitude band (Fig. 12.9), and all are associated with active regions, and thus they are very important for understanding the heating of active regions, which may be different from the heating of the corona in *"Quiet Sun"* regions (Sect. 6.8)

Some early statistics of nanoflares/microflares in Quiet Sun regions has been gathered from analyzing images in EUV wavelengths with the *EUV Imaging Telescope (EIT)* onboard SOHO, yielding a power law distribution of $N(E) \propto E^{-\alpha}$, with power law slopes of $\alpha \approx 2.3$–2.6, in the energy range of $E \approx 8 \times 10^{24}$–$1.6 \times 10^{26}$ erg (Krucker and Benz 1998). It was concluded that the extrapolation of the same power law slope down to energies of 3×10^{23} erg would constitute sufficient

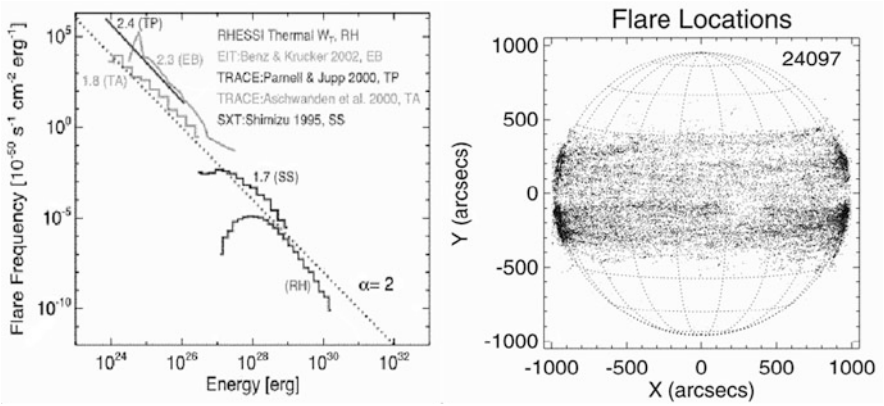

Fig. 12.9 *Left:* Synthesis of frequency distributions of the thermal energy of 8161 RHESSI microflares (RH) in the context of thermal energy distributions of nanoflares (TA, TP, and EB) and active region transient brightenings (SS). The dotted line indicates a power-law index of $\alpha = 2$. *Right:* Flare locations of 24,097 microflares detected with RHESSI, which spread over the two low-latitude bands. Note that the (centroid) locations have all a very low coronal height (Hannah et al. 2008; Christe et al. 2008)

energy to match the coronal heating requirement in the Quiet Sun (Krucker and Benz 1998), but the extrapolation of the power law size distribution to unobserved energies is questionable (Benz and Krucker 2002), especially for power law slopes above the critical value $\alpha \geq 2$, where the size distribution diverges at the low end (Hudson 1991). From multi-wavelength observations of small heating events in the Quiet Sun, using EIT/SOHO, CDS/SOHO, and the *Very Large Array (VLA)* in centimeter wavelengths, it was established that heating events with thermal energies of $\approx 10^{26}$ erg share many common thermal and non-thermal characteristics of larger flares, and thus they can be considered as miniature versions of regular flares, with an energy size corresponding to microflares (as detected in hard X-rays earlier) or large nanoflares (Krucker and Benz 2000).

Nanoflare statistics in the Quiet Sun was then obtained with the *Transition Region And Coronal Explorer (TRACE)* instrument, which had a pixel size of $0.5''$ that was three times smaller than EIT ($1.59''$), which yielded energy size distributions in the range of $E \approx 10^{24}$–10^{26} erg (Parnell and Jupp 2000; Aschwanden et al. 2000b). Although the energy estimates were compatible with data from EIT and TRACE, the power law slope of the size distributions differed significantly, being $\alpha \approx 2.3$–2.6 for EIT (Krucker and Benz 1998), $\alpha \approx 2.4$–2.6 (Parnell and Jupp 2000) or $\alpha \approx 1.8$ (Aschwanden et al. 2000b) for TRACE, a mismatch that resulted from different assumptions of the geometric flare volume model, incomplete temperature coverage, event detection thresholds, and event selection methods (Aschwanden et al. 2000a,b; Benz and Krucker 2002). Nevertheless, the best-fitting size distribution that is consistent with nanoflare statistics in EUV and

microflare statistics in soft X-rays was found to scale as (Aschwanden et al. 2000b),

$$N(E) \approx 10^{-46} \left(\frac{E}{10^{24}\ \mathrm{erg}} \right)^{-1.8} \qquad \mathrm{s}^{-1}\ \mathrm{cm}^{-2}\ \mathrm{erg}^{-1}\ . \tag{12.7.1}$$

which is shown in Fig. 6.14. Heating events in the picoflare regime $E \approx 10^{21}$–10^{24} erg were found to be implausible, because the scaling laws of the flare area, flare temperature, flare density, and chromospheric height extrapolated to these lower energies violate physical conditions that are conducive to coronal heating (Aschwanden et al. 2000b). Further studies on nanoflare statistics improved on the fractal geometry of nanoflares and on more complete temperature coverage (combining EUV data from TRACE with soft X-ray data from Yohkoh), yielding fractal Hausdorff dimensions of $D = 1.5 \pm 0.2$ and flatter size distributions of the thermal energy with a power law slope of $\alpha = 1.54 \pm 0.11$ (Aschwanden and Parnell 2002).

Since the coronal heating problem remained undecided after the controversial results of nanoflare statistics in EUV and soft X-ray wavelengths, the search for a hot component in microflares (using RHESSI data) continued. Open-shutter RHESSI observations of 3–15 keV X-rays revealed active region brightenings with a thermal component of $T = 6$–14 MK, which dominates in the 3–9 keV energy range and was interpreted in terms of beam-driven evaporation (Benz and Grigis 2002). Hard X-ray microflares were detected down to 3 keV, corresponding to the GOES-class level of B6 to A6, which exhibited a non-thermal component down to $\approx$ 6–7 keV, with energies of 10^{26}–10^{27} erg, and steep power law slopes of $\gamma \approx 5$–8 (Krucker et al. 2002). Systematic studies of microflares detected by RHESSI yielded temperatures of $T \approx 11$–15 MK, which are likely to be biased towards too high values, because they fit the high-temperature tail of the *differential emission measure (DEM)* distributions only and because RHESSI is not sensitive to emission measures at lower temperatures (Stoiser et al. 2007), a bias that affects also other published results as comparisons between GOES and high RHESSI temperatures demonstrate (e.g., Battaglia et al. 2005; Ryan et al. 2014; Hannah et al. 2008; McTiernan 2009; Reale et al. 2009).

RHESSI provided also the first limits on the 3–200 keV X-ray spectrum of the Quiet Sun, using a newly developed chopping technique (fan-beam modulation) during seven off-pointing periods during 2005–2006, when the GOES level was down to a background flux of 10^{-8}–10^{-7} W m^{-2}. These lower limits at 3–6 keV correspond to coronal temperatures of $T \leq 6$ MK and can even be used to estimate the axion-to-photon coupling constant or cosmic ray effects (Hannah et al. 2007, 2010).

Large statistics of RHESSI-detected microflares have been undertaken, yielding 25,705 microflares during the years of 2002–2007, using an automated flare-finding algorithm in the 6–12 keV energy range (Christe et al. 2008). The main microflare duration is $\approx$ 6 min, the time-averaged energy is $\lesssim 10^{26}$ erg, and the peak count rate size distributions show power law slopes of 1.50 ± 0.03 at 3–6 keV, or a

range of 1.50–1.58 for different energy ranges and years (Christe et al. 2008). Statistical distributions of thermal and nonthermal energies, emission measures, and temperatures of RHESSI-detected microflares are presented in Hannah et al. (2008), which demonstrate that they fit a natural extension of the size distributions of nanoflares and active region brightenings, in the energy range of $E = 10^{27}$–10^{30} erg (Fig. 12.9). See also Hannah et al. (2011) for a review on microflare statistics.

Evidence for nonthermal particles in coronal microflares, hypothetically being heated impulsively by Parker-type nanoflares, was sought by analysis of chromospheric brightenings in *Interface Region Imaging Spectrograph (IRIS)* data, which revealed small events with rapid variability ($\approx$ 20–60 s) of intensity and velocity on small spatial scales of $\lesssim$ 500 km, and blueshifted components (Testa et al. 2014; Polito et al. 2015; Young et al. 2015). Numerical simulations with the RADYN code can reproduce small heating events with thermal energies of $E \approx 6 \times 10^{24}$ erg, produced by electron beams that penetrate into the transition region (Testa et al. 2014), but it is not clear whether those events correspond to the microflares detected by RHESSI. Similarly small flares ($\lesssim$ 500 km) were observed also with the 1.6-m *New Solar Telescope (NST)* (Jing et al. 2016).

12.8 Flare Hard X-Ray Oscillations

There are two basic types of oscillations: (i) Resonance phenomena or normal modes (with eigen-values), such as a standing MHD wave, and (ii) *nonlinear limit cycles*, which are manifestations of self-organizing systems, where a driving force is counteracted by a negative feedback force. The two types of oscillations can be distinguished by their degree of periodicity, i.e., MHD waves generally show a strict periodicity (although often with a damped oscillation amplitude), while nonlinear limit cycles are quasi-periodic (with occasional glitches). The physical mechanism of an oscillator system needs to be identified indirectly, while the detection of oscillations is generally faciliated by a secondary (radiation) mechanism, such as free-free bremsstrahlung in hard X-ray wavelengths, or plasma emission and gyrosynchrotron emission in radio wavelengths. While numerous observations of oscillations were reported earlier, much progress in the new millennium has been made from imaging observations in many wavelengths (for reviews see Aschwanden 1987; Nakariakov and Melnikov 2009).

A sequence of 4 periodic pulses with a period of $P = 6.6$ s was detected during a flare with the *Hard X-ray Telescope (HXT)* onboard Yohkoh in three energy bands between 14 keV and 53 keV, as well as with the *Nobeyama Radio Heliograph (NoRH)* (Asai et al. 2001). Because the period is close to the Alfvén transit time along the flare loop, it was concluded that the number of accelerated electrons is modulated by macroscopic magnetic structures, such as MHD oscillations in flare loops (Asai et al. 2001).

First high-resolution imaging observations of *quasi-periodic pulsations (QPP)* during flares were obtained from RHESSI (3–25 keV), from which evidence for the

presence of a trans-equatorial loop with kink-mode MHD oscillations was obtained (Foullon et al. 2005). The QPPs were interpreted as periodic pumping of electrons in a compact flaring loop, modulated by oscillations in a magnetically linked and larger loop acting as a long-period MHD resonator, for the 2004 February 5–6 flare with a loop length of $L \approx 500$–600 Mm, periods of $P = 8$–12 min, and Alfvénic phase speeds of $v_{ph} = 2L/P = 1400$–2500 km s^{-1} (Foullon et al. 2005). QPP events can be subdivided into a long-periodic class where an external large-loop resonator is involved, and into a short-periodic class that contains single-loop fast kink-mode MHD oscillations (Foullon et al. 2010).

A considerable number of flare pulsation events in hard X-rays were reported from RHESSI observations (P=480–720 s, Foullon et al. 2005; P=240 s, Dauphin et al. 2005; P=120–240 s, Ofman and Sui 2006; P=227–280 s, Li and Gan 2008; P=16 s, Inglis et al. 2008; P=14.5–18.4 s, Fleishman et al. 2008; P=15, 36 s, Zimovets and Struminsky 2010; P=600–1080 s, Foullon et al. 2010; P=1–30 s, Dolla et al. 2012; P=25–120 s, Ning 2014; P=8–270 s, Kuznetsov et al. 2016; P=180 s, Kumar et al. 2016). An interpretation in terms of a physical model that fits the data with a unique solution could often not be established. Observational constraints include not only the periods, densities, temperatures, and magnetic fields, but also the microwave modulation depth, the spectral index of optically thin radio emission, the degree of circular polarization, and the electron pitch-angle distribution (Fleishman et al. 2008). Double-periodic emission was detected ($P_1 = 16$ s, $P_2 = 36$ s), which was attributed to MHD oscillations in two spatially separated, but interacting systems of flaring loops (Zimovets and Struminsky 2010).

For the > 25 keV quasi-periodic oscillations of the 2005 January 19 flare it was suggested that the oscillations are due to variations of the current magnitude in the reconnection region, induced by Alfvénic or super-Alfvénic beams. The electric current fluctuations modulate the electric field magnitude, and consequently modulate the electron acceleration and associated thick-target hard X-ray emission (Ofman and Sui 2006).

Besides RHESSI, quasi-periodic pulsations of hard X-ray or gamma-ray emission was also detected with *WATCH/Granat* (P=143.2±0.8 s, Terekhov et al. 2002); with the *Hard X-ray Spectrometer (HXRS)* onboard the *Energy Multi-Spectral Thermal Imager (MTI)* (P=25–48 s, Farnik et al. 2003); with SONG/CORONAS-F (P=40 s, Nakariakov et al. 2010), with HXT/Yohkoh (Jakimiec and Tomczak 2010, 2012), with the *Fermi Gamma-Ray Burst Monitor (GBM)* (Gruber et al. 2011; Li et al. 2015; with the *Euv Spectro Photometer (ESP)* onboard SDO and the *Project of On-Board Autonomy (PROBA)* (Dolla et al. 2012); The detection of quasi-periodic pulsations in solar flare gamma-rays was disputed for data that are governed by red-noise (Gruber et al. 2011).

The modulation of quasi-periodic hard X-rays has also been interpreted in terms of magnetic trapping in the temporary cusps above flare loops where X-type reconnection occurs according to standard flare models. During the compression of an oscillating magnetic trap, particles are accelerated, while chromospheric

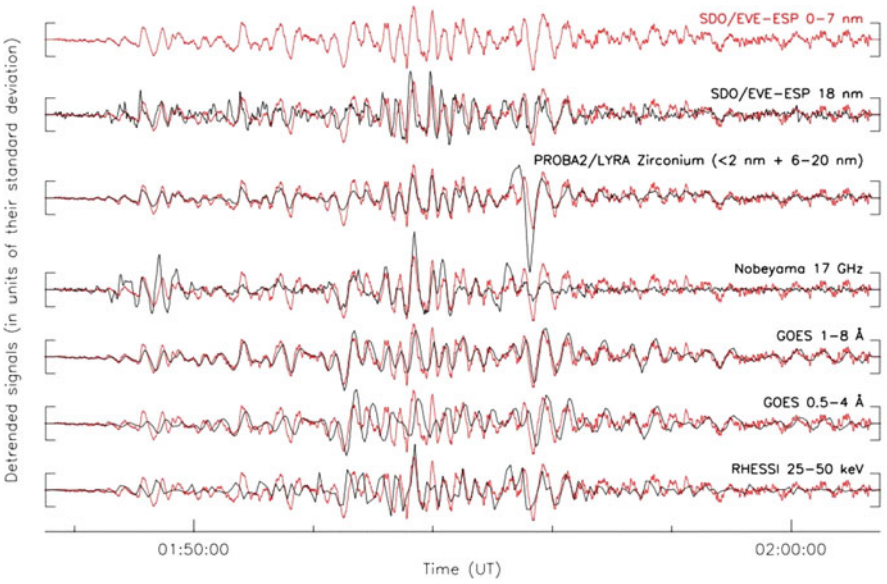

Fig. 12.10 Normalized time profiles of different instruments during the 2011 February 15, X2.2 flare. The time profiles are detrended by subtracting a signal that is smoothed with a 20 s boxcar. The ESP0–7/SDO light curve (red) is overplotted on each curve for comparison (Dolla et al. 2012)

evaporation fills the trap and quenches particle acceleration (Jakimiec and Tomczak 2010, 2012), leading to a quasi-periodic nonlinear limit cycle between the two competing processes.

The 2011 February 15 (GOES X2.2-class) flare was observed with many instruments (ESP/AIA, PROBA, GOES, NoRH), where a time lag of $\approx$ 9 s was measured between EUV and soft X-ray pulsations (Fig. 12.10). This was interpreted in terms of the time difference between the directly-precipitating electrons and the trapped electrons (with larger pitch angles) that are scattered into the loss-cone after a collisional deflection time, before they produce bremsstrahlung in hard X-rays (Dolla et al. 2012). The relative time delays, however, are subject to corrections due to a later revision of the GOES time stamps (Dolla, private communication). Although pulsations in hard X-rays and UV are often well-correlated temporally, the detailed spatial evolution of UV ribbons and hard X-ray sources is not understood (Inglis and Gilbert 2013).

One observation of quasi-periodic pulsations has been interpreted as a two-ribbon flare with subsequent reflections of slow waves that propagate in up and downward direction (Nakariakov and Zimovets 2011), which has been disputed by Inglis and Dennis (2012), because no correlation between the hard X-ray footpoint separation and the pulse timing was found.

Analyzing quasi-periodic pulsations from both gamma-rays (GBM/Fermi) and chromospheric Doppler velocities (with IRIS) leads to the conclusion that QPPs are

produced by non-thermal electrons that are accelerated by induced quasi-periodic magnetic reconnection in a flare (Li et al. 2015; Hayes et al. 2016). The observations are consistent with a series of energy injections by nonthermal particle beams into the chromosphere (Brosius et al. 2016).

A systematic analysis of 29 hard X-ray flares with quasi-periodic pulsations in the 50–100 keV range suggests that an eruptive flux rope can act as a trigger of the pulsating flare energy release (Kuznetsov et al. 2016).

In one case a 3-min QPP was observed that was highly correlated with the 3-min oscillations in a nearby sunspot (Kumar et al. 2016). It was suggested that the periodic reconnection (modulated either by a sunspot slow-mode wave or by an untwisting filament) at a magnetic null point most likely causes the repetitive particle acceleration.

QPPs in hard X-rays can also be detected from the time derivative of the GOES soft X-ray light curves. For instance, the X3.2 flare on 2013 May 14 reveals a total of 163 distinct pulses over a duration of 2 hours (Dennis et al. 2017).

12.9 Flare Radio Emission

Solar radio bursts are usually subdivided into coherent and incoherent emission mechanisms. Incoherent mechanisms (such as free-free bremsstrahlung, gyro-emission, or gyro-synchrotron emission) are additive, in the sense that the number of emitted photons is linear to the volume in which they are emitted. Coherent radio emission, in contrast, is multiplicative, in the sense that they have a nonlinear scaling between the observed flux and the emitting volume. Coherent radio bursts undergo some resonant wave-particle interaction process that displays exponential growth during some time interval, driven by some unstable anisotropic particle distribution (in momentum and pitch angle space), such as the (bump-in-tail) beam instability (giving rise to type III bursts), or the loss-cone instability (producing quasi-periodic decimetric oscillations or electron cyclotron maser spikes). The physical mechanisms of solar radio bursts are difficult to pin down by remote-sensing observations, but some progress occurred by identifying the underlying instabilities using new multi-frequency imaging data. For recent reviews see Benz et al. (2005), Chernov (2006), Nindos et al. (2008), and White et al. (2011).

Statistics of radio fluxes, spectral peaks, and spectral slopes have been obtained from 412 solar radio bursts observed during 2001–2002 at 40 frequencies in the 1.2–18 GHz range with the *Owens Valley Solar Array (OVSA)* (Nita et al. 2004). A survey of radio emission during 201 selected X-ray solar flares in the frequency range of 100 MHz to 4 GHz was carried out with the *Phoenix-2 spectrometer* of ETH Zürich, which yielded the following morphological burst types: type III's, pulsations, diffuse continua, narrowband spikes, type IV bursts, and high-frequency broadband (gyro-synchrotron) bursts (Benz et al. 2005). A survey of solar radio bursts with drifting (zebra-like) stripes in emission and absorption offers two possible interpretations: (i) interactions between electrostatic plasma

waves and whistlers, and (ii) radio emission at the *double plasma resonance (DPR)* (Chernov 2006). Standing and propagating sausage-mode oscillations are expected to modulate the DPR layers differently, which could be used as a diagnostic (Yu et al. 2016).

Both microwave and hard X-ray spectra are sensitive to low- and high-energy cutoffs of the electron distribution function. The optically thick portion of a microwave spectrum is enhanced and smoothed by a low-energy cutoff, while a hard X-ray spectrum is flattened below the cutoff energy. The determination of the high-energy cutoff from these spectra establishes the highest electron energies produced by the acceleration mechanism, while determination of the low-energy cutoff is crucial for establishing the total energy in accelerated electrons (Holman 2003). Joint modeling of microwave and hard X-ray spectra suggests a break point of the electron spectra at a few hundred keV, and harder spectra at higher energies that contribute to microwave gyro-synchrotron emission (Asai et al. 2013). Modeling of the gyro-synchrotron emission of an impulsive, but X-ray-poor impulsive flare (Fig. 12.11; Bastian et al. 2007), indicated the absence of chromospheric evaporation, and possibly a large magnetic mirror ratio that disables electron trapping (Bastian et al. 2007).

From microwave imaging with the *Nobeyama Radio Heliograph (NoRH)* at frequencies of 17 and 34 GHz (gyro-synchrotron emission), an initial shrinkage of radio flare loops was observed (Li and Gan 2005), which corresponds to the initial downward motion of coronal flare loops seen in soft and hard X-rays (Sect. 12.3).

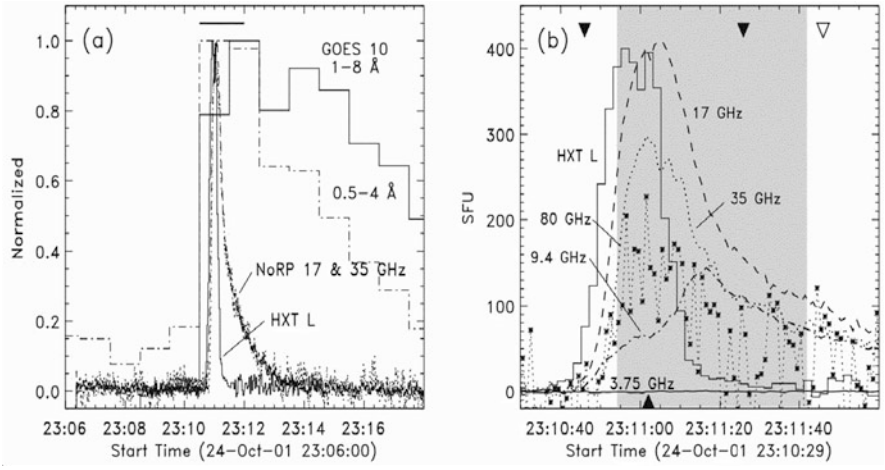

Fig. 12.11 Time profiles of the 2001 October 24, 23:11 UT, flare. (**a**) Nobeyama Radio Heliograph (NoRH 17 and 35 GHz), GOES (1–8, and 0.5–4 Å), HXT/Yohkoh L-band 13.9–22.7 eV. (**b**) Detail of the NoRP (17 and 35 GHz) and HXT L observations, with additional data from the *Owens Valley Solar Array (OVSA)*, (3.75, 9.4, 80 GHz, and *TRACE 171 Å* (histogram), Bastian et al. 2007)

Quasi-periodic decimetric radio emission in the frequency range of $\nu = 0.6$–2 GHz during the flare of 1992 October 25, 09:25 UT, has been interpreted in terms of a dynamic magnetic reconnection scenario. Quasi-periodic particle acceleration episodes are thought to result from dynamic processes in a large-scale current sheet, where reconnection is dominated by repeated formation and subsequent coalescence of magnetic islands (known as "secondary tearing" or "impulsive bursty" regime of reconnection), while a continuously growing plasmoid is fed by newly coalescing islands (Fig. 12.8, Kliem et al. 2000). 2-D MHD simulations reproduce bursty or quasi-periodic electric currents at the main X-points of Petschek-like reconnection. Related studies focus on the reconnection of a kinking flux rope that triggers the ejection of a microwave and hard X-ray plasmoid (Kliem et al. 2010; Karlicky and Kliem 2010), or on electromagnetic emission generated by Langmuir waves during a coalescence of plasmoids (Karlicky et al. 2010; Karlicky and Barta 2011).

Quasi-periodic broadband radio emission was observed during the 2003 June 15 flare, for which a model with quasi-periodic acceleration and injection of fast electrons was found to be fit the observed modulation and spectra better than a model with MHD oscillations (Fleishman et al. 2008). The 1998 May 8 flare, which showed quasi-periodic pulsations in microwave (17 GHz) and soft X-ray wavelengths, was found to be consistent with the interpretation of sausage-type MHD oscillations which periodically modulate the flare loop cross-section and magnetic field (Inglis et al. 2008). Except for this particular event, the prevalence of oscillatory signals in other solar flares was questioned, based on a Bayesian analysis of power law-like Fourier power spectra of hard X-ray and microwave data (Inglis et al. 2015). An alternative way to analyze periodic signals was attempted with the *Hilbert-Huang transform* applied to an *ensemble empirical mode decomposition (EEMD)* technique (Kolotkov et al. 2015).

Occulted coronal hard X-ray sources during Masuda-type flares (above the limb) have been observed not only in hard X-rays (with RHESSI), but also in microwaves (with NoRH), which both could be modeled with a single electron population that produces free-free bremsstrahlung and gyro-synchrotron emission, suggesting that the above-the-loop-top source is the electron acceleration region (Krucker et al. 2010). Taking the starting frequency of type III bursts into account, the height of the acceleration region was inferred to be well above the soft X-ray loop-top, i.e., at $h \approx 40$–60 Mm (Reid et al. 2011).

Evidence for a termination shock in standard solar flare models was put forward with high-cadence radio spectroscopy, where it is shown that a disruption of the shock coincides with an abrupt reduction of the energetic electron population (Chen et al. 2015).

Numerical simulation tools have been developed for modeling and forward-fitting of microwave and X-ray images, which allows to import magnetic field extrapolation models, to populate loops with non-uniform plasma densities and temperatures, as well as nonthermal electron distributions, and to compute radio and X-ray spectra, based on gyro-synchrotron emission, using SDO, NoRH, and RHESSI data (Nita et al. 2015).

For the 2011 September 23–24 flare, a filament was observed with a periodic alternate rotation in the clockwise and counter-clockwise directions with a 3-min period, which moreover was highly correlated with a 3-min global p-mode oscillation in a nearby sunspot (Kumar et al. 2016). It was suggested that the periodic reconnection at a magnetic null point causes the repetitive particle acceleration, the QPP observed in hard X-rays, microwaves, and type III radio bursts (Kumar et al. 2016).

12.10 White-Light Flares

"*White light*" refers to continuum emission in excess of the photospheric background. White-light flares have an excess intensity (normalized to local Quiet Sun values) by factors in the range of $\approx$ 0.1–4.1, in a sample of 11 events observed with TRACE and RHESSI during 2002–2004 (Hudson et al. 2006). TRACE was able to detect white-light flares by using the full broad-band response of the CCD sensor, producing images that were not compromised by ground-based seeing, and TRACE had excellent pointing stability, as well as high spatial (pixel size of $0.5''$) and temporal resolution. There is a strong association of the TRACE white-light emission (including UV and optical wavelengths) with hard X-ray sources observed with RHESSI. Although white-light emission is observed in the largest flares, it is also observed down to the GOES C1.6 class level. It is believed that white-light continuum is produced in essentially all flares, but its detection is subject to photon statistics, contrast, and background solar fluctuations (see reviews by Hudson et al. 2006, and Hudson 2016).

An earlier catalog of white-light flares has been compiled by using data from the aspect camera of the *Soft X-ray Telescope (SXT)* onboard Yohkoh, made in the Fraunhofer g-band with a pixel size of $2.46''$ and a typical sample interval of $\approx$ 10 s (Matthews et al. 2003). The catalog comprises 28 flare events, observed during 1991–1992, down to the GOES C7.8-class level. A maximum average contrast factor of 0.3 relative to the pre-flare continuum brightness was detected at the flare location. Comparing flares with and without white-light continuum, is was noted that white-light flare emission is also strongly related to coronal overpressure, indicating a component with a thermal, rather than a non-thermal origin (Matthews et al. 2003). On the other hand, a recent statistical study of 43 M- and X-class flares observed in hard X-rays (RHESSI) and white-light (HMI/SDO) has been conducted by Kuhar et al. (2016), which confirms a high correlation between the white-light flux and $>$ 30 keV hard X-rays, or with the $>$ 50 keV electron flux, and corroborates the interpretation that white-light emission is produced by $>$ 50 keV electrons (Kuhar et al. 2016).

A white-light flare occurring on 2007 August 24 was observed with the *Swedish Solar Telescope (SST)* on La Palma, which acquired $H\alpha$ continuum with a sampling of $0.068''$ per pixel at the telescope's diffraction limit, and Ca II continuum with a sampling of $0.034''$ per pixel, both with a cadence of 0.12 s. Because of this much

higher spatial resolution than previously used (with TRACE), the flare displayed smaller kernels with a diameter of 300 km, with a contrast ratio of a factor 3 above the quiescent flux, and a delay of $\approx$ 2 min between the continuum emission of the impulsive flare phase and the chromospheric emission. It was concluded that the observed white-light emission is caused by radiative back-warming, and that white-light emission is a common feature of all solar flares (Jess et al. 2008).

A detailed analysis of the 2001 August 25, 16:30 UT, white-light flare observed with TRACE and HXT/Yohkoh concluded that the enhanced white-light emission originates in the chromosphere and temperature minimum region via nonequilibrium hydrogen ionization induced by direct collisions with the electron beam and by backwarming of the lower atmosphere. The three flare kernels observed in hard X-rays move along a magnetic separatrix at 400 km s^{-1}, which is considered as evidence of particle acceleration models that energize the electrons via magnetic reconnection at magnetic separators (Metcalf et al. 2003). In the 2003 October 29 white-light flare observed with the *Dunn Solar Telescope (DST)* at NSO/Sacramento Peak in near-infrared continuum at 1.56 μm, it was concluded that an interpretation in terms of back-warming is more likely than high-energy electron precipitation (Xu et al. 2004). On the other side, from analysis of the same flare it was concluded that photospheric heating by high-energy protons is likely to explain seismic emission from acoustically active flares (Donea and Lindsey 2005). Modeling a set of 9 white-light flares observed with RHESSI and TRACE led to the conclusion that the power required by the white-light luminosity enhancement is comparable to the electron beam power required to produce hard X-ray emission only if the low-energy cutoff to the spectrum is less than 25 keV, and thus such low-energy electrons cannot penetrate deep into a collisional thick-target, which places the co-spatial white-light sources into the upper chromosphere (Fletcher et al. 2007). The centroid heights of hard X-ray and white-light footpoints were directly measured (at the limb) to amount to $h = 305 \pm 170$ km (for $\approx$ 40 keV photons) and $h = 195 \pm 70$ km (at the opacity level of $\tau = 1$ of the 5000 Å wavelength) for the 2011 February 24, 07:35 UT, M3.5 flare (Martinez Oliveros et al. 2012), which is consistent with the electron beam precipitation model of white-light emission (Fig. 12.12). Another study finds altitudes of $h \approx 800$ km above the photosphere for co-spatial white-light and $>$ 30 keV hard X-ray sources (Krucker et al. 2015).

Possible mechanisms of white-light emission are heating in the chromosphere causing optically thin or thick emission from free-bound transitions of hydrogen, and heating of the photosphere causing enhanced H^- continuum brightness. These processes were studied by combining observations from IRIS, HMI/SDO, Hinode, IBIS, and RHESSI, yielding blackbody temperatures of $T \approx$ 6000–6300 K. The energy in $>$ 40 keV electrons was found to be sufficient to explain the extra continuum emission of (4–8) $\times 10^{10}$ erg s^{-1} cm^{-2} (Kleint et al. 2016). For the X1.6-class flare of 2014 October 22, 14:02 UT, the deposited energy in nonthermal electrons was calculated to be (3–7.7) $\times 10^{10}$ erg cm^{-2} s^{-1} for a low-energy cutoff of 30–40 keV, while the energy flux estimated from the changes in temperature in the chromosphere (inferred from Mg II lines) was found to be 6%–22% of the deposited energy, which further confirms that the continuum enhancement is caused by $\gtrsim$ 30

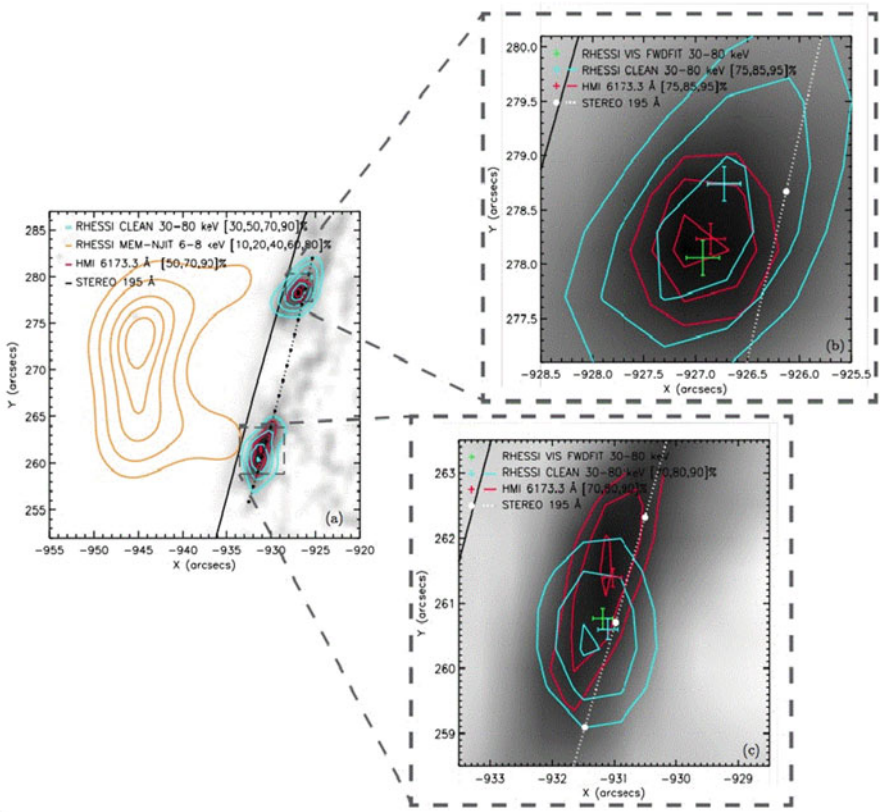

Fig. 12.12 HMI intensity continuum difference images (grey scale), white-light difference images (red), and RHESSI hard X-ray images 30–80 keV (blue), soft X-ray 6–8 keV RHESSI image (orange), and EUVI/STEREO source positions (white dots), of the 2011 February 24, 07:35 UT, flare (Martinez Oliveros et al. 2012)

keV nonthermal electrons (Lee et al. 2017). Recent numerical simulations with *radiative hydrodynamic (RHD)* codes investigate various emission mechanisms for white-light flares, such as hydrogen recombination continuum (Paschen) or the Thomson continuum due to scattering of disk radiation on flare electrons. For electron densities higher than 10^{12} cm^{-3}, the Paschen recombination continuum significantly dominates the Thomson scattering continuum (Heinzel et al. 2017).

Sampling the solar irradiance fluctuations in white-light with SOHO and GOES during solar flares, using a superposed epoch analysis, the white-light emission was found to be consistent with blackbody emission at $T \approx 9000$ K, while the white-light emission amounts to about 70% of the total radiated energy (Kretzschmar 2011). Using SOT/Hinode with optical continuum data taken in broadband red, green, and blue filters, blackbody temperatures of $T \approx 5000$–6000 K and a power of $E \approx 10^{26}$ erg emitted in optical wavelengths were found (Kerr and Fletcher 2014).

Statistical correlations between flare energies E and durations τ were determined in white-light superflares on solar-type stars also, and was found to be similar for both the Sun and the stars, i.e., $\tau \propto E^{0.4}$.

Velocity and magnetic transients were detected near the umbral boundary of the main sunspot during white-light flares with HMI/SDO, which are related to line profile changes of the Stokes parameters (Maurya et al. 2012).

Besides white-light (chromospheric) footpoint sources, there exist also (rarely reported) white-light ejecta, which are seen in coronal heights as continuum emission, rather than as line emission (Martinez Oliveros et al. 2014).

References

(12.1) Flare Gamma-Rays

Ackermann, M., Ajello, M., Albert, A., et al. 2014, *High-energy gamma-ray emission from solar flares: Summary of Fermi Large Area Telescope (LAT) detections and analysis of two M-class flares*, ApJ 787, 15, [46 c, 13 c/y].

Ackermann, M., Allafort, A., Baldini, L., et al. 2017, *Fermi-LAT observations of high-energy behind-the-limb solar flares*, ApJ 835, 219, [13 c, 13 c/y].

Ajello, M., Albert, A., Allafort, A., et al. 2014, *Impulsive and long duration high-energy emission from the very bright 2012 March 7 solar flares*, ApJ 789, 20, [53 c, 15 c/y].

Holman, G.D., Aschwanden, M.J., Aurass, H., et al. 2011, *Implications of X-ray observations for electron acceleration and propagation in solar flares*, SSRv 159, 107, [146 c, 22 c/y].

Holman, G.D. 2016, *Scientific considerations for future spectroscopic measurements from space of activity on the Sun*, JGR 121/12, 11,667, [7 c, 5 c/y].

Hurford, G.J., Schwartz, R.A., Krucker, S., et al. 2003, *First gamma-ray images of a solar flare*, ApJ 595, L77, [96 c, 7 c/y].

Hurford, G.J., Krucker, S., Lin, R.P., et al. 2006, *Gamma-ray imaging of the 2003 October/November solar flares*, ApJ 644, L93, [84 c, 7 c/y].

Kurt, V.G., Yushkov, B.Y., Kudela, K., et al. 2010, *High-energy gamma radiation of solar flares as an indicator of acceleration of energetic protons*, Cosmic Research 48, 70, [15 c, 2 c/y].

Kuznetsov, A.A., Nita, G.M., and Fleishman, G.D. 2011, *Gamma-ray and high-energy neutron measurements on CORONAS-F during the solar flare of 28 October 2003*, SoPh 268, 175, [24 c, 4 c/y].

Lin, R.P., Krucker, S., Hurford, G.J., et al. 2003, *RHESSI observations of particle acceleration and energy release in an intense solar gamma-ray line flare*, ApJ 595, L69, [264 c, 18 c/y].

Lin, R.P. 2006, *Particle acceleration by the Sun: Electrons, hard X-ray / Gamma-rays*, SSRv 124, 233, [19 c, 2 c/y].

Masson, S., Klein, K.L., Bütikofer, R., et al. 2009, *Acceleration of relativistic protons during the 20 January 2005 flare and CME*, SoPh 257, 305, [30 c, 4 c/y].

Murphy, R.J., Kozlovsky, B., Share, G.H., et al. 2007, *Using gamma-ray and neutron emission to determine solar flare accelerated particle spectra and composition and the conditions within the flare magnetic loop*, ApJSS 168, 167, [41 c, 4 c/y].

Nakariakov, V.M., Foullon, C., Myagkova, I.N., et al. 2010, *Quasi-periodic pulsations in the gamma-ray emission of a solar flare*, ApJ 708, L47, [44 c, 6 c/y].

Pesce-Rollins, M., Omodei, N., Petrosian, V., et al. 2015, *First detection of* $\geq$ *100 MeV gamma rays associated with a behind-the-limb solar flare*, ApJ 805, L15, [20 c, 8 c/y].

Schrijver, C.J., Hudson, H.S., Murphy, R.J., et al. 2006, *Gamma rays and the evolving, compact structure of the 2003 October 28 X17 flare*, ApJ 650, 1184, [20 c, 2 c/y].

Share, G.H., Murphy, R.J., Smith, D.M., et al. 2004, *RHESSI e+e- annihilation radiation observations: Implications for conditions in the flaring solar chromosphere*, ApJ 615, L169, [40 c, 3 c/y].
Shih, A.Y., Lin, R.P., and Smith, D.M. 2009, *RHESSI observations of the proportional acceleration of relativistic > 0.3 MeV electrons and > 30 MeV protons in solar flares*, ApJ 698, L152, [51 c, 6 c/y].
Smith, D.M., Share, G.H., Murphy, R.J., et al. 2003, *High-resolution spectroscopy of gamma-ray lines from the X-class solar flare of 2002 July 23*, ApJ 595, L81, [61 c, 4 c/y].
Tatischeff, V., Kozlovsky, B., Kiener, J., et al. 2006, *Delayed X- and gamma-ray line emission from solar flare radioactivity*, ApJSS 165, 606, [24 c, 2 c/y].
Trottet, G., Krucker, S., Lüthi, T., et al. 2008, *Radio submillimeter and gamma-ray observations of the 2003 October 28 solar flare*, ApJ 678, 509, [35 c, 4 c/y].
Vilmer, N., MacKinnon, A.L., and Hurford, G.J. 2011, *Properties of energetic ions in the solar atmosphere from gamma-ray and neutron observations*, SSRv 159, 167, [56 c, 9 c/y].

(12.2) Flare Hard X-Ray Ribbons

Asai, A., Isii, T.T., Kurokawa, H., et al. 2003, *Evolution of conjugate footpoints inside flare ribbons during a great two-ribbon flare on 2001 April 10*, ApJ 586, 624, [44 c, 3 c/y].
Asai, A., Yokoyama, T., Shimojo, M., et al. 2004, *Flare ribbon expansion and energy release rate*, ApJ 611, 557, [71 c, 5 c/y].
Aschwanden, M.J. and Alexander, D. 2001, *Flare plasma cooling from 30 MK down to 1 MK modeled from Yohkoh, GOES, and TRACE observations during the Bastille Day event (14 July 2000)*, SoPh 204, 91, [122 c, 7 c/y].
Dennis, B.R. and Pernak, R.L. 2009, *Hard X-ray flare source sizes measured with the RHESSI*, ApJ 698, 2131, [61 c, 7 c/y].
Fletcher, L. and Hudson, H.S. 2001, *The magnetic structure and generation of EUV flare ribbons*, SoPh 204, 69, [104 c, 6 c/y].
Fletcher, L. and Hudson, H.S. 2002, *Spectral and spatial variations of flare hard X-ray footpoints*, SoPh 210, 307, [84 c, 5 c/y].
Fletcher, L., Dennis, B.R., Hudson, H.S., et al. 2011, *An observational overview of solar flares*, SSRv 159, 19, [238 c, 37 c/y].
Fletcher, L., Hannah, I.G., Hudson, H.S., et al. 2013, *Flare ribbon energetics in the early phase of an SDO flare*, ApJ 771, 104, [22 c, 5 c/y].
Gallagher, P.T., Dennis, B.R., Krucker, S. et al. 2002, *RHESSI and TRACE observations of the 21 April 2002 X1.5 flare*, SoPh 210, 341, [97 c, 6 c/y].
Grigis, P.C. and Benz, A.O. 2005, *The evolution of reconnection along an arcade of magnetic loops*, ApJ 625, L143, [82 c, 7 c/y].
Jing, J., Lee, J., Liu, C., et al. 2007, *Hard X-ray intensity distribution along Hα ribbons*, ApJ 664, L127, [21 c, 2 c/y].
Kontar, E.P., MacKinnon, A.L., Schwartz, R.A., et al. 2006, *Compton backscattered and primary X-rays from solar flares: angle dependent Green's function correction for photospheric albedo*, A&A 446, 1157, [68 c, 6 c/y].
Krucker, S., Hurford, G.J., and Lin, R.P. 2003, *Hard X-ray source motions in the 2002 July 23 Gamma-ray flare*, ApJ 595, L103, [119 c, 8 c/y].
Krucker, S., Hudson, H.S., Jeffrey, N.L.S. 2011, *High-resolution imaging of solar flare ribbons and its implications on the thick-target model*, ApJ 739, 96, [69 c, 11 c/y].
Liu, C., Lee, J., Gary, D., et al. 2007, *The ribbon-like hard X-ray emission in a sigmoidal solar active region*, ApJ 658, L127, [28 c, 3 c/y].
Liu, C., Lee, J., Jing, J. et al. 2008, *The spatial distribution of the hard X-ray spectral index and the local magnetic reconnection rate*, ApJ 672, L69, [12 c, 1 c/y].

Masuda, S., Kosugi, T., and Hudson, H.S. 2001, *A hard X-ray two-ribbon flare observed with Yohkoh/HXT*, SoPh 204, 55, [71 c, 4 c/y].
Qiu, J. and Cheng, J. 2017, *Gradual solar coronal dimming and evolution of coronal mass ejection in the early phase*, ApJ 838, L6, [2 c, 2 c/y].
Savcheva, A., Pariat, E., McKillop, S., et al. 2015, *The relation between solar eruption topologies and observed flare features. I. Flare ribbons*, ApJ 810, 96, [36 c, 14 c/y].
Savcheva, A., Pariat, E., McKillop, S., et al. 2016, *The relation between solar eruption topologies and observed flare features. II. Dynamical evolution*, ApJ 817, 43, [20 c, 13 c/y].
Temmer, M., Veronig, A.M., Vrsnak, B., et al. 2007, *Energy release rates along Hα ribbons and the location of hard X-ray sources*, ApJ 654, 665, [43 c, 5 c/y].
Wang, H. and Liu, C. 2012, *Circular ribbon flares and homologous jets*, ApJ 760, 101, [65 c, 12 c/y].
Warren, H.P. and Warshall, A.D. 2001, *Ultraviolet flare ribbon brightenings and the onset of hard X-ray emission*, ApJ 560, 87, [43 c, 3 c/y].
Yang, K., Guo, Y., and Ding, M.D. 2015, *On the 2012 October 23 circular ribbon flare: Emission features and magnetic topology*, ApJ 806, 171, [27 c, 11 c/y].

(12.3) Coronal Hard X-Rays

Asai, A., Yokoyama, T., Shimojo, M., et al. 2004, *Downflow motions associated with impulsive nonthermal emissions observed in the 2002 July 23 solar flare*, ApJ 605, L77, [119 c, 9 c/y].
Aschwanden, M.J., Hudson, H.S., Kosugi, T., et al. 1996, *Electron time-of-flight measurements during the Masuda flare, 1992 January 13*, ApJ 464, 985, [74 c, 3 c/y].
Bain, H.M. and Fletcher, L. 2009, *Hard X-ray emission from a flare-related jet*, A&A 508, 1443, [16 c, 2 c/y].
Battaglia, M. and Benz, A.O. 2006, *Relations between concurrent hard X-ray sources in solar flares*, A&A 456, 751, [83 c, 7 c/y].
Battaglia, M. and Benz, A.O. 2007, *Exploring the connection between coronal and footpoint sources in a thin-thick target solar flare model*, A&A 466, 713, [22 c, 2 c/y].
Caspi, A. and Lin, R.P. 2010, *RHESSI line and continuum observations of super-hot flare plasma*, ApJ 725, L161, [71 c, 9 c/y].
Ishikawa, S., Krucker, S., Takahashi, T., et al. 2011, *On the relation of above-the-loop and footpoint hard X-ray sources in solar flares*, ApJ 737, 48, [20 c, 3 c/y].
Ji, H., Wang, H., Liu, C., et al. 2008, *A hard X-ray sigmoidal structure during the initial phase of the 2003 October 29 X10 flare*, ApJ 680, 734, [30 c, 3 c/y].
Krucker, S., White, S.M., and Lin, R.P. 2007a, *Solar flare hard X-ray emission from the high corona*, ApJ 669, L49, [38 c, 4 c/y].
Krucker, S., Hannah, I.G., and Lin, R.P. 2007b, *RHESSI and Hinode X-ray observations of a partially occulted solar flare*, ApJ 671, L193, [18 c, 2 c/y].
Krucker, S. and Lin, R.L. 2008, *Hard X-ray emissions from partially occulted solar flares*, ApJ 673, 1181, [84 c, 9 c/y].
Krucker, S., Battaglia, M., Cargill, P.J., et al. 2008, *Hard X-ray emission from the solar corona*, A&AR 16, 155, [123 c, 13 c/y].
Krucker, S., Hudson, H.S., Glesener, L., et al. 2010, *Measurements of the coronal acceleration region of a solar flare*, ApJ 714, 1108, [109 c, 15 c/y].
Lin, R.P., Krucker, S., Hurford, G.J., et al. 2003, *RHESSI observations of particle acceleration and energy release in an intense solar gamma-ray line flare*, ApJ 595, L69, [264 c, 28 c/y].
Liu, W., Petrosian, V., Dennis, B.R., et al. 2008, *Double coronal hard and soft X-ray source observed by RHESSI: Evidence for magnetic reconnection and particle acceleration in solar flares*, ApJ 676, 704, [75 c, 8 c/y].
Masuda, S., Kosugi, T., Hara, H., et al. 1994, *A loop-top hard X-ray source in a compact solar flare as evidence for magnetic reconnection*, Nature 371, 495, [726 c, 31 c/y].

Sui, L., and Holman, G.D. 2003, *Evidence for the formation of a large-scale current sheet in a solar flare*, ApJ 596, 251, [223 c, 14 c/y].
Sui, L., Holman, G.D., Dennis, B.R. 2004, *Evidence for magnetic reconnection in three homologous solar flares observed by RHESSI*, ApJ 612, 546, [167 c, 12 c/y].
Veronig, A.M. and Brown, J.C. 2004, *A coronal thick-target interpretation of two hard X-ray loop events*, ApJ 603, L117, [127 c, 9 c/y].
Veronig, A.M., Karlicky, M., Vrsnak, B., et al. 2006, *X-ray sources and magnetic reconnection in the X3.9 flare of 2003 November 3*, A&A 446, 675, [97 c, 8 c/y].

(12.4) Modeling of Hard X-ray Spectra

Aschwanden, M.J., Bynum, R.M., Kosugi, T., et al. 1997, *Electron trapping times and trap densities in solar flare loops measured with Compton and Yohkoh*, ApJ 487, 936, [60 c, 3 c/y].
Aschwanden, M.J. 2007, *RHESSI timing studies: Multithermal delays*, ApJ 661, 1242, [24 c, 2 c/y].
Aschwanden, M.J., Holman, G., O'Flannagain, A., et al. 2016, *Global energetics of solar flares. III. Nonthermal energies*, ApJ 832, 27, [16 c, 11 c/y].
Bain, H.M. and Fletcher, L. 2009, *Hard X-ray emission from a flare-related jet*, A&A 508, 1443, [16 c, 2 c/y].
Chen, Q. and Petrosian, V. 2013, *Determination of stochastic acceleration model characteristics in solar flares*, ApJ 777, 33, [16 c, 4 c/y].
Dennis, B.R., Duval-Poo, M.A., Piana, M., et al. 2018, *Coronal hard X-ray sources revisited*, ApJ 867, 82.
Emslie, A.G. 2003, *The determination of the total injected power in solar flare electrons*, ApJ 595, L119, [41 c, 3 c/y].
Grigis, P.C. and Benz, A.O. 2004, *The spectral evolution of impulsive solar X-ray flares*, A&A 426, 1093, [98 c, 7 c/y].
Holman, G.D. 2003, *The effects of low- and high-energy cutoffs on solar flare microwave and hard X-ray spectra*, ApJ 586, 606, [71 c, 5 c/y].
Holman, G.D., Sui, L., Schwartz, R.A., et al. 2003, *Electron bremsstrahlung hard X-ray spectra, electron distributions, and energetics in the 2002 July 23 solar flare*, ApJ 595, L97, [213 c, 15 c/y].
Kasparova, J., Kontar, E.P., and Brown, J.C. 2007, *Hard X-ray spectra and positions of solar flares observed by RHESSI: photospheric albedo, directivity and electron spectra*, A&A 466, 705, [38 c, 4 c/y].
Kontar, E.P., Brown, J.C., and McArthur, G.K. 2002, *Nonuniform target ionization and fitting thick target electron injection spectra to RHESSI data*, SoPh 210, 419, [40 c, 3 c/y].
Kontar, E.P., MacKinnon, A.L., Schwartz, R.A., et al. 2006, *Compton backscattered and primary X-rays from solar flares: angle dependent Green's function correction for photospheric albedo*, A&A 446, 1157, [68 c, 6 c/y].
Kontar, E.P., Brown, J.C., Emslie, A.G., et al. 2011, *Deducing electron properties from hard X-ray observations*, SSRv 159, 301, [85 c, 13 c/y].
Kontar, E.P., Jeffrey, N.L.S., Emslie, A.G., et al. 2015, *Collisional relaxation of electrons in a warm plasma and accelerated nonthermal electron spectra in solar flares*, ApJ 809, 35, [12 c, 5 c/y].
Krucker, S. and Lin, R.L. 2008, *Hard X-ray emissions from partially occulted solar flares*, ApJ 673, 1181, [84 c, 9 c/y].
Massone, A.M., Emslie, A.G., Kontar, E.P., et al. 2004, *Anisotropic bremsstrahlung emission and the form of regularized electron flux spectra in solar flares*, ApJ 613, 1233, [31 c, 2 c/y].
Oka, M., Ishikawa, S., Saint-Hilaire, P., et al. 2013, *Kappa distribution model for hard X-ray coronal sources of solar flares*, ApJ 764, 6, [41 c, 9 c/y].
Petrosian, V. and Chen, Q. 2010, *Derivation of stochastic acceleration model characteristics for solar flares from RHESSI hard X-ray observations*, ApJ 712, L131, [20 c, 3 c/y].

Saint-Hilaire, P. and Benz, A.O. 2005, *Thermal and non-thermal energies of solar flares*, A&A 435, 743, [81 c, 6 c/y].
Su Y., Holman, G.D., and Dennis, B.R. 2011, *Evidence for the full hard X-ray spectral signature of nonuniform ionization in a solar flare*, Ap[J 731m 106, [13 c, 2 c/y].
Sui, L., Holman, G.D., and Dennis, B.R., et al. 2005, *Determination of low-energy cutoffs and total energy of nonthermal electrons in a solar flare on 2002 April 15*, ApJ 626, 1102, [57 c, 5 c/y].
Xu, Y., Emslie, A.G., and Hurford, G.J. 2008, *RHESSI hard X-ray imaging spectroscopy of extended sources and the physical properties of electron acceleration regions in solar flares*, ApJ 673, 576, [57 c, 6 c/y].

(12.5) Rapid Magnetic Changes During Flares

Aschwanden, M.J., Xu, Y., and Jing, J. 2014, *Global energetics of solar flares. I. Magnetic energies*, ApJ 797, 50, [27 c, 8 c/y].
Kleint, L. 2017, *First detection of chromospheric magnetic field changes during an X1-flare*, ApJ 834, 26, [7 c, 7 c/y].
Liu, C., Deng, N., Liu, Y., et al. 2005, *Rapid change of δ spot structure associated with 7 major flares*, ApJ 622, 722, [97 c, 8 c/y].
Liu, C., Deng, N., Liu, R., et al. 2012, *Rapid changes of photospheric magnetic field after tether-cutting reconnection and magnetic implosion*, ApJ 745, L4, [61 c, 11 c/y].
Petrie, G.J.D. 2013, *A spatio-temporal description of the abrupt changes in the photospheric magnetic and Lorentz-force vectors during the 15 February 2011 X2.2 flare*, SoPh 287, 415, [46 c, 8 c/y].
Petrie, G.J.D. 2014, *Estimating flare-related photospheric Lorentz force vector changes within active regions*, SoPh 289, 3663, [6 c, 2 c/y].
Schrijver, C.J., DeRosa, M.L., Metcalf, T., et al. 2008, *Nonlinear force-free field modeling of a solar active region around the time of a major flare and coronal mass ejection*, ApJ 675, 1637, [191 c, 20 c/y].
Sudol, J.J. and Harvey, J.W. 2005, *Longitudinal magnetic field changes accompanying solar flares*, ApJ 635, 647, [166 c, 13 c/y].
Sun, X., Hoeksema, J.T., Liu, Y., et al. 2012, *Evolution of magnetic field and energy in a major eruptive active region based on SDO/HMI observations*, ApJ 748, 77, [191 c, 34 c/y].
Sun, X., Bobra, M.G., Hoeksema, J.T., et al. 2015, *Why is the great solar active region 12192 flare-rich but CME-poor ?* ApJ 804, L28, [71 c, 28 c/y].
Wang, H., Spirock, T.J., Qiu, J., et al. 2002, *Rapid changes of magnetic fields associated with 6 X-class flares*, ApJ 576, 497, [104 c, 7 c/y].
Wang, H. 2006, *Rapid changes of photospheric magnetic fields around flaring magnetic neutral lines*, ApJ 649, 490, [78 c, 7 c/y].
Wang, H. and Liu, C. 2010, *Observational evidence of back reaction on the solar surface associated with coronal magnetic restructuring in solar eruptions*, ApJ 716, L195, [84 c, 11 c/y].
Wang, H., Liu, C., Ahn, K., et al. 2017, *High-resolution observations of flare precursors in the low solar atmosphere*, Nature Astronomy 1, 0085, [15 c, 15 c/y].
Wang, S., Liu, C., Lu, R., et al. 2012, *Response of the photospheric field to the X2.2 flare on 2002 February 15*, ApJ 745, L17, [95 c, 17 c/y].
Xu, Z, Yang, K., Guo, Y., et al. 2017, *Homogolous circular-ribbon flares driven by flux emergence*, ApJ 851, 30, [5 c, 5 c/y].
Yurchyshyn, V., Wang, H., Abramenko, V., et al. 2004, *Magnetic field, Hα, and RHESSI observations of the 2002 July 23 gamma-ray flare*, ApJ 605, 546, [42 c, 3 c/y].

(12.6) Magnetic Reconnection and Particle Acceleration

Aschwanden, M.J., Kosugi, T., Hudson, H.S., et al. 1996, *The scaling law between electron time-of-flight distances and loop lengths in solar flares*, ApJ 470, 1998, [78 c, 4 c/y].

Aulanier, G., Pariat, E., Démoulin, P., et al. 2006, *Slip-running reconnection in quasi-separatrix layers*, SoPh 238, 347, [136 c, 12 c/y].

Aulanier, G., Janvier, M., and Schmieder, B. 2012, *The standard flare model in 3-D. I. Strong-to-weak shear transition in post-flare loops*, A&A 543, A110, [80 c, 15 c/y].

Che, H., Drake, J.F., and Swisdak, M. 2011, *A current filamentation mechanism for breaking magnetic field lines during reconnection*, Nature 474, 184, [75 c, 12 c/y].

Chen, L.J., Bhattacharjee, A., Puhl-Quinn, P.A., et al. 2008, *Observation of energetic electrons within magnetic islands*, Nature Physics 4, 19, [130 c, 14 c/y].

Drake, J.F., Swisdak, M., Che, H., et al. 2006, *Electron acceleration from contracting magnetic islands during reconnection*, Nature 443, 553, [438 c, 38 c/y].

Drake, J.F., Swisdak, M., and Fermo, R. 2013, *The power-law spectra of energetic particles during multi-island magnetic reconnection*, ApJ 763, L5, [61 c, 14 c/y].

Dudik, J., Janvier, M., Aulanier, G., et al. 2014, *Slipping magnetic reconnection during an X-class flare observed by SDO/AIA*, ApJ 784, 144, [57 c, 16 c/y].

Fletcher, L. and Hudson, H.S. 2008, *Impulsive phase flare energy transport by large-scale Alfvén waves and the electron acceleration problem*, ApJ 675, 1645, [202 c, 21 c/y].

Janvier, M., Aulanier, G., Pariat, E., et al. 2013, *The standard flare model in 3-D: III. Slip-running reconnection properties*, A&A 555, A77, [66 c, 15 c/y].

Janvier, M., Aulanier, G., Bommer, V., et al. 2014, *Electric currents in flare ribbons: Observations and 3-D standard model*, ApJ 788, 60, [58 c, 16 c/y].

Janvier, M., Savcheva, A., Pariat, E., et al. 2016, *Evolution of flare ribbons, electric currents, and quasi-separatrix layers during an X-class flare*, A&A 591, A141, [15 c, 10 c/y].

Ji, H., Wang, H., Liu, C., et al. 2008, *A hard X-ray sigmoidal structure during the initial phase of the 2003 October 29 X10 flare*, ApJ 680, 734, [30 c, 3 c/y].

Kliem, B., Karlicky, M., and Benz, A.O. 2000, *Solar radio pulsations as a signature of dynamic magnetic reconnection*, A&A 360, 715, [280 c, 16 c/y].

Li, T. and Zhang, J. 2015, *Quasi-periodic slipping magnetic reconnection during an X-class solar flare observed by the SDO and IRIS*, ApJ 804, L8, [43 c, 17 c/y].

Li, Y., Qiu,J., Longcope, D.W., et al. 2016, *Observation of an X-shaped ribbon flare in the Sun and its 3-D magnetic reconnection*, ApJ 823, L13, [7 c, 5 c/y].

Liu, W., Petrosian, V., Dennis, B.R. 2008, *Double coronal hard and soft X-ray source observed by RHESSI: Evidence for magnetic reconnection and particle acceleration in solar flares*, ApJ 676, 704, [75 c, 8 c/y].

Qiu, J., Lee, J., Gary, E.D., et al. 2002, *Motion of flare footpoint emission and inferred electric field in reconnecting current sheets*, ApJ 656, 1335, [129 c, 8 c/y].

Shibata, K. and Tanuma, S. 2001, *Plasmoid-induced reconnection and fractal reconnection*, Earth, Planets and Space 53, 473, [247 c, 15 c/y].

Sui, L. and Holman, G.D. 2003, *Evidence for the formation of a large-scale current sheet in a solar flare*, ApJ 596, L251, [223 c, 15 c/y].

Sui, L., Holman, G.D., and Dennis, B.R. 2004, *Evidence for magnetic reconnection in three homologous solar flares observed by RHESSI*, ApJ 612, 546, [167 c, 12 c/t].

Sun, X., Hoeksema, J.T., Liu, Y., et al. 2013, *Hot spine loops and the nature of a late-phase solar flare*, ApJ 778, 139, [64 c, 14 c/y].

Takasao, S., Asai, A., Isobe, H., et al. 2012, *Simultaneous observation of reconnection inflow and outflow associated with the 2010 August 18 solar flare*, ApJ 745, L6, [73 c, 13 c/y].

Toriumi, S. and Takasao, S. 2017, *Numerical simulations of flare-productive regions: δ-sunspots, sheared polarity inversion lines, energy storage, and prediction*, ApJ 850, 39, [4 c, 4 c/y].

Toriumi, S., Schrijver, C.J., Harra, L.K. 2017, *Magnetic properties of solar active regions that govern large solar flares and eruptions*, ApJ 834, 56, [16 c, 16 c/y].

Veronig, A.M., Karlicky, M., Vrsnak, B., et al. 2006, *X-ray sources and magnetic reconnection in the X3.9 flare of 2003 November 3*, A&A 446, 675, [97 c, 8 c/y].
Yokoyama, T., Akita, K., Morimoto, T., et al. 2001, *Clear evidence of reconnection inflow of a solar flare*, ApJ 546, L69, [212 c, 13 c/y].
Zhao, J., Gilchrist, S.A., Aulanier, G., et al. 2016, *Hooked flare ribbons and flux-rope-related QSL footprints*, ApJ 823, 62, [19 c, 13 c/y].

(12.7) Microflares and Nanoflares

Aschwanden, M.J., Nightingale, R., Tarbell, T., et al. 2000a, *Time variability of the quiet Sun observed with TRACE. I. Instrumental effects, event detection, and discrimination of EUV nanoflares*, ApJ 535, 1027, [58 c, 3 c/y].
Aschwanden, M.J., Tarbell, T., Nightingale, R., et al. 2000b, *Time variability of the quiet Sun observed with TRACE. II. Physical parameters, temperature evolution, and energetics of EUV nanoflares*, ApJ 535, 1047, [219 c, 13 c/y].
Aschwanden, M.J. and Parnell, C.E. 2002, *Nanoflare statistics from first principles: Fractal geometry and temperature synthesis*, ApJ 572, 1048, [113 c, 7 c/y].
Battaglia, M., Grigis, P.C., and Benz, A.O. 2005, *Size dependence of solar X-ray flare properties*, A&A 439, 737, [67 c, 5 c/y].
Benz, A.O. and Grigis, P. 2002, *Microflares and hot component in solar active regions*, SoPh 210, 431, [41 c, 3 c/y].
Benz, A.O. and Krucker, S. 2002, *Energy distribution of microevents in the quiet solar corona*, ApJ 568, 413, [80 c, 5 c/y].
Christe, S., Hannah, I.G., Krucker, S., et al. 2008, *RHESSI microflares statistics. I. Flare-finding and frequency distributions*, ApJ 677, 1385, [71 c, 7 c/y].
Hannah, I.G., Hurford, G.J., Hudson, H.S., et al. 2007, *First limits on the 3–200 keV X-ray spectrum of the Quiet Sun using RHESSI*, ApJ 659, L77, [17 c, 2 c/y].
Hannah, I.G., Christe, S., Krucker, S., et al. 2008, *RHESSI microflare statistics. II. X-ray imaging, spectroscopy, and energy distribution*, ApJ 677, 704, [98 c, 10 c/y].
Hannah, I.G., Hudson, H.S., Hurford, G.J., et al. 2010, *Constraining the hard X-ray properties of the Quiet Sun with new RHESSI observations*, ApJ 724, 487, [25 c, 3 c/y].
Hannah, I.G., Hudson, H.S., Battaglia, M., et al. 2011, *Microflares and the statistics of X-ray flares*, SSRv 159, 263, [60 c, 9 c/y].
Hudson, H.S. 1991, *Solar flares, microflares, nanoflares, and coronal heating*, SoPh 133, 357, [358 c, 14 c/y].
Jing, J., Xu, Y., Cao, W., et al. 2016, *Unprecedented fine structure of a solar flare revealed by the 1.6 m New Solar Telescope*, Scientific Reports 6, 24319, [25 c, 17 c/y].
Krucker, S. and Benz, A.O. 1998, *Energy distribution of heating processes in the quiet solar corona*, ApJ 501, L213, [195 c, 10 c/y].
Krucker, S. and Benz, A.O. 2000, *Are heating events in the quiet solar corona small flares? Multiwavelength observations of individual events*, SoPh 191, 341, [55 c, 3 c/y].
Krucker, S., Christe, S., Lin, R.P. 2002, *Hard X-ray microflares down to 3 keV*, SoPh 210, 445, [54 c, 3 c/y].
McTiernan, J.M. 2009, *RHESSI/GOES observations of the nonflaring Sun from 2002 to 2006*, ApJ 697, 94, [41 c, 5 c/y].
Parnell, C.E. and Jupp, P.E. 2000, *Statistical analysis of the energy distribution of nanoflares in the Quiet Sun*, ApJ 529, 554, [193 c, 11 c/y].
Polito, V., Reeves, K.K., Del Zanna, G., et al. 2015, *Joint high temperature observation of a small C6.5 solar flare with IRIS/EIS/AIA*, ApJ 803, 84, [26 c, 10 c/y].
Reale, F., McTiernan, J.M., and Testa, P. 2009, *Comparison of Hinode/XRT and RHESSI detection of hot plasma in the non-flaring solar corona*, ApJ 704, L58, [29 c, 3 c/y].

Ryan,D.F., O'Flannagain,A.M., Aschwanden, M.J., Gallagher,P.T. 2014, *The compatibility of flare temperatures observed with AIA, GOES, and RHESSI*, SoPh 289, 2547, [15 c, 4 c/y].
Stoiser, S., Veronig, A.M., Aurass, H., et al. 2007. *RHESSI microflares: I. X-ray properties and multiwavelength characteristics*, SoPh 246, 339, [10 c, 1 c/y].
Testa, P., De Pontieu, B., Allred, J., et al. 2014, *Evidence of nonthermal particles in coronal loops heated impulsively by nanoflares*, Science 346, 1255724, [50 c, 14 c/y].
Young, P.R., Tian, H., and Jaeggli, S. 2015, *The 2014 March 29 X-flare: Subarcsecond resolution observations of Fe XXI λ1354.1*, ApJ 799, 218, [42 c, 17 c/y].

(12.8) Flare Hard X-Ray Oscillations

Asai, A., Shimojo, M., Isobe, H., et al. 2001, *Periodic acceleration of electrons in the 1998 November 10 solar flare*, ApJ 562, L103, [91 c, 6 c/y].
Aschwanden, M.J. 1987, *Theory of radio pulsations in coronal loops* SoPh 111, 113, [214 c, 7 c/y].
Brosius, J.W., Daw, A.N., and Inglis, A.R. 2016, *Quasi-periodic fluctuations and chromospheric evaporation in a solar flare ribbon observed by Hinode/EIS, IRIS, and RHESSI*, ApJ 830, 101, [14 c, 9 c/y].
Dauphin, C., Vilmer, N., Lüthi, T., et al. 2005, *Modulations of broad-band radio continua and X-ray emissions in the large X-ray flare on 03 November 2003*, Adv.Spac.Res. 35, 1805, [10 c, 1 c/y].
Dennis, B.R., Tolbert, A.K., Inglis, A., et al. 2017, *Detection and interpretation of long-lived X-ray quasi-periodic pulsations in the X-class solar flare on 2013 May 14*, ApJ 836, 84, [9 c, 9 c/y].
Dolla, L., Marque, C., Seaton, D.B., et al. 2012, *Time delays in quasi-periodic pulsations observed during the X2.2 solar flare on 2011 February 15.* ApJ 749, L16, [30 c, 5 c/y].
Farnik, F., Karlicky, M., and Svestka, Z. 2003, *Hard X-ray pulsations in the initial phase of flares*, SoPh 218, 183, [18 c, 1 c/y].
Fleishman, G.D., Bastian, T.S., and Gary, D.E. 2008, *Broadband quasi-periodic radio and X-ray pulsations in a solar flare*, ApJ 684, 1433, [32 c, 3 c/y].
Foullon, C., Verwichte, E., Nakariakov, V.M. et al., 2005, *X-ray quasi-periodic pulsations in solar flares as MHD oscillations*, A&A 440, L59, [54 c, 4 c/y].
Foullon, C., Fletcher, L., Hannah, I.G., et al. 2010, *From large-scale loops to the sites of dense flaring loops: Preferential conditions for long-period pulsations in solar flares*, ApJ 719, 151, [18 c, 2 c/y].
Hayes, L.A., Gallagher, P.T., Dennis, B.R. et al. 2016, *Quasi-periodic pulsations during the impulsive and decay phases of an X-class flare*, ApJ 827, L30, [16 c, 11 c/y].
Gruber, D., Lachowica, P., Bissaldi, et al. 2011, *Quasi-periodic pulsations in solar flares: New clues from the Fermi Gamma-Ray Burst Monitor*, A&A 533. A61, [27 c, 4 c/y].
Inglis, A.R., Nakariakov, V.M., and Melnikov, V.F. 2008, *Multi-wavelength spatially resolved analysis of quasi-periodic pulsations in a solar flare*, A&A 487, 1147, [50 c, 5 c/y].
Inglis, A.R. and Gilbert, H.R. 2013, *Hard X-ray and ultraviolet emission during the 2011 June 6 solar flare*, ApJ 777, 30, [17 c, 4 c/y].
Inglis, A.R. and Dennis, B.R. 2012, *The relationship between hard X-ray pulse timings and the locations of footpoint sources during flares*, ApJ 748, 139, [11 c, 2 c/y].
Kumar, P., Nakariakov, V.M., and Cho, K.S. 2016, *Observation of a quasi-periodic pulsation in hard X-ray, radio, and EUV'*, ApJ 822, 7, [16 c, 11 c/y].
Kuznetsov, S.A., Zimovets, I.V., Morgachev, A.S., et al. 2016, *Spatio-temporal dynamics of sources of hard X-ray pulsations in solar flares*, SoPh 291, 3385, [6 c, 4 c/y].
Jakimiec,J. and Tomczak, M. 2010, *Investigation of quasi-periodic variations in hard X-rays of solar flares*, SoPh 261, 233, [13 c, 2 c/y].
Jakimiec,J. and Tomczak, M. 2012, *Investigation of quasi-periodic variations in hard X-rays of solar flares II. Further investigation of oscillating magnetic traps*, SoPh 278, 393, [5 c, 1 c/y].

Li, D., Ning, Z.J., and Zhang, Q.M. 2015, *Imaging and spectral observations of quasi-periodic pulsations in a solar flare*, ApJ 807, 72, [23 c, 9 c/y].
Li, Y.P. and Gan, W.Q. 2008, *Observational studies of the X-ray quasi-periodic oscillations of a solar flare*, SoPh 247, 77, [20 c, 3 c/y].
Nakariakov, V.M., Foullon, C., Myagkova, I.N., et al. 2010, *Quasi-periodic pulsations in the gamma-ray emission of a solar flare*, ApJ 708, L47, [45 c, 6 c/y].
Nakariakov, V.M. and Melnikov, V.F. 2009, *Quasi-periodic pulsations in solar flares*, SSRv 149, 119, [187 c, 21 c/y].
Nakariakov, V.M. and Zimovets, I.V., 2011, *Slow magneto-acoustic waves in two-ribbon flares*, ApJ 730, L27, [41 c, 6 c/y].
Ning, Z. 2014, *Imaging observations of X-ray quasi-periodic oscillations at 3–6 keV in the 26 December 2000 solar flare*, SoPh 289, 1239, [15 c, 4 c/y].
Ofman, L. and Sui, L. 2006, *Oscillations of hard X-ray flare emission observed by RHESSI: Effects of super-Alfvénic beams ?* ApJ 644, L149, [45 c, 4 c/y].
Terekhov, O.V., Shevchenko, A.V., Kuzmin, A.G. et al. 2002, *Observation of quasi-periodic pulsations in the flare SF 900610*, Astron.Lett. 28, 397, [11 c, 0.7 c/y].
Zimovets, I.V. and Struminsky, A.B. 2010, *Observations of double-periodic X-ray emission in interacting systems of solar flare loops*, SoPh 263, 163, [16 c, 2 c/y].

(12.9) Flare Radio Emission

Asai, A., Kiyohara, J., Takasaki, H., et al. 2013, *Temporal and spatial analyses of spectral indices of nonthermal emissions derived from hard X-rays and microwaves*, ApJ 763, 87, [17 c, 4 c/y].
Bastian, T.S., Fleishman, G.D., and Gary, D.E. 2007, *Radio spectral evolution of an X-ray poor impulsive solar flare: Implications for plasma heating and electron acceleration*, ApJ 666, 1256, [33 c, 3 c/y].
Benz, A.O., Grigis, P.C., Csillaghy, A., et al. 2005, *Survey on solar X-ray flares and associated coherent radio emissions*, SoPh 226, 121, [55 c, 4 c/y].
Chen, B., Bastian, T.S., Chen, C. 2015, *Particle acceleration by a solar flare termination shock*, Science 350, 1238, [20 c, 8 c/y].
Chernov, G.P. 2006, *Solar radio bursts with drifting stripes in emission and absorption*, SSRv 127, 195, [64 c, 6 c/y].
Fleishman, G.D., Bastian, T.S., and Gary, D.E. 2008, *Broadband quasi-periodic radio and X-ray pulsations in a solar flare*, ApJ 684, 1433, [32 c, 3 c/y].
Holman, G.D. 2003, *The effects of low- and high-energy cutoffs on solar flare microwave and hard X-ray spectra*, ApJ 586, 606, [71 c, 5 c/y].
Inglis, A.R., Nakariakov, V.M., and Melnikov, V.F. 2008, *Multi-wavelength spatially resolved analysis of quasi-periodic pulsations in a solar flare*, A&A 487, 1147, [50 c, 5 c/y].
Inglis, A.R., Ireland, J., Dominique, M. 2015, *Quasi-periodic pulsations in solar and stellar flares: Re-evaluating their nature in the context of power-law flare Fourier spectra*, ApJ 798, 108, [28 c, 11 c/y].
Karlicky, M. and Kliem, B. 2010. *Reconnection of a kinking flux rope triggering the ejection of a microwave and hard X-ray source. I. Observations and interpretation*, SoPh 266, 71, [30 c. 4 c/y].
Karlicky, M., Barta, M., and Rybak, J. 2010, *Radio spectra generated during coalescence processes of plasmoids in a flare current sheet*, A&A 514, 28, [23 c, 3 c/y].
Karlicky, M. and Barta, M. 2011, *Successive merging of plasmoids and fragmentation in a flare current sheet and their X-ray and radio signatures*, ApJ 733, 107, [32 c, 5 c/y].
Kliem, B., Karlicky, M., and Benz, A.O. 2000, *Solar radio pulsations as a signature of dynamic magnetic reconnection*, A&A 360, 715, [280 c, 16 c/y].

Kliem, B., Linton, M.G., Török, T., et al. 2010, *Reconnection of a kinking flux rope triggering the ejection of a microwave and hard X-ray source. II. Numerical modeling*, SoPh 266, 91, [41 cm, 5 c/y].
Kolotkov, D.Y., Nakariakov, V.M., Kupriyanova, E.G., et al. 2015, *Multi-mode quasi-periodic pulsations in a solar flare*, A&A 574, A53, [25 c, 10 c/y].
Krucker, S., Hudson, H.S., Glesener, L., et al. 2010, *Measurements of the coronal acceleration region of a solar flare*, ApJ 714, 1108, [109 c, 15 c/y].
Kumar, P., Nakariakov, V.M., Cho, K.S. 2016, *Observation of a quasiperiodic pulsation in hard X-ray, radio, and EUV wavelengths*, ApJ 822, 7, 16 c, 11 c/y].
Li, Y.P. and Gan, W.Q. 2005, *The shrinkage of flare radio loops*, ApJ 629, 137, [48 c, 4 c/y].
Nindos, A., Aurass, H., Klein, K.L. et al. 2008, *Radio emission of flares and coronal mass ejections. Invited review*, SoPh 253, 3, [48 c, 5 c/y].
Nita, G.M., Gary, D.E., and Lee, J.W. 2004, *Statistical study of two years of solar flare spectra obtained with the Owens Valley Solar Array (OVRA)*, ApJ 605, 528, [62 c, 5 c/y].
Nita, G.M., Fleishman, G.D., Kuznetsov, A.A. et al. 2015, *3-D radio and X-ray modelling and data analysis software: Revealing flare complexity*, ApJ 799, 236, [28 c, 11 c/y].
Reid, H.A.S., Vilmer, N., and Kontar, E.P. 2011, *Characteristics of the flare acceleration region derived from simultaneous hard X-ray and radio observations*, A&A 529, 66, [28 c, 4 c/y].
White, S.M., Benz, A.O., Christe, S., et al., 2011, *The relationship between solar radio and hard X-ray emission*, SSRv 159, 225, [62 c, 10 c/y].
Yu, S., Nakariakov, V.M., an Yan, Y. 2016, *Effect of a sausage oscillation on radio zebra pattern structures in a solar flare*, ApJ 826, 78, [6 c, 4 c/y].

(12.10) White-Light Flares

Donea, A.C. and Lindsey, C. 2005, *Seismic emission from the solar flares of 2003 October 28 and 29*, ApJ 630, 1168, [92 c, 7 c/y].
Fletcher, L., Hannah, I.G., Hudson, H.S., et al. 2007, *A TRACE white light and RHESSI hard X-ray study of flare energetics*, ApJ 656, 1187, [88 c, 8 c/y].
Heinzel, P., Kleint, L., Kasparova, J., et al. 2017, *On the nature of off-limb flare continuum sources detected by SDO/HMI*, ApJ 847, 48, [4 c, 4 c/y].
Hudson, H.S., Wolfson, C.J., and Metcalf, T.R. 2006, *White-light flares: A TRACE/ RHESSI overview*, SoPh 234, 79, [82 c, 7 c/y].
Hudson, H.S. 2016, *Chasing white-light flares*, SoPh 291, 1273, [8 c, 5 c/y].
Jess, D.B., Mathioudakis, M., Crockett, P.J., et al. 2008, *Do all flares have white-light emission ?* ApJ 688, 119, [62 c, 7 c/y].
Kerr, G.S. and Fletcher, L. 2014, *Physical properties of white-light sources in the 2011 February 15 solar flare*, ApJ 783, 98, [28 c, 8 c/y].
Kleint, L., Heinzel, P., Judge, P., et al. 2016, *Continuum enhancements in the ultraviolet, the visible and the infrared during the X1 flare on 2014 March 29*, ApJ 816, 88, [28 c, 19 c/y].
Kretzschmar, M. 2011, *The Sun as a star: Observations of white-light flares*, A&A 530, 84, [64 c, 10 c/y].
Krucker, S., Saint-Hilaire, P., Hudson, H.S., 2015, *Cospatial white light and hard X-ray flare footpoints seen above the solar limb*, ApJ 802, 19, [26 c, 10 c/y].
Kuhar, M., Krucker, S., Martinez Oliveros, J.C., et al. 2016, *Correlation of hard X-ray and white-light emission in solar flares*, ApJ 816, 6, [21 c, 14 c/y].
Lee, K.S., Imada, S., Watanabe, K., et al. 2017, *IRIS, Hinode, SDO, and RHESSI observations of a white light flare produced directly by nonthermal electrons*, ApJ 836, 150, [13 c, 13 c/y].
Martinez Oliveros, J.C., Hudson, H.S., Hurford, G.J., et al., 2012, *The height of a white-light flare and its hard X-ray sources*, ApJ 753, 26, [49 c, 9 c/y].
Martinez Oliveros, J.C., Krucker, S., Hudson, H.S., et al. 2014, *Chromospheric and coronal observations of solar flares with the HMI*, ApJ 780, L28, [12 c, 3 c/y].

Matthews, S.A., van Driel-Gesztelyi, L., Hudson, H.S., et al. 2003, *A catalogue of white-light flares observed by Yohkoh*, A&A 409, 1107, [51 c, 4 c/y].

Metcalf, T.R., Alexander, D., Hudson, H.S., et al. 2003, *TRACE and Yohkoh observations of a white-light flare*, ApJ 595, 483, [90 c, 6 c/y].

Maurya, R.A., Vemareddy, P., and Ambastha, A. 2012, *Velocity and magnetic transient driven by the X2.2 white-light flare of 2011 February 15 in NOAA 11158*, ApJ 747, 134, [36 c, 7 c/y].

Xu, Y., Cao, W., Liu,C., et al. 2004, *Near-infrared observations at 1.56 microns of the 2003 October 29 X10 white-light flare*, ApJ 607, L131, [69 c, 5 c/y].

Chapter 13
Flares: Thermal Emission

13.1 Direct Heating of Chromosphere

While a description of the quiescent chromosphere outside of flaring time intervals and away from flare locations is presented in Chap. 5, a complementary view of the chromosphere under flaring conditions is given here. There are a number of physical mechanisms that produce a chromospheric response during flares, which affect the physical density and temperature structure of the chromosphere, mostly in form of enhanced heating from coronal agents: (i) precipitation of accelerated electrons, protons, and ions from the coronal acceleration site to the chromospheric thin- or thick target; (ii) direct heating of the chromosphere by thermal conduction fronts that propagate from a coronal magnetic reconnection site towards the chromosphere, (iii) downward motions, (iv) reconnection outflows, (v) *coronal rain*, (vi) shocks, and (vii) associated waves. Combined models of particle acceleration, particle transport, and hydrodynamic response of the chromosphere exist (e.g., Liu et al. 2009; Rubio da Costa et al. 2015).

The 1989 April 29, 16:00 UT, flare is one of the few events where thermal conduction was considered to be the most likely mechanism to heat the chromosphere, rather than precipitation by nonthermal particles (Czaykowska et al. 2001). This conclusion is based on the observation of chromospheric evaporation more than an hour after the impulsive flare phase, where a significant amount of $\geq$ 15 keV hard X-ray emission would be required to produce the observed upflow velocities, which however is not observed at this phase of the flare (Czaykowska et al. 2001). Other diagnostics, using the Hα and the Ca II 8542 Å lines, can distinguish between thermal and nonthermal heating of the chromosphere also, finding nonthermal heating to be stronger in the outer edge of flare ribbons, and measuring a higher chromospheric temperature at the inner edge of the ribbons (Cheng et al. 2006). Flare observations in G-band and Fe I 6302 Å filters of SOT/Hinode revealed sharp leading edges of the flare ribbons associated with electron-beam heating, and diffusive parts, supposedly produced by back-warming (Isobe et al. 2007), or by

M. J. Aschwanden, *New Millennium Solar Physics*, Astrophysics and Space Science Library 458, https://doi.org/10.1007/978-3-030-13956-8_13

the free-bound continuum produced by both thermal and nonthermal collisions (Xu et al. 2006; Kerr and Fletcher 2014).

Evidence for conduction-driven (rather than beam-driven) evaporation was also found in the early phase of flares, based on RHESSI observations of coronal (rather than chromospheric) hard X-ray sources, where the driver is a saturated heat flux (Battaglia et al. 2009). However, from RHESSI spectral fitting alone, the two options of thermal or nonthermal heating cannot unambiguously be distinguished, while RHESSI modeling combined with XRT/Hinode and EIS/Hinode can discriminate between the two models (Graham et al. 2011).

While early hydrostatic 1-D chromospheric models inferred an average height of 2000 km above the photosphere as an upper boundary, new measurement methods (based on radio and hard X-ray data) found a more dynamic and a more *extended chromosphere*. In the theoretical flare model of hard X-rays in a collisional thick-target chromosphere, the dependence of the electron density n_e on the altitude h can be modeled with a power law function, $n_e(h) = n_0(h/h_0)^{-b}$, (Brown et al. 2002). A compilation of various chromospheric density models (Fig. 13.1)

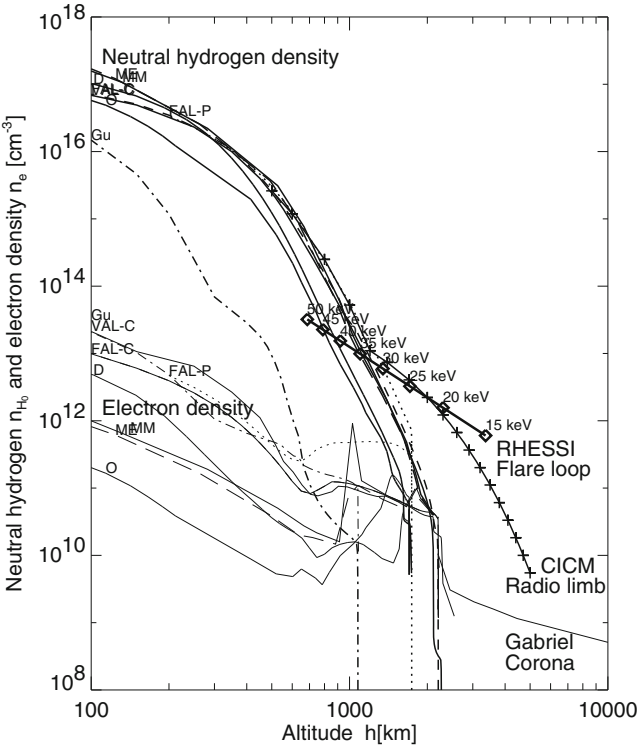

Fig. 13.1 A compilation of (non-flaring) chromospheric density models at altitudes of h = 100–2500 km, and the (flaring) extended component at altitudes of $h \approx$ 1000–5000 km, measured with CICM and RHESSI (Aschwanden et al. 2002)

shows that the radio-based *Caltech Irreference Chromospheric Model (CICM)* in sub-millimeter wavelengths and a RHESSI-inferred chromospheric density model extend the chromosphere up to $h \lesssim 5000$ km, at densities of $n_e \gtrsim 10^{10}$ cm^{-3} (Aschwanden et al. 2002). The standard collisional thick-target model, however, faces some problems regarding the high electron beam density and anisotropy, and thus may need some modification (Brown et al. 2009). Hard X-ray source motions along the flare loops were used as a constraint to distinguish between thermal and nonthermal chromospheric heating, but the two models could not be discriminated, nor could the source motion be reproduced with purely thermal models (Reep et al. 2016).

EUV spectroscopy during a small (C-class) flare revealed a sudden brightening of coronal Fe XIX line emission (formed at a temperature of $T \approx 8$ MK) in the preflare phase, which showed no bulk velocity flows, and thus could not be explained with chromospheric evaporation, indicating direct coronal heating in the preflare phase, while the brightening during the subsequent flare phase requires thermal conduction heating of the chromosphere (Brosius 2012). Evidence for heating over extended periods on very small spatial scales (of a single IRIS pixel) is seen in small flares (Warren et al. 2016). Impulsive heating above $T > 10$ MK has been observed in two-ribbon flares (Simoes et al. 2015; Graham et al. 2015).

A mechanism for direct heating of the chromosphere by downward propagating Alfvénic waves from coronal flare sites was considered by Russell and Fletcher (2013). A 1-D two-fluid model (of plasma and neutrals) was used to study the propagation of waves from the fully ionized corona through the underlying partially ionized chromosphere, and it was found that damping strongly depends on the wave frequency: waves with periods of 10 s or longer pass through the chromosphere with relatively little damping, while for periods of 1 s or less, a substantial fraction (37%–100%) of wave energy entering the chromosphere is damped by ion-neutral friction in the upper chromosphere, and by electron resistivity in the lower chromosphere and in the umbra. Thus it was concluded that Alfvénic waves with periods of a few seconds or less are capable of heating the chromosphere during flares (Russell and Fletcher 2013). However, the chromospheric response to heating due to the dissipation of Alfvén waves can be strikingly similar to heating by an electron beam (Reep and Russell 2016; Kerr et al. 2016).

Chromospheric radiative loss can be a significant part of the flare energy budget (Milligan 2015). The response of the lower chromosphere to a major flare was measured in the EUV continuum and EUV emission lines, UV continuum, and white-light continuum, and it was found that the summed radiated energy amounted to $\approx 10^{30}$ erg, about 15% of the total nonthermal energy (Milligan et al. 2014). Making use of IRIS data and the RADYN code, it was shown for the 2014 March 29 X1 flare that the chromospheric response to a high beam flux density satisfactorily achieved the observed continuum brightness in near-ultraviolet (Kowalski et al. 2017).

13.2 Chromospheric Evaporation

Chromospheric evaporation is the response of the chromosphere to precipitating particles (according to the collisional thick-target model), or to thermal conduction fronts (also called *direct heating*) that propagate from a coronal flare site down to the chromosphere. Thus we have two heating mechanisms: beam-driven impulsive heating that leads to *explosive evaporation*, and thermal conduction-driven heating that leads to *gentle evaporation*. Typical (blueshifted) upflow speeds of the evaporating plasma are $v \approx$ 100–300 km s^{-1}. In addition, impulsive wave heating can lead to chromospheric evaporation also (Reep and Russell 2016; Kerr et al. 2016), while weak beam heating can lead to gentle evaporation also (Milligan et al. 2006).

Observations related to the chromospheric evaporation process include: the Neupert-type relationship between soft and hard X-rays (Veronig et al. 2002; Liu et al. 2006), double-peaked *differential emission measure (DEM)* distributions that exhibit a cool background plasma and a hot evaporated flare plasma (Battaglia and Kontar 2012), episodes of chromospheric upflows in single loop strands as well as in multi-stranded flare loops (Brosius 2013; Graham and Cauzzi 2015), the radiated energy budget of chromospheric plasma compared with the heating power (Milligan et al. 2014), imaging and spectroscopic observations of chromospheric evaporation tested with the standard magnetic reconnection flare scenario (Tian et al. 2014), quasi-periodic intensity and velocity fluctuations in chromospheric and transition region lines during a flare (Brosius and Daw 2015; Brosius et al. 2016), the effects of slipping magnetic reconnection in chromospheric evaporation (Dudik et al. 2016), in circular ribbon flare geometries (Zhang et al. 2016), in the magnetic topology of quasi-separatrix layers (Sadykov et al. 2016), and in X-shaped separator geometries (Li et al. 2017b).

Observations of chromospheric evaporation that are consistent with energy transport by nonthermal particle beams include cases where (i) momentum balance between the hot upflowing material and the cool downflowing material was demonstrated (Brosius and Phillips 2004), (ii) where the thick-target model (using RHESSI data) predicts evaporative velocities that are consistent with those measured from spectroscopy (using CDS/SOHO, EIS/Hinode, IRIS data) (Milligan et al. 2006b; Milligan and Dennis 2009; Doschek et al. 2013; Tian et al. 2015; Li et al. 2015a), (iii) where coronal lines show blueshifts and chromospheric lines show redshifts (Li et al. 2015b, 2017a; Zhang et al. 2016; Li et al. 2017b), or (iv) quasi-periodic injections of electron beams (Brosius et al. 2016). Low fluxes of incident nonthermal electrons ($\gtrsim 5 \times 10^9$ erg cm^{-2} s^{-1}) during the impulsive flare phase can produce upflows also (Milligan et al. 2006a; Li et al. 2015a), although such low fluxes have previously been associated with *gentle evaporation* during the decay phase of flares, or during the *EUV late phase* (Woods et al. 2011), while optimal electron energies for driving chromospheric evaporation in solar flares are typically higher (Reep et al. 2015). In contrast, during the 2014 March 29 flare, conduction-driven evaporation was found to be present during the entire flare, supported by a stationnary hot (25 MK) coronal source, which may have driven evaporation during both the impulsive

and decay phase (Battaglia et al. 2015). The chromospheric dynamics observed by IRIS shows features of *gentle evaporation* that are driven both by accelerated electrons and by heat flux (Sadykov et al. 2015).

Numerical 2-D MHD simulations have been carried out that include the effect of anisotropic heat conduction and chromospheric evaporation based on a magnetic reconnection model, leading to the scaling law (Yokoyama and Shibata 2001),

$$T_{top} \approx \left(\frac{B^3 L}{2\pi \kappa_0 \sqrt{4\pi \rho}} \right)^{2/7} , \tag{13.2.1}$$

where T_{top} is the temperature at the flare loop top, B is the coronal magnetic field strength, ρ is the coronal mass density, and κ_0 is the heat conduction coefficient. The energy release rate is found to be a linearly increasing function of time,

$$\left| \frac{dE_m}{dt} \right| \approx \frac{B^2}{4\pi} V_{in} C_A t , \tag{13.2.2}$$

where V_{in} is the inflow velocity and C_A is the Alfvén velocity. The MHD simulations show that heat conduction produces adiabatic slow-mode MHD shocks, which are split into thermal conduction fronts and isothermal shocks by the heat conduction effect. The upper chromosphere is unable to radiate the flare energy deposited there by collision of nonthermal electrons, and is therefore heated rapidly to coronal temperatures in the *explosive evaporation* scenario (Yokoyama and Shibata 2001). Polito et al. (2016) simulated a flare loop undergoing heating, using the HYDRAD 1-D hydrodynamic code, and could reproduce the observed densities and temperatures (Fig. 13.2) in the framework of electron beam heating, rather than purely thermal conduction heating.

The physics of the (empirical) *Neupert effect*, which states that the time derivative of the soft X-ray flux $F_{SXR}(t)$ corresponds to the hard X-ray flux $F_{HXR}(t)$,

$$\frac{d}{dt} F_{SXR}(t) \propto F_{HXR}(t) , \tag{13.2.3}$$

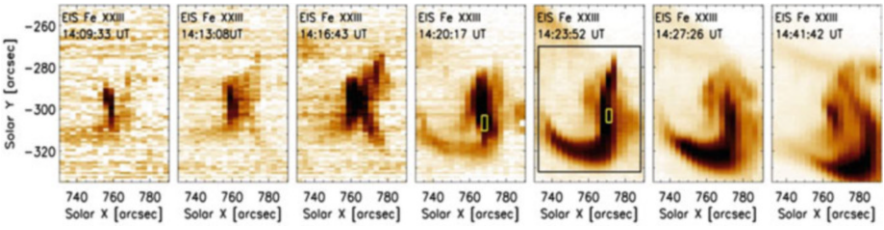

Fig. 13.2 Time sequence of images recorded with EIS/Hinode in the Fe XXIII 263.77 Å line. The time evolution shows the progressive filling of two loops, one starting in the left-most panel, and a second connected loop in the panels 4–7. The increase in brightness represents the increase in emission measure and electron density (Polito et al. 2016)

has been related to the *theoretical Neupert effect*, which states that the beam power supply $P_{beam}(t)$ inferred from the hard X-ray spectrum should match the actual power $P_{in}(t)$ that is required to explain the soft X-ray flux and spectrum (Veronig et al. 2005). However, the theoretical model did not reveal a better correlation than the empirical Neupert model, which implies that either (i) fast electrons are not the main source of the soft X-ray plasma supply and heating, (ii) the beam low energy cutoff varies with time, or (iii) the theoretical Neupert effect is affected by the source geometry (Veronig et al. 2005).

13.3 Coronal Condensation and Rain

Downflows were detected in long-duration flares above newly generated post-flare arcades, at altitudes where outflows from vertical large-scale current sheets in X-point magnetic reconnection regions are expected (McKenzie and Hudson 1999; McKenzie 2000). The supra-arcadal downflow was identified in the form of X-ray voids moving with speeds of $v \approx 100$–200 km s^{-1}, which is much smaller than the free-fall speed or the local Alfvén speed, and has been interpreted in terms of cross-sections of evacuated flux tubes resulting from intermittent reconnection following a coronal mass ejection (McKenzie and Hudson 1999).

While the SXT/Yohkoh observations reveal *hot coronal rain* (at flare temperatures of typically $T_e \approx 10$–20 MK), EUV observations (in Lyman-α and C IV) from TRACE reveal *cold coronal rain* in active regions at temperatures of $T_e \approx 0.1$–2 MK (Schrijver 2001). The cool downflows occur at speeds up to $v \approx 100$ km s^{-1}, accelerated no more than a third of the surface gravity. The intermittent downflows in quiescent coronal loops, occurring over a large altitude range in intervals of 2–7 days, has been attributed to catastrophic cooling of thermally unstable active region loops (Schrijver 2001).

Analysis of a dozen of such events observed with SXT/Yohkoh revealed both dark voids and bright X-ray emitting features, while no cool counterparts in Hα or EUV were found, leading to two opposing interpretations, either in terms of the *above-the-arcade coronal rain* scenario, or the *shrinking magnetic flux tube* scenario (McKenzie 2000). Sequential dark supra-arcadal downflows (observed with SUMER/SOHO, AIA/SDO) were interpreted in terms of plasma voids (Innes et al. 2003; Reeves and Golub 2011). Collapsing hot flare loops were found to deform from initial cusp shapes to circular shapes (observed with TRACE) (Sheeley et al. 2004),

A further alternative interpretation of supra-arcade downflows was proposed in terms of wakes that are generated by the retraction of much thinner flux tubes (Savage et al. 2012).

Warm rain with temperatures of $T \approx 0.08$–8.0 MK has been detected spectroscopically with CDS/SMM in the O III, O V, Mg X, and Fe XIX lines following chromospheric evaporation episodes, consistent with electron beam precipitation scenarios (Brosius 2003). IRIS observations of Mg II, C II, and Si IV line profiles

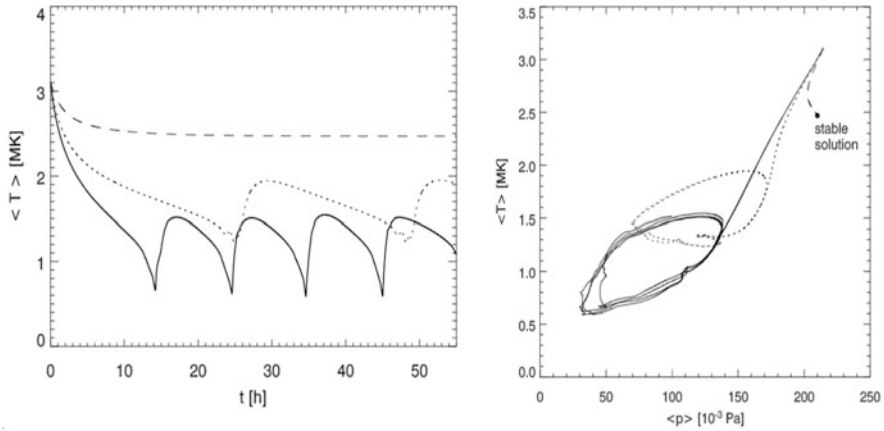

Fig. 13.3 *Left:* Evolution of mean temperature, $< T >$, as a function of time, for different damping lengths of the heating function: $H_m = 2$ Mm (solid), $H_m = 5$ Mm (dotted), and $H_m = 12$ Mm (dashed) for hydrodynamic 1-D simulations of evaporation-condensation cycles. *Right:* Mean temperature, $< T >$, of the loop, as a function of mean pressure, $< p >$, for a loop of total length $L = 300$ Mm. Solid line: $H_m = 2$ Mm, dotted: $H_m = 5$ Mm, dashed: $H_m = 12$ Mm (Müller et al. 2005)

revealed apparent downflows higher than the free-fall velocity, supposedly from thermally unstable loops (Kleint et al. 2014). IRIS observations of Si IV and Mg II line profiles reveal downflows in a circular-ribbon flare geometry with quasi-periodic pulsations (Zhang et al. 2016). Warm rain, however, occurs also frequently in active regions without an obvious relationship to flares.

The dynamics of condensation of cool coronal loops has been numerically simulated with 1-D hydrodynamic codes, which reproduce the thermal instability that occurs as a consequence of radiative cooling when a critical gradient dT/ds is reached, and can undergo a nonlinear limit cycle behavior between evaporation and condensation (Fig. 13.3), even when a constant heating function in time is applied (Müller et al. 2003). This suggests that catastrophic cooling is not initiated by a drastic decrease of the total loop heating rate, but rather by a loss of equilibrium at the loop apex as a natural consequence of heating concentrated at the footpoints of the loop, but constant in time (Müller et al. 2004). These simulations can explain propagating intensity enhancements in EUV wavelengths (Müller et al. 2005). Catastrophic cooling occurs also for (repetitive) impulsively heated loops, as long as they are heated at the footpoints (Mendoza-Briceno et al. 2005). While thermal non-equilibrium can explain catastrophic cooling and coronal rain in loops, it cannot simultaneously satisfy all other observed loop features, such as the excess density, the flat temperature profile, super-hydrostatic scale height, unstructured intensity profiles, and 1000–5000 s life times (Klimchuk et al. 2010)

1.5-D MHD simulations of loops heated (i) by small-scale discrete events concentrated at the footpoints, or (ii) by Alfvén waves generated at the photospheric

level show a strong sensitivity to internal pressure changes rather than to gravity. Heating by Alfvén waves leads to inhibition of coronal rain due to the characteristic uniform heating they produce, and thus can be used as a marker of coronal heating mechanisms (Antolin et al. 2010). The wave pressure from transverse (propagating torsional Alfvén or fast kink) waves can be responsible for the observed low downward acceleration of coronal rain (Antolin and Verwichte 2011). The appearance of rain causes the excitation of small-amplitude oscillations that may explain the observed events and provide a seismological tool to measure the rain mass (Verwichte et al. 2017).

Some aspects of coronal rain have been studied with semi-analytical models. Multi-dimensional modeling of loop arcades with individual heating rates yields statistical distributions of coronal rain and condensations (Fang et al. 2013, 2015), as well as information on rebound shocks, limit cycles, and shear flows (Fang et al. 2015). Analytical approximations of scaling laws can be used to simulate chromospheric evaporation and condensation driven by thermal conduction (Longcope 2014).

Coronal rain has even be inferred from on-disk observations, using the *CRisp Imaging SpectroPolarimeter (CRISP)* at the *Swedish 1-m Solar Telescope (SST)* (Antolin et al. 2012), with average temperatures $T_e \lesssim 7000$ K, speeds of $v \approx 70$ km s^{-1}, area coverage of 7%–30%, occurrence time of $\Delta t = 5$–20 hrs, mass draining rate of $dm/dt \approx 5 \times 10^9$ g s^{-1}, but unrelated to a flare (Antolin and Rouppe van der Voort 2012). Rain core densities are estimated to be $n_e \approx 1 \times 10^{10} - 2.5 \times 10^{11}$ cm^{-3}, while downflow mass fluxes are about a factor 20 lower, but still represent a significant part of the chromosphere-corona mass cycle (Antolin et al. 2015). The time evolution can be subdivided into 5 phases: (i) heating, (ii) evaporation, (iii) dominant conductive cooling for ≈ 120 s, (iv) dominant radiative/enthalpy cooling for ≈ 4700 s, and (v) catastrophic cooling within 35–124 s, leading to rain strands with a periodicity of 55–70 s (Scullion et al. 2016). Coronal rain was observed in a transequatorial loop, where a prominence formed after an eruptive CME, exhibiting magnetic dips and sustained condensation and drainage (Liu et al. 2012). Blobs associated with coronal rain leave trails, which may be a result of continuous cooling in their tails (Vashalomidze et al. 2015). Falling blobs have also been observed above helmet streamers, also called *raining inflows* (Sanchez-Diaz et al. 2017).

The quasi-periodic evaporation-condensation cycle produced by a thermal non-equilibrium has also been inferred from long-duration AIA observations of coronal loops, where the mean electron density exhibits a phase delay to the mean electron temperature, and undergoes a nonlinear limit cycle (Froment et al. 2015, 2017).

13.4 Flare Oscillations and Waves

Quasi-periodic emission during solar flares can be classified (on the most general level) into two groups: (i) MHD oscillations, and (ii) limit cycles of nonlinear systems, such as a quasi-periodic magnetic reconnection process, or a *load/unload*

system. Among the MHD resonances, torsional, fast-kink, fast-sausage, and slow magneto-acoustic wave modes are all possible candidates. Progress has been made in the new millennium by observations with spatially resolved oscillating flare loops (Nakariakov and Melnikov 2009; Nakariakov et al. 2010b, 2016; Van Doorsselaere et al. 2016).

The first imaging observations of *quasi-periodic pulsations (QPP)* were reported for the C7.9 flare on 1998 November 10, observed with the *Hard X-ray Telescope (HXT)* onboard Yohkoh and the *Nobeyama Radio Heliograph (NoRH)* (Asai et al. 2001). Since the Alfvén transit time along the loop was found to be equal to the period ($P \approx 5.1$ s), it was interpreted in terms of oscillating loops that modulate the efficiency of particle injection/acceleration (Asai et al. 2001).

The mechanism for microwave pulsations is attributed either to (i) variations of the magnetic field strength in the loop, (ii) to variations of the angle between the line-of-sight and the magnetic field vector, (iii) to variations of the mirror ratio and loss-cone angle in the loop, or (iv) to a quasi-periodic regime of the energetic electron acceleration/injection in the loop (Melnikov et al. 2005). QPPs were also observed in trans-equatorial loops that exhibited standing fast kink-mode oscillations, which were interpreted in terms of periodic pumping of electrons in a compact flare loop, modulated by oscillations in a magnetically linked larger loop that acts as MHD resonator (Foullon et al. 2005). A similar model was proposed where MHD oscillations of a nearby loop couple with X-ray emitting flare loops via the magnetic field and the associated electric current density, inducing current-driven plamsa micro-instabilities in the flare-related magnetic reconnection regions (Nakariakov et al. 2006). QPPs in the flaring energy release region can also be triggered by 3-min slow magneto-acoustic waves leaking from sunspots (Sych et al. 2009; Kumar et al. 2016), which was refuted by Milligan et al. (2017) because of the lack of a 3-min period in hard X-rays. Alternative interpretations consider fast sausage mode oscillations (Kopylova et al. 2007; Inglis et al. 2008; Dennis et al. 2017).

Multi-periodic oscillations have been observed in some cases, with up to three different periods (P = 12, 18, and 28 s), which were interpreted in terms of the fast kink-mode, which periodically triggers magnetic reconnection (Inglis and Nakariakov 2009). Triple periods (P≈10 s, P≈20 s, P $\gtrsim$ 30 s) were observed during the 2002 July 3 flare, which were interpreted as fundamental, second, and third harmonics of kink-mode standing waves (Kupriyanova et al. 2013). Two modes with periods of P=15 and P=100 s were found during the X3.2 flare of 2013 May 14, which were interpreted as fundamental kink mode and sausage mode (Kolotkov et al. 2015). Two periods ($P = 20, 55$ s) were reported during the X1.0 flare of 2013 October 28, the shorter period for all channels, and the longer for the nonthermal emission only (Hayes et al. 2016). Multi-periods of P=27, 46, 60 s were detected during the 2014 September 10 flare (Li and Zhang 2017).

Typical periods in microwaves are found in the range of P=5–60 s, which can be stable, or drift to shorter or longer periods (Kupriyanova et al. 2010). Up to 163 distinct pulses have been detected in GOES soft X-ray light curves (Dennis et al. 2017).

QPPs were also observed in gamma-ray emission, at photon energies of 2–6 MeV with the SONG/CORONAS-F instrument (Nakariakov et al. 2010a), or with the *Gamma-ray Burst Monitor (GBM)* onboard *Fermi* (Li et al. 2015; Li and Zhang 2017; Inglis et al. 2016).

Numerical 1-D hydrodynamic simulations of an impulsive energy release episode reveals quasi-periodic perturbations of the electron density in the heated flare loops, with periods corresponding to the second standing harmonics of an acoustic wave (Nakariakov et al. 2004). 2-D hydrodynamic simulations that include magnetic reconnection, heat conduction, and chromospheric evaporation revealed that the generation of quasi-periodic propagating fast-mode magneto-acoustic waves is spontaneously excited by above-the-loop-top oscillations (Takasao and Shibata 2016).

Disturbances propagating along the axis of the arcade in two-ribbon flares have been observed with speeds of a few tens of km s^{-1}, which were interpreted in terms of slow magneto-acoustic waves (Nakariakov and Zimovets 2011).

The availability of a high instrumental cadence (12 s for AIA/SDO) led to the discovery of quasi-periodic (concentrically) propagating fast-mode magnetosonic waves, which propagated up to a distance of $\approx$ 400 Mm with a phase velocity of $v = 2200 \pm 130$ km s^{-1} (Fig. 13.4; Liu et al. 2011). These waves were modeled with MHD simulations (Ofman et al. 2011) and were found to be the limb counterpart of the so-called global *EIT waves* (Liu et al. 2012). The observations provide evidence for the fast-mode MHD waves, where the primary (outer) fast component is running ahead of the secondary (inner) slow component with CME-caused restructuring (Liu et al. 2012).

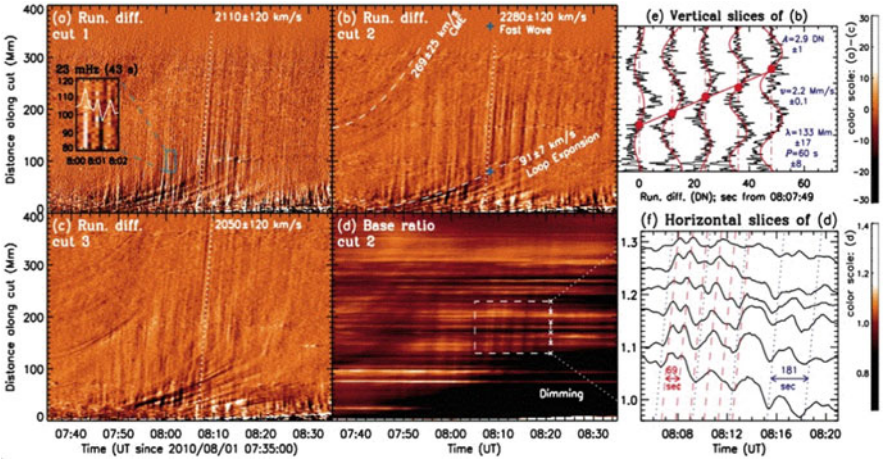

Fig. 13.4 Running difference space-time diagrams obtained from AIA 171 Å during the 2010 August 01 flare, showing quasi-periodically triggered propagating fast-mode waves (Liu et al. 2011)

QPPs were observed in many wavelength bands during the X2.2 flare of 2011 February 15, but with relative delays up to ±6 s, possibly be caused by the energy dependence of electron trapping (although it became also subject to a time correction of GOES data) (Dolla et al. 2012). A survey of 35 soft X-ray flares confirmed the common occurrence of QPPs and the relatively small time delays between different wavelength bands (Simoes et al. 2015).

Compression of the flare loop magnetic field can be associated with hard X-ray pulsations in the betatron acceleration model, which starts with the initial implosion of flare loops at the onset of the impulsive flare phase (Simoes et al. 2013). Sometimes, downward propagating disturbances cannot be distinguished from periodically shrinking loops (Kumar et al. 2017).

A strictly periodic signal should produce a narrow peak in the power spectrum, but most solar flare QPPs are consistent with a power law function for the power spectrum, while peaks are very rare, and thus the prevalence of regular oscillation eigen-modes in solar flare QPPs has been over-estimated in past literature (Inglis et al. 2015, 2016).

Extending the search of flare-related oscillations into the transition region and chromosphere, an oscillation with a 3-min period in the EUV irradiance (Lyman-α and Lyman continuum) was detected during a flare with EVE/SDO full-disk data, probably be caused by a flare-induced excitation of the chromospheric cavity at the acoustic cutoff frequency (Milligan et al. 2017). Quasi-periodic oscillations of the flare ribbon position and of the Doppler velocities with periods of $\approx$ 140 s were also detected in the Si IV (1403 Å) line with IRIS data (Brannon et al. 2015).

13.5 High-Temperature Components

The temperature distribution of flares or active regions can in principle be determined with standard *differential emission measure (DEM)* analysis methods (Sect. 2.6), which yield reliable results in EUV wavelengths ($T \approx$ 1–10 MK), but produces less robust results in soft X-ray wavelengths ($T \approx$ 10–50 MK) for a number of reasons, such as (i) the lack of high-temperature diagnostic lines, (ii) order of magnitude lower emission measures in soft X-rays compared with EUV, (iii) inadequate parameterization of the hotter part of the DEM, and (iv) confusion of thermal with nonthermal spectral components (especially when using RHESSI data), etc.

More than 50 intense spectral lines (Fe, Ni, Ca, Mg, Si) are present in the EUV spectra that provide diagnostics in the temperature range of $T = 0.5$–16 MK, for the SPIRIT instrument on CORONAS-F (Shestov et al. 2010) , or for AIA/SDO (Reeves and Golub 2011). Spectral lines with sensitivity to high-temperature ($\gtrsim$ 20 MK) plasma include the TRACE 195 Å channel, because of the Fe XXIV 192 Å resonance line, in addition to the low-temperature Fe XII 195 Å line (Warren and Reeves 2001). The XRS/GOES channels have a good line-ratio diagnostic in the temperature range of $T \approx$ 15–35 MK, but without spatial resolution, and with a

dependence on the photospheric and coronal elemental abundances (White et al. 2005). The RHESSI energy spectrum provides a high-temperature diagnostic of the Fe line (Fe XXIV/Fe XXV) and Ne/Ni line features at $E \approx 7.7$–8.6 keV (Phillips 2008; Caspi and Lin 2010). In many flares, the thermal component dominates the nonthermal component at energies of $E \lesssim 25$ keV, in which case an isothermal temperature can be fitted unambiguously (e.g., Milligan 2008).

Characterizing the thermal components in large flares yields at least two components, a super-hot ($T_e > 30$ MK) component and a lower-altitude hot ($T_e \lesssim 25$ keV) component whose temperature and emission measure closely track those derived from GOES measurements (Caspi and Lin 2010). A statistical study of 37 large (GOES M and X-class) flares suggests that the hot component (at the GOES DEM peak temperature) and the super-hot component (from RHESSI spectral fitting) are due to physically different conditions (Caspi et al. 2014). Different heating mechanisms could be operational, such as impulsive heating by precipitating electrons (the thick-target model), or direct heating by thermal conduction fronts. In one flare it was found that collisional beam-heating can only marginally explain the power necessary to heat the 10 MK plasma at the ribbons (Simoes et al. 2015). One or two thermal components (below and above 15 keV) were identified also with RHESSI and AIA/SDO (Battaglia and Kontar 2013). The temperature in the dark lanes of *supra-arcadal downflows* were found to be heated up to temperatures of $T_e \gtrsim 20$ MK, which is hotter than the background, but cooler than the surrounding plasma (Fig. 13.5, Hanneman and Reeves 2014). Although many DEM or spectral

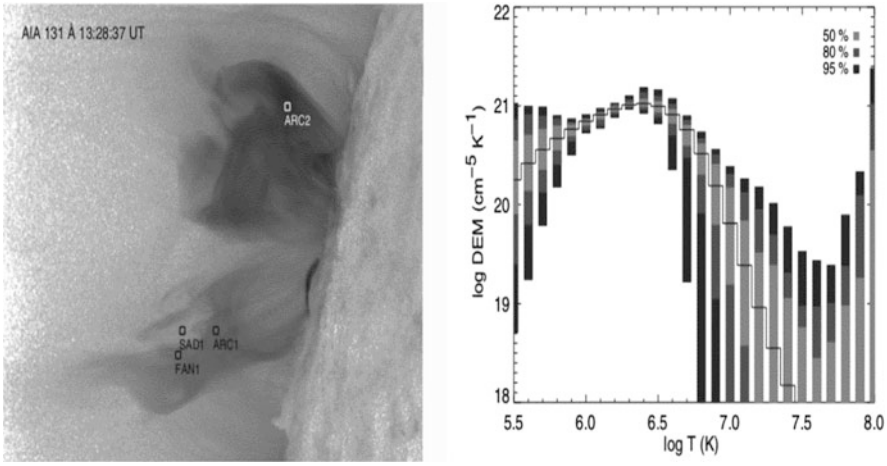

Fig. 13.5 *Left:* AIA 131 Å image of the 2012 January 14 flare showing the locations of the regions used for DEM calculations (in small square boxes). *Right:* DEMs resulting from Monte Carlo simulations for SAD1 (supra-arcadal downflow source 1) for the 2012 January 14 flare. The DEM calculated from the observed intensities is shown as a black line. The dark gray (gray, light gray) boxes encompass 95% (80%, 50%) of the Monte Carlo simulations in each temperature bin (Hanneman and Reeves 2014)

fits are consistent with a single (isothermal) temperature, or with a bi-modal two-temperature combination, multi-thermal models are ultimately more realistic. Hard X-ray imaging with RHESSI allows multiple isothermal components to be separated (Caspi et al. 2015). Also, different instruments sample complementary temperature regimes and should be combined in forward-fitting models. Isothermal fits yield systematic temperature discrepancies of $T_{GOES}/T_{AIA} = 1.4 \pm 0.4$, and $T_{RHESSI}/T_{AIA} = 1.9 \pm 1.0$ (Ryan et al. 2014), which clearly implies that multi-thermal models are needed. A GOES temperature measurement of $T = 33$ MK has been criticized as an artefact of the line-ratio method (Sharykin et al. 2015).

There is a theoretical hypothesis of a nanoflare-heated corona that predicts the existence of high temperatures $T \approx 10$–20 MK in active regions even in non-flaring conditions. However, studies of the nonequilibrium of ionization show that rapid and short heat pulses may never be detected above ≈ 5 MK, for heat pulses shorter than ≈ 1 min (Reale and Orlando 2008). Also the new RHESSI upper limits in the 3–200 keV energy range for solar hard X-ray emission in the absence of flares and active regions make it unlikely for nanoflares involving nonthermal effects to heat the corona, because such events would require a steep electron spectrum $E^{-\delta}$ with index $\delta > 5$ extending to very low energies (< 1 keV) (Hannah et al. 2010). Also *Nuclear Spectroscopic Telescope ARray (NuSTAR)* observations derive an upper limit for nanoflare fluxes that is 8 orders of magnitude fainter than the soft X-ray flux of the largest solar flares (Kuhar et al. 2018).

Evidence for a hot plasma temperature ($T \approx 4$–15 MK) in an active region was claimed from XRT/Hinode data, but the DEM of the hotter plasma is two orders of magnitude smaller than the cold plasma ($T \approx 2$–3 MK) (Reale et al. 2009a; Patsourakos and Klimchuk 2009; Petralia et al. 2014), and comparison of XRT with RHESSI results reveals a discrepancy within a factor of a few (Reale et al. 2009b; Schmelz et al. 2009). Since the absolute calibration of EUV instruments is of order $\approx 10\%$–20% (according to DEM benchmark tests, see Aschwanden et al. 2015), it is questionable whether hot temperature tails of the DEM can be measured down to a level of a few percents of the DEM peak. The emission measure distribution of EIS/Hinode was found to be a factor of two smaller than that of XRT/Hinode (Testa et al. 2011). Combined XRT/Hinode and EIS/Hinode DEM modeling indicates a hot temperature component of $T \geq 8$ MK, which however, is contradicted by FOXSI observations, and thus suggests larger uncertainties in the Hinode DEM analysis (Ishikawa et al. 2014). In contrast, analysis of the Ca XVII line at 192.858 Å line (formed at $T \approx 6$ MK) by extraction from the blend of Fe XI and O V lines yielded a ratio as high as 10 for the emission measure of the 6 MK plasma relative to the cooler 1 MK plasma (Ko et al. 2009). However, no thermal emission has been detected above $T_e = 5$ MK with NuSTAR (Hannah et al. 2016). In contrast, hard X-ray emission detected with FOXSI-2 above 7 keV was interpreted as thermal emission ($T_e \gtrsim 10$ MK), possibly produced by nanoflare heating (Ishikawa et al. 2017). Nanoflare modeling predicts an emission measure distribution extending well above $T \gtrsim 10$ MK, for "single nanoflares" (Barnes et al. 2016a), as well as for "nanoflare trains" (Barnes et al. 2016b), but observational evidence for such high temperatures in the Quiet Sun is scant.

13.6 Flare Size Distributions and SOC Systems

There is neither a typical size of a solar flare, nor a statistical mean of a random distribution with a Gaussian-like shape and an exponential-like tail. In contrast, solar flares exhibit a scale-free power law distribution function with "fat tails", as it is expected for nonlinear energy dissipation processes that are modeled with *self-organized criticality (SOC) models* (Aschwanden et al. 2000, 2016; Charbonneau et al. 2001). The power law distribution of flare energies extends over almost 9 orders of magnitude ($E = 10^{24}$–10^{31} erg, Fig. 12.9), which includes nanoflares observed in EUV (e.g., Aschwanden et al. 2000), microflares detected in hard X-rays with RHESSI (Christe et al. 2008; Qiu et al. 2004), and large (GOES M and X-class) hard X-ray flares detected with RHESSI, HXRBS/SMM, BATSE/CGRO (Aschwanden 2011a; Aschwanden et al. 2014a) and WATCH (Georgoulis et al. 2001; Wheatland 2000). The synthesized power law slopes are $\alpha_P = 1.73 \pm 0.07$ for the hard X-ray peak flux (Fig. 13.6), $\alpha_E = 1.62 \pm 0.12$ for the total flux, and $\alpha_T = 1.99 \pm 0.35$ for flare durations.

The power law slope is in principle independent of the intensity threshold (Baiesi et al. 2006), as long as the sample is complete in the detection of events above some threshold level. The threshold can be modeled by a generalized Pareto (type-II) or Lomax distribution (Aschwanden 2015). The power law slope of the hard X-ray peak flux is found to be slightly anti-correlated with the sunspot number (Fig. 13.7; Aschwanden 2011a,b), while the power law slope of the soft X-ray peak flux is found to be independent of the solar cycle (Aschwanden and Freeland 2012). The flare occurrence rate depends on the magnetic structure of sunspots (such as the $\beta\gamma\delta$ classification), as well as on the size of the flaring active regions (Sammis et al. 2000).

While the power law slope of flare size distributions is a strong indicator of SOC models, a physical model requires the knowledge of the underlying scaling laws. A statistical fractal-diffusive avalanche model of a slowly-driven SOC system has been proposed where the time evolution of avalanches follows a diffusive random walk, and the spatial structure of an avalanche obeys a fractal scaling law (Aschwanden 2012, 2014). Fractal current sheets in an avalanching impulsive reconnection region has been inferred from sub-bursts in flare kernels (Nishizuka et al. 2009). A fractal geometry of $V \propto A^{1.41\pm0.04}$ between avalanche volumes and areas has been inferred from cellular automaton simulations (McIntosh and Charbonneau 2001), and $N(A) \propto A^{-2.45}$ (Morales and Charbonneau 2008). Another model mimics solar flares as cascades of reconnecting magnetic loops, where loops injected at small scales are anchored by footpoints of opposite polarity and follow a random walk until they collide and reconnect (Hughes et al. 2003). Other models propose the coexistence of SOC and intermittent turbulence in the solar corona, based on the statistics of inter-occurrence (waiting) times between subsequent bursts (Uritsky et al. 2007). A turbulent environment immediately before flares that triggers an avalanche of coronal reconnection events is also implied by the observed rapid magnetic field changes (Abramenko et al. 2003).

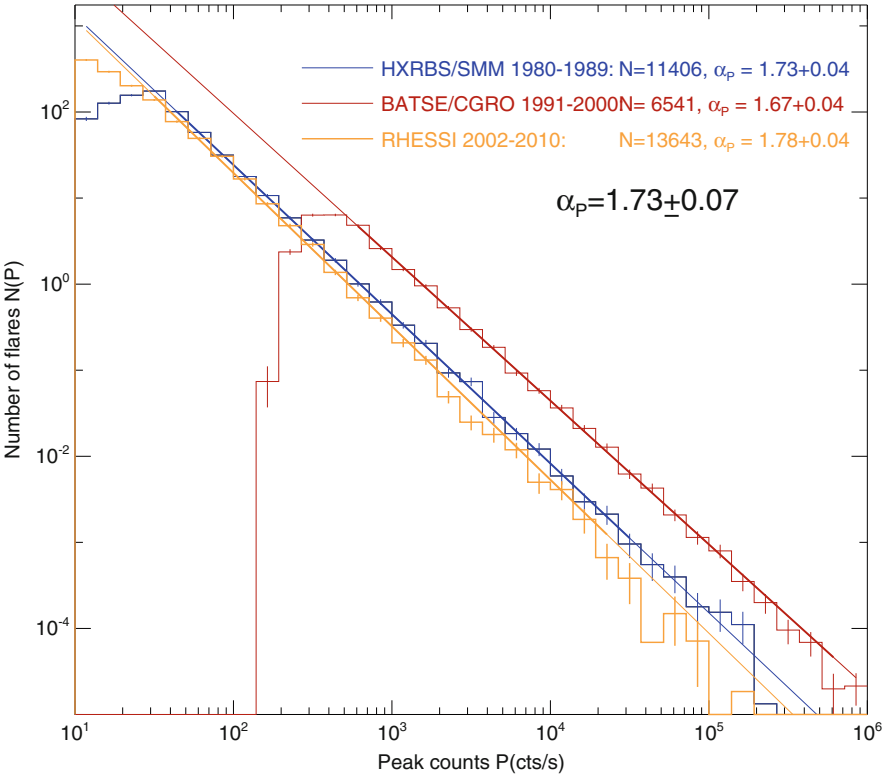

Fig. 13.6 Occurrence frequency distributions of hard X-ray peak count rates observed with SMM/HXRBS (1980–1989), BATSE (1991–2000), and RHESSI (2002–2010), with power law fits. An average preflare background of 40 cts s^{-1} was subtracted from the HXRBS count rates. BATSE/CGRO has larger detector areas and thus records higher count rates (Aschwanden 2011a)

Numerical simulations of avalanches are generally conducted with so-called *cellular automaton* models, which reduce the complexity of spatial structures of a nonlinear energy dissipation process with a statistical model of next-neighbor interactions (Isliker et al. 2000), which can be transformed into diffusive transport of the MHD equations and mimics Joule dissipation (Isliker et al. 2001). 3-D MHD simulations produce power law distributions of Ohmic (nanoflare) heating events with energies of $E \approx 10^{24}$ erg (Bingert and Peter 2013). Cellular automaton simulations can re-arrange randomly-placed localized electric currents and can accelerate particles in a SOC system (Anastasiadis et al. 2004; Dauphin et al. 2007). More advanced studies use dynamic data-driven input (magnetograms of active regions) to drive cellular automaton simulations (Dimitropoulou et al. 2013).

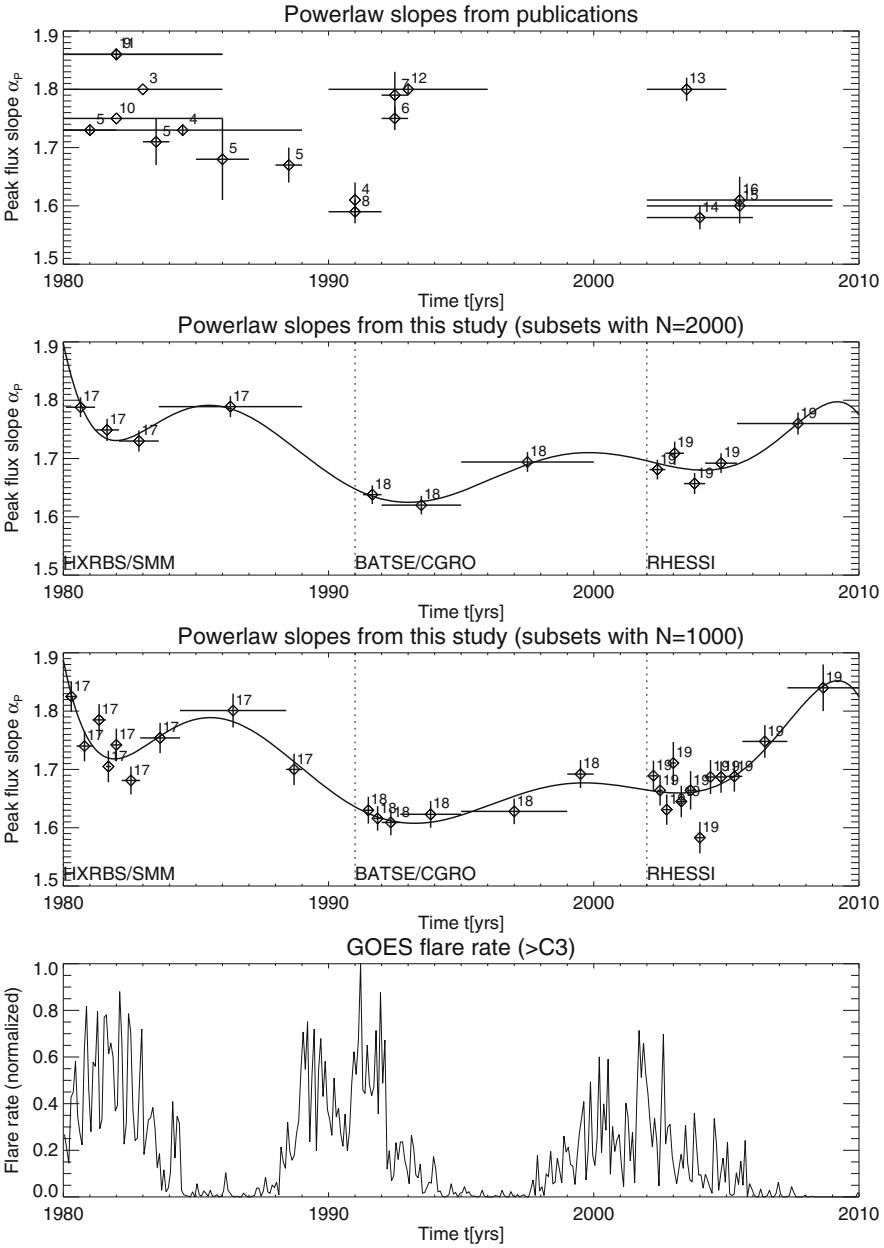

Fig. 13.7 The power law slope α_P of the peak flux P as a function of time during the last three solar cycles is shown for values quoted in the literature (top panel), for HXRBS, BATSE, and RHESSI data, with equal-sized subsets of $\approx$ 2000 events per subset (second panel) or $\approx$ 1000 events per subset (third panel), along with the flare rate observed by GOES (bottom panel) (Aschwanden 2011a)

13.7 Flare Energy Partition

The global energetics of solar flares and associated eruptive phenomena (Benz 2008, 2017) can be studied by measuring all components of the energy input, by quantifying the partitioning of energies in secondary processes, and by testing whether the sum of their parts matches the whole of the energy output. A frequent assumption is that all primary energy input is provided by dissipation of magnetic energies, which supply the energy output of secondary processes, such as the thermal energies of the heated flare plasma, the nonthermal energies of accelerated particles that produce hard X-rays, gamma-rays, or are detected as *solar energetic particles (SEP)*, and kinetic energies of coronal mass ejections (CMEs).

The global energetics of solar flare/CME events and their energy partition was initially studied for a small number of cases only (Emslie et al. 2004, 2005; Feng et al. 2013). More substantial statistics on the global energetics has been obtained for 38 large solar eruptive events (Emslie et al. 2012) and for 173 M and X-class flares (Aschwanden et al. 2014b). These papers study various contents of energy, such as (i) the radiated energy in soft X-rays detected by GOES, (ii) the total energy radiated in soft X-rays, (iii) the peak energy in soft X-rays, (iv) the bolometric radiated energy, (v) the non-thermal energy in accelerated >20 keV electrons, (vi) in >1 MeV ions, (vii) the kinetic energies in CMEs, and (viii) in solar energetic particles (SEP) in interplanetary space, and later (ix) the free magnetic energy based on *nonlinear force-free field (NLFFF)* codes. The free magnetic energy was found to cover a range of $E_{free}/E_{pot} \approx 1\%–25\%$, with potential energies of $E_{pot} \approx 1 \times 10^{31} - 4 \times 10^{33}$ erg (Sun et al. 2012; Aschwanden et al. 2014b). The magnetic energy is generally found to decrease after an eruption (Bleybel et al. 2002). The free energy above the minimum-energy state (which is a linear force-free field if the magnetic helicity of the configuration is conserved), however, was found to yield a better estimate of the flare process than the free energy above the potential field state (Régnier and Priest 2007).

The EUV images provide spatial information (length scales, areas, and volumes of flares) which is a prerequiste to calculate the volume-integrated thermal energies in flares. The flare volume has some filling factor, which can be modeled with the fractal-diffusive avalanche model (Aschwanden et al. 2013). Measuring the length scale L, the peak temperature T_p, the peak density n_p, and the magnetic field B, universal scaling laws can be estimated (e.g., Shibata and Yokoyama 1999). It is found that these parameters fulfill the *Rosner-Tucker-Vaiana (RTV)* scaling laws, $T_p^2 \propto n_p L$ and $H \propto T^{7/2} L^{-2}$ (Aschwanden and Shimizu 2013). The ratio of the thermal to the magnetically dissipated energy is found to have a ratio of $E_{th}/E_{magn} \approx 2\%–40\%$ (Aschwanden et al. 2015).

The thermal and nonthermal energies were found to be of the same magnitude, which implies an efficient conversion of nonthermal energy into hot flare plasma (Saint-Hilaire and Benz 2005; Oka et al. 2015). In the early phase of solar flares, the energy partition between thermal and nonthermal energy can be complicated by delayed acceleration and injection due to an energy threshold (Altyntsev et al. 2012).

Combined spectral modeling of GOES and RHESSI X-ray observations indicates two hot temperature components, a cooler component ($\approx$ 10–25 MK) produced by electron-precipitation driven chromospheric evaporation, and a hotter component ($\gtrsim$ 25 MK) that is more consistent with direct in situ heating of coronal plasma (Warmuth and Mann 2016a). Heating the hot thermal plasma and supplying radiated energy requires an additional non-beam heating mechanism. Strong conductive losses are a necessary additional energy transport that transfers the energy released in the corona to the chromosphere, where the bulk of released energy is efficiently radiated away in EUV, UV, and white light (Warmuth and Mann 2016b). In another study, no additional ad hoc heating mechanism other than heating by nonthermal electrons was required (Falewicz et al. 2011).

The radiated energy in UV and optical lines (Lyα, He II, Ca II H) and continua (in UV, C IV, LyC, He I, He II, green, red, blue) were found to amount to $\approx 3 \times 10^{30}$ erg, about 15% of the total nonthermal energy (Milligan et al. 2014).

The estimate of the nonthermal energy strongly depends on the assumption of the low-energy cutoff of the electron energy spectrum, usually assumed to be somewhere in the range of $\approx$ 10–25 keV. An example of nonthermal energies generated in the flare ribbon plasma is given in Fletcher et al. (2013), where a low energy cutoff of 5 keV was required to balance thermal losses. Using the warm-target bremsstrahlung model of Kontar et al. (2015), a mean electron temperature of $T_e = 8.6$ MK was found for the warm thick-target plasma and a low-energy cutoff of 6.2 ± 1.6 keV (Aschwanden et al. 2014b). In the statistical average, the nonthermal energy exceeds the thermal energy in 85% of the events, which largely confirms the warm thick-target model (Aschwanden et al. 2014b).

The EUV images from AIA/SDO and EUVI/STEREO yield detailed information on EUV dimming during the launch of a CME and thus allow us to determine masses, velocities, and kinetic energies of CMEs at any location on the solar disk (Aschwanden 2016, 2017), while the traditional measurements of CME masses using the polarized brightness of white-light images are only feasible near the solar limb. 2.5-D numerical MHD simulations were also used to calculate the energy partition in current sheet outflows during an eruption (Reeves et al. 2010).

The results of the studies on the global energetics of solar flares and associated coronal mass ejections (CMEs), which include magnetic, thermal, nonthermal, and CME energies in 399 solar M and X-class flare events observed during the first 3.5 years of the SDO mission are synthesized in Table 13.1 (Aschwanden et al. 2017): (i) The sum of the mean nonthermal energy of flare-accelerated particles ($E_{\rm nt}$), the energy of direct heating ($E_{\rm dir}$), and the energy in coronal mass ejections ($E_{\rm CME}$), which are the primary energy dissipation processes in a flare, is found to have a ratio of $(E_{\rm nt} + E_{\rm dir} + E_{\rm CME})/E_{\rm mag} = 0.87 \pm 0.18$, compared with the dissipated magnetic free energy $E_{\rm mag}$, which confirms energy closure within the measurement uncertainties and corroborates the magnetic origin of flares and CMEs; (ii) The energy partition of the dissipated magnetic free energy is: 0.51 ± 0.17 in nonthermal energy of $\geq$ 6 keV electrons, 0.17 ± 0.17 in nonthermal $\geq$ 1 MeV ions, 0.07 ± 0.14 in CMEs, and 0.07 ± 0.17 in direct heating; (iii) The thermal energy is almost always less than the nonthermal energy, which is consistent with the thick-

Table 13.1 Summary table of statistical energy ratios in flares. The sum of primary energies includes nonthermal electrons, ions, direct heating, and CME (kinetic and potential) energies (Aschwanden et al. 2017)

Energy type type	Number of flares	Fraction of energies
Free magnetic energy	172	$E_{\rm mag}/E_{\rm mag} = 1.00 \pm 0.00$
Nonthermal electrons	55	$E_{\rm nt,e}/E_{\rm mag} = 0.51 \pm 0.17$
Nonthermal ions	55	$E_{\rm nt,i}/E_{\rm mag} = 0.17 \pm 0.17$
CME energy	157	$E_{\rm CME}/E_{\rm mag} = 0.07 \pm 0.14$
SEP energy	4	$E_{\rm SEP}/E_{\rm mag} = 0.10 \pm 1.64$
Direct heating	106	$E_{\rm dir}/E_{\rm mag} = 0.07 \pm 0.17$
Thermal energy	170	$E_{\rm th}/E_{\rm mag} = 0.08 \pm 0.13$
Radiated energy in SXR	171	$E_{\rm rad}/E_{\rm mag} = 0.004 \pm 0.130$
Bolometric energy	172	$E_{\rm bol}/E_{\rm mag} = 0.07 \pm 0.10$
Sum of primary energies	52	$E_{\rm sum}/E_{\rm mag} = 0.87 \pm 0.18$
Thermal energy	391	$E_{\rm th}/E_{\rm th} = 1.00 \pm 0.00$
Radiated energy in SXR	389	$E_{\rm rad}/E_{\rm th} = 0.07 \pm 0.06$
Bolometric energy	391	$E_{\rm bol}/E_{\rm th} = 1.14 \pm 0.05$

target model; (iv) The bolometric luminosity in white-light flares is comparable with the thermal energy in soft X-rays (SXR); (v) Solar Energetic Particle (SEP) events carry a fraction ≈ 0.03 of the CME energy, which is consistent with CME-driven shock acceleration; and (vi) The warm-target model predicts a lower limit of the low-energy cutoff at $e_c \approx 6$ keV, based on the mean differential emission measure (DEM) peak temperature of $T_e = 8.6$ MK during flares. This work represents the first statistical study that establishes energy closure in solar flare/CME events.

The largest solar flares are estimated to have an energy of $E \approx 10^{32}$–10^{33} erg, they cover about 30% of the area of a sunspot group, and they are about six times as energetic (in total solar irradiance fluence) as the strongest flares observed in history (Aulanier et al. 2013).

13.8 Magnetic Topology in Flares

The topology or configuration of the magnetic field before and after a flare provides the most relevant observables to identify which magnetic reconnection process operates during a flare or a *coronal mass ejection (CME)* event (see review by Priest and Forbes 2002). Irreversible magnetic field changes during flares are detected in the photospheric field (Sudol and Harvey 2005; Wang et al. 2012). The most important tracers of magnetic field line footpoints that are involved in a magnetic reconnection process are rooted in the so-called chromospheric *flare ribbons*, which are illuminated in hard X-rays and ultraviolet, due to the intense bombardment of

precipitating electrons and ions that are accelerated in coronal particle acceleration sites.

A paradigm of a well-observed large flare is the Bastille-Day flare of 1998 July 14. Magnetic field extrapolations reveal the presence of a null point in the corona, with its associated "spine" field line, and its "fan" surface surrounding the parasitic polarity (Aulanier et al. 2000), which was considered to support the "magnetic breakout model" in a multipolar field configuration (Antiochos et al. 1999). The classical *magnetic breakout model* consists of two dipole sources, where the resulting field configuration defines a two-flux system with two distinct polarity inversion lines, a domelike separatrix surface at the interface of the two flux systems, and a single null point at the intersection of the spine field lines with the separatrix surface (Antiochos et al. 1999; Lynch et al. 2008).

In flares with coronal null points, flare ribbons are located along footpoints of separatrices or quasi-separatrix layers (QSLs) (Masson et al. 2009), and the footprint of the dome-shaped fan surface does map out a closed circular ribbon. Since all fan lines pass through the null point, the entire circular ribbon is expected to brighten simultaneously, but observations show that the fan field lines slip or slip-run according to their distance from the spine (Masson et al. 2009). In the X-class circular ribbon flare of 2012 October 12, three topological structures were identified: (i) a 3-D null point, (ii) a flux rope below the fan of the null point, and (3) a large-scale quasi-separatrix layer (QSL) induced by the quadrupolar-like magnetic field of the active region (Yang et al. 2015). In active regions with QSLs it was found that so-called "fans" (field lines filled with EUV-emitting plasma that fan out from sunspot penumbrae) are primarily related to the pronounced change in connectivity across a QSL to widely separated clusters of magnetic flux (Schrijver et al. 2010).

Another Bastille-Day flare, observed on 2000 July 14, exhibited a classical two-ribbon topology, where the ribbons run from west to east with an almost constant separation distance, which systematically widens during the flare progression. However, some anomalies were noted, such as the asymmetry of the fine structure, ribbon bifurcation, unbalanced magnetic flux, and the strongest hard X-rays occur in the stronger field regions (Fletcher and Hudson 2001). Ribbons are usually located on both sides of a neutral line and they tend to separate with flare progression, with speeds of $v \approx 1$–15 km s^{-1} (Wang et al. 2003).

Homologous flares display morphologically near-identical magnetic configurations, although they occur some time apart. For instance, two homologous flares observed on 2003 November 20 show both four homologous Hα ribbons, both were accompanied by CMEs, both displayed similar photospheric traces of *quasi-separatrix layers (QSL)* and both match well the locations of the four Hα ribbons. The globally unchanged topology and the continuous shearing by the rotating bipole are two key factors responsible for the flare homology (Chandra et al. 2011).

Investigating the topological structure of the coronal magnetic field arising from the interaction of two bipolar regions, four distinct, topologically stable states were found. The changes from one topology to another are produced either by a global separator bifurcation, a local double-separator bifurcation, a new global separatrix quasi-bifurcation, or a new global spine quasi-bifurcation (Beveridge et al. 2002).

The magnetic topology during the evolution of the kink instability in a solar coronal loop has been simulated with a 3-D MHD code. The system starts with an axisymmetric twisted magnetic flux tube that carries a vanishing axial electric current that evolved towards a kinked configuration containing an intense current concentration along the loop, which then becomes resistive and allows a stationary reconnection (Baty 2000). The system reaches a relaxed configuration of lower magnetic energy with three topologically distinct regions; two interwoven flux tubes surrounded by a weakly non-axisymmetric flux tube (Baty 2000).

On the largest (global) scale, the solar surface exhibits a poloidal (during the solar minimum) and a toroidal topology (during the solar maximum), forming a trailing-polarity hole on its pole-ward side that evolves into the new-cycle polar hole, while the leading-polarity open flux on the equatorward side of the bipole progressively closes down by merging with its opposite-hemisphere counterpart (Wang and Sheeley 2003). The global magnetic topology of coronal holes can be characterized by a squashing factor or a *"slog Q distribution* (Fig. 13.8; Titov et al. 2011),

$$slog\,Q = sign(B_r)\ \log[Q/2 + (Q^2/4 - 1)]^{1/2}\,. \tag{13.8.1}$$

Another way to display the topological large-scale structure of the solar corona is a visualization of the separatrix surfaces between different magnetic polarity domains,

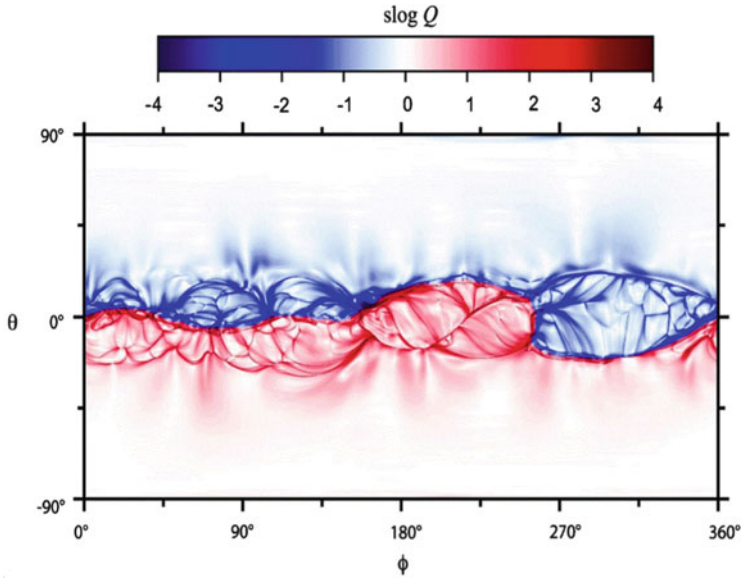

Fig. 13.8 The slog-Q distribution of the solar wind model during the total solar eclipse 2008 August 1, at the sphere of $r = 3R_{\odot}$. The high-Q lines border the regions of open magnetic flux that appear at the photosphere as disconnected or nearly disconnected ones. Blue and red colors correspond to negative and positive magnetic fluxes (Titov et al. 2011)

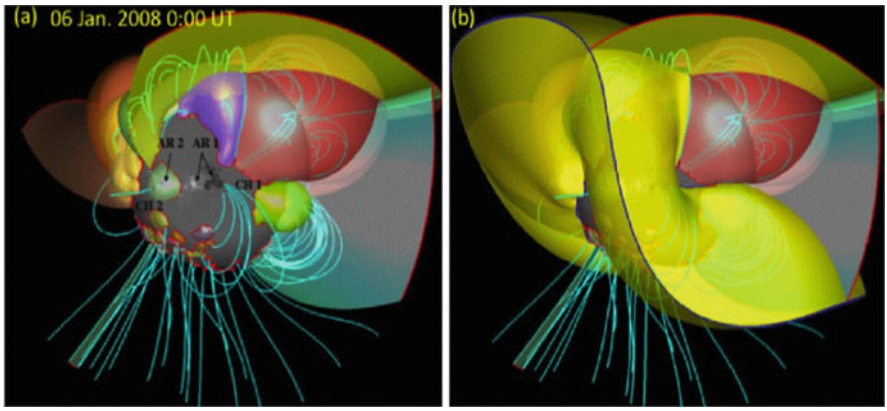

Fig. 13.9 Potential-field source surface model and topological structures of the solar corona for 2008 January 11, showing the separatrices between open and closed field line domains (yellow), as well as different magnetic polarity domains (colored), of active regions, streamers, pseudo-streamers, and associated fans. Null-points are marked with red dots, and photospheric boundaries of separatrices with red curves (van Driel-Gesztelyi et al. 2012)

using the *Potential-field source surface (PFSS)* model, as shown in Fig. 13.9, which depicts active region (domes), coronal holes, streamers, pseudo-streamers, null-points, and their associated fan surfaces and spine fields (van Driel-Gesztelyi et al. 2012).

13.9 MHD Modeling of Flares

There are three types of MHD modeling that have been applied in modeling the magnetic field and hydrodynamics of flares: (i) 1-D flux tubes, (ii) composite multi-threaded 1-D flux tubes, and (iii) 2-D, 2.5D, or 3-D MHD simulations, all of them time-dependent, conceived either as an initial boundary problem, or constrained by data-driven time-dependent boundary motions. For relevant reviews see Shibata and Magara (2011), and Janvier et al. (2015). The physical key processes for producing a flare are: (i) the emergence of magnetic field from the solar interior to the solar atmosphere (flux emergence), (ii) the local enhancement of electric current in the corona (formation of current sheets), and (iii) rapid dissipation of electric currents (magnetic reconnection), which causes shock heating, mass ejection (CMEs), and particle acceleration. The first two processes require (macroscopic) MHD fluid codes, while the latter is modeled with (microscopic particle) kinetic codes. A further distinction is made between eruptive and confined flares.

Among the numerous magnetic field configurations used in MHD simulations of flares we find the following models: (i) the 2-D standard *Carmichael-Sturrock-Hirayama-Kopp-Pneuman (CSHKP)* flare model (Yokoyama and Shibata 2001;

Reeves et al. 2010); (ii) the flux emergence model (Miyagoshi and Yokoyama 2004; Jiang et al. 2012); (iii) the magnetic breakout model with a coronal null point, a spine field line, and a fan surface surrounding the parasitic polarity (Aulanier et al. 2000; Karpen et al. 2012); (iv) magnetic reconnection between oppositely sheared magnetic loops that involves the resistive-tearing mode instability (Kusano et al. 2004; Landi et al. 2015); (v) twisting motion and eruption as response to the converging shearing motion (Zuccharello et al. 2012); (vi) a sigmoidal core with an envelope that contains a coronal null and is prone to a torus instability (Jiang et al. 2013); (vii) spontaneous current-layer fragmentation and cascading reconnection (Barta et al. 2011; Che et al. 2011; Shen et al. 2011); (viii) reconnection of a kinking flux rope (Kliem et al. 2010); (ix) 3-D null point reconnection (Baumann et al. 2013); and (x) vortex and sink flows in eruptive flares as a model for coronal implosions (Zuccharello et al. 2017).

Two examples of 3-D MHD simulations forming twisted flux tubes in the corona are shown in Fig. 13.10 from Janvier et al. (2015): Leake et al. (2013) conducted a flux-rope emergence simulation, where the twisting motion of the polarities resulting from the emergence leads to current-carrying coronal loops (Fig. 13.10a–d). The simulation of Aulanier et al. (2010) forms a flux rope structure via photospheric motions (twisting) and diffusion at the photospheric level, creating a set of field lines running above the inversion line and a sigmoidal distribution of currents (Fig. 13.10e–h).

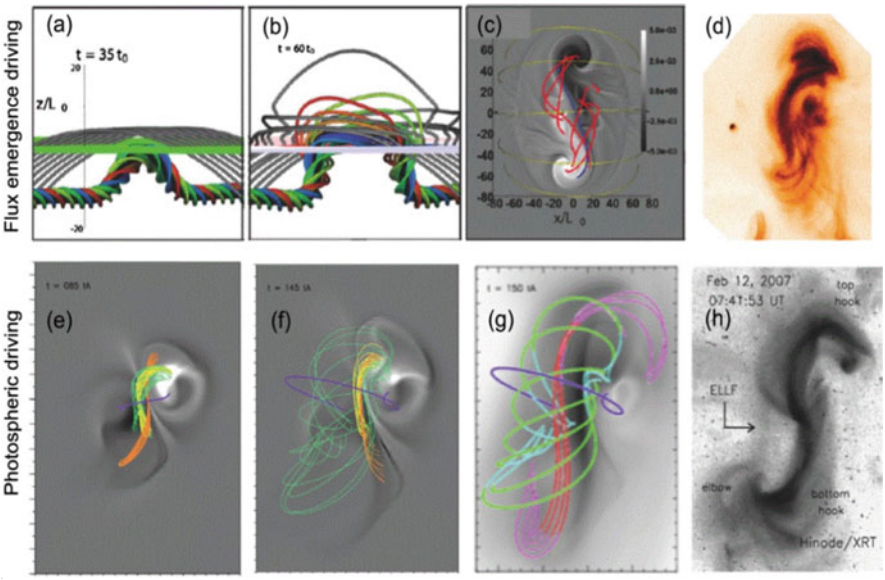

Fig. 13.10 3-D MHD simulation of Leake et al. (2013) (**a–c**) and comparison with observations of a sigmoid on 2007 February 12 (**d**). 3-D MHD simulation of Aulanier et al. (2010) (**e–g**) and comparison with XRT/Hinode observations of a sigmoid on 2007 February 12 (**f**), Janvier et al. (2015)

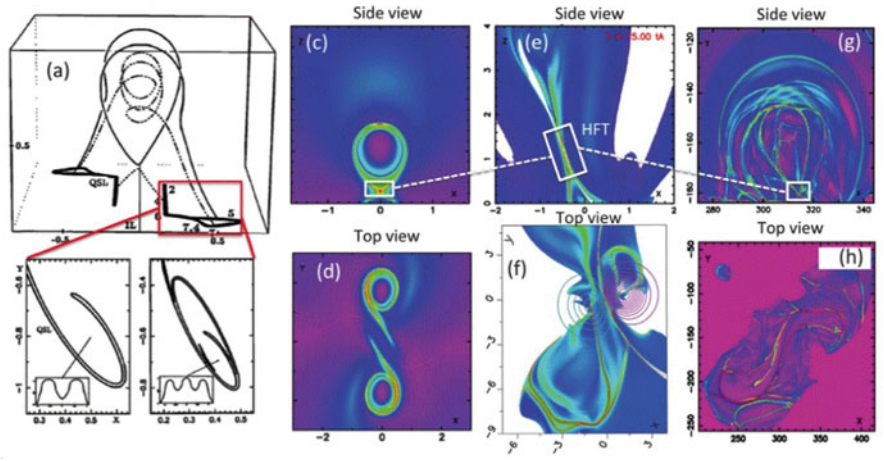

Fig. 13.11 QSLs footprints and field lines for an analytical model of a flux rope (Démoulin et al. 1996) (**a**), with different hook shapes (**b**), central cut (**c**), top view (**d**), QLSs seen from a 2-D cut in the 3-D flux rope (**e**), photospheric footpoints of the QSLs (**f**), and QSLs computed from the flux rope insertion extrapolation model of the 2007 February 12 event (Savcheva et al. 2012; Janvier et al. 2015)

An example of 3-D MHD simulations with *quasi-separatrix layers (QSLs)* is shown in Fig. 13.11. QSLs footpoints and field lines are shown for an analytical model of a flux rope of Démoulin et al. (1996), with numerical computation of the QSLs from Pariat and Démoulin (2012), according to the analytical flux-rope model of Titov and Démoulin (1999) and a flux-rope ejection numerical model of Janvier et al. (2013).

High-resolution MHD simulations have been conducted to study the energy transfer from large scales of flare plasma accumulation to small dissipation length scales, which shows a cascade of consecutively smaller flux ropes (plasmoids), analogous to the vortex-tube cascade in incompressible fluid dynamics, where both tearing and fragmenting coalescence processes are found to be equally important to drive the cascading magnetic reconnection (Barta et al. 2011). When current layers that form during magnetic reconnection become too intense, they disintegrate and spread into a complex web of filaments that causes the rate of reconnection to increase abruptly (Che et al. 2011).

Recent (1-D) hydrodynamic codes include the equations of radiative transfer, the statistical equilibrium is treated in *non-local thermal equilibrium (non-LTE)*, and is solved for numerous transitions of hydrogen, helium, and Ca II. It is found that soft X-ray and EUV back-warming contributes less than 10% of the heating, even in strong flares (Allred et al. 2005).

In a multi-threaded flare loop model, using the electron flux inferred from RHESSI as input and the radiative hydrodynamic code RADYN to simulate the atmospheric response, better agreement of the Mg II line profile was found with

observations when using a higher micro-turbulent velocity of 27 km s^{-1} in a narrow chromospheric layer (Rubio da Costa et al. 2016). The atmospheric response to a high beam flux density satisfactorily achieves the observed continuum brightness in the *near-ultraviolet (NUV)*, consistent with hydrogen (Balmer) recombination radiation that originates from low optical depth in a dense chromospheric condensation (Kowalski et al. 2017).

13.10 Stellar Flares

Do stars produce flares of similar magnitude as the Sun does? Are solar flares detectable at stellar distances? If not, we expect a sensitivity-related bias towards larger events in stellar flare databases. Are there universal physical processes of energy dissipation on Sun and stars that can be quantified by physical scaling laws? Possible physical mechanisms include: MHD oscillations, self-oscillatory (self-organizing) mechanisms, oscillatory reconnection/reconnection reversal, wave-driven reconnection, two-loop coalescence, MHD flow over-stability, the equivalent LCR-contour mechanism, and thermal-dynamical cycles (McLaughlin et al. 2018).

Coronae of late-type stars are formed with soft X-ray structures very similar to those of the Sun, since their behavior is identical to that of the solar coronal structures and of the whole solar corona (Peres et al. 2004). This claim is based on tight correlations that were found between the soft X-ray surface flux (F_X) versus the spectral hardness ratio (HR), which corresponds to $F_X \propto T^6$, yielding scaling laws between density, pressure, length scale, and the volumetric heating rate with the temperature ($p \propto T^{5.2}$) (Peres et al. 2004). The *Rosner-Tucker-Vaiana (RTV)* predicts a scaling law of the emission measure (EM) versus temperature (T), i.e., $EM \propto T^4 L^{(D_3-2)}$ (with D_3 the fractal dimension), which agrees with both solar and stellar flare statistics, although the emission measures of stellar flares are about a factor of 200 higher than in solar flares at the same temperature, a possible sensitivity bias (Aschwanden 2007).

Coronal seismology has been extended from solar to stellar flaring loops (for reviews see Nakariakov and Melnikov 2009; Van Doorsselaere et al. 2016; McLaughlin et al. 2018). In particular, second harmonics of standing acoustic waves are likely to produce quasi-periodic pulsations with periods in the range of 10–300 s (Nakariakov et al. 2004, 2006; Tsiklauri et al. 2004), which overlap with the periods of 220 s observed in white-light emission associated with stellar flaring loops (Mathioudakis et al. 2003), with periods of 160 s during a flare on Ad-Leonis (Houdebine et al. 1993), and periods of 13 and 26 s observed during EV Lac flares (Zhilyaev et al. 2000). X-ray observations of oscillations during a flare on the active M-type dwarf AT Mic were obtained with XMM-Newton, which display a period $P \approx 750$ s and an exponential damping time of $\tau_d \approx 2000$ s, apparently produced in a trans-equatorial loop with a length of $L \approx 250$ Mm (Mitra-Kraev et al. 2005).

Flare oscillations on ξ Boo with a period of $P \approx 1019$ s, observed with XMM-Newton, were interpreted in terms of the fundamental fast-kink mode (Pandey and Srivastava 2009). Long periods of $P \approx 32$ min were observed in the U-band on the dM4.5e star YZ CMi, which could be interpreted with either standing slow magneto-acoustic waves or standing kink oscillations (Anfinogentov et al. 2013). Double periods of $P_1 = 1261$ s and $P_2 = 687$ were observed with XMM-Newton on Proxima Centauri, yielding a period ratio of $P_1/P_2 = 1.83$, possibly attributed to the fundamental and first overtone of slow magneto-acoustic oscillations in the flare loop (Srivastava et al. 2013). Selecting flare events with quasi-periodic pulsations in 42 solar flares and 36 stellar flares observed with XMM-Newton, and performing *empirical mode decomposition (EMD)* of the damped time profiles, correlations were found between the damping times and periods ($\tau_d/P = 1.69 \pm 0.56$ for solar, and $\tau_d/P = 1.74 \pm 0.77$ for stellar events), which was interpreted as evidence for standing slow magneto-acoustic and kink modes in coronal loops (Cho et al. 2016).

A huge new dataset of superflares observed on solar-type stars has been recently provided by the *Kepler* mission. A search during 500 days brought 1547 superflares on 279 G-type dwarfs to the table, which were found to obey a power law distribution of $dN/dE \propto E^{-2}$, as expected from solar flares, but covering by several orders of magnitude higher energies of 10^{33}–10^{36} erg (Fig. 13.12; Shibayama et al.

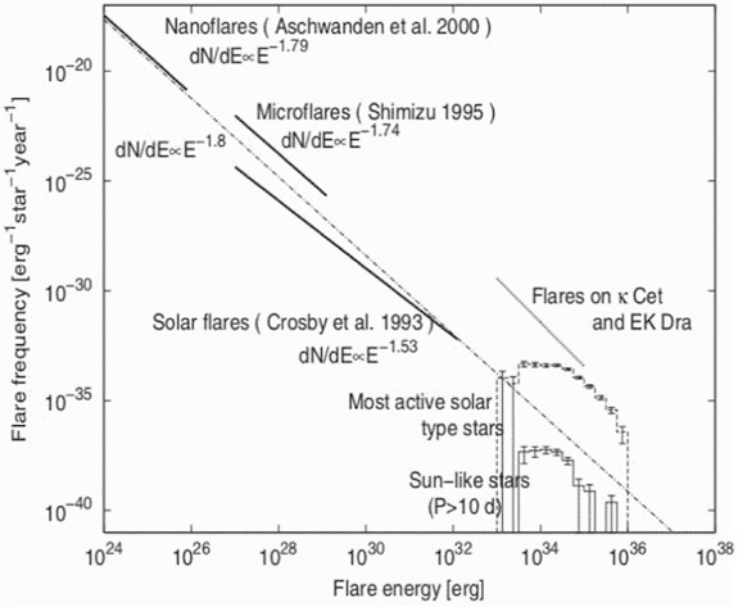

Fig. 13.12 Occurrence rate of superflares on G-type dwarfs and solar flares, including EUV nanoflares (Aschwanden et al. 2000), soft X-ray brightenings (Shimizu 1995), and hard X-ray flares (Crosby et al. 1993). Solar data fit an overall slope of ≈ -1.8, but the most active solar-type stars have a several order of magnitude higher energy (Shibayama et al. 2013)

2013; Maehara et al. 2015). Analysis of short-cadence Kepler data reveal distinct bumps in the flare decay time profile, but no correlation of the periods with any stellar parameter was found (Balona et al. 2015). Another Kepler study with 1439 stellar flares on 216 different stars yielded 56 flares with pronounced quasi-periodic pulsations, where no correlation was found between the stellar temperature, radius, rotation period, and surface gravity, nor with the flare energy (Pugh et al. 2016). A possible correlation was found between the oscillation period and the damping time for the case of a Gaussian damping function, but not for an exponential damping function (Pugh et al. 2016), similar to solar flares.

Radiative hydrodynamic models of optical and ultraviolet emission from M-dwarf flares have been developed in order to infer the strength of weak versus strong beam heating, which is compared with the observed He II 304 line profile and hydrogen Balmer line profiles (Allred et al. 2006). With a unified computational model, heating of the chromosphere by precipitating flare-accelerated charged particles was simulated using a Fokker-Planck kinetic code, which is used to model solar and stellar (dMe) abundances (Allred et al. 2015). The theoretically modeled hydrogen Balmer line broadening was compared with stellar data from A0 Vega and a YZ CMi megaflare, yielding filling factors of $\approx 0.1\%$–1.0% (Kowalski et al. 2017).

Extreme events of giant flares have been observed from magnetars, soft gamma repeaters, and neutron stars. Such stars have extremely strong magnetic fields up to $\lesssim 10^{15}$ G, where extreme energy dissipation episodes are thought to occur by interaction of shearing and reconnection with magnetar-strength external magnetic fields (Thompson and Duncan 2001).

References

(13.1) Direct Heating of Chromosphere

Aschwanden, M.J., Brown, J.C., and Kontar, E.P. 2002, *Chromospheric height and density measurements in a solar flare observed with RHESSI II. Data analysis*, SoPh 210, 383, [69 c, 5 c/y].

Battaglia, M., Fletcher, L., and Benz, A.O. 2009, *Observations of conduction driven evaporation in the early rise phase of solar flares*, A&A 498, 891, [61 c, 7 c/y].

Brosius, J.W. 2012, *EUV spectroscopic observation of direct coronal heating during a C-class solar flare*, ApJ 754, 54, [9 c, 2 c/y].

Brown, J.C., Aschwanden, M.J., and Kontar, E.P. 2002, *Chromospheric height and density measurements in a solar flare observed with RHESSI I. Theory*, SoPh 210, 373, [39 c, 3 c/y].

Brown, J.C., Turkmani, R., Kontar, E.P., et al. 2009, *Local re-acceleration and a modified thick target model of solar flare electrons*, A&A 508, 993, [81 c, 10 c/y].

Cheng, J.X., Ding, M.D., and Li, J.P. 2006, *Diagnostics of the heating processes in solar flares using chromospheric spectral lines*, ApJ 653, 733, [11 c, 1 c/y].

Czaykowska, A., Alexander, D., and De Pontieu, B. 2001, *Chromospheric heating in the late phase of two-ribbon flares*, ApJ 552, 849, [37 c, 2 c/y].

Graham, D.R., Fletcher, L., and Hannah, I.G. 2011, *Hinode/EIS plasma diagnostics in the flaring solar chromosphere*, A&A 532, 27, [28 c, 4 c/y].

Graham, D.R., Fletcher, L., and Labrosse, N. 2015, *Determining energy balance in the flaring chromosphere from oxygen V line ratios*, A&A 584, A6, [3 c, 1 c/y].
Isobe, H., Kubo, M., Minoshima, T., et al. 2007, *Flare ribbons observed with G-band and Fe I 6302 A filters of the SOT onboard Hinode*, PASJ 59 No.SP3, S807, [65 c, 6 c/y].
Kerr, G.S. and Fletcher, L. 2014, *Physical properties of white-light sources in the 2011 February 15 solar flare*, ApJ 783, 98, [32 c, 9 c/y].
Kerr, G.S., Fletcher, L., Russell, A.J.B., et al. 2016, *Simulations of the Mg II k and Ca 8542 lines from an Alfvén wave-heated flare chromosphere*, ApJ 827, 101, [19 c, 13 c/y].
Kowalski, A.F., Allred, J.C., Daw, A., et al. 2017, *The atmospheric response to high nonthermal electron beam fluxes in solar flares. I. Modelling the brightest NUV footpoints in the X1 solar flare of 2014 March 29*, ApJ 836, 12, [16 c, 16 c/y].
Liu, W., Petrosian, V., and Mariska, J.T. 2009, *Combined modeling of acceleration, transport, and hydrodynamic response in solar flares. I. The numerical model*, ApJ 702, 1553, [43 c, 5 c/y].
Milligan, R.O., Kerr, G.S., Dennis, B.R., et al. 2014, *The radiated energy budget of chromospheric plasma in a major solar flare deduced from multi-wavelength observations*, ApJ 793, 70, [44 c, 13 c/y].
Milligan, R.O. 2015, *EUV spectroscopy of the lower solar atmosphere during solar flares (Invited review)*, SoPh 290, 3399, [19 c, 13 c/y].
Milligan, R.O., Gallagher, P.T., Mathioudakis, M. et al. 2006, *Observational evidence of gentle evaporation during the impulsive phase of a solar flare*, ApJ 642, L169, [71 c, 6 c/y].
Reep, J.W. and Russell, A.J.B. 2016, *Alfvénic wave heating of the upper chromosphere in flares*, ApJ 818, 20, [25 c, 17 c/y].
Reep, J.W., Bradshaw, S.J., and Holman, G.D. 2016, *X-ray source heights in a solar flare: Thick-target versus thermal conduction front heating*, ApJ 818, 44, [8 c, 5 c/y].
Rubio da Costa, F., Liu, W., Petrosian, V., et al. 2015, *Combined modeling of acceleration, transport, and hydrodynamic response in solar flares. II. Inclusion of radiative transfer with RADYN*, ApJ 813, 133, [14 c, 6 c/y].
Russell, A.J.B. and Fletcher, L. 2013, *Propagation of Alfvén waves from the corona to chromosphere and consequences for solar flares*, ApJ 765, 81, [37 c, 8 c/y].
Simoes, P.J.A., Graham, D.R., and Fletcher, L. 2015, *Impulsive heating of solar flare ribbons above 10 MK*, SoPh 290, 3573, [9 c, 4 c/y].
Warren, H.P., Reep, J.W., Crump, N.A., et al. 2016, *Transition region and chromospheric signatures of impulsive heating events. I. Observations*, ApJ 829, 35, [8 c, 5 c/y].
Xu, Y., Cao, W., Liu, C., et al. 2006, *High-resolution observations of multiwavelength emissions during two X-class white-light flares*, ApJ 641, 1210, [51 c, 4 c/y].

(13.2) Chromospheric Evaporation

Battaglia, M. and Kontar, E.P. 2012, *RHESSI and SDO/AIA observations of the chromospheric and coronal plasma parameters during a solar flare*, ApJ 760, 142, [27 c, 5 c/y].
Battaglia, M., Kleint, L., Krucker, S., et al. 2015, *How important are electron beams in driving chromospheric evaporation in the 2014 March 29 flare ?* ApJ 813, 113, [24 c, 10 c/y].
Brosius, J.W. and Phillips, K.J.H. 2004, *EUV and X-ray spectroscopy of a solar flare loop observed at high time resolution: A case study in chromospheric evaporation*, ApJ 613, 580, [79 c, 6 c/y].
Brosius, J.W. 2013, *Chromospheric evaporation in solar flare loop strands observed with the EIS on board Hinode*, ApJ 762, 133, [32 c, 7 c/y].
Brosius, J.W. and Daw, A.N. 2015, *Quasi-periodic fluctuations and chromospheric evaporation in a solar flare ribbon observed by IRIS*, ApJ 810, 45, [26 c, 10 c/y].
Brosius, J.W., Daw, A.N., and Inglis, A.R. 2016, *Quasi-periodic fluctuations and chromospheric evaporation in a solar flare ribbon observed by Hinode/EIS, IRIS, and RHESSI*, ApJ 830, 101, [14 c, 9 c/y].

Doschek, G.A., Warren, H.P., and Young P.R. 2013, *Chromospheric evaporation in an M1.8 flare observed by the EIS on Hinode*, ApJ 767, 55, [35 c, 8 c/y].

Dudik, J., Polito, V., Janvier, M. et al. 2016, *Slipping magnetic reconnection, chromospheric evaporation, implosion, and precursors in thie 2014 September 10 X1.6-class solar flare*, ApJ 823, 41, [27 c, 18 c/y].

Graham, D.R. and Cauzzi, G. 2015, *Temporal evolution of multiple evaporating ribbon sources in a solar flare*, ApJ 807, L22, [43 c, 17 c/y].

Kerr, G.S., Fletcher, L., Russell, A.J.B., et al. 2016, *Simulations of the Mg II k and Ca II 8542 lines from an Alfvén wave-heated flare*, ApJ 827, 101, [24 c, 16 c/y].

Li, D., Ning, Z.J., Huang, Y. et al. 2017a, *Explosive chromospheric evaporation driven by nonthermal electrons around one footpoint of a solar flare loop*, ApJ 841, 9, [8 c, 8 c/y].

Li, Y., Ding, M., Qiu, J., et al. 2015a, *Chromospheric evaporation in an X1.0 flare on 2014 March 29 observed with IRIS and EIS*, ApJ 811, 7, [25 c, 10 c/y].

Li, Y., Ning, Z.J., and Zhang, Q.M. 2015b, *Observational evidence of electron-driven evaporation in two solar flares*, ApJ 813, 59, [18 c, 7 c/y].

Li, Y., Kelly, M., Ding, M.D. 2017b, *Spectroscopic observations of magnetic reconnection and chromospheric evaporation in an X-shaped solar flare*, ApJ 848, 118, [5 c, 5 c/y].

Liu, W., Liu, S., Jiang, Y.W. 2006, *RHESSI observations of chromospheric evaporation*, ApJ 649, 1124, [61 c, 5 c/y].

Milligan, R.O., Gallagher, P.T., Mathioudakis, M. et al. 2006a, *Observational evidence of gentle evaporation during the impulsive phase of a solar flare*, ApJ 642, L169, [71 c, 6 c/y].

Milligan, R.O., Gallagher, P.T., Mathioudakis, M. et al. 2006b, *RHESSI and SOHO CDS observations of explosive chromospheric evaporation*, ApJ 638, L117, [81 c, 7 c/y].

Milligan, R.O. and Dennis, B.R. 2009, *Velocity characteristics of evaporated plasma using Hinode/EUV Imaging Spectrometer*, ApJ 699, 968, [116 c, 14 c/y].

Milligan, R.O., Kerr, G.S., Dennis, B.R., et al. 2014, *The radiated energy budget of chromospheric plasma in a major solar flare deduced from multi-wavelength observations*, ApJ 793, 70, [44 c, 13 c/y].

Polito, V., Reep, J.W., Reeves, K.K. 2016, *Simultaneous IRIS and Hinode/EIS observations and modelling of the 2014 October 27 X2.0 class flare*, ApJ 816, 89, [27 c, 18 c/y].

Reep, J.W., Bradshaw, S.J., and Alexander, D. 2015, *Optimal electron energies for driving chromospheric evaporation in solar flares*, ApJ 808, 177, [21 c, 8 c/y].

Reep, J.W. and Russell, A.J.B. 2016, *Alfvénic wave heating of the upper chromosphere in flares*, ApJ 818, L20, [31 c, 21 c/y].

Sadykov, V.M., Vargas Dominguez, S., Kosovichev, A.G. et al. 2015, *Properties of chromospheric evaporation and plasma dynamics of a solar flare from IRIS*, ApJ 805, 167, [20 c, 8 c/y].

Sadykov, V.M., Kosovichev, A.G., Sharykin, I.N. et al. 2016, *Relationship between chromospheric evaporation and magnetic field topology in an M-class solar flare*, ApJ 828, 4, [9 c, 9 c/y].

Tian, H., Li, G., Reeves, K.K., et al. 2014, *Imaging and spectroscopic observations of magnetic reconnection and chromospheric evaporation in a solar flare*, ApJ 797, L14, [43 c, 12 c/y].

Tian, H., Young, P.R., Reeves, K.K., et al. 2015, *Temporal evolution of chromospheric evaporation: Case study of the M1.1 flare on 2014 September 6 and X1.6 flare on 2014 September 10*, ApJ 811, 139, [38 c, 15 c/y].

Veronig, A.M., Vrsnak, B., Dennis, B.R. 2002, *Investigation of the Neupert effect in solar flares. I. Statistical properties and the evaporation model*, A&A 392, 699, [93 c, 14 c/y].

Veronig, A.M., Brown, J.C., Dennis, B.R., et al. 2005, *Physics of the Neupert effect: Estimates of the effects of source energy, mass transport, and geometry using RHESSI and GOES data*, ApJ 621, 482, [109 c, 9 c/y].

Woods, T.N., Hock, R., Eparvier, F., et al. 2011, *New solar EUV irradiance observations during flares*, ApJ 739, 59, [70 c, 11 c/y].

Yokoyama, T. and Shibata, K. 2001, *MHD simulation of a solar flare with chromospheric evaporation effect based on the magnetic reconnection model*, ApJ 549, 1160, [146 c, 9 c/y].

Zhang, Q.M., Li, D., Ning, Z.J., et al. 2016, *Explosive chromospheric evaporation in a circular-ribbon flare*, ApJ 827, 27, [17 c, 11 c/y].

(13.3) Coronal Condensation and Rain

Antolin, P., Shibata, K., Vissers, G. 2010, *Coronal rain as a marker for coronal heating mechanisms*, ApJ 716, 154, [58 c, 8 c/y].
Antolin, P. and Verwichte, E. 2011, *Transverse oscillations of loops with coronal rain observed by Hinode/SOT*, ApJ 736, 121, [41 c, 6 c/y].
Antolin, P., Vissers, G., and Rouppe van der Voort, L. 2012, *On-disk coronal rain*, SoPh 280, 457, [27 c, 5 c/y].
Antolin, P. and Rouppe van der Voort, L. 2012, *Observing the fine structure of loops through high-resolution spectroscopic observations of coronal rain with the CRISP instrument at the Swedish Solar Telescope*, ApJ 745, 152, [84 c, 15 c/y].
Antolin, P., Vissers, G., Pereira, T.M.D., et al. 2015, *The multithermal and multi-stranded nature of coronal rain*, ApJ 806, 81, [35 c, 14 c/y].
Brosius, J.W. 2003, *Chromospheric evaporation and warm rain during a solar flare observed in high time resolution with the CDS aboard SOHO*, ApJ 586, 1417, [54 c, 4 c/y].
Fang, X., Xia, C., and Keppens, R. 2013, *Multidimensional modeling of coronal rain dynamics*, ApJ 771, 29, [32 c, 7 c/y].
Fang, X., Xia, C., and Keppens, R., et al. 2015, *Coronal rain in magnetic arcades: rebound shocks, limit cycles, and shear flows*, ApJ 807, 142, [13 c, 5 c/y].
Froment, C., Auchère, F., Bocchialini, K. 2015, *Evidence for evaporation-incomplete condensation cycles in warm solar coronal loops*, ApJ 807, 158, [18 c, 7 c/y].
Froment, C., Auchère, F., Aulanier, G., 2017, *Long-period intensity pulsations in coronal loops explained by thermal non-equilibrium cycles*, ApJ 835, 272, [6 c, 6 c/y].
Innes, D.E., McKenzie, D.E., and Wang, T. 2003, *SUMER spectral observations of post-flare supra-arcade inflows*, SoPh 217, 247, [92 c, 6 c/y].
Kleint, L., Antolin, P., Tian, H., et al. 2014, *Detection of supersonic downflows and associated heating events in the transition region*, ApJ 789, 42, [30 c, 9 c/y].
Klimchuk, J.A., Karpen, J.T., and Antiochos, S.K. 2010, *Can thermal nonequilibrium explain coronal loops ?* ApJ 714, 1239, [55 c, 7 c/y].
Liu, W, Berger, T.E., and Low, B.C. 2012, *First SDO/AIA observation of solar prominence formation following an eruption: Magnetic dips and sustained condensation and drainage*, ApJ 745, 21, [51 c, 9 c/y].
Longcope, D.W. 2014, *A simple model of chromospheric evaporation and condensation driven conductivity in a solar flare*, ApJ 795, 10, [15 c, 4 c/y].
McKenzie, D.E. and Hudson, H.S. 1999, *X-Ray observations of motions and structure above a solar flare arcade*, ApJ 519, L93, [214 c, 12 c/y].
McKenzie, D.E. 2000, *Supra-arcade downflows in long-duration solar flare events*, SoPh 195, 381, [100 c, 6 c/y].
Mendoza-Briceno, C.A., Sigalotti, L.D.G., and Erdelyi, R. 2005, *Catastrophic cooling of impulsively heated coronal loops*, ApJ 624, 1080, [34 c, 3 c/y].
Müller, D.A.N., Hansteen, V.H., Peter, H. 2003, *Dynamics of coronal loops: I. Condensation in cool loops and its effect on transition region lines*, A&A 411, 605, [102 c, 7 c/y].
Müller, D.A.N., Peter, H., Hansteen, V.H., 2004, *Dynamics of coronal loops: II. Catastrophic cooling and high-speed downflows*, A&A 424, 289, [86 c, 7 c/y].
Müller, D.A.N., De Groof, A., Hansteen, V.H., et al. 2005, *High-speed coronal rain*, A&A 436, 1067, [59 c, 5 c/y].
Reeves, K.K. and Golub, L. 2011, *AIA observations of hot flare plasma*, ApJ 727, L52, [66 c, 10 c/y].
Sanchez-Diaz, E., Rouillard, A.P., Davies, J.A., et al. 2017, *Observational evidence for the associated formation of blobs and raining inflows in the solar corona*, ApJ 835, 7, [7 c, 7 c/y].
Savage, S.L., McKenzie, D.E., and Reeves, K.K. 2012, *Re-interpretation of supra-arcade downflows in solar flares*, ApJ 747, L40, [58 c, 11 c/y].

Schrijver, C.M. 2001, *Catastrophic cooling and high-speed downflow in quiescent solar coronal loops observed with TRACE*, SoPh 198, 325, [123 c, 7 c/y].
Scullion, E., Rouppe van der Voort L., Antolin, P., et al. 2016, *Observing the formation of flare-driven coronal rain*, ApJ 833, 184, [5 c, 5 c/y].
Sheeley, N.R.Jr., Warren, H.P., and Wang, Y.M. 2004, *The origin of postflare loops*, ApJ 616, 1224, [86 c, 6 c/y].
Vashalomidze, Z., Kukhianidze, V., Zaqarashvili, T.V., et al. 2015, *Formation and evolution of coronal rain observed by SDO/AIA on February 22, 2012*, A&A 577, 136, [9 c, 4 c/y].
Verwichte, E., Antolin, P., Rowlands, G., et al. 2017, *Kinematics of coronal rain in a transversely oscillating loop: Ponderomotive force and rain-excited oscillations*, A&A 598, 57, [5 c, 5 c/y].
Zhang, Q.M., Li, D., Ning, Z.J. 2016, *Chromospheric condensation and quasi-periodic pulsations in a circular-ribbon flare*, ApJ 832, 65, [11 c, 7 c/y].

(13.4) Flare Oscillations and Waves

Asai, A., Shimojo, M., Isobe, H., et al. 2001, *Periodic acceleration of electrons in the 1998 November 10 solar flare*, ApJ 562, L103, [91 c, 6 c/y].
Brannon, S.R., Longcope, D.W., and Qiu, J. 2015, *Spectroscopic observations of an evolving flare ribbon substructure suggesting origin in current sheet waves*, ApJ 810, 4, [24 c, 10 c/y].
Dennis, B.R., Tolbert, A.K., Inglis, A., et al. 2017, *Detection and interpretation of long-lived X-ray quasi-periodic pulsations in the X-class solar flare on 2013 May 14*, ApJ 836, 84, [9 c, 9 c/y].
Dolla, L., Marque, C., Seaton, D.B., et al. 2012, *Time delays in quasi-periodic pulsations observed during the X2.2 solar flare on 2011 February 15*, ApJ 749, L16, [31 c, 6 c/y].
Foullon, C., Verwichte, E., Nakariakov, V.M., et al. 2005, *X-ray quasi-periodic pulsations in solar flares and MHD oscillations*, A&A 440, L59, [54 c, 4 c/y].
Hayes, L.A., Gallagher, P.T., Dennis, B.R. 2016, *Quasi-periodic pulsations during the impulsive and decay phases of an X-class flare*, ApJ 827, L30, [15 c, 10 c/y].
Inglis, A.R., Nakariakov, V.M., and Melnikov, V.F. 2008, *Multi-wavelength spatially resolved analysis of quasi-periodic pulsations in a solar flare*, A&A 487, 1147, [50 c, 5 c/y].
Inglis, A.R. and Nakariakov, V.M. 2009, *A multi-periodic oscillatory event in a solar flare*, A&A 493, 259, [56 c, 7 c/y].
Inglis, A.R., Ireland, J., and Dominique, M. 2015, *Quasi-periodic pulsations in solar and stellar flares: Re-evaluating their nature in the context of power-law flare Fourier spectra*, ApJ 798, 108, [28 c, 11 c/y].
Inglis, A.R., Ireland, J., Dennis, B.R., et al. 2016, *A large-scale search for evidence of quasi-periodic pulsations in solar flares*, ApJ 833, 284, [12 c, 8 c/y].
Kolotkov, D.Y., Nakariakov, V.M., Kupriyanova, E.G., et al. 2015, *Multi-mode quasi-periodic pulsations in a solar flare*, A&A 574, A53, [25 c, 10 c/y].
Kopylova, Y.G., Melnikov, A.V., Stepanov, A.V. et al. 2007, *Oscillations of coronal loops and second pulsations of solar radio emission*, Astron.Lett. 33/10, 706, [31 c, 7 c/y].
Kumar, P., Nakariakov, V.M., Cho, K.S. 2016, *Observations of quasiperiodic pulsations in hard X-ray, radio, and EUV wavelengths*, ApJ 822, 7, [16 c, 11 c/y].
Kumar, P., Nakariakov, V.M., Cho, K.S. 2017, *Quasi-periodic radio bursts associated with fast-mode waves near a magnetic null point*, ApJ 836, 121, [10 c, 10 c/y].
Kupriyanova, E.G., Melnikov, V.F., Nakariakov, V.M., et al. 2010, *Types of microwave quasi-periodic pulsations in single flaring loops*, SoPh 267, 329, [67 c, 9 c/y].
Kupriyanova, E.G., Melnikov, V.F., and Shibasaki, K. 2013, *Spatially resolved microwave observations of multiple periodicities in a flaring loop*, SoPh 284, 559, [31 c, 7 c/y].
Li, D., Ning, Z.J., and Zhang, Q.M. 2015, *Imaging and spectral observations of quasi-periodic pulsations in a solar flare*, A[K 807, 72, [24 c, 10 c/y].
Li, D. and Zhang, Q.M. 2017, *Quasi-periodic pulsations with multiple periods in hard X-ray emission*, MNRAS 471, L6, [5 c, 5 c/y].

Liu,W., Title, A.M., Zhao, J.W., et al. 2011, *Direct imaging of quasi-periodic fast propagating waves of 2000 km/s in the low solar corona by the ADO/AIA*, ApJ 736, L13, [84 c, 13 c/y].
Liu,W., Ofman, L., Nitta, N.V., et al. 2012, *Quasi-periodic fast-mode trains within a global EUV wave and sequential transverse oscillations detected by SDO/AIA*, ApJ 753, 52, [79 c, 14 c/y].
Melnikov, V.F., Reznikova, V.E., Shibasaki, K., et al. 2005, *Spatially resolved microwave pulsations of a flare loop*, A&A 439, 727, [84 c, 7 c/y].
Milligan, R.O., Fleck, B., Ireland, J., et al. 2017, *Detection of 3-minute oscillations in full-disk Lyα during a solar flare*, ApJ 848, L8, [3 c, 3 c/y].
Nakariakov, V.M., Tsiklauri, D., Kelly, A., et al. 2004, *Acoustic oscillations in solar and stellar flaring loops*, A&A 414, L25, [96 c, 7 c/y].
Nakariakov, V.M., Foullon, C., Verwichte, E., et al. 2006, *Quasi-periodic modulation of solar and stellar flaring emission by MHD oscillations in a nearby loop*, A&A 452, 343, [101 c, 9 c/y].
Nakariakov, V.M. and Melnikov, V.F. 2009, *Quasi-periodic pulsations in solar flares*, SSRv 149, 119, [187 c, 21 c/y].
Nakariakov, V.M., Foullon, C., Myagkova, I.N., et al. 2010a, *Quasi-periodic pulsations in the gamma-ray emission of a solar flare*, ApJ 708, L47, [45 c, 6 c/y].
Nakariakov, V.M., Inglis, A.R., Zimovets, I.V., et al. 2010b, *Oscillatory processes in solar flares*, Plasma Physics and Controlled Fusion 52/12, 124009, [34 c, 5 c/y].
Nakariakov, V.M. and Zimovets, I.V. 2011, *Slow magneto-acoustic waves in two-ribbon flares*, ApJ 730, L27, [41 c, 6 c/y].
Nakariakov, V.M., Pilipenko, V., Heilig, B., et al. 2016, *MHD oscillations in the solar corona and Earth's magnetosphere: Towards consolidated understanding*, SSRv 200, 75, [48 c, 32 c/y].
Ofman, L., Liu, W., Title, A., et al. 2011, *Modeling super-fast MHD waves observed by SDO in active region funnels*, ApJ 740, L33, [32 c, 5 c/y].
Simoes, P.J.A., Fletcher, L., Hudson, H.S., et al. 2013, *Implosion of coronal loops during the impulsive phase of a solar flare*, ApJ 777, 152, [30 c, 7 c/y].
Simoes, P.J.A., Hudson, H.S., and Fletcher, L. 2015, *Soft X-ray pulsations in solar flares*, SoPh 290, 3625, [28 c, 11 c/y].
Sych, R., Nakariakov, V.M., Karlicky, M., et al. 2009, *Relationship between wave processes in sunspots and quasi-periodic pulsations in active region flares*, A&A 505, 791, [91 c, 11 c/y].
Takasao, S. and Shibata, K. 2016, *Above-the-loop-top oscillation and quasi-periodic coronal wave generation in solar flares*, ApJ 823, 150, [15 c, 10 c/y].
Van Doorsselaere, T., Kupriyanova, E.G., and Yuan, D. 2016, *Quasi-periodic pulsations in solar and stellar flares: An overview of recent results (Invited review)*, SoPh 291, 3143, [33 c, 22 c/y].

(13.5) High-Temperature Components

Aschwanden, M.J., Boerner, P., Caspi, A., et al. 2015, *Benchmark test of differential emission measure codes and multi-thermal energies in solar active regions*, SoPh 290, 2733, [8 c, 3 c/y].
Barnes, W.T., Cargill, P.J., and Bradshaw, S.J. 2016a, *Inference of heating properties from "hot" non-flaring plasmas in active region cores. I. Single nanoflares*, ApJ 829, 31, [7 c, 5 c/y].
Barnes, W.T., Cargill, P.J., and Bradshaw, S.J. 2016b, *Inference of heating properties from "hot" non-flaring plasmas in active region cores. II. Nanoflare trains*, ApJ 833, 217, [4 c, 3 c/y].
Battaglia, M. and Kontar, E.P. 2013, *Electron distribution functions in solar flares from combined X-ray and EUV observations*, ApJ 779, 107, [19 c, 4 c/y].
Caspi, A. and Lin, R.P. 2010, *RHESSI line and continuum observations of super-hot flare plasma*, ApJ 725, 161, [72 c, 10 c/y].
Caspi, A., Krucker, S., and Lin, R.P. 2014, *Statistical properties of super-hot solar flares*, ApJ 781, 43, [26 c, 7 c/y].
Caspi, A., Shih, A.Y., McTiernan, J.M., et al. 2015, *Hard X-ray imaging of individual spectral components in solar flares*, ApJ 811, L1, [7 c, 3 c/y].

Hannah, I.G., Hudson, H.S., Hurford, G.J., et al. 2010, *Constraining the hard X-ray properties of the Quiet Sun with new RHESSI observations*, ApJ 724, 487, [25 c, 3 c/y].
Hannah, I.G., Grefenstette, B.W., Smith, D.M., et al. 2016, *The first X-ray imaging spectroscopy of quiescent solar active regions with NuSTAR*, ApJ 820, L14, [19 c, 13 c/y].,
Hanneman, W.J. and Reeves, K.K. 2014, *Thermal structure of current sheets and supra-arcade downflows in the solar corona*, ApJ 786, 95, [18 c, 5 c/y].
Ishikawa, S.N., Glesener, L., Christe, S., et al. 2014, *Constraining hot plasma in a non-flaring region with FOXSI hard X-ray observations*, PASJ 66S, 15, [14 c, 4 c/y].
Ishikawa, S.N., Glesener, L., Krucker, S., et al. 2017, *Detection of nanoflare-heated plasma in the solar corona by the FOXSI-2 sounding rocket*, Nature Astronomy 1, 771, [7 c, 7 c/y].
Ko, Y.K., Doschek, G.A., Warren, H.P., et al. 2009, *Hot plasma in nonflaring active regions observed by the EIS on Hinode*, ApJ 697, 1956, [31 c, 21 c/y].
Kuhar, M., Krucker, S., Glesener, L., et al. 2018, *NuSTAR detection of X-ray heating events in the Quiet Sun*, ApJ 856, L32.
Milligan, R.O. 2008, *A hot microflare observed with RHESSI and Hinode*, ApJ 680, 157, [23 c, 2 c/y].
Patsourakos, S. and Klimchuk, J.A. 2009, *Spectroscopic observations of hot lines constraining coronal heating in solar active regions*, ApJ 696, 760, [36 c, 4 c/y].
Petralia, A., Reale, F., Testa, P., et al. 2014, *Thermal structure of a non-flaring corona from Hinode/EIS*, A&A 564, 3, [10 c, 3 c/y].
Phillips, K.J.H. 2008, *Highly ionized Fe X-ray lines at energies 7.7–8.6 keV*, A&A 490, 823, [7 c, 1 c/y].
Reale, F. and Orlando, S. 2008, *Nonequilibrium of ionization and the detection of hot plasma in nanoflare-heated coronal loops*, ApJ 684, 715, [57 c, 6 c/y].
Reale, F., Testa, P., Klimchuk, J.A., et al. 2009a, *Evidence of widespread hot plasma in a nonflaring coronal active region from Hinode/XRT*, ApJ 698, 756, [66 c, 8 c/y].
Reale, F. McTiernan, J.M., and Testa, P. 2009b, *Comparison of Hinode/XRT and RHESSI detection of hot plasma in the non-flaring solar corona*, ApJ 704, 58, [29 c, 3 c/y].
Ryan, D.F., O'Flannagain, A.M., Aschwanden, M.J., et al. 2014, *The compatibility of flare temperatures observed with AIA, GOES, and RHESSI*, SoPh 289, 2547, [15 c, 4 c/y].
Schmelz, J.T., Kashyap, V.L., Saar, S.H., et al. 2009, *Some like it hot: Coronal heating observations from Hinode X-ray Telescope and RHESSI*, ApJ 704, 863, [38 c, 4 c/y].
Sharykin, I.N., Struminskii, A.B., and Zimovets, I.V. 2015, *Plasma heating to super-hot temperatures (>30 MK) in the August 9, 2011 solar flare*, Astron.Lett. 41, 53, [5 c, 2 c/y].
Shestov, S.V., Kuzin, S.V., Urnov, A.M., et al. 2010, *Solar plasma temperature diagnostics in flares and active regions from spectral lines in the range 280–330 A in the SPIRIT/CORONAS-F experiment*, Astron.Lett. 36, 44, [16 c, 2 c/y].
Simoes, P.J.A., Graham, D.R., and Fletcher, L. 2015, *Impulsive heating of solar flare ribbons above 10 MK*, SoPh 290, 3573, [9 c, 4 c/y].
Testa, P., Reale, F., Landi, E., et al. 2011, *Temperature distribution of a non-flaring active region from simultaneous Hinode XRT and EIS*, ApJ 728, 30, [39 c, 6 c/y].
Warren, H.P. and Reeves, K.K. 2001, *High spatial resolution observations of a hot region in a solar flare with the TRACE*, ApJ 554, L103, [16 c, 1 c/y].
White, S.M., Thomas, R.J., and Schwartz, R.A. 2005, *Updated expressions for determining temperatures from GOES soft X-ray measurements*, SoPh 227, 231, [106 c, 8 c/y].

(13.6) Flare Size Distributions and SOC Systems

Abramenko, V.I., Yurchyshyn, V.B., Wang, H., et al. 2003, *Signature of an avalanche in solar flares as measured by photospheric magnetic fields*, ApJ 597, 1135, [42 c, 3 c/y].
Anastasiadis, A., Gontikakis, C., Vilmer, N., et al. 2004, *Electron acceleration and radiation in evolving complex active regions*, A&A 422, 323, [13 c, 1 c/y].

Aschwanden, M.J., Tarbell, T., Nightingale, R., et al. 2000, *Time variability of the quiet Sun observed with TRACE. II. Physical parameters, temperature evolution, and energetics of EUV nanoflares*, ApJ 535, 1047, [219 c, 13 c/y].

Aschwanden, M.J. 2011a, *The state of self-organized criticality of the Sun during the last three solar cycles. I. Observations*, SoPh 274, 99, [27 c, 4 c/y].

Aschwanden, M.J. 2011b, *The state of self-organized criticality of the Sun during the last three solar cycles. II. Theoretical model*, SoPh 274, 119, [9 c, 1 c/y].

Aschwanden, M.J. 2012, *A statistical fractal-diffusive avalanche model of a slowly-driven self-organized criticality system*, A&A 539, A2, [41 c, 7 c/y].

Aschwanden, M.J. and Freeland, S.L. 2012, *Automated solar flare statistics in soft X-rays over 37 years of GOES observations: The invariance of self-organized criticality during three solar cycles*, ApJ 754, 112, [51 c, 9 c/y].

Aschwanden, M.J. 2014, *A macroscopic description of a generalized self-organized criticality system: Astrophysical applications*, ApJ 782, 54, [21 c, 6 c/y].

Aschwanden, M.J., Xu, Y., and Jing, J. 2014a, *Global energetics of solar flares. I. Magnetic energies*, ApJ 797, 50, [27 c, 8 c/y].

Aschwanden, M.J. 2015, *Thresholded power law size distributions of instabilities in astrophysics*, ApJ 814, 19, [9 c, 4 c/y].

Aschwanden, M.J., Crosby N.B., Dimitropoulou, M., et al. 2016, *25 Years of self-organized criticality: Solar and astrophysics*, SSRv 198, 47, [56 c, 37 c/y].

Baiesi, M., Paczuski, M., and Stella, A.L. 2006, *Intensity threshold and the statistics of the temporal occurrence os solar flares*, Phys.Rev.Lett 96/5. 051103, [75 c, 6 c/y].

Bingert, S. and Peter, H. 2013, *Nanoflare statistics in an active region 3-D MHD coronal model*, A&A 550, A30, [25 c, 6 c/y].

Charbonneau, P., McIntosh, S.W., Liu, H.L., et al. 2001, *Avalanche models for solar flares*, SoPh 203, 321, [130 c, 8 c/y].

Christe, S., Hannah, I.G., Krucker, S., et al. 2008, *RHESSI microflares statistics. I. Flare-finding and frequency distributions*, ApJ 677, 1385, [73 c, 8 c/y].

Dauphin, C., Vilmer, N., and Anastasiadis, A. 2007, *Particle acceleration and radiation in flaring complex solar active regions modeled by cellular automata*, A&A 468, 273, [12 c, 1 c/y].

Dimitropoulou, M., Isliker, H., Vlahos, L., et al. 2013, *Dynamic data-driven integrated flare model based on self-organized criticality*, A&A 553, A65, [8 c, 2 c/y].

Georgoulis, M.K., Vilmer, N., and Crosby, N.B. 2001, *A comparison between spatial properties of solar X-ray flares and avalanche predictions in cellular automata statistical flare models*, A&A 367, 326, [28 c, 2 c/y].

Hughes, D., Paczuski, M., Dendy, R.O., et al. 2003, *Solar flares as cascades of reconnecting magnetic loops*, Phys.Rev.Lett. 90/13, 131101, [74 c, 5 c/y].

Isliker, H., Anastasiadis, A., and Vlahos, L. 2000, *MHD consistent cellular automata (CA) models. I. Basic features*, A&A 363, 1134, [40 c, 2 c/y].

Isliker, H., Anastasiadis, A., and Vlahos, L. 2001, *MHD consistent cellular automata (CA) models. II. Applications to solar flares*, A&A 377, 1068, [35 c, 2 c/y].

McIntosh, S.W. and Charbonneau, P. 2001, *Geometric effects in avalanche models of solar flares: Implications for coronal heating*, ApJ 563, L165, [20 c, 1 c/y].

Morales, L.F. and Charbonneau, P. 2008, *Scaling laws and frequency distributions of avalanche areas in a self-organized criticality model of solar flares*, GRL 35/4, L04108, [8 c, 1 c/y].

Nishizuka, N., Asai, A., Takasaki, H., et al. 2009, *The power-law distribution of flare kernels and fractal current sheets in a solar flare*, ApJ 694, L74, [26 c, 3 c/y].

Qiu, J., Liu, C., Gary, D., et al. 2004, *Hard X-ray and microwave observations of microflares*, ApJ 612, 530, [30 c, 2 c/y].

Sammis, I., Tang, F., and Zirin, H. 2000, *The dependence of large flare occurrence on the magnetic structure of sunspots*, ApJ 540, 583, [117 c, 7 c/y].

Uritsky, V.M., Paczuski, M., Davila, J.M., et al. 2007, *Coexistence of self-organized criticality and intermittent turbulence in the solar corona*, Phys.Rev.Lett. 99/2, 025001, [42 c, 4 c/y].

Wheatland, M.S. 2000, *Flare frequency-size distributions for individual active regions*, ApJ 532, 1209, [25 c, 1 c/y].

(13.7) Flare Energy Partition

Altyntsev, A.A., Fleishman, G.D., Lesovoi, S., et al. 2012, *Thermal to nonthermal energy partition at the early rise phase of solar flares*, ApJ 758, 138, [13 c, 3 c/y].

Aschwanden, M.J. and Shimizu, T. 2013, *Multi-wavelength observations of the spatio-temporal evolution of solar flares with AIA/SDO. II. Hydrodynamic scaling laws and thermal energies*, ApJ 776, 132, [15 c, 3 c/y].

Aschwanden, M.J., Zhang, J., and Liu, K. 2013, *Multi-wavelength observations of the spatio-temporal evolution of solar flares with AIA/SDO. I. Universal scaling laws of space and time parameters*, ApJ 775, 23, [8 c, 2 c/y].

Aschwanden, M.J., Xu, Y., and Jing, J. 2014b, *Global energetics of solar flares. III. Nonthermal energies*, ApJ 832, 27, [17 c, 5 c/y].

Aschwanden, M.J., Boerner, P., Caspi, A., et al. 2015, *Benchmark test of differential emission measure codes and multi-thermal energies in solar active regions*, SoPh 290, 2733, [8 c, 3 c/y].

Aschwanden, M.J. 2016, *Global energetics of solar flares. IV. Coronal mass ejection energetics*, ApJ 831, 105, [10 c, 7 c/y].

Aschwanden, M.J. 2017, *Global energetics of solar flares. VI. Refined energetics of coronal mass ejections*, ApJ 847, 27, [2 c, 2 c/y].

Aschwanden, M.J., Caspi, A., Cohen, C., et al. 2017, *Global energetics of solar flares. V. Energy Closure in Flares and Coronal Mass Ejections*, ApJ 836, 17, [13 c, 13 c/y].

Aulanier, G., Démoulin, P., Schrijver, C.J., et al. 2013, *The standard flare model in three dimensions. II. Upper limit on solar flare energy*, A&A 549, A66, [48 c, 4 c/y].

Benz, A.O. 2008, *Flare observations*, LRSP 5/1, 1, [155 c, 16 c/y].

Benz, A.O. 2017, *Flare observations*, LRSP 14/1, 1, [24 c, 24 c/y].

Bleybel, A., Amari, T.,van Driel-Gesztelyi, L. 2002, *Global budget for an eruptive active region. I. Equilibrium reconstruction approach*, A&A 395, 685, [57 c, 4 c/y].

Emslie, A.G., Kucharek, H., Dennis, B.R., et al. 2004, *Energy partition in two solar flare/CME events*, JGR 109/A10, A10104, [163 c, 12 c/y].

Emslie, A.G., Dennis, B.R., Holman, G.D., et al. 2005, *Refinements to flare energy estimates: A followup to "Energy partition in two solar flare/CME events" by A.G.Emslie et al.*, JGR 110/A11, A11103, [120 c, 10 c/y].

Emslie, A.G., Dennis, B.R., Shih, A.Y., et al. 2012, *Global energetics of 38 large solar eruptive events*, ApJ 759, 71, [150 c, 27 c/y].

Falewicz, R., Siarkowski, M., and Rudawy, P. 2011, *Plasma heating in the very early and decay phases of solar flares*, ApJ 733, 37, [10 c, 2 c/y].

Fletcher, L., Hannah, I.G., Hudson, H.S., et al. 2013, *Flare ribbon energetics in the early phase of an SDO flare*, ApJ 771, 104, [22 c, 5 c/y].

Feng, L., Wiegelmann, T., Su, Y., et al. 2013, *Magnetic energy partition between the coronal mass ejection and flare from AR 11382*, ApJ 765, 37, [30 c, 7 c/y].

Kontar, E.P., Jeffrey, N.L.S., Emslie, A.G., et al. 2015, *Collisional relaxation of electrons in a warm plasma and accelerated nonthermal electron spectra in solar flares*, ApJ 809, 35, [12 c, 5 c/y].

Milligan, R.O., Kerr, G.S., Dennis, B.R., et al. 2014, *The radiated energy budget of chromospheric plasma in a major solar flare deduced from multi-wavelength observations*, ApJ 793, 70, [45 c, 13 c/y].

Oka, M., Krucker, S., Hudson, H.S. et al. 2015, *Electron energy partition in the above-the-looptop solar hard X-ray sources*, ApJ 799, 129, [29 c, 12 c/y].

Reeves, K.K., Linker, J.A., Mikic, Z., et al. 2010, *Current sheet energetics, flare emissions, and energy partition in a simulated solar eruption*, ApJ 721, 1547, [60 c, 8 c/y].

Régnier, S. and Priest, E.R. 2007, *Free magnetic energy in solar active regions above the minimum-energy relaxed state*, ApJ 669, L53, [47 c, 4 c/y].
Saint-Hilaire, P. and Benz, A.O. 2005, *Thermal and non-thermal energies of solar flares*, A&A 435, 743, [81 c, 6 /y].
Shibata, K. and Yokoyama, T. 1999, *On the universal correlation between the flare temperature and the emission measure for solar and stellar flares*, ApJ 526, L49, [74 c, 4 c/y].
Sun, X., Hoeksema, J.T., Liu, Y., et al. 2012, *Evolution of magnetic field and energy in a major eruptive active region based on SDO/HMI observations*, ApJ 748, 77, [191 c, 34 c/y].
Warmuth, A. and Mann, G. 2016a, *Constraints on energy release in solar flares from RHESSI and GOES X-ray observations. I. Physical parameters and scalings*, A&A 588, A115, [10 c, 7 c/y].
Warmuth, A. and Mann, G. 2016b, *Constraints on energy release in solar flares from RHESSI and GOES X-ray observations. II. Energetics and energy partition*, A&A 588, A116, [8 c, 5 c/y].

(13.8) Magnetic Topology in Flares

Antiochos, S.K., DeVore, C.R., and Klimchuk, J.A. 1999, *A model for solar coronal mass ejections*, ApJ 510, 485, [844 c, 46 c/y].
Aulanier, G., DeLuca, E.E., Antiochos, S.K. 2000, *The topology and evolution of the Bastille Day flare*, ApJ 540, 1126, [179 c, 10 c/y].
Baty, H. 2000, *Magnetic topology during the reconnection process in a kinked coronal loop*, A&A 360, 345, [28 c, 2 c/y].
Beveridge, C., Priest, E.R., and Brown, D.S. 2002, *Magnetic topologies due to two bipolar regions*, SoPh 209, 333, [39 c, 3 c/y].
Chandra, R., Schmieder, B., Mandrini, C.H., et al. 2011, *Homologous flares and magnetic field topology in active region NOAA 10501 on 20 November 2003*, SoPh 269, 83, [51 c, 8 c/y].
Fletcher, L. and Hudson, H. 2001, *The magnetic structure and generation of EUV flare ribbons*, SoPh 204, 71, [104 c, 6 c/y].
Lynch, B.J., Antiochos, S.K., DeVore, C.R., et al. 2008, *Topological evolution of a fast magnetic breakout CME in 3-D*, ApJ 683, 1192, [135 c, 14 c/y].
Masson, S., Pariat, E., Aulanier, G., et al. 2009, *The nature of flare ribbons in coronal null-point topology*, ApJ 700, 559, [176 c, 21 c/y].
Priest, E.R. and Forbes, T.G. 2002, *The magnetic nature of solar flares*, Astron.Astroph. Rev. 10/4, 313, [443 c, 29 c/y].
Schrijver, C.J., DeRosa, M.L., and Title, A.M. 2010, *Magnetic field topology and the thermal structure of the corona over solar active regions*, ApJ 719, 1083, [18 c, 2 c/y].
Sudol, J.J. and Harvey, J.W. 2005, *Longitudinal magnetic field changes accompanying solar flares*, ApJ 635, 647, [167 c, 13 c/y].
Titov, V.S., Mikic, Z., Linker, J.A., et al. 2011, *Magnetic topology of coronal hole linkages*, ApJ 731, 111, [52 c, 8 c/y].
Wang, H., Qiu, J., and Zhang, H. 2003, *Study of ribbon separation of a flare associated with a quiescent filament eruption*, ApJ 593, 564, [88 c, 6 c/y].
Wang, Y.M. and Sheeley, N.R.Jr. 2003, *On the topological evolution of the coronal magnetic field during the solar cycle*, ApJ 599, 1404, [55 c, 4 c/y].
Wang, S., Liu, C., Liu, R., et al. 2012, *Response of the photospheric magnetic field to the X2.2 flare on 2011 February 15*, ApJ 745, L17, [98 c, 18 c/y].
van Driel-Gesztelyi, L., Culhane, J.L., Baker, D., et al. 2012, *Magnetic topology of active regions and coronal holes: Implications for coronal outflows and the solar wind*, SoPh 281, 237, [36 c, 7 c/y].
Yang, K., Guo, Y., and Ding, M.D. 2015, *On the 2012 October 23 circular ribbon flare: Emission features and magnetic topology*, ApJ 806, 171, [29 c, 12 c/y].

(13.9) MHD Modeling of Flares

Allred, J.C., Hawley, S.L., Abbett, W.P., et al. 2005, *Radiative hydrodynamic models of the optical and ultraviolet emission from solar flares*, ApJ 630, 573, [169 c, 14 c/y].

Aulanier, G., DeLuca, E.E., Antiochos, S.K. 2000, *The topology and evolution of the Bastille Day flare*, ApJ 540, 1126, [179 c, 10 c/y].

Aulanier, G., Török, T., Démoulin, P., et al. 2010, *Formation of torus-unstable flux ropes and electric currents in erupting sigmoids*, ApJ 708, 314, [258 c, 34 c/y].

Barta, M., Büchner, J., Karlicky, M., et al. 2011, *Spontaneous current-layer fragmentation and cascading reconnection in solar flares. I. Model and analysis*, ApJ 737, 24, [95 c, 15 c/y].

Baumann, G., Galsgaard, K., Nordlund, A. 2013, *3-D solar null point reconnection MHD simulations*, SoPh 284, 467, [24 c, 5 c/y].

Che, H., Drake, J.F., and Swisdak, M. 2011, *A current filamentation mechanism for breaking magnetic field lines during reconnection*, Nature 474, 7350, [75 c, 12 c/y].

Démoulin, P., Priest, E.R., and Lonie, D.P. 1996, *3-D magnetic reconnection without null points. II. Application to twisted flux tubes*, JGR 101, 7631, [120 c, 6 c/y].

Janvier, M., Aulanier, G., Pariat, E. et al. 2013, *The standard flare model in 3-D. III. Slip-running reconnection properties*, A&A 555, A77, [66 c, 15 c/y].

Janvier, M., Aulanier, G., and Démoulin, P. 2015, *From coronal observations to MHD simulations, the building blocks for 3D models of solar flares (Invited Review)*, SoPh 290, 3425, [40 c, 16 c/y].

Jiang, R.L., Fang, C., and Chen, P.F. 2012, *Numerical simulation of solar microflares in a canopy-type magnetic configuration*, ApJ 751, 152, [24 c, 4 c/y].

Jiang, C., Feng, X., Wu, S.T., et al. 2013, *MHD simulation of a sigmoid eruption of active region 11283*, ApJ 771, L30, [60 c, 13 c/y].

Karpen, J.T., Antiochos, S.K., and DeVore, C.R. 2012, *The mechanisms for the onset and explosive eruption of coronal mass ejections and eruptive flares*, ApJ 760, 81, [86 c, 16 c/y].

Kliem, B., Linton, M.G., Török, T., et al. 2010, *Reconnection of a kinking flux rope triggering the ejection of a microwave and hard X-ray source. II. Numerical modeling*, SoPh 266, 91, [41 c, 5 c/y].

Kowalski, A.F., Allred, J.C., Daw, A., et al. 2017, *The atmospheric response to high nonthermal electron beam fluxes in solar flares. I. Modeling the brightest NUV footpoints in the X1 solar flare of 2014 March 29*, ApJ 836, 12, [17 c, 17 c/y].

Kusano, K., Maeshiro, T., Yokoyama, T., et al. 2004, *The trigger mechanism of solar flares in a coronal arcade with reversed magnetic shear*, ApJ 610, 537, [124 c, 9 c/y].

Landi, S., Del Zanna, L., Papini, E. et al. 2015, *Resistive MHD simulations of the ideal tearing mode*, ApJ 806, 131, [26 c, 10 c/y].

Leake, J.E., Linton, M.G., and Török, T. 2013, *Simulations of emerging magnetic flux. I. The formation of stable coronal flux ropes*, ApJ 778, 99, [52 c, 12 c/y].

Miyagoshi, T. and Yokoyama, T. 2004, *MHD simulation of solar coronal chromospheric evaporation jets caused by magnetic reconnection associated with magnetic flux emergence*, ApJ 614, 1042, [38 c, 3 c/y].

Pariat, E. and Démoulin, P. 2012, *Estimation of the squashing degree within a 3-D domain*, A&A 541, A78, [56 c, 10 c/y].

Reeves, K.K., Linker, J.A., Mikic, Z., et al. 2010, *Current sheet energetics, flare emissions, and energy partition in a simulated solar eruption*, ApJ 721, 1547, [60 c, 8 c/y].

Rubio da Costa, F., Kleint, L., Petrosian, V., et al. 2016, *Data-driven radiative hydrodynamic modeling of the 2014 March 29 X1.0 solar flare*, ApJ 827, 38, [27 c, 18 c/y].

Savcheva, A., Pariat, E., van Ballegooijen, A., et al. 2012, *Sigmoidal active region on the Sun: Comparison of a MHD simulation and a nonlinear force-free field model*, ApJ 750, 15, [71 c, 13 c/y].

Shen, C., Lin, J., and Murphy, N.A. 2011, *Numerical experiments on fine structure within reconnecting current sheets in solar flares*, ApJ 737, 14, [57 c, 9 c/y].

Shibata,K., and Magara, T. 2011, *Solar flares: Magnetohydrodynamic processes*, LRSP 8, 6, [238 c, 37 c/y].
Titov, V.S. and Démoulin, P. 1999, *Basic topology of twisted magnetic configurations in solar flares*, A&A 351, 707, [402 c, 22 c/y].
Yokoyama, T. and Shibata, K. 2001, *MHD simulation of a solar flare with chromospheric evaporation effect based on the magnetic reconnection model*, ApJ 549, 1160, [146 c, 9 c/y].
Zuccharello, F.P., Meliani, Z., and Poedts, S. 2012, *Numerical modeling of the initiation of coronal mass ejections in active region NOAA 9415*, ApJ 758, 117, [20 c, 4 c/y].
Zuccharello, F.P., Aulanier, G., Dudik, J., et al. 2017, *Vortex and sink flows in eruptive flares as a model for coronal implosions*, ApJ 837, 115, [5 c, 5 c/y].

(13.10) Stellar Flares

Allred, J.C., Hawley, S.L., Abbett, W.P., et al. 2006, *Radiative hydrodynamic models of optical and UV emission from M dwarf flares*, ApJ 644, 484, [66 c, 6 c/y]
Allred, J.C., Kowalski, A.F., and Carlsson, M. 2015, *A unified computational model for solar and stellar flares*, ApJ 809, 104, [46 c, 18 c/y].
Anfinogentov, S., Nakariakov, V.M., Mathioudakis, M., et al. 2013, *The decaying long-period oscillation of a stellar megaflare*, ApJ 773, 156, [29 c, 6 c/y].
Aschwanden, M.J. 2007, *From solar nanoflares to stellar giant flares: Scaling laws and non-implications for coronal heating*, Adv.Spac.Res. 39/12, 1867, [8 c, 1 c/y].
Aschwanden, M.J., Tarbell, T.D., Nightingale, R.W., et al. 2000, *Time variability of the "Quiet" Sun observed with TRACE. II. Physical parameters, temperature evolution and energetics of EUV Nanoflares*, ApJ 535, 1047, [214 c, 12 c/y].
Balona, L.A., Broomhall, A.M., Kosovichev, A., et al. 2015, *Oscillations in stellar superflares*, MNRAS 450, 956, [16 c, 11 c/y].
Cho, I,H., Cho, K.S., Nakariakov, V.M., et al. 2016, *Comparison of damped oscillations in solar and stellar X-ray flares*, ApJ 830, 110, [11 c, 7 c/y].
Crosby, N.B., Aschwanden, M.J., Dennis, B.R. 1993, *Frequency distributions and correlations of solar X-ray flare parameters*, SoPh 143, 275, [345 c, 14 c/y].
Houdebine, E.R., Foing, B.H., Doyle, J.G. et al. 1993, *Dynamics of flares on late type DMe stars. Part II: Mass motions and prominence oscillations during a flare on Ad Leonis*, A&A 274, 245, [30 c, 1 c/y].
Kowalski, A.F., Allred, J.C., Uitenbroek, H., et al. 2017, *Hydrogen Balmer line broadening in solar and stellar flares*, ApJ 837, 125, [7 c, 7 c/y].
Maehara, H., Shibayama, T., Notsu, Y., et al. 2015, *Statistical properties of superflares on solar-type stars based on 1-min cadence data*, Earth Planets and Space 67, 59, [44 c, 18 c/y].
Mathioudakis, M., Seiradakis, J.H., Williams, D.R. et al. 2003, *White-light oscillations during a flare on II Peg*, A&A 403, 1101, [76 c, 5 c/y].
McLaughlin, J.A., Nakariakov, V.M., Dominique, M., et al. 2018, *Modelling quasi-periodic pulsations in solar and stellar flares*, SSRv 214, 45, [10 c, 10 c/y].
Mitra-Kraev, U., Harra, L.K., Williams, D.R., et al. 2005, *The first observed stellar X-ray flare oscillation: Constraints on the flare loop length and the magnetic field*, A&A 436, 1041, [70 c, 6 c/y].
Nakariakov, V.M., Tsiklauri, D., Kelly, A., et al. 2004, *Acoustic oscillations in solar and stellar flaring loops*, A&A 414, L25, [96 c, 7 c/y].
Nakariakov, V.M., Foullon, C., Verwichte, E., et al. 2006, *Quasi-periodic modulation of solar and stellar flaring emission by MHD oscillations in a nearby loop*, A&A 452, 343, [101 c, 9 c/y].
Nakariakov, V.M. and Melnikov, V.F. 2009, *Quasi-periodic pulsations in solar flares*, SSRv 149, 119, [187 c, 21 c/y].
Pandey, J.C. and Srivastava, A.K. 2009, *Observations of X-ray oscillations in ξ Bootis: Evidence of a fast-kink mode in the stellar loops*, ApJ 697, 153, [33 c, 4 c/y].

Peres, G., Orlando, S., and Reale, F. 2004, *Are coronae of late-type stars made of solar-like structures ? The X-ray surface flux versus hardness ratio diagram and the pressure-temperature correlation*, ApJ 612, 472, [16 c, 1 c/y].

Pugh, C.E., Armstrong, D.J., Nakariakov, V.M. et al. 2016, *Statistical properties of quasi-periodic pulsations in white-light flares observed with Kepler*, MNRAS 459, 3659, [18 c, 12 c/y].

Shibayama, T., Maehara, H., Notsu, S., et al. 2013, *Superflares on solar-type stars observed with Kepler. I. Statistical properties of superflares*, ApJS 209, 5, [113 c, 25 c/y].

Shimizu, T. 1995, *Energetics and occurrence rate of active-region transient brightenings and implications for the heating of the active-region corona*, PASJ 47, 251, [279 c, 12 c/y].

Srivastava, A.K., Lalitha, S., and Pandey, J.C. 2013, *Evidence of multiple slow acoustic oscillations in the stellar flaring loops of Proxima Centauri*, ApJ 778, 28, [12 c, 3 c/y].

Thompson, C. and Duncan, R.C. 2001, *The giant flare of 1998 August 27 from SGR 1900+14. II. Radiative mechanism and physical constraints on the source*, ApJ 561, 980, [201 c, 12 c/y].

Tsiklauri, D., Nakariakov, V.M., Arber, T.D., et al. 2004, *Flare-generated acoustic oscillations in solar and stellar coronal loops*, A&A 422, 351, [54 c, 4 c/y].

Van Doorsselaere, T., Kupriyanova, E.G., and Yuan, D. 2016, *Quasi-periodic pulsations in solar and stellar flares: An overview of recent results (Invited Review)*, SoPh 291, 3143, [29 c, 19 c/y].

Zhilyaev, B.E., Romanyuk, Y.O., Verlyuk, I.A. et al. 2000, *Detection of high-frequency optical oscillations on the flare star EV Lacertae*, A&A 364, 641, [43 c, 2 c/y].

Chapter 14
CME Initiation

14.1 CME Observables, Catalogs, and Classifications

Recent reviews on *coronal mass ejections (CMEs)* can be grouped into observational aspects (Cane 2000; Gopalswamy 2004, 2016; Hudson et al. 2006; Schmieder et al. 2015; Webb and Howard 2012; Wimmer-Schweingruber et al. 2006), and theoretical aspects (Forbes 2000; Zhang and Low 2005; Forbes et al. 2006; Chen 2011, 2017; Lin et al. 2015).

Statistical properties of CMEs have been gathered for the CME rates, the apparent speeds (projected in the plane-of-sky), heights as a function of time, acceleration, central position angles, angular widths, and the Kp geomagnetic storm index. The velocity time profiles of CMEs can be described with a three-phase scenario: the initiation phase, the impulsive acceleration phase (coinciding with the impulsive flare rise phase), and the propagation phase (Zhang et al. 2001). Electron temperatures and electron densities of CMEs have been calculated based on *differential emission measure (DEM)* analysis in the dimming regions, the footprints of CMEs, which provide information on CME core heating, plasma compression in the leading front, and adiabatic expansion in the dimming region (Cheng et al. 2012; Aschwanden 2016, 2017). The spatial structure of CMEs is hard to define. Standard detections report the apparent position angle and angular width of CMEs, which becomes problematic for halo CMEs. However, full 3-D reconstructions of CMEs have been attempted with 3-D polarimetric imaging of C2/LASCO/SOHO data (Moran and Davila 2004), and with stereoscopic observations (Thernisien et al. 2009).

M. J. Aschwanden, *New Millennium Solar Physics*, Astrophysics and Space Science Library 458, https://doi.org/10.1007/978-3-030-13956-8_14

CME parameters have been measured from LASCO/SOHO white-light observations during 1996–1998 (St.Cyr et al. 2000), a set of 3217 CME events during 1996–2000 (Moon et al. 2002), and of $\approx$ 7000 CME events during 1996–2002 (Yashiro et al. 2004). This continually updated list (1996–2017) of CME events, based on visual detection, the so-called *LASCO/SOHO CME catalog* or *CDAW CME catalog*, is available at the website http://cdaw.gsfc.nasa.gov/CME_list/, providing the central position angle, the angular width, linear and quadratic speed profiles, acceleration, CME mass, and kinetic energy (Gopalswamy et al. 2009). CMEs during solar cycle 23 are compiled in Gopalswamy (2006). LASCO/SOHO appears to miss faint (or low-mass) CMEs, compared with earlier observations (St.Cyr et al. 2000). A study of all major solar eruptions during the solar cycle 24 is conducted in Gopalswamy et al. (2014). Most existing CME catalogs (CACTUS, SEEDS, ARTEMIS, CORIMP) have been compiled with automated detection. The only manually compiled catalog is the CDAW catalog (Yashiro et al. 2004; Gopalswamy et al. 2009). A new automated algorithm, called *coronal image processing catalog (CORIMP)*, has been developed, which applies a Savitzky-Golay filter, along with quadratic and linear fits for the height-time measurements of CME trajectories (Byrne 2015).

Large statistics of CME parameters has been pursued with automated detection of CMEs in LASCO/SOHO data, using the Hough transform to create height-time maps, which yields an overall success rate of 94% for CME detection (Robbrecht and Berghmans 2004). Another method, the *Solar Eruptive Event Detection System (SEEDS)* code, performs pre-processing, detection, tracking, and event cataloging, based on a 2-D image to 1-D radial profile projection method, with a success rate of 75% in the CME detection, compared with the official LASCO catalog (Olmedo et al. 2008). Another automated CME detection algorithm using LASCO data is the *Computer Aided CME Tracking software (CACTUS)*, which is about a factor of two more sensitive than the visual LASCO CME catalog (Fig. 14.1), and reveals a scale-free power law distribution of CME sizes (Robbrecht et al. 2009). A catalog of $\approx$ 300 near-Earth *Interplanetary Coronal Mass Ejection (ICME)* events was created during 1996–2009 that covers the complete cycle 23, containing geomagnetic parameters, the interplanetary magnetic field, solar wind composition, and charge states (Richardson and Cane 2010). A comprehensive study of the solar cycle dependence on the CME mass and energy over a full solar cycle (1996–2009) was conducted by Vourlidas et al. (2010), which showed that "normal CMEs" reach a constant mass for $> 10 R_\odot$ in the C2 coronagraph, while "pseudo-CMEs" disappear in the C3 field-of-view.

Distinctions are made for CMEs that propagate side-ward to the line-of-sight, in contrast to halo CMEs that are Earth-directed, or move in anti-Earth direction when originating from the backside of the Sun. CMEs associated with flares were found to have a higher median speed than those associated with eruptive filaments, which was considered as evidence for two different classes of CMEs (Moon et al. 2002). This bimodality, however, did not hold up in a statistical study of 545 flare-associated CMEs and 104 non-flare CMEs using LASCO/SOHO data from 1996–2001 (Vrsnak et al. 2005). A different power law slope of the frequency distributions

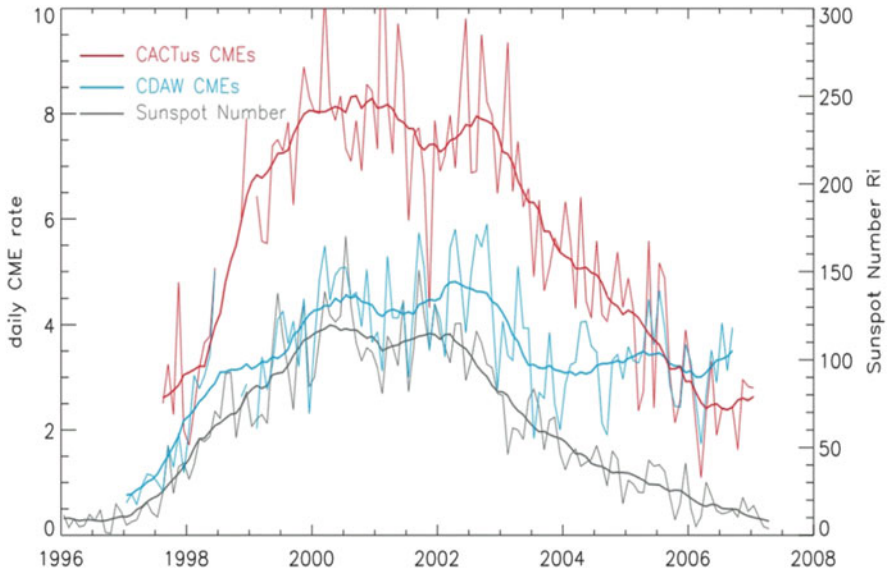

Fig. 14.1 Daily LASCO/SOHO CME rates for cycle 23 (thin curves: smoothed per month, thick curves: smoothed over 13 months) from 1997 to 2006, extracted from the CACTUS (red) and the CDAW (blue) CME catalog. As a reference, the daily and monthly sunspot number (SSN, gray) is overplotted, produced by the SIDC-Royal Observatory of Belgium. The CME rates have been corrected for duty cycle (Robbrecht et al. 2009)

has been obtained when selecting flares with, and without CMEs (Yashiro et al. 2006), which may be related to the two types of eruptive and confined (compact) flares. Generally, it is expected that massive CMEs are correlated with large eruptive flares. However, not all CMEs follow this *"big flare syndrome"*, because some great solar active regions are flare-rich but CME-poor (Sun et al. 2015).

14.2 CME Energetics

The importance of *coronal mass ejections (CMEs)*, like the importance of solar flares, is concealed in their energetics. The energy of a CME can be measured from various parameters, such as from the kinetic energy, the gravitational potential energy, the magnetic energy, the thermal energy, or the particle energies accelerated in CME-driven shocks. The synergy of various energy parameters in solar flares has often been characterized with the term *"big-flare syndrome"*. In addition, the term *"solar flare myth"* has been coined by Jack Gosling (1993), in order to emphasize that the flare-associated electromagnetic emission has a lesser geoeffective impact than CMEs, because it causes only a brief change in the conductivity of the ionosphere, compared with the much larger impacts of CMEs during major space

weather events, such as the generation of geomagnetic storms and large solar energetic particle events, which both last much longer than the impulsive flare duration. Of course, flares and CMEs are two different aspects of the same eruptive event, the former referring to the electromagnetic emission (in X-rays, EUV, and microwaves), while the latter is referring to the mass motion. Nevertheless, the total energies contained in flares and CMEs require detailed models and measurements with large statistics over many orders of magnitude.

White-light observations with LASCO/SOHO provided direct measurements of the mass, velocity, and geometry of CMEs (Vourlidas et al. 2000). The CME mass m_{CME} is obtained by subtracting a brightness image before a CME launch, while the excess number of electrons is determined by the ratio of the excess observed brightness B_{obs} over the brightness $B_e(\theta)$ of a single electron at some angle θ, computed from the Thomson scattering function,

$$m_{CME} = \frac{B_{obs}}{B_e(\theta)} \, 1.97 \times 10^{24} \, \mathrm{g} \, , \tag{14.2.1}$$

where the angle θ is usually assumed to be zero (corresponding to the plane-of-sky above the solar limb).

The gravitational potential energy of a CME is obtained from

$$E_{grav} = \sum_{fluxrope} \int_{R_\odot}^{R} \frac{G M_\odot m}{r^2} dr_i \, , \tag{14.2.2}$$

and the kinetic energy of a CME is,

$$E_{kin} = \frac{1}{2} \sum_{fluxrope} m_i v_{CME}^2 \, , \tag{14.2.3}$$

while the magnetic energy is modeled from the flux rope volume $V = L \, A$, with conservation of the magnetic flux $\Phi = A \, B$,

$$E_{mag} = \frac{1}{8\pi} \int_{fluxrope} B^2 dV = \frac{1}{8\pi} L \, A \, B^2 \, , \tag{14.2.4}$$

with A being the area of the flux rope and L the length of the flux rope (which can be measured from LASCO images). LASCO measurements showed that the gravitational potential energy and the kinetic energy increase at the expense of the magnetic energy as the CME moves out, keeping the total energy roughly constant (Vourlidas et al. 2000). The mass and kinetic energy of CMEs asymptotically approach a constant at $> \; 10 R_\odot$, while the mass density $(g/R_\odot^2)$ of CMEs varies relatively little, indicating a small range of coronal heights for the CME source regions (Vourlidas et al. 2010). The energy partition of (magnetic, kinetic, gravitational) CME energies computed with a 2.5-D MHD code has been compared

with observations and an order-of-magnitude agreement was found (Reeves et al. 2010). The best correlation of any CME parameter was found between the CME mass m_{CME} and the soft X-ray GOES flare flux F $[Wm^2]$, i.e., $m_{CME} \approx 10^{18.5} F^{0.7}$ (Aarnio et al. 2011).

The thermal energy of CMEs requires a measurement of the temperature and density evolution, which could be obtained from UV spectroscopy using UVCS/SOHO (Ciaravella and Raymond 2008). A *differential emission measure (DEM)* analysis, using AIA/SDO data revealed temperatures of $T \approx$ 8–14 MK in the core of an eruptive plasmoid, yielding thermal energies of $E_{th} = 5 \times 10^{29}, 1 \times 10^{29}$, and 2×10^{30} erg, while the kinetic energy for the core and envelope was slightly lower, suggesting continuous influx of energy in the growing current sheet during the eruption (Hannah and Kontar 2013). Using AIA/SDO 131, 171, and 304 Å data, 32% of the flares were found to host hot flux ropes, or 49% of the eruptive events (Nindos et al. 2015). Similar numbers were obtained from coronagraphic observations (Vourlidas et al. 2013).

The CME speed distributions for accelerating or decelerating events were found to be nearly identical, and they could be fitted with a single log-normal distribution (which is similar to a power-law distribution, see Yashiro et al. 2006), suggesting that the same driving mechanism of a nonlinear nature is acting in both slow and fast dynamical types of CMEs (Yurchyshyn et al. 2005). A reciprocal relationship between the acceleration magnitude and the acceleration duration was found (Zhang and Dere 2006). Only a weak correlation was found between CME post-impulsive-phase acceleration and flare decay time (Cheng et al. 2010). The CME peak accelerations were found in the range of $a =$ 20–6800 m s^{-2} and are inversely correlated with the acceleration duration and the height at peak acceleration (Bein et al. 2011). Occasionallyh the acceleration can reach $a \lesssim 10$ km s^{-2} (Gopalswamy et al. 2018). A majority (74%) of CMEs reach their peak acceleration at distances below $r < 1.5 R_\odot$, suggesting that the Lorentz force in the lower corona acts as prime accelerator (Bein et al. 2011). Stereoscopic reconstructions yield acceleration heights up to (2–4) $R_\odot$ (Joshi and Srivastava 2011).

A second method of determining the CME mass is based on the *coronal dimming* in the CME source region (Fig. 14.2), where the mass loss due to the evacuation of CME material diminishes the EUV and soft X-ray brightness locally. This interpretation is corroborated by a high association rate of CMEs with EUV dimming events, where 55% of the dimming events are associated with CMEs, and 84% of CMEs are associated with dimmings (Bewsher et al. 2008). A stereoscopic study of 34 CMEs that were observed in quadrature by both STEREO A and B revealed that about 1 out of 3 CMEs was a "stealth CME" without low coronal signatures, and the speeds of these stealth CMEs are typically below 300 km s^{-1} (Ma et al. 2010). In a statistical study of 1078 CME events observed with LASCO/SOHO, 21% of the CMEs could not be localized due to poor data, 22% of the CMEs occurred above the limb, and 32% (stealth) CMEs showed no eruption in EIT/SOHO (Wang et al. 2011).

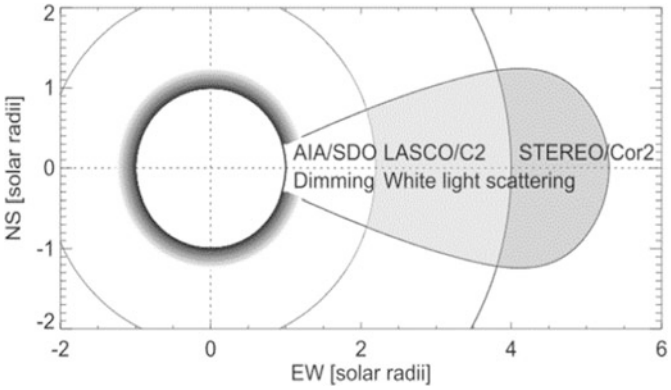

Fig. 14.2 Schematic of CME mass determination methods in EUV vs. white light. Using the EUV method, the CME mass is calculated from the missing mass that causes the EUV dimming in the lower corona at $r \lesssim 1.1 R_{\odot}$, while the white-light method measures the excess brightness in a coronagraph image, e.g., at $r \gtrsim 1.5$ ($2.5 R_{\odot}$) beyond the occulting disk of the C2/LASCO/SOHO (COR2/STEREO) coronagraphs

The largest statistics on the energetics of CMEs, using the EUV dimming effect as observed with AIA/SDO, has been furnished for 399 GOES M- and X-class flare events, and was compared with simultaneous LASCO/SOHO data (Aschwanden 2016, 2017). The EUV dimming method, which measures the CME expansion in the lowest hydrostatic scale height ($h \lesssim 0.1 R_{\odot}$) is truly complementary to the Thomson scattering method in white light, which detects the CME evolution in the outer corona $r \gtrsim (2\text{–}10) R_{\odot}$ (Fig. 14.2). An initial EUV dimming model (Aschwanden 2016) is based on (i) radial (wedge-shaped) adiabatic expansion of the CME volume, (ii) the hydrostatic scale height before eruption, (iii) the kinematics of acceleration in lowest altitudes, and (iv) the gravitational potential of energy, which sets a limit of $v_{esc} \approx 618$ km s^{-1} for the escape velocity. The energy partition between kinetic and gravitational energy is time- and height-dependent, but their sum is found to be systematically lower than the dissipated magnetic energies, which is consistent with a magnetic origin of CMEs. A refined EUV dimming model has been applied to 860 events, featuring the following improvements (Aschwanden 2017): (i) a CME geometry with self-similar adiabatic expansion, (ii) the deceleration of CMEs caused by solar gravity, (iii) a self-consistent relationship between the CME center-of-mass motion (measured from EUV dimming) and the leading-edge motion (detected in white-light, being about twice the center-of-mass speed), (iv) the equipartition of the CME's kinetic and thermal energies, and (iv) the application of the Rosner-Tucker-Vaiana scaling law. Comparing the results from the two (white-light scattering and EUV dimming) methods it is found that (i) LASCO is less sensitive than AIA in detecting CMEs, (ii) CME masses below $m_{CMS} \lesssim 10^{14}$ g are underestimated by LASCO, (iii) AIA and LASCO masses, speeds, and energies agree closely in the statistical mean, and (iv) the CME parameters of the speed v, the emission measure-weighted flare peak temperature T_e, and the length scale L

of a CME footprint area are consistent with the following scaling laws: $v \propto T_e^{1/2}$, $v \propto m_{CME}^{1/4}$, and $m_{CMS} \propto L^2$.

14.3 CME Helicity

While we discussed the magnetic helicity in active regions in Sect. 8.3, we now consider the role of magnetic helicity during *coronal mass ejections (CMEs)*. On the most fundamental level, each CME contributes a systematic permanent change to the coronal magnetic field (Low 2001). Reviews on helicity aspects of CMEs can be found in Low (2001), Démoulin (2007), Démoulin and Pariat (2009), Chen (2011), Pevtsov et al. (2014), and Chen (2017).

Observing active region NOAA 7978 during seven solar rotations, Démoulin et al. (2002a) analyze the long-term budget of the relative magnetic helicity and find that the helicity injection caused by the differential rotation can neither explain the helicity of coronal fields (at least a factor of 2.5–4 larger), nor the helicity of CMEs ejected into the interplanetary space (a factor of 4–20 larger), and thus conclude that the main source of helicity is the inherent twist of the magnetic flux tube (sigmoid) forming in active regions, transferred to the corona either by continuous emergence of the flux tube or by torsional Alfvén waves. Démoulin et al. (2002b) also conclude that shearing motions are a relatively inefficient way to bring magnetic helicity to the corona, compared with helicity carried by a significantly twisted emerging flux tube. However, the opposite conclusion was reached by Liu and Schuck (2012) and Liu et al. (2014). Thus, CMEs are thought to expel accumulated magnetic helicity that has been injected into the corona, most likely by the twist in the sub-photospheric part of the magnetic flux tube forming an active region (Green et al. 2002). Five active regions have been observed to rotate around each other (during several solar rotations), while 35 CMEs erupted and carried helicity away, producing a non-monotonic change and even a sign change of the helicity, caused by the varying aspect angle (Green et al. 2002). Nindos et al. (2003) confirm that the helicities carried away by CMEs are a factor of $\lesssim 4$ larger than injected by differential rotation, but the authors note large uncertainties in the length scale of magnetic clouds that are used in helicity calculations. Newly emerging flux often brings up helicity of opposite sign to the dominant helicity of active regions, and thus the interaction and reconnection of flux systems with opposite helicity are key elements in the magnetism of CME initiation (Wang et al. 2004).

Transient coronal sigmoids have been found to be associated with filaments whose apex rotates upon eruption, for which the helicity sign of the erupting field and the direction of filament rotation was found to be consistent with the conversion of twist into writhe under the ideal MHD constraints of helicity conservation (Green et al. 2007), and being consistent with the model by Titov and Démoulin (1999), which identify transient sigmoids with steepened current layers below rising flux ropes.

The coronal helicity can be expressed as (Berger 1985),

$$H_c = 2\alpha \sum_{n_x=1}^{N_x} \sum_{n_y=1}^{N_y} \frac{|\tilde{B}^2_{n_x,n_y}|}{(k_x^2 + k_y^2)^{3/2}} , \tag{14.3.1}$$

where $\tilde{B}_{n_x,n_y}$ is the magnetic field's Fourier amplitude of the (n_x, n_y) harmonic, and $k_x = 2\pi n_x/L$, $k_y = 2\pi n_y/L$, with L being the horizontal extension of the computation box used in force-free magnetic field extrapolation methods. Another formulation of the magnetic helicity H_m includes the sum of the self $H_{m,self}$ and the mutual $H_{m,mut}$ terms (Georgoulis et al. 2012),

$$H_c = H_{m,self} + H_{m,mut} = 8\pi d^2 A \sum_{i=1}^{N} a_l \Phi_l^{2\delta} + \sum_{l=1}^{N} \sum_{m=1, j\neq m}^{N} L^{arch} \Phi_l \Phi_m , \tag{14.3.2}$$

where α_l are the force-free parameters for different flux tubes l.

Calculating a linear force-free magnetic field model (with constant α) for 78 active regions, the preflare value of α and helicity of active regions that produce big flares without CMEs was found to be smaller than the coronal helicity of those that produce CME-associated flares, from which it was concluded that the stored preflare coronal helicity may determine whether a big flare will be eruptive or confined (Nindos and Andrews 2004).

The magnetic energy and relative-helicity budgets have been calculated during the evolution of active region 11158 for 600 time steps (Fig. 14.3), which led to the conclusion that the active region builds large budgets for both the free magnetic energy and the relative magnetic helicity, which follow almost a proportional relationship (Fig. 14.4), sufficient to power many more eruptions than reported (Tziotziou et al. 2013). It was also concluded that self terms of free energy and relative helicity most likely originate from the mutual terms, following a progressive mutual-to-self conversion pattern that stems most likely from magnetic reconnection (Tziotziou et al. 2013).

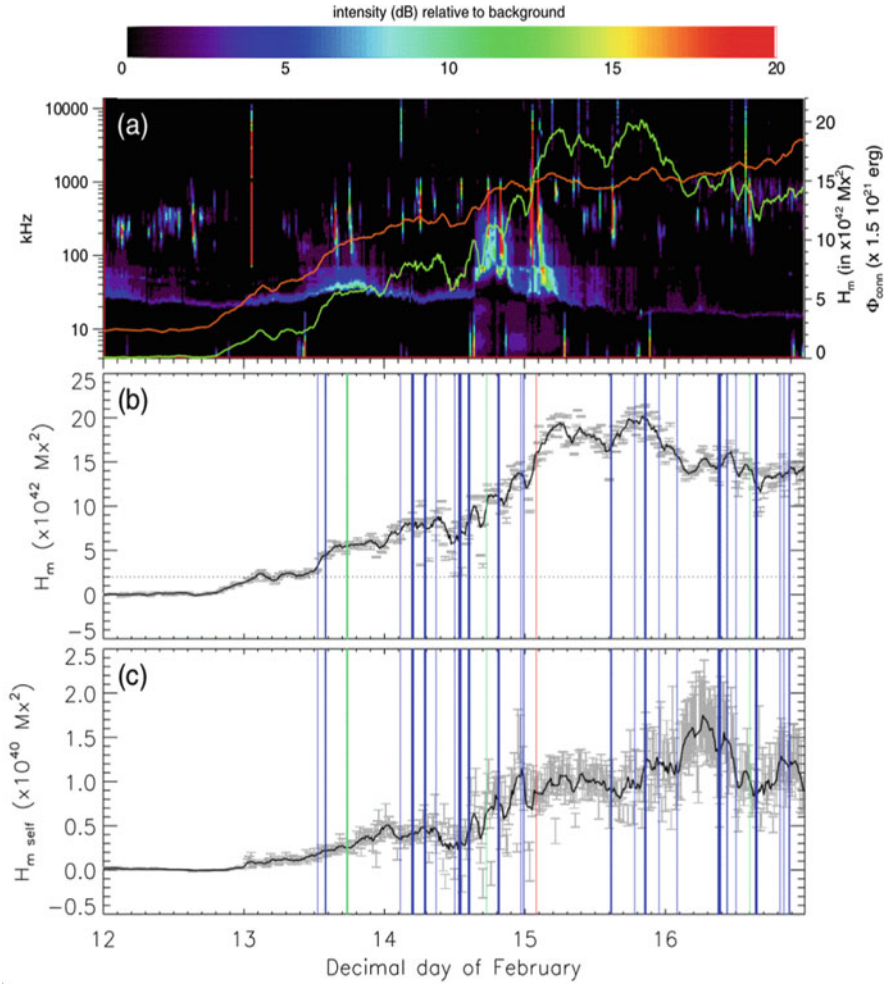

Fig. 14.3 Time evolution of the Wind/WAVES radio spectrum (**a**), the magnetic helicity (**b**), and the self-helicity (**c**), for 5 days during 2011 February 12–17. Vertical blue, green, and red lines in (**b**) and (**c**) denote the peak times of C-, M-, and X-class GOES flares. The dotted horizontal line in (**b**) indicates the $\approx 2 \times 10^{42}$ Mx^2 threshold for relative magnetic helicity (Tziotziou et al. 2013)

Numerical simulations show that erupting CMEs occur at a fixed magnitude of free energy in the corona, independent of the value of helicity, and the eruption can actually lead to an increase in the helicity of the remaining corona, suggesting that there is no critical helicity buildup and shedding as the determining factors for CME initiation (Phillips et al. 2005).

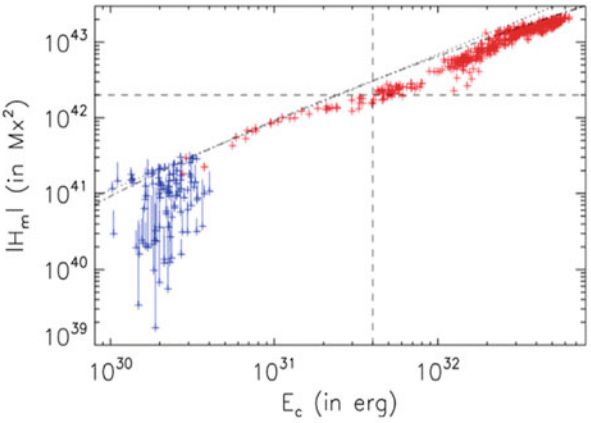

Fig. 14.4 Correlation between the relative magnetic helicity H_m and the free magnetic energy E_c, sampled from the time interval of 2011 February 12–17. Blue symbols refer to the first 20 hrs of 2011 February 12. A least-square fit is indicated with a dot-dashed line (Tziotziou et al. 2013)

14.4 CME Magnetic Configuration

Theoretical models of the initiation of *coronal mass ejections (CMEs)* can be categorized in terms of whether they occur in force-free or non-force-free magnetic fields, whether they can be described in the framework of ideal MHD or non-ideal MHD (Forbes 2000; Forbes et al. 2006), or whether a flux rope is pre-existing or not (Lin et al. 2004, 2015). Some of the most-cited theoretical magnetic field models for the generation of CMEs include: (i) magnetic reconnection in an initially closed, highly sheared and twisted sigmoid (Moore et al. 2001); (ii) an ideal-MHD catastrophic loss of force-free current equilibrium in the corona (Forbes and Isenberg 1991; Forbes et al. 2006); (iii) eruption due to the kink instability or torus instability (Titov and Démoulin 1999; Isenberg and Forbes 2007; Török and Kliem 2003; Kliem and Török 2006; Fan and Gibson 2007); (iv) the magnetic breakout model (Antiochos et al. 1999), or (v) long-distance triggering by waves (Schrijver and Title 2011).

(i) The magnetic explosion scenario of Moore et al. (2001) occurs in an initially closed single bipole, in which the core field is sheared and twisted in the shape of a sigmoid, having an oppositely curved elbow on each end (Fig. 14.5, top left). The arms of the opposite elbows are shaped past each other so that they overlap and are crossed low above the neutral line in the middle of the bipole. They are brought into contact by converging and shearing photospheric flows. The magnetic explosion can be ejective or confined. The magnetic explosion is thought to be unleashed by runaway tether-cutting via implosive/explosive reconnection in the middle of the sigmoid, as it occurs in the standard flare model (Moore et al. 2001). The magnetic configuration of a magnetic flux rope

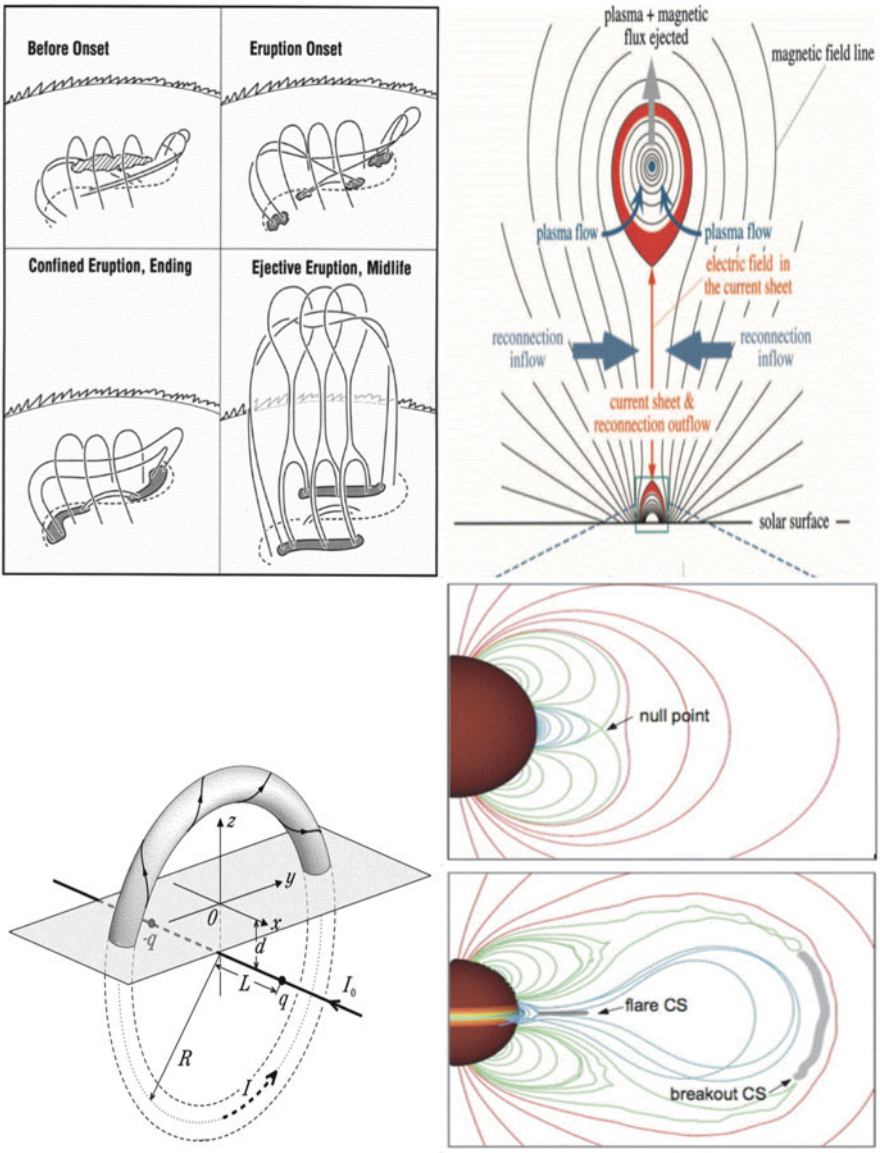

Fig. 14.5 *Top left:* Magnetic field explosion in single-bipole active region, leading to a confined eruption or an ejective eruption (Moore et al. 2001); *Top right:* Emerging flux and loss-of-equilibrium model (Lin et al. 2004); *Bottom left:* Force-free circular flux tube model with azimuthal currents, with the photospheric level indicated as a horizontal plate (Titov and Démoulin 1999; Isenberg and Forbes 2007); *Bottom right:* Magnetic breakout model with quadrupolar geometry (Karpen et al. 2012)

of field lines that twist about an axial field line is produced (final stage in Fig. 14.5 top left). The related evolution of sigmoids before, during, and after CMEs is reviewed in Gibson et al. (2006). The double J-shaped pattern of electric currents in the photosphere show clear evidence of the existence of currents parallel to the magnetic field and can be the signature of a flux rope that is detectable in CMEs (Schmieder et al. 2015).

(ii) A model involving a pre-existing flux rope envisions a CME according to a catastrophe model (Fig. 14.5, top right), where roughly half of the total mass and magnetic flux are contained in the initial flux rope, while the remaining plasma and poloidal magnetic flux are brought by magnetic reconnection from the corona into the current sheet and from there into the CME bubble (Lin et al. 2004). The magnetic reconnection geometry of this model has been verified by direct observations during the 2003 November 18 partial-halo CME event, which stretches out an elongated vertical current sheet behind the expanding wake of the CME (Lin et al. 2005). The formation of a current sheet and an associated streamer-like structure has been observed in the 2002 January 8 CME event (Ko et al. 2003). MHD simulations of emerging flux ropes predict the formation of sigmoids in soft X-rays, which under dynamic forcing forms current sheets and leads to reconnection and eruption (Gibson et al. 2004). Evidence for this type of magnetic reconnection is also supported by observations of downward directed reconnection outflows and supra-arcadal downflows (Savage et al. 2010). Magnetic modeling with the flux-rope insertion method developed by Ballegooijen indicates that a CME is initiated by catastrophic loss of equilibrium, caused by an increase of the axial flux in the flux rope, which is driven by magnetic flux cancellations (Su et al. 2011).

(iii) A special type of an emerging flux tube is the geometry of a twisted torus (Fig. 14.5, bottom left), which is a force-free magnetic field model embedded into a potential magnetic field (Titov and Démoulin 1999). This configuration evolves when the flux tube emerges quasi-statically from below the photosphere to a certain height in the corona and then becomes unstable and erupts (Titov and Démoulin 1999). This model may undergo a catastrophic loss of equilibrium and trigger an eruption. The flux rope will tend to form an aneurysm-like structure once it erupts (Isenberg and Forbes 2007). A possible instability is the kink instability or the torus instability (Török and Kliem 2003, 2005; Kliem and Török 2006).

(iv) The magnetic breakout model (Fig. 14.5, bottom right) of Antiochos et al. (1999) can explain that very low-lying magnetic field lines down to the photospheric neutral line can open toward infinity during eruption, and the eruption is driven solely by magnetic free energy stored in a closed, sheared arcade. The magnetic configuration of the breakout model consists of a multi-polar (quardupolar) topology in which reconnection between a sheared arcade and neighboring flux systems triggers the eruption. Reconnection removes the unsheared field above the low-lying, sheared core flux near the neutral line, thereby allowing this core flux to burst open (Antiochos et al. 1999). The

explosive behavior in the breakout model may be aided by a resistive instability and tearing mode instability (Karpen et al. 2012).

(v) There may exist a long-range magnetic coupling between CME source regions that are prone to erupt, as evidenced by near-synchronous and long-distance global triggering (over more than a solar radius), found between magnetic domains that exhibit flares, CMEs, and filament eruptions (Schrijver and Title 2011). The global magnetic configuration of the Sun causes CMEs to arise in a self-similar manner from pre-existing small scale loop systems, overlying regions of opposite magnetic polarities. The long-range interactions weaken the overlying field of the current carrying core regions by magnetic reconnection analogous to the breakout model (Török et al. 2011). From the characteristic pattern of the CMEs source regions in both solar hemispheres, a generic scheme was found in which the projected white-light topology of a CME primarily depends on the orientation and position of the source region's neutral line on the solar disk (Cremades and Bothmer 2004).

14.5 CME Trigger Mechanisms

What we mean with a *trigger mechanism* is simply a physical instability that occurs above some critical threshold, where an equilibrium becomes unstable. In the case of *coronal mass ejections (CMEs)*, a number of magneto-hydrodynamic instabilities were suggested to initiate a CME, such as a resistive instability (like the tearing instability), or an ideal instability (like the torus instability), or the kink instability. In the breakout model, for instance, the explosive behavior is aided by a resistive instability related to the tearing mode instability (Karpen et al. 2012). In ideal MHD, the onset of a CME has also been described as a catastrophic loss of a force-free flux rope equilibrium (van Tend and Kuperus 1978; Forbes and Isenberg 1991; Lin and Forbes 2000; Lin et al. 2005).

A twisted magnetic flux rope, displaying a sigmoid-shaped geometry in 3-D, surrounded by an overlaying arcade, is a commonly described situation for the pre-eruption phase of a CME (e.g., Amari et al. 2000). Imposing slow motions in the footpoints of a sheared arcade that converge toward the inversion line, leads (after a phase of quasi-static evolution) to the formation of a twisted flux rope by a reconnection process (van Ballegooijen and Martens 1989) and to the global disruption of the configuration (Amari et al. 2003). Although flux ropes play a central role in many CME models, a debate occurred whether the flux ropes pre-exist or whether they are formed on-the-fly during the eruption. The observations indicate increasingly the former (Patsourakos et al. 2013; Amari et al. 2014), but the latter viewpoint continues to receive support as well (Wang et al. 2017). This issue is not settled, because observations indicate that the total reconnected flux during an eruption is about the same as the poloidal flux of the resulting flux rope at 1 AU (Longcope et al. 2007; Qiu et al. 2007; Gopalswamy et al. 2017, 2018). This means that a pre-existing flux rope, if any exists, needs to have a very small poloidal flux.

A parametric study of CME MHD simulations revealed two different small magnetic structures that favor the onset of solar eruptions, which should appear near the magnetic polarity inversion line: (i) newly emerging magnetic fluxes reversed to the potential component of a pre-existing large-scale sheared arcade, or (ii) new flux reversed to the shear component of the arcade (Kusano et al. 2012).

A subphotospheric trigger mechanism of CMEs is the emerging flux scenario. The onset of CMEs starts when emerging flux occurs within a filament channel (or at the outer edge of a filament channel), cancelling the magnetic field below the flux rope, leading to the rise of the flux rope (owing to loss of equilibrium), and forming a current sheet below it (Chen and Shibata 2000). Magnetic flux and helicity injection are considered to be favorable triggers for fast plasma ejections (Roussev et al. 2012).

Alternatively to the flux emergence scenario, a mechanism of photospheric flux cancellation for flux rope formation and eruption was proposed also (van Ballegooijen and Martens 1989; Green et al. 2011). In one observation, about a third of the magnetic flux of the active region cancelled at the internal polarity inversion line in the 2.5 days leading up to the eruption, and the amount of cancellation implies that up to 60% of the magnetic flux could be in the body of the flux rope (Green et al. 2011).

The initiation of a CME has been studied with the 3-D flux rope configuration of Titov and Démoulin (1999). It was found that it is possible to achieve a loss of equilibrium even though the ends of the flux rope are anchored to the solar surface, while this configuration needs to be changed by eliminating the unrealistically strong arcade field, in order to have the flux rope to escape (Roussev et al. 2003). Besides the development of the long-wavelength ($m = 1$) kink mode, the upward-kinking loops form also a second, vertical current sheet below the loop apex at the position of the hyperbolic flux tube, which make up the sigmoids seen during flares and CMEs (Kliem et al. 2004).

Instabilities that can occur in twisted coronal magnetic flux tubes are the *kink instability* or *torus instability*. The critical end-to-end twist is found to lie in the range of $2.5\pi < \Phi_c < 2.75\pi$, based on simulations with the ideal MHD equations (Török and Kliem 2003). For a loop aspect ratio of ≈ 5, unstable growth of the kink mode starts for average twists of $\Phi_c \geq 3.5\pi$, and this instability threshold increases with a larger major loop radius (Török and Kliem 2004). 3-D MHD simulations with the Titov and Démoulin (1999) topology could reproduce the development, both the geometry of a helical shape and the rise profile of a confined (or failed) filament eruption), in agreement with observations (Török and Kliem 2005). The helical kink instability is identified as the most likely trigger of CMEs in a series of confined and ejective flares (Liu et al. 2016). Alternatively, an eruption could be triggered by decreasing the magnetic field more rapidly with altitude. Thus, the decrease of the overlying field with height is a main factor in deciding whether the kink instability leads to a confined or an eruptive CME (Török and Kliem 2005). 3-D MHD simulations demonstrate the loss of confinement and eruption of a flux rope emerging quasi-statically into a pre-existing coronal arcade field, where the overlying arcade field declines with height slowly, such that the emerging flux rope

remains confined until its self-relative magnetic helicity (normalized by the square) of the rope's flux reaches −1.4 and the flux becomes significantly kinked (Fan and Gibson 2007). The morphology of sigmoids or S-shaped field lines in coronal loops provides important diagnostics, since active regions that exhibit sigmoids are more likely to erupt than non-sigmoidal ones. The amount of twist or shear in helical structures can be quantified by the magnetic helicity. For a magnetic flux rope, the helicity is proportional to the sum of its twist and writhe (Török et al. 2010). Kink-unstable erupting flux ropes are found to transform a far smaller fraction of their twist helicity into writhe than often assumed, while confined flux rope eruptions tend to show stronger writhe at low heights than ejective eruptions in CMEs, which argues against suggestions that the writhing enables the rise of the rope through the overlying field (Török et al. 2010).

It has been shown that the torus instability and catastrophic loss of equilibrium are equivalent descriptions for the onset of a CME (Démoulin and Aulanier 2010; Kliem et al. 2014). For all catastrophes found in Forbes and Isenberg (1991) and subsequent papers, torus instability occurs at the same point on the equilibrium manifold in parameter space. For 3-D MHD simulations see Fig. 14.6. Observational evidence of the torus instability was furnished for the 2011 August 4 filament eruption (Zuccarello et al. 2014).

14.6 MHD Evolution of CME

MHD simulations of *coronal mass ejections (CMEs)* are particularly challenging due to the many complex aspects, such as (i) the type of MHD (ideal, resistive, 2-D, 2.5D, 3-D), (ii) the large spatial range from chromospheric to heliospheric scales (requiring adaptive grids), (iii) the complexity of magnetic configurations (Sect. 14.4), (iv) initial physical conditions (CME footpoint area, density, temperature, heating rate, cooling rate), (v) pre-CME evolution (stability, metastability, non-equilibrium), (vi) the unknown onset mechanism (loss of equilibrium, catastrophe, resistive instability, tearing instability, torus instability, kink instability, magnetic reconnection), (vii) the global energetics (confined, eruptive, helicity budget), and (viii) the use of boundary conditions (data-inspired, data-driven). It is therefore no surprise that each numerical MHD simulation addresses only a subset of these characteristics, while making assumptions for other aspects, inspired by observations. Forward-fitting to observations has been attempted for specialized geometries only (e.g., Thernisien et al. 2006), but has not been performed with MHD codes so far. However, data-driven simulations that include time-dependent boundary data can be used to constrain global 3-D MHD models with the capability of forecasting (Jin et al. 2017).

Amari et al. (2003a) simulates the initiation of a CME by driving the footpoints of sheared arcade field with slow motions, converging toward the inversion line. This process leads after a phase of quasi-static evolution to the formation of a twisted flux rope by a reconnection process and to global disruption. Since the flux

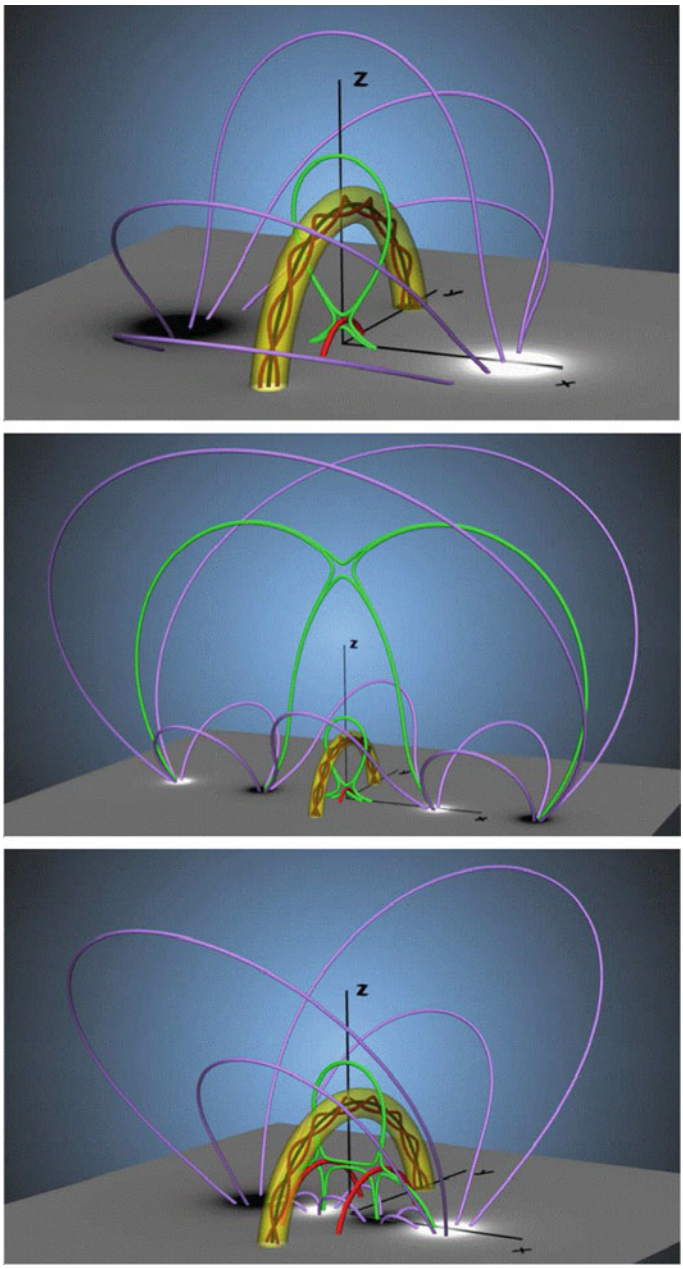

Fig. 14.6 *Top:* Bipolar active-region model with topology of Titov and Démoulin (1999); *Middle:* Quadrupolar active-region model with generalized Titov-Démoulin equilibrium; *Bottom:* Quadrupolar active-region model with generalized Titov-Démoulin equilibrium and different ratio of curvature radius to inner (cross-sectional) radius. The toroidal flux rope in an external bipolar or quadrupolar field represents a model for the current-carrying flux that evolves through a sequence of equilibria (Kliem et al. 2014)

rope is never in equilibrium, its pre-existence in the pre-eruptive phase is not a necessary condition, but may be the product of the disruption (Amari et al. 2003a). In a similar set up, a different driver is used, where the magnetic field of the initial condition is due to turbulent diffusion of the photospheric flux generated by small-scale horizontal plasma motions (Amari et al. 2003b). The system evolves in two phases: The first one, during which a twisted flux rope is created, is slow and almost quasi-static, while the second one is associated with a disruption, which is confined for a small initial helicity and global for a large initial helicity (Amari et al. 2003b). Photospheric flux cancellation and tether-cutting coronal reconnection are found not to trigger CMEs in bipolar magnetic fields, but are key pre-eruptive mechanisms for flux ropes to build up and to rise to the critical height above the photosphere at which the torus instability causes the eruption (Aulanier et al. 2010; Savcheva et al. 2012; Jiang et al. 2013).

In the ideal MHD simulations of Török and Kliem (2003), the initially potential coronal flux tube is twisted by photospheric vortex motions, centered a two photospheric flux concentrations, and is slowly driven while it evolves quasi-statically along a sequence of force-free equilibria, rising slowly with increasing twist and forming a sigmoid structure. There exists a critical twist above which no equilibrium can be found in the simulation and the flux tube starts to ascend rapidly, due to the torus or kink instability (Török and Kliem 2007; Kliem et al. 2013). The outer part of the twisted flux tube expands, especially if the density is falling off sufficiently rapidly with height (Török and Kliem 2003). Based on numerous MHD simulations of kink-unstable flux ropes, there is no bimodal distribution of fast and slow CME generation mechanisms, while complex (quadrupolar) active regions lead to the fastest CMEs (Török and Kliem (2007).

The 3-D MHD simulations of Manchester et al. (2004) start with a global steady-state model of the corona and solar wind, typical for conditions near solar minimum, which includes a helmet streamer belt with a current sheet at the equator, and the fast and slow solar wind. Within this steady-state heliospheric model, conditions for a CME are created by superimposing the magnetic field and plasma density of the 3-D Gibson-Low flux rope model, which launches a CME by the initial force imbalance and results into acceleration with speeds of $v \gtrsim 1000$ km s^{-1}. Other large-scale models of the solar corona include the effects of differential rotation and small-scale flows of the surface diffusion (Mackay and van Ballegooijen 2006). The 3-D MHD simulations of Manchester et al. (2004) that use solar wind data for the global background and the Gibson-Low configuration to generate individual events, is used as a forecasting tool (Jin et al. 2017).

A first 2.5-D MHD simulation of the complete breakout process (Fig. 14.7) include the initiation, plasmoid formation and ejection, and the eventual relaxation of the coronal field to a more potential state (MacNeice et al. 2004). The magnetic configuration consists of four (trans-equatorial) X-line flux systems, bounded by two separatrix surfaces that intersect in the corona at an X-point. A footpoint shear is applied to the inner equatorial flux system, which causes it to expand outward and push against the overlying field, deforming the X-point to a current sheet. The code covers a field-of-view out to $30R_{\odot}$, which enables to track the acceleration of

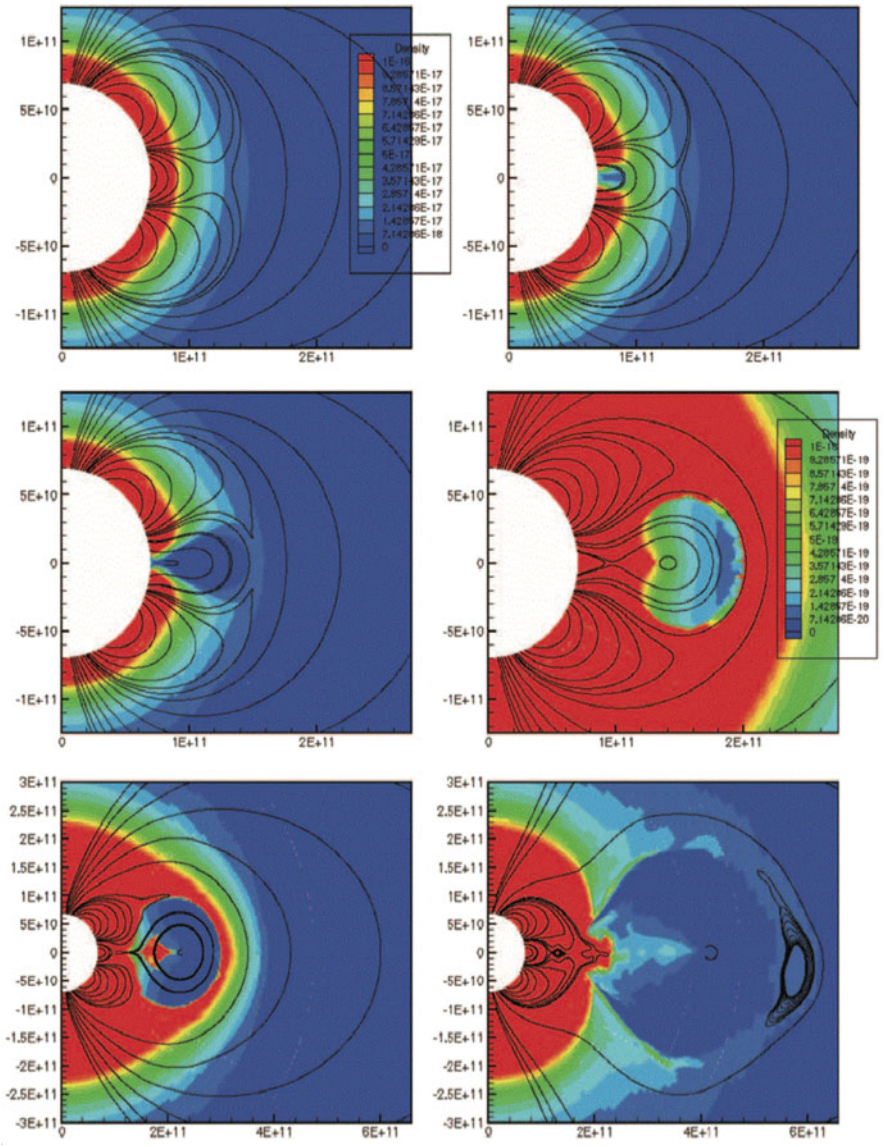

Fig. 14.7 A 2.5-D MHD simulation of the magnetic breakout model, showing the mass density (color scale) and the axi-symmetric magnetic field configuration (black curves). The 6 panels depict different time steps (from left to right, and from top to bottom). The simulation box extends out to $\approx 30 R_{\odot}$ and the numeric grid varies from 128×256 at the base to an equivalent of 512×1024 at the outermost zone (MacNeice et al. 2004)

the ejected plasmoid up to coronal Alfvén speed, which proves that the breakout model can produce fast CMEs (MacNeice et al. 2004). Simulations with boundary shearing flows introduce free magnetic energy and eventually lead to a fast magnetic breakout CME (Lynch et al. 2008). Similar quadrupolar configurations with two flux ropes located within a pseudo-streamer lead to two consecutive reconnections and eruptions, a scenario for twin-filament eruptions that can explain coupled sympathetic eruptions also (Török et al. 2011).

Emerging flux rope models require MHD simulation codes that start with insertion of sub-photospheric flux ropes that emerge into the chromosphere and corona. Gibson et al. (2004) conceives such a code with two assumptions: (i) X-ray sigmoids appear in regions of the flux rope known as *"bald-patch-associated separatrix surfaces* where the flux rope touches the photospheric boundary and where current sheets can form by dynamic forcing, leading to reconnection and localized heating, and (ii) filaments are regions of enhanced density contained within dips in the magnetic flux rope. The current layers form along the sigmoids as the flux rope is driven by the kink instability (Gibson et al. 2004). The loss of confinement and eruption of a flux rope emerging quasi-statically into a pre-existing coronal arcade field occurs either when the magnetic field declines with height sufficiently rapid, or when the kinking motion causes rotation of the tube to an orientation that makes it easier for it to rupture through the arcade field, leading to eruption (Fan and Gibson 2007), although the latter process was questioned by Török et al. (2010). Kusano et al. (2012) use a model similar to Fan and Gibson (2007) for a parametric study to dynamically form a variety of magnetic structures and they find two types of CME-prone magnetic field configurations: (i) emerging fluxes reversed to the potential field component, and (ii) emerging flux opposite to the nonpotential component of major fields above the polarity inversion line. The emergence of magnetic flux is a common mechanism to produce CME eruptions, but the erupting CME plasmoid is formed in situ, independently of the emerging flux tube (Roussev et al. 2012; Archontis and Hood 2012; Leake et al. 2014).

14.7 Confined Eruption

The fate of whether an expanding CME escapes during the eruption from the Sun, or whether it turns into a stalled (failed) eruption that comes to a halt and falls back to the Sun, depends on whether or not the CME reaches the critical escape velocity during the initial acceleration phase,

$$v_{esc} = \sqrt{\frac{2GM_{\odot}}{R_{\odot}}} \approx 618\ [\mathrm{km\ s^{-1}}]\,, \tag{14.7.1}$$

where G is the gravitational constant, $M_{\odot}$ the solar mass, and $R_{\odot}$ the solar radius. The effect of solar gravity is a deceleration that is strongest at the launch time of

the CME and decreases almost exponentially with height. However, the upward stretching of overlying flux builds up much larger tension forces, what may stop the eruption. Magnetic reconnection in a vertical ("flare") current sheet that forms under the erupting flux cuts the overlying flux and removes its downward tension force in a successful CME (Fig. 14.5 top right; Lin and Forbes 2000). Additionally, breakout reconnection above the eruption can also help the escape if the source region is sufficiently complex, so that a magnetic X-line or null point exists above the erupting flux. Gilbert et al. (2007) distinguish between failed, partial, and full eruptions, depending on whether the bulk of the mass and the magnetic structure ("full") erupts, the magnetic structure but only part of the mass ("partial") erupts (Olmedo and Zhang 2010), or none erupts ("failed"). Furthermore, transverse motion of a prominence without a CME (Gopalswamy et al. 2003), or changes in an overlying streamer without an eruption was observed also (Gopalswamy et al. 2004).

For examples of failed eruptions see Fig. 14.8 and Table 1 in Schrijver (2009). Observations of a confined (or failed) eruption were reported for filament threads that approach a peak height of $h \approx 80$ Mm and then drain back to the Sun, where the deceleration of the filament exceeded the gravitational deceleration by more than a

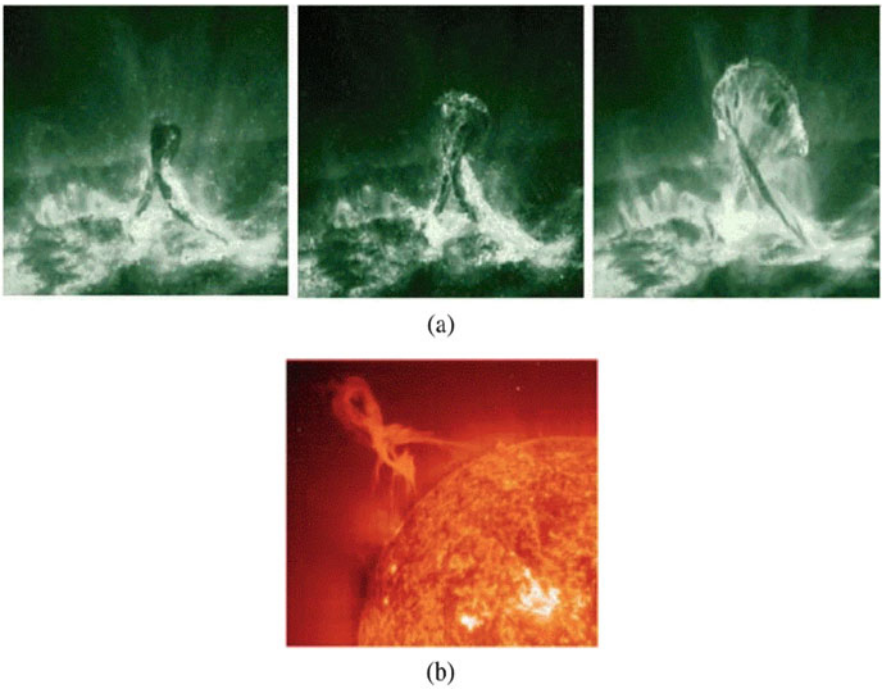

Fig. 14.8 (**a**) Failed filament eruption on 2002 May 27, showing an "inverted-gamma" structure as a result of significant kinking, observed with TRACE 195 Å. (**b**) Filament eruption observed with EIT/SOHO 304 Å on 2000 January 18, also showing an inverted-gamma structure (Gilbert et al. 2007)

factor of 10, which suggests that the filament material was pulled back by magnetic tension (Ji et al. 2003). The asymmetry of coronal background fields provides a stronger confinement for flux rope eruptions than symmetric background fields (Liu et al. 2009). Statistical studies indicate that 90% of X-class flares (from a set of 104 events) are eruptive, while the remaining 10% are confined, and the eruption (or confinement) was found to depend on the displacement of the location of the energy release between the flare site and the magnetic center (Wang and Zhang 2007; Akiyama et al. 2007; Cheng et al. 2011), as found also at the periphery of active regions (Chen et al. 2015). Stereoscopic observations of failed and successful eruptions reveal little difference in the magnetic configuration (Shen et al. 2011). In the 2005 May 27 M1.1 flare, magnetic reconnection started at several locations, and the evolution of the UV flare ribbons stopped at the border of the closest large-scale quasi-separatrix layer (Guo et al. 2012). Although the statistical probability of confined flares decreases with flare magnitude, X-class confined flares have been found also (in about 10%), such as in the unusually large active region NOAA 12192 on 2014 October (Fig. 14.9; Thalmann et al. 2015; Sun et al. 2015; Chen et al. 2015), which produced major two-ribbon flares without CMEs, but only a small fraction ($\approx$ 10%) of non-thermal electrons was accelerated to high energies (Thalmann et al. 2015), also characterized as flare-rich but CME-poor (Sun et al. 2015). Confined flares can occur a long time (from one day to several days)

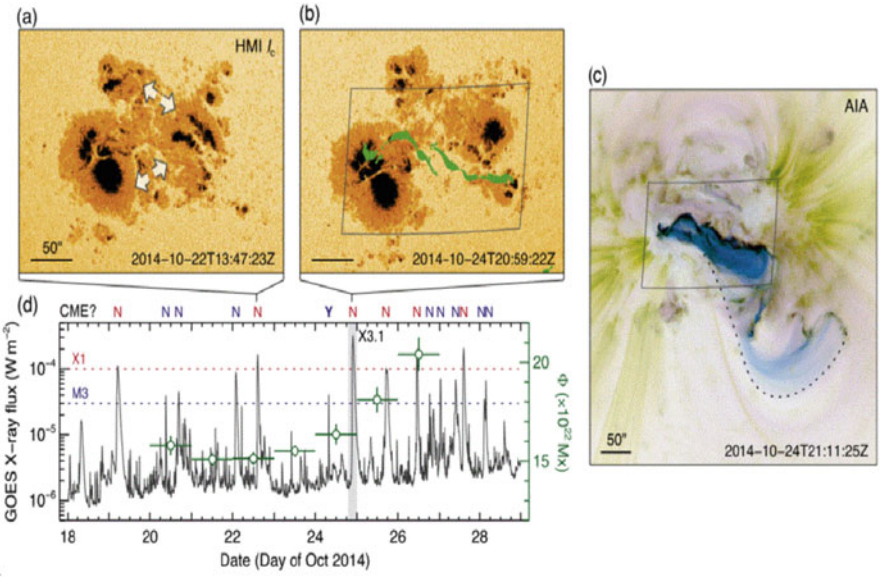

Fig. 14.9 Active region NOAA 12192: (**a**) and (**b**) HMI/SDO continuum intensity before two X-class flares. Arrows in (**a**) denote two locations with significant sunspot separation. AIA 1600 Å ribbons for the X3.1 flare are overplotted in (**b**). (**c**) Negative composite AIA image during the X3.1 flare. (**d**) GOES 1–8 Å flux and unsigned magnetic flux (green) (Sun et al. 2015)

before large eruptive flares occur (Chintzoglou et al. 2015; Cheng et al. 2015a). SDO and IRIS observations show that a failed magnetic flux rope eruption is also able to produce a two-ribbon flare and high-energy electrons that heat the lower atmosphere, causing an enhancement of the white-light and FUV/NUV continuum emissions and chromospheric evaporation (Cheng et al. 2015b).

Confined eruptions could successfully be reproduced by MHD simulations of magnetic flux ropes that were initially force-free and then driven towards the helical kink instability (Török and Kliem 2005). The decrease of the overlying field with height is a main factor in deciding whether the instability leads to a confined event or to an ejective CME (Török and Kliem 2005; Guo et al. 2010). Tether weakening by breakout-like quadrupolar reconnection is likely to be the release mechanism for the previously confined flux rope in one of the fastest CMEs ever observed (> 3000 km s^{-1}) (Williams et al. 2005). The 3-D MHD simulations of the *magnetic breakout* model reproduce confined eruptions also, which can explain the filament disappearance followed by re-formation, also called *homologous confined filament eruptions* (DeVore and Antiochos 2008; Gilbert et al. 2007; Joshi et al. 2014; Yang et al. 2014) . A flux rope erupts when the primary emerging field reconnects with the pre-existing coronal field, otherwise it remains confined by the ambient field of the the initial emerging system (Archontis and Török 2008). Confined flux rope eruptions tend to show stronger writhe at low heights than ejective eruptions (CMEs), which argues against suggestions that writhing faciliates the rise of the flux rope through the overlying field (Sturrock et al. 2001; Fan 2005; Török et al. 2010).

14.8 Coronal Dimming

Observations of the Sun in optically thin wavelengths (UV, EUV, soft X-rays) often show brightness (or intensity) variations, either in form of brightness increases (i.e., brightenings) or decreases (i.e., dimmings). Both the brightenings or dimmings can have two different interpretations, either in terms of an emission measure change, or in terms of a temperature change, which varies the flux (or intensity) in a given wavelength band. In the context of *coronal mass ejections (CMEs)*, EUV dimming in the corona due to mass ejection is a common phenomenon, which provides a sensitive diagnostics on the CME volume, mass, speed, and acceleration.

Observations of EUV dimmings that were interpreted as CME-related mass depletions have been reported initially from EIT/SOHO data. These EUV dimmings appeared about a half hour before the white-light counterparts of CMEs became visible, and the extended dimming areas are considered as *"footprints"* of CMEs (Thompson et al. 2000). Spectroscopic studies corroborate that the EUV dimming is due to a density decrease, rather than due to a temperature change (Harrison and Lyons 2000; Harrison et al. 2003). Direct evidence for ejection of CME masses in EUV dimming regions comes also from Doppler shifts of the mass motions in the footprint areas, with outflow speeds in the range of $v \approx$ 20–100 km s^{-1} (Harra and Sterling 2001; Harra et al. 2007; Tian et al. 2012). Modeling the EUV fluxes

with both AIA/SDO and full-disk EVE/SDO data, nearly 100% of the dimming was found to be due to mass loss in the corona (Mason et al. 2014). The gradual pre-CME evolution (several hours before) indicates that source regions have a continuous driver (Harrison et al. 2003; Zhang et al. 2017). The EUV dimmings may be accompanied by successive openings of magnetic field lines during the CME lift-off (Zhukov and Auchère 2004). A so-called *streamer-puff CME* type was found to produce coronal dimming at the footpoints also (Moore and Sterling 2007), as well as *mini-CMEs* (Innes et al. 2010).

The evolution of the coronal dimming regions can be used to probe the large-scale magnetic structure involved in a CME (Attrill et al. 2006, 2009). A correlation is expected between the EUV dimming and the associated magnetic flux in an associated interplanetary magnetic cloud, but flux comparisons of the 2003 October 28 event with EIT/SOHO and ACE were found to be incompatible (Mandrini et al. 2007).

A statistical analysis of 96 CME-associated EUV coronal dimmings (between 1998 and 2000) finds durations of 3–12 hours, locations in mid-latitudes of 10°–50°, latitudinal and longitudinal symmetries, sharp rise and gradual recovery, and two-step decay phases (Reinard and Biesecker 2008). A high association rate is found between CME with EUV dimming events, with 55% of dimming events associated with CMEs, and 84% of CMEs associated with dimmings (Bewsher et al. 2008). However, there are exceptions, such as the famous CME of 2008 June 2, that *"left no trace behind"* (Robbrecht et al. 2009), which belongs to the *streamer-blowout CME class* and had a starting height in relatively large altitudes. In summary, it appears that energetic source regions at large heights produce fast CMEs that are accompanied by larger flares and detectable dimmings, while less energetic sources produce slow CMEs that are accompanied by smaller flares and may, or may not, have dimmings (Reinard and Biesecker 2009).

Modeling of EUV dimming events requires 3-D geometries and modeling of the emission measure in terms of the line-of-sight depth. An automated detection algorithm was developed that is capable to distinguish between EUV dimming events and *"EIT waves"* (Podladchikova and Berghmans 2005; Attrill and Wills-Davey 2010).

Stereoscopic measurements of the EUV dimming regions allows us to determine the time-dependent 3-D volume $V(t)$, electron density $n_e(t)$, and propagation speed $v(t)$ of the dimming region, from which it was found that the CME volume expands adiabatically with a self-similar geometry (Aschwanden 2009), and that the CME masses agree well between the white-light estimates and the EUV dimming model (Aschwanden et al. 2009). The largest statistical study with modeling of EUV dimming has been conducted with AIA/SDO and LASCO/SOHO data of 399 M- and X-lass flares (Aschwanden 2016, 2017). The dimming model is based on the adiabatic self-similar expansion of the source region of CMEs, the hydrostatic density scale height of the corona, the center-of-mass speed, equi-partition of CME kinetic and thermal energy, and the hydrodynamic scaling law of Rosner-Tucker-Vaiana, which yielded agreement of the CME mass and speed between the LASCO-inferred white-light method and the EUV dimming method (Fig. 14.10).

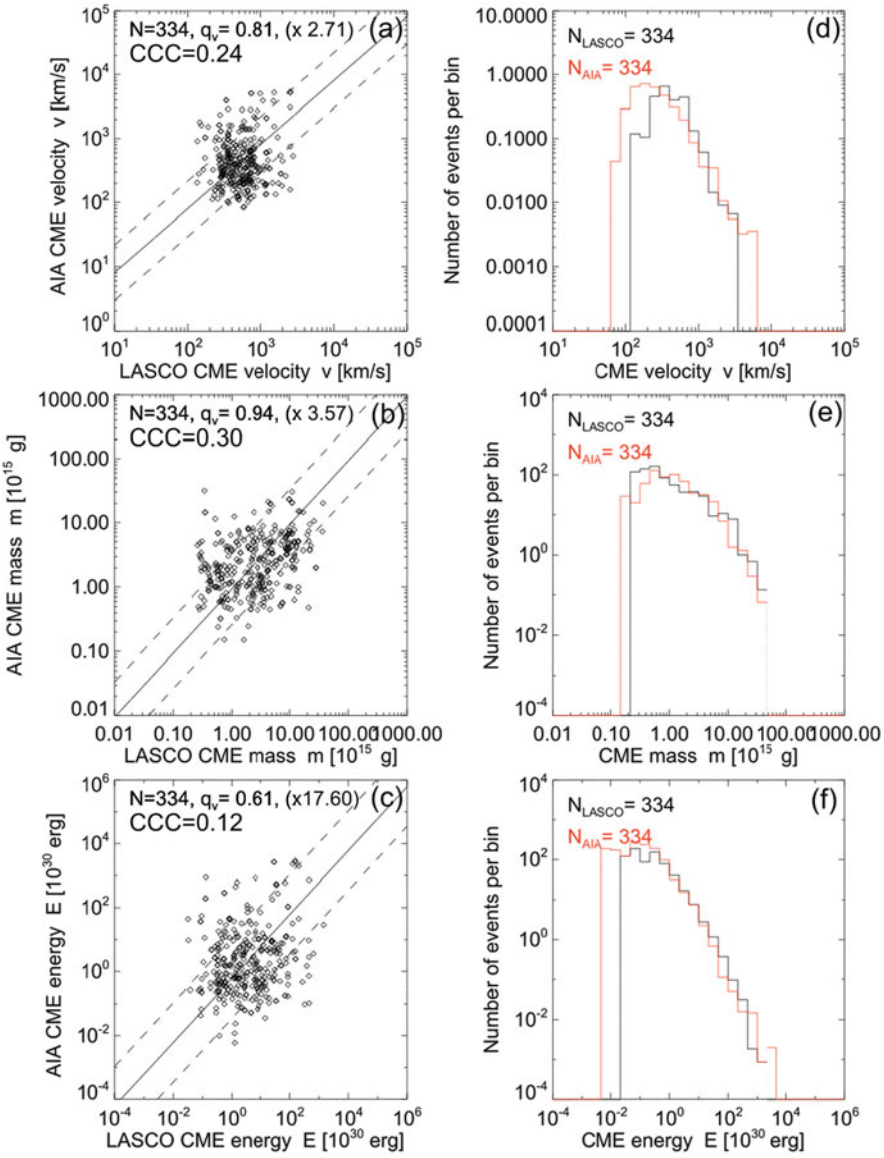

Fig. 14.10 EUV-inferred (from AIA/SDO) versus white light-inferred (from LASCO/SOHO) parameters: (**a**) CME velocity, (**b**) CME mass, and (**c**) CME energy. The ratios q_v are obtained from the logarithmic averages (indicated with a solid line), and the standard deviation factors are indicated with dashed lines. The corresponding size distributions, panels (**d**), (**e**), (**f**), are shown with a black histogram for the LASCO events and with a red histogram for the AIA events (Aschwanden 2017)

Theoretical 2.5-D MHD modeling of the EUV dimming in the context of a giant arcade formation during a flare indicates that soft X-ray twin dimming (above the two ribbons) corresponds to the rarefaction induced by magnetic reconnection. The inner boundary of the dimming corresponds to the slow shocks (Shiota et al. 2005). Rapid dimming starts after the onset of fast reconnection and CME acceleration, and its evolution tracks the CME height and flare reconnection (Cheng and Qiu 2016).

14.9 Halo CMEs

Coronal mass ejections (CMEs) can be categorized by their directional motion or source location: on-disk, near-limb, or behind the Sun. CMEs near the limb can be observed from a side view, with an approximate motion in the plane-of-sky, while CMEs originating on the front disk or behind the Sun move more or less along the line-of-sight and are called *"halo CMEs"*. However, halo CMEs are identified as such only when the brightness enhancement associated with the CME is detected above the occulting disk at all position angles, which requires also a minimum radial speed and transverse (super-radial) expansion speed. Halo CMEs are challenging to reconstruct in white-light data because of the projection effects, but have the advantage to reveal their footpoint area in EUV wavelengths almost unobstructed for on-disk CMEs. Halo CMEs allow the measurement of the expansion speed, which is related to the radial speed by a width-dependent function. This gives a simple method to obtain the deprojected speed (Schwenn et al. 2005; Gopalswamy et al. 2009; Mäkelä et al. 2015). Stereoscopic observations came in use since 2006, which provided additional perspectives for 3-D reconstructions of halo CMEs.

The importance of halo CMEs lies in their potential geoeffectiveness. During the post-solar minimum period from December 1996 to June 1997, six halo CME events were detected, being likely Earthward-directed, associated with shocks, magnetic clouds, and moderate geomagnetic storms at Earth 3–5 days later (Webb et al. 2000). Not all on-disk CMEs hit Earth, but it is found that all of the Earth-encountered CMEs satisfy a simple criterion that the angular width is larger than twice the deviation angle between the CME propagation direction and the Sun-Earth line-of-sights (Shen et al. 2014).

A subset of halo CMEs displays sigmoid structures in soft X-rays (Sterling et al. 2000). Halo CMEs are also accompanied by radio type II bursts, which signify the steepening of a shock wave by the expanding CME (Zucca et al. 2018). Six recurrent halo CMEs during a 60-hour period in November 2000 showed associations with major flares on the disk, the dynamic restructuring was due to flux emergence, the flares were not long-decay events, and no global changes in EUV or soft X-rays were detected during the preflare phase (Nitta and Hudson 2001).

A statistical study of 197 frontside halo CMEs from 1997 to 2001 confirmed that all CMEs were accompanied by local brightenings in the CME source regions (observed with EIT/SOHO and Hα), while 88% of the Earth-directed CMEs are associated with flares, 79% of the CMEs were initiated from active regions, 21%

originate from outside active regions, 59% of the CME initiations preceded the flare onset, and 41% are preceded by flares (Zhou et al. 2003). An expanded statistical study of 378 halo CMEs in cycle 23 (1996–2005) finds that 71% of all frontside halos are geoeffective, and that the most intense geomagnetic storms occur when there are successive CMEs, while there is no significant difference in flare size between geoeffective and other CMEs (Gopalswamy et al. 2007). A online catalog of halo CMEs based on LASCO/SOHO data since 1996–2007 (with 396 events) was compiled by Gopalswamy et al. (2010), which contains the heliographic location, the soft X-ray flare importance, the flare onset time, and the CME speed based on a cone model. A statistical result from this catalog is that halo CMEs are twice faster than ordinary CMEs, and that halo CME events are subject to a bias of being associated with the large flares (Aarnio et al. 2011). This bias could be explained by undersampling of halo CMEs with LASCO/SOHO (Webb and Howard 2012). The statistics of halo CME parameters is not identical during different solar cycles, for instance halo CMEs are more abundant in cycle 24 than in cycle 23, although the sunspot number in cycle 24 has dropped by $\approx$ 40% (Gopalswamy et al. 2015), which could be explained by a weaker heliospheric (magnetic and thermal) pressure that produces more CMEs to appear as halos.

The 3-D reconstruction of halo CMEs is difficult because of the inhomogeneity in the mass distribution and the rapid time variation. Initial geometric models include cones, which can be characterized by the angular width and the central position of the halo CME (Zhao et al. 2002; Xie et al. 2004). The widths, velocities, and source locations of halo CMEs can also be estimated based on a model that assumes constant velocity, symmetry, and constant angular width during propagation (Michalek et al. 2003). Using additional Dopplershift measurements reveals that the fronts of halo CMEs generally correspond to coronal plasma swept up by a shock or a compression wave (Sheeley et al. 2000), and thus favors the cone model (or a spherical shell model), rather than an expanding arcade of loops (Ciaravella et al. 2006). Stereoscopic reconstruction and the geometric cone model have been combined with the *Wang-Sheeley-Arge (WSA)* numerical *solar corona-solar wind* model to estimate the arrival time at Earth, which crucially depends on the accuracy of the modeled solar wind background (Lee et al. 2013, 2015). Multi-spacecraft analysis of the 3-D geometry of a halo-CME reveals two fronts, one that can be represented by an ellipsoid or bubble shape, and one that is reproduced with the graduated cylindrical shell model, indicating the flux rope structure. The bubble-shaped component is a fast magnetosonic shock wave (Veronig et al. 2010; Patsourakos et al. 2010; Ma et al. 2011; Gopalswamy et al. 2012), while the flux-rope component is mass that is carried outward by the underlying magnetic structure (Fig. 14.11; Kwon et al. 2014; Kwon and Vourlidas 2017). Halo-like CMEs are not solely caused by geometric projection effects, since 66% (out of a sample of 62 events) of halo CMEs were observed as halo CMEs simultaneously from all viewing angles of C2/LASCO/SOHO and COR2-A and COR2-B/STEREO in quadrature (Kwon et al. 2015).

The spatial relationship between solar flares and CMEs has been investigated for 496 events with LASCO and it was found that many X-class flares lie at the center

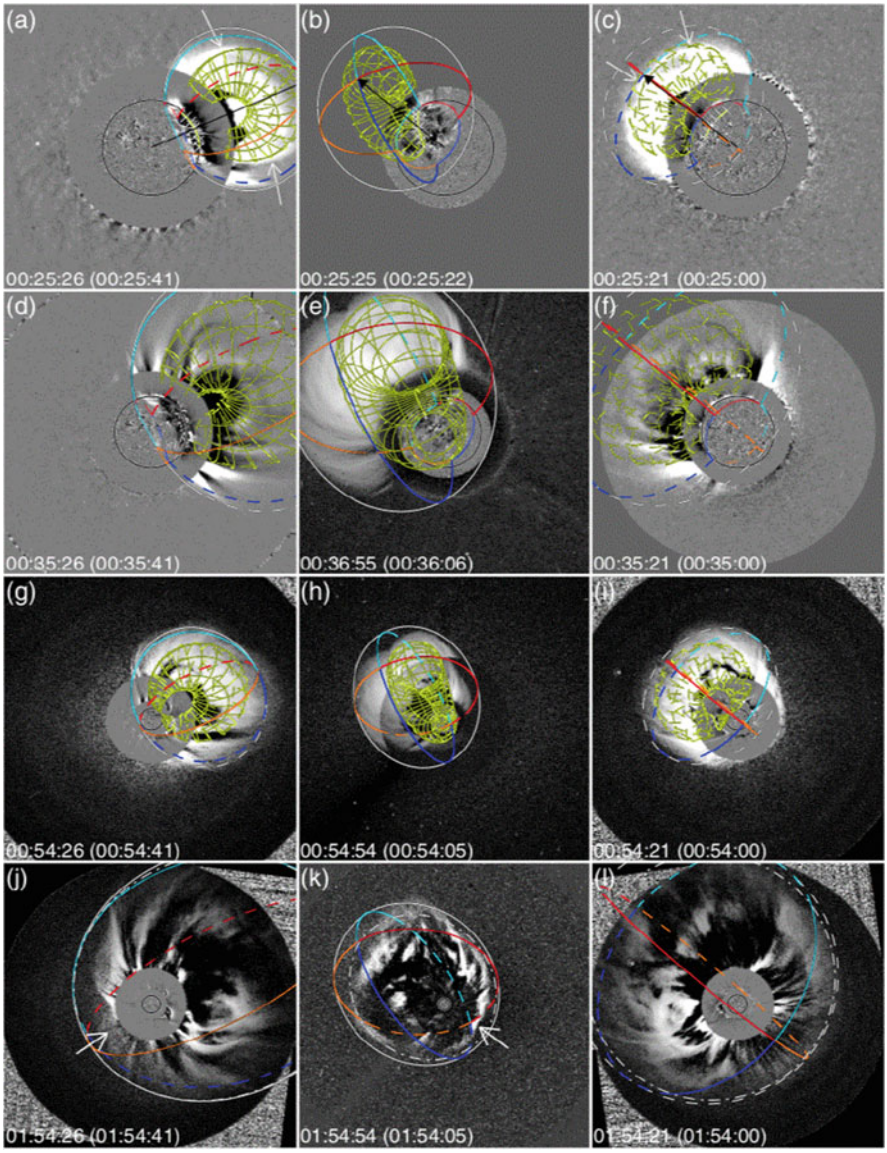

Fig. 14.11 3-D reconstruction of the halo CME on 2012 March 7, using data from STEREO-Behind (left), AIA/SDO (middle), and STEREO-Ahead (right). White-light images are shown as running difference images. Yellow curves represent the ejecta front with the *graduated cylindrical shell model (GCS)*, and the others represent the outermost front with the *ellipsoid model*. Top panels show intensity images, while the bottom panels show the running difference ratio (AIA) images (Kwon et al. 2014)

of the associated CME, while C-class flares widely spread to the outside of the CME span (Yashiro et al. 2008).

Magnetic models of halo CMEs were attempted with global potential fields, using the boundary element method, which revealed that the footpoint area of a halo CME extended over trans-equatorial distances (Wang et al. 2002). *Nonlinear force-free field (NLFFF)* modeling of a particular halo-CME has been used to determine the dissipated magnetic energy (with a difference of $\Delta E_{mag} = 6.4 \times 10^{31}$ erg before and after the flare), while the sum of the kinetic and potential energy of the CME amounts to $E_{cme} = 6.5 \times 10^{31}$ erg, which is consistent with equipartition between the energy dissipated in the flare and CME (Feng et al. 2013).

The kinematics of fast halo-CME events reveals a close synchronization between the CME acceleration profile and the flare energy release in hard X-rays (observed with RHESSI), which suggests a physical relationship between the CME dynamics and the reconnection process in the current sheet beneath the CME (Temmer et al. 2008).

14.10 CMEs and Coronal Radio Emission

Most of the solar radio bursts (of type II, III, and IV) occur during flares, which explains also their intimate association with CMEs, from which unique diagnostic techniques have been developed (for a review see Kontar and Nindos 2018). Type II bursts occur within 2–3 min of the impulsive flare phase in hard X-rays, while the CME liftoffs start before the flare and type II sources by 1–24 min (Leblanc et al. 2001). The most common radio emission that is associated with *coronal mass ejections (CMEs)* is the *radio type II burst* (Gopalswamy et al. 2001), which is most likely to be produced by the CME-related shock wave. Since the plasma frequency ν_p is a strict function of the ambient electron density n_e, yielding $n_e \approx 10^8$–10^{10} cm^{-3} in the frequency range of $\nu_p \approx$ 100–1000 MHz, the radio type II emission traces out the propagation of CME-related shock waves in the lower corona, close to the source region of CMEs. Theoretical models predict a start frequency of $\nu \approx 150$ MHz and starting height of $\approx 0.5 R_\odot$ for type II bursts (Lin et al. 2006), coinciding with the distance at which the Alfvén speed profile has a minimum (Gopalswamy et al. 2009). CMEs were found to be located at heliocentric distances of (1.20–1.93)$R_\odot$ at the onset times of type II bursts, and shock formation was found at heights substantially below $1.5 R_\odot$ and up to $2.0 R_\odot$ (Gopalswamy et al. 2013). The starting frequencies of metric type II bursts have a weak correlation with the measured CME/shock heights and are consistent with the rapid decline of density with height in the inner corona (Gopalswamy et al. 2013). For a high-frequency type II burst (425 MHz), an extremely low distance of shock formation was inferred ($\approx 0.05 R_\odot$), and a correspondingly low height of $\approx 0.08 R_\odot$ for the start frequency of the type II burst (Cho et al. 2013).

A CME was observed with SOHO (EIT, LASCO, UVCS) and simultaneously with WAVES on the Wind spacecraft at 4 MHz and by ground-based instruments.

The density in the shock wave implied by the higher frequency is close to that inferred from UVCS, the type II drift rate suggests shock speeds lower than the CME speed, and the UVCS shows enhanced emission in the O^{5+} and Si^{11+} lines, consistent with modest compression in an MHD shock (Raymond et al. 2000).

The first direct imaging of a CME was made with the *Clark Lake Radioheliograph* (Gopalswamy and Kundu 1992). Bastian et al. (2001) performed the first direct 2-D imaging of nonthermal emission from the CME shock, using the *Nançay Radioheliograph* at frequencies of 164–432 MHz. This radio emission was classified as type IV burst, which is produced by nonthermal synchrotron emission from electrons with energies of $\approx$ 0.5–5 MeV, interacting with magnetic fields of $\approx$ 0.1 to a few Gauss (Bastian et al. 2001). Another observation with Nançay radio imaging data shows that the type II source coincides with the interface between the CME EUV wave front and a nearby coronal ray structure, providing evidence that the type II emission is physically related to the CME-ray interaction (Chen et al. 2014). Radio type IVM emission (interpreted as gyrosynchrotron emission) was found to be cospatial with the CME core in the 2010 August 14 event (Bain et al. 2014), or with the CME leading edge in the case of harmonic plasma emission (Hariharan et al. 2016). Solar type III bursts, which are signatures of plasma emission generated by electron beams, have been mapped with the *LOw frequency ARray (LOFAR)* in the frequency range of 30–90 MHz (corresponding to heights of $\approx 4R_{\odot}$), and were found to be associated with the expanding flank of a CME. The CME compresses the neighboring streamer plasma and produces larger electron densities at high altitudes. The non-radial burst trajectories then become extended by the deflection of radial magnetic fields, as the CME expands in the low corona (Morosan et al. 2014).

The magnetic field could also be measured from multi-frequency imaging of a *moving type IV radio burst* in recent observations, using the gyrosynchrotron spectrum, produced by mildly relativistic electrons with energies of $E \lesssim 100$ keV in relatively strong magnetic fields of $B \lesssim 15$ G (Tun and Vourlidas 2013). Type II bursts can also be used to measure the coronal magnetic field from the shock standoff distance from the flux rope, provided that the type II burst has split-band structure (Gopalswamy et al. 2012).

A timing analysis in a statistical sample of type II bursts led to the conclusion that radio emission can be generated either by blast wave shocks (30%), at shocks driven by the leading edge of the CME (30%), or at shocks driven by internal parts or the flanks of CMEs (29%) (Classen and Aurass 2002). Rapid CME acceleration in 6 analyzed cases was found to be almost coincident with the onset time of metric type II bursts (Cliver et al. 2004). A piston-driven origin was found to be consistent with the timing also, if the radio emission originates above the top of the CME flanks (Mancuso and Raymond 2004). Another study finds that the interface of the CME flank and the streamer is favorable for shock formation (Cho et al. 2007). 3-D reconstruction of a bow-shock model constrains the origin of type II bursts in the flank of the shock (Feng et al. 2015). Dual type II bursts can also be generated by a single shock, first at the CME nose, and second at the CME-streamer interaction site (Cho et al. 2011). Bump features in type II bursts have been interpreted by the source

density variation when the CME shock propagates through nearby dense streamers (Feng et al. 2013).

The majority of type II bursts are associated with *solar energetic particle (SEP)* events (Gopalswamy et al. 2005). There is a trend that the SEP association rate increases with CME speed, width, and energy (Gopalswamy et al. 2008). Nevertheless, a clear-cut distinction between flare-associated and CME-associated SEP events is difficult to establish (Nindos et al. 2008).

Stereoscopic observations have been used to model the expansion of a large-scale dome-shaped CME transient. All of its properties found from EUV, white light, and a metric type II burst were found to match the model of a freely expanding coronal shock wave (Fig. 14.12; Grechnev et al. 2011).

A novel technique that deduces the imaging data compression ratio of AIA images in EUV, and compares it with the compression ratio deduced from the band-split of the type II metric radio bursts observed in ARTEMIS IV dynamic spectra, was used to localize the source locations of the CME-associated shock wave (Kouloumvakos et al. 2014).

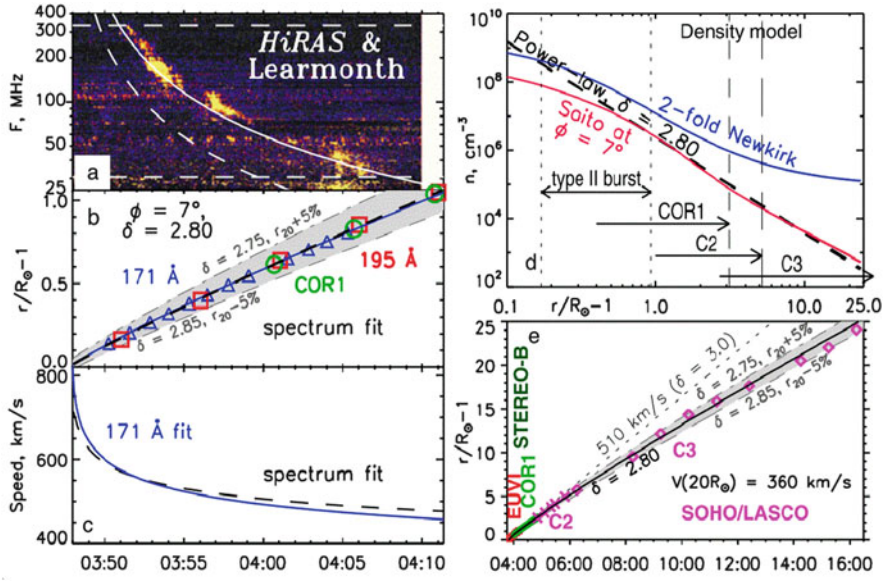

Fig. 14.12 The off-limb expansion of the EUV wave and type II burst are shown: (**a**) Composite radio dynamic spectrum, (**b**) Height-time measurements from EUVI at 195 Å (red), 171 Å (blue), and COR1/STEREO (green); shock power law (blue line) and fit of the type II burst converted into heights (dashed black); (**c**) Speed-time plots calculated from the shock power law fit of the 171 Å data (blue) and from the dynamic spectrum (dashed black); (**d**) Coronal density models: Power law model with $\delta = 2.8$ (dashed black) fitting the dynamic spectrum and models of Newkirk (blue) and Saito for $\Phi = 7°$. (**e**) Overall height-time plot including the CME catalog data (pink) embraced by the gray band (also shown in panel **b**). The dotted line is a linear fit of data in panel **b**), (Grechnev et al. 2011)

References

(14.1) CME Observables, Catalogs, and Classifications

Aschwanden, M.J. 2016, *Global energetics of solar flares. IV. Coronal mass ejection energetics*, ApJ 831, 105, [10 c, 7 c/y].

Aschwanden, M.J. 2017, *Global energetics of solar flares. VI. Refined energetics of coronal mass ejections*, ApJ 847, 27, [2 c, 2 c/y].

Byrne, J.P. 2015, *Investigating the kinematics of coronal mass ejections with the automated CORIMP catalog*, J.Space Weather and Space Climate 5, A19, [6 c, 2 c/y].

Cane, H.V. 2000, *Coronal mass ejections and Forbush decreases*, SSRv 93, 55, [215 c, 12 c/y].

Chen, P.F. 2011, *Coronal mass ejections: Models and their observational basis*, LRSP 8, 1, [182 c, 28 c/y].

Chen, J. 2017, *Physics of erupting solar flux ropes: Coronal mass ejections (CMEs) - Recent advances in theory and observation*, Physics of Plasmas 24/9, 090501.

Cheng, X., Zhang, J., Saar, S.H., et al. 2012, *Differential emission measure analysis of multiple structural components of coronal mass ejections in the inner corona*, ApJ 761, 62, [105 c, 19 c/y].

Forbes, T.G. 2000, *A review on the genesis of coronal mass ejections*, JGR 105/A10, 23153, [362 c, 21 c/y].

Forbes, T.G., Linker, J.A., Chen, J., et al. 2006, *CME theory and models*, SSRv 123, 251, [251 c, 22 c/y].

Gopalswamy, N. 2004, *A global picture of CMEs in the inner heliosphere*, in The Sun and Heliosphere as an Integrated System, (eds. G.Poletto and S.T.Suess), ASSL 317, Dordrecht: Kluwer, p.201, [74 c, 5 c/y].

Gopalswamy, N. 2006, *Coronal mass ejections of solar cycle 23*, J.Astroph.Astron. 27/2, 243, [81 c, 7 c/y].

Gopalswamy, N., Yashiro, S., Michalek, G., et al. 2009, *The SOHO/LASCO CME catalog*, Earth, Moon, and Planets 104, 295, [226 c, 27 c/y].

Gopalswamy, N., Xie, H., Akiyama, S., et al. 2014, *Major solar eruptions and high-energy particle events during solar cycle 24*, Earth, Moon, and Planets 66, 104, [48 c, 14 c/y].

Gopalswamy, N. 2016, *History and development of coronal mass ejections as a key player in solar terrestrial relationship*, Geoscience Letters 3, 8, [17 c, 11 c/y].

Hudson, H.S., Bougeret, J.L., and Burkepile, J. 2006, *Coronal mass ejections: Overview of observations*, SSRv 123, 13, [43 c, 4 c/y].

Lin, J., Murphy, N.A., Shen, C., et al. 2015, *Review on current sheets in CME development: Theories and observations*, SSRv 194, 237, [24 c, 10 c/y].

Moon, Y.J., Choe, G.S., Wang, H., et al. 2002, *A statistical study of two classes of coronal mass ejections*, ApJ 581, 694, [143 c, 9 c/y].

Moran, T.G. and Davila, J.M. 2004, *3-D polarimetric imaging of coronal mass ejections*, Science, 305, 66, [74 c, 5 c/y].

Olmedo, O., Zhang, J., Wechsler, H., et al. 2008, *Automatic detection and tracking of coronal mass ejections in coronagraph time series*, SoPh 248, 485, [65 c, 7 c/y].

Richardson, I.G., and Cane, H.V. 2010, *Near-Earth interplanetary coronal mass ejections during solar cycle 23 (1996–2009) and summary of properties*, SoPh 264, 189, [290 c, 39 c/y].

Robbrecht, E. and Berghmans, D. 2004, *Automated recognition of coronal mass ejections (CMEs) in near-real-time data*, A&A 425, 1097, [133 c, 10 c/y].

Robbrecht, E., Berghmans, D., and Van der Linden, A.M. 2009, *Automated LASCO CME catalog for solar cycle 23: Are CMEs scale-invariant ?* ApJ 691, 1222, [128 c, 15 c/y].

Schmieder, B., Aulanier, G., and Vrsnak, B. 2015, *Flare-CME models: An observational perspective* (Invited review), SoPh 290, 3457, [31, 12 c/y].

St.Cyr, O.C., Plunkett, S.P., Michels, D.J., et al. 2000, *Properties of coronal mass ejections: SOHO LASCO observations from January 1996 to June 1998*, JGR 105/A8, 18169, [321 c, 18 c/y].

Sun, X., Bobra, M., Hoeksema, J.T., et al. 2015, *Why is the great solar active region 12192 flare-rich but CME-poor ?* ApJ 804, L28, [74 c, 30 c/y].
Thernisien, A., Vourlidas, A., and Howard, R.A. 2009, *Forward modeling of coronal mass ejections using STEREO/SECCHI data*, SoPh 156, 111, [235 c, 28 c/y].
Vourlidas, A., Howard, R.A., Esfandiari, E., et al. 2010, *Comprehensive analysis of coronal mass ejection properties over a full solar cycle*, ApJ 722, 1522, [104 c, 14 c/y].
Vrsnak, B., Sudar, D., and Ruzdjak, D. 2005, *The CME-flare relationship: Are there really two types of CMEs ?* A&A 435, 1149, [85 c, 7 c/y].
Webb, D.F. and Howard, T.A. 2012, *Coronal mass ejections: Observations*, LRSP 9, 3, [109 c, 20 c/y].
Wimmer-Schweingruber, R.F., Crooker, N.U., Balogh,A., et al. 2006, *Understanding interplanetary coronal mass ejection signatures*, SSRv 123, 177, [75 c, 7 c/y].
Yashiro, S., Gopalswamy, N., Michalek, G., et al. 2004, *A catalog of white light coronal mass ejections observed by the SOHO spacecraft*, JGR 109/A7, A07105, [528 c, 39 c/y].
Yashiro, S., Akiyama, S., Gopalswamy, N., et al. 2006, *Different power-law indices in the frequency distributions of flares with and without coronal mass ejections*, ApJ 650, L143, [98 c, 9 c/y].
Zhang, J., Dere, K.P., Howard, R.A., et al. 2001, *On the temporal relationship between coronal mass ejections and flares*, ApJ 559, 452, [429 c, 26 c/y].
Zhang, M. and Low, B.C. 2005, *The hydrodynamic nature of solar coronal mass ejections*, ARAA 43, 103, [133 c, 10 c/y].

(14.2) CME Energetics

Aarnio, A.N., Stassun, K.G., Hughes, W.J., et al. 2011, *Solar flares and coronal mass ejections: A statistically determined flare flux - CME mass correlation*, SoPh 268, 195, [39 c, 6 c/y].
Aschwanden, M.J. 2016, *Global energetics of solar flares. IV. Coronal mass ejection energetics*, ApJ 831, 105, [10 c, 7 c/y].
Aschwanden, M.J. 2017, *Global energetics of solar flares. VI. Refined energetics of coronal mass ejections*, ApJ 847, 27, [2 c, 2 c/y].
Bein, B.M., Berkebile-Stoiser, S., Veronig, A.M., et al. 2011, *Impulsive acceleration of coronal mass ejections. I. Statistics and coronal mass ejection source region*, ApJ 738, 191, [54 c, 8 c/y].
Bewsher, D., Harrison, R.A., and Brown, D.S. 2008, *The relationship between EUV dimming and coronal mass ejections. I. Statistical study and probability model*, A&A 478, 897, [39 c, 4 c/y].
Cheng, X., Zhang, J., Ding, M.D., et al. 2010, *A statistical study of the post-impulsive acceleration of flare-associated coronal mass ejections*, ApJ 712, 752, [16 c, 2 c/y].
Ciaravella, A. and Raymond, J.C. 2008, *The current sheet associated with the 2003 November 4 coronal mass ejection: Density, temperature, thickness, and line width*, ApJ 686, 1372, [114 c, 12 c/y].
Gopalswamy, N., Yashiro, S., Mäkelä, P., et al. 2018, *Extreme kinematics of the 2017 September 10 solar eruption and the spectral characteristics of the associated energetic particles*, ApJ 863, L39, [7 c, 7 c/y].
Gosling, J.T. 1993, *The solar flare myth*, JGR 98/A11, 18937, [569 c, 23 c/y].
Hannah, I.G. and Kontar, E.P. 2013, *Multi-thermal dynamics and energetics of a coronal mass ejection in the low solar atmosphere*, A&A 553, A10, [49 c, 11 c/y].
Joshi, A.D. and Srivastava, N. 2011, *Acceleration of coronal mass ejections from 3-D reconstruction of STEREO images*, ApJ 739, 8, [13 c, 2 c/y].
Ma, S., Attrill, G.D.R., Golub, L., et al. 2010, *Statistical study of coronal mass ejections with and without distinct low coronal signatures*, ApJ 722, 289, [39 c, 5 c/y].
Nindos, A., Patsourakos, S., Vourlidas, A., et al. 2015, *How common are hot magnetic flux ropes in the low solar corona? A statistical study of EUV observations*, ApJ 808, 117, [24 c, 10 c/y].

Reeves, K.K., Linker, J.A., Mikic, Z. et al. 2010, *Current sheet energetics, flare emissions, and energy partition in a simulated solar eruption*, ApJ 721, 1547, [60 c, 8 c/y].
Vourlidas, A., Subramanian, P., Dere, K.P., et al. R.A. 2000, *Large-angle spectroscopic coronagraph measurements of the energetics of coronal mass ejections*, ApJ 534, 456, [180 c, 10 c/y.]
Vourlidas, A., Howard, R.A., Esfandiari, E., et al. 2010, *Comprehensive analysis of coronal mass ejection mass and energy properties over a full solar cycle*, ApJ 722, 1522, [105 c, 13 c/y].
Vourlidas, A., Lynch, B.J., Howard, R.A., et al. 2013, *How many CMEs have flux ropes ? Deciphering the signatures of shocks, flux ropes, and prominences in coronagraph observations of CMEs*, SoPh 284, 179, [139 c, 31 c/y].
Wang, Y., Chen, C., Gui, B., et al. 2011, *Statistical study of coronal mass ejection source locations: Understanding CMEs viewed in coronagraphs*, JGR (Space Physics), 116, 4104.
Yashiro, S., Akiyama, S., Gopalswamy, N., et al. 2006, *Different power-law indices in the frequency distributions of flares with and without coronal mass ejections*, ApJ 650, L143, [98 c, 9 c/y].
Yurchyshyn, V.B., Yashiro,S., Abramenko,V., et al. 2005, *Statistical distributions of speeds of coronal mass ejections*, ApJ 619, 599, [65 c, 5 c/y].
Zhang, J. and Dere, K.P. 2006, *A statistical study of main and residual accelerations of coronal mass ejections*, ApJ 649, 1100, [141 c, 12 c/y.

(14.3) CME Helicity

Berger, M.A. 1985, *Structure and stability of constant-alpha force-free fields*, ApJS, 59, 433, [106 c, 3 c/y].
Chen, J. 2017, *Physics of erupting solar flux ropes: Coronal mass ejections (CMEs) - Recent advances in theory and observation*, Physics of Plasmas 24/9, 090501.
Chen, P.F. 2011, *Coronal mass ejections: Models and their observational basis*, LRSP 8, 1, [182 c, 28 c/y].
Démoulin, P., Mandrini, C.H., van Driel-Gesztelyi, L., et al. 2002a, *What is the source of the magnetic helicity shed by CMEs? The long-term helicity budget of AR 7978*, A&A 382, 650, [163 c, 11 c/y].
Démoulin, P., Mandrini, C.H., van Driel-Gesztelyi, L., et al. 2002b, *The magnetic helicity injected by shearing motions*, SoPh 207, 87, [73 c, 5 c/y].
Démoulin, P. 2007, *Recent theoretical and observational developments in magnetic helicity studies*, AdvSpR 39/11, 1674, [57 c, 5 c/y].
Démoulin, P. and Pariat, E. 2009, *Modelling and observations of photospheric magnetic helicity*, AdvSpR 43/7, 1013, [63 c, 7 c/y].
Georgoulis, M.K., Tziotziou, K., and Raouafi, N.E. 2012, *Magnetic energy and helicity budget in the active region solar corona. II. Nonlinear force-free approximation*, ApJ 759, 1, [29 c, 5 c/y].
Green, L.M., Lopez Fuentes, M.C., Mandrini, C.H., et al. 2002, *The magnetic helicity budget of a CME-prolific active region*, SoPh 208, 43, [126 c, 8 c/y].
Green, L.M., Kliem, B., Török, T. et al. 2007, *Transient coronal sigmoids and rotating erupting flux ropes*, SoPh 246, 365, [125 c, 12 c/y].
Liu, Y. and Schuck, P.W. 2012, *Magnetic energy and helicity in two emerging active regions in the Sun*, ApJ 761, 105, [64 c, 12 c/y].
Liu, Y., Hoeksema, J.T., Bobra, M., et al. 2014, *Magnetic helicity in emerging solar active regions*, ApJ 785, 13, [25 c, 7 c/y].
Low, B.C. 2001, *Coronal mass ejections, magnetic flux ropes, and solar magnetism*, JGR 106, A11, [285 c, 17 c/y].
Nindos, A., Zhang, J., and Zhang, H. 2003, *The magnetic helicity budget of solar active regions and coronal mass ejections*, ApJ 594, 1033, [112 c, 8 c/y].
Nindos, A. and Andrews, M.D. 2004, *The association of big flares and coronal mass ejections: What is the role of magnetic helicity*, ApJ 616, L175, [66 c, 5 c/y].

Pevtsov, A.A., Berger, M.A., Nindos, A., et al. 2014, *Magnetic helicity, tilt, and twist*, SSRv 186, 285, [34 c, 10 c/y].
Phillips, A.D., MacNeice, P.J., and Antiochos, S.K. 2005, *The role of magnetic helicity in coronal mass ejections*, ApJ 624, L129, [40 c, 3 c/y].
Titov, V.S. and Démoulin, P. 1999, *Basic topology of twisted magnetic configurations in solar flares*, ApJ 351, 707, [402 c, 22 c/y].
Tziotziou, K., Georgoulis, M.K., and Liu, Y. 2013, *Interpreting eruptive behavior in NOAA AR 11158 via the region's magnetic energy and relative helicity budgets* ApJ 772, 115, [42 c, 9 c/y].
Wang, J., Zhou, G., and Zhang, J. 2004, *Helicity patterns of coronal mass ejection-associated active regions*, ApJ 615, 1021, [44 c, 3 c/y].

(14.4) CME Magnetic Configuration

Antiochos, S.K., DeVore, C.R., and Klimchuk, J.A. 1999, *A model for solar coronal mass ejections*, ApJ 510, 485, [844 c, 46 c/y].
Cremades, H. and Bothmer, V. 2004, *On the 3-D configuration of coronal mass ejections*, A&A 422, 307, [198 c, 15 c/y].
Fan, Y. and Gibson, S.E. 2007, *Onset of coronal mass ejections due to loss of confinement of coronal flux ropes*, ApJ 668, 1232, [182 c, 17 c/y].
Forbes, T.G. and Isenberg, P.A. 1991, *A catastrophe mechanism for coronal mass ejections*, ApJ 373, 294, [312 c, 12 c/y].
Forbes, T.G. 2000, *A review on the genesis of coronal mass ejections*, JGR 105/A10, 23153, [362 c, 21 c/y].
Forbes, T.G., Linker, J.A., Chen, J., et al. 2006, *CME theory and models*, SSRv 123, 251, [251 c, 22 c/y].
Gibson, S.E., Fan, Y., Mandrini, C., et al. 2004, *Observational consequences of a magnetic flux rope emerging into the corona*, ApJ 617, 600, [108 c, 8 c/y].
Gibson, S.E., Fan, Y., Török, T., et al. 2006, *The evolving sigmoid: Evidence for magnetic flux ropes in the corona before, during, and after CMEs*, SSRv 124, 131, [68 c, 6 c/y].
Isenberg, P.A. and Forbes, T.G. 2007, *A 3-D line-tied magnetic field model for solar eruptions*, ApJ 670, 1453, [82 c, 8 c/y].
Karpen, J.T., Antiochos, S.K., DeVore, C.R. 2012, *The mechanisms for the onset and explosive eruption of coronal mass ejections and eruptive flares*, ApJ 760, 81, [87 c, 16 c/y].
Kliem, B. and Török, T. 2006, *Torus instability*, Phys. Rev. Lett. 96/25, 255002, [410 c, 36 c/y].
Ko, Y.K., Raymond, J.C., Lin, J., et al. 2003, *Dynamical and physical properties of a post-coronal mass ejection current sheet*, ApJ 594, 1068, [160 c, 11 c/y].
Lin, J., Raymond, J.C., and van Ballegooijen, A.A. 2004, *The role of magnetic reconnection in the observable features of solar eruptions*, ApJ 602, 422, [104 c, 8 c/y].
Lin, J., Ko, Y.K., Sui, L., et al. 2005, *Direct observations of the magnetic reconnection site of an eruption on 2003 November 18*, ApJ 622, 1251, [195 c, 16 c/y].
Lin, J., Murphy, N.A., Shen, C., et al. 2015, *Review on current sheets in CME development: Theories and observations*, SSRv 194, 237, [24 c, 10 c/y].
Moore, R.L., Sterling, A.C., Hudson, H.S., et al. 2001, *Onset of the magnetic explosion in solar flares and coronal mass ejections*, ApJ 552, 833, [477 c, 29 c/y].
Savage, S.L., McKenzie, D.E., Reeves, K.K., et al. 2010, *Reconnection outflows and current sheet observed with Hinode/XRT in the 2008 April 0 "Carthweel CME" flare*, ApJ 722, 329, [93 c, 12 c/y].
Schmieder,B., Aulanier, G., and Vrsnak, B. 2015, *Flare-CME models: An observational perspective* (Invited review), SoPh 290, 3457, [31, 12 c/y].
Schrijver, C.J. and Title, A.M. 2011, *Long-range magnetic couplings between solar flares and coronal mass ejections observed by SDO and STEREO*, JGR 116/A4, A0408, [92 c, 14 c/y].

Su, Y., Surges, V., van Ballegooijen, A.A. et al. 2011, *Observations and magnetic field modeling of the flare/coronal mass ejection event on 2010 April 8*, ApJ 734, 53, [71 c, 11 c/y].
Titov, V.S. and Démoulin, P. 1999, *Basic topology of twisted magnetic configurations in solar flares*, ApJ 351, 707, [402 c, 22 c/y].
Török, T. and Kliem, B. 2003, *The evolution of twisting coronal magnetic flux tubes*, A&A 406, 1043, [182 c, 16 c/y].
Török, T. and Kliem, B. 2005, *Confined and ejective eruptions of kink-unstable flux ropes*, ApJ 630, L97, [477 c, 38 c/y].
Török, T., Panasenco, O., Titov, V.S., et al. 2011, *A model for magnetically coupled sympathetic eruptions*, ApJ 739, L63, [95 c, 15 c/y].

(14.5) CME Trigger Mechanisms

Amari, T., Luciani, J.F., Mikic, Z., et al. 2000, *A twisted flux rope model for coronal mass ejections and two-ribbon flares*, ApJ 529, L49, [285 c, 16 c/y].
Amari, T., Luciani, J.F., Aly, J.J., et al. 2003, *Coronal mass ejection: Initiation, magnetic helicity, and flux ropes. I. Boundary motion-driven evolution*, ApJ 585, 1073, [184 c, 13 c/y].
Amari, T., Canou, A., and Aly, J.J. 2014, *Characterizing and predicting the magnetic environment leading to solar eruptions*, Nature 514/7523, 465, [55 c, 16 c/y].
Chen, P.F. and Shibata, K. 2000, *An emerging flux trigger mechanism for coronal mass ejections*, ApJ 545, 524, [306 c, 17 c/y].
Démoulin, P. and Aulanier, G. 2010, *Criteria for flux rope eruption: Non-equilibrium versus torus instability*, ApJ 718, 1388, [128 c, 17 c/y].
Fan, Y. and Gibson, S.E. 2007, *Onset of coronal mass ejections due to loss of confinement of coronal flux ropes*, ApJ 668, 1232, [178 c, 17 c/y].
Forbes, T.G. and Isenberg, P.A. 1991, *A catastrophe mechanism for coronal mass ejections*, ApJ 373, 294, [312 c, 12 c/y].
Gopalswamy, N., Yashiro, S., Akiyama, S. et al. 2017, *Estimation of reconnection flux using post-eruption arcades and its relevance to magnetic clouds at 1 AU*, SoPh 292/4, 65, [13 c, 13 c/y].
Gopalswamy, N., Akiyama, S., Yashiro, S. et al. 2018, *Coronal flux ropes and their interplanetary counterparts*, JASTP 180, 35, [5 c, 5 c/y].
Green, L.M., Kliem, B., and Wallace, A.J. 2011, *Photospheric flux cancellation and associated flux rope formation and eruption*, A&A 526, A2, [102 c, 16 c/y].
Karpen, J.T., Antiochos, S.K., DeVore, C.R. 2012, *The mechanisms for the onset and explosive eruption of coronal mass ejections and eruptive flares*, ApJ 760, 81, [87 c, 16 c/y].
Kusano, K., Bamba, Y., Yamamoto, T.T., et al. 2012, *Magnetic field structures triggering solar flares and coronal mass ejections*, ApJ 760, 31, [90 c, 16 c/y].
Kliem, B., Titov, V.S., and Török, T. 2004, *Formation of current sheets and sigmoidal structure by the kink instability of a magnetic loop*, A&A 413, L23, [131c, 10 c/y].
Kliem, B., Lin, J., Forbes, T.G., et al. 2014, *Catastrophe versus instability for the eruption of a toroidal solar magnetic flux rope*, ApJ 789, 46, [43 c, 12 c/y].
Lin, J. and Forbes, T.G. 2000, *Effects of reconnection on the coronal mass ejection process*, JGR 105/A2, 2375, [384 c, 22 c/y].
Lin, J., Ko, Y.K., Sui, L., et al. 2005, *Direct observations of the magnetic reconnection site of an eruption on 2003 November 18*, ApJ 622, 1251, [195 c, 16 c/y].
Liu, R., Kliem, B., Itov, V.S. et al. 2016, *Structure, stability, and evolution of magnetic flux ropes from the perspective of magnetic twist*, ApJ 818, 148, [54 c, 36 c/y].
Longcope, D., Beveridge, C., Qiu, J., et al. 2007, *Modeling and measuring the flux reconnected and ejected by the two-ribbon flare/CME event on 7 November 2004*, SoPh 244, 45, [69 c, 7 c/y].
Qiu, J., Hu, Q., Howard, T.A. et al. 2007, *On the magnetic flux budget in low-corona magnetic reconnection and interplanetary coronal mass ejections*, ApJ 659, 758, [153 c, 15 c/y].

Patsourakos, S., Vourlidas, A., and Stenborg, G. 2013, *Direct evidence for a fast coronal mass ejection driven by the prior formation and subsequent destabilization of a magnetic flux rope*, ApJ 764, 125, [92 c, 20 c/y].

Roussev, I.I., Forbes, T.G., Gombosi, T.I., et al. 2003, *A 3-D flux rope model for coronal mass ejections based on a loss of equilibrium*, ApJ 588, L45, [152 c, 10 c/y].

Roussev, I.I., Galsgaard, K., Cooper, D., et al. 2012, *Explaining fast ejections and exotic X-ray emission from the solar corona*, Nature Physics 8/11, 845, [25 c, 5 c/y].

Titov, V.S. and Démoulin, P. 1999, *Basic topology of twisted magnetic configurations in solar flares*, ApJ 351, 707, [402 c, 22 c/y].

Török, T. and Kliem, B. 2003, *The evolution of twisting coronal magnetic flux tubes*, A&A 406, 1043, [182 c, 16 c/y].

Török, T. and Kliem, B. 2004, *Ideal kink instability of a magnetic loop equilibrium*, A&A 413, L27, [236 c, 17 c/y].

Török, T. and Kliem, B. 2005, *Confined and ejective eruptions of kink-unstable flux ropes*, ApJ 630, L97, [463 c, 37 c/y].

Török, T., Berger, M.A., and Kliem, B. 2010, *The writhe of helical structures in the solar corona*, A&A 516, A49, [66 c, 9 c/y].

van Ballegooijen, A.A. and Martens, P.C.H. 1989, *Formation and eruption of solar prominences*, ApJ 343, 971, [548 c, 19 c/y].

van Tend, W. and Kuperus, M. 1978, *The development of coronal electric current systems in active regions and their relation to filaments and flares*, SoPh 59, 115, [247 c, 6 c/y].

Wang, W., Lui, R., Wang, Y. 2017, *Buildup of a highly twisted magentic flux rope during a solar eruption*, Nature Comm. 8, 1330, [14 c, 14 c/y].

Zuccarello, F.P., Seaton, D.B., Mierla, M. 2014, *Observational evidence of torus instability as trigger mechanism for coronal mass ejections: The 2011 August 4 filament eruption*, ApJ 785, 88, [34 c, 10 c/y].

(14.6) MHD Evolution of CMEs

Amari, T., Luciani, J.F., Aly, J.J., et al. 2003a, *Coronal mass ejection: Initiation, magnetic helicity, and flux ropes. I. Boundary motion-driven evolution*, ApJ 585, 1073, [184 c, 13 c/y].

Amari, T., Luciani, J.F., Aly,k J.J. et al. 2003b, *Coronal mass ejection: Initiation, magnetic helicity, and flux ropes. II. Turbulent diffusion-driven evolution*, ApJ 595, 1231, [143 c, 10 c/y].

Archontis, V. and Hood, A.W. 2012, *Magnetic flux emergence: a precursor of solar plasma expulsion*, A&A 537, A62, [33 c, 6 c/y].

Aulanier, G., Török, T., Démoulin, P., et al. 2010, *Formation of torus-unstable flux ropes and electric currents in erupting sigmoids* ApJ 708, 314, [259 c, 35 c/y].

Fan, Y. and Gibson, S.E. 2007, *Onset of coronal mass ejection due to loss of confinement of coronal flux ropes*, ApJ 668, 1232, [178 c, 17 c/y].

Gibson, S.E., Fan, Y., Mandrini, C., et al. 2004, *Observational consequences of a magnetic flux rope emerging into the corona*, ApJ 617, 600, [108 c, 8 c/y].

Jiang, C., Feng, Z., Wu, S.T., et al. 2013 *MHD simulation of a sigmoid eruption of active region 11283*, ApJ 771, L30, [60 c, 13 c/y].

Jin, M., Manchester, W.B., van der Holst, B., et al. 2017, *Data-constrained coronal mass ejections in a global MHD model*, ApJ 834, 173, [13 c, 13 c/y].

Kliem, B., Su, Y.N., van Ballegooijen, A.A. et al. 2013, *MHD modeling of the solar eruption on 2010 April 8*, ApJ 779, 129, [49 c, 11 c/y].

Kusano, K., Bamba, Y., Yamamoto, T.T., et al. 2012, *Magnetic field structures triggering solar flares and coronal mass ejections*, ApJ 760, 31, [90 c, 16 c/y].

Leake, J.E., Linton, M.G., and Antiochos, S.K. 2014, *Simulations of emerging magnetic flux. II. The formation of unstable coronal flux ropes and the initiation of coronal mass ejections*, ApJ 787, 46, [31 c, 9 c/y].

Lynch, B.J., Antiochos, S.K., DeVore, C.R. 2008, *Topological evolution of a fast magnetic breakout CME in 3D*, ApJ 683, 1192, [135 c, 14 c/y].
Mackay, D.H. and van Ballegooijen, A.A. 2006, *Models of the large-scale corona. I. Formation, evolution, and liftoff of magnetic flux ropes*, ApJ 641, 577, [136 c, 12 c/y].
MacNeice, P., Antiochos, S.K., Phillips, A., et al. 2004, *A numerical study of the breakout model for coronal mass ejection initiation*, ApJ 614, 1028, [98 c, 7 c/y].
Manchester, W.B., Gombosi, T.I., Roussev, I.I. et al. 2004, *3-D MHD simulation of a flux rope driven CME* JGR 109/A1, A01102, [103 c, 8 c/y].
Roussev, I.I., Galsgaard, K., Cooper, D., et al. 2012, *Explaining fast ejections and exotic X-ray emission from the solar corona*, Nature Physics 8/11, 845, [25 c, 5 c/y].
Savcheva, A., Pariat, E., van Ballegooijen, A.A. et al. 2012, *Sigmoidal active region on the Sun: Comparison of a MHD simulation and a nonlinear force-free field model*, ApJ 750, 15, [71 c, i13 c/y].
Thernisien, A.F.R., Howard, R.A., and Vourlidas, A. 2006, *Modeling of flux rope CMEs*, ApJ 652, 763, [203 c, 28 c/y].
Török, T. and Kliem, B. 2003, *The evolution of twisting coronal magnetic flux tubes*, A&A 406, 1043, [182 c, 16 c/y].
Török, T. and Kliem, B. 2007, *Numerical simulations of fast and slow CMEs*, Astron.Nachrichten 328/8, 743, [114 c, 11 c/y].
Török, T., Berger, M.A., and Kliem, B. 2010, *The writhe of helical structures in the solar corona*, A&A 516, A49, [66 c, 9 c/y].
Török, T., Panasenco, O., Titov, V.S., et al. 2011, *A model for magnetically coupled sympathetic eruptions*, ApJ 739, L63, [93 c, 14 c/y].

(14.7) Confined Eruption

Akiyama, A., Yashiro, S., and Gopalswamy, N. 2007, *The CME-productivity associated with flares from two active regions*, AdvSpR 39/9, 1467, [5 c, 0.4 c/y].
Archontis, V. and Török, T. 2008, *Eruption of magnetic flux ropes during flux emergence*, A&A 492, L35, [86 c, 9 c/y].
Chen, H., Zhang, J., Ma, S., et al. 2015, *Confined flares in solar active region 12192 October 18 to 29*, ApJ 808, L24, [30 c, 12 c/y].
Cheng, X., Zhang, J., Ding, M.D., et al. 2011, *A comparative study of confined and eruptive flares in NOAA AR 10720*, ApJ 732, 87, [46 c, 7 c/y].
Cheng, X., Ding, M.D., and Fang, C. 2015a, *Imaging and spectroscopic diagnostics on the formation of two magnetic flux ropes revealed by SDO/AIA and IRIS* ApJ 804, 82, [35 c, 14 c/y].
Cheng, X., Hao, Q., Ding, M.D., et al. 2015b, *A two-ribbon white-light flare associated with a failed solar eruption observed by ONSET, SDO, and IRIS*, ApJ 809, 46, [11 c, 4 c/y].
Chintzoglou, G., Patsourakos, S., and Vourlidas, A. 2015, *Formation of magnetic flux ropes during a confined flaring well before the onset of a pair of major CMEs*, ApJ 809, 34, [23 c, 9 c/y].
DeVore, C.R. and Antiochos, S.K. 2008, *Homologous confined filament eruptions via magnetic breakout*, ApJ 680, 740, [102 c, 11 c/y].
Fan, Y. 2005, *Coronal mass ejections as loss of confinement of kinked magnetic flux ropes*, ApJ 630, 543, [114 c, 9 c/y].
Gilbert, H.R., Alexander, D., and Liu, R. 2007, *Filament kinking and its implications for eruption and re-formation*, SoPh 245, 287, [64 c, 6 c/y].
Gopalswamy, N., Shimojo, M., Lu, W. et al. 2003, Prominence eruptions and coronal mass ejection: A statistical study using microwave observations, ApJ 586, 562, [196 c, 14 c/y].
Gopalswamy, N., Nunes, S., Yashiro, S., et al. 2004, *Variability of solar eruptions during cycle 23*, AdvSpR 34, 391, [19 c, 1.4 c/y].

Guo, Y., Ding, M.D., Schmieder, B., et al. 2010, *Driving mechanism and onset condition of a confined eruption*, ApJ 725, L38, [70 c, 9 c/y].
Guo, Y., Ding, M.D., Schmieder, B., et al. 2012, *Evolution of hard X-ray sources and ultraviolet solar flare ribbons for a confined eruption of a magnetic flux rope*, ApJ 746, 17, [21 c, 4 c/y].
Ji, H., Wang, H., Schmahl, E.J., et al. 2003, *Observations of the failed eruption of a filament*, ApJ 595, L135, [140 c, 10 c/y].
Joshi, N.C., Srivastava, A.K., Filippov, B., et al. 2014, *Confined partial filament and its reformation within a stable magnetic flux rope*, ApJ 787, 11, [24 c, 7 c/y].
Lin, J. and Forbes, T.G. 2000, *Effects of reconnection on the coronal mass ejection process*, JGR 105/A2, 2375, [384 c, 22 c/y].
Liu, Y., Su, J., Lin, H., et al. 2009, *New observations of failed filament eruptions: The influence of asymmetric coronal background fields on solar eruptions*, ApJ 696, L70, [31 c, 4 c/y].
Olmedo, O. and Zhang, J. 2010, *Partial torus instability*, ApJ 718, 433, [62 c, 8 c/y].
Schrijver, C.J. 2009, *Driving major solar flares and eruptions: A review*, Adv.Spac.Res. 43/5, 739, [111 c, 13 c/y].
Shen, Y.D., Liu,Y., and Liu,R. 2011, *A time series of filament eruptions observed by three eyes from space: From failed to successful eruptions.* Res.Astron.Astrophys. 11/5, 594, [43 c, 7 c/y].
Sturrock, P.A., Weber, M., Wheatland, M.S., et al. 2001, *Metastable magnetic configurations and their significance for solar eruptive events*, ApJ 548, 492, [57 c, 3 c/y].
Sun, X., Bobra, M., Hoeksema, J., et al. 2015, *Why is the great solar active region 12192 flare-rich but CME-poor ?* ApJ 804, L28, [74 c, 30 c/y].
Thalmann, J.K., Su, Y., Temmer, M., et al. 2015, *The confined X-class flares of solar active region 2192*, ApJ 801, L23, [49 c, 20 c/y].
Török, T. and Kliem, B. 2005, *Confined and ejective eruptions of kink-unstable flux ropes*, ApJ 630, L97, [463 c, 37 c/y].
Török, T., Berger, M.A., and Kliem, B. 2010, *The writhe of helical structures in the solar corona*, A&A 516, A49, [66 c, 9 c/y].
Wang, Y. and Zhang, J. 2007, *A comparative study between eruptive X-class flares associated with CMEs and confined X-class flares*, ApJ 665, 1428, [88 c, 8 c/y].
Williams, D.R., Török, T., Démoulin, P., et al. 2005, *Eruption of a kink-unstable filament in NOAA active region 10696*, ApJ 628, L163, [144 c, 12 c/y].
Yang, S., Zhang, J., and Xiang, Y. 2014, *Fine structures and overlying loops of confined solar flares*, ApJ 793, L28, [22 c, 6 c/y].

(14.8) Coronal Dimming

Aschwanden, M.J., Nitta, N.V., Wuelser, J.P., et al. 2009, *First measurements of the mass of CMEs from EUV dimming observed with STEREO EUVI A+B spacecraft*, ApJ 706, 376, [36 c, 4 c/y].
Aschwanden, M.J. 2009, *4-D modeling of CME expansion and EUV dimming observed with STEREO/EUVI*, Annales Geophysicae 27/8, 3275, [18 c, 2 c/y].
Aschwanden, M.J. 2016, *Global energetics of solar flares. IV. Coronal mass ejection energetics*, ApJ 831, 105, [10 c, 7 c/y].
Aschwanden, M.J. 2017, *Global energetics of solar flares. VI. Refined energetics of coronal mass ejections*, ApJ 847, 27, [2 c, 2 c/y].
Attrill, G., Nakwacki, M.S., Harra, L.K., et al. 2006, *Using the evolution of coronal dimming regions to probe the global magnetic field topology*, SP 238, 117, [83 c, 7 c/y].
Attrill, G.D.R., Engell, A.J., Wills-Davey, M.J., et al. 2009, *Hinode/XRT and STEREO observations of a diffuse coronal wave-CME-dimming event*, ApJ 704, 1296, [37 c, 4 c/y].
Attrill, G.D.R. and Wills-Davey, M.J. 2010, *Automatic detection and extraction of coronal dimming from SDO/AIA data*, SoPh 262, 461, [15 c, 2 c/y].

Bewsher, D., Harrison, R.A., and Brown, D.S. 2008, *The relationship between EUV dimming and CMEs. I. Statistical study and probability model*, A&A 478, 897, [39 c, 4 c/y].
Cheng, J.X. and Qiu, J. 2016, *The nature of CME-flare-associated coronal dimming*, ApJ 825, 37, [7 c, 5 c/y].
Harra, L.K. and Sterling, A.C. 2001, *Material outflows from coronal intensity "dimming regions" during CME onset*, ApJ 561, L215, [114 c, 7 c/y].
Harra, L.K., Hara, H., Imada, S. 2007, *Coronal dimming observed with Hinode outflows related to a coronal mass ejection*, PASJ 59, SP3, [61 c, 6 c/y].
Harrison, R.A. and Lyons, M. 2000, *A spectroscopic study of coronal dimming associated with a coronal mass ejection*, A&A 358, 1097, [100 c, 6 c/y].
Harrison, R.A., Bryans, P., Simnett, G.M., et al. 2003, *Coronal dimming and the coronal mass ejection onset*, A&A 400, 1071, [83 c, 6 c/y].
Innes, D.E., McIntosh, S.W., and Pietarila, A. 2010, *STEREO quadrature observations of coronal dimming at the onset of mini-CMEs*, A&A 517, L7, [25 c, 3 c/y].
Mandrini, C.H., Nakwacki, M.S., Attrill, G., et al. 2007, *Are CME-related dimmings always a simple signature of interplanetary magnetic cloud footpoints ?* SoPh 244, 25, [57 c, 5 c/y].
Mason, J.P., Woods, T.N., Caspi, A., et al. 2014, *Mechanisms and observations of coronal dimming for the 2010 August 7 event*, ApJ 789, 61, [15 c, 4 c/y].
Moore, R.L. and Sterling, A.C. 2007, *The coronal-dimming of a streamer-puff coronal mass ejection: Confirmation of the magnetic-arch-blowout scenario*, ApJ 661, 543, [33 c, 3 c/y].
Podladchikova, O. and Berghmans, D. 2005, *Automated detection of EIT waves and dimmings*, SoPh 228, 265, [67 c, 5 c/y].
Reinard, A.A. and Biesecker, D.A. 2008, *CME-associated coronal dimmings*, ApJ 674, 576, [41 c, 4 c/y].
Reinard, A.A. and Biesecker, D.A. 2009, *The relationship between coronal dimming and CME properties*, ApJ 705, 914, [21 c, 2 c/y].
Robbrecht, E., Patsourakos, S., and Vourlidas, A. 2009, *No trace left behind: STEREO observations of a coronal mass ejection without low coronal signatures*, ApJ 701, 283, [93 c, 11 c/y].
Shiota, D., Isobe, H., Chen, P.F., et al. 2005, *Self-consistent MHD modeling of a CME, coronal dimming, and a giant cusp-shaped arcade*, ApJ 634, 663, [51 c, 4 c/y].
Thompson, B.J., Cliver, E.W., Nitta, N., et al. 2000, *Coronal dimming and energetic CMEs in April-May 1998*, GRL 27, 1431, [133 c, 8 c/y].
Tian, H., McIntosh, S.W., Xia, L., et al. 2012, *What can we learn about solar CMEs, coronal dimmings, and EUV jets through spectroscopic observations ?* ApJ 748, 106, [45 c, 8 c/y].
Zhang, Q.M., Su, Y.N., and Ji, H.S. 2017, *Pre-flare coronal dimmings*, A&A 598, A3, [7 c, 7 c/y].
Zhukov, A.N. and Auchère, F. 2004, *On the nature of EIT waves, EUV dimmings and their link to CMEs*, A&A 427, 705, [152 c, 11 c/y].

(14.9) Halo CMEs

Aarnio, A.N., Stassun, K.G., Hughes, W.J., et al. 2011, *Solar flares and CMEs: A statistically determined flare flux-CME mass correlation*, SoPh 268, 195, [39 c, 6 c/y].
Ciaravella, A., Raymond, J.C., and Kahler, S.W. 2006, *CMEs: Doppler shifts, angles, shocks, and bulk morphology*, ApJ 652, 774, [29 c, 3 c/y].‘
Feng, L., Wiegelmann, T., Su, Y., et al. 2013, *Magnetic energy partition between the CME and flare from AR 11283*, ApJ 765, 37, [31 c, 7 c/y].
Gopalswamy, N., Yashiro, S., and Akiyama, S. 2007, *Geoeffectiveness of halo CMEs*, JGR 112/A6, A06112, [107 c, 10 c/y].
Gopalswamy, N., Dal Lago, A., Yashiro, S., et al. 2009, *The expansion and radial speeds of coronal mass ejections*, Central European Astrophys. Bulletin 33, 115, [23 c, 3 c/y].
Gopalswamy, N., Yashiro, S., Michalek, G., et al. 2010, *A catalog of halo CMEs from SOHO*, Sun and Geosphere 5/1, 7, [43 c, 6 c/y].

Gopalswamy, N., Nitta, N., Akiyama, S., et al. 2012, *Coronal magnetic field measurement from EUV images made by the solar dynamics*, ApJ 744, 72, [55 c, 10 c/y].
Gopalswamy, N., Xie, H., Akiyama, S., et al. 2015, *The peculiar behavior of halo CMEs in solar cycle 24*, ApJ 804, L23, [23 c, 9 c/y].
Kwon, R.Y., Zhang, J., and Olmedo, O. 2014, *New insights into the physical nature of CMEs and associated shock waves within the framework of the 3-D structure*, ApJ 794, 148, [24 c, 7 c/y].
Kwon, R.Y., Zhang, J., and Vourlidas, A. 2015, *Are halo-like solar CMEs merely a matter of geometric projection effects ?* ApJ 799, L29, [19 c, 8 c/y].
Kwon, R.Y. and Vourlidas, A. 2017, *Investigating the wave nature of the outer envelope of halo and CMEs*, ApJ 836, 246, [6 c, 6 c/y].
Lee, C.O., Arge, C.N., Odstrcil, D., et al. 2013, *Ensemble modeling of CME propagation*, SoPh 285, 349, [29 c, 4 c/y].
Lee, C.O., Arge, C.N., Odstrcil, D., et al. 2015, *Ensemble modeling of successive halo CMEs: A case study*, SP 290, 1207, [8 c, 3 c/y].
Ma, S., Raymond, J.C., Golub, L., et al. 2011, *Observations and interpretation of a low coronal shock wave observed in the EUV by the SDO/AIA*, ApJ 738, 160, [86 c, 13 c/y].
Mäkelä, P., Gopalswamy, N., Akiyama et al. 2015, *Estimating the height of CMEs associated with a major SEP event at the onset of the metric type II radio burst during solar cycles 23 and 24*, ApJ 806, 13, [11 c, 4 c/y].
Michalek, G., Gopalswamy, N., and Yashiro, S., et al. 2003, *A new method for estimating widths, velocities, and source location of halo CMEs*, ApJ 584, 472, [95 c, 7 c/y].
Nitta, N.V. and Hudson, H.S. 2001, *Recurrent flare/CME events from an emerging flux region*, GRL 28/19, 3801, [58 c, 4 c/y].
Patsourakos, S., Vourlidas, A., and Stenborg, G. 2010, *The genesis of an impulsive coronal mass ejection observed at ultra-high cadence by AIA on SDO*, ApJ 724, L188, [69 c, 9 c/y].
Schwenn, R., dal Lago, A., Huttunen, E., et al. 2005, *The association of coronal mass ejections with their effects near the Earth*, Annales Geophysicae 23/3, 1033, [191 c, 15 c/y].
Sheeley, N.R., Hakala, W.N., and Wang, Y.M. 2000, *Detection of coronal mass ejection associated shock waves in the outer corona*, JGR 105, A4, 5081, [102 c, 6 c/y].
Shen, C., Wang, Y., Pan, Z., et al. 2014, *Full-halo CMEs: Arrival at the Earth*, JGR 119/7, 5107, [15 c, 4 c/y].
Sterling, A.C., Hudson, H.S., Thompson, B., et al. 2000, *Yohkoh SXT and SOHO EIT observations of sigmoid-to-arcade evolution of structures associated with halo CMEs*, ApJ 532, 628, [121 c, 7 c/y].
Temmer, M., Veronig, A.M., Vrsnak, B., et al. 2008, *Acceleration in fast halo CMEs and synchronized flare hard X-ray bursts*, ApJ 673, L95, [115 c, 12 c/y].
Veronig, A.M., Muhr, N., Kienreich, I.W., et al. 2010, *First observations of a dome-shaped large-scale coronal EUV wave*, ApJ 716, L57, [130 c, 17 c/y].
Wang, T., Yan, Y., Wang, J., et al. 2002, *The large-scale coronal field structures and source region features for a halo CME*, ApJ 572, 580, [73 c, 5 c/y].
Webb, D.F., Cliver, E.W., Crooker, N.U., et al. 2000, *Relationship of halo CMEs, magnetic clouds, and magnetic storms*, JGR 105/A4, 7491, [229 c, 13 c/y].
Webb, D.F. and Howard, T.A. 2012, *Coronal mass ejections: Observations*, LRSP 9/1, 3, [133 c, 24 c/y].
Xie, H., Ofman, L., and Lawrence, G. 2004, *Cone model for halo CMEs: Application to space weather forecasting*, JGR 109/A3, A03109, [134 c, 10 c/y].
Yashiro, S., Michalek, G., Akiyama, S., et al. 2008, *Spatial relationship between solar flares and coronal mass ejections*, ApJ 673, 1174, [51 c, 5 c/y].
Zhao, X.P., Plunkett, S,P., and Liu, W. 2002, *Determination of geometrical and kinematical properties of halo CMEs using the cone model*, JGR 107/A8, 1223, [93 c, 6 c/y].
Zhou, G., Wang, J., and Cao, Z. 2003, *Correlation between halo CMEs and solar surface activity*, A&A 397, 1057, [63 c, 4 c/y].
Zucca, P., Morosan, D.E., Rouillard, A.P. 2018, *Shock location and CME 3D reconstruction of a solar type II radio burst with LOFAR*, A&A 615, A89.

(14.10) CMEs and Coronal Radio Emission

Bain, H.M., Krucker, S., Saint-Hilaire, P, et al. 2014, *Radio imaging of a type IVM radio burst on the 14th of August 2010*, ApJ 782, 43, [15 c, 4 c/y].

Bastian, T.S., Pick, M., Kerdraon, A., et al. 2001, *The CME of 1998 April 20: Direct imaging at radio wavelengths*, ApJ 558, L65, [92 c, 6 c/y].

Chen, Y., Du, G., Feng, L., et al. 2014, *A solar type II radio burst from CME-coronal ray interaction: Simultaneous radio and EUV imaging*, ApJ 787, 59, [24 c, 7 c/y].

Cho, K.S., Lee, J., Moon, Y.J., et al. 2007, *A study of CME and type II shock kinematics based on coronal density measurements*, A&A 461, 1121, [43 c, 4 c/y].

Cho, K.S., Bong, S.C., Moon, Y.J. et al. 2011, *Relationship between multiple type II solar radio bursts and CME observed by STEREO/SECCHI*, A&A 530, A16, [30 c, 5 c/y].

Cho, K.S., Gopalswamy, N., Kwon, R.Y., et al. 2013, *A high-frequency type II solar radio burst associated with the 2011 February 13 CME*, ApJ 765, 148, [17 c, 4 c/y].

Classen, H.T. and Aurass, H. 2002, *On the association between type II radio bursts and CMEs*, A&A 384, 1098, [76 c, 5 c/y].

Cliver, E.W., Nitta, N.V., Thompson, B.J., et al. 2004, *Coronal shocks of November 1997 revisited: The CME type II timing problem*, SoPh 225, 105, [73 c, 5 c/y].

Feng, S.W., Chen, Y., Kong, X.L. 2013, *Diagnostics on the source properties of a type II radio burst with spectral bumps*, ApJ 767, 29, [27 c, 6 c/y].

Feng, S.W., Du, G.H., Chen, Y., et al. 2015, *Simultaneous radio and EUV imaging of a mutli-lane coronal type II radio burst*, SoPh 290, 1195, [11 c, 4 c/y].

Gopalswamy, N. and Kundu, M.R. 1992, *Estimation of the mass of a coronal mass ejection from radio observations*, ApJ 390, L37, [41 c, 2 c/y].

Gopalswamy, N., Lara, A., Kaiser, M.L., et al. 2001, *Near-Sun and near-Earth manifestations of solar eruptions*, JGR 106, Aqq, 25261, [141 c, 9 c/y].

Gopalswamy, N., Aguilar-Rodriguez, E., Yashiro, S., et al. 2005, *Type II radio bursts and energetic solar eruptions*, JGR 110/A12, A12S07, [78 c, 6 c/y].

Gopalswamy, N., Yashiro, S., Akiyama, S., et al. 2008, *CMEs, type II radio bursts, and solar energetic particle events in the SOHO era*, Annales Geophysicae 26/10, 3033, [63 c, 7 c/y].

Gopalswamy, N., Thompson, W.T., Davila, J.M., et al. 2009, *Relation between type II bursts and CMEs inferred from STEREO observations*, SoPh 259, 227, [99 c, 12 c/y].

Gopalswamy, N., Nitta, N., Akiyama, S., et al. 2012, *Coronal magnetic field measurement from EUV images made by the SDO*, ApJ 744, 72, [44 c, 10 c/y].

Gopalswamy, N., Xie, H., Mäkelä, P., et al. 2013, *Height of shock formation in the solar corona inferred from observations of type II radio bursts and CMEs*, Adv.Space Res. 51, 1981, [7 c/y].

Grechnev, V.V., Afanasyev, A.N., Uralov, A.M., et al. 2011, *Coronal shock waves, EUV waves, and their relation to CMEs. III. Shock-associated CME/EUV wave in an event with a two-component EUV transient*, SoPh 273, 461, [31 c, 5 c/y].

Hariharan, K., Ramesh, R., Kathiravan, C., et al. 2016, *Simultaneous near-Sun observations of a moving type IV radio burst and the associated white-light CME*, SoPh 291, 1405, [8 c, 5 c/y].

Kouloumvakos, A., Patsourakos, S., Hillaris, A., et al. 2014, *CME expansion as the driver of metric type II shock emission as revealed by self-consistent analysis of high-cadence EUV images and radio spectrograms*, SoPh 289, 2123, [16 c, 5 c/y].

Kontar, E.P. and Nindos, A. 2018, *Combined radio and space-based solar observations: From techniques to new results - Preface*, SoPh 293/6, 90.

Leblanc, Y., Dulk, G., Vourlidas, A., et al. 2001, *Tracing shock waves from the corona to 1 AU: Type II radio emission and relationship with CMEs*, JGR 106/A11, 25301, [60 c, 8 c/y].

Lin, J., Mancuso, S., and Vourlidas, A. 2006, *Theoretical investigation of the onset of type II radio bursts during solar eruptions*, Astron. J. 649, 1110, [42 c, 4 c/y].

Mancuso, S. and Raymond, J.C. 2004, *Coronal transients and metric type II radio bursts. I. Effects of geometry*, A&A 413, 363, [64 c, 5 c/y].

Morosan, D.E., Gallagher, P.T., Zucca, P., et al. 2014, *LOFAR tied-array imaging of type III solar radio bursts*, A&A 568, A67, [27 c, 8 c/y].

Nindos, A., Aurass, H., Klein, K.L. et al. 2008, *Radio emission of flares and coronal mass ejections. Invited review*, SoPh 253, 3, [48 c, 5 c/y].

Raymond, J.C., Thompson, B.J., St.Cyr, O.C., et al. 2000, *SOHO and radio observations of a CME shock wave*, GRL 27/10, 1439, [71 c, 4 c/y].

Tun, S.D. and Vourlidas, A. 2013, *Derivation of the magnetic field in a CME core via multi-frequency radio imaging*, ApJ 766, 130, [21 c, 5 c/y].

Chapter 15
CME Propagation

15.1 CME Coronagraph Observations

Coronal mass ejections (CMEs) have been observed most commonly with white-light coronagraphs, which have a built-in occulting disk that eclipses the bright solar disk. This has the consequence that the lowest possible altitude of a CME detection is given by the diameter of the occulting disk. The three coronagraphs of LASCO/SOHO have the following nominal field-of-views in distances from Sun center: C1: 1.1–3.0 $R_\odot$, C2: 1.5–6.0 $R_\odot$, and C3: 3.7–30.0 $R_\odot$ (Brueckner et al. 1995). The COR1/STEREO coronagraph has a field-of-view of 1.4–4 $R_\odot$, while the COR2/STEREO coronagraph has 7–15 $R_\odot$ (Howard et al. 2008). Given these constraints we should be aware that detection times of CMEs with white-light coronagraphs typically lag by a time delay of $\Delta t \approx 0.5$–1.0 hrs after the beginning of the impulsive flare phase, or the starting time of EUV dimming in the lower corona. White-light coronagraphs therefore miss the initial acceleration phase of a CME in the lower corona.

Although the pointing stability of LASCO/SOHO provided by an L1 orbit and the use of CCD detectors have resulted in superior brightness sensitivity for LASCO over earlier coronagraphs, it has been realized that no significant population of faint CMEs with low masses ($\lesssim 10^{14}$ g) has been detected with the C2 and C3/LASCO coronagraphs (St.Cyr et al. 2000). Ground-based coronagraphs have occulting disks that observe much closer to the solar surface, for instance the *Mauna Loa Solar Observatory (MLSO)* has a field-of-view beginning at $1.01 R_\odot$ and extending to 2.25 $R_\odot$, which allows to observe CMEs and prominences in much lower altitudes (e.g., Gilbert et al. 2000), including fainter CMEs that have a higher brightness in the lower corona ($\gtrsim 1.01 R_\odot$) than in the upper corona ($\gtrsim 1.5 R_\odot$) as seen with C2/LASCO.

The CME structure seen in white-light was originally characterized by their 3-part structure (leading edge, dark cavity, and filament), recently expanded to a 5-part structure (Vourlidas et al. 2013). Besides the 3-part structure of CMEs, a number

M. J. Aschwanden, *New Millennium Solar Physics*, Astrophysics and Space Science Library 458, https://doi.org/10.1007/978-3-030-13956-8_15

of additional phenomena have been observed in white light, such as: active and eruptive prominences (Gilbert et al. 2000); polar white-light jets, appearing at the outward extensions of EUV jets and observed during the solar maximum (Wang and Sheeley 2002); disturbances found ahead of the CME noses and along the flanks and rear ends, producing kinks in the streamers and other ray-like features, probably associated with shock waves (Sheeley et al. 2000); propagating waves in the CME flanks, causing density enhancements, probably from a fast-mode MHD shock that is reflected at streamers (Vourlidas et al. 2003); relatively sharp fronts ahead of the bright CME front, from which the upstream/downstream density compression ratio and shock direction can be measured (Ontiveros and Vourlidas 2009); a faint front followed by diffuse emission ahead of the bright loop-like CME front, probably caused by density compression at a wave or shock, which may be called the 5-part CME structure (Vourlidas et al. 2013); and CME rays that appear on average 3–4 hours after the CME core (Webb and Vourlidas 2016). Magnetic reconnection models of CMEs take the geometry of the post-CME current sheet and reconnection outflows into account (e.g., Vrsnak et al. 2009).

The projected white-light topology of a CME depends primarily on the orientation and position of the source region's neutral line on the solar disk (Cremades and Bothmer 2004), and hence projection effects play a significant role in the determination of CME parameters. White-light observations measure CME speeds projected in the plane-of-sky. A statistical study of selected CME events associated with the limb yielded greater speeds (than average), (520 ± 50) km s^{-1}, larger masses, $(4.5 \pm 0.5) \times 10^{15}$g, smaller angular widths ($\lesssim 110°$), and a stronger correlation between the kinetic CME energy and the GOES soft X-ray peak flux (Burkepile et al. 2004). A statistical study of 7000 CMEs detected with LASCO during 1996–2000 yields average CME speeds increasing from 300 km s^{-1} during the solar minimum to 500 km s^{-1} during the solar maximum, a speed of 960 km s^{-1} for halo CMEs, which is twice that of normal CMEs (430 km s^{-1}) (Yashiro et al. 2004). Statistics on the visibility of 1078 CMEs revealed 231 CMEs (21%) whose source location cannot be identified due to poor data, 288 CMEs (27%) with a location identified on the frontside solar disk, 234 CMEs (22%) appearing above the limb, and 325 CMEs (30%) without evident eruptive signature (Wang et al. 2011).

Coronagraph observations record the Thomson-scattered white-light emission from the coronal or heliospheric CME plasma, which has a sensitive dependence on the geometry between the observed and the scattering material. Usually one makes the assumption that the CME propagates in the plane-of-the sky in perpendicular direction to the line-of-sight. However, this assumption fails increasingly with the propagation distance from Sun center. If one drops this assumption and uses the "true" sphere of maximum Thomson scattering, one finds CME mass underestimations by a factor of 2 compared with the standard method, for elongations beyond 60° (Vourlidas and Howard 2006). Reconstruction of the 3-D structure of CMEs have been tested by comparing 2-D single-view observations with 3-D stereoscopy using STEREO data (Colaninno and Vourlidas 2009; Lee et al. 2015).

Another difficulty in analyzing and rendering the structure of a CME in a white-light image is the very steep decrease in density with heliocentric distance. This challenge has been overcome by applying a *normalizing radial-graded filter (NRGF)* in order to remove the strong radial gradient, which has been successfully used for processing C2/LASCO images (Fig. 15.1). The contrast strongly depends on the background subtraction, for which the unpolarized brightness is used, since it remains virtually unchanged during the solar cycle (Morgan et al. 2006). Also the rate of CMEs follows the solar cycle well, as evident from 17 years of C2/LASCO data (Lamy et al. 2014).

15.2 CME Stereoscopy and Tomography

The first tomographic reconstruction of the 3D density distribution of the solar corona has been accomplished by Altschuler (1979), based on a time series of coronagraph images from *Skylab* in white light. Tomographic inversions of coronagraph images from Mark III K-coronameter on Hawaii and from C1/LASCO/SOHO, which contain CME-associated streamers, were conducted by Zidowitz (1999). Tomography of the solar corona in an altitude range of a few solar radii has been systematically investigated by regularization inversion methods (Frazin 2000; Frazin and Kamalabadi 2005a,b; Frazin et al. 2005a,b), and applied to white-light coronagraph images from C2/LASCO on the SOHO spacecraft (Frazin and Janzen 2002; Quemerais and Lamy 2002; Frazin et al. 2007; Morgan et al. 2009; Morgan and Habbal 2010; Morgan 2011), to Mauna Loa Solar Observatory Mark-IV coronameter data (Butala et al. 2005), to COR1/STEREO datasets (Kramar et al. 2009; Barbey et al. 2013), and by separating contributions of the K- and F-corona (Frazin and Kamalabadi 2005b). The qualitative tomographic method of Morgan et al. (2009) uses background subtraction and a normalized radial gradient filter, instead of an inversion of the polarized brightness data.

Tomographic reconstruction of polarized brightness images from C2/LASCO/SOHO was also extended to CMEs (Moran and Davila 2004; Moran et al. 2010), or simulated for a CME generated with the ENLIL (Fig. 15.2) kinematic model (Odstrcil et al. 2004; Howard et al. 2013). The polarimetric technique has been validated with the triangulation method (Moran et al. 2010). A modified *Computer Aided Tomography (CAT)* technique that uses the velocity field as additional constraint, called *co-rotational tomography*, was used to model the co-rotating background solar wind component with observations from the SMEI spacecraft (Jackson et al. 1988; Jackson and Hick 2002; Jackson et al. 2011; Dunn et al. 2005). The strongest restriction of any solar-rotation based tomographic method is the steady-state requirement, which amounts to a time scale of about two weeks for a half rotation of the Sun.

Stereoscopic observations do help not only to obtain a 3-D reconstruction of coronal features, such as streamers or CMEs (Byrne et al. 2010), but permit also to correct the effects of the Thomson scattering geometry, because the intensity of

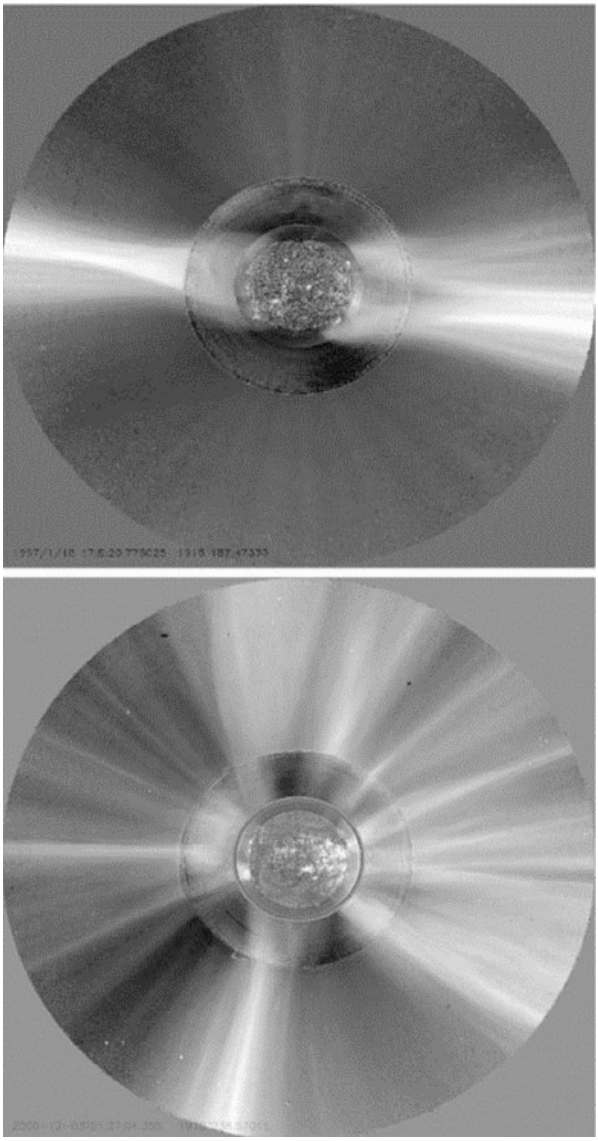

Fig. 15.1 Composite coronal images processed with the *normalizing radial-graded filter (NRGF)* at all heights above the solar limb for 1997 January 18 at solar minimum (top) and 2000 December 3 at solar maximum (bottom). The innermost views of the disk and low corona are EIT images of the He II 304 Å line. The corona from 1.15 to 2.3 $R_{\odot}$ are from MLSO MKIII (minimum) and MKIV (maximum) observations, and the outer fields of view from 2.3 to 5 $R_{\odot}$ are from C2/LASCO observations (Morgan et al. 2006)

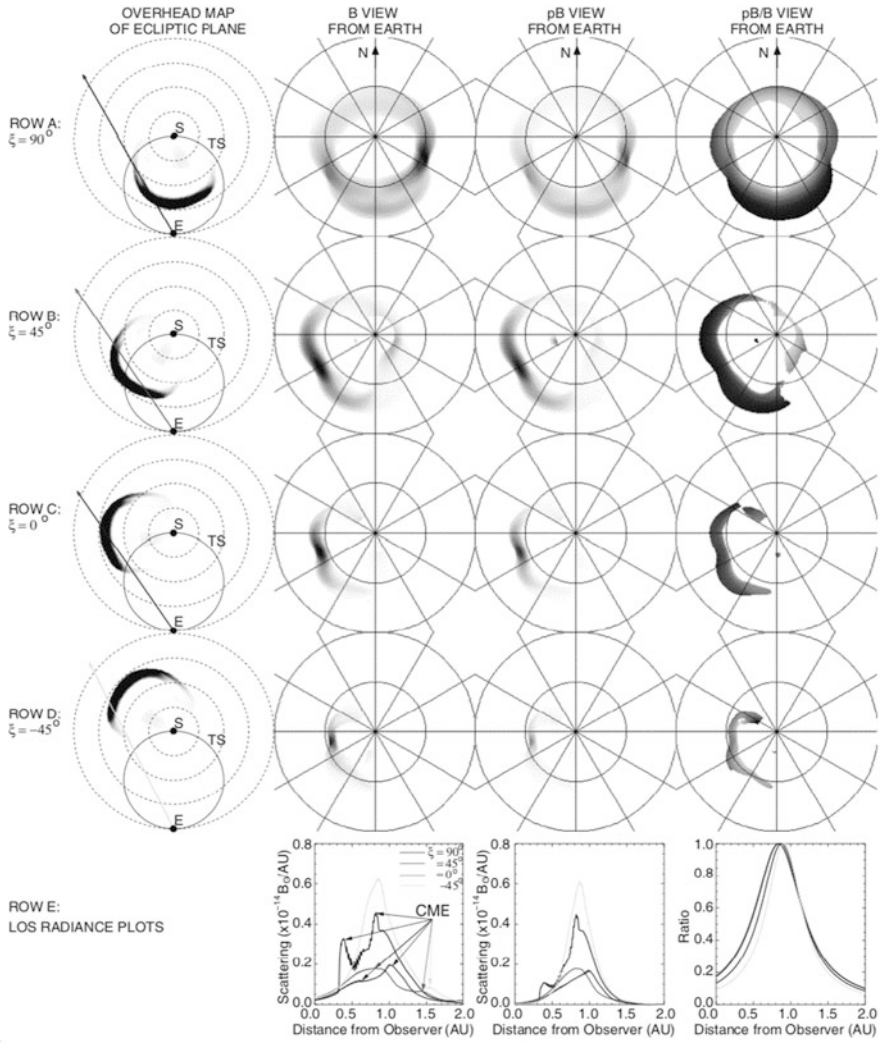

Fig. 15.2 CME simulations of a CME and the solar wind with the ENLIL code, with the solar wind and CME conditions chosen for the period from early 2010 April, when a large geoeffective CME erupted from the Sun. The CME is located at S25W03 and has an initial speed of 960 km s^{-1}, and the initial density is 4 times that of the fast solar wind stream (Howard et al. 2013)

an observed CME is dependent on the angle to the plane-of-sky, which then yields the *"true"* electron density and CME mass. This technique to determine the true CME mass has been applied to COR2/STEREO data from the STEREO/A and B spacecraft, for the white-light method (Colaninno and Vourlidas 2009), as well as for the EUV dimming method (Aschwanden et al. 2009).

A statistical study of 565 CMEs (2007–2010) was conducted to forward-fit 3-D flux ropes to data from from the two COR2/STEREO/A and B coronagraphs, using the method of Thernisien et al. (2006). It was found that the majority of the CME flux ropes (82%) lie within 30° of the solar equator, and 82% of the events were displaced from their source region, to lower latitudes of $\lesssim 25°$ (Bosman et al. 2012), which provides support for the deflection of CMEs towards the solar equator reported in earlier observations (Cremades and Bothmer 2004).

The 3-D trajectory of CMEs in the outer corona and heliosphere (out to 1 AU) is measured and triangulated from the elongation angles of a CME as a function of time (Liu et al. 2010), as provided by COR2, HI1, HI2/SECCHI and SMEI. They are then transformed into a 3-D trajectory by using the so-called *"Point-P"* and *"Fixed-Φ"* approximations, which complement 3-D fitting of CMEs by cone models or flux rope shapes (Lugaz et al. 2009), or self-similar expansion (Davies et al. 2012), and allow to predict the arrival times of CMEs at Earth (Liu et al. 2010). It relies on fewer assumptions than the single-track fitting technique, and thus the solution should be more accurate (Liu et al. 2010). A review of the 3-D configuration of CMEs in the coronagraph field-of-view out to 15 $R_\odot$ can be found in Mierla et al. (2010).

15.3 CME Acceleration

Since the Lorentz forces that accelerate a *coronal mass ejection (CME)* are located in the lower corona, the acceleration phase is often missed in white-light coronagraph observations (e.g., at $\gtrsim 1.5 R_\odot$ with C1/LASCO/SOHO), but can be measured from the evolution of EUV dimming. A theoretical understanding of the acceleration of CMEs requires quantitative models of the Lorentz forces, such as storage models, directly-driven models, pre-eruption current sheet models, or 2-D force-free models (e.g., Forbes 2010).

Generally there is a pre-flare phase with very little acceleration, followed by the impulsive flare phase with rapid acceleration, typically in heights of $h \approx 100$–350 Mm (≈ 0.1–$0.5 R_\odot$ above the surface), with an acceleration rate as high as $a \approx 0.5$ km s^{-2} (Neupert et al. 2001). A fraction of 74% of CMEs reach their peak acceleration at heights below $0.5 R_\odot$ (Bein et al. 2011). Gallagher et al. (2003) observed a CME with a very fast acceleration of $a \approx 1.5$ km s^{-2} over an e-folding time scale of $t_{rise} \approx 138$ s and e-folding decay time of $t_{decay} \approx 1000$ s, reaching an almost constant speed of $v \approx 2500$ km s^{-1} at a distance of $r \approx 3.4 R_\odot$ (Fig. 15.3). Statistical studies yield for the peak acceleration a range of $a = 0.003$–4.5 km s^{-2}, with a median of $a = 0.17$ km s^{-2}, and durations of $\tau_{acc} \approx 6$–1200 min, with a median of 54 min. The two parameters are related to each other reciprocally, i.e., a[km s^{-2}] $\approx 10 \tau_{acc}^{-1}[min]$ (Zhang and Dere 2006; Bein et al. 2011). Statistics of kinematic CME parameters are now available from the automatically processed CORIMP catalog (Byrne 2015), besides the CDAW, SEEDS, and CACTUS catalogs.

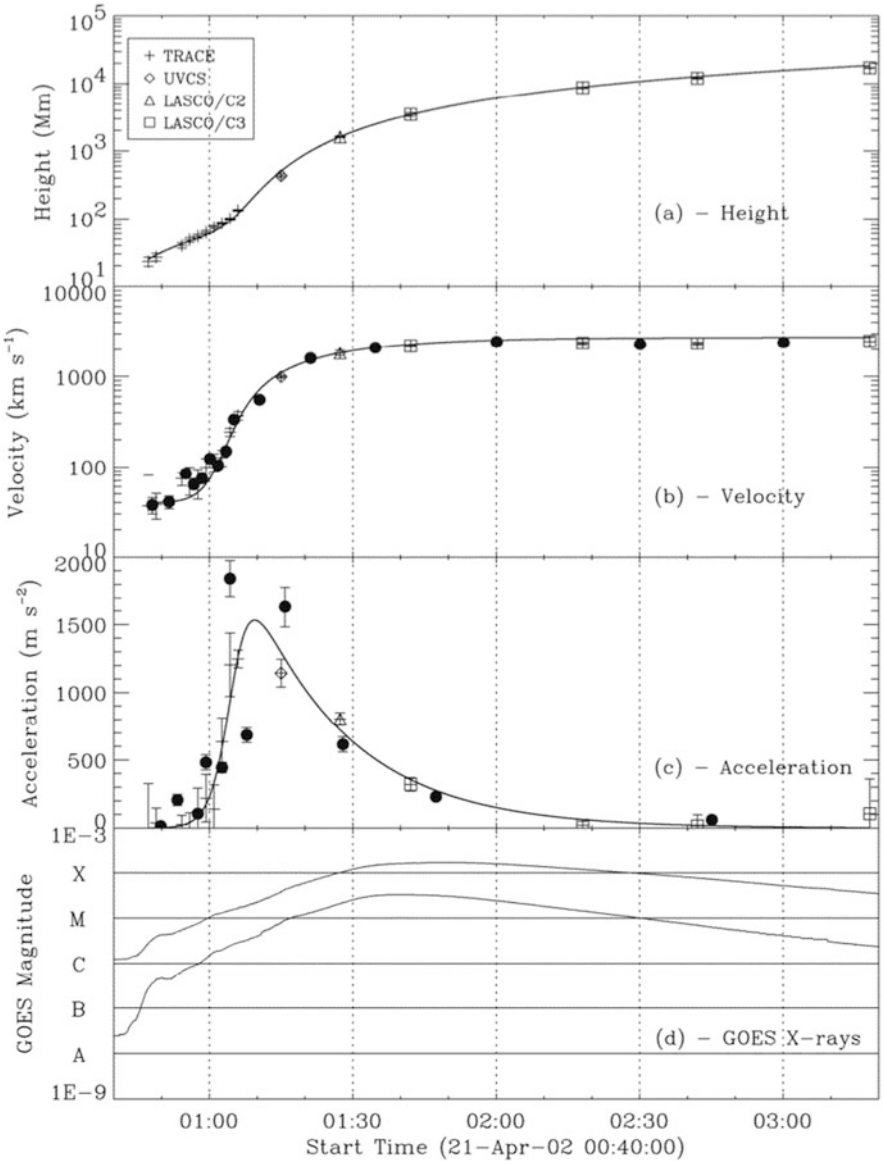

Fig. 15.3 (**a**) The height-time profile of a CME observed on 2002 April 21, 00:47–03:20 UT; (**b**) and (**c**) give the velocity and acceleration profiles, obtained by taking the first and second numerical derivatives, respectively. The first-difference values are given as circles, while the 3-point difference values are given using the same symbol scheme as (**a**). The solid line gives the best fit to the data from an empirical function. (**d**) The GOES-10 soft X-ray flux for the corresponding time period (Gallagher et al. 2003)

The timing of acceleration was found to be synchronized with the impulsive flare phase in at least half of the CME events (Maricic et al. 2007), typically within ±5 min (Bein et al. 2012; Berkebile-Stoiser et al. 2012). The evolution observed in EUV shows generally three phases of the CME formation: a slow self-similar expansion, a short-lived period of strong lateral over-expansion, and another phase of self-similar expansion (Patsourakos et al. 2010). For the majority of CMEs acceleration starts before the flare onset (75%), and the CME acceleration ends after the soft X-ray peak (77%).

A temporal correlation between the magnetic reconnection rate (measured from the magnetic flux swept through by flare ribbons) and the directly observed acceleration of the CME was discovered for two large X-class flares by Qiu et al. (2004), yielding electric fields of $E_{rec} \approx 0.5$–5.8 V cm^{-1}, and peak accelerations of $a \approx 0.2$–3 km s^{-2}. A similar relationship was found by Vrsnak et al. (2004b). This correlation strongly supports reconnection-driven CME models. Along the same lines, simultaneous observations with STEREO and RHESSI reveal a synchronized evolution of the CME acceleration profile in altitude and the evolution of the hard X-ray flux or acceleration of nonthermal particles also, which can be explained with the standard flare/CME magnetic reconnection flare model (Temmer et al. 2008, 2010). A study of 37 impulsive flare-CME events exhibits the strongest correlation ($CC = 0.85$) between the CME peak velocity and the total energy in accelerated electrons, supporting the model of a common source for both energies, probably magnetic reconnection in the current sheet in the wake of the erupting structure (Berkebile-Stoiser et al. 2012).

Based on an observed relationship between CME speeds v_{cme} near the Sun and the solar wind speed v_{wind}, an *"effective acceleration"* that acts on CMEs can be defined, i.e., $a = (v_{CME} - v_{wind})/\Delta t$. Gopalswamy et al. (2000) find a linear relation between this effective acceleration and the initial speed of CMEs, so that the average solar wind speed naturally divides CMEs into fast and slow ones. The kinematics of over 5000 CMEs measured in the distance range of 2–30 $R_\odot$ revealed a distinct anti-correlation between the acceleration a and velocity v, i.e., $a = -k_1(v - v_0)$ with $v_0 = 400$ km s^{-1}, where most of the CMEs faster than 400 km s^{-1} decelerate, whereas slower ones accelerate (Vrsnak et al. 2004a). This acceleration-velocity relationship was interpreted in terms of the aerodynamic drag (Sect. 15.5; Vrsnak et al. 2004a).

A most-cited investigation how magnetic reconnection affects the acceleration of *CMEs* and how the acceleration in turn affects the reconnection process can be found in Lin and Forbes (2000), for the case of a 2-D flux rope model, which drives the ejection by means of a catastrophic loss of mechanical equilibrium. For a hydrostatic coronal density model (with the density decreasing exponentially with height), a relatively small reconnection inflow with an Alfvén Mach number of $M_A = 0.005$ is sufficient to produce an eruption, and $M_A = 0.1$ yields a best fit (Lin and Forbes 2000). This model predicts an almost constant velocity (without acceleration), or even increasing with time (with positive acceleration).

Another popular model of CMEs is the 3-D magnetic flux rope model, which predicts a critical height of $h = s_f/2$ as a function of the footpoint separation

s_f, above which maximum acceleration is attained, consistent with observations (Chen and Krall 2003; Chen et al. 2006). The flux rope first appears as a twisted channel in high temperatures, then rises and develops into a semi-circular flux-rope-like structure during the impulsive acceleration phase, while the hot channel acts as a continuous driver of the CME formation and eruption (Cheng et al. 2013). The 3-D geometry of the expanding flux rope is determined by its inductive properties and the Lorentz self-force.

The early phase of near-limb filament destabilization involving CMEs was found to have a height dependence of $h(t) \propto t^3$, which appears to be incompatible with the breakout model, MHD instability models, or catastrophe models, while the torus instability can approximately match this height dependence (Schrijver et al. 2008).

15.4 CME Interplanetary Propagation

The study of interplanetary propagation of *coronal mass ejections (CMEs)* is motivated by a number of questions, such as: Which CMEs are geoeffective and which are not? What is the evolution of speed, density, temperature, and magnetic field on their way from the Sun to Earth? How can the remote-sensing observations of CMEs near the Sun be connected over a large gap with in-situ particle measurements near Earth ? What is the most robust method to predict the arrival time of CMEs at Earth orbit ? How can we model CME deflections and CME-CME interactions ? At which heliospheric distance does the drag force become dominant and the CME adjusts to the solar wind flow speed ?

We discussed the CME acceleration phase in the previous Sect. 15.3. A kinematic study of the CME acceleration phase characterizes 3 typical regimes: fast acceleration ($\approx$ 300 m s^{-2}) at distances of 1.2–4.6$R_\odot$, intermediate acceleration ($\approx$ 100 m s^{-2} at distances of (4.3–7.0)$R_\odot$, and gradual acceleration, sometimes persistent over 24 hours (Zhang et al. 2004). Multiple homologous CMEs that appear in rapid succession can be separated in the initial fast acceleration phase only, while they blend into each other in white-light images at larger heliospheric distances. Such an episode with four CME events ejected in rapid succession occurred on 2010 August 1 (Harrison et al. 2012). Often, a gradual acceleration precedes a fast acceleration phase, such as for instance in the 2013 May 22 event (Cheng et al. 2014). CME-CME interactions are described in more detail in Sect. 15.6.

A number of CMEs have been tracked over their entire trajectory from the Sun to Earth (e.g., for a sample of 22 CME events see Moestl et al. 2014). The X5.7 solar flare on 2000 July 14 was accompanied by a classical halo CME, being one of the most intense reported proton events. The trajectory of this CME (Fig. 15.4) could be tracked with imaging by the Nançay radioheliograph at low coronal heights ($\lesssim 2R_\odot$), with the white-light coronagraph LASCO/SOHO in the upper corona, $\approx$ (2–10)$R_\odot$, and with *interplanetary scintillation (IPS)* measurements with the *Ooty Radio Telescope (ORT)* in India and the multi-antenna system of Nagoya University, Japan, $\approx$ (100–225)$R_\odot$ (Manoharan et al. 2001). The speed-distance

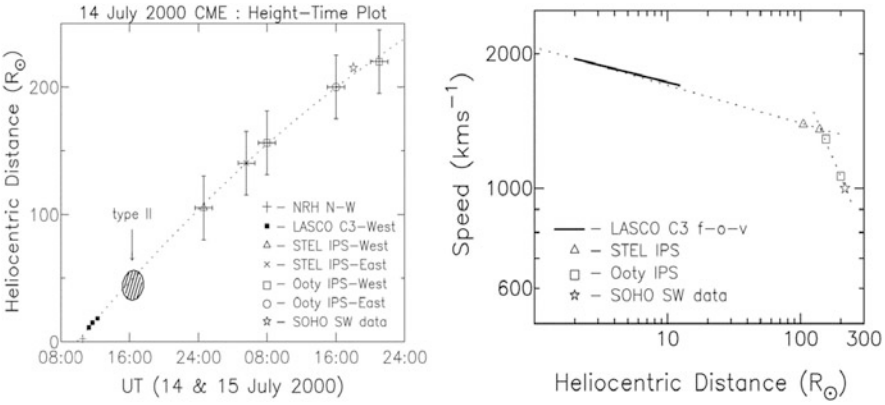

Fig. 15.4 *Left:* Height-time plot of the CME of 2000 July 14, based on Nançay NRH, LASCO/SOHO, STEL IPS, and Ooty IPS data. *Right:* Speed-distance plot of the CME, based on the time derivative $v(t) = dh(t)/dt$ of the height time plot $h(t)$ in the left panel (Manoharan et al. 2001)

plot $v(r)$ indicates a two-level deceleration: a low decline in speed from $v \approx 2000$ km s^{-1} to $\approx$ 1400 km s^{-1} at distances $r \lesssim 100 R_\odot$, and a rapid decrease down to $v \approx 1000$ km s^{-1} in the range of $r \approx (100\text{–}225) R_\odot$ (Fig. 15.4; Manoharan et al. 2001). Similar speed patterns in the propagation of CMEs from Sun to Earth have been reported in other observations (e.g., Liu et al. 2013, 2016; Rollett et al. 2014). One of the fastest CMEs was observed on 2012 July 23, which produced an extremely short transit time from the Sun to 1 AU, being shorter than 21 hours (Liu et al. 2014; Temmer and Nitta 2015). The maximum speed was $v \approx 2580 \pm 280$ km s^{-1} for the CME shock, and $v \approx 2270 \pm 420$ km s^{-1} for the magnetic structure.

A survey of *interplanetary CMEs (ICMEs)* based on *Helios* 1 and 2, *Ulysses*, *WIND*, and *ACE* spacecraft data, gathered from in-situ measurements at heliocentric distances of (0.3–5.4) AU finds that: (i) the radial width evolves as $r(t) \propto r^{0.92}$, (ii) most of the ICMEs are co-moving with the ambient solar wind, and (iii) the temperature decreases more slowly inside ICMEs than in the ambient solar wind, which requires heating of ICMEs, and (iv) the expansion behaves more like an isothermal than an adiabatic process, with a polytropic index of $\gamma \approx 1.15$ (Liu et al. 2005). Other statistical studies of ICMEs quantify their occurrence rate, scale size, shock association rate, peak pressure, and velocity (Jian et al. 2006).

Models of the propagation of ICMEs include the *aerodynamic drag model* and the *snow-plow model* (Howard et al. 2007). Mass accretion of CMEs due to the snowplow effect in the solar wind has been measured (DeForest et al. 2013). Simple theoretical assumptions of CME propagation models, such as radial expansion (rather than super-radial), or self-similar expansion, have been invalidated (with precise STEREO measurements) for some CME events that show over-expansion, rotation along the propagation axis, and CME deflections (Nieves-Chinchilla et al. 2013). A deflection of 20° towards the west has been measured for the 2008

September 12–19 CME, resulting in a significant change in the probability that the CME encounters Earth (Wang et al. 2014). Similarly, a deflection of 12° towards Earth was inferred in the 2015 March 15–17 event (Wang et al. 2016). The assumption of constant angular momentum beyond 10 $R_\odot$ yields underestimates of the total deflection at 1 AU of only 1%–5%, and underestimates of the rotation of 10% (Kay and Opher 2015).

MHD models are also used to "interpolate" ICME in-situ observations out to heliospheric distances of 5 AU (Liu et al. 2008). Fast and slow CMEs exhibit different distance ranges for acceleration and deceleration (Liu et al. 2016). Observations from STEREO and SMEI are used to constrain the drive/drag model, 3-D tomographic reconstruction, the HAFv2 kinematic model, the ENLIL MHD model (Webb et al. 2009; Vrsnak et al. 2014), and the EUHFORIA MHD model (Pomoell and Poedts 2018), which uses spheromak flux ropes. 3-D reconstructions of the heliospheric density distribution, which also reveals transients such as CMEs, have been carried out with data from STEREO, SMEI, and IPS with EISCAT (Bisi et al. 2010). 3-D reconstruction of ICMEs from STEREO data are able to quantify the deflected trajectory from high latitudes along the ecliptic, to measure its increasing angular width, and its propagation at (2–46)$R_\odot \approx 0.2$ AU (Byrne et al. 2010).

Using MHD models based on the ENLIL solar wind model, such as the *Wang-Sheeley-Arge (WSA)* model and the *MHD Algorithm outside a Sphere (MAS)* model, the distance where the drag force starts to dominate can be evaluated, which is found to spread from 30 $R_\odot$ to 1 AU (Temmer et al. 2011). For the 2015 May 5 CME, a propagation speed of $\geq$ 800 km s^{-1} was measured between the Sun and 1 AU, and the authors conclude that the drag exerted the ambient/background solar wind, with the support of its internal magnetic energy (Johri and Manoharan 2016). Forecasting of CME arrival times at the *Community Coordinated Modeling Center (CCMC)* is accomplished with the triple combination of the WSA+ENLIL+Cone model (e.g., Mays et al. 2015; Vrsnak et al. 2014).

From 3-D reconstruction of CME trajectories in terms of the *graduated cylindrical shell (CGS)* model (Thernisien et al. 2006) it was found that the propagation directions of CMEs change, consistent in strength and direction with the magnetic energy density, which is quantitatively described by the *magnetic density gradient (MEDG)* model (Gui et al. 2011).

Two different acceleration models are sometimes applied to the same event, slow magnetic reconnection in a quasi-separatrix layer in the preflare phase, and fast magnetic reconnection after onset of the torus instability in the impulsive phase (Cheng et al. 2014).

For most CMEs, the amount of twisted flux per AU in magnetic clouds is comparable with the total reconnection flux on the Sun, typically $\gtrsim$ 5 turns per AU (Hu et al. 2014). In a statistical study it was found that flux rope structures are seen in 94%, that they are closely aligned with the magnetic polarity inversion line, and that the erupted flux rope propagates through the interplanetary space with its orientation maintained (Marubashi et al. 2015).

The high-speed solar wind streams produce a continuous outflow, causing large deviations from the quiet solar wind conditions. A statistical study indicates that the interplanetary space needs $\approx$ 2–5 days to recover from the impact of ICMEs (Temmer et al. 2017).

15.5 Aerodynamic Drag Force

The interaction of an *interplanetary coronal mass ejection (ICME)* with the solar wind leads to an adjustment or equalization of both velocities at heliocentric distances out to $\approx$ 1 AU. Generally, an ICME has initially a higher velocity than the solar wind, which is then slowed down to a lower value that is closer to the solar wind speed. Vice versa, there are also slow ICMEs that become accelerated to about solar wind speed.

The equation of motion for an ICME moving in the solar wind can be expressed in most general form (Cargill 2004),

$$M_* \frac{dV_i}{dt} = F_L + F_g + F_D \,, \tag{15.5.1}$$

as the sum of the Lorentz force F_L, the gravitational force F_g, and the *aerodynamic drag force* F_D, where the drag force is defined as,

$$F_D = -\rho_e A C_D (v_i - v_e)\,|v_i - v_e| \,, \tag{15.5.2}$$

where A is the cross-sectional area of the ICME, C_D is the dimensionless drag coefficient, ρ is the mass density, and subscript i (or e) refers to the quantities inside (or external to) the ICME, e.g., v_e is the solar wind velocity. The mass $M_* = M + M_V$ is the sum of the ICME mass M and the so-called virtual mass $M_v \approx \rho_e V/2$ with V the volume of the ICME. The optimum radial parameterization of the drag coefficient F_D has been calculated by Cargill (2004), beyond approximately $15 R_\odot$, which varies slowly between the Sun and 1 AU, and is of order of unity (Fig. 15.5). The heavy ICME shown in Fig. 15.5 shows a slow-down of the velocity from $v_i (R = 0.09\ \text{AU}) \approx 800\ \text{km s}^{-1}$ to $v_i (R = 1.09\ \text{AU}) \approx 600\ \text{km s}^{-1}$, while the ambient (slow) solar wind has an almost constant velocity of $v_e \approx 430\ \text{km s}^{-1}$. When the ICME and solar wind densities are similar, the drag coefficient C_D is larger (between 3 and 10), but remains approximately constant with radial distance. For tenuous ICMEs, the ICME and solar wind velocities equalize rapidly due to the very effective drag force. When the ICME density is similar to or less than that of the solar wind, inclusion of the virtual mass M_v becomes important (Cargill 2004).

An analytical solution of the momentum equation (Eq. 15.5.2) is provided for the drag-based model by Vrsnak et al. (2013), which is for a constant solar wind speed v_e,

$$v(t) = \frac{v_i - v_e}{1 \pm \gamma (v_i - v_e) t} + v_e \,, \tag{15.5.3}$$

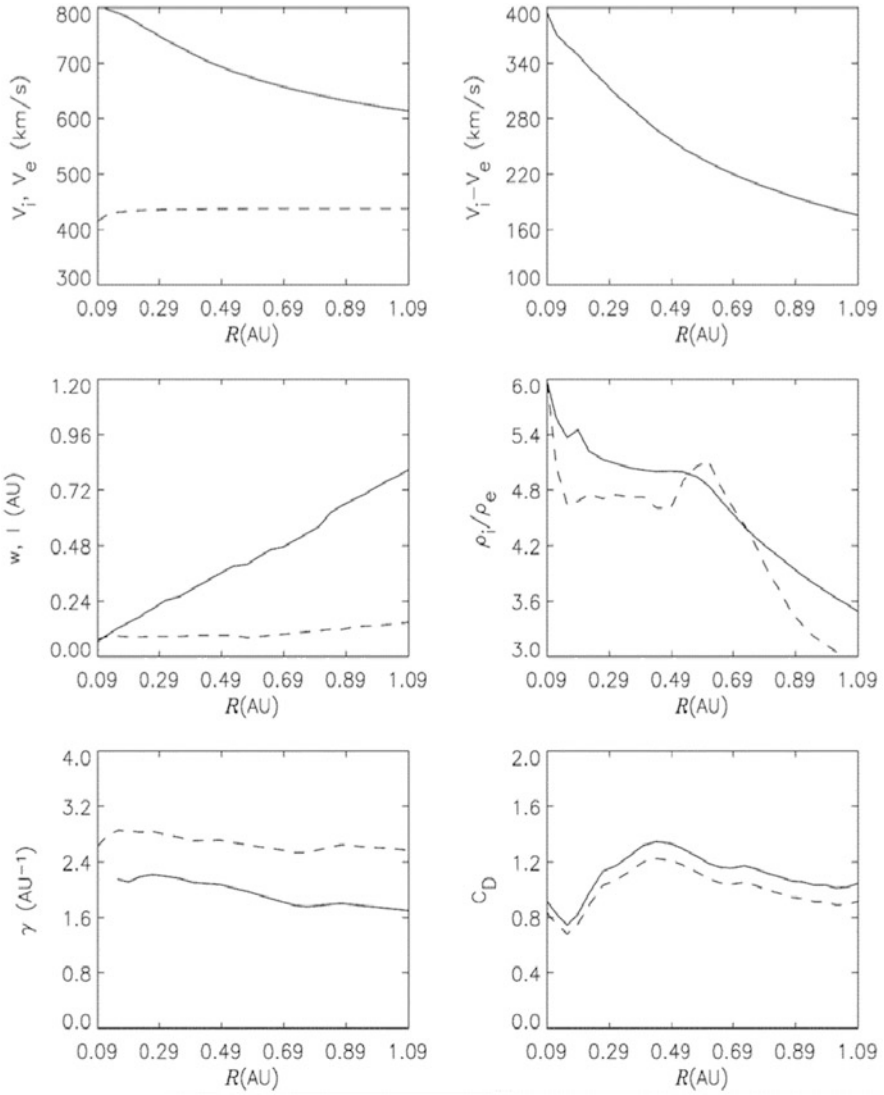

Fig. 15.5 The interaction of a fast, heavy ICME with the solar wind. The initial ICME density and velocity (solid curves) are a factor of 5 and 2 larger than the ambient solar wind values (dashed curves). The six panels show: the ICME and solar wind velocities v_i, v_e (top left), the difference between the two velocities $(v_e - v_i)$ (top right), the ICME width w and thickness I (center left), the ratio of the ICME to solar wind density (ρ_i/ρ_e) (solid curve: computational; dashed curve: analytical) (middle right), the inverse length $\gamma = \rho_e A/V(\rho_i + \rho_e/2)$ (bottom left), and the drag coefficient C_D, which is of order unity (bottom right), (Cargill 2004)

and yields the heliocentric distance $r(t)$ as a function of time,

$$r(t) = \pm\frac{1}{\gamma}\ln\left[1+\gamma(v_i - v_e)t\right] + v_e t + r_0 \,, \tag{15.5.4}$$

which allows a straightfoward application to real-time space-weather forecasting.

The kinematics of over 5000 CMEs has been measured in the distance range of (2–30) $R_\odot$ (Vrsnak et al. 2004). These data revealed a distinct anti-correlation between the acceleration a and velocity v,

$$a = -k(v - v_0)|v - v_0| \,, \tag{15.5.5}$$

with $v_0 = 400$ km s^{-1}, where most of the CMEs faster than 400 km s^{-1} decelerate, whereas slower ones accelerate (Vrsnak et al. 2004). This acceleration-velocity relationship has been interpreted in terms of the aerodynamic drag (Vrsnak et al. 2004). Comparing with the drag force (Eqs. 15.5.2 and 15.5.5), as defined in Cargill (2004), the solar wind speed corresponds to $v_e = v_0 \approx 400$ km s^{-1}, $v_i = v$ is the ICME speed, the acceleration is $a = F_D/M_*$, and $k = \rho_e A C_D$.

Vrsnak et al. (2008) investigate the mass dependence of aerodynamic drag. The slope k in the anti-correlation of ICME acceleration a and ICME velocity v_i is less steep for ICMEs with higher masses, revealing that massive CMEs are less affected by the aerodynamic drag. The slope follows the scaling $k \propto M^{-1/3}$ (Vrsnak et al. 2008).

Two drag models were applied to ICME data observed with LASCO and SMEI (Howard et al. 2007): the *aerodynamic drag model* (Cargill 2004), and the *snow-plow model* (Tappin 2006). In the so-called snow-plow model, the transient (ICME) sweeps up material from the surrounding solar wind during its transit, and hence accumulates mass, which can be described with a pair of coupled differential equations (Tappin 2006),

$$\frac{d^2R}{dt^2} = -\frac{dM}{dt}\frac{(v_i - v_e)}{M} \,, \tag{15.5.6}$$

$$\frac{dM}{dt} = \sigma\Omega(v_i - v_e) \,. \tag{15.5.7}$$

Howard et al. (2007) finds little difference between these two models, and the distance-time plots match well the SMEI data in one case, while an additional Lorentz force is necessary in another case. Comparisons of four different ICME propagation models (aerodynamic drag model, 3-D tomographic reconstruction, the HAFv2 kinematic model, the ENLIL MHD model) were found to be in general agreement (Webb et al. 2009). A further drag model is the *"sheath-accumulating propagation" model*, which deals with similar mass accumulation effects at the CME front as the snow-plow model (Takahashi and Shibata 2017).

The most accurate 3-D trajectories of ICMEs were obtained from stereoscopic observations, which corroborated the aerodynamic drag model successfully for the three cases of faster, slower, and equal speeds of ICMEs, which asymptotically approach the ambient solar wind speed (Maloney and Gallagher 2010). However, the heliospheric distance at which the aerodynamic drag becomes dominant can vary a lot, from $30R_{\odot}$ to beyond 1 AU, depending on the ambient solar wind characteristics (Temmer et al. 2011). In addition, the momentum exchange between the solar wind and the moving ICMEs can cause acceleration and deceleration of the ICME (Shen et al. 2012). Furthermore, the 3-D reconstruction of the trajectory of a moderate or small-sized ICME event, using a constant background solar wind model, can be affected by the deflection due to larger ICMEs (Rollett et al. 2014). The interplanetary propagation of the fast ICME on 2012 July 23 indicated that an extremely small aerodynamic drag force is exerted on the CME shock, smaller by an order of magnitude. As a consequence, the CME hardly decelerates in interplanetary space and maintains its high initial speed, which can only be explained by a low density ($\rho \approx$ 1–2 cm^{-3}) in the solar wind (Temmer and Nitta 2015). Similarly, the intense CME event of 2015 May 5 maintained a swift speed of $\geq$ 800 km s^{-1} without slowing down by the drag force (Johri and Manoharan 2016).

15.6 CME-CME Interactions

Coronal mass ejections (CMEs) have been detected with speeds of $v \approx$ 300–2500 km s^{-1}, which travel the distance of $R = 1$ AU from the Sun to Earth during a time interval of $\Delta t = R/v \approx$ 0.7–5.8 days. Given this extended range of travel times, there is a large probability that sometimes a fast CME "rams" and "overtakes" a slower CME ahead, which is now referred to as *CME-CME interaction*, originally also hailed as "CME cannibalism" (Gopalswamy et al. 2001). Reviews on the interaction of successive CMEs can be found in Lugaz et al. (2017) and Shen et al. (2017).

The first detection of an interaction between a fast and slow CME in the interplanetary medium (at a distance of $\gtrsim 10R_{\odot}$) at long radio wavelengths (decametric, 21–280 m, or 1–14 MHz in frequency) has been reported by Gopalswamy et al. (2001). An interplanetary type II burst (followed by intense continuum-like radio emission) was observed that suddenly exhibited a strong enhancement, coinciding with the event of a fast CME overtaking a slow CME (Figs. 15.6 and 15.7). The radio enhancement was interpreted as a consequence of shock strengthening when the shock ahead of the fast CME plows through the core of the preceding slow CME. The collision of CMEs caused also a change in the trajectory of the slow CME, which like other CME deflection events, contain relevant information to accurately calculate the CME arrival time at 1 AU in space weather predictions.

Simultaneous observations with STEREO A and B, and in-situ probing with the *Wind* spacecraft allowed for a more detailed disentanglement of CME-CME

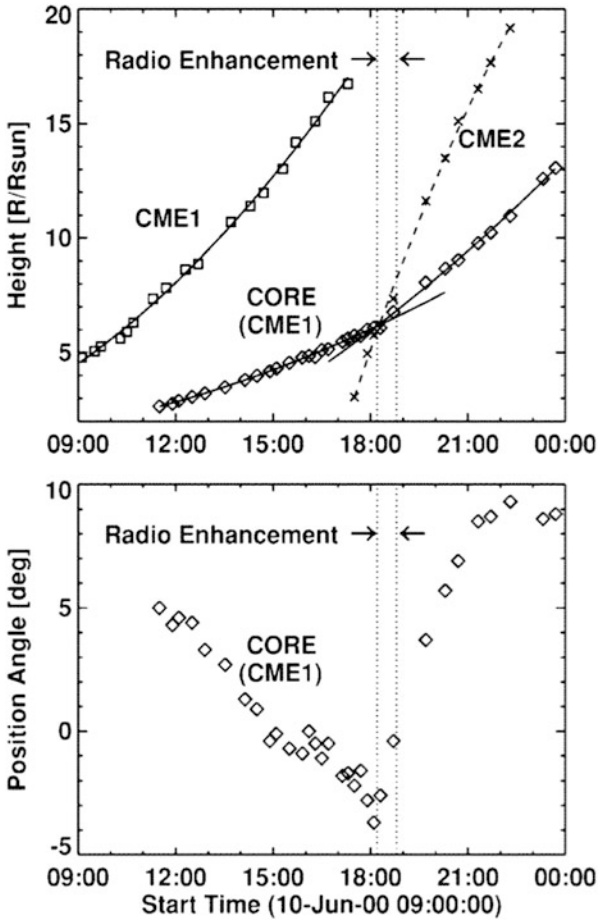

Fig. 15.6 *Top:* Height-time plot of the slow and fast CMEs showing an increase in the speed of the slow-CME core due to the impact of the fast CME. There is a sudden change in the speed of the slow-CME core at the time of type II burst enhancement (bracketed by the vertical dotted lines). *Bottom:* Time variation of the position angle of the slow-CME core. Note the change in position angle at the time of the impact, resulting in an eastward motion of the slow-CME core (Gopalswamy et al. 2001)

interactions in the 2010 July 30 to August 1 events (Liu et al. 2012; Harrison et al. 2012; Temmer et al. 2012). Two cases of CME-CME interactions are observed: merging of two CMEs launched close in time, and overtaking of a preceding CME by a shock wave. The merged front is identified to be a shock wave. In-situ measurements show that the overtaken CME is significantly compressed, accelerated, and heated. The interaction between the preceding ejecta and shock also results in variations of the shock strength (Liu et al. 2012). The speed of the faster CME 2 (≈ 1200 km s^{-1}) shows a strong deceleration over the distance range

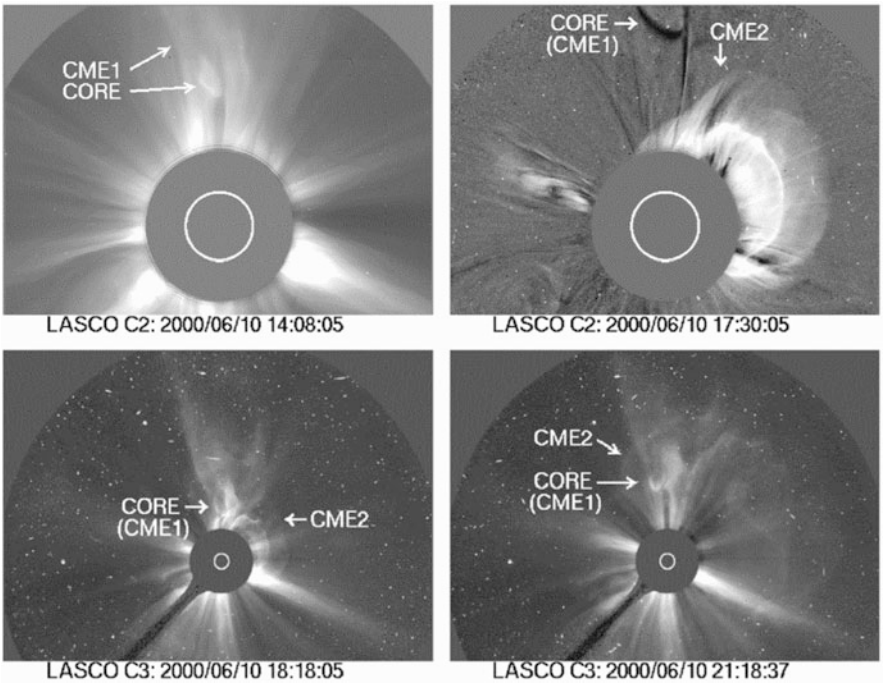

Fig. 15.7 Series of SOHO/LASCO images on 2000 June 10, 14:08 UT to 21:18 UT, showing the fast CME 2 approaching the core of the slow CME 1. The radio enhancement occurs at 18:18 UT (Gopalswamy et al. 2001)

at which it reaches the slower, preceding CME 1 ($\approx$ 700 km s^{-1}), suggesting that besides the aerodynamic drag, magnetic forces contribute to the enhanced deceleration of CME 2 (Temmer et al. 2012).

In the 2010 May 23–24 events, the interaction of 2 CMEs decelerated the speed of the leading edge of the first CME from 500 km s^{-1} to 380 km s^{-1}, and the first CME was deflected by about 10° toward the Sun-Earth line (Lugaz et al. 2012). However, due to the over-expansion of the CME after collision, only few signs of the interaction in in-situ observations are detectable (Lugaz et al. 2012; Wang et al. 2014). The Earth underwent a two-step geomagnetic storm during 2012 September 30 to October 1, caused by a CME-CME interaction of two CMEs at 1 AU, but a magnetic cloud-like structure without clear signs of CME interactions is anticipated when the merging process is finished (Liu et al. 2014).

Analysis of the 2011 February 14–15 CMEs reveals differences in the kinematics inferred from position angles for the interacting flanks and apices. CME 1 accelerates and CME 2 decelerates to an almost identical final speed. However, the measurements indicate that a simplified scenario of inelastic collision is not sufficient to describe the CME-CME interaction. The magnetic field structures of the intertwining flux ropes and the momentum transfer due to shocks, each play an

important role in the interaction process (Temmer et al. 2014). Mishra and Srivastava (2014) identified the interaction of three CMEs during 2011 February 13–15.

Two successive flux rope eruptions were found to be responsible for two successive CMEs in the 2012 January 23 events, where both flux ropes appeared in high-temperature EUV channels. The eruption of the first flux rope is believed to be caused by the torus instability, while the eruption of the second flux rope benefitted from the resulting partial opening of the magnetic field (Cheng et al. 2013). CME-CME interactions seem to be a common phenomenon close to solar maximum, according to analysis of this and other events (Liu et al. 2013).

Numerical simulations of the interaction of two CMEs have been performed with a 3-D compressible MHD code, where two identical CMEs are launched in the exact same direction into a pre-existing solar wind, and the second one 10 hrs after the first one (Lugaz et al. 2005). After an initial phase, when the trailing shock and the second CME propagate into the disturbed solar wind medium, they reach the edge of the first magnetic cloud, leading to complex magnetic interactions and a steep acceleration of the shock, followed by deceleration and merging of the two shocks, while a stronger, faster shock forms in the contact discontinuity between the "old" and "new" downstream regions (Lugaz et al. 2005). Merging CMEs are associated with a momentum exchange from the faster to the slower one due to the propagation of the shock wave associated with the fast eruption through the slow eruption (Lugaz et al. 2009; Farrugia and Berdichevsky 2004).

15.7 CME-Driven Global Waves

The impulsive dynamics that launches a *coronal mass ejection (CME)* almost always triggers also spherically expanding waves that propagate globally over the entire solar surface, detectable in the photosphere, chromosphere, and lower corona. Such global wave phenomena have been called *"EIT waves"* or *"EUV waves"*, but are also related to the so-called *Moreton waves*. Signatures of global waves have been observed directly in the corona, in EUV, soft X-rays (Khan and Aurass 2002), metric/decimetric radio (Vrsnak et al. 2005), and white light (Kwon et al. 2013). In addition, their signature (or "imprints") has also been detected in the chromosphere in H-alpha (Moreton waves), Helium I 10,830 Å (Vrsnak et al. 2001) and in microwaves (Warmuth et al. 2004a). A major conclusion of numerous studies is that all these signatures in different wavelength ranges and in different atmospheric layers are consistent with a single underlying physical disturbance. Reviews on these global waves can be found in Wills-Davey and Attrill (2009), Gallagher and Long (2011), Patsourakos et al. (2010), Liu and Ofman (2014), Warmuth (2015), and Long et al. (2017).

An unambiguous correlation between EIT waves and CMEs has been established (Biesecker et al. 2002). The high statistical association rate (90%) of radio type II bursts with EIT waves suggests that both wave phenomena can be explained with fast magnetosonic (shock) waves (Klassen et al. 2000; Warmuth et al. 2004b).

Moreover, Moreton and EIT waves were found to be co-spatial, a deceleration of the wave fronts was observed, a broadening of the perturbation profile, a decrease in the perturbation amplitude, and the wave fronts have a near-spherical geometry, which all favor the fast-mode shock interpretation (Warmuth et al. 2001, 2004a), driven by a *"blast wave"*, a freely propagating shock wave, or a piston-driven shock wave.

Consistent with earlier detections of global waves (Khan and Aurass 2002; Hudson et al. 2003), the detection of EIT waves in the coronal temperature band of Fe (284 Å) confirmed their propagation in coronal (rather than in transition region) altitudes (Zhukov and Auchère 2004; Long et al. 2008). An observationally constrained model of the Alfvén speed in the quiet corona indicates that the EIT wave and associated type II radio bursts are consistent with the propagation of coronal shock waves with an initially high super-magnetosonic Mach number of $M_{ms} \approx 2$–3, which then decelerates during propagation until $M_{ms} \approx 1$ is reached (Warmuth and Mann 2005). EIT waves are found to stop at a frontal boundary of a coronal hole, which was explained in terms of a wave refraction effect (Veronig et al. 2006; Long et al. 2008; Gopalswamy et al. 2009; Li et al. 2012). The kinematics of the coronal EUV wave is slower than the leading edge of the CME and decelerates, suggesting a wave initiation by the CME expanding flanks (Veronig et al. 2008). All these effects are consistent with an impulsively generated fast-mode magneto-acoustic wave (Long et al. 2017).

The high image cadence of EUVI/STEREO yields a higher velocity and acceleration of the EIT wave than previous EIT/SOHO measurements (Long et al. 2008; Patsourakos et al. 2009). Stereoscopic triangulation yields an average height of $h \approx 90$ Mm for the propagation of EIT waves (Patsourakos et al. 2009), or $h \approx 80$–100 Mm (Kienreich et al. 2009). Quadrature observations with STEREO have been available during early 2009, when the STEREO/A and B spacecraft had an angular separation of $\approx 90°$ (Fig. 15.8), which allowed to separate the CME structure from the EUV wave signature (Patsourakos and Vourlidas 2009). One of the first STEREO quadrature observations revealed a global EIT wave that propagated with a constant speed of $v = 236 \pm 16$ km s^{-1} close to the fast magneto-sonic speed in the Quiet corona, initiated by the CME lateral expansion (Fig. 15.8; Kienreich et al. 2009). *EIT waves* are found to undergo wave reflection (as well as transmission and refraction), which is another characteristic of their wave nature (Gopalswamy et al. 2009). EIT waves can assume the geometric shape of a dome (Narukage et al. 2004), which expands not self-similarly, but instead with an upward expansion speed of $v \approx 650$ km s^{-1} and a different lateral speed of $v \approx 280$ km s^{-1} (Veronig et al. 2010).

Using time sequences of AIA images, which have an unprecedented cadence of 12 s, further details of global EUV waves have been discovered, such as a superimposed *diffuse pulse* that maintains a stable profile during ≈ 30 min, on which multiple slow and fast components of *sharp fronts* occur, which overtake the slow front and produce multiple *ripples* and steepening of the local pulse (Liu et al. 2010), or produce secondary waves after encountering coronal bright structures (Li et al. 2012). Diffuse wave fronts are found to be separated from the front of the expanding CME bubble shortly after the expansion slows down (Patsourakos et al.

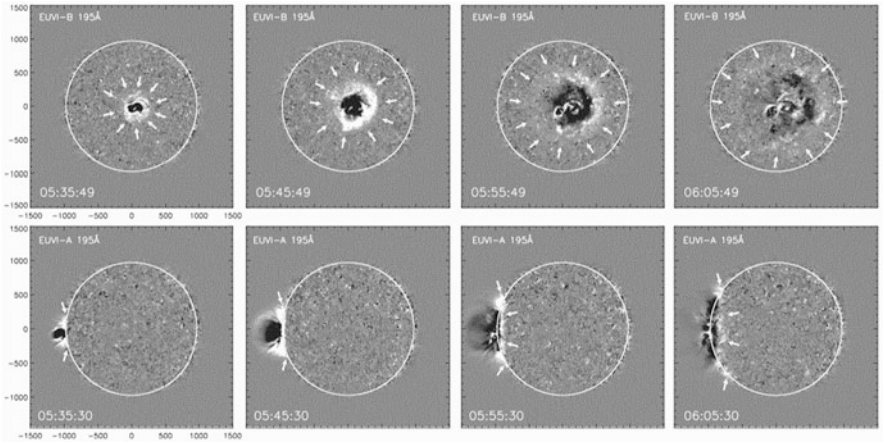

Fig. 15.8 Sequence of median-filtered running difference images of the CME of 2009 February 13, recorded with EUVI/STEREO 195 Å in quadrature (with a spacecraft separation angle of 91°) and with a cadence of 10 min. STEREO/B sees the CME on the disk as a halo-CME event (top row), while STEREO/A sees the CME at the limb (bottom row), (Kienreich et al. 2009)

2009, 2010; Ma et al. 2011; Cheng et al. 2012). A large statistical study (with 171 AIA-observed events during 2010–2013) of *large-scale coronal propagation fronts (LCPF)* were analyzed by Nitta et al. (2013), finding that the highest propagation speed of the fronts is often considerably higher than measured in EIT waves, which is debated to be an artifact of the analysis technique (Warmuth 2010).

An alternative interpretation for EIT waves was proposed in terms of magnetic field evolution, rather than a flare-triggered, propagating wave (Delannee 2000), which triggered a debate about the wave or non-wave interpretation of EIT waves (Wills-Davey and Attrill 2009; Warmuth 2010). It was suggested that interchange reconnection between the expanding CME structure with open field lines leads to an asymmetric temporal and spatial evolution of two main dimming regions (Attrill et al. 2006, 2007). Evidence for a statistical clustering of three velocity regimes was put forward by Warmuth and Mann (2011), from which the two fast groups (with $v \approx 170$–320 km s^{-1} and $v \geq 320$ km s^{-1}), appear to be consistent with the fast magneto-acoustic wave interpretation, while the slowest group ($v \leq 130$ km s^{-1}) could possibly be associated with the non-wave interpretation. Chen and Wu (2011) propose that EIT waves are the apparent propagation of the plasma compression due to successive stretching of the magnetic field lines pushed by the eruptive flux rope. Perhaps a hybrid model of wave and non-wave components is necessary to explain all observations (Liu et al. 2010; Warmuth 2010).

Quasi-periodic propagating fast-mode magneto-acoustic waves with phase speeds of $v = 2200 \pm 130$ km s^{-1} were discovered also, which are much faster than the EIT waves (Liu et al. 2011). Such quasi-periodic fast-mode magneto-acoustic wave trains were found to have the same periodicity ($T \approx 2$ min) as the

flare-associated X-rays, which suggests a causal connection (Liu et al. 2012). Such quasi-periodic fast-mode waves exhibit a weakly-damped time profile (with a high quality), detectable in 10 (or more) subsequent wave periods (Nistico et al. 2014). For a review see Liu and Ofman (2014).

15.8 CME-Driven Shocks

White-light coronal images from the LASCO/SOHO coronagraphs show disturbances that propagate ahead of *coronal mass ejections (CMEs)*, faintly visible ahead of the ejected material at the noses of CMEs, but strongly visible along the flanks and rear ends of CMEs, which have been interpreted as shock waves (Sheeley et al. 2000). For instance, a CME-driven shock with a speed of 1100 km s^{-1} was inferred from the type II radio burst drift rate and from electron densities obtained from UVCS observations (defining the plasma frequency for radio emission, $f_p \propto \sqrt{n_e}$), which ran ahead of the CME leading edge with a (projected) speed of 920 km s^{-1} (Mancuso et al. 2002), or 1500 km s^{-1} (Ciaravella et al. 2005). In some cases, the plasma physical parameters (compression ratio, density, temperature) of both the pre- and post-shock phase could be derived, using the Rankine-Hugoniot relationship for the magnetic field change (Bemporad and Mancuso 2010). Both the ejected material in the noses of CMEs, as well as the accumulated material piled up by the expanding flux rope, contribute to the mass density in the coronal shock wave. Tracing of coronal shocks can even be used to derive a 2-D map of the coronal magnetic field strength over intervals of 10 $R_\odot$ and $\approx 110°$ latitude (Susino et al. 2015). In summary, there is a concensus now that coronal global waves (Sect. 15.7) and CME-driven shocks (Sect. 15.8) are responses to the same underlying physical processes that trigger a CME, but observed in different wavelengths and coronal altitudes.

While indirect evidence of shocks has been furnished often (type II bursts, distant streamer deflections), a direct detection of a shock wave has been inferred from the speed and density of a propagating disturbance in the CME front and flanks (Vourlidas et al. 2003). Faint and sharp fronts ahead of bright CME fronts were found in 86% from a selection of 15 fast ($v \gtrsim 1500$ km s^{-1}) CMEs, with density compression ratios that are typical for CME-driven bow-shock structures (Ontiveros and Vourlidas 2009). Shock formation heights can be determined from the CME kinematics (Bein et al. 2011), which agrees well with *ground level enhancement (GLE)* particle energy release heights triangulated from STEREO observations (Gopalswamy et al. 2013).

AIA/SDO data provide higher temporal and spatial resolution. A well-observed shock ahead of a bubble-like CME, using AIA data, was found to have a density compression of 1.56, a temperature of 2.8 MK, a thickness of $\approx$ 20 Mm, a speed of 600 km s^{-1} decreasing to 550 km s^{-1}, and a lateral expansion speed of 400 km s^{-1} (Ma et al. 2011). A good temporal and height association between the EUV

wavefront and the radio type II trajectory suggests that (off-limb) propagating EUV waves may be the signatures of coronal shocks (Kozarev et al. 2011).

Complimentary evidence for CME-driven shocks comes from in-situ detections of high-energetic particles, such as observed in "gradual" *solar energetic particle (SEP)* events, which suggest that SEPs are accelerated by a *diffusive shock acceleration mechanism* in the front of CMEs or in the solar wind, rather than in high-temperature flare plasma (Zank et al. 2000; Li et al. 2003). Monte-Carlo simulations can mimic intensity profiles, angular distributions, particle anisotropies, and spectra of high-energy particles (up to 1 GeV), arriving at various distances from the Sun, where they can be compared with spectra obtained from in-situ particle detectors onboard ACE, WIND, IMP-8, GOES (Li et al. 2003). Large, gradual SEP events exhibit a high variability above a few tens of MeV, likely to be caused by the shock geometry and a compound seed population, typically consisting of both solar-wind and flare suprathermal particles (Tylka et al. 2005; Tylka and Lee 2006). Quasi-parallel shocks generally draw their seeds from solar-wind suprathermals, while quasi-perpendicular shocks preferentially accelerate seed particles from flares (because they require a higher initial speed for effective injection (Tylka et al. 2005). Multi-point in-situ observations of shocks (STEREO, WIND, ACE, ARTEMIS, VEX, MESSENGER), however, demonstrated that local in-situ views are difficult to link to a consistent global picture of ICME shocks (Moestl et al. 2012), which may persist to the far outer heliosphere (Liu et al. 2017).

A theoretical model of the Alfvén speed in terms of a (poloidal) magnetic dipole has been derived that yields a local minimum of the Alfvén speed in the range of $(1.2–1.8)\,R_\odot$, as well as a maximum of 740 km s^{-1} at a distance of $3.8\,R_\odot$, which has important consequences for the formation and development of shock waves in the corona and interplanetary space, and the onset of radio type II bursts (Mann et al. 2003). An alternative analytical model is formulated in terms of the *stand-off distance* of the shock wave ahead of the CME flux rope, which can be used to determine the shock speed in the lower corona (at $\approx 1.4\,R_\odot$), from which an Alfvén speed increase from $\approx$ 140 km s^{-1} to 460 km s^{-1} was inferred over a distance range of $(1.2–1.5)\,R_\odot$, and a coronal magnetic field strength of 1.3–1.5 G (Gopalswamy et al. 2012).

A numerical simulation with a fully 3-D global MHD code (Fig. 15.9), driven by a slowly-varying velocity field at the lower boundary, until the system reaches a critical point with loss of equilibrium, produces the eruption of a flux rope with a maximum speed in excess of 1000 km s^{-1}, and forms a shock in front of the flux rope, with a fast-mode Mach number in excess of 4 and a compression ratio $\gtrsim 3$ at a distance of $5\,R_\odot$ (Roussev et al. 2004). For such values, diffusive shock acceleration theory predicts a distribution of solar energetic protons with a cutoff energy of $\approx$ 10 GeV.

There are two related major controversies: (i) Is the origin of large-scale coronal shock waves caused by CMEs or flares ? And similarly: (ii) Are high-energy particles (up to 1 GeV) accelerated in CME-driven shocks or in coronal flares ? Both questions could in principle be answered from timing measurements, besides the methods discussed above. However, particle time-of-flight measurements often

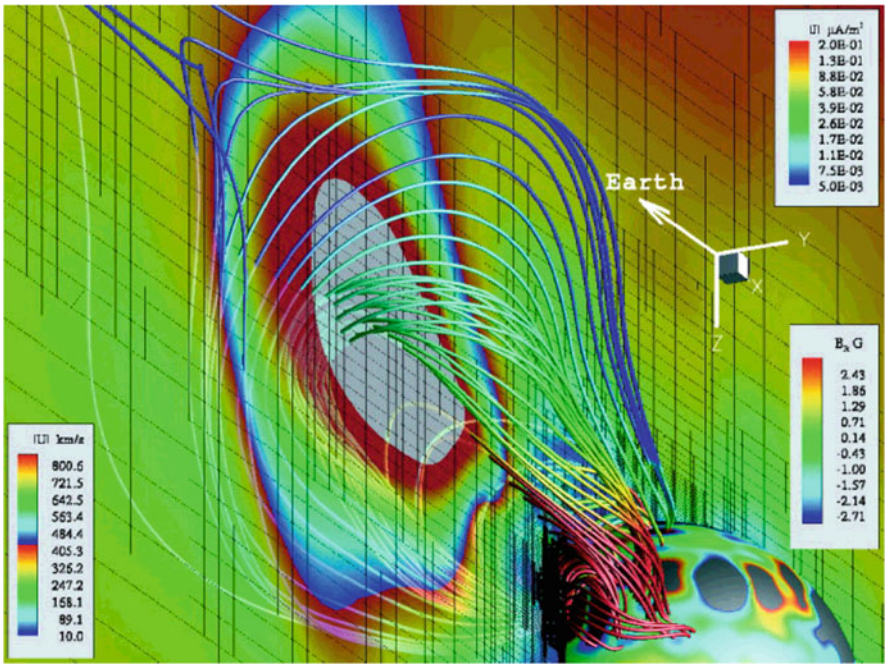

Fig. 15.9 3-D view of a MHD simulation of a CME, showing magnetic field lines (solid lines), the magnitude of the current density in units of μA m^{-2} (color scale at the top right), the magnitude of the flow velocity, in units of km s^{-1} (translucent plane), the radial magnetic field strength on the solar surface in units of G (sphere at bottom right), (Roussev et al. 2004)

have too large uncertainties to determine the time coincidence between the flare hard X-ray peak (i.e., the time of maximum acceleration) and the particle release time with sufficient accuracy, by back-extrapolation of the time-of-flight delays. Another promising approach is to combine 3D reconstructions of coronal shocks with extrapolations of the magnetic field of full MHD models of the corona. This allows to derive crucial shock parameters and to check whether this is consistent with in-situ SEP data (e.g., Rouillard et al. 2016). For tentative conclusions, see review by Vrsnak and Cliver (2008).

15.9 CMEs and Interplanetary Radio Emission

Interplanetary radio bursts provide a rich diagnostic on the acceleration and propagation of energetic particles and shock waves (Fig. 15.10). Radio bursts with plasma frequencies $f_p \gtrsim 20$ MHz (above the Earth's ionospheric cutoff frequency) can be observed with ground-based radio telescopes. These radio bursts originate only in low coronal altitudes ($\lesssim 2R_\odot$), while all interplanetary radio bursts further

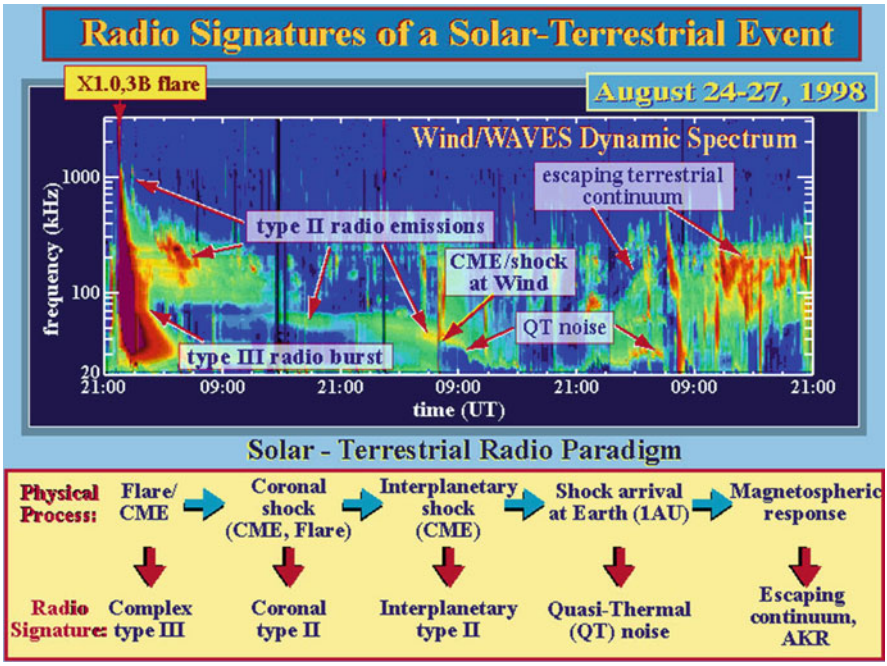

Fig. 15.10 Overview of physical processes and corresponding radio signatures produced by a flare/CME event. The radio dynamic spectrum is observed by the WIND spacecraft for the 1998 Aug 24–27 geoeffective event (Credit: NASA, STEREO, S-WAVES)

out have a lower plasma frequency and require space-based detectors, such as the S-WAVES/STEREO instrument. S-WAVES is able to triangulate interplanetary type II and type III radio emission, which can be combined with the particle in-situ measurements of the IMPACT/STEREO and PLASTIC/STEREO instruments. The radio signatures of a solar-terrestrial event is depicted in Fig. 15.10, displayed in form of a dynamic spectrum $\nu(t)$: (i) A flare/CME event produces complex type III bursts at metric/decimetric frequencies in the corona; (ii) Electron acceleration in a coronal shock accompanying a CME or flare produces metric coronal type II bursts; (iii) Interplanetary shocks ahead of CMEs produce *interplanetary type II bursts*; (iv) The arrival of shock fronts at Earth (1 AU) is detected as *quasi-thermal noise*; and (v) The magnetospheric response generates *escaping continuum* and *auroral kilometric radiation (AKR)*.

Long-wavelength type II radio bursts are observed in the *decameter-hectometric (DH)* frequency regime and indicate powerful MHD shocks that leave the inner solar corona and enter the interplanetary medium. Almost all of these type II bursts are associated with wider and faster-than-average CMEs, and a large fraction of these radio-rich CMEs decelerate in the coronagraph field-of-view, most likely due to aerodynamic drag (Gopalswamy et al. 2001a). Shocks originating from both limbs of the Sun were found to arrive at Earth, contradicting earlier claims that

shocks from the west limb do not reach Earth (Gopalswamy et al. 2001c). Selecting type II bursts that have more spectral components, such as the entire *decameter-hectometer plus kilometric (m-to-km)* frequency regime, the associated CMEs were found to be more energetic, the majority (78%) of the m-to-km type II bursts were associated with *solar energetic particle (SEP)* events, and they are associated with larger flares (Gopalswamy et al. 2005). If a CME originating from the western hemisphere is accompanied by a DH type II burst, there is a high probability to produce a SEP event, which is a crucial prediction for space weather applications (Gopalswamy et al. 2008). A fraction of 34% of interplanetary shocks (detected with SOHO in-situ at the L1 point) are found to be radio-quiet, i.e., shocks that lack type II radio bursts, for which it was found that the CME kinetic energy is the most deciding factor in the radio-emission properties of shocks (Gopalswamy et al. 2010).

Since the type II emitting radio bursts are preferably associated with fast CMEs, it is likely that these fast CMEs "slam" into a slower CME ahead, which causes a shock strengthening and enhanced radio emission, a phenomenon that was coined as "CME cannibalism" (Gopalswamy et al. 2001b). However, the spatial relationship between the type II sources and the CME shocks is often not clear, because the type II emission (which requires a density enhancement) could be generated where the shock front intersects with dense streamers, rather than at the CME front (Reiner et al. 2003; Shen et al. 2013).

Modeling the coronal and interplanetary electron density and magnetic field, a general decrease of type II burst source velocities and broadening of the band-splitting (of the fundamental and harmonic plasma frequencies) is inferred, which is interpreted in terms of the deceleration of the CME-driven shocks (Vrsnak et al. 2004). A correlation was found between the initial CME (or shock) speed and the CME (or shock) deceleration (Reiner et al. 2007), which is expected from the aerodynamic drag force model (Sect. 15.5). Combining coronal density models, the CME speeds from white-light images using the cone model, and interplanetary scintillation measurements, the travel time of interplanetary shocks between the Sun and Earth has been compared for three halo-CME events. However, substantial uncertainties have been assessed due to the density model, the CME geometry, the CME propagation direction, the shock stand-off distance, and the influence of successive CMEs on the background solar wind, and the aerodynamic drag force (Pohjolainen et al. 2007).

STEREO observations opened up a new perspective in the localization and kinematic reconstruction of interplanetary type II bursts. The heliocentric distance at which CME-driven shocks form has been determined to $\approx 1.5 R_\odot$, which coincides with the distance at which the Alfvén speed profile has a minimum value (Gopalswamy et al. 2009). Observations from S-WAVES/STEREO and WAVES/WIND indicate that shocks seem to be most efficient in accelerating electrons at a heliocentric distance of $(1.5–4.0) R_\odot$ (Gopalswamy et al. 2009). The statistical height of CMEs at the time of type II burst starts was found to be lower ($\approx 1.5 R_\odot$) when measured with STEREO than detected with SOHO ($\approx 2.2 R_\odot$),

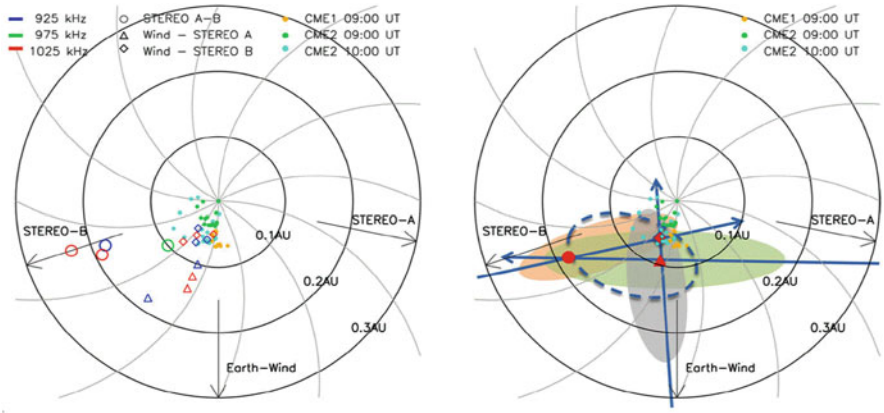

Fig. 15.11 *Left:* Location of the geometrically triangulated positions of the radio sources in interplanetary space from 3 spacecraft (STEREO A, B, WIND), with Parker spiral. *Right:* Combining the direction-finding positions yields the most likely CME area (dashed ellipse), (Martinez Oliveros et al. 2012)

which is likely to be due to the solar cycle-dependent variation of the average coronal density as a function of the solar cycle (Gopalswamy et al. 2009).

A type II burst associated with a CME-CME interaction was observed with the STEREO and the WIND spacecraft (Fig. 15.11). Applying a radio direction-finding technique for the two spacecraft and combining it with white-light coronagraphic positions, all three position measurements were found to be consistent with each other, and confirmed that the type II burst radio emission is causally related to the CME-CME interaction (Martinez Oliveros et al. 2012). The positions of a CME, the CME-driven shock, and its associated radio type II burst have been triangulated with gonio-polarimetric observations from the S-WAVES/STEREO and WAVES/WIND spacecraft, and it was found that the interaction of the shock wave with a nearby coronal streamer resulted in the interplanetary type II radio emission (Magdalenic et al. 2014), similar to previous results on the interaction with dense streamers (Reiner et al. 2003; Shen et al. 2013).

The interaction of two CMEs during the large 2013 May 22 SEP event has been located at a heliocentric distance of $\approx 6R_{\odot}$, while the leading edges of the two CMEs merged at a height of $\approx 20R_{\odot}$, based on HET/STEREO, S-WAVES/STEREO, and WIND measurements. On the other side, the *solar particle release (SPR)* time was found to coincide with the time interval when the second CME caught up with the trailing edge of the first CME, indicating that the CME-CME interaction (and shock-CME interaction) plays an important role in the acceleration of energetic particles (Ding et al. 2014).

Predictions of arrival times of CME-driven shocks at Earth, based on distance-time diagrams resulting from a combination of white-light corona, interplanetary type II radio, and in-situ data, have been improved by almost 50% by a linear method based on WAVES/WIND data (Cremades et al. 2015).

15.10 MHD Simulations of CME Propagation

The focus of recent MHD simulations of *coronal mass ejections (CMEs)* are the following two major applications: (i) The generation and propagation of global waves triggered at the launch site of a CME (e.g., Wang 2000; Wu et al. 2001; Ofman and Thompson 2002; Chen et al. 2005a,b; Delannee et al. 2008; Cohen et al. 2009; Wang et al. 2009; Downs et al. 2011, 2012), and (ii) the propagation of CMEs from the corona through the heliosphere and to Earth (e.g., Groth et al. 2000; Low 2001; Riley et al. 2003; Odstrcil et al. 2004; Manchester et al. 2004, 2008; Jin et al. 2017a,b). Complementary to this section, see also Sect. (13.9) on MHD modeling of flares, and Sect. 14.6 on MHD evolution of CME initiation.

The generation and propagation of global *EIT waves* or *EUV waves* has been simulated in the short-wavelength *Wentzel-Kramers-Brillouin (WKB)* approximation of fast-mode MHD waves, where a hydromagnetic wave is propagating along rays that are refracted by the non-uniform coronal medium. The coronal magnetic field is specified by a current-free extrapolation from the photospheric lower boundary, given by an observed monthly synoptic map. Wang (2000) simulated two observed events this way and found that the globally propagating fast-mode MHD waves are reflected away from active regions and coronal holes, where the phase speed is large, and that they are also refracted upward as they propagate away from their initiation point. Wu et al. (2001) conducted similar 3-D time-dependent MHD simulations and obtained distance-time curves of the spherically propagating fast-mode waves on the disk, the 3-D evolution of the disturbed magnetic field, electron densities at various viewing angles, and Friedrich's diagrams to identify the MHD wave characteristics. Ofman and Thompson (2002) performed 3-D MHD simulations of an active region with a force-free bipolar magnetic field and gravitational stratification, where an EIT wave is launched at the boundary of the region, and found that the EIT wave undergoes strong reflection and refraction, induces transient currents in the active region, generates secondary waves, and destabilizes the active region. Chen et al. (2005a) use a setup of a rising flux rope, where a piston-driven shock is formed along the envelope of the expanding CME and sweeps over the solar surface. They suggest that the legs of the shock produce Moreton waves, the chromospheric counterpart of coronal EIT waves (Chen et al. 2002, 2005a,b). Further experiments with the ZEUS-2D MHD code simulate the generation of slow- and fast-mode shocks in an unstable flux rope configuration, which causes disturbances at the chromospheric boundary that accounts for Moreton waves observed in H-α (Wang et al. 2009).

An alternative model for propagating EIT waves has been proposed in terms of a current shell in a CME (Delannee et al. 2008). In this scenario, propagating EIT waves are a direct signature of a gradual opening of magnetic field lines during a CME. 3-D MHD simulations were performed for a slowly rotating magnetic bipole, which progressively results in the formation of a twisted magnetic flux tube and its fast expansion during a CME. A current shell is produced by the return currents of the rotating bipole, which separate the twisted flux tube from the surrounding

fields, leading to the conjecture that propagating EIT waves are the observable signature of Joule heating in electric current shells (Delannee et al. 2008). Numerical MHD simulations (with the BATS-R-US code) of the 2009 February 13 CME event, which has been observed in quadrature by STEREO, reveal a diffuse coronal bright front that is made up of two components, where the expansion is faciliated by magnetic reconnection between the expanding CME core and the surrounding magnetic environment, producing many secondary dimmings, many far away from the initial CME source region, while the CME expansion leads to opening of coronal field lines on a global scale. Thus, both MHD wave and non-wave models are required to explain the complexity of the EIT wave phenomenon (Cohen et al. 2009). Downs et al. (2011) perform parametric 3-D MHD simulations of EIT waves by varying the ambient magneto-sonic speed, the free (eruptive) energy, and the eruption handedness (chirality), leading to different possible interpretations in terms of fast-mode magneto-sonic waves, plasma compression, or magnetic reconnection fronts (Downs et al. 2011, 2012).

The second major aspect of MHD simulations deals with the coronal launch and propagation of CMEs out to the heliosphere. A most comprehensive code that covers the CME formation, the interplanetary propagation, as well as interactions with the magnetosphere, is the parallel adaptive mesh refinement (AMR) code (Groth et al. 2000). CMEs are simulated with this code by driving local plasma density enhancements on the solar surface, with the background initial state of the corona and solar wind represented by a steady-state solution, and including coronal holes, helmet streamers with a neutral line and current sheet, the (Archimedean) Parker spiral topology of the interplanetary magnetic field, and the fast and slow solar wind. The density-driven CME causes a rapid acceleration after disruption, and a nearly constant speed of ≈ 560 km s^{-1} through interplanetary space. The CME produces a large magnetic cloud, which however is not geoeffective, but illustrates the capability of the AMR code as a space weather prediction tool (Groth et al. 2000). A similar MHD simulation, but using the constraints from two in-situ instruments (ACE at 1 AU and Ulysses at 5 AU) led to the problems of a force-free magnetic field model (because the ejecta underwent significant distortions from the solar wind) and the chemical composition (because significant spatial inhomogeneities exist within a single CME) (Riley et al. 2003). It became clear that MHD simulations of CMEs should always include an ambient solar wind model derived from photospheric magnetic field data for the background, and geometrical and kinematic fitting of coronagraph observations of CMEs for the transient disturbances, which should enable a prediction of the arrival of the shock and ejecta at Earth (Odstrcil et al. 2004). Another 3-D numerical ideal MHD code, called the *Block Adaptive Tree Solar-Wind Rope Upwind Scheme (BATS-R-US)*, includes a global steady-state model, a helmet streamer structure with a current sheet at the equator, Archimedean spiral topology for the interplanetary magnetic field, fast and slow solar wind, and the introduction of a Gibson-Low magnetic flux rope. After rapid flux-rope expansion, the CME produces a large magnetic cloud at 1 AU in which B_z rotates from north to south, and is geoeffective by generating strong geomagnetic activity at Earth (Manchester et al. 2004). Initiation of two CMEs, where the first

CME pre-conditions the solar wind, while the second CME drives a strong forward shock, was simulated with the same BATS-R-US code, but this simulation demonstrates that the CME shape is largely determined by its interaction with the ambient solar wind and may not be sensitive to the initiation process (Manchester et al. 2008). A new code was developed, called *Alfvén Wave Solar Model (AWSoM)*, which describes the background solar wind starting from the upper chromosphere and extends to 24 $R_{\odot}$ (Jin et al. 2017a). Coupling AWSoM to an inner heliosphere model with the *Space Weather Modeling Framework (SWMF)* extends the total domain beyond the Earth orbit. Physical processes included in the model are multi-species thermodynamics, electron heat conduction (in collisional and collisionless formulations), optically thin radiative cooling, and Alfvén-wave turbulence that accelerates and heats the solar wind. This new model can reproduce many of the stereoscopically observed features near the Sun, e.g., the CME-driven EIT waves, deflection of the flux rope from the coronal hole, and the "double-front" in the white-light images, and in the heliosphere, e.g., shock direction and shock properties observed by STEREO (Jin et al. 2017a). A remaining problem of such a data-constrained MHD model is the lack of direct observations of the eruptive magnetic field, which in the most recent (first-principle-based) codes is substituted with a data-driven *Eruptive Event Generator using Gibson-Low (EEGGL)* configuration (Jin et al. 2017b). Such a first-principle global MHD code is a forecasting tool that is capable of predicting the CME direction of propagation, the arrival time at Earth, and the ICME magnetic field at 1 AU (Fig. 15.12).

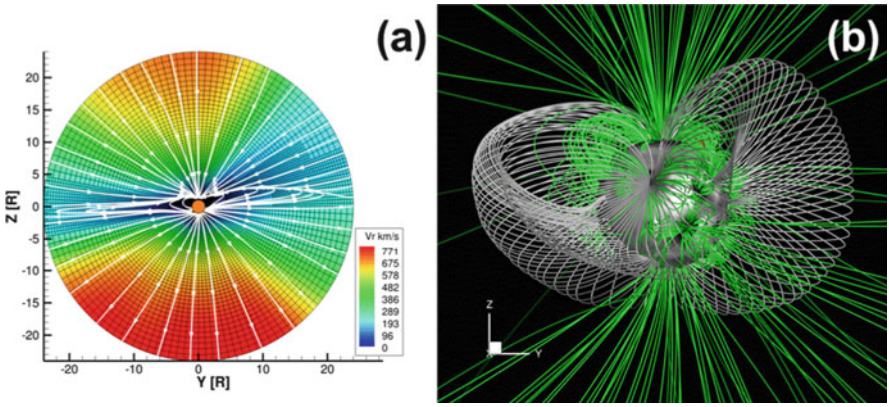

Fig. 15.12 (**a**) Carrington rotation 2107 steady-state solar wind radial velocity of the meridional slice with magnetic field lines. The black grid shows the simulation cells used in the AWSoM code. (**b**) 3-D field configuration of the steady-state solution. The white field lines represent the large=scale streamer belt. The active region and open fields are marked in green (Jin et al. 2017b)

References

(15.1) CME Coronagraph Observations

Burkepile, J.T., Hundhausen, A.J., Stanger, A.L., et al. 2004, *Role of projection effects on solar coronal mass ejection properties*, JGR 109/A3, A03103, [88 c, 7 c/y].

Brueckner, G.E., Howard, R.A., Koomen, M.J., et al. 1995, *The Large Angle Spectroscopic Coronagraph (LASCO)*, SoPh 162, 357, [1680 c, 75 c/y].

Colaninno, R.C. and Vourlidas, A. 2009, *First determination of the true mass of coronal mass ejections: A novel approach to using the two STEREO viewpoints*, ApJ 698, 852, [71 c, 8 c/y].

Cremades, H. and Bothmer, V. 2004, *On the 3-D configuration of coronal mass ejections*, A&A 422, 307, [198 c, 15 c/y].

Gilbert, H.R., Holzer, T.E., Burkepile, J.T., et al. 2000, *Active and eruptive prominences and their relationship to coronal mass ejections*, ApJ 537, 503, [127 c, 7 c/y].

Howard, R.A., Moses, J.D., Vourlidas, A., et al. 2008, *Sun Earth Connection Coronal and Heliospheric Investigation (SECCHI)*, SSRv 136, 67, [830 c, 87 c/y].

Lamy, P., Barlyaeva, T., Llebaria, A., et al. 2014, *Comparing the solar minima of cycles 22/23 and 23/24: The view from LASCO white light coronal images*, JGRA 119, 47, [18 c, 5 c/y].

Lee, H., Moon, Y.J., Na, H., et al. 2015, *Are 3-D coronal mass ejection parameters from single-view observations consistent with multiview ones ?* JGR 120/12, 10,237, [8 c, 3 c/y].

Morgan, H., Habbal, S., and Woo, R. 2006, *The depiction of coronal structure in white-light images*, SoPh 236, 263, 58 c, 5 c/y].

Ontiveros, V. and Vourlidas, A. 2009, *Quantitative measurements of CME-driven shocks from LASCO observations*, ApJ 693, 267, [109 c, 13 c/y].

Sheeley, N.R., Hakala, W.N., and Wang, Y.M. 2000, *Detection of coronal mass ejection associated shock waves in the outer corona*, JGR 105/A3, 5081, [101 c, 6 c/y].

St.Cyr, O.C., Plunkett, S.P., Michels, D.J., et al. 2000, *Properties of coronal mass ejections: SOHO LASCO observations from January 1996 to June 1998*, JGR 105/A8, 18169, [321 c, 18 c/y].

Vourlidas, A., Wu, S.T., Wang, A.H., et al. 2003, *Direct detection of coronal mass ejection-associated shock in LASCO experiment white-light images*, ApJ 598, 1392, [140 c, 10 c/y].

Vourlidas, A. and Howard, R.A. 2006, *The proper treatment of coronal mass ejection brightness: A new methodology and implications for observations*, ApJ 642, 1216, [120 c, 10 c/y].

Vourlidas, A., Lynch, B.J., Howard, R.A., and Li, Y. 2013, *How many CMEs have flux ropes? Deciphering the signatures of shocks, flux ropes, and prominences in coronagraph observations of CMEs*, SoPh 284, 179, [129 c, 29 c/y].

Vrsnak, B., Poletto, G., Vujic, E., et al. 2009, *Morphology and density structure of post-CME current sheets*, A&A 499, 905, [32 c, 4 c/y].

Wang, Y.M. and Sheeley, N.R.Jr. 2002, *Coronal white-light jets near sunspot maximum*, ApJ 575, 542, [61 c, 4 c/y].

Wang, Y., Chen, C., Gui, B., et al. 2011, *Statistical study of coronal mass ejection source locations: Understanding CMEs viewed in coronagraphs*, 2011 JGR 116/A4, A04104, [46 c, 7 c/y].

Webb, D.F. and Vourlidas, A. 2016, *LASCO white-light observations of eruptive current sheets trailing CMEs*, SoPh 291, 3725, [9 c, 6 c/y].

Yashiro, S., Gopalswamy, N., Michalek, G., et al. 2004, *A catalog of white light coronal mass ejections observed by the SOHO spacecraft*, JGR 109/A7, A07105, [528 c, 39 c/y].

(15.2) CME Stereoscopy and Tomography

Altschuler, M.D. 1979, *Reconstruction of the global-scale 3-D corona*, in Image Reconstruction from projections. Topics in Applied Physics, Vol. 32, p.105, [12 c, 0.3 c/y].

Aschwanden, M.J., Nitta, N.V., Wuelser,J.-P., et al. 2009, *First measurements of the mass of coronal mass ejections from the EUVI dimming observed with EUVI/STEREO/A and B Spacecraft*, ApJ 706, 376, [36 c, 4 c/y].

Barbey, N., Guennou, C., and Auchère, E. 2013, *TomograPy: A fast, instrument-independent, solar tomography software*, SoPh 283, 227, [11 c, 2 c/y].

Bosman, E., Bothmer, V., Nistico, G., et al. 2012, *Three-dimensional properties of coronal mass ejections from STEREO/SECCHI observations*, SoPh 281, 167, [18 c, 3 c/y].

Butala, M.D., Frazin, R.A., and Kamalabadi, F. 2005, *3-D estimates of the coronal electron density at times of extreme solar activity*, JGR 110(A9), A09S09, [9 c, 0.7 c/y].

Byrne, J.P., Maloney, S.A., McAteer, R.T., et al. 2010, *Propagation of an Earth-directed coronal mass ejection in 3D*, Nature Comm. 1/6, 74, [82 c, 11 c/y].

Colaninno, R.C. and Vourlidas, A. 2009, *First determination of the true mass of coronal mass ejections: A novel approach to using the two STEREO viewpoints*, ApJ 698, 852, [71 c, 8 c/y].

Cremades, H. and Bothmer, V. 2004, *On the 3-D configuration of coronal mass ejections*, A&A 422, 307, [198 c, 15 c/y].

Davies, J.A., Harrison, R.A., Perry, C.H., et al. 2012, *A self-similar expansion model for use in solar wind transient propagation studies*, ApJ 750, 23, [56 c, 10 c/y].

Dunn, T., Jackson, B.V., Hick, P.P. et al. 2005, *Comparative analysis of the CSSS calculation in the UCSD tomographic solar observations*, SoPh 227, 339, [19 c, 2 c/y].

Frazin, R.A. 2000, *Tomography of the solar corona. I. A robust, regularized, positive estimation method*, ApJ 530, 1026, [44 c, 3 c/y].

Frazin, R.A. and Janzen, P. 2002, *Tomography of the solar corona. II. Robust, regularized, positive estimation of the 3-D electron density distribution from LASCO-C2 polarized white-light images*, ApJ 570, 408, [56 c, 4 c/y].

Frazin, R.A. and Kamalabadi, F. 2005a, *Rotational tomography for 3-D reconstruction of the white-light and EUV corona in the post-SOHO era*, SoPh 228, 219, [23 c, 2 c/y].

Frazin, R.A. and Kamalabadi, F. 2005b, *On the use of total brightness measurements for tomography of the solar corona*, ApJ 628, 1061, [13 c, 1 c/y].

Frazin, R.A., Butala, M.D., Kemball, M.D., and Kamalabadi, F. 2005a, *Time-dependent reconstruction of nonstationary objects with tomographic or interferometric measurements*, ApJL 635, L197, [19 c, 2 c/y].

Frazin, R.A., Kamalabadi, F., and Weber, M.A. 2005b, *On the combination of differential emission measure analysis and rotational tomography for 3-D solar EUV imaging*, ApJ 628, 1070, [27 c, 2 c/y].

Frazin, R.A., Vasquez, A.M., Kamalabadi, F., et al. 2007, *3-D tomographic analysis of a high-cadence LASCO-C2 polarized brightness sequence*, ApJ 671, L201, [23 c, 2 c/y].

Howard, T.A., Tappin, S.J., Odstrcil, D. et al. 2013, *The Thomson surface. III. Tracking features in 3D*, ApJ 765, 45, [13 c, 3 c/y].

Jackson, B.V., Rompolt, B., and Svestka, Z. 1988, *Solar and interplanetary observations of the mass ejection on 7 May, 1979*, SoPh 115, 327, [19 c, 0.6 c/y].

Jackson, B.V. and Hick, P.P. 2002, *Corotational tomography of heliospheric features using global Thomson scattering data*, SoPh 211, 345, [17 c, 1 c/y].

Jackson, B.V., Hamilton, M.S., Hick, P.P. et al. 2011, *Solar mass ejection imager (SMEI) 3-D reconstruction of density enhancements behind interplanetary shocks: in-situ comparison near Earth and at STEREO*, JASTP 73/11, 1317, [5 c, 1 c/y].

Kramar, M., Jones, S., Davila, J. et al. 2009, *On the tomographic reconstruction of the 3-D electron density for the solar corona from STEREO Cor1 data*, SoPh 259, 109, [27 c, 3 c/y].

Liu, Y., Davies, J.A., Luhmann, J.G., et al. 2010, *Geometric triangulation of imaging observations to track coronal mass ejections continuously out to 1 AU*, ApJ 710, L82, [124 c, 17 c/y].

Lugaz, N., Vourlidas, A., and Roussev, I.I. 2009, *Deriving the radial distances of wide CMEs from elongation measurements in the heliosphere - Application to CME-CME interaction*, Annales Geophysicae 27/9, 3479, [93 c, 11 c/y].

Mierla, M., Inhester, B., Antunes, A., et al. 2010, *On the 3D reconstruction of coronal mass ejections using coronagraph data*, Annales Geophysicae 28, 203, [62 c, 8 c/y].

Moran, T.G. and Davila, J.M. 2004, *3-D polarimetric imaging of coronal mass ejections*, Science, 305, 66, [74 c, 5 c/y].
Moran, T.G., Davila, J.M., and Thompson, W.T. 2010, *3-D polarimetric coronal mass ejection localization tested through triangulation*, ApJ 712, 453, [25 c, 3 c/y].
Morgan, H., Habbal, S.R., and Lugaz, N. 2009, *Mapping the structure of the corona using Fourier backprojection tomography*, ApJ 690, 1119, [17 c, 2 c/y].
Morgan, H. and Habbal, S.R. 2010, *A method for separating coronal mass ejections from the quiescent corona*, ApJ 711, 631, [10 c, 1 c/y].
Morgan, H. 2011, *The rotation of the white light solar corona at height 4 $R_\odot$ from 1996 to 2010: A tomographical study of LASCO C2 observations*, ApJ 738, 189, [11 c, 2 c/y].
Odstrcil, D., Riley, P., and Zhao, X.P. 2004, *Numerical simulation of the 12 May 1997 interplanetary CME event*, JGR 109, A2, A02116, [123 c, 9 c/y].
Quemerais, E. and Lamy, P. 2002, *2-D electron density in the solar corona from inversion of white light images - Application to SOHO/LASCO-C2 observations*, A&A 393, 295, [41 c, 3 c/y].
Thernisien, A.F.R., Howard, R.A., and Vourlidas, A. 2006, *Modeling of flux rope CMEs*, ApJ 652, 763, [203 c, 28 c/y].
Zidowitz, S. 1999, *Coronal structure of the While Sun Month: A tomographic reconstruction*, JGR 104, A5, 9727, [26 c, 1 c/y].

(15.3) CME Acceleration

Bein, B.M., Berkebile-Stoiser, S., Veronig, A.M., et al. 2011, *Impulsive acceleration of coronal mass ejections. I. Statistics and coronal mass ejection source region characteristics*, ApJ 738, 191, [54 c, 8 c/y].
Bein, B.M., Berkebile-Stoiser, S., Veronig, A.M., et al. 2012, *Impulsive acceleration of coronal mass ejections. II. Relation to soft X-ray flares and filament eruptions*, ApJ 755, 44, [30 c, 5 c/y].
Berkebile-Stoiser, S., Veronig, A.M., Bein, B.M., et al. 2012, *Relation between the coronal mass ejection acceleration and the non-thermal flare*. ApJ 753, 88, [19 c, 3 c/y].
Byrne, J.P. 2015, *Investigating the kinematics of coronal mass ejections with the automated CORIMP catalog*, J.Space Weather and Space Climate 5, A19, [6 c, 2 c/y].
Chen, J. and Krall, J. 2003, *Acceleration of coronal mass ejections*, JGR 108, 1410, [81 c, 6 c/y].
Chen, J., Marque, C., Vourlidas, A., et al. 2006, *The flux rope scaling of the acceleration of coronal mass ejections and eruptive prominences*, ApJ 649, 452, [36 c, 3 c/y].
Cheng, X., Zhang, J., Ding, M.D., et al. 2013, *The driver of coronal mass ejections in the low corona: A flux rope*, ApJ 763, 43, [58 c, 13 c/y].
Forbes, T. 2010, *Models of coronal mass ejections and flares*, in "Heliophysics, Space Storms and Radiation: Causes and Effects" (eds. Schrijver C.J. and Siscoe, G.L.), Cambridge University Press: Cambridge, p.159.
Gallagher, P.T., Lawrence, G.R., and Dennis, B.R. 2003, *Rapid acceleration of a CME in the low corona and implications for propagation* ApJ 588, L53, [116 c, 8 c/y].
Gopalswamy, N., Lara, A., Lepping, R.P., et al. 2000, *Interplanetary acceleration of coronal mass ejections*, GRL 27, 145, [291 c, 17 c/y].
Qiu, J., Wang, H., Cheng, C.Z., et al. 2004, *Magnetic reconnection and mass acceleration in flare-coronal mass ejection events*, ApJ 604, 900, [128 c, 9 c/y].
Lin, J. and Forbes, T.G. 2000, *Effects of reconnection on the coronal mass ejection process*, JGR 105/A2, 2375, [384 c, 22 c/y].
Maricic, D., Vrsnak, B., Stanger, A.L., et al. 2007, *Acceleration phase of coronal mass ejections: II Synchronization of the energy release in the associated flare*, SoPh 241, 99, [83 c, 8 c/y].
Neupert, W.M., Thompson, B.J., Gurman, J.P. et al. 2001, *Eruption and acceleration of flare-associated coronal mass ejection loops in the low corona*, JGR 106 A11, 25215, [50 c, 3 c/y].

Patsourakos, S., Vourlidas, A., and Stenborg, G. 2010, *The genesis of an impulsive coronal mass ejection observed at ultra-high cadence by AIA and SDO*, ApJ 724, L188, [67 c, 7 c/y].

Schrijver, C.J., Elmore,C., Kliem, B., et al. 2008, *Observations and modeling of the early acceleration phase of erupting filaments involved in coronal mass ejections*, ApJ 674, 586, [97 c, 10 c/y].

Temmer, M., Veronig, A.M., Vrsnak, B. et al. 2008, *Acceleration in fast halo CMEs and synchronized flare hard X-ray bursts*, ApJ 673, L95, [121 c, 13 c/y].

Temmer, M., Veronig, A.M., Kontar, E.P., et al. 2010, *Combined STEREO/RHESSI study of coronal mass ejection acceleration and particle acceleration in solar flares*, ApJ 712, 1410, [104 c, 14 c/y].

Vrsnak, B., Ruzdjak, D., Sudar, D., et al. 2004a, *Kinematics of coronal mass ejections between 1 and 30 solar radii. What can be learned about forces governing the eruption*, A&A 423, 717, [77 c, 6 c/y].

Vrsnak, B., Maricic, D., Stanger, A., et al. 2004b, *Coronal mass ejection of 15 May 2001: Coupling of the CME acceleration and the flare energy release*, SoPh 225, 355, [58 c, 4 c/y].

Zhang, J. and Dere, K.P. 2006, *A statistical study of main and residual accelerations of coronal mass ejections*, ApJ 649, 1100, [141 c, 12 c/y].

(15.4) CME Interplanetary Propagation

Bisi, M.M., Breen, A.R., Jackson, B.V., et al. 2010, *From the Sun to the Earth: The 13 May 2005 coronal mass ejection*, SoPh 265, 49, [40 c, 5 c/y].

Byrne, J.P., Maloney, S.A., McAteer, R.T., et al. 2010, *Propagation of an Earth-directed coronal mass ejection in 3D*, Nature Comm. 1/6, 74, [82 c, 11 c/y].

Cheng, X., Ding, M.D., Guo, Y. et al. 2014, *Tracking the evolution of a coherent magnetic flux rope continuously from the inner to the outer corona*, ApJ 780, 28, [42 c, 12 c/y].

DeForest, C.E., Howard, T.A., and McComas, D.J. 2013, *Tracking coronal features from the low corona to Earth: A qualitative analysis of the 2008 December 12 coronal mass ejection*, ApJ 769, 43, [43 c, 10 c/y].

Gui, B., Shen, C., Wang, Y., et al. 2011, *Quantitative analysis of CME deflections in the corona*, SoPh 271, 111, [47 c, 7 c/y].

Harrison, R.A., Davies, J.A., Moestl, C., et al. 2012, *An analysis of the origin and propagation of the multiple coronal mass ejections of 2010 August 1*, ApJ 750, 45, [57 c, 10 c/y].

Howard, T.A., Fry, C.D., Johnston, J.C., et al. 2007, *On the evolution of coronal mass ejections in the interplanetary medium*, ApJ 667, 610, [58 c, 6 c/y].

Hu, Q., Qiu, J., Dasgupta, B., et al. 2014, *Structures of interplanetary magnetic flux ropes and comparison with their solar sources*, ApJ 793, 53, [37 c, 11 c/y].

Jian, L., Russell, C.T., Luhmann, J.G., et al. 2006, *Properties of interplanetary coronal mass ejections at 1 AU during 1995–2004*, SoPh 239, 393, [187 c, 16 c/y].

Johri, A. and Manoharan, P.K. 2016, *An intense flare-CME event in 2015: Propagation and interaction effects between the Sun and Earth's orbit*, SoPh 291, 1433, [7 c, 5 c/y].

Kay, C. and Opher, M. 2015, *The heliocentric distance where the delections and rotations of solar coronal mass ejections occur*, ApJL 811, L36, [12 c, 5 c/y].

Liu, Y., Richardson J.D., and Belcher, J.W. 2005, *A statistical study of the properties of interplanetary coronal mass ejections from 0.3 to 5.4 AU*, Planetary and Space Science 53, 3, [84 c, 7 c/y].

Liu, Y., Luhmann, J.G., Müller-Mellin, R., et al. 2008, *A comprehensive view of the 2006 December 13 CME: From the Sun to interplanetary space*, ApJ 689, 563, [65 c, 7 c/y].

Liu, Y.D., Luhmann, J.G., Lugaz, N., et al. 2013, *On Sun-to-Earth propagation of coronal mass ejections*, ApJ 769, 45, [72 c, 16 c/y].

Liu, Y.D., Luhmann, J.G., Lugaz, N., et al. 2014, *Observations of an extreme strorm in interplanetary space caused by successive coronal mass ejections*, Nature Comm. 5, 3841, [73 c, 21 c/y].
Liu, Y.D., Hu, H., Wang, C., et al. 2016, *On Sun-to-Earth propagation of coronal mass ejections: II. Slow events and comparison with others*, ApJSS 222, 23, [20 c, 13 c/y].
Marubashi, K., Akiyama, S., Yashiro, S., et al. 2015, *Geometrical relationship between interplanetary flux ropes and their solar sources*, SoPh 290, 137, [22 c, 9 c/y].
Manoharan, P.K., Tokumaru, M., Pick, M., et al. 2001, *Coronal mass ejection of 2000 July 14 flare event: Imaging from near-Sun to Earth environment*, ApJ 559, 1180, [62 c, 16 c/y].
Mays, M.L., Taktakishvili, A., Pulkkinen, A., et al. 2015, *Ensemble modeling of CMEs using the WSA-ENLIL-Cone model*, SoPh 290, 1775, [66 c, 26 c/y].
Moestl, C., Amla, K., Hall, J.R., et al. 2014, *Connecting speeds, directions and arrival times of 22 coronal mass ejections from the Sun to 1 AU*, ApJ 787, 119, [81 c, 23 c/y].
Nieves-Chinchilla, T., Vourlidas, A., Stenborg, G., et al. 2013, *Inner heliospheric evolution of a "stealth" CME derived from multi-view imaging and multipoint in situ observations. I. Propagation to 1 AU*, ApJ 779, 55, [21 c, 5 c/y].
Pomoell, J. and Poedts, S. 2018, *EUHFORIA: European heliospheric forecasting information asset*, J. Space Weather and Space Climate 8/27, A35.
Rollett, T., Moestl, C., Temmer, M., et al. 2014, *Combined multipoint remote and in situ observations of the asymmetric evolution of a fast solar coronal mass ejection*, ApJ 790, 6, [20 c, 6 c/y].
Temmer, M., Rollett, T., Moestl, C., et al. 2011, *Influence of the ambient solar wind flow on the propagation behavior of interplanetary coronal mass ejections*, ApJ 743, 101, [56 c, 9 c/y].
Temmer, M. and Nitta, N.V., 2015, *Interplanetary propagation behavior of the fast coronal mass ejection on 23 July 2012*, SoPh 290, 919, [31 c, 12 c/y].
Temmer, M., Reiss, M.A., Nikolic, L. et al. 2017, *Preconditioning of interplanetary space due to transient CME disturbances*, ApJ 835, 141, [11 c, 11 c/y].
Thernisien, A.F.R., Howard, R.A., and Vourlidas, A. 2006, *Modeling of flux rope CMEs*, ApJ 652, 763, [203 c, 28 c/y].
Vrsnak, B., Temmer, M., Zic, T., et al. 2014, *Heliospheric propagation of coronal mass ejections: Comparison of numerical WSA-ENLIL+Cone model and analytical drag-based model*, ApJSS 213, 21, [37 c, 11 c/y].
Wang, H., Wang, B., Shen, C., et al. 2014, *Deflected propagation of a coronal mass ejection from the corona to interplanetary space*, JGR 119/7, 5117, [31 c, 9 c/y].
Wang, Y., Zhang, Q., Liu, J., et al. 2016, *On the propagation of a geoeffective coronal mass ejection during 15–17 March 2015*, JGR 121/8, 6723, [10 c, 7 c/y].
Webb, D.F., Howard, T.A., Fry, C.D., et al. 2009, *Study of CME propagation in the inner heliosphere: SOHO LASCO, SMEI and STEREO HI observations of the January 2007 events*, SoPh 256, 239, [49 c, 6 c/y].
Zhang, J., Dere, K.P., Howard, R.A., et al. 2004, *A study of the kinematic evolution of coronal mass ejections*, ApJ 604, 420, [152 c, 11 c/y].

(15.5) Aerodynamic Drag Force

Cargill, P.J. 2004, *On the aerodynamic drag force acting on interplanetary coronal mass ejections*, SoPh 221, 125, [133 c, 10 c/y].
Howard, T.A., Fry, C.D., Johnston, J.C., et al. 2007, *On the evolution of coronal mass ejections in the interplanetary medium*, ApJ 667, 610, [58 c, 6 c/y].
Johri, A. and Manoharan, P.K. 2016, *An intense flare-CME event in 2015: Propagation and interaction effects between the Sun and Earth's orbit*, SoPh 291, 1433, [7 c, 5 c/y].
Maloney, S.A. and Gallagher, P.T. 2010, *Solar wind drag and the kinematics of interplanetary coronal mass ejections*, ApJ 724, L127, [19 c, 3 c/y].

Rollett, T., Moestl, C., Temmer, M., et al. 2014, *Combined multipoint remote and in situ observations of the asymmetric evolution of a fast solar coronal mass ejection*, ApJ 790, 6, [20 c, 6 c/y].

Shen, F., Wu, S.T., Feng, X., et al. 2012, *Acceleration and deceleration of coronal mass ejections during propagation and interaction*, JGR 117, A11, A11101, [16 c, 3 c/y].

Takahashi, T. and Shibata, K. 2017, *Sheath-accumulating propagation of interplanetary coronal mass ejection*, ApJ 837, 17, [4 c, 4 c/y].

Tappin S.J. 2006, *The deceleration of an interplanetary transient from the Sun to 5 AU*, SoPh 233, 233, [52 c, 5 c/y].

Temmer, M., Rollett, T., Moestl, C., et al. 2011, *Influence of the ambient solar wind flow on the propagation behavior of interplanetary coronal mass ejections*, ApJ 743, 101, [56 c, 9 c/y].

Temmer, M. and Nitta, N.V., 2015, *Interplanet propagation behavior of the fast coronal mass ejection on 23 July 2012*, SoPh 290, 919, [31 c, 12 c/y].

Vrsnak, B., Ruzdjak, D., Sudar, D., et al. 2004, *Kinematics of coronal mass ejections between 1 and 30 solar radii. What can be learned about forces governing the eruption*, A&A 423, 717, [77 c, 6 c/y].

Vrsnak, B., Vrbanec, D., and Calogovic, J. 2008, *Dynamics of coronal mass ejections. The mass-scaling of the aerodynamic drag*, A&A 490, 811, [17 c, 2 c/y].

Vrsnak, B., Zic, T., Vrbanec, D., et al. 2013, *Propagation of interplanetary coronal mass ejections: The drag-based model*, SoPh 285, 295, [99 c, 22 c/y].

Webb, D.F., Howard, T.A., Fry, C.D., et al. 2009, *Study of CME propagation in the inner heliosphere: SOHO LASCO, SMEI and STEREO HI observations of the January 2007 events*, SoPh 256, 239, [49 c, 6 c/y].

(15.6) CME-CME Interactions

Cheng, X., Zhang, J., Ding, M.D., et al. 2013, *Investigating two successive flux rope eruptions in a solar active region*, ApJ 769, L25, [39 c, 9 c/y].

Farrugia, C. and Berdichevsky, D. 2004, *Evolutionary signatures in complex ejecta and their driven shocks*, Annales Geophysicae 22/10, 3679, [56 c, 4 c/y].

Gopalswamy, N., Yashiro, S., Kaiser, M.L., et al. 2001, *Radio signatures of CME interaction: CME Cannibalism ?* ApJ 548, L91, [197, 12 c/y].

Harrison, R.A., Davies, J.A., Moestl, C., et al. 2012, *An analysis of the origin and propagation of the multiple coronal mass ejections of 2010 August 1*, ApJ 750, 45, [57 c, 10 c/y].

Liu, Y.D., Luhmann, J.G., Moestl, C., et al. 2012, *Interactions between coronal mass ejections viewed in coordinated imaging and in situ observations*, ApJ 746, L15, [64 c, 12 c/y].

Liu, Y.D., Luhmann, J.G., Lugaz, N., et al. 2013, *On Sun-to-Earth propagation of coronal mass ejections*, ApJ 769, 45, [72 c, 16 c/y].

Liu, Y.D., Yang, Z., Wang, R., et al. 2014, *Sun-to-Earth characteristics of two coronal mass ejections interacting near 1 AU: Formation of a complex ejecta and generation of a two-step geomagnetic storm*, ApJ 793, L41, [33 c, 9 c/y].

Lugaz, N., Manchester, W.B.IV., Gombosi, T.I., et al. 2005, *Numerical simulation of the interaction of two coronal mass ejections from Sun to Earth*, ApJ 634, 651, [92 c, 7 c/y].

Lugaz, N., Vourlidas, A., and Roussev, I.I. 2009, *Deriving the radial distances of wide CMEs from elongation measurements in the heliosphere - Application to CME-CME interaction*, Annales Geophysicae 27/9, 3479, [93 c, 11 c/y].

Lugaz, N., Farrugia, C.J., Davies, J.A., et al. 2012, *The deflection of the two interacting coronal mass ejections of 2010 May 23–24 as revealed by combined in situ measurements and heliospheric imaging*, ApJ 759, 68, [78 c, 14 c/y].

Lugaz, N., Temmer, M., Wang, Y., et al. 2017, *The interaction of successive CMEs: A review*, SoPh 292, 64, [21 c, 21 c/y].

Mishra, W. and Srivastava, N. 2014, *Morphological and kinematic evolution of three interacting coronal mass ejections of 2011 February 13–15*, ApJ 794, 64, [15 c, 4 c/y].
Shen, F., Wang, Y., Shen, C., et al. 2017, *On the collision nature of two coronal mass ejections: A review*, SoPh 292, 104, [4 c, 4 c/y].
Temmer, M., Bojan, V., Rollett, T., et al. 2012, *Characteristics of kinematics of a coronal mass ejection during the 2010 August 1 CME-CME interaction*, ApJ 749, 57, [81 c, 15 c/y].
Temmer, M., Veronig, A.M., Reinhart, V., et al. 2014, *Asymmetry in the CME-CME interaction process for the events from 2011 February 14–15*, ApJ 785, 85, [35 c, 10 c/y].
Wang, Y., Wang, B., Shen, C., et al. 2014, *Deflected propagation of a coronal mass ejection from the corona to interplanetary space*, JGR 119/7, 5117, [32 c, 9 c/y].

(15.7) CME-Driven Global Waves

Attrill, G., Nakawacki, M.S., Harra, L.K., et al. 2006, *Using the evolution of coronal dimming regions to probe the global magnetic field topology*, SoPh 238, 117, [84 c, 7 c/y].
Attrill, G.D.R., Harra, L.K., van Driel-Gesztelyi, L. et al. 2007, *Coronal wave: Magnetic footprint of a coronal mass ejection ?* ApJ 656, L101, [173 c, 16 c/y].
Biesecker, D.A., Myers, D.C., Thompson, B.J., et al. 2002, *Solar phenomena associated with EIT waves*, ApJ 569, 1009, [181 c, 12 c/y].
Chen, P.F. and Wu, Y. 2011, *First evidence of coexisting EIT wave and coronal Moreton wave from SDO/AIA observations*, ApJ 732, L20, [73 c, 11 c/y].
Cheng, X., Zhang, J., Olmedo, O., et al. 2012, *Investigation of the formation and separation of an EUV wave from the expansion of a coronal mass ejection*, ApJ 745, L5, [68 c, 12 c/y].
Delannee C. 2000, *Another view of the EIT wave phenomen*, ApJ 545, 512, [126 c, 7 c/y].
Gallagher, P.T. and Long, D.M. (2011), *Large-scale bright fronts in the solar corona: A review of "EIT waves"*, SSRv 158, 365, [86 c, 13 c/y].
Gopalswamy, N., Yashiro, S., Temmer, M., et al. 2009, *EUV wave reflection from a coronal hole*, ApJ 691, L123, [113 c, 13 c/y].
Hudson, H.S., Khan, J.I., Lemen, J.R., et al. 2003, *Soft X-ray observation of a large-scale coronal wave and its exciter*, SoPh 212, 121, [92 c, 6 c/y].
Khan, J.I. and Aurass, H. 2002, *X-ray observations of a large-scale solar coronal shock wave*, A&A 383, 1018, [107 c, 7 c/y].
Kienreich, I.W., Temmer, M., and Veronig, A.M. 2009, *STEREO quadrature observations of the 3-D structure and driver of a global coronal wave*, ApJ 703, L118, [80 c, 9 c/y].
Klassen, A., Aurass, H., Mann, G., et al. 2000, *Catalogue of the 1997 SOHO/EIT coronal transient waves and associated type II radio burst spectra*, A&AS 141, 357, [166 c, 9 c/y].
Kwon, R.Y., Kramar, M., Wang, T.J., et al. 2013, *Global coronal seismology in the extended solar corona through fast magnetosonic waves observed by STEREO SECCHI COR1*, ApJ 766, 55, [13 c, 1 c/y].
Li, T., Zhang, J., Yang, S., et al. 2012, *SDO/AIA observations of secondary waves generated by interaction of the 2011 June 7 global EUV wave with solar coronal structures*, ApJ 746, 13, [54 c, 10 c/y].
Liu, W., Nitta, N.V., Schrijver, C.J., et al. 2010, *First SDO AIA observations of a global coronal EUV wave: Multiple components and ripples*, ApJ 723, L53, [94 c, 13 c/y].
Liu, W., Title, A.M., Zhao, J., et al. 2011, *Direct imaging of quasi-periodic fast propagating waves of* $\approx$*2000 km* s^{-1} *in the low solar corona by the SDO AIA*, ApJ 736, L13, [85 c, 13 c/y].
Liu, W., Ofman, L., Nitta, N.V., et al. 2012, *Quasi-periodic fast-mode wave trains within a global EUV wave and sequential transverse oscillations detected by SDO/AIA*, ApJ 753, 52, [81 c, 15 c/y].
Liu, W. and Ofman, L. 2014, *Advances in observing various coronal EUV waves in the SDO Era and their seismological applications* (Invited review), SoPh 289, 3233, [75 c, 21 c/y].

Long, D.M., Gallagher, P.T., McAteer, R.T.J., et al. 2008, *The kinematics of a globally propagating disturbance in the solar corona*, ApJ 680, L81, [113 c, 12 c/y].
Long, D.M., Bloomfield, D.S., Chen, P.F., et al. 2017, *Understanding the physical nature of coronal "EIT waves"*, SoPh 292, 7, [22 c, 22 c/y].
Ma, S., Raymond, J.C., Golub, L., et al. 2011, *Observations and interpretation of a low shock wave observed in the EUV by the SDO/AIA*, ApJ 738, 160, [86 c, 13 c/y].
Narukage, N., Morimoto, T., Miwako, K., et al. 2004, *X-ray expanding features associated with a Moreton wave*, PASJ 56, L5, [21 c, 2 c/y].
Nistico, G., Pascoe, D.J., and Nakariakov, V.M. 2014, *Observation of a high-quality quasi-periodic rapidly wave train using SDO/AIA*, A&A 569, A12, [35 c, 10 c/y].
Nitta, N.V., Schrijver, C.J., Title, A.M., et al. 2013, *Large-scale coronal propagating fronts in solar eruptions as observed by the AIA on board the SDO - An ensemble study*. ApJ 776, 58, [53 c, 12 c/y].
Patsourakos, S., Vourlidas, A., Wang, Y.M., et al. 2009, *What is the nature of EUV waves ? First STEREO 3D observations and comparison with theoretical models*, SoPh 2009, 259, 49, [81 c, 10 c/y].
Patsourakos, S. and Vourlidas, A. 2009, *EUV waves are waves: First quadrature observations of an EUV wave from STEREO*, ApJ 700, L182, [112, 13 c/y].
Patsourakos, S., Vourlidas, A., and Kliem, B. 2010, *Toward understanding the early stages of an impulsively accelerated coronal mass ejection. SECCHI observations*, A&A 522, A100, [48 c, 6 c/y].
Veronig, A.M., Temmer, M., Vrsnak, B., et al. 2006, *Interaction of a Moreton/EIT wave and a coronal hole*, ApJ 647, 1466, [69 c, 6 c/y].
Veronig, A.M., Temmer, M., and Vrsnak, B. 2008, *High cadence observations of a global coronal wave by STEREO EUVI*, ApJ 681, L113, [116 c, 12 c/y].
Veronig, A.M., Muhr, N., Kienreich, I.W., et al. 2010, *First observations of a dome-shaped large-scale coronal EUV wave*, ApJ 716, L57, [129 c, 17 c/y].
Vrsnak, B., Warmuth, A., Brajsa, R., et al. 2001, *Flare waves observed in Helium I 10,830 A. A link between Hα Moreton and EIT waves*, A&A 394, 299, [88 c, 6 c/y].
Vrsnak, B., Magdalenic, J., Temmer, M., et al. 2005, *Broadband metric-range radio emission associated with a Moreton/EIT wave*, ApJ 625, L67, [30 c, 2 c/y].
Warmuth, A., Vrsnak, B., Aurass, H., et al. 2001, *Evolution of two EIT/Hα Moreton waves*, ApJ 560, L105, [130 c, 8 c/y].
Warmuth, A., Vrsnak, B., Magdalenic, J., et al. 2004a, *A multiwavelength study of solar flare waves. I. Observations and basic properties*, A&A 418, 1101, [121 c, 9 c/y].
Warmuth, A., Vrsnak, B., Magdalenic, J., et al. 2004b, *A multiwavelength study of solar flare waves. II. Perturbation characteristics and physical interpretation*, A&A 418, 1117, [111 c, 8 c/y].
Warmuth, A. and Mann, G. 2005, *A model of the Alfvén speed in the solar corona*, A&A 435, 1123, [68 c, 5 c/y].
Warmuth, A. 2010, *Large-scale waves corona debate: The continuing debate*, Adv.Space Res. 45, 527, [65 c, 9 c/y].
Warmuth, A. and Mann, G. 2011, *Kinematical evidence for physically different classes of large-scale coronal EUV waves*, A&A 532, A151, [54 c, 8 c/y].
Warmuth, A. 2015, *Large-scale globally propagating coronal waves*, LRSP 12, 3, [24 c, 10 c/y].
Wills-Davey, M.J. and Attrill, G.D.R. 2009, *EIT waves: a changing understanding over a solar cycle*, SSRv 149, 325, [87 c, 10 c/y].
Zhukov, A.N. and Auchère, F. 2004, *On the nature of EIT waves, EUV dimmings and their link to CMEs*, A&A 427, 705, [152 c, 11 c/y].

(15.8) CME-Driven Shocks

Bein, B.M., Berkebile-Stoiser, S., Veronig, A.M., et al. 2011, *Impulsive acceleration of coronal mass ejections. I. Statistics and coronal mass ejection source region characteristics*, ApJ 738, 191, [54 c, 8 c/y].

Bemporad, A. and Mancuso, S. 2010, *First complete determination of plasma physical parameters across a coronal mass ejection-driven shock*, ApJ 720, 130, [43 c, 6 c/y].

Ciaravella, A., Raymond, J.C., Kahler, S.W., et al. 2005, *Detection and diagnostics of a coronal shock wave driven by a partial-halo coronal mass ejection on 2000 June 28*, ApJ 621, 1121, [42 c, 3 c/y].

Gopalswamy, N., Nitta, N., Akiyama, S., et al. 2012, *Coronal magnetic field measurement from EUV images made by the SDO*, ApJ 744, 72, [55 c, 10 c/y].

Gopalswamy, N., Xie, H., Akiyama, S., et al. 2013, *The first ground level enhancement of solar cycle 24: Direct observation of shock formation*, ApJ 765, L30, [54 c, 12 c/y].

Kozarev, K.A., Korreck, K.E., Lobzin, V.V., et al. 2011, *Off-limb solar coronal wavefronts from SDO/AIA EUV observations - Implications for particle production*, ApJ 733, L25, [61 c, 9 c/y].

Li, G., Zank, G.P., Rice, W.K.M., et al. 2003, *Energetic particle acceleration and transport at coronal mass ejection-driven shocks*, JGR 108/A2, 1082, [98 c, 7 c/y].

Liu, Y.D., Hu, H., Zhu, B., et al. 2017, *Structure, propagation, and expansion of a CME-driven shock in the heliosphere: A revisit of the 2012 July 23 extreme storm*, ApJ 834, 158, [8 c, 8 c/y].

Ma, S., Raymond, J.C., Golub, L., et al. 2011, *Observations and interpretation of a low corona shock wave observed in the EUV by the SDO/AIA*, ApJ 738, 160, [86 c, 13 c/y].

Mancuso, S., Raymond, J.C., Kohl, J., et al. 2002, *UVCS/SOHO observations of a CME-driven shock: Consequences on ion heating mechanisms behind a coronal shock*, A&A 383, 267, [75 c, 5 c/y].

Mann, G., Klassen, A., Aurass, H., et al. 2003, *Formation and development of shock waves in the solar corona and the near-Sun interplanetary space*, A&A 400, 329, [126 c, 9 c/y].

Moestl, C., Farrugia, C.J., Kilpua, E.K.J., et al. 2012, *Multi-point shock and flux rope analysis of multiple interplanetary coronal mass ejections around 2010 August 1 in the inner heliosphere*, ApJ 758, 10, [62 c, 11 c/y].

Ontiveros, V. and Vourlidas, A. 2009, *Quantitative measurements of CME-driven shocks from LASCO observations*, ApJ 693, 267, [109 c, 13 c/y].

Rouillard, A.P., Plotnikov, I., Pinto, R.F., et al. 2016, *Deriving the properties of coronal pressure frongs in 3D: Application to the 2012 May 17 ground level enhancement*, ApJ 833, 45, [23 c, 9 c/y].

Roussev, I.I., Sokolov, I.V., Forbes, T.G., et al. 2004, *A numerical model of a coronal mass ejection: Shock development with implications for the acceleration of GeV protons*, ApJ 605, L73, [95 c, 7 c/y].

Sheeley, N.R., Hakala, W.N., and Wang, Y.M. 2000, *Detection of coronal mass ejection associated shock waves in the outer corona*, JGR 105/A3, 5081, [101 c, 6 c/y].

Susino, R., Bemporad, A., and Mancuso, S. 2015, *Physical conditions of coronal plasma at the transit of a shock driven by a coronal mass ejection*, ApJ 812, 119, [8 c, 3 c/y].

Tylka, A.J., Cohen, C.M.S., Dietrich, W.F., et al. 2005, *Shock geometry, seed populations, and the origin of variable elemental composition at high energies in large gradual solar particle events*, ApJ 625, 474, [241 c, 19 c/y].

Tylka, A.J. and Lee, M.A. 2006, *A model for spectral and compositional variability at high energies in large, gradual solar particle events*, ApJ 646, 1319, [141 c, 12 c/y].

Vourlidas, A., Wu, S.T., Wang, A.H., et al. 2003, *Direct detection of a coronal mass ejection-associated shock in LASCO white-light images*, ApJ 598, 1292, [140 c, 10 c/y].

Vrsnak, B. and Cliver, E.W. 2008, *Origin of coronal shock waves. Invited Review* SoPh 253, 215, [133 c, 14 c/y].

Zank, G.P., Rice, W.K.M., and Wu, C.C. 2000, *Particle acceleration and coronal mass ejection driven shocks. A theoretical model*, JGR 105/A11, 25079, [197 c, 11 c/y].

(15.9) CMEs and Interplanetary Radio Emission

Cremades, H., Iglesias, F.A., St.Cyr, O.C., et al. 2015, *Low-frequency type-II radio detections and coronagraph data employed to describe and forecast the propagation of 71 CMEs/shocks*, SoPh 290, 2455, [9 c, 4 c/y].

Ding, L.G., Li, G., Jiang, Y., et al. 2014, *Interaction between two coronal mass ejections in the 2013 May 22 large solar energetic particle event*, ApJ 793, L35, [17 c, 5 c/y].

Gopalswamy, N., Yashiro, S., Kaiser, M.L., et al. 2001a, *Characteristics of CMEs associated with long-wavelength type II radio bursts*, JGR 106, A12, [134 c, 8 c/y].

Gopalswamy, N., Yashiro, S., Kaiser, M.L., et al. 2001b, *Radio signatures of CME interaction: CME Cannibalism ?* ApJ 548, L91, [197, 12 c/y].

Gopalswamy, N., Lara, A., Kaiser,M.L. 2001c, *Near-Sun and near-Earth manifestations of solar eruptions*, JGR 106, A11, [139 c, 8 c/y].

Gopalswamy, N., Aguilar-Rodriguez, E., Yashiro, S., et al. 2005, *Type II radio bursts and energetic solar eruptions*, JGR 110, A12, A12S07, [78 c, 6 c/y].

Gopalswamy, N., Yashiro, S., Akiyama, S., et al. 2008, *Coronal mass ejections, type II radio bursts, and solar energetic particle events in the SOHO era*, Annales Geophysicae 26/10, 3033, [63 c, 7 c/y].

Gopalswamy, N. Thompson, W.T., Davila, J.M., et al. 2009, *Relation between type II bursts and CMEs inferred from STEREO observations*, SoPh 259, 227, [103 c, 12 c/y].

Gopalswamy, N., Xie, H., Mäkelä, P., et al. 2010, *Interplanetary shocks lacking type II radio bursts*, ApJ 710, 1111, [60 c, 8 c/y].

Magdalenic, J., Marque, C., Krupar, V., et al. 2014, *Tracking the CME-driven shock wave on 2012 March 5 and radio triangulation of associated radio emission*, ApJ 791, 115, [18 c, 5 c/y].

Martinez Oliveros, J.C., Raftery, C.L., Bain, H.M., et al. 2012, *The 2010 August 1 type II burst: A CME-CME interaction and its radio and white-light manifestations*, ApJ 748, 66, [39 c, 7 c/y].

Reiner, M.J., Vourlidas, A., St.Cyr, O.C., et al. 2003, *Constraints on CME dynamics from simultaneous radio and white-light observations*, ApJ 590, 533, [63 c, 4 c/y].

Reiner, M.J., Kaiser, M.L., and Bougeret, J.L. 2007, *Coronal and interplanetary propagation of CME/Shocks from radio, in situ and white-light observations*, ApJ 663, 1369, [45 c, 4 c/y].

Pohjolainen, S., van Drie-Gesztelyi, L., Culhane, J.L. 2007, *CME propagation characteristics from radio observations*, SoPh 244, 167, [40 c, 4 c/y].

Shen, C., Liao, C., Wang, Y., et al. 2013, *Source region of the decameter-hectometric type II radio burst: Shock-streamer interaction region*, SoPh 282, 543, [20 c, 4 c/y].

Vrsnak, B., Magdalenic, J., and Zlobec, P. 2004, *Band-splitting of coronal and interplanetary type II bursts. III. Physical conditions in the upper corona and interplanetary space*, A&A 413, 753, [73, 5 c/y].

(15.10) MHD Simulations of CME Propagation

Chen, P.F., Wu, S.T., Shibata, K., et al. 2002, *Evidence of EIT and Moreton waves in numerical simulations*, ApJ 572, L99, [210 c, 14 c/y].

Chen, P.F., Fang, C., and Shibata, K. 2005a, *A full view of EIT waves*, ApJ 622, 1202, [152 c, 12 c/y].

Chen, P.F., Ding, M.D., and Fang, C. 2005b, *Synthesis of CME-associated Moreton and EIT wave features from MHD simulations*, SSRv 121, 201, [31 c, 2 c/y].

Cohen, O., Attrill, G.D.R., and Manchester, Ward B.IV. et al. 2009, *Numerical simulation of an EUV coronal wave based on the 2009 February 13 CME event*, ApJ 705, 587, [108 c, 13 c/y].

Delannee, C., Török, T., Aulanier, et al. 2008, *A new model for propagating parts of EIT waves: A current shell in a CME*, SoPh 247, 123, [99 c, 10 c/y].

Downs, C., Roussev, I.I., van der Holst, B., et al. 2011, *Studying EUV transients with a digital laboratory: Direct comparison of EUV observations to global MHD simulations*, ApJ 728, 2, [75 c, 12 c/y].

Downs, C., Roussev, I.I., van der Holst, B., et al. 2012, *Understanding SDO/AIA observations of the 2010 June 13 EUV wave event: Direct insight from a global thermodynamic simulation*, ApJ 750, 134, [51 c, 9 c/y].

Groth Clinton P.T., DeZeeuw, D.L., Gombosi, T.I., et al. 2000, *Global 3-D MHD simulation of a space weather event: CME formation, interplanetary propagation, and interaction with the magnetosphere*, JGR 105, A11, 25053, [126 c, 7 c/y].

Jin, M., Manchester, W.B., van der Holst, B. 2017a, *Chromosphere to 1 AU simulation of the 2011 March 7th event: A comprehensive study of coronal mass ejection propagation*, ApJ 834, 172, [12 c, 12 c/y].

Jin, M., Manchester, W.B., van der Holst, B. 2017b, *Data-constrained coronal mass ejections in a global MHD model*, ApJ 834, 173, [14 c, 14 c/y].

Low, B.C. 2001, *Coronal mass ejections, magnetic flux ropes, and solar magnetism*, JGR 106, A11, 25141, [284 c, 17 c/y].

Manchester, W.B., Gombosi, T.I., Roussev, I., et al. 2004, *Modeling a space weather event from the Sun to the Earth: CME generation and interplanetary propagation*, JGR 109/A2, A012107, [144 c, 11 c/y].

Manchester, W.B.IV., Vourlidas, A., Toth, G., et al. 2008, *3-D MHD simulation of the 2003 October 28 coronal mass ejection: Comparison with LASCO coronagraph observations*, ApJ 684, 1448, [83 c, 9 c/y].

Odstrcil, D., Riley, P., and Zhao, X.P. 2004, *Numerical simulation of the 12 May 1997 interplanetary CME event*, JGR 109, A2, A02116, [123 c, 9 c/y].

Ofman, L. and Thompson, B.J. 2002, *Interaction of EIT waves with coronal active regions*, ApJ 574, 440, [129 c, 8 c/y].

Riley, P., Linker, J.A., Mikic, Z., et al. 2003, *Using an MHD simulation to interpret the global context of a coronal mass ejection observed by two spacecraft*, JGR 108, A7, 1272, [69 c, 5 c/y].

Wang, H., Shen, C., and Lin, J. 2009, *Numerical experiments of wave-like phenomena caused by the disruption of an unstable magnetic configuration*, ApJ 700, 1716, [73 c, 9 c/y].

Wang, Y.M. 2000, *EIT waves and fast-mode propagation in the solar corona*, ApJ 543, L89, [158 c, 9 c/y].

Wu, S.T., Zheng, H., Wang, S., et al. 2001, *3-D numerical simulation of MHD waves observed by the EIT*, JGR 106, A11, 25089, [149 c, 9 c/y].

Chapter 16
Sun-Earth Connections

16.1 The Slow Solar Wind

The solar wind permeates the heliosphere and influences the near-Earth ("space weather") environment. While it is certain that the *fast solar wind* originates in coronal holes, the question where and how the *slow solar wind* is formed, remains an outstanding puzzle in solar physics, even in the new millennium (for a review of the slow solar wind see Abbo et al. 2016).

The slow speed solar wind as measured at the Earth orbit and beyond is characterized by its velocity ($v \approx 400$ km s^{-1}), by its coronal composition (of nearly 40 ion species of He, C, N, O, Ne, Mg, Si, S, Fe; von Steiger et al. 2000), and by its frozen-in temperature from carbon charge-states ($T = (1.4–1.6)$ MK; Feldman et al. 2005). The solar wind is believed to originate very close to the solar surface, but since it is accelerated significantly above the solar surface, its velocity cannot be correlated with remote observations to trace its origin (Feldman et al. 2005). Two physical paradigms emerged in the interpretation of solar wind fluctuations: (i) Fluctuations described as non-interacting Alfvén waves propagating away from sources near the Sun, and (ii) fluctuations due to active, evolving hydrodynamic turbulence. Slow wind streams, which appear to be more fully evolved turbulence, are dominated by quasi-perpendicular fluctuation wave vectors (Dasso et al. 2005). Parametric studies with 1-D MHD simulations for the heating and acceleration in coronal holes by low-frequency Alfvén waves find that both the fast and slow solar winds can be explained by a single process, namely by the dissipation of low-frequency Alfvén waves, which explains the negative correlation between the solar wind speed and the coronal temperature, as well as the larger amplitudes of Alfvénic fluctuations in the fast wind (Suzuki and Inutsuka 2006). From analysis of three polar orbits of *Ulysses* observations, it was found that the slow-wind proton temperature falls less rapidly with distance than the fast wind does, which indicates a source of enhanced heating in the low-speed solar wind (Ebert et al. 2009).

M. J. Aschwanden, *New Millennium Solar Physics*, Astrophysics and Space Science Library 458, https://doi.org/10.1007/978-3-030-13956-8_16

The availability of STEREO data, especially the *Heliospheric Imager (HI)* onboard the STEREO spacecraft, has helped to disentangle the 3-D structure of the solar wind. HI/STEREO data show the variability of the slow solar wind that originates inside and in the vicinity of the streamer belt, exhibiting intermittent mass flows, twisted flux rope structures, V-shaped structures, "blobs", and *co-rotating interaction regions (CIRs)*. These features indicate emergence of flux ropes near helmet streamers, magnetic reconnection at the tip of helmet streamers, or disconnection of open magnetic field lines (Rouillard et al. 2010). Besides the origination of the slow solar wind near streamers, changes of coronal hole boundaries and coronal bright points have also been invoked as possible sources of the slow solar wind (Subramanian et al. 2010). Evidence for two types of slow solar wind has also been been shown in the interplanetary space, one coming from coronal streamers or active regions and characterized by non-Alfvénic structures, and the other being highly Alfvénic and originating from the boundary of coronal holes (D'Amicis and Bruno 2015). While previous studies attributed current sheets to be the main cause of intermittency at ion scales, more recent studies show that a large variety of coherent structures contribute to the intermittency of the slow solar wind (Perrone et al. 2016). Among the intermittent structures seen in the solar wind, an MHD Alfvén vortex was intersected with the *Cluster* spacecraft (Roberts et al. 2016).

The power spectrum of magnetic fluctuations in the solar wind, depends strongly on the type of (slow or fast) wind (Bruno and Telloni 2015). A large spectral change (of the power law slope from -3.75 to -1.75) at proton scales has been observed in high-speed streams that move from fast to slow wind regions (Bruno et al. 2014).

Global magnetic modeling is necessary to unify the apparent difference of standard dipolar streamers and unipolar (or *pseudo-streamers*), both being dipolar when viewed from the "correct" orientation, which has crucial consequences for modeling the slow solar wind speed (Riley and Luhmann 2012). The source of the slow solar wind is not only located in the streamer belt region surrounding the *heliospheric current sheet*, but extends also into a global-wide web of separatrix surfaces (Crooker et al. 2012). The open-field area measured from Hinode data is sufficiently large to account for a significant fraction of the mass loss rate of the slow solar wind (Brooks et al. 2015).

An important defining characteristic of the slow solar wind is the highly variable nature of plasma properties and composition. Periodic density structures have been identified in white-light coronagraph images, which form below $2.5 R_{\odot}$, have periodicities of ≈ 90 min, and occur near streamers, possibly revealing the sources of the slow solar wind (Viall and Vourlidas 2015). Each 90 min parcel of slow wind has near-constant speed yet exhibits repeatable, systematic charge state and composition variations that span the entire range of statistically determined slow solar wind values (Kepko et al. 2016).

A long-standing puzzle is that the slow wind is frequently found far from the *heliospheric current sheet (HCS)*, which poses the conundrum of how the slow wind can originate at or very near the HCS at the Sun, but is found very far from the HCS in the heliosphere. 3-D MHD simulations that mimic a coronal hole with a geometry

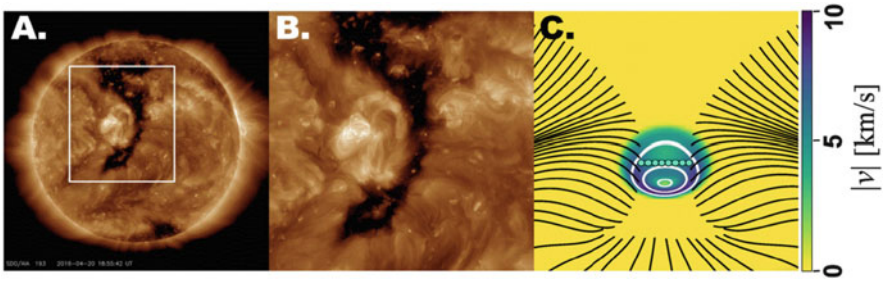

Fig. 16.1 (**a**) EUV image from SDO with (dark) coronal hole extending across the equator. (**b**) Zoom-in of white box from (**a**), showing the equatorial coronal hole connecting with the northern polar coronal hole. (**c**) Simulated S-Web corridor shown with field lines (black), footpoints across the corridor (cyan dots), and driving velocity field (green) in the simulation of Higginson et al. (2017)

that includes a narrow corridor flanked by closed field (Fig. 16.1) produce giant arcs of closed-field plasma that originate at the open-closed boundary in the corona, but extend far from the HCS and span tens of degrees in latitude and longitude at Earth, which apparently solves the HCS conundrum (Higginson et al. 2017).

The solar wind provides information on the isotopic composition for most volatile elements (oxygen, nitrogen, and noble gases) of the solar atmosphere. The difference between fast and slow solar wind has been explained in terms of an isotopic fractionation process, which was found to be in good agreement with the values predicted by the *inefficient Coulomb drag* model (Heber et al. 2012). While some of the slow solar wind parameters show variations during a solar cycle (speed, the C^{+6}/C^{+4} and He/H ratios), other parameters (Fe/O ratios) show very little change, which implies that the solar wind sources cannot be defined by isotopic composition alone (Kilpua et al. 2016). The implications of the deep 2008–2009 solar cycle minimum on the variability of the isotopic composition is discussed in Cliver and von Steiger (2017).

Besides the slow solar wind ($v \approx 400$ km s^{-1}), a so-called *very slow solar wind* with speeds of < 300 km s^{-1} was also discovered, at < 0.7 AU with the *Helios* spacecraft, apparently containing the heliospheric plasma sheet and current sheet, with higher density and lower temperature than the regular slow solar wind (Sanchez-Diaz et al. 2016).

16.2 The Fast Solar Wind

The source regions of the *fast solar wind* (measured with a speed of $v \gtrsim 700$ km s^{-1} at a distance of 1 AU) have been localized early on in polar coronal holes based on the blueshift of He and Ne^{7+} spectral lines (with average Doppler shifts of ≈ 3 km s^{-1}), measured with the *Solar Ultraviolet Measurements of Emitted*

Radiation (SUMER) onboard SOHO (Wilhelm et al. 2000; Tu et al. 2005). The fast solar wind has also been inferred from the Doppler dimming of the intensities of O VI (1032 Å, 1037 Å), and H I Ly α (1216 Å) between 1.5 $R_\odot$ and 3.5 $R_\odot$ with the *Ultraviolet Coronagraph Spectrometer (UVCS)* onboard SOHO, implying an average acceleration of order $a \approx 4.5 \times 10^3$ cm s^{-2} (Antonucci et al. 2000). Furthermore, the UVCS observations revealed surprisingly large temperatures, outflow speeds, and velocity distribution anisotropies for positive ions in coronal holes (for reviews see Cranmer 2002; Zurbuchen and Richardson 2006; Marsch 2006).

Extremely high solar wind speeds have been detected during the 2003 October 29–30 event with the *Solar Wind Electron Proton Alpha Monitor (SWEPAM)* on board the *Advanced Composition Explorer (ACE)* spacecraft, with a value in excess of 1850 km s^{-1} (Skoug et al. 2004), which is more than twice the average fast wind speed. These higher measured speeds were observed following two CME-driven shocks, which apparently were so fast and heavy that slowing down by aerodynamic drag was inefficient.

Coronal holes are not the only locations where the fast solar wind originates. Additional locations of fast solar wind sources have been identified with Hinode/XRT at the edge of active regions, where continuous outflows of soft X-ray emitting plasma along open magnetic field lines was observed, with a total mass loss rate of $\approx 1/4$ of the solar wind (Sakao et al. 2007). From the O^{7+}/O^{6+} ratio measured with ACE, three fast solar wind components were distinguished: a non-transient solar wind from coronal holes, a non-transient solar wind originating from outside of coronal holes, and a transient solar wind component that is associated with interplanetary CMEs (Zhao et al. 2009). Besides the slow and fast solar wind, Stakhiv et al. (2015) postulate a third component of the solar wind, the so-called *boundary wind*, which originates in mid-latitudes between the equatorial slow wind and the polar fast wind, based on the observation that the charge-state distribution is similar to the slow wind, while its elemental composition is coronal hole like.

The propagation of the solar wind has been characterized by the time evolution of velocity distribution anisotropies of electrons and ions. The protons receive about 60% of the total plasma heating in the inner heliosphere, and this fraction increases to 80% by the orbit of Jupiter (Cranmer et al. 2009). Only small differences were observed in the radial dependence for the proton density $n_p(r)$ and magnetic field strength $B(r)$ (Ebert et al. 2009). The observed electron distribution functions consist of three different components: a thermal core, a suprathermal halo (present at all pitch angles), and a sharply magnetic field aligned *"strahl"* that is usually anti-sunward moving. Using data from the Helios, Wind, and Ulysses spacecraft it was concluded that the heliospheric electron halo population consists partly of electrons that have been scattered out of the strahl (Maksimovic et al. 2005). Fluctuations in the *fast solar wind* are dominated by fluctuations with wave vectors quasi-parallel to the local magnetic field, in contrast to the quasi-perpendicular fluctuations for the *slow solar wind* (Dasso et al. 2005). Phase coherence analysis shows the presence of sporadic quasi-parallel Alfvén ion cyclotron waves, as well as coherent structures in

the form of large-amplitude, quasi-perpendicular Alfvén vortex-like structures and current sheets (Lion et al. 2016).

Data from NASA's Genesis space mission returned samples of solar wind collected over 2.3 years. Isotopic compositions of He, Ne, and Ar reveal heavy isotope depletion in the slow solar wind, compared with the fast wind composition, which suggests that fractionation processes between fast and slow solar wind are mass dependent, as it is reproduced by the inefficient Coulomb drag model (Heber et al. 2012).

Earlier estimates of the the magneto-convective energy that is transported upward from the photosphere to the base of the corona by means of Alfvénic waves, revealed amplitudes of 0.5 km s^{-1} to supply the energy flux of (1–2) $\times$ 10^7 erg cm^{-2} s^{-1} to heat the corona. Recent estimates yield evidence for ubiquitous outward-propagating Alfénic motions with amplitudes of order 20 km s^{-1} and periods of order 100–500 s, which is sufficient to accelerate the fast solar wind and to heat the Quiet corona (McIntosh et al. 2011). However, previous measurements of the energy carried and dissipated by Alfvén waves have been unable to quantify the energy lost by the waves, because the line widths depend on both the non-thermal velocity v_{nt} and the ion temperature T_i. A new method that provides a means to separate the T_i and v_{nt} contributions, based on the observations that the waves are undamped at low heights, and that the ion temperatures do not change with height (Fig. 16.2). From this model, an initial energy flux of $(6.7 \pm 0.7) \times 10^5$ erg cm^{-2} s^{-1} was inferred, which is sufficient to heat the coronal hole and to accelerate the solar wind during the years of 2007–2009, where 85% of this energy is dissipated below 2.5 $R_\odot$ (Hahn and Savin 2013).

Comparing the solar cycle minimum 23/24 with historical solar wind records at 1 AU, one finds that this solar minimum has the slowest, least dense, and coolest solar wind, and the weakest magnetic field, but more shocks are produced during

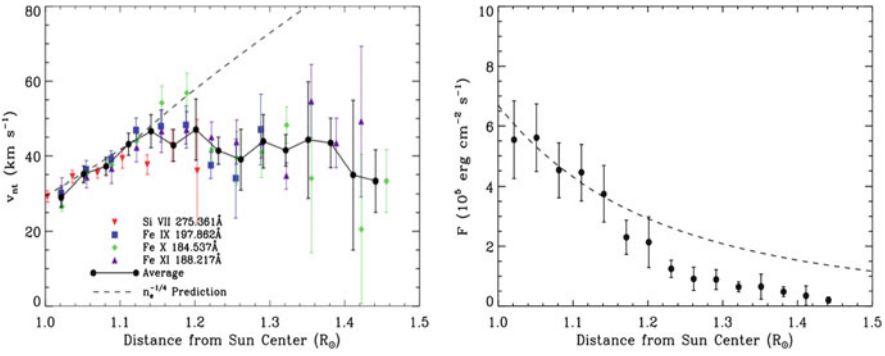

Fig. 16.2 *Left:* The nonthermal velocity v_{nt} is shown for the strongest lines (Si VII, Fe IX, Fe X, Fe XI) as a function of the solar center distance. The dashed line illustrates the predicted electron density $n_e^{1/4}$ trend for undamped waves. *Right:* Wave energy density flux F as a function of height (filled circles). The dashed curve illustrates the predicted trend for undamped waves (Hahn and Savin 2013)

the solar minimum, probably caused by the slower fast magnetosonic speed of the solar wind (Jian et al. 2011; de Toma 2011). Compared to typical values observed during 1970–1990, the following proton parameters are lower on average during 2009–2013: solar wind speed and beta ($\approx$ 11%), temperature ($\approx$ 40%), thermal pressure ($\approx$ 55%), mass flux ($\approx$ 34%), momentum flux or dynamic pressure ($\approx$ 40%), energy flux ($\approx$ 48%), interplanetary magnetic field (IMF) ($\approx$ 31%), and radial component of the IMF ($\approx$ 38%) (McComas et al. 2013). Comparing with the Maunder minimum (1650–1710), the solar wind shows a factor 2 reduction in near-Earth heliospheric magnetic field strength and solar wind speed, and up to a factor 4 increase in solar wind Mach number (Owens et al. 2017).

16.3 Solar Wind Models

In-situ measurements of the solar wind and remote sensing observations of coronal holes strongly indicate resonant interaction with ion-cyclotron waves as the responsible mechanism for heating and acceleration of coronal hole ions to generate the fast solar wind (Hollweg and Isenberg 2002). The plasma response to the resonant dissipation of ion-cyclotron waves is often approximated by treating the ion populations as fluids (protons, electrons, and heavy ions), while the resonant interaction (in a nearly collisionless extended corona) is most accurately treated by kinetic theory (Hollweg and Isenberg 2002; Cranmer 2002; Marsch 2006). In one MHD turbulence model, ions are energized by the dissipation of ion-cyclotron resonant waves, but such high-frequency small-wavelength fluctuations have never been observed. A turbulent cascade is one possibility of generating small-scale fluctuations from a pre-existing population of low-frequency MHD waves, but for the most realistic values of advection and diffusion in an MHD cascade, there is insufficient power to heat protons and heavy ions (Cranmer and van Ballegooijen 2003). However, a coupling between the fast MHD mode and the Alfvén mode to excite high-frequency ion-cyclotron resonance is possible, which is efficient at heating protons and other ions in the direction perpendicular to the background magnetic field (Cranmer and van Ballegooijen 2012). Nevertheless, a direct signature that Alfvén-cyclotron waves are ubiquitous in solar wind turbulence has not yet been found (He et al. 2011).

However, a new ingredient is the reflection of Alfvénic waves (Cranmer and van Ballegooijen 2005), which produces a Kolmogorov-like spectrum (Fig. 16.3) that does not change dramatically from the photosphere to the solar wind (Verdini and Velli 2007). The model of Verdini et al. (2010) demonstrates solar wind acceleration due to heating by a quasi-incompressible turbulent cascade triggered by coronal stratification and supplemented by compressive heating near the coronal base. The turbulent cascade causes the power anisotropy at smaller scales: close to $k^{-5/3}$ across, and k^{-2} along the local magnetic field, consistent with critically balanced Alfvénic turbulence (Wicks et al. 2010), while the first measurements of the scale-dependent power anisotropy of Elsasser variables in imbalanced fast solar wind

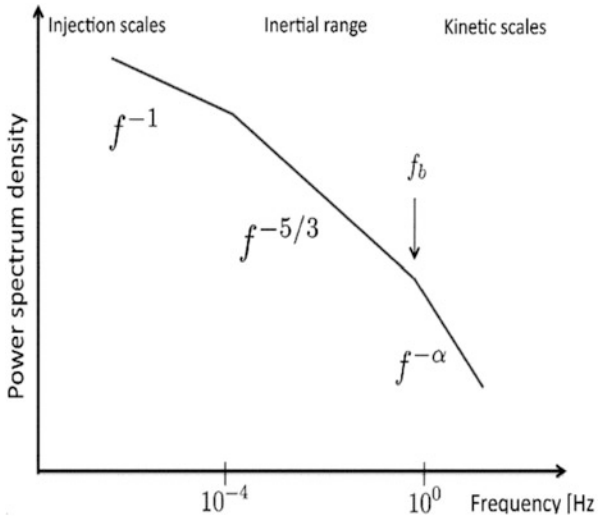

Fig. 16.3 Generic Kolmogorov turbulence spectrum with a power law slope of $-5/3$ in the inertial range

turbulence show that the dominant Elsasser mode is isotropic at low frequencies, but becomes increasingly anisotropic at higher frequencies (Wicks et al. 2011).

Self-consistent solutions that combine (i) chromospheric heating driven by an empirically guided acoustic wave spectrum; (ii) coronal heating from Alfvén waves that have been partially reflected, then damped by anisotropic turbulent cascade; and (iii) solar wind acceleration from gradients of gas pressure, acoustic wave pressure, and Alfvén wave pressure, have been obtained that produce a range of slow and fast solar wind conditions (Cranmer et al. 2007).

The inertial range of solar wind turbulence consists of a mixture of incompressible and compressible motions, with at least 90% of the energy due to the incompressible component, such as the Alfvén mode. Observations show that the compressible component of inertial range solar wind turbulence is primarily in the kinetic *slow mode*, which has the consequence that the kinetic Alfvén wave mode is favored for the cascade of kinetic turbulence to short wavelengths (Howes et al. 2012). The energy cascade rate in the inertial range of solar wind turbulence has been derived for compressible, isothermal MHD turbulence, for the fast and slow solar wind, and it was found that the energy cascade rate is amplified particularly in the slow solar wind (Hadid et al. 2017).

Models of the solar wind proton temperature anisotropy have been attempted with the Vlasov linear theory. In the slow solar wind the observed proton temperature anisotropy seems to be constrained by oblique instabilities, by the mirror instability and the oblique fire hose instability, contrary to the results of the linear theory which predicts a dominance of the proton cyclotron instability and the parallel fire hose instability (Hellinger et al. 2006). The simulations of perpendicular

ion heating by low-frequency Alfvén wave turbulence show anisotropic heating, while Landau damping and transit-time damping of *kinetic Alfvén waves (KAWs)* lead to strong parallel heating of protons (Chandran et al. 2010). Hellinger et al. (2011) report that parallel cooling and perpendicular heating is required close to the Sun, while heating in both directions is needed at a distance of 1 AU. The fast solar wind turbulence may be populated by KAWs, small-scale current sheets, and Alfvén vortices at ion kinetic scales (Roberts et al. 2013), kinetic slow and ion-Bernstein modes, coherent structures with very small intrinsic frequencies, and nonlinear or sideband modes (Roberts et al. 2017). New proposed dissipation mechanisms in MHD turbulence comprise the proton Landau damping of the quasi-perpendicular kinetic slow mode, which has a different Alfvén resonance parameter, the proton Landau resonance parameter, magnetic compressibility, and the electric field polarization of the kinetic Alfvén mode (Narita and Marsch 2015).

3-D MHD numerical models of a realistic ambient and transient solar wind include global 3-D interaction of a CME propagating in a structured background solar wind and merging of coronal and heliospheric models to track CMEs, which are increasingly used for space weather forecasting near Earth (Odstrcil 2003). The 3-D *Solar-InterPlanetary Conservation Element / Solution Element MHD (SIP-CESE MHD)* model achieves solar wind simulations with time-dependent boundary conditions (Feng et al. 2010). The photospheric boundary conditions has also been modeled in terms of a separatrix-web concept (Antiochos et al. 2011). Another choice of the photospheric boundary was made by assuming that MHD Alfvén wave turbulence and its nonlinear dissipation to be the only momentum and energy source for heating the coronal plasma and driving the solar wind (Sokolov et al. 2013). A 2.5-D MHD simulation reproduced the propagation and dissipation for Alfvén waves in the solar atmosphere *ab initio*, i.e., without any initial corona or solar wind (Matsumoto and Suzuki 2014).

1-D MHD codes have been used to simulate outgoing Alfvén waves which contribute to coronal heating and acceleration of the fast solar wind, mainly by the nonlinear generation of compressive waves and shocks (Suzuki and Inutsuka 2005, 2006).

16.4 Heliospheric Magnetic Structures

There are a number of magnetic structures or processes occurring in the heliosphere, such as the heliospheric magnetic field (Owens and Forsyth 2013; Lockwood 2013), *the heliospheric current sheet (HCS)*, the background fast and slow solar wind, magnetic clouds, interplanetary flux ropes, the Parker spiral, *co-rotating interaction regions (CIR)*, magnetic reconnection in the solar wind, and turbulent regions.

Magnetic fields of the inner heliosphere (30 $R_\odot$ to 5 AU) are often modeled solely based on extrapolation from line-of-sight photospheric magnetograms (Fig. 16.4), using synoptic maps from an entire solar rotation (e.g., Riley et al. 2001, 2011). There are open questions, such as: What are the global properties of the

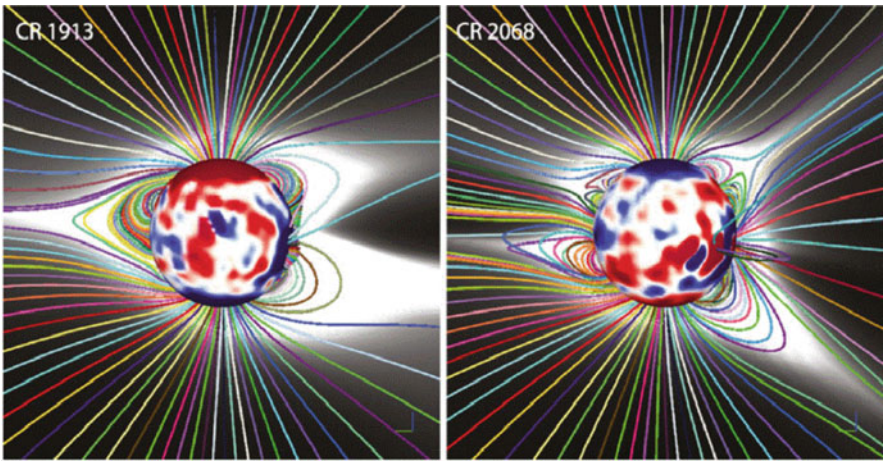

Fig. 16.4 Composite images of the photospheric magnetic field at the solar surface (saturated at ± 1 G, with a selection of magnetic field lines originating in the plane of the paper, and a color contour of the coronal density (scaled by r^2) for Carrington rotations CR1913 (left) and CR2068 (right), produced by the 3-D time-dependent algorithm *MHD Algorithm outside a Sphere (MAS)*, (Riley et al. 2011)

HCS near solar maximum? and How faithfully are they reproduced by *potential field source surface models (PFSS)*? (Smith 2001). While the heliospheric field is mostly fed by the open fields from coronal holes, active regions were found to contribute to the total absolute magnetic flux from $\lesssim$ 10% at the solar cycle minimum up to 50% during the maximum, sometimes with direct connections from sunspots to the heliosphere (Schrijver and DeRosa 2003). At larger coronal and heliospheric heights, a comparison between MHD models and PFSS models was carried out by Riley et al. (2006), which demonstrated that PFSS solutions often closely match MHD results for configurations based on untwisted coronal fields, but more significant differences are expected when magnetograms are used rather than vector data (Riley et al. 2006). Later it was confirmed that the PFSS model cannot account for the magnetic field of dynamic structures, such as the toroidal/axial flux component of an interplanetary (streamer-blowout) coronal mass ejection (Lynch et al. 2010). Also the agreement between flare locations and type III bursts using the PFSS model was found not to be satisfactory, either due to the inadequacy to reproduce the coronal magnetic field above evolving active regions, or due to the lack of a simultaneous full-surface magnetic map (Nitta and DeRosa 2008). Interplanetary magnetic field comparisons during low activity (during solar cycle minima) imply that the PFSS source surface radius should be lowered to $\approx$ 1.5–1.8 solar radii (Lee et al. 2011), or raised by 15%–30% during the solar minimum (Arden et al. 2014). Applications of the PFSS model during the solar minimum provided key evidence of the coronal field restructuring (Liu et al. 2009). Comparisons between the PFSS and the *current sheet surface (CSSS)*

model demonstrated that a source surface located at $\geq 10 R_\odot$ and a cusp surface at $1.7 R_\odot$ yields the best agreement, which certifies the CSSS model to produce a good extrapolation of the heliospheric field, based on solar surface data (Schüssler and Baumann 2006).

An alternative method to measure the magnetic field in the outer solar corona and heliosphere is the measurement of *Faraday rotation*, which can be accomplished with spacecraft on the far side of the Sun or with astrophysical pulsars. An experiment with pulsar PSR B0950+08 in 2015 August, compared with visible light coronagraph data, yielded an upper limit of the magnetic field and electron densities in agreement (Howard et al. 2016).

While the solar wind has a steady-flowing background component, there occur superimposed transient events, so-called *magnetic clouds*, which are defined as a region of enhanced magnetic field strength, smooth rotation of the magnetic field vector, and low proton temperature. Earth-directed halo *coronal mass ejections (CMEs)* were found to be associated with magnetic clouds, shocks, and geomagnetic storms (Webb et al. 2000a), with a higher percentage near solar minimum (Cane and Richardson 2003). The magnetic flux of magnetic clouds is found to be correlated with the total magnetic reconnection flux (Qiu et al. 2007).

The two footpoints of a halo CME-associated flux rope expand earth-ward into the solar wind and form a magnetic cloud that is detectable upstream the Earth (Webb et al. 2000a). The smallest magnetic cloud source region ever observed had a sigmoidal geometry with a size of $\approx$ 30 Mm and a magnetic flux of $F_z \approx 10^{19}$ Mx (Mandrini et al. 2005).

Evidence for local magnetic reconnection in the solar wind has been obtained from accelerated ion flows observed within magnetic field reversal regions in the solar wind, using ACE data, consistent with the Walen relationship, which relates changes in flow velocity to density-weighted changes in the magnetic field vector (Gosling et al. 2005), implying a magnetic reconnection X-line extending more than 390 Earth radii in the solar wind (Phan et al. 2006).

The orientation of a *magnetic interplanetary flux rope* was found to be consistent with that of the expelled filament (disappearing in the solar corona) in a geoeffective event, which implies that the geoeffectiveness depends also on the magnetic helicity (Yurchyshyn et al. 2001).

CMEs expel magnetic fields into the interplanetary medium and produce shocks. If both, *ejecta* and *shocks* are present, the resulting cosmic ray event is called a *"classical, two-step" Forbush decrease* (Cane 2000).

Magnetic flux buildup in the heliosphere from CMEs requires timescales of $\approx$ 50 days in order to match the observed doubling in the magnetic field intensity at 1 AU over a solar cycle (Owens and Crooker 2006).

First imaging of CIRs was accomplished with the HI/STEREO cameras, revealing the formation of a CIR where the fast solar wind from an equatorial coronal hole is interacting with the slow solar wind from the streamer belt (Rouillard et al. 2008). A succession of solar wind wave fronts sweeping past Earth were observed with the HI-2/STEREO cameras from distance, synchronized with the Earth-detected arrival of density enhancements at the leading edges of high-speed solar wind streams

(Sheeley et al. 2008). Synoptic views of Earth-directed CMEs (Harrison et al. 2008), Earth-impacting CMEs (Davies et al. 2009), or other solar transients propagating to 1 AU can be tracked with HI/STEREO time-elongation plots (Davies et al. 2009).

On the outermost scale of the heliosphere, the local interstellar medium, the inner heliosheath, the termination shock, and the heliopause are explored with *Voyager 1* and 2. It is speculated that the reasons for the recent decrease in the termination shock particles (ions accelerated to anomalous cosmic-ray energies) flux observed by *Voyager 1* is caused by the variability of the solar cycle (Pogorelov et al. 2013).

16.5 Impulsive SEP Events

Evidence for two different physical mechanisms for acceleration of *solar energetic particles (SEPs)* has been accumulated over the last 50 years, leading to the paradigm of two sources: (i) flare-accelerated particles that are associated with type III bursts, called *impulsive SEP events*, and (ii) shock-accelerated particles that are accompanied by type II bursts, called *gradual SEP events* (Reames 2013). CME-driven shocks appear to be the dominant acceleration mechanism of relativistic electron events, but most near-relativistic electron events result from flares (Kahler 2007). The CME speed and the soft X-ray fluence were found to be well-correlated, consistent with the *big-flare syndrome*, which entails in large SEP events also correlations between flare-related electron acceleration, CME shock-driven acceleration, protons, and near-relativistic electrons populations (Trottet et al. 2015). The probability of observing SEPs at Earth increases with flare intensity, more western location, higher CME speed, and halo CMEs (Dierckxsens et al. 2015). A catalog of 314 SEP events with properties has been compiled by Papaioannou et al. (2016).

Flare-accelerated particles that contribute to impulsive SEP events, are commonly attributed to a resonant stochastic acceleration process, which occurs during magnetic reconnection and involves open magnetic field lines (in order to enable transport of SEP particles to 1 AU), and accelerates not only electrons, but also produces 1000-fold enhancements of ^{3}He/^{4}He and 10-fold enhancements of Fe/O (Reames 2013). Impulsive SEP events originate in a coronal flare site, which subtends a small angle, while gradual SEP events show extensive acceleration that can fill half of the inner heliosphere, beginning when the shock reaches $\approx 2R_\odot$ (Reames 2013). The longitudinal spread of the 2010 January 17 SEP event covered nearly 360° at 1 AU (Dresing et al. 2012), which is also the case in other circumsolar SEP events (Gomez-Herrero et al. 2015; Klassen et al. 2016). The large longitudinal range could be due to pecularities of the magnetic field in the corona, due to a broad accelerator, due to cross-field transport of the particles (which might be expected to be similar for both impulsive and gradual events), or due to a combination of these processes (Salas-Matamoros et al. 2016). In addition, an association between the longitudinal extent of the perturbed corona and the longitudinal extent of the SEP event in the heliosphere was found (Rouillard et al 2012).

A timing analysis of SEP events observed with the WIND spacecraft in the energy range of $\approx$ 30 keV to 6 MeV revealed two different classes of proton events, which were interpreted in terms of flare-associated and CME-shock-associated acceleration (Krucker and Lin 2000). A comparison of the $>$ 500 keV peak electron intensity versus the $>$ 10 MeV peak proton intensity confirms the dichotomy of two distinct populations (flare vs. CME-shock) for well-connected SEP events, based on their e/p ratios, trans-Fe enhancements, and association with decameter-hectometric type II radio bursts (Cliver and Ling 2007). A statistical study of 1191 solar electron events observed by the WIND instrument from 1 keV to $\geq$ 300 keV revealed a 98.75% association rate with type III radio bursts (Wang et al. 2012).

Two types of SEP events were also inferred from the abundance ratios of (Fe/O), which was found to be higher for flare-associated SEP events and lower for shock-associated SEP events (Cane et al. 2003).

The *solar particle release time (SPR)* (or time-of-flight method) of 16 GLE events was found to vary from 1.1 to 2.2 AU in 13 events (Fig. 16.5). The SPR times occur after the onset of the shock wave-induced type II radio bursts, and the distribution of source longitudes had a wide span, as expected from CME-shock acceleration models (Reames 2009a), and similarly for historic GLE events (Reames 2009b). In the 2013 May 22 SEP event, which was a CME-CME interaction event, the SPR times for electrons and protons where found to be close at the time of CME-CME or shock-CME interaction (Ding et al. 2014). However, a statistical study of SEP events found no differences among the transient, fast, and slow solar wind streams for SEP 20 MeV proton event time scales (Kahler and Vourlidas 2014).

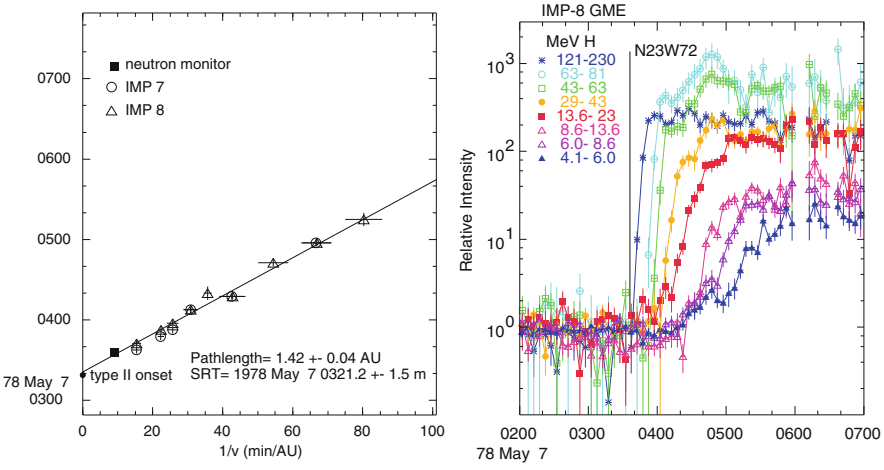

Fig. 16.5 Example of a velocity dispersion (or time-of-flight) measurement of GLE arrival times of protons at IMP-7, IMP-8, or neutron monitors (y-axis in left panel) versus the reciprocal velocity (1/v) (x-axis in left panel), which allows to extrapolate the energy release time t_{SPR} at the source location ($1/v \mapsto 0$), for the GLE event of 1978 May 7. The timing of the relative intensity of the protons with different energies is shown in the right-hand-side panel (Reames 2009b)

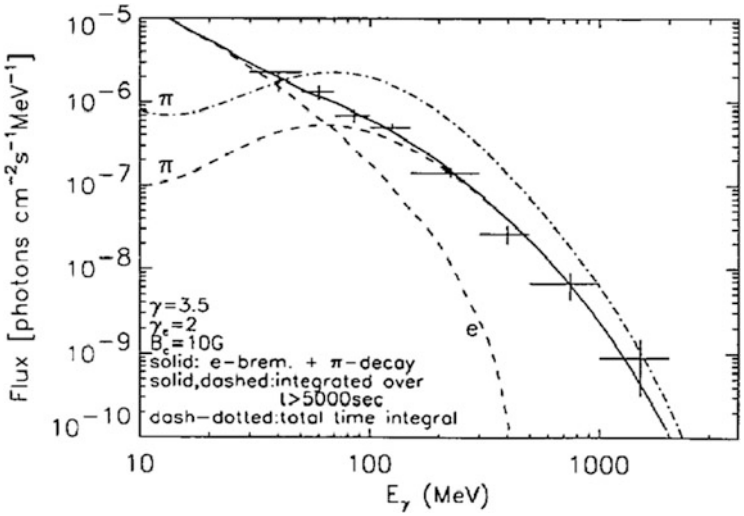

Fig. 16.6 A gamma-ray spectrum observed with EGRET/CGRO during the GLE event on 1991 June 11, 02:04 UT flare, accumulated during 03:26:06:00 UT. The spectrum is fitted with a combination of primary electron bremsstrahlung and pion-decay radiation. Note that pion decay is dominant at energies $\gtrsim$ 40 MeV (adapted from Mandzhavidze and Ramaty 1992)

The extreme event of 2005 January 25 exhibited gamma-rays up to 200 MeV and produced a *ground-level enhancement (GLE)* event with π^0-decay emission (Fig. 16.6), preceded by a co-spatial flare of similar energy but without a GLE event, and thus appears to be the main acceleration mechanism for sub-relativistic electrons and protons, rather than the CME shock (Grechnev et al. 2008) Although flare-accelerated particles were found to be ^{3}He-rich (e.g., Murphy et al. 2016) and Fe-rich, a long-standing problem is that the expected charged secondaries (^{2}H, Li, Be, B) have never been detected in-situ along with gamma-ray bursts.

In the largest solar proton events ($>$ 25 MeV), type III emissions occur after the impulsive phase, which possibly could be due to a change in chemical composition (Cane et al. 2010).

Ground level enhancement (GLE) events represent the most energetic class of SEP events, requiring acceleration processes to produce $\gtrsim$ 1 GeV ions (Fig. 16.6) in order to produce showers of secondary particles in the Earth's atmosphere with sufficient intensity to be detected by ground level neutron monitors, above the background of cosmic rays. In a statistical study of 12 GLE events, the timing was consistent with a flare origin for 50% of the events (Aschwanden 2012). From the 16 GLE events during solar cycle 23 it was found that $\approx$ 50% have properties in common with impulsive ^{3}He-rich SEP events, which contribute to the seed population accelerated by CME-driven shocks (Mewaldt et al. 2012).

16.6 Gradual SEP Events

While impulsive *solar energetic particle (SEP)* events are attributed to acceleration of particles in the coronal flare site (Sect. 16.5), *gradual SEP events* are interpreted in terms of acceleration in coronal and interplanetary shock waves (Fig. 16.7), generally accompanied by shock signatures in radio type II bursts (Reames 2013). Essentially all type II bursts in the decameter-hectometric wavelength range are associated with SEP events (Gopalswamy et al. 2008). Gradual events produce by far the highest SEP intensities near Earth. Shock acceleration occurs as ions are scattered back and forth across the shock by resonant Alfvén waves amplified by the accelerated protons themselves as they stream away (Reames 2013). Behind the shock develops a large "reservoir" of trapped SEPs, which provide a seed population for acceleration by a second CME-driven shock wave (in the case where a faster CME overtakes a slower one; Sect. 15.6). Further evidence for CME-driven shock acceleration comes also from the abundances detected by in situ solar wind or coronal plasma, rather than from high-temperature flare material. The kinetic energy of SEPs is found to amount to a significant fraction of the CME kinetic energy in large SEP events, which implies that shock acceleration must be relatively efficient in those SEP events (Mewaldt et al. 2005).

A correlation of peak intensities of SEP events with the speeds of the associated CMEs is expected in a CME-driven shock acceleration model, but the data reveal a scatter over 4 orders of magnitude, as well as no strong correlation between SEP

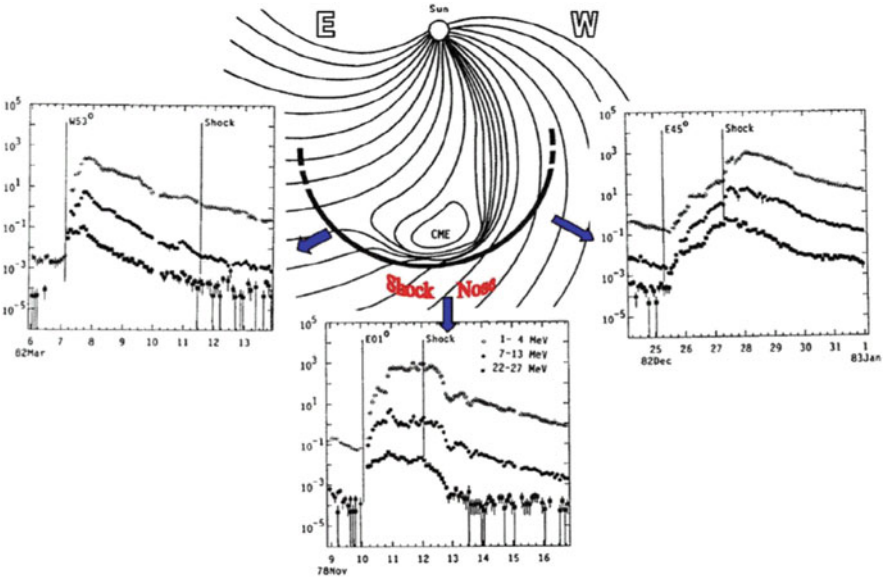

Fig. 16.7 Typical intensity vs. time plots seen for a gradual SEP event viewed from three different solar longitudes relative to the CME shock wave (Reames 2013)

spectral hardening and SEP peak intensity (Kahler 2001; Kahler et al. 2001). This lack of expected correlations could be explained by the fact that SEPs provide only sources of energetic seed particles for the shock acceleration process. Nevertheless, the SEP intensity is better correlated with the CME speed than with the X-ray flare class (Gopalswamy et al. 2003), while intensities of energetic electrons are better correlated with flare size than with CME speed (Gopalswamy et al. 2004). *Ground-level enhancement (GLE)* events are a subset of SEP events, but show essentially the same behavior (for a review of GLE events during Cycle 23 see Gopalswamy et al. 2012a; or Cycle 24 in Gopalswamy et al. 2014a). The solar cycle 24 showed an anomalous expansion of CMEs, which implied a reduced pressue and a weaker magnetic field, and consequently a lack of SEPs accelerated to very high energies (Gopalswamy et al. 2014b).

Near-relativistic electrons measured by ACE, *Proton*, and *Alpha Monitor* revealed delayed ($\approx$ 10 min) injection that is consistent with acceleration of the escaping near-relativistic electrons by an outgoing coronal shock ($v \approx 1000$ km s^{-1}) launched near the time of the prompt electromagnetic emissions of radio type III bursts (Haggerty and Roelof 2002). A kinematic study of the 2012 May 17 GLE event exhibited relativistic protons to be released $\approx$ 10 min later than the electrons, probably accelerated by the CME-driven shock when it travels to $\approx 3R_{\odot}$ (Li et al. 2013).

Statistics on SEP production during CME-CME interactions reveals that a faster CME overtakes a slower one within heliocentric distances of $\approx 20R_{\odot}$, and that fast CMEs (with a speed of > 900 km s^{-1}) and wide CMEs ($> 60°$) are 4 times more likely to be preceded by CME-CME interaction (Gopalswamy et al. 2002). The efficiency of the CME-driven shock thus is enhanced as they propagate through the preceding CMEs and they accelerated SEPs from the material of the preceding CMEs, rather than from the quiet solar wind.

An analysis of elemental abundances (C/O and Fe/O ratios) in 72 interplanetary shocks is found to be inconsistent with shock acceleration of ions originating mainly from the bulk solar wind or a suprathermal tail, but rather requires a seed population that is previously accelerated in impulsive and gradual SEPs, and it is also found that higher rigidity ions are less efficiently accelerated by shocks than lower rigidity ions (Desai et al. 2003). The C/O and Fe/O abundances were found to be enhanced with increasing mass-to-charge M/Q ratio, but since ions with higher M/Q ratios are accelerated less efficiently by shocks, the actual Fe/O ratios decrease with increasing energy (Desai et al. 2006). In extreme events, enhanced wave power enables faster CME shocks to accelerate impulsive suprathermal ions more efficiently than ambient coronal ions (Desai et al. 2016b). SEP spectral properties result from many complex and competing effects, namely Q/M-dependent scattering, shock properties, and the origin of the seed populations, which must be taken into account to develop a comprehensive picture of CME-driven shock acceleration of large gradual SEP events (Desai et al. 2016a).

While gradual SEP events generally have been associated with CME-driven shock acceleration (Reames 2013), some newly found correlations between the sizes

of X-ray and/or microwave bursts with associated (proton) SEP events led to a more flare-centric paradigm shift (Grechnev et al. 2015; Cliver 2016).

A theoretical model of particle acceleration at a propagating, evolving interplanetary shock is presented by Zank et al. (2000), which includes the determination of the particle injection energy (into the diffusive shock acceleration mechanism), the maximum energy of particles accelerated at the shock, energetic particle spectra at all spatial and temporal locations, and the dynamical distribution of particles that escape upstream and downstream from the evolving shock complex. In another analytical model based on quasi-linear theory, the upstream ion transport is described by the two-stream moments of the focused transport equation, which accomodate the large streaming anisotropies observed near event onset, and the model includes diffusive shock acceleration, ion advection with the solar wind, spatial diffusion upstream of the shock, magnetic focusing, wave excitation by the energetic protons, and minor ions as test particles (Lee 2005). The predictions reproduce the observed phases of most gradual SEP events: onset, a plateau with large streaming anisotropy, and energetic storm particle enhancement prior to shock passage, and the decaying invariant spectra after shock passage (Lee 2005). Analytical modeling is complemented with numerical simulations with the ENLIL code, from the Sun at $\approx 10 R_{\odot}$ to 1 AU and beyond, yielding shock compression ratios that are compared with STEREO data (Rouillard et al. 2011), or with the BATS-R-US code, which reveals strong acceleration in sheath regions immediately behind the shock (Kozarev et al. 2013).

16.7 Geomagnetic Storms

Geomagnetic storms are temporary disturbances in the Earth's magnetosphere that are caused by *coronal mass ejections*, solar flares, solar wind transients (shock waves), solar energetic particles (accelerated in CME shocks), or *ground level enhancements (GLE)* (produced by $\gtrsim 1$ GeV particles). Since CME-driven shocks propagate with typical speeds of $v \approx$ 1000–2000 km s^{-1}, geomagnetic storms commence about 20–40 hours after the impulsive phase of a solar flare.

Although front-side halo CMEs (detected by LASCO/SOHO) generally precede geomagnetic storms, three quarters of halo-CMEs do not produce even moderate geomagnetic activity, which has been explained by the facts that only half of the CMEs encounter the Earth, and that the geoeffectiveness of ejecta strongly depends on the southward magnetic field strength B_z (Cane et al. 2000), as well as on the initial speed of the CME, and the ram pressure (Srivastava and Venkatakrishnan 2004). All unipolar *magnetic clouds* (defined by the inclination angle $\gtrsim 45°$ relative to the ecliptic plane) with the magnetic field southward at the axis are found to be geoeffective, while those with the field pointing northward did not cause magnetic storms at all (Huttunen et al. 2005).

The sources of geomagnetic storms are fast solar wind structures in the form of CME-related, co-rotating high-speed streams, as well as slow wind structures,

but 97% of the most intense storms (defined by the geomagnetic K_p index) are generated by fast transient structures associated with CMEs, while the slow solar wind generates a small fraction of weaker storms only (Richardson et al. 2001). About 71% of all front-side halo-CMEs are geoeffective, while the most intense geomagnetic storms are produced when there are successive CMEs (Gopalswamy et al. 2007). A statistical study of 132 Earth-directed halo-CMEs confirmed that 45% caused geomagnetic storms with $K_p \geq 5$ (with a maximum of 9), that halo-CMEs accompanied by solar flares are more geoeffective, and that a significant correlation exists between the CME speed and the transit time for severe geomagnetic storms (with $K_p \geq 7$) (Wang et al. 2002), which has been quantified by $T[\text{hrs}] = 96 - (v[\text{km s}^{-1}]/21)$, with an average speed of $v \approx 700$ km s^{-1} and Sun-Earth transit time of $T = 64$ hrs (Zhang et al. 2003).

Halo-CMEs are mostly located under the bipolar coronal streamer belt, sandwiched between coronal holes of opposite magnetic polarity. The inclination of the heliospheric current sheet increases towards solar maximum, and this way explains the solar cycle effect of the geoeffectiveness of front-side halo-CMEs (Zhao and Webb 2003).

The most extreme geomagnetic storm in history occurred on 1859 September 1–2, which had an associated intense magnetic cloud ejection leading to a geomagnetic storm with a *disturbance storm index* of $D_{st} \approx -1760$ nT, and a local noon magnetic response of $\Delta H = 1600 \pm 10$ nT (Tsurutani et al. 2003). Another extreme ionospheric response to the large interplanetary electric fields occurred during the so-called *"Halloween" storms* during 2003 October 20–30, when $\approx$ 40% and $\approx$ 250% increases of the day-site total electron content were registered (Mannucci et ãl. 2005). This geomagnetic storm-time phenomenon of promptly penetrating electric fields is thought to be a contributing cause of these electron content increases, where the day-side ionospheric uplift, combined with equatorial plasma diffusion along magnetic field lines to higher latitudes, creates a *" day-time super-fountain" effect.* The biggest CME since the Halloween storm occurred on 2006 December 13, which produced the largest shock extent ever detected, i.e., 74° in latitude and 117° in longitude (Fig. 16.8; Liu et al. 2008). During the 2015 March 15 geomagnetic storm, being the largest event during cycle 24, the following prerequisites have been identified: (i) a CME with strong southward magnetic fields both in the sheath and in the ejecta was followed by a high-speed stream from a nearby coronal hole, and (ii) preceding slow and high-density solar wind was piled up ahead of the CME just before the arrival at Earth, and (iii) enhanced solar wind speed, magnetic field, and density worked all together to drive the major magnetic storm (Kataoka et al. 2015; Liu et al. 2015).

The flux enhancements of ring current electrons and ions at the L-shell location of $L > 3.5$ (Earth radii) during the recovery phase of a geomagnetic storm largely depend on the solar wind structure, while at $L \leq 3.0$ they largely depend on the strength of the storm (Miyoshi and Kataoka 2005; Thorne et al. 2007). CIRs are significantly more effective for the evolution of the outer belt than are CMEs (Miyoshi and Kataoka 2005). CME-driven storms are brief, have denser plasma sheets, have strong ring currents and D_{st}, have *solar energetic particle (SEP)* events,

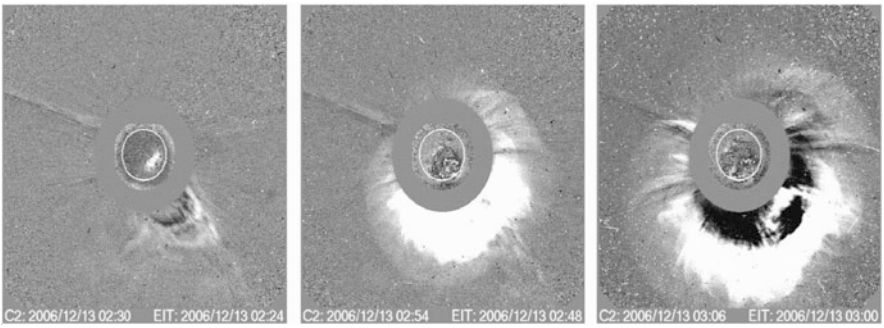

Fig. 16.8 Difference images of the CME and the source region at three different times. EIT difference images at 195 Å are shown within the white circles. A transition layer is visible around the CME front, indicating the existence of a shock (middle and right) (Liu et al. 2008)

and can produce great auroras and dangerous geomagnetically induced currents, while CIR-driven storms are of longer duration, have hotter plasmas and stronger spacecraft charging, and produce high fluxes of relativistic electrons (Borovsky and Denton 2006). Further statistical studies juxtaposed the properties of CME-driven versus CIR-Driven geomagnetic storms (Denton et al. 2006; Richardson et al. 2006; Zhang et al. 2007). It was found that during storms with $D_{st} < -250$ nT the tail-like deformation of the night-side magnetic field penetrates so close to Earth that the quasi-dipolar approximation breaks down at distances as small as $L = 3$–4, which explains why the auroras expand to unusually low latitudes during extremely strong storms (Tsyganenko et al. 2003).

Modeling the dynamics of the inner magnetosphere during strong geomagnetic storms, each principal source of the external magnetic field (magnetopause, cross-tail current sheet, axisymmetric and partial ring current, and Birkeland current systems) is driven during its growth and decay time interval by a separate variable, calculated as a time integral of a combination of geoeffective parameters, $n^{\lambda} v^{\beta} B_s^{\gamma}$, with n the solar wind density, v the speed of the solar wind, and B_s the southward component of the interplanetary magnetic field, from which the *disturbance storm index* D_{st} can be calculated (Tsyganenko and Sitnov 2005).

A new approach to model the magnetic field in CMEs is based on a method that combines magnetic helicity calculations in the the photosphere or low corona and geometrical modeling in the outer corona (13 $R_{\odot}$), which yields a field strength in the range of $B = 0.01$–0.16 G at this distance (Patsourakos et al. 2016).

The geomagnetic activity index *aa* has been used to predict the solar cycle 24 maximum of the sunspot number, where the index *aa* is split into two components, a flare/CME component that follows the solar activity cycle, and a second component that is associated with the recurrent high-speed solar wind streams, which are out of phase with the solar activity cycle (Hathaway and Wilson 2006).

Interestingly, although the interplanetary CME (ICME) shock detected by the WIND spacecraft on 2010 April 5 was followed by a moderate geomagnetic storm

only (with a minimum of $D_{st} = -72$ nT and a maximum $K_p = 8$), communication with the *Galaxy 15* satellite was lost during the time of the geomagnetic storm (Möstl et al. 2010; Liu et al. 2011). It was concluded that the observations with STEREO and WIND confirm the hypotheses that parts of ICME classified as (i) long-duration *magnetic cloud* or (ii) magnetic-cloud-like structures can be a consequence of a spacecraft trajectory through the ICME flank (Möstl et al. 2010).

16.8 Solar Flare Predictions

The business of flare predictions or forecasting requires reliable statistics of physical parameters that are sensitive to flare-related processes, as well as to capture processes that exhibit a causality between pre-flare conditions and the actually observed flare magnitude. Considering various driver mechanisms of solar flares and eruptions, Schrijver (2009) concludes that it remains to be seen whether deterministic forecasting is possible, in principle.

An *Active Region Monitor (ARM)* program has been installed at the *Big Bear Solar Observatory (BBSO)*, which uses full-disk Hα images and magnetic gradient maps from the GONG network, EUV images from EIT/SOHO, and GOES soft X-ray time profiles to predict the probability for each active region to produce C, M, or X-class flares, and has been in operation for 8 years (Gallagher et al. 2002). The 24-hour prediction probabilities are derived from the following observables: (i) the modified Zürich sunspot classification, (ii) the penumbra type of the largest spot, and (iii) the type of sunspot distribution (Gallagher et al. 2002). A Poisson distribution is assumed for the flare waiting time distribution, while a power law distribution would be more adequate to match the observations (Aschwanden and McTiernan 2010). Power law distributions should also be used for other flare parameters, such as peak fluxes, fluences, or flare durations, as they have been established for the largest flare data sets, with over 300,000 GOES events (Aschwanden and Freeland 2012). A Bayesian approach was applied to GOES data for solar flare prediction (Wheatland 2005). Note that the prediction scheme of Gallagher et al. (2002) is entirely based on statistical probabilities, without attempting a deterministic forecast of an individual event based on precursor conditions.

A sample of 289 M and X-class flares and over 2500 active region magnetograms has been analyzed by Schrijver (2007) and it was found that (i) large flares, without exception, are associated with pronounced high-gradient polarity-separation lines, while (ii) the free energy that emerges within these fibrils is converted into flare energy in a broad spectrum of flare magnitudes that can be characterized by a power law distribution. The unsigned magnetic flux Φ near the polarity-separation lines can be used effectively for flare forecasting. The probability for major flares to occur within 24 hours of the measurement of Φ approaches unity for active regions with the highest values of Φ around 2×10^{21} Mx. For active regions with $\Phi \leq 10^{19}$ Mx, no M or X-class flare occurs within a day (Schrijver 2007).

Based on the assumption of the *effective connected magnetic field* B_{eff}, defined by all possible connectivities between unipolar magnetic areas in a flux-partitioned MDI/SOHO magnetogram, the probability of flaring for an active region was calculated in 298 (93 X and M-flaring, 205 nonflaring) active regions during 10 years (Georgoulis and Rust 2007). The criterion of B_{eff} is found to be a robust criterion for distinguishing flaring from nonflaring regions, with a probability of 95% for M-class flares if $B_{eff} > 1600$ G, and for X-class flares if $B_{eff} > 2100$ G. Active regions do not produce flares if $B_{eff} < 200$ G (for M-class), or if $B_{eff} < 750$ G (for X-class) (Georgoulis and Rust 2007). The performance of solar flare forecasting methods (Schrijver 2007; Georgoulis and Rust 2007; Leka and Barnes 2003; Barnes et al. 2007; Barnes and Leka 2008) has been evaluated with standard verification statistics in terms of skill scores (Barnes and Leka 2008). It has been recommended to use the *True Skill Statistic (TSS)* as a standard for forecast comparison, over the commonly used *Heidke Skill Score (HSS)* (Bloomfield et al. 2012).

An *Automated Solar Activity Prediction (APAS)* platform has been developed with real-time processing of solar data (MDI/SOHO magnetograms), which has a machine learning-based capability to classify sunspot configurations, including the McIntosh sunspot classification scheme, and has been qualified with a quadratic score and compared with results from the NOAA *Space Weather Prediction Center (SWPC)*, (Colak and Qahwaji 2009). Similar solar flare prediction techniques that use advanced feature extraction, machine learning, and feature selection, are described in Ahmed et al. (2013), or *Support Vector Machine (SVM)* and *K-Nearest Neighbors (KNN)* (Li et al. 2007).

Some parameters that proved to be useful for flare forecasting are: the length of the (neutral) *polarity inversion line (PIL)*, and the overall twist and shear of the non-potential magnetic field, which can be characterized by the length segment over which the transverse magnetic field is strong (Falconer et al. 2003). Calculating the free magnetic energy, a new space weather forecasting tool has been created (Falconer et al. 2011). From 71,000 MDI/SOHO magnetograms and 6000 flares, a *gradient-weighted inversion-line length (GWILL)* was defined as a flare-predictive parameter, which combines the primary PIL length and the transverse gradient. GWILL increases by 35% during the 40 hrs prior to X-class flares, by 16% before M-class flares, and by 17% prior to B-C-class flares, but was found not to be a reliable parameter for predicting solar flares in real time (Mason and Hoeksema 2010). Another study defined similar criteria, assuming that solar flare productivity closely connects with the three measures: the maximum horizontal gradient in longitudinal magnetograms, the length of the neutral line, and the number of singular points, which increases with magnetic nonpotentiality or complexity, but it was found that none of these measures can absolutely determine whether solar flares would occur or not (Cui et al. 2006). On the other side, applying a machine-learning algorithm to distinguish two populations (of flare vs. CME occurrence), a True Skill Statistic value of $\approx 0.8 \pm 0.2$ was achieved (Bobra and Ilonidis 2016).

The most comprehensive evaluation of 25 magnetic parameters was carried out with vector magnetograph HMI/SDO data (including 2071 active regions), using

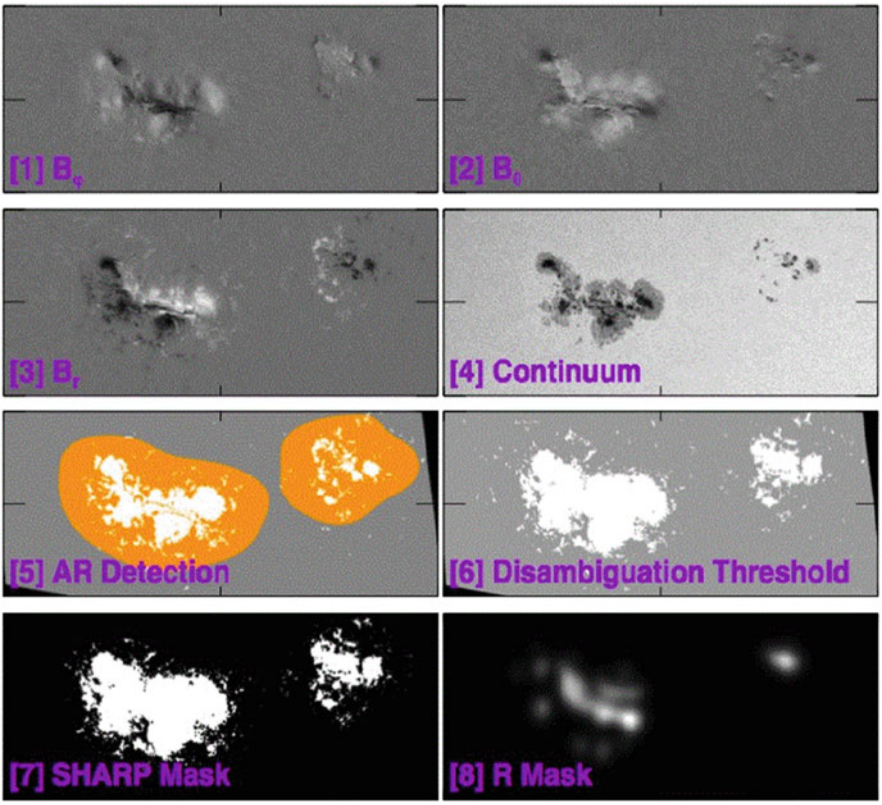

Fig. 16.9 Vector magnetic field data, B_ϕ [1]; B_θ [2]; B_r [3]; continuum intensity for NOAA active region 11429 on 2012 March 7, 00:24 UT [4]; automatic detection algorithm [5]; disambiguation threshold [6]; sharp mask [7]; and active region parameter R, computed with the polarity inversion line automatic detection algorithm [8], (Bobra and Couvidat 2015)

a machine-learning algorithm, in order to test the reliability and predictability of various magnetic parameters for flare forecasting (Fig. 16.9; Bobra and Couvidat 2015). Physical parameters that are most relevant for flare forecasting include the total unsigned current helicity, the total magnitude of the Lorentz force, the total photospheric magnetic free energy density, and the total unsigned vertical current. These parameters essentially are all directly related to the free energy (E_{free}), which is the difference between the nonpotential (E_{np}) and the potential energy (E_p), i.e., $E_{free} = E_{np} - E_p$. However, the free energy of an active region appears not to be a sufficient criterion to predict the flare magnitude, while additional (unknown) flare parameters must play a more decisive role, such as the history of prior flaring (Falconer et al. 2012). A similar study, but using UV brightenings and soft X-ray data, besides the vector magnetograph data, and extending to 60 feature parameters, has been conducted by Nishizuka et al. (2017). The ranking of the

feature importance showed that previous flare activity is most effective, followed by the length of magnetic neutral lines, the unsigned magnetic flux, the area of UV brightening, and the time differentials of features over 24 hrs, all of which are strongly correlated with the flux emergence dynamics in active regions (Nishizuka et al. 2017). Synthesizing photospheric and coronal data was found to be helpful for flare prediction too (Jonas et al. 2018). Other studies use magnetic helicity injection in active regions as a flare-predictability parameter (Park et al. 2010), or the *mean weighted shear angle* (Tiwari et al. 2010). Alternatively, measures of fractality, multi-fractality, or turbulence were tested on their ability for flare predictions, but none of these parameters was able to distinguish flaring from non-flaring active regions (Georgoulis 2012).

A benchmark test has been conducted during an inter-agency workshop on "all clear" forecast, where the performance of a number of existing flare prediction algorithms was compared with common data sets (from MDI/SOHO), but it was found that no single method outperformed all others, similar to the situation in climatological forecasts (Barnes et al. 2016).

An estimation of the magnitude of the largest possible solar flare has been attempted from statistics of solar-like stars observed with the *Kepler* spacecraft, which revealed the existence of superflares with energies of 10^{33}–10^{35} erg, where the largest event with an energy of 10^{35} erg has a statistical probability for occurrence once in 5000 years (Shibata et al. 2013).

There is still no concensus whether flare forecasting is deterministic or chaotic. Avalanche models are used to replicate the (unobservable) stochastic nature of the driving and triggering mechanisms in flares (Bélanger et al. 2007). Although the avalanche models have a high sensitivity to the embedded stochastic process, deterministically driven models can still be efficiently used for prediction of large events (Strugarek and Charbonneau 2014).

16.9 Space Weather Forecasting

The success rate of *"space weather forecasting"* strongly depends on the model assumptions in the chain of events that are initiated by a flare and/or CME and that propagate from the corona to the heliosphere all the way to the Earth, and beyond in interplanetary space. The first link in the chain of solar-terrestrial relationships is the prediction of flares and/or CMEs, which we discussed in the last section 16.8. For reviews on space weather phenomena see Schwenn (2006), Bothmer and Daglis (2006), Pulkkinen (2007), Schrijver and Siscoe (2010), Knipp (2011), and Schrijver et al. (2016).

An early comprehensive space weather forecasting tool was developed with a parallel *adaptive mesh refinement (AMR)* scheme for predicting ideal MHD flows to simulate the initiation, structure, and evolution of a CME and its interaction with the magnetosphere-ionosphere system (Groth et al. 2000). The code starts with an initial "steady-state solution for the time-averaged solar wind, which

contains: (i) a magnetic field model with a high-latitude polar coronal hole, closed magnetic flux tubes at low latitudes, and a helmet streamer structure with a neutral line and current sheet; (ii) the Archimedean spiral topology of the interplanetary magnetic field; (iii) the two-component fast solar wind at high latitudes and slow solar wind at low latitudes; and (iv) the predicted solar wind plasma properties as measured in situ at 1 AU (Groth et al. 2000). Similarly, 3-D MHD space-weather simulations were performed with the *Block Adaptive Tree Solar-Wind Roe Upwind Scheme (BATS-R-US)* code, which in addition includes a Gibson-Low magnetic flux rope embedded in the streamer (Manchester et al. 2004). An even more complete framework for physics-based space weather simulations is the *Space Weather Modeling Framework (SWMF)*, which integrates numerical models of the solar corona, an eruptive event generator, the inner heliosphere, solar energetic particles, the global magnetosphere, the inner magnetosphere, the radiation belt, ionospheric electrodynamics, and the upper atmosphere (Toth et al. 2005). It was pointed out early on that the most needed parameters for space weather predictions are the variations of storm time electron, proton, and ion populations within the magnetosphere, the CME initiation, the CME acceleration in the corona, and the SEP acceleration and propagation, rather than the sunspot number or the K_p geomagnetic index (Feynman and Gabriel 2000).

Several studies focus on the best strategy to predict the CME arrival time at Earth (at a distance of 1 AU). An empirical model includes interplanetary acceleration and cessation, and minimization of projection effects by using multi-spacecraft data in quadrature (Gopalswamy et al. 2001). The *Hakamada-Akasofu-Fry version 2 (HAFv.2)* model uses the drift rate of metric type II radio bursts, as well as a realistic background solar wind structure, to predict the shock arrival time at Earth (Fry et al. 2003). An ensemble of four physics-based models has been used to predict (in real-time) the shock arrival times for the 2003 November 19–20 *"Halloween"* events, using inputs from both CME leading edge speeds as well as type II shock speeds, which matched the "hit windows" of ± 15 hours with a success rate of 74% (Dryer et al. 2004). The statistical properties of the Halloween events were significantly different from average CME events; being faster, wider, more energetic, and more geoeffective (Gopalswamy et al. 2005). Another ensemble study conducts forecast in near-real time using the *Shock Time of Arrival model (STOA)*, *the interplanetary shock propagation model (ISPM)*, and the HAFv.2 model, which predict the arrival time of 166 flare-related shocks at Earth with similar success rates of $\approx$ 50%–60% in a ± 24 hours window (McKenna-Lawlor et al. 2006).

A major uncertainty in all CME arrival time prediction models is the unknown radial propagation speed of halo-CMEs (in direction towards the observer), but the lateral expansion speed v_{exp} is a good proxy that can be used instead, which is found to be correlated with the travel time T_{tr} of the shock, i.e., $T_{tr} \approx 203–2.77 \log(v_{exp})$ (Schwenn et al. 2005). Geometric triangulation techniques (using STEREO A and B) show a promising capability to link solar observations with corresponding in situ signatures at 1 AU and to predict CME arrival at the Earth (Liu et al. 2010). Comparing the performance of 6 methods for predicting the CME time of arrival using STEREO data yields an error of ± 6 hours for 78% of the CMEs, or ± 13

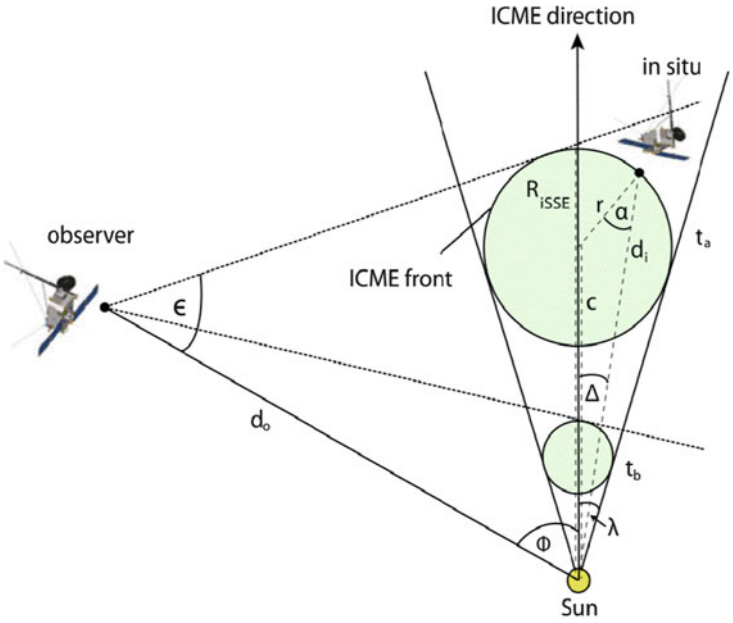

Fig. 16.10 The geometry of stereoscopic triangulation of a spherical CME with two spacecraft (observed and in situ). The expansion of the CME is indicated with a small and a large green sphere (Möstl and Davies 2013)

hours for the full sample, which is a half-day improvement over past methods based on LASCO/SOHO data (Colaninno et al. 2013). Using STEREO data, Möstl and Davies (2013) derive analytical formulas for the geometric correction of the ICME speed, path, and arrival time (Fig. 16.10). A more extended study with 22 CMEs and using PLASTIC/STEREO, IMPACT/STEREO, WIND, MFI/SWE data, yields arrival times of 26.4 ± 15.3 hours. Comparing the arrival times between three different geometric models (including self-similar expansion), none of the three geometric models was found to yield superior results (Möstl et al. 2014).

A new tool, called *Forecasting a CME's altered trajectory (ForeCAT)*, has been designed to calculate deflection due to magnetic sources, which includes CME expansion, a 3-part propagation model, the effects of drag on the CME's deflection, type II radio burst profiles, and a *potential field source surface (PFSS)* magnetic field background model (Kay et al. 2013). The ForeCat tool reproduces the in situ magnetic field for each vector component with an error equivalent to ≈35% (Kay and Gopalswamy 2017).

A technique to provide short-term warnings of *solar energetic proton* events has been developed based on the flare location, the flare size, and evidence of particle acceleration/escape as parameterized by flare longitude, time-integrated soft X-ray intensity, and time-integrated intensity (fluence) of type III radio emission at ≈ 1

MHz, which gives a median warning time of ≈ 55 min, with a detection probability of 63% and a false alarm rate of 42% (Laurenza et al. 2009).

The last link in the chain of solar-terrestrial connections is the ionosphere, which becomes turbulent and develops density irregularities, which in turn cause amplitude and phase scintillations, and affect communication and the *Global Positioning System (GPS)*. The effects are most intense in the equatorial region, moderate at high latitudes, and minimal at middle latitudes (Basu et al. 2002).

16.10 Solar Irradiance

The constancy of solar irradiance (luminosity, energy flux, or brightness) integrated over the entire wavelength spectrum has become the focus of new studies in the context of the Earth's global climate changes. The variability of the Sun's total energy output is caused by changing dark (sunspots) and bright (faculae) structures on the solar disk during the 11-year sunspot cycle, modulated by the solar rotation (for a review see Kopp 2016). The variations measured from spacecraft since 1978 (in the order of ≈ 0.2%) are found to be too small to have contributed appreciably to accelerated (man-made) global warming over the past 30 years (Foukal et al. 2006).

In historical records, a reduction of the total solar irradiance variation from contemporary levels is expected during the 17th century (Maunder minimum), due to the almost total absence of sunspots, which indeed was confirmed in increases in the Ca II brightness, in broad ultraviolet (0.7%), visible/near infrared (0.2%), infrared (0.07%), and total irradiance (0.2%) since 1675 (Lean 2000). Chromospheric lines, such as Ca II K 3933 Å track the 11-year cycle of the sunspot number. The temperature-sensitive C I 5380 Å appears to be constant in intensity to 0.2% (Livingston et al. 2007).

On the other hand, larger decreases in the total irradiance are expected due to the presence of larger sunspots, which was indeed the case during the 2003 October 18 extraordinary storms, when over 140 flares occurred, primarily from two different large sunspot groups, resulting in a unprecedented drop of the *total solar irradiance (TSI)* index by 0.34%, as measured by the *Solar Radiation and Climate Experiment (SORCE)*, and by the *Thermosphere, Ionosphere, Mesosphere, Energetic, and Dynamics (TIMED)* spacecraft (Woods et al. 2004).

The SATIRE-S data set (MDI/SOHO, TIM/SORCE) recreates TSI observations on all time scales of a day (and longer) over 31 years starting in 1978 (Fig. 16.11), providing strong evidence that changes in photospheric magnetic flux alone are responsible for almost all solar irradiance variations over the last three solar cycles (Ball et al. 2012). The SATIRE-S model was extended with KPVT, MDI/SOHO, and HMI/SDO data covering the time interval of 1974–2013 with the new solar cycle (Yeo et al. 2014a,b). The most recent reconstruction of the SSI and TSI using data from AIA/SDO during 2010–2015 can be found in Fontenla et al. (2017). The SSI estimates were used to drive a thermosphere-ionosphere physical simulation model, where the predictions of neutral mass density at low Earth orbit

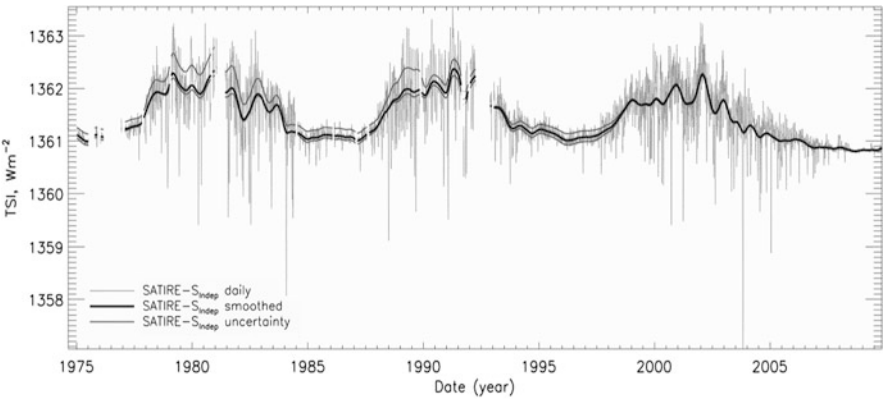

Fig. 16.11 The *Total Solar Irradiance (TSI)* index from the entire SATIRE-S_{Ind} dataset. Daily data are shown as solid grey lines when dates are contiguous. The thick flack line is smoothed data and the uncertainty range is shown, smoothed only, as thin black lines. Gaps in the curves are present when data gaps are larger than 27 days (Ball et al. 2012)

altitudes in the thermosphere and peak plasma densities at mid-latitudes are in reasonable agreement. The solar Lyman α radiation is the brightest ultraviolet emission (VUV: $\lambda < 2000$ Å), and this radiation is deposited in the Earth's atmosphere above an altitude of 70 km. Long-term Lyman α data have been gathered by the *Atmospheric Explorer E (AE-E)*, the *Solar Mesospheric Explorer (SME)*, and the *Upper Atmosphere Research Satellite (UARS)* back to 1947. The 1-σ uncertainty of the long-term Lyman α is estimated to be $\approx$ 10%, and the solar rotation variability is $\approx$ 9% (Woods et al. 2000).

The recent revision of the sunspot number, such as the Sunspot Index and Long-term Solar Observations (SILSO), has an impact on the solar irradiance reconstructions, such as the NRLTSI2 and the SATIRE model (Kopp et al. 2016). The SILSO record has little effect on either model after 1885, but leads to solar-cycle fluctuations with greater amplitude in the TSI reconstructions prior, suggesting that many 18th and 19th century cycles could be similar in amplitude to those of the current maxima (Kopp et al. 2016).

Evidence for a long-term trend in the TSI has been found by comparing the last two solar cycle minima, where the TSI was more than 0.2 W m^{-2} lower than during the last minimum in 1996 (Fröhlich 2009). However, the chromospheric indices and hence the solar UV irradiance do not exhibit a similar change, and thus the long-term trend of TSI is most possibly caused by a global temperature change of the Sun that does not influence the UV irradiance in the same way as the surface magnetic fields (Fröhlich 2009). The *solar spectral irradiance (SSI)* values for wavelengths with a brightness temperature greater than 5770 K show a brightening with decreasing solar activity, whereas those with lower brightness temperatures show a dimming, which confirms that different parts of the solar atmosphere contribute differently to the TSI, almost opposite in the lower and upper

photospheric layers (Harder et al. 2009). High-resolution SSI calculations include the effects of the the upper chromosphere and full non-LTE radiative transfer of level populations and ionizations, and the photodissociation continuum opacity of molecular species CH and OH, which may explain the missing near-UV opacity in the spectral range of the near-UV (Fontenla et al. 2011, 2015).

Modeling of the irradiance variations have initially been conducted from the rotational modulation of disk-integrated magnetic proxies (sun spot areas), while more detailed work takes into account the variations of the surface distributions of the magnetic field, the center-to-limb variation of sunspot and facular contrast as a function of wavelengths, and magnetic filling factors (Fligge et al. 2000). The TSI reconstructed from the end of the Maunder minimum to the present, based on variations of the surface distribution of the solar magnetic field, successfully reproduces the photospheric magnetic flux since 1974 and the open magnetic flux since 1868, predicting an increase of $\approx 1.3 \pm 0.3$ W m^{-2} in the TSI (Krivova et al. 2007). Long-term modeling of the irradiance requires additional parameters that are depending on the solar cycle, such as meridional flow speeds that control the polar field reversals (Wang et al. 2005). Because the diffusive decay rate accelerates as the average spacing between active regions decreases, the photospheric magnetic flux and facular brightness grow more slowly than the sunspot number and the TSI saturates during the highest amplitude cycles (Wang et al. 2005).

Envisioning the longest time scales in stars, the solar photospheric luminosity was about 30% lower 4.6 Gyr ago, when the Sun arrived on the main sequence, compared to present-day levels, when its faster rotation generates enhanced magnetic activity (Güdel 2007).

References

(16.1) The Slow Solar Wind

Abbo, L., Ofman, L., Antiochos, S.K., et al. 2016, *Slow solar wind: Observations and modeling*, SSRv 201, 55, [24 c, 16 c/y].

Brooks, D.H., Ugarte-Urro, I., and Warren, H.P. 2015, *Full-sun observations for identifying the source of the slow solar wind*, Nature Comm. 6, 5947. [34 c, 17 c/y].

Bruno, R., Trenchi, L., and Telloni, D. 2014, *Spectral slope variation at proton scales from fast to slow solar wind*, ApJ 793, L15, [26 c, 7 c/y].

Bruno, R. and Telloni, D. 2015, *Spectral analysis of magnetic fluctuations at proton scales from fast to slow solar wind*, ApJ 811, 17, [16 c, 6 c/y].

Cliver, E.W. and von Steiger, R. 2017, *Minimal magnetic states of the Sun and the solar wind: Implications for the origin of the slow solar wind*, SSRv 210, 227, [6 c, 6 c/y].

Crooker, N.U., Antiochos, S.K., Zhao, X., et al. 2012, *Global network of slow solar wind*, JGR 117, A4, A04104, [32 c, 6 c/y].

D'Amicis, R. and Bruno, R. 2015, *On the origin of highly Alfvénic slow solar wind*, ApJ 805, 84, [12 c, 5 c/y].

Dasso, S., Milano, L.J., Matthaeus, W.H., et al. 2005, *Anisotropy in fast and slow solar wind fluctuations*, ApJ 635, L181, [137 c, 11 c/y].

Ebert, R.W., McComas, D.J., Elliott, H.A., et al. 2009, *Bulk properties of the slow and fast solar wind and interplanetary coronal mass ejections measured by Ulysses: Three polar orbits of observation*, JGR 114, A1, A01109, [79 c, 9 c/y].
Feldman, U., Landi, E., and Schwadron, N.A. 2005, *on the sources of fast and slow solar wind*, JGR 110, A7, A07109, [65 c, 5 c/y].
Heber, V.S., Baur, H., Bochsler, P., et al. 2012, *Isotopic mass fractionation of solar wind: Evidence from fast and slow solar wind collected by the Genesis mission*, ApJ 759, 121, [27 c, 5 c/y].
Higginson, A.K., Antiochos, S.K., DeVore, C.R. et al. 2017, *Formation of heliospheric arcs of slow solar wind*, ApJ 840, L10, [5 c, 5 c/y].
Kepko, L., Viall, N.M., Antiochos, S.K., et al. 2016, *Implications of L1 observations for slow solar wind formation by solar reconnection*, GRL 43, 4089, [14 c, 9 c/y].
Kilpua, E.K.J., Madjarska, M.S., Karna, N., et al. 2016, *Sources of the slow solar wind during the solar cycle 23/24 minimum*, SoPh 291, 2441, [9 c, 6 c/y].
Perrone, D., Alexandrova, O., Mangeney, A., et al. 2016, *Compressive coherent structures at ion scales in the solar wind*, ApJ 826, 196, [23 c, 15 c/y].
Riley, P. and Luhmann, J.G. 2012, *Interplanetary signatures of unipolar streamers and the origin of the slow solar wind*, SoPh 277, 355, [51 c, 9 c/y].
Roberts, O.W., Li, X., Alexandrova, O., et al. 2016, *Observation of an MHD Alfvén vortex in the slow solar wind*, JGR 121, 3870, [11 c, 7 c/y].
Rouillard, A.P., Davies, J.A., Lavraud, B., et al. 2010, *Intermittent release of transients in the slow solar wind: I. Remote sensing observations*, JGR 115, A4, A04103, [52 c, 7 c/y].
Sanchez-Diaz, E., Rouillard, A.P., Lavraud, B., et al. 2016, *The very slow solar wind: Properties, origin, and variability*, JGR 121, 2830, [10 c, 7 c/y].
Subramanian, S., Madjarska, M.S., and Doyle, J.G. 2010, *Coronal hole boundaries evolution at small scales. II. XRT view. Can small-scale outflows at CHBs be a source of the slow solar wind ?* A&A 516, A50, [43 c, 6 c/y].
Suzuki, T.K. and Inutsuka, S.I. 2006, *Solar winds driven by nonlinear low-frequency Alfvén waves from the photosphere: Parametric study for fast/slow winds and disappearance of solar winds*, JGR 111, A6, A06101, [122 c, 11 c/y].
Viall, N.M. and Vourlidas, A. 2015, *Periodic density structures and the origin of the slow solar wind*, ApJ 807, 176, [18 c, 7 c/y].
von Steiger, R., Schwadron, N.A., Fisk, L.A., et al. 2000, *Composition of quasi-stationary solar wind flows from Ulysses/Solar wind ion composition spectrometer*, JGR 105/A12, 27217, [278 c, 16 c/y].

(16.2) The Fast Solar Wind

Antonucci, E., Dodero, M.A., and Giordano, S. 2000, *Fast solar wind velocity in a polar coronal hole during solar minimum*, SoPh 197, 115, [88 c, 5 c/y].
Cranmer, S.R. 2002, *Coronal holes and the high-speed solar wind*, SSRv 101, 229, [160 c, 10 c/y].
Cranmer, S.R., Matthaeus, W.H., Breech, B.A., et al. 2009, *Empirical constraints on proton and electron heating in the fast solar wind*, ApJ 702, 1604, [101 c, 12 c/y].
Dasso, S., Milano, L.J., Matthaeus, W.H., et al. 2005, *Anisotropy in fast and slow solar wind fluctuations*, ApJ 635, L181, [137 c, 11 c/y].
de Toma, G. 2011, *Evolution of coronal holes and implications for high-speed solar wind during the minimum between cycles 23 and 24*, SoPh 274, 195, [66 c, 10 c/y].
Ebert, R.W., McComas, D.J., Elliott, H.A., et al. 2009, *Bulk properties of the slow and fast solar wind and interplanetary coronal mass ejections measured by Ulysses: Three polar orbits of observation*, JGR 114, A1, A01109, [79 c, 9 c/y].
Hahn, M. and Savin, D.W. 2013, *Observational quantification of the energy dissipated by Alfvén waves in a polar coronal hole: Evidence that waves drive the fast solar wind*, ApJ 776, 78, [22 c, 5 c/y].

Heber, V.S., Baur, H., Bochsler, P., et al. 2012, *Isotopic mass fractionation of solar wind: Evidence from fast and slow solar wind collected by the Genesis mission*, ApJ 759, 121, [27 c, 5 c/y].
Jian, L.K., Russell, C.T., and Luhmann, J.G. 2011, *Comparing solar minimum 23/24 with historical solar wind records at 1 AU*, SP 274, 321, [72 c, 11 c/y].
Lion, S., Alexandrova, O., and Zaslavsky, A. 2016, *Coherent events and spectral shape at ion kinetic scales in the fast solar wind turbulence*, ApJ 824, 47, [33 c, 22 c/y].
Maksimovic, M., Zouganelis, I., Chaufray, J.Y. 2005, *Radial evolution of the electron distribution functions in the fast solar wind between 0.3 and 1.5 AU*, JGR 110/A9, A09104, [120 c, 10 c/y].
Marsch, E. 2006, *Kinetic physics of the solar corona and solar wind*, LRSP 3, 1, [290 c, 27 c/y].
McComas, D.J., Angold, N., Elliott, H.A., et al. 2013, *Weakest solar wind of the space age and the current "mini" solar maximum*, ApJ 779, 2, [76 c, 17 c/y].
McIntosh, S.W., De Pontieu, B., Carlsson, M., et al. 2011, *Alfvénic waves with sufficient energy to power the quiet solar corona and fast solar wind*, Nature 475, 7357, [283 c, 44 c/y].
Owens, M.J., Lockwood, M., and Riley, P. 2017, *Global solar wind variations over the last four centuries*, Scientific Reports 7, 41548, [9 c, 9 c/y].
Sakao, T., Kano, R., Narukage, N., et al. 2007, *Continuous plasma outflows from the edge of a solar active region as a possible source of solar wind*, Science 318/5856, 1585, [142 c, 14 c/y].
Skoug, R.M., Gosling, J.T., Steinberg, J.T., et al. 2004, *Extremely high speed solar wind: 29–30 October 2003*, JGR 109/A9, A09102, [135 c, 10 c/y].
Stakhiv, M., Landi, E., Lepri, S.T., et al. 2015, *On the origin of mid-latitude fast wind: Challenging the two-state solar wind paradigm*, ApJ 801, 100, [16 c, 6 c/y].
Tu, C.Y., Zhou, C., Marsch, E., et al. 2005, *Solar wind origin in coronal funnels*, Science 308/5721, 519, [178 c, 14 c/y].
Wilhelm, K., Dammasch, I.E., Marsch, E., et al. 2000, *On the source regions of the fast solar wind in polar coronal holes*, A&A 353, 749, [92 c, 5 c/y].
Zhao, L., Zurbuchen, T.H., and Fisk, L.A. 2009, *Global distribution of the solar wind during solar cycle 23: ACE observations*, GRL 36/14, L14104, [77 c, 9 c/y].
Zurbuchen, T.H. and Richardson, I.G. 2006, *In-situ solar wind and magnetic field signature of interplanetary coronal mass ejections*, SSRv 123, 31, [216 c, 19 c/y].

(16.3) Solar Wind Models

Antiochos, S.K., Mikic, Z., Titov, V.S. et al. 2011, *A model for the sources of the slow solar wind*, ApJ 731, 112, [112 c, 17 c/y].
Chandran, B.D.G., Li, B., Rogers, B.N., et al. 2010, *Perpendicular ion heating by low-frequency Alfvén wave turbulence in the solar wind*, ApJ 720, 503, [126 c, 17 c/y].
Cranmer, S.R. 2002, *Coronal holes and the high-speed solar wind*, SSRv 101, 229, [160 c, 10 c/y].
Cranmer, S.R. and van Ballegooijen, A.A. 2003, *Alfvénic turbulence in the extended solar corona: Kinetic effects and proton heating*, ApJ 594, 573, [145 c, 10 c/y].
Cranmer, S.R. and van Ballegooijen, A.A. 2005, *On the generation, propagation, and reflection of Alfvén waves from the solar photosphere to the distant heliosphere*, ApJSS 156, 265, [252 c, 20 c/y].
Cranmer, S.R., van Ballegooijen, A.A., and Edgar, R.J. 2007, *Self-consistent coronal heating and solar wind acceleration from anisotropic MHD turbulence*, ApJSS 171/2, 520, [310 c, 30 c/y].
Cranmer, S.R. and van Ballegooijen, A.A. 2012, *Proton, electron, and ion heating in the fast solar wind from nonlinear coupling between Alfvénic and fast-mode turbulence*, ApJ 754, 92, [33 c, 6 c/y].
Feng, Z., Yang, L., Xiang, X., et al. 2010, *3-D solar WIND modeling from the Sun to Earth by a SIP-CESE MHD model with a six-component grid*, ApJ 723, 300, [67 c, 9 c/y].
Hadid, L.Z., Sahraoui, F., and Galtier, S. 2017, *Energy cascade rate in compressible fast and slow solar wind turbulence*, ApJ 838, 9, [14 c, 14 c/y].

He, J., Marsch, E., Tu, C., et al. 2011, *Possible evidence of Alfvén-cyclotron waves in the angle distribution of magnetic helicity of solar wind turbulence*, ApJ 731, 85, [106 c, 16 c/y].
Hellinger, P., Travnicek, P., Kasper, J.C., et al. 2006, *Solar wind proton temperature anisotropy: Linear theory and WIND/SWE observations*, GRL 33/9, L09101, [230 c, 20 c/y].
Hellinger, P., Matteini, L., Stverak, S., et al. 2011, *Heating and cooling of protons in the fast solar wind between 0.3 and 1 AU: Helios revisited*, JGR 116/A9, A09105, [38 c, 6 c/y].
Hollweg, J.V. and Isenberg, P.A. 2002, *Generation of the fast solar wind: A review with emphasis on the resonant cyclotron interaction*, JGR 107/A7, 1147, [203 c, 13 c/y].
Howes, G.G., Bale, S.D., Klein, K.G., et al. 2012, *The slow-mode nature of compressible wave power in solar wind turbulence*, ApJ 753, L19, [90 c, 16 c/y].
Marsch, E. 2006, *Kinetic physics of the solar corona and solar wind*, LRSP 3, 1, [290 c, 27 c/y].
Matsumoto, T. and Suzuki, T.K. 2014, *Connecting the Sun and the solar wind: The self-consistent transition of heating mechanisms*, MNRAS 440, 971, [35 c, 10 c/y].
Narita, Y. and Marsch, E. 2015, *Kinetic slow mode in the solar wind and its possible role in turbulence dissipation and ion heating*, ApJ 805, 24, [23 c, 9 c/y].
Odstrcil, D. 2003, *Modeling 3-D solar wind structure*, Adv.Space Res. 32/4, 497, [121 c, 8 c/y].
Roberts, O.W., Li, X., and Li, B. 2013, *Kinetic plasma turbulence in the fast solar wind measured by Cluster*, ApJ 769, 58, [51 c, 11 c/y].
Roberts, O.W., Narita, Y., Li, X., et al. 2017, *Multipoint analysis of compressive fluctuations in the fast and slow solar wind*, JGR 122, 6940, [5 c, 5 c/y].
Sokolov, I.V., van der Holst, B., Oran, R., et al. 2013, *MHD waves and coronal heating: Unifying empirical and MHD turbulence models*, ApJ 764, 23, [58 c, 13 c/y].
Suzuki, T. and Inutsuka, S.I. 2005, *Making the corona and the fast solar wind: A self-consistent simulation for the low-frequency Alfvén waves from the photosphere to 0.3 AU*, ApJ 632, L49, [157 c, 14 c/y].
Suzuki, T.K. and Inutsuka, S.I. 2006, *Solar winds driven by nonlinear low-frequency Alfvén waves from the photosphere: Parameteric study for fast/slow winds and disappearance of solar winds*, JGR 111, A6, A06101, [122 c, 11 c/y].
Verdini, A. and Velli, M. 2007, *Alfvén waves and turbulence in the solar atmosphere and solar wind*, ApJ 662, 669, [133 c, 13 c/y].
Verdini, A., Velli, M., Matthaeus, W.H. et al. 2010, *A turbulence-driven model for heating and acceleration of the fast wind in coronal holes*, ApJ 708, L116, [91 c, 12 c/y].
Wicks, R.T., Horbury, T.S., Chen, C.H.K. et al. 2010, *Power and spectral index anisotropy of the entire inertial range of turbulence in the fast solar wind*, MNRAS 407, L31, [89 c, 5 c/y].
Wicks, R.T., Horbury, T.S., Chen, C.H.K., et al. 2011, *Anisotropy of imbalanced Alfvénic turbulence in fast solar wind*, Phys.Rev.Lett. 106,/4, 045001, [62 c, 10 c/y].

(16.4) Heliospheric Magnetic Structures

Arden, W.M., Norton, A.A., and Sun, X. 2014, *A "breathing" source surface for cycles 23 and 24*, JGR 119/3. 1476, [15 c, 4 c/y].
Cane, H.V. 2000, *Coronal mass ejections and Forbush decreases*, SSRv 93, 55, [219 c, 13 c/y].
Cane, H.V. and Richardson, I.G. 2003, *Interplanetary coronal mass ejections in the near-Earth solar wind during 1996–2002*, JGR 108/A4, 1156, [302 c, 21 c/y].
Davies, J.A., Harrison, R.A., Rouillard, A.P., et al. 2009, *A synoptic view of solar transient evolution in the inner heliosphere using the heliospheric imagers on STEREO*, GRL 36/2, L02102, [117 c, 14 c/y].
Gosling, J.T., Skoug, R.M., McComas, D.J., et al. 2005, *Direct evidence for magnetic reconnection in the solar wind near 1 AU*, JGR 110/A1, A01107, [185 c, 15 c/y].
Harrison et al., Davis, C., Eyles, C.J., et al. 2008, *First imaging of coronal mass ejections in the heliosphere viewed from outside the Sun-Earth line*, SoPh 247, 171, [73 c, 8 c/y].

Howard, T.A., Stovall, K., Dowell, J., et al. 2016, *Measuring the magnetic field of CMEs near the Sun using pulsars*, ApJ 831, 208, [9 c, 6 c/y].
Lee, C.O., Luhmann, J.G., Hoeksema, J.T., et al. 2011, *Coronal field opens at lower height during the Solar Cycles 22 and 23 minimum periods: IMF comparison suggests the source surface should be lowered*, SoPh 269, 367, [39 c, 6 c/y].
Liu, Y., Luhmann, J.G., Lin, R.P., et al. 2009, *Coronal mass ejections and global coronal magnetic field reconfiguration*, ApJ 698, L51, [28 c, 3 c/y].
Lockwood, M. 2013, *Reconstruction and prediction of variations in the open solar magnetic flux and interplanetary conditions*, LRSP 10, 4, [45 c, 10 c/y].
Lynch, B.J., Li, Y., Thernisien, A.F.R., et al. 2010, *Sun to 1 AU propagation and evolution of a slow streamer-blowout coronal mass ejection*, JGR 115, A7, A07106, [33 c, 4 c/y].
Mandrini, C.H., Pohjolainen, S., Dasso, S., et al. 2005 *Interplanetary flux rope ejected from an X-ray bright point. The smallest magnetic cloud source-region ever observed*, A&A 434, 725, [115 c, 9 c/y].
Nitta, N.V. and DeRosa, M.L. 2008, *A comparison of solar open field regions found by type III radio bursts and the potential field source surface model*, ApJ 673, L207, [23 c, 2 c/y].
Owens, M.J. and Crooker, N.U. 2006, *Coronal mass ejections and magnetic flux buildup in the heliosphere*, JGR 111/A10, A10104, [76 C, 7 C/Y].
Owens, M.J., and Forsyth, R.J. 2013, *The heliospheric magnetic field*, LRSP 10, 5, [50 c, 11 c/y].
Phan, T.D., Gosling, J.T., Davis, M.S., et al. 2006, *A magnetic reconnection X-line extending more than 390 Earth radii in the solar wind*, Nature 439/7073, 175, [159 c, 14 c/y].
Pogorelov, N.V., Suess, S.T., Borovikov, S.N., et al. 2013, *3D features of the outer heliosphere due to coupling between the interstellar and interplanetary magnetic fields. IV. Solar cycle model based on Ulysses observations*, ApJ 777, 2, [60 c, 13 c/y].
Qiu, J., Hu, Q., Howard, T.A., et al. 2007, *On the magnetic flux budget in low-corona magnetic reconnection and interplanetary coronal mass ejections*, ApJ 659, 758, [151 c, 14 c/y].
Riley, P., Linker, J.A., and Mikic, Z. 2001, *An empirically-driven global MHD model of the solar corona and inner heliosphere*, AGR 106/A8, 15889, [131 c, 8 c/y].
Riley, P., Linker, J.A., Mikic, Z., et al. 2006 *A comparison between global solar MHD and potential field source surface model results*, ApJ 653, 1510, [147 c, 13 c/y].
Riley, P., Lionello, R., Linker, J.A., et al. 2011, *Global MHD modeling of the solar corona and inner heliosphere for the Whole Heliosphere Interval*, SoPh 274, 361, [55 c, 8 c/y].
Rouillard, A.P., Davies, J.A., Forsyth, R.J. et al. 2008, *First imaging of corotating interaction regions using the STEREO spacecraft*, GRL 35/10, L10110, [127 c, 13 c/y].
Schrijver, C.J. and DeRosa, M.L. 2003, *Photospheric and heliospheric magnetic fields*, SoPh 212, 165, [385 c, 27 c/y].
Schüssler, M. and Baumann, I. 2006, *Modeling the Sun's open magnetic flux*, A&A 459, 945, [41 c, 4 c/y].
Sheeley, N.R.Jr., Herbst, A.D., Palatchi, C.A., et al. 2008, *Heliospheric images of the solar wind at Earth*, ApJ 675, 853, [98 c, 10 c/y].
Smith, E.J. 2001, *The heliospheric current sheet*, JGR 106/A8, 15819, [119 c, 7 c/y].
Webb, D.F., Cliver, E.W., Crooker, N.U., et al. 2000a, *Relationship of halo coronal mass ejections, magnetic clouds, and magnetic storms*, JGR 105/A4, 7491, [230 c, 13 c/y].
Yurchyshyn, V.B., Wang, H., Goode, P.R., et al. 2001, *Orientation of the magnetic fields in interplanetary flux ropes and solar filaments*, ApJ 563, 381, [104 c, 6 c/y].

(16.5) Impulsive SEP Events

Aschwanden, M.J. 2012, *GeV particle acceleration in solar flares and ground level enhancement (GLE) events*, SSRv 171, 3, [62 c, 11 c/y].
Cane, H.V., von Rosenvinge, T.T., Cohen, C.M.S., et al. 2003, *Tow components in major solar particle events*, GRL 30/12, 8017, [95 c, 7 c/y].

Cane, H.V., Richardson, I.G., and von Rosenvinge, T.T. 2010, *A study of solar energetic particle events of 1997–2006: Their composition and associations*, JGR 115/A8, A08101, [86 c, 11 c/y].
Cliver, E.W. and Ling, A.G. 2007, *Electrons and protons in solar energetic particle events*, ApJ 658, 1349, [37 c, 4 c/y].
Dresing, N., Gomez-Herrero, R., Klassen, A., et al. 2012, *The large longitudinal spread of solar energetic particles during the 17 January 2010 solar event*, SoPh 281, 281, [88 c, 16 c/y].
Dierckxsens, M., Tziotziou, K., Dalla, S., et al. 2015, *Relationship between solar energetic particles and properties of flares and CMEs: Statistical analysis of solar cycle 23 events*, SoPh 290, 841, [48 c, 19 c/y].
Ding, L.G., Li, G., Jiang, Y., et al. 2014, *Interaction between two coronal mass ejections in the 2013 May 22 large solar energetic particle event*, ApJ 793, L35, [17 c, 5 c/y].
Gomez-Herrero, R., Dresing, N., Klassen, A., et al. 2015, *Circumsolar energetic particle distribution on 2011 November 3*, ApJ 799, 55, [39 c, 16 c/y].
Grechnev, V.V., Kurt, V.G., Chertok, I.M., et al. 2008, *An extreme solar event on 20 January 2005: Properties of the flare and the origin of energetic particles*, SoPh 252, 149, [70 c, 7 c/y].
Kahler, S.W. 2007, *Solar sources of heliospheric energetic electron events - Shocks or flares ?* SSRv 129, 359, [28 c, 3 c/y].
Kahler, S.W. and Vourlidas, A. 2014, *Solar energetic particle events in different types of solar wind*, ApJ 791, 4, [5 c, 1 c/y].
Klassen, A., Dresing, N., Gomez-Herrero, R., et al. 2016, *Unexpected spatial intensity distributions and onset timing of solar electron events observed by closely spaced STEREO spacecraft*, A&A 593, A31, [9 c, 6 c/y].
Krucker, S. and Lin, R.P. 2000, *Two classes of solar proton events derived from onset time analysis*, ApJ 542, L61, [45 c, 3 c/y].
Mandzhavidze, N. and Ramaty, R. 1992, *High energy gamma ray emission from pion decay in a solar flare magnetic loop*, ApJ 389, 739, [45 c, 2 c/y].
Mewaldt, R.A., Looper, M.D., Cohen, C.M.S., et al. 2012, *Energy spectra, composition, and other properties of ground-level events during solar cycle 23*, SSRv 171, 97, [73 c, 13 c/y].
Murphy, R.J., Kozlovsky, B., and Share, G.H. 2016, *Evidence for enhanced 3He in flare-accelerated particles based on new calculations of the gamma-ray line spectrum*, ApJ 833, 196, [4 c, 3 c/y].
Papaioannou, A., Sandberg, I., Anastasiadis, A., et al. 2016, *Solar flares, CMEs and solar energetic particle event characteristics*, J.Space Weather and Space Climate 6, A42, [16 c, 11 c/y].
Reames, C.V. 2009a, *Solar release times of energetic particles in ground-level events*, ApJ 693, 812, [85 c, 10 c/y].
Reames, C.V. 2009b, *Solar energetic-particle release times in historic ground-level events*, ApJ 706, 844, [77 c, 9 c/y].
Reames, D.V. 2013, *The two sources of solar energetic particles*, SSRv 175, 53, [129 c, 29 c/y].
Rouillard, A.P., Sheeley, N.R., Tylka, A., et al. 2012 *The longitudinal properties of a solar energetic particle event investigated using modern solar imaging*, ApJ 752, 44, [95 c, 17 c/y].
Salas-Matamoros, C., Klein, K.L., and Rouillard, A.P. 2016, *CME-related particle acceleration regions during a simple eruptive event*, A&A 590, A135, [9 c, 6 c/y].
Trottet, G., Samwel, S., Klein, K.L., et al. 2015, *Statistical evidence for contributions of flares and coronal mass ejections to major solar energetic particle events*, SoPh 290, 819, [28 c, 11 c/y].
Wang, L., Lin, R.P., Krucker, S., et al. 2012, *A statistical study of solar electron events over one solar cycle*, ApJ 759, 69, [29 c, 5 c/y].

(16.6) Gradual SEP Events

Cliver, E.W. 2016, *Flare vs. shock acceleration of high-energy protons in solar energetic particle events*, ApJ 832, 128, [10 c, 7 c/y].

Desai, M.I., Mason, G.M., Dwyer, J.R., et al. 2003, *Evidence for a supra-thermal seed population of heavy ions accelerated by interplanetary shocks near 1 AU*, ApJ 588, 1149, [105 c, 7 c/y].

Desai, M.I., Mason, G.M., Gold, R.E., et al. 2006, *Heavy-ion elemental abundances in large solar energetic particle events and their implications for the see population*, ApJ 649, 470, [87 c, 8 c/y].

Desai, M.I., Mason, G.M., Dayeh, M.A., et al. 2016a, *Spectral properties of large gradual solar energetic particle events. I. Fe, O, and seed material*, ApJ 816, 68, [12 c, 8 c/y].

Desai, M.I., Mason, G.M., Dayeh, M.A., et al. 2016b, *Spectral properties of large gradual solar energetic particle events. II. Systematic Q/M dependence of heavy ion spectra breaks*, ApJ 828, 106, [8 c, 5 c/y].

Gopalswamy, N., Yashiro, S., Michalek, G., 2002, *Interacting coronal mass ejections and solar energetic particles*, ApJ 572, L193, [156 c, 10 c/y].

Gopalswamy, N., Yashiro, S., Lara, A., et al. 2003, *Large solar energetic particle events of cycle 23: A global view*, GRL 30/12, 8015, [60 c, 4 c/y].

Gopalswamy, N., Yashiro, S., Krucker, S., et al. 2004, *Intensity variation of large solar energetic particle events associated with coronal mass ejections*, JGR 109, A12, A12105, [159 c, 12 c/y].

Gopalswamy, N., Yashiro, S., Akiyama, S., et al. 2008, *CMEs, type II radio bursts, and solar energetic particle events in the SOHO era*, Annales Geophysicae 26/10, 3033, [66 c, 7 c/y].

Gopalswamy, N., Xie, H., Yashiro, S., et al. 2012a, *Properties of ground level enhancement events and the associated solar eruptions during solar cycle 23*, SSRv 171, 23, [126 c, 23 c/y].

Gopalswamy, N., Xie, H., Akiyama, S., et al. 2014a, *Major solar eruptions and high-energy particle events during solar cycle 24*, Earth, Planets and Space 66, 104, [48 c, 14 c/y].

Gopalswamy, N., Akiyama, S., Yashiro, S., et al. 2014b, *Anomalous expansion of coronal mass ejections during solar cycle 24 and its space weather implications*, GRL 41, 2673, [47 c, 13 c/y].

Grechnev, V.V., Kiselev, V.I., Meshalkina, N.S., et al. 2015, *Relations between microwave bursts and near-Earth high-energy proton enhancements and their origin*, SoPh 190, 2827, [15 c, 6 c/y].

Haggerty, D.K. and Roelof, E.C. 2002, *Impulsive near-relativistic solar electron events: Delayed injection with respect to solar electromagnetic emission*, ApJ 579, 841, [128 c, 8 c/y].

Kahler, S.W. 2001, *The correlation between solar energetic particle peak intensities and speeds of coronal mass ejections: Effects of ambient particle intensities and energy spectra*, JGR/A 106, A10, 20947, [153 c, 9 c/y].

Kahler, S.W., Reames, D.V., and Sheeley, N.R.Jr. 2001, *Coronal mass ejections associated with impulsive solar energetic particle events*, ApJ 562, 558, [100 c, 6 c/y].

Kozarev, K.A., Evans, R.M., Schwadron, N.A., et al. 2013, *Global numerical modeling of energetic proton acceleration in a coronal mass ejection traveling through the solar corona*, ApJ 778, 43, [23 c, 5 c/y].

Lee, M.A. 2005, *Coupled hydromagnetic wave excitation and ion acceleration at an evolving coronal/interplanetary shock*, ApJSS 158, 38, [153 c, 12 c/y].

Li, C., Firoz,, K.A., Sun, L.P., et al. 2013, *Electron and proton acceleration during the first ground level enhancement event of solar cycle 24*, ApJ 770, 34, [26 c, 6 c/y].

Mewaldt, R.A., Cohen, C.M.S., Labrador, A.W., et al. 2005, *Proton, helium, and electron spectra during large solar particle events of October-November 2003*, JGR 110, A9, A09S18, [95 c, 8 c/y].

Reames, D.V. 2013, *The two sources of solar energetic particles*, SSRv 175, 53, [129 c, 29 c/y].

Rouillard, A.P., Odstrcil, D., Sheeley, N.R., et al. 2011, *Interpreting the properties of solar energetic particle events by suing combined imaging and modeling of interplanetary shocks*, ApJ 735, 7, [69 c, 11 c/y].

Zank, G.P., Rice, W.K.M., and Wu, C.C. 2000, *Particle acceleration and coronal mass ejection driven shocks: A theoretical model*, JGR 105/A11, 25079, [197 c, 11 c/y].

(16.7) Geomagnetic Storms

Borovsky, J.E. and Denton, M.H. 2006, *Differences between CME-driven and CIR-driven storms*, JGR 111/A7, A07S08, [200 c, 17 c/y].

Cane, H.V., Richardson, I.G., and St.Cyr, O.C. 2000, *Coronal mass ejections, interplanetary ejecta, and geomagnetic storms*, GRL 27/21, 3591, [127 c, 7 c/y].

Denton, M.H., Borovsky, J.E., Skoug, R.M., et al. 2006, *Geomagnetic storms driven by ICME- and CIR-dominated solar wind*, JGR 111/A7, A07S07, [113 c, 10 c/y].

Gopalswamy, N., Yashiro, S., and Akiyama, S. 2007, *Geoeffectiveness of halo coronal mass ejections*, JGR 112/A6, A06112, [107 c, 10 c/y].

Hathaway, D.H. and Wilson, R.M. 2006, *Geomagnetic activity indicates large amplitude for sunspot cycle 24*, GRL 33/18, L18101, [80 c, 7 c/y].

Huttunen, K.E.J., Schwenn, R., Bothmer, V., et al 2005, *Properties and geoeffectiveness of magnetic clouds in the rising, maximum and early declining phases of solar cycle 23*, Annales Geophysicae 23/2, 625, [97 c, 8 c/y].

Kataoka, R., Shiota, D., Kilpua, E., et al. 2015, *Pileup accident hypothesis of magnetic storm on 17 March 2015*, GRL 42/13, 5155, [42 c, 17 c/y].

Liu, Y.D., Hu, H., and Wang, R. 2015, *Plasma and magnetic field characteristics of solar coronal mass ejections in relation to geomagnetic storm intensity and variability*, ApJ 809/2, L34, [37 c, 15 c/y].

Liu, Y., Luhmann, J.G., Müller-Mellin, R. 2008, *A comprehensive view of the 2006 December 13 CME: From the Sun to interplanetary space*, ApJ 689, 563, [65 c, 7 c/y].

Liu, Y., Luhmann, J.G., Bale, S.D., et al. 2011, *Solar source and heliospheric consequences of the 2010 April 3 coronal mass ejection: A comprehensive view*, ApJ 734, 84, [54 c, 8 c/y].

Mannucci, A.J., Tsurutani, B.T., Iijima, B.A., et al. 2005, *Dayside global ionospheric response to the major interplanetary events of October 29–30 "Halloween Storms"*, GRL 32/12, L12S02, [244 c, 20 c/y].

Miyoshi, Y. and Kataoka, R. 2005, *Ring current ions and radiation belt electrons during geomagnetic storms driven by coronal mass ejections and corotating interaction regions*, GRL 32/21, L21105, [94 c, 8 c/y].

Möstl, C., Temmer, M., Rollett, T., et al. 2010, *STEREO and Wind observations of a fast ICME flank triggering a prolonged geomagnetic storm on 5–7 April 2010*, GRL 37/24, L24103, [76 c, 10 c/y].

Patsourakos, S., Georgoulis, M.K., Vourlidas, A., et al. 2016, *The major geoeffective solar eruptions of 2012 March 7: Comprehensive Sun-to-Earth analysis*, ApJ 817, 14, [17 c, 11 c/y].

Richardson, I.G., Cliver, E.W., and Cane, H.V. 2001, *Sources of geomagnetic storms for solar minimum and maximum conditions during 1972–2000*, GRL 28/13, 2569, [108 c, 6 c/y].

Richardson, I.G., Webb, D.F., Zhang, J., et al. 2006, *Major geomagnetic storms (Dst<-100 nT) generated by corotating interaction regions*, JGR 111, A7, A07S09, [79 c, 7 c/y].

Srivastava, N. and Venkatakrishnan, P. 2004, *Solar and interplanetary sources of major geomagnetic storms during 1996–2002*, JGR 109, A10, A10103, [71 c, 5 c/y].

Thorne, R.M., Shprits, Y.Y., Meredith, N.P., et al. 2007, *Refilling of the slot region between the inner and outer electron radiation belts during geomagnetic storms*, JGR 112, A6, A06203, [62 c, 6 c/y].

Tsurutani, B.T., Gonzalez, W.D., Lakhina, G.S., et al. 2003, *The extreme magnetic storm of 1–2 September 1859*, JGR 108, A7, 1268, [182 c, 13 c/y].

Tsyganenko, N.A., Singer, H.J., and Kaper, J.C. 2003, *Storm-time distortion of the inner magnetosphere: How severe can it get ?* JGR 108, A5, 1209, [141 c, 11 c/y].

Tsyganenko, N.A. and Sitnov, M.I. 2005, *Modeling the dynamics of the inner magnetosphere during strong geomagnetic storms*, JGR 110, A3, A03208, [410 c, 33 c/y].

Wang, Y.M., Ye, P.Z., Wang, S., et al. 2002, *A statistical study on the geoeffectiveness of Earth-directed coronal mass ejections from March 1997 to December 2000*, JGR 107, A11, 1340, [106 c, 7 c/y].

Zhang, J., Dere, K.P., Howard, R.A. et al. 2003, *Identification of solar sources of major geomagnetic storms between 1996 and 2000*, ApJ 582, 520, [140 c, 10 c/y].
Zhang, J., Richardson, I.G., Webb, D.F., et al. 2007, *Solar and interplanetary sources of major geomagnetic storms (Dst <-100 nT) during 1996–2005*, JGR 112, A10, A10102, [276 c, 26 c/y
Zhao, X.P. and Webb, D.F. 2003, *Source regions and storm effectiveness of frontside full halo coronal mass ejections*, JGR 108, A6, 1234, [77 c, 5 c/y].

(16.8) Solar Flare Predictions

Ahmed, O.W., Qahwaji, R., Colak, T., et al. 2013, *Solar flare prediction using advanced feature extraction, machine learning, and feature selection*, SoPh 283, 157, [36 c, 8 c/y].
Aschwanden, M.J. and McTiernan, J.M. 2010, *Reconciliation of waiting time statistics of solar flares observed in hard X-rays*, ApJ 717, 683, [24 c, 3 c/y].
Aschwanden, M.J. and Freeland, S.L. 2012, *Automated solar flare statistics in soft X-rays over 37 years of GOES observations: The invariance of self-organized criticality during three solar cycles*, ApJ 754, 112, [51 c, 9 c/y].
Barnes, G. and Leka, K.D. 2008, *Evaluating the performance of solar flare forecasting methods*, ApJ 688, L107, [55 c, 6 c/y].
Barnes, G., Leka, K.D., Schumer, E.A., et al. 2007, *Probabilistic forecasting of solar flares from vector magnetogram data*, Space Weather 5/9, S09002.
Barnes, G., Leka, K.D., Schrijver, C.J., et al. 2016, *A comparison of flare forecasting methods. I. Results from the "All-Clear" workshop*, ApJ 829, 89, [22 c, 15 c/y].
Bélanger, E., Vincent, A., and Charbonneau, P. 2007, *Predicting solar flares by data assimilation in avalanche models. I. Model design and validation*, SoPh 245, 141, [13 c, 1 c/y].
Bloomfield, D.S., Higgins, P.A., McAteer, R.T.J., et al. 2012, *Toward reliable benchmarking of solar flare forecasting methods*, ApJ 747, L41, [50 c, 9 c/y].
Bobra, M.G. and Couvidat S. 2015, *Solar flare prediction using SDO/HMI vector magnetic field data with a machine-learning algorithm*, ApJ 798, 125, [43 c, 17 c/y].
Bobra, M.G. and Ilonidis, S. 2016, *Predicting coronal mass ejections using machine learing methods*, ApJ 821, 127, [16 c, 11 c/y].
Colak, T. and Qahwaji, R. 2009, *Automated solar activity prediction: A hybrid computer platform using machine learning and solar imaging for automated prediction of solar flares*, Space Weather 7/6, S06001.
Cui, Y., Li, R., Zhang, L. et al. 2006, *Correlation between solar flare productivity and photospheric magnetic field properties*, SoPh 237, 45, [50 c, 4 c/y].
Falconer, D.A., Moore, R.L., and Gary, G.A. 2003, *A measure from line-of-sight magnetograms for prediction of coronal mass ejections*, JGR 108, A10, 1380, [36 c, 2 c/y].
Falconer, D.A., Abdulnasser, F., Khazanov, I., et al. 2011, *A tool for empirical forecasting of major flares, coronal mass ejections, and solar particle events from a proxy of active-region free magnetic energy*, Space Weather 9/4, S04003, [37 c, 6 c/y].
Falconer, D.A., Moore, R.L., Barghouty, A.F., et al. 2012, *Prior flaring as a complement to free magnetic energy for forecasting solar eruptions*, ApJ 757, 32, [18 c, 3 c/y].
Gallagher, P.T., Moon, Y.J., and Wang, H. 2002, *Active-region monitoring and flare forecasting*, SoPh 209, 171, [93 c, 6 c/y].
Georgoulis, M.K. and Rust, D.M. 2007, *Quantitative forecasting of major solar flares*, ApJ 661, L109, [83 c, 8 c/y].
Georgoulis, M.K. 2012, *Are solar active regions with major flares more fractal, multifractal, or turbulent than others ?* SoPh 276, 161, [22 c, 4 c/y].
Jonas, E., Bobra, M., Shankar, V., et al. 2018, *Flare prediction using photospheric and coronal image data*, SoPh 293, 48, [1 c, 1 c/y].

Leka, K.D. and Barnes, G. 2003, *Photospheric magnetic field properties of flaring versus flare-quiet active regions. I. Data, general approach, and sample results*, ApJ 595, 1277, [100 c, 7 c/y].

Li, R., Wang, H.N., He, H. et al. 2007, *Support Vector Machine combined with K-Nearest Neighbors for solar flare forecasting*, Chinese J. Astron.Astrophys. 7/3, 441, [26 c, 2 c/y].

Mason, J.P. and Hoeksema, J.T. 2010, *Testing automated solar flare forecasting with 13 years of MDI magnetograms*, ApJ 723, 634, [50 c, 7 c/y].

Nishizuka, N., Sugiura, K., Kubo, Y., et al. 2017, *Solar flare prediction model with three machine-learning algorithms using UV brightening and vector magnetograms*, ApJ 835, 156, [10 c, 10 c/y].

Park, S.H., Chae, J., and Wang, H. 2010, *Productivity of solar flares and magnetic helicity injection in active regions*, ApJ 718, 43, [25 c, 3 c/y].

Schrijver, C.J. 2007, *A characteristic magnetic field pattern associated with all major solar flares and its use in flare forecasting*, ApJ 655, L117, [140 c, 13 c/y].

Schrijver, C.J. 2009, *Driving major solar flares and eruptions: A review*, Adv.Space Res. 43, 739, [108 c, 13 c/y].

Shibata, K., Isobe, H., Hillier, A., et al. 2013, *Can superflares occur on our Sun ?* PASJ 65/3, 49, [69 c, 15 c/y].

Strugarek, A. and Charbonneau, P. 2014, *Predictive capabilities of avalanche models for solar flares*, SoPh 289, 4137, [7 c, 2 c/y].

Tiwari, S.K., Venkatakrishnan, P., and Gosain, S. 2010, *Magnetic non-potentiality of solar active regions and peak X-ray flux of the associated flares*, ApJ 721, 622, [12 c, 2 c/y].

Wheatland, M.S. 2005, *A statistical solar flare forecast method*, Space Weather 3/7, S07003, [35 c, 3 c/y].

(16.9) Space Weather Forecasting

Basu, S., Groves, K.M., Basu, S., et al. 2002, *Specification and forecasting of scintillations in communication/navigation links: Current status and future plans*, JASTP 64/16. 1745, [105 c, 7 c/y].

Bothmer, V. and Daglis, I.A. 2006, *Space weather - Physics and effects*, PRAXIS Publishing Ltd. and Springer:Berlin, 490p.

Colaninno, R.C., Vourlidas, A., and Wu, C.C. 2013, *Quantitative comparison of methods for predicting the arrival of coronal mass ejections at Earth based on multiview imaging*, JGR 118/11, 6866, [44 c, 10 c/y].

Dryer, M., Smith, Z., Fry, C.D., et al. 2004, *Real-time shock arrival predictions during the "Halloween 2003 epoch"*, Space Weather 2/9, S09001, [65 c, 5 c/y].

Feynman, J. and Gabriel, S.B. 2000, *On space weather consequences and predictions*, JGR 105/A5, 10543, [68 c, 4 c/y].

Fry, C.D., Dryer, M., Smith, Z., et al. 2003, *Forecasting solar wind structures and shock arrival times using an ensemble of models*, JGR 108/A2, 1070, [94 c, 6 c/y].

Gopalswamy, N., Lara, A., Yashiro, S., et al. 2001, *Predicting the 1 AU arrival times of coronal mass ejections*, JGR 106/A12, 29207, [225 c, 14 c/y].

Gopalswamy, N., Yashiro, S., Liu, Y., et al. 2005, *Coronal mass ejections and other extreme characteristics of the 2003 October-November solar eruptions*, JGR 110/A9, A09S15, [81 c, 6 c/y].

Groth, C.P.T., De Zeeuw, D.L., and Gombosi, T.I. 2000, *Global 3-D MHD simulation of a space weather event: CME formation, interplanetary propagation, and interaction with the magnetosphere*, JGR 105/A11, 25053, [127 c, 7 c/y].

Kay, C., Opher, M., and Evans, R.M. 2013, *Forecasting a coronal mass ejection's altered trajectory: ForeCAT*, ApJ 775, 5, [44 c, 10 c/y].

Kay, C. and Gopalswamy, N. 2017, *Using the coronal evolution to successfully forward model CMEs' in situ magnetic profiles*, JGR 122/12, 11,810.
Knipp, D.J. 2011, *Understanding space weather and the physics behind it*, McGraw Hill.
Laurenza, M., Cliver, E.W., Hewitt, J., et al. 2009, *A technique for short-term warning of solar energetic particle events based on flare location, flare size, and evidence of particle escape*, Space Weather 7/4, S04008, [51 c, 6 c/y].
Liu, Y., Thernisien, A., Luhmann, J.G., et al. 2010, *Reconstructing coronal mass ejections with coordinated imaging and in situ observations: Global structure, kinematics, and implications for space weather*, ApJ 722, 1762, [84 c, 11 c/y].
McKenna-Lawlor, S.M.P., Dryer, M., Kartalev, M.D., et al. 2006, *Near real-time predictions of the arrival at Earth of flare-related shocks during solar cycle 23*, JGR 111/A11, A11103, [60 c, 5 c/y].
Manchester, W.B., Gombosi, T.I., Roussev, I., et al. 2004, *Modeling a space weather event from the Sun to the Earth: CME generation and interplanetary propagation*, JGR 109/A2, A02107, [146 c, 11 c/y].
Möstl, C. and Davies, J.A. 2013, *Speeds and arrival times of solar transients approximated by self-similar expanding circular fronts*, SoPh 285, 411, [49 c, 11 c/y].
Möstl, C., Amla, K., Hall, J.R., et al. 2014, *Connecting speeds, directions and arrival times of 22 coronal mass ejections from the Sun to 1 AU*, ApJ 787, 119, [79 c, 23 c/y].
Pulkkinen, T.I. 2007, *Space weather: Terrestrial perspective*, LRSP 4, 1, [63 c, 6 c/y].
Schrijver, C.J. and Siscoe, G.L. (eds.) 2010, *Heliophysics II. Space storms and radiation: Causes and effects*, Cambridge University Press: Cambridge, [6 c, 0.8 c/y].
Schrijver, C.J., Kauristie, K., Aylward, A.D., et al. 2016, *Understanding space weather to shield society: A global road map for 2015–2015 commissioned by COSPAR and ILWS*, Adv.Spac.Res. 55/12, 2745, [53 c, 35 c/y].
Schwenn, R., dal lago, A., Huttunen, E., et al. 2005, *The association of coronal mass ejections with their effects near the Earth*, Annales Geophysicae 23/3, 1033, [189 c, 15 c/y].
Schwenn, R. 2006, *Space weather: The solar perspective*, LRSP 3, 2, [102 c, 9 c/y].
Toth, G., Sokolov, I.V., Gombosi, T.I., et al. 2005, *Space weather modeling framework: A new tool for the space science community*, JGR 110/A12, A12226, [326 c, 26 c/y].

(16.10) Solar Irradiance

Ball, W.T., Unruh, Y.C., Krivova, N.A., et al. 2012, *Reconstruct of total solar irradiance 1974–2009*, A&A 541, A27, [65 c, 12 c/y].
Fligge, M., Solanki, S.K., and Unruh, Y.C. 2000, *Modeling irradiance variations from the surface distribution of the solar magnetic field*, A&A 353, 380, [124 c, 7 c/y].
Fontenla, J.M., Harder, J., Livingston, W., et al. 2011, *High-resolution solar spectral irradiance from extreme ultraviolet to far infrared*, JGR 116/D20, D20108, [90 c, 14 c/y].
Fontenla, J.M., Stancil, P.C., and Landi, E. 2015, *Solar spectral irradiance, solar activity, and the near-ultra-violet*, ApJ 809, 157, [17 c, 7 c/y].
Fontenla, J.M., Codrescu, M., Fedrizzi, M., et al. 2017, *Five years of synthesis of solar spectral irradiance from SDID/SISA and SDO/AIA images*, ApJ 834, 54, [5 c, 5 c/y].
Fröhlich, C. 2009, *Evidence of a long-term trend in solar solar irradianc* A&A 501, L27, [138 c, 13 c/y].
Güdel, M. 2007, *The Sun in time: Activity and Environment*, LRSP 4/1, 3, [77 c, 7 c/y].
Harder, J.W., Fontenla, J.M., Pilewskie, P., et al. 2009, *Trends in solar spectral irradiance variability in the visible and infrared*, GRL 36/7, L07801, [146 c, 17 c/y].
Kopp, G. 2016, *Magnitudes and timescales of total solar irradiance variability*, J.Space Weather and Space Climate 6/A30, [19 c, 13 c/y].
Kopp, G., Krivova, N., Wu, C.J., et al. 2016, *The impact of the revised sunspot record on solar irradiance reconstructions*, SoPh 291, 2951, [12 c, 8 c/y].

Lean, J. 2000, *Evolution of the Sun's spectral irradiance since the Maunder minimum*, GRL 27/16, 2425, [370 c, 21 c/y].

Foukal, P., Fröhlich, C., Spruit, H., et al. 2006, *Variations in solar luminosity and their effect on the Earth's climate*, Nature 443/7108, 161, [154 c, 13 c/y].

Krivova, N.A., Balmaceda, L., and Solanki, S.K. 2007, *Reconstruction of solar total irradiance since 2007 from the surface magnetic flux*, A&A 467, 335, [186 c, 18 c/y].

Livingston, W., Wallace, L., White, O.R. 2007, *Sun-as-a-star spectrum variations 1974–2006*, ApJ 657, 1137, [81 c, 8 c/y].

Wang, Y.M., Lean, J.L., and Sheeley, N.R.Jr. 2005, *Modeling the Sun's magnetic field and irradiance since 1713*, Apj 625, 522, [334 c, 27 c/y].

Woods, T.N., Tobiska, W.K., Rottman, G.J., et al. 2000, *Improved Lyman α irradiance modeling from 1947 through 1999 based on UARS observations*, JGR 105/A12, 27195, [211 c, 12 c/y].

Woods, T.N., Eparvier, F.G., Fontenla, J., et al. 2004, *Solar irradiance variability during the October 2003 solar storm period*, GRL 31/10, L10802, [113 c, 8 c/y].

Yeo, K.L., Krivova, N.A., Solanki, S.K., et al. 2014a, *Reconstruction of total and spectral solar irradiance from 1974 to 2013 based on KPVT, SoHO/MDI, and SDO/MDI observations*, A&A 570, A85, [57 c, 16 c/y].

Yeo, K.L., Krivova, N.A., and Solanki S.K. 2014b, *Solar cycle variation in solar irradiance*, SSRv 186, 137, [37 c, 11 c/y].

Appendix A: Reviews (2000–2018)

Plasma Physics (General)

Balogh, A., Bykov, A., Lin, R.P., et al. (eds.) 2013, *Particle acceleration in cosmic plasmas*, ISSI Space Science Series, Vol. 45.

Bellan, P.M. 2006, *Fundamentals of plasma physics*, Cambridge University Press: Cambridge, [150 c, 13 c/y].

Biskamp, D. 2000, *Magnetic reconnection in plasmas*, Cambridge University Press: Cambridge, [435 c, 25 c/y].

Boyd, T.J.M. and Sanderson,J.J. 2003, *The physics of llasmas*, Cambridge University Press: Cambridge, [132 c, 9 c/y].

Davidson, P.A. 2001, *An introduction to magnetohydrodynamics*, Cambridge Texts in Applied Mathematics, University of Cambridge: Cambridge, [237 c, 14 c/y].

Goedbloed, H., Keppens, R., and Poedts, S. 2019, *Magnetohydrodynamics of Laboratory and Astrophysical Plasmas*, Cambridge University Press: Cambridge.

Goossens, M. 2003, *An introduction to plasma astrophysics and magnetohydrodynamics*, ApSS Library 294, Kluwer Academic Publishers: Dordrecht, 405 pp., [24 c, 2 c/y].

Priest, E.R. and Forbes, T. 2000, *Magnetic reconnection (MHD Theory and applications)*, Cambridge University Press: Cambridge, [582 c, 33 c/y].

Somov, B.V. 2000, *Cosmic plasma physics*, ApSS Library, Vol. 251, (672 pp.), Kluwer Academic Publishers: Dordrecht, [48 c, 3 c/y].

Spitzer, L. 2006, *The physics of fully ionized gases*, Republication of 2nd edition, Dover Publ. Inc.: New York.

Spruit, H.C. 2013, *Essential magnetohydrodynamics for astrophysics*, Electronic textbooklet, available from website of Henk Spruit, http://www.mpa-garching.mpg.de/~henk/mhd12.pdf.

Tajima, T. and Shibata, K. 2002, *Plasma astrophysics*, Perseus Publishing: Cambridge, Massachusetts, [18 c, 1 c/y].

Thompson, M.J. 2006, *An introduction to astrophysical fluid dynamics*, London: Imperial College Press, [20 c, 2 c/y].

M. J. Aschwanden, *New Millennium Solar Physics*, Astrophysics and Space Science Library 458, https://doi.org/10.1007/978-3-030-13956-8

Solar Physics (General)

Alexander, D. 2009, *The Sun*, Greenwood Guides to the Universe, Greenwood Press: Santa Barbara, California.

Aschwanden, M.J. 1999 (1st edition), 2007 (2nd edition), *The Sun*, in *Encylopedia of the solar system*, (eds. L.A. McFadden, P.R. Weissman, and T.V. Johnson), Elsevier, Academic Press, p.71

Aschwanden,M.J. 2004a, *Physics of the solar corona - An introduction*, Praxis Springer, New York, First Edition (hardbound), 842p; Second Edition (paperback), 892p, [632 c, 49 c/y].

Aschwanden, M.J. 2010, *Image processing techniques and feature recognition in solar physics* (Invited review), SoPh 262, 235, [34 c, 5 c/y].

Bhatnagar, A., and Livingston, W. 2005, *Fundamentals of solar astronomy*, World Scientific Series in Astronomy and Astrophysics Vol.6, Singapore: WOrld Scientific, 468p, [9 c, 1 c/y].

Foukal, P.V. 2004, *Solar Astrophysics*, (2nd edition), ISBN 3-527-40374-4, Wiley-VCH, [51 c, 4 c/y].

Golub, L. and Pasachoff, J.M. 2001, *Nearest star: The surprising ccience of our Sun*, Harvard University Press: Cambridge Massachusetts, [10 c, 0.6 c/y].

Golub, L. and Pasachoff, J.M. 2009, *The solar corona* (2nd Edition), Cambridge University Press: Cambridge, [20 c, 2 c/y].

Hill, S.M. and Carlowicz, M. 2006, *The Sun*, Harry N. Abrams, Inc. (http://www.abramsbooks.com).

Lang, K.R. 2000, *The Sun from space*, Springer: Berlin, [20 c, 1 c/y].

Lang, K.R. 2001, *The Cambridge encyclopedia of the Sun*, Cambridge University Press: Cambrdge, [29 c, 2 c/y].

Mullan, D. 2010, *Physics of the sun. A first course*, CRC Series in Pure and Applied Physics, CRC Press: New York

Priest, E. 2014, *Magnetohydrodynamics of the Sun*, Carmbridge, UK: Cambridge University Press, [159 c, 45 c/y].

Stix, M. 2002, *The Sun: An introduction*, (2nd edition), Berlin: Springer, [151 c, 10 c/y].

Atomic Physics and Spectroscopy (Chap. 2)

Allende Prieto,C. 2016, *Solar and stellar photospheric abundances*, LRSP 13, 1, [2 c, 1 c/y].

Asplund, M., Grevesse, N., and Sauval, A.J. 2005, *The solar chemical composition*, in "Cosmic abundances as records of stellar evolution and nucleosynthesis", ASP Conference Series, (eds., T.G.Barnes III and Frank N.Bash), Astronomical Society of the Pacific Conference Series Vol. 336, 25, [1508 c, 121 c/y].

Asplund, M., Grevesse, N., Sauval, A.J. and Scott, P. 2009, *The chemical composition of the Sun*, ARAA 47, 481, [3261 c, 384 c/y].

Cox,A.N. (ed.) 2000, *Allen's astrophysical quantities*, AIP Press, 4th edition, Springer: New York, [686 c, 39 c/y].

DelToro-Iniesta, J.C. 2001, *Introduction to spectropolarimetry*, Cambridge University Press: Cambridge.

DelToro-Iniesta, J.C. and Ruiz Cobo B. 2016, *Inversion of the radiative transfer equation for polarized Light*, LRSP 13, 4, [2 c, 1 c/y].

Del Zanna, G. and Mason, H.E. 2017, *Solar UV and X-ray spectral diagnostics*, LRSP, arXiv:1809.01618v.

Doschek, G.A. and Feldman, U. 2010, *The solar UV-X-ray spectrum from 1.5 to 2000 A*, J. Phys. B: At.Mol.Opt.Phys. 43, 232001, [15 c, 2 c/y].

Feldman, U. and Widing, K.G. 2003, *Elemental abundances in the solar upper atmosphere derived by spectroscopic means*, SSRv 107/3, 665, [84 c, 6 c/y].

Feldman, U. and Widing, K.G. 2007, *Spectroscopic measurement of coronal compositions*, SSRv 130, 115, [18 c, 2 c/y].
Grevesse, N., Asplund, M., and Sauval, A.J. 2007, *The solar chemical composition*, SSRv 130, 105, [387 c, 37 c/y].
Kohl, J.L., Noci, G., Cranmer, S.R., et al. 2006, *Ultraviolet spectrocopy of the extended corona*, A&AR 13, 31, [118 c, 10 c/y].
Laming, J.M. 2015, *The FIP and inverse FIP effects in solar and stellar coronae*, LRSP 12, 2, [33 c, 13 c/y].
Milligan, R.O. 2015, *Extreme ultra-violet spectrocopy of the lower solar atmosphere during solar flares (Invited review)*, SoPh 290, 3399, [15 c, 6 c/y].
Penn, M.J. 2014, *Infrared solar physics*, LRSP 11, 2, [15 c, 1 c/y].
Phillips, K.J.H., Feldman, U., and Landi, E. 2008, *Ultraviolet and X-ray Spectroscopy of the Solar Atmosphere*, Cambridge Astrophysics Series Vol., 44, Cambridge University Press, Cambridge, [74 c, 8 c/y].

Solar Interior and Solar Dynamo (Chap. 3)

Basu, S. 2016, *Global seismology of the Sun*, LRSP 13, 2, [8 c, 5 c/y].
Charbonneau, P. 2005, 2010, *Dynamo models of the solar cycle*, LRSP 2, 2 (2005), 7:3 (2010), [410 c, 47 c/y].
Charbonneau, P. 2013, *Solar and stellar dynamos*, in Saas-Fee Advanced Course 38, Swiss Society for Astrophysics and Astronomy, Steiner (ed.), 237p, e-book, [9 c, 1 c/y].
Cheung, M.C.M. and Isobe, H. 2014, *Flux emergence (theory)*, LRSP 11, 3, [38 c, 11 c/y].
Christensen-Dalsgaard, J. 2002, *Helioseismology*, Rev.Modern Phys. 74/4, 1073, [305 c, 20 c/y].
Fan, Y. 2004, 2009, *Magnetic fields in the solar convection zone*, LRSP 1, 1 (2004), 6:4 (2009), [197 c, 23 c/y].
Gizon, L., and Birch, A.C. 2005, *Local helioseismology*, LRSP 2, 6, [124 c, 10 c/y].
Gough, D. 2013, *What have we learned from helioseismology, what have we really learned, and what do we aspire to learn?*, SoPh 287, 9, [13 c, 3 c/y].
Guedel, M. 2007, *The Sun in time: Activity and environment*, LRSP 4, 3, [70 c, 7 c/y].
Hathaway, D.H. 2010, 2015, *The solar cycle*, LRSP 7, 1 (2010), 12:4 (2015), [311 c, 61 c/y].
Hood, A.W. and Hughes, D.W. 2011, *Solar magnetic fields*, Physics of the Earth and Planetary Interiors 187, [3 c, 0.5 c/y].
Howe, R. 2009, *Solar interior rotation and its variation*, LRSP 6, 1, [116 c, 14 c/y].
Kosovichev, A.G., Duvall, T.L.Jr., and Scherrer, P.H. 2000, *Time-distance inversion methods and results (Invited review)*, SoPh 192, 159, [240 c, 14 c/y].
Kosovichev, A.G. 2011, *Advances in global and local helioseismology: An introductory review*, Lecture Notes in Physics 832, 3, [12 c, 2 c/y].
Miesch, M.S. 2005, *Large-scale dynamics of the convection zone and tachocline*, LRSP 2, 1, [149 c, 12 c/y].
Narayanan, A.S. 2013, *An introduction to waves and oscillations in the Sun*, Series Astronomy and Astrophysics Library, XII, 222 p, Springer: Berlin.
Nordlund, A, Stein, R.F., and Asplund, M. 2009, *Solar surface convection*, LRSP 6, 2, [169 c, 20 c/y].
Petrovay, K. 2010, *Solar cycle prediction*, LRSP 7, 6, [73 c, 10 c/y].
Schrijver, C.J. and Zwaan, C. 2000, *Solar and stellar magnetic activity*, Cambridge University Press: Cambridge, [195 c, 11 c/y].
Sheeley, N.R. 2005, *Surface evolution of the Sun's magnetic field: A historical review of the flux-transport mechanism*, LRSP 2, 5, [50 c, 4 c/y].
Soon, W.H. and Yaskell, S.H. 2003, *The Maunder minimum and the variable Sun-Earth connection*, World Scientific: New Jersey, [12 c, 1 c/y].

Stein, R.F. 2012, *Solar surface magneto-convection*, LRSP 9, 4, [33 c, 6 c/y].
Usoskin, I.G. 2008, 2013, 2017, *A history of solar activity over millennia*, LRSP 5, 3 (2008); 10, 1 (2013); 14, 3 (2017), [191 c, 52 c/y].

Photosphere and Sunspots (Chap. 4)

Borrero, J.M., and Ichimoto, K. 2011, *Magnetic structure of sunspots*, LRSP 8, 4, [67 c, 10 c/y].
Damiani, C., Rozelot, J.P., Lefebvre, S. et al. 2011, *A brief history of the solar oblateness. A review*, J.Atmos Solar-Terr. Phys. 73, 241, [24 c, 4 c/y].
Khomenko, E., and Collados, M. 2015, *Oscillations and waves in sunspots*, LRSP 12, 6, [15c, 6 c/y].
Lagg, A., Lites, B., Harvey, J. et al. 2017, *Measurements of photospheric and chromospheric magnetic fields*, SSRv 210, 37, [6 c, 6 c/y].
Mackay,D.H., and Yeates, A. 2012, *The Sun's global photospheric and coronal magnetic fields: Observations and models*, LRSP 9, 6, [66 c, 12 c/y].
Rempel,M. and Schlichenmaier,R. 2011, *Sunspot modeling: From simplified models to radiative MHD Simulations*, LRSP 8, 3, [35 c, 5 c/y].
Rieutord,M., and Rincon, F. 2010, *The Sun's supergranulation*, LRSP 7, 2, [72 c, 10 c/y].
Solanki, S.K. 2003, *Sunspots: An overview*, A&ARv 11/2, 153, [387 c, 27 c/y].
Solanki, S.K., Inhester, B., and Schuessler, M. 2006, *The solar magnetic field*, Reports on Progress in Physics 69/3, 563, [118 c, 10 c/y].
Thomas, J.H. and Weiss, N.O. 2004, *Fine structure in sunspots*, ARvA&A 42, 517, [85 c, 6 c/y].
Thomas, J.H. and Weiss, N.O. 2008, *Sunspots and starspots*, Cambridge, UK: Cambridge Unviersity Press, [61 c, 6 c/y].

Chromosphere and Spicules (Chap. 5)

Carlsson, M. 2007, *Modeling the Solar Chromosphere*, in ASP Conf. Ser. 368, The Physics of Chromospheric Plasmas, (ed. P. Heinzel, R. Dorotovic, and R.J.Rutten), (San Francisco: ASP), 49, [15 c, 1 c/y].
Carlsson, M. 2008, *3D radiative transfer in stellar atmospheres*, Physica Scripta 133, 014012, [7 c, 1 c/y].
Jess, D.B., Morton, R.J., Verth, G., et al. 2015, *Multiwavelength studies of MHD waves in the solar chromosphere. An overview of recent results*, SSRv 190, 103, [33 c, 13 c/y].
Sterling, A.C. 2000, *Solar spicules: A review of recent models and targets for future observations*, SoPh 196,79, [170 c, 20 c/y].
Tsiropoula, G., Tziotziou, K., Kontogiannis, I., et al. 2012, *Solar fine-scale structures. I. Spicules and Other small-scale, jet-like events at the chromospheric level: Observations and physical parameters*, SSRv 169, 181, [60 c, 11 c/y].
Zaqarashvili,T.V. and Erdelyi,R. 2009, *Oscillations and waves in solar spicules*, SSRv 149, 355, [93 c, 11 p/y].

The Quiet-Sun Corona (Chap. 6)

Longcope, D.W. 2005, *Topological methods for the analysis of solar magnetic fields*, LRSP 2, 7, [107 c, 9 c/y].
Wiegelmann,T., and Sakurai, T. 2012, *Solar force-free magnetic fields*, LRSP 9, 5, [97 c, 18 c/y].

Wiegelmann,T., Thalmann, J. K., and Solanki, S.K. 2014, *The magnetic field in the solar atmosphere*, A&AR 22, 78, [38 c, 11 c/y].
Wiegelmann,T., Petrie, G.J.D., and Riley,P. 2017, *Coronal magnetic field models*, SSRv 210, 249, [10 c, 20 c/y].

Coronal Holes and Jets (Chap. 7)

Cranmer, S.R. 2002, *Coronal holes and the high-speed solar wind*, SSRv 101, 229, [156 c, 10 c/y].
Cranmer, S.R. 2009, *Coronal holes*, LRSP 6, 3, [126 c, 15 c/y].
Gloeckler, G, and Geiss, J. 2007, *The composition of the solar wind in polar coronal holes*, SSRv 130, 139, [42 c, 4 c/y].
Petrie, G.J.D. 2015, *Solar magnetism in the polar regions*, LRSP 12, 5, [12 c, 5 c/y].
Petrie,G. and Ettinger,S. 2017, *Polar field reversals and active region decay*, SSRv 210, 77, [5 c, 2 c/y].
Poletto,G. 2015, *Solar Coronal Plumes*, LRSP 12, 7, [4 c, 2 c/y].
Raouafi, N.E., Patsourakos, S., Pariat, E., Young, P.R., et al. 2016, *Solar coronal jets: Observations, theory, and modeling*, Space Science Reviews, 201, 1, [30 c, 20 c/y].
Wilhelm, K., Abbo, L., Auchère, F., et al. 2011, *Morphology, dynamics and plasma parameters of plumes and inter-plume regions in solar coronal holes*, A&ARv 19, 35, [42 c, 6 c/y].

Active Regions and Loops (Chaps. 8, 9)

Aschwanden, M.J. 2011, *Solar stereoscopy and tomography*, LRSP 8, 5, [19 c, 3 c/y].
Cheung, M.C.M., van Driel-Gesztelyi, L., Martinez Pillet, V., and Thompson, M.J. 2017, *The life cycle of active region magnetic fields*, SSRv 210, 317.
DeMoortel, I. and Browning, P. 2015, *Recent advances in coronal heating*, Philosophical Transactions Royal Society A 373, 2042, p.20140269, [27 c, 11 c/y].
Klimchuk, J.A. 2015, *Key aspects of coronal heating*, Royal Society of London Philosophical Transactions Series A, 373, p.20140256, [44 c, 18 c/y].
Reale, F. 2010, 2014, *Coronal loops: Observations and modeling of confined plasma*, LRSP 7, 5 (2010); 11, 4 (2014), [129 c, 17 c/y].
VanDriel-Gesztelyi,L. and Green,L.M. 2015, *Evolution of active regions*, LRSP 12, 1, [15 c, 6 c/y].

Loop Oscillations and Waves (Chap. 10)

Banerjee,D., Erdelyi,R., Oliver,R., and O'Shea,E. 2007, *Present and future observing trends in atmospheric magneto-seismology*, SoPh 246, 3, [156 c, 15 c/y].
Nakariakov,V.M. and Verwichte, E. 2005, *Coronal waves and oscillations*, LRSP 2, 3, [246 c, 20 c/y].
Nakariakov, V.M., Pilipenko, V., Jelinek, B., et al. 2016, *Magnetohydrodynamic oscillations in the solar corona and Earth's magnetosphere: Towards consolidated understanding*, SSRv 200, 75, [48 c, 32 c/y].
Roberts, B. 2000, *Waves and oscillations in the corona (Invited review)*, SoPh 193, 139, [200 c, 11 c/y].
Ruderman, M.S., and Erdelyi,R. 2009, *Transverse oscillations of coronal loops*, SSRv 149, 199, [98 c, 12 c/y].

Stepanov, A.V., Zaitsev, V.V., and Nakariakov, V.M. 2012, *Coronal seismology. Waves and Oscillations in Stellar Coronae*, Verlag GmbH & Co., KGaA, Weinheim, Germany, [27 c, 5 c/y].
VanDoorsselaere,T., Kupriyanova, E.G., and Yuan, D. 2016, *Quasi-periodic pulsations in solar and stellar flares: An overview of recent results (Invited review)*, SoPh 291, 3143, [17 c, 11 c/y].
Wang, T.J. 2011, *Standing slow-mode waves in hot coronal loops: Observations, modeling, and coronal seismology*, SSRv 158, 397, [66 c, 10 c/y].
Wang, T.J., 2016, *Waves in Solar Coronal Loops in Low-Frequency Waves in Space Plasmas*, (eds. by A. Keiling, D.H. Lee, V. Nakariakov), Geophysical Monograph Series, Vol. 216, Wiley, p.395, [9 c, 6 c/y].

Filaments and Prominences (Chap. 11)

Arregui, I., Oliver, R., and Ballester, J.L. 2012, *Prominence oscillations*, LRSP 9, 2, and 15, 3, [61 c, 11 c/y].
Parenti,S. 2014, *Solar prominences: Observations*, LRSP 11, 1, [53 c, 15 c/y].
Vial, J.C. and Engvold,O. (eds.) 2015, *Solar prominences*, Astrophysics. Space Sience Library ASSL 415, Springer: Berlin, [21 c, 8 c/y].

Flares (Chaps. 12, 13)

Aschwanden, M.J. 2002, *Particle acceleration and kinematics in solar flares. A synthesis of recent observations and theoretical concepts* (Invited review), SSRv 101:(1–2), 1–227, [323 c, 21 c/y].
Aschwanden, M.J. 1987, *Theory of radio pulsations in coronal loops*, SoPh 111, 113, [211 c, 7 c/y].
Benz, A.O. 2008, 2017, *Flare observations*, LRSP 5, 1 (2008), 14, 2 (2017), [159 c, 17 c/y].
Charbonneau, P., McIntosh, S.W., Liu, H.L., and Bogdan,T.J. 2001, *Avalanche models for solar flares*, SoPh 203, 321, [130 c, 8 c/y].
Chernov, G.P. 2011, *Fine structure of solar radio bursts*, Astrophysics and Space Science Library Vol. 375, Springer: Berlin, [15 c, 2 c/y].
Fletcher, L., Dennis, B.R., Hudson, H.S., et al. 2011, *An observational overview of solar flares*, SSRv 159, 19, [238 c, 37 c/y].
Hannah, I.G., Hudson, H.S., Battaglia, M., et al. 2011, *Microflares and the statistics of X-ray flares*, SSRv 159, 263, [60 c, 9 c/y].
Holman, G.D., Aschwanden, M.J., Aurass, H., et al. 2011, *Implications of X-ray observations for electron acceleration and propagation in solar flares*, SSRv 159, 107, [146 c, 22 c/y].
Holman, G.D. 2016, *Scientific considerations for future spectroscopic measurements from space of activity on the Sun*, JGR 121/12, 11,667, [7 c, 5 c/y].
Hudson, H.S., Wolfson, C.J., and Metcalf, T.R. 2006, *White-light flares: a TRACE/ RHESSI overview*, SoPh 234, 79, [78 c, 7 c/y].
Hudson,H.S. 2011, *Global properties of solar flares*, SSRv 158, 5, [80 c, 12 c/y].
Janvier, M., Aulanier, G., and Démoulin, P. 2015, *From coronal observations to MHD simulations, the building blocks for 3D models of solar flares*, (Invited Review), SoPh 290, 3425, [40 c, 16 c/y].
Kontar, E.P., Brown, J.C., Emslie, A.G., et al. 2011, *Deducing electron properties from hard X-ray observations*, SSRv 159, 301, [85 c, 13 c/y].
Krucker, S., Battaglia, M., Cargill, P.J., et al. 2008, *Hard X-ray emission from the solar corona*, A&AR 16, 155, [123 c, 13 c/y].

Janvier,M., Aulanier, G., and Démoulin, P. 2015, *From coronal observations to MHD simulations, the building blocks for 3-D Models of solar flares* (Invited review), SoPh 290, 3425, [34 c, 14 c/y].
McLaughlin, J.A., Nakariakov, V.M., Dominique, M., et al. 2018, *Modelling quasi-periodic pulsations in solar and stellar flares*, SSRv 214, 45, [10 c, 10 c/y].
Milligan, R.O. 2015, *EUV spectroscopy of the lower solar atmosphere during solar flares (Invited review)*, SoPh 290, 3399, [19 c, 13 c/y].
Nakariakov, V.M. and Melnikov, V.F. 2009, *Quasi-periodic pulsations in solar flares*, SSRv 149, 119, [187 c, 21 c/y].
Nakariakov, V.M., Inglis, A.R., Zimovets, I.V., et al. 2010, *Oscillatory processes in solar flares*, Plasma Physics and Controlled Fusion 52/12, 124009, [34 c, 5 c/y].
Nakariakov, V.M. and Melnikov, V.F. 2009, *Quasi-periodic pulsations in solar flares*, SSRv 149, 119, [187 c, 21 c/y].
Nakariakov, V.M., Pilipenko, V., Heilig, B., et al. 2016, *MHD oscillations in the solar corona and Earth's magnetosphere: Towards consolidated understanding*, SSRv 200, 75, [48 c, 32 c/y].
Nindos, A., Aurass, H., Klein, K.L. et al. 2008, *Radio emission of flares and coronal mass ejections. Invited review*, SoPh 253, 3, [48 c, 5 c/y].
Pick, M., and Vilmer, N. 2008, *Sixty-five years of solar radioastronomy: flares, coronal mass ejections and Sun-Earth connection*, A&AR 16, 1, [68 c, 7 c/y].
Priest, E.R. and Forbes, T.G. 2002, *The magnetic nature of solar flares*, Astron.Astroph.Rev. 10/4, 313, [443 c, 9 c/y].
Shibata,K., and Magara, T. 2011, *Solar flares: Magnetohydrodynamic processes*, LRSP 8, 6, [238 c, 37 c/y].
Zharkova, V.V. 2012, *Electron and proton kinetics and dynamics in flaring atmospheres*, Wiley-VCH Verlag GmbH and Co.
Zharkova, V.V., Arzner, K., Benz, A.O., et al. 2012, *Recent advances in understanding particle acceleration processes in solar flares*, SSRv 159, 257, [104 c, 19 c/y].
Van Doorsselaere, T., Kupriyanova, E.G., and Yuan, D. 2016, *Quasi-periodic pulsations in solar and stellar flares: An overview of recent results (Invited Review)*, SoPh 291, 3143, [33 c, 22 c/y].
Vilmer, N., MacKinnon, A.L., and Hurford, G.J. 2011, *Properties of energetic ions in the solar atmosphere from gamma-ray and neutron observations*, SSRv 159, 167, [56 c, 9 c/y].
White, S.M., Benz, A.O., Christe, S., et al., 2011, *The relationship between solar radio and hard X-ray emission*, SSRv 159, 225, [62 c, 10 c/y].

Coronal Mass Ejections (Chaps. 14, 15)

Cane, H.V. 2000, *Coronal mass ejections and Forbush decreases*, SSRv 93, 55, [215 c, 12 c/y].
Chen, P.F., Ding, M.D., and Fang, C. 2005, *Synthesis of CME-associated Moreton and EIT wave features from MHD simulations*, SSRv 121, 201, [31 c, 2 c/y].
Chen, P.F. 2011, *Coronal mass ejections: Models and their observational basis*, LRSP 8, 1, [182 c, 28 c/y].
Chen, J. 2017, *Physics of erupting solar flux ropes: Coronal mass ejections (CMEs) - Recent advances in theory and observation*, Physics of Plasmas 24/9, 090501.
Forbes, T.G. 2000, *A review on the genesis of coronal mass ejections*, JGR 105/A10, 23153, [362 c, 21 c/y].
Forbes, T.G., Linker, J.A., Chen, J., et al. 2006, *CME theory and models*, SSRv 123, 251, [251 c, 22 c/y].
Forbes, T. 2010, *Models of coronal mass ejections and flares*, in "Heliosphysics, Space Storms and Radiation: Causes and Effects" (eds. Schrijver C.J. and Sicoe, G.L.), Cambridge University Press: Cambridge, p.159.

Gibson, S.E., Fan, Y., Tŕök, T., et al. 2006, *The evolving sigmoid: Evidence for magnetic flux ropes in the corona before, during, and after CMEs*, SSRv 124, 131, [68 c, 6 c/y].
Gopalswamy, N. 2004, *A global picture of CMEs in the inner heliosphere*, in The Sun and Heliosphere as an Integrated System, (eds. G. Poletto and S.T. Suess), ASSL 317, Dordrecht: Kluwer, p.201, [74 c, 5 c/y].
Hudson, H.S., Bougeret, J.L., and Burkepile, J. 2006, *Coronal mass ejections: overview of observations*, SSRv 123, 13, [43 c, 4 c/y].
Kontar, E.P. and Nindos, A. 2018, *Combined radio and space-based solar observations: From techniques to new results - Preface*, SoPh 293/6, 90.
Lin, J., Murphy, N.A., Shen, C., et al. 2015, *Review on current sheets in CME development: Theories and observations*, SSRv 194, 237, [24 c, 10 c/y].
Long, D.M., Bloomfield, D.S., Chen, P.F., et al. 2017, *Understanding the physical nature of coronal "EIT waves"*, SoPh 292, 7, [22 c, 22 c/y].
Low, B.C. 2001, *Coronal mass ejections, magnetic flux ropes, and solar magnetism*, JGR 106, A11, 25141, [284 c, 17 c/y].
Lugaz, N., Temmer, M., Wang, Y., et al. 2017, *The interaction of successive CMEs: A review*, SoPh 292, 64, [21 c, 21 c/y].
Mierla, M., Inhester, B., Antunes, A., et al. 2010, *On the 3D reconstruction of coronal mass ejections using coronagraph data*, Annales Geophysicae 28, 203, [62 c, 8 c/y].
Rouillard, A.P. 2011, *Relating white light and in situ observations of coronal mass ejections: A review*, JASTP 73, 1201, [43 c, 7 c/y].
Schmieder,B., Aulanier, G., and Vrsnak, B. 2015, *Flare-CME models: An observational perspective* (Invited review), SoPh 290, 3457, [31, 12 c/y].
Schrijver, C.J. 2009, *Driving major solar flares and eruptions: A review*, Adv.Spac.Res. 43/5, 739, [111 c, 13 c/y].
Shen, F., Wang, Y., Shen, C., et al. 2017, *On the collision nature of two coronal mass ejections: A review*, SoPh 292, 104, [4 c, 4 c/y].
Vrsnak, B. and Cliver, E.W. 2008, *Origin of coronal shock waves. Invited Review* SoPh 253, 215, [133 c, 14 c/y].
Webb, D.F. and Howard, T.A. 2012, *Coronal mass ejections: Observations*, LRSP 9, 3, [109 c, 20 c/y].
Wimmer-Schweingruber, R.F., Crooker, N.U., Balogh,A., et al. 2006, *Understanding interplanetary coronal mass ejection signatures*, SSRv 123, 177, [75 c, 7 c/y].
Zhang, M. and Low, B.C. 2005, *The hydrodynamic nature of solar coronal mass ejections*, ARAA 43, 103, [133 c, 10 c/y].

CME-Driven Global Waves (Sect. 15.7)

Gallagher, P.T., and Long, D.M. 2011, *Large-scale bright fronts in the solar corona: A review of "EIT waves"*, SSRv 158, 365, [82 c, 13 c/y].
Liu, W. and Ofman, L. 2014, *Advances in observing various coronal EUV waves in the SDO Era and their seismological applications* (Invited review), SoPh 289, 3233, [75 c, 21 c/y].
Patsourakos,S., and Vourlidas, A. 2012, *On the nature and genesis of EUV waves: A synthesis of observations from SOHO, STEREO, SDO, and Hinode* (Invited review), SoPh 281, 187, [76 c, 14 c/y].
Warmuth, A. 2015, *Large-scale globally propagating coronal waves*, LRSP 12, 3, [24 c, 10 c/y].
Wills-Davey, M.J., and Attrill, G.D.R. 2009, *EIT waves: A changing ynderstanding over a solar cycle*, SSRv 149, 325, [86 c, 10 c/y].

Sun-Earth Connections (Chap. 16)

Balogh, A., Hudson, H.S., Petrovay, K., and von Steiger, R. 2014, *Introduction to the solar activity cycle: Overview of causes and consequences*, SSRv 186, 1, [3 c, 1 c/y].
Bothmer, V. and Daglis, I.A. 2006, *Space weather - Physics and effects*, PRAXIS Publishing Ltd. and Springer:Berlin, 490p.
Carlowicz, M.J. and Lopez, R.E. 2002, *Storms from the Sun - The emerging science of space weather*, The Joseph Henry Press: Washington DC.
Foukal, P., Fröhlich, C., Spruit, H., et al. 2006, *Variations in solar luminosity and their effect on the Earth's climate*, Nature 443/7108, 161, [154 c, 13 c/y].
Güdel, M. 2007, *The Sun in time: Activity and Environment*, LRSP 4/1, 3, [77 c, 7 c/y].
Haigh, J.D. 2007, *The Sun and the Earth's climate*, LRSP 4, 2, [52 c, 5 c/y].
Kamide, Y., and Chian, A.C. (eds.) 2007, *Handbook of the solar-terrestrial environment*, Springer: New York, [7 c, 0.7 c/y].
Knipp, D.J. 2011, *Understanding space weather and the physics behind it*, McGraw Hill.
Poletto, G. and Suess, S.T. 2004, *The Sun and the heliosphere as an integrated system*, Springer Verlag: Berlin.
Pulkkinen, T.I. 2007, *Space weather: Terrestrial perspective*, LRSP 4, 1, [63 c, 6 c/y].
Schrijver, C.J. 2009, *Driving major solar flares and eruptions: A review*, AdSpR 43, 739, [102 c, 12 c/y].
Schrijver, C.J. and Siscoe, G.L. (eds.) 2010, *Heliophysics II. Space storms and radiation: Causes and effects*, Cambridge University Press: Cambridge, [6 c, 0.8 c/y].
Schwenn, R. 2006, *Space weather: The solar perspective*, LRSP 3, 2, [102 c, 9 c/y].
Yeo, K.L., Krivova, N.A., and Solanki S.K. 2014, *Solar cycle variation in solar irradiance*, SSRv 186, 137, [37 c, 11 c/y].

Solar Wind (Sects. 16.1–16.3)

Abbo,L., Ofman, L., Antiochos, S. K., et al. 2016, *Slow solar wind: Observations and modeling*, SSRv 201, 55, [14 c, 9 c/y].
Antonucci, E. 2006, *Wind in the solar corona: Dynamics and composition*, SSRv 124, 35, [15 c, 1 c/y].
Bruno,R. and Carbone, V. 2005, 2013, *The solar wind as a turbulence laboratory*, LRSP 2, 4 (2005); 10, 2 (2013), [564 c, 45 c/y].
Burgess, D., Drake, J., Marsch, E., et al. (eds.) 2013, *Multi-scale physics in coronal heating and solar wind acceleration*, ISSI Space Science Series Vol.38.
Cranmer, S.R. 2002, *Coronal holes and the high-speed solar wind*, SSRv 101, 229, [160 c, 10 c/y].
Gombosi, T.I., van der Holst, B., Mancheser, W.B., et al. 2018, *Extended MHD modeling of the steady solar corona and the solar wind*, LRSP 15, 4.
Hollweg, J.V. and Isenberg, P.A. 2002, *Generation of the fast solar wind: A review with emphasis on the resonant cyclotron interaction*, JGR A 107, 1147, [195 c, 13 c/y].
Marsch, E. 2006, *Kinetic physics of the solar corona and solar wind*, LRSP 3, 1, [290 c, 27 c/y].
Ofman, L. 2010, *Wave modeling of the solar wind*, LRSP 7, 4, [49 c, 7 c/y].
Reisenfeld, B.B., Burnett, D.S., Becker, R.H., et al. 2007, *Elemental abundances of the bulk solar wind: Analysis from Genesis and ACE*, SSRv 130, 79, [35 c, 3 c/y].
Richardson, I.G. 2004, *Energetic particles and corotating interaction regions in the solar wind*, SSRv 111, 267, [88 c, 7 c/y].
Tsurutani, B.T., Gonzalez, W.D., Gonzalez, A.L.C. 2006, *Corotating solar wind streams and recurent geomagnetic activity: A review*, JGR 111, A7, A07S01, [225 c, 21 c/y].
Zurbuchen, T.H. and Richardson, I.G. 2006, *In-situ solar wind and magnetic field signature of interplanetary coronal mass ejections*, SSRv 123, 31, [216 c, 19 c/y].

Heliospheric Magnetic Structures (Sect. 16.4)

Balogh, A., Marsden, R.G. and Smith,E.J. (eds.) 2001, *The heliosphere near solar minimum - The Ulysses perspective*, Springer-Praxis Books in Astrophysics and Astronomy.
Lockwood, M. 2013, *Reconstruction and prediction of variations in the open solar magnetic flux and interplanetary conditions*, LRSP 10, 4, [45 c, 10 c/y].
Owens, M.J., and Forsyth, R.J. 2013, *The heliospheric magnetic field*, LRSP 10, 5, [50 c, 11 c/y].
Schrijver, C.J. and Siscoe, G.L. (eds.) 2009, *Heliophysics I. Plasma physics of the local cosmos*, Cambridge University Press: Cambridge.
Schrijver, C.J. and Siscoe, G.L. (eds.) 2010, *Heliophysics III. Evolving solar activity and the climates of space and Earth*, Cambridge University Press: Cambridge.
Zurbuchen, T.H. 2007, *A new view of the coupling of the Sun and the heliosphere*, ARAA 45, 297, [76 c, 7 c/y].

Solar Energetic Particles (Sects. 16.5–16.6)

Aschwanden, M.J. 2012, *GeV particle acceleration in solar flares and ground level enhancement (GLE) Events*, SSRv 171, 3, [54 c, 10 c/y].
Cohen, C.M.S., Mewaldt, R.A., Leski, R.A. et al. (2007), *Solar elemental composition based on studies of solar energetic particles*, SSRv 130, 183, [22 c, 2 c/y].
Desai, M.I. and Giacalone, J. 2016, *Large gradual solar energetic particle events*, LRSP 13, 3, [18 c, 12 c/y].
Gopalswamy, N., Xie, H., Yashiro, S., et al. 2012, *Properties of ground level enhancement events and the associated solar eruptions during solar cycle 23*, SSRv 171, 23, [109 c, 20 c/y].
Kahler, S.W. 2007, *Solar sources of heliospheric energetic electron events - Shocks or flares ?* SSRv 129, 359, [28 c, 3 c/y].
Mewaldt, R.A., Looper, M.D., Cohen, C.M.S., et al. 2012. *Energy spectra, composition, and other properties of ground-level events during solar cycle 23*, SSRv 171, 97, [61 c, 11 c/y].
Reames, D.V. 2013, *The two sources of solar energetic particles*, SSRv 175, 53, [129 c, 29 c/y].
Reames, D.V. 2017, *Solar Energetic Particles*, Lecture Notes in Physics 932, Springer: New York

Appendix B: Journal Abbreviations

A&A	Astronomy and Astrophysics
A&AS	Astronomy and Astrophysics Supplement Series
A&ARv	Astronomy and Astrophysics Review
AdSpR	Advances in Space Research
ApJ	The Astrophysical Journal
ApJL	The Astrophysical Journal Letters
ApJS	The Astrophysical Journal Supplement Series
ARAA	Annual Review of Astronomy and Astrophysics
ASSL	Astrophysics and Space Science Library
BAAS	Bulletin of the American Astronomical Society
GRL	Geophysics Research Letters
JASTP	Journal of Atmospheric and Solar-Terrestrial Science
JGR	Journal of Geophysics Research
JKAS	Journal of Korean Astronomical Society
LRSP	Living Reviews in Solar Physics
MNRAS	Monthly Notices of the Royal Astronomical Society
PASA	Publications of the Astronomical Society of Australia
PASJ	Publications of the Astronomical Society of Japan
PASP	Publications of the Astronomical Society of the Pacific
SoPh	Solar Physics
SoSyR	Solar System Research
SPIE	Proc. SPIE (International Society for Optical Engineering)
SSRv	Space Science Reviews

M. J. Aschwanden, *New Millennium Solar Physics*, Astrophysics and Space Science Library 458, https://doi.org/10.1007/978-3-030-13956-8

Appendix C: Acronyms

1-D, 2-D, 3-D	One, two, three-dimensional
AC	Alternating current
ACE	Advanced Composition Explorer (spacecraft)
ACHF	Adaptive Circular Highpass Filter
ACRIM	Active Cavity Radiometer Irradiance Monitor (on SMM)
ADS	Astronomical Database System (NASA)
AE-E	Atmospheric Explorer E (satellite)
AIA	Atmospheric Imaging Assembly (on SDO)
AKR	Auroral Kilometric Radiation
ALMA	Atacama Large Millimeter/Submillimeter Array (Chile)
AMATERAS	Assembly of Metric-band Aperture TElescope and Real-time Analysis System (Japan)
AMR	Adaptive Mesh Refinement (MHD code)
ANMHD	Anelastic 3-D MHD code
ARGOS	Adaptive Refined Godunov Solver (HD code)
ARM	Active Region Monitor (data system)
ARMS	Adaptively-Refined MHD Solver (numerical code)
ARTB	Active Region Transient Brightenings
ARTEMIS	Acceleration, Reconnection, Turbulence and Electrodynamics of Moon's Interction with the Sun (multichannel solar radio spectrograph (Athens)
ASE	American Science and Engeneering (rocket)
ASTRON	Netherlands Astronomical Foundation
ATA	Allen Telescope Array (California)
ATM	Apollo Telescope Mount (on Skylab)
AU	Astronomical unit
AVS	Time-Amplitude Spectrometer (on CORONAS-F)
AWSOM	Alfvén Wave Solar Model (MHD code)

M. J. Aschwanden, *New Millennium Solar Physics*, Astrophysics and Space Science Library 458, https://doi.org/10.1007/978-3-030-13956-8

BATSE	Burst and Transient Source Experiment (on CGRO)
BATSRUS	Block Adaptive Tree Solar-Wind Roe Upwind Scheme (MHD code)
BBSO	Big Bear Solar Observatory (in California)
BCS	Bent Crystal Spectrometer (on SMM)
BCS	Bragg Crystal Spectrometer (on Yohkoh)
BDA	Brazilian Decimetric Array (Brazil)
BFI	Broadband Filter Imager (on Hinode)
Bifrost	Nymerical MHD code
BISON	Burmingham Solar Oscillations Network (helioseismology)
BRM	Fast X-Ray Monitor (on CORONAS-PHOTON)
CACTUS	Computer Aided CME Tracking Software (method)
CAT	Computer-Aided Tomography
CC	Charged Current (neutrino interaction)
CCD	Charge Coupled Device (camera)
CCMC	Community Coordinated Modeling Center (MHD codes)
CDAW	Coordinated Data Analysis Workshop (data center at GSFC)
CDS	Coronal Diagnostic Spectrometer (on SOHO)
CELIAS	Charge, ELement and Isotope Analysis (on SOHO)
CEM	Column Emission Measure
CGRO	Compton Gamma Ray Observatory (spacecraft)
CHIANTI	Atomic Database
CICM	Caltech Irreference Chromospheric Model
CIR	Co-rotating Interaction Regions (in heliosphere)
CME	Coronal Mass Ejection
CNO	Carbon Nitrogen Oxygen cycle
CO5BOLD	COnservative COde for the COmputation of COmpressible COnvection in a BOX of L dimensions (MHD code)
CoMP	Coronal Multi-Channel Polarimeter (at NSO)
COR1, COR2	Coronagraph 1 and 2 (on SECCHI/STEREO)
CORIMP	Coronal Image Processing (method)
CORONAS	Complex ORbital Observatory Near-earth of Activity of the Sun
CRISP	CRisp Imaging Spectro-Polarimeter (instrument on SST)
CSHKP	Carmichael-Sturrock-Hirayama-Kopp-Pneuman (flare model)
CSIRO	Commonwealth Scientific and Industrial Research Organisation
CSSS	Current Sheet Source Surface (magnetic field model)
CT	Correlation Tracker (on Hinode)
CT	Computed Tomography (method)

DC	Direct current
DEM	Differential emission measure (distribution)
DIFOS	Optical photometer (on CORONAS-I)
DIFOS	Solar photometer (on CORONAS-F)
DIOGENESS	X-Ray Spectrometer and Photometer (on CORONAS-F)
DH	Decameter-Hectrometric wavelength range
DKIST	Daniel K. Inouye Solar Telescope (Maui, USA)
DM	Dipole moment (solar magnetic field)
DOT	Dutch Open Telescope (La Palma, Spain)
DPR	Double Plasma Resonance
DST	Dunn Solar Telescope (Sacramento Peak, USA)
EBTEL	Enthalpy-Based Thermal Evolution of Loops (HD code)
E-CALLISTO	Compound Astronomical Low-Cost Low-Frequency Instrument for Spectroscopy
EDT	Eastern Daylight Time
EEMD	Ensemble Empirical Mode Decomposition (method)
EEGGL	Eruptive Event Generator using Gibson-Low (MHD code)
EGRET	Energetic Gamma Ray Experiment Telescope (on CGRO)
EIS	EUV Imaging Spectrometer (on Hinode)
EISCAT	European Incoherent Scatter Scientific Association
EIT	Extreme-ultraviolet Imaging Telescope (on SOHO)
ELECTRON-M-PESCA	Charged Particle Analyzer (on CORONAS-PHOTON)
EMD	Empirical Mode Decomposition (method)
EMI	Emission Measure Loci (data analysis method)
ENLIL	Solar wind model
ERB	Earth Radiation Budget (on NIMBUS)
ES	Elastic Scattering (neutrino reaction)
ESA	European Space Agency
ESP	EUV Spectro-Photometer (onboard SDO)
ETH	Eidgenössische Technische Hochschule (Zurich, Switzerland)
EUI	EUV full-Sun and high-resolution imager (on Solar Orbiter)
EULAG	Eulerian/semi-Lagrangian fluid solver (numerical code)
EUNIS	Extreme Ultraviolet Normal-Incidence Spectrograph (rocket)
EUV	Extreme ultraviolet
EUVI	Extreme-UltraViolet Imager (on SECCHI/STEREO)
EUVS	Extreme-UltraViolet Sensor (on GOES)
EVE	Extreme Ultraviolet Variability Experiment (on SDO)
FAL	Fontenla−Avrett−Loeser (atmospheric model)
FASR	Frequency-Agile Solar Radiotelescope

FBR	Fourier-Based Reconnection (algorithm)
FCS	Flat Crystal Spectrometer (on SMM)
FERMI	Hard X-ray (NASA spacecraft)
FFR	Fixed Frequency Receiver (on S-WAVES/STEREO)
FIAN	Lebedev Institute of Physics (Moscow, Russia)
FIELDS	FIELDS experiments (on Parker Solar Probe)
FIP	first ionization potential
FISS	Fast Imaging Solar Spectrograph (NST, BBSO)
FNRGF	Fourier Normalizing Radial-Graded Filter (method)
ForeCAT	Forecasting a CME's Altered Trajectory (method)
FOXSI	Focussing Optics X-ray Solar Imager (rocket)
FPP	Focal Plane Package (on Hinode)
FUV	Far Ultra Violet (on IRIS)
FWHM	Full width half maximum
GALLEX	Gallium Experiment (neutrino detector)
GBM	Gamma-Ray Burst Monitor (on FERMI)
GCS	Graduated Cylindrical Shell (model)
GEANT-4	Software for simulations of high-energy particles
GENESIS	Flare Genesis Experiment (balloon)
GLE	Ground Level Enhancement (particle events)
GN	Group Number (sunspots)
GNST	Goode New Solar Telescope (BBSO)
GOES	Geostationary Orbiting Earth Satellite (spacecraft)
GOLF	Global Oscillations at Low Frequency (on SOHO)
GONG	Global Oscillation Network Group (helioseismology)
GPS	Global Positioning System
GRANAT	Gamma Ray spacecraft (Russia)
GREGOR	GREGOR Solar Telescope (Tenerife, Spain)
GRH	Gauribidanur Radioheliograph (India)
GRIPS	Gamma-Ray Imager/Polarimeter for Solar Flares (balloon)
GSFC	Goddard Space Flight Center (NASA)
GSAT-2	Indian Geostationary Satellite
GWILL	Gradient-Weighted Inversion Line Length (magnetic field)
HAFv2	Hakamada-Akasofu-Fry version 2 (solar wind model)
HAO	High-Altitude Observatory (Mauna Loa, Hawaii)
HCS	Heliospheric Current Sheet
HD	Hydrodynamic (code)
HELICON	Solar gamma-ray detector (on CORONAS-I)
HELICON	Gamma spectrometer (on CORONAS-F)
HET	High Energy Telescope (on IMPACT/STEREO)
HFR	High Frequency Receiver (on S-WAVES/STEREO)
HI1, HI2	Heliospheric Imager 1 and 2 (on SECCHI/STEREO)
Hi-C	High-Resolution Coronal Imager (rocket)

HIREGS	High Resolution Gamma-Ray and Hard X-Ray Spectrometer (balloon)
HMF	Heliospheric Magnetic Field
HMI	Helioseismic and Magnetic Imager (on SDO)
HSS	Heidke Skill Score (statistical method)
HXRBS	Hard X-Ray Burst Spectrometer (on SMM)
HXRS	Hard X-Ray Spectrometer (onboard MTI)
HXT	Hard X-ray Telescope (on Yohkoh)
HYDRAD	Hydrodynamic Radiative (code)
IBIS	Interferometric Bidimensional Spectrometer (instrument at DST)
ICME	Interplanetary Coronal Mass Ejection
IDL	Interactive Data Language (software used by most solar physicists)
IMAX	Imaging Vector Polarimeter (on Sunrise)
IMF	Interplanetary Magnetic Field
IMP-7,8	Interplanetary Monitoring Platform (spacecraft)
IMPACT	In-situ Measurments of PArticles and CME Transients (on STEREO)
INTEGRAL	INTErnational Gamma-Ray Astrophysics Laboratory (ESA spacecraft)
IPHIR	InterPlanetary Helioseismology with IRadiance observations (photometer)
IPS	Interplanetary Scintillation
IRIS	Interface Region Imaging Spectrograph (spacecraft)
IRIS	Flare Spectrometer (on CORONAS-F)
IS$\odot$IS	Integrated Science Investigation of the Sun (instrument on PSP)
ISPM	Interplanetary Shock Propagation Model
ISAS	Institute of Space and Astronautical Science (Japan)
JHU/APL	Johns Hopkins University Applied Physics Laboratory
KAW	Kinetic Alfvén Waves
keV	Kilo electron Volt
KHI	Kelvin-Helmholtz Instability
KIS	Kiepenheuer Institute for Solar Physics (Germany)
KMAS	Kislovodsk Mountain Astronomical Station
KNN	K-Nearest Neighbours (statistical method)
KONUS-RF	X-ray and Gamma-Ray Spectrometer (on CORONAS-PHOTON)
KPNO	Kitt Peak National Observatory (Arizona, USA)
KPSO	Kitt Peak Solar Obaservatory
KPVT	Kitt Peak Vacuum Telescope (Arizona, USA)
LARE2D	LAgrangian-REmap 2-D (MHD code)
LASCO	Large Angle Solar COronagraph (on SOHO)

LASP	Laboratory for Atmospheric and Space Physics, University of Colorado
LCPF	Large-Scale Coronal Propagation Fronts
LCR	Inductor Capacitor Resistor (electronic circuit)
LEDA	resistive MHD code (University of Leuven)
LET	Low Energy Telescope (on IMPACT/STEREO)
LFFF	Linear Force Free Field (code)
LFR	Low Frequency Receiver (on S-WAVES/STEREO)
LMSAL	Lockheed Martin Solar and Astrophysics Laboratory
LOFAR	Low-Frequency Array (Europe)
LOWL	Low-degree solar oscillations instrument (helioseismology)
LPSP	Laboratoire de Physique Stellaire et Planetaire (on OSO-8)
LTE	Local Thermal Equilibrium
LWS	Living With a Star program
MAG	Magnetometer (on IMPACT/STEREO)
MAG	Magnetometer (on Solar Orbiter)
MAS	MHD Algorithm outside a Sphere (MHD code)
MCMC	Monte Carlo Markov Chain (data analysis method)
MDI	Michelson Doppler Imager (on SOHO)
MDI/HR	Michelson Doppler Imager High Resolution data (on SOHO)
MDI/FD	Michelson Doppler Imager Full Disk data (on SOHO)
MEDG	Magnetic Density Gradient (method)
MEGS-A, B	Multiple EUV Grating Spectrographs A and B (on EVE/SDO)
MEM	Maximum entropy method
METIS	Multi Element Telescope for Imaging and Spectroscopy (on Solar Orbiter)
MeV	Mega electron Volt
MHD	Magneto-Hydrodynamics
MHS	Magneto-Hydrostatics
MK	Mega Kelvin
MKL	Cosmic Ray Monitor (on CORONAS-F)
MLT	Mulitple-Level Tracking (algorithm)
MLSO	Mauna Loa Solar Observatory (Maui, USA)
MMF	Moving Magnetic Features
MOSES	Multi-Order Solar EUV Spectrograph (rocket)
MFI	Magnetic Field Investigation (instrument on SWE/ACE)
MPS	Moving Paricle Semi-implicit method
MSDP	Multi Channel Subtractive Double Pass (on THEMIS)
MSH	Millionth Solar Hemisphere (physical unit)
MSO	Mees Solar Observatory (Haleakala, Maui, USA)
MTR	MulTi-Raies instrument (France)

MTI	Energy Multi-Spectral Thermal Imager (Russian spacecraft)
MURAM	MPS/University of Chicago Radiative MHD (numerical code)
MWA	Murchison Widefield Array
MWO	Mount Wilson Observatory (California)
NASA	National Aeronautics and Space Administration
NATALYA-2M	High Energy Spectrometer (on CORONAS-Photon)
NAVE	Non-linear Affine Velocithy Estimator (algorithm)
NBP	Network Bright Points
NC	Neutral Current (neutrino interaction)
NFI	Narrowband Filter Imager (on Hinode)
NICOLE	Non-LTE inversion COde using the Lorien Engine (MHD code)
NIS	Normal Incidence Spectrometer (of CDS instrument on SOHO)
NJIT	New Jersey Institute of Technology (New Jersey)
NLFFF	Non-Linear Force Free Field (code)
NLTE	Non-Local Thermal Equilibrium
NOAA	National Oceanic and Atmospheric Administration
NoRH	Nobeyama Radioheliograph
NRGF	Normalizing Radial-Graded Filter (method)
NRL	Naval Research Laboratory (in Washington DC)
NRLTSI2	Naval Research Laboratory Total Solar Irradiance (database)
NRH	Nancay Radioheliograph (France)
NSO	National Solar Observatory (in USA)
NSO/KP	National Solar Observatory, Kitt Peak (USA)
NST	New Solar Telescope (BBSO)
NuSTAR	Nuclear Spectroscopic Telescope Array (spacecraft)
NUV	Near Ultra Violet (on IRIS)
NVST	New Vacuum Solar Telescope (Yunnan Observatories, China)
OSO	Orbiting Solar Observatory (spacecraft)
OVRO	Owens Valley Radio Observatory (California)
OVSA	Owens Valley Solar Array (California)
pB	Polarized Brightness (white-light image)
PCSA	Pulkovo's Catalog of Solar Activity
PDF	Probability (Density) Distribution Function
PENGUIN-M	Hard X-Ray Polarimeter-Spectrometer (on CORONAS-PHOTON)
PFSS	Potential Field Source Surface (magnetic field model)
PHI	Polarimetric and Helioseismic Imager (instrument on Solar Orbiter)

PHOKA	Multi-Channel Ultraviolet Monitor (on CORONAS-PHOTON)
PIL	Polarity Inversion Line (magnetic field)
PLASTIC	PLAsma and SupraThermal Ion Composition (on STEREO)
PMTRAS	Photo-Multiplier Tube Roll Angle System (on RHESSI)
PR-N	X-ray polarimeter (on CORONAS-F)
PROBA2	PRoject for OnBoard Autonomy 2 (spacecraft)
PRW	Radio and Plasma Wave Analyser (instrument on Solar Orbiter)
PSP	Parker Solar Probe mission
QPO	Quasi-Periodic Oscillations
QPP	Quasi-Periodic Pulsations
QSL	Quasi-Separatrix Layer (magnetic field)
RADYN	Flare radiation hydrodynamics (code)
RAS	Roll Angle System (on RHESSI)
RATAN-600	Special Astrophysical Observatory (Russia)
RES	X-ray Spectroheliograph (on CORONAS-F)
RESIK	X-ray Spectrometer (on CORONAS-F)
RES-K	Solar X-ray spectrograph (on CORONAS-I)
RF15	Solar Photometer and imager (on Interball)
RHESSI	Reuven Ramaty High Energy Solar Spectroscopic Imager (spacecraft)
RGO	Royal Greenwich Observatory
RHD	Radiative HydroDynamic (code)
RMHD	Radiation Magneto-Hydrodynamic (model)
RMHS	Radiative-Magnetohydrostatic (model)
ROSA	Rapid Oscillations in the Solar Atmosphere (at DST)
ROUGH	Random, Observationally motivated, Unphysical, Granulation-based Heliosphysics (MHD code)
RPS	X-Ray Spectrometer (on CORONAS-F)
RT-2	Roentgen Telescope 2 (CORONAS-PHOTON)
RT-2/CZT	Coded Aperture Mask and Fresnel Zone Plates (on CORONAS-PHOTON)
RTV	Rosner−Tucker−Vaiana (coronal loop model)
SAGE	Soviet-American Gallium Experiment (gallium detector)
SAS	Solar Aspect System (on RHESSI)
SATIRE	Spectral And Total Irradiance REconstructions (method)
SBRS	Solar Broadband Radio Spectrometer (China)
SDO	Solar Dynamics Observatory (spacecraft)
SDS	Solar Diameter Sextant experiment
SECCHI	Sun Earth Connection Coronal and Heliospheric Investigation (on STEREO)

SEM	Solar EUV Monotor (of CELIAS instrument on SOHO)
SECIS	Solar Eclipse Coronal Eclipse Imaging System
SEE	Solar EUV Experiment (onboard TIMED)
SEEDS	Solar Eruptive Event Detection System (method)
SEP	Solar Energetic Particle
SEPT	Solar Elecftron Proton Telescope (on IMPACT/STEREO)
SERTS	Solar EUV Research Telescope and Spectrograph (rocket)
SFO	San Fernando Observatory
SG	SpectroGraph (on IRIS)
SIT	Suprathermal-Ion Telescope (on IMPACT/STEREO)
SIM	Spectral Irradiance Monitor (on SORCE)
SIP-CESE	Solar InterPlanetary Conservation Element / Solution Element (MHD code)
SILSO	Sunspot Index and Long-term Solar Observations (database)
SJI	Slit Jaw Image (on IRIS)
SKI	Spectrometer of Energy and Ion Chemical Composition (on CORONAS-F)
SLIPCAT	Solar Limb Prominence Catcher (algorithm)
SM-8M	Magnetometer (on CORONAS-PHOTON)
SME	Solar Mesospheric Explorer (satellite)
SMEI	Solar Mass Ejection Imager (spacecraft)
SMEX	SMall EXplorer mission (NASA mission category)
SKL	Solar Cosmic Rays Complex (on CORONAS-F)
SMART	Solar Magnetic Activity Research Telescope (Hida Observatory)
SMM	Solar Maximum Mission (spacecraft)
SNO	Sudbury Neutrino Observatory
SNU	Solar Neutrino Units
SO	Self-Organization system
SOC	Self-Organized Criticality (nonlinear system)
SOHO	Solar and Heliospheric Observatory (spacecraft)
SOKOL	Global Solar Oscillation Experiment (on CORONAS-PHOTON)
SOLIS	Synoptic Optical Long-Term Investigations of the Sun (KPNO)
SoloHI	Solar Orbiter Heliospheric Imager
SOLSTICE	Solar Stellar Irradiance Comparison Experiment (on SORCE)
SONG	Solar Neutron and Gamma Ray Spectrometer (on CORONAS-F)
SOON	Solar Observing Opticl Network (instrument)
SORCE	Solar Radiation and Climate Experiment (spacecraft)

SOT	Solar Optical Telescope (on Hinode)
SOT/NFI	Solar Optical Telescope Narrowband Filter Imager (on Hinode)
SOUP/SST	Solar Optical Universal Polarimeter (instrument on SST)
SOXS	Solar X-Ray Spectrometer (on GSAT-2)
SP	Spectro-Polarimeter (on Hinode)
SP/MSO	Solar Polarimeter at MSO
SPHINX	Soft X-Ray Spectro-Photometer (on CORONAS-PHOTON)
SPICE	Spectral Imager (on Solar Orbiter)
SPIRIT	Full Sun XUV spectroscopy (on CORONAS-F)
SPINOR	Spectro-Polarimeter for Infrared and Optical Regions (DST)
SPP	Solar Probe Plus mission (renamed to PSP)
SPR	Solar Spectropolarimeter (on CORONAS-F)
SPR	Solar Particle Release time
SRBL	Solar Radio Burst Locator (California)
SRT	Solar X-Ray Telescope (on CORONAS-F)
SSRT	Siberian Solar Radio Telescope (Irkutsk)
SN	Sunspot Number
SSI	Solar Spectrtal Irradiance
SSN	Smoothed Sunspot Number
SST	Swedish 1-m Solar Telescope (La Palma, Spain)
SSW	Solar SoftWare (software package in IDL)
STE	Super Thermal Electron instrument (on IMPACT/STEREO)
STEP-F	Satellite Telescope of Electrons and Protons (on CORONAS-PHOTON)
STEREO-A, B	Solar TErrestrial RElations Observatory (spacecraft A and B)
STIX	Spectrometer Telescope for Imaging X-rays (on Solar Orbiter)
STO	Stratospheric Terahertz Observatory (balloon)
STOA	Shock Time of Arrival model (heliosphere)
SUFI	Sunrise Filter Imager (instrument on Sunrise)
SUFR	Solar UV Radiometer (on CORONAS-F)
SUMER	Solar Ultraviolet Measurements of Emitted Radiation (on SOHO)
Sunrise	UCAR balloon flight with 1-meter solar telescope (balloon)
SUVI	Soft X-ray Ultraviolet Imager (onboard GOES-R and GOES-S)
SUVR-SP-C	Ultraviolet radiometer (on CORONAS-I)

SVST	Swedish Vacuum Solar Telescope (La Palma, Canary Islands)
SWA	Solar Wind Analyser (instrument on Solar Orbiter)
SWAP	Sun Watcher using Active Pixel System detector (on PROBA2)
S-WAVES	STEREO waves experiment (on STEREO)
SWE	Solar Wind Experiment (onboard WIND spacecraft)
SWEA	Solar Wind Electron Analyzer (on IMPACT/STEREO)
SWEAP	Solar Wind Electrons Alphas and Protons (instrument on PSP)
SWEPAM	Solar Wind Electron Proton Alpha Monitor (instrument on ACE)
SWRI	South West Research Institute
SWS	Solar Wind Sector instrument (on PLASTIC/STEREO)
SVM	Support Vector Machine (statistical method)
SWMF	Space Weather Modeling Framework (MHD codes)
SWPC	Space Weather Prediction Center
SXI	Solar X-ray Imager (onboard GOES-M to GOES-P)
SXT	Soft X-ray Telescope (on Yohkoh)
TDS	Time domain sammpler (on S-WAVES/STEREO)
TEREK	Spetro-heliometer (on CORONAS-I)
TESIS	Solar Telescope/Imaging Spectrometer (on CORONAS-PHOTON)
TESOS	Fabry-Perot Interferometer (at VTT)
THEMIS	Themis Solar Telescope (France)
THEMIS	Télescope Héliographique pour l'Etude due Magnétisme et des Instabilités Solaires
TIM	Total Irradiance Monitor (on SORCE)
TIMED	Thermosphere Ionosphere Mesosphere Energetics and Dynamics (spacecraft)
TRACE	Transition Region And Coronal Explorer (spacecraft)
TSI	Total Solar Irradiance
TSS	True Skill Statistic (method)
UARS	Upper Atmosphere Research Satellite
UCAR	University Corporation for Atmospheric Research
ULA	United Launch Alliance
UTC	Coordinated Universal Time
UV	Ultraviolet
UVCS	UltraViolet Coronagraph Spectrometer (on SOHO)
VIRGO	Variability of solar IRradiance and Gravity Oscillations (on SOHO)
VAC	Versatile Advection Code (numeric code)
VAL	Vernazza−Avrett−Loeser (atmospheric model)
VAULT	Very High Angular Resolution Ultraviolet Telescope (sounding rocket)

VCA-NLFFF	Vertical Current Approximation Non-Linear Force Free Field (code)
VEX	Venus Express (spacecraft)
VFISV	Very Fast Inversion of the Stokes Vector (for HMI)
VIP	Visible Imaging Polarimeter (on TESOS at VTT)
VLA	Very Large Array (radiointerferometer, New Mexico)
VSM	Vector Spectro-Magnetograph (on SOLIS instrument)
VTT	Vacuum Tower Telescope (Sacramento Peak)
VUSS	Solar UV Radiometer (on CORONAS-F)
WAP	Wide Angle Partition Sector (on PLASTIC/STEREO)
WATCH	Wide Angle Telescope for Cosmic Hard X-Rays (onboard GRANAT)
WAVES	instrument on WIND spacecraft
WIND	(spacecraft)
WISPR	Wide-field Imager for Solar PRobe (instrument on PSP)
WKB	Wentzel-Brillouin-Kramers approximation (wave physics)
WSA	Wang-Sheeley-Arge (solar wind model)
WSO	Wilcox Solar Observatory (Stanford Unversity)
XDT	XUV Doppler Telescope (rocket)
XMM	X-Ray Multi-Mirror Newton (ESA observatory)
XPS	XUV Photometer System (on SORCE)
XRS	X-ray Sensor (instrument on GOES)
XRT	X-Ray Telescope (on Hinode)
XUV	Extreme ultraviolet
ZEUS-3D	MHD code (University Princeton)
ZIMPOL	Zürich Imaging Polarimeter

Index

M. J. Aschwanden, *New Millennium Solar Physics*, Astrophysics and Space Science Library 458, https://doi.org/10.1007/978-3-030-13956-8